AGARD-CP-551

AGARD-CP-551

AGARD

ADVISORY GROUP FOR AEROSPACE RESEARCH & DEVELOPMENT
7 RUE ANCELLE, 92200 NEUILLY-SUR-SEINE, FRANCE

DTIC
ELECTE
MAR 15 1995
B

AGARD CONFERENCE PROCEEDINGS 551

Application of Direct and Large Eddy Simulation to Transition and Turbulence

(L'application de la simulation directe et de la simulation des gros tourbillons à la transition et à la turbulence)

Papers presented and discussions recorded at the 74th Fluid Dynamics Symposium held at Chania, Crete, Greece, in April 1994.

DISTRIBUTION STATEMENT A
Approved for public release;
Distribution Unlimited

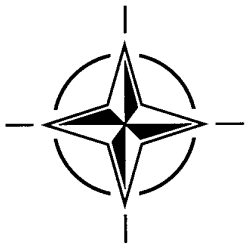

NORTH ATLANTIC TREATY ORGANIZATION

19950313 003

Published December 1994

istribution and Availability on Back Cover

AGARD-CP-551

AGARD

ADVISORY GROUP FOR AEROSPACE RESEARCH & DEVELOPMENT
7 RUE ANCELLE, 92200 NEUILLY-SUR-SEINE, FRANCE

AGARD CONFERENCE PROCEEDINGS 551

Application of Direct and Large Eddy Simulation to Transition and Turbulence

(L'application de la simulation directe et de la simulation des gros tourbillons à la transition et à la turbulence)

Papers presented and discussions recorded at the 74th Fluid Dynamics Symposium held at Chania, Crete, Greece, in April 1994.

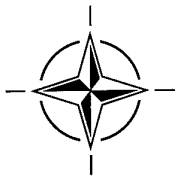

North Atlantic Treaty Organization
Organisation du traité de l'Atlantique Nord

The Mission of AGARD

According to its Charter, the mission of AGARD is to bring together the leading personalities of the NATO nations in the fields of science and technology relating to aerospace for the following purposes:

- Recommending effective ways for the member nations to use their research and development capabilities for the common benefit of the NATO community;
- Providing scientific and technical advice and assistance to the Military Committee in the field of aerospace research and development (with particular regard to its military application);
- Continuously stimulating advances in the aerospace sciences relevant to strengthening the common defence posture;
- Improving the co-operation among member nations in aerospace research and development;
- Exchange of scientific and technical information;
- Providing assistance to member nations for the purpose of increasing their scientific and technical potential;
- Rendering scientific and technical assistance, as requested, to other NATO bodies and to member nations in connection with research and development problems in the aerospace field.

The highest authority within AGARD is the National Delegates Board consisting of officially appointed senior representatives from each member nation. The mission of AGARD is carried out through the Panels which are composed of experts appointed by the National Delegates, the Consultant and Exchange Programme and the Aerospace Applications Studies Programme. The results of AGARD work are reported to the member nations and the NATO Authorities through the AGARD series of publications of which this is one.

Participation in AGARD activities is by invitation only and is normally limited to citizens of the NATO nations.

The content of this publication has been reproduced
directly from material supplied by AGARD or the authors.

Published December 1994

Copyright © AGARD 1994
All Rights Reserved

ISBN 92-836-0006-1

Printed by Canada Communication Group
45 Sacré-Cœur Blvd., Hull (Québec), Canada K1A 0S7

Recent Publications of the Fluid Dynamics Panel

AGARDOGRAPHS (AG)

Computational Aerodynamics Based on the Euler Equations
AGARD AG-325, September 1994

Scale Effects on Aircraft and Weapon Aerodynamics
AGARD AG-323, July 1994

Design and Testing of High-Performance Parachutes
AGARD AG-319, November 1991

Experimental Techniques in the Field of Low Density Aerodynamics
AGARD AG-318 (E), April 1991

Techniques Expérimentales Liées à l'Aérodynamique à Basse Densité
AGARD AG-318 (FR), April 1990

A Survey of Measurements and Measuring Techniques in Rapidly Distorted Compressible Turbulent Boundary Layers
AGARD AG-315, May 1989

Reynolds Number Effects in Transonic Flows
AGARD AG-303, December 1988

REPORTS (R)

Optimum Design Methods for Aerodynamics
AGARD R-803, Special Course Notes, November 1994

Missile Aerodynamics
AGARD R-804, Special Course Notes, May 1994

Shock-Wave/Boundary-Layer Interactions in Supersonic and Hypersonic Flows
AGARD R-792, Special Course Notes, August 1993

Unstructured Grid Methods for Advection Dominated Flows
AGARD R-787, Special Course Notes, May 1992

Skin Friction Drag Reduction
AGARD R-786, Special Course Notes, March 1992

Engineering Methods in Aerodynamic Analysis and Design of Aircraft
AGARD R-783, Special Course Notes, January 1992

Aircraft Dynamics at High Angles of Attack: Experiments and Modelling
AGARD R-776, Special Course Notes, March 1991

ADVISORY REPORTS (AR)

A Selection of Experimental Test Cases for the Validation of CFD Codes
AGARD AR-303, Vols I and II, Report of WG-14, August 1994

Quality Assessment for Wind Tunnel Testing
AGARD AR-304, Report of WG-15, July 1994

Air Intakes for High Speed Vehicles
AGARD AR-270, Report of WG13, September 1991

Appraisal of the Suitability of Turbulence Models in Flow Calculations
AGARD AR-291, Technical Status Review, July 1991

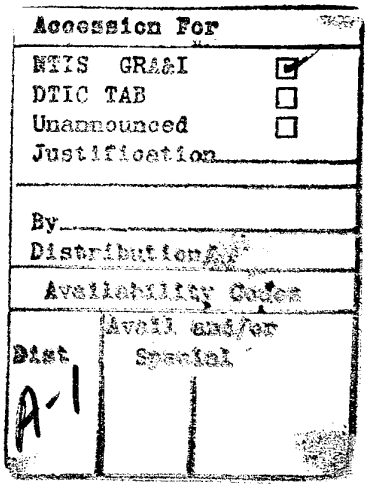

Rotary-Balance Testing for Aircraft Dynamics
AGARD AR-265, Report of WG11, December 1990

Calculation of 3D Separated Turbulent Flows in Boundary Layer Limit
AGARD AR-255, Report of WG10, May 1990

Adaptive Wind Tunnel Walls: Technology and Applications
AGARD AR-269, Report of WG12, April 1990

CONFERENCE PROCEEDINGS (CP)

Wall Interference, Support Interference and Flow Field Measurements
AGARD CP-535, July 1994

Computational and Experimental Assessment of Jets in Cross Flow
AGARD CP-534, November 1993

High-Lift System Aerodynamics
AGARD CP-515, September 1993

Theoretical and Experimental Methods in Hypersonic Flows
AGARD CP-514, April 1993

Aerodynamic Engine/Airframe Integration for High Performance Aircraft and Missiles
AGARD CP-498, September 1992

Effects of Adverse Weather on Aerodynamics
AGARD CP-496, December 1991

Manoeuvring Aerodynamics
AGARD CP-497, November 1991

Vortex Flow Aerodynamics
AGARD CP-494, July 1991

Missile Aerodynamics
AGARD CP-493, October 1990

Aerodynamics of Combat Aircraft Controls and of Ground Effects
AGARD CP-465, April 1990

Computational Methods for Aerodynamic Design (Inverse) and Optimization
AGARD CP-463, March 1990

Applications of Mesh Generation to Complex 3-D Configurations
AGARD CP-464, March 1990

Fluid Dynamics of Three-Dimensional Turbulent Shear Flows and Transition
AGARD CP-438, April 1989

Validation of Computational Fluid Dynamics
AGARD CP-437, December 1988

Aerodynamic Data Accuracy and Quality: Requirements and Capabilities in Wind Tunnel Testing
AGARD CP-429, July 1988

Aerodynamics of Hypersonic Lifting Vehicles
AGARD CP-428, November 1987

Aerodynamic and Related Hydrodynamic Studies Using Water Facilities
AGARD CP-413, June 1987

Applications of Computational Fluid Dynamics in Aeronautics
AGARD CP-412, November 1986

Foreword

During the past two decades significant progress has been made in the numerical simulation of turbulent flows. Vast improvements in speed and memory size of modern supercomputers and recent progress in simulation algorithms and parallel computation have put us on the threshold of being able to simulate flows in configurations of engineering interest. The purpose of this symposium is to disseminate the accumulated experience in this fast moving field which can be expected to play a vital role in future aeronautical developments.

The proposal to hold an AGARD Symposium on Direct and Large Eddy Simulation of Turbulence had its origins in a Technical Status Review held at Friedrichshafen, Germany April 26 1990 on the "Appraisal of the Suitability of Turbulence Models in Flow Calculations" (AGARD Advisory Report 291). This report includes contributions from a number of experts in the field and provides a useful and interesting summary of the state of the art in turbulence modeling at that time. The TSR was carried out in recognition of the fact that the proper treatment of turbulence is a crucial factor in the development of successful prediction codes and that it is of utmost importance for AGARD to stay abreast of developments in this field.

Among the contributions to the TSR is a description by Peter Bradshaw (Stanford University) of the initiation of a worldwide effort in the Collaborative Testing of Turbulence Models organized by Bradshaw, Brian Launder (UMIST) and John Lumley (Cornell). At the peak of this effort approximately 120 participants were involved from 16 countries around the world computing results for approximately 25 test cases. A unique ingredient of the CTTM project was that the test cases included low Reynolds number "experimental" data generated numerically. This represented the first attempt on a broad scale to use the results of direct numerical simulations of turbulence for the evaluation of turbulence models.

The continuing importance of the proper treatment of turbulence for accurate prediction together with the emerging importance of simulation as a tool for evaluating turbulence models formed the initial motivation for the present Symposium. Recent events have reinforced interest in the subject. The CTTM project has come to a close (a final report will appear in J. Fluids Eng.) and one of the main conclusions was that no one model, or type of model, could predict all the test cases to good engineering accuracy. The implication of this result is that for certain cases Large Eddy Simulation or Direct Numerical Simulation may be the only recourse for obtaining an accurate prediction. This is consistent with an increasing recognition by researchers that turbulent flows can be very sensitive to small details in the initial and boundary conditions. Turbulence models may not be able to reproduce this sensitivity faithfully. Since 1990, there has been significant progress in the development of improved subgrid scale models for large Eddy Simulation. As a result, LES is beginning to be applied to flows in moderately complex geometries. The Symposium contains several papers describing this progress.

The content of the Symposium includes papers on fundamental building block flows as well as flows of aeronautical interest which are difficult to predict by classical means. Among the subjects addressed in the Symposium are:

— Subgrid scale modeling (8 papers)

— Basic turbulence structure (8 papers)

— Simulation of transition, bypass transition (10 papers)

— Simulation of jets, wakes and wall bounded flows (5 papers)

— Simulation of complex flows, recirculating flows (5 papers)

The Symposium concluded with general remarks by the Technical Evaluator, Professor John Lumley of Cornell University. This was followed by a lively open discussion during which a number of the issues raised during the Symposium were considered.

The Programme Committee would like to extend thanks to Prof. Panaras, Prof. Georgantopoulos, Colonel Metochianakis and the Greek National Coordinator, Capt. Kormas as well as all the local organizers and authors for their hard work in preparing for this meeting on the lovely and historic island of Crete.

B. Cantwell, J. Jiménez and S. Lekoudis
Programme Committee Co-Chairmen

Avant-propos

Des progrès importants ont été réalisés dans le domaine de la simulation numérique des écoulements turbulents. Grâce à l'évolution fulgurante de la vitesse de calcul et de la capacité memoire des supercalculateurs modernes, ainsi que des avancées récentes dans le domaine des algorithmes de simulation et du calcul en parallèle. Il est vraisemblable que dans un avenir proche, nous pourrons simuler des écoulements autour de configurations présentant un intérêt technogénique. L'objet de ce symposium est de diffuser l'expérience acquise dans ce secteur en pleine évolution qui aura, sans doute, un rôle capital à jouer dans l'évolution de l'aéronautique.

L'idée de tenir un symposium AGARD sur la simulation directe et la simulation des gros tourbillons (LES) doit son origine à la revue de l'état de l'art (TSR) tenue à Friedrichshafen, en Allemagne, le 26 avril 1990 sur «Une appréciation de la pertinence de la modélisation de la turbulence aux calculs d'écoulement» (Rapport consultatif AGARD N° 291). Ce rapport contient des contributions d'un certain nombre d'experts dans le domaine et il constituait à cette époque un sommaire utile et intéressant de l'état de l'art de la modélisation de la turbulence. Le TSR a été réalisé en raison du fait que le traitement adéquat de la turbulence est l'un des facteurs essentiels dans l'élaboration de codes de prédiction performants et qu'il est de première importance pour l'AGARD de se tenir au courant des derniers développements dans ce domaine.

Parmi les contributions au TSR figure la description, donnée par Peter Bradshaw de l'université de Stanford, du lancement d'un projet à l'échelle mondiale d'essais coopératifs de modèles de la turbulence organisé par Bradshaw, Brian Launder d'UMIST et John Lumley de l'université de Cornell. Pendant la période d'activités la plus intensive, quelques 120 participants de 16 pays différents étaient occupés à calculer les résultats d'environ 25 cas d'essais. Le projet CTTM est unique en ce sens que les cas d'essais comprenaient des données «expérimentales» à petit nombre de Reynolds, produites numériquement. Il s'agissait de la première tentative à grande échelle de se servir des résultats de la simulation numérique directe de la turbulence pour l'évaluation de la modélisation de la turbulence.

L'importance continue du traitement adéquat de la turbulence pour permettre sa prédiction précise, ainsi que l'importance croissante de la simulation en tant qu'outil pour l'évaluation des modèles de la turbulence constituaient la motivation initiale du présent symposium. Certains développements récents ont confirmé l'intérêt témoigné pour ce sujet. Le projet CTTM est achevé (le rapport final sera publié dans J. Fluids Eng.). L'une de ses principales conclusions a été qu'il n'existe aucune modèle unique, ni type de modèle unique, capable de prédire l'ensemble de cas d'essais dans des limites de précision technogéniques acceptables. Il s'ensuit que dans certains cas d'espèce, il se pourrait que la simulation de gros tourbillons ou la simulation directe numérique soit le seul recours pour obtenir une prédiction précise. Ceci s'accorde avec la reconnaissance de plus en plus fréquente de la part des chercheurs du fait que les écoulements turbulents peuvent être sensibles à de très petites variations des conditions initiales et de couche limite. Il se peut que les modèles de la turbulence ne puissent pas reproduire cette sensibilité de façon exacte.

Depuis 1990, des progrès considérables ont été réalisés dans le développement de modèles à l'échelle des sous-maillages améliorés pour la simulation de gros tourbillons (LES). Par conséquent, LES commence à trouver des applications pour les écoulements autour de géométries moyennement complexes. Le symposium présente plusieurs communications qui décrivent ces progrès.

Le symposium comprend des communications sur les écoulements de base, ainsi que sur les écoulements d'intérêt aéronautique, qui sont diffiçiles à prédire à l'aide des moyens classiques. Parmi les sujets examinés lors du symposium on distingue:

— la modélisation à l'échelle des sous-maillages (8 communications)

— la structure de base de la turbulence (8 communications)

— la simulation de la transition, la transition bipasse (10 communications)

— la simulation de jets, de sillages et d'écoulements pariétaux (5 communications)

— la simulation d'écoulements complexes, d'écoulements de retour (5 communications)

Le symposium s'est conclu par des remarques d'ordre général exprimées par l'évaluateur technique, le Professeur John Lumley de l'université de Cornell. Ces remarques ont été suivies d'une discussion générale animée, lors de laquelle un certain nombre de questions soulevées lors du symposium ont été considérées.

Le comité du programme tient à remercier le Professeur Panaras, le Professeur Georgantopoulos, le Colonel Metochianakis et le coordonnateur local, le Capitain Kormas et son équipe, ainsi que les auteurs pour les efforts qu'ils ont bien voulu consacrer à la préparation de cette réunion qui s'est tenue sur la belle et antique île de la Crète.

B. Cantwell, J. Jiménez et S. Lekoudis
Co-Présidents du Comité du Programme

FLUID DYNAMICS PANEL

Chairman: M. C. DUJARRIC
ASE-Programme HERMES
Bâtiment Copernic
18 Avenue Edouard Belin
31055 Toulouse Cedex - France

Deputy Chairman: Professor Dr. C. CIRAY
Aeronautical Eng. Department
Middle East Technical Univ.
Inonu Bulvari PK: 06531
Ankara - Turkey

PROGRAMME COMMITTEE

Prof. B. CANTWELL (Co-Chairman)
Dept. of Aeronautics & Astronautics
Stanford University
Stanford, CA 94305 - USA

Prof. J. JIMENEZ (Co-Chairman)
Dept. de Mecanica de Fluidos
Escuela Tecnica Superior de
Ingenieros Aeronauticos
Plaza del Cardenal Cisneros 3
28040 Madrid - Spain

Dr. S. LEKOUDIS (Co-Chairman)
Director (Acting) Mechanics Div.
Code 332
Office of Naval Research
Arlington, VA 22217-5660 - USA

Prof. H. DECONINCK
Von Karman Institute for Fluid Dynamics
Chaussée de Waterloo 72
1640 Rhode-Saint-Génèse - Belgium

Prof. R.J. KIND
Dept. of Mechanical & Aerospace Eng.
Carleton University
Ottawa, Ontario K1S 5B6 - Canada

Prof. A. BONNET
Ecole Nationale Supérieure de
l'Aéronautique et de l'Espace
10 Avenue Edouard Belin - BP 4032
31055 Toulouse Cedex - France

Dr. B. WAGNER
Dornier Lufthahrt GmbH
Abteilung Aerodynamik
D-88039 Friedrichshafen - Germany

Dr. G. SIDERIDIS
Aristotle University of Thessaloniki
Department of Chemical Engineering
University Box 453
Thessaloniki 54006 - Greece

Prof. G.A. GEORGANTOPOULOS
Laboratory of Aerodynamics
Hellenic Air Force Academy
52 G Kolokotroni Street
11741 Athens - Greece

Prof. C. GOLIA
Centro Italiano Ricerche Aerospaziali
Via Maiorise
81043 Capua (CE) - Italy

Prof. Dr. Ir. J.L. van INGEN
Dept. of Aerospace Eng.
Delft University of Technology
Kluyverweg 1
2629 HS Delft - Netherlands

Prof. Dr. T. YTREHUS
Division of Applied Mechanics
The University of Trondheim
The Norwegian Institute of Technology
N-7034 Trondheim - NTH - Norway

Prof. A.F. de O. FALCAO
Depart. Engenharia Mecanica
Instituto Superior Tecnico
1096 Lisboa Codex - Portugal

Dr. U. KAYNAK
TUSAS
Havacilik ve Uzay San A.S.
P.K. 18 Kavaklidere 06690
Ankara - Turkey

Prof. D.I.A. POLL
Dept. of Eng. (Aeronautical)
Simon Building
University of Manchester
Oxford Road
Manchester M13 9PL - UK

PANEL EXECUTIVE

Mr. J.K. MOLLOY

Mail from Europe
AGARD-OTAN
Attn: FDP Executive
7 rue Ancelle
92200 Neuilly-sur-Seine
France

Mail from USA and Canada
AGARD-NATO
Attn: FDP Executive
Unit 21551
APO AE 09777

Contents

	Page
Recent Publications of the Fluid Dynamics Panel	iii
Foreword	v
Avant-propos	vi
Fluid Dynamics Panel	vii
Technical Evaluation Report **by J. Lumley**	T
SESSION I — SUBGRID SCALE MODELING I **Chairman: A.G. PANARAS**	
Developments and Applications of Dynamic Models for Large Eddy Simulation of Complex Flows (Invited) by P. Moin, D. Carati, T. Lund, S. Ghosal and K. Akselvoll	1
Subgrid Scale Models in Finite Difference Simulations of Complex Wall Bounded Flows by E. Balaras and C. Benocci	2
Large Eddy Simulation of Rotating Channel Flows Using a Localized Dynamic Model by U. Piomelli and J. Liu	3
The Asymptotic State of Rotating Homogeneous Turbulence at High Reynolds Numbers by K.D. Squires, J.R. Chasnov, N.M. Mansour and C. Cambon	4
Comparison of DNS and LES of Transitional and Turbulent Compressible Flow: Flat Plate and Mixing Layer by B. Geurts, B. Vreman and H. Kuerten	5
SESSION II — RECIRCULATING FLOWS **Chairman: B. WAGNER**	
Direct Numerical Simulation of Turbulent Flow in a Sudden Pipe Expansion by C. Wagner and R. Friedrich	6
Simulation d'Ecoulements Décollés by B. Troff, T.H. Lê, P. Sagaut and T.P. Loc	7
Large Eddy Simulation of Turbulent Flows Over a Cavity by J.C.F. Pereira and J.M.M. Sousa	8
Large-Eddy Simulation of Separated Flow in a Ribbed Duct by H. Braun, M. Fiebig and N.K. Mitra	9

SESSION III — TURBULENCE STRUCTURE I
Chairman: H. DECONINCK

Analysis of Subgrid Models Using Direct and Large-Eddy Simulations of Isotropic Turbulence 10
by S. Menon and P.K. Yeung

A Cheap DNS Tool for Turbulence Models Testing 11
by A. Baron and M. Quadrio

Direct Simulation of Turbulent Flow in a Square Duct: Reynolds-Stress Budgets 12
by A. Huser, S. Biringen and F.F. Hatay

SESSION IV — TRANSITION I
Chairman: D.I.A. POLL

Numerical Simulation of Supersonic Boundary Layer Transition (Invited) 13
by Y. Guo, N.A. Adams, N.D. Sandham and L. Kleiser

Simulation des Grandes Echelles d'Ecoulements Transitionnels 14
by P. Comte, F. Ducros, J. Silvestrini, E. David,
E. Lamballais, O. Métais and M. Lesieur

SESSION V — SUBGRID SCALE MODELING II
Chairman: J. JIMENEZ

Large Eddy Simulation of Channel Flow Using a Vorticity Transport Subgrid Model 15
by A.L. Rovelstad, R.A. Handler, P.S. Bernard and J.M. Thomas

Modeling Anisotropy and Backscatter Effects in the Subgrid Scale Stress Tensor 16
by T. Goutorbe and D. Laurence

Simulation of Pipe Flow 17
by Y. Zhang, A. Gandi, A.G. Tomboulides and S.A. Orszag

SESSION VI — TRANSITION II
Chairman: J.L. van INGEN

Simulations of Bypass Transition for Spatially Evolving Disturbances 18
by A. Lundbladh, P.J. Schmid, S. Berlin and D.S. Henningson

Direct Numerical Determination of the Minimum Bypass Reynolds Number in Boundary Layers 19
by R. Corral and J. Jiménez

SESSION VII — TURBULENCE STRUCTURE II
Chairman: S. LEKOUDIS

A Flamelet Model for Turbulent Unpremixed Combustion (Invited) 20
by V.R. Kuznetsov

Direct Numerical Simulation for Premixed Turbulent Combustion Modeling 21
by R.S. Cant

Entrainment in a Shear-Free Turbulent Mixing Layer 22
by D.A. Briggs, J.H. Ferziger, J.R. Koseff and S.G. Monismith

SESSION VIII — WAKES, JETS AND VORTICES
Chairman: R.J. KIND

Direct Simulation of a Self-Similar Plane Wake 23
by R.D. Moser and M.M. Rogers

The Effect of Initial Conditions on the Development of Temporally Evolving Planar Three-Dimensional Incompressible Wakes 24
by R. Sondergaard, N.N. Mansour and B.J. Cantwell

Simulation Directe du Sillage Tridimensionnel du Profil NACA0012 25
by J. Dušek and Ph. Fraunié

Numerical Simulation of Spatially-Developing Planar Jets 26
by G. Hoffmann and C. Benocci

Rib Vortices in Round Jets: Direct and Large Eddy Simulation 27
by M. Factica, R. Verzicco and P. Orlandi

Direct Numerical Simulation of Transition to Turbulence From a High-Symmetry Initial Condition 28
by O.N. Boratav and R.B. Pelz

SESSION IX — TRANSITION III
Chairman: W.S. SARIC

Direct Numerical Simulations of Leading-Edge Receptivity to Freestream Sound 29
by D.A. Fuciarelli and H.L. Reed

Numerical Study of Realistic Perturbations in Three-Dimensional Boundary Layers 30
by P.R. Spalart, J.D. Crouch and L.L. Ng

On Subcritical Instability of the Attachment Line Boundary Layer 31
by V. Theofilis

Spatial Direct Numerical Simulation of Boundary Layer Transition Under Strong Adverse Pressure Gradient 32
by H. Bestek, M. Kloker and W. Müller

Navier-Stokes Simulations of the Effects of Suction Holes on a Flat Plate Boundary Layer 33
by H.L. Meitz and H.L. Fasel

Direct Numerical Simulation of 2-D and 3-D Instability Waves in a Laminar Separation Bubble 34
by U. Rist and U. Maucher

SESSION X — NUMERICAL METHODS
Chairman: G. GEORGANTOPOULOS

Investigation of Shear Layer Transition Using Various Turbulence Models 35
by J.K. Kaldellis and G.A. Georgantopoulos

DNS of Turbulent Flow in a Driven Cavity and their Analysis Using Proper Orthogonal Decomposition 36
by W. Cazemier, R.W.C.P. Verstappen and A.E.P. Veldman

Direct Simulation and Graphics Post-Processing of Three-Dimensional Turbulent Flows 37
by J. Ryan, P. Leoncini, U. Berrino and B. Troff

GENERAL DISCUSSION GD

Technical Evaluation Report[1]

John L. Lumley
Sibley School of Mechanical and Aerospace Engineering
Cornell University
Ithaca, NY 14853
USA

ABSTRACT

The subject Symposium, "Application of Direct and Large Eddy Simulation to Transition and Turbulence", sponsored by the Fluid Dynamics Panel of AGARD, took place in Chania, Crete (Greece) 18-21 April 1994. The objectives of the Symposium, which consisted of ten sessions, including 36 papers, were to report and assess advances within the AGARD community in Direct Numerical Simulation (DNS) and Large Eddy Simulation (LES) of transitional and turbulent flows.

INTRODUCTION

The role of technical evaluator is an unusual one. After all, when the Metropolitan Opera mounts a new production of Faust, it does not usually invite the critic from the New York Times to come to the stage after the final curtain, and share with the audience his perception of the positive and negative aspects of the performance. I am happy, however, to have an opportunity to play this part relative to this symposium.

There are many positive aspects to this symposium, and the organizing committee is to be commended in particular for putting together an interesting meeting, with many countries and points of view represented, and a number of excellent papers.

I would like to open the substantive part of my discussion with some general comments about the field of computational fluid dynamics. What should we expect from a simulation of a turbulent or transitional flow; what should be its position among the other various types of papers, experimental and theoretical? It is natural to compare Direct Numerical Simulation (DNS) and Large Eddy Simulation (LES) with experiments. They are, in effect, numerical experiments. Experiments, on the one hand, and DNS and LES on the other, have specific positive and negative attributes that make one or the other suitable tools in particular circumstances; there are clearly some circumstances in which DNS and LES should replace laboratory experiments. DNS and LES are also of differing maturity - DNS is more or less mature, while LES is still under development. The concept of the minimal flow unit in DNS, introduced by Moin and Jimenez only three years ago, is essentially mature. Spectral element methods are still under development. For that reason, the kind of paper we should expect from each sub-field should be different. However, certain general principles apply to all, whether experiments, DNS or LES.

With few exceptions, the best experiments and simulations are constructed around a theoretical inquiry, to explore a concept, or a mechanism, or an unfamiliar effect. There is also another kind of experiment, the archival data collection experiment, which is designed to explore a flow in great depth to provide a data set which can be used subsequently by others, but does not have a particular fluid mechanical point to make. Important as these are, the number needed is relative small. Many DNS and LES papers look a little too much like the archival data collection experiments, with relatively little fluid mechanical point to make.

There are certainly many experiments and simulations that are neither one nor the other; they are not of archival quality, nor do they have a clear underlying conceptual / theoretical structure. We might wish that experimentalists and computors who found themselves in this kind of trouble had joined forces with a theoretician to help in the planning of the experiment or calculation and the interpretation of the results.

Experimental fluid mechanics sometimes suffers from another syndrome - the unending development of instrumentation. It is, of course, desirable to develop new instrumentation, but the development should come to an end, and the instrumentation should be used in an experiment with fluid mechanical motivation. An example is the development of laser diagnostics in combustion, which for many years produced more and more elaborate diagnostic systems without contributing much to the understanding of the physics of the flow. It is undeniable that some aspects of DNS and LES are still under development, and it is certainly

[1] Supported in part by Contract No. F49620-92-J-0287 jointly funded by the U. S. Air Force Office of Scientific Research (Control and Aerospace Programs), and the U. S. Office of Naval Research, in part by Grant No. F49620-92-J-0038, funded by the U. S. Air Force Office of Scientific Research (Aerospace Program), and in part by the Physical Oceanography Programs of the U. S. National Science Foundation (Contract No. OCE-901 7882) and the U. S. Office of Naval Research. (Grant No. N00014-92-J-1547).

legitimate to give greater emphasis to the developmental aspect in a paper, but not to the exclusion of the fluid mechanical point.

Of course, it is normal in an experimental paper to discuss the experimental setup, the instrumentation, the data reduction, etc. In DNS or LES it is legitimate to discuss algorithms, outflow conditions, and so forth, particularly if a new twist has been added. However, the emphasis should still be on the fluid mechanics.

To summarize: the best DNS and LES should be devised to illuminate a fluid mechanical concept or explain a difficulty or explore a phenomenon. It is not enough to reproduce an experiment, or simply to present a flow without analysis, as if to say "here it is - take it or leave it". To avoid misunderstanding, I should emphasize that there are numerous groups that for many years have consistently produced simulation papers that more than meet the criteria I have outlined. There are a number of such papers at this meeting, and I will mention them explicitly.

It should not be necessary to point out that a paper at a meeting like this should be something new, or a new application of an existing idea. Material that is in the literature should be given proper attribution, and briefly summarized. If the author doesn't have enough new material to make a paper, he probably should not come to the meeting. Several of the papers at this meeting were largely re-doing of things that have been in the literature for one or more decades. Exploring one of these classic ideas may be a voyage of discovery for you, but that does not make it suitable for a paper.

By rather arbitrary criteria I have identified roughly half of the papers at this meeting as having a fluid mechanical focus, while the other half are focused on development of a method, including validation of a computation against experiment. One might expect the LES papers to emphasize development, since LES is a less well-developed subject, while the DNS papers, from a more mature area, might be expected to emphasize fluid mechanics. In fact, by my count, a third of the DNS papers I have classified as developmental, while 20% of the LES papers seem to me to emphasize fluid mechanics.

Of the 36 papers, I would rate fifteen of them very good - containing new material, illuminated by theoretical insight, and well presented; I would rate nine as weak and derivative, containing much old material, displaying little or no theoretical insight; the remaining twelve lie in between, of good quality, but not exceptional. The proportions of very good / good / weak are 42% / 33% / 25%. In this respect, this meeting is not markedly different from many other meetings. The precise ratings could be quibbled with, and papers on the borders between categories might be reclassified; however, I do not believe it would change the percentages very much.

COMMENTS ON SPECIFIC TALKS

I would like to mention just a few papers that I thought were particularly interesting.

Moin's talk (1. Moin, P., Application of Dynamic Localization Model for Large Eddy Simulation of Complex Flows) I found particularly clear and useful. Toward the end of the talk, Moin mentioned that the group at CTR were considering adding dependence of the sub-grid-scale stresses on rotation and on non-linear terms in the strain rate of the resolved scales. This, of course, was the historical path followed by continuum mechanics, and may be the right choice. My group has been toying with another idea from continuum mechanics: adding a history dependence, so that the present sub-grid-scale stress is dependent on a weighted average of the strain rate experienced by the material neighborhood over its past. This would require carrying a differential equation for the sub-grid-scale stresses.

The excellent talk delivered by Kleiser (13. Kleiser, L., Adams, N.A., Sandham, N. D. and Guo, Y., Numerical Simulation of Supersonic Boundary Layer Transition) particularly impressed me by his code validation procedures. Essentially, he dropped the non-linear terms from his code, and compared his results with linear stability theory, obtaining very satisfactory agreement, as a preliminary to doing the simulation. Code validation like this was not discussed frequently at this meeting, and of course, it is essential to instill confidence in the code.

In the paper delivered by Comte (Comte, P., Lesieur, M., Metais, O., Ducros, F., David, E., Silvestrini, J., and Prestemon, S., Large Eddy simulation of Transitioning Shear Flows)), while I have heard some question raised as to whether the structure function technique is truly different from the more traditional Smagorinsky technique, I thought the *selective application* of the structure function technique was a new idea, which seemed to produce convincing results.

The paper delivered by Goutorbe (17. Goutorbe, T. & Laurence, D., Modelling Anisotropy and Backscatter Effects in the Subgridscale Stress Tensor) I thought had an interesting technique and showed very nice results. However, I could not help wondering why the authors did not relate the normalized deviatoric part of the sub grid scale stresses and the normalized deviatoric part of the resolved stresses by the square root of the Reynolds number? ${}^{d}\tau_{ij} \propto R_e^{-1/2}\, {}^{d}R_{ij}{}^{rs}$. This is similar to the argument that I present to my turbulence class, (and that is contained in chapter three of Tennekes, H. & Lumley, J. L., *A First Course in Turbulence*); namely, that the anisotropy of the small scales

should be less than the anisotropy of the large scales, by the ratio of the time scales.

The paper presented by Orszag (18. Zhang, Y., Gandhi, A., Tomboulides, A. G. & Orszag, S. A., Direct and Large Eddy Simulations of Pipe Flow) was very interesting. My former boss, George Wislicenus, would have been very pleased to know that the superpipe experiment will take place. For several years during the early sixties he tried unsuccessfully to get support for a superpipe experiment in the penstock of Grand Coulee Dam, with the same goal. Regarding Orszag's suggestion of Very Large Eddy Simulation (VLES) - that is, doing unsteady, non-symmetric calculations with turbulence models, second order or otherwise - it seems to me that this is essentially unconnected with the Renormalization Group Expansion; it can be done with any turbulence model, no matter how it might have been derived. The use of this technique is quite old in the meteorological community, and dates at least from Deardorff's work in 1973 (Deardorff, J. W. 1973. The use of subgrid transport equations in a three-dimensional model of atmospheric turbulence. *J. Fluids Engineering* 95(3):429-438). I have been pushing this idea for several years, and in fact, I thought I had invented the term VLES about 1992; however, I am afraid we must both defer to Bill Reynolds (Reynolds, W. C. 1990. The potential and limitations of direct and large eddy simulations. In *Whither Turbulence? Turbulence at the Crossroads.* Ed. J. L. Lumley. pp. 313-343. Berlin etc.: Springer.) I am sure the idea is correct: only the very largest scales are resolved, and the sub-grid-scale model is correspondingly elaborate, but the constants, of course, must be different from those used in a model intended to produce a steady flow, since they do not include the transport of the large scale unsteadiness, as Orszag pointed out.

The very delicate and complex physical reasoning at the beginning of Orszag's talk, which was reminiscent of Onsager and Corrsin, was too complex to be evaluated without considerable work, but looked interesting.

The two papers on bypass transition, (20. Lundbladh, A., Schmidt, P., Berlin, S., & Henningson, D. Simulations of bypass transition for spatially Evolving Disturbances; 21. Corral, R., & Jimenez, J. Direct Numerical Estimation of the Bypass Transition Reynolds Number for a Flat Plate) both had good physics. I particularly liked the discussion in 20. of the causal relations between the oblique waves, the streamwise vortices, the wall-normal vorticity and the ultimate breakdown. In 21. I thought the use of suction to keep the layer from growing (I understand an idea of P. Spalart), and of reverse transition, were both clever.

I hope that Kuznetsov (22. Kuznetsov, V. R. Flamelet Model for Turbulent Unpremixed Combustion) will forgive me for saying that his beautiful, simple, clever analysis shows what one can do if access to computation is limited. I have thought for a long time that we in the west have been severely hampered by having too much computer time available, and therefore not being required to think as much about the physics.

I found numbers 25 and 26 (25. Moser, R. D., & Rogers, M. Direct Simulation of a Self-Similar Plane Wake; 26. Sondergaard, R., Mansour, N. & Cantwell, B. The Effect of Initial Conditions on Temporally Evolving Planar Incompressible Wakes) very interesting, with a great deal of good physics. This is an interesting problem, and far from resolved, I think. Since the relevant time scale is logarithmic, neither the calculations nor the experiments covers enough downstream distance or time to tell if the flow is really self-preserving, or if the artificially stimulated flow would revert eventually to a universal form, or if an instability would eventually develop. Experimental values, for example, exist in the range $500 < x/d < 1000$; to answer any questions about the ultimate state of the wake, it would be necessary to examine it at $x/d = 5000$ and perhaps 50,000. I would like to explore the idea of a DNS in stretched coordinates, in which the mean velocity grows as $t^{1/2}$, and the length scales shrink as $t^{-1/2}$, that would perhaps allow us to follow the flow much longer. Such a wake would not appear to grow laterally, and would have an unchanging time scale, although there would, of course be computational difficulties associated with the ever increasing mean velocity, and the shrinking grid.

I will consider together the several excellent presentations on boundary layer instability and transition, particularly those of Spalart, Bestek and Fasel (32. Spalart, P., Crouch, J. D., & Ng, L. L. Numerical Study of Realistic Perturbations in Three-Dimensional Boundary Layers.; 34. Bestek, H., Kloker, M. & Muller, W. Spatial Direct Numerical Simulation of Boundary Layer Transition Under Strong Adverse Pressure Gradient; 35. Fasel, H. Numerical Simulation of the effect of Suction Holes on Transition in a Turbulent Boundary Layer). This is a very complicated area, and certainly not my specialty. However, it is difficult to escape the impression of natural history - that is, what I sometimes call butterfly collecting. It seems to me that this material cries out for a better physical/theoretical framework, beyond the linear, or weakly non-linear, stability theory. Recently we have been having a great deal of success with the application of dynamical systems theory to the construction of low-dimensional models of the turbulent boundary layer. This should work even better on the transitional boundary layer, where there are fewer active modes - it should help make clear some of the mechanisms. What is being done now are numerical experiments, which is excellent, but to determine <u>significance</u>, you need dynamical models. I am delighted to be able to point to two papers by Rempfer and Fasel which have just

appeared, and will shortly appear, respectively, which in fact follow this road. (Rempfer, D., & Fasel, H. 1994. Evolution of three-dimensional coherent structures in a flat-plate boundary layer. *J. F. M. 260: 351-375.* and Rempfer, D. & Fasel, H. 1994. Dynamics of three-dimensional coherent structures in a flat plate boundary layer. *J. F. M.* To appear this summer.)

I thought paper number 38 (38. Piomelli, U., & Liu, J. Large Eddy Simulation of Rotating Channel Flows using a Localized Dynamic Model) presented a simple, clever, effective idea for obtaining the value of the constant in the dynamic sub-grid-scale model. I found the simulation of the extremely intermittent state on the stable side of the channel very interesting.

Despite the question of P. Moin from the floor, suggesting that Cazemier (39. Cazemier, W., Verstappen, R. & Veldman, A. E. P. DNS of Turbulent Flow in a Driven Cavity and Their Analysis Using Proper Orthogonal Decomposition) had not established an application for his decomposition, I think Cazemier is to be commended for trying a technique a little out of the ordinary, and of great potential. There are ways of predicting eigenfunctions cheaply, without a Direct Numerical Simulation (e.g.- Poje, A. & Lumley, J. L. 1994 A model for large scale structures in turbulent shear flows, submitted to *JFM*), and these models can provide cheap surrogates for practical purposes - e.g. - to predict panel vibration or sonar self-noise or multi-path interference of signals transmitted through a heated, turbulent atmosphere in battlefield conditions. They can also provide test beds to explore mechanisms, for example that of drag reduction in the turbulent boundary layer by polymers, or by magnetic fields.

Finally, I must mention the beautiful soft-ware engineering and post-processing of the last paper (40. Ryan, J., Troff, B., Berrino, U. & Leoncini, P. Direct Simulation and Graphics Post-Processing of Three-Dimensional Turbulent Flows). I understand that fluid mechanics was not the point of this paper; nevertheless, I feel it is important that such visualization be accompanied by comparisons with theory where possible, to lend credence to the results. It is particularly true of such a delicate mechanism as vortex breakdown, that the results can look plausible and be wrong. A great deal is understood regarding vortex breakdown, and predictions are possible (see Leibovich, S. 1984. Vortex stability and breakdown: survey and extension. *AIAA J.* 22: 1192-1206.); I would have been happier to see some comparisons with theory.

ACKNOWLEDGMENTS

I would like to thank my colleagues Sidney Leibovich and Zellman Warhaft for helpful discussions.

DEVELOPMENTS AND APPLICATIONS OF DYNAMIC MODELS FOR LARGE EDDY SIMULATION OF COMPLEX FLOWS

P. Moin, D. Carati, T. Lund, S. Ghosal, K. Akselvoll

Center for Turbulence Research
Stanford University & NASA Ames Research Center
Stanford, CA 94305
USA

1. SUMMARY

The dynamic modeling procedure for large eddy simulation of turbulent flows is reviewed and recent developments in the theoretical aspects and applications are described. Methods for inclusion of backscatter of energy from small to large scale motions are presented. New formulations of the dynamic procedure are proposed which are optimized based on the subgrid scale flux vector or the energy dissipation rate instead of the subgrid scale stress tensor. Recent results from application of the model to forced isotropic turbulence with an inertial subrange, flow over a backward facing step at Reynolds number of 28000, and flow over a concave curved surface are presented.

2. INTRODUCTION

Introduction of the dynamic subgrid scale modeling procedure in 1990 has brought about a renaissance in large eddy simulation (LES). There are significant ongoing efforts devoted to its further theoretical developments and applications to challenging flow configurations. A recent review and the relevant background information is provided in[1]. This paper is largely an account of the developments since then.

The key feature of the dynamic procedure is the means to compute rather than prescribe the subgrid scale model coefficients during the computations. The model coefficients are functions of space and time which of course is an attractive feature allowing for "automatic" adjustment of the coefficients in different flow regimes and near boundaries. The model coefficients are determined using the mathematical identity[2]

$$L_{ij} = T_{ij} - \hat{\tau}_{ij} \tag{1}$$

that relates the subgrid scale stresses corresponding to two different filter widths. Here, τ_{ij} and T_{ij} are the subgrid scale stresses corresponding to the so called grid and test filters respectively, and $L_{ij} = \widehat{\overline{u}_i\overline{u}_j} - \hat{\overline{u}}_i\hat{\overline{u}}_j$. In this paper $\overline{(.)}$ indicates a grid filtered quantity and $\hat{(.)}$ is a test filtered quantity. The test filter width is usually taken to be twice the grid filter width. L_{ij} in Eq. (1) can be computed in a straight forward manner since it involves only the resolvable velocities and filtered resolvable velocities. In the simplest parameterization, τ_{ij} is modeled according to Smagorinsky's eddy viscosity closure

$$\tau_{ij} - \frac{1}{3}\delta_{ij}\tau_{kk} = -2\nu_t\overline{S}_{ij} \qquad \nu_t = C\Delta^2|\overline{S}|, \tag{2}$$

where $\overline{S}_{ij}$ is the large scale strain rate tensor,

$$\overline{S}_{ij} = \frac{1}{2}\left(\frac{\partial\overline{u}_i}{\partial x_j} + \frac{\partial\overline{u}_j}{\partial x_i}\right), \tag{3}$$

and $|\overline{S}| = |2\overline{S}_{ij}\overline{S}_{ij}|^{1/2}$. It is also assumed that the subgrid scale stresses are self-similar, that is $T_{ij} = \widehat{\overline{u}_i\overline{u}_j} - \hat{\overline{u}}_i\hat{\overline{u}}_j$ can be modeled analogously

$$T_{ij} - \frac{1}{3}\delta_{ij}T_{kk} = -2C\hat{\Delta}^2|\hat{\overline{S}}|\hat{\overline{S}}_{ij} \tag{4}$$

where, $|\hat{\overline{S}}| = |2\hat{\overline{S}}_{ij}\hat{\overline{S}}_{ij}|^{1/2}$. Germano *et al.* substituted the Eqs. (2) and (4) into Eq. (1), thereby obtaining an equation for C. The equation for C is actually a set of integral equations, but it was assumed that C was not a function of space, which led to a set of algebraic equations for C. The resulting tensorial equations were contracted with $\overline{S}_{ij}$, and C was computed from a scalar equation. Moin *et al.*[3] extended the dynamic procedure to compressible flows and scalar transport; where the latter involves dynamic evaluation of turbulent Prandtl number. Lilly[4] used a local least square technique, instead of contraction with $\overline{S}_{ij}$, to obtain C. His method amounts to a different projection of the algebraic tensor equation to obtain the scalar C. However, both models suffered from numerical instabilities in the subsequent computational experiments. The source of instability appears to be *prolonged* presence of negative C in some locations[5]. This problem has been circumvented by spatial averaging of the equation for C in directions of flow homogeneity. Later, it was shown by Ghosal, Lund & Moin[6] that, for flows with directions of homogeneity, the solutions for C obtained using this seemingly *ad hoc* averaging operation were the same as those obtained from a more rigorous variational formulation of the dynamic model. In this paper we refer to these early formulations of the dynamic model as the *algebraic formulations*.

The main inconsistency in both algebraic formulations of the dynamic model was the assumption that C did not have

Paper presented at the 74th Fluid Dynamics Symposium on "Application of Direct and Large Eddy Simulation to Transition and Turbulence" held at Chania, Crete, Greece, in April 1994.

spatial variations. However, tests of the dynamic model showed that, in fact, C varies significantly in the flow domain (probably a reflection of the inadequacy of the basic eddy viscosity parameterization). Ghosal *et al.*[6] proposed a variational formulation of the model which removes this inconsistency. Their model also imposes the constraint that C remains positive. In this formulation, called the *constrained variational formulation*, C is obtained from numerical solution of an integral equation

$$C(\mathbf{x}) = \left[\int K(\mathbf{x},\mathbf{y})C(\mathbf{y})\mathbf{dy} + f(\mathbf{x}) \right]_+ \qquad (5)$$

where, the operation denoted by the suffix '+' is defined as $x_+ = \frac{1}{2}(x + |x|)$ for any real number x, and K and f are known functions of $\alpha_{ij} = -2\hat{\Delta}^2|\widehat{\overline{S}}|\widehat{\overline{S}}_{ij}$, and $\beta_{ij} = -2\Delta^2|\overline{S}|\overline{S}_{ij}$, L_{ij} and the filter function. It was reasoned that although backscatter of energy from small scales to large scales does occur in turbulent flows, it should be modeled in a different framework. Inclusion of backscatter in subgrid scale modeling is discussed in §3 of this paper.

Applications of the algebraic formulations of the dynamic model have been remarkably successful. Correct energy decay rates and spectra were obtained in simulations of isotropic turbulence[3], and isotropic turbulence subjected to rotation[7]. The latter predictions are particularly impressive because of the well known reduction in turbulence energy transfer rate with system rotation. The dynamic procedure responded to rotation by predicting a reduction in the model coefficient. Simulations of fully developed turbulence and laminar/turbulence transition in channel flow have also been very successful[2, 8]. In the transition simulations the model coefficient is correctly activated in response to the onset of transition. Other applications include simulation of an idealized cloud-topped planetary boundary layer[9], weakly turbulent flow in a driven cavity[10], three-dimensional channel flow[11], channel flow with system rotation[12], and boundary layer with embedded streamwise vortices[13]. In general, satisfactory solutions have been obtained in all of these simulations, which have diverse turbulence physics, without any adjustments of the model parameters.

In §3 recent theoretical developments in dynamic modeling are reviewed. The results from applications of the dynamic model to flow over a backward facing step at a moderately high Reynolds number and flow over a concave wall are presented in §4. Concluding remarks are given in §5.

3. RECENT THEORETICAL DEVELOPMENTS

3.1. Backscatter

In the algebraic and constrained variational formulations the Smagorinsky coefficient C is required to be positive. This constraint appears to be dictated by numerical stability reasons much more than physical arguments. Indeed, negative values of C would correspond to a reverse transfer of energy from the unresolved scales to the large scale velocity field. This phenomenon is usually referred to as backscatter and has long been recognized as a feature of turbulent flows.

Two different approaches to modeling backscatter in LES are presented. In the first approach (*the k-equation formulation*) C is determined as in the constrained variational formulation except that C is allowed to be negative. However, the backscatter rate is limited by coupling the Navier-Stokes equations with the equation for the subgrid-scale energy (k). The backscatter rate goes to zero in a natural way when no energy is left in the subgrid scales, thus preventing unphysical instabilities. The second approach (*the stochastic backscatter formulation*) represents backscatter by a stochastic eddy forcing instead of negative eddy viscosity effects. This is motivated by the theoretical arguments that backscatter is not a deterministic function of the large scales.

3.1.1. The k-equation formulation

In this formulation, $C(\mathbf{x},t)$ is computed[6] by solving a Fredholm integral equation of the second kind

$$C(\mathbf{x}) = f(\mathbf{x}) + \int \mathcal{K}(\mathbf{x},\mathbf{y})C(\mathbf{y})d\mathbf{y} \qquad (6)$$

at each time-step, where f and $\mathcal{K}$ are as in Eq. (5) with the eddy-viscosity scaled in terms of k rather than $|\overline{S}|$. Thus, $\alpha_{ij} = -2\hat{\Delta}\sqrt{\widehat{K}}\widehat{\overline{S}}_{ij}$ and $\beta_{ij} = -2\Delta\sqrt{k}\overline{S}_{ij}$ where k is the subgrid scale kinetic energy and K is the test level subgrid kinetic energy. From the trace of Eq. (1), $K = \hat{k} + L_{ii}/2$. To close the system one now needs to use an evolution equation for k

$$\partial_t k + \overline{u}_j\partial_j k = \overline{u}_i\partial_j\tau_{ij} + Re^{-1}\nabla^2 k + \nabla\cdot(D\Delta\sqrt{k}\nabla k) - \frac{C_* k^{3/2}}{\Delta}. \qquad (7)$$

The (nonnegative) coefficients $C_*(\mathbf{x},t)$ and $D(\mathbf{x},t)$ are obtained by solving integral equations analogous to (5). It is noteworthy that here the dynamic procedure is used to compute rather than prescribe the model coefficients in the equation for k. In fact this manner of determination of C_* and D ensures correct limiting behavior near walls for the various terms in the k-equation.

This formulation of the dynamic model was used to simulate the experiment of decaying isotropic turbulence of Comte-Bellot and Corrsin[14]. In a reference frame moving downstream with the mean flow, the turbulence can be regarded as decaying in time instead of in the streamwise direction. The fluid is considered to be inside a cubical box with periodic boundary conditions. A fully dealiased pseudo-spectral method is used for the numerical simulation of the LES equations. The integral equations are solved at each time-step using an iterative scheme. The initial conditions are chosen so as to match the experimental 3D energy spectrum at the first downstream station, and the simulations are used to predict the flow at the remaining two downstream stations where the experimental data are available.

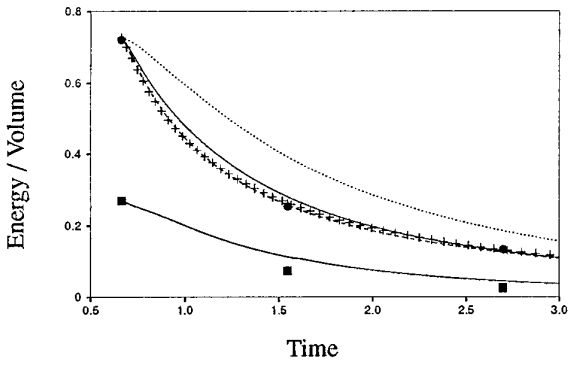

Figure 1. Decay of energy in homogeneous isotropic turbulence ——— : DLM(k)(resolved and sgs energy), +: DLM(+), - - - - : DM, ····· : no model, •: experiment (resolved) ▪ : experiment (sgs).

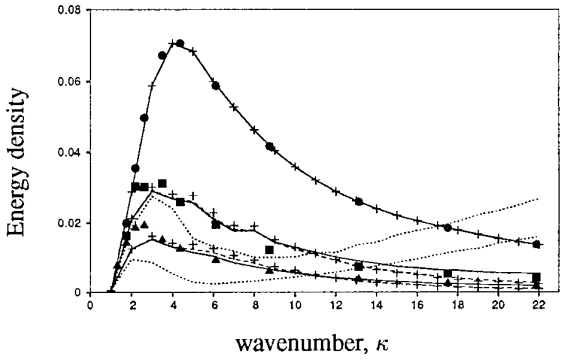

Figure 2. Time evolution of spectra in decaying homogeneous isotropic turbulence ——— : DLM(k), +: DLM(+), - - - - : DM, ····· : no model, •: experiment ($t = 0.66$) ▪ : experiment ($t = 1.55$) ▲ : experiment ($t = 2.70$).

Figures 1 and 2 show the result of a simulation performed using 48 grid points in each direction. The k-equation formulation, the constrained variational formulation and the algebraic formulation are denoted by DLM(k), DLM(+) and DM respectively. The non-dimensional time, t in Figures 1 and 2 are related to the downstream distance x in the experiment by $t = xu_*/U_0L_*$. Where $U_0 = 10$m/s is the inflow velocity and $u_* = 2.7$ m/s and $L_* = 0.55$ m are units of velocity and distance. The predicted rate of decay of the resolved energy is in good agreement with the experiment. In addition, the subgrid scale energy, k computed from the model agrees well with the experiment, even though this quantity has been computed purely from the information in the resolved scales. The dotted line is the result of running the simulation with no subgrid scale model. It is clear that the subgrid scale model can be credited with an important role in the successful prediction of the experimental result.

Figure 2 shows the energy spectrum at the three different times $t = 0.66$, $t = 1.55$ and $t = 2.70$ corresponding to the three downstream locations in the experiment. It is seen that the model predicts the spectra reasonably well. When the model is "turned off" (dotted line), the prediction is very poor with energy piling up at the high wavenumber 'tails'. In the present computations with the k-equation formulation, the CPU overhead was about 15 percent over computations without a model. The simulations were performed on a CRAY C90.

Next, a statistically steady field of homogeneous isotropic turbulence is simulated by applying a force to the smallest wavenumbers. The Reynolds number is taken to be infinite so there are no viscous terms. The number of grid points in each direction is 32. The 3D energy spectrum, $E(\kappa)$, is averaged over ten well spaced fields from a statistically steady flow. The dissipation ϵ can be computed by one of several equivalent methods which give identical results. Figure 3 shows $C_\kappa = \epsilon^{-2/3}\kappa^{5/3}E(\kappa)$ plotted against κ. It is seen that with the k-equation formulation, the spectrum is consistent with Kolmogorov's 5/3 law with a Kolmogorov constant $C_\kappa \approx 1.75$. Experimental measurements usually yield a value in the range $1.3 - 2.1$[15] though $C_\kappa \approx 1.5$ is the most commonly accepted value. The constrained variational and the algebraic formulations give a spectrum that decays somewhat faster than the 5/3 law, $E_\kappa \sim \kappa^{-m}$ where $m \approx 2.2$ instead of $5/3 \approx 1.67$.

The k-equation formulation has also been applied to turbulent channel flow where the numerical issues associated with the implementation of the k-equation with a stretched mesh were successfully addressed[16].

3.1.2. The stochastic backscatter formulation

In the k-equation formulation, backscatter is modeled through a negative eddy-viscosity. It has long been believed that the small eddies influence the large scales in the same way molecular motion affects the hydrodynamic scales of a fluid. In the kinetic theory of gases, the mean transfer of momentum is accounted for by a viscosity. Due to the large separation of scales, the fluctuations about the mean (thermal noise) are negligible. However, in turbulence, there is no clear separation of scales between the small unresolved eddies and the large eddies. Thus, the noise generated by these small eddies (the "thermal noise") is no longer negligible and is believed to be the

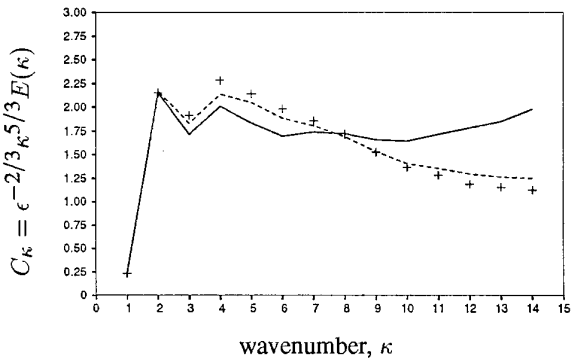

Figure 3. Prediction of Kolmogorov's 5/3 law and Kolmogorov's constant in forced homogeneous isotropic turbulence at steady state ——— : DLM(k) + : DLM(+) - - - - : DM.

source of backscatter. Therefore, it seems reasonable that backscatter should be modeled by a stochastic force.

Some subgrid scale models have been proposed that add a stochastic forcing to a purely dissipative viscous term. Chasnov[15] extensively studied the influence of this "eddy forcing" in LES of isotropic turbulence within the framework of the EDQNM approximation. The inclusion of the eddy-forcing term significantly improved the results. The influence of adding such a stochastic term to the Smagorinsky model has also been explored in the context of boundary layers[17] and plane mixing layers[18].

In the model presented here, stochastic backscatter is included in the dynamic model framework which includes local determination of all the coefficients. We model the subgrid scale force as

$$\partial_j(\tau_{ij} - \frac{1}{3}\tau_{kk}\delta_{ij}) = -2\partial_j(C_1\,\overline{\mathcal{E}}^{1/3}\,\Delta^{4/3}\overline{S}_{ij}) + \frac{C_2}{\sqrt{\Delta t}}\,\overline{\mathcal{E}}^{1/2}\,\overline{e}_i, \qquad (8)$$

where $\overline{\mathcal{E}}$ is the net energy transfer rate from the resolved to unresolved scales and Δt is the time-step. This model is very similar to the one used by Leith[18], with the important difference that we determine C_1 and C_2 dynamically. The simplest choice for $\overline{e}_i$ is a normalized (dimensionless) white noise in space and time. The net energy transfer rate $\overline{\mathcal{E}}$ can be determined as follows. The net transfer is the difference between the eddy-dissipation and the backscatter rates. Therefore,

$$\overline{\mathcal{E}} = C_1\,\overline{\mathcal{E}}^{1/3}\,\Delta^{4/3}\,|\overline{S}|^2 - \frac{1}{2}C_2^2\,\overline{\mathcal{E}} \qquad (9)$$

so that

$$\overline{\mathcal{E}} = \left(\frac{2C_1\,\Delta^{4/3}\overline{S}^2}{2+C_2^2}\right)^{3/2}. \qquad (10)$$

Since f_i enters as a force in the LES equations rather than as a stress tensor, some modification is needed in the usual dynamic procedure. This is implemented by converting Eq. (1) into a vector rather than a tensor relation by taking the divergence of each side.

3.2. Alternative minimization procedures

We have mentioned in the previous section that the stochastic backscatter formulation requires the use of the divergence of Eq. (1). Since the sgs stress itself never appears in the LES equations except as a divergence, there is no reason to search for a good model for τ_{ij}. A good description of its divergence is more appropriate. In current formulations one attempts to make an optimal choice for a single parameter C so as to "best satisfy" five scalar equations. In the divergence formulation only three scalar equations need be satisfied. It is therefore reasonable to expect that the C field in the divergence formulation would have less variability in space.

One may take the argument one step further and work at a scalar level. Indeed, it is likely that the critical feature in sgs modeling is to correctly determine the dissipation rate rather than have an accurate model for the sgs stresses. Clark *et al.*[19] have compared Smagorinsky's model and the "exact" sgs stresses computed by DNS. They found that the correlation coefficient between $2\nu_t\overline{S}_{ij}$ and τ_{ij} was as low as 0.37. However, the correlation between $2\partial_j\nu_t\overline{S}_{ij}$ and $\partial_j\tau_{ij}$ was 0.43 and between $2\overline{u}_i\partial_j\nu_t\overline{S}_{ij}$ and $\overline{u}_i\partial_j\tau_{ij}$ was 0.7. Thus, even though the Smagorinsky model is not a good model for the local subgrid scale stresses, its account of the rate of kinetic energy dissipation is reasonably accurate. Inspired by these results, one may base the dynamic procedure for determining the dimensionless coefficients in any subgrid scale model on the scalar equation obtained by multiplying the velocity with the divergence of Eq. (1) In this case, some information on the dynamic evolution of the large scale field will be lost, but it allows the model to be optimized for a good description of the energy transfer rate.

The vectorial and scalar versions of Eq. (1) are presently being investigated for the constrained variational formulation. They both lead to integro-differential equations for the coefficient C. Preliminary results in isotropic turbulence show that the probability distribution of C is not strongly altered by using the vectorial or scalar identities, but tests in complex flows are necessary to further discriminate between the various models.

4. APPLICATIONS IN COMPLEX FLOWS

The dynamic model has been highly successful in benchmark tests involving homogeneous and channel flows (*c.f.* Refs. [2, 3, 8, 11]). Having demonstrated the potential of the dynamic model in these simple flows, the overall direction of the LES effort at CTR has shifted toward an evaluation of the model in more complex situations. The general objective of these simulations is to evaluate the effectiveness of the dynamic model as an engineering tool for flows (or flow regions) where Reynolds averaged approaches have faced difficulties. The current test cases do not necessarily take place in complex geometries, but the flow fields contain complex turbulent phenomena that are very difficult to model successfully via Reynolds averaged approaches. Flows currently under investigation include a backward-facing step, wake behind a circular cylinder, airfoil at high angles of attack, separated flow in a diffuser, and boundary layer over a concave surface. Some results from the backward-facing step and concave surface boundary layer are presented below.

4.1. Backward-facing step

Large Eddy Simulations have been performed for turbulent flow over a backward facing step at Reynolds number 28000 based on the inlet free-stream velocity and step height. The flow is complex by virtue of the massive separation behind the step, the associated adverse pressure gradient and the recovery downstream of the reattachment region. The LES results are compared with experimental results of Adams *et al.*[20]. The subgrid scale model used in the calculations is the constrained variational model.

The experimental facility used by Adams *et al.* consists of a single sided expansion with a fixed upper wall. The expansion ratio is 1.25 (upstream channel width is 4 step heights). The flow upstream of the step consists of two developing boundary layers, each of thickness roughly 1.2 step-heights. A potential core exists between the boundary layers. An aspect ratio (spanwise extent/step height) of 11.4 was used in order to enhance two-dimensionality of the mean flow in the separated region.

The computational domain starts 10 step-heights upstream of the step in order to allow the flow to recover from the inflow boundary condition, and extends 20 step-heights downstream of the step. The spanwise extent of the computational domain is 3 step heights. As in the experiment, a solid wall is used at the top boundary. The inflow boundary condition consists of a mean velocity profile with superimposed random fluctuations[21]. A convective boundary condition is used at the domain exit. In the homogeneous spanwise direction periodic boundary conditions are used and no slip conditions are employed along all solid walls.

The computational mesh is uniform in the spanwise direction and stretched in both the streamwise and wall-normal directions. Wall-normal stretching of the mesh is necessary in order to be able to resolve the boundary layers. The mesh in the wall-normal direction is designed to resolve the boundary-layers upstream as well as downstream of the step. The mesh is also stretched in the streamwise direction, increasing the density of grid-points around the corner of the step. This is necessary in order to resolve sharp mean gradients in that region. Earlier simulations clearly demonstrated the need for adequate streamwise resolution at the corner of the step. The computational mesh has 244x96x96 grid points in the streamwise, wall-normal and spanwise direction, respectively. Based on the friction velocity at the inlet of the domain, the resolution (in wall units) in the streamwise direction is : $\Delta x^+_{min} = 17$ and $\Delta x^+_{max} = 273$. The minimum resolution occurs at the corner of the step. For the wall-normal direction the corresponding numbers are : $\Delta y^+_{min} = 1.8$ and $\Delta y^+_{max} = 227$. The spanwise (uniform) resolution is $\Delta z^+ = 36$. The calculation required about 70 CPU hours on a CRAY-C90. Evaluation of the subgrid scale model increases the CPU time spent per time step in the code by about 30%.

An important parameter for comparing the results of the backward facing step flows is the reattachment location. Adams *et al.* report a reattachment length of 6.7 step heights which is identical to the value calculated in the present simulation. Figure 4 shows the mean streamwise velocity profiles at three locations downstream of the step. $x/h = 4.5$ is in the recirculation region, $x/h = 7.2$ is in the reattachment region and $x/h = 12.2$ is in the recovery region. Overall good agreement between the computation and experiment is observed at all locations. The slight lag of the LES velocity profile compared with the experimental values in the recovery region is believed to be due to the blocking effect of the side-wall boundary layers in the experiment. Figure 5 shows the streamwise turbulent

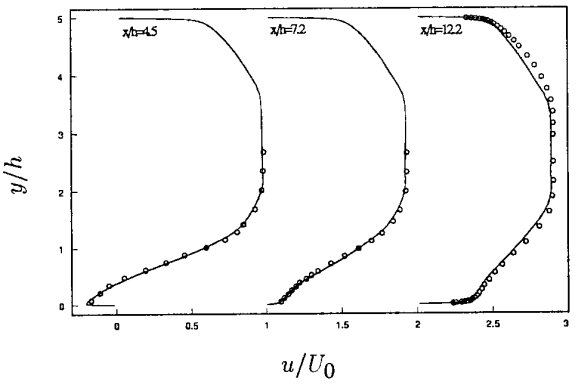

Figure 4. Mean streamwise velocity profiles downstream of the step. ——— : LES; o : experimental results of Adams *et al.* [20]

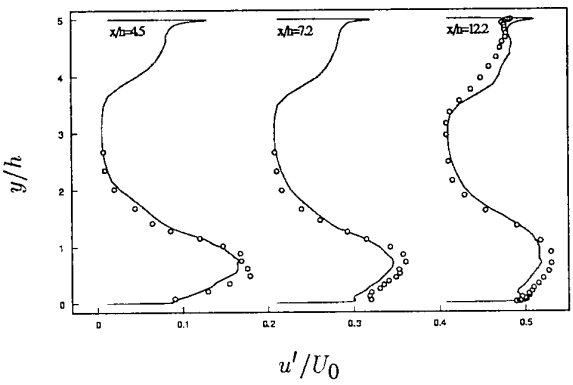

Figure 5. Streamwise turbulence intensities downstream of the step. ——— : LES; o : experimental results of Adams *et al.* [20]

intensity. As with the mean velocity profiles, the overall agreement between the experiment and computation is excellent.

4.2. Concave surface boundary layer

Large eddy simulations of a turbulent boundary layer on a concave surface at momentum thickness Reynolds number of 1300 have been performed. Although the geometry of a concave wall is not very complex, the boundary layer that develops on its surface is difficult to model due to the presence of streamwise Taylor-Görtler vortices. These vortices arise as a result of a centrifugal instability associated with the concave curvature. The vortices are of the same scale as the boundary layer thickness, alternate in sense of rotation, and are strong enough to induce significant changes in the boundary layer statistics. Owing to their streamwise orientation and alternate signs, the Taylor-Görtler vortices induce alternating bands of flow toward and away from the wall. The induced upwash and downwash motions serve as effective agents to transport streamwise momentum normal to the wall, thereby increasing the skin friction. As evidenced by the 1980 AFOSR-Stanford conference on complex turbulent flows, Reynolds averaged models perform poorly for concave curvature since the Taylor-Görtler vortices

are not resolved in these calculations. Historically the *ad hoc* corrections for the effects of curvature have been unsatisfactory.

The flow solver is a variant of the code described by Choi and Moin[22]. The incompressible Navier-Stokes equations are solved in a coordinate space where two directions are curvilinear and the third (spanwise) direction is Cartesian. Spatial derivatives are approximated with second-order finite differences on a staggered mesh. A fully-implicit second-order fractional step algorithm is used for the time advancement.

The algebraic formulation of the dynamic model is used with test filtering being restricted to the streamwise and spanwise directions. The equations for the Smagorinsky coefficient are averaged over the spanwise direction. In this simulation, the number of grid points in the spanwise direction is not large enough to ensure that the model coefficient is always positive. For this reason, the constraint is imposed that the total viscosity (eddy plus molecular) remain non-negative. In this case, the constraint binds for less than 0.01% of the points within the domain.

The LES corresponds to the water-tunnel experimental configuration of Barlow and Johnston[23] and Johnson and Johnston[24]. In the experiment, the boundary layer develops on a long flat entry section and is then subjected to a 90^o constant radius of curvature bend. In the simulation, the calculation begins approximately 10 boundary layer thicknesses upstream of the curved section and ends at the 75^o station (the boundary layer thickness measured at the onset of curvature, δ_0 is used as the normalizing length scale). Unsteady turbulent inflow data is generated in a separate simulation of a parallel-flow boundary layer. This auxiliary simulation is run in parallel with the main simulation in a time-synchronous fashion. At each time step, the velocity field is extracted from a $y-z$ plane in the inflow simulation and used as boundary data for the main simulation. A convective boundary condition is applied at the outflow station. The opposing (convex) wall in the experiment is contoured to minimize the streamwise pressure gradient on the concave wall. The same contoured geometry is used in the LES, with the exception that the calculation extends only to the streamline that lies along the channel centerline. The position of the streamline is determined from an inviscid analysis that accounts for the displacement of the boundary layers on both walls. No flow-through and no-stress boundary conditions are applied on the streamline boundary. The spanwise extent of the domain is 2 boundary layer thicknesses. According to the experimental measurements, the computational domain is wide enough to enclose 4 streamwise Taylor-Görtler vortices. Periodic boundary conditions are used in the spanwise direction.

The momentum thickness Reynolds number (at the onset of curvature) in both the experiment and simulation is $R_{\theta_0} = 1300$. The ratio of the boundary layer thickness to the radius of curvature, δ_0/R, is 0.055, which is sufficiently large to create significant curvature effects on turbulent statistics.

The computational grid contains $178 \times 40 \times 64$ points in the streamwise, wall-normal, and spanwise directions respectively. The mesh is stretched in the wall-normal direction and uniform in the other two.

In order to eliminate starting transients, the simulation is run for an initial period of 60 boundary layer inertial time scale units (1.7 flow-through times). Statistics are then sampled over a period of 300 inertial time scales (8.5 flow-through times). Mean quantities are formed by averaging over both the spanwise direction and time.

Mean velocity profiles at several streamwise stations are compared with the experimental data in Figure 6. The first station is on the flat inlet section, 8 boundary layer thicknesses ahead of the curved section. The other 4 stations are at 15^o, 30^o, 45^o, and 60^o (4.7, 9.5, 14.2, and 18.9 boundary layer thicknesses into the curved section). Overall the agreement between simulation and experiment is good. Near the start of the curve, the simulation produces profiles that are a bit fuller near the wall as compared with the experiment. The fuller profiles also result in higher skin friction as compared with the experiment up to about 30^o into the the curve.

Streamwise and wall-normal turbulent intensities are shown in Figure 7. The differences between the simulation and experiment at the first station are largely due to the approximate turbulent fluctuations supplied at the inflow station in the simulation. The agreement is much better further downstream within the curved section. The only significant differences in the curved section is the overprediction of the streamwise intensity near the wall. This is a well-known feature of marginal resolution in the near wall region. Note that the shapes of the experimental profiles (especially v') have changed significantly from the first to the last station. In particular a pronounced bulge develops in the middle of the layer which shifts the maximum in v' to the central portion of the profile. It is believed that the Taylor-Görtler vortices are responsible for this bulge. The LES does a good job of predicting this transition in the profile shape.

5. CONCLUDING REMARKS

Results from applications of dynamic models to a diverse set of turbulent flows have been encouraging. The model has proven to be very robust. Research on further improvement of the model is continuing; these improved versions should be validated in challenging flows. In particular, the effect of including subgrid scale backscatter on large scale turbulence statistics needs to be quantitatively documented.

Proper resolution of the eddies in the viscous sublayer remains a pacing item for LES of high Reynolds number wall-bounded flows. The viscous drag in attached boundary layers is directly related to the dynamics of the streamwise vortices near the wall. The use of embedded grids may be necessary in the wall layer as well as for resolving thin shear layers that frequently occur in complex flows.

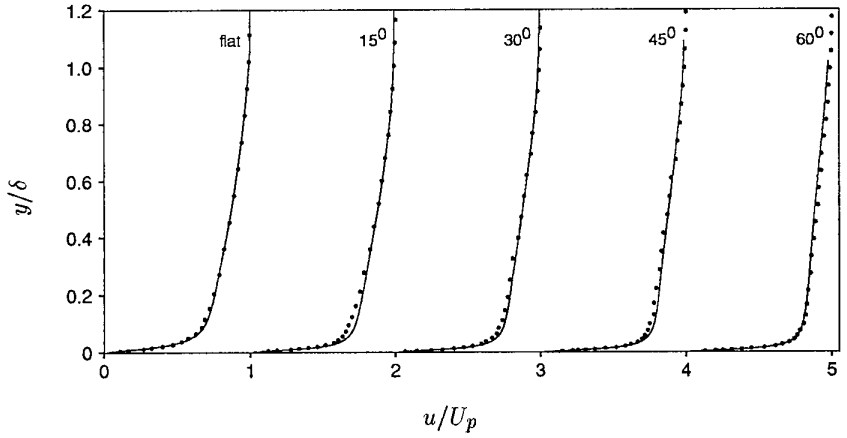

Figure 6. Mean streamwise velocity profiles. The velocity is scaled by U_p, the streamwise profile that would be developed in an inviscid flow through the curved section. The first station is on the flat inlet section, 8 boundary layer thicknesses ahead of the curve. ——: LES; •: Johnson and Johnston [24].

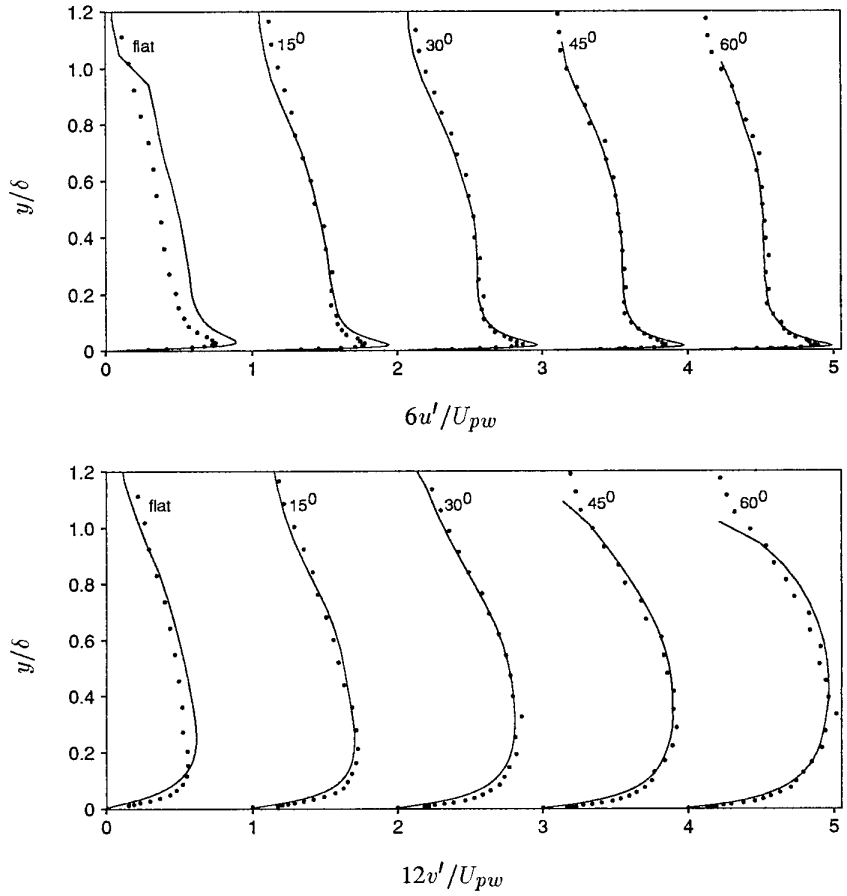

Figure 7. Turbulent intensity profiles. (a) streamwise, (b) wall-normal. The RMS values are scaled by $U_p w$, the streamwise velocity that would be developed at the curved wall in an inviscid flow through the curved section. The first station is on the flat inlet section, 8 boundary layer thicknesses ahead of the curve. ——: LES; •: Johnson and Johnston [24].

ACKNOWLEDGEMENT

The LES program at the Center for Turbulence Research is supported by the U.S. Office of Naval Research and the Air Force Office of Scientific Research.

REFERENCES

1. P. Moin and J. Jimenez, "Large eddy simulation of complex turbulent flows", AIAA paper 93-3099, (1993), presented at the AIAA 24th Fluid Dynamics Conference, Orlando, Fl.

2. M. Germano, U. Piomelli, P. Moin, and W. Cabot, "A dynamic subgrid-scale eddy-viscosity model," Phys. Fluids A **3(7)**, 1760 (1991).

3. P. Moin, K. Squires, W. Cabot, and S. Lee, "A dynamic subgrid-scale model for compressible turbulence and scalar transport," Phys. Fluids A **3(11)**, 2746 (1991).

4. D. Lilly, "A proposed modification of the Germano subgrid-scale closure method," Phys. Fluids A **4(3)**, 633 (1992).

5. T. S. Lund, S. Ghosal, and P. Moin, "Numerical experiments with highly variable eddy viscosity models," in *Engineering applications of large eddy simulations*, edited by S. A. Ragab and U. Piomelli (ASME, New York, 1993), pp. 7–11, presented at the ASME fluid engineering conference, Washington D. C. June 20-24, 1993.

6. S. Ghosal, T. Lund, and P. Moin, "A local dynamic model for LES,"*1992 Annual Research Briefs* (Center for Turbulence Research, Stanford Univ., Stanford CA, 1993), pp. 3–25.

7. J. P. Bertoglio, 1993, private communication.

8. W. Cabot and P. Moin, "Large-eddy simulation of scalar transport with the dynamic subgrid-scale model," in *Large Eddy Simulation of complex engineering and geophysical flows*, edited by B. Galperin and S. A. Orzag (Cambridge Univ. Press, Cambridge, England, 1993).

9. M. Bohnert and J. H. Ferziger, "The dynamic sgs model in LES of the stratified Eckman layer," in *Engineering turbulence modelling and experiments 2*, edited by W. Rodi and M. Martelli (Elsevier Science Publishers, 1993), pp. 315–324.

10. Y. Zang, R. L. Street, and J. R. Koseff, "A dynamic mixed subgrid-scale model and its application to turbulent recirculating flows," Phys. Fluids A **5(12)**, 3186 (1993).

11. W. Cabot, "Large eddy simulations of time-dependent and buoyancy-driven channel flows,"*1992 Annual Research Briefs* (Center for Turbulence Research, Stanford Univ., Stanford CA, 1993), pp. 45–60.

12. K. D. Squires and U. Piomelli, in *Proc. Ninth Symp. on Turbulent Shear Flows* (Kyoto, Japan, 1993).

13. J. Liu and U. Piomelli, "Interaction of embedded streamwise vortices with a spatially-developing boundary layer," in *Engineering applications of large eddy simulations*, edited by S. A. Ragab and U. Piomelli (ASME, New York, 1993), pp. 45–52, presented at the ASME fluid engineering conference, Washington D. C. June 20-24, 1993.

14. G. Comte-Bellot and S. Corrsin, "Simple Eulerian time correlations of full and narrow band velocity signals in grid generated 'isotropic' turbulence," J. Fluid Mech. **48**, 273 (1971).

15. J. Chasnov, "Simulation of the Kolmogorov inertial subrange using an improved subgrid model," Phys. Fluids A **3(1)**, 188 (1991).

16. W. Cabot, "Dynamic localization and second-order subgrid-scale models in large eddy simulations of channel flow,"*1993 Annual Research Briefs* (Center for Turbulence Research, Stanford Univ., Stanford CA, 1993), pp. 129–144.

17. P. J. Mason and D. J. Thomson, "Stochastic backscatter in large eddy simulations of boundary layers," J. Fluid Mech. **242**, 51 (1992).

18. C. E. Leith, "Stochastic backscatter in a subgrid-scale model: plane shear mixing layer," Phys. of Fluids A **2**, 297 (1990).

19. R. A. Clark, J. H. Ferziger, and W. C. Reynolds, "Evaluation of subgrid-scale models using an accurately simulated turbulent flow," J. Fluid Mech. **91**, 1 (1979).

20. E. W. Adams, J. P. Johnston, and J. K. Eaton, "Experiments on the structure of turbulent reacting flow", report MD-43, Thermosciences Division, Dept of Mech. Eng., Stanford University (1984).

21. H. Le and P. Moin, "Direct numerical simulation of flow over a backward-facing step", report TF-58, Thermosciences Division, Dept of Mech. Eng., Stanford University (1994).

22. H. Choi and P. Moin, The effect of computational timestep on numerical simulation of turbulent flow, 1994, also published as *Rep. TF-55*, Dept. of Mech. Eng., Stanford Univ., 1992.

23. R. S. Barlow and J. P. Johnston, "Structure of a turbulent boundary layer on a concave surface," J. Fluid Mech. **191**, 137 (1988).

24. P. L. Johnson and J. P. Johnston, "The effects of grid-generated turbulence on a flat and concave turbulent boundary layer", report MD-53, Thermosciences Division, Dept of Mech. Eng., Stanford University (1989).

Subgrid scale models in finite difference simulations of complex wall bounded flows

Elias Balaras
Carlo Benocci
von Karman Institute for Fluid Dynamics
Environmental and Applied Fluid Dynamics Department
Chaussée de Waterloo 72
1640 Rhode St Génèse, Belgium

1 SUMMARY

The dynamic subgrid scale model has been used in the Large Eddy Simulation (LES) of turbulent flow in a straight square duct. The Reynolds numbers considered, (based on the friction velocity and the duct halfwidth), are varying from 150 to 1125. The results obtained are in good agreement with the reference Direct Numerical Simulation (DNS) and experimental data. The accuracy and suitability of the model in high Reynolds number finite difference computations of three dimensional non-equilibrium flows is investigated. The influence of approximate wall boundary conditions in such flow cases is also addressed.

2 INTRODUCTION

Since the pioneering work of Deardoff [1] in the beginning of the 70^s, the LES approach has become an attractive tool for the accurate prediction of turbulent and transitional flows. However, the lack of general subgrid scale (SGS) models, able to account for all the complicated phenomena present in turbulent flows of practical interest, has restricted, up to now, the applicability of LES to simple geometries at moderate Reynolds numbers. Over the past decades, one of the most widely used SGS closures in LES is the Smagorinsky model [2]. Although it has been used in a variety of turbulent flows, it has some significant drawbacks. The model coefficient is an *a priori* input which has to be optimized for each type of flow. It was also found to be very dissipative in transitional flows [3], partly because it does not account for backscatter (transfer of energy form the small to the large scales), and partly because it does not vanish in laminar regions. In addition, ad hoc dumping functions have to be introduced in order to ensure the correct limiting behaviour close to solid boundaries.

One of the most promising developments in the field of subgrid scale modelling, which has the potential to overcome the limitations mentioned above, is the dynamic eddy viscosity model proposed by Germano et. al. [4]. In this case, in addition to the grid filter which defines the resolved field and the subgrid scale stresses τ_{ij}, a test filter, which is wider than the grid filter is introduced. In a similar manner it defines the subtest scale stresses T_{ij}. If a simple eddy viscosity model is used as a subgrid scale closure, the algebraic identity [5] which relates τ_{ij} and T_{ij} with the resolved stresses $\mathcal{L}_{ij}$, can be exploited to compute the model coefficient. The dynamic eddy viscosity model has been used in a variety of turbulent incompressible [4],[6], [7] [8] and compressible flows [9] with impressive results. In most of the above studies the Reynolds number was kept at relatively low levels. Recently, Piomelli [10] and Balaras et. al. [11] reported channel flow computations at high Reynolds numbers, (ranging between 5000 and 120000, based on the bulk velocity and channel width), with good agreement with the reference data. In this study the model is extended to more complicated flows at high Reynolds numbers. More specifically, the flow in a straight square duct is computed.

In this flow case, a non zero mean flow occurs in the transverse planes of the duct, referred as secondary flow. It has been thought to arise due to the anisotropy and inhomogeneity of the Reynolds stresses. Speziale [12], had shown analytically that the secondary flow in ducts with non-circular cross sections originates from the fact that the axial mean velocity gives rise to a non-zero difference in the transverse normal Reynolds stresses responsible for the production of axial mean vorticity. The above argument is also supported by the experimental findings of Brundrett and Baines [13]. However, Gessner [14] in his experimental investigation reported that the gradients of turbulent shear stresses normal to the corner bisector play an important role in the generation of secondary flow, and he suggested that the mechanisms responsible for the production of the mean streamwise vorticity are not necessarily initiating the secondary motions. Eventhough the secondary flow is very small in magnitude $(1\% - 2\%)$, it has a significant effect on the overall flow structure and its accurate prediction is quite important. Taking also into account that this is one of the simplest configurations related to fully three dimensional flows, this flow problem can be an attractive test case for problems related to SGS modelling.

Another issue which is addressed in this study, is the effect of approximate wall boundary conditions in the accuracy of the computations. In such case the first computational point in the vicinity of the wall is located in the fully turbulent region ($y^+ = 30 - 100$), and the wall stresses required to impose boundary conditions are estimated in terms of the core flow velocities. This way the grid can be coarse in the other flow directions as well, leading in big savings in CPU time. Most of the currently available approximate wall boundary conditions [15] are based on some semi-empirical correlation between the wall stress and the velocity in the fully turbulent region. Very good results have been obtained using the above models in turbulent channel flow computations, combined either with the Smagorinsky [15] or the dynamic SGS [11] closure. However, extension to complex flows were the log-law is not valid in an average sense and semi-empirical information is not available, could introduce considerable inaccuracies. Recently, Bagwell et. al. [16] has used the Linear Stochastic Estimation approach to derive approximate wall boundary conditions.

Paper presented at the 74th Fluid Dynamics Symposium on "Application of Direct and Large Eddy Simulation to Transition and Turbulence" held at Chania, Crete, Greece, in April 1994.

A priori calculations using the DNS data of Kim et. al. [17] for a turbulent channel flow gave improved results compared to existing models. This model yet has to be extended to turbulent flows in more complex geometries. In the present study a more general approximate wall boundary condition is proposed. It is based on the solution of a simplified model equation for each velocity component in the wall region. In a previous study [18] the model was used in the computation of turbulent channel flows. The results obtained were in good agreement with the reference DNS and experimental data. Since the model requires no input based on semi-empirical correlations, it is more suitable for the square duct flow case where such information is not available.
In the next section the governing equations and the dynamic eddy viscosity model will be described. In section 4 the numerical method and the approximate wall boundary conditions will be presented. Results will be given in section 5 and conclusions will be drawn in section 6.

3 MATHEMATICAL FORMULATION

In the LES approach the large scale velocity field can be obtained from the direct solution of the filtered Navier-Stokes equations, while the scales smaller than the grid size are modelled. In finite difference computations, the filtering operation which defines the large scale variables (denoted by overbar), is a simple top-hat filter in physical space applied implicitly by the finite difference operators :

$$\overline{f}(\mathbf{x}) = \frac{1}{\overline{\Delta}_1\overline{\Delta}_2\overline{\Delta}_3}\int_D f(\mathbf{x}')d\mathbf{x}', \qquad (1)$$

where D is a finite-difference cell. The resulting filtered form of the equations for the conservation of mass and momentum for an incompressible fluid is the following:

$$\frac{\partial\overline{u}_i}{\partial t} + \frac{\partial}{\partial x_j}(\overline{u}_i\overline{u}_j) = -\frac{\partial P}{\partial x_i} + F_i - \frac{\partial\tau_{ij}}{\partial x_j} + \frac{1}{Re_\tau}\frac{\partial^2\overline{u}_i}{\partial x_j\partial x_j} \qquad (2)$$

$$\frac{\partial\overline{u}_i}{\partial x_i} = 0, \qquad (3)$$

where Re_τ is the Reynolds number, based on the friction velocity u_τ and duct halfwidth h, and F_i is a forcing term representing the average streamwise pressure gradient. In the following, x is the streamwise direction, y and z are the transverse directions. A schematic representation of the duct geometry and coordinate system is given in figure 1.
The effect of the small scales upon the resolved part of turbulence appears in the subgrid-scale stress term, $\tau_{ij} = \overline{u_iu_j} - \overline{u}_i\overline{u}_j$. Taking into account that the small scales are more isotropic than the resolved scales, τ_{ij} can be modelled using a simple eddy viscosity model [2] :

$$\tau_{ij} - \frac{\delta_{ij}}{3}\tau_{kk} = -2\nu_T\overline{S}_{ij} = -2C\overline{\Delta}^2|\overline{S}|\overline{S}_{ij}, \qquad (4)$$

in which δ_{ij} is Kronecker's delta, $\overline{\Delta}$ is the filter width defined as:

$$\overline{\Delta} = (\overline{\Delta}_1\overline{\Delta}_2\overline{\Delta}_3)^{\frac{1}{3}}, \qquad (5)$$

and $|\overline{S}| = (2\overline{S}_{ij}\overline{S}_{ij})^{1/2}$ is the magnitude of the large-scale strain rate tensor

$$\overline{S}_{ij} = \frac{1}{2}\left(\frac{\partial\overline{u}_i}{\partial x_j} + \frac{\partial\overline{u}_j}{\partial x_i}\right). \qquad (6)$$

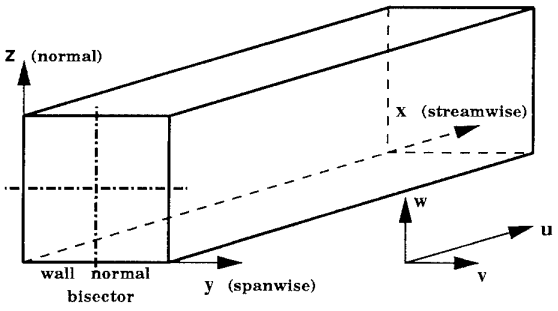

Fig. 1: Duct geometry and coordinate system.

The trace of the subgrid-scale stresses is included in the pressure term. The application of a second filter, the test filter, to equations (2) and (3), defines the subtest-scale stresses $T_{ij} = \widehat{u_iu_j} - \widehat{\overline{u}}_i\widehat{\overline{u}}_j$. Using the same closure as above to model T_{ij} one can obtain:

$$T_{ij} - \frac{\delta_{ij}}{3}T_{kk} = -2C\widehat{\Delta}^2|\widehat{\overline{S}}|\widehat{\overline{S}}_{ij}. \qquad (7)$$

Equations (4) and (7) can be substituted into the identity [5] :

$$\mathcal{L}_{ij} = T_{ij} - \widehat{\tau_{ij}}, \qquad (8)$$

which relates the subgrid-scale and the subtest-scale stresses to the resolved turbulent stresses $\mathcal{L}_{ij} = \widehat{\overline{u}_i\overline{u}_j} - \widehat{\overline{u}}_i\widehat{\overline{u}}_j$. C can be computed from equation (8), which represents a set of five independent equations in one unknown. Following Lilly [19], C can be derived from (8) using a least squares approximation, which leads to an expression for the model coefficient which is well conditioned. However, Cabot and Moin [7] found numerical instabilities resulting from the negative total viscosities predicted by the local model. As it was also done by previous investigators [7], [6], to avoid ill-conditioning and make the model mathematically self-consistent, in the present study Lilly's expression was averaged over the homogenous streamwise direction :

$$C(y,z,t) = -\frac{1}{2}\frac{<\mathcal{L}_{ij}M_{ij}>}{<M_{ij}M_{ij}>}, \qquad (9)$$

where $<\cdot>$ denotes averaging over the streamwise direction, and

$$M_{ij} = \widehat{\Delta}^2|\widehat{\overline{S}}|\widehat{\overline{S}}_{ij} - \overline{\Delta}|\widehat{\overline{S}}|\widehat{\overline{S}}_{ij}. \qquad (10)$$

This procedure was found to be more accurate than an earlier one [20], in which C was computed locally on the test filter. Ill-conditioning was eliminated by truncating the values of C exceeding an upper and a lower bound. Although the results obtained for high Reynolds number square duct flow were in good agreement with the experimental data, it was found that on coarse grids the percentage of C values that had to be truncated increased, and the accuracy depended on the choice of the bounds. Following Germano *et al.* (1991) the ratio of the two filter widths was set to $\widehat{\Delta}/\overline{\Delta} = 2$.

4 NUMERICAL ASPECTS

4.1 Numerical method

Equations (2) and (3) are integrated in time using an Adams-Bashforth fractional-step method:

$$U_i^* = U_i^n + (1.5H_i^n - 0.5H_i^{n-1} + 0.5\frac{\partial P^{n-1}}{\partial x_i})\,\Delta t \quad (11)$$

$$1.5\Delta t\,\frac{\partial^2 P^n}{\partial x_i^2} = \frac{\partial U_i^*}{\partial x_i} \quad (12)$$

$$U_i^{n+1} = U_i^* - 1.5\Delta t\,\frac{\partial P^n}{\partial x_i} \quad (13)$$

where H includes all the right hand side terms minus the contribution of the pressure.
Equation (12) is solved using a Direct Poisson Solver based on Fast Fourier Transforms. The constraints imposed by the Direct Poisson solver lead to choose a staggered discretization with uniform mesh spacing in the three coordinate directions x_i. Both advective and diffusive terms are treated explicitly. All spatial derivatives are approximated by second-order central differences. The overall accuracy of the code is second order in space and in time.
The value of C is computed from equation (9). All the necessary test filtered quantities were computed at each grid cell, using weighted volume averages over the surrounding cells. A detailed study on the application of the model in finite difference computations and on the implementation details concerning the use of staggered grids can be found in [11]. Although spatial averaging of numerator and denominator of (9) was found to give stable computations in channel flows [4], [10], where two spatial homogenous directions exist, in the present study it was found that averaging only in the streamwise direction was not sufficient to remove ill-conditioning. A number of negative total viscosities was appearing during the calculations, leading to computational instabilities. For the high Reynolds number case, negative total viscosities were detected at approximately 1% of the total number of grid points. The problem was removed by replacing total viscosity with zero whenever was negative. This way also a small amount of backscatter is allowed. A similar approach was followed by Akselvoll and Moin [6] in the computation of a backward facing step with good results.

4.2 Boundary conditions

Periodic boundary conditions were used in the streamwise direction. As it was mentioned in the first section, a more critical problem is related with the modeling of the region close to solid boundaries. Due to the lack of empirical information in complex wall bounded flows currently available approximate wall boundary conditions are impractical and may introduce inaccuracies in the computations. The treatment which is proposed in this study is based on the solution of a simplified model equation for each velocity component, on a refined mesh embedded in the main one. Also in this case the first computational point is located in the logarithmic region and the mesh is refined from this point to the solid boundary. The equation proposed, obtained from the two dimensional boundary layer equations, has the form:

$$\frac{\partial \overline{u}_i}{\partial t} + u_n\frac{\partial \overline{u}_i}{\partial x_n} = -\frac{\partial P}{\partial x_i} + (\nu + \nu_t)\frac{\partial^2 \overline{u}_i}{\partial x_n \partial x_n} \quad (14)$$

where $\overline{u}_i$ is the unknown, P is the pressure and ν and ν_t are the molecular and turbulent viscosity accordingly. The lower index n denotes direction normal to the boundary. The normal advection term and the pressure term account for the sweep and ejection events in the region, taking information from the first actual grid point. The viscous term accounts for most of the activity in the region via the turbulent viscosity. In this study a simple eddy viscosity model is used to represent ν_t :

$$\nu_t = \kappa z D(z)|S| \quad (15)$$

where κ is the von Karman constant, z is the distance from the solid boundary, $|S|$ is the magnitude of the total strain rate, and D is a dumping function used to ensure the correct limiting behaviour for ν_t. An expression proposed by Piomelli et. al. [15] is adopted:

$$D(z) = [1 - exp(-(\frac{z^+}{A^+})^3)]^{0.5} \quad (16)$$

Equation (14) is discretized with 2^{nd} order finite differences in an implicit fashion to avoid stability restrictions. w_n is obtained by applying the continuity equation at each cell. The solution obtained at each time step, gives a velocity profile for the component of interest, which provides an estimate of the wall stress, required to impose boundary conditions.

Table 1: Summary of the computations

Case	Grid size	Re_τ	Re_b
1	82×22×22	150	4410
2	82×34×34	1125	42000

5 RESULTS

Two computations were performed at two different Reynolds numbers. The calculation parameters are summarized in table 1, in which Re_τ is the Reynolds number based on friction velocity u_τ and the duct halfwidth, and Re_b is the Reynolds number based on the bulk velocity U_b and the hydraulic diameter. The size of the computational box was taken equal to $5.5\pi h \times 2h \times 2h$. This streamwise length was found to be sufficient to contain the largest structures present in the flow, by *postpriori* examination of the two point correlations. Case 1 is a low Reynolds number case, fairly resolved, for which detailed DNS data [21] are available. Case 2 is a high Reynolds

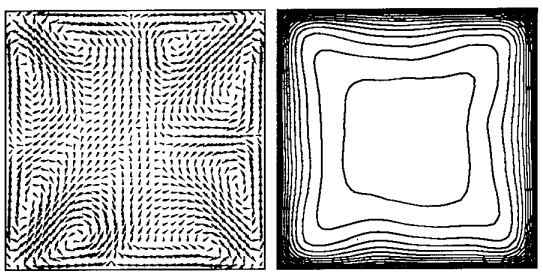

Fig. 2: Left: Mean secondary velocity vectors, Right: contours of mean streamwise velocity at a cross-sectional plane for case 2

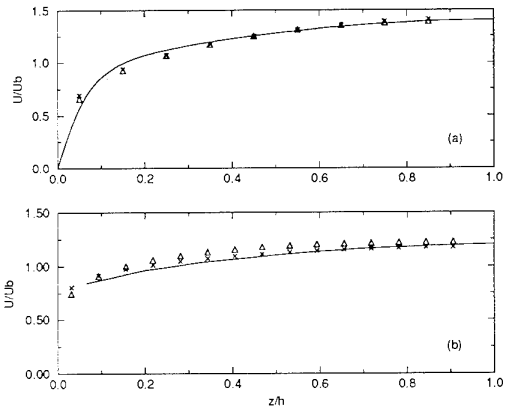

Fig. 3: Mean streamwise velocity profiles at the normal wall bisector. (a) $Re_\tau = 150$, $\times$ case 1, $\triangle$ Smagorinsky model, ——— DNS data [21] , (b) $Re_\tau = 1125$, $\times$ case 2, $\triangle$ Smagorinsky model, ——— experimental data [13]

number case (7.5 times larger compared with case 1), were the accuracy of the model and adequacy of the approximate wall boundary conditions can be investigated for high Reynolds numbers. The results from this computation will be compared with available experimental data in the literature, [13], [22].

The initial solution was obtained taking the experimental [23] and DNS [21] mean velocity profiles, and superimpose divergence free perturbations. The equations were integrated in time until steady state was reached. Statistics were accumulated over 7-8 units, (tu_τ/δ). Further integration in time was found to have negligible influence on the mean flow quantities and turbulent statistics. In figure 2 isolines of the mean streamwise velocity and velocity vectors of the mean secondary flow, are shown at a cross section for case 2. Although some asymmetry in the results is present, the main flow features are evident. In the following comparisons all the corresponding quantities are averaged over the four quadrants. In figure 3 mean streamwise velocity profiles normalized with U_b are given at the normal wall bisector. Computations done with the Smagorinsky model with $cs = 0.12$, are also included. The agreement with the reference data is very good. A small improvement can be observed when the dynamic model is used. The predicted ratio of U_c/U_b for case 1 is 1.32, which is in good agreement

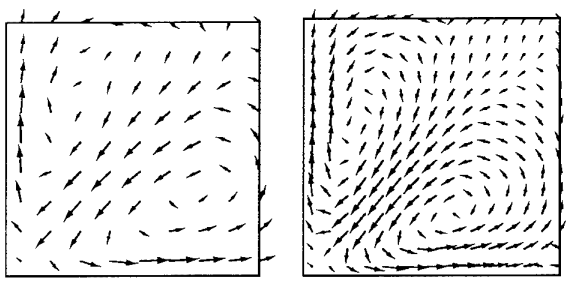

Fig. 4: Mean secondary velocity vectors at a quadrant. Left: case 1, Right: case 2

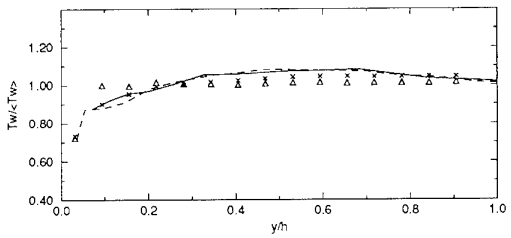

Fig. 5: $T_w/ < T_w >$ profile along the lower wall. $\times$ proposed model, $\triangle$ shifted model, ——— experimental data in [25], ——— experimental data in [26]

with the value 1.33 reported by Gavrilakis, [21]. For case 2 this ratio was 1.18. Brandrett and Baines [13] reported a value of $U_c/U_b = 1.2$ for a higher Reynolds number ($Re_b = 80000$). The predicted values are also consistent with the trend given by Demuren and Rodi [24], meaning that the value of U_c/U_b is decreasing as the Reynolds number increases. In figure 4 the mean secondary flow velocity vectors averaged over the four quadrants, are given for case 1 and case 2. The magnitudes of the maximum secondary velocity were found to be 2.51% and 2.23% of the bulk velocity accordingly. The second one is in good agreement with the value of 2.2% reported in [13].

For the low Reynolds number case Gavrilakis predicted

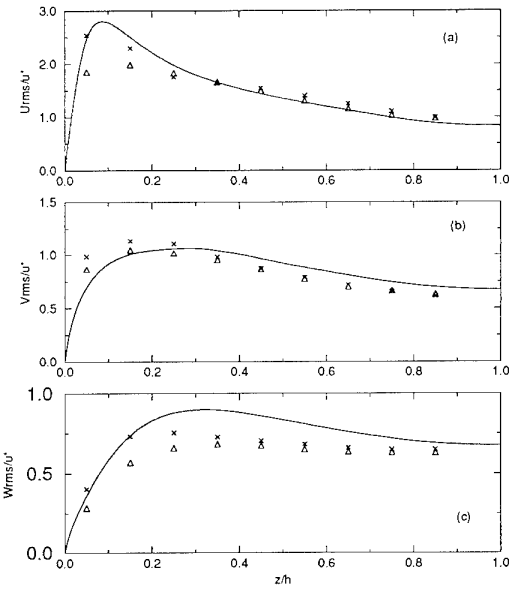

Fig. 6: Turbulent intensities along the normal wall bisector at $Re_\tau = 150$. $\times$ case 1, $\triangle$ Smagorinsky model ——— DNS data [21], (a) U_{rms}, (b) V_{rms}, (c) W_{rms}

a relatively lower value of 1.9%. The difference could be due to the limited resolution, since in case 2 the number of points at the cross section is marginal to capture all details of the secondary flow.

The distribution of $\tau_w/ < \tau_w >$ along the lower duct wall for case 2 is given in figure 5. The measured values in [25]

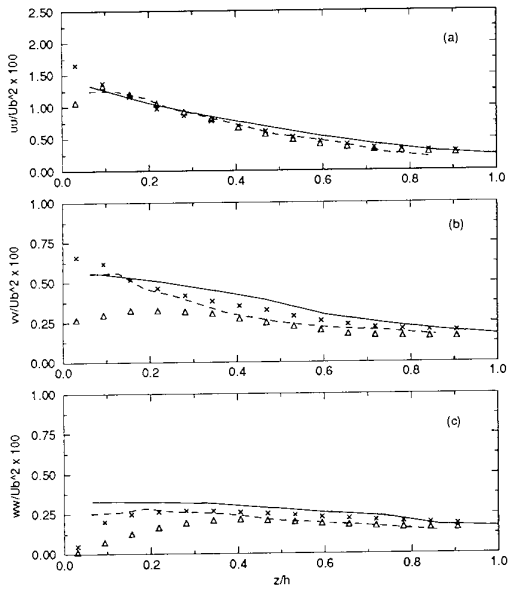

Fig. 7: Normal Reynolds stresses along the normal wall bisector at $Re_\tau = 1125$. $\times$ case 2, $\triangle$ Smagorinsky model ——— experimental data in [13], — — — experimental data in [22], (a) uu, (b) vv, (c) ww

and [26] at $Re_b = 50000$ and $Re_b = 34000$ respectively, are also included. The prediction given by the new wall model is in good agreement with the experimental data. It follows quite closely the measured values with a mid-wall value of $1.005 < \tau_w >$. For case 1 the mid-wall value was $1.12 < \tau_w >$; slightly lower than the one reported in [21], which is $1.18 < \tau_w >$. The computation for case 2 was repeated using the shifted model [15] as approximate wall boundary condition. The resulting $\tau_w / < \tau_w >$ distribution is also given in figure 5. It can be seen that the predicted value close to the corner region is higher than the measured one, probably because in this region the average streamwise velocity is far from satisfying the log-law which is required by the model.

In figure 6 and 7 the normal Reynolds stress profiles along the normal wall bisector are given for case 1 and 2 respectively. The choice of the velocity scales is different for each case, in order to be able to have comparisons with the reference data, minimizing the uncertainties introduced by rescaling the data using empirical correlations.

The local shear velocity (referred as u^*) is chosen for case 1 and the bulk velocity U_b for case 2. In figure 5 the velocity fluctuations obtained with the dynamic model compare well with the DNS data, [21]. An improvement can be observed compared with the Smagorinsky model. A similar behaviour can be seen in fig 7 for case 2, which is more evident probably due to the lower resolution. For both cases the Smagorinsky model is performing purely mainly in the wall region. This can be attributed to the less dissipative character of the dynamic model in this region. In figure 8 isolines of $< C >$ are given at a quadrant. In the centerline region $< C >$ varies between $0.012 - 0.020$, corresponding to C_s values of $0.11 - 0.14$, which are very close to the value of $C_s = 0.12$ used in the actual Smagorinsky computation. Approaching the solid boundaries, C is reduced rapidly and reaches a value of approximately 0.004, corresponding to $C_s = 0.06$ which is half of the one used in the simulation.

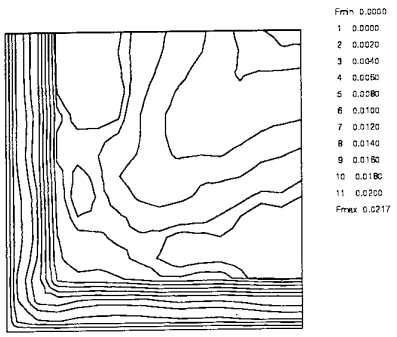

Fig. 8: Isolines of model coefficient at a quadrant for case 2

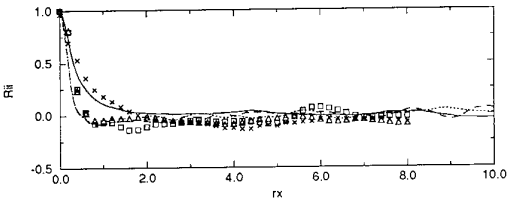

Fig. 9: Streamwise two point correlations for case 1. The symbols denote LES data, the lines denote DNS data [21], $\times$ ——— R_{11}, $\triangle$ — — — R_{22}, $\square$ ····· R_{33}

In figure 9 two point streamwise correlations are given for case 1. The agreement with the DNS data is very good despite the mesh coarseness in this direction.

6 CONCLUSIONS

In the present study, the dynamic eddy viscosity model was used in finite difference computations of turbulent flow in a square duct at high Reynolds numbers. The accuracy and suitability of the model for such flow cases was demonstrated. The mean velocity field and low order turbulent statistics compare well with the reference data. A considerable improvement can be observed for most of the statistics in comparison with the Smagorinsky model. The line averaging performed to eliminate ill-conditioning and make the model mathematically self-consistent, was found to be more accurate and robust than a straitforward localization procedure used in a previous study [20]. However, this averaging procedure is limiting the applicability of the model to flows were at least one homogeneous direction exists. For flows in which no homogeneous direction is available, a localized model should be introduced.

An other issue addressed in this study is the accuracy and suitability of approximate wall boundary conditions, which could be crucial in extending LES to complex wall bounded flows at high Reynolds numbers. The proposed model was found to be more accurate than existing models in such flow cases. However, a more sophisticated tur-

bulence model able to account for the complicated flow phenomena present in the wall region is more desirable and could improve the accuracy of the model.
Further developments in both fields mentioned above are quite important in extending LES to engineering applications. Considering also the flexibility of finite difference methods in complex geometries and the fact that the cost of the simulations reported in this study is not exiting $15h$ on a fast desktop workstation, LES can be considered a promising tool for the prediction of practical flow problems at high Reynolds numbers.

ACKNOWLEDGMENTS

This work is supported by E.E.C. under grand No. $ERBCHDICT930257$. The authors are grateful to Prof. U. Piomelli for many useful discussions during the coarse of this work, and to Dr. S. Gavrilakis for kindly providing detailed data from his DNS.

REFERENCES

[1] J. W. Deardorff. A numerical study of three-dimensional turbulent channel flow at large Reynolds numbers. *J. Fluid Mech.*, 41:453–480, 1969.

[2] J. Smagorinsky. General circulation experiments with the primitive equations, i. the basic experiment. *Mon. Weather Rev.*, 91:99, 1963.

[3] U. Piomelli, H. Cabot, P. Moin, and S. Lee. Subgrid-scale backscatter in turbulent and transitional flows. *Phys. Fluids A*, 3(7):1766–1771, July 1991.

[4] M. Germano, U. Piomelli, P. Moin, and W.H. Cabot. A dynamic subgrid-scale eddy viscosity model. *Phys. Fluids A*, 3(7):1760–1765, July 1991.

[5] M. Germano. Turbulence : the filtering approach. *J. Fluid Mech.*, 238:325–336, 1992.

[6] K. Akselvoll and P. Moin. Application of the dynamic localization model to large eddy simulation of turbulent flow over a backward facing step. In Engineering applications of large eddy simulations, editor, *S. A. Ragab and U. Piomelli.* The Amarican Society of Fluids Engineering, New York, 1993.

[7] W. H. Cabot and P. Moin. Large eddy simulation of scalar transport with the dynamic subgrid-scale model. In Large eddy simulation of complex engineering and geophysical flows, editors, *B. Galperin and S. Orzag.* Cambridge University Press, Cambridge, 1993.

[8] Y. Zang, R. L. Street, and J. R. Koseff. A dynamic mixed subgrid-scale model and its application to turbulent recirculating flows. *Phys. Fluids A*, 12(5):3186–3196, December 1993.

[9] P. Moin, K. Squires, W. Cabot, and S. Lee. A dynamic subgrid scale model for compressible turbulence and scalar transport. *Phys. Fluids A*, 11(3):2746–2757, November 1991.

[10] U. Piomelli. High Reynolds number calculations using the dynamic subgrid-scale stress model. *Phys. Fluids A*, 5(6):1484–1490, June 1993.

[11] E. Balaras, C. Benocci, and U. Piomelli. Finite difference computations of high Reynolds number flows using the dynamic subgrid-scale model. *Theoretical and Computational Fluid Dynamics*, 1994. submitted for publication.

[12] C. G. Speziale. The dissipation rate correlation and turbulent secondary flows in noncircular ducts. *J. Fluids Eng., Transactions of ASME*, 108:118–120, 1986.

[13] E. Brundrett and W. D. Baines. The production and diffusion of vorticity in a duct flow. *J. Fluid Mech.*, 19:375–394, 1964.

[14] F. B. Gessner. The origin of secondary flow in turbulent flow along a corner. *J. Fluid Mech.*, 58:1–25, 1973.

[15] U. Piomelli, J. Ferziger, P. Moin, and J. Kim. New approximate boundary conditions for large eddy simulations of wall-bounded flows. *Phys. Fluids A*, 1(6):1061–1068, June 1989.

[16] G. Bagwell, R. J. Andrian, R. D. Moser, and J. Kim. Improved approximation of wall shear stress boundary conditions for large eddy simulation. In Near wall turbulent flows, editor, *C. G. Speziale and B. P. Launder*, pages 265–275. Elsevier Science Publishers, 1993.

[17] J. Kim, P. Moin, and R. Moser. Turbulent statistics in fully developed channel flow at low Reynolds number. *J. Fluid Mech.*, 177:133–166, 1987.

[18] E. Balaras, C. Benocci, and P. F. Trecate. A new model for estimating the wall shear stress in large eddy simulations. In *Proceedings of international workshop on large eddy simulations of turbulent flows in engineering and the environment*, Montreal, Quebec, Canada, September 27-28 1993. CERCA.

[19] D. K. Lilly. A proposed modification of the germano subgrid-scale closure method. *Phys. Fluids A*, 4(3):633–635, March 1992.

[20] E. Balaras and C. Benocci. Large eddy simulation of flow in a square duct. In *Proceedings of the thirteenth symposium on turbulence.* University of Missuri Rolla, September 21-23 1992.

[21] S. Gavrilakis. Numerical simulation of low Reynolds number tutbulent in a straight duct. *J. Fluid Mech.*, 244:101–129, 1993.

[22] F. B. Gessner. PhD thesis, Purdue University, 1964.

[23] A. Melling and J. H. Whitelaw. Turbulent flow in a rectangular duct. *J. Fluid Mech.*, 78:289–314, 1976.

[24] A. O. Demuren and W. Rodi. Calculation of turbulence-driven secondary motion in non-circular ducts. *J. Fluid Mech.*, 140:189–222, 1984.

[25] E. G. Lund. Mean flow and turbulence characteristics in the near corner region of a square duct. Master's thesis, University of Washington, 1977.

[26] H. J. Leutheusser. Turbulent flow in rectungular ducts. *J. Hydraulics Division*, 89(HY3):1–19, 1963.

LARGE-EDDY SIMULATION OF ROTATING CHANNEL FLOWS USING A LOCALIZED DYNAMIC MODEL

Ugo Piomelli and Junhui Liu
Department of Mechanical Engineering
University of Maryland
College Park, MD 20742, USA

ABSTRACT

Most applications of the dynamic subgrid-scale stress model use volume- or planar-averaging to avoid ill-conditioning of the model coefficient, which may result in numerical instabilities. A spatially-varying coefficient is also mathematically inconsistent with the model derivation. A localization procedure is proposed here that removes the mathematical inconsistency to any desired order of accuracy in time. This model is applied to the simulation of rotating channel flow, and results in improved prediction of the turbulence statistics.

INTRODUCTION

The dynamic subgrid-scale stress model, introduced by Germano *et al.* [1], has been widely used for the large-eddy simulation (LES) of incompressible and compressible flows. The model is based on the introduction of two filters; in addition to the *grid* filter (denoted by an overbar), which defines the resolved and subgrid scales, a *test* filter (denoted by a circumflex) is used, whose width is larger than the grid filter width. The stress terms that appear when the grid filter is applied to the Navier-Stokes equations are the subgrid-scale (SGS) stresses τ_{ij}; in an analogous manner, the test filter defines a new set of stresses, the subtest-scale stresses T_{ij}. An identity [2] relates T_{ij} and τ_{ij} to the resolved turbulent stresses, $\mathcal{L}_{ij}$. If an eddy-viscosity model is used to parametrize τ_{ij} and T_{ij}, this identity can be exploited to determine the model coefficient.

This yields a coefficient that is function of space and time, and whose value is determined by the energy content of the smallest resolved scales, rather than input *a priori* as in the standard Smagorinsky model [3]. Two difficulties, however, arise in the determination of C: the first is that the model is ill-conditioned because the denominator of the expression for C becomes very small at a few points in the flow. Furthermore, the procedure described above is not mathematically self-consistent since it requires that a spatially-dependent coefficient be extracted from a filtering operation [4]. To overcome this problem, C is usually assumed to be only a function of time and of the spatial coordinates in inhomogeneous directions. The mathematical inconsistency is thus eliminated, and the ill-conditioning problem is alleviated.

The resulting eddy viscosity has several desirable features: it vanishes in laminar flow, it can be negative (indicating that the model is capable of predicting backscatter, i.e., energy transfer from the small to the large scales) and it has the correct asymptotic behavior near a solid boundary. The dynamic eddy viscosity model has been used successfully to solve a variety of flows such as transitional and turbulent channel flows [1, 5], and compressible isotropic turbulence [6]. Since the model coefficient adjusts itself to the energy content of the smallest resolved scales, it can also be applied to relaminarizing or intermittent flows, and has given accurate prediction of problems in which the Smagorinsky model did not work well. Esmaili and Piomelli [7], who used it in the LES of sink flows, observed that C vanishes when the boundary layer relaminarizes even if inactive fluctuations are still present. Squires and Piomelli [8] applied it to rotating flows, and found that C decreases as a result of the stabilizing effect of rotation.

Orszag *et al.* [9] moved a number of criticisms to the dynamic model; in the first place, they attributed its success in the prediction of low Reynolds number flows to the fact that it acts as a damping function for the eddy viscosity in the wall region, where, they state, the test filter width $\widehat{\Delta}$ is in the inertial range and the grid filter width $\overline{\Delta}$ is in the dissipation range; this results in $T_{ij} << \tau_{ij}$ and $< \mathcal{L}_{ij} > \simeq < \tau_{ij} > \sim y^3$ ($< \cdot >$ denotes plane-averaging). It is easy to show analytically that this statement is incorrect since, for most filters of interest, $< T_{ij} > \geq < \tau_{ij} >$ independent of the shape of the spectrum. Furthermore, in the wall region, both $\overline{\Delta}$ and $\widehat{\Delta}$ are in flat regions of the spectrum, and the ratios of $\mathcal{L}_{ij}$, T_{ij} and τ_{ij} to the resolved energy and stresses become constant [5]. Orszag and coworkers [9] also hypothesized that the model will depend very strongly on the ratio of test to grid filter width, a point that had already been addressed by Germano *et al.* [1], who showed that the model is rather insensitive to this ratio. Fi-

Paper presented at the 74th Fluid Dynamics Symposium on "Application of Direct and Large Eddy Simulation to Transition and Turbulence" held at Chania, Crete, Greece, in April 1994.

nally, they conjecture that application of the model may become problematic at high Reynolds numbers; however, Piomelli [5] and Balaras *et al.* [10] have computed channel flow at Reynolds numbers (based on channel width and bulk velocity) ranging between 5,000 and 250,000 ($200 < Re < 5,000$ based on channel halfwidth and friction velocity), obtaining results in good agreement with the data.

A limitation of the dynamic model is, however, the plane averaging mentioned above. For flows in which no homogeneous directions exist, the model coefficient should be a function of all spatial coordinates. Even flows that are homogeneous in planes parallel to the wall may be intermittent, in which case the eddy viscosity should be non-zero only in regions of significant turbulent activity, and zero elsewhere, a behavior that is not always possible if plane averaging is performed.

Although straightforward localization of the dynamic model gives rise to the problems mentioned above, it has nonetheless been used by Zang and coworkers in simulations of the turbulent flow in a driven cavity [11]. They performed some local averaging (over the test filter cell) and also constrained the total viscosity (sum of molecular and eddy viscosity) to be non-negative, thus allowing a small amount of backscatter. Since large (positive and negative) values of the eddy viscosity were observed only in the corner of the cavity, probably due to the low Reynolds number of the flow they studied, neither the local averaging nor the cutoff applied to avoid backscatter affected the results very much. In later work [12] the same authors adopted a mixed model that was also localized in a similar manner.

Ghosal and coworkers [13] recast the problem in variational form, obtaining an integral equation for C that they solved iteratively. This removed the mathematical inconsistency, but the overhead associated with the iterative solution of the integral equation could be significant. The ill-conditioning that led to locally large values of C was removed by the integral formulation, and negative values of the model coefficient were avoided by the additional constraint that $C \geq 0$. This model was used for the LES of isotropic decay [13] and to study the flow over a backward-facing step [14], with results in good agreement with DNS data.

In this paper a localized version of the dynamic model will be proposed and implemented in which the mathematical inconsistency is removed only approximately (i.e., to some order of accuracy in time). The present formulation, however, does not require any iteration; thus, its cost, in terms of CPU and memory, is essentially the same as the plane-averaged model. A small amount of backscatter will be allowed, but negative total viscosities will be avoided for numerical stability.

The new localized model will be used for the computation of rotating channel flow. System rotation has some important effects on turbulence: for instance, it inhibits energy transfer from large to small scales; this leads to a reduction in turbulence dissipation and a decrease in the decay rate of turbulence energy. Furthermore, the turbulence length scales along the rotation axis increase relative to those in non-rotating turbulence. The presence of mean shear normal to the axis of rotation may have either a stabilizing or a destabilizing effect, depending on whether the angular velocity and mean shear have the same or opposite signs. In turbulent channel flow, for example, system rotation acts to both stabilize and destabilize the flow. On the unstable side Coriolis forces resulting from system rotation enhance turbulence-producing events, leading to an increase in turbulence levels, while on the stable side Coriolis forces inhibit turbulence production and decrease turbulence levels. The increase in the component energies, however, is dependent on the rotation rate: at sufficiently high rotation rates streamwise fluctuations on the unstable channel wall are suppressed relative to the non-rotating case. The stabilizing/destabilizing effects of rotation on turbulence in channel flow make this problem an attractive test for subgrid-scale models, which are required to capture relaminarization with inactive turbulent motions as well as fully-developed turbulence.

In the next Section, the numerical method will be discussed; then the model will be presented and applied to the simulation of rotating channel flow. The results will then be discussed, and conclusions and recommendations for future work will be drawn.

NUMERICAL METHOD

In large-eddy simulations the flow variables are decomposed into a large scale (or resolved) component, denoted by an overbar, and a subgrid scale component. The large scale component is defined by the filtering operation:

$$\overline{f}(\mathbf{x}) = \int_D f(\mathbf{x}')G(\mathbf{x},\mathbf{x}')d\mathbf{x}', \qquad (1)$$

where D is the computational domain, and G is the filter function.

Appling the filtering operation to the incompressible Navier-Stokes and continuity equations yields the filtered equations of motion,

$$\frac{\partial \overline{u}_i}{\partial t} + \frac{\partial}{\partial x_j}\left(\overline{u}_i\overline{u}_j\right) = -\frac{1}{\rho}\frac{\partial \overline{p}}{\partial x_i} - \frac{\partial \tau_{ij}}{\partial x_j} + \nu\frac{\partial^2 \overline{u}_i}{\partial x_j \partial x_j} + 2\epsilon_{ij3}\Omega\overline{u}_j \qquad (2)$$

$$\frac{\partial \overline{u}_i}{\partial x_i} = 0, \qquad (3)$$

where ϵ_{ijk} is Levi-Civita's alternating tensor and Ω the angular velocity of the system. The axis of rotation is in the positive z, or x_3 direction. The subgrid-scale stresses, $\tau_{ij} = \overline{u_i u_j} - \overline{u}_i\overline{u}_j$, need to be modeled to represent the effect of the subgrid scales on the resolved field. Since the small scales tend to be more isotropic than the large scales, their effects can be

modeled by fairly simple eddy viscosity models of the form [3]

$$\tau_{ij} - \frac{\delta_{ij}}{3}\tau_{kk} = -2\nu_T \overline{S}_{ij} = -2C\overline{\Delta}^2 |\overline{S}| \overline{S}_{ij}, \qquad (4)$$

in which δ_{ij} is Kronecker's delta, $\overline{\Delta}$ is the length scale, related to the filter width (see below) and $|\overline{S}| = (2\overline{S}_{ij}\overline{S}_{ij})^{1/2}$ is the magnitude of the large-scale strain rate tensor

$$\overline{S}_{ij} = \frac{1}{2}\left(\frac{\partial \overline{u}_i}{\partial x_j} + \frac{\partial \overline{u}_j}{\partial x_i}\right). \qquad (5)$$

The trace of the subgrid-scale stresses is incorporated in the pressure term. The method used to compute the coefficient C will be described in the next section. The length scales $\overline{\Delta}$ and $\widehat{\Delta}$ are given by

$$\overline{\Delta} = (\overline{\Delta}_1\overline{\Delta}_2\overline{\Delta}_3)^{1/3}; \qquad \widehat{\Delta} = (\widehat{\Delta}_1\widehat{\Delta}_2\widehat{\Delta}_3)^{1/3}, \qquad (6)$$

where $\overline{\Delta}_i$ is the grid spacing in the i-th direction, and $\widehat{\Delta}_1 = 2\overline{\Delta}_1$, $\widehat{\Delta}_2 = \overline{\Delta}_2$, $\widehat{\Delta}_3 = 2\overline{\Delta}_3$. In addition to the definitions given in (6), the length scale proposed by Scotti *et al.* [17] has also been used in this work; this length scale includes a correction evaluated semi-analitically to account for grid anisotropy:

$$\overline{\Delta} = f(a_2, a_3)\left[\overline{\Delta}_1\overline{\Delta}_2\overline{\Delta}_3\right]^{1/3}, \qquad (7)$$

(where $a_i = \overline{\Delta}_i/\overline{\Delta}_1$, $i = 2, 3$); a similar expression holds for $\widehat{\Delta}$. In the present work the approximate form of the correction,

$$f(a_2, a_3) = \cosh\left\{\frac{4}{27}\left[(\ln a_2)^2 - 2\ln a_2 \ln a_3 + (\ln a_3)^2\right]\right\}^{1/2} \qquad (8)$$

is used; it was found to vary between 1 (at the channel centerline) and 2.5 (near the wall).

The governing equations (2) and (3) are integrated in time using a Fourier-Chebychev pseudospectral collocation scheme [18]. The skew-symmetric form of the momentum equation (2) is employed, and the time-advancement is performed by a fractional time step method with a semi-implicit scheme; the wall-normal diffusion term is advanced using the Crank-Nicolson scheme, and the remaining terms by a low-storage third-order Runge-Kutta scheme. Periodic boundary conditions are applied in the streamwise (x) and spanwise (z) directions, and no-slip conditions at the solid walls. No dealiasing is performed. The computational domain in the streamwise, wall-normal and spanwise directions was $4\pi\delta \times 2\delta \times 4\pi\delta/3$ (where δ is the channel halfwidth). All LES calculations used $32\times65\times48$ mesh points, a grid significantly coarser than those used in previous simulations of similar flows.

APPROXIMATE LOCALIZATION

The dynamic model is based on an identity relating the resolved turbulent stresses $\mathcal{L}_{ij} = \widehat{\overline{u}_i\overline{u}_j} - \widehat{\overline{u}}_i\widehat{\overline{u}}_j$ to the subgrid- and subtest-scale stresses [2]:

$$\mathcal{L}_{ij} = T_{ij} - \widehat{\tau_{ij}}, \qquad (9)$$

where $T_{ij} = \widehat{\overline{u}_i\overline{u}_j} - \widehat{\overline{u}}_i\widehat{\overline{u}}_j$. The subgrid- and subtest-scale stresses are then parameterized by eddy viscosity models of the form (4):

$$\tau_{ij} - \frac{\delta_{ij}}{3}\tau_{kk} = -2C\overline{\Delta}^2|\overline{S}|\overline{S}_{ij} = -2C\beta_{ij}, \qquad (10)$$

$$T_{ij} - \frac{\delta_{ij}}{3}T_{kk} = -2C\widehat{\Delta}^2|\widehat{\overline{S}}|\widehat{\overline{S}}_{ij} = -2C\alpha_{ij}. \qquad (11)$$

Substituting (10) and (11) into (9) yields

$$\mathcal{L}^a_{ij} = \mathcal{L}_{ij} - \frac{\delta_{ij}}{3}\mathcal{L}_{kk} = -2C\alpha_{ij} + 2\widehat{C\beta_{ij}}. \qquad (12)$$

This is a set of five independent equations that cannot be solved explicitly for C, which appears inside a filtering operation. If, however, one assumes that $C = C(y,t)$, then $\widehat{C\beta_{ij}} = C\widehat{\beta_{ij}}$. The sum of the squares of the residual,

$$E_{ij} = \mathcal{L}^a_{ij} + 2C\alpha_{ij} - 2C\widehat{\beta_{ij}}, \qquad (13)$$

can then be minimized by contracting both sides of (12) with $\alpha_{ij} - \widehat{\beta_{ij}}$ to yield [19]:

$$C(y,t) = -\frac{1}{2}\frac{<\mathcal{L}^a_{ij}(\alpha_{ij} - \widehat{\beta}_{ij})>}{<(\alpha_{mn} - \widehat{\beta}_{mn})(\alpha_{mn} - \widehat{\beta}_{mn})>}, \qquad (14)$$

where $<\cdot>$ denotes plane-averaging. This form of the coefficient has been widely used in LES calculations. In studies of homogeneous isotropic turbulence, averaging is performed over the entire computational domain, and $C = C(t)$ only, whereas averaging over the spanwise direction is used for spatially-developing flows.

As mentioned above, a straightforward localization of the model was used in references [11] and [12], in which C was given by (14) with the plane-averaging replaced by a local average over the test filter cell. The problem of the mathematical inconsistency of the localized application of (14) is not addressed in that work, but the results are in good agreement with experimental data; however, the Reynolds number of those calculations is quite low, and the SGS contribution to the stresses is rather small, which makes it difficult to draw definite conclusions from those simulations.

Ghosal and coworkers [13] noted that, if C is assumed to be fully dependent on space, the residual cannot be minimized in the least-squares sense locally; therefore, they introduced a constrained variational problem consisting of the minization of the integral of the square of the sum of the residuals over the entire domain, with the additional constraint that C be non-negative. The result was of the form of Fredholm's integral equation of the second kind, that they

solved iteratively using under-relaxation to improve convergence.

In the present work a simpler approach is taken: the expression (12) is recast in the form

$$-2C\alpha_{ij} = \mathcal{L}^a_{ij} - \widehat{C^*\beta_{ij}}, \qquad (15)$$

where on the right-hand-side an estimate of the coefficient, denoted by C^* and assumed to be known, is used. Since C^* is known, the sum of the squares of the residual can now be minimized locally; the contraction that minimizes it, in this case, is:

$$C = -\frac{1}{2}\frac{\left(\mathcal{L}^a_{ij} - \widehat{C^*\beta_{ij}}\right)\alpha_{ij}}{\alpha_{mn}\alpha_{mn}}. \qquad (16)$$

The denominator of (16) is positive definite, like that of (14), but has the advantage that it does not involve a difference between two terms of the same order of magnitude. In wall-bounded flows, $\alpha_{mn}\alpha_{mn}$ becomes small only where the mean shear vanishes (in the freestream of a boundary layer, for example); the numerator is also expected to vanish there. In these regions, moreover, the flow is essentially uniform, so that spurious high values of C obtained from the ratio of very small numbers do not result in large values of the eddy viscosity or of the SGS stresses.

There are various ways to obtain C^* at timestep n:

1. Use the value at the previous timestep:
$$C^* = C^{n-1}. \qquad (17)$$
2. Estimate the value at the present timestep by some backward extrapolation scheme:
$$C^* = C^{n-1} + \Delta t \left.\frac{\partial C}{\partial t}\right|_{n-1} + \ldots \qquad (18)$$
3. Use an iterative scheme: set $C^* = C^{n-1}$ and calculate the left-hand-side of (16); then replace C^* with the newly obtained value and repeat the procedure until convergence to the desired order of accuracy is reached.

In this work, the second approach will be taken; a first-order extrapolation schemes will be used in which $\partial C/\partial t|_{n-1}$ is evaluated using an explicit Euler scheme:

$$\left.\frac{\partial C}{\partial t}\right|_{n-1} = \frac{C^{n-1} - C^{n-2}}{t_{n-1} - t_{n-2}}, \qquad (19)$$

which gives

$$C^* = C^{n-1} + \frac{t_n - t_{n-1}}{t_{n-1} - t_{n-2}}\left(C^{n-1} - C^{n-2}\right). \qquad (20)$$

Equation (17) will be referred to as the "zeroth-order approximation", equation (20) as the "first-order approximation". No attempt was made to use higher-order schemes, since little difference was observed between the results obtained with the first- and zeroth-order approximations.

Use of an extrapolation scheme such as the one proposed here contains some inherent dangers: numerical instabilities are possible, and the difference between C^* and the actual value C^n could be quite large if C varied on a short time-scale. In practice, however, C is a fairly slowly-varying function of time because of the temporal filtering introduced implicitly by the spatial filtering. By eliminating the smallest scales of motion, the highest frequencies are also filtered out. Typically, the time-scale of the structures whose length scale is the filter width is 5 to 10 times larger than the timestep, and this results in long correlation times for C [20].

The coefficient C obtained from (17) or (20) can be either positive or negative. Since negative total viscosities that are correlated over long times can lead to numerical instabilities, the total viscosity was constrained to be non-negative.

RESULTS AND DISCUSSION

Calculations were performed for a Reynolds numbers $Re_b = U_b(2\delta)/\nu = 5700$ (based on the channel width, 2δ, and bulk velocity, U_b), and for a range of

Table 1: Summary of the numerical calculations.

Case	Re_τ	Ro_τ	Ro_b	Model	Length scale
0	177	1.14	0.144	DNS	
1	192	0.00	0.000	Eqn. (16), (18)	Eqn. (6)
2	185	0.54	0.069	Eqn. (16), (18)	Eqn. (6)
3	176	1.17	0.144	Eqn. (16), (18)	Eqn. (6)
4	185	1.63	0.210	Eqn. (16), (18)	Eqn. (6)
5	181	1.14	0.144	Eqn. (14)	Eqn. (6)
6	175	1.18	0.144	Eqn. (16), (17)	Eqn. (6)
7	177	1.17	0.144	Eqn. (16), (18)	Eqn. (7)

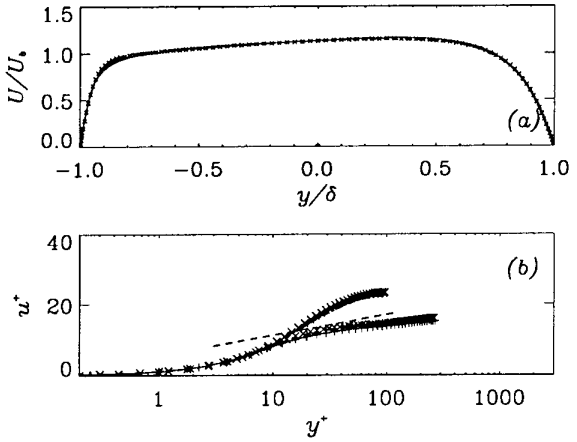

Figure 1: Mean velocity in the rotating channel. $Re_b = 5,700$, $Ro_b = 0.144$. —— First-order; --- zeroth order; —·— SML length scale; ····· plane-averaged; × DNS. (a) global coordinates; (b) wall coordinates.

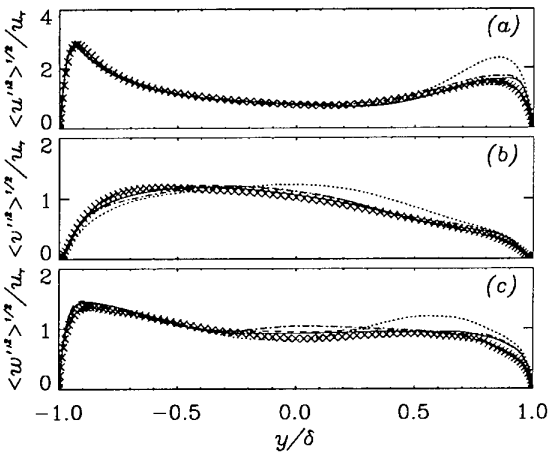

Figure 2: Turbulence intensities in the rotating channel. $Re_b = 5,700$, $Ro_b = 0.144$. —— First-order; --- zeroth order; —·— SML length scale; ····· plane-averaged; × DNS. (a) u; (b) v; (c) w.

rotation numbers $Ro_b = \Omega(2\delta)/U_b$. A summary of the calculations is shown in Table 1. The initial conditions for the cases with non-zero rotation rates were obtained from equilibrium cases at $\Omega = 0$, and were in very good agreement with experimental and DNS data [5]. After rotation was applied the simulations were integrated forward in time to a new steady state, statistics being obtained by averaging over at least 4 dimensionless time units tu_τ/δ. Experimental measurements in this flow exist [15] but at higher Reynolds numbers, whereas a series of DNS calculations was performed by Kristoffersen and Andersson [16] that span the range of Re_b and Ro_b examined in this work. A direct simulation of the intermediate ($Ro_b = 0.144$) case was also performed to compare with the LES results. The DNS used 128×129×128 grid points, and was in very good agreement with the DNS results of Ref. [16].

The mean velocity profiles for cases 3 through 6 (i.e., the calculations for $Re_b = 5,700$ and $Ro_b = 0.144$) are compared with DNS data in Figure 1. Very little difference can be observed between the various results. The localized models, however, give better prediction of the turbulent fluctuations $u_i'' = \overline{u}_i - < \overline{u}_i >$ (where $< \cdot >$ from here on denotes averaging over planes parallel to the wall and time), than the plane-averaged model, especially on the stable side of the channel (Figure 2). The localized models are slightly more dissipative than the plane-averaged one (in which backscatter acts to lower the plane-averaged C). This results in better prediction of the quasi-laminar flow on the stable side.

The average values of C are shown in Figure 3. There is very little difference between the zeroth- and first-order approximations. The length scale proposed in Ref. [17] results in smaller values of C, only partially offset by the larger length scale $f\overline{\Delta}$; the model is less dissipative than the ones with the standard length scale, as evidenced by the higher levels of u'' turbulent fluctuations near the stable wall and of w'' in the

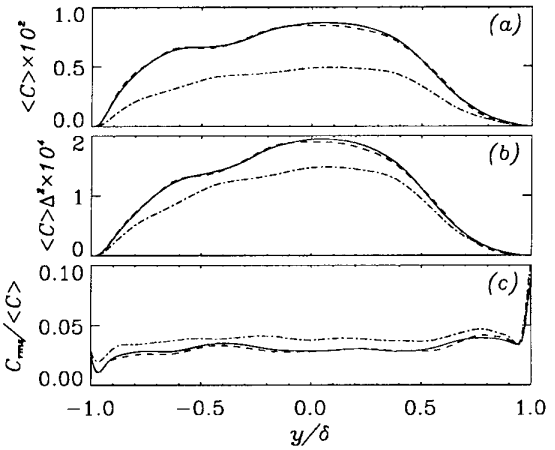

Figure 3: Average model coefficient. $Re_b = 5,700$, $Ro_b = 0.144$. —— Case 3; --- case 5; —·— case 6. (a) $< C >$; (b) $< C > \overline{\Delta}^2$; (c) rms difference.

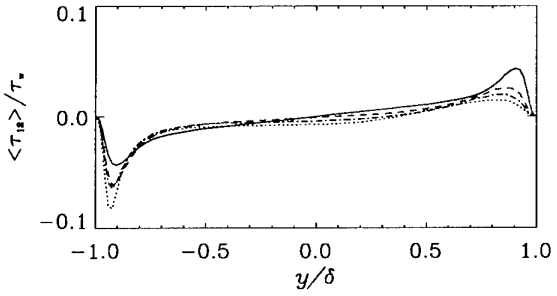

Figure 4: Subgrid-scale stresses τ_{12}. $Re_b = 5,700$. —— $Ro_b = 0$; - - - $Ro_b = 0.069$; —·— $Ro_b = 0.144$; ····· $Ro_b = 0.21$.

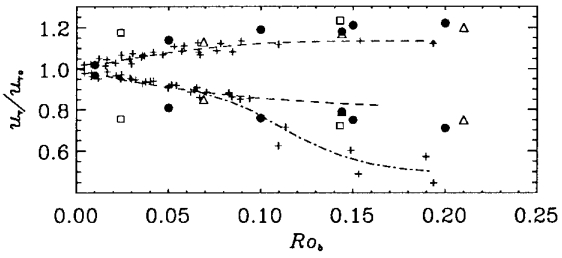

Figure 5: Friction velocity on the two sides of the channel. + Experiments; • DNS; □ LES, Ref. [21]; △ LES, present calculation.

channel center that can be observed in Figure 2. The rms difference between the predicted coefficient C^* and the actual value C^n is also shown in Figure 3c (normalized by the average C). The difference is fairly small (less than 5%) throughout the channel, except on the stable side, where it increases because of the low value of $< C >$; almost no difference can be observed between the zeroth-and first-order approximations.

The average value of C is lower on the unstable than on the stable side, as expected. The maximum value of C corresponds to a Smagorinsky constant $C_s \simeq 0.1$; the SGS stresses on the unstable side (Figure 4) are slightly larger than in the zero rotation rate (about 10% of the resolved ones, vs. 8% in the no-rotation case) while on the stable side they are about half the value they have when no rotation is applied. As the rotation number is increased, the SGS stress decreases on the unstable side and increases on the stable side, but it never vanishes entirely as it would if the flow relaminarized completely.

Full relaminarization on the stable side was observed in experiments [15] and in the LES calculations of Tafti and Vanka [21]; in the DNS calculations of Kristoffersen and Andersen [16] and in the present ones, however, the fluctuations on the stable side remained significant, and the mean velocity never reached the laminar profile, even at large rotation rates and at a Reynolds number at which relaminarization is expected to occur. The friction velocity u_τ normalized by the friction velocity in the absence of rotation $u_{\tau o}$, is plotted in Figure 5 (the results of the numerical calculations are also tabulated in Table 2).

The LES, DNS and experimental data are in good agreement on the unstable side; in the experiment the bulk velocity was obtained from the volume flow rate, which led to underestimation of the bulk velocity (and an overestimation of Ro_b) because of the presence of boundary layers on the sides of the channel (see also [16]).

A more significant difference can be observed on the stable side, where the numerical results tend to lie close to the extrapolation of the results of experiments in which the flow remained turbulent on the stable side (the dashed line), and are significantly higher than those for fully relaminarized flow (the chain-dot line). Possible reasons for the difference between the experimental and DNS results on the stable side are the relatively small aspect ratio of the experimental apparatus and the fact that the flow was not fully developed, which may have added a streamwise pressure gradient that could have increased the tendency of the flow towards relaminarization. The results obtained with the dynamic model are in much better agreement with the DNS results than those obtained by Tafti and Vanka [21] with the Smagorinsky model, which tended to overdamp the fluctuations on the stable side, leading to excessively low wall stress even at the lower rotation rate they examined.

Table 2: Normalized friction velocity $u_\tau/u_{\tau,o}$ on the unstable and stable side.

Case	Ro_b	Unstable	Stable	Model	Length scale
0	0.144	1.17	0.80	DNS	
1	0.000	1.00	1.00	Eqn. (16), (18)	Eqn. (6)
2	0.069	1.13	0.85	Eqn. (16), (18)	Eqn. (6)
3	0.144	1.17	0.79	Eqn. (16), (18)	Eqn. (6)
4	0.210	1.20	0.75	Eqn. (16), (18)	Eqn. (6)
5	0.144	1.15	0.82	Eqn. (14)	Eqn. (6)
6	0.144	1.18	0.77	Eqn. (16), (17)	Eqn. (6)
7	0.144	1.17	0.80	Eqn. (16), (18)	Eqn. (7)

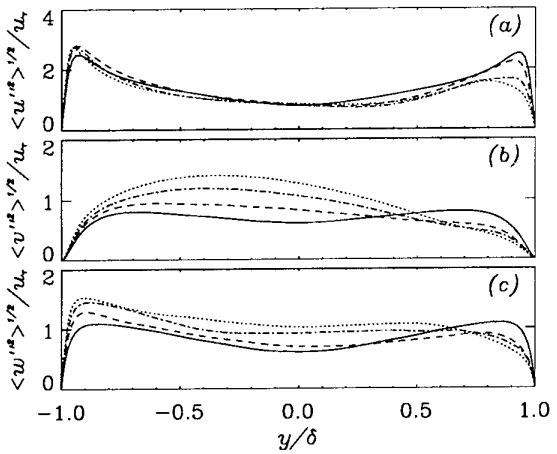

Figure 6: Turbulence intensities in the rotating channel. —— $Ro_b = 0.0$, --- $Ro_b = 0.069$, —·— $Ro_b = 0.144$, ····· $Ro_b = 0.210$. (a) u; (b) v; (c) w.

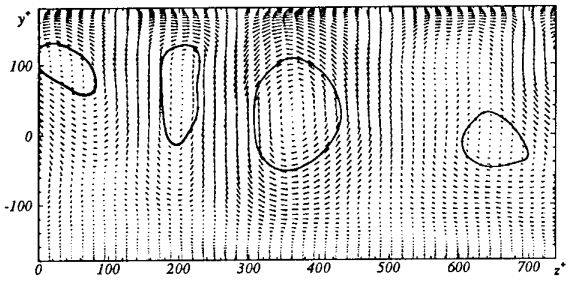

Figure 7: Averaged velocity vectors in the yz-plane at $tu_\tau/\delta \simeq 6$, $Ro_b = 0.210$. Streamlines are used to visualize the roll cells.

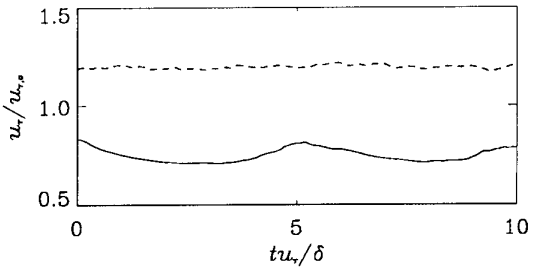

Figure 8: History of the friction velocity on the upper and lower walls. $Ro_b = 0.210$. —— Stable wall, --- unstable wall.

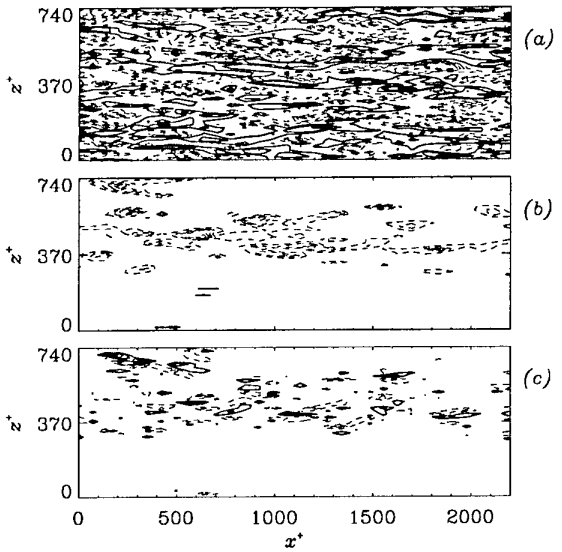

Figure 9: Velocity fluctuation contours in the xz-plane. $Ro_b = 0.210$, $tu_\tau/\delta \simeq 5$. (a) u'' at $y^+ = 3.5$, unstable wall; (b) u'' at $y^+ = 3.5$, stable wall; (c) v'' at $y^+ = 3.5$, stable wall. Contour lines are at intervals of ± 1 in parts (a) and (b), ± 0.07 in part (c). Dashed lines indicate negative contours.

The turbulence intensities normalized by the average shear velocity for various rotation rates are shown in Figure 6. The DNS results of [16] show that, on the unstable side, the peak rms streamwise fluctuation is maximum for $Ro_b \simeq 0.1$ and then decreases; the present calculations show the same trend.

At the high rotation rates the formation of roll cells, which has been observed in experiments and numerical simulations, is quite evident. Usually, two strong cells could be observed accompanied, sometimes, by two weaker ones. In Figure 8 the average velocity vectors in the xy planes are shown, averaged over the streamwise directions and 2 realizations.

The vortical structures tend to drift both in the y and z directions. The vortices convect high momentum fluid in the downwash region between them, and, as they drift towards the stable wall, the wall stress there can fluctuate significantly. While on the unstable wall the friction velocity (Figure 8) is nearly constant in time, on the stable wall it exhibits an oscillations with a period of about 4 tu_τ/δ time units, and with significant amplitude.

Figure 9 shows contours of the u'' and v'' velocity fluctuations in two xz-planes near the unstable and stable walls. The downwash of the roll cells appears as an elongated region of increased u'' and v'' velocity fluctuations at $z^+ \simeq 400$. On the unstable side the elongated streaky structure typical of wall bounded flows is present, and little effect of the vortices can be observed. When the roll cells move away from the stable wall, the fluctuations in the near-wall layer become extremely small (Figure 10). The flow on the unstable side, however, is not affected much by the roll cell motions.

CONCLUDING REMARKS

A new localization procedure for the dynamic eddy-viscosity model has been proposed. The localization is only approximate, in the sense that it is based on a Taylor series expansion of the model coefficient in time, in which the time derivatives are evaluated numerically. Nonetheless, it results in more accurate results compared with the plane-averaged formulation of the model. The localization proposed here, moreover, is better conditioned than the original for-

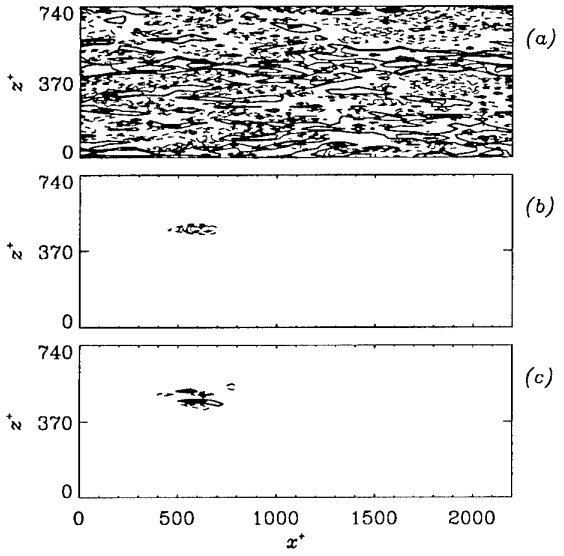

Figure 10: Velocity fluctuation contours in the xz-plane. $Ro_b = 0.210$, case 4, $tu_\tau/\delta \simeq 8$. (a) u'' at $y^+ = 3.5$, unstable wall; (b) u'' at $y^+ = 3.5$, stable wall; (c) v'' at $y^+ = 3.5$, stable wall. Contour lines are at intervals of ± 1 in parts (a) and (b), ± 0.07 in part (c). Dashed lines indicate negative contours.

mulation, and does not result in numerical instabilities.

The proposed localization has been tested by computing the flow in a rotating channel. Although the grids used are very coarse, the localized model predicts statistics in good agreement with DNS data; some discrepancy between all the numerical results (both DNS and LES) and the experiments can be explained based on the different boundary conditions. First-order accurate localization, which can be performed without any increase in cost or memory, appears to be sufficient to reduce the mathematical inconsistency to acceptable levels.

The vortical structures characteristic of rotating flows of this type were captured. Their time evolution has significant effects on the flow field, especially on the stable side of the channel.

ACKNOWLEDGMENTS

Research supported by the Office of Naval Research under Grant N00014-89-J-1638. The computer time was supplied by the Pittsburgh Supercomputing Center.

REFERENCES

[1] Germano, M., Piomelli, U., Moin, P., and Cabot, W.H. "A dynamic subgrid-scale eddy viscosity model." *Phys. Fluids A* **3** 1760, 1991.

[2] Germano, M. "Turbulence: the filtering approach." *J. Fluid Mech.* **238** 325, 1992.

[3] Smagorinsky, J. "General circulation experiments with the primitive equations. I. The basic experiment." *Monthly Weather Review* **91** 99, 1963.

[4] Cabot, W.H. and Moin, P. "Large eddy simulation of scalar transport with the dynamic subgrid-scale model." In *Large Eddy Simulation of Complex Engineering and Geophysical Flows*, ed. by B. Galperin and S.A. Orszag, (Cambridge University Press, Cambridge) 141, 1993.

[5] Piomelli, U. "High Reynolds number calculations using the dynamic subgrid-scale stress model. " *Phys. Fluids A* **5** 1484, 1993.

[6] Moin, P., Squires, K.D., Cabot, W.H. and Lee, S. "A dynamic subgrid-scale model for compressible turbulence and scalar transport." *Phys. Fluids A* **3** 2746, 1991.

[7] Esmaili, H. and Piomelli, U. "Large-eddy simulation of relaminarizing sink flow boundary layers." In *Near-Wall Turbulent Flows*, ed. by R.M.C. So, C.G. Speziale and B.E. Launder, (Elsevier, Amsterdam) 287, 1993.

[8] Squires, K.D. and Piomelli, U. "Dynamic modeling of rotating turbulence." In press, *Turbulent Shear Flows 9*, edited by F. Durst, N. Kasagi, B.E. Launder, F.W. Schmidt and J.H. Whitelaw, (Springer Verlag, Heidelberg), 1994.

[9] Orszag, S.A., Staroselsky, I., and Yakhot, V.Y. "Some basic challenges for large eddy simulation research." In *Large Eddy Simulation of Complex Engineering and Geophysical Flows*, ed. by B. Galperin and S.A. Orszag, (Cambridge University Press, Cambridge) 55, 1993.

[10] Balaras, E., Benocci, C., and Piomelli, U. "Finite difference computations of high Reynolds number flows using the dynamic subgrid-scale model." Submitted to *Theoret. Comput. Fluid Dyn.*, 1994.

[11] Zang, Y., Street, R.L., and Koseff, J. "Application of a dynamic subgrid-scale model to turbulent recirculating flows." *CTR Annual Research Briefs*, Center for Turbulence Research, Stanford University 85, 1993.

[12] Zang, Y., Street, R.L., and Koseff, J. "A dynamic mised subgrid-scale model and its application to turbulent recirculating flows." *Phys. Fluids A* **5** 3186, 1993.

[13] Ghosal, S., Lund, T.S., and Moin, P. "A local dynamic model for LES." *CTR Annual Research Briefs*, Center for Turbulence Research, Stanford University 3, 1993.

[14] Akselvoll, K. and Moin, P. "Application of the dynamic localization model to large-eddy simulation of turbulent flow over a backward facing step." In *Engineering Applications of Large*

Eddy Simulations-1993, ed. by S.A. Ragab and U. Piomelli, (The American Society of Fluids Engineering, New York) 1, 1993.

[15] Johnston, J.P., Halleen, R.M., and Lezius, D.K. "Effects of spanwise rotation on the structure of two-dimensional fully developed turbulent channel flow." *J. Fluid Mech.* **56** 533, 1972.

[16] Kristoffersen, R. and Andersson, H.I. "Direct simulation of low Reynolds number turbulent flow in a rotating channel." Submitted to *J. Fluid Mech.*, 1993.

[17] Scotti, A., Meneveau, C., and Lilly, D.K. "Generalized Smagorinsky model for anisotropic grids." *Phys. Fluids A* **5** 2306, 1993.

[18] Zang, T.A. and Hussaini, M.Y. "On spectral multigrid methods for the time-dependent Navier-Stokes equations." *Appl. Math. Comp.* **19** 359, 1986.

[19] Lilly, D.K, "A proposed modification of the Germano subgrid-scale closure method." *Phys. Fluids A* **4**, 633, 1992.

[20] Lund, T., Ghosal, S., and Moin, P. "Numerical experiments with highly-variable eddy viscosity models." In *Engineering Applications of Large Eddy Simulations-1993*, ed. by S.A. Ragab and U. Piomelli, (The American Society of Fluids Engineering, New York) 7, 1993.

[21] Tafti, D.K. and Vanka, S.P. " A numerical study of the effects of spanwise rotation on turbulent channel flow." *Phys. Fluids A* **3** 642, 1991.

THE ASYMPTOTIC STATE OF ROTATING HOMOGENEOUS TURBULENCE AT HIGH REYNOLDS NUMBERS

Kyle D. Squires*, Jeffrey R. Chasnov†,
Nagi N. Mansour‡ & Claude Cambon§
Center for Turbulence Research
Stanford University
Stanford, CA 94305, USA

ABSTRACT

The long-time, asymptotic state of rotating homogeneous turbulence at high Reynolds numbers has been examined using large-eddy simulation of the incompressible Navier-Stokes equations. The simulations were carried out using $128 \times 128 \times 512$ collocation points in a computational domain that is four times longer along the rotation axis than in the other directions. Subgrid-scale motions in the simulations were parameterized using a spectral eddy viscosity modified for system rotation. Simulation results show that in the asymptotic state the turbulence kinetic energy undergoes a power-law decay with an exponent which is independent of rotation rate, depending only on the low-wavenumber form of the initial energy spectrum. Integral lengthscale growth in the simulations is also characterized by power-law growth; the correlation length of transverse velocities exhibiting much more rapid growth than observed in non-rotating turbulence.

INTRODUCTION AND BACKGROUND

Study of turbulent flows in rotating reference frames has long been an area of considerable scientific and engineering interest. Because of its importance, the subject of turbulence in rotating reference frames has motivated over the years a large number of theoretical, experimental, and computational studies. The bulk of these studies have served to demonstrate that the effect of system rotation on turbulence is subtle and remains exceedingly difficult to predict. For example, it is well recognized that the standard models for the dissipation rate of the turbulent kinetic energy do not accurately predict the effects of system rotation. Yet, these models are widely used in engineering predictive schemes for technologically important areas such as turbomachinery and rotorcraft aerodynamics.

A rotating flow of particular interest in many studies, including the present work, is examination of the effect of steady system rotation on the evolution of an initially isotropic turbulent flow. Aside from the simplifications associated with analysis and computation of homogeneous flows, one of the principal reasons for the interest in this problem is that solid-body rotation of initially isotropic turbulence represents the most basic turbulent flow whose structure is altered by system rotation but without the complicating effects introduced by mean strains or flow inhomogeneities.

For initially isotropic turbulence it is well known that solid-body rotation inhibits the non-linear cascade of energy from large to small scales. Consequently, the turbulence dissipation rate is reduced relative to non-rotating flows and there is an associated decrease in the decay rate of turbulence kinetic energy [1], [2], [3], [4]. Some computations and experiments have also noted an increase in the integral lengthscales along the rotation axis relative to non-rotating turbulence [5], [6], [7], [8]. Increase in the integral lengthscales has been thought by some to be a prelude to a Taylor-Proudman reorganization to two-dimensional turbulence. However, direct numerical simulation (DNS) has demonstrated that, for very rapid rates of rotation, initially isotropic turbulence remains isotropic and three dimensional [3]. The results in Ref. [3] confirm the essential role of nonlinear interactions for the transition towards two-dimensional turbulence to occur; such a transition, first studied using a spectral approach, can be started only for intermediate Rossby numbers at sufficiently large Reynolds numbers [6], [9].

While some of the effects summarized above are reasonably well documented, e.g., reduction in the decay rate of turbulence kinetic energy, other features of rotating flows are less well resolved, e.g., the behavior of the integral scales. There are also other fundamentally important questions associated with rotating turbulence which cannot be resolved from previous investigations. For example, while the decrease

*University of Vermont, Burlington, VT, USA
†The Hong Kong University of Science and Technology, Clear Water Bay, Hong Kong
‡NASA Ames Research Center, Moffett Field, CA, USA
§Ecole Centrale de Lyon, Ecully Cedex, France

Paper presented at the 74th Fluid Dynamics Symposium on "Application of Direct and Large Eddy Simulation to Transition and Turbulence" held at Chania, Crete, Greece, in April 1994.

in the kinetic energy power-law exponent relative to non-rotating turbulence is clear, the actual value is unknown (nor even its dependence on the rotation rate). It is not possible to determine, based upon previous work, whether the effects of rotation on initially isotropic turbulence are transient in nature or an inherent property of rotating flows. Such issues can only be resolved through an examination of the asymptotic state of rotating turbulence; i.e., its long-time evolution. Recent large-eddy simulations of (non-rotating) high Reynolds number isotropic turbulence have demonstrated the universal nature of the flow at long evolution times, including the existence of asymptotic similarity states [10]. It is extension of the ideas in Ref. [10] to rotating turbulence which has been the primary interest of the present work. Knowledge of the asymptotic state of rotating homogeneous turbulence at high Reynolds numbers is further motivated since it will also determine the asymptotic state that engineering turbulence models should yield.

Therefore, the objective of this work has been to examine the long-time evolution of rotating homogeneous turbulence. Of particular interest is the quantification of the asymptotic state at high Reynolds numbers. Important issues in this regard include determining whether the turbulence kinetic energy and integral lengthscales evolve as power laws and, if so, the appropriate exponents for rotating flows. While the power-law decay of the kinetic energy in non-rotating isotropic turbulence is widely accepted, the asymptotic decay of kinetic energy in rotating turbulence is unknown. The behavior of the integral lengthscales at long times in the evolution of rotating flows is also not clear. As discussed above, some previous work suggests an increased growth rate of the integral scales along the rotation axis relative to non-rotating isotropic turbulence. As with the kinetic energy decay, however, it is not clear if this is an effect inherent to rotating flows. Asymptotic power-law behavior of the kinetic energy and integral scales imply the possible existence of similarity states, analogous to those found in the non-rotating flow [10]. Existence of asymptotic similarity states would be of considerable interest since it would permit prediction of the statistical evolution of rotating flows at high Reynolds numbers without requiring knowledge of the complex, and not well understood, non-linear transfer processes.

Large-eddy simulation (LES) is ideally suited for examination of the long-time evolution of rotating homogeneous turbulence. Unlike direct numerical simulation, LES is not restricted to low Reynolds numbers. Aside from the Reynolds number restriction, DNS is further limited to the initial evolution of rotating flows. The need for high Reynolds numbers and long time integrations, as can be obtained using LES, is further motivated by previous studies [3], [6], [9], [10]. The principal drawback to the use of LES is that it requires use of a model to parameterize subgrid-scale stresses. However, in a decaying homogeneous turbulence, the dominant non-linear transfer is from large to small scales so that large-scale statistics may not be unduly influenced by the errors in a small-scale subgrid model.

The governing equations and an overview of the simulations are provided in the following section. Results from the simulations are then discussed and a summary of the work is contained in the final section.

SIMULATION OVERVIEW

In the present study the filtered Navier-Stokes equations for an incompressible fluid were solved in a rotating reference frame:

$$\nabla \cdot \mathbf{u} = 0 \tag{1}$$

$$\frac{\partial \mathbf{u}}{\partial t} + \mathbf{u} \cdot \nabla \mathbf{u} = -\frac{1}{\rho}\nabla p - \nabla \cdot \boldsymbol{\tau} + \nu \nabla^2 \mathbf{u} - 2\boldsymbol{\Omega} \times \mathbf{u} . \tag{2}$$

In (1) and (2), $\mathbf{u}$ is the (filtered) velocity vector, p and ρ the fluid pressure and density, respectively, and ν the kinematic viscosity. The Coriolis term in (2) accounts for reference frame rotation, the rotation vector is denoted $\boldsymbol{\Omega}$ and, for the purposes of discussion, is considered to act along the z or "vertical" axis, $\boldsymbol{\Omega} = (0, 0, \Omega)$. Filtering of the convective terms yields the subgrid-scale stress $\boldsymbol{\tau}$ in (2) and this term requires a model in order to represent the effect of subgrid-scale motions on the resolved scales.

In this work the subgrid-scale stresses have been parameterized in the Fourier space using a spectral eddy viscosity which accounts for system rotation. The form of the eddy viscosity for non-rotating turbulence is [11]:

$$\nu_e(k|k_m, t) = \left[0.145 + 5.01 \exp\left(\frac{-3.03 k_m}{k}\right)\right] \times \left[\frac{E(k_m, t)}{k_m}\right]^{1/2} \tag{3}$$

where ν_e is the eddy viscosity, k_m the maximum wavenumber magnitude of the simulation and $E(k,t)$ is the spherically integrated three-dimensional Fourier transform of the co-variance $\frac{1}{2}\langle u_i(\mathbf{x},t) u_i(\mathbf{x}+\mathbf{r},t)\rangle$ ($\langle\cdot\rangle$ denotes a volume average). In this work the eddy viscosity ν_e has been modified to account for the weakening of the energy cascade in a rotating turbulence:

$$\nu_\Omega = \nu_e f(\alpha) . \tag{4}$$

In (4), ν_Ω is the eddy viscosity in rotating turbulence with the function $f(\alpha)$ accounting for the reduction by system rotation. Using an EDQNM model modified to take into account the effect of rotation on the energy cascade [12], it is possible to calculate the factor $f(\alpha)$ (see Ref. [13], later corrected by [14]):

$$f(\alpha) = \frac{2\left[(1+\alpha^2)^{3/2} - \alpha^3 - 1\right]}{3\alpha^2} \tag{5}$$

where

$$\alpha = \frac{8\Omega^2}{3E(k_m)k_m^3} . \tag{6}$$

As can be seen from (5) and (6), the eddy viscosity is reduced for increasing Ω. It is also worth noting that (4)-(6) yields an expression similar in form to the reduction in velocity derivative skewness by rotation found in Ref. [3] using DNS of rotating isotropic turbulence. Some comparisons between different subgrid models (including a dynamic model [4]) and the one used in this study (4), (5), and (6) are reported in [15].

The initial energy spectrum of the simulations was of the form

$$E(k,0) = \frac{1}{2} C_s \frac{u_0^2}{k_p} \left(\frac{k}{k_p}\right)^s \exp\left[-\frac{1}{2} s \left(\frac{k}{k_p}\right)^2\right], \tag{7}$$

where C_s is given by

$$C_s = \sqrt{\frac{2}{\pi}} \frac{s^{\frac{1}{2}(s+1)}}{1 \cdot 3 \cdot \ldots \cdot (s-1)} \tag{8}$$

and k_p is the wavenumber at which the initial energy spectrum is maximum. In this study simulations with $s = 2$ and $s = 4$ were performed, corresponding to the initial energy spectrum having a low wavenumber form proportional to either k^2 or k^4.

Because the principal interest of this work was examination of the long-time evolution of rotating homogeneous turbulence, it was necessary to use as large a value of k_p as possible in order that the flow evolution not be adversely affected by the periodic boundary conditions used in the simulations. Adverse affects occur when the integral lengthscales of the flow become comparable to the box size. Another important consideration in these simulations was the aspect ratio of the computational domain. Because of the rapid growth of the integral scales along the direction of the rotation axis, it was necessary to use a computational box which was longer along the rotation axis than in the other directions. Preliminary calculations of rotating turbulence on cubic domains demonstrated a relatively rapid degradation in the integral scales in the vertical direction because of periodic boundary conditions. Numerical experiments showed that it was optimal to use a computational box which was four times longer along the rotation axis than in the directions orthogonal to the rotation vector. Four times as many collocation points were used in the vertical direction in order to avoid any effects of grid anisotropy at the smallest resolved scales.

Simulations were performed using resolutions of $128 \times 128 \times 512$ collocation points. The governing equations (1) and (2) were solved using a pseudo-spectral method [16]. The length of the computational box along the vertical axis was $\sqrt[3]{128}\pi$, corresponding to a minimum wavenumber of 0.397 and maximum of 95. The lengths of the computational volume in the horizontal plane (orthogonal to the rotation axis) were $\sqrt[3]{2}\pi$, corresponding to a minimum wavenumber of 1.587 and maximum of 95. The initial root-mean-square velocity fluctuation u_0 in (7) was equal to 1/2 and the wavenumber at which the initial spectrum was initially maximum, k_p, was 75. The initial energy spectrum was set to zero for wavenumbers greater than 93 to allow the subgrid-scale eddy viscosity to build up from zero values. For each spectrum type, i.e., low wavenumber part proportional to k^2 or k^4, simulations were performed with $\Omega = 0$, 0.5, and 1.0.

Finally, it is also noted that statistics from simulations performed on a domain having resolutions of $96 \times 96 \times 384$ collocation points were in good agreement with the results presented in this paper. The principal advantage of the higher resolution simulations is the increase in time the flow field maintains its asymptotic state before the simulation results are impacted by the finite computational domain.

RESULTS

The time development of the resolved-scale turbulence kinetic energy, $\langle \mathbf{u}^2 \rangle$, for both initial spectrum types is shown in Figure 1 for each rotation rate. The time axis in Figure 1 and following figures has been made dimensionless using the eddy turnover time in the initial field

$$\tau(0) = L_u(0)/\langle \mathbf{u}^2 \rangle \tag{9}$$

where $L_u(t)$ is the velocity integral scale at time t defined as

$$L_u(t) = \frac{\pi}{2} \frac{\int_0^\infty k^{-1} E(k,t) dk}{\int_0^\infty E(k,t) dk}. \tag{10}$$

In isotropic turbulence, L_u is two-thirds the usual longitudinal integral scale measured in experiments. Throughout this work, "k^2 spectrum" refers to an initial energy spectrum $E(k)$ with low wavenumber part proportional to k^2 while "k^4 spectrum" refers to an initial $E(k)$ with low wavenumbers proportional to k^4. The characteristic effect of increasing Ω on the evolution of $\langle \mathbf{u}^2 \rangle$ is evident in Figure 1, i.e., inhibition of the energy cascade with increasing rotation rate resulting in a less rapid decay of kinetic energy.

The effect of rotation on the evolution of turbulence kinetic energy is even more clearly seen in Figure 2. Plotted in Figure 2 is the power-law exponent of $\langle \mathbf{u}^2 \rangle$ for each rotation rate and initial spectrum type. It is evident from Figure 2 that, following an initial transient, the power-law exponent becomes independent of time.

The values of the power-law exponents for the simulations at zero rotation rate are in good agreement with the simulations of Ref. [10] despite the anisotropic computational box. Comparison of the power-law exponents for a given initial spectrum type clearly show the reduction in the decay rate of kinetic energy in rotating turbulence. It may be observed that for both initial spectrum types, the power-law exponent is reduced by approximately a factor of two in rotating turbulence relative to its value at $\Omega = 0$. Finally, in the asymptotic region the

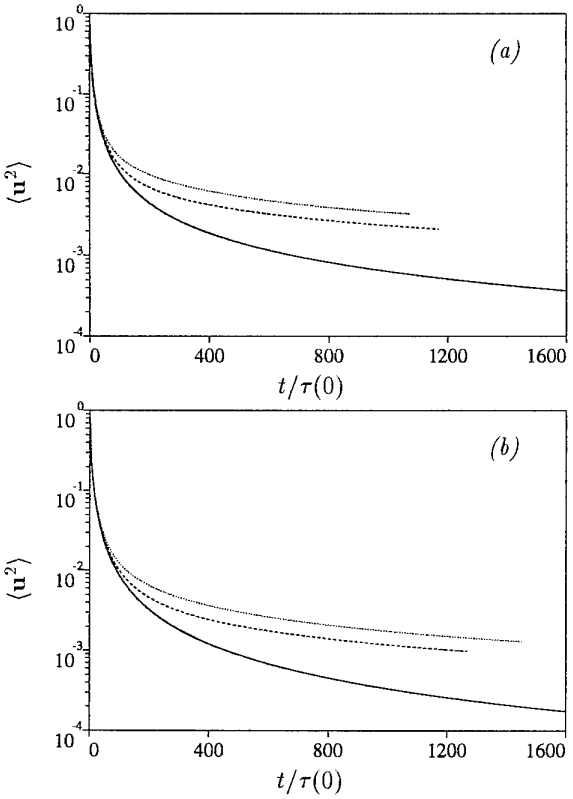

Figure 1: Time development of resolved-scale kinetic energy in rotating turbulence. ——— , $\Omega = 0$; - - - - , $\Omega = 0.5$; ····· , $\Omega = 1.0$. (*a*) k^2 spectrum; (*b*) k^4 spectrum.

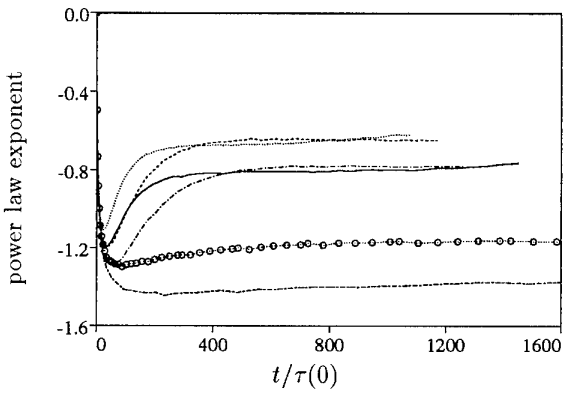

Figure 2: Time development of the power-law exponent of $\langle \mathbf{u}^2 \rangle$ in rotating turbulence. k^2 spectrum: o·····o , $\Omega = 0$; - - - - , $\Omega = 0.5$; ····· , $\Omega = 1.0$. k^4 spectrum: — — — , $\Omega = 0$; —·— , $\Omega = 0.5$; ——— , $\Omega = 1.0$.

power-law exponent of $\langle \mathbf{u}^2 \rangle$ is independent of the rotation rate, depending only on the form of the initial energy spectrum.

Chasnov [10] showed that, at high Reynolds numbers, the asymptotic decay of $\langle \mathbf{u}^2 \rangle$ in isotropic turbulence could be accurately described using simple scaling arguments and dimensional analysis. The analysis is predicated on the assumption that the asymptotic scaling of $\langle \mathbf{u}^2 \rangle$ is dependent on the form of $E(k)$ at low wavenumbers and independent of viscosity. For high Reynolds number turbulence this is reasonable since the direct effect of viscosity occurs at much higher wavenumber magnitudes than those scales which contain most of the energy. The asymptotic forms found in [10] can be obtained by first considering an asymptotic series expansion of the energy spectrum near $k = 0$

$$E(k) = 2\pi k^2 \left(B_0 + B_2 k^2 + \ldots \right) . \qquad (11)$$

The initial $E(k)$ with low wavenumbers proportional to k^2 corresponds to a non-zero value of B_0 while the k^4 spectrum is obtained for $B_0 = 0$ and non-zero B_2. Saffman [17] considered a homogeneous turbulence field generated by a distribution of random impulsive forces and showed that as a consequence of momentum conservation B_0 is invariant in time. Batchelor & Proudman [18] considered an initial flow field in which all of the velocity cumulants of the turbulence are exponentially small at large separations distances. For this flow B_2 (the Loitsianski integral) is non-zero but not time invariant. Closure calculations [19] and large-eddy simulations [20] have shown that the time dependence of B_2 is weak relative to the overall turbulence decay, however, and is therefore assumed constant for the sake of obtaining an approximate asymptotic scaling law for $\langle \mathbf{u}^2 \rangle$. Thus, assuming the appropriate dependence of $\langle \mathbf{u}^2 \rangle$ on either B_0 or B_2, dimensional analysis yields the asymptotic scaling of $\langle \mathbf{u}^2 \rangle$ for non-rotating turbulence [10]

$$\langle \mathbf{u}^2 \rangle \propto B_0^{2/5} t^{-6/5} \qquad (k^2 \text{ spectrum}) \qquad (12)$$

and

$$\langle \mathbf{u}^2 \rangle \propto B_2^{2/7} t^{-10/7} \qquad (k^4 \text{ spectrum}) . \qquad (13)$$

as previously obtained by Saffman [21] and Kolmogorov [22].

The results above may be generalized for rotating homogeneous turbulence by considering the additional dimensionless group for this flow, Ωt. For the rotating flow a dimensional analysis yields the following possible asymptotic decay:

$$\langle \mathbf{u}^2 \rangle \propto B_0^{2/5} t^{-6/5} (\Omega t)^x \qquad (k^2 \text{ spectrum}) \qquad (14)$$

$$\langle \mathbf{u}^2 \rangle \propto B_2^{2/7} t^{-10/7} (\Omega t)^{x'} \qquad (k^4 \text{ spectrum}) . \qquad (15)$$

For rotating turbulence at high Reynolds numbers and low Rossby numbers it is possible to offer plausibility arguments to determine the unknown exponents x and x'. In this regime rotating turbulence is characterized by two disparate timescales, a long

timescale representative of the turbulence evolution and a short timescale associated with the rotation frequency, Ω. If it is assumed that the correlation time of the non-linear triadic interactions is directly proportional to the short timescale $1/\Omega$, then the transport equation of $\langle \mathbf{u}^2 \rangle$ may be written as

$$\frac{d\langle \mathbf{u}^2 \rangle}{dt} = \frac{1}{\Omega} f(T, B_0 \text{ or } B_2) \qquad (16)$$

for the two initial spectrum types. The long timescale of the non-linear interactions in (16) is denoted T and may be constructed on dimensional grounds from $\langle \mathbf{u}^2 \rangle$ and B_0 or B_2. Dimensional analysis may be used to determine the unknown function f, yielding

$$\frac{d\langle \mathbf{u}^2 \rangle}{dt} = \frac{1}{\Omega} B_0^{-2/3} \langle \mathbf{u}^2 \rangle^{8/3} \qquad (17)$$

for non-zero B_0 and

$$\frac{d\langle \mathbf{u}^2 \rangle}{dt} = \frac{1}{\Omega} B_2^{-2/5} \langle \mathbf{u}^2 \rangle^{12/5} \qquad (18)$$

for zero B_0. Integrating (17) and (18) results in the predicted asymptotic decay for $\langle \mathbf{u}^2 \rangle$ in rotating turbulence:

$$\langle \mathbf{u}^2 \rangle \propto B_0^{2/5} \Omega^{3/5} t^{-3/5} \qquad (k^2 \text{ spectrum}) \qquad (19)$$

and

$$\langle \mathbf{u}^2 \rangle \propto B_2^{2/7} \Omega^{5/7} t^{-5/7} \qquad (k^4 \text{ spectrum}). \qquad (20)$$

The scaling laws (19) and (20) predict that in rotating turbulence the kinetic energy decay exponent is reduced by a factor of two relative to its value in the non-rotating flow (cf. 14 and 15). More importantly, the exponents predicted from (19) and (20) and the actual values obtained in the simulations (Figure 2) are in very good agreement. The actual value of the power-law exponent for cases with non-zero B_0 is around -0.65, compared to a predicted value of -0.6, while the exponent in the asymptotic region for simulations with zero B_0 is approximately -0.78, slightly smaller than the predicted value of -0.71. Thus, neglecting the weak time dependence of the leading order term B_2, necessary in order to obtain (20), appears justified.

While the asymptotic scaling laws (19) and (20) yield exponents for the dependence of $\langle \mathbf{u}^2 \rangle$ on time which are in good agreement with the large-eddy simulations, it is not possible to verify the power-law dependence of the kinetic energy on Ω using the results in Figure 2. To test the scaling of $\langle \mathbf{u}^2 \rangle$ on Ω, the quantities

$$\frac{\langle \mathbf{u}^2 \rangle}{B_0^{2/5} \Omega^{3/5} t^{-3/5}} \qquad (21)$$

and

$$\frac{\langle \mathbf{u}^2 \rangle}{B_2^{2/7} \Omega^{5/7} t^{-5/7}} \qquad (22)$$

are plotted in Figure 3. Note that the value of B_2 used in (22) is from the initial condition. Provided that the dependence on Ω shown in (19) and (20) is correct, (21) and (22) in Figure 3 should asymptote to the same dimensionless constant at long times (for a given initial spectrum type). The results in Figure 3 show that the collapse of the kinetic energy obtained using the asymptotic scaling laws is excellent for the k^2 spectrum. For the k^4 spectrum the collapse is reasonable considering the assumption of a time-invariant B_2. It may be concluded that Figure 3 validates the scalings on rotation rate as obtained from the analysis leading to (19) and (20).

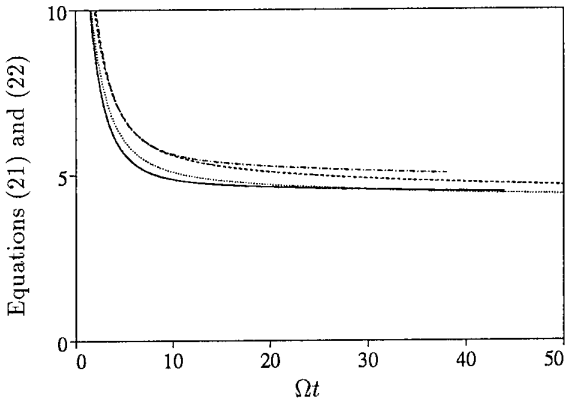

Figure 3: Check of asymptotic scaling laws (19) and (20). k^2 spectrum: ——— , $\Omega = 0.5$; ····· , $\Omega = 1.0$. k^4 spectrum: —·— , $\Omega = 0.5$; ---- , $\Omega = 1.0$.

In rotating turbulence it is possible that the velocity fluctuations along the rotation axis may possess a different power-law decay than those in the plane normal to the rotation vector (i.e., the horizontal plane). It is not clear based upon previous numerical and experimental results as to the behavior of the vertical fluctuations $\langle w^2 \rangle$ relative to the velocity scale in the horizontal plane, $(\langle u^2 \rangle + \langle v^2 \rangle)/2$. Shown in Figure 4 is the ratio of $(\langle u^2 \rangle + \langle v^2 \rangle)/2$ to the vertical fluctuations, $\langle w^2 \rangle$. With the exception of the highest rotation rate in the simulations with non-zero B_0, the results in Figure 4 show that in the asymptotic region the ratio of mean-square velocity fluctuations is approximately 0.8. This result is further significant since it also implies the existence in the asymptotic region of a single velocity scale in rotating turbulence.

For the rotating flow, by axisymmetry, there are possibly five independent lengthscales. These integral scales are obtained from integration of the two-point correlation function

$$L_{\alpha\alpha;\beta} = \frac{1}{\langle u_\alpha^2 \rangle} \int \langle u_\alpha(\mathbf{x}) u_\alpha(\mathbf{x} + r_\beta) \rangle dr_\beta \,. \qquad (23)$$

The lengthscale $L_{\alpha\alpha;\beta}$ measures the correlation between the α velocity components with separation in the β direction. In the horizontal plane the independent lengthscales may be expressed using (23) as

$$\begin{aligned} L_{h1} &= (L_{11,1} + L_{22,2})/2 \\ L_{h2} &= (L_{11,2} + L_{22,1})/2 \\ L_{h3} &= (L_{33,1} + L_{33,2})/2 \,. \end{aligned} \qquad (24)$$

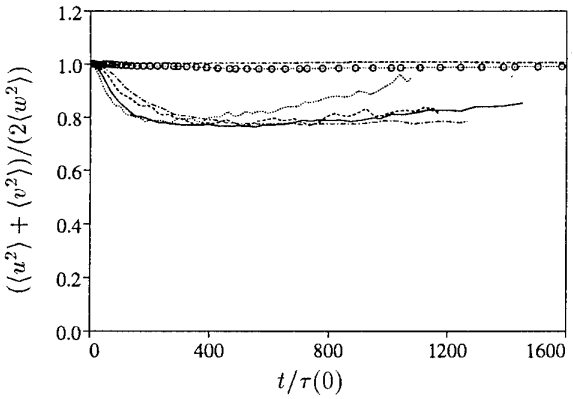

Figure 4: Time development of mean-square velocity ratio in rotating turbulence. k^2 spectrum: o·····o , $\Omega = 0$; ---- , $\Omega = 0.5$; ····· , $\Omega = 1.0$. k^4 spectrum: —-— , $\Omega = 0$; —·— , $\Omega = 0.5$; ——— , $\Omega = 1.0$.

The integral scale L_{h1} measures the horizontal correlation of longitudinal velocities, L_{h2} the horizontal correlation of lateral velocities, and L_{h3} the correlation in the horizontal plane of vertical velocity fluctuations. For the vertical direction (along the rotation axis) the two independent integral scales are

$$\begin{aligned} L_{v1} &= (L_{11,3} + L_{22,3})/2 \\ L_{v2} &= L_{33,3} \end{aligned} \qquad (25)$$

where L_{v1} measures the vertical correlation of lateral velocities and L_{v2} the vertical correlation of vertical velocities.

For the non-rotating flow dimensional analysis yields directly the asymptotic scalings of the integral scales for high Reynolds number isotropic turbulence [10]

$$L_u \propto B_0^{1/5} t^{2/5} \qquad (k^2 \text{ spectrum}) \qquad (26)$$

$$L_u \propto B_2^{1/7} t^{2/7} \qquad (k^4 \text{ spectrum}). \qquad (27)$$

For the rotating flow the appropriate dependence of the integral scales on the invariant B_0 and approximate invariant B_2 can be approached in the same manner as for the kinetic energy, i.e., through introduction of the additional dimensionless group Ωt with appropriate exponents. For example, for the vertical lengthscales L_{v2} the development in the asymptotic state may be expressed as

$$L_{v2} \propto B_0^{1/5} t^{2/5} (\Omega t)^{y_2} \qquad (k^2 \text{ spectrum}) \qquad (28)$$

and

$$L_{v2} \propto B_2^{1/7} t^{2/7} (\Omega t)^{y_2'} \qquad (k^4 \text{ spectrum}). \qquad (29)$$

Using (24) and (25) one could write similar expressions for the other lengthscales; each with a possibly distinct exponent as in (28) and (29). Unlike the kinetic energy, however, we do not yet have an argument for predicting *a priori* the appropriate exponents for the integral lengthscale growth in the rotating flow. Rather, the results of the large-eddy

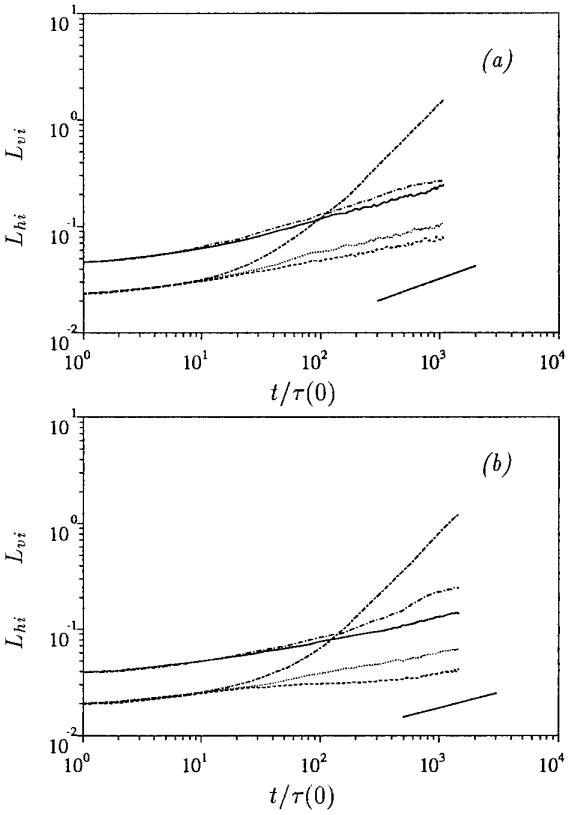

Figure 5: Time development of integral lengthscales in rotating turbulence, $\Omega = 1$. Asymptotic growth rate in non-rotating turbulence also shown in lower portion of Figure. ——— , L_{h1}; ---- , L_{h2}; ····· , L_{h3}; —-— , L_{v1}; —·— , L_{v2}. (*a*) k^2 spectrum; (*b*) k^4 spectrum.

simulations are used to supply the unknown exponents.

Shown in Figure 5 is the time development of the integral scales for both initial spectrum types. The curves shown in Figure 5 are for the highest rotation rate used with each initial condition. Also shown for reference in both Figures is the slope corresponding to the asymptotic growth rate in non-rotating isotropic turbulence. It is clear from Figure 5 that the growth of L_{v1} is much more rapid than the asymptotic growth rate in non-rotating turbulence as well as the other integral scales in the rotating flow. With the exception of L_{v1}, the growth rate of the integral scales in the rotating flow are slightly suppressed relative to the non-rotating case. More importantly, the simulation results demonstrate that in the asymptotic region the integral lengthscales do in fact exhibit power-law growth and, with the exception of L_{v1}, the power-law exponents of the integral scales are identical. Thus, in the horizontal plane there is a single independent lengthscale, L_h, while there exist two independent integral scales in the vertical, L_{v1} and L_{v2}. The asymptotic scaling laws obtained from the simulations for the k^2 spectrum are approximately

$$\begin{aligned} L_h &\propto B_0^{1/5}\Omega^{-3/20}t^{1/4} \\ L_{v1} &\propto B_0^{1/5}\Omega^{3/5}t^{1} \\ L_{v2} &\propto B_0^{1/5}\Omega^{-3/20}t^{1/4} \end{aligned} \qquad (30)$$

while for the k^4 spectrum the long-time evolution of the lengthscales determined from the large-eddy simulations are approximately

$$\begin{aligned} L_h &\propto B_2^{1/7}\Omega^{-3/35}t^{1/5} \\ L_{v1} &\propto B_2^{1/7}\Omega^{32/35}t^{6/5} \\ L_{v2} &\propto B_2^{1/7}\Omega^{-3/35}t^{1/5} \end{aligned} \qquad (31)$$

Perhaps the most striking feature of the integral scale behavior is that even in the asymptotic region the growth of L_{v1} is much more rapid than the other lengthscales. Surprisingly, the vertical correlation of vertical velocities, L_{v2}, is relatively unaffected by rotation which would seem to indicate a "de-coupling" between the two vertical lengthscales. However, this de-coupling occurs while there is close coupling between L_h and L_{v2} as well as between the velocity components in the vertical and horizontal planes (Figure 4).

The relations (30) and (31) yield the appropriate dependence of the integral lengthscales on time but, similar to the kinetic energy considered earlier, it is not possible to verify the dependence on rotation rate from the results in Figure 5. Shown in Figure 6 are the ratio of the integral lengthscales to the appropriate combination of B_0, B_2, Ω, and t, i.e.,

$$\begin{aligned} L_h,\quad L_{v2} \;&/\; \left(B_0^{1/5}\Omega^{-3/20}t^{1/4}\right) \\ L_{v1} \;&/\; \left(B_0^{1/5}\Omega^{3/5}t^{1}\right) \end{aligned} \qquad (32)$$

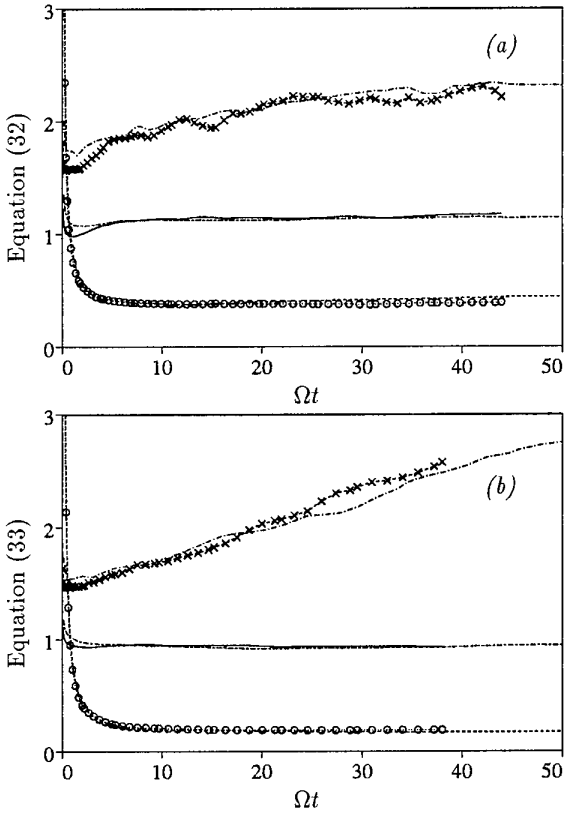

Figure 6: Check of asymptotic scaling laws (30) and (31). $\Omega = 0.5$: ——— , L_h; o·····o , L_{v1}; ×---× , L_{v2}. $\Omega = 1.0$: — — — , L_h; - - - - , L_{v1}; —·— , L_{v2}. (*a*) k^2 spectrum; (*b*) k^4 spectrum.

for the k^2 spectrum (Figure 6*a*) and

$$\begin{aligned} L_h,\quad L_{v2} \;&/\; \left(B_2^{1/7}\Omega^{-3/35}t^{1/5}\right) \\ L_{v1} \;&/\; \left(B_2^{1/7}\Omega^{32/35}t^{6/5}\right) \end{aligned} \qquad (33)$$

for the k^4 spectrum (Figure 6*b*). The collapse of the lengthscales for the different rotation rates in Figure 6 demonstrates that the scalings (30) and (31) possess the proper dependence on the rotation rate. The collapse of the integral scales L_{v1} is especially striking given the relatively strong dependence on Ω. Figure 6 also demonstrates an excellent collapse of the horizontal integral scale L_h. The collapse of L_{v2} using the (30) and (31) for different Ω possesses the greatest amount of statistical variation, presumably due to the fewer number of samples available to compute this lengthscale.

SUMMARY

Large-eddy simulations of high Reynolds number rotating homogeneous turbulence have been performed. The calculations were evolved sufficiently far in time to observe the development of the asymptotic state for initial conditions with low wavenumbers proportional to both k^2 and k^4. The simula-

tions demonstrate the characteristic effect of solid body rotation on initially isotropic turbulence, i.e., inhibition of non-linear energy transfer from large to small scales and less rapid decay of kinetic energy. In the asymptotic region the decay exponent of the turbulence kinetic energy is also observed to be independent of time as well as rotation rate.

Simple scaling arguments and dimensional analysis were used to obtain predictions of the asymptotic behavior of the kinetic energy. Assuming that the non-linear triadic interactions have a correlation time directly proportional to the rotation time scale allows one to predict *a priori* the asymptotic scaling laws for the turbulence kinetic energy. The predicted values were found to be in very good agreement with the simulation results, supporting the analytical results.

In the rotating flow simulation results indicate that in the asymptotic region the integral lengthscales undergo a power-law growth. With the exception of the correlation length along the rotation axis of horizontal velocities, integral lengthscale growth in the rotating flows is found to be slightly suppressed relative to non-rotating isotropic turbulence. In the asymptotic region there is a single horizontal lengthscale but two independent vertical lengthscales. The de-coupling between the vertical lengthscales was unexpected, especially considering the strong coupling between the vertical and horizontal velocity fluctuations.

More work is required to better understand the asymptotic state of rotating turbulent flows at high Reynolds numbers. Application of the scaling laws to the appropriately defined energy spectra is needed to further validate the similarity states indicated by the power-law evolution in the kinetic energy and integral lengthscales found in this work. Use of the database accumulated during the course of this work will also be invaluable for future studies directed towards extension of engineering turbulence models to high Reynolds number rotating flows.

ACKNOWLEDGMENTS

The authors gratefully acknowledge the support of Dr. Robert Rogallo and Dr. Alan Wray at the NASA Ames Research Center. Partial support for this work was obtained from the American Society for Engineering Education. The computations were performed on the Cray C-90 at NASA Ames.

REFERENCES

[1] Traugott, S.C., "Influence of solid-body rotation on screen-produced turbulence", *NACA TN 4135*, 1958.

[2] Veeravalli, S.V., "An experimental study of the effects of rapid rotation on turbulence", *Annual Research Briefs - 1991*, NASA-Stanford Center for Turbulence Research, 1991.

[3] Mansour, N.N., Cambon, C. & Speziale, C.G., "Theoretical and computational study of rotating isotropic turbulence", in *Studies in Turbulence*, edited by T. B. Gatski, S. Sarkar & C. G. Speziale, Springer-Verlag, 1992.

[4] Squires, K.D. & Piomelli, U., "Dynamic modeling of rotating turbulence", in press, *Turbulent Shear Flows 9*, edited by F. Durst, N. Kasagi, B.E. Launder, F.W. Schmidt and J.H. Whitelaw, Springer Verlag, 1994.

[5] Bardina, J., Ferziger, J.H. & Rogallo, R.S., "Effect of rotation on isotropic turbulence: computation and modeling", *J. Fluid Mech.* **154**, 321, 1985.

[6] Jacquin, L., Leuchter, O., Cambon, C. & Mathieu, J., "Homogeneous turbulence in the presence of rotation", *J. Fluid Mech.* **220**, 1, 1990.

[7] Bartello, P., Métais, O. & Lesieur, M., "Coherent structures in rotating three-dimensional turbulence", submitted to *J. Fluid Mech.*

[8] Hossain, M., "Reduction in the dimensionality of turbulence due to a strong rotation", *Phys. Fluids A* **6**, 1077, 1994.

[9] Cambon, C. & Jacquin, L., "Spectral approach to non-isotropic turbulence subjected to rotation", *J. Fluid Mech.* **202**, 295, 1989.

[10] Chasnov, J.R., "Similarity states of passive scalar transport in isotropic turbulence", *Phys. Fluids A* **6**, 1036, 1994.

[11] Chollet, J.P. & Lesieur, M., "Parameterization of small scales of three-dimensional isotropic turbulence utilizing spectral closures", *J. Atmos. Sci*, **38**, 2747, 1981.

[12] Cambon C., Bertoglio, J.P. & Jeandel, D., "Spectral closure of homogeneous turbulence", AFOSR–Stanford Conf. on Complex Turb. Flows, 1981.

[13] Aupoix, B., "Eddy viscosity subgrid-scale models for homogeneous turbulence", in *Proc. of Macroscopic Mod. Turb. Flows, Lecture Notes in Phys.*, **230**, 45, 1984.

[14] Alexandre A. & Bertoglio, J.P., private communication, 1992.

[15] Cambon, C., Bertoglio, J.P., Godeferd, F.S. & Le Penven, L., in *Report on the 1993 Summer School/Workshop: Modelling Turbulent Flows - ERCOFTAC Bulletin # 19*, 1993.

[16] Rogallo, R.S., "Numerical experiments in homogeneous turbulence", *NASA TM 81315*, 1981.

[17] Saffman, P.G., "The large-scale structure of homogeneous turbulence", *J. Fluid Mech.* **27**, 581, 1967.

[18] Batchelor, G. K. & Proudman, I., "The large-scale structure of homogeneous turbulence", *Phil. Trans. Roy. Soc*, **248**, 369, 1956.

[19] Lesieur, M., *Turbulence in Fluids*, Nijhoff, 1990.

[20] Chasnov, J.R., "Computation of the Loitsianski integral in decaying isotropic turbulence", *Phys. Fluids A* **5**, 2579, 1993.

[21] Saffman, P.G., "Note on decay of homogeneous turbulence", *Phys. Fluids* **10**, 1349, 1967.

[22] Kolmogorov, A.N., "On degeneration of isotropic turbulence in an incompressible viscous liquid", *Dokl. Akad. Navk. SSSR*, **31**, 538, 1941.

Comparison of DNS and LES of transitional and turbulent compressible flow: flat plate and mixing layer

Bernard Geurts, Bert Vreman and Hans Kuerten
Department of Applied Mathematics, University of Twente
P.O.Box 217, 7500 AE Enschede, The Netherlands

Abstract

We present *a priori* and *a posteriori* test results of LES of compressible flow over a flat plate and in a mixing layer. Through a comparison with filtered DNS data the 'quality' of subgrid-models for the turbulent stress can be assessed. In particular, the scale similarity model of Bardina and the dynamic mixed model arising from a combination of Bardina's model with the Germano eddy-viscosity model show excellent correlations *a priori*, and give rise to accurate LES simulations *a posteriori*. Moreover, the filtering approach close to solid walls is considered and the contribution to the filtered equations arising from the non-commutation of the filter operator with the partial derivatives is calculated. It appears, in *a priori* tests for 2D simulations, that these non-commutation terms can be comparable to the turbulent stress. The scale similarity hypothesis yields models for these terms which show a good correlation.

1 Introduction

The numerical simulation of natural transition as well as the early stages of fully developed turbulent flow in compressible fluids forms a subject of intensive research [1, 2, 3, 4, 5, 6]. Basically two different approaches can be distinguished: direct numerical simulation (DNS) and large eddy simulation (LES). In DNS the flow is simulated on a sufficiently fine grid in order to accurately capture the wide range of length-scales encountered in turbulent flow. In LES the filtered Navier-Stokes equations are considered and a time-accurate treatment is given of the large, geometry dependent eddies occurring in the flow. The effects of the small scale phenomena on the resolved scales are modeled through the introduction of so called subgrid-scale models in the momentum and energy equations [7, 8]. Since in a LES approach the governing equations are filtered, the flow is usually either simulated on a coarser grid or at a somewhat higher Reynolds number when compared to a DNS [9]. This represents the main virtue of LES. The basic problem, however, is how to devise models for the small scale contributions which accurately represent the subgrid phenomena. A number of different models have been formulated in literature. In this paper we will compare results of DNS with large eddy simulations employing several subgrid models in order to test the accuracy of different proposals for the turbulent stresses.

Recently, a class of subgrid scale models has been proposed which are 'dynamic' in the sense that the properties of the resolved scales directly and dynamically determine the model coefficients. In the formulation of the models that will be considered here Germano's identity [10] and the scale similarity hypothesis of Bardina *et.al.* [11] play a central role. The dynamic 'eddy-viscosity' model results after imposing Germano's identity to the Smagorinsky model [12]. Moreover, the non-eddy viscosity model of Bardina, which is based on the scale similarity hypothesis, as well as a dynamic 'mixed' model resulting from a combination of these two approaches will be considered [13, 14]. Since we will restrict ourselves to compressible flow at relatively low Mach numbers, the modeling of the subgrid terms in the energy equation will not be addressed here (for a discussion and results at higher Mach numbers see [15]). When comparing LES and DNS two principally different tests can be distinguished.

Paper presented at the 74th Fluid Dynamics Symposium on "Application of Direct and Large Eddy Simulation to Transition and Turbulence" held at Chania, Crete, Greece, in April 1994.

First, *a priori* tests can be performed in which the DNS results are used to calculate the norms of all terms appearing in the filtered equations and to determine the correlations of the subgrid scale models, evaluated on the filtered DNS fields, with the actual turbulent stresses. Since the interactions between the different scales in the flow field are not included in these *a priori* tests, so called *a posteriori* tests should be performed as well in which the results of an actual LES are directly compared with the filtered DNS results. We will present results of this analysis for compressible flow over a flat plate in 2D and for the mixing layer in 3D.

In section 2 we present the filtered Navier-Stokes equations and in particular pay attention to the filtering near a solid wall. The commutation of the filter operation with partial derivatives, which is usually assumed in the filtering approach, can no longer be maintained in that case. This gives rise to additional contributions in the filtered equations. In section 3 we explicitly define the above mentioned subgrid models for the turbulent stress in compressible flow. The DNS results representing the transition process in 2D flat plate flow, i.e. the evolution of the flow starting from the linear stability regime up to a well developed flow field, are presented in section 4. Moreover, several *a priori* test results are discussed. A major drawback of this analysis is that it is based on a flow field in 2D which is quite different from a turbulent flow field in 3D. In section 5 we will present results obtained for the compressible mixing layer in 3D and consider the quality of the subgrid models in compressible, free, turbulent shear layers. This is a first step towards the assessment of the capabilities of the subgrid models for flows in different geometries. Finally, we summarize our findings in section 6.

2 Filtering the Navier-Stokes equations

In this section we present the filtered Navier-Stokes equations and focus on the filtering close to a solid wall. A generalisation of the box filter is proposed and the contribution to the filtered equations arising from the non-commutation of the filtering with the partial derivatives near a solid wall is considered.

The equations describing compressible flow are the well known Navier-Stokes equations, which represent conservation of mass, momentum and energy:

$$\begin{aligned} \partial_t \rho &+ \partial_j(\rho u_j) = 0 \\ \partial_t(\rho u_i) &+ \partial_j(\rho u_i u_j) + \partial_i p - \partial_j \tau_{ij} = 0 \\ \partial_t e &+ \partial_j((e+p)u_j) - \partial_j(\tau_{ij}u_i - q_j) = 0 \end{aligned} \qquad (2.1)$$

Here the symbols ∂_t and ∂_j are abbreviations of the partial differential operators $\partial/\partial t$ and $\partial/\partial x_j$ respectively. The components of the velocity vector are denoted by u_i, while ρ is the density and p the pressure which is related to the total energy density e by:

$$p = (\gamma - 1)\{e - \frac{1}{2}\rho u_i u_i\} \qquad (2.2)$$

in which γ denotes the adiabatic gas constant. The viscous stress tensor τ_{ij} is a function of temperature T and velocity vector $\mathbf{u}$

$$\tau_{ij}(T, \mathbf{u}) = \frac{\mu(T)}{Re}(\partial_j u_i + \partial_i u_j - \frac{2}{3}\delta_{ij}\partial_k u_k) \qquad (2.3)$$

where $\mu(T)$ is the dynamic viscosity for which we use either Sutherland's law for air or treat it as a constant. In addition q_j represents the viscous heat flux vector, given by

$$q_j(T) = -\frac{\mu(T)}{(\gamma - 1)RePrM^2}\partial_j T \qquad (2.4)$$

where Pr is the Prandtl number. Finally, the temperature T is related to the density and the pressure by the ideal gas law

$$T = \gamma M^2 \frac{p}{\rho} \qquad (2.5)$$

These governing equations have been made dimensionless by introducing a reference length L_0, velocity u_0, density ρ_0, temperature T_0 and viscosity μ_0. The values of the Reynolds number $Re = (\rho_0 u_0 L_0)/\mu_0$ and the Mach number $M = u_0/a_0$, where a_0 is a reference value for the speed of sound, are given for each case separately.

A direct numerical simulation is based on a discretisation of (2.1) whereas the governing equations for large eddy simulation are obtained by applying a spatial filter to these equations. A filter operation extracts the large scale part $\bar{f}$ from a quantity f:

$$\bar{f}(\mathbf{x}) = \int_\Omega G_\Delta(\mathbf{x}, \xi) f(\xi) d\xi \qquad (2.6)$$

where Ω is the flow domain and Δ denotes the filter width of the kernel G which is assumed to be normalized, i.e. the integral of G over Ω equals 1 independent of $\mathbf{x}$. For compressible flow Favre [16] introduced a related filter operation $\tilde{f} = \overline{\rho f}/\bar{\rho}$. The filtered equations that are presented next, are valid when the 'bar-filter' is any linear operator that commutes with the partial differential operators ∂_t and ∂_j. For the spatial filter adopted in LES a necessary and sufficient condition for commutation in unbounded flow domains is that the filter is a convolution, i.e. the kernel G depends on $\mathbf{x} - \xi$ only. In general the filter operation does not commute with ∂_j, which gives rise to additional terms in the LES-equations to which we turn later.

When a convolution bar-filter is applied to the continuity and momentum equations we find

$$\partial_t \bar{\rho} + \partial_j(\bar{\rho}\tilde{u}_j) = 0 \tag{2.7}$$

$$\begin{aligned}\partial_t(\bar{\rho}\tilde{u}_i) &+ \partial_j(\bar{\rho}\tilde{u}_i\tilde{u}_j) + \partial_i\bar{p} - \partial_j(\hat{\tau}_{ij}) \\ &+ \{\partial_j(\bar{\rho}a_{ij}) - \partial_j(\bar{\tau}_{ij} - \hat{\tau}_{ij})\} = 0\end{aligned} \tag{2.8}$$

where $\hat{\tau}_{ij}$ is the stress tensor based on $\tilde{T}$ and $\tilde{\mathbf{u}}$ cf. eq. (2.3). The quantity $A_{ij}^{(-)} \equiv \bar{\rho}a_{ij}$ is the turbulent stress tensor, defined as

$$\begin{aligned}A_{ij}^{(-)}(\rho\,,\rho\mathbf{u}) &= \bar{\rho}[\widetilde{u_iu_j} - \tilde{u}_i\tilde{u}_j] \\ &= \overline{(\rho u_i)(\rho u_j)/\rho} - (\overline{\rho u_i})(\overline{\rho u_j})/\bar{\rho}\end{aligned} \tag{2.9}$$

We introduced the notation $A_{ij}^{(-)}$ for later convenience (section 3). In this notation we explicitly indicate the variables and the filter that are used. In (2.7,8) we recognize the Navier-Stokes equations in terms of the filtered fields and some additional terms which are referred to as subgrid terms. The turbulent stress term arises as a subgrid term from the filtering of the nonlinear convection term $\partial_j(\rho u_i u_j)$. An additional subgrid term appears since the stress tensor in the filtered equations is evaluated in the filtered fields which differs from $\bar{\tau}_{ij}$. A similar filter can be applied to the energy equation. The definition of the filtered pressure $\bar{p}$ by (2.2), however, would require $\overline{\rho u_i u_i}$ which can not be expressed in terms of $\bar{\rho}$ and $\tilde{u}_i$. One can either introduce a modified pressure by (2.2) evaluated in the filtered fields $\{\bar{\rho}, \tilde{\mathbf{u}}, \bar{e}\}$ or introduce a modified energy $\hat{e}$ defined by

$$\hat{e} = \frac{\bar{p}}{\gamma - 1} + \frac{1}{2}\bar{\rho}\tilde{u}_k\tilde{u}_k = \bar{e} - \frac{1}{2}\bar{\rho}a_{kk} \tag{2.10}$$

The evolution equation for $\hat{e}$ is obtained when the bar-filter is applied to the energy equation and the transport equation for the turbulent kinetic energy $(\bar{\rho}a_{kk}/2)$ is subtracted. Since we will not consider the subgrid terms arising in the energy equation in this paper we will not present this equation (see [17]).

As mentioned, the filtered Navier-Stokes equations (2.7,8) are derived under the assumption that the filter operation commutes with the partial differential operators ∂_j. In an unbounded domain commutation is satisfied if and only if the filtering is a convolution. This requirement poses a strong restriction on the filtering approach in LES near solid walls. Maintaining the requirement implies that the flow field needs to be extended inside the wall region which is unphysical and leads to *ad hoc* approaches. Another drawback of convolution filters is that the filter width is constant throughout the flow domain. Since the length scales of the different structures in the flow field typically are strongly position dependent, the use of a constant filter width implies that the smoothing due to the filtering is not optimal. In a region with predominantly small scale structures it would be desirable to use a smaller filter width than in the far-field regions of the flow. Usually one adopts a nonuniform grid for an efficient simulation of the regions in which the flow field varies rapidly in space. Requiring a similar, grid associated filter width function leads to a more realistic smoothing of the flow and implies that the small scale structures are filtered using a 'matching' filter width. These observations suggest to relax the commutation requirement and to use the more general filter definition (2.6) instead. For filters with a compact support the no-slip condition is satisfied provided the support reduces to zero as $\mathbf{x}$ approaches the wall, i.e. the filtering in the direction normal to the wall is effectively switched off in the near wall region. This correlates quite naturally with the existence of a laminar sublayer in this region and avoids the introduction of 'wall-damping' functions frequently used in combination with eddy viscosity models. An extension of this approach to curved geometries can be developed as well.

The introduction of non-commuting filters implies that each term in the Navier-Stokes equations gives rise to filtered terms which can be decomposed

as follows:

$$\overline{\partial_j F(\mathcal{U})} = \partial_j F(\overline{\mathcal{U}}) + [\partial_j(\overline{F(\mathcal{U})} - F(\overline{\mathcal{U}}))] + (\overline{\partial_j F(\mathcal{U})} - \partial_j \overline{F(\mathcal{U})}) \quad (2.11)$$

The first term on the right hand side is the corresponding term evaluated in the filtered field, denoted here by $\overline{\mathcal{U}}$. The second is the subgrid term as always appears in the filtered equations, independent of commutation, and the last term arises due to the non-commutation of the filter-operation with the partial derivatives. In the flat plate flow application which will be presented the norm of the terms arising from the non-commuation will be determined.

The additional terms arising from the non-commutation will be further specified for a generalised box filter which is used in the sequel. For convenience we consider filtering in 1D first and sketch the extension to higher dimensions afterwards. The generalised box filter is defined by

$$G(x,\xi) = (h_+(x) + h_-(x))^{-1} \quad (2.12)$$

if $-h_-(x) \leq \xi - x \leq h_+(x)$ and 0 elsewhere. Here the positive upper and lower 'bounding functions' h_+, h_- and an x-dependent filter width $\Delta(x) = h_+ + h_-$ are introduced. After some calculation one obtains for the non-commutation:

$$\overline{\partial_x f} - \partial_x \overline{f} = \Delta^{-1}\{\overline{f}\partial_x(h_+ + h_-) - [f(x+h_+)\partial_x h_+ + f(x-h_-)\partial_x h_-]\} \quad (2.13)$$

This expression reduces to zero if h_+ and h_- are constant, i.e. a box filter with constant filter width. The upper- and lower bounding functions $h_\pm(x)$ can be chosen independently. Expression (2.13) can be made more transparent by considering the example in which we set $h_+(x) = h_-(x) = h(x)/2$. The non-commutation simplifies to

$$\overline{\partial_x f} - \partial_x \overline{f} = \frac{\partial_x h}{h}\{\overline{f} - \frac{1}{2}[f(x+h_+) + f(x-h_-)]\} \quad (2.14)$$

which shows that non-commutation arises from x-dependence in the filter width. The term between brackets can be interpreted as the difference between two approximations to a local average of f. In fact $\bar{f}$ is obtained by integrating f over $[x-h_-, x+h_+]$, whereas the term between square brackets is related to an application of the trapezoidal rule to this integration. Hence the term between braces in (2.14) is of second order in the filter width Δ. It appears that the non-commutation terms could be comparable in magnitude to the turbulent stresses and should be considered in detail. In case the flow domain is bounded from below, say at $x = 0$, the requirement that the filtering does not involve values of f outside the domain implies that $x - h(x)/2 \geq 0$ which leads to $\bar{f}(x) \to f(0)$ as $x \to 0$. Hence, close to $x = 0$ the non-commutation term will become small and the filter is switched off. This extension of the box filter contains the special case in which no filtering in the normal direction is performed at all [18]. In 3D the non-commutation term has a structure comparable to the 1D expression with the exception that an additional integation over the remaining directions appears. If the upper and lower bounding functions $h_\pm^{(i)}$ $(i = 1, 2, 3)$ are chosen independently and possibly depend on $\mathbf{x}$ instead of x_i only the non-commutation terms become less transparent although the basic properties are maintained. Modeling the non-commutation terms is not considered in detail in this paper but will be presented elsewhere. Here, the norms of these terms will be determined in *a priori* tests in order to obtain a first impression of the relevance of these terms in LES.

3 Subgrid models

The discussion of the filtering of the Navier-Stokes equations has indicated that models for the turbulent stress $\bar{\rho}a_{ij}$ in terms of the filtered density and velocity should be introduced in order to close the system of equations. Since we will restrict ourselves to low Mach numbers the subgrid terms appearing in the energy equation will not be considered, which is justified in view of the magnitude of these terms in *a priori* tests and the negligible influence in *a posteriori* tests (see ref. [15, 19]). In order to arrive at a concise formulation of the models that will be considered, use is made of Germano's identity and the scale similarity hypothesis. Imposing Germano's identity to a particular model allows for dynamically adjusting the model coefficients. The properties of the instantaneous local flow field determine directly the magnitude of the coefficients. The scale similarity hypothesis presumes that the

turbulent stress $\bar{\rho}a_{ij}$ is well approximated using the resolved scales only. These two presumptions are independent, which implies that combinations of the scale similarity model with other models can be introduced in which the model coefficients may be determined dynamically by imposing Germano's identity. We also discuss some implementation aspects of these models.

The most widely used subgrid-scale model is the Smagorinsky eddy-viscosity model [20]. It is based on the gradient hypothesis and a dimension argument. The modeled turbulent stress (m^S) is given by:

$$m^S = -\bar{\rho}C_S\Delta^2|S(\tilde{\mathbf{u}})|S(\tilde{\mathbf{u}}) \qquad (3.1)$$

in which C_S is the Smagorinsky constant which we set $C_S = (0.17)^2$ and $|S| = |S_{ij}^2|^{1/2}$. Moreover, $S(\tilde{\mathbf{u}})$ is the rate of strain tensor based on $\tilde{\mathbf{u}}$, i.e.

$$S_{ij}(\tilde{\mathbf{u}}) = \partial_j\tilde{u}_i + \partial_i\tilde{u}_j - \frac{2}{3}\delta_{ij}\partial_k\tilde{u}_k \qquad (3.2)$$

The main advantage of using the Smagorinsky model is that it represents an efficient drain for the energy to subgrid-scales which makes actual simulations based on this model relatively easy to perform. The evaluation of m^S has only a small computational cost and due to the dissipative character of the model the calulations are well stabilized. There are, however, some serious drawbacks to this model. First, it has been shown to be too dissipative near solid walls and in transitional flow. Through the *ad hoc* introduction of wall-damping functions and/or intermittency functions some of these problems can be partially resolved. Another major drawback of the Smagorinsky model is that the gradient hypothesis is proven to be inadequate and leads to a poor correlation with the turbulent stress [15, 19, 21].

This calls for models which do not require that the principal axes of the turbulent stress tensor are aligned with those of the rate of strain tensor, i.e. non-eddy viscosity models. An elegant model which satisfies this requirement is obtained by invoking the scale similarity hypothesis [11]. Basically it is assumed that the turbulent stress formulated on the resolved flow field is a good approximation of the actual turbulent stress. This is expressed in Bardina's scale similarity model (m^B):

$$\begin{aligned} m_{ij}^B &= A_{ij}^{(\overline{\ })}(\bar{\rho}, \overline{\rho\mathbf{u}}) \\ &= \overline{(\overline{\rho u_i})(\overline{\rho u_j})/\bar{\rho}} - (\overline{\rho u_i})(\overline{\rho u_j})/\bar{\rho} \end{aligned} \qquad (3.3)$$

The scale similarity model was shown to correlate quite well with the actual turbulent stress and also provides an accurate representation of the norm [15]. This model does not require wall damping functions near solid walls. A drawback of this model is that it requires a certain minimal resolution in a LES in order for the similarity hypothesis to be accurate. A certain amount of eddy viscosity may be introduced in order to additionally represent the subgrid scales. Simply adding the Smagorinsky model would introduce the disadvantages of this model [11]. However, an alternative approach can be followed which is presented next.

In order to overcome some of the drawbacks of the Smagorinsky model, Germano [10] proposed to obtain the model coefficient (C_S) from a dynamic procedure based on an identity which relates the turbulent stress obtained when using two different filter levels [12]. In fact we introduce, next to the bar filter, an explicit test filter denoted by $\widehat{f}$. This test filter has a filter width $\widehat{\Delta} = m\Delta$ and we use $m = 2$. The Germano identity can be written as:

$$A^{(\widehat{\ })}(\rho, \rho\mathbf{u}) - \widehat{A^{(\overline{\ })}}(\rho, \rho\mathbf{u}) = A^{(\widetilde{\ })}(\bar{\rho}, \overline{\rho\mathbf{u}}) \qquad (3.4)$$

In this expression the right hand side can be evaluated using data from a LES whereas the evaluation of the left hand side requires the turbulent stress itself. However, if we introduce a model for the turbulent stress, and require the model to satisfy the identity (3.4) as well, a system of equations for the model coefficients is obtained. Applying this procedure to the Smagorinsky model one arrives at Germano's dynamic subgrid model which has been succesfully applied to a variety of flows (e.g. refs. [12, 18, 21]). If we substitute the Smagorinsky model (3.1) into the identity (3.4) one obtains $C_S M = L$ with

$$M = -\widehat{\bar{\rho}}\widehat{\bar{\Delta}}^2|S(\widehat{\bar{\mathbf{u}}})|S(\widehat{\bar{\mathbf{u}}}) + \left[\overline{\rho}\Delta^2|\widehat{S(\tilde{\mathbf{u}})}|S(\tilde{\mathbf{u}})\right] \qquad (3.5)$$

where $\widehat{\bar{\mathbf{u}}} \equiv \widehat{\overline{\rho\mathbf{u}}}/\widehat{\bar{\rho}}$ and

$$L = A^{(\widetilde{\ })}(\bar{\rho}, \overline{\rho\mathbf{u}}) \qquad (3.6)$$

Notice that the test filter is applied to the complete term between square brackets in (3.5). To obtain the expression for M we have neglected the variation of C_S on the scale of the test filter width. Since the expression for C_S represents a system of

equations for the single unknown C_S, a least-square approach [22] is used to calculate this coefficient: $C_S = \langle M_{ij}L_{ij}\rangle / \langle M_{ij}M_{ij}\rangle$. The brackets $\langle \cdot \rangle$ denote an average over the homogeneous directions which is introduced additionally in order to stabilize actual calculations with this model. More sophisticated procedures for the determination of C_S have been proposed (see ref. [21] for a survey). The value of C_S is dynamically obtained from the above procedure; in particular C_S becomes small in regions of the flow in which the small scale structures are not important. This implies that the use of wall damping functions is not required in combination with the dynamic model.

A drawback of the dynamic model is that it is of the eddy viscosity type. This can be overcome by applying the Germano identity to a 'mixed' model consisting of a combination of the Bardina model (3.3) and the Smagorinsky model in which the model coefficient is dynamically determined as was done by Zang *et.al.* [13]. We will use an alternative formulation of this model which is more consistent in the treatment of the Bardina part of the model in the Germano identity (see [14]). We adopt the mixed model, rather than the Smagorinsky model as base model, i.e.

$$m_{ij}^m = m_{ij}^B + m_{ij}^S \tag{3.7}$$

The model coefficient C_S is obtained by substituting this model into the Germano identity which yields: $H + C_S M = L$,with M and L as given above and the tensor H defined as:

$$H = A^{\widehat{(-)}}(\widehat{\rho}, \widehat{\rho\mathbf{u}}) - \widehat{A^{(-)}}(\overline{\rho}, \overline{\rho\mathbf{u}}) \tag{3.8}$$

and C_S is determined by a least squares fit in which M_{ij} is contracted with $L_{ij} - H_{ij}$ rather than with L_{ij} alone as was done in the dynamic model.

We conclude this section with some remarks on implementation aspects of the models introduced above. These models require an efficient filtering of DNS or LES fields. The implementation of the generalised box filter is considerably simplified if the upper and lower bounding functions $h_\pm$ are related to the (stretched) grid that is being used. Given a grid $\{\mathbf{x}_{\alpha,\beta,\gamma}\}$, which may be clustered in regions of the flow in which large gradients appear, the filter width is defined in the associated computational space. In particular a filter width covering $2n$ intervals in the x_1-direction implies that $\Delta_1 = |\mathbf{x}_{\alpha+n,\beta,\gamma} - \mathbf{x}_{\alpha-n,\beta,\gamma}|$. In case a solid wall is present, say at $\alpha = 0$ then for $0 \leq \alpha \leq n$ the requirement that the filter involves only points in the interior of the flow field is represented by $\Delta_1 = |\mathbf{x}_{2\alpha,\beta,\gamma} - \mathbf{x}_{0,\beta,\gamma}|$, i.e. the filter width in the x_1-direction reduces to zero as we approach the solid wall from above.

The total filter width Δ which appears in the definition of the Smagorinsky model and in the definition of the tensor M appearing in the dynamic formulation is given by $\Delta = \sqrt{(\Delta_1^2 + \Delta_2^2 + \Delta_3^2)/3}$ and the combined filter width $\widehat{\overline{\Delta}}$ is equal to $\sqrt{5}\Delta$. The value $\sqrt{5}$ is exact for Gaussian filters [10] which have the property that the combined filter is a Gaussian filter as well. If the box filter is used the combined filter is not a box filter which makes it somewhat more difficult to define $\widehat{\overline{\Delta}}$. The value $\sqrt{5}$ appears to be optimal for box filters in the following sense. The filter operations $\widehat{f}$ and $\overline{f}$ correspond to filter functions with rectangular shapes. The combined filter operator $\widehat{\overline{f}}$ corresponds to a 'tent' filter function, say F. The best approximation of F, in the L_2 norm, with a rectangular filter function $G_{\widehat{\overline{\Delta}}}$ gives $\widehat{\overline{\Delta}}^2 = \Delta^2 + \widehat{\Delta}^2$ which yields the factor $\sqrt{5}$ in view of the choice $\widehat{\Delta} = 2\Delta$.

The integrations required when evaluating the box filter were performed using the trapezoidal rule. A similar technique was adopted for the integration over the homogeneous directions as required when calculating C_S. Finally, at the boundaries of the computational domain the field is extended according to the boundary conditions which are locally applied. In particular zeroth order extrapolation is used at far field boundaries and periodic conditions are imposed for the homogeneous directions.

4 LES tests for transition in 2D flat plate flow

In this section we present some results obtained from a DNS of the flow over a flat plate in 2D. Subsequently some *a priori* tests are described. Two different simulations have been conducted which differ only in the perturbation which is added to the mean field in order to define the initial state. We consider either simulations initialised on a low amplitude random noise perturbation confined to the

near wall region or simulations in which a specific eigensolution as predicted by linear stability theory [23, 24] is added to the mean field. In these simulations the evolution of the flow starting in the linear stability regime up to a well developed flow field is observed. *A priori* tests which are based on a well developed flow field will be presented subsequently.

First we describe the set-up of the simulation. A temporal simulation is performed, i.e. the flow field is periodic in the streamwise (x_1) direction. The wall is treated as isothermal at a temperature equal to the value obtained from the solution to the boundary layer equations using an adiabatic wall condition. The physical situation envisaged is that of flow over an adiabatic wall in which the fluctuations in the flow are too rapid for the wall temperature to respond. At the far-field boundary we adopt free-slip conditions. A Mach number $M = 1/2$ and a Reynolds number $Re = 1000$ based on the displacement thickness δ^* are used. The computational domain has a length $L_1 = 31$ in the streamwise and $L_2 = 30$ in the normal direction [9]. The mean field used to define the initial state is obtained from a solution to the compressible boundary layer equations using adiabatic wall conditions. Forcing terms are added to the x_1-momentum and the energy equation such that this mean field is a steady state solution of the forced equations. The initial state is generated by adding a specific, low amplitude perturbation to this mean field. In particular we consider either random noise perturbations multiplied by $x_2^2 \exp(-x_2^2)$ in order to confine these perturbations to the near wall region or we add the eigenfunction corresponding to the most unstable mode for the specific computational box considered according to linear stability theory. A stretched grid is used in the normal (x_2) direction clustering points in the near wall region:

$$x_j^{(2)} = \frac{\alpha L_2 \eta_j}{1 + \alpha - \eta_j} \quad ; \quad \eta_j = j/n_2 \qquad (4.1)$$

in which n_2 is the number of cells in the normal direction and the parameter $\alpha = 0.2$. The grid in the streamwise direction is uniform. A second order accurate finite volume method with central spatial differencing and explicit four stage Runge-Kutta time stepping is used [25]. This method was validated using results from linear stability theory [26]. By considering the exponential growth of fluctuations in the velocities at several distances $x_j^{(2)}$ from the wall it was observed that the growth rate ω was predicted with an accuracy well within 0.5 % using 128 points in the normal direction and 32 — 128 points in the streamwise direction. This error of 0.5 % was observed at locations close to the wall; in the region $x_2 \geq 1$ the error in ω reduced rapidly to less than 10^{-5} relative error. Moreover, a comparison of the results obtained for ω at different resolutions showed a clear convergence rate consistent with a second order accurate method.

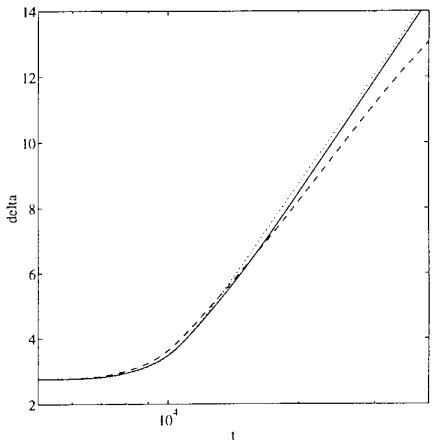

Figure 1: Evolution of the boundary layer thickness δ at different resolutions: 64×128 (solid), 64×64 (dashed) and 32×128 (dotted)

In figure 1 we show the evolution of the boundary layer thickness δ which was obtained from the simulation using random noise perturbations of the mean field of amplitude 10^{-4}. The boundary layer thickness remains almost constant up to $t = 10^4$ after which a logarithmic time-dependence is observed, i.e. $\delta \sim \log(t)$. The simulation was repeated on different grids as illustrated, showing that the resolution in the x_2-direction is much more critical than the resolution in the x_1-direction. The evolution of the fluctuations in the velocities close to the wall shows a transient period in which these fluctuations are quite erratic and decay (see fig.2). This corresponds to the stable modes contained in the random initial state. After this transient the most unstable mode as predicted by linear stability theory becomes dominant and is captured accurately using 128 points in the normal direction. Around $t = 10^4$ the nonlinear interactions lead to a saturation of the fluctuations in the kinetic energy and an

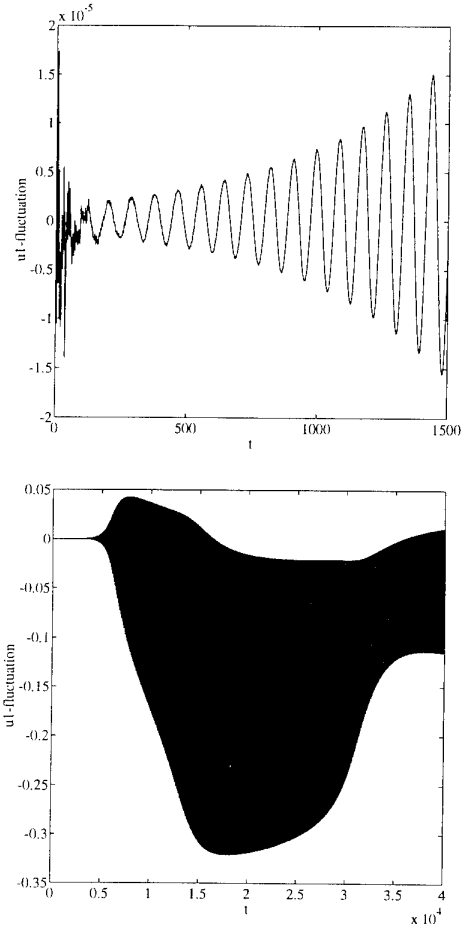

Figure 2: Evolution of the fluctuations in u_1 at $x_1 = 0$ and $x_2 = 1/2$ at a resolution of 64×128. Top figure shows the initial behavior and bottom figure the envelope of the long time fluctuations.

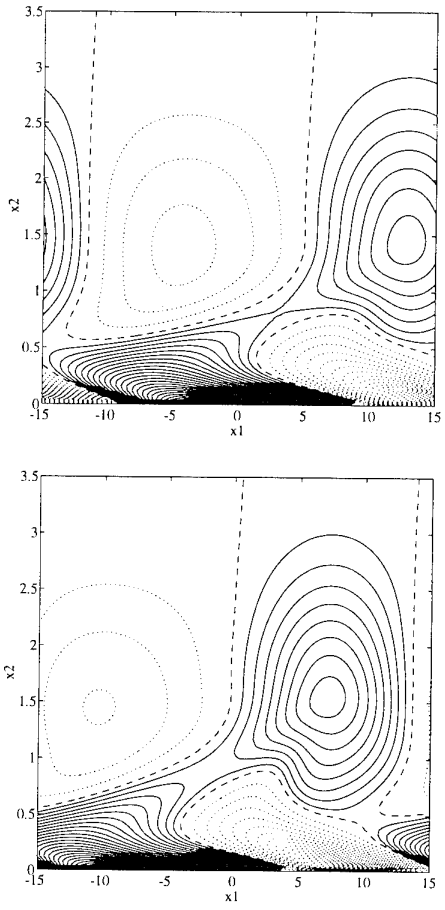

Figure 3: Contours of vorticity-fluctuations at $t = 10000$ (top) and $t = 15000$ (bottom). The solid curves denote negative values, dotted refer to positive values and dashed to 0.

unsteady saturated state sets in. The shape factor evolves from 2.74 to a value of 1.86 and the skin-friction was observed to initially rise considerably above the laminar value and to decrease again in the long time regime. For $t > 10^4$ the mean velocity profile develops a steeper gradient close to the wall while the boundary layer thickness gradually increases. The fluctuations in u_1, relative to the mean initial velocity profile, in the center of the computational box at a distance $x_2 = 1/2$ from the plate is shown in figure 2. In the top figure the initial evolution is shown demonstrating the transient leading to the most unstable mode becoming dominant. The envelope of the fluctuations for a long time run is shown in the bottom figure. The fluctuations are oscillatory with a frequency that corresponds closely to the eigenvalue as obtained from linear stability theory in the initial stages. In the long time regime this frequency increases only slightly. A similar behavior was observed for the fluctuations in the other flow variables. Since the simulation is 2D the strongly destabilizing 'oblique mode' mechanisms which are responsible for the rapid transition in 3D simulations are absent [1, 27]. This absence has several consequences. The 'transition' process in 2D is very slow, e.g. the above mentioned decrease in the shape factor takes place

in a time span of about 2×10^4 units which is two orders of magnitude larger than in 3D. Moreover, the tail of the energy spectrum is much steeper, showing that only very little small scale structures are generated in 2D. The well developed flow field bears little resemblance to a turbulent flow in 3D; mainly a large scale structure of the size of the computational box is observed.

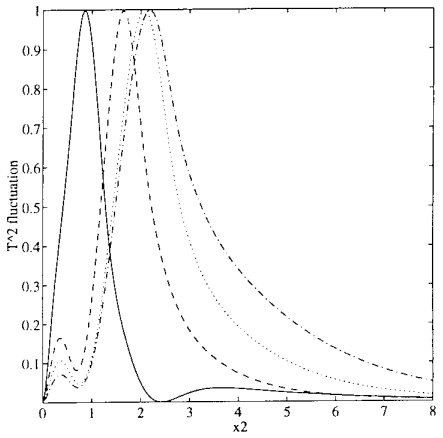

Figure 4: Spatial distribution of the fluctuations in T for $t = 0$ (solid), $t = 5000$ (dashed), $t = 10000$ (dotted) and $t = 15000$ (dash-dotted).

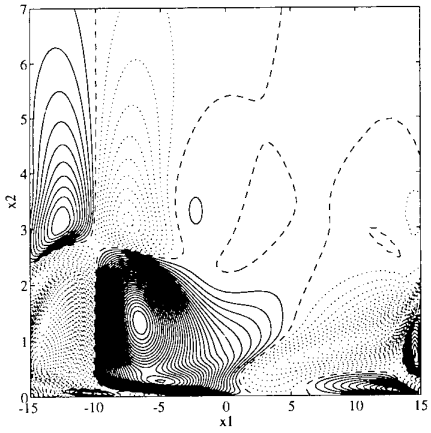

Figure 5: Contours of the (1,2)-component of the turbulent stress at $t = 15000$.

The simulations starting from a random noise perturbation show that the most unstable mode as predicted by linear stability theory becomes dominant after a certain transient period. The evolution beyond the time in which this mode has become dominant is hence virtually identical to the evolution initialised on an eigenfunction perturbation. We consider this second set of simulations next. The amplitude of the linear stability perturbation was set 10^{-2}. In figure 3 the spatial distribution of the fluctuations in the vorticity is presented for different times. In the linear regime two separated layers of vorticity fluctuations in the near wall region are present. Both positive and negative vorticity fluctuations are observed. The regions of negative vorticity fluctuation are seen to connect near the moment beyond which the boundary layer thickness increases logarithmically with time (cf. fig.1). For later times the connection between regions of negative vorticity fluctuation remains and becomes more pronounced as shown in figure 3. This global development of the flow is reminiscent of the early stages of subsonic transitional flow in 3D simulations of flat plate flow [27]. In the early stages the dominant mode is two-dimensional at the combination of Mach and Reynolds number adopted here. The evolution of the spatial structure of the fluctuations in the temperature is shown in figure 4. In particular we plot the x_1-integrated square fluctuations $(T')^2$ normalised such that the maximum equals 1 (this implies different normalizations for the different curves). Initially the spatial structure of these fluctuations corresponds closely with the predictions from linear stability theory. In the later stages an additional structure arises near $x_2 = 1/2$ and the maximum shifts away from the plate.

In figure 5 we show the spatial distribution of $\overline{\rho} a_{12}$ at $t = 15000$. The simulation is based on 128×128 grid cells and we used a filter width Δ corresponding to 2 intervals on a 64×64 grid. Similar results were obtained when using different filter-widths and even coarser LES-grids. One clearly observes the saddle structure in this component of the turbulent stress [19]. Moreover, since use is made of a 'positive' filter, i.e. the kernel of the generalized box filter is positive, the other components of the turbulent stress are positive as well and in addition we verified that $|\overline{\rho} a_{12}| \leq [(\overline{\rho} a_{11})(\overline{\rho} a_{22})]^{1/2}$ [28]. These 'realizability conditions' [29] can be shown to hold if and only if the filter-kernel is a positive function. The use of a non-positive filter such as the spectral cut-off filter can give rise to negative values of the generalized turbulent kinetic energy k. This has some consequences on the combinations of fil-

ters and subgrid-models that can be used in LES, in particular when using so called one-equation models involving k to be positive.

Based on these data we next determine the correlation of the models introduced in section 3 with the actual turbulent stresses. Moreover, we consider the contribution to the filtered equations arising from the non-commutation of the filter operator with the partial differential operators. If we consider the correlations of the subgrid models introduced in section 3 with the turbulent stresses we observe a large range of different values. If we compare the models on tensor-level, i.e. we compare the modeled stress tensor with the turbulent stress tensor obtained from filtering the DNS-data, we find correlations with $\overline{\rho}a_{12}$ very close to 1 for the Bardina and mixed models and practically 0 for the Smagorinsky and the Germano models using Δ equal to 2 intervals on a 64×64 grid. Increasing Δ or coarsening the grid does not lead to essential changes in the correlations although a decrease by about 1% is observed e.g. for Bardina's model. The low correlation of the Smagorinsky and Germano models seems to indicate that the gradient hypothesis for the turbulent stress tensor is inaccurate; the principal axes of the turbulent stress tensor are not aligned with those of the rate of strain tensor. These results were obtained for the field at $t = 15000$ and are typical for other times. When comparing the models at vector-level, i.e. considering the divergence of the turbulent stress, the correlation of the Bardina and mixed models decreases slightly ($\approx 2\%$) whereas the Smagorinsky and Germano models show no improvement. A comparison of the L_2-norms exhibits a similar pattern; the Smagorinsky model generates a far too high value, the Bardina model and the mixed model give rise to virtually the correct norm and the Germano model underestimates the norm considerably. Typically the Bardina model underestimates the norm by less than 1 % and the mixed model overestimates it by about 5 % .

The extension of the box-filter introduced in section 2 implies the occurence of additional terms in the filtered equations due to the non-commutation. In figure 6 we show the spatial distribution of the three terms arising from the filtering of the nonlinear convection term $\partial_j(\rho u_1 u_j)$ using the decomposition as introduced in eq.(2.11). We distinguish between a mean term ($\partial_j(\overline{\rho}\tilde{u}_1\tilde{u}_j)$), a turbulent stress term ($\partial_j(\overline{\rho}a_{1j})$) and an associated non-commutation term. In order to represent all three results in one graph the turbulent stress term and the non-commutation term have been multiplied by a factor of 10. Hence, the mean term is clearly dominant. The magnitude of the turbulent stress term and the non-commutation are comparable. Since the simulation is in 2D, these observations may well be quite different in 3D simulations and in *a posteriori* tests; this is subject of future investigation. The non-commutation terms have largely been disregarded in the LES-modeling so far because, almost exclusively, convolution filters have been applied. Following the approach outlined in section 2, however, it appears from the 2D results that a careful consideration of these terms is necessary. Modeling these terms using the scale similarity hypothesis seems a natural first attempt. In particular we propose

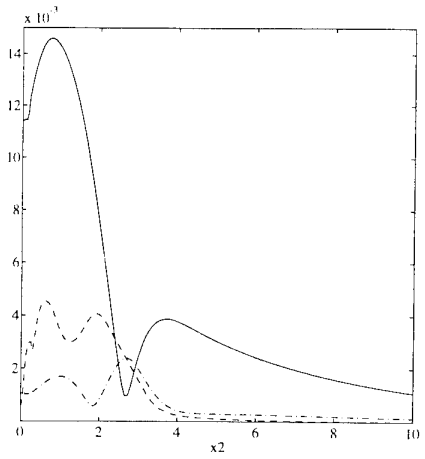

Figure 6: Norm of mean terms (solid), turbulent stress (dashed) and non-commutation term (dash-dotted) in the x_1-momentum equation at $t = 15000$. The latter two curves have been multiplied by a factor of 10 in order to represent the results in one graph.

$$\overline{\partial_j F(\mathcal{U})} - \partial_j \overline{F(\mathcal{U})} \rightarrow \overline{\partial_j F(\overline{\mathcal{U}})} - \partial_j \overline{F(\overline{\mathcal{U}})} \qquad (4.2)$$

which bears a strong resemblance with the Bardina model for the turbulent stress itself. *A priori* test results showed a correlation of at least 0.95 for the present 2D-data which seems to indicate that accurate models for the non-commutation terms can

be formulated. In order to further establish these results it is, however, required to perform simulations in 3D, both DNS and actual LES (*a posteriori* tests). The results of this study are anticipated in the near future and will be published elsewhere.

5 LES of the compressible mixing layer in 3D

In this section we present some LES results obtained for the compressible mixing layer in 3D. In this application a convolution filter is used, which implies that the non-commutation terms are absent. Instead we focus on a comparison of actual LES using the subgrid models introduced in section 3 with the filtered DNS results for a 3D flow in which a well developed turbulent flow field develops [15, 19, 30]. In this way we can assess the quality of these subgrid models for a turbulent flow, supplementing the results obtained for the flat plate flow in 2D. First we describe the DNS results and present some *a posteriori* test results afterwards.

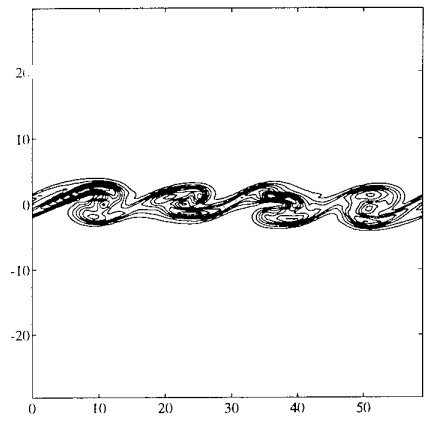

Figure 7: Contours of spanwise vorticity for the plane $x_3 = (3/4)L_3$ at $t = 20$. Solid contours and dotted contours indicate negative and positive vorticity respectively. The contour increment is 0.2.

The Navier-Stokes equations were solved in a rectangular geometry $[0, L_1] \times [-L_2/2, L_2/2] \times [0, L_3]$ with $L_1 = L_2 = L_3 = 59$ corresponding to four wave-lengths of the most unstable mode as predicted by linear stability [26] at $M = 0.2$ and $Re = 50$ using half the initial vorticity thickness as length scale. Periodic boundary conditions are imposed in the x_1 and x_3 directions, while in the normal x_2 direction the boundaries are free slip walls. The basic initial velocity profile is the hyperbolic tangent profile $u_1 = \tanh(x_2)$. The initial mean temperature profile is obtained from the Busemann-Crocco law and the initial pressure distribution is uniform. Superimposed on the mean profile we put a three-dimensional large amplitude eigenfunction perturbation as described by Sandham and Reynolds [30]. A simulation on a uniform grid with 192^3 cells is performed which proved to be well resolved through a comparison with lower resolution runs using 64^3 and 128^3 cells. The convective terms are treated with a fourth order accu-

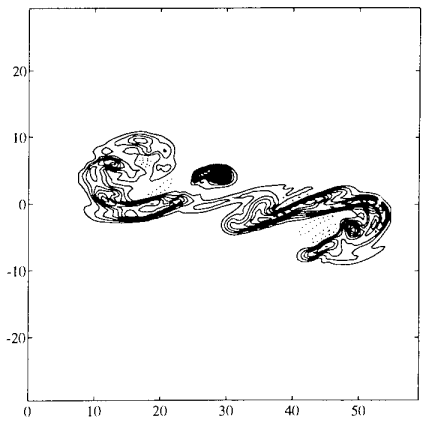

Figure 8: Contours of spanwise vorticity for the plane $x_3 = (3/4)L_3$ at $t = 40$.

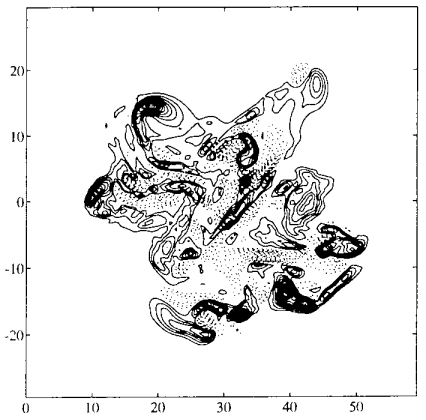

Figure 9: Contours of spanwise vorticity for the plane $x_3 = (3/4)L_3$ at $t = 80$.

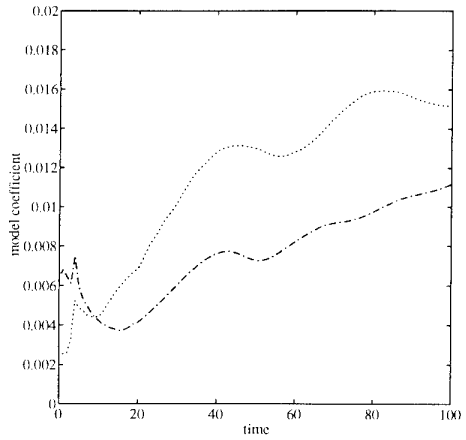

Figure 10: The evolution of C_S for the Germano model (dotted) and the mixed model (dash-dotted).

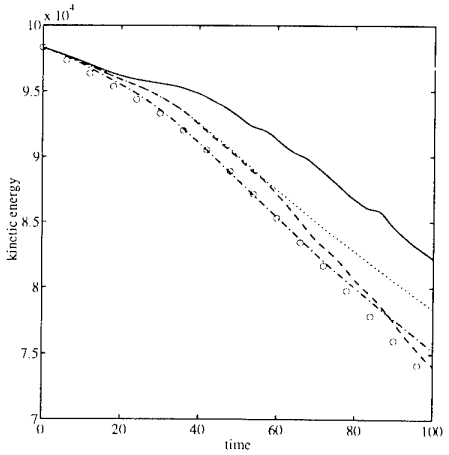

Figure 11: The evolution of the kinetic energy: coarse DNS (solid), filtered fine DNS (markers), Germano model (dotted), Bardina model (dashed) and mixed model (dash-dotted).

rate finite difference method. The growth rates of the dominant two- and three-dimensional modes are predicted with an error of at most one percent. The DNS demonstrates the roll-up of the fundamental instability and successive pairings. Four rollers with mainly negative span-wise vorticity are observed at $t = 20$ (fig. 7). After the first pairing ($t = 40$) the flow has become highly three-dimensional (fig. 8). Another pairing ($t = 80$), yields a single roller in which the flow exhibits a complex structure, with many regions of positive span-wise vorticity (fig. 9). This structure is a result of the transition to turbulence which has been triggered by the pairing process at $t = 40$ [15, 31]. The simulations are stopped at $t = 100$, at which time a single well developed roller remains.

In *a priori* tests it was found that the correlations of the subgrid models with the turbulent stress on vector level is close to zero for the Smagorinsky and Germano model, whereas it is about 0.9 for the Bardina model and 0.8 for the dynamic mixed model. A calculation of the subgrid terms in the energy equation showed that at $M = 0.2$ these terms are very small, approximately two orders of magnitude smaller than the corresponding mean terms. Hence these terms were disregarded in the *a posteriori* tests [15]. For the actual LES we selected a 32^3 grid in order to represent a demanding testcase for the *a posteriori* tests and used $\Delta = 2h$ with h the grid spacing on the coarse grid. We used the filtered initial state for the DNS to define the initial state for the LES.

In figure 10 we show the evolution of the average value of C_S for the Germano model and the mixed model. It is apparent that the model coefficient in the Germano model is significantly larger than in the mixed model which is a consequence of the introduction of the Bardina term in this model. The latter term correlates very well with the turbulent stress which implies that the eddy-viscosity part has to account for a strongly reduced 'portion' of the total turbulent stress [14].

In figure 11 the evolution of the total kinetic energy is shown for several models. The results for the Smagorinsky model are not shown here since they correspond very poorly with the filtered DNS results. For all three models we observe that the results of LES are better than those corresponding to a coarse grid DNS. Moreover, the results obtained with the mixed model seem to be somewhat better than those resulting from the Bardina model. Turning to the evolution of the momentum thickness (fig. 12) we observe a similar improvement of the results using the Bardina and mixed models. The Germano model appears to give no improvement over the coarse grid DNS. The correspondence of the LES and filtered DNS results is not as good as was obtained for the kinetic energy. The remaining difference between the LES and the filtered DNS results can be attributed to two aspects. First, further improvement in the subgrid modeling is necessary. Moreover, the effects of the discretisation

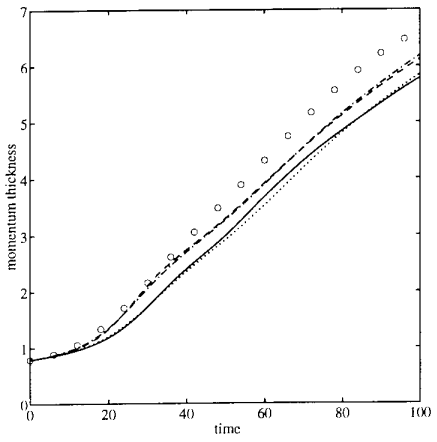

Figure 12: The evolution of the momentum-thickness: identification of lines as in figure 11.

errors cannot be disregarded [19, 32].

6 Conclusions

We compared DNS and LES results for compressible flow over a flat plate in 2D and in a mixing layer in 3D. Both *a priori* and *a posteriori* tests have been performed and attention was paid to the contributions of the non-commutation terms in the filtered equations. It was shown that in particular the scale similarity hypothesis in combination with the Germano-identity can be exploited to formulate accurate models for the turbulent stress. Both for the flat plate and the mixing layer excellent correlation of the scale similarity model of Bardina and the dynamic mixed model, with the turbulent stress was observed. This agreement was seen to hold for the entire evolution of the flow, i.e. in the transitional regime as well as in the early stages of fully developed turbulent flow. This correlation is almost absent for the eddy-viscosity models considered which suggests that the 'gradient hypothesis' is inaccurate. More precisely, it appears that the principal axes of the rate of strain tensor are not aligned with those of the turbulent stress tensor. These *a priori* observations partially clarify the differences in the performance of these models in actual LES, i.e. *a posteriori* testing. The Bardina and mixed models yielded accurate predictions of the filtered DNS results whereas the Smagorinsky model yielded very inaccurate results. The need to perform both types of LES-tests is apparent in view of the results obtained with the dynamic eddy-viscosity model of Germano. In *a priori* tests the correlation proved to be very small and strongly fluctuating in time for this model whereas in *a posteriori* tests a considerable improvement when compared to a coarse grid DNS was obtained for some flow properties.

The filtering of the Navier-Stokes equations close to solid walls was considered in detail. Usually convolution filters are used in LES which have a number of drawbacks. These drawbacks can be removed for filters with a compact support when allowing the filter-width Δ to be a function of the spatial coordinates. With such an extension a filter-width variation can be determined which 'matches' the variation of the small scale structures in the flow and leads to a more efficient filtering of the equations. A complication that arises from this approach, however, is that additional terms in the filtered equations should be taken into account. These arise from the non-commutation of the filter operator with the partial differential operators. Such terms were shown in 2D to be comparable in norm to the subgrid terms. Hence, it is necessary to study the contribution of these terms to the filtered equations in detail, in particular in physically more relevant 3D simulations. It appeared that the scale similarity hypothesis can be used to provide models for these terms which have a high correlation.

These results obtained for the flat plate flow were based on simulations in 2D which were shown to give rise to well developed flow fields which bear little resemblance to well developed turbulent flow fields that are reported for flat plate flow in 3D. Hence, in order to obtain physically relevant conclusions it is required to repeat the analysis for a 3D simulation. Results of this study are anticipated in the near future and will give a first impression about the sensitivity of the small scale contributions to the geometry of the flow. This is required if LES is to be developed systematically for turbulent flow in more complex geometries which forms the long-terms objective of the present research.

References

[1] L. Kleiser and T.A. Zang, Ann. Rev. Fluid Mech., **23**, 495, (1991)

[2] G. Erlebacher and M.Y. Hussaini, Phys. Fluids A **2**, 94, (1990)

[3] T. Herbert, Ann. Rev. Fluid Mech., **20**, 487, (1988)

[4] L. Ng and G. Erlebacher, Phys. Fluids A **4**, 710, (1992)

[5] Lesieur M., 'Turbulence in Fluids', Kluwer Academic Publishers, (1987)

[6] N.D. Sandham and L. Kleiser, J. Fluid Mech. **245**, 319, (1992)

[7] R.S. Rogallo and P. Moin, Ann. Rev. Fluid Mech. **16**, 99, (1984)

[8] G. Erlebacher, M.Y. Hussaini, C.B. Speziale and T.A. Zang, J. Fluid Mech. **238**, 155, (1992)

[9] X. Normand and M. Lesieur, Theoret. Comput.Fl. Dyn., **3**, 231-252, (1992)

[10] M. Germano, J. Fluid Mech. **238**, 325 (1992)

[11] J. Bardina, J.H. Ferziger and W.C. Reynolds, Department of Mechanical Engineering, Report No. TF-19, Stanford (1984)

[12] M. Germano, U. Piomelli, P. Moin and W.H. Cabot, Phys. Fluids A **3**, 1760 (1991)

[13] Y. Zang, R. L. Street and J.R. Koseff, Phys. Fluids A **5** 3186 (1993)

[14] A.W. Vreman, B.J. Geurts and J.G.M. Kuerten, Memorandum 1192, University of Twente, (1994)

[15] A.W. Vreman, B.J. Geurts, J.G.M. Kuerten, First ERCOFTAC workshop on Direct and Large Eddy simulation, 28-30 March, Guildford, England, To appear, (1994)

[16] A.Favre, Physics of Fluids, **26**, 2851, (1983)

[17] B.J. Geurts, B. Vreman, H. Kuerten, V. Theofilis, Proceedings 2nd International Symposium on Engineering Turbulence Modelling and Measurements, Florence 31 May- 2 June 1993, Ed: W. Rodi, F. Martelli, Elsevier, 325, (1993)

[18] N.M. El-Hady, T.A. Zang and U. Piomelli, ASME FED-Vol. **162**, 103 (1993)

[19] B. Vreman, B.J. Geurts and J.G.M. Kuerten, J. Engg. Math, To appear, (1994)

[20] J. Smagorinsky, Mon. Weather Rev. **91**, 99 (1963)

[21] P. Moin and J. Jimenez, AIAA-93-3099, AIAA 24th Fluid Dynamics Conference, Orlando (1993)

[22] D.K. Lilly, Phys. Fluids A **4**, 633 (1992)

[23] L.M. Mack, AGARD-Rep. No. 709, Lecture Series VKI, (1984)

[24] M.R. Malik, NASA Rep. 3584, (1982)

[25] J.G.M.Kuerten, B.J.Geurts, J. van der Burg, A.W.Vreman, P.J.Zandbergen, Proceedings 13th International conference on numerical methods in fluid dynamics, Eds: M. Napolitano, F. Sabetta, Springer, 529, (1993)

[26] V.Theofilis, A.W.Vreman, B.J. Geurts, J.G.M. Kuerten, ASME FED-Vol. **155**, 71, (1993)

[27] W. Eissler and H. Bestek, Proceedings ASME FED **151**, 69, (1993)

[28] A.W. Vreman, B.J. Geurts and J.G.M. Kuerten, Memorandum 1181, University of Twente, (1993)

[29] U. Schumann, Phys. Fluids **20**, 721, (1977)

[30] N.D. Sandham and W.C. Reynolds, J. Fluid Mech. **224**, 133, (1991)

[31] R.D. Moser and M. Rogers, J. Fluid Mech. **247**, 275 (1993)

[32] B. Vreman, B.J. Geurts, H. Kuerten, Comm. Num. Meth. Eng. Math., To appear (1994)

Direct Numerical Simulation of Turbulent Flow in a Sudden Pipe Expansion

C. Wagner and R. Friedrich
Lehrstuhl für Fluidmechanik
Munich University of Technology
Arcisstr. 21
80290 München
Germany

1. SUMMARY

Direct numerical simulations (DNS) of fully developed turbulent pipe flow and sudden pipe expansion flow with an expansion ratio of ER = 1.2 have been performed. The former DNS provides inflow conditions for the latter. The upstream Reynolds number, based on friction velocity and pipe diameter is 360 or 6950 based on mean centerline velocity. This is too low a Reynolds number to obtain a universal logarithmic law of the wall. Moreover, tranverse curvature effects are observed when the data are compared with DNS data of Kim, Moin, Moser (1987) in the plane channel. The reason for these effects is that the streak spacing is of the same order of magnitude as the pipe radius. Hence, the pipe expansion flow will also reflect transverse curvature effects. The mean reattachment length is 10.1 step heights. Instantaneous and statistical flow variables are presented. They give an impression of the complex flow dynamics in the free shear layer, the recirculation and reattachment regions.

2. PREFACE

The turbulent flow through a sudden pipe expansion is of great theoretical and practical importance since it involves several fundamental flow phenomena and is found in a wide variety of applications. The configuration is used for dump combustors where swirl is introduced before the expansion and the recirculation zone serves as a flame holder. It also appears e.g. in piping junctions. The major features of this flow are a free shear layer which rapidly develops downstream of the expansion by entraining fluid from the main stream and from a primary recirculation zone. The shear layer curves towards the wall and hits it forming a broad reattachment region. Downstream recovery of the flow is so slow that there is no possibility of studying it in a DNS. The prediction of pipe expansion flow is a challenge for statistical turbulence modelers, even today. Unless the complex turbulence dynamics within the free shear layer and the reattachment region are fully understood, real improvement of turbulence models is not possible. The present paper attempts to provide more insight into the physics of this flow based on instantaneous and statistical data than the experiment can, at least at low Reynolds number.

3. NUMERICAL METHOD

In order to obtain a spatially discretized version of the incompressible Navier-Stokes equations in cylindrical coordinates we apply Schumann's volume balance procedure (1973) and use his definitions of surface averaged velocity components $\overline{u_\alpha}$ and volume-averaged pressure $\overline{p}$, viz :

$$\overline{u_\alpha} = \frac{1}{\Delta A_\alpha}\int u_\alpha \, dA_\alpha \quad \text{(no summation)} \tag{1}$$

$$\overline{p} = \frac{1}{\Delta V}\int p \, dV \tag{2}$$

with $\Delta A_z = r\Delta r\Delta\varphi$, $\Delta A_\varphi = \Delta r\Delta z$, $\Delta A_r = r\Delta\varphi\Delta z$, $\Delta V = r\Delta r\Delta\varphi\Delta z$. Using the diameter of the upstream pipe D and the wall shear velocity u_τ for nondimensionalization, the dimensionless and finite volume form of the Navier-Stokes equations reads:

$$\sum_\alpha \left(\Delta A_\alpha \, \overline{u_\alpha}\,|_{\xi_\alpha +} \; - \Delta A_\alpha \, \overline{u_\alpha}\,|_{\xi_\alpha -}\right) \; = \; 0 \tag{3}$$

$$\begin{aligned} &\Delta V \tfrac{\partial \overline{u_\alpha}}{\partial t} + \\ &\textstyle\sum_\beta \Big[\Delta A_\beta \left(\overline{u_\beta}\,\overline{u_\alpha} \; + \; \overline{p}\delta_{\alpha\beta} \; - \; \overline{\tau_{\alpha\beta}}\right)|_{\xi_\beta +} \\ &- \Delta A_\beta \left(\overline{u_\beta}\,\overline{u_\alpha} \; + \; \overline{p}\delta_{\alpha\beta} \; - \; \overline{\tau_{\alpha\beta}}\right)|_{\xi_\beta -}\Big] \\ &- (\text{Term})_\alpha \; = \; 0 \end{aligned} \tag{4}$$

$\alpha, \beta \; = \; z, \varphi, r$.

$(\text{Term})_\alpha$ contains the curvature terms:

$$(\text{Term})_z \;\; = \;\; 0, \tag{5}$$

$$(\text{Term})_\varphi \;\; = \;\; \frac{\Delta V}{r}\left(-\,\overline{u_\varphi}\,\overline{u_r} \; + \; \overline{\tau_{\varphi r}}\right), \tag{6}$$

$$(\text{Term})_r \;\; = \;\; \frac{\Delta V}{r}\left(\,\overline{u_\varphi}\,\overline{u_\varphi} \; + \; \overline{p} \; - \; \overline{\tau_{\varphi\varphi}}\right). \tag{7}$$

The shear stress is defined as

$$\overline{\tau_{\alpha\beta}} \; = \; \frac{1}{Re_\tau}\overline{S_{\alpha\beta}} \tag{8}$$

with the Reynolds number $Re_\tau = u_\tau D/\nu$ and the deformation tensor

Paper presented at the 74th Fluid Dynamics Symposium on "Application of Direct and Large Eddy Simulation to Transition and Turbulence" held at Chania, Crete, Greece, in April 1994.

$$\overline{S_{\alpha\beta}} =$$

$$\begin{bmatrix} 2\delta_z\overline{u_z} & \frac{1}{r}\delta_\varphi\overline{u_z}+\delta_z\overline{u_\varphi} & \delta_r\overline{u_z}+\delta_z\overline{u_r} \\ \dots & \frac{2}{r}\left(\delta_\varphi\overline{u_\varphi}+\overline{u_r}\right) & r\delta_r\left(\frac{\overline{u_\varphi}}{r}\right)+\frac{1}{r}\delta_\varphi\overline{u_r} \\ \dots & \dots & 2\delta_r\overline{u_r} \end{bmatrix} \quad (9)$$

δ_α represents a central difference operator

$$\delta_\alpha\phi = \frac{\phi(\xi_\alpha+\Delta\xi_\alpha/2)-\phi(\xi_\alpha-\Delta\xi_\alpha/2)}{\Delta\xi_\alpha}. \quad (10)$$

The momentum equations (4) are integrated in time on staggered grids using a semi-implicit scheme in which all convection and diffusion terms containing derivatives in the circumferential direction are treated implicitly. A leap-frog scheme being second-order accurate serves to integrate the remaining convection terms in time. Diffusive terms with derivatives in the (r,z)-directions are treated with a 1st order Euler-backward step. Both, leapfrog and Euler steps are explicit and consequently, the admissible time-step Δt must be limited to avoid numerical instabilities. A conservative choice for Δt is:

$$\Delta t \le \frac{1}{2\left[\left(\frac{|\overline{u_r}|}{\Delta r}+\frac{|\overline{u_z}|}{\Delta z}\right)_{max}+4\nu\left(\frac{1}{\Delta r^2}+\frac{1}{\Delta z^2}\right)\right]} \quad (11)$$

A variant of Chorin's (1968) fractional-step method is applied to provide the coupling between the pressure and the velocity fields. The divergence of the pressure-correction equation leads to a Poisson-equation which is solved using Fast Fourier transforms in φ-direction. The remaining set of 2D Helmholtz problems in irregular domains is treated with a cyclic reduction algorithm in combination with the influence matrix technique (Schumann 1980).

On the pipe centerline the basic partial equations are singular. In their finite-volume form and on staggered grids these equations do not pose serious problems, but require an approximation concerning the radial velocity component at its position closest to the axis. This component is extrapolated from neighbouring (inner) mesh points.

3.1 Boundary conditions

Due to the elliptical nature of the flow equations boundary conditions are needed at all boundaries of the computational domain. At the wall the impermeability condition leads to vanishing radial, respectively axial (at the expansion) velocity components. Instead of two tangential velocity components - which are not defined at the walls within this finite volume scheme - two wall shear stresses

$$\overline{\tau_{rz}} = \frac{2}{Re_\tau}\frac{\overline{u_z}(R-\Delta r/2,\varphi,z,t)}{\Delta r},$$
$$\overline{\tau_{r\varphi}} = \frac{2}{Re_\tau}\frac{\overline{u_\varphi}(R-\Delta r/2,\varphi,z,t)}{\Delta r}, \quad (12)$$

have to be specified. (12) corresponds to the discretized forms of these stresses for the pipe sections. Corresponding stresses $\overline{\tau_{z\varphi}}$, $\overline{\tau_{zr}}$ are prescribed at the expansion.

The specification of boundary conditions for the incoming flow poses the greatest problem. Random velocity fluctuations satisfying certain constraints could have been superimposed on a mean velocity profile as in Le et al. (1993). We preferred to choose a more accurate and tedious way of obtaining inflow boundary conditions. A DNS of fully developed pipe flow at $Re_\tau = u_\tau D/\nu = 360$ was performed simultaneously with the DNS of the sudden pipe expansion flow to obtain the 3D time-dependent velocity vector in the inflow plane at each time step of the simulation.

The mean outgoing flow is linearly extrapolated, whereas the fluctuating velocity components are computed from a convection equation with a local mean velocity as convective speed.

Boundary conditions for the Poisson equation are derived from the pressure correction equation.

3.2 Initial conditions

To start the DNS of fully developed pipe flow artificial initial conditions are used for the velocity components in each cell. They consist of experimental mean values and random fluctuations satisfying the constraints of incompressibility and rms profiles. In order to avoid the subsequent decay of the initial fluctuations the Re-number is increased at the start of the simulation by a factor of 5 and then gradually decreased in the course of one eddy-turnover time (D/u_τ) down to the desired value. This is ample time for the energy spectrum to build up. The initial conditions for the DNS of the pipe expansion flow are constant values for the remaining components in the field downstream of the inflow plane. Due to the boundary conditions for the inlet plane these false initial values are totally swept out of the computational domain in the course of 6 eddy-turnover times.

4. COMPARISON BETWEEN FULLY DEVELOPED PIPE AND CHANNEL FLOW

The flow entering the sudden pipe expansion is fully developed and has a Reynolds number $Re_\tau = u_\tau D/\nu$ of 360. This corresponds to Reynolds numbers based on bulk velocity u_b or centerline velocity u_{cl} and diameter D of $Re_b = 5300$, respectively, $Re_{\mathrm{cl}} = 6950$. Re_τ has been chosen such that it coincides with $Re_\tau = u_\tau h/\nu$ of Kim et al.'s (1987) channel flow simulation (h being the channel width). The computational domain is 5 pipe diameters long. An equidistant cylindrical grid system has been chosen with

$$\Delta z^+ = 7.031, (r\Delta\varphi)^+ = 0.046, .., 8.789,$$
$$\Delta r^+ = 1.874 \quad (13)$$

The minimal Kolmogorov length scale close to the wall is $l_k^+ = 5.15$. The grid consisting of $256 \times 128 \times 96$ cells in (z, φ, r) directions is thus fine enough to resolve all scales. Essential parameters of the simulation are summarized in table 1. Only 20000 time steps i.e. 4 problem times have been used for statistical averaging.

Grid (z, φ, r)	$256 \times 128 \times 96$
Geometry (z, φ, r)	$5 \times 2\pi \times 0.5$
Timestep Δt	$2 \cdot 10^{-4}$
Number of timesteps	184000
CPU-time per Δt	6.8 sec
CPU-time per Δt and point	$2.2 \cdot 10^{-6}$ sec
total CPU-time	400 h
Required memory	29.7 MWords

Table 1: DNS parameters of pipe flow

	DNS Unger/ Wagner	LDA Wester- weel	DNS Kim et al.	DNS Gavri- lakis
Geom.	⊕	⊕	=	⊞
Re_{cl}	**6950**	7200	6600	5880
Re_b	**5300**	5450	5600	4421
Re_τ	**360**	371	360	300
u_{cl}/u_τ	**19.29**	19.39	18.20	19.56
u_b/u_τ	**14.74**	14.68	15.63	14.70
u_{cl}/u_b	**1.31**	1.32	1.16	1.33
$c_f \cdot 10^3$	**9.21**	9.28	8.18	-
δ_1/R	**0.126**	0.130	0.141	-
δ_2/R	**0.068**	0.071	0.087	-
δ_1/δ_2	**1.85**	1.83	1.62	-

Table 2: Comparison of integral parameters, $Re_{cl} = u_{cl}D/\nu$, $Re_b = u_bD/\nu$, $Re_\tau = u_\tau D/\nu$, $c_f = \tau_w/\frac{1}{2}\rho {u_b}^2$

The number of 184000 time steps equals that needed for averaging of flow quantities in the pipe expansion.

While the mean velocity profiles of pipe and channel flow coincide close to the wall, they diverge in the core regions and the pipe flow does not follow the universal logarithmic law. To achieve this, remarkably higher Reynolds numbers have to be used. Table 2 compares integral parameters of the present pipe DNS with LDA data of Westerweel et al. (1992), with DNS data of Kim et al. (1987) and DNS data of Gavrilakis (1992) for fully developed flow in a duct of square cross section. The DNS data are confirmed by the LDA experiment and they are closer to the data for the duct than for the channel, which is due to the fact that sidewalls are missing in the case of plane channel flow. Fig.1 shows a comparison of computed and measured mean velocity profiles. It is obvious that the flow in the pipe follows the universal log-law only for a Reynolds number greater/equal that of Durst et al. (1993), i.e. $Re_{cl} = 9600$. On the other hand the longitudinal rms-velocity fluctuations, normalized with the mean axial velocity, show good agreement for pipe and channel flow, see fig.2. The remaining two rms fluctuations are somewhat lower than in the channel. We see the cause for this behaviour in the transverse curvature of the pipe wall which the fluid experiences when

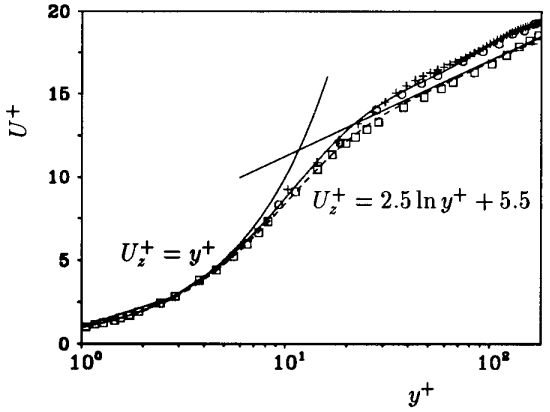

Figure 1: Mean velocity profiles versus log-law, Pipe: ——— present DNS, □ LDA Durst et al. (1993), ○ LDA Westerweel et al. (1992), + PIV Westerweel et al. (1992). Channel: – – – – Kim et al. (1987).

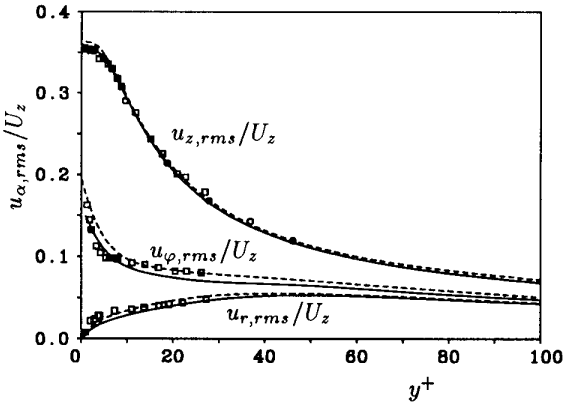

Figure 2: Rms velocity fluctuations, normalized with the mean axial velocity. Symbols as in figure 1.

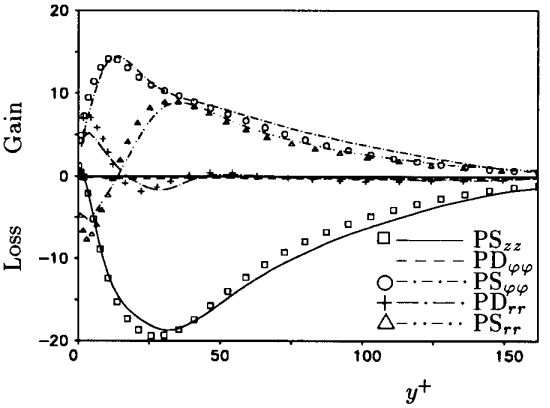

Figure 3: Pressure strain and pressure diffusion terms for pipe (lines) and channel flow (symbols, data of Kim et al. (1987)).

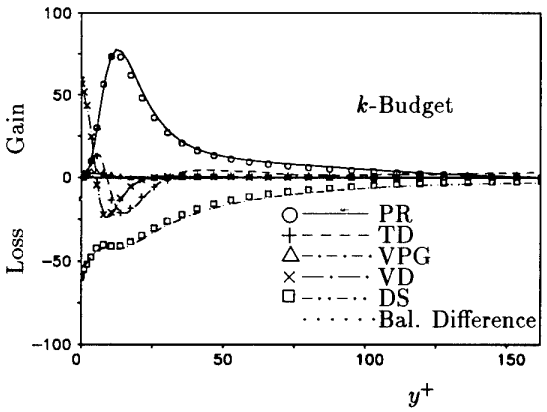

Figure 4: TKE budget for pipe (lines) and channel flow (symbols). PR = production, TD = turb. diffusion, VPG = velocity pressure gradient correlation, VD = viscous diffusion, DS = turbulent dissipation.

it approaches the wall in sweep events. In the present case the radius of curvature, expressed in wall units, Ru_τ/ν, is 180 which is comparable to the streak spacing of 120 (Ferziger (1993)). Transverse curvature effects are also reflected in the pressure strain (PS) and pressure diffusion (PD) terms appearing in the transport equations for the radial and circumferential velocity components. In figure 3 we present profiles of these terms. While PS_{zz} does not show any difference between pipe and channel flow in the viscous and buffer layers, the other terms are lower in the pipe than in the channel. In the core regions the geometrical differences between the two flows again show up. A comparison of the kinetic energy budgets for both flows is given in figure 4. Minor differences of the TKE production rate away from the wall are due to the shapes of the two velocity profiles. We feel that these results demonstrate that DNS with central finite difference schemes of second order accuracy provides very reliable results as long as the smallest turbulent scales are properly resolved. For more details, see Unger et al. (1993), Unger (1994) and Eggels et al. (1994).

5. RESULTS FOR PIPE EXPANSION FLOW

The computational domain consists of an upstream pipe section of diameter D and length 1.484D and a downstream section of diameter 1.2D and length 2.03D. $180 \times 128 \times 115$ mesh cells are used in (z, φ, r)-directions to resolve this domain. The grid spacing is the same as that for the incoming flow, see (13). A few more details of the DNS are summarized in table 3. This flow has only one homogeneous direction to be used for statistical averaging. A great number of realizations is therefore needed to obtain stable averages. Each 250th time step provides one of the 700 realizations used for averaging.

The Reynolds number based on centerline velocity of the incoming flow and step height 0.1 D is $Re_H = 695$. The reattachment length in terms of step height is

Grid (z, φ, r)	$180 \times 128 \times 115$
Geometry (z, φ, r)	$3.51 \times 2\pi \times 0.6$
Timestep Δt	$2 \cdot 10^{-4}$
Number of timesteps	184000
CPU-time per Δt	10.4 sec
CPU-time per Δt and point	$3.9 \cdot 10^{-6}$ sec
total CPU-time	600 h
Required memory	29 MWords

Table 3: DNS parameters of pipe expansion flow

10.1. This is in agreement with experimental data of Nitsche and Haberland (1993) for fully developed incoming flow, but a three times higher Reynolds number.

5.1 Instantaneous flow field

Figure 5 presents perspective views of the instantaneous velocity field in terms of contour lines of the three velocity components. They have their own characteristic features. The formation of shear layers with locally high gradients in the near wall region and in the mixing layer is a typical feature of the longitudinal velocity component (top). The circumferential velocity is organized in flow structures which are inclined in a characteristic manner with respect to the axis. The spotty character of the wall normal velocity component (bottom) is well known from wall-bounded turbulent shear layers. The increase in turbulence activity in the mixing layer due to extra rates of strain is reflected from all components. The flow dynamics within the recirculation and mixing layer regions are demonstrated in the following 3 figures showing contour lines and velocity vectors in two cross sections, one immediately downstream of the expansion ($z = 1.484$), the other slightly upstream of the mean reattachment line. At $z = 1.6$ the longitudinal velocity in figure 6 reflects a smooth external shape of the mixing layer. Further downstream we notice that this layer is extremly corrugated by high speed fluid which comes from the core region and penetrates the recirculation zone causing local patches of downstream momentum although the mean flow is reversed. It is useful discussing figures 7 and 8 simultaneously. They show projections of the velocity vector into (z = const)-planes and contour lines of pressure fluctuations. In fig. 7 each fourth velocity vector has been plotted only. There seem to be zones with high longitudinal vorticity. The lines $\varphi = \pi$ and $\varphi = 15\pi/8$ e.g. pass through these zones with velocity vectors turning round clockwise and anticlockwise, respectively. The pressure fluctuations in these spots, see fig. 8, show minimum values which underlines their vortical nature.

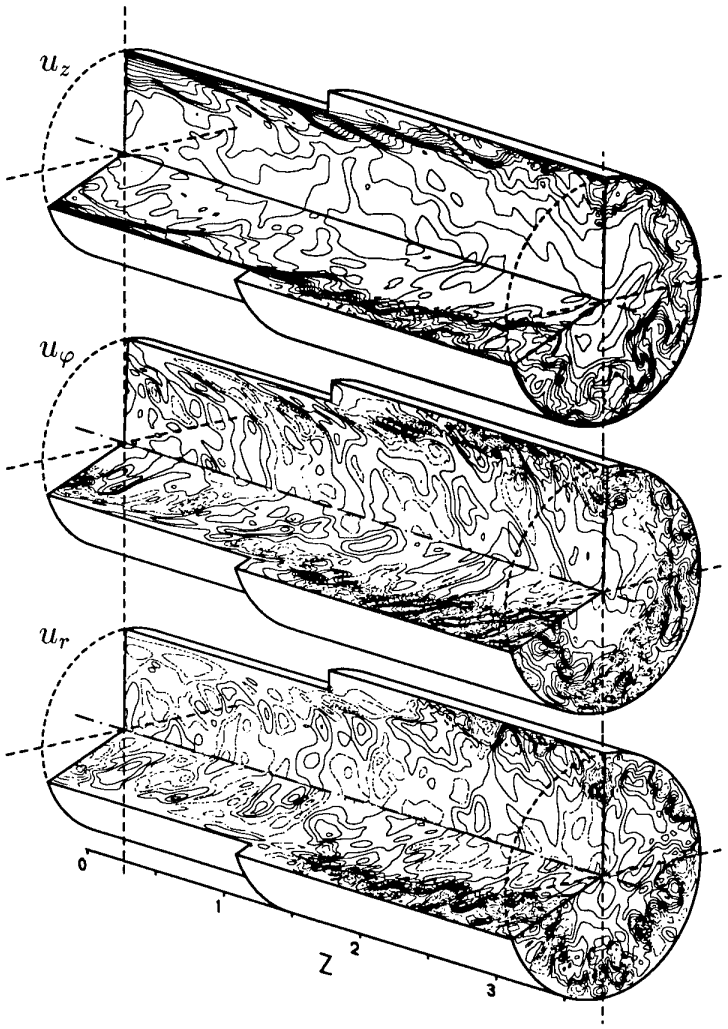

Figure 5: Snapshots of contour lines of the three velocity components

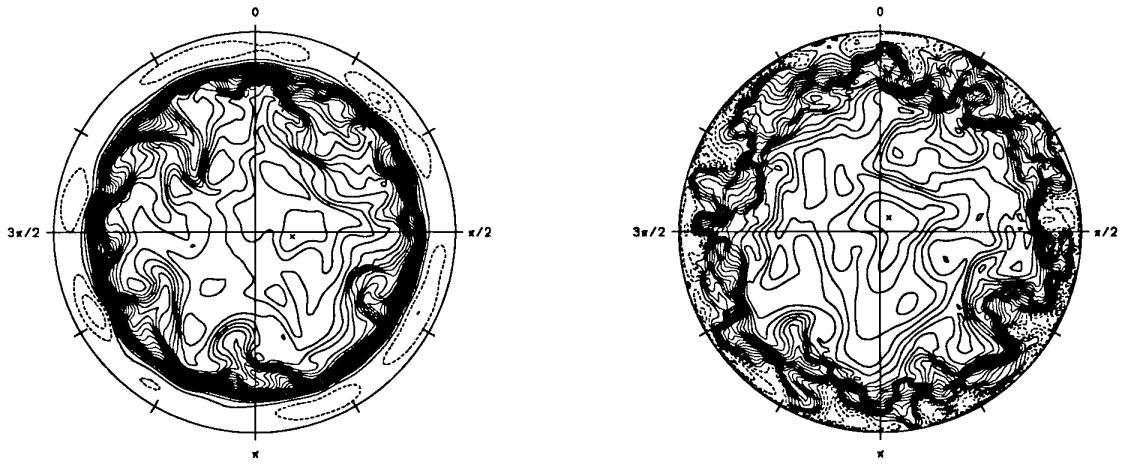

Figure 6: Contour lines of the instantaneous longitudinal velocity in planes $z = 1.6$ (left) and $z = 2.2$ (right). Values range from: $-1.957 < u_z < 20.61$, $-4.813 < u_z < 20.35$. Solid/dashed lines represent positive/negative values.

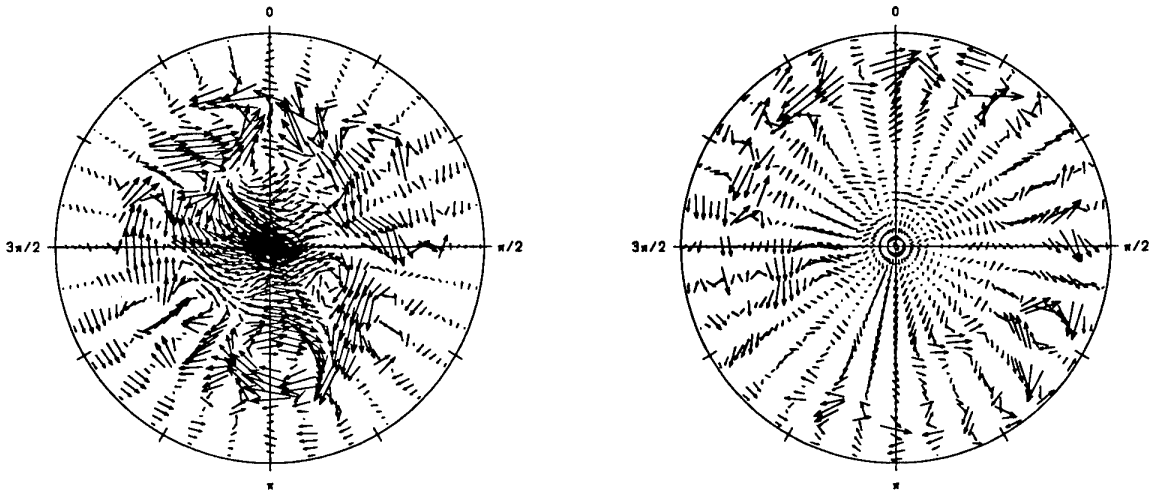

Figure 7: Projections of the instantaneous velocity vector into planes $z = 1.6$ (left) and $z = 2.2$ (right). The scaling in the two plots differs by a factor of two.

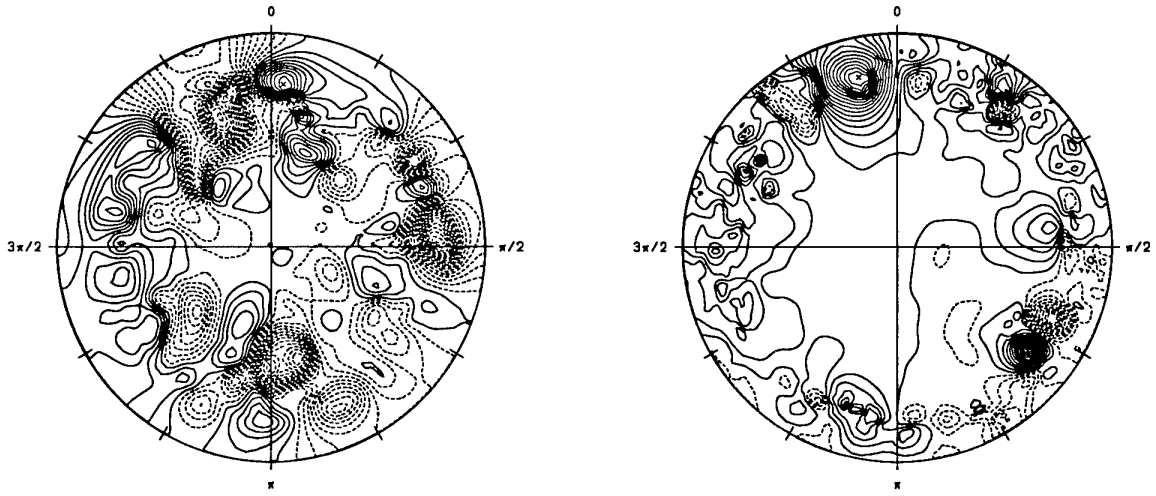

Figure 8: Pressure fluctuations in planes $z = 1.6$ (left) and $z = 2.2$ (right). Solid/dashed lines represent positive/negative values. Values range from $-7.157 < p' < 3.885$ (left), $-28.14 < p' < 47.03$ (right).

5.2 Statistically averaged flow field

Since the incoming flow is swirlfree, the statistically averaged flow field is axially symmetric. The mean velocity vector has only two components, namely those for axial and radial flow, $\langle u_z \rangle$, $\langle u_r \rangle$. Their profiles at different positions are plotted in fig. 9. The dotted line separates foreward from backward flow. It is the line of zero mean axial velocity, starting at the expansion and ending at the mean reattachment point. Especially the radial velocity shows that the flow at the outlet is still developing in axial direction.

Contour lines of the four non-zero components of the Reynolds stress tensor are plotted in figures 10 and 11.

It is obvious that the highest turbulence activity occurs in the mixing layer. Maximum/minimum values exceed those in the wall layer of the incoming flow by roughly an order of magnitude. The biggest amplification rates are achieved in the radial component, the lowest in the longitudinal component. The fact that the maximum values of the Reynolds stress components appear at different downstream positions reflects the complexity of the turbulence dynamics of this flow and the difficulties to correctly predict it with turbulence models. A close inspection of the contour lines, especially of the circumferential turbulence intensity, shows perturbations near the outlet plane which are due to the boundary condition used. They do not travel far upstream and are therefore irrelevant.

The importance of turbulence transport in the reattachment zone is underlined by contour plots of the triple correlations $\langle u_r' u_z'^2 \rangle$, $\langle u_r' u_\varphi'^2 \rangle$ and $\langle u_r'^3 \rangle$ in figure 12 from top to bottom. In the reattachment zone all quantities show qualitatively the same behaviour, namely a transport towards the wall and further away from the wall an even stronger transport towards the axis. Both effects are dominated by the characteristics of the mixing layer and exceed similiar effects in fully developed pipe flow by an order of magnitude.

The increase in turbulence activity in the mixing layer entails an increase in turbulent dissipation rate. Fig.13 shows profiles at three axial positions $z = 0.1$, 1.6 and 2.2. While ϵ reaches values of 48 close to the wall (nondimensionalized with $(u_\tau^3/D)_{z=0}$ in fully developed pipe flow, the mixing layer produces maximum rates of 120. Even the reversed flow dissipates turbulent kinetic energy at a maximum rate of 90 close to the wall.

A quantity which is extremly difficult to measure close to the wall even with non-intrusive devices like the LDA, is the flatness factor of the velocity fluctuations. From Kim et al.'s (1987) spectral data for fully developed channel flow it is well known that the wall normal fluctuation has a flatness factor of 20 in the vicinity of the wall. Fig. 14-16 show profiles of the three flatness factors for the same axial positions as in fig. 13, one close to the inflow, the other two within the recirculation zone.

In the mixing layer slightly downstream of the expansion the flatness factor of the axial velocity fluctuations achieves the biggest values in contrary to its behaviour in the wall layer of fully developed flow. This again is a manifestation of the complexity of the turbulence dynamics of the present flow.

We conclude the discussion of mean flow quantities with profiles of the rms vorticity fluctuations in fig. 17-19. Near reattachment the axial vorticity fluctuations are enhanced and reach values close to those of the circumferential component. This is true for the region close to the wall (reversed flow) and for the mixing layer zone, and it is in contrast to the flow behaviour upstream.

6. CONCLUDING REMARKS

A DNS based on second order accurate central differencing has been performed to study the turbulent flow in a sudden pipe expansion. Comparison of the incoming flow with fully developed channel flow of the same Reynolds number based on friction velocity (Kim et al.'s (1987) spectral data) underlines the reliability of the present data and reveals transverse curvature effects. The pipe expansion flow is characterized by a primary recirculation zone, a mixing layer and a reattachment zone. Extra rates of strain within the mixing layer provide a strong increase of turbulence activity and turbulent dissipation rate. The complexity of the turbulence dynamics is demonstrated in terms of snapshots of instantaneous flow quantities and in terms of 1-point correlations up to fourth order. The DNS results form a database which can be used to test and improve turbulence models.

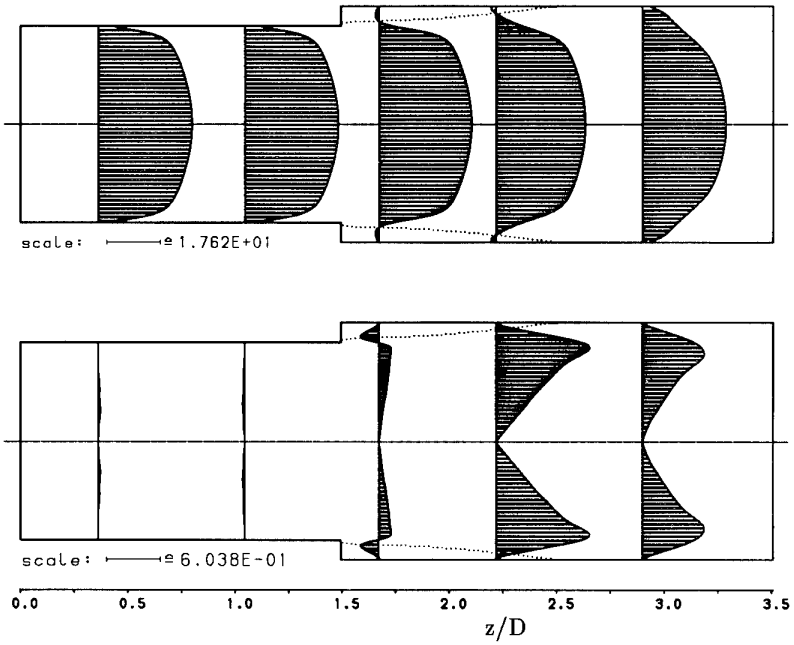

Figure 9: Profiles of mean axial (top) and radial velocity (bottom). The dashed line connects points of zero mean axial velocity

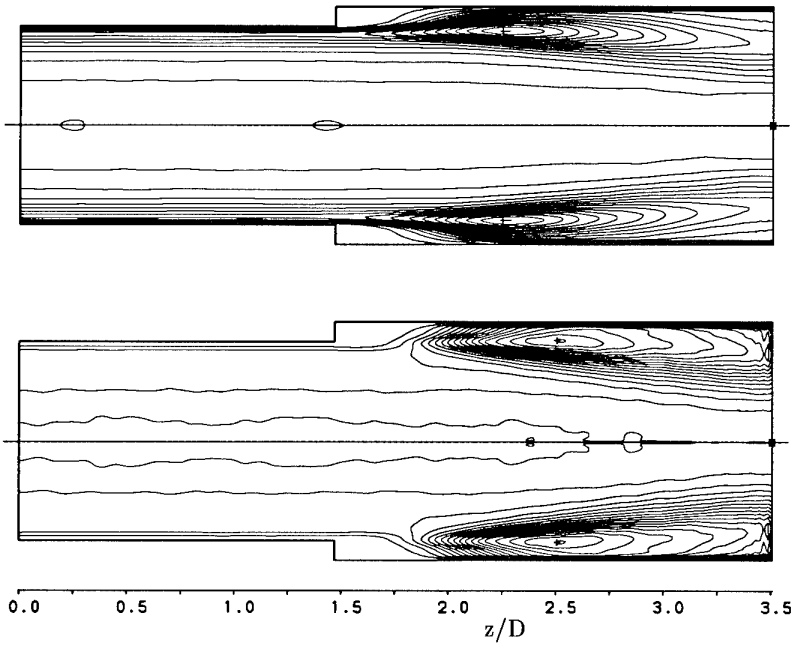

Figure 10: Contour lines of turbulence intensities, in axial (top) and circumferential directions (bottom). Range of values: $0.685 < \langle u_z'^2 \rangle < 16.30$ (top), $4.98 < \langle u_\varphi'^2 \rangle < 5.79$ (bottom). Solid/dashed lines represent positive/negative values.

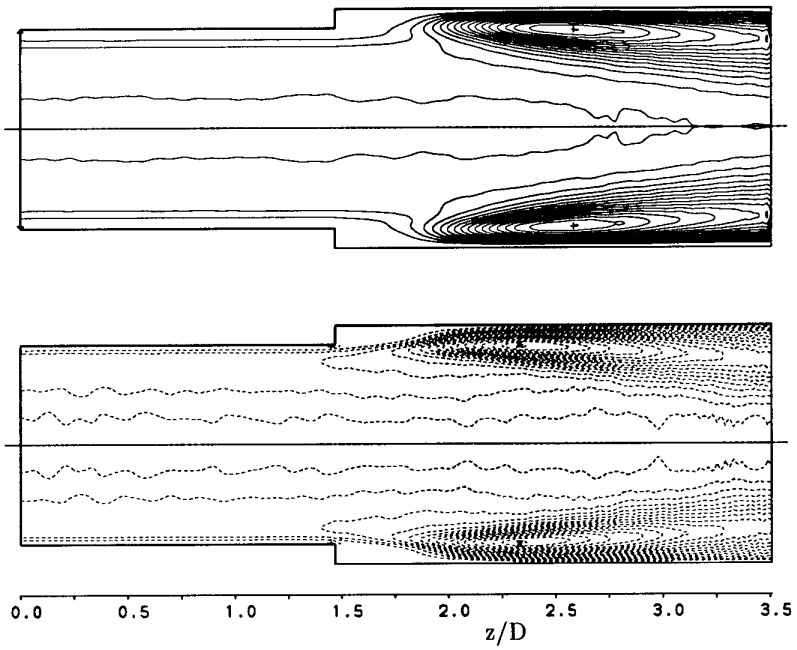

Figure 11: Contour lines of radial turbulence intensity and Reynolds shear stress. Range of values: $0.534 < \langle u_r{}'^2 \rangle < 4.63$ (top), $-4.343 < \langle u_z{}' u_r{}' \rangle < 0.00273$ (bottom).

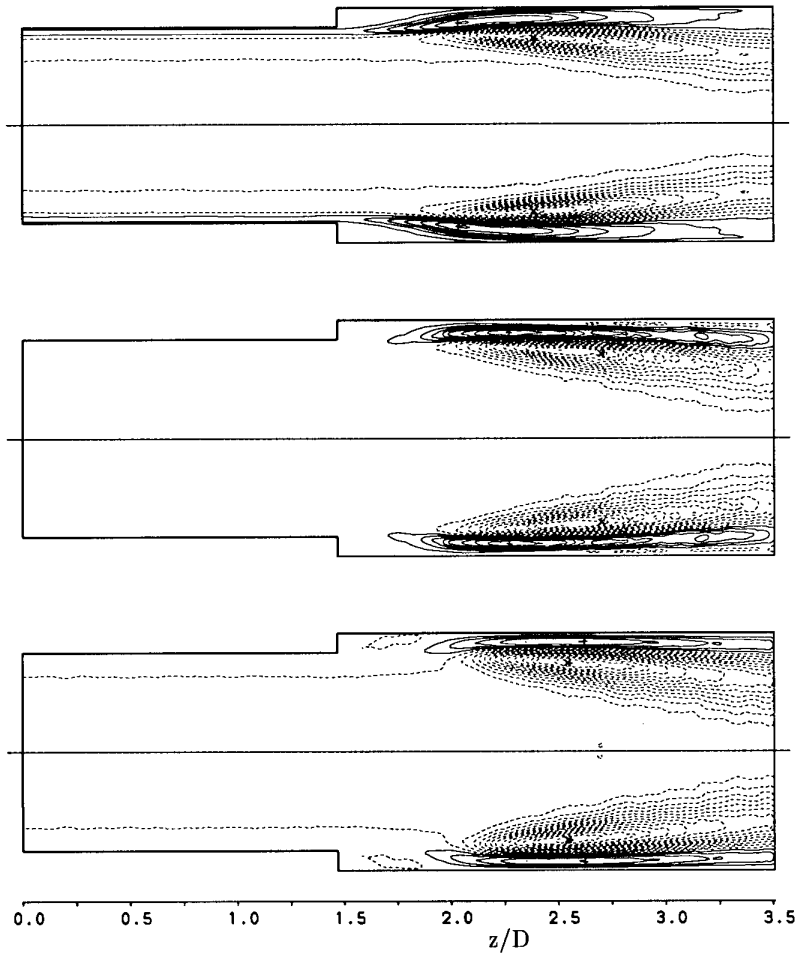

Figure 12: Contour lines of triple correlations. Range of values: $-10.4 < \langle u_r{}' u_z{}'^2 \rangle < 5.06$ (top), $-1.64 < \langle u_r{}' u_\varphi{}'^2 \rangle < 1.29$ (middle), $-5.22 < \langle u_r{}'^3 \rangle > 1.88$ (bottom).

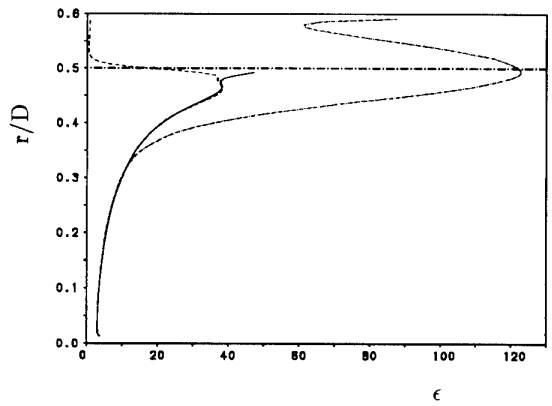

Figure 13: Profiles of turbulent dissipation rate at three axial positions: ——— :$z = 0.1$, – – – – : $z = 1.6$, –·–·–·– : $z = 2.2$.

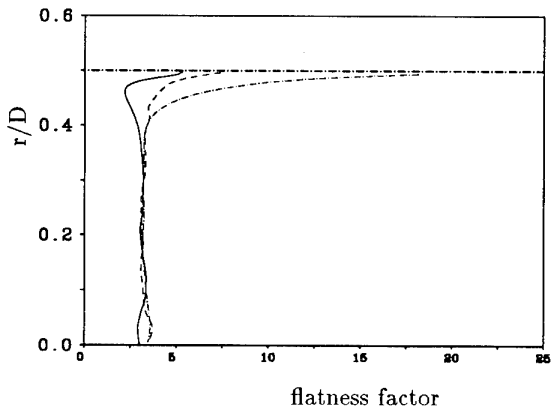

Figure 14: Profiles of the flatness factors of the 3 velocity fluctuations at the axial position $z = 0.1$, ——— :$u_{z,flat}$, – – – – : $u_{\varphi,flat}$, –·–·–·– : $u_{z,flat}$.

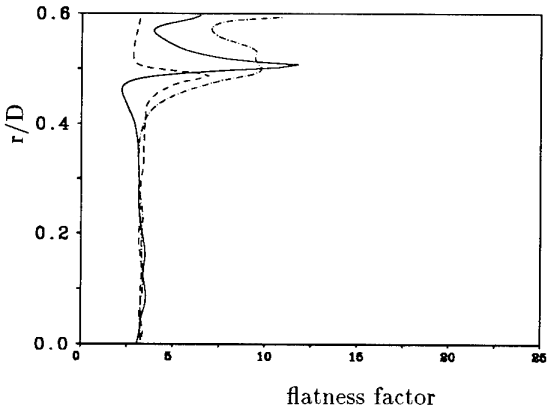

Figure 15: Profiles of flatness factors at the axial position $z = 1.6$, notation see fig. 14.

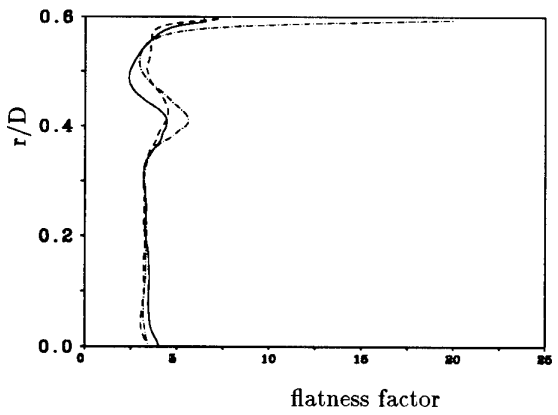

Figure 16: Profiles of flatness factors at the axial position $z = 2.2$, notation see fig. 14.

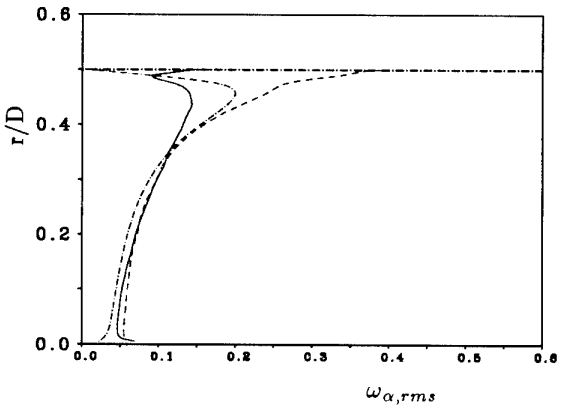

Figure 17: Profiles of the rms vorticity fluctuations $(\omega_z, \omega_\varphi, \omega_r)_{rms}$ (solid, dashed, dashed-dotted lines, respectively) at the axial position $z = 0.1$, Values are non-dimensionalized with $(u_\tau{}^2/\nu)_{z=0}$.

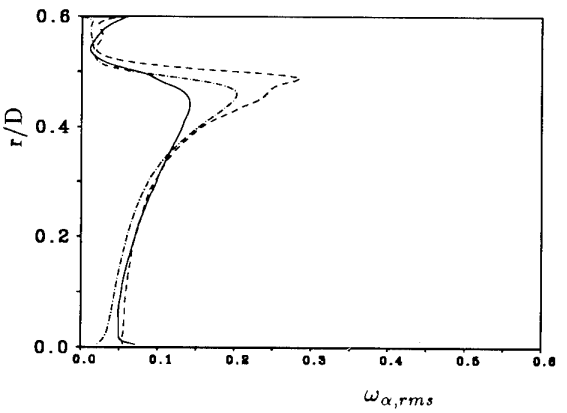

Figure 18: Profiles of the rms vorticity fluctuations at the axial position $z = 1.6$, notation see fig.17.

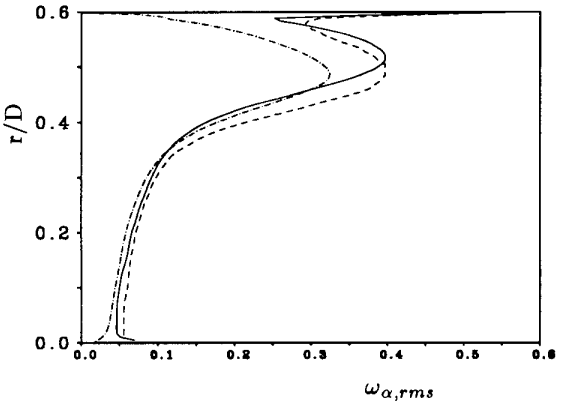

Figure 19: Profiles of the rms vorticity fluctuations at the axial position $z = 2.2$, notation see fig.17.

6. REFERENCES

1. Chorin, A.J., "Numerical solution of the Navier-Stokes equations", Mathematics of Computation, 22, 1968, pp.745-762.
2. Durst, F., Jovanovič, J., Sender, J., "Detailed measurements of the near wall region of turbulent pipe flows," in " Proc. 9th Symp. on Turbulent Shear Flows", August 16-18, 1993, Kyoto, Japan, pp. 2/2/1-2/2/6.
3. Eggels, J.G.M., Unger, F., Weiss, M.H., Westerweel, J., Adrian, R.J., Friedrich, R., Nieuwstadt, F.T.M., "Fully developed turbulent pipe flow: A comparison between numerical simulation and experiment", to appear in J. Fluid Mech., 1994.
4. Ferziger, J.H., Private communication, 1993.
5. Gavrilakis, S., "Numerical simulation of low-Reynolds number turbulent flow through a straight square duct", J. Fluid Mech., **244**, 1992, pp. 101-129.
6. Kim, J., Moin, P., Moser, R., "Turbulence statistics in fully developed channel flow at low Reynolds number", J. Fluid Mech., **177**, 1987, pp.133-166.
7. Le. H., Moin, P., Moser, R., "Direct numerical simulation of turbulent flow over a backward-facing step", in "Proc. 9th Symp. on Turbulent Shear Flows", August 16-18, 1993, Kyoto, Japan, pp. 13/2/1-13/2/6.
8. Nitsche, W., Haberland, C., "On turbulent-separated flows in axisymmetric diffusers",in "Notes on Numerical Fluid Mechanics", Vol. 40, 1993, pp. 116-124.
9. Schumann, U., "Ein Verfahren zur direkten numerischen Simulation turbulenter Strömungen in Platten- und Ringspaltkanälen und über seine Anwendung zur Untersuchung von Turbulenzmodellen", 1973, Dissertation, Univ. Karlsruhe.
10. Schumann, U., "Fast elliptic solvers and their application in fluid dynamics", in "Computational Fluid Dynamics", W.Kollmann (Ed.), Washington: Hemisphere, 1980, pp.402-430.
11. Unger, F., "Numerische Simulation turbulenter Rohrströmungen", 1994, Dissertation, TU München.
12. Unger, F., Eggels, J.G.M., Friedrich, R., Nieuwstadt, F.T.M., "On second and higher order statistics in fully-developed turbulent pipe flow", in "Proc. 9th Symp. on Turbulent Shear Flows", August 16-18, 1993, Kyoto, Japan, pp. 2/1/1-2/1/6.
13. Westerweel, J., Adrian, R.J., Eggels, J.G.M., Nieuwstadt, F.T.M., "Measurements with particle image velocimetry of fully turbulent pipe flow at low Reynolds number", in "Proc. 6th Int. Symp. on Applications of Laser Techniques to Fluid Mechanics", July 20-23, 1992, Lisbon, Portugal.

SIMULATION D'ECOULEMENTS DECOLLES

B. TROFF, T.H. LÊ, P. SAGAUT
O.N.E.R.A. BP 72, 92322 Châtillon Cedex, FRANCE

TA PHUOC LOC
O.N.E.R.A. and L.I.M.S.I. BP 133, 91403 Orsay Cedex, FRANCE.

Résumé

Des simulations numériques d'écoulements décollés ont été effectuées à l'aide du code PEGASE (version 1.1) en simulation directe et en simulation des grosses structures. La résolution des équations de Navier-Stokes incompressibles est basée sur une méthode de projection. La discrétisation spatiale est effectuée par une approche hybride différences finies / éléments finis. Les résultats dans le cas de la marche descendante bidimensionnelle concernant une validation en simulation directe effectuée à des nombres de Reynolds de valeur inférieure ou égale à 800 et un cas avec modélisation de sous-maille à un nombre de Reynolds égal à 11 200 sont présentés.

Summary

Direct Numerical Simulations and Large Eddy Simulations of separated flows have been carried out using the PEGASE code (release 1.1). The incompressible Navier-Stokes equations are solved using a projection method. The spatial discretization is performed via a hybrid finite difference / finite element approach. Results related to the bidimensional backward facing step provided in DNS at Reynolds numbers up to 800 and in LES at a Reynolds number equal to 11 200 are shown.

1 Introduction

Les progrès récents des algorithmes de Simulation Directe (Direct Numerical Simulation ou DNS) permettent aujourd'hui d'aborder l'étude numérique d'écoulements instationnaires décollés présents dans de nombreuses applications industrielles.
La compréhension du comportement de tels écoulements est très importante, dans le domaine aéronautique par exemple, car ils conditionnent les performances des voilures (en terme de portance et de trainée) en particulier lors du phénomène de décrochage.
Ces écoulements complexes, difficiles à modéliser, représentent un champ de recherche privilégié pour la simulation d'écoulements de fluide réel. Les expériences numériques, à caractère fondamental, devraient contribuer à une meilleure compréhension des mécanismes régissant ces écoulements complexes et constituer à terme une base de référence pour les calculs à caractère plus industriel utilisant des modèles classiques de turbulence.
C'est dans ce but qu'a été développé à l'ONERA le code de simulation directe PEGASE (version 1.1). La méthode adoptée pour la résolution des équations de Navier-Stokes, écrites en formulation vitesse-pression, est une méthode de projection résolvant une équation de Poisson pour la pression. La discrétisation des équations se fait sur un maillage non-décalé. L'approximation des opérateurs aux dérivées partielles est basée sur un schéma hybride différences finies/éléments finis d'ordre 2 en espace. Le schéma temporel est de type Euler explicite.
La méthode est appliquée ici au cas de l'écoulement derrière une marche descendante. Cette configuration représentative des écoulements instationnaires fortement décollés constitue un cas-test très sévère pour la validation des méthodes numériques et des modélisations de sous-maille (Large Eddy Simulation ou LES). Les résultats présentés ici constituent une étape préliminaire de simulation numérique sur des géométries bidimensionnelles permettant de préparer les futures simulations tridimensionnelles. Ils montrent les capacités du code développé à simuler correctement les écoulements à nombre de Reynolds inférieur ou égal à 800 et ont permis d'illustrer un cas d'écoulement à nombre de Reynolds plus élevé égal à 11 200 nécessitant l'introduction d'une modélisation de sous-maille.

2 Formulation mathématique

La méthode mise en œuvre dans le code PEGASE est une méthode de projection qui permet de résoudre les équations de Navier-Stokes instationnaires d'un fluide incompressible. Le système d'équations de base, composé de l'équation de continuité et des équations de conservation de quantité de mouvement, est dérivé de manière à obtenir un système équivalent constitué des équations de quantité de mouvement et d'une équation de Poisson pour la pres-

Paper presented at the 74th Fluid Dynamics Symposium on "Application of Direct and Large Eddy Simulation to Transition and Turbulence" held at Chania, Crete, Greece, in April 1994.

sion. Le terme non-linéaire des équations de quantité de mouvement est traité soit sous la forme conservative, soit sous la forme semi-conservative.
Le système discret correspondant aux équations de quantité de mouvement et à l'équation de Poisson sur la pression est obtenu à l'aide de schémas précis à l'ordre 2. Ces schémas sont dérivés au moyen d'une approche hybride faisant intervenir une méthodologie différences finies pour certains d'entre eux et une méthodologie éléments finis pour les autres, cette dernière étant basée sur une décomposition de type Q1. Ces schémas, mis en oeuvre sur des maillages non-décalés, ont demandé une attention particulière, en particulier en ce qui concerne le traitement des termes de convection et plus généralement la discrétisation des dérivées premières composant l'opérateur divergence. Le schéma résultant évite le découplage des points de discrétisation qui apparaît lorsque l'on utilise les schémas classiques et qui se traduit par l'apparition de modes parasites dans la solution.

2.1 Problème continu

La résolution dans un domaine Ω des équations de Navier-Stokes instationnaires adimensionnées d'un fluide incompressible s'exprime en variables primitives vitesse $\vec{v} = (u, w)$ et pression cinématique p (i.e divisée par la densité) en coordonnées cartésiennes $\vec{x} = (x, z)$ par l'un des systèmes suivants :
termes non linéaires sous forme conservative :

$$\vec{\nabla} \cdot \vec{v} = 0 \quad \text{dans} \quad \Omega \tag{1}$$

$$\frac{\partial \vec{v}}{\partial t} + \vec{\nabla} \cdot (\vec{v} \otimes \vec{v}) = -\vec{\nabla} p + \frac{1}{Re} \nabla^2 \vec{v} \tag{2}$$

ou termes non linéaires sous forme semi-conservative :

$$\vec{\nabla} \cdot \vec{v} = 0 \quad \text{dans} \quad \Omega$$

$$\frac{\partial \vec{v}}{\partial t} + \frac{1}{2} (\nabla \cdot (\vec{v} \otimes \vec{v}) + \vec{v} \cdot \nabla \vec{v}) = -\nabla p + \frac{1}{Re} \nabla^2 \vec{v} \tag{3}$$

où Re est le nombre de Reynolds. Le choix de la formulation est guidé par les caractéristiques de l'écoulement. La formulation semi-conservative sera préférée à la formulation conservative dans le cas d'écoulements dominés par les phénomènes convectifs, plus précisément lorsque le nombre de Reynolds, qui est une mesure du rapport entre termes convectifs et termes diffusifs, prend des valeurs élevées.
Ce problème est résolu par une méthode de projection qui consiste à substituer à l'équation de continuité (1) une équation portant sur la pression. Cette équation est obtenue en appliquant l'opérateur divergence à l'équation de quantité de mouvement (2), dont les termes non linéaires sont sous forme conservative.

$$-\nabla^2 p = \vec{\nabla} \cdot \vec{\nabla} \cdot (\vec{v} \otimes \vec{v}) + \frac{\partial}{\partial t} \left(\vec{\nabla} \cdot \vec{v} \right) \tag{4}$$

Les termes visqueux ont été éléminés dans l'équation (4) en tenant compte de (1) et du fait que, dans le cas continu, les opérateurs Laplacien et divergence commutent.
Le système continu effectivement considéré se compose de l'une des équations (2) ou (3) et de l'équation de Poisson (4).
A ces équations sont associées des conditions initiales et des conditions aux limites portant sur la vitesse et sur la pression.
Sur des frontières d'entrée ou des parois solides on impose une condition de Dirichlet portant sur la vitesse associée à une condition de Neumann portant sur la pression :

$$\begin{cases} \vec{v} & = \vec{W} \\ \frac{\partial P}{\partial n} & = \vec{n} . \left[\frac{1}{Re} \nabla^2 \vec{u} - \nabla . (\vec{u} \otimes \vec{u}) \right] \end{cases}$$

où $\vec{W}$ est un champ de vitesse donné et $\vec{n}$ le vecteur unitaire normal à la frontière. La seconde équation est obtenue par projection de l'équation de quantité de mouvement sur cette normale.
Sur des frontières de type sortie on impose des conditions portant sur la contrainte à la frontière :

$$\begin{cases} \frac{\partial v_\tau}{\partial n} & = 0 \\ -P + \frac{2}{Re} \frac{\partial v_n}{\partial n} & = 0 \end{cases}$$

où v_τ et v_n sont respectivement les composantes tangentielle et normale de la vitesse à la frontière. La première de ces équations est une approximation de la relation imposant la contrainte tangentielle nulle, la seconde traduit la relation imposant la contrainte normale nulle.
Le problème requiert de plus la donnée d'une condition initiale $\vec{v}(x, 0) = \vec{v}_0(x)$ satisfaisant à l'équation de continuité $\nabla \cdot \vec{v}_0 = 0$. Cette solution est obtenue en deux étapes : la première consiste à calculer un champ de vitesse régulier compatible avec la donnée des conditions aux limites, la seconde est une étape de correction inspirée de la technique utilisée par P.M. Gresho [7] consistant à projeter le champ obtenu dans un espace à divergence nulle, afin de satisfaire la contrainte d'incompressibilité à l'instant initial.

2.2 Problème discret

Le domaine de calcul, supposé rectangulaire, est décomposé en quadrangles formant un maillage sur lequel on définit des variables collocatives.
Les dérivées premières définissant l'opérateur divergence du terme de convection écrit sous forme conservative, ainsi que la divergence de la vitesse au second membre de l'équation de pression, doivent être discrétisées avec soin. Le schéma classique différences finies s'écrit pour deux variables ϕ et ψ :

$$\left(\frac{\partial \phi}{\partial x} \right)_{i,k} + \left(\frac{\partial \psi}{\partial z} \right)_{i,k} =$$

$$\delta_x \phi_{i,k} + \delta_z \psi_{i,k} + O(\Delta x^2) + O(\Delta z^2)$$

avec,

$$\delta_x \phi_{i,k} + \delta_z \psi_{i,k} =$$

$$\frac{1}{2\Delta x}\left(\phi_{i+1,k} - \phi_{i-1,k}\right) + \frac{1}{2\Delta z}\left(\psi_{i,k+1} - \psi_{i,k-1}\right)$$

Il génère des oscillations dues au découplage des noeuds d'indice (i+k) pair et (i+k) impair [9]. D'autres schémas développés dans les approches volumes finis et éléments finis ont été proposés afin d'éviter cet effet.
La méthode décrite ici utilise un schéma centré du second ordre définie en 2-D par :

$$\begin{aligned}
\delta_x^* \phi_{i,k} + \delta_z^* \psi_{i,k} &= \frac{1}{12\Delta x}\{\left(\phi_{i+1,k+1} - \phi_{i-1,k+1}\right) \\
&+ 4 \times \left(\phi_{i+1,k} - \phi_{i-1,k}\right) \\
&+ \left(\phi_{i+1,k-1} - \phi_{i-1,k-1}\right) \} \\
&+ \frac{1}{12\Delta z}\{\left(\psi_{i+1,k+1} - \psi_{i+1,k-1}\right) \\
&+ 4 \times \left(\psi_{i,k+1} - \psi_{i,k-1}\right) \\
&+ \left(\psi_{i-1,k+1} - \psi_{i-1,k-1}\right) \}
\end{aligned}$$

Ce schéma est issu d'une approche discrète de type éléments finis dans le cas d'une décomposition sur une base de fonctions bilinéaires par morceaux définies sur des éléments quadrangulaires. Les sommets de ces quadrangles définissent les noeuds de calcul. Bien que le schéma soit plus coûteux, huit points pour la divergence comparé à quatre pour le schéma standard différences finies, il possède de meilleures propriétés concernant le couplage des points dans les deux directions x et z.
L'approche éléments finis utilisée ici est cependant différente de la méthodologie classique. La première différence concerne la prise en compte discrète des conditions aux limites qui est effectuée en utilisant un schéma aux différences finies. La seconde tient au fait que ces schémas sont appliqués également aux termes non linéaires issus du terme convectif [3]. Cette dernière caractéristique conduit d'ailleurs à une expression plus simple et moins coûteuse. Dans le cas de l'utilisation de la forme semi-conservative du terme de convection, la partie purement convective de ce terme est discrétisée au moyen d'un schéma décentré d'ordre 3 en espace, similaire à celui exposé dans la référence [10]. L'utilisation de ce schéma permet de stabiliser le calcul en introduisant un terme de dissipation d'ordre 4 sans réduire l'ordre global du schéma.
Les opérateurs de dérivées secondes et de dérivées croisées qui apparaissent dans l'équation de pression sont issus d'une approche différences finies classique. Ce qui conduit aux expressions suivantes :

$$\left(\frac{\partial^2 \phi}{\partial x^2}\right)_{i,k} = \delta_{xx}\phi_{i,k} + O(\Delta x^2)$$

$$\delta_{xx}\phi_{i,k} = \frac{1}{\Delta x^2}\left\{\phi_{i+1,k} - 2\phi_{i-1,k} + \phi_{i-1,k+1}\right\}$$

$$\left(\frac{\partial^2 \phi}{\partial x \partial z}\right)_{i,k} = \delta_{xz}\phi_{i,k} + O(\Delta x \Delta z)$$

$$\delta_{xz}\phi_{i,k} = \frac{1}{4\Delta x \Delta z}\left\{\phi_{i+1,k+1} - \phi_{i,k+1} - \phi_{i+1,k-1} + \phi_{i-1,k-1}\right\}$$

Dans le cas d'une frontière de type Dirichlet sur la vitesse, la prise en compte de la condition de type Neumann sur la pression est obtenue par des développements de type différences finies au point demi-entier voisin du point frontière. Dans le cas d'une frontière de sortie, la composante tangentielle de vitesse est évaluée en discrétisant la dérivée normale par un schéma décentré au second ordre. Dans le cas d'une frontière i=Imax par exemple on a :

$$(w)_{Imax,k} = \frac{1}{3}\left(4 \times w_{Imax-1,k} - w_{Imax-2,k}\right)$$

La composante normale est obtenue à l'aide d'une formule d'extrapolation du second ordre :

$$(u)_{Imax,k} = 3 \times u_{Imax-1,k} - 3 \times u_{Imax-2,k} + u_{Imax-3,k}$$

la pression est alors une donnée, si l'on se réfère au paragraphe 2.1.
Le calcul de la vitesse utilise le schéma de type Euler explicite. La méthode de projection du premier ordre permet de découpler les problèmes en vitesse et en pression et d'imposer la contrainte d'incompressibilité. On peut noter que ce type d'approximation temporelle est bien adaptée aux architectures parallèles des nouveaux supercalculateurs.
Les composantes de la vitesse à l'instant n+1 sont données, dans le cas de la formulation conservative par :

$$\vec{v}^{n+1} = \vec{v}^n - \Delta t\left(D^* p^n - \frac{1}{Re} L\vec{v}^n + D^* \cdot (\vec{v} \otimes \vec{v})^n\right)$$

et, dans le cas de la formulation semi-conservative par :

$$\vec{v}^{n+1} = \vec{v}^n - \Delta t\left(D^* p^n - \frac{1}{Re} L\vec{v}^n + \frac{1}{2}\left(D^* \cdot (\vec{v}^n \otimes \vec{v}^n) + C(\vec{v}^n)\right)\right)$$

où l'opérateur discret $C(\vec{v}^n)$ correspond au schéma décentré mentionné plus haut et les opérateurs discrets D^* et L sont définis comme suit :

$$D^* = (\delta_x^*, \delta_z^*)^T, \quad L = \delta_{xx} + \delta_{zz}$$

On peut remarquer que la vitesse peut être calculée par simple substitution algébrique dès que la pression est donnée en chaque noeud.
Dans le but de résoudre (2) ou bien (3) tout en satisfaisant (1), la pression est calculée à partir de l'équation (4) dans laquelle le terme $\frac{\partial}{\partial t}\left(\vec{\nabla} \cdot \vec{v}\right)$ est discrétisé par $\left(D^* \cdot \vec{v}^{n+1} - D^* \cdot \vec{v}^n\right)/\Delta t$ et en posant $D^* \cdot \vec{v}^{n+1} = 0$

afin de satisfaire l'équation de continuité à l'instant n+1. L'équation discrète en pression s'exprime alors sous la forme :

$$\begin{aligned} -(\delta_{xx}p^n_{i,k} + \delta_{zz}p^n_{i,k}) &= \delta_{xx}(u^2)^n_{i,k} + \delta_{zz}(w^2)^n_{i,k} \\ &+ 2\delta_{xz}(uw)^n_{i,k} - \frac{1}{\Delta t}(\delta^*_x u^n_{i,k} + \delta^*_z w^n_{i,k}) \end{aligned}$$

Le dernier terme du membre de droite est retenu dans l'équation comme un terme correcteur, puisque l'équation de continuité n'est pas directement satisfaite. Ceci permet d'empêcher l'accumulation d'erreurs qui conduit à des instabilités polluant la solution des équations de quantité de mouvement [8].
Les propriétés de stabilité d'un tel schéma sont données par le critère bidimensionnel suivant :

$$\Delta t \leq Min\,(\alpha;\beta)$$

où

$$\alpha = \frac{2\nu}{Max\,(u^2+w^2)} \quad , \quad \beta = \frac{\Delta x^2}{4\nu}$$

Le système linéaire associé au problème en pression est résolu à l'aide d'une méthode itérative de minimisation de résidus de type gradient conjugué, le Bi-CGSTAB proposé par H.A. Van der Vorst [15]. Cette technique permet de résoudre des systèmes non-symétriques et nécessite de faibles ressources mémoire. Elle a été utilisée avec un préconditionnement de type Jacobi dans le cas de maillage à pas variable.
Une description plus détaillée des propriétés de la méthode numérique du code PEGASE est fournie dans la référence [11].

3 Résultats

Les résultats présentés concernent la configuration de la marche descendante. Deux types de calcul ont été entrepris avec cette configuration. Le premier concerne l'écoulement dans une plage de Reynolds correspondant à un régime laminaire ayant pour but de valider la méthode présentée plus haut. Le second constitue une application de la méthode dans le cas d'un écoulement turbulent nécessitant l'utilisation d'une modélisation de sous-maille. Dans les deux cas, il s'agit de calculs bidimensionnels constituant une étude préliminaire aux développements futurs de la méthode dans le cas tridimensionnel.

3.1 Cas laminaire

Dans le but de valider la méthode, une étude a été effectuée sur le cas de la marche descendante pour des nombres de Reynolds inférieurs à 800. Le choix de cette configuration a été guidé par l'aspect fortement décollé de l'écoulement et la présence d'une singularité sur le profil de vitesse amont. Des résultats concernant la longueur de la zone de recirculation en fonction du nombre de Reynolds sont comparés à des résultats expérimentaux. Pour un nombre de Reynolds égal à 800 les résultats obtenus sont comparés aux résultats numériques présentés dans le cadre du Minisymposium sur les conditions aux limites de sortie organisé à Stanford en 1990 [4]. La configuration, correspondant au cas test, qui a été utilisée pour l'ensemble de ces calculs est schématisée sur la figure 1. Le rapport entre la hauteur du canal de sortie et la hauteur du canal d'entrée est égal à 2. Les conditions aux limites sur la vitesse correspondent à un profil parabolique sur la frontière d'entrée, des conditions d'adhérence sur les parois et des conditions d'écoulement libre sur la frontière de sortie. La longueur L correspond à la distance séparant la marche de la frontière aval. Le nombre de Reynolds est basé sur la vitesse débitante amont et sur la hauteur H du canal.

Sur la figure 2 ont été reportés les résultats portant sur la longueur de la zone de recirculation (caractérisée par l'abscisse x_r du point de recollement) en fonction du nombre de Reynolds. Les résultats numériques sont en bon accord pour des nombres de Reynolds inférieurs à 400 avec les résultats expérimentaux obtenus par Armaly et *al.* [1]. Pour des nombres de Reynolds supérieurs, l'écart observé peut être expliqué par le changement de régime de l'écoulement qui devient tri-dimensionnel. Ceci est illustré par le schéma de la figure 3 où les différents régimes de l'écoulement (en particulier l'aspect bi- ou tridimensionnel et le caractère laminaire, transitionnel ou turbulent de l'écoulement) sont reportés en fonction du nombre de Reynolds. Numériquement, cette explication semble confirmée par le fait que l'utilisation d'un maillage deux fois plus fin conduit au même résultat.

Les résultats suivants concernent un nombre de Reynolds égal à 800. Dans ce cas le pas de temps est égal à 0.0005, le maillage est composé de 801×41 points correspondant à un domaine de longueur égale à 40 hauteurs de marche. Le calcul a été mené sur 800 000 pas de temps correspondant à un temps adimensionné de 400. Le coût correspondant est de l'ordre de 20 heures CPU sur CRAY-YMP pour 32000 points.

Sur la figure 4 sont tracées les lignes iso-pression et iso-vorticité aux temps adimensionnés 10, 20 et 300. Elles mettent en évidence les structures de l'écoulement et leur évolution au cours du temps. L'écoulement généré derrière la marche est composé d'une succession de structures tourbillonnaires localisées près des parois supérieure et inférieure du canal. Seules deux structures principales, correspondant à la zone de recirculation située juste en aval de la marche et à la zone de recirculation située plus en aval sur la paroi supérieure, subsistent à l'état stationnaire.

La figure 5 montre l'évolution au cours du temps des composantes de vitesse longitudinale u et tranversale w en différents points de l'écoulement. Ces résultats sont en parfait accord avec les résultats numériques obtenus par Gresho et al. [6] et montrent en particulier que l'on atteint un état stationnaire à partir d'un temps égal à 150.

Les résultats obtenus à l'état stationnaire, correspondant au temps adimensionné de 400., sont reportés sur les figures 6 et 7. Les profils de vitesse dans deux sections du canal sont comparés aux résultats numériques obtenus par Gartling [4]. L'accord entre les différents résultats est très bon. L'écart sur la composante w dans une section située à 7 hauteurs de canal correspond à une sous-estimation de l'ordre de 1% de la longueur de recirculation. Par ailleurs les répartitions de pression et de frottement sur les parois du canal tracées sur la figure 7 coincident également avec les résultats donnés dans la référence [4].
L'influence de la position de la frontière aval a été évaluée en effectuant un calcul complémentaire avec L=7H. On peut observer sur les figures 8 et 9 que la position de cette frontière, même lorsqu'elle est placée dans une zone critique de l'écoulement (en l'occurence au voisinage du point de recollement dans le cas L=7H) ne perturbe pas de façon significative l'écoulement. D'un point de vue qualitatif, les lignes iso-pression et iso-vorticité portées sur la figure 8 montrent que les structures de l'écoulement sont tout à fait similaires dans les deux cas. Il est à remarquer que le résultat obtenu est valable non seulement pour la solution stationnaire mais également pour les temps intermédiaires de la phase transitoire. D'un point de vue quantitatif, les courbes des coefficients de pression et de frottement sur les parois du canal, tracées sur la figure 9, confirment ce résultat malgré les différences au voisinage de l'extrémité du canal. Cependant, les écarts observés sont faibles et les structures de l'écoulement sont encore bien représentées.

3.2 Cas turbulent

Le cas de la marche descendante est simulé ici à un nombre de Reynolds égal à 11200. La géométrie de la marche, illustrée par la figure 10, correspond à celle étudiée expérimentalement par Eaton et Johnston [2]. Par rapport à la configuration précédente, outre le nombre de Reynolds élevé correspondant à un régime turbulent, la présence d'une singularité géométrique représente une difficulté supplémentaire qui a été traitée de manière satisfaisante. Les caractéristiques du calcul correspondent à un rapport canal de sortie sur canal d'entrée égal à 5/3, à une position de la frontière aval du domaine située à 50H et un canal d'entrée d'une longueur de 0.75 H. Le nombre de points et les resserrements de maillage utilisés ne permettent pas de résoudre toutes les structures de l'écoulement turbulent au nombre de Reynolds choisi. Il est donc nécessaire d'effectuer une simulation des grosses structures à l'aide d'une modélisation de sous-maille. Trois types de modèles de sous-maille basés sur le concept de viscosité turbulente ont été implémentés dans PEGASE : le modèle de Smagorinsky, le modèle dynamique [13] [5] et le modèle stochastique de cascade inverse d'énergie (Stochastic Backscatter) [12].
Quatre calculs ont été effectués sur cette configuration : trois calculs à l'aide des modèles de sous-maille mentionnés plus haut avec un maillage de 301 × 31 points et un calcul de simulation directe avec un maillage de 601 × 61 points. Chaque calcul a été effectué jusqu'à un temps adimensionné de 400. Le coût d'un calcul sur un maillage de 10 000 points et pour 80 000 pas de temps est de l'ordre de 2 heures CPU sur un CRAY-YMP.
La figure 11 montre les lignes iso-pression et iso-vorticité qui mettent en évidence les structures présentes dans l'écoulement à un temps adimensionné de 200 dans le cas d'une simulation avec le modèle dynamique.
La figure 12 montre les profils de vitesse, moyennés sur un temps de 300, dans 3 sections du canal situées en aval de la marche. Les résultats obtenus, dont une analyse détaillée est fournie dans la référence[14], sont très sensibles au modèle de sous-maille utilisé. L'écart avec les résultats expérimentaux (et en particulier l'écart avec la simulation directe) montrent qu'il est difficile de reproduire par un calcul bidimensionel une expérience par essence tridimensionnelle.

4 Conclusion

Le code PEGASE a été développé à l'ONERA dans le but d'effectuer des simulations directes et des simulations des grosses structures. Les tests numériques effectués ont montré que la technique de discrétisation mise en oeuvre fournit des résultats d'excellente qualité à nombre de Reynolds modéré. De plus, l'utilisation d'une modélisation de sous-maille a permis d'effectuer ,à titre d'illustration, un cas de calcul à nombre de Reynolds plus élevé.
L'expérience acquise et les résultats prometteurs obtenus sur une géométrie bidimensionnelle permettent d'envisager le calcul de configurations complexes tridimensionnelles à faible ou haut nombre de Reynolds.

Remerciement

Cette étude a bénéficié du soutien financier de la Délégation Générale de l'Armement (DGA/DRET).

References

[1] Armaly, B.F., Durst, F., Pereira, J.C. and Schonung, B. "Experimental and theoritical investigation of backward-facing step." J. Fluid Mech. 127 1983, pp 473-496.

[2] Eaton, J.K., Johnston, J.P., "Turbulent flow reattachment: an experimental study of the flow and structure behind a backward-facing step." Stanford University MD-39, june 1980.

[3] Fletcher, C.A.J., "Computational techniques for Fluid Dynamics", Springer Verlag, 1988 (IBSN 3 540 18151 2) pp 355-360.

[4] Gartling, D.K., "A test problem for outflow boundary conditions - flow over a backward-facing step" Int. J. Num. Meth. Fluids 11 1990, pp 953-967.

[5] Germano, M., Piomelli, U., Moin, P., Cabot, W.H., "A dynamic subgrid-scale eddy viscosity model" Phys. Fluids A 3 (7) 1991, pp 1760-1765.

[6] Gresho, P.M., Gartling, D.K., Torczynski, J.R., Cliffe, K.A., Winters, K.H., Garratt, T.J., Spence, A., Goodrich, J.W., "Is the steady viscous incompressible two-dimensional flow over a backward-facing step at Re=800 stable?" Int. J. Num. Methods Fluids 17 1993, pp 501-541.

[7] Gresho, P.M., "Incompressible fluid dynamics: some fundamental formulation issues" Annu. Rev. Fluid Mech. 23 1991, pp 413-453.

[8] Harlow, F.H. and Welch, J.E., "Numerical calculation of time-dependent viscous incompressible flow of fluid with free surface." Phys. Fluids 8 1965, pp 2181-2189.

[9] Hirsch, C., "Numerical Computation of Internal and External Flows" vol. 1, John Wiley and Sons 1987.

[10] Kondo, N., Tosaka, N., and Nishimura, T., Comput. Methods Appl. Mech. Engrg. 93 1991, pp 169-187.

[11] Lê, T.H., Troff, B., Sagaut, P., Dang-Tran, K., Ta Phuoc Loc, "PEGASE: a Navier-Stokes solver for direct numerical simulation of incompressible flows." submitted to Int. J. Numer. Methods Fluids.

[12] Leith, C.E., "Stochastic backscatter in a subgrid-scale model: Plane shear mixing layer." Phys. Fluids A 2 (3) 1990, pp 297-299.

[13] Lilly, D.K., "A proposed modification of the Germano subgrid-scale closure method." Phys. Fluids A 4 (3) 1992, pp 633-635.

[14] Sagaut, P., Troff, B., Lê, T.H., Ta Phuoc Loc, "Numerical Simulation with Subgrid Scale Models for Separated Flow." First ERCOFTAC Workshop on Direct and Large-Eddy Simulation, March 1994, Guildford, U.K.

[15] Van der Vorst, H.A. "Bi-CGSTAB: A fast and smoothly converging variant of Bi-CG for the solution of nonsymmetric linear systems" J. Sci. Statist. Comput. 13, 1992 , pp 631-644.

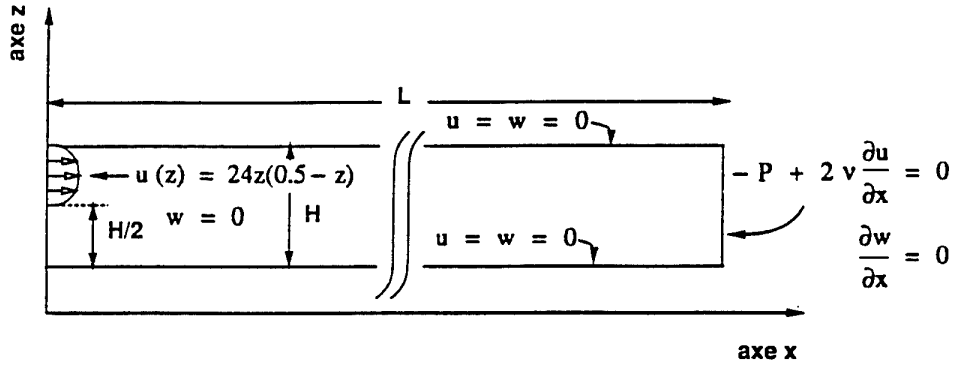

Figure 1 : Géométrie de la marche descendante (cas laminaire)
Dimensions et Conditions aux Limites.

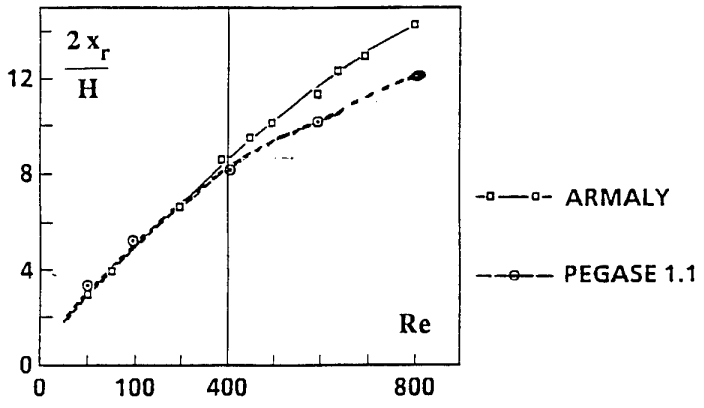

Figure 2 : Evolution du point de recollement en fonction du nombre de Reynolds.

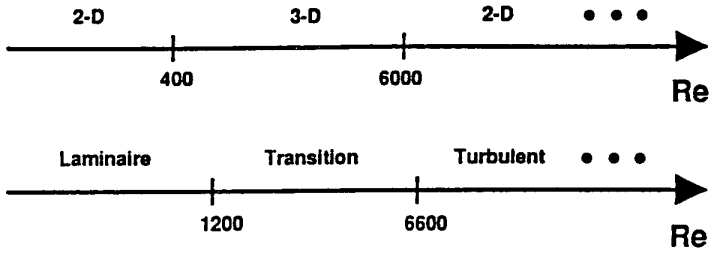

Figure 3 : Régimes de l'écoulement derrière la marche, d'après la référence [1].

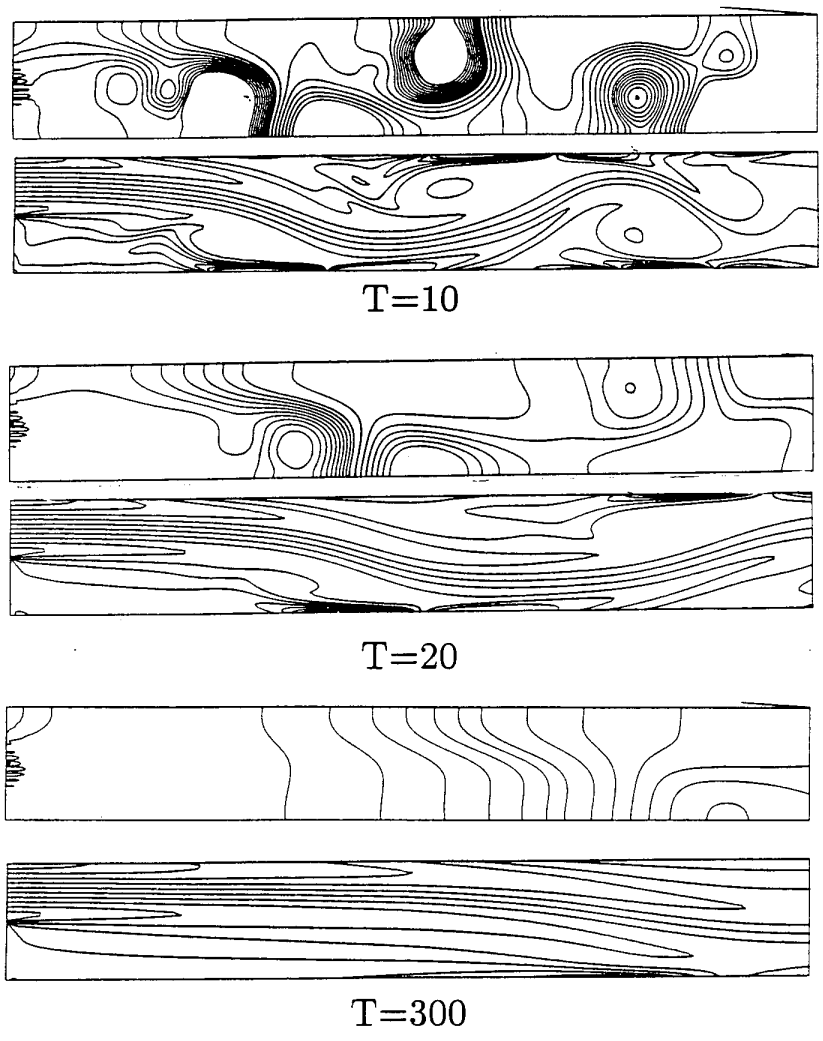

Figure 4 : Evolution des structures de l'écoulement en fonction du temps
Lignes iso-pression et iso-vorticité.

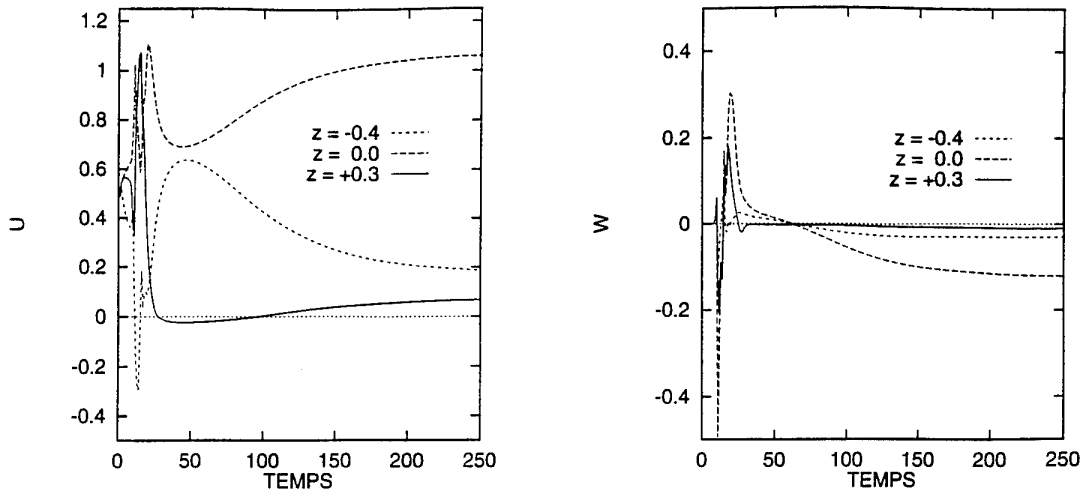

Figure 5 : Evolution temporelle des composantes de vitesse en x/H=6.

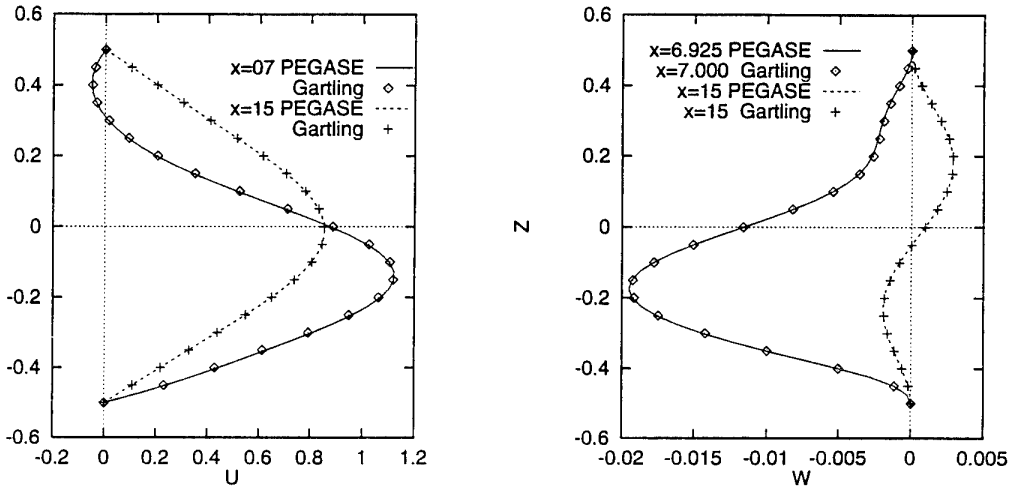

Figure 6 : Résultats à l'état stationnaire
profils de vitesse en 2 sections du canal.

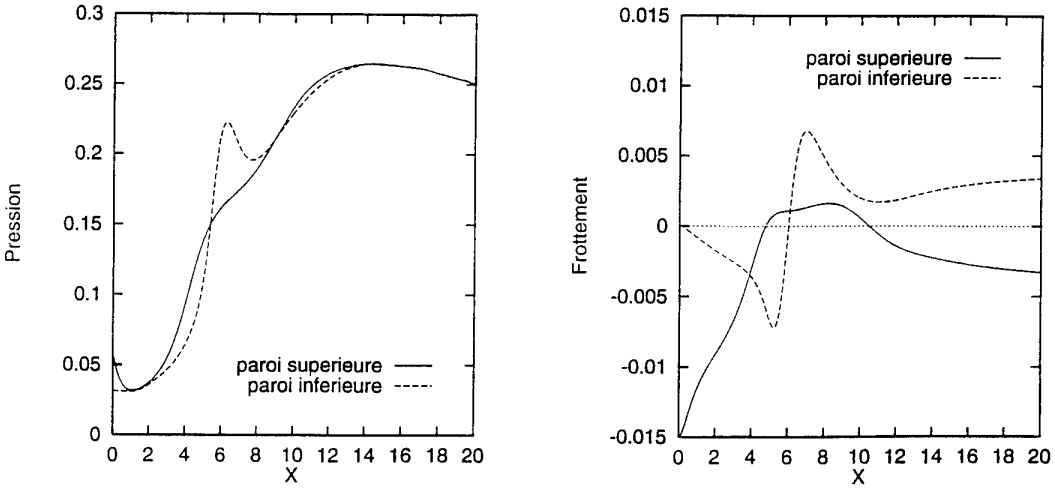

Figure 7 : Résultats à l'état stationnaire
pression et frottement sur les parois du canal.

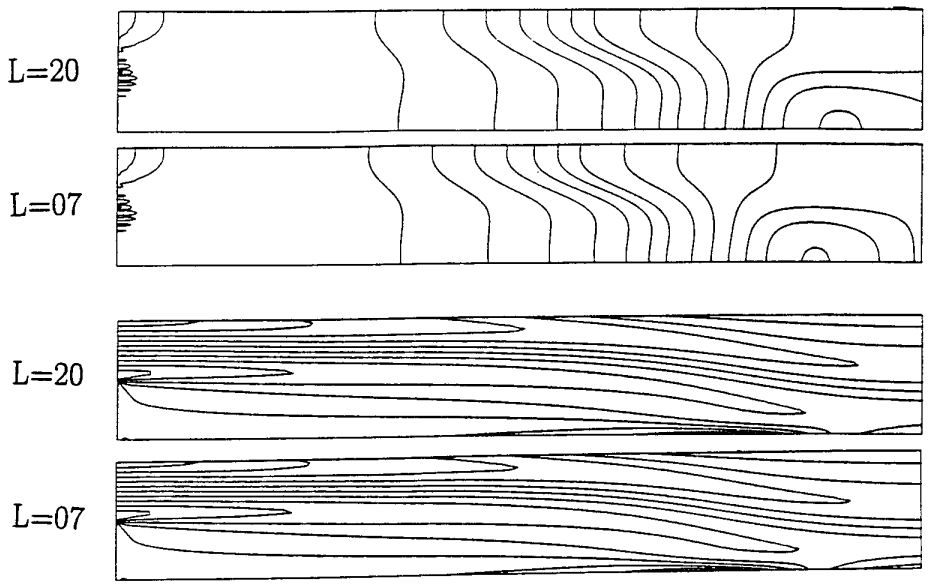

Figure 8 : Influence de la position de la frontière aval
Lignes iso-pression et iso-vorticité.

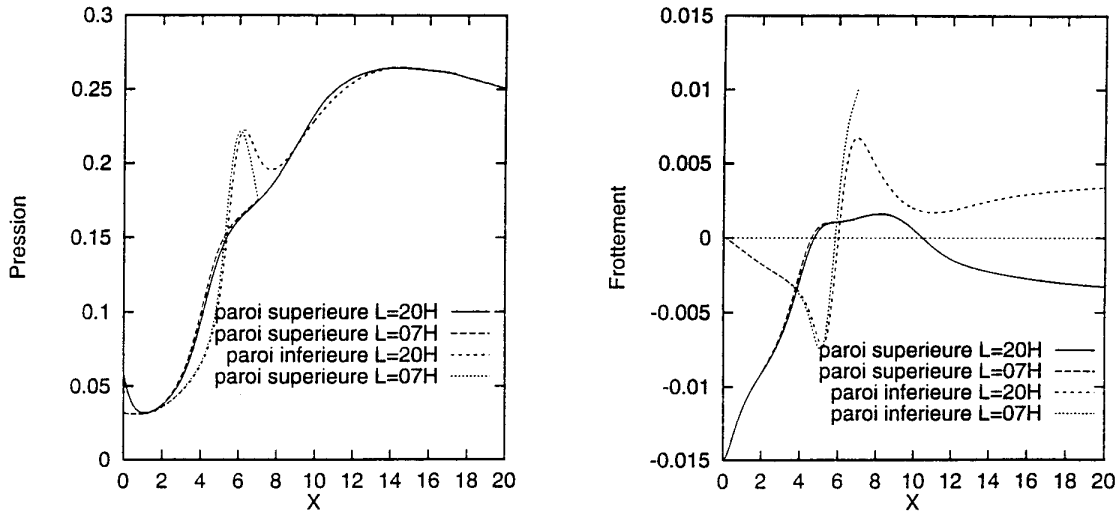

Figure 9 : Influence de la position de la frontière aval
pression et frottement sur les parois du canal.

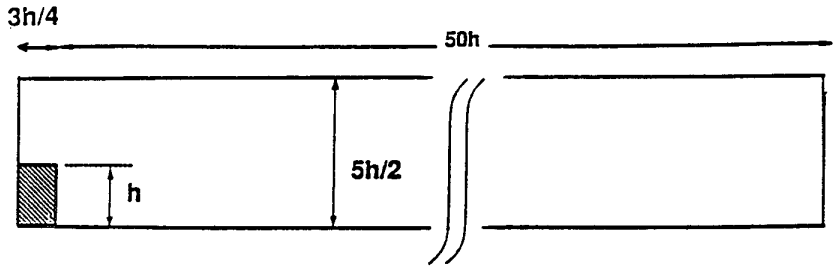

Figure 10 : Géométrie de la marche descendante Re=11 200

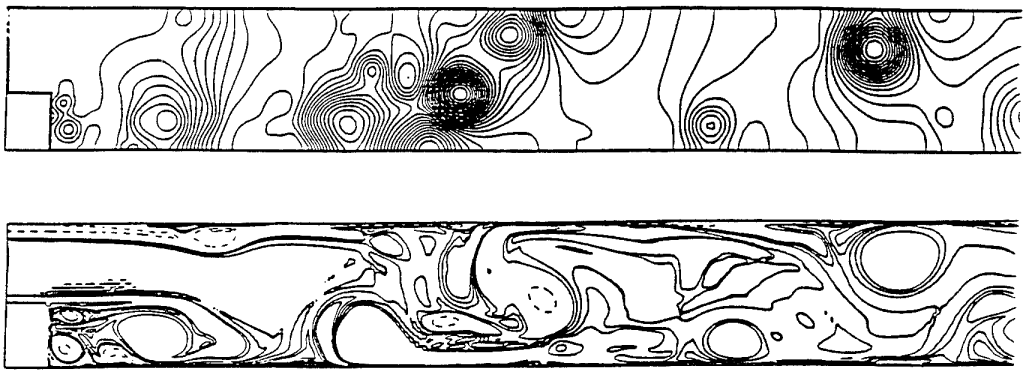

Figure 11 : Lignes iso-pression et iso-vorticité
Re=11200 - T=200. Modèle dynamique.

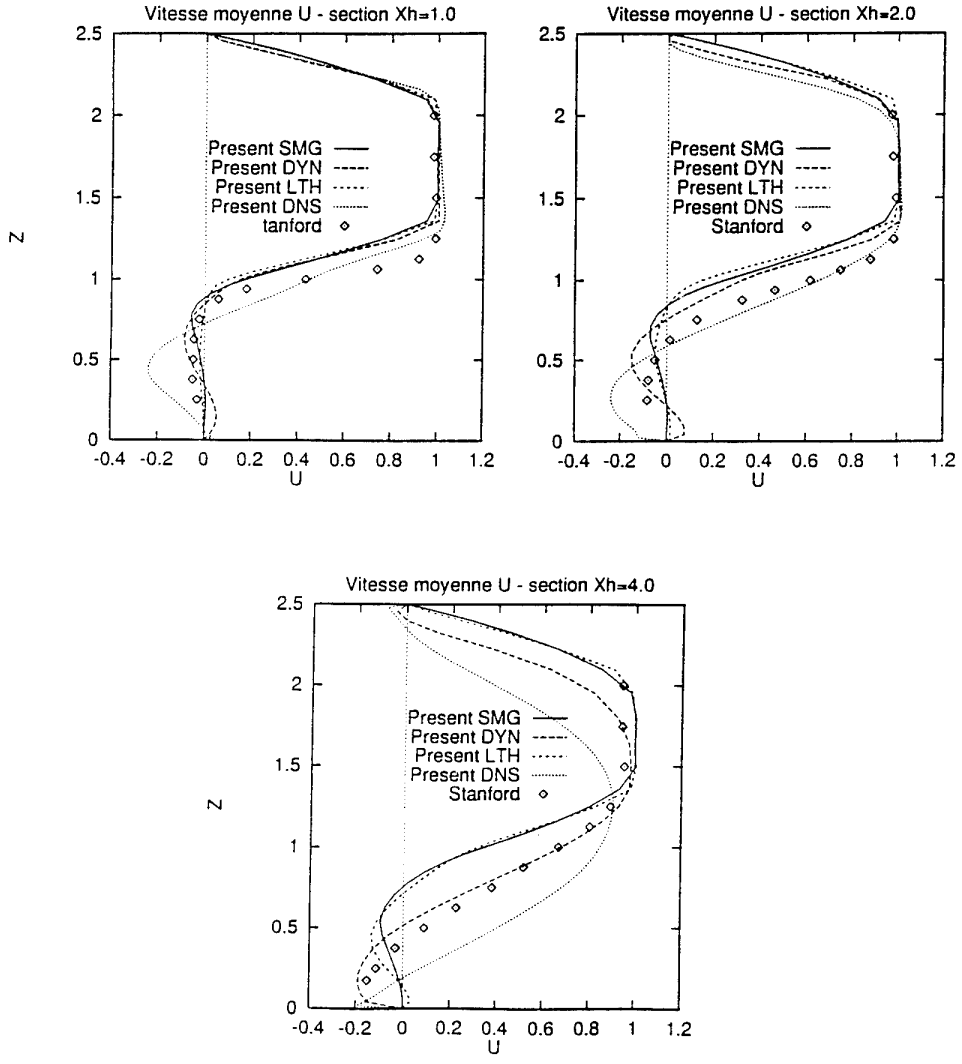

Figure 12 : profils de vitesse moyenne dans diffrentes sections du canal
Comparaison des différents modèles.

Large Eddy Simulation of Turbulent Flow Over a Cavity

J. C. F. Pereira and J. M. M. Sousa

Instituto Superior Técnico/Technical University of Lisbon
Mechanical Engineering Department
Av. Rovisco Pais
1096 Lisbon Codex
Portugal

SUMMARY

Smagorinsky and structure-function models are applied to the large eddy simulation of the turbulent flow over a cavity at a Reynolds number Re = 63,600. The near-wall flow region is modeled by implementing either a logarithmic law-of-the-wall or an exponential damping function. Results obtained with two values of the Smagorinsky constant, C_S = 0.10 and 0.20, have been compared. Further, the results provided by the mentioned subgrid-scale models are compared with those obtained using the standard k-ε model. As a basis for the comparison, LDV measurements of mean and fluctuating turbulent quantities are also reported. The computational results have demonstrated that the use of large eddy simulation is clearly rewarding in face of k-ε model computation, yielding better results employing a similar number of grid nodes.

1. INTRODUCTION

There is a consensus upon the fact that the direct simulation of the time-dependent Navier-Stokes equations represent a complete and accurate description of the behavior of turbulent flows. However, the enormous costs of computer time required by the full simulations have restricted the investigations to flows at low or moderate Reynolds numbers. Therefore, the direct numerical simulation (DNS) of geometrically-complex flows of engineering interest seems to be beyond the actual computing capabilities. The engineers and planetary scientists argue that cheaper prediction methods are needed, which explains why turbulence modeling has ruled until nowadays. Limited by the aforementioned restrictions, DNS has mainly performed the role of provider of a deeper understanding of the basic processes involved in turbulence, although definitely contributing to the improvement of the foundations of existing models. Nevertheless, it has been proved that the universal application of these models is unattainable, as they cannot predict a significant range of perturbed (exhibiting streamline curvature, in the presence of unsheared free-stream turbulence, etc.) non-trivial turbulent flows, without arbitrary adjustment of the empirical constants.

It is within this landscape that one technique which was developed a few decades ago rejuvenates, as it has received renewing interest for the purpose of common turbulence calculations. We are, of course, speaking about large eddy simulation (LES), where the large-scale turbulent eddies (resolved scales of motion) are calculated explicitly and only the effects of the small-scale motions (subgrid-scale) are parametrized. The prospects of success of such procedure are anticipated, because the properties of most turbulent flows are dominated by the influence of the large-scales which are problem dependent. Another implicit advantage is that the small-scale eddies display a much more isotropic character than the energy-containing ones, that facilitates its necessary modeling. On the other hand, as LES only requires the resolution of the large eddies by the numerical method, much coarser grids than those that must be used in DNS calculations can be employed. Both the reduction of the demand of computational efforts and the continuous increase of computing power, have made LES a serious competitor of the standard one-point closure turbulence models. In contrast to DNS, successful calculations of more and more complex flows, with undeniable engineering relevance, are likely to be available in a very near future.

The encouraging results obtained by Deardorff[1] for the simulation of turbulent plane channel flow, based on the formulation first proposed by Smagorinsky[2], have been retrieved with several improvements by, e.g., Schumann[3], and Moin and Kim[4], among others. The immediate evolution of such a simple geometry, rolling out to approach problems of direct and practical application is the backward-facing step, where phenomena like curvature, recirculation and reattachment are already present. This geometry has deserved the careful studies accomplished by Kobayashi et al.[5], Amal and Friedrich[6], and Neto et al.[7], the latter employing a new formulation, known as the structure-function model. Also, a slightly more complicated geometry, i.e. the flow around a cubic obstacle, was investigated by Werner and Wengle[8], and Yang and Ferziger.[9]

The subject of the present work stands out as a natural sequence of the aforementioned geometry evolution towards problems of engineering interest, i.e. we propose to study the turbulent flow over a cavity. This geometry arises in several practical flowfields, such as slotted-wall wind and water tunnels[10], aircraft components and the cooling of electronic chips.[11] Therefore, the main aim of the present study is to explore the possibilities of extending LES to real day by day problems. With this objective in mind, experiments

Paper presented at the 74th Fluid Dynamics Symposium on "Application of Direct and Large Eddy Simulation to Transition and Turbulence" held at Chania, Crete, Greece, in April 1994.

have been carried out for a Reynolds number of 63,600, embracing laser-Doppler measurements of the mean and fluctuating turbulent velocities. Considering the engineering purpose of this work and due to the impossibility of resolving accurately the wall regions, wall functions were implemented for the grid nodes next to the solid surface. For the remaining flow, two subgrid-scale models were utilized: Smagorinsky and structure-function proposed by Métais and Lesieur.[12] The numerical predictions have been obtained using an explicit differencing scheme, known as QUICKEST.[13]

2. EXPERIMENTAL PROCEDURE

2.1 Flow Configuration

The experimental setup, illustrated in Fig. 1, consisted of a rectangular cavity model formed on the floor of a PERSPEX water tunnel, 0.170 m in depth, 0.200 m in width and 7 m in length. The water was drawn from a constant-head discharge tank and pumped, in a closed-circuit, into a pressurized tank. Further details concerning the water tunnel were given by Durão et al.[14]. The cavity model spanned the width of the test section by the combination of appropriate upstream and downstream PERSPEX plates, yielding a depth-to-cavity length ratio $h/b = 0.5$ and a depth-to-width ratio $h/w = 0.12$, where $h/H = 0.141$ (see Fig. 1).

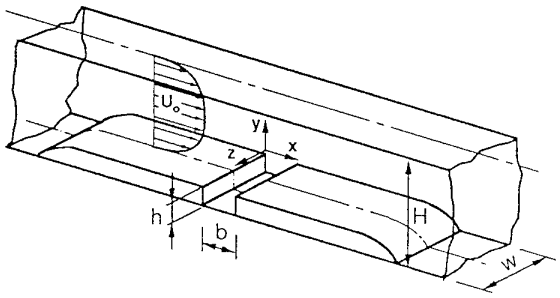

Figure 1 Geometrical Flow Configuration.

The present results were obtained for a fully developed channel flow, characterized by a Reynolds number, based on the cavity depth, $Re = U_o h/\nu = 63{,}600$.

2.2 LDV Measurements

The use of Laser-Doppler velocimetry (LDV) allowed to obtain accurate measurements of turbulent velocity characteristics in the growing shear-layer and inside the separated flow regions as well. The measurement procedure used in this investigation has been explained in detail by Durão et al.[15], therefore only a brief description will be given here. The velocimeter was operated in the dual-beam forward-scatter mode and sensitivity to the flow direction was provided by acousto-optic modulation from a Bragg cell unit. Measurements of the longitudinal and transverse velocity components ($\overline{u}$, $\overline{v}$) at the channel centerplane, as well as the corresponding variances ($\overline{u'^2}$, $\overline{v'^2}$) were performed. The time averaged velocities and the velocity statistics were evaluated by ensemble averaging, calculated from blocks containing 10,000 samples.

The velocity measurements may be affected by non-turbulent Doppler broadening errors, due to gradients of mean velocity across the measuring volume (see, e.g., Durst et al.[16]). Particles moving through the scattering volume at different lateral locations scatter light at varying frequencies, independently of the turbulent velocity fluctuations. However, velocity gradient broadening is usually significant only near the walls. The maximum error in variance of the velocity fluctuations was estimated to be normally at least five orders of magnitude smaller than the bulk velocity. Also, the large number of individual values used to form the averages indicates maximum measurement errors (systematic plus random) below 1% and 4%, respectively for the mean and variance values, according to the analysis referred by Yanta and Smith[17] for a 95% confidence level.

3. NUMERICAL METHOD

3.1 Numerical Discretization

The basic equations for the incompressible fluid flow problem under study are the unsteady, three-dimensional Navier-Stokes and continuity equations. These have been expressed in a Cartesian reference frame, as

$$\frac{\partial u_i}{\partial x_i} = 0 \tag{1}$$

$$\frac{\partial u_i}{\partial t} + \frac{\partial u_i u_j}{\partial x_j} = -\frac{1}{\rho}\frac{\partial p}{\partial x_i} + \nu \nabla^2 u_i \,, \tag{2}$$

where the summation convention applies and u_i is the velocity, p is the pressure, ν is the kinematic viscosity, as ρ stands for the fluid density. Integral conservation relations for mass and momentum can be derived by integrating Eqs. (1) and (2) over finite grid volumes, yielding the equations describing the resolvable flow quantities

$$\frac{\partial \tilde{u}_i}{\partial x_i} = 0 \tag{3}$$

$$\frac{\partial \tilde{u}_i}{\partial t} + \frac{\partial \widetilde{u_i u_j}}{\partial x_j} = -\frac{1}{\rho}\frac{\partial \tilde{p}}{\partial x_i} + \nu \nabla^2 \tilde{u}_i \,. \tag{4}$$

In Eqs. (3) and (4) a tilde denotes an averaged quantity over a grid volume or its corresponding surface, which

is equivalent to a filtering procedure as proposed by Shumann.[3]

Afterwards, the above Eqs. (3) and (4) have been discretized in a staggered grid system, employing an explicit quadratic Leith-type of temporal discretization.[13] The resulting finite differences equation, simply written here under the assumption of one-dimensional flow, with $\tilde{u}_i > 0$, for the sake of simplicity, is then

$$\hat{u}_i = \tilde{u}_i^n - \frac{1}{2} C \left(\tilde{u}_{i+1}^n - \tilde{u}_{i-1}^n\right)$$
$$+ \left(\alpha + \frac{1}{2} C^2\right)\left(\tilde{u}_{i+1}^n - 2\tilde{u}_i^n + \tilde{u}_{i-1}^n\right)$$
$$+ C\left(\frac{1}{6} - \alpha - \frac{1}{6} C^2\right)\left(\tilde{u}_{i+1}^n - 3\tilde{u}_i^n + 3\tilde{u}_{i-1}^n - \tilde{u}_{i-2}^n\right)$$
$$+ \frac{\Delta t}{\rho \Delta x}\left(\tilde{p}_i^n - \tilde{p}_{i-1}^n\right). \qquad (5)$$

Thus, each time step has been split into three sub-steps. Firstly, the flowfield dependent variable $\hat{u}_i$ is obtained explicitly from expressions similar to (5), without implicit pressure terms, where C is the Courant number and α denotes the non-dimensional diffusion coefficient. Secondly, the pressure field is determined from a three-dimensional Poisson equation, by introducing the quantity $\tilde{\phi}_i$ as in

$$\nabla^2 \tilde{\phi}_i^{n+1} = \frac{1}{\Delta t} \nabla . \hat{u}_i , \qquad (6)$$

which results from combining the corresponding velocity adjustment with the continuity equation, i.e.

$$\frac{\tilde{u}_i^{n+1} - \hat{u}_i}{\Delta t} = - \nabla \tilde{\phi}_i^{n+1} \qquad (7)$$

and $$\nabla . \tilde{u}_i^{n+1} = 0 . \qquad (8)$$

Finally, the divergence-free velocity field at the $(n+1)$ time step is obtained by taking into account the velocity correction

$$\tilde{u}_i^{n+1} = \hat{u}_i + \frac{\Delta t}{\rho \Delta x}\left(\tilde{\phi}_i^{n+1} - \tilde{\phi}_{i-1}^{n+1}\right). \qquad (9)$$

Further details concerning the numerical discretization can be found in Pereira and Sousa.[18] However, it should still be mentioned that the numerical method is fully second-order accurate in space and in time.

It is recognized that the specification of the initial and, particularly, of the boundary conditions plays a very important role in LES, because the success of the calculations depends much upon it. In the present case, the inflow conditions have been specified in order to respect the measured mean velocity profile at one step height upstream of the cavity and the corresponding turbulence energy. At the spanwise boundaries, periodic conditions have been implemented, thus assuming quasi-two-dimensionality of the mean flow and statistically homogeneous turbulence in the so-treated direction. Aiming to select the periodicity length, previous computations, covering the whole domain and using a coarser grid (32^3) than the one utilized to produce the reported results have been performed. A domain width of $w/3$ have proved to contain the largest scales of motion. To avoid undesirable wave reflections from the outlet region, a Sommerfeld-type of radiation condition (see, e.g., Kobayashi et al.[19]) was applied at this location. At solid walls, a logarithmic law-of-the-wall has been employed, similarly to Schumann[3] and Werner[20], making use of the concept of local equilibrium. This allowed to express the volume averaged wall shear stress as

$$\tilde{\tau}_w = \frac{\rho \tilde{u}_c C_\mu^{0.25} \sqrt{k_c} K}{\ln (E y_c)} , \qquad (10)$$

where $C_\mu = 0.09$, $K = 0.41$, $E = 9.79$ and the index c denotes the nearest grid volume center. Alternatively, an exponential damping function has been coupled to the subgrid-scale model to account for the proximity of the wall as

$$f(y^+) = \left[1 - \exp\left(- y^+ / A^+\right)\right], \qquad (11)$$

where y^+ indicates the distance to the wall in wall coordinates and A^+ takes the value of 25. Concerning the initial conditions, these have been obtained from a standard k-ε model calculation.

A mesh comprising 64x64x48 control volumes overlapped the computational domain, extending up to $7h$ in the streamwise direction. The time step was chosen in order to keep the Courant number $C < 0.5$, due to accuracy requirements.

3.2 Subgrid-Scale Modeling

The subgrid scale velocity may be defined by

$$u_i'' = u_i - \tilde{u}_i , \qquad (12)$$

then resulting from the convective term in Eq. (4)

$$\widetilde{u_i u_j} = \tilde{u}_i \tilde{u}_j + \widetilde{u_i'' \tilde{u}_j} + \widetilde{\tilde{u}_i u_j''} + \widetilde{u_i'' u_j''} . \qquad (13)$$

The first three terms on the right-hand side can be combined in such a form (see Ferziger[21]) that originates one term expressing the contribution of the large scales of motion and a few extra terms (including the so-called

Leonard term) which can be included in the finite difference scheme truncation error, i.e.

$$\widetilde{\widetilde{u_i}\widetilde{u_j}} + \widetilde{u_i''\widetilde{u_j}} + \widetilde{\widetilde{u_i}u_j''} = \widetilde{u_i}\widetilde{u_j} + O(\Delta^2) \ . \qquad (14)$$

For this reason, the latter terms have been neglected in the present study, similarly as performed by Deardorff[1] and Shumann.[3] However, the remaining term on Eq. (13) has to be modeled, in a procedure resembling the one usually adopted for the Reynolds stress term appearing in the time averaged equations. An extensively used model is that proposed by Smagorinsky[2], using the local grid scale strain-rate tensor, $\tilde{S}_{ij}$, to approximate an assumed eddy viscosity coefficient, ν_t, as

$$- \widetilde{u_i''u_j''} + \frac{1}{3}\delta_{ij}\widetilde{u_k''u_k''} = 2\,\nu_t\,\tilde{S}_{ij}$$
$$= 2\,(C_s\Delta)^2\,\left(2\tilde{S}_{ij}\tilde{S}_{ij}\right)^{1/2}\tilde{S}_{ij} \ . \qquad (15)$$

In any case, the model implies the apriori specification of the constant C_s, for which the values of 0.10 and 0.20 have been used in the present study. Several studies have been carried out to determine an optimum value for this constant[1,22,23], but an universal value could not be obtained. Various attempts have also been made to generalize the method by computing a dynamically adjustable value for C_s, as described in Lilly[24] and more recently in Germano.[25] Nevertheless, this procedure will not be followed in the presently reported investigation.

Another way of modeling the eddy viscosity coefficient for the unresolved scales was suggested by Métais and Lesieur.[13] The so-called structure-function model has been derived in the physical space by using the "Batchelor-Orszag formula", yielding

$$\nu_t = 0.063\,\Delta\,[F_2(x_i, \Delta, t)]^{1/2} \ , \qquad (16)$$

where

$$F_2(x_i, \Delta, t) =$$
$$\left(||u_i(x_i, t) - u_i(x_i + r_i, t)||^2\right)_{||r_i|| = \Delta} \ . \qquad (17)$$

In the following section, both Smagorinsky and Métais and Lesieur subgrid scale models will be used in LES calculations and its performance will be investigated. It is our purpose to compare the results produced by these two methods and to assess the improvements obtained with respect to the predictions carried out using the standard k-ε model.

4. RESULTS

The calculations have that have been performed in the present study are summarized in Table 1.

Table 1
Summary of Calculations

Ref.	Model	Near-wall
LES1	Smagorinsky (C_s = 0.20)	Log. law
LES2	Smagorinsky (C_s = 0.10)	Log. law
LES3	Smagorinsky (C_s = 0.20)	Exp. damp.
LES4	Smagorinsky (C_s = 0.20)	No-slip
LES5	Structure-Function	Log. law
k-ε	Standard k-ε Model	Log. law

The results include five LES computations, using two different values of the Smagorinsky model constant, three different near-wall treatments, the structure-function model and a standard k-ε model computation using a similar computational grid. The LES results reported here have been obtained by computing statistics over approximately 70 characteristic time units ($U_o t/h$).

Our first concern is to find the most suitable value for the Smagorinsky model constant, C_s, to be used in the present fluid flow problem. Figures 2a and 2b display profiles of mean velocity and longitudinal normal stress, respectively, at x/h = 17/10 inside the cavity, calculated using LES1 and LES2. It can be observed in Fig. 2a that LES1 allows to get slightly more curvature in the mean velocity profile inside the separated flow region than LES2 and, therefore, it is closer to the measurements. This fact indicates that C_s = 0.20 should be used instead of C_s = 0.10. Also, the peak value of the longitudinal normal stress (see Fig. 2b) is better predicted with LES1. In the foregoing calculations, a logarithmic law-of-the-wall was employed as near-wall treatment. Figures 3a and 3b show that this procedure (LES1) is in fact the best compromise, as the flow adjacent to the wall cannot be resolved utilizing so few grid nodes. These figures portray profiles of mean velocity and longitudinal normal stress, at a location upstream inside the cavity, x/h = 3/10. Both plots clearly demonstrate that the no-slip condition (LES4) does not allow to capture the details of the flow near the wall, resulting severe consequences for the remaining recirculating flow. Furthermore, it can be seen that, in the present case, the use of an exponential damping function (LES3) did not produce clear improvements to the implementation of a no-slip condition.

It is recognized that the flow inside a cavity exhibits strong unsteadiness when the Reynolds number is above a certain threshold level.[10,26] For this reason, it was expected to obtain significant improvements in using a LES formulation instead of a standard k-ε model. Figures 4a - 4d and 5a - 5d prove the former expectations and the statement applies for both the separated shear layer and the recirculation region. In

these figures, the results of LES1, LES5 (structure-function model) and the k-ε calculation have been superimposed, covering longitudinal and transverse components of mean velocity and normal stress, at two locations inside the cavity, x/h = 3/10 and 17/10. The results show that the standard k-ε model is unable to predict the curvature of the streamwise velocity profile, particularly near the wall, as can clearly be seen in Figs. 4a and 5a. Consequently, the best predictions of the transverse velocity component have also been obtained for the LES computations, as shown in Figs. 4b and 5b, although there is a certain uncertainty on the experiments at the downstream location, due to effects of impingement. Again, better predictions were obtained with LES1 and LES5 for the longitudinal normal stress at the analyzed stations. As shown in Figs. 4c and 5c, the k-ε model cannot predict the peak values on the separated shear layer and, once again, it is incapable of producing a correct evolution inside the recirculation region. The latter is also true for the transverse component of the normal stress but, in this case, the LES calculations show a slight underprediction in the shear layer, patent at the downstream location, as can be confirmed by viewing Figs. 4d and 5d.

It has been mentioned before but it should be emphasized that the better agreement with respect to the experimental results obtained using LES approaches is not a surprising event, since roll-up of the separated shear layer occurs, as evidenced by Fig. 6. Instantaneous velocity time-series indicated the presence of periodic shedding of vortical structures from the separation corner of the cavity, characterized by a Strouhal number, $St = fh/U_o$ = 0.5. This value is in agreement with previous experimental investigations.[26]

5. CONCLUSIONS

LDV measurements of turbulent flow over a cavity at a Reynolds number Re = 63,600 have been used to investigate the ability of LES to predict the flow in the separated shear layer and inside the recirculation region as well. Two different LES approaches have been used: Smagorinsky and the structure-function model. Globally, both models have proved to perform much better in the present flow problem than the standard k-ε model, using a similar computational grid. Further, the logarithmic law-of-the-wall have demonstrated to be the best compromise for near-wall treatment in a flow with engineering application.

ACKNOWLEDGMENTS

The authors gratefully acknowledge to Prof. M. Lesieur for several helpful discussions during his visit to IST in the framework of an AGARD mission. Computing facilities were made available by "Fundação para o Desenvolvimento dos Meios Nacionais de Cálculo Científico".

REFERENCES

1. Deardorff, J.W., "A Numerical Study of Three-Dimensional Turbulent Channel Flow at Large Reynolds Numbers", J. Fluid Mech., *41*, 2, 1969, pp 453-480.

2. Smagorinsky, J., "General Circulation Experiments with the Primitive Equations. I. The Basic Experiment", Mon. Weather Rev., *91*, 1963, pp 99-164.

3. Shumann, U., "Subgrid Scale Model for Finite Difference Simulations of Turbulent Flows in Plane Channels and Anulli", J. Comp. Physics, *18*, 1975, pp 376-404.

4. Moin, P. and Kim, J., "Numerical Investigation of Turbulent Channel Flow", J. Fluid Mech., *118*, 1982, pp 341-377.

5. Kobayashi, T., Morinishi, Y. and Oh, K., "Large Eddy Simulation of Backward-Facing Step Flow", Comm. in Appl. Num. Meth., *8*, 1992, pp 431-441.

6. Arnal, M. and Friedrich, R., "Large Eddy Simulation of a Turbulent Flow with Separation", Eighth Symp. on Turbulent Shear Flows, Munich, Germany, 1991, Paper II-2.

7. Neto, A.S., Grand, D., Métais, O. and Lesieur, M., "A Numerical Investigation of Coherent Vortices in Turbulence behind a Backward-Facing Step", J. Fluid Mech., *256*, 1993, pp 1-25.

8. Werner, H. and Wengle, G., "Large Eddy Simulation of Turbulent Flow over and around a Cube in a Plate Channel", Eighth Symp. on Turbulent Shear Flows, Munich, Germany, 1991, Paper 19-4.

9. Yang, K. and Ferziger, J.H., "Large Eddy Simulation of Turbulent Obstacle Flow Using a Dynamic Subgrid-Scale Model", AIAA J., *31*,8,1993, pp 1406-1413.

10. King, J.L., Boyle, P. and Ogle, J.B., "Instability in Slotted Wall Tunnels", J. Fluid Mech., *4*, 1958, pp 283 - 305.

11. Sparrow, E.M., Vemuri, S.B. and Kadle, D.S., "Enhanced and Local Heat Transfer, Pressure Drop, and Flow Visualization for Arrays of Block-Like Electronic Components", Int. J. Heat Mass Transfer, *26*, 1983, pp 689 - 699.

12. Métais, O. and Lesieur, M., "Spectral Large Eddy Simulation of Isotropic and Stably Stratified Turbulence", J. Fluid Mech., *239*, 1992, pp 157-194.

13. Leonard, B.P., "A Stable and Accurate Convective Modelling Procedure Based on Quadratic Upstream Interpolation", Comp. Meth. in Appl. Mech. Eng., *19*, 1979, pp. 59 - 98.

14. Durão, D.F.G., Heitor, M.V. and Pereira, J.C.F., "A Laser Anemometry Study of Separated Flow Over a Model Three-Dimensional Hill", *in* "Applications of Laser Anemometry to Fluid Mechanics" (ed. Adrian et al.), Springer-Verlag, 1989, pp 93 - 118.

15. Durão, D.F.G., Pereira, J.C.F. and Sousa, J.M.M., "LDV Measurements of Turbulent Separated Flow Over a Cavity", Sixth Int. Symp. on Applications of Laser Techniques to Fluid Mechanics, Lisbon, Portugal, 1992, Paper 7-2.

16. Durst, F., Melling, A. and Whitelaw, J.H., "Principles and Practice of Laser-Doppler Anemometry", 2nd ed., Academic Press, New York, 1981.

17. Yanta, W.J. and Smith, R.A., "Measurements of Turbulent-Transport Properties with a Laser Doppler Velocimeter", AIAA-73-169, Eleventh Aerospace Science Meeting, Washington, 1978.

18. Pereira, J.C.F. and Sousa, J.M.M., "Finite Volume Calculations of Self-Sustained Oscillations in a Grooved Channel", J. Comp. Physics, *106*, 1, 1993, pp 19 - 29.

19. Kobayashi, M.H., Pereira, J.C.F. and Sousa, J.M.M., "Comparison of Several Open Boundary Numerical Treatments for Laminar Recirculating Flows", Int J. Num. Meth. in Fluids, *16*, 1993, pp 403 - 419.

20. Werner, H., "Grobstruktursimulation der Turbulenten Strömung über eine Querliegende Rippe in einem Plattenkanal bei Hoher Reynoldszahl", Ph.D. Dissertation, Technische Universität München, 1991.

21. Ferziger, J.H., "Large Eddy Numerical Simulations of Turbulent Flows", AIAA J., *15*, 9, 1977, pp 1261-1267.

22. Deardorff, J.W., "On the Magnitude of the Subgrid-Scale Eddy Coefficient", J. Comp. Physics, 7, 1971, pp 120-133.

23. Mason, P.J. and Callen, N.S., "On the Magnitude of the Subgrid-Scale Eddy Coefficient in LES of Turbulent Channel Flow", J. Fluid Mech., *162*, 1986, pp 439-462.

24. Lilly, D.K., "On the Application of the Eddy Viscosity Concept in the Inertial Sub-Range of Turbulence", NCAR, Boulder, Colorado, 1966, Paper 123.

25. Germano, M., "Turbulence: The Filtering Approach", J. Fluid Mech., *238*, 1992, pp 325-336.

26. Rockwell, D. and Naudascher, E., 1978, "Review — Self-Sustaining Oscillations of Flow Past Cavities", ASME J. of Fluids Eng., *100*, pp 152-165.

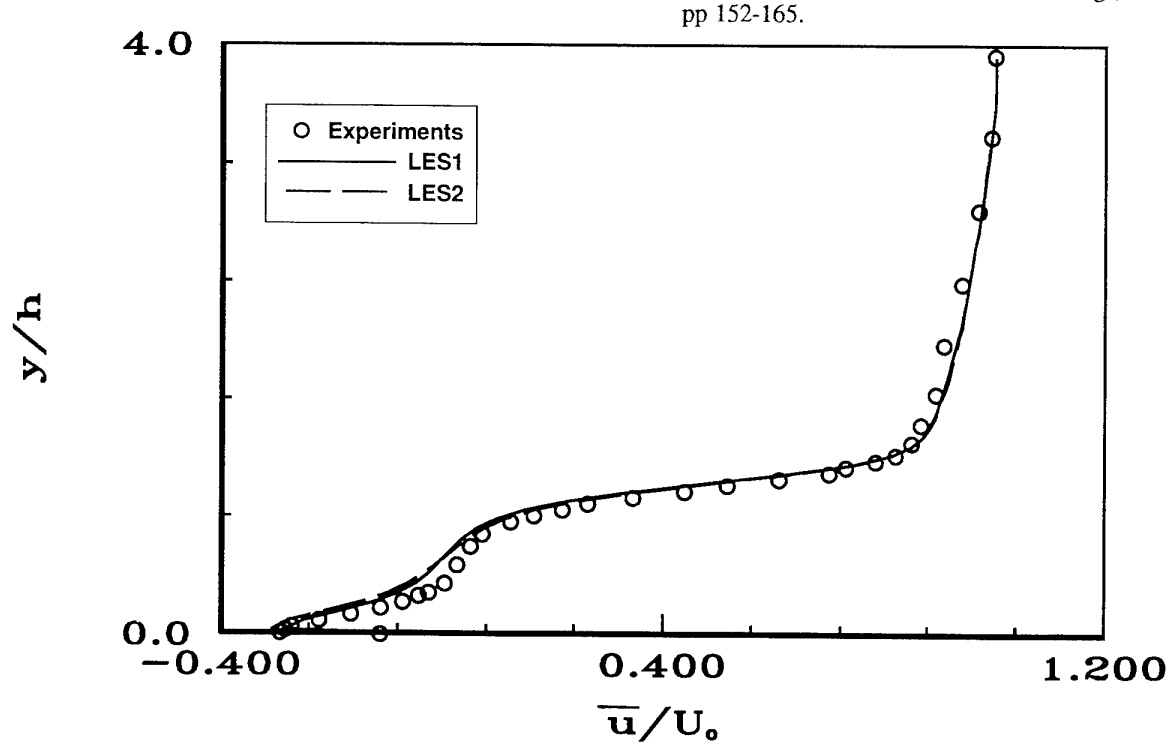

Figure 2a Longitudinal velocity profile at x/h = 17/10 predicted with the Smagorinsky model.

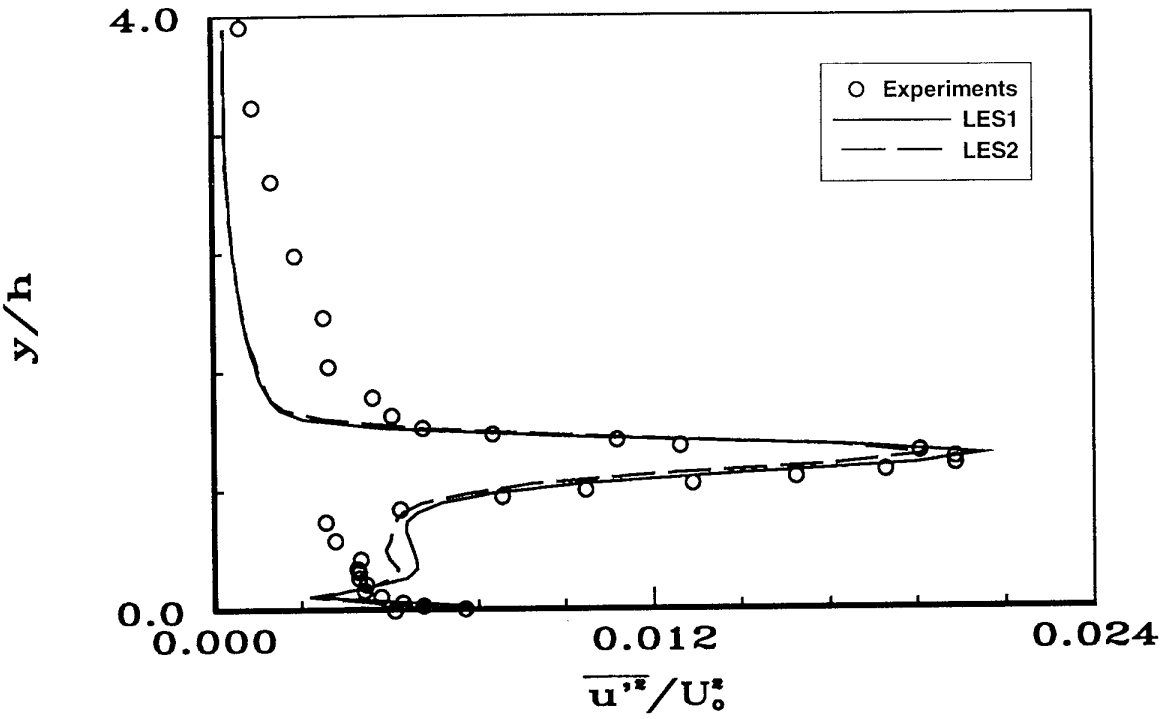

Figure 2b Longitudinal normal stress at x/h = 17/10 predicted with the Smagorinsky model.

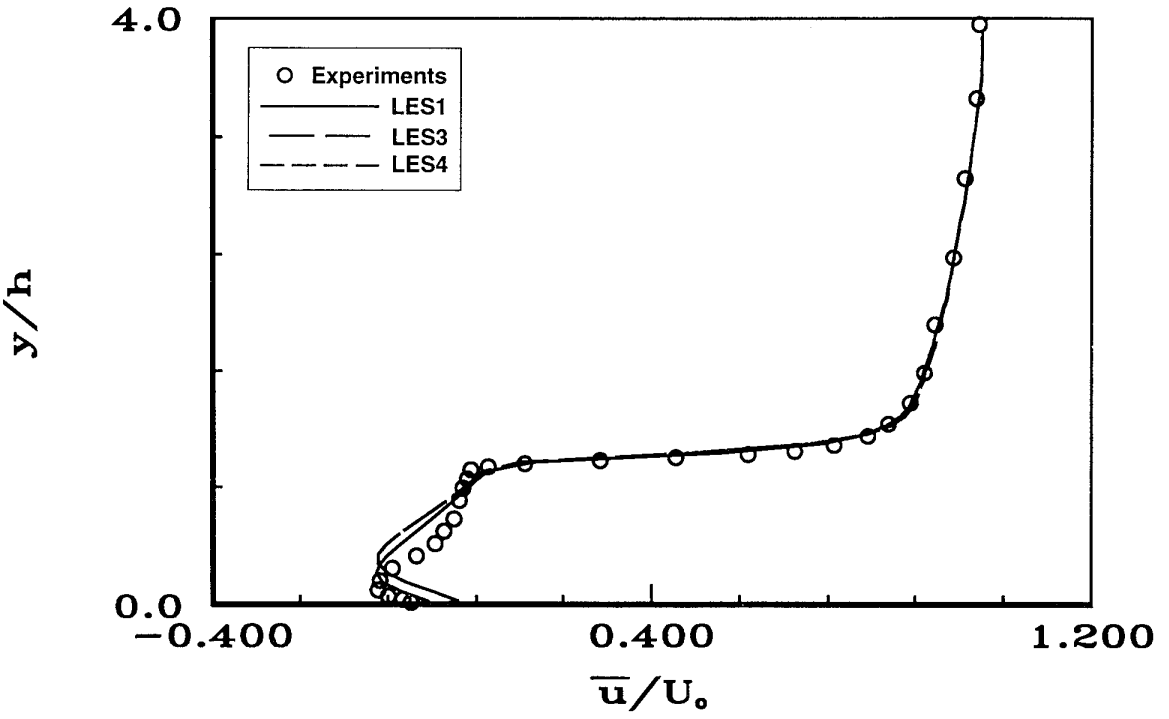

Figure 3a Longitudinal velocity profile at x/h = 3/10 predicted using different near-wall treatments.

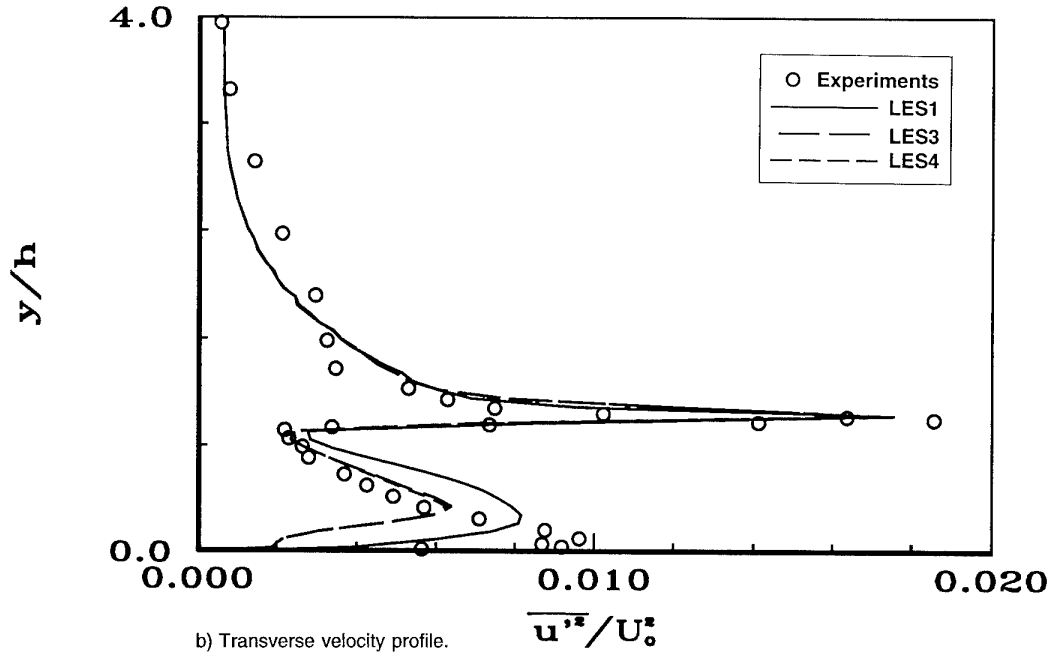

b) Transverse velocity profile.

Figure 3b Longitudinal normal stress at x/h = 3/10 predicted using different near-wall treatments.

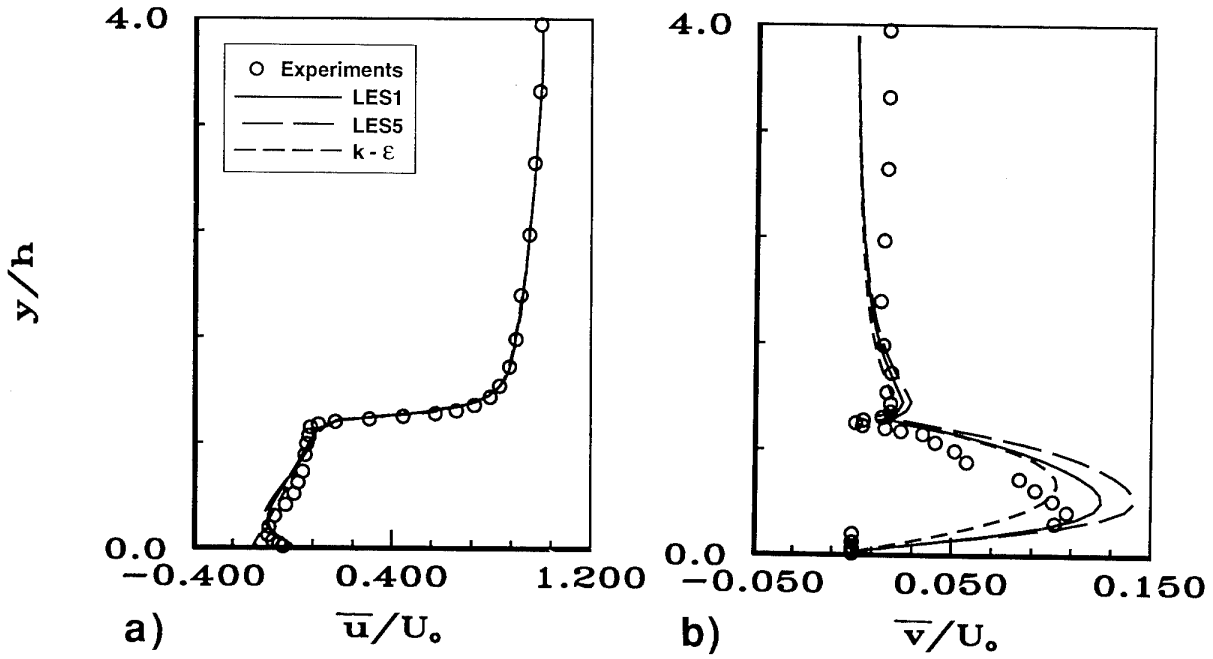

a) Longitudinal velocity profile.

Figure 4 Predictions at x/h = 3/10 using Smagorinsky, structure-function and k-ε models.

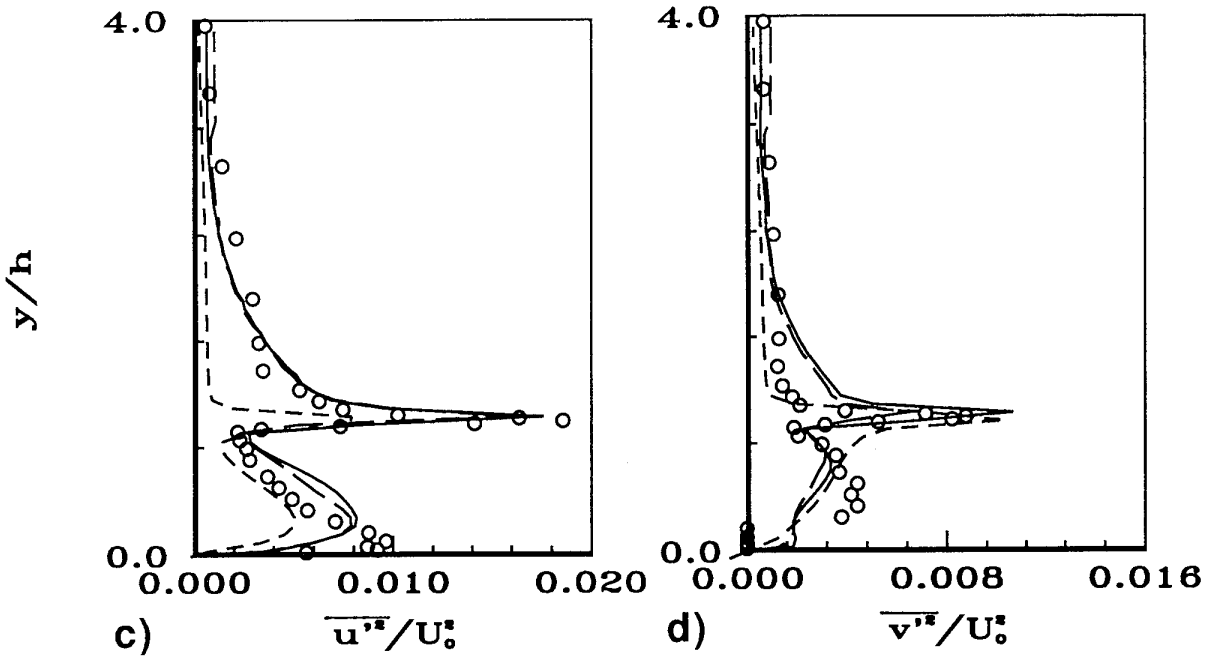

c) Longitudinal normal stress.

d) Transverse normal stress.

Figure 4 Concluded

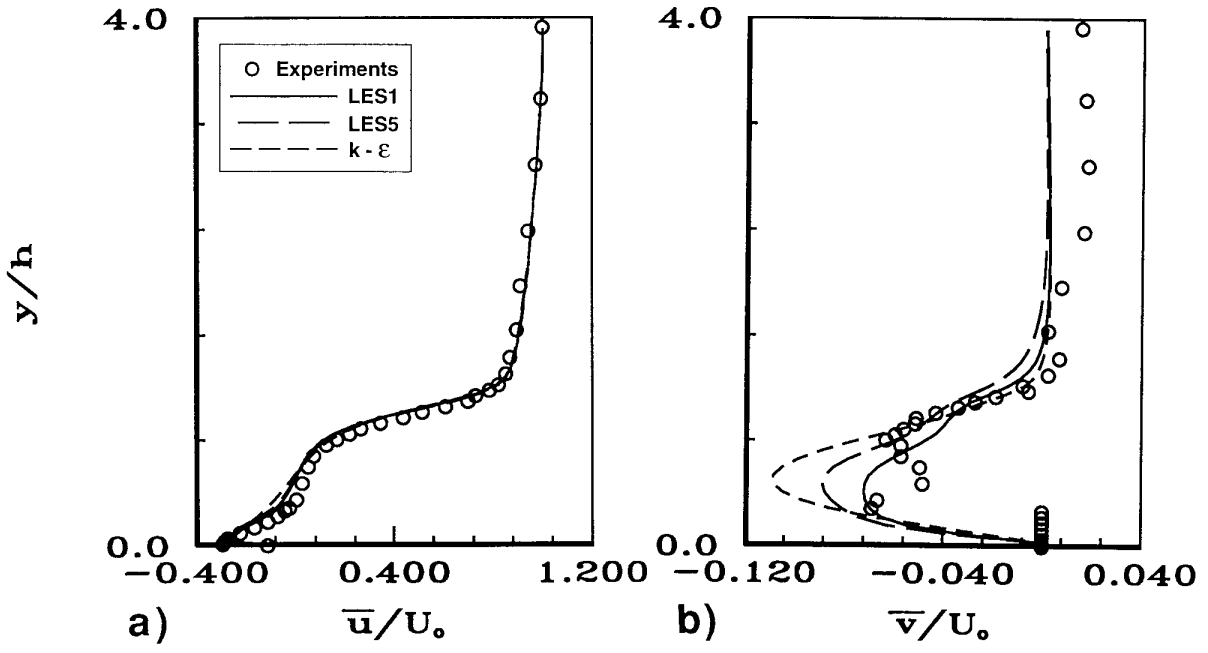

a) Longitudinal velocity profile.

b) Transverse velocity profile.

Figure 5 Predictions at x/h = 17/10 using Smagorinsky, structure-function and k-ε models.

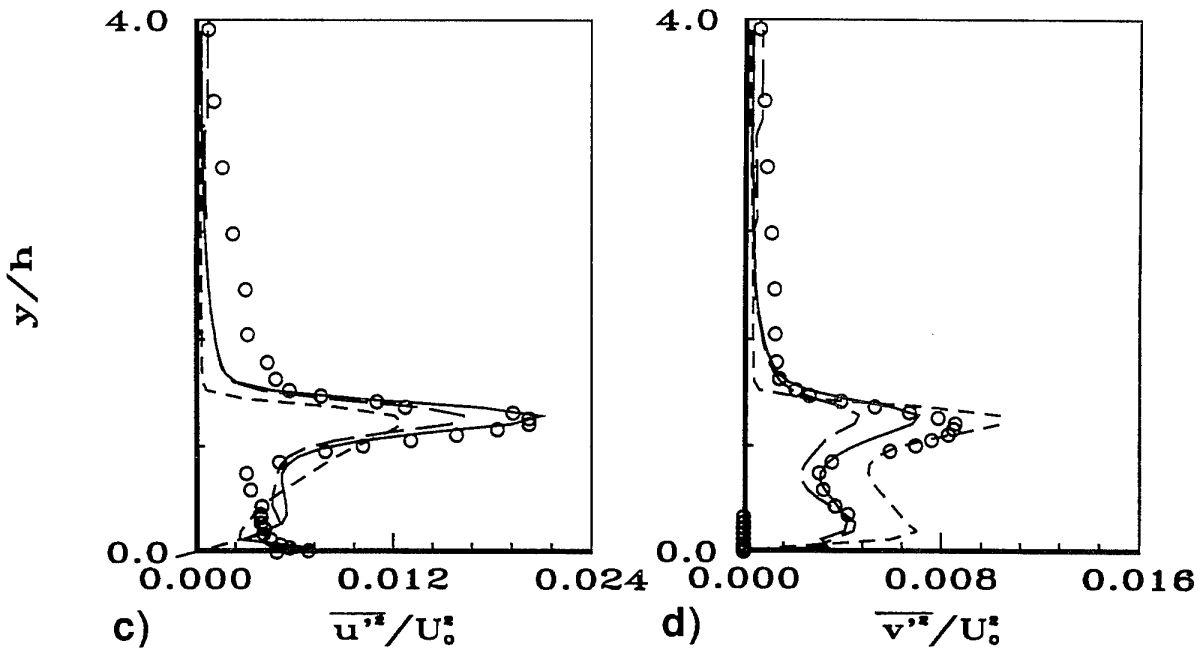

c) Longitudinal normal stress.

d) Transverse normal stress.

Figure 5 Concluded

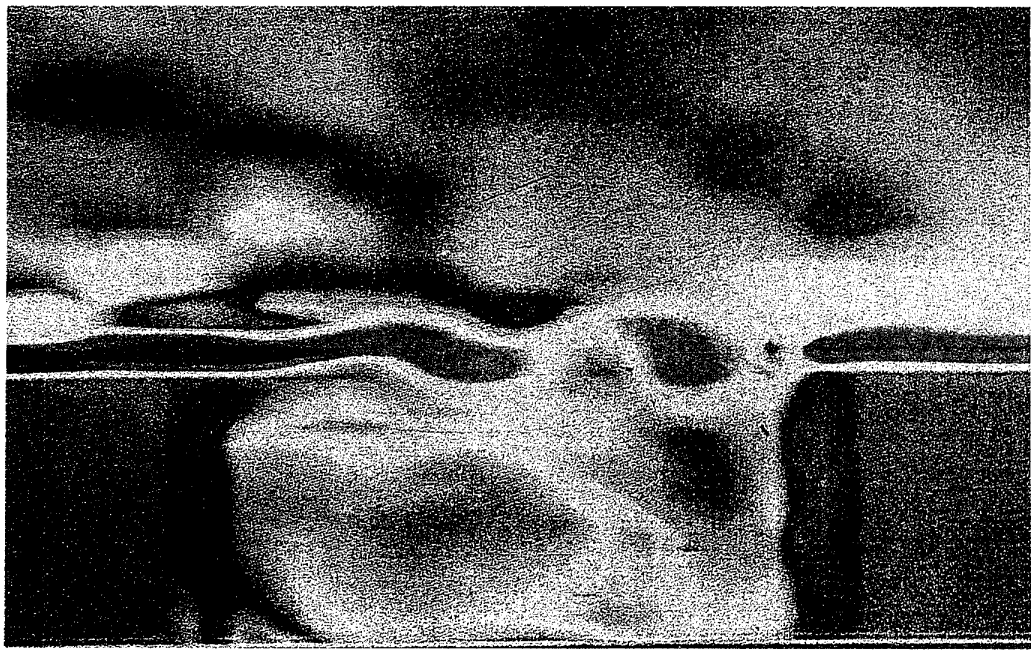

Figure 6 Instantaneous vorticity contours obtained using the structure-function model.

LARGE-EDDY SIMULATION OF SEPARATED FLOW IN A RIBBED DUCT

Harald BRAUN, Martin FIEBIG and Nimai Kumar MITRA

Institut für Thermo- und Fluiddynamik, Ruhr-Universität Bochum,
44780 Bochum, Germany

SUMMARY

Large-eddy simulation of turbulent channel flow over an one-sided periodically ribbed wall has been performed. Large-scale nonsteady structures have been correlated with the statistical values of the turbulent flow field. It is shown, that high turbulent kinetic energy and vortex shedding appear at the same location. The shedding of vortical structures from the edge of the rib is the dominating turbulent phenomena of the flow. The instantaneous behaviour of the large-scale vortical structures is visualized and their interaction with the highly fluctuating recirculation zones is observed.

NOMENCLATURE

C_s	subgrid model constant
c_τ	Schumann's coefficient
h	channel half width
p	absolute pressure
p'	local periodic pressure
Re	Reynolds number based on $\bar{u}_m$ and channel half width h
Re_x	Reynolds number based on $\bar{u}_x$ and channel half width h
S_{ij}	deformation tensor
$\bar{u}_i$	filtered velocity component
$\bar{u}_i \mid_w$	filtered velocity component nearest to the wall
$\bar{u}_m$	mean velocity
$\bar{u}_x$	unknown reference velocity
X_R	nondimensional distance between the edge of the rib and the reattachment line
x_i	cartesian coodinates
β	fixed pressure gradient
τ_w	wall shear stress
ν_{ij}	eddy viscosity

1. INTRODUCTION

Many flows of technical interest are turbulent and hence unsteady and vortical. Simulation of such flows by traditional Reynolds-averaging fail to model properly the large-scale structures of the flow and the associated momentum and energy transport. Franke & Rodi (1991) tried to simulate vortex shedding behind a rectangular cylinder with standard k-ε model and Reynolds stress equation model. The predicted turbulent kinetic energy was in all presented cases too small and the Strouhal number was strongly dependent on the wall boundary conditions. A more accurate, but more expensive technique is large-eddy simulation (LES). In contrast to the Reynolds-averaging approach a filtering of the Navier-Stokes equations is applied in LES. The large-scale structure of the flow field is simulated directly, only the small-scales are approximated by turbulence modelling.

Large-eddy simulation of various flows with separation have been reported. Wengle and Werner investigated a single cube and a single square rib (1989). They found complex vortex structures around the cube, the results were confirmed by experiments. For Reynolds number Re= 85,000 the reattachment length X_R was 7.0. In case of the single rib they noticed large-scale structures over the complete channel width. Murakami, Mochida and Hayashi (1990) also calculated turbulent flow over a single cube. A comparison with results of the standard k-ε model showed a fundamental shortcoming of Reynolds-averaging; the systematic fluctuations of Karman's vortex street were eleminated. Friedrich and Arnal (1990) simulated flow over a backward facing step. They reported on separation bubbles and fluctuating reattachment zones. Akselvoll & Moin (1993) also reported a LES of flow over a backward facing step and compared their results with direct numerical simulation. Yang and Ferziger (1993) calculated flow over periodically ribs with the dynamical subgrid-model of Germano (1992). The periodic length was 31h to minimize the interaction between the neighboring ribs. They reported on vortex merging and splitting behind the ribs and instantaneous reattachment and separation zones. The Reynolds number of the calculations was 3,300 and the reattachment length X_R was 7.01.

In contrast to the results of the Reynolds-averaging, the large-eddy simulations show the strong interaction of small-scale turbulent fluctuations and large-scale coherent structures like periodic and non-periodic vortex shedding. These large-scale effects are highly non-isotropic, this explains the failure of traditional turbulence modelling in separated flow.

The purpose of the present work is to investigate the three-dimensional turbulent flow in an infinitely wide duct with an one-sided ribbed wall by large-eddy simulation for a Reynolds number, based on channel half width h and mean velocity $\bar{u}_m$, of 16,000.

2. COMPUTATIONAL DOMAIN

The computational domain is an element of the periodically ribbed channel, see fig.1. The periodic element has a length of 10h. The channel height is 2h and the width is 4h.

The height of the rib is half of the channel height. The grid size is 162 * 34 * 34 with variable mesh width, see fig. 2. The grid is equidistant in the homogenous y-direction. At the middle of the periodic element, there is an equidistant block of 4h length with 96 grid points. On both sides are blocks of 3h length with variable grid size. In z-direction two variable grid blocks are employed with grid refinement at the center line and near walls.

Paper presented at the 74th Fluid Dynamics Symposium on "Application of Direct and Large Eddy Simulation to Transition and Turbulence" held at Chania, Crete, Greece, in April 1994.

2. Numerical Method

The filtered nondimensional momentum and mass conserving equations in index form are given by eq. (1). All variables are nondimensionalized by the reference velocity $\bar{u}_x$ and the channel half width h.

$$\frac{\partial \overline{u_i}}{\partial x_i}=0$$

$$\frac{\partial \overline{u_i}}{\partial t} = -\frac{\partial \overline{p'}}{\partial x_i}-\frac{\partial \overline{u_i}\,\overline{u_j}}{\partial x_j}-\frac{\partial \overline{u_i' u_j'}}{\partial x_j}+\frac{1}{Re_x}\frac{\partial^2 \overline{u_i}}{\partial x_j^2}+\delta_{i1}\beta \qquad (1)$$

The pressure gradient in streamwise direction is splitted in the fixed periodical gradient β and a local part to realize the periodicity condition accurately, see eq. (2).

$$\frac{\partial \overline{p}}{\partial x_1} = \beta + \frac{\partial \overline{p'}}{\partial x_1} \qquad (2)$$

For the calculation of turbulent shear stresses, see eq. (3), the subgrid model of Smagorinsky and Lilly (1967) has been implemented, see eq. (4). The model constant C_s is set to 0.1.

$$-\overline{u_i' u_j'} = 2\,\overline{\nu_{ij}}\,\overline{S_{ij}} - \frac{1}{3}\,\overline{u_k' u_k'}\,\delta_{ij} \qquad (3)$$

$$\overline{\nu_t} = (C_s * \Delta)^2 \sqrt{2\overline{S_{ij}}\,\overline{S_{ij}}} \qquad (4)$$

This model is widely used in meteorological and engineering applications. This simple model is in good agreement with experiments in recirculating flows. In equation (3) and (4) the filtered deformation tensor is used as defined in equation (5).

$$\overline{S_{ij}} = \frac{1}{2}\left(\frac{\partial \overline{u_i}}{\partial x_j} + \frac{\partial \overline{u_j}}{\partial x_i}\right) \qquad (5)$$

The inflow and outflow conditions are of critical importance when turbulent structures are calculated directly. Turbulent fluctuations have to exist at the entrance of the computational domain to avoid a laminar/turbulent transition and they should not be damped at the exit. For the present case the geometry is assumed periodically, so that periodicity conditions can be used in the axial and lateral boundaries of the computational domain. Possible errors resulting from the in- and outflow conditions are avoided by this way. For the convective terms a no-slip boundary condition is used, for the diffusive terms the formulation of Schumann (1975) as given in eq. (6) is employed.

$$c_\tau = \frac{\overline{\tau_w}}{\overline{u_1}|_w} = \frac{\tau_w}{u_1|_w} \qquad (6)$$

Equation (6) implies, that the quotient of the filtered mainstream velocity nearest to the wall and the filtered wall shear stress in the main flow direction is assumed equal to the quotient of the unsteady velocity nearest to the wall and the unsteady wall shear stress.

The present computational scheme is similar to the fractional step method of Kim and Moin (1985). The spatial arrangement of the variables is cell-centered. The discretization scheme in space is second order. The convective terms have been discretized by the Adams-Bashforth scheme and the Crank-Nicholson scheme has been used for viscous terms, so that the discretization in time is also of second order. For the solution of the resulting Poisson equation for pressure a SIP solver is employed.

For the calculations the periodic pressure gradient and β the reference Reynolds number Re_x are fixed, so that the flow field adjusts to a mean mass flow. After a calculation the results are normalized with the mean velocity $\bar{u}_m$.

The calculations were performed on an IBM RS6000/580H workstation.

4. Statistical Results

For the statistical evaluation of the turbulent flow field 331 samples of the instantaneous flow field are accumulated over 100000 time steps, i.e. approximately 500 dimensionless time units. The statistics are carried out with ensemble-averaging respectively in time and in y-direction. The samples are stored on a hard-disk. During the calculations the statistical evaluation is used to check the convergence of the solution. The ensemble-averaged results presented in this paper are determined from 6800 samples per grid point.

The streamlines of the time-averaged two-dimensional flow field and the distribution of wall shear stress at the lower and upper wall are presented in fig. 3. The streamlines disclose corner eddies (cef and ceb) on both sides of the rib and a large separation vortex (sv) behind the rib. The distribution of wall shear stress on the lower wall shows two minimum values, which correspond to the locations of the clockwise rotating vortices, these are the corner eddy in front of the rib and the large separation vortex behind the rib. Only the primary corner eddy behind the rib is rotating counter-clockwise. At the upper wall a maximum of wall shear stress appears approximately 1.3h behind the rib. The shift of 1.3h behind the rib can be explained from the development of the velocity profile, see fig.4. In the rib cross section the time-averaged velocity profile is nearly uniform, the turbulent kinetic energy k has a maximum close to the rib, see fig. 5. The strong fluctuations on the centerline lead to a high turbulent momentum diffusion in normal direction, so that the u-velocity is decreased on the centerline of the channel and it is increased near the upper wall because of the mass conservation.

The location of the time-averaged reattachment line X_R is 6.01h behind the rib. The value of Werner & Wengle (1989) with a single rib was 1h larger, the periodic ribs of Yang & Ferziger have also a reattachment length X_R of 7h. This reduction of X_R is caused by the interaction of the periodic ribs. In contrast to the single rib and to the periodic ribs with a periodic distance of 31h an upstream influence from obstacles downstream exists for the present geometry. The flow at the lower channel half is slowed down through the repeated blokkage.

The contour lines of equal rms-values of the large-scales are interesting with respect to the structure of the instantaneous flow field. Areas of high u_{rms}-values appear near the edge of

the rib and spread out in normal direction downstream, see fig. 5. This is an indication of a fluctuating shear layer similar to those of the turbulent backward-facing step. This area reaches approximately 2.5h downstream from the rib. With the spreading the fluctuations decay downstream and are reinforced at the edge of the next rib. The distributions of v_{rms} and w_{rms} are similar to the one of the u_{rms}-values. There is also a spreading area which is 2.5-3h long. The location of origin is different, which is indicated by the maximum rms-value. The v-fluctuations develop in front of the rib. Observations of the instantaneous flow field show a splashing of vortical structures on the front side of the rib, which result in large lateral and normal velocity-components. The maxima of the w_{rms}-values support this observation, they appear at the upper half of the rib. Due to the change of the local flow direction from xz-direction to x-direction at the edge of the rib the v- and w-fluctuations are transfered into u-fluctuations. Secondary maxima of the v- und w-fluctuations occur 2.5h behind the rib, whereas the u-fluctuations decay. Owing to instabilities of the shear layer turbulent kinetic energy of the u-velocity components is transfered into the v- and w-velocity components.

The distribution of turbulent kinetic energy of the large-scale fluctuations is presented in fig. 5. It gives an overview of local intensity of fluctuations. Furthermore the stretched area of maximum values supports the conjecture of turbulent energy transfer between the velocity components, because the extension of the area encloses the maximum areas of u_{rms}, v_{rms} and w_{rms}.

5. Instantaneous flow field

It is not possible to present a comprehensive view of the instantaneous large-scale flow field, because only a small coherent time record of the instantaneous flow field information is stored on hard disks. For this reason the investigation of the instantaneous flow field presented in this paper is a brief survey of the unsteady flow characteristics.

The distributions of the rms-values show, that the fluctuations of the large-scale field are generated at the rib and decay downstream. The fluctuations are caused by non-periodically shedding vortices, which separate from the edge of the rib. After a short growing time, which corresponds approximately to a length of 2.5h behind the rib, the vortical structures begin to decay downstream. Fig. 6 shows a typical snapshot of pressure minima in the vicinity of the rib. They indicate the vortex cores of the shedding vortices. At the edge of the rib a new transverse vortex develops, downstream there are two vortices with a double-core. Video animations of the instantaneous pressure field have shown, that these double-cores are typical before vortex division. The spreading of the u_{rms}-values downstream to the lower wall can be explained by the effect of vortex division and decaying from large-scale structures to small-scale structures.

In fig. 7 a top view on the u-velocity components on the mesh cells nearest to the walls is presented, the dashed lines indicate areas of back flow. In contrast to the time-averaged results no linear reattachment lines appear. The different areas of forward and backward flows are characterized by highly fluctuating separation lines. The area of dashed lines in front of the rib is the corner eddy "cef", the area of solid lines behind the rib is the corner eddy "ceb". Compared with the two-dimensional time-averaged results of fig. 3, it is conspicuous, that the range of both corner eddies fluctuates from 0.0h to 1.5h in this snapshot. Whereas the area of "cef" is nearly closed, the areas of "ceb" and of the separation vortex "sv" overlap. Isolated small areas of forward flow are found inside the back flow areas of the separation vortex. The same effect exists in the main reattachment area in the vicinity of X_R. The maximum extension of the reattachment line can not be determined, because in special cases the areas of back flow of "cef" and "sv" grow together.

Fig. 8 presents three-dimensional snapshots of surfaces of equal pressure, which wrap the vortical structures behind the rib. The shedding of the vortices is clearly structured during the growing time, in some cases the axes of the vortices are nearly parallel to the ribs. Downstream the axes develop into three-dimensional threads or worm-like structures, which break up into small vortical structures. The views of three different time steps suggest the considerable changes of the instantaneous flow field and the transfer of turbulent kinetic energy from large-scale to small-scale structures.

6. Conclusions

The large-eddy simulation of turbulent channel flow over a one-sided periodically ribbed wall gives the instantaneous large-scale structure of the flow field. Non-periodical shedding of transverse vortices at the edge of the ribs occurs. The vortices pass through a growing phase as they move downstream. Approximately 2.5h behind the ribs they begin to decay and break up into small-scale vortical structures. The shedding appears two- or three-dimensional, the axes of the vortices are not always parallel to the ribs. During the growing phase they roll up and form worm-like structures. The reattachment lines at the lower wall are highly fluctuating and the areas of back flow enclose isolated areas of forward flow.

Acknowledgements

This work is supported by the Deutsche Forschungsgemeinschaft (DFG) through the special research group "Wirbel und Wärmeübertragung". The authors also thank Prof. H. Wengle for his help and interest.

References

K. Akselvoll, P.Moin
"Large-eddy simulation of a backward facing step flow"
In: W.Rodi (ed.), Engineering Turbulence Modelling and Experiments 2, pp. 303-313, 1993

M. Arnal, R. Friedrich
"On the effects of spatial resolution and subgrid-scale modelling in the large-eddy simulation of a recirculating flow"
In: J.B. Vos (ed.), Proceedings of the 9th GAMM Conference on Numerical Methods in Fluids, Notes on Numerical Fluid Mechanics 35, Vieweg, pp. 3-13, 1992

R. Franke, W. Rodi
"Calculation of vortex shedding past a square cylinder with various turbulence models"
Proceedings of the 8th Symposium of Turbulent Shear Flows, pp. 20.1.1-20.1.6, Munich, 1991

M. Germano, U. Piomelli, P. Moin, W.H. Cabot
"A dynamic subgrid-scale eddy viscosity model"
Physics of Fluids A 3, pp. 1760-1765, 1991

J. Kim, P. Moin
"Application of a fractional-step method to incompressible Navier-Stokes equations"
Journal of Computational Physics 59, pp. 308-323, 1985

D.K. Lilly
"The representation of small-scale turbulence in numerical simulation experiments"
Proceedings of the IBM Scientific Computing Symposium on Environmental Sciences, IBM Form No. 320-1951, pp. 195-210, 1967

S. Murakami, A. Mochida, K. Hibi
"Three-dimensional numerical simulation of air flow around a cubic model by means of large-eddy simulation"
Journal of Wind Engineering and Industrial Aerodynamics 25, pp. 291-305, 1987

U. Schumann
"Subgrid scale model for finite difference simulations of turbulent flows in plane channels and annuli"
Journal of Computational Physics 18, pp. 376-404, 1975

H. Werner, H. Wengle
"Large-eddy simulation of turbulent flow over a square rib in a channel"
In: H.H. Fernholz (ed.), Advances in Turbulence 2, pp. 418-423, Springer, 1989

H. Werner, H. Wengle
"Large-eddy simulation of turbulent flow over and around a cube in a plate channel"
8th Symposium of Turbulent Shear Flows, München, 1991

K.S. Yang, J. H. Ferziger
"Large-eddy simulation of turbulent obstacle flow using a dynamic subgrid-scale model"
AIAA Journal 31, No. 8, pp. 1406-1413, 1993

FIGURES

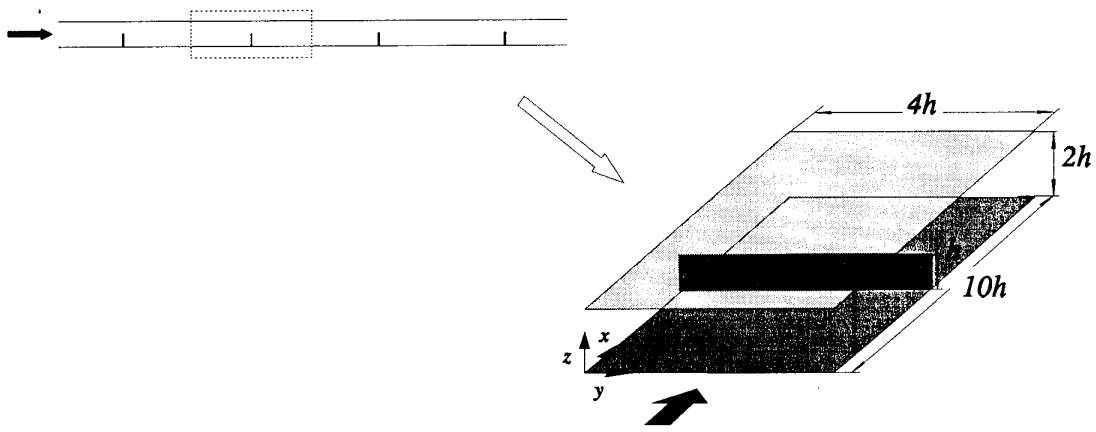

Fig. 1 Computational domain

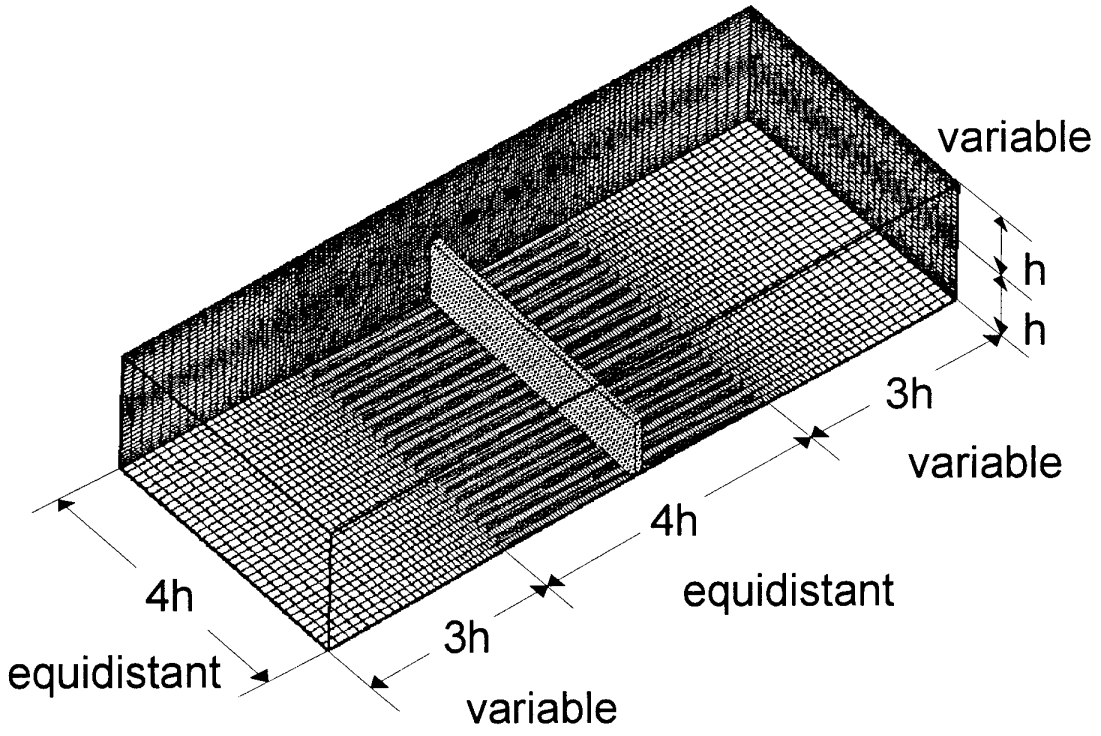

Fig. 2 Computational grid

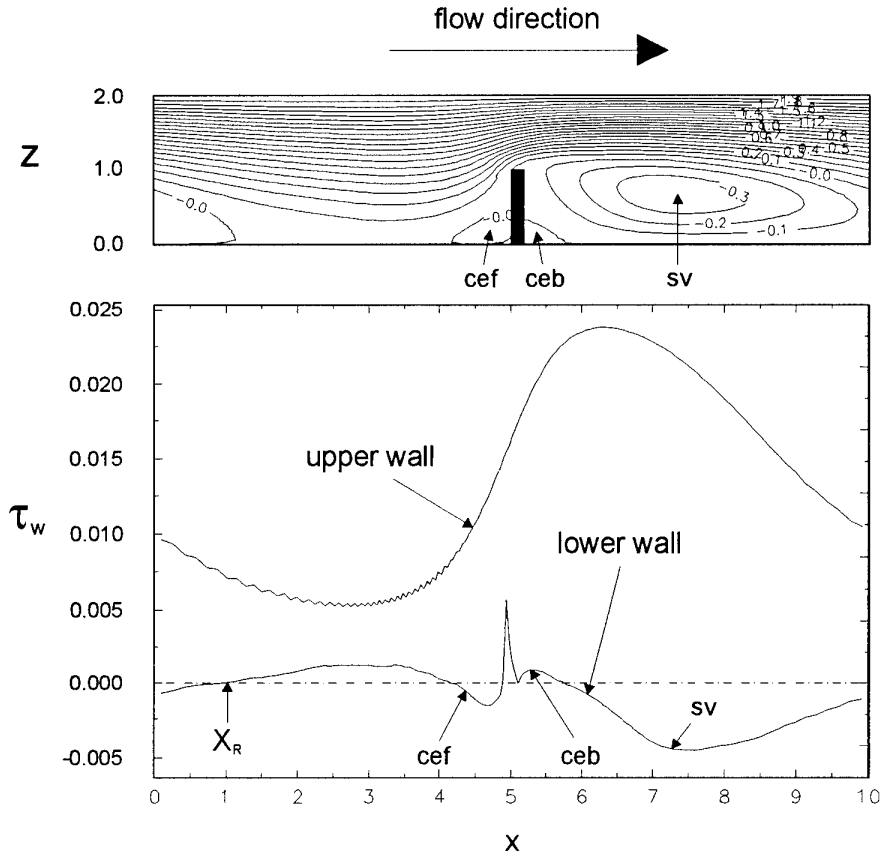

Fig. 3 Streamlines and wall shear stress distribution of time-averaged flow field
(cef - corner eddy in front of the rib, ceb - corner eddy behind the rib, sv - separation vortex)

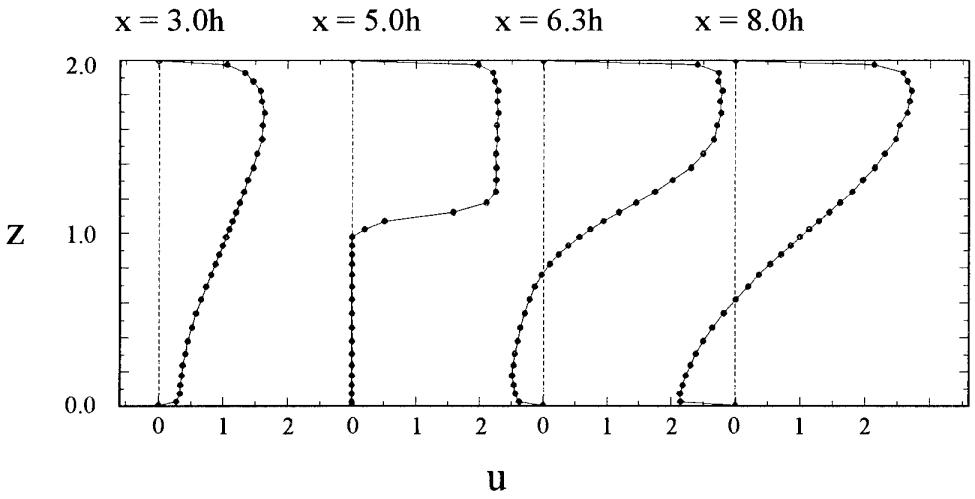

Fig. 4 Time-averaged velocity profiles at x =3h, 5h, 6.3h and 8h

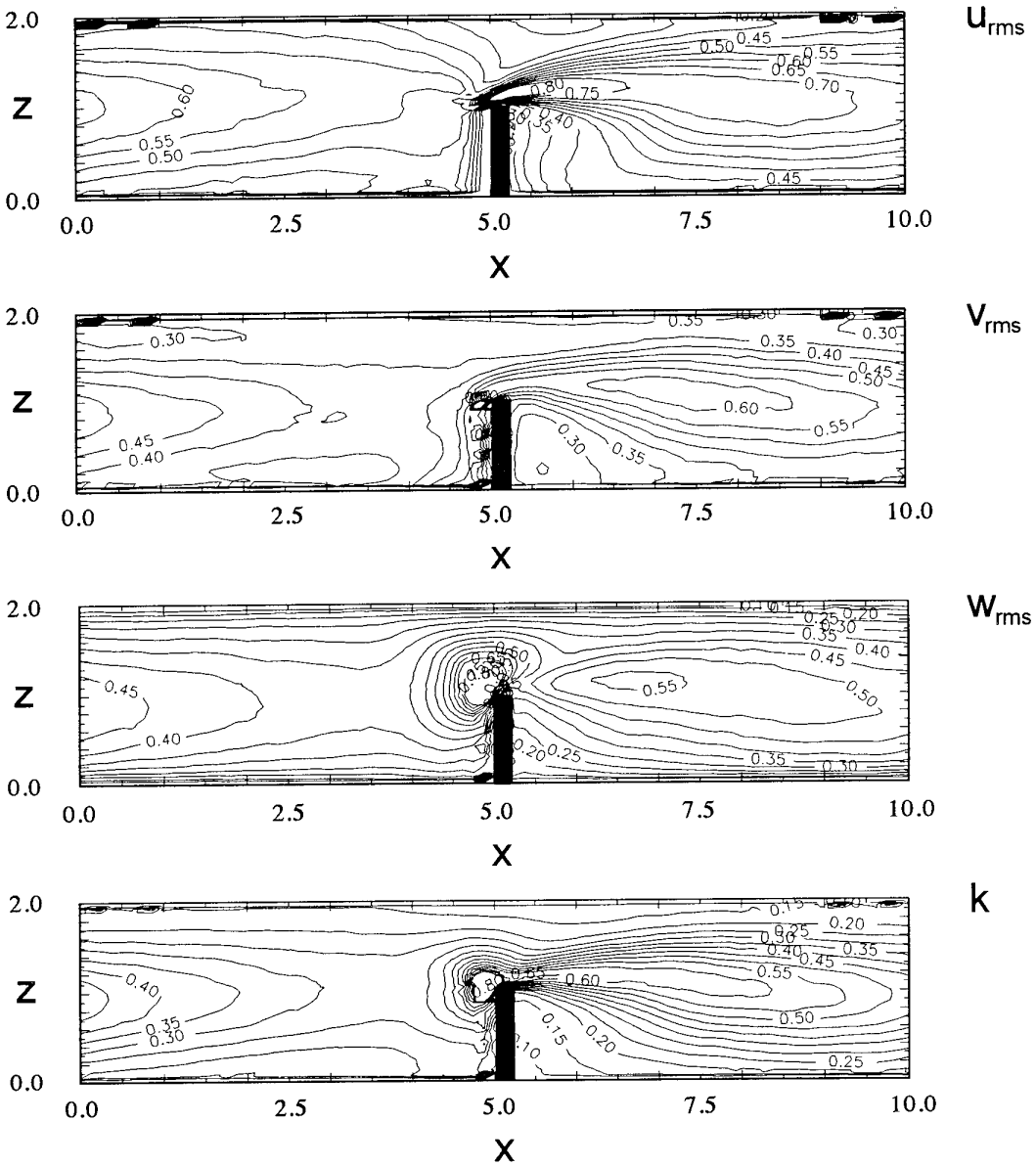

Fig. 5 Contour lines of u_{rms}, v_{rms}, w_{rms} and turbulent kinetic energy k

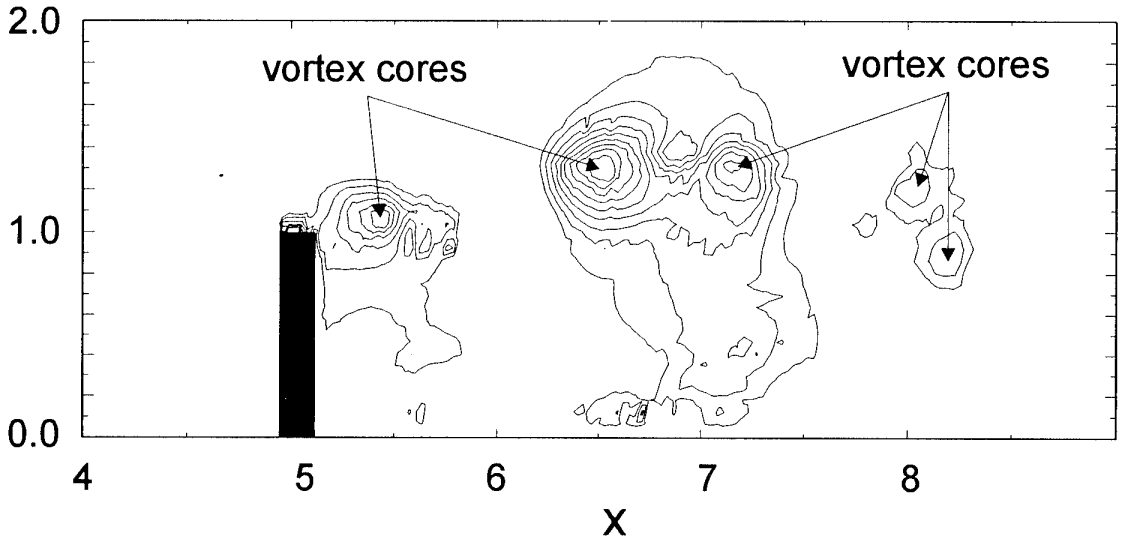

Fig. 6 Vortex shedding in the vicinity of the rib visualized by pressure minima in vortex cores

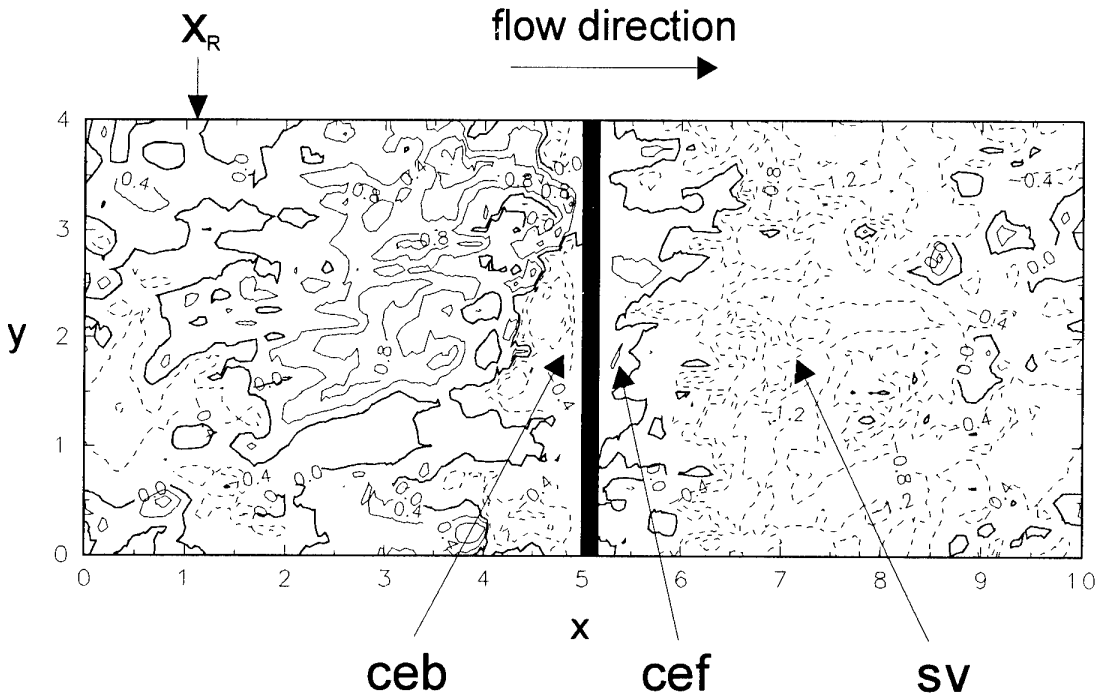

Fig. 7 Top view of contour lines of constant u-velocity components near the wall (z = 0.022)
Dotted lines refer to back flow

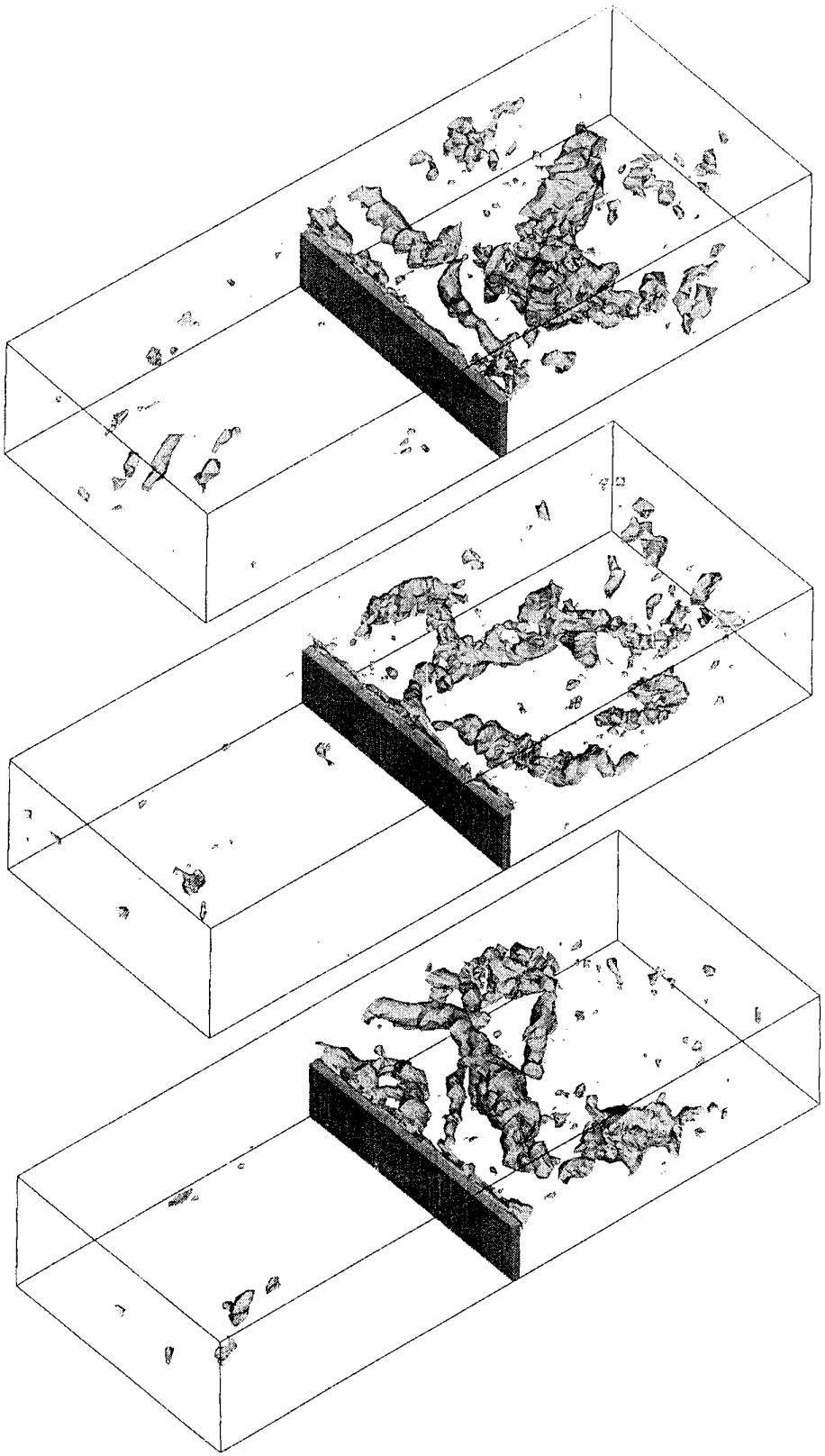

Fig. 8 Perspective views of isobar surfaces at three different times

ANALYSIS OF SUBGRID MODELS USING DIRECT AND LARGE-EDDY SIMULATIONS OF ISOTROPIC TURBULENCE

S. Menon and P.K. Yeung
School of Aerospace Engineering
Georgia Institute of Technology
Atlanta, Georgia, 30332-0150
USA

ABSTRACT

Direct and large eddy simulations of forced and decaying isotropic turbulence have been performed using a pseudospectral and a finite-difference code. Subgrid models that include a one-equation subgrid kinetic energy model with and without a stochastic backscatter forcing term and a new scale similarity model have been analyzed in both Fourier space and physical space. The Fourier space analysis showed that the energy transfer across the cutoff wavenumber k_c is dominated by local interaction. The correlation between the exact and the modeled (by a spectral eddy viscosity) nonlinear terms and the subgrid energy transfer in physical space was found to be quite low. In physical space, a similar correlation analysis was carried out using top hat filtering. Results show that the subgrid stress and the energy flux predicted by the subgrid models correlates very well with the exact data. The scale similarity model showed very high correlation for reasonable grid resolution. However, with decrease in grid resolution, the scale similarity model became more uncorrelated when compared to the kinetic energy subgrid model. The subgrid models were then used for large-eddy simulations for a range of Reynolds number. It was determined that the dissipation was modeled poorly and that the correlation with the exact results was quite low for all the models. In general, for coarse grid resolution, the scale similarity model consistently showed very low correlation while the kinetic energy model showed a relatively higher correlation. These results suggest that to use the scale similarity model relatively fine grid resolution may be required, whereas, the kinetic energy model could be used even in coarse grids.

1. INTRODUCTION

For large-eddy simulation (LES) methods to become a viable tool for simulating high Reynolds number flows in complex geometries, models that faithfully represent the effects of the unresolved scales of motion on the resolved motion have to be developed and validated. The unresolved scales act on the resolved field as new unknown stresses that must be modeled (by the so-called subgrid models). The most popular subgrid model used for LES is the eddy viscosity model, first proposed by Smagorinsky in 1963. Inherent limitations of this model were identified quite early and methods were developed to address these limitations. Key modifications involved the adjustment of the "constant" (the Smagorinsky constant) for different flows [e.g., 1] and the use of damping functions to model near-wall effects [2].

Although LES using these models has provided fairly acceptable results, recently, more serious limitations have been identified. For example, backscatter of energy from the unresolved to the resolved scales has been observed to occur in direct numerical simulations (DNS) data [3] demonstrating that the subgrid processes cannot be modeled by a purely dissipative mechanism. Recent attempts to improve the eddy viscosity model include the application of the dynamic procedure to evaluate the model constant [4], and, an explicit modeling of the subgrid backscatter process [5,6]. The dynamic model has proven quite versatile and results show that it can model correctly the behavior of the subgrid stresses both near and away from the wall, and has a capability to model backscatter [4,7]. However, it is not yet clear if algebraic subgrid models are adequate for LES of high Reynolds (Re) number flows, especially when coarse grid resolutions are employed. This is due to the possibility that the unresolved scales could contain significant amount of turbulent kinetic energy resulting in significant backscatter. Furthermore, anisotropy effects in the unresolved scales may have to be taken into account.

To evaluate subgrid models, *a priori* evaluation of the model(s) using DNS data (obtained in simple, low-Re flows) is typically carried out. Then, the subgrid model is used in an LES using coarse grid resolution and comparisons with DNS predictions are used to determine the validity of the subgrid model. However, models validated using *a priori* analysis of low-Re DNS data appear to have problems when used for LES of high Re flows. High Reynolds number DNS cannot be carried out and, therefore, *a priori* analysis is not possible. The *a priori* methods also have some limitations, since, such analysis is typically carried out in Fourier space which is only possible for flows in configurations that employ periodic boundary conditions. Thus, for high-Re flows in complex domains, new methods to investigate the applicability and validity of the chosen subgrid model have to developed in physical space. Furthermore, such analysis has to be carried out using only LES. Of course, comparison with experimental data will remain the final test of the model, but if the agreement is poor, methods are needed that will allow the modeler an avenue for improving the subgrid model.

In this paper, the ability of the chosen subgrid model to predict accurately the energy transfer between the resolved and unresolved scales in LES, will be investigated. We will address this issue by carrying out DNS and LES of both decaying and forced, incompressible, isotropic turbulence and analyze the data in both physical and spectral space. In the Fourier space, an earlier developed technique [8] was used, while in the physical space, methods such as correlation analysis [9] was used. The results of these studies are described below.

2. NUMERICAL METHODS

Two simulation methods have been used in this research. The first method is a well known pseudo-spectral method [10] and has been primarily used to obtain high resolution DNS data.

Paper presented at the 74th Fluid Dynamics Symposium on "Application of Direct and Large Eddy Simulation to Transition and Turbulence" held at Chania, Crete, Greece, in April 1994.

No LES has been performed with this code. The second code is a new finite-difference Navier-Stokes solver that is fifth-order accurate in space and second-order accurate in time. This code has been developed in a very general manner and is used for both LES and DNS. Both simple, (e.g., isotropic turbulence) and relatively complex (e.g., rearward facing steps) flows have been simulated using this code. The numerical algorithm is based on the artificial compressibility method. To obtain time-accuracy at each time step, iterations in pseudotime are carried out using a multigrid technique until the incompressibility condition has been met. This code has been validated by comparing its predictions to those of the spectral DNS code.

2.1. DNS using the Pseudo-Spectral Method

Direct simulations of both (a) naturally decaying isotropic turbulence and, (b) statistically stationary isotropic turbulence in which the turbulent kinetic energy is maintained by stochastic forcing of the large scales [11], have been performed with both 64^3 and 128^3 grid resolution.

Decaying isotropic turbulence has been simulated by beginning with an isotropic Gaussian random field with a specified initial energy spectrum, and then allowing the hydrodynamic field to evolve until a "realistic" self-similar state has been reached [12]. This developed isotropic state is characterized by Kolmogorov similarity in the high wavenumber energy spectrum, power law decay of energy, and non-Gaussian velocity gradients. DNS data used for analysis in this paper is approximately at a Taylor-scale Reynolds number Re_λ of 20. A higher Reynolds number can be reached by forcing the large scales [11]. The limitation is that the energy transfer characteristics at the large scales are distorted as a result of artificial forcing. However, the structure of the small scales is not directly affected. The parameters of the forcing scheme are chosen to reproduce one realization of the stationary isotropic turbulence at a $\mathrm{Re}_\lambda \approx 90$.

The energy spectra for both decaying and forced isotropic turbulence, is shown in Fig. 1a, with Kolmogorov scaling of the variables. It is clearly seen that the energy in the large scales is greatly increased by the forcing. On the other hand, the spectral shapes at the small scales are very similar. The small spectral turn-ups at the high wavenumber end are caused by imperfect resolution with a finite number of grid points. A nondimensional measure of the numerical resolution is given by $k_{\max}\eta$, where $k_{\max}$ is the highest wavenumber (60) reached in the simulations, and η is the Kolmogorov length scale. It may be seen from the figure that in both data sets, $k_{\max}\eta$ is about 1.6, which is sufficiently high for adequate resolution of the small-scale motions in the simulations.

2.2. DNS using Finite-Difference Method

Decaying and forced isotropic turbulence was also simulated using the finite-difference code. The forced simulation employed a forcing method [13] that differed from the stochastic forcing employed for DNS in spectral space. Therefore, direct comparison of the predictions could not be carried out. However, using identical initialization, decaying isotropic turbulence was simulated using both the codes in a 64^3 grid resolution. Figure 1b shows the Kolmogorov-scaled energy and the dissipation spectra from the DNS results obtained using both the psuedospectral and finite-difference codes. The results are shown after nearly the same time of evolution ($t = 12$, $\mathrm{Re}_\lambda \approx 10$). Good agreement is obtained in nearly the entire wavenumber space except near the very low wave numbers. More detailed evaluations of the various statistical quantities (such as the dissipation rate skewness, etc.) showed that the physical space code is capable of reproducing statistics very similar to those obtained by the spectral code.

3. SUBGRID ENERGY TRANSFER AND MODELS

Two different methodologies have been employed to analyze the results of the simulations. The first, relies entirely on the Fourier space information and closely follows the method developed earlier by Domaradzki et al.[8]. The second, relies entirely on the physical space information and, employs correlation analysis to characterize the behavior of the models.

3.1. Subgrid Transfer and Modeling in Fourier Space

The Fourier space representation of the Navier-Stokes equations may be written as:

$$\left[\frac{\partial}{\partial t} + \nu k^2\right] u_n(\mathbf{k}) = N_n(\mathbf{k}) \qquad (1)$$

where $u_n(\mathbf{k})$ is the velocity field in the Fourier space at a wavenumber mode $\mathbf{k}$ (of magnitude k), ν is the kinematic viscosity, and $N_n(\mathbf{k})$ is the nonlinear term which includes the effects of advection, pressure and incompressibility and is given by

$$N_n(\mathbf{k}) = -\frac{i}{2} P_{nlm}(\mathbf{k}) \int u_l(\mathbf{p})\, u_m(\mathbf{k}-\mathbf{p})\, d\mathbf{p} \qquad (2)$$

where $P_{nlm}(k) \equiv k_l(\delta_{nm} - k_n k_m/k^2) + k_m(\delta_{nl} - k_n k_l/k^2)$, and δ_{ij} is the Kronecker delta tensor. A triad in wavenumber space is a closed triangle formed by the modes $\mathbf{k}$, $\mathbf{p}$, and $\mathbf{k}-\mathbf{p}$. The integral above is taken over all possible triads that may be formed with the mode $\mathbf{k}$ as a member.

Domaradzki et al. [8] introduced a technique in Fourier space which involves a decomposition of the various terms into "resolved" and "subgrid" components. This is accomplished by introducing a wavenumber cutoff at k_c and then, for example, the nonlinear term may be decomposed into:

$$N_n(\mathbf{k}) = N_n(\mathbf{k}\,|\,k_c) + N_n^s(\mathbf{k}\,|\,k_c) \quad (k \le k_c) \qquad (3)$$

The resolved nonlinear term, $N_n(\mathbf{k}\,|\,k_c)$, represents contributions from those triad interactions that couple a resolved mode $k \le k_c$ to two other resolved modes (i.e., with both $\mathbf{p}$ and $\mathbf{k}-\mathbf{p}$ in the resolved range below k_c). On the other hand, the rest of the triad interactions, which couple the resolved modes to subgrid modes (with at least one of $\mathbf{p}$ and $\mathbf{k}-\mathbf{p}$ in the subgrid range $k > k_c$), are represented by the subgrid nonlinear term, $N_n^s(\mathbf{k}\,|\,k_c)$.

Energy transfer between different scales is represented by triadic interactions. The total (rate of) energy transfer to a Fourier mode $\mathbf{k}$, due to its interactions with the subgrid scales, is given by $T^s(\mathbf{k}\,|\,k_c) = \mathrm{Re}\left[u_n^*(\mathbf{k}) N_n(\mathbf{k}\,|\,k_c)\right]$, where the asterisk denotes complex conjugate and Re indicates the real part. The subgrid transfer spectrum function is then given by:

$$T^s(k\,|\,k_c) = \sum_{k-\frac{\Delta k}{2} \le |\mathbf{k}'| < k+\frac{\Delta k}{2}} T^s(\mathbf{k}'\,|\,k_c) \qquad (4)$$

Here, $T^s(k\,|\,k_c)$ is a function of wavenumber magnitude k only, and the shell thickness Δk, is taken as unity for conveni-

ence. Summation over spectral shells, denoted by $\sum_{\Delta k}$ for short, is also used in the formation of the energy spectrum function $E(k)$ from the energy of discrete Fourier modes: $E(k) = \frac{1}{2}\sum_{\Delta k} u_n(\mathbf{k}')\, u_n^*(\mathbf{k}')$. The energy spectrum $E^L(k)$ of the resolved scales (i.e., for $k \le k_c$, signified by superscript L) at wavenumber k evolves by:

$$\frac{\partial}{\partial t}E^L(k) = -2\nu k^2 E^L(k) + T(k\,|\,k_c) + T^s(k\,|\,k_c) \qquad (5)$$

where $T(k\,|\,k_c)$ represents energy transfer from interactions with resolved scales only, and $T^s(k\,|\,k_c)$ represents interactions with subgrid modes which must be modeled in an LES.

A subgrid eddy viscosity is often used to parametrize the subgrid motions, with the spectral subgrid scale (SGS) eddy viscosity defined as [8]:

$$\nu_e(k\,|\,k_c) = -\frac{T^s(k\,|\,k_c)}{2k^2 E^L(k)}, \quad k \le k_c \qquad (6)$$

The corresponding modeled subgrid nonlinear term is given by: $N_n^{sm}(\mathbf{k}\,|\,k_c) = -\nu_e(k\,|\,k_c)k^2 u_n(\mathbf{k})$, and the modeled subgrid transfer is $T^{sm}(\mathbf{k}\,|\,k_c) = \mathrm{Re}\left[u_n^*(\mathbf{k})N_n^{sm}(\mathbf{k}\,|\,k_c)\right]$. A straightforward substitution of the definitions presented above leads to the relation:

$$\frac{T^{sm}(\mathbf{k}\,|\,k_c)}{T^s(k\,|\,k_c)} = \frac{1}{2}\frac{u_n(\mathbf{k})\,u_n^*(\mathbf{k})}{E^L(k)}, \quad k \le k_c \qquad (7)$$

A further summation over the spectral shell k would yield unity on the right hand side, which indicates that the spectral eddy viscosity model accounts for the total energy transfer to a spectral shell correctly. However, it may be seen that this model assumes that energy and energy transfer have the same form of distribution within a given spectral shell. In other words, energy and energy transfer are assumed to be entirely in phase with each other in wavenumber space. This assumption, of course, deviates from the exact spectral equations.

The exact and modeled subgrid nonlinear terms and energy transfers obtained from DNS and LES have been analyzed for a range of k_c. These results will be discussed in Section 4.

3.2. Subgrid Transfer and Modeling in Physical Space

In physical space, the incompressible Navier-Stokes equations are filtered using a spatial filter of characteristic width Δ (typically, the grid resolution) resulting in the filtered LES equations:

$$\frac{\partial \bar{u}_i}{\partial x_i} = 0 \qquad (8a)$$

$$\frac{\partial \bar{u}_i}{\partial t} + \bar{u}_j\frac{\partial \bar{u}_i}{\partial x_j} = -\frac{\partial}{\partial x_j}\left[\frac{\bar{p}}{\rho}\delta_{ij} + \tau_{ij}\right] + \nu\nabla^2\bar{u}_i \qquad (8b)$$

where $\bar{u}_i(\mathbf{x}, t)$ is the resolved velocity field and the subgrid scale (SGS) stress tensor τ_{ij} is defined as: $\tau_{ij} = \overline{u_i u_j} - \bar{u}_i\bar{u}_j$. It has been shown that proper choice of the filtering process is essential to maintain model consistency [14]. Various types of filtering processes have been studied in the past, such as the top hat, the Gaussian, and the Fourier cut off filters [9,14]. In the present study, we employ the top hat filter which is considered appropriate for finite-difference methods.

The goal of SGS modeling is to represent the SGS stress τ_{ij} in terms of the resolved field $\bar{u}_i(\mathbf{x}, t)$ in such a manner that the modeled SGS stresses represent as much as possible the exact stresses. In addition, the energy flux to the unresolved scales given by $E(\Delta) = -\tau_{ij}\bar{S}_{ij}$ must also be modeled reasonably well by the subgrid model. These issues will be addressed in this study.

Various models have been proposed, the most popular one being the Smagorinsky's model:

$$\tau_{ij}^S = -2(C_S\Delta)^2\,|\bar{S}|\,\bar{S}_{ij} \qquad (9)$$

where, the superscript S indicates the model, C_S is the Smagorinsky's constant and

$$\bar{S}_{ij} = \frac{1}{2}\left(\frac{\partial \bar{u}_i}{\partial x_j} + \frac{\partial \bar{u}_j}{\partial x_i}\right) \qquad (10)$$

is the resolved rate-of-strain tensor, where $|\bar{S}| = |2\bar{S}_{ij}\bar{S}_{ij}|^{1/2}$. The dynamic modeling approach [4,7] can be used to compute the constant C_S as a part of the solution, as described elsewhere. At present, we have not implemented the dynamic model in the LES but will consider it in the near future.

Here, in addition to the Smagorinsky's model, two new SGS models are considered. The first is a one-equation model for the subgrid kinetic energy $k_{sgs} = \frac{1}{2}\left(\overline{u_i^2} - \bar{u}_i^2\right)$. The motivation behind the choice of this model is two-fold. First, as noted earlier, it is conceivable that in high Reynolds number flows (or when very coarse grids are employed), the unresolved scales may contain energy-containing scales. In this case, the contribution of the subgrid energy to the resolved SGS stresses may have to be explicitly computed. Second, we are also interested in LES of reacting flows. For LES of premixed combustion using a thin flame model, the turbulent flame speed must be determined as a function of the laminar flame speed and the resolved subgrid kinetic energy [15]. In such a case, explicit evaluation of the SGS kinetic energy is required. A compressible version of the k_{sgs} model is currently being used for LES of premixed combustion in a ramjet [15]. One-equation models have been also used earlier for channel flows [17,18], and it was shown that it gave more accurate results when very coarse grids were used [18].

The exact equation for k_{sgs} is first derived by filtering the exact equations for the kinetic energy $u_i^2/2$ and subtracting from it the exact equation for the resolved kinetic energy $\bar{u}_i^2/2$. A possible closure for the terms in the k_{sgs} equation is considered in the following form:

$$\frac{\partial k_{sgs}}{\partial t} + \bar{u}_i\frac{\partial k_{sgs}}{\partial x_i} = -\tau_{ij}^k\frac{\partial \bar{u}_i}{\partial x_j} - C_\varepsilon\frac{k_{sgs}^{3/2}}{\Delta} + \frac{\partial}{\partial x_i}\left(\frac{\nu_k}{\sigma_k}\frac{\partial k_{sgs}}{\partial x_i}\right)$$

where the three terms on the right-hand-side of Equation (11) represent, respectively, the production, dissipation and transport processes. Here, the subgrid stresses τ_{ij}^k (considered equivalent to τ_{ij}) are modeled in terms of the SGS eddy viscosity ν_k as:

$$\tau_{ij}^k = -2\nu_k\bar{S}_{ij} + \frac{2}{3}k_{sgs}\delta_{ij} \qquad (12)$$

where the SGS eddy viscosity is $\nu_k = C_k\sqrt{k_{sgs}}\,\Delta$. The model constants are chosen based on earlier study [16] to be $C_k = 0.09$, $C_\varepsilon = 0.916$ and $\sigma_k = 1.0$. It has not yet been esta-

blished if these constants or the form of the terms in Eq. 11 are appropriate for high-Re LES. For example, it has been noted using a *a priori* study in channel flow, that the dissipation model in equation (11) is extremely poor [19].

To investigate the behavior of the k_{sgs} model, the production, the dissipation and the transport terms in the exact equation were computed by filtering the DNS data and then correlated with the model terms in Equation (11). The results (not shown) suggests that the transport and production terms in the model equation are correlated quite well with the exact terms (with a correlation greater that 0.6). However, the dissipation term was poorly correlated. This result agrees with the earlier observation that the dissipation model needs to be further improvement. This will be addressed in a future study by using the dynamic procedure to evaluate the constants in the k_{sgs} model.

If subgrid scales contain energy-containing eddies, then there is a good chance for backscatter of energy from the subgrid scales to the resolved scales. Furthermore, earlier studies [5,6] have shown that forward scatter (by the eddy viscosity term) and backscatter are two distinct processes. Therefore, these two effects must be modeled separately. Using the results of Chasnov [5], a phenomenological model for stochastic backscatter was derived earlier [15] by assuming that the backscatter effect can be modeled by a random force which satisfies certain constraints. The resulting form of the backscatter contribution to the subgrid stress model can be written as:

$$\tau_{ij}^{bs} = C_{bs} \prod \frac{\Delta^2}{\sqrt{\Delta t}} |\bar{S}| \bar{S}_{ij}^{1/2} \qquad (13)$$

Here, C_{bs} is a constant of order unity, Δt is the time step of the LES, and $\prod$ is a random number with zero mean and unit variance. Then, the modeled SGS stresses τ_{ij}^{k} become

$$\tau_{ij}^{k} = -2\nu_k \bar{S}_{ij} + \frac{2}{3} k_{sgs} \delta_{ij} + \tau_{ij}^{bs} \qquad (14)$$

The second model used is a modified scale similarity model proposed by Liu et al. [9]. This model was derived using *a priori* analysis of high Re_λ (= 310) experimental data obtained from a turbulent jet and is of the form:

$$\tau_{ij}^{m} = c_L f(I_{LS}) L_{ij} \qquad (15)$$

where the stress $L_{ij} = \tilde{\bar{u}}_i \tilde{\bar{u}}_j - \tilde{\bar{u}}_i \tilde{\bar{u}}_j$ can be computed entirely from the resolved velocity field. Here, the tilde indicates filtering at a scale 2Δ and is reminiscent of the Germano identity [4]. The constant c_L was determined in [9] to be around 0.45 at high Re_λ. This model is similar to the scale similarity model proposed earlier [20]; and it can be shown that the energy flux to the subgrid scale $E_L = -L_{ij} \bar{S}_{ij}$ will exhibit both positive (forward scatter) and negative (backscatter) in the flow. However, it was noted earlier [9,20], and in the present study, that this backscatter (which may not be real) can result in numerical instability. Hence, to control the backscatter, a scalar function $f(I_{LS})$ is used in terms of I_{LS}, a dimensionless invariant:

$$I_{LS} = -\frac{L_{mn} \bar{S}_{mn}}{\sqrt{L_{ij} L_{ij}} \sqrt{\bar{S}_{ij} \bar{S}_{ij}}} \qquad (16)$$

Here, I_{LS} represents the alignment between L_{ij} and $\bar{S}_{ij}$ [9]. Various forms of the scalar function $f(I_{LS})$ were proposed in [9] but their validity in LES have not been investigated. Furthermore, the experimental data was a two-dimensional slice of the flow field and Liu et al. [9] had to make some assumptions to determine the contribution from the third dimension. Therefore, to evaluate this subgrid model, both *a priori* analysis using DNS results and LES, were carried out. Various forms of backscatter control were studied. However, for LES, $f(I_{LS})$ was chosen following the suggestion by Liu et al. [9] such that $f(I_{LS}) = \left[1 - \exp(-10 I_{LS}^2)\right]$, if $I_{LS} \geq 0$, and $f(I_{LS}) = 0$, if $I_{LS} < 0$.

To carry out analysis in physical space, methods that rely entirely on physical space information have been employed. To obtain a measure of the accuracy of the model, correlation coefficient (defined in the usual manner) has been used to quantify the results. These results are discussed below.

4. RESULTS AND DISCUSSIONS

In this section, we describe the results of our analysis of the subgrid models described above.

4.1. Spectral Space Analysis

Energy transfer information extracted from the DNS data was analyzed to determine the effect of a variable cutoff wavenumber k_c, on energy transfer between the resolved (in an LES sense, $k \leq k_c$) and subgrid ($k \geq k_c$) scale ranges. The SGS eddy viscosity, the subgrid and the resolved energy transfer defined earlier in Section 3.1, are shown in Fig. 2 (a,b,c) for decaying isotropic turbulence (at $Re_\lambda \simeq 20$). It can be seen that the SGS eddy viscosity takes negative, albeit, small values at low k/k_c for relatively high values of the cutoff wavenumber. This indicates that the SGS energy transfer $T^s(k|k_c)$ takes on positive values - representing a non-negligible backscatter of energy from the subgrid scales to the resolved scales. The eddy viscosity displays a cusp-like behavior at resolved wavenumbers approaching k_c, consistent with the results of Domaradzki et al. [8] at higher Reynolds number. The formation of these cusps may be understood in terms of the local nature of energy transfer in turbulence. An active forward-cascading transfer of energy occurring between scales close to k_c causes a large and negative value of $T^s(k|k_c)$, and, hence, a large and positive SGS eddy viscosity. The strength of this local transfer, which is evident in Fig. 2(b), depends, of course, on the energy in scales of size in the order of $1/k_c$, and, hence, weakens with increasing k_c.

In Fig. 2(a) it may be seen that the SGS eddy viscosity at the lowest cutoff wavenumber k_c=10.5 (line A) has a much greater value than the data at higher spectral cutoffs. This is a consequence of the subgrid transfer taking on a more local character as the spectral cutoff is moved to lower wavenumbers. That is, energy transfer between the largest scales and the subgrid scales becomes much more significant if the subgrid range is expanded to include intermediate scales that are closer to the largest scales. The upturn in line A at the low wavenumber end is partly a result of the fall-off in the energy spectrum (see Fig. 1a) as the low wavenumber limit is approached.

The behavior of the resolved energy transfer ($T(k|k_c)$, in Fig. 2(c)), which represents interactions wholly among the resolved scales, is also of interest. The signs of this transfer indicate it is consistently a forward cascade, drawing energy from lower to higher wavenumber modes. At large k_c the resolved interactions close to $k=k_c$ takes on a nonlocal charac-

ter, and is much weaker than the more local transfer that take place at lower values of k_c.

It is of interest to compare the spectral properties of stationary forced turbulence (at $Re_\lambda \simeq 90$) with turbulence in viscous decay. Because of space limitations, we show only the eddy viscosity for stationary forced turbulence, in Fig. 2(d), although, the resolved and subgrid energy transfers have also been calculated. The cusp-like behavior of the SGS eddy viscosity near k_c is preserved, although, more pronounced than for decaying turbulence. The influence of k_c on the magnitudes of the SGS eddy viscosity and subgrid transfer near k_c is qualitatively similar to decaying isotropic turbulence. A qualitative difference is observed for k_c=15.5, with backscatter and negative eddy viscosity found in the forced turbulence data. For the lowest spectral cutoff k_c=10.5 (line A), the subgrid viscosity is also much larger than that for higher cutoffs, as in the case of decaying turbulence. On the other hand, no upturn at the low wavenumber end is observed; this can be understood by noting that in the expression for eddy viscosity, the energy spectrum appears in the denominator and in the low wavenumber range, the spectrum is nearly flat (see Fig. 1a).

Since the lowest wavenumber modes are forced in stationary turbulence, the resolved energy transfer is greatly distorted. In this forced turbulent flow, the peak in the energy spectrum occurs at the lowest nonzero wavenumber shell in the simulations. While the nature of a forward cascade remains unchanged, these forced modes, being highly energetic, lose a large amount of energy to other resolved modes (and, for low spectral cutoffs, to the subgrid scales as well).

To assess the performance of the SGS eddy viscosity model (Eq. 6), an important criterion is how well the energy transfer is predicted in physical space. The Fourier space considerations illustrated by Eq. 8 indicates, in homogeneous turbulence, the space average of the energy transfer is reproduced exactly by this model. However, incorrect phase information in Fourier space translates to deviations from exact values at each grid point in physical space. A quantitative measure of model accuracy is the correlation coefficient between the exact and modeled SGS transfer in physical space, denoted by $T^s(\mathbf{x}\,|\,k_c)$ and $T^m(\mathbf{x}\,|\,k_c)$, respectively. This correlation coefficient, $\rho(T^s,T^m)$, which is computed over all grid points in physical space, is shown in Fig. 3 as a function of the cutoff wavenumber k_c. Also shown, is the corresponding correlation coefficient, averaged over the coordinate components, between the exact and modeled SGS nonlinear terms, denoted by $\rho(N^s,N^m)$.

Several observations may be made in Fig. 4. First, for all of the quantities considered, model performance improves steadily with increasing cutoff wavenumber. This is clearly consistent with the general expectation that SGS models should improve if a wider range of scales are resolved in an LES by increasing the number of grid points, leaving only the smallest scales to be modeled. Second, except at low cutoff wavenumbers, the nonlinear term is predicted more accurately than the energy transfer. Since in physical space this (subgrid) transfer is given by the dot product between the resolved velocity vector and the subgrid nonlinear vector, we may conclude that the alignment between these vectors is not well predicted. Third, the model produces better agreement with DNS data in the decaying case compared to the forced case. This is not surprising, since the artificial forcing has a distorting effect on energy transfer, especially at the large scales, which generally dominate the correlation coefficients.

As discussed above, one of the weaknesses of the SGS spectral eddy viscosity model is that it is based on quantities summed over spectral shells. As a result, ν_e is represented as an isotropic function of the wavenumber magnitude k in Fourier space. A modification can be made to accommodate the phase variations inside spectral shells by using the modal transfer and energy instead. We define the modified SGS spectral eddy viscosity by

$$\nu'_e(\mathbf{k}\,|\,k_c) = -\frac{T^s(\mathbf{k}\,|\,k_c)}{k^2\,u_n(\mathbf{k})u_n^*(\mathbf{k})} \qquad k \le k_c \tag{17}$$

The modeled SGS nonlinear term becomes $\mathrm{Re}[u_n^*(\mathbf{k})N_n^s(\mathbf{k}\,|\,k_c)]/u_n^*(\mathbf{k})$, which is, clearly, still not exact. This modified model requires too much information - the energy and SGS transfer at individual Fourier modes - to be useful in practice. However, because it accounts for phase variations within spectrals shells, this modified model does give better agreement with DNS data. The correlation coefficients in physical space discussed above, but computed from the modified model, are shown as lines E and F in Fig. 4 for the decaying turbulence case. As may be seen, these correlation coefficients are consistently higher than those obtained from the conventional model.

The spectral space analysis method was then used to analyze the behavior of the subgrid models described in Section 3.2. Figure 4a shows the Kolmogorov scaled energy spectra for the 64^3 DNS (at a $Re \simeq 10$), and for the 32^3 and 16^3 LES using the k_{sgs} model with stochastic backscatter (Eq. 14), and the scale-similarity model (Eq. 15). These results are shown at a time, $t = 12$ which corresponds to around 21.7 large-eddy turnover time. By this time, the flow field has evolved into realistic isotropic turbulence. The flow field for the LES was initialized by filtering the 64^3 initial (i.e., at $t = 0$) flow field in *physical space*. Thus, at $t = 0$, the initial fields for the DNS and the LES were highly correlated in the physical space. (Results of the physical space analysis will be discussed in the next section). However, in Fourier space, due to the form of the transfer function for the top hat filter, the initial energy spectra will be quite different. This would show up in the eventual evolution of the flow field when analyzed in the Fourier space. However, if the simulations are self consistent, the Kolmogorov scaled spectra should exhibit similarity, as seen in Fig. 4a.

Figure 4b and 4c show, respectively, the energy spectra (normalized by the kinetic energy) and disspation spectra (normalized by the dissipation rate) as a function of wavenumber. The disagreement between the DNS and LES results is more apparent in these figures. The normalized energy spectra shows that all the LES data predict higher peak energy at a lower wavenumber than predicted by DNS. Both the k_{sgs} and similarity models predict nearly the same peak value (about 25 percent higher than exact) and location with 32^3 resolution. However, as the grid is coarsened, the k_{sgs} model shows a much larger peak energy than the similarity model. Further, near $k = k_{max}$, the energy in the high wavenumbers is much lower for the LES. The dissipation spectra peaks at larger wavenumbers (by a factor of 2) and all the data shows similar trends. However, since energy is lower near $k = k_{max}$, the LES results predict lower dissipation when compared to the DNS results. These results suggest that the dissipation modeled by

the subgrid models is insufficient and needs to be improved.

The energy transfer in the spectral space was also analyzed using these LES data. Using the DNS and LES fields shown in Fig. 4, the spectral eddy viscosity and the subgrid transfer at a cutoff wavenumber $k_c = 10$ was computed and are shown in Figs. 5a and 5b, respectively. Note that, for the DNS, $k_{max} = 30$, while for the LES, $k_{max} = 15$. Therefore, a k_c of 10 is in the range of resolved scales for all the simulations. Figure 5a shows that the spectral eddy viscosity behavior in all cases is nearly identical suggesting that the LES models are behaving quite well. However, this is somewhat misleading. Figure 5b shows that at $k/k_c \rightarrow 1$ both the scale similarity model and the k_{sgs} model predict lower negative values for the subgrid transfer $T^s(k|k_c)$. A low value for the transfer would result in a lower peak in the eddy viscosity. However, less energy is being transferred to the subgrid scales, as seen in Fig. 4. Therefore, the combination of low (negative) value of $T^s(k|k_c)$ and lower $E^L(k)$ near k_c, results in an eddy viscosity (from Eq. 6) that appears to agree with the *a priori* results.

In summary, the *a priori* analysis of the DNS data showed that the eddy viscosity model in spectral space has a distinct cusp at the wavenumber cutoff k_c, suggesting that the energy transfer across k_c is dominated by interaction of scales (both resolved and unresolved) in the neighborhood of k_c. The spectral subgrid transfer was found to be quite dependent on k_c and inverse transfer (backscatter) was found to occur for relatively high values of k_c. Correlation analysis of the nonlinear terms and SGS energy transfer in physical space showed very low values (around 0.3-0.4) which increased with k_c. The correlation of the nonlinear term was higher than for the energy transfer indicating that the resolved velocity field and the nonlinear term were not correlated very well.

The analysis of the LES data using a similar method showed that there were significant differences in the energy and dissipation spectra for all the cases studied. This is understandable since the initial spectra for the LES and the DNS was different due to the initialization that maintained high correlation in the physical space. All the SGS models appear to model dissipation very poorly and, also, predict much higher energy in lower wavenumbers than predicted by the DNS data. Using a spectral cutoff at $k_c = 10$, it was shown that the spectral eddy viscosity computed using the LES data agrees reasonably well with the eddy viscosity computed using DNS data. However, it was shown that this agreement was due to a combination of lower energy at k_c, and a lower (negative) value for the subgrid transfer.

4.2. Physical Space Analysis

The analysis in the physical space was carried out using methods that attempted to quantify the behavior of the models in terms of the resolution of the large-scale structures and, the correlation between the exact and the modeled stresses and energy flux to the subgrid scales. The *a priori* analysis was carried out on all the DNS data sets. Here, we will discuss only representative results.

Figure 6a shows contours of the energy flux ($E(\Delta) = -\tau_{ij}\bar{S}_{ij}$) to the subgrid scales on a 32^3 grid obtained by filtering of the 128^3 DNS data for forced stationary turbulence. This result is compared to the prediction by the k_{sgs} model without backscatter (Fig. 6b), and the scale similarity model without backscatter control (Fig. 6c), and with backscatter control (Fig. 6d). The contour interval is the same for all figures, and an arbitrary (but same) slice of the 3D field is shown. Comparison with the exact results (Fig. 6a) shows that there is significant similarity in regions with high positive transfer. However, only the similarity model without backscatter control (Fig. 6c) is capable of resolving regions with backscatter, although, the peak negative value is around 35% lower than in the exact case. The peak positive value is, also, not predicted very well, with the k_{sgs} model predicting a maximum level that is nearly 60% lower than the exact value while the similarity model predicting peak level around 35 % lower without backscatter control. With backscatter control, the similarity model predicts a peak level around 42% lower.

To further quantify the differences and similarity between the model predictions and the exact values, Figure 7a shows the correlation between the exact and the modeled stresses for the forced 128^3 DNS data. The correlation shown in Fig. 7a is an average of the correlation coefficient of the three stress components ($\tau_{xx}, \tau_{yy}, \tau_{zz}$). The data shows that the correlation decreases with an increase in filter width for all cases, with the similarity model showing the largest decrease. The similarity model with backscatter control has lower correlation when compared to the same model without backscatter control. This is consistent with the results shown by Liu et al. [9]. The eddy viscosity model of Smagorinsky consistently shows the lowest correlation. This result is also consistent with observations made in earlier studies. The k_{sgs} model shows quite high correlation for these stresses with only a weak dependence on the filter width. The correlation for the stresses τ_{ij}, $i \neq j$ (not shown) was lower than the correlation shown here; however, they too showed only a weak dependence on the filter width. This suggests that as the grid resolution becomes coarse, the k_{sgs} model should behave much better than the other models shown in Fig. 7a.

Figure 7b shows the stress correlation for the subgrid models for two different Reynolds number. The k_{sgs} model consistently shows higher correlation than the similarity model (with backscatter control) which shows a decrease in the correlation with decrease in Re_λ. The decrease in the stress correlation for the similarity model with increase in filter width and with decrease in Re_λ can be understood by noting that this model was developed based on analysis of very high Re_λ experimental data with at least a decade of wavenumbers in the inertial range. For the present DNS data, there is no appreciable inertial range and this situation is even worse for the low Re_λ case. Furthermore, the model assumes that there is similarity between the stresses resolved at 2Δ grid and the stresses resolved at the Δ grid. In the present case, as the filter width increases (or as the grid coarsens), this assumption breaks down.

Figure 8a shows the energy flux correlation for Re_λ of 90 for the models shown in Fig. 7 and Fig. 8b shows the energy flux correlation for the models for two different Reynolds numbers. As noted earlier, the energy flux to the unresolved scales is defined as $E(\Delta) = -\tau_{ij}\bar{S}_{ij}$ for a filter width Δ. For the subgrid models, τ_{ij} is replaced by the appropriate model (e.g., Eqns. 12 or 15). For small values of Δ/η, where η is the Kolmogorov scale, the correlation for the scale similarity model is much higher than for the other models. In all cases, the correlation decreases with decrease in Reynolds number with the largest decrease seen for the similarity model.

Since the ensemble-averaged value of the energy flux $<E(\Delta)>$

should be of the order of the dissipation rate ε, a comparison was carried out for all the models studied here. The results (not shown) indicate that all models predicted values lower than the dissipation rate computed from the exact field. However, the predicted $<E(\Delta)>$ was of the same order as the dissipation rate. This agreed with the observations by Liu et al. [9]. The energy flux at scales larger than Δ is also of interest. For example, it was shown [9] that the energy flux at a scale 2Δ can be represented by contributions from the 'local' and 'not-so-local' contributions. Using the Germano identity, the energy flux at 2Δ can be written as: $E(2\Delta) = -(L_{ij}\bar{\bar{S}}_{ij} + \tilde{\tau}_{ij}\tilde{\bar{S}}_{ij})$, where as before, the tilde filter indicates filtering at the 2Δ scale. The first term represents the 'local' transfer of energy flux from large scales to scales between Δ and 2Δ, while the second term represents the energy transfer to the scales smaller than Δ [9]. A correlation between these two terms was computed for various filter width. The results (again, not shown for brevity) indicates a very high correlation in the range of 0.8, and since $E(2\Delta)$ was always positive, this suggests that both the energy fluxes were forward scattered. A similar high correlation and behavior was noted by Liu et al. [9] in their *a priori* analysis of the experimental data.

The coefficient c_L in Eq. 15 was determined by Liu et al. [9] by assuming that the correct amount of dissipation must be predicted by the model. Thus, $c_L = <\tau_{ij}\bar{S}_{ij}> / <f(I_{LS})L_{ij}\bar{S}_{ij}>$ where $< >$ denotes ensemble averaging. A value of around 0.45±0.15 was estimated for the high Reynolds number experimental data [9]. For the correlation analysis shown in Figs. 7 and 8, $c_L = 0.45$ was employed. However, in the present study a significant variation in the correlation was observed as a function of both the filter width and Re_λ. Therefore, this coefficient was recomputed using the above noted relation. Figure 9 shows the variation of c_L as a function of filter width and Re_λ. The results suggest that this coefficient increases with increase in filter width and decrease in Re_λ. However, for small filter widths, the predicted value is in the range of the value determined by Liu et al. [9] from the high Re_λ data. The large variation in the value of c_L may be an artifact of the limited range of scales resolved in the present DNS data and the problems with the similarity model (discussed above) when the grid is coarsened. This issue needs further study.

A priori analysis of the DNS data at $Re_\lambda \approx 10$ was also carried out since this data is used for comparison with LES predictions (as discussed in Fig. 4). Comparison of the flow structures, and, the stress and energy flux correlations showed a picture very similar to that seen at the higher Re_λ (and therefore, not shown). The scale similarity model consistently showed a much better correlation for both stresses and the energy flux when compared to the k_{sgs} model while the Smagorinsky's model consistently gave very low correlation. In all cases, the correlation decreased with increase in the filter width. The scale similarity model again showed the largest decrease in correlation.

Large-eddy simulations were then carried out using 32^3 and 16^3 grid resolutions. As noted above, for LES, the flow field was initialized by filtering the initial field used for the 64^3 DNS. Hence, at $t = 0$ the physical space fields were highly correlated (although, in the Fourier space there was quite a bit of discrepancy, see Fig. 4). However, the results showed that as time evolved, the DNS and LES became highly uncorrelated.

To determine the behavior of the subgrid models, the correlation analysis was carried out as done earlier for the *a priori* study. To analyze the LES results, the DNS data obtained on the 64^3 grid resolution, and the LES data obtained on the 32^3 grid were filtered to the 16^3 grid. Then, the energy flux predicted from these two simulations at the 16^3 grid resolution was compared to the model prediction in the actual 16^3 grid LES. The results showed that all the models predicted very poor correlation (less than 0.1) when the 16^3 grid LES was compared to the filtered DNS data set at the same grid level. The comparison between the two LES showed that the energy flux correlation for the scale similarity model was very low (around 0.12) while the k_{sgs} model predicted a relatively higher value of around 0.35. This again suggests that when coarse grids are employed in an LES, the k_{sgs} model appears to behave much better. At this juncture, however, the scale similarity model cannot be disregarded since, as noted above, even the *a priori* estimates showed that, in coarse grids the scale similarity assumptions may be breaking down. It is, therefore, necessary to revisit this analysis using LES at much higher Re_λ with a reasonable resolution of the inertial range. This has not yet been attempted since it would require excessive grid resolution and computational resources.

A series of simulations were also carried out using the 32^3 and 16^3 grid resolution for an initial $Re_\lambda \approx 10^3$. The results of this study are qualitatively analyzed by carrying out relative comparison of the behavior of the subgrid models. However, note that, in high Reynolds number flows, the grid resolution that is economically practical is likely to be too coarse to resolve the inertial range.

Figure 10 shows the energy spectra for these high Reynolds number simulations at a time of $t = 12$. It was found that the scale similarity model did not contain sufficient dissipation and therefore, for these simulations, the Eq. 15 (with $f(I_{LS}) = 1.$) was supplemented by a Smagorinsky's eddy viscosity model, in effect, making this model a modified version of the mixed model proposed earlier [20]. The spectra shows that both the modified similarity model and the k_{sgs} model behaves in a similar manner. The spectra for all cases appears to be leveling off at around the same location and it is clear that the cutoff occurs at a wavenumber at which significant energy containing scales remain unresolved. This is as expected for such high Reynolds number simulations.

The stress and energy flux correlation between the 32^3 grid and the 16^3 grid LES was carried out for this case. Figures 11a and 11b show, respectively, the stress and energy flux correlations (obtained in the 16^3 grid) as a function of the initial Re_λ. As discussed before, the computed correlation in the LES is much lower that in the *a priori* analysis. Furthermore, with increase in Re_λ, the correlation for all the models decrease indicating a serious problem with the dissipation modeling. The k_{sgs} model without the stochastic backscatter model (Eq. 13) showed a slightly lower correlation indicating that the backscatter model (although not very effective) does result in a higher correlation. More importantly, for all the cases studied here, the k_{sgs} model showed a much higher correlation at this grid resolution. This suggests that although the k_{sgs} model needs improvements, it warrants further investigation for application in high Reynolds number flows.

5. CONCLUSIONS

Direct and large eddy simulations of forced and decaying isotropic turbulence have been performed using a pseudospectral and a finite-difference code. Subgrid models that include a one-equation subgrid kinetic energy model with and without a stochastic backscatter forcing term and a new scale similarity model have been analyzed in both the Fourier space and the physical space using high resolution DNS data. The spectral space analysis showed that energy transfer across the cutoff wavenumber k_c is dominated by local interaction. Correlation analysis of the modeled and exact nonlinear terms and the subgrid energy transfer in physical space showed very low values.

In physical space, *a priori* analysis of the stress and energy transfer correlation between the exact value and the modeled terms was carried out for a range of Re_λ. Results show that the stress and energy flux predicted by both the subgrid models correlates very well with the DNS data with the scale similarity model showing very high correlation for reasonable grid resolution. However, with decrease in grid resolution, the scale similarity model becomes more uncorrelated when compared to the kinetic energy model.

When the subgrid models were used for LES, correlation with the DNS results was very low. This was in spite of keeping the initial flow field for all the simulations highly correlated. This suggests that the results of *a priori* analysis cannot be used to predict the behavior of the subgrid models in actual LES. The analysis of the LES data obtained on very coarse grids showed that the scale similarity model behaves very poorly when compared to the k_{sgs} model which consistently showed higher correlation. These results suggest that the scale similarity model can be used only for relatively fine grid resolution, whereas, the kinetic energy model can be used even in coarse grids. This was further demonstrated by carrying out LES at a very high Re_λ for which the scale similarity model had nearly zero correlation while the k_{sgs} model still had (albeit) finite value. It is expected that the application of the dynamic procedure (to be carried out in the future) will improve the disspation and production models in the k_{sgs} model.

ACKNOWLEDGEMENTS

This work is supported by the Office of Naval Research under Grant No. N00014-93-1-0342. Computing time was provided by the Numerical Aerodynamic Simulation (NAS) at NASA Ames Research Center and is gratefully acknowledged. Support provided by graduate students W. Kim and K. Chakravarty is also acknowledged.

REFERENCES

1. McMillan, O.J., Ferziger, J.H., and Rogallo, R.S., "Tests of new Subgrid-Scale Models in Strained Turbulence", AIAA Paper No. 80-1339, 1980.

2. Moin, P. and Kim, J., "Numerical Investigation of Turbulent Channel Flow", J. Fluid Mech., *118*, pp. 341-377, 1982.

3. Piomelli, U., Cabot, W.H., Moin, P., and Lee, S., "Subgrid-scale Backscatter in Turbulent and Transitional Flows", Phys. Fluids A, *3*, pp. 1766-1771, 1991.

4. Germano, M., Piomelli, U., Moin, P., and Cabot, W. H., "A Dynamic Subgrid-Scale Eddy Viscosity Model," Phys. Fluids A, *3*, pp. 1760-1765, 1991.

5. Chasnov, J. R., "Simulation of the Kolmogorov Inertial Subrange Using an Improved Subgrid Model," Phys. Fluids A, *3*, pp. 188-220, 1991.

6. Leith, C.E., "Stochastic Backscatter in a Subgrid-scale Model: Plane Shear Mixing Layer", Phys. Fluids A, *2*, pp. 297-299, 1990.

7. Piomelli, U., "High Reynolds Number Calculations using the Dynamic Subgrid-Scale Stress Model", Phys. Fluids A, *5*, pp. 1484-1490, 1993.

8. Domaradzki, J. A., Liu, W., and Brachet, M. E., "An Analysis of Subgrid Scale Interactions in Numerically Simulated Isotropic Turbulence", Phys. Fluids A, *5*, pp. 1747-1759, 1993.

9. Liu, S., Meneveau, C., and Katz, J., "On the Properties of Similarity Subgrid-scale Models as Deduced from Measurements in a Turbulent Jet", preprint, submitted for publication, 1993.

10. Rogallo, R. S., "Numerical Experiments in Homogeneous Turbulence," NASA TM 81315, 1981.

11. Eswaran, V. and Pope, S. B., "An Examination of Forcing in Direct Numerical Simulations of Turbulence", Comput. & Fluids, *16*, pp. 257-278, 1988.

12. Yeung, P. K. and Brasseur, J. G., "The Response of Isotropic Turbulence to Isotropic and Anisotropic Forcing at the Large Scales," Phys. Fluids A, *3*, pp. 884-896, 1991.

13. Kerr, R.M., "Velocity, Scalar and Transfer Spectra in Numerical Turbulence", J. Fluid Mech., *211*, pp. 309-332, 1990.

14. Piomelli, U., Moin, P., and Ferziger, J.H., "Model Consistency in Large Eddy Simulation of Turbulent Channel Flows", Phys. Fluids, *31*, pp. 1884-1891, 1988.

15. Menon, S., "A Numerical Study of Secondary Fuel Injection Control of Combustion Instability in a Ramjet", AIAA Paper No. 92-0777, 1992.

16. Yoshizawa, A., "Bridging between Eddy-viscosity-type and Second-order Models using a Two-Scale DIA", Ninth Symposium on "Turbulent Shear Flows", Kyoto, Japan, August, 1993.

17. Schumann, U., "Subgrid Scale Model for Finite Difference Simulation of Turbulent Flows in Plane Channels and Annuli", J. Comput. Phys., *18*, pp. 376-404, 1975.

18. Horiuti, K., and Yoshizawa, A., "Large Eddy Simulation of Turbulent Channel Flow by 1-Equation Model", in Finite Approximations in Fluid Mechanics, ed. E. H. Hirschel, pp. 119-134, 1985.

19. Piomelli, U., "Applications of Large Eddy Simulations in Engineering: An Overview", in "Large eddy Simulations of Complex Engineering and Geophysical Flows", B. Galperin and S. Orszag, Eds., Cambridge University Press, 1993, pp. 119-137.

20. Bardina, J., Ferziger, J.H., and Reynolds, W.C., "Improved Subgrid Scale Models for Large Eddy Simulations", AIAA Paper 90-1357, 1980.

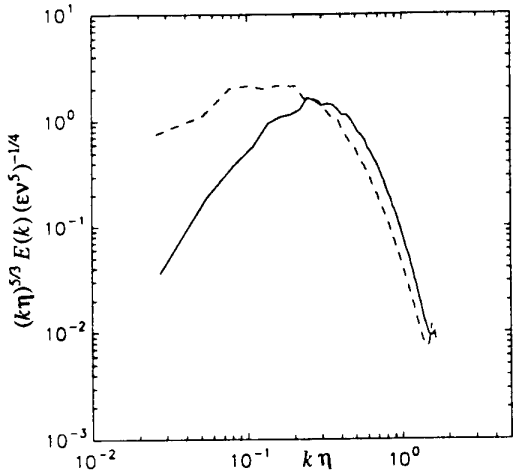

(a) Energy spectra for 128^3 DNS of forced stationary isotropic turbulence at $Re_\lambda \approx 90$ (dashed line) and decaying turbulence at $Re_\lambda \approx 20$ (solid line).

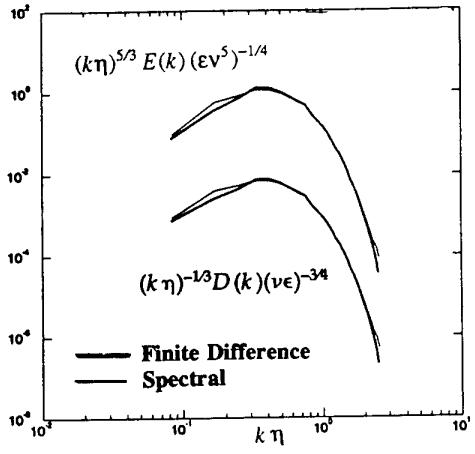

(b) Energy and dissipation spectra for 64^3 DNS.

Figure 1. Kolmogorov scaled energy and disspation spectra for decaying and forced isotropic turbulence.

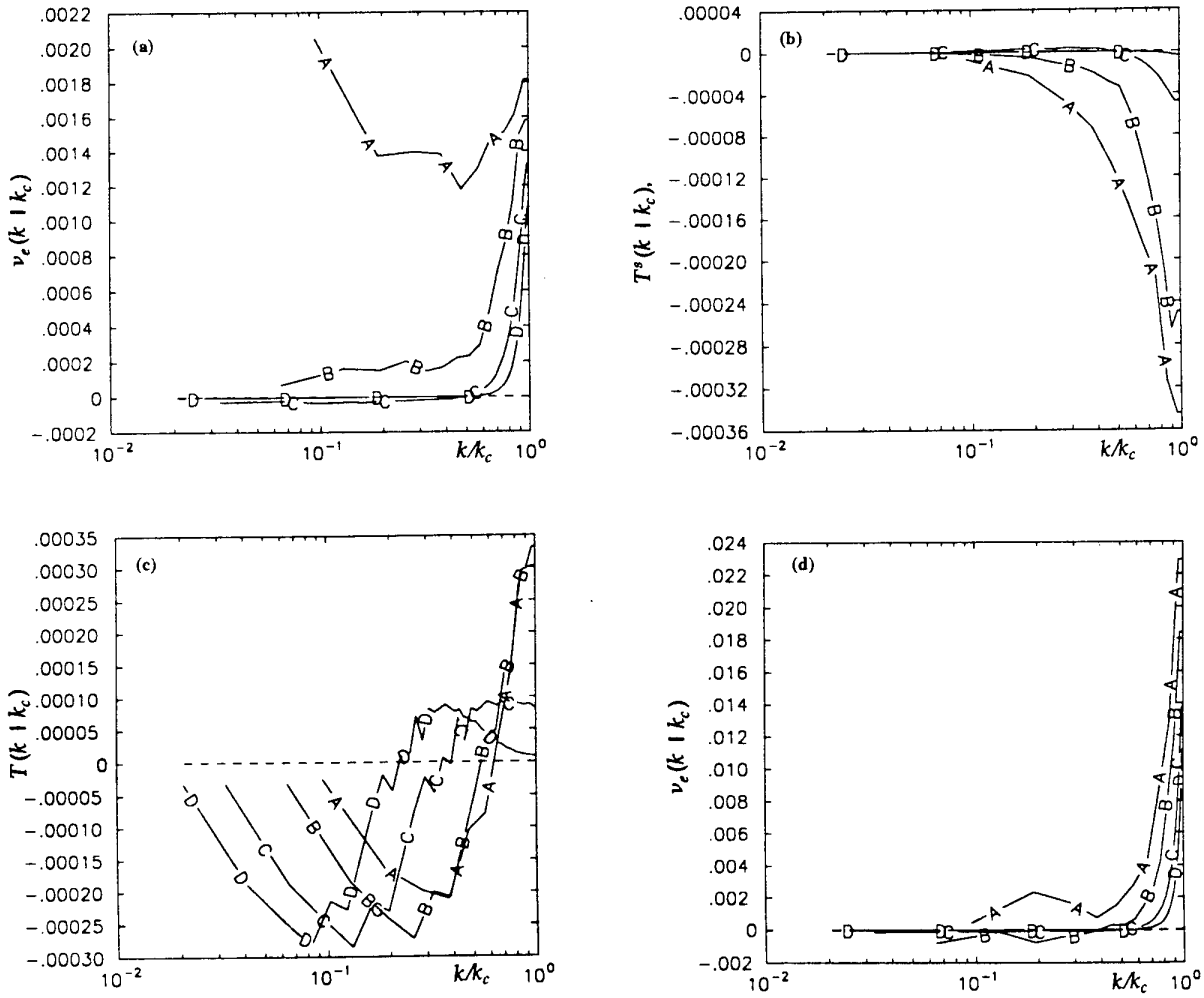

Figure 2. (a) SGS eddy viscosity, $\nu_e(k|k_c)$, (b) subgrid energy transfer, $T^s(k|k_c)$, and (c) resolved energy transfer, $T(k|k_c)$, computed from decaying isotropic turbulence DNS data for different k_c: Curves A-D are k_c: 10.5, 15.5, 30.5 and 48.5 respectively. (d) SGS eddy viscosity for forced stationary isotropic turbulence.

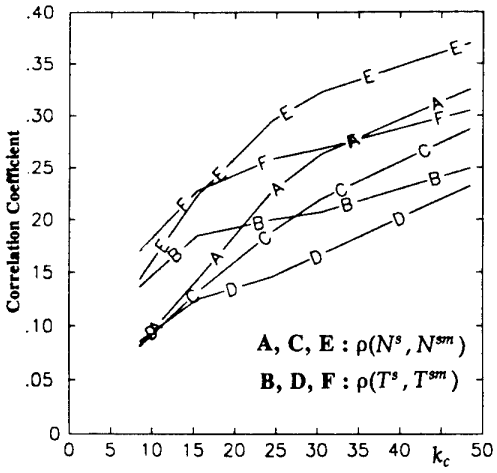

Figure 3. Correlation coefficients between exact and modeled quantities computed in physical space. Lines A, B, E, and F are for the decaying case and lines C and D are for the forced case. Also, lines A, C and E are for the non-linear term while lines B, D and F are for energy transfer.

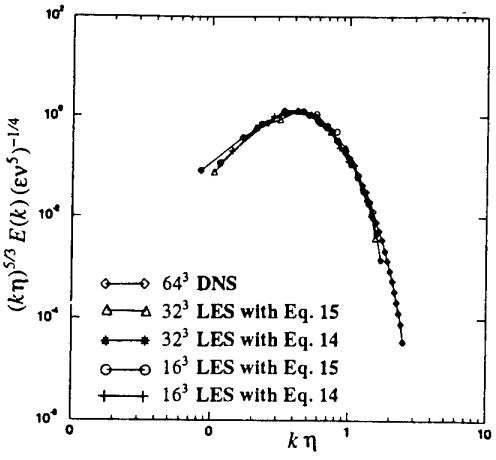

(a) Kolmogorov scaled energy spectra

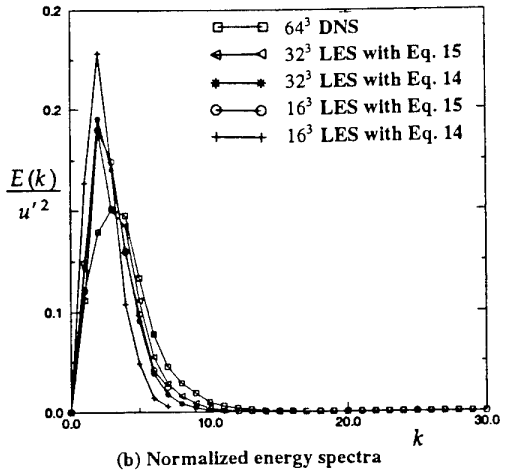

(b) Normalized energy spectra

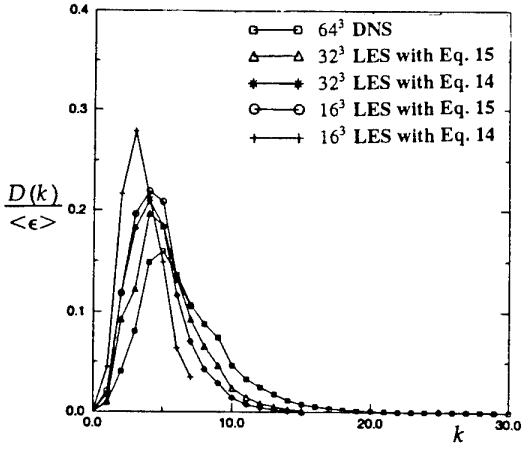

(c) Normalized dissipation spectra

Figure 4. Comparison of the energy and dissipation spectra for the DNS and LES with various models at $t = 12$ ($Re_\lambda \approx 10$).

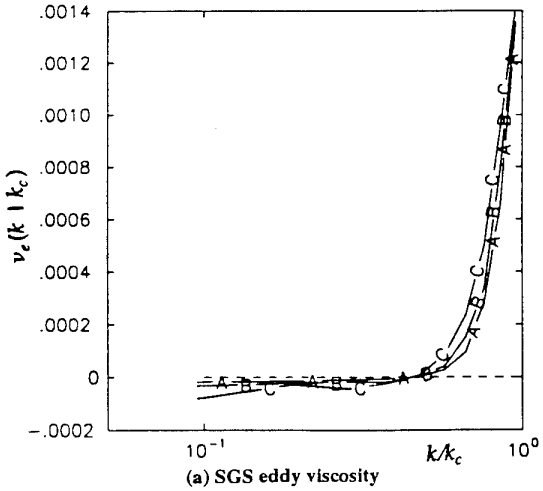

(a) SGS eddy viscosity

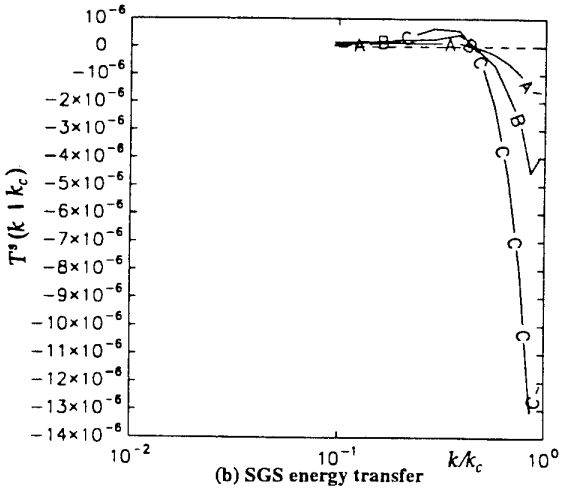

(b) SGS energy transfer

Figure 5. Subgrid eddy viscosity, $\nu_e(k|k_c)$ and subgrid energy transfer, $T^s(k|k_{kc}$ for $k_c = 10.5$ for the DNS and LES data. Curve A: 32^3 LES with Eq. 14, Curve B: 32^3 LES with Eq. 15, Curve C: 64^3 DNS.

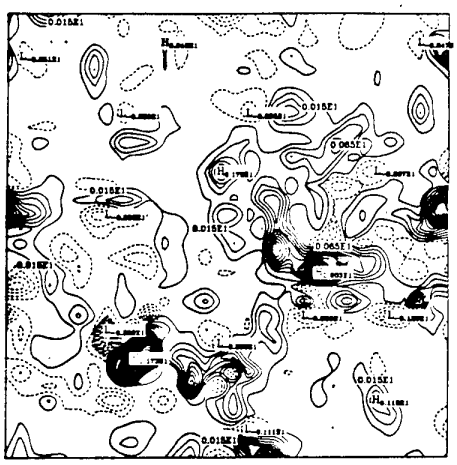

(a) Exact energy transfer from DNS

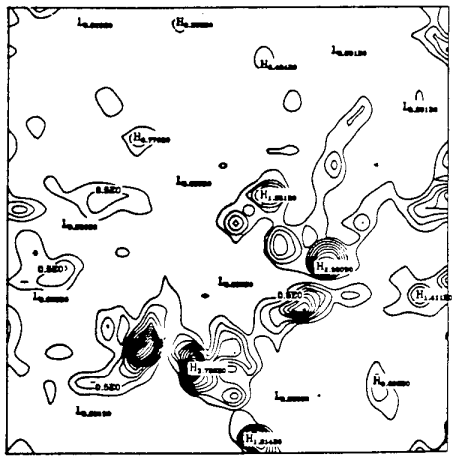

(b) Energy transfer predicted by Eq. 14

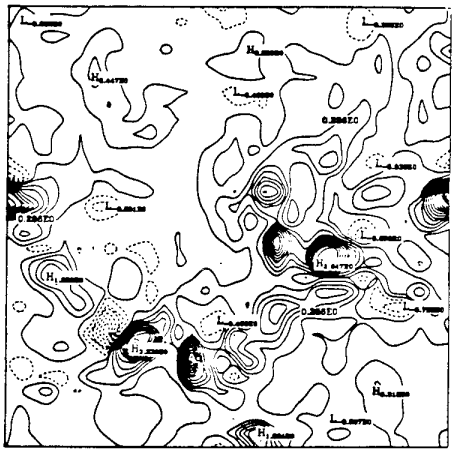

(c) Energy transfer predicted by Eq. 15 with $f(l_{LS}) = 1$.

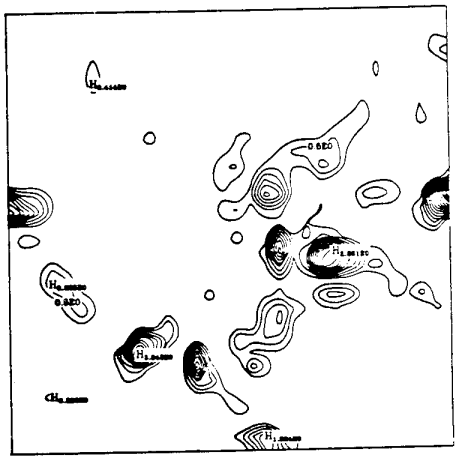

(d) Energy transfer predicted by Eq. 15

Figure 6. Comparison of the contours of the energy transfer for the forced DNS case and the SGS models resolved on 32^3 grid. Same contour interval and location for all cases. Solid contours indicate forward scatter and negative contours indicate backscatter.

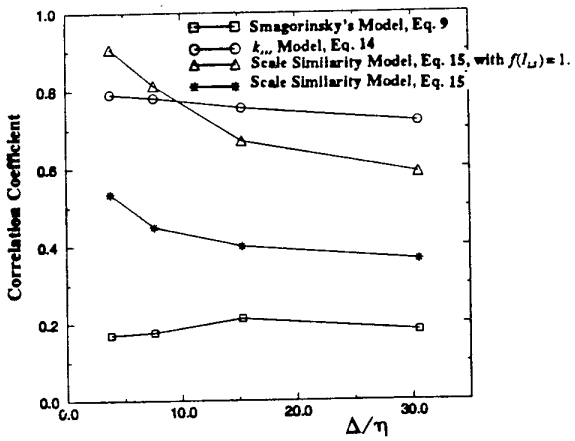

(a) Correlation at $Re_\lambda \simeq 90$

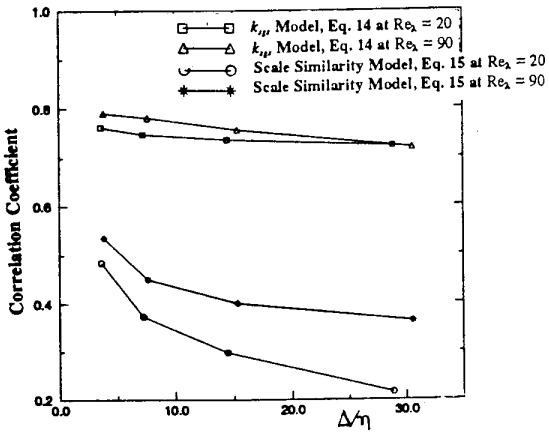

(b) Correlation at $Re_\lambda \simeq 90$ and 20

Figure 7. Correlation between the exact stresses from the 128^3 DNS data and the stresses computed from the SGS models as a function of filter width.

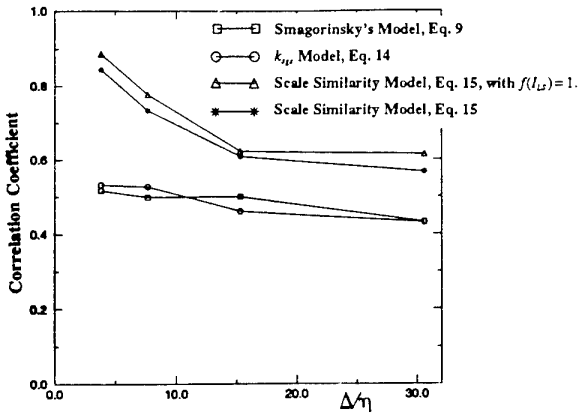

(a) Correlation at $Re_\lambda \simeq 90$

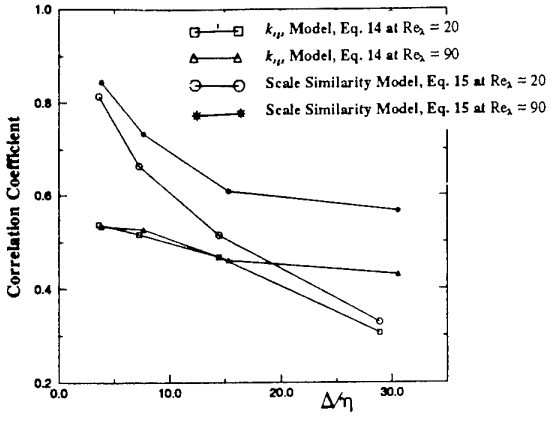

(b) Correlation at $Re_\lambda \simeq 90$ and 20

Figure 8. Correlation between the exact energy transfer from the 128^3 DNS data and the energy transfer computed from the SGS models as a function of filter width.

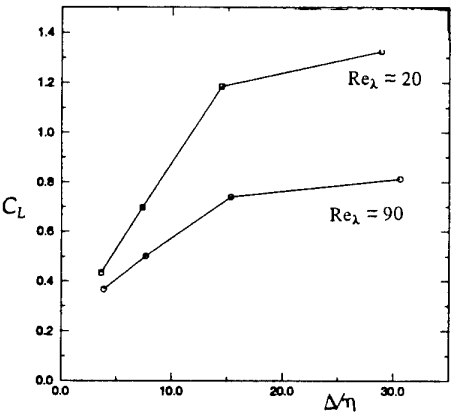

Figure 9. Variation of the coefficient c_L in the scale similarity model (Eq. 15) with filter width and Re_λ

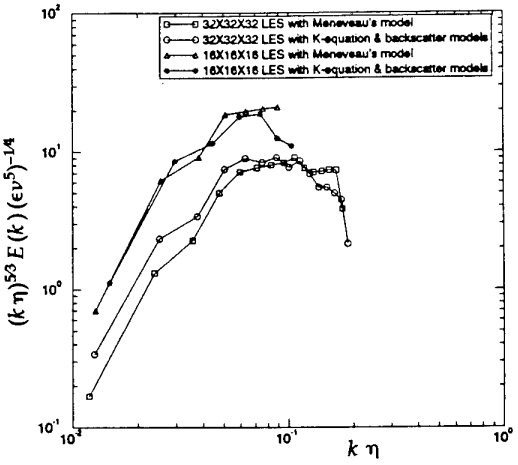

Figure 10. The Kolmogorov scaled energy spectra for $Re_\lambda = 10^3$.

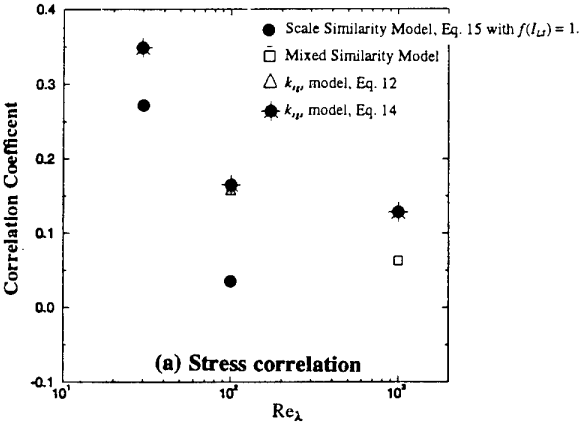

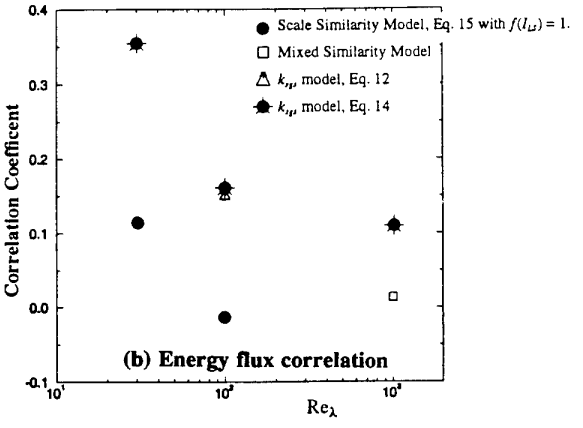

Figure 11. The variation of the stress and energy flux correlations as a function of Re_λ at $t = 0$. Correlations computed in the 16^3 grid.

A cheap DNS tool for turbulence models testing

A.Baron and M.Quadrio

Dipartimento di Ingegneria Aerospaziale del Politecnico di Milano
40, via C. Golgi - 20133 Milano - Italy

1. SUMMARY

The *Narrow Channel* (NC) assumption, together with a simple although efficient numerical scheme are adopted in order to perform the Direct Numerical Simulation (DNS) of turbulent channel flows at moderate Reynolds numbers with extremely reduced computational resources.
Typical results are presented for a constant property fluid, which certify the reliability of the numerical tool and the quality of the simulations.
The closure problem of turbulence modelling is then considered and the transport equations for the Reynolds stresses and for the dissipation rate of the turbulence kinetic energy are solved on the basis of the *Narrow Channel* data.
The comparison of the distributions of the various terms in the transport equations with published full channel DNS data confirms that, although the NC assumption substantially reduces the computational cost of the simulations, it does not affect the accuracy of the numerical predictions.
Finally, as an example of the use that can be done of the numerical tool, an algebraic stress model and a one-equation model for the dissipation rate tensor for low Reynolds number flows are considered, and the modelled quantities are compared with their directly computed counterparts.

2. INTRODUCTION

In recent years, the advancement of large-scale computers made the Direct Numerical Simulation of turbulence an affordable task. The DNS of turbulent flows, although still limited to relatively simple geometries and moderate Reynolds numbers, is nevertheless producing a dramatic impact on many turbulence-related fields, ranging from fundamental research to routine simulation of industrial and atmospheric flows.

In basic turbulence research, the DNS provides the scientists with an unparalleled tool for the comprehension of those complicated mechanisms through which turbulent structures interact mutually and with the solid boundaries of the flow domain, so that a much deeper insight is currently being gained into the dynamics of those basic events and structures that for many years since have been identified as the essential components of the bursting cycle in near-wall turbulence.

On the other hand, nowadays satisfactory predictions of a number of industrial and natural turbulent flows can be obtained by using simplified mathematical models of the flow, such as the Large Eddy Simulation technique or the averaged or Reynolds form of the Navier-Stokes equations. Although the DNS will probably never become an engineering tool itself, it can incomparably help in developing those turbulence models which the solution of any simplified form of the Navier-Stokes equations is based on.

All of the work on the development of turbulence modelling makes recourse to indirect procedures to test the various closure models. So far, the only source of physical comparative data was in fact of experimental nature, but difficulties in measuring pressure and velocity with a sufficient spatial accuracy always prevented from the possibility of a direct comparison of the closure models with experiments.

As a result of a DNS, on the contrary, the instantaneous values of the primitive variables are known with such a spatial resolution, that each term in the budget of the Reynolds stresses can be accurately computed. It is then immediate to test the closure models by direct comparison of the closure formula with the term being modelled. This procedure has been adopted by Mansour, Kim and Moin in a paper appeared in the Journal of Fluid Mechanics in 1988, where the Authors presented outstanding results obtained by using DNS data for a channel flow.

However, a DNS of a channel flow is so expensive from a computational point of view that it still remains beyond the computing power of most research laboratories. This is why in the present work an attempt is made aimed at preserving all of the advantages intrinsic in the use of DNS data, while reducing the computational cost of their production. Two strategies are adopted: the *Narrow Channel* assumption (Jiménez and Moin, 1991) is applied in order to abate the size of the computational domain and an extremely simple, although efficient, numerical scheme is used for the integration of the complete Navier-Stokes equations.

The transport equations for the Reynolds stresses and for the scalar trace of the turbulence kinetic energy dissipation-rate tensor provide the essential information for the development and testing of many turbulence models. In the present paper these equations are considered, their terms are evaluated by using the *Narrow Channel* flow fields, and used for a direct comparison with quantities modelled by an algebraic and a one-equation turbulence model.

It might be objected that, since exhaustive and well documented DNS data for the distribution of each single term in the transport equations are public domain, researchers involved in the development of turbulence models might not be interested in producing these data themselves. However new closure procedures could be envisaged, requiring the evaluation of terms different from those considered so far (e.g. terms involving correlations of fluctuating vorticity components). In that case, the capability of exactly computing, through a cheap DNS tool, the quantities to be modelled, seems to be an extremely attractive one.

Paper presented at the 74th Fluid Dynamics Symposium on "Application of Direct and Large Eddy Simulation to Transition and Turbulence" held at Chania, Crete, Greece, in April 1994.

3. MATHEMATICAL FORMULATION AND COMPUTATIONAL ALGORITHMS

The turbulent flow of a constant property fluid is governed by the Navier-Stokes equations, which express the momentum equation and the mass conservation principle. For a plane channel flow, the Navier-Stokes equations can be written as:

$$\begin{cases} \dfrac{\partial u_i}{\partial t} + \dfrac{\partial}{\partial x_j}(u_i u_j) + \dfrac{\partial p}{\partial x_i} = \dfrac{1}{\mathrm{Re}} \dfrac{\partial^2 u_i}{\partial x_j \partial x_j} + f_i \\ \dfrac{\partial u_i}{\partial x_i} = 0 \end{cases} \quad (1)$$

In these equations, velocities and lengths are made dimensionless with the friction velocity $u_\tau = \sqrt{\tau_w/\rho}$ and the channel half-height h. The dimensionless form of pressure and stresses is consequently obtained by dividing the physical quantities by ρu_τ^2. Re denotes the Reynolds number, defined throughout this paper as $\mathrm{Re} = u_\tau h/\nu$, where ν is the kinematic viscosity of the fluid. f_i denotes the dimensionless forcing term, which represents the pressure gradient necessary, in a plane channel, to drive the flow by balancing the viscous losses. In the present numerical scheme, the forcing term is kept constant and equal to one, so that the volume flux through the channel is allowed to vary in time.

Spatial derivatives are evaluated by using a second-order accurate central finite difference scheme. The non-linear terms are written in the Arakawa form (Horiuti, 1987), so that conservation of momentum is preserved also in the discrete sense.

Time integration of the momentum equations is performed by using an efficient, low-storage, partially implicit scheme, with an iterative Crank-Nicholson method for the diffusive terms and a third-order self-starting Runge-Kutta method for the remaining terms. The algorithm is discussed in detail in Rai and Moin (1991), and is divided in 3 substeps (see Annex A). Each single substep of the algorithm closely resembles the fractional step scheme used by Kim and Moin (1985), to which the reader is referred for a detailed description.
Although this scheme is shown to be stable for CFL numbers up to $\sqrt{3}$ on uniform grids and 1.45 for smoothly stretched grids, the results presented in the following are obtained by keeping the CFL number around 1, since it brings to the use of time steps of the order of the inner viscous time scale $t^+ = t u_\tau^2/\nu$, which are essential to sample the time evolution of the physical quantities governed by equation (1). This means in practice that the limitation in the time step is mainly due to physical requirements, rather than to stability problems.

Continuity is enforced at every substep by solving a Poisson equation for the pressure-related scalar variable Φ. A spectral method based on Fast Fourier Transforms is used in this section of the code (Schmidt *et al*, 1984), thanks to the simple geometry of the computational domain.

The no-slip condition is imposed on the solid walls, and the usual periodic conditions are used in the streamwise and spanwise (homogeneous) directions.

Grid spacing is uniform in the homogeneity directions, while a smooth stretching (from a geometrical 2% stretching near the solid walls to an approximately constant spacing in the central portion of the channel, according to the local turbulence length scales) is used in the direction normal to the walls. The dimensions of the computational domain are discussed in the following paragraph.

4. THE *NARROW CHANNEL* ASSUMPTION

An interesting computational technique has been suggested in 1991 by Jiménez and Moin. In this technique, all of the beneficial features of the DNS of channel flows in terms of both space and time resolution are retained, while the computational effort is consistently reduced. They called this new approach to the Direct Numerical Simulation of turbulence the *Narrow Channel* assumption.
It basically consists in performing a DNS with space and time discretizations adequate for resolving all of the essential turbulence scales (so that no turbulence model is required), but over a computational domain of very limited size in the spanwise and streamwise directions. This allows a reduction of almost two orders of magnitude in the number of the required grid points (and computational resources), with respect to a standard DNS performed over a full-size channel, at the same Reynolds number.

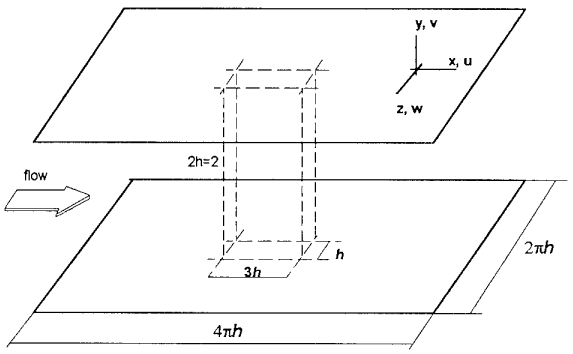

Fig.1 - Sketch of the computational domain

As mentioned in section 3, periodic boundary conditions are imposed in the homogeneous streamwise (x) and spanwise (z) directions. In a full channel flow, the dimensions λ_x and λ_z of the computational domain have to be such that all of the computed two-point spatial autocorrelation functions along x and z decay sufficiently at half the streamwise and spanwise extents of the domain, which are usually fixed at $\lambda_x = 4\pi h$ and $\lambda_z = 2\pi h$ respectively (Kim and Moin, 1982). When assuming the *Narrow Channel* hypothesis, on the contrary (Fig.1), the dimensions of the domain in the homogeneity directions are kept much smaller than those usually suggested for the full channel case. The size of the computational box, however, cannot be reduced arbitrarily since minimal values for λ_x and λ_z are found to exist, below which turbulence cannot self-sustain. Self-sustained turbulence here means that each fluctuating quantity, computed for a time interval long enough for establishing its asymptotic behaviour, does not show to be damped to a non-fluctuating, laminar value.

Incidentally we can notice that, when the dimensions of the computational box are close to the minimal ones, the interesting phenomenon of one-walled turbulence naturally appears. This peculiar feature of the flow can be monitored, for instance, through the spatially averaged instantaneous wall shear Ω, defined as:

$$\Omega(\pm 1) = \frac{1}{\lambda_x \lambda_z} \int_0^{\lambda_x} \int_0^{\lambda_z} \frac{\partial U}{\partial y}(x, \pm 1, z)\, dx dz$$

which is a physical quantity strictly related to turbulent activity. If we examine (Fig.2) the time evolution of the ratio between Ω and its laminar value, computed for $Re_\tau = 145$, in four different simulations in which the channel span is progressively reduced, we can observe that the flow moves from a two-walled turbulent situation (Fig.2a) to a decaying one (Fig.2d), through a series of one-sided conditions.

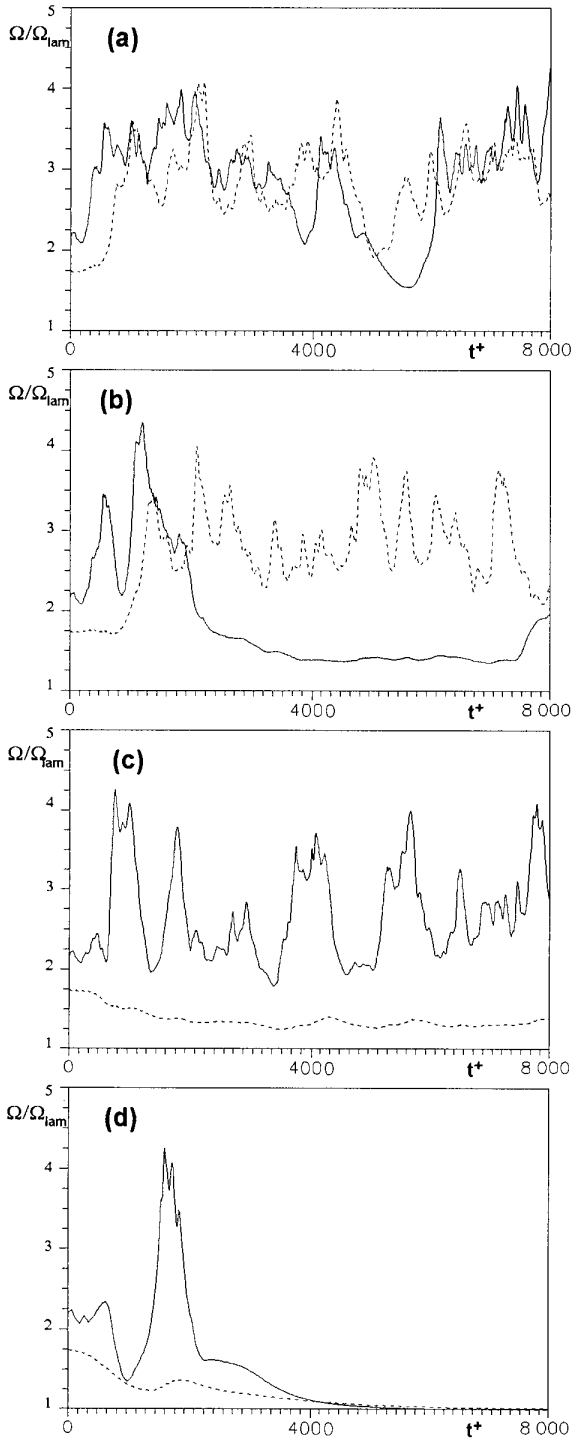

Fig.2 - Time evolution of the wall-averaged instantaneous shear stress, divided by its laminar value, for $Re_\tau = 145$. Continuous and dotted lines refer to the lower and upper wall, respectively. Dimensions of the computational domain: λ_x=3h; λ_z=0.85h (a), λ_z=0.80h (b), λ_z=0.75h (c), λ_z=0.70h (d).

Although the initial conditions are the same for all of the four simulations, nevertheless, turbulent activity is observed to switch randomly between the upper and the lower wall of the channel. While in Fig.2b, for instance, turbulence mainly resides near the upper wall, Fig.2c, on the contrary, clearly shows a quiescent flow on the upper wall of the channel and an intense turbulent activity near the lower one.

Provided the dimensions of the computational domain are not reduced below some critical threshold values, recourse to the *Narrow Channel* hypothesis proves to produce no undue effect on the mean flow, the main turbulent quantities and low-order statistical moments, neither in the logarithmic nor in the near-wall region of the flow. Otherwise, on the contrary, not only the turbulent structures are affected, but also the mean velocity distribution is found to deviate from the usual law-of-the-wall behaviour, due to the unrealistic constraining effect of a too small computational domain.

From a physical point of view, channel dimensions must be such to contain at least a complete hierarchy of turbulent structures, so that the complete dynamic cycle of turbulence can be correctly reproduced within the computational domain. The existence of minimal dimensions can also be interpreted in terms of energetic considerations. The well-known energy cascade theory of turbulence states that the large-scale structures extract their turbulent kinetic energy from the mean flow, while intermediate scales simply transfer energy to the smaller ones which have a predominant dissipative nature. Reduced dimensions of the computational domain obviously limit the maximum size of the large-scale structures contained in the flow, while leaving the dissipative action of the small scales unaffected. This produces a lack of turbulent kinetic energy production with respect to dissipation, and forces turbulence to a natural decay.

The parametric study performed by Jiménez and Moin (1991), aimed at determining the influence of the Reynolds number of the flow on the minimal dimensions of the computational domain, has been repeated with the present numerical scheme (Baron and Quadrio, 1993), finding full support to their results. In particular, the parametric analysis confirmed that the minimal dimensions of the computational domain are roughly constant when expressed in wall units. This is especially true for the spanwise dimension of the channel, for which this approximately constant value has an evident physical meaning, since it turns out to be very close to the mean spanwise spacing (around 100 wall units) of the low speed streaks, which are a characteristic feature of near-wall turbulent flows, as reported by a number of experimental observations (see for instance Smith and Metzler, 1983).

Although the volume of the computational domain cannot be reduced indefinitely, nevertheless its minimal dimensions are so small compared to those usually required for a full-size channel flow, that a substantial reduction of the computational resources is achieved.
For the Reynolds number Re_τ equal to 180 considered in the following of the present work, for instance, it turns out that a streamwise extent λ_x of the flow domain equal to three times the half height of the channel h and a spanwise one λ_z equal to h are sufficient, not only to preserve self-sustained turbulence, but also to avoid any undue effect on both fluctuating and mean flow variables. This allows a very realistic and accurate DNS of turbulence to be performed on a computational mesh of only 32x32x120 grid points in the

streamwise, spanwise and normal-to-the-wall directions respectively.

It should be noted that the amount of grid points in the spanwise direction could be further reduced to approximately a half the number here adopted, with but negligible effects on the results. However the finer grid has been preferred, since it brings to a spatial resolution which is approximately proportional to the gradients of the solutions along each spatial coordinate, which are strongly non-isotropic in the near-wall region of a turbulent flow. Despite of this, the CPU time for a single time step is only 25 seconds on a HP 715 workstation (a small machine capable of approximately 15 MFlops peak performance), while the typical integration time required to obtain stable and accurate low-order statistics is of the order of 24 hours.

A Navier-Stokes solver, used under the *Narrow Channel* assumption, can be consequently considered as an extremely efficient tool for performing realistic DNS of turbulent channel flows with a reduced computational effort.

5. TYPICAL RESULTS

Prior to using the DNS data to evaluate the capabilities of turbulence models, the mean flow and complete turbulence statistics have been computed. Some of the results are reported in this section, aimed at assessing the quality and the reliability of the present numerical tool.

Results concern $Re_\tau = 180$, a value chosen because it allows a direct comparison with the results of Mansour *et al* (1988) in terms of Reynolds-stress budgets. The computations have been carried out for box dimensions of $\lambda_x=3h$ and $\lambda_z=h$, by using 32x32x120 grid points in the spanwise, streamwise and normal to the wall directions respectively. An integration time $\overline{T} = T u_\tau / h = 20$ has been used, which is approximately twice the minimum time necessary to obtain stable statistics. Examples of two-point spatial autocorrelation functions are shown in Fig.3 and, as expected, they do not fall down to zero at half the streamwise and spanwise dimensions of the computational domain. This implies that the effect of the larger turbulence structures will probably not be accurately accounted for and suggests that the *Narrow Channel* data are a preferred choice when testing subgrid or near wall turbulence models.

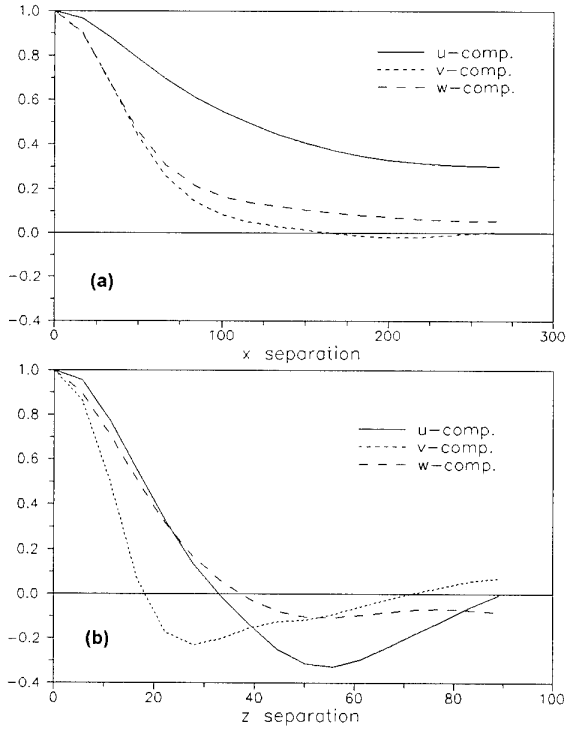

Fig.3 - Two-point spatial autocorrelation function along (a) the streamwise and (b) the spanwise directions, at y^+=15. In both cases the plot spans half of the computational domain.

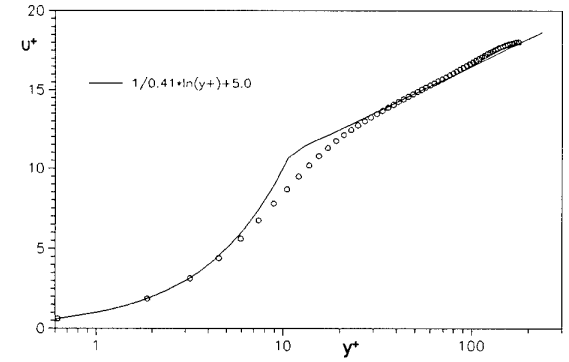

Fig. 4 - Mean velocity distribution in law-of-the-wall form.

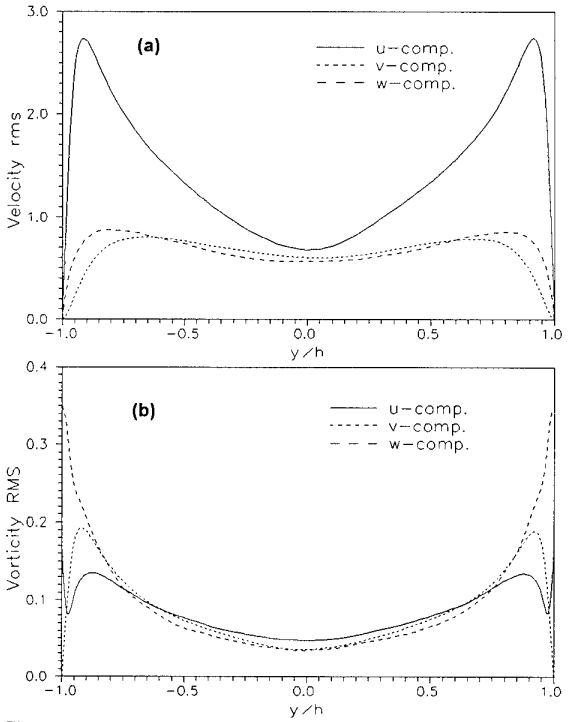

Fig. 5 - RMS values of (a) velocity and (b) vorticity fluctuations, across the channel, in global coordinates.

The mean velocity distribution, in the form of the law of the wall, is reported in Fig.4, and it closely agrees with experimental data and results from other DNS. The perfect agreement of the computed mean velocity distribution with the universal law of the wall confirms the adequacy of both the sample size and the integration time adopted in the numerical simulations.

The RMS values of the velocity and vorticity components are shown in Fig.5. Their agreement with published narrow and

full channel DNS results, can be considered excellent, both in terms of general spatial distribution and wall values.

As a result of a Direct Numerical Simulation, the instantaneous velocity, vorticity and pressure fields are completely known, so that the spatial distribution of each fluid dynamic variable can be visualized and followed in time, much better than any experimental technique can do.
A sample is given in Figg.6-8 of the physical insight which can be gained even through the analysis of simple cross-sections of a computed flowfield.

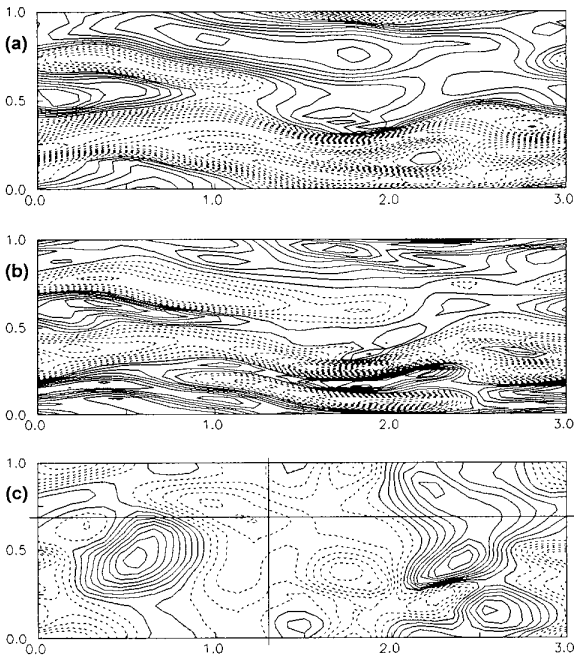

Fig.6 - Horizontal (x,z) section in the wall region of the flow, $y^+=15$ below the upper wall. Flow is from left to right, $\lambda_x=3h$; $\lambda_z=h$. Solid lines denote positive instantaneous values of the observed variable, dotted lines negative ones. All the variables are nondimensionalized in wall units. (a) Streamwise component of velocity, isolines increment = 0.5. (b) Vorticity component normal to the wall, isolines increment 0.05. (c) Pressure contours, isolines increment = 0.5.

Contours of the instantaneous fluctuating component u of the velocity vector (the mean velocity distribution has been detracted) are shown in Fig.6a, in a plane parallel to the solid walls of the channel, 15 wall units below the upper wall. Flow is from left to right, contour increment is $\Delta u = 0.5$ and solid lines denote positive values, dotted lines negative ones. In the same plane (Fig.6b) the contour plot for the instantaneous vorticity component normal to the wall ω_y is reported (contour increment 0.05). The distinctive feature in both the velocity and vorticity contour plots is the existence of those well-known elongated streaks of low speed fluid adjacent to high speed fluid regions. The instantaneous distribution of the associated fluctuating pressure (contour increment 0.5) is also shown in Fig.6c.

In Fig.7 contour plots of u and ω_x are reported in a plane normal to the walls of the channel and to the direction of the mean flow, located at approximately half the channel length (the trace of this plane is represented by the vertical line

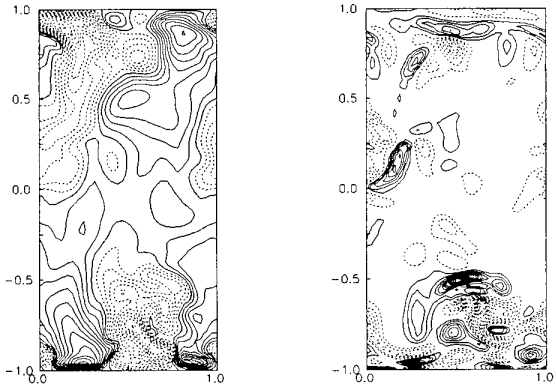

Fig.7 - Transversal (y,z) section of the flow, at $x=1.27h$. Flow enters the page. Symbols as in Fig.6. (Left) Streamwise component of velocity, isolines increment = 0.5. (Right) Streamwise component of vorticity, isolines increment 0.05.

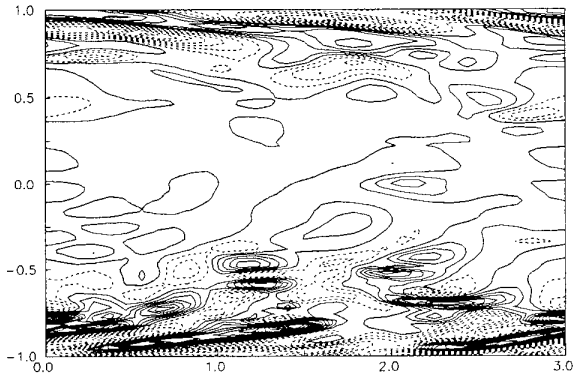

Fig.8 - Contour plot of the instantaneous spanwise component of vorticity, in a vertical (x,y) section of the flow, at $z=0.67h$. Flow is from left to right. Isolines increment 0.05.

superimposed to the pressure field of Fig.6c). It is quite interesting to observe how multiple vorticity regions of opposite sign can be contained in the same low speed streak.

Finally, the typical structure of the shear layers in the near-wall region is clearly evidenced by the contour plot of the instantaneous spanwise component of vorticity ω_z (the mean shear has been detracted), shown in Fig.8, in a plane normal to the solid walls and aligned with the mean flow, whose trace is represented by the horizontal line in Fig.6c.

The capability of capturing all of the essential features of the near-wall turbulent structures and reproducing in a realistic way their dynamics ensures that a DNS tool based on the *Narrow Channel* assumption can be reliably used in the development and testing of turbulence models.

6. THE CLOSURE PROBLEM

In most engineering problems there is no need to consider the finer details of turbulence and reliable predictions of turbulent flows can be obtained by only accounting for the time-averaged properties of turbulence, even if the mean flow is unsteady. The time-averaging process of the Navier-Stokes equations, however, causes statistical correlations involving fluctuating quantities to appear in the momentum and energy equations. As we have no direct way to know the magnitude of these terms, their effects must be approximated through

turbulence models, namely sets of assumptions and equations which, when solved with the mean flow equations, allow to determine the relevant correlations involving the fluctuating quantities.

In single-point closures, turbulent fluxes and stresses can be expressed in terms of effective turbulent diffusion coefficients for momentum, heat, chemical species, etc. In one- and multi-equation models, these effective diffusion coefficients are determined from local values of one or more turbulent quantities which, in turn, are obtained from exact transport equations similar to those describing the mean flow quantities and educed by manipulating the Navier-Stokes equations. These transport equations, however, are still unclosed, as they contain correlations that are not exactly determinable and which must therefore be approximated, i.e. modelled, in terms of quantities that are.

6.1- The transport equation for the Reynolds stresses

Turbulence models at the second-moment level require the solution of a transport equation for the Reynolds stresses, which can be derived by ensemble averaging the Navier-Stokes equations, then deriving equations for the fluctuating stresses and ensemble averaging these equations.

In general, as the Reynolds stress tensor is symmetric, there are six independent Reynolds stress components. However, in a fully developed channel flow, the relevant non-zero stresses are $\overline{uu}$, $\overline{vv}$, $\overline{ww}$ and $\overline{uv}$, because of the reflection properties of the Navier-Stokes equations in the spanwise (z) direction.

If lengths and primitive variables are expressed in wall units, i.e. made dimensionless with the friction velocity and the kinematic viscosity of the fluid, for the turbulent flow of a constant property fluid, one obtains:

$$\frac{\overline{D}}{Dt}\overline{u_i u_j} = P_{ij} + T_{ij} + D_{ij} + \Pi_{ij} - \varepsilon_{ij} \qquad (2)$$

where $\overline{D}/Dt = \partial/\partial t + U_k \partial/\partial x_k$ and the terms on the right hand side are listed below and denote production, turbulent transport, viscous diffusion, velocity pressure-gradient and dissipation rates respectively:

$$P_{ij} = -\left[\overline{u_j u_k}\frac{\partial U_i}{\partial x_k} + \overline{u_i u_k}\frac{\partial U_j}{\partial x_k}\right]$$

$$T_{ij} = -\frac{\partial}{\partial x_k}\left[\overline{u_i u_j u_k}\right]$$

$$D_{ij} = \nu\frac{\partial^2}{\partial x_k \partial x_k}\left[\overline{u_i u_j}\right]$$

$$\Pi_{ij} = -\frac{1}{\rho}\left[\overline{u_i\frac{\partial p}{\partial x_j} + u_j\frac{\partial p}{\partial x_i}}\right]$$

$$\varepsilon_{ij} = 2\nu\overline{\left(\frac{\partial u_i}{\partial x_k}\right)\left(\frac{\partial u_j}{\partial x_k}\right)}$$

In equation (2), tensor notation is used, with repeated suffices indicating summation. Lower and upper case u's denote fluctuating and time averaged velocity components respectively, p is the fluctuating pressure and overbars indicate the usual time average operator.

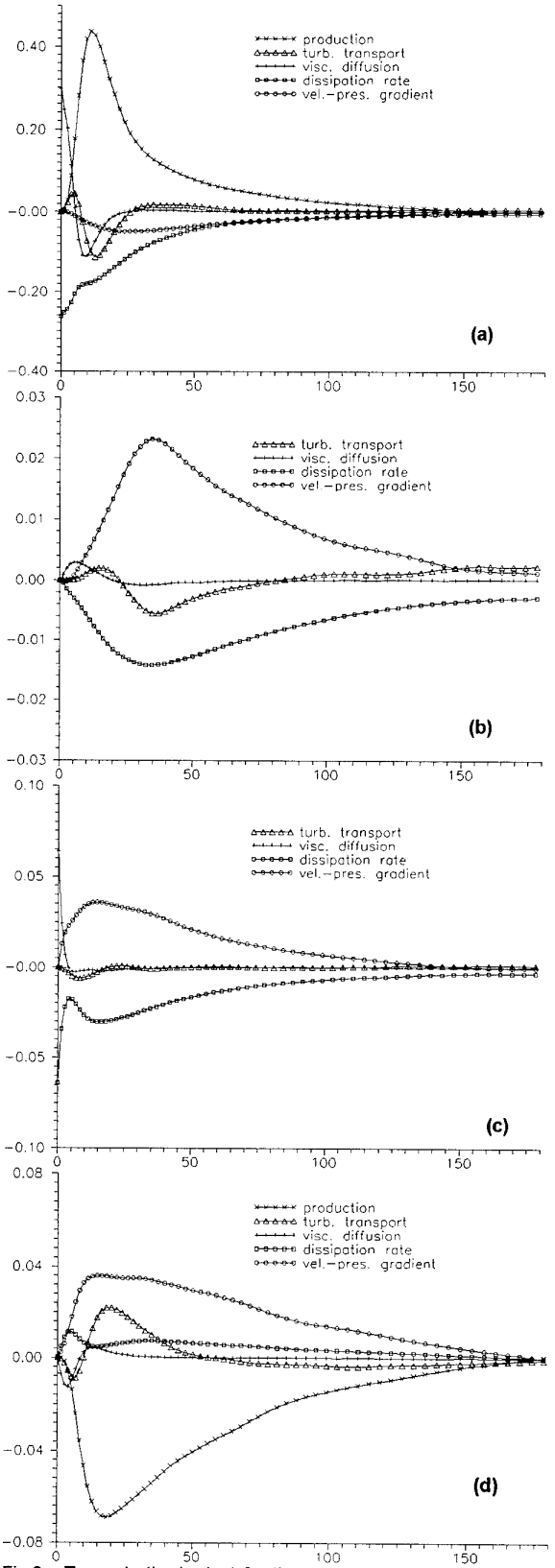

Fig.9 - Terms in the budget for the components of the Reynolds stresses, in wall coordinates. (a) u_1u_1 ; (b) u_2u_2 ; (c) u_3u_3 ; (d) u_1u_2

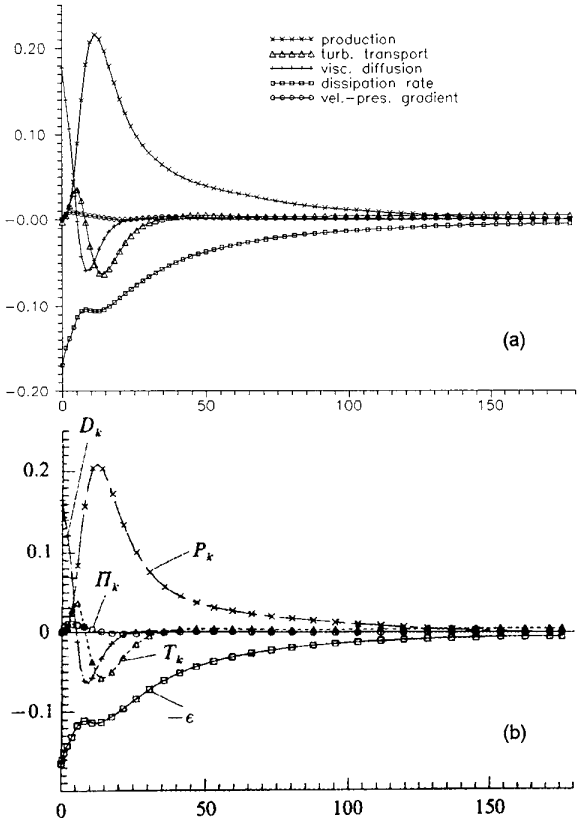

Fig.10 - Terms in the budget of the turbulence kinetic energy, in wall coordinates. (a) present NC based results; (b) full channel results of Mansour, Kim and Moin.

The five terms in the right hand side of equation (2) have been computed by using the instantaneous and average values of velocity and pressure supplied by the direct solution of the Navier-Stokes equations in the *Narrow Channel*, and their distribution is shown in Fig.9, for the four non-zero components of the Reynolds-stress tensor.
The present results perfectly match the ones obtained by Mansour *et al* (1988) for the full channel flow, and those of Spalart (1988), for the turbulent boundary layer on a flat plate, which is very similar to the channel flow as far as the wall region is concerned.

The terms in the budget for the turbulence kinetic energy, defined as half the trace of the Reynolds stress tensor, are shown in Fig.10a. In order to assess the quality of the present NC based predictions, they are compared with the analogous ones obtained by Mansour *et al* (1988) for the full channel case.

6.2- The transport equation for the dissipation rate of the turbulence kinetic energy

In the transport equation for the Reynolds stresses, the production-rate term P_{ij} is a function of the mean velocity and the Reynolds-stresses themselves, so that it does not need modelling. For the remaining terms, however, closure requires modelling of the dissipation-rate tensor ε_{ij} in terms of the Reynolds stresses and a turbulence lengthscale or timescale. Such a timescale, in the case of isotropic turbulence, can be expressed as a function of the turbulence kinetic energy K, defined as a half of the sum of the squares of the fluctuating velocities $(u^2+v^2+w^2)$, and the dissipation-rate tensor ε_{ij}. The latter, in turn, can be modelled in terms of its scalar trace ε, which is twice the dissipation-rate of the turbulence kinetic energy (i.e. the scalar trace of the Reynolds stress tensor), and the Reynolds stresses themselves.

Closure is therefore obtained by solving the following transport equation for the scalar quantity ε, derived from the Navier-Stokes equations by differentiating the equation of motion for u_i with respect to x_j and multiplying through by $2\nu\partial u_i/\partial x_j$:

$$\frac{\overline{D}}{Dt}\varepsilon = P_\varepsilon^1 + P_\varepsilon^2 + P_\varepsilon^3 + P_\varepsilon^4 + T_\varepsilon + D_\varepsilon + \Pi_\varepsilon - Y \qquad (3)$$

where:

$$P_\varepsilon^1 = -2\overline{\frac{\partial u_i}{\partial x_j}\frac{\partial u_k}{\partial x_j}}S_{ik}$$

$$P_\varepsilon^2 = -2\overline{\frac{\partial u_i}{\partial x_j}\frac{\partial u_i}{\partial x_k}}S_{jk}$$

$$P_\varepsilon^3 = -2\overline{u_k\frac{\partial u_i}{\partial x_j}}\frac{\partial^2 U_i}{\partial x_j\partial x_k}$$

$$P_\varepsilon^4 = -2\overline{\frac{\partial u_i}{\partial x_k}\frac{\partial u_i}{\partial x_j}\frac{\partial u_k}{\partial x_j}}$$

$$T_\varepsilon = -\frac{\partial}{\partial x_k}\left[\overline{u_k\frac{\partial u_i}{\partial x_j}\frac{\partial u_i}{\partial x_j}}\right]$$

$$D_\varepsilon = \nu\frac{\partial^2\varepsilon}{\partial x_k\partial x_k}$$

$$\Pi_\varepsilon = -\frac{2}{\rho}\frac{\partial}{\partial x_k}\left[\overline{\frac{\partial p}{\partial x_j}\frac{\partial u_k}{\partial x_j}}\right]$$

$$Y = 2\nu\overline{\frac{\partial^2 u_i}{\partial x_j^2}\frac{\partial^2 u_i}{\partial x_j^2}}$$

$S_{ij} = 1/2\left[\partial U_i/\partial x_j + \partial U_j/\partial x_i\right]$ is the mean strain rate, and the terms listed above denote the mixed production, the production by mean velocity gradient, the gradient production, the turbulent production, the turbulent transport, the viscous diffusion, the pressure transport and the dissipation rate terms respectively.

All of the terms in the budget for the dissipation rate of the turbulence kinetic energy are shown in Fig.11a, where the sum of T_ε and Π_ε is reported, instead of the single terms, for comparison purposes. Again the comparison between the NC data and the full channel ones (Fig.11b) obtained by Mansour *et al* (1988) is extremely satisfactory. However, the distribution of the dissipation rate term Y shows to be poorly resolved by the present scheme. This is only due to the relatively low number of grid points in the near-wall region, and must not be ascribed to a limitation of the *Narrow Channel* itself.

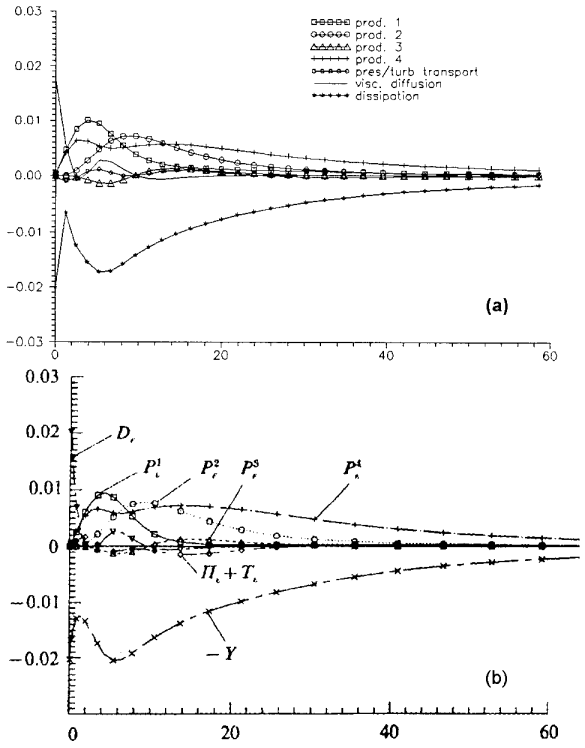

Fig.11 - Terms in the budget of the dissipation rate of the turbulence kinetic energy, in wall coordinates. (a) present NC results; (b) full channel results of Mansour, Kim and Moin.

7. SOME EXAMPLES OF TURBULENCE MODEL TESTING

An exhaustive review of the performances of the various turbulence models is beyond the scope of the present work. As an example of the use which can be done of the NC data, however, two turbulence models are considered in this section and their performances are assessed by comparing the modelled quantities with DNS. This kind of analysis is not innovative in itself: the aspect which has to be emphasised is the use of relatively inexpensive comparative DNS data computed under the *Narrow Channel* assumption.

Model testing is carried out by simply computing the terms which appear in the expressions for the model on the basis of the DNS results.

In the choice of the particular models to be tested, the work of Mansour, Moin and Kim (1988) has been followed and, because of the peculiar properties of the *Narrow Channel* technique, attention has been focused on low Reynolds number closures.

7.1. Algebraic stress models

The main hypotheses underlying the development of algebraic stress models are based on the following physical considerations on the dissipation-rate tensor (Rotta, 1951). In the limit of Re→∞, the dissipation rate tensor tends to isotropy, according to the essentially isotropic structure of turbulence. This implies that

$$2\nu\overline{\frac{\partial u_i \partial u_j}{\partial x_k \partial x_k}} = \frac{2}{3}\delta_{ij}\varepsilon$$

On the other hand, in the limit of Re→0 the energy containing scales and the dissipative ones tend to coincide. The relationship between the two tensors can be consequently written as:

$$\varepsilon_{ij} = \frac{\varepsilon}{K}\overline{u_i u_j}$$

with the possible addition (see for instance Hanjalic and Launder, 1976) of an empirical function of the turbulence Reynolds number which drives the shift between the two above mentioned expressions.

In Fig. 12 the distributions along the coordinate normal to the wall are shown of the four non-zero components of the dissipation rate tensor, compared to the ones predicted by a typical algebraic model. The diagonal terms are quite well predicted by the algebraic model, even if an empirical function different for each component of the dissipation rate tensor would probably further improve the performances of

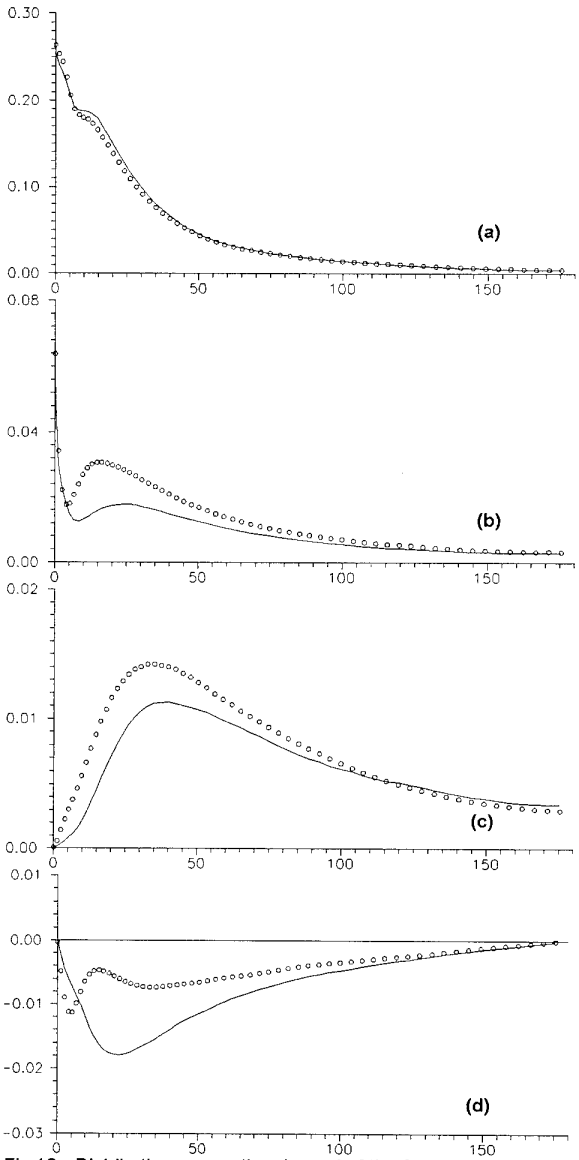

Fig.12 - Distribution across the channel of the four non-zero terms of the turbulence kinetic energy dissipation-rate tensor, compared with the model $\varepsilon_{ij} = \varepsilon/K\,\overline{u_i u_j}$. (a) ε_{11}; (b) ε_{22}; (c) ε_{33}; (d) ε_{12}. Solid line: model. Symbols: NC data.

the model. The off-diagonal component, on the contrary, shows poor agreement with the computed data.
In addition to these considerations on the model itself, what is interesting is again the fact that no substantial differences exist between the present plots and those reported in Mansour *et al* (1988).

7.2 Transport models for ε

The equation describing the transport of ε, defined as twice the trace of the dissipation rate tensor, is often used in turbulence modelling. Models for this equation usually incorporate the sum of a term of production, a term of dissipation and a term of turbulent transport, in addition to a term of viscous diffusion which does not need modelling. For the equation:

$$\frac{\overline{D}}{Dt}\varepsilon = C_{\varepsilon 1}\frac{\varepsilon}{K}P_k - C_{\varepsilon 2}\frac{\varepsilon^2}{K} + C_\varepsilon \frac{\partial}{\partial x_i}\left(\frac{K}{\varepsilon}\overline{u_i u_j}\frac{\partial \varepsilon}{\partial x_j}\right) + \frac{\partial^2 \varepsilon}{\partial x_j \partial x_j}$$

the various coefficients can be considered as constants or functions of the turbulence Reynolds number. In various models the terms in the right hand side are associated with the terms of the transport equation for ε_{ij}. Following for instance Hanjalic and Launder (1976), the sum of P_ε^1 and P_ε^2 is considered and modelled as:

$$P_\varepsilon^1 + P_\varepsilon^2 = C_{\varepsilon 1}\frac{\varepsilon}{K}P_k$$

being P_k the production term in the K equation, and $C_{\varepsilon 1} = 1.275$.

Fig.13 shows the comparison between the modelled term and the exact term computed from the *Narrrow Channel* data: the near-wall peak of the production term is underpredicted by the model, while the behaviour in the outer region is perfectly

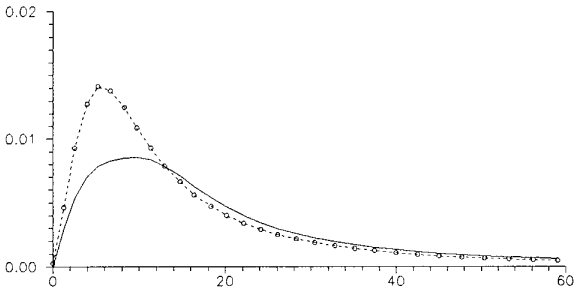

Fig.13 - Distribution of the production term $P_\varepsilon^1 + P_\varepsilon^2$ in the budget of ε, across the channel. Solid line: model. Symbols: NC data.

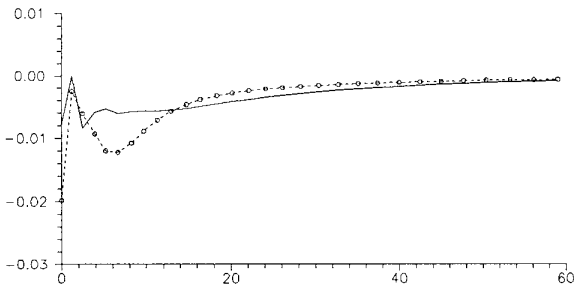

Fig. 14 - Distribution of the dissipation term $-P_\varepsilon^4 + Y$ in the budget of ε, across the channel. Solid line: model. Symbols: NC data.

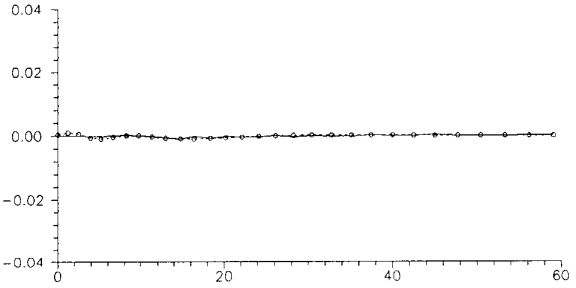

Fig.15 - Distribution of the turbulent transport term T_ε, in the budget of ε, across the channel. Solid line: model. Symbols: NC data.

matched. Similar observations have been drawn by Mansour *et al*, on the basis of the full channel data.

The dissipative term is often modelled introducing a modified dissipation rate $\tilde{\varepsilon}$, in order to get, when approaching the wall, a correct behaviour of the ratio $\varepsilon\tilde{\varepsilon}/K$, which would otherwise be unbounded. This modified dissipation rate is defined by Hanjalic and Launder as:

$$\tilde{\varepsilon} = \varepsilon - \left(\frac{\partial\sqrt{K}}{\partial y}\right)^2$$

The same Authors also introduce a dependence on the turbulence Reynolds number, on the basis of experimental information, so that the modelled terms can be written as:

$$-P_\varepsilon^4 + Y = C_{\varepsilon 2} f_\varepsilon \frac{\varepsilon\tilde{\varepsilon}}{K}$$

where $C_{\varepsilon 2} = 1.8$ and $f_\varepsilon = 1 - \frac{0.4}{1.8}\exp\left[\left(-K^2/6\varepsilon\right)^2\right]$.
Again, Fig.14 shows the model compared with the DNS data. It can be observed, as in Mansour *et al*, that the model underpredicts the data in the near-wall region. It has to be noted, in addition, that steep gradients in the normal direction in the very-near wall region are present. The inadequacy of the results for say $y^+<3$ should anyway be attributed to the poor resolution allowed by the present numerical method (finite differences with geometrical stretching), and not to the *Narrow Channel* hypothesis itself.

The last term of the ε equation which is usually modelled is the turbulent transport term:

$$T_\varepsilon = C_\varepsilon \frac{\partial}{\partial x_i}\left(\frac{K}{\varepsilon}\overline{u_i u_j}\frac{\partial \varepsilon}{\partial x_j}\right)$$

with $C_\varepsilon = 0.15$.

From Fig.15 it is quite evident that this term is so small everywhere in the channel, that modelling errors can but negligibly affect the accuracy of the results.
Quite often the terms P_ε^3 and Π_ε are ignored in the models, on the basis of order-of-magnitude considerations (Tennekes and Lumley, 1972). The results in Fig.11, however, indicate, as observed by Mansour *et al*, that in the near wall region they may become significant, and that their inclusion in the models could be useful.

8. CONCLUSIONS

Numerical data obtained through the Direct Numerical Simulation of *Narrow Channel* flows have been used to compute the various terms in the transport equations for the Reynolds stresses and for the dissipation rate of the turbulence kinetic energy.

The efficiency of the numerical scheme here presented is remarkable, although its accuracy, in terms of spatial resolution in the near-wall region of the flow should be improved. Nevertheless, an illustrative application of the code to the evaluation of an algebraic and a one-equation turbulence model has been presented, which produced satisfactory results.

Despite of the reduced size of the computational domain, which is essential to reduce the computational cost of the numerical simulations, the *Narrow Channel* assumption surprisingly does not seem to affect the quality of the predictions, in terms of production, transport and dissipation of turbulent quantities, as clearly demonstrated by the comparisons with published results based on the DNS of full channel flows.

It can be concluded that, although still limited to relatively low Reynolds numbers, the *Narrow Channel* assumption makes the DNS of channel flows affordable with limited computational resources and offers the researchers involved in the numerical simulation of turbulent flows a cheap and unparalleled tool for testing the performances of various existing or newly formulated turbulence models.

9. REFERENCES

- Baron, A. and Quadrio, M., 1993. Direct Numerical Simulation of Turbulent Flows under the Narrow Channel Assumption, Proceedings of the XIIth Congresso Nazionale AIDAA, Como.
- Hanjalic, K. and Launder, B.E. 1976. Contribution towards a Reynolds-stress closure for low-Reynolds-number turbulence. *J.Fluid Mech.* vol.74, Part IV, pp.593-610
- Horiuti, K., 1987. Comparison of conservative and rotational forms in Large Eddy Simulation of turbulent channel flow. *J. Comp. Physics* vol.71, pp.343-370
- Jiménez, J. and Moin, P., 1991. The minimal flow unit in near-wall turbulence. *J. Fluid Mech.* vol.225, pp.213-240.
- Kim, J., Moin, P. and Moser, R., 1987. Turbulence statistics in fully developed channel flow at low Reynolds number. *J. Fluid Mech.* vol.177, pp.133-166.
- Kim, J. and Moin, P., 1982. Numerical investigation of turbulent channel flow. *J. Fluid Mech.* vol.118, pp.341-377
- Kim, J. and Moin, P., 1985. Application of a fractional-step method to incompressible Navier-Stokes equations. *J. Comp. Physics* vol.59, pp.308-323
- Mansour, N.N., Kim , J. and Moin, P., 1988. Reynolds-stress and dissipation-rate budgets in a turbulent channel flow. *J. Fluid Mech.* vol. 194, pp.15-44
- Rai, M.M. and Moin, P., 1991. Direct Simulations of Turbulent Flow Using Finite-Difference schemes. *J. Comp. Physics* vol.96, pp.15-53
- Rotta, J. 1951. Statistical theory of inhomogeneous turbulence. Part I. *Zeitschrift für Physik* vol.129, p.257
- Schmidt, H., Schumann, U. and Volkert, H. 1984. Three-dimensional, direct and vectorized elliptic solvers for various boundary conditions. DFVLR, Köln
- Smith, C.R. and Metzler, S.P., 1983. The characteristics of low-speed streaks in the near wall region of a turbulent boundary layer. *J.Fluid Mech.* vol.129, pp.27-54
- Spalart, P.R. 1988. Direct simulation of a turbulent boundary layer up to $\mathrm{Re}_\theta = 1400$. *J. Fluid Mech.* vol.187, pp.61-98.
- Tennekes, H. and Lumley, J.L. 1972. A first course in turbulence. MIT Press

10. ACKNOWLEDGMENTS

The Authors are indebted to their collegue L. Vigevano, for several useful discussions.

The present work has been supported by the MURST, Ministero dell'Università e della Ricerca Scientifica e Tecnologica. Some of the computations have been performed thanks of the support of the CILEA, Consorzio Interuniversitario Lombardo per l'Elaborazione Automatica.

ANNEX A

The numerical scheme for advancing the solution of equation (1) from the time level n to the time level $n+1$ is described by the three following substeps, which constitute an explicit Runge-Kutta scheme of third order accuracy for the convective terms and an implicit Cranck Nicholson scheme of second order accuracy for the viscous ones.

For each substep, an intermediate velocity field (u_i^a, u_i^b and u_i^c respectively) is computed, which does not satisfy the mass conservation equation. This last condition is accounted for by solving a related Poisson equation which yields the correction necessary to get the solenoidal fields $\tilde{u}_i$, $\tilde{\tilde{u}}_i$ and eventually u_i^{n+1}

$$u_i^a = u_i^n + \Delta t\left(\gamma_1 H_i\left(u_i^n\right) + \frac{\alpha_1}{\mathrm{Re}}\frac{\partial^2}{\partial x_j \partial x_j}\left(u_i^n + u_i^a\right) + f_i^a\right)$$

$$\frac{\tilde{u}_i - u_i^a}{\Delta t} = -G(\gamma_1\Phi) \qquad D(\tilde{u}_i) = 0$$

$$u_i^b = \tilde{u}_i + \Delta t\left(\gamma_2 H_i(\tilde{u}_i) + \zeta_1 H_i\left(u_i^n\right) + \frac{\alpha_2}{\mathrm{Re}}\frac{\partial^2}{\partial x_j \partial x_j}\left(\tilde{u}_i + u_i^b\right) + f_i^b\right)$$

$$\frac{\tilde{\tilde{u}}_i - u_i^b}{\Delta t} = -G\left(\gamma_2\tilde{\Phi} + \zeta_1\Phi\right) \qquad D\left(\tilde{\tilde{u}}_i\right) = 0$$

$$u_i^c = \tilde{\tilde{u}}_i + \Delta t\left(\gamma_3 H_i\left(\tilde{\tilde{u}}_i\right) + \zeta_2 H_i(\tilde{u}_i) + \frac{\alpha_3}{\mathrm{Re}}\frac{\partial^2}{\partial x_j \partial x_j}\left(\tilde{\tilde{u}}_i + u_i^c\right) + f_i^c\right)$$

$$\frac{u_i^{n+1} - u_i^c}{\Delta t} = -G\left(\gamma_3\tilde{\Phi} + \zeta_2\tilde{\Phi}\right) \qquad D\left(u_i^{n+1}\right) = 0$$

In these equations, G and D stand for the gradient and divergence operators respectively, δ is the finite difference operator, H denotes the discrete counterpart of convective terms and Φ is a pressure-related scalar.

The coefficients assume the following values:

$$\alpha_1 = \frac{4}{15} \quad \alpha_2 = \frac{1}{15} \quad \alpha_3 = \frac{1}{6} \quad \xi_1 = -\frac{17}{60}$$
$$\gamma_1 = \frac{8}{15} \quad \gamma_2 = \frac{5}{12} \quad \gamma_3 = \frac{3}{4} \quad \xi_2 = -\frac{5}{12}$$

$$f_i^a = f_i^b = f_i^c = \begin{cases} 1/3 f_i & \text{for } i = 1 \\ 0 & \text{for } i = 2,3 \end{cases}$$

Direct Simulation of Turbulent Flow in a Square Duct: Reynolds-Stress Budgets

Asmund Huser[1], Sedat Biringen[2] and Ferhat F. Hatay[2]

[1]DNV Technica, P.O.Box 300, N-1322 Høvik, Norway
[2]University of Colorado at Boulder, Boulder, Colorado 80309, USA

Abstract

The data base from a direct numerical simulation of turbulent flow in a square duct is used to calculate all the terms in the Reynolds stress transport equations. The simulation of this complex turbulent flow was performed at a Reynolds number of 600 based on the friction velocity and the duct width. The distributions of the Reynolds stress budget terms along the wall bisector show similar dynamics to wall-bounded turbulent flows with one inhomogeneous direction. Budget terms in the vicinity of the corner demonstrate how transport and redistribution of energy and shear stresses between the Reynolds stress components takes place, promoting the turbulence characteristics of secondary flows of the second kind. The redistribution of energy by pressure velocity correlations can be explained by the low pressures at the cores of streamwise vortices. The data base is also used to evaluate a nonlinear turbulence model in its ability to accommodate the anisotropy of the Reynolds stress tensor in this flow. This anisotropy is known to be entirely responsible for the formation of the secondary flow in noncircular ducts and cannot be captured by linear models.

1 Introduction

The development of transport equations for turbulence, such as for the turbulent kinetic energy and dissipation rate (i.e., first-order closures) and Reynolds stresses and dissipation rate (i.e., second-order closures), has received wide attention (see Speziale[1], Launder[2] and Rodi[3] for reviews). Recent studies indicate that "mild" inhomogeneities may be adequately resolved by first-order closures (Yakhot, Thangam, Gatski, Orszag & Speziale[4]). Second-order closures are more likely to be effective for turbulent flows with strong inhomogeneities. Demuren & Rodi[5] and Speziale[1] demonstrated that an algebraic Reynolds stress model (first-order closure) is able to predict mean secondary flows in a square duct, confirming that the inhomogeneities are relatively mild. However, such models can only predict trends in the mean flow properties, and lack the ability to predict Reynolds stress distributions with sufficient accuracy. The first- and second-order turbulence closures are usually derived by considering homogeneous turbulence and consequently have to be modified when used near solid boundaries. Typically, the "law of the wall" together with damping functions are used to bridge the solution down to the wall. These wall-boundary corrections use a length scale proportional to the wall distance. In the square duct flow, the ambiguity of the wall distance when the corner is approached creates difficulties, and the definition of a length scale independent of the wall distance becomes critical. Michelassi & Shih[6] compared a length-scale model that is independent of the wall distance with other existing length-scale models when calculating flow over a backward-facing step, providing good agreement with existing models. Demuren[7] derived a useful algebraic stress model for calculating secondary flows in ducts with arbitrary cross section, but the model cannot predict shear stresses accurately. Consequently, at the present time there is no turbulence model that is completely capable of predicting the turbulence characteristics of Prandtl's secondary flows of the second kind.

The most important connection between Reynolds stresses and the driving mechanisms for the secondary flow is in the velocity-pressure interaction terms in the full Reynolds stress transport equations. However, these equations have not been investigated in experimental studies or in direct numerical simulations (DNS) for the present flow configuration and closure approximations for the high-order correlations (e.g. the pressure strain terms) are obtained only by physical arguments and order-of-magnitude

Paper presented at the 74th Fluid Dynamics Symposium on "Application of Direct and Large Eddy Simulation to Transition and Turbulence" held at Chania, Crete, Greece, in April 1994.

analyses. By calculating all the terms in the Reynold stress budget directly, the dynamics of the system of equations can be displayed and the fundamental concepts used in the development of second-order turbulence models can be tested and assessed. Along these lines, Mansour, Kim & Moin[8] showed that in turbulent channel flow, all the terms in the turbulence budgets become important near the wall and that existing turbulence models behave poorly in this region. Moser & Moin[9] studied the effects of a mild curvature on Reynolds stress budgets in curved channel flow, demonstrating that DNS results of channel flows can give valuable insight into the dynamics of the turbulent transport equations over a solid wall in the presence of a centrifugal force. In the present work, the effects of two intersecting walls are considered which requires the inclusion of a greater number of terms in the transport equations, resulting in transport and redistribution effects that do not exist in channel and boundary layer flows.

The main purpose of the present work is to obtain a detailed description of turbulent flow in a square duct with emphasis on the origin of the secondary flows. Our earlier work (Huser & Biringen[10]) revealed that the location of and the interaction between bursts from both walls near the corner are responsible for the turbulence characteristics of the square duct flow. Also the instantaneous streamwise vortices are associated with low pressure regions (Kim[11]); this has a significant effect on pressure velocity correlations. Of particular interest in this paper is the high-order terms involving pressure velocity correlations, which contribute significantly to the Reynolds stress balance. We also provide an assessment of a nonlinear $k-\epsilon$ model using the present data base in an attempt to uncover why such models fail to predict the strength of secondary flows of the second kind.

2 Solution Procedure

The present results are generated from a DNS of turbulent flow in a square duct (see Huser[12] and Huser & Biringen[10]). The numerical solution of the Navier-Stokes equations incorporates a time-splitting method and the decoupled equations are solved semi-implicitly by a Runge Kutta procedure. Spatial discretization is done by high-order finite differences and by the Fourier pseudo-spectral method.

The calculations were performed in the fully-developed turbulence regime at a Reynolds number $Re_\tau = u_\tau D/\nu = 600$, where u_τ is the mean friction velocity and D is the duct width; the bulk Reynolds number was $Re_B = U_B D/\nu = 10320$, where U_B is the bulk velocity. The computational mesh consisted of $96 \times 101 \times 101$ grid points in the x, y, z directions, respectively, where x is the streamwise direction and y, z are the wall normal directions; the computational box length was $L_x/D = 6.4$. Statistics presented in this paper were collected during a period of $t = Tu_\tau/D = 10$ time units (T is the dimensional time) after the flow reached a statistically steady state.

3 Reynolds stress budget

Transport equations for the Reynolds stresses are given by:

$$\frac{\partial \tau_{ij}}{\partial t} + \bar{u}_k \frac{\partial \tau_{ij}}{\partial x_k} = P_{ij} + \Pi_{ij} + T_{ij} - \epsilon_{ij} + D_{ij}, \quad (1)$$

where $\tau_{ij} = \overline{u_i' u_j'}$ is the Reynolds stress tensor. The terms in this equation represent the following processes:

$$P_{ij} = -\tau_{ik}\frac{\partial \bar{u}_j}{\partial x_k} - \tau_{jk}\frac{\partial \bar{u}_i}{\partial x_k}, \quad (2)$$

$$\Pi_{ij} = -\overline{u_i'\frac{\partial p'}{\partial x_j}} - \overline{u_j'\frac{\partial p'}{\partial x_i}}, \quad (3)$$

$$T_{ij} = -\frac{\partial}{\partial x_k}\overline{u_i' u_j' u_k'}, \quad (4)$$

$$\epsilon_{ij} = 2\overline{\frac{\partial u_i'}{\partial x_k}\frac{\partial u_j'}{\partial x_k}}, \quad (5)$$

$$D_{ij} = \nabla^2 \tau_{ij}, \quad (6)$$

where P_{ij}, Π_{ij}, T_{ij}, ϵ_{ij}, and D_{ij} denote the production, velocity-pressure gradient, turbulent transport (diffusion), the dissipation rate, and viscous diffusion, respectively. Equations (2-6), are written in $\{\}^+$ variables, which involves using u_τ and ν/u_τ as velocity and length scale, respectively. When presenting distributions of these terms, both $y = Y/D$ (Y is a dimensional coordinate) and y^+ coordinates are considered. The coordinate notation y^+ is given by,

$$y^+ = yRe_\tau. \quad (7)$$

The velocity-pressure gradient correlation, Eq. (3), is usually split into a pressure strain correlation and a pressure diffusion correlation (by the chain rule),

$$\Pi_{ij} = \Phi_{ij} + T_{ij}^P \quad (8)$$

and each term is written,

$$\Phi_{ij} = 2\overline{p' s_{ij}'}, \quad (9)$$

$$T_{ij}^P = -\frac{\partial}{\partial x_k}(\overline{p' u_i'}\delta_{jk} + \overline{p' u_j'}\delta_{ik}), \quad (10)$$

where Φ_{ij} is the pressure strain, T_{ij}^P is the pressure diffusion, $s'_{ij} = (\partial u'_i/\partial x_j + \partial u'_j/\partial x_i)/2$ is the fluctuating strain rate, and δ_{ij} is the Kronecker delta. The pressure-strain correlation is modeled directly, and the pressure-diffusion term is modeled together with the turbulent transport term, Eq. (4). Results from DNS of turbulent channel flow indicate that Π_{ij} should be modeled directly instead of Φ_{ij} because near the wall, Φ_{ij} and T_{ij}^P are opposite-valued and cancel each other when added[8].

Moser & Moin[9] demonstrated the importance of all the terms in the Reynolds stress equations in the presence of a wall, and consequently in the present work, these terms are considered when presenting the budgets along the wall bisector. In the square duct flow, the additional Reynolds stress equations are those for $\overline{u'w'}$ and $\overline{v'w'}$; the $\overline{u'w'}$ equation is similar to the $\overline{u'v'}$ equation, and the effect of the vertical wall on the $\overline{u'v'}$ equation is the same as the effect of the horizontal wall on the $\overline{u'w'}$ equation. Therefore only the $\overline{u'v'}$ equation is presented here, and the terms in the $\overline{u'w'}$ equation can be obtained by rotating the distribution of the terms in the $\overline{u'v'}$ equation by 90° in the transverse plane. The same argument is valid for the $\overline{w'^2}$ and the $\overline{v'^2}$ equations and a presentation of the $\overline{v'^2}$ equation in the transverse plane also describes the $\overline{w'^2}$ equation.

Mean convection occurs in the Reynolds stress budgets describing the square duct flow, but does not occur in budgets describing channel flow. All the other processes noted in Eq. (1) also occur in channel flow, but, due to the intersecting walls in the square duct flow, each term will contain spatial derivatives of the mean quantities in two directions; the mean quantities contain two-dimensional distributions of the three velocity components, the pressure field, and the full Reynolds stress tensor.

The terms in Eq. (1) are ensemble-averaged over the eight similar triangles, and line plots and contour diagrams are presented to show their distributions in the lower left quadrant of the duct, highlighting the effect of the corner and the interaction between the terms.

3.1 Primary normal stress equation

The transport equation for $\overline{u'^2}$ is obtained from Eq. (1) after averaging in x and t,

$$\bar{v}\frac{\partial \overline{u'^2}}{\partial y} + \bar{w}\frac{\partial \overline{u'^2}}{\partial z} = \underbrace{-2(\overline{u'v'}\frac{\partial \bar{u}}{\partial y} + \overline{u'w'}\frac{\partial \bar{u}}{\partial z})}_{P_{11}}$$

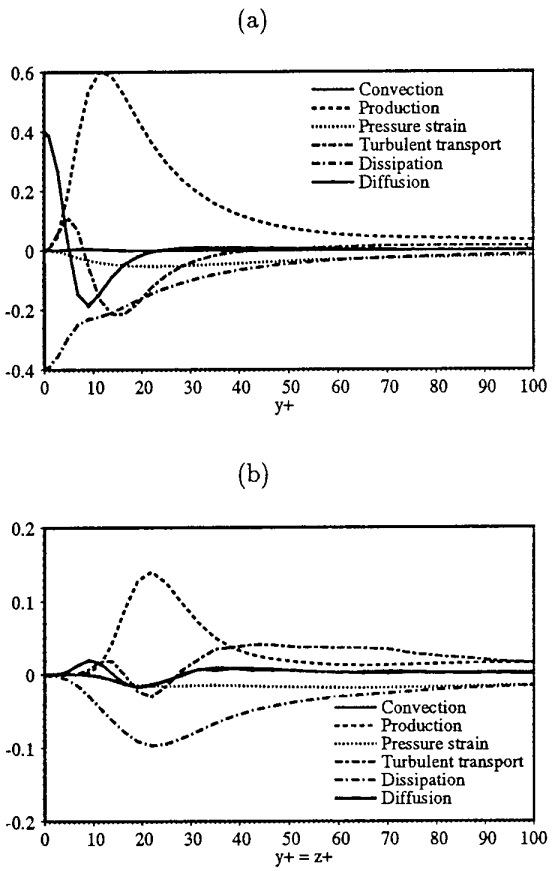

Figure 1: Primary normal stress ($\overline{u'^2}$) budget distributions at different locations: (a) wall bisector; (b) corner bisector.

$$\underbrace{-2\overline{u'\frac{\partial p'}{\partial x}}}_{\Pi_{11}} \underbrace{-(\frac{\partial}{\partial y}\overline{u'u'v'} + \frac{\partial}{\partial z}\overline{u'u'w'})}_{T_{11}} \underbrace{-\epsilon_{11}}_{D_{11}} + \nabla^2_{yz}\overline{u'^2}. \quad (11)$$

Along the wall bisector (Fig. 1a), the peak in production at $y^+ = 12$ is diffused both toward the wall and toward the core of the duct by viscous and turbulent diffusion. Dissipation also increases in the high production area indicated by an inflection point on each side of $y^+ = 12$. At the wall, viscous effects are dominant, and viscous diffusion balances dissipation. The pressure strain correlation is a relatively small term in the $\overline{u'^2}$ budget (note that $\Phi_{11} = \Pi_{11}$), however, this term is important because it is the source of energy to $\overline{v'^2}$ and $\overline{w'^2}$ via Π_{22} and Π_{33}.

Both D_{11} and ϵ_{11} must be zero in the corner (origin), and the maximum value of ϵ_{11} on the corner

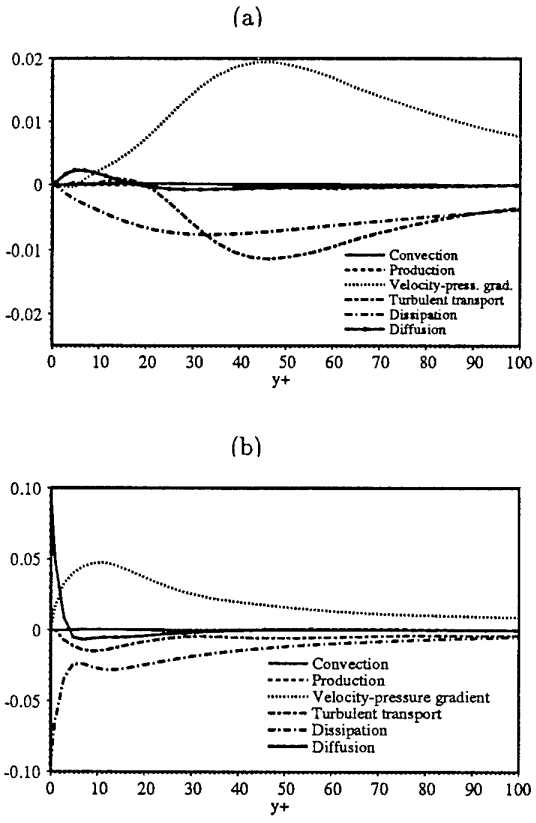

Figure 2: Secondary normal stress budget distributions at the wall bisector, $z = 0.5(z^+ = 300)$: (a) $\overline{v'^2}$; (b) $\overline{w'^2}$.

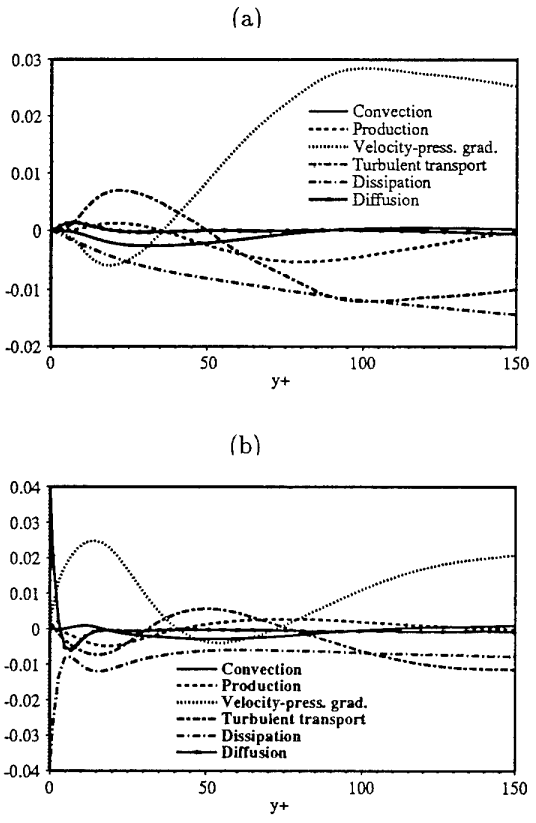

Figure 3: Secondary normal stress budget distributions near the vertical wall at $z^+ = 38(z = 0.064)$: (a) $\overline{v'^2}$; (b) $\overline{w'^2}$.

bisector is caused by the production there (with a saddle point at $y = z = 0.037$, Fig. 1b); this is the same effect that causes the "hump" in dissipation at the wall bisector (at $y^+ = 12$, Fig. 1a).

The imbalance in the budget reaches 10% at the high production areas which may be attributed the slow convergence to statistically steady state. The turbulent diffusion term requires the longest integration time in order to converge because these terms involves derivatives of third-order moments, therefore, in general, the balance in the budgets is added to the turbulent diffusion, i.e. $T^*_{ij} = T_{ij} + \text{balance}$.

3.2 Secondary normal stress equation

The transport equation for $\overline{v'^2}$ is obtained from Eq. (1) after averaging in x and t and reads,

$$\bar{v}\frac{\partial \overline{v'^2}}{\partial y} + \bar{w}\frac{\partial \overline{v'^2}}{\partial z} = \underbrace{-2(\overline{v'^2}\frac{\partial \bar{v}}{\partial y} + \overline{v'w'}\frac{\partial \bar{v}}{\partial z})}_{P_{22}}$$

$$\underbrace{-2v'\overline{\frac{\partial p'}{\partial y}}}_{\Pi_{22}} \underbrace{-(\frac{\partial}{\partial y}\overline{v'^3} + \frac{\partial}{\partial z}\overline{v'v'w'})}_{T_{22}} \underbrace{-\epsilon_{22}}_{D_{22}} + \nabla^2_{yz}\overline{v'^2}. \quad (12)$$

First, considering the distributions of the terms in both $\overline{v'^2}$ and $\overline{w'^2}$ budgets along the wall bisector, $z = 0.5$ (Figs. 2a,b), it can be observed that the energy is gained by the velocity-pressure gradient terms (Π_{22} and Π_{33} provide energy to $\overline{v'^2}$ and $\overline{w'^2}$, respectively, and Π_{11} redistributes energy from $\overline{u'^2}$), transported by the diffusion terms and lost by dissipation; this process is similar to the scenario in turbulent channel flow[9]. When considering the $\overline{v'^2}$ budget distributions near the vertical wall at $z^+ = 34(z = 0.064)$, a strong reduction in Π_{22} is observed at low y-values (Fig. 3a). The negative velocity-pressure gradient correlation, Π_{22}, near the corner below the corner bisector, is associated with a gain in the $\overline{w'^2}$ budget through Π_{33} at the same location[10] (Figs. 3 a and b).

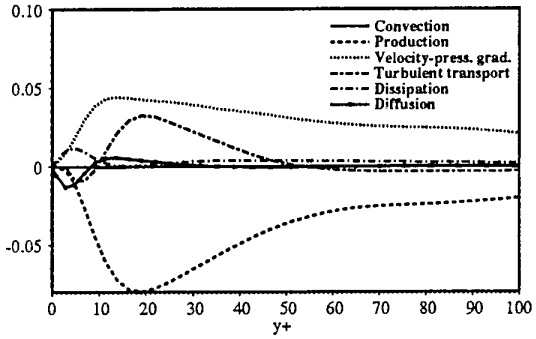

Figure 4: Primary shear stress ($\overline{u'v'}$) budget distributions at the wall bisector, $z^+ = 300(z = 0.5)$.

This effect is called the "corner effect" and is caused by the upward motion of ejections from the horizontal wall directed toward the vertical wall, thus causing a transport from $\overline{v'^2}$ to $\overline{w'^2}$ (vice versa above the corner bisector)[10].

3.3 Primary shear stress equation

Turbulent energy is produced by the interaction of the mean velocity gradient with the primary shear stress[13], and this interaction determines the mean velocity profile. Therefore, an accurate representation of the primary shear stress is the key to turbulence modeling, where usually the mean velocity profile is of primary concern (for the calculation of drag or of any mean flux quantity through the boundary layer). Convection of $\bar{u}$ in the transverse directions is caused by primary shear stress gradients as evident from the $\bar{u}$ transport equation[10], and in the present flow it is promoted by a strong difference in turbulence production between the corner bisector and the wall bisector[14]. The effect which is responsible for the $\bar{u}$ convection is therefore also indirectly responsible for the secondary flow, thus indicating the significance of the $\overline{u'v'}$ (and $\overline{u'w'}$) equations.

Averaging Eq. (1) in x and t for the $\overline{u'v'}$ shear stress, a connection between primary and secondary shear stresses is seen (in the P_{12} term):

$$\bar{v}\frac{\partial \overline{u'v'}}{\partial y} + \bar{w}\frac{\partial \overline{u'v'}}{\partial z} =$$

$$\underbrace{-(\overline{v'^2}\frac{\partial \bar{u}}{\partial y} + \overline{v'w'}\frac{\partial \bar{u}}{\partial z} + \overline{u'v'}\frac{\partial \bar{v}}{\partial y} + \overline{u'w'}\frac{\partial \bar{v}}{\partial z})}_{P_{12}}$$

$$\underbrace{-(\overline{u'\frac{\partial p'}{\partial y}} + \overline{v'\frac{\partial p'}{\partial x}})}_{\Pi_{12}} \quad \underbrace{-(\frac{\partial}{\partial y}\overline{u'v'v'} + \frac{\partial}{\partial z}\overline{u'v'w'})}_{T_{12}}$$

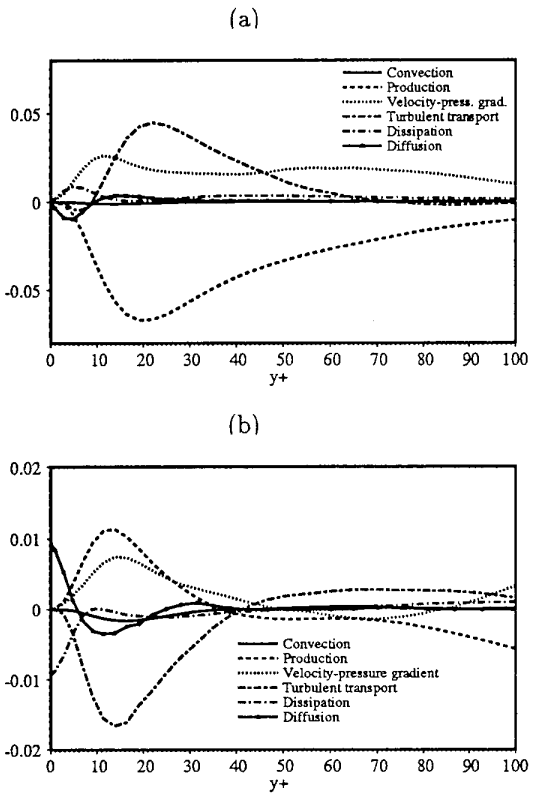

Figure 5: Primary shear stress budget distributions near the vertical wall, $z^+ = 114(z = 0.19)$: (a) $\overline{u'v'}$; (b) $\overline{u'w'}$.

$$\underbrace{-\epsilon_{12}}_{D_{12}} \quad +\nabla^2_{yz}\overline{u'v'}. \tag{13}$$

The shear stresses can be both positive and negative as opposed to the normal stresses which must be positive; a gain to the $\overline{u'v'}$ budget is positive (negative) on the right-hand-side of Eq. (13) if $\overline{u'v'}$ itself is positive (negative); a loss to the $\overline{u'v'}$ budget is positive (negative) on the right-hand-side of Eq. (13) if $\overline{u'v'}$ itself is negative (positive).

Considering first the effects that also occur in channel flow, we investigate the flow field along the wall bisector at $z = 0.5$ (Fig. 4). The distributions compare qualitatively well with data from Mansour *et al.*[8] (not shown in Fig. 4). For $z < 0.3$, the effect of the corner becomes pronounced, and the budget distributions at $z^+ = 114(z = 0.19)$ (Fig. 5a) show that the maximum value in Π_{12} is reduced from 53% to 36% of the maximum local production value. The reduction of Π_{12} appears as a gain to the $\overline{u'w'}$ budget through Π_{13} for $y^+ < 40$ (Fig. 5b), which is one of the mechanisms by which positive $\overline{u'w'}$ shear stress

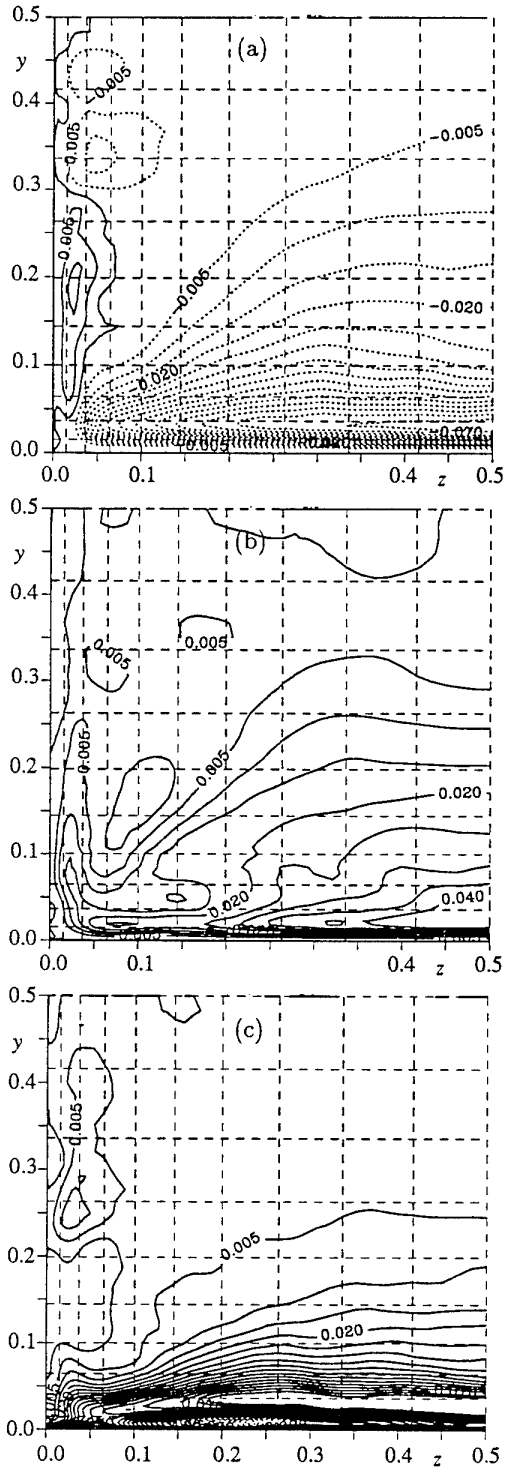

Figure 6: Ensemble-averaged contour plots of terms in the $\overline{u'v'}$ transport equation. Increment=0.005; negative (nonzero) contour levels are dotted: (a) production; (b) velocity-pressure gradient; (c) pressure strain.

is produced[10]. The other source of the positive primary shear stress near the corner is the production term, represented by P_{13} in Fig. 5(b). Positive $\overline{u'v'}$ is produced above the corner bisector similar to the production of $\overline{u'w'}$ below the corner bisector, and the main contributors are P_{12} and Π_{12} (Figs. 6 a and b).

The pressure-strain term, Φ_{12}, which is the term usually modeled, behaves similar to the Π_{12} term near the corner, but the gain in Φ_{12} along the vertical wall for $y < 0.2$ is much less than the gain in Π_{12} (Figs. 6 b and c). Also, due to the "splatting" effect[15], the pressure strain term, Φ_{12}, has a local minimum value near the wall in channel flow, making it more complicated to model than the velocity-pressure gradient term. As implied by Mansour *et al.*[8], modeling of Π_{ij} may be easier than modeling of Φ_{ij} because the pressure transport term acts differently than the turbulent transport term and lumping them in a model for $(T_{12} + T_{12}^P)$ requires the model to describe two different effects.

3.4 Secondary shear stress equation

This is perhaps the most interesting equation among the turbulent transport equations considered in this work because it does not exist in simple turbulent shear flows, and little is known about this equation from experimental or numerical studies. Modelling of this equation is reviewed by Demuren & Rodi[5], indicating that present turbulence models are not capable of capturing the turbulence characteristics of this stress component. The significance of the secondary shear stress is manifested in its appearance in the production term in the mean streamwise vorticity equation. The secondary shear stress also appears in the $\overline{v'^2}$ and the $\overline{u'v'}$ budgets in the production terms.

The transport equation for $\overline{v'w'}$ is obtained from Eq. (1) after averaging in x and t,

$$\bar{v}\frac{\partial \overline{v'w'}}{\partial y} + \bar{w}\frac{\partial \overline{v'w'}}{\partial z} =$$

$$\underbrace{-\left(\overline{v'w'}\frac{\partial \bar{v}}{\partial y} + \overline{w'^2}\frac{\partial \bar{v}}{\partial z} + \overline{v'^2}\frac{\partial \bar{w}}{\partial y} + \overline{v'w'}\frac{\partial \bar{w}}{\partial z}\right)}_{P_{23}}$$

$$\underbrace{-\left(\overline{w'\frac{\partial p'}{\partial y}} + \overline{v'\frac{\partial p'}{\partial z}}\right)}_{\Pi_{23}} \quad \underbrace{-\left(\frac{\partial}{\partial y}\overline{v'v'w'} + \frac{\partial}{\partial z}\overline{v'w'w'}\right)}_{T_{23}}$$

$$\underbrace{-\epsilon_{23}}_{} \quad \underbrace{+\nabla^2_{yz}\overline{v'w'}}_{D_{23}}. \qquad (14)$$

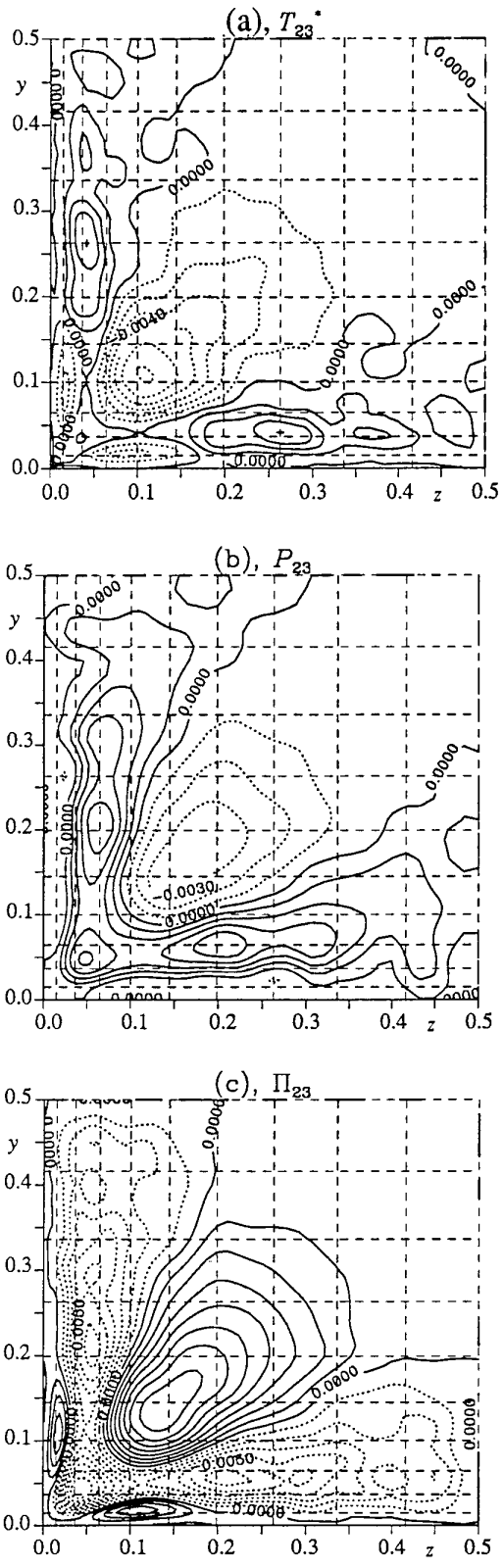

Figure 7: Ensemble-averaged contour plots of the terms in the $\overline{v'w'}$ transport equation. Increment=0.001; negative (nonzero) contour levels are dotted: (a) turbulent transport + balance; (b) production; (c) velocity-pressure gradient; (d) pressure strain.

Contour plots of the three dominant terms in Eq. (14), and contour plot of Φ_{23}, reveal that transport processes are concentrated near the corner and along the walls (Fig. 7). Along the wall bisectors, all the terms in Eq. (14) are zero. In §3.5, the interaction between velocity-pressure gradient terms are considered together with the typical turbulence structure in order to offer an explanation of the particular arrangement of Π_{23}.

The imbalance of this budget is small for $y, z < 0.3$ (less than 10%) and therefore the transport processes are truly represented by T_{23}^*. Along both walls, there is a positive production of $\overline{v'w'}$ (Fig. 7b) caused by the secondary Reynolds stresses, and this P_{23} balances part of the negative contribution from Π_{23}. The turbulent diffusion term, T_{23}, is negative along the corner bisector for y and $z > 0.06$ (Fig. 7a); hence, parts of the production of negative $\overline{v'w'}$ by Π_{23} along the walls (for $z > 0.12$ at the horizontal wall) is diffused to the corner bisector by T_{23} (Fig. 7a).

Also for the secondary shear stress equation, Π_{23} appears to be easier to model than Φ_{23} because the wall behavior is simpler in the former (compare Figs. 7c and d).

3.5 Shear stress interactions

The coupling between the shear stress budgets is a troublesome issue for turbulence modelers both

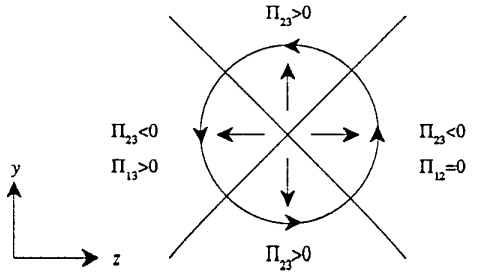

Figure 8: Schematic division of counter-clockwise rotating streamwise vortex in four sectors by the sign of $\Pi_{23} = -\overline{w'\partial p'/\partial y} - \overline{v'\partial p'/\partial z}$. The straight arrows indicates the direction of the pressure gradients.

in deriving the models and in solving the coupled equations numerically[7]. Interactions and the interaction mechanisms between shear stresses must be addressed to resolve the first issue and this is attempted here.

Returning to the secondary shear stress budget, Figure 7(c) illustrates that Π_{23} is the main source of negative secondary shear stress with a rather complicated arrangement of the contours in the transverse plane. The particular arrangement of the Π_{23} contours (Fig. 7c) can be explained by a model of the two mean streamwise vortices near the corner. Considering only the counter-clockwise rotating streamwise vortex near the corner, below the corner bisector, this vortex can be divided in four sectors, as displayed schematically in Fig. 8. By determining the sign of the Π_{23} term in each of these sectors, it can be seen that the combined effects of low pressure in the center of the vortex and the sense of rotation of the vortex result in positive Π_{23} in the upper and lower sectors and negative Π_{23} in the left and right sectors. This pattern is clearly observed in the contour plot of Π_{23} (Fig. 7c) where the center of the streamwise vortex below the corner bisector is located at $(y, z) = (0.05, 0.11)$, close to the local minimum in mean streamwise vorticity.

These effects on the $\overline{v'w'}$ budget are observed to occur concurrently with similar effects on the primary shear stress budgets. Near the corner there is an interaction between the secondary shear stress and the primary shear stresses; this interaction becomes one of the source of $-\overline{v'w'}$. Considering the $\overline{u'v'}$ budget, Π_{12} is positive in the triangle near the vertical wall, above the corner bisector (Fig. 6b) for $y < 0.1, z < 0.05$. This "gain" in the $\overline{u'v'}$ budget does not appear as an increase in $\overline{u'v'}$ itself at this location, but is redistributed to $-\overline{v'w'}$ by Π_{23} (explaining the strong $-\overline{v'w'}$ at this location). The off-diagonal velocity-pressure gradient terms together with the simplified model of the ejection structure near the corner (Fig. 8), can provide an explanation of this co-occurrence of high Π_{12} and $-\Pi_{23}$ above the corner bisector. The same mechanism is present below the corner bisector with co-occurrence of Π_{13} and $-\Pi_{23}$ (considering ejections from the horizontal wall). Assuming that the main contributions to Π_{13} is from $-\overline{u'\partial p'/\partial z}$ ($\overline{w'\partial p'/\partial x}$ is small), it can be deduced that this term has positive maximum values at the corner (below the corner bisector) because negative instantaneous transverse pressure gradients are most frequently correlated with positive u' in this region as a result of the occurrence of a streamwise vortex during an ejection. The left side of the vortex belonging to an ejection from the horizontal wall that can occur close to the left corner has a negative $\partial p'/\partial z$ associated with a positive u'. Again, this may be explained by the low pressure at the vortex core and the transfer of high momentum fluid towards the corner by the same vortex.

In this section we have discussed how the co-occurrence the off-diagonal velocity-pressure gradient correlations can explain connections between the three shear stresses. Also it is implied that these connections may interchange shear forces, and that this redistribution can proceed in both directions depending on the rotational sense of the vortex in an ejection. In channel flow, the redistribution effects cancel out in the mean since the streamwise vortices do not have any preferred location. In other geometries which experience turbulence driven secondary flows, such observations may be applied towards a general model.

4 Evaluation of a Nonlinear Closure Model

4.1 Model Description

Nonlinear eddy-viscosity models comprise the simplest closure set to predict secondary flows and include nonlinear strain-dependent terms in addition to the Newtonian stress terms. Nonlinearity and anisotropy are therefore introduced in the closure set without adding new closure equations. The nonlinear $k - \epsilon$ model of Speziale[16] is based on arguments from continuum mechanics whereas Yoshizawa[17] formulated a similar model by exploiting the two-scale Direct-Interaction Approximation (DIA) theory of Kraichnan[18]. Rubinstein and Barton[19] obtained a nonlinear model through renormalization group for-

mulation of Yakhot and Orszag[20].

In this section, we will examine the nonlinear turbulence model of Speziale[16] in its capability to represent the anisotropy induced by the intersecting walls of the square duct flow. This particular model differs from other $k-\epsilon$ models in only the specified model constants; therefore, the following evaluation is qualitatively valid for the other models referenced above[17,19].

The evaluation of the Speziale model[16] will be based on the results from the present data base using ensemble-averaged mean flow quantities, mean strain rate, turbulent kinetic energy, and turbulent dissipation rate. These quantities are used in the model to make estimates of the Reynolds stress distributions in the cross-flow plane. The model predictions are then directly compared with the results from the DNS.

In the present problem, the formation of the secondary flow is directly associated with the generation of streamwise vorticity, $\overline{\Omega}_x = \frac{\partial \overline{w}}{\partial y} - \frac{\partial \overline{v}}{\partial z}$; the transport equation for this quantity can be written as

$$\overline{v}\frac{\partial \overline{\Omega}_x}{\partial y} + \overline{w}\frac{\partial \overline{\Omega}_x}{\partial z} = \nu\left(\frac{\partial^2 \overline{\Omega}_x}{\partial y^2} + \frac{\partial^2 \overline{\Omega}_x}{\partial z^2}\right) + \Phi. \quad (15)$$

From this formulation, the source term, Φ, for the secondary flow can be shown to be solely a function of the anisotropy of the turbulent stresses which reads[16]:

$$\Phi = -\frac{\partial^2 (R_{22} - R_{33})}{\partial y \partial z} + \frac{\partial^2 R_{23}}{\partial y^2} - \frac{\partial^2 R_{23}}{\partial z^2}. \quad (16)$$

Linear turbulence models are based on the eddy-viscosity hypothesis of Boussinesq and assume Newtonian (isotropic) behavior of the turbulent stress tensor and are not capable of predicting the secondary flow in this situation. Any alternative Reynolds-averaged approach to the problem should allow for the anisotropic nature of the turbulent stresses. Speziale[16] proposed the following $k-\epsilon$ model satisfying both realizability and invariance constraints as the next highest algebraic approximation:

$$R_{ij} = \frac{2}{3}k\delta_{ij} - 2C_\mu \frac{k^2}{\epsilon}\overline{S}_{ij} - 4C_D C_\mu^2 \frac{k^3}{\epsilon^2}\left(\overset{o}{\overline{S}}_{ij} + \overline{S}_{ik}\overline{S}_{kj} - \frac{1}{3}\overline{S}_{kl}\overline{S}_{kl}\delta_{ij} - \frac{1}{3}\overset{o}{\overline{S}}_{kk}\,\delta_{ij}\right) \quad (17)$$

where

$$\overline{S}_{ij} = \frac{1}{2}\left(\frac{\partial \overline{u}_i}{\partial x_j} + \frac{\partial \overline{u}_j}{\partial x_i}\right) \quad (18)$$

is the mean strain rate tensor and

$$\overset{o}{\overline{S}}_{ij} = \frac{\partial \overline{S}_{ij}}{\partial t} + \overline{u}_k\frac{\partial \overline{S}_{ij}}{\partial x_k} - \overline{S}_{kj}\frac{\partial \overline{u}_i}{\partial x_k} - \overline{S}_{ki}\frac{\partial \overline{u}_j}{\partial x_k} \quad (19)$$

is the frame-indifferent Oldroyd derivative of $\overline{S}_{ij}$. The optimized model constants are $C_\mu = 0.09$ and $C_D = 1.68$ as used by Speziale for the turbulent rectangular duct flow[16].

4.2 Evaluation of the Model

Quantitative estimates of both the mean strain rate and the Reynolds-stress tensors are obtained from the DNS data base. The turbulence model is then employed to predict the Reynolds stresses by using the mean strain rate tensor available from the DNS data. In the same way, the source terms in the streamwise vorticity equation are evaluated by numerical means. The model *approximations* to the source terms are then compared with the DNS data. The model constants used in the evaluation process are those given by Speziale as optimized values. No attempt was made in the present study to further optimize these quantities.

Figures 9 and 10 compare cross-stream plane distributions of $R_{22} - R_{33}$ and R_{23} obtained from the DNS and from the model. The form of the anisotropy is found to be reasonably represented by the model only in the close vicinity of the corner. Away from the corner, discrepancies become significant.

Figure 11 displays the source terms for the secondary flow as they appear in the streamwise vorticity equation from DNS and from the model. It is apparent that the dynamo of the secondary flow is situated close to the walls and its strength increases towards the corner while at the very close proximity of the corner the strength actually diminishes as evident from both the model predictions and from the DNS data. However, there are some significant differences between the model behavior and the DNS results. For example, there is a difference of two orders of magnitude between the model predictions and DNS data for the source terms which are based on the second order spatial derivatives of the predicted stresses. Moreover, this is caused by grossly negative values predicted by the model for the secondary normal stresses leading to an unrealistic partition of the turbulent kinetic energy between the primary and the secondary flows and to a weak secondary flow pattern.

5 Conclusions

The data base from a direct numerical simulation of fully developed turbulent flow in a square duct is employed to find all the terms in the Reynolds stress transport equations. By considering the turbulent

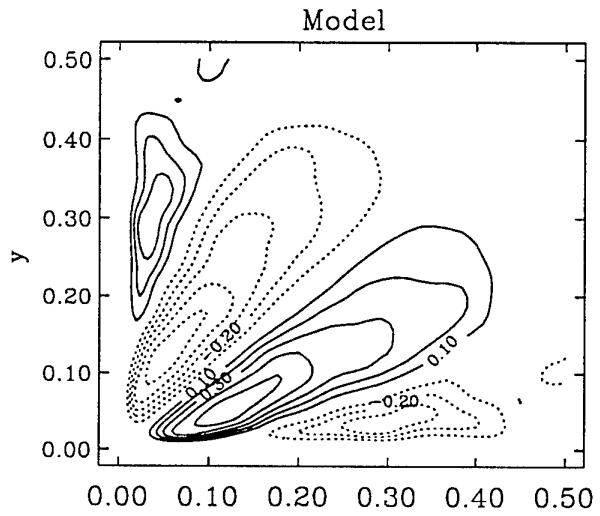

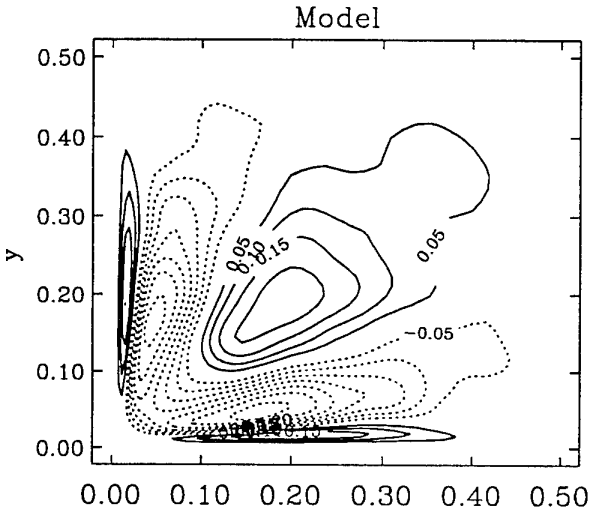

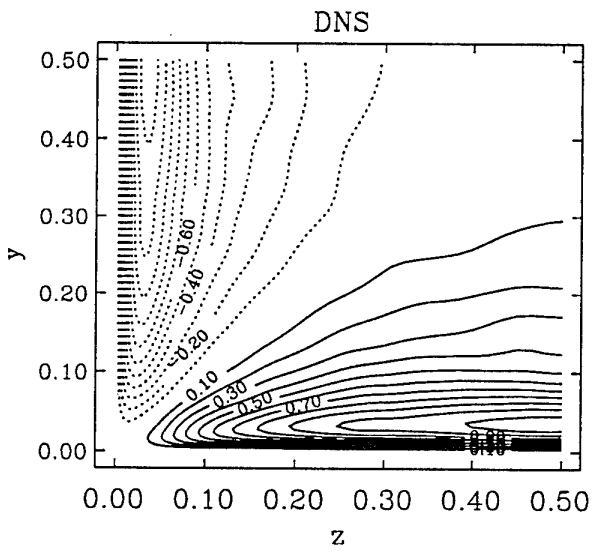

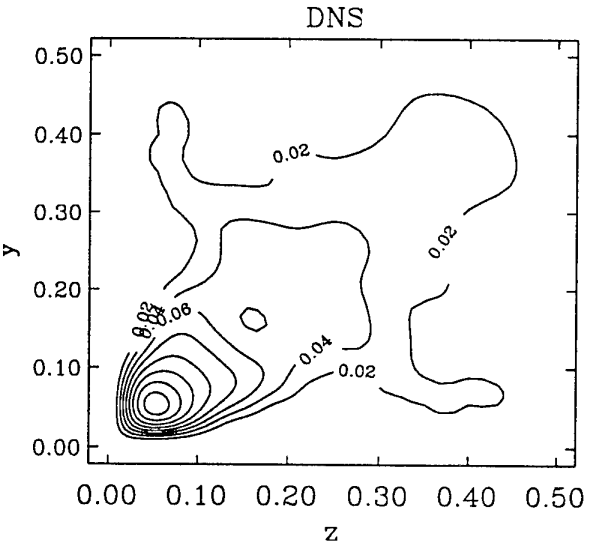

Figure 9: Comparison of anisotropy term R_{23} from DNS data and the Speziale's model[16].

Figure 10: Comparison of anisotropy term $R_{22} - R_{33}$ from DNS data and the Speziale's model[16].

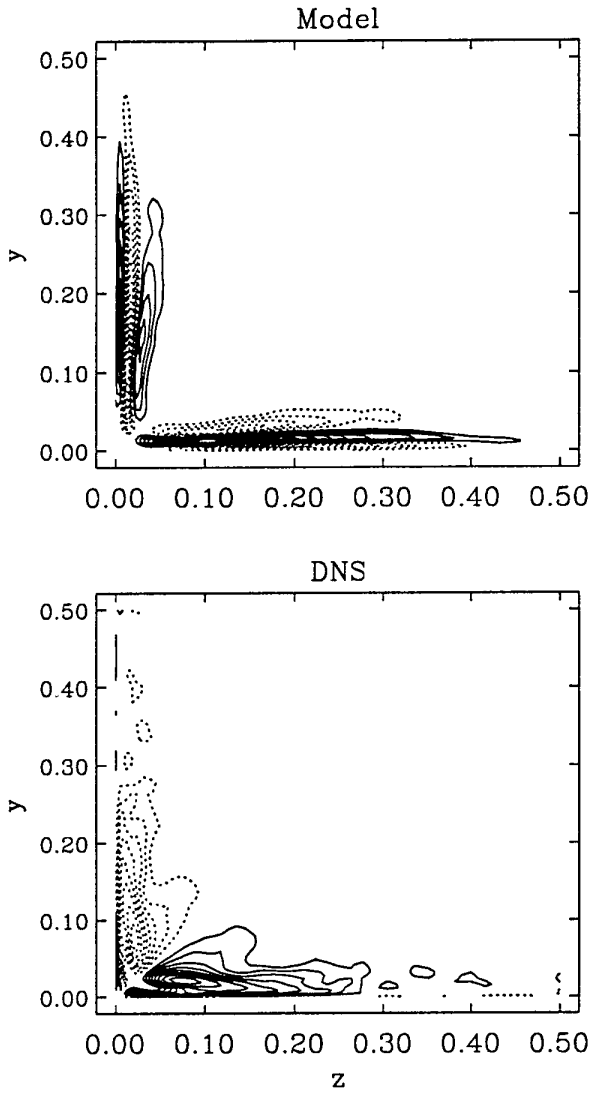

Figure 11: Comparison of the source term in the $\overline{\Omega}_x$ equation, $-\frac{\partial^2(R_{22}-R_{33})}{\partial y \partial z} + \frac{\partial^2 R_{23}}{\partial y^2} - \frac{\partial^2 R_{23}}{\partial z^2}$, from the DNS data and the Speziale's model[16]. The model-predicted values lie between -5000 and +5000 in the upper plot whereas the range of DNS values in the lower plot is between -250 and 250.

transport equations, the complete dynamics of the shear stress and energy transport in the transverse plane of the square duct is displayed; the terms in this set of equations are used to explain the mechanisms responsible for the turbulence characteristics of secondary flow of the second kind. It is shown that the exchange between the two primary *shear* stresses through the production and the velocity-pressure gradient terms is the main contributor to the anisotropic primary shear stress in the corner; these effects are responsible for the convection of mean streamwise velocity. Similar effects are also responsible for the redistribution of energy between the secondary *normal* stresses which become partly responsible for the secondary flow. A redistribution of stresses from the *primary* shear stress to the *secondary* shear stress through the velocity-pressure gradient terms also contributes to the secondary shear stress which in turn plays an important role in the production of the mean secondary flow. However, there is also energy transfer from the secondary shear stress to the primary shear stresses through the transfer terms. In essence, all the shear stress components are linked through the velocity-pressure gradient terms and exchange energy with each other. These effects are explained by the location of the ejection structure near the corner, and the interaction between bursts from the two intersecting walls, where the redistribution mechanisms are directly related to the low pressure and high streamwise velocity in the core of streamwise vortices. It is suggested that the redistributive effects are described by a model for the velocity-pressure gradient instead of the traditional pressure strain model. The data base is also used to evaluate the nonlinear $k-\epsilon$ Speziale model[16]. Evaluation of this nonlinear model with the DNS data reveals that although some anisotropy close to the corners is captured by the model, the distributions and the magnitudes of the source terms of the $\overline{\Omega}_x$ equation are not in agreement.

Acknowledgments

The first author acknowledges The Fulbrigth Foundation, The Norwegian Space Agency and The Royal Norwegian Council for Scientific and Industrial Research (NTNF) for financial support. Acknowledged is also Cray Research for providing computer-time. Partial support for this study was provided by ONR Grant N00014-91-J-1086 with J.A. Fein as the Technical Monitor.

References

[1]Speziale, C.G. 1991 Analytical Methods for the Development of Reynolds- stress Closures in Turbulence. *Ann. Rev. Fluid Mech.* **23**, 107.

[2]Launder, B.E. 1989 Phenomenological Modelling: Present ... and Future? *Lecture Notes in Physics* **357**, 439.

[3]Rodi, W. 1980 *Turbulence Models and Their Application in Hydraulics.* International Association for Hydraulic Research.

[4]Yakhot, V., Thangam, S., Gatski, T.B., Orszag, S.A., and Speziale, C.G. 1991 Development of Turbulence Models for Shear Flows by a Double Expansion Technique. *ICASE report no.* **91-65**.

[5]Demuren, A.O. and Rodi, W. 1984 Calculation of Turbulence-driven Secondary Motion in Noncircular Ducts. *J. Fluid Mech.* **140**, 189.

[6]Michelassi, V. and Shih, T.-H. 1991 Low Reynolds Number Two-Equation Modeling of Turbulent Flows. *NASA* **TM-104363**.

[7]Demuren, A.O. 1990 Calculation of Turbulence-driven Secondary Motion in Ducts with Arbitrary Cross-section. *AIAA* **90-0245**.

[8]Mansour, N.N., Kim, J. and Moin, P. 1988 Reynolds-stress and Dissipation Rate Budgets in a Turbulent Channel Flow. *J. Fluid Mech.* **194**, 15.

[9]Moser, R.D. and Moin, P. 1987 The Effects of Curvature in Wall-bounded Turbulent Flows. *J. Fluid Mech.* **175**, 479.

[10]Huser, A. and Biringen, S. 1993 Direct Numerical Simulation of Turbulent Flow in a Square Duct. *J. Fluid Mech.* **257**, 65.

[11]Kim, J. 1989 On the Structure of Pressure Fluctuations in Simulated Turbulent Flow. *J. Fluid Mech.* **205**, 421.

[12]Huser, A. 1992 Direct Numerical Simulation of Turbulent Flow in a Square Duct. Doctoral thesis, University of Colorado, Boulder, USA.

[13]Hinze, J.O. 1959 *Turbulence* p. 252 New York: Mc.Graw-Hill.

[14]Gessner, F.B. 1973 The Origin of Secondary Flow in Turbulent Flow Along a Corner. *J. Fluid Mech.* **58**, 1.

[15]Moin, P. and Kim, J. 1982 Numerical Investigation of Turbulent Channel Flow. *J. Fluid Mech.* **118**, 341.

[16]Speziale, C. G. 1987 On Nonlinear $k-l$ and $k-\epsilon$ Models of Turbulence. *J. Fluid Mech.* **178**, 450.

[17]Yoshizawa, A. 1984 Statistical analysis of the deviation of the Reynolds Stress from its eddy-viscosity representation. *The Physics of Fluids*, **27**, 1377.

[18] Kraichnan, R. H. 1964 Direct-Interaction Approximation for shear and thermal driven turbulence. *The Physics of Fluids*, **7**, 1048.

[19] Rubinstein, R. & Barton, J. M. 1990 Nonlinear Reynolds stress models and the renormalization group. *Phys. of Fluids,* **A**, **2**, 1472.

[20] Yakhot, V. & Orszag, S. A. 1986 Renormalization group theory. *J. Sci. Comput.*, **1**, 3.

Numerical Simulation of Supersonic Boundary Layer Transition

Y. Guo[1], N.A. Adams[2], N.D. Sandham[3], L. Kleiser[1]
DLR, Institute for Fluid Mechanics,
Bunsenstr. 10, D-37073 Göttingen, Germany

ABSTRACT

The present contribution reviews some of the recent progress obtained at our group in the direct numerical simulation (DNS) of compressible boundary layer transition. Elements of the different simulation approaches and numerical techniques employed are surveyed. Temporal and spatial simulations, as well as comparisons with results obtained from Parabolized Stability Equations, are discussed. DNS results are given for flat plate boundary layers in the Mach number range 1.6 to 4.5. A temporal DNS at Mach 4.5 has been continued through breakdown all the way to the turbulent stage. In addition results obtained with a recently developed extended temporal DNS approach are presented, which takes into account some nonparallel effects of a growing boundary layer. Results from this approach are quite close to those of spatial DNS, while preserving the efficiency of the temporal DNS.

1. INTRODUCTION

Reliable prediction and modeling of transition in boundary layers on high-speed vehicles is still an unsolved problem. Much of the present theoretical knowledge on transition stems from linearized theories or the parabolized stability equations (PSE) (cf. Arnal [5], Bertolotti [8], Chang & Malik [11], Cheng [12], Herbert [34, 35], Kufner *et al.* [41], Mack [44, 45, 46], Malik *et al.* [47], Ng & Erlebacher [48], Zang *et al.* [72]). These theories describe the behavior of small-amplitude disturbances relevant for the initial stages of transition in a low-noise environment. Significantly less is known on the nonlinear phenomena and mechanisms in the later stages of transition. Due to enormous difficulties encountered in high-speed flow experiments (Fernholz & Finley [21], Kendall [38], Kosinov *et al.* [40], Spina *et al.* [67]), few experimental results uncovering flow phenomena at the nonlinear stages of transition have been published. This is quite different from the incompressible flow case (cf. Saric [58]). Thus presently there is a strong interest in numerical simulation techniques for studying transition (Kleiser & Zang [39], Reed [55]) and for obtaining databases in more "realistic" turbulent shear flows. In recent years significant progress has been made with direct numerical simulations (DNS) of transition in compressible flows by several research groups. Different instability mechanisms have been investigated, and in some cases transition has been simulated up to the beginning turbulence. Detailed information on the formation and evolution of transitional flow structures, as well as on the distribution of statistical turbulence data in the transitional regime, has become available. It appears that some basic mechanisms responsible for the transitional flow development in high-speed flows are now being understood. In the present contribution, we review some recent progress made at our group. Some related development at other groups is also included, but no extensive review of the field is given, due to space limitation.

In the DNS of a transitional boundary layer, the computational domain is usually a truncation of the physical domain, as is shown by the dashed lines in figure 1. We designate x as the streamwise direction, y as the spanwise direction and z as the wall-normal direction. The boundary layer thickness, δ_0, increases in the streamwise direction. Currently, there are two approaches used in DNS: spatial DNS (SDNS) and temporal DNS (TDNS). In an SDNS, inflow boundary conditions are prescribed and the flow develops spatially in the streamwise direction. This is the closest numerical realization of a transition experiment. Due to the difficulties in finding appropriate inflow and outflow boundary conditions at the domain truncation planes, the computational box is usually quite long in the streamwise direction (typically several dozen wavelengths of the primary instability waves at high Mach number). This requires very large computing resources. So far except for a few cases (Pruett & Chang [53], Rai & Moin [54]), SDNS has been mainly limited to the earlier stages of the transition (Eißler & Bestek [17], Fasel *et al.* [19], Pruett *et al.* [52], Reed [55], Saric & Reed [59], Thumm *et al.* [69]).

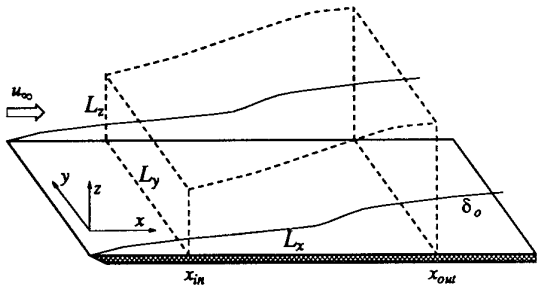

Figure 1: Sketch of the computational domain of a growing boundary layer.

Since the development of boundary layers in the streamwise direction is rather slow in comparison to that of an instability wave, a local parallel flow assumption is often made and the inflow/outflow boundary conditions are replaced by periodic boundary conditions. This is the TDNS approach (cf. Kleiser & Zang [39]). Because the flow is assumed to be periodic in the streamwise direction, the computational box can be very short (one or a few primary instability wavelengths) and Fourier spectral schemes can be used in this direction. Thus TDNS is a highly efficient approach. Using this approach, the DNS of a complete subharmonic transition process from

[1]Present address: Institute of Fluid Dynamics, ETH Zentrum, CH-8092 Zürich, Switzerland.

[2]Present address: Center for Turbulence Research, NASA-Ames Research Center, Moffett Field, CA 94035-1000, U.S.A.

[3]Present address: Queen Mary and Westfield College, London E1 4NS, U.K.

Paper presented at the 74th Fluid Dynamics Symposium on "Application of Direct and Large Eddy Simulation to Transition and Turbulence" held at Chania, Crete, Greece, in April 1994.

laminar to turbulent boundary layer at $M_\infty = 4.5$ has recently been performed by Dinavahi, Pruett & Zang [15] and by our group (see section 3). For other recent work on DNS of compressible boundary layer transition, readers are referred to Adams [1], Adams & Kleiser [2, 3, 4], Delfs [14], Ducros *et al.* [16], Erlebacher & Hussaini [18], Pruett & Zang [50], Sandham & Adams [56] and Sandham *et al.* [57].

One drawback of TDNS is its inability to take into account nonparallel effects, due to the use of the local parallel flow assumption. In order to study the effect of a growing boundary layer on instability waves and transition, the computational box is moved downstream at a speed, c_T, which is close to the group speed of the dominant instability waves under consideration, and the boundary layer grows in time (cf. Spalart & Yang [66]). For convenience, we refer to Spalart & Yang's approach as the standard TDNS approach in this study. However, unlike for incompressible flow, this approach turns out to be unsatisfactory for compressible boundary layer flows. Considerable discrepancies were found in the obtained growth rates of the instability waves between this approach and other sources, e.g., parabolized stability equations (PSE, Bertolotti [6]) and SDNS (Guo *et al.* [30]). In order to improve the accuracy of temporal DNS for nonparallel boundary layer flows, a new temporal approach was proposed by Guo *et al.* [29], which takes into account the nonparallelity of the basic flow and linear perturbations within the temporal simulation method.

In order make a quantitative comparison between temporal and spatial DNS, we have also made significant efforts recently towards spatial DNS. Two spatial DNS codes have been developed. One is a "conventional" approach which employs a sixth order Padé scheme in the nonperiodic streamwise and wall-normal directions and a Fourier collocation scheme in the spanwise direction (Guo & Adams [25]). The other is rather "unconventional": it utilizes a "spatial window function" to truncate the computational domain from a physical system in the streamwise direction, and as a result a Fourier scheme can be used efficiently in the non-periodic streamwise direction (Guo *et al.* [28]). Extensive comparison between the extended temporal DNS approach and our two spatial DNS approaches has shown that the use of the extended DNS is essential in obtaining quantitative agreement with the spatial approaches at high Mach numbers (Guo *et al.* [30]). This technique has also been used in our newly developed temporal DNS approach for numerical simulation of compressible turbulent boundary layers (Guo & Adams [26]).

The structure of this paper is as follows. In section 2, numerical techniques employed are briefly discussed. Results obtained with temporal DNS for transition at various Mach numbers are summarized in section 3. In section 4, we present our recent efforts towards both temporal and spatial DNS of nonparallel boundary layer flows. Issues such as modeling nonparallel effects in a temporal DNS and inflow/outflow boundary treatments in a spatial DNS are discussed. Our recent progress in the DNS of compressible turbulent boundary layers using a temporal approach is also outlined. Concluding remarks are given in section 5.

2. NUMERICAL METHODS

This section contains a brief discussion of the numerical methods used to obtain the simulation results presented later. The discretization of the equations of motion follows the method-of-lines approach. That is, in a first step the system of partial differential equations given by the Navier-Stokes equations is transformed into a system of ordinary differential equations by a discrete approximation of the spatial derivatives. The resulting system is then projected forward in time using a standard method.

2.1 Spatial Discretization

Computational efficiency requires a scheme of high order (Kleiser & Zang [39]). Typical members are spectral schemes (Canuto *et al.* [10]). For direct simulation of transitional and turbulent flows, where flow phenomena are dominated by convection and diffusion of eddies, besides the approximation order also the resolution becomes important. Both are not necessarily equivalent (this holds only for periodic functions). We measure the resolution by the largest wavenumber ξ (normalized with the grid spacing), for which the dispersion relation can be accurately represented by the scheme. Exponential convergence and superior resolution properties of spectral methods make them the most efficient spatial approximation methods. In addition, for the most common of theses schemes fast transform algorithms exist. Numerical stability of spectral methods is discussed in detail in Canuto *et al.* [10].

With periodic boundary conditions it is natural to employ Fourier expansions. In the present work the periodic directions are treated by Fourier collocation. Flow variables are stored in real space. Differentiation is done in spectral space, transforming back and forth by FFT. Convolutions are calculated in real space as well and are thus affected by aliasing errors (Canuto *et al.* [10]). For compressible Navier-Stokes equations an exact dealiasing is usually impossible due to the viscosity law. But even if one considers the convective terms only, dealiasing is practically unfeasible since contributions from all three coordinate directions need to be considered, which makes the storage requirements prohibitive. Our experience shows that indeed *dealiasing by resolving* (Boyd [9]) is practicable.

In non-periodic directions we use Padé-methods (Lele [42]). Based on order conditions derived by local Taylor analysis, these schemes are finite difference methods. However, unlike the usual explicit finite-difference methods, the finite difference stencil makes use of neighboring derivative values, rendering the scheme implicit. Together with suitable (linearly independent) boundary closures one gets a linear equation system which can be solved for the derivative values $\mathbf{f}'$ in terms of the function values $\mathbf{f}$ by $\mathbf{A}\mathbf{f}' = \mathbf{B}\mathbf{f}$, where the matrices $\mathbf{A}$ and $\mathbf{B}$ are densely banded and constant. The overhead due to the necessity of solving a linear system for each derivative evaluation is small since the LU-decomposition of $\mathbf{A}$ can be precomputed and stored. Additional free parameters, after satisfying a desired approximation order, can be used to tune the resolution properties of the scheme (Lele [42]) in such a way that they become nearly as good as spectral polynomial approximations, while retaining the less severe stability restriction of explicit finite difference methods (order $1/N$ for the convective and $1/N^2$ for the diffusive operator). A side benefit is that even high order schemes have a relatively narrow stencil, so that high order boundary closures can be formulated (Lele [42]). The schemes we use are of 6th order at inner points, of 4th order at the next-to-boundary points and of 3rd order at the boundary. Theoretically (Gustafsson [31]) these schemes are thus of 4th order globally. However the higher local order within the domain has been found to be advantageous. The inner

schemes are symmetric and thus non-dissipative, whereas boundary schemes introduce a small amount of numerical dissipation.

The linear stability analysis for these schemes for the scalar advection equation and the scalar diffusion equation leads to the following conclusions (Adams [1]): (a) the methods are stable in the sense of Lax (this has been shown by an analysis following the theory of Gustafsson, Kreiss and Sundström [32]) and (b) the methods are asymptotically (or time) stable if all second derivatives are treated by second-derivative schemes (and not by repeated application of first derivative schemes).

2.2 Coordinate Transformation

The finite-difference schemes being formulated for equidistant grid spacings may be easily extended to non-uniform grid spacings by applying an analytic mapping. During transition high gradients are usually concentrated near the wall and near the critical layer (detached shear layer evolution). This can be accounted for by employing a mapping which clusters grid point in these regions. The computational space $\zeta_j \in [0, 1]$ is mapped onto the physical space $z_j \in [0, z_{max}]$ by a function

$$z_j = \frac{z_{max} z_{1/2} d}{(z_{max} - z_{1/2}) + d(2z_{1/2} - z_{max})} , \qquad (1)$$

where

$$d = \left[a\zeta_j + b + a_1 \sinh\left(\frac{\zeta_j - a_2}{a_3}\right)\right] ,$$

and a_1, a_2, a_3 are tuning parameters. This is a combination of a sinh-function which condenses grid points near $z_{mv} = z(a_2)$, and a hyperbola which concentrates grid points near the wall (about 50% of all grid points are below $z_{1/2}$). The parameter a_3 controls the spreading of grid points (due to sinh) at the interval limits. The effect of this mapping is similar to the hyperbola/tanh-mapping used in Erlebacher & Hussaini [18] and Pruett & Zang [50], however it has the advantage of requiring the solution of only one transcendental equation $z(a_2) - z_{mv} = 0$ at regridding.

2.3 Time Integration

Problems concerning implicit time integration (preconditioning of the Jacobian of the viscous fluxes, preconditioning of the discrete derivative operators) lead us to the conclusion that presently explicit methods are preferable for the present purpose. Linear explicit Runge-Kutta schemes have - besides being relatively easy to implement - the advantage of being compact (even for high order) and to become identical with the respective first terms of the Taylor series for the exponential function for the equation $y' = y$ (Dahlquist equation). Since this equation is a model for the initial growth processes during transition, Runge-Kutta schemes are specially favorable to represent the dispersion relation for small amplitude waves. Linear explicit Runge-Kutta schemes are in general locally stable even for systems of equations. We use a method proposed by Wray [70]. This scheme can be cast into a compact storage form.

The time step size is controlled at each time step by a CFL criterion. Derived from a linearized advection-diffusion equation the time step is required to be bounded by

$$\tau \leq \frac{CFL}{A_{max}} , \qquad (2)$$

where

$$A_{max} = \pi \max \left[\frac{|u|+\sqrt{T}/M_\infty}{\Delta_x} + \frac{|v|+\sqrt{T}/M_\infty}{\Delta_y} + \frac{|w|+\sqrt{T}/M_\infty}{\Delta_z} + \pi d_{max} \left(\frac{1}{\Delta_x^2} + \frac{1}{\Delta_y^2} + \frac{1}{\Delta_z^2} \right) \right] , \qquad (3)$$

where

$$d_{max} = \max\left(\frac{\mu}{Re\rho}, \frac{\mu}{(\kappa - 1) M_\infty^2 Pr Re \rho} \right) .$$

The results shown in the subsequent sections are typically obtained with $CFL = 2$.

3. TEMPORAL DNS RESULTS

Basic features of transition processes for flat plate boundary layers at various Mach numbers have been summarized by Mack [44, 45] using linear stability theory point. In a low-disturbance environment, the most unstable disturbances in a supersonic boundary layer below $M_\infty = 3$ are oblique waves. Weakly nonlinear interactions among such oblique waves usually lead to rapid growth of higher modes, which results in transition (cf. Fasel *et al.* [20], Sandham & Adams [56], Sandham *et al.* [57]). Here the transition process skips a secondary linear instability stage. The transition of this type is referred to as an "oblique wave breakdown" in Fasel *et al.* [20]. At higher Mach numbers the linear stability characteristics become substantially more complex. A two-dimensional second-mode (Mack mode) wave becomes the most unstable one at about $M_\infty > 3$ (Mack [44]). A secondary instability due to the finite-amplitude second-mode wave may initialize a subharmonic resonance which may lead the transition process towards turbulence (Herbert [34], Ng & Erlebacher [48]). Since the instability domain of the second mode waves is rather narrow, the most unstable first mode waves, which are oblique waves, may still have larger growth. Thus both oblique wave breakdown and subharmonic resonance may be observed at high Mach numbers. Using the temporal DNS approach, we have studied both transition processes at $M_\infty = 4.5$. The results are outlined in §3.1 and §3.2. In §3.3, temporal DNS results of an oblique wave breakdown at $M_\infty = 2$ are presented.

3.1 Subharmonic Transition at $M_\infty = 4.5$

The flow parameters were chosen to match the secondary instability investigations of Ng & Erlebacher [48]: $T_\infty = 61.15K$, $M_\infty = 4.5$, $Re = 10000$. A second-mode primary instability near branch II of the neutral curve with a streamwise wavenumber $\alpha = 2.52$ is excited initially with an amplitude of 0.4% with respect to the maximum streamwise velocity fluctuation. The most amplified secondary instability wave with wavenumbers $\alpha = 1.26$ and $\beta = 2.1$, which is of subharmonic type, is allowed to grow from additionally imposed random noise with an amplitude of 10^{-5}. These parameters happen to be close to those used by Pruett & Zang [50] for the hollow cylinder

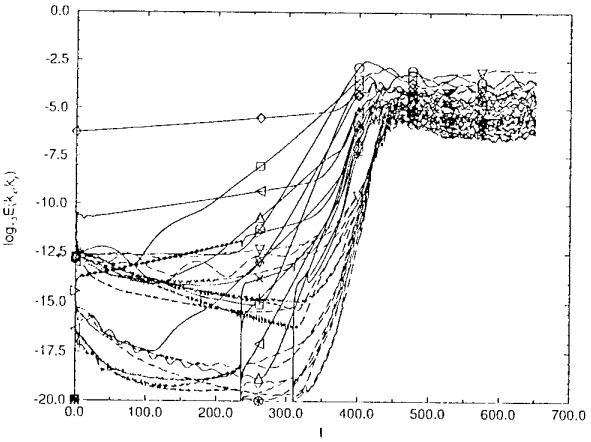

Figure 2: Temporal development of the mode energy of the leading modes in DNS of subharmonic transition. Legends: solid line for even $k_x + k_y$ modes; dashed line for odd $k_x + k_y$ modes; $\diamond$ for $(1,1)$; $\square$ for $(2,0)$; $\triangle$ for $(0,2)$; $\triangleleft$ for $(3,1)$; ∇ for $(1,3)$; $\triangleright$ for $(0,4)$; $+$ for $(4,0)$; $\times$ for $(2,1)$.

problem. This simulation was started by Adams & Kleiser [3, 4] up to the breakdown stage ($t = 440$), and was continued into the beginning turbulence recently ($t = 653$). The history of grid refinement is shown in table 1.

Table 1. Grid refinement history for subharmonic transition simulation at $M_\infty = 4.5$ case.

Time	N_x	N_y	N_z
235	12	12	100
310	16	16	100
329	24	16	100
364	32	24	120
368	48	32	120
373	64	48	140
384	64	64	140
431	128	128	190
439	128	128	220
502	128	128	240
538	128	108	240
610	128	108	200
653	128	96	200

For an assessment of the disturbance growth the mode-energy is used, which is defined as the magnitude of the Fourier-transformed velocity vector integrated over z. An overview of the temporal development of the leading modes is shown in figure 2. The primary wave mode $(2,0)$ grows initially with its linear growth rate up to about 70 period T_w ($T_w = 2.7646$). Meanwhile the secondary wave develops from background noise. After about $85T_w$ the correct secondary eigenfunction and growth rate can be extracted (cf. Adams & Kleiser [3, 4]). Primary and secondary modes travel downstream with a common velocity. This phase-locking yields the most effective environment for wave interaction.

After a phase of weakly nonlinear development a strongly nonlinear interaction among the dominant modes sets in at about $130T_w$, where the mode-energy of the $(0,2)$ mode overtakes the $(1,1)$ mode. The dominant mode during the breakdown is the $(0,2)$ mode, which represents two pairs of high- and low-speed streaks to be observed just below the Λ-vortices. These streaks are moving down towards the wall during the transition process. At this stage a shear layer generated by the Λ-vortices

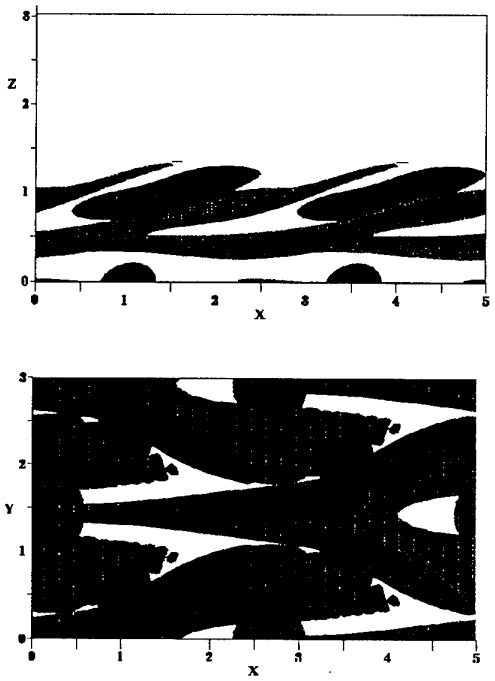

Figure 3: Λ-vortices (iso-surface $p = 0.03237$, dark) and Y-shaped shear layers (iso-surface $\omega_y = 1.4$, light), $t = 392.70$. (From [1], figure 7.22.)

becomes visible, which possesses a Y-shape and is located between two neighboring Λ-vortices, shown in figure 3. This lower shear layer winds slightly around the leg of the neighboring Λ-vortex and becomes stretched and elongated. Several levels of subsequent shear-layer roll-up have been observed in our simulation. The first roll-up happens near the center of the associated Λ-vortex leg and leads to a first inverted hairpin-like structure. The Y-shaped shear-layer elongates, its tips reach the head region of the preceding Λ-vortex and the second roll-up begins. Again an inverted hairpin-like vortical structure forms.

In the following stages, it appears that the first-appearing hairpin-like vortex weakens while the second one gains strength. During the later breakdown stage, the staggered subharmonic symmetry is lost, which is indicated by the sudden, rapid growth of the odd $k_x + k_y$ modes shown in figure 2. The remaining large scale vortical structures are formed by the legs of the second hairpin-like vortices and the remnants of the Λ-vortex. The breakdown to turbulent flow is indicated by a strong decrease of the shape factor and increase of the skin friction coefficient, shown in figure 4. From figures 2 and 4 it can be concluded that the breakdown is complete.

The temporal evolutions of the mean (i.e. x-y-averaged) profiles of the streamwise velocity and temperature are shown in figure 5. The experimental data compiled by Fernholz & Finley [21] for turbulent flow at somewhat different parameters are also shown for comparison. Starting from the laminar profiles, the transitional mean velocity and temperature profiles evolve towards the experimental results. Note that after the breakdown stage the profiles continue to grow thicker with time. This is a problem inherent in a temporal DNS approach. A method was designed recently by Guo & Adams [26] to avoid this problem in the DNS of compressible turbulent boundary

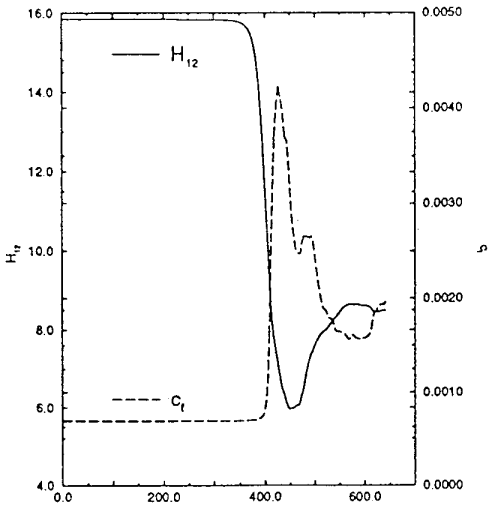

Figure 4: Shape factor H and skin friction coefficient C_f.

layers (see section 4.3).

3.2 Oblique Wave Breakdown at $M_\infty = 4.5$

The flow parameters are similar to those in section 3.1. Initially the laminar basic flow is superimposed with a pair of the most unstable oblique first mode primary waves, which have the wavenumbers $\alpha = 0.48$ and $\beta = 0.83$ and thus are oblique at an angle of 60^0 with respect to the freestream. The amplitudes of the oblique waves are 0.4% of the freestream velocity. The simulation was initialized with a discretization of $N_x = 16$, $N_y = 16$ and $N_z = 129$, and was refined up to $N_x = 96$, $N_y = 128$ and $N_z = 161$ finally.

Figure 6 shows the temporal evolution of the mode-energy of the leading modes. The period of the primary wave is $T_w = 16.20$. The finite-amplitude primary wave immediately initiates weakly nonlinear interactions of second order. The growth rate of the $(1,1)$ mode remains at the linear value until about $10T_w$. The $(0,2)$ mode is generated by second order interactions of the $(1,1)$ mode and the $(-1,1)$ mode, the $(2,0)$ mode by the $(1,1)$ mode and the $(1,-1)$ mode, as expected. The onset of strongly nonlinear interactions occurs after about $15T_w$. It is characterized by the amplification of modes with an odd sum of wavenumbers $k_x + k_y$, which begin to grow exponentially from machine zero. This stage is accompanied by the build-up of a staggered system of streamwise vortices and Y-shaped shear layers, shown in figure 7. It should be noted that in contrast to the subharmonic transition, during which the $(0,2)$ mode is dominant throughout the whole breakdown, now a dominant $(1,3)$ mode overtakes the $(0,2)$ mode in the late stages. More detailed discussions of this transition process are given in Adams & Kleiser [2].

3.3 Oblique Wave Breakdown at $M_\infty = 2$

Mach 2 boundary layers are representative of a particular stability regime where compressibility is sufficient to stabilize the two-dimensional waves that are most unstable in incompressible flow, but not strong enough to give

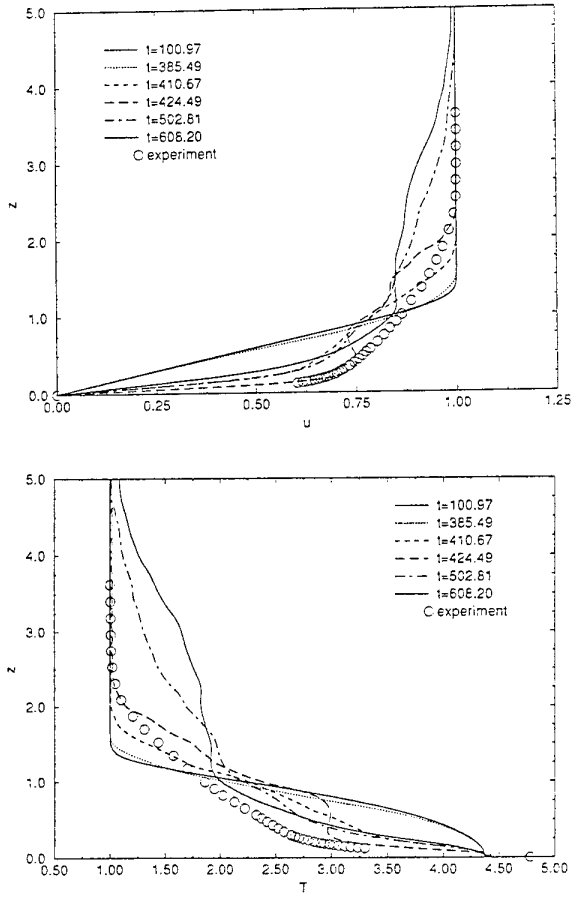

Figure 5: Temporal evolution during subharmonic transition of the mean profiles of (a) the streamwise velocity and (b) temperature, and comparison with experimental data for turbulent flows.

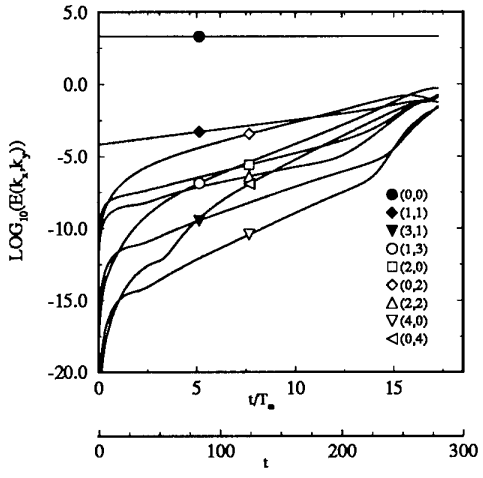

Figure 6: Temporal evolution of the mode-energy of the leading mode during oblique breakdown at $M_\infty = 4.5$. (From [2], figure 3.)

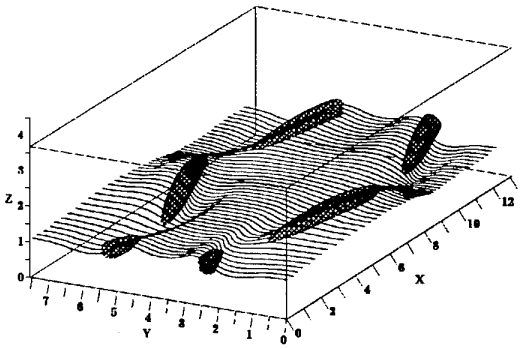

Figure 7: Pressure iso-surface $p = 0.034$ and vortex lines in DNS of oblique wave breakdown at $t = 247.11$. (From [2], figure 8.)

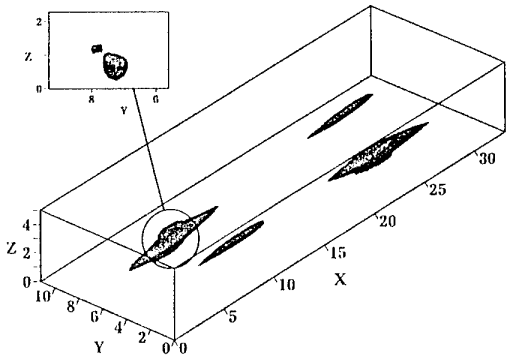

Figure 8: Flow structure just before the breakdown stage in $M_\infty = 2$ boundary layer. The surface of constant pressure shows the quasi-streamwise vortices, and the inset figure shows the location of the new vortex caused by vorticity stretching.

the acoustic Mack modes. The initial instability characteristics were studied in temporal simulations by Sandham & Adams [56]. With random initial conditions it was shown that oblique modes, with the wavelengths and orientations predicted by linear stability theory, soon dominated the flow. Evidence for radiating two-dimensional instability waves was found, but these were only weakly unstable. In the nonlinear phase of disturbance growth quasi-streamwise vortices form, in agreement with spatial simulations (Fasel *et al.* [20]).

Detailed mechanisms of breakdown to turbulence following oblique instability waves were studied by Sandham *et al.* [57]. The simulations were initialized with a pair of equal and opposite oblique waves and were continued up until a breakdown to small scale vortices and a sharp increase in skin friction. A delay is found in the transition process after the appearance of quasi-streamwise vortices. These do not lead directly to breakdown, and in this phase of the transition process the disturbance energies actually decrease. Other changes take place during this phase that eventually lead to breakdown. Shear layers are formed by a process of vorticity convection and stretching and secondary vortices form near the quasi-streamwise vortices. The flow structure at this time is shown in figure 8 using iso-surfaces of static pressure. There are four main quasi-streamwise vortices which arise from the nonlinear evolution of streamwise vorticity already present in the linear eigenfunctions. The inset shows a view in the downstream direction of the flow structure near one of the vortices. A secondary vortex has formed above and to one side of the original vortex. In Sandham *et al.* [57] terms in the vorticity transport equation were analyzed and it was found that the slight inclination (2°) and skewness (5°) of the original vortices was sufficient to cause the formation of these vortices. These new vortices form in the vicinity of the shear layer, and force a shear layer roll-up into many small vortices. After this breakdown the flow evolves slowly towards a turbulent state, initially producing turbulence in streaks with small spanwise extent. This breakdown process is expected to be relevant to other situations (not necessarily compressible) where quasi-streamwise vortices are present at the outset of transition.

4. RECENT DEVELOPMENTS

In this section, we first report our recent efforts on spatial DNS. Attention is given to the treatment of inflow and outflow boundary conditions. Our recent efforts towards modeling nonparallel effects in temporal DNS of transitional and turbulent boundary layers are reported section 4.2 and section 4.3.

4.1 Spatial DNS Codes

In a spatial DNS, the correct specification of the inflow and outflow boundary conditions is a crucial issue. This is especially important for high-order finite-difference schemes where the numerical diffusivity is very low. Improper treatments of inflow/outflow conditions usually lead to unacceptable wave reflection problems (cf. Thumm *et al.* [69], Poinsot & Lele [49], Pruett *et al.* [52], Guo & Adams [25]). In this subsection, we outline our recent studies on the treatment of inflow/outflow boundary conditions. These treatments have been implemented in our two recently developed DNS codes.

Our first code is a "conventional" code (Guo & Adams [25]): it employs a Fourier collocation scheme in the periodic spanwise direction, and sixth order central-difference (Padé) schemes in the nonperiodic streamwise and wall-normal directions. Time advancement is achieved by the Runge-Kutta scheme mentioned earlier. Grid stretching is used in the streamwise and wall-normal directions. At the inflow boundary, the flow field is first decomposed into three parts: the given basic flow, the prescribed perturbation and the unknown remaining "residual" disturbance. At the supersonic section of the inflow boundary, the residual disturbance can be assumed to be zero, and all the variables of the basic flow and the prescribed perturbation are imposed. At the subsonic section, the basic flow and the prescribed perturbation are imposed while a characteristic boundary condition is applied to the residual disturbance part, which allows the out-going waves to pass the boundary with minimum reflection. The advantage of this inflow treatment

over the one in Poinsot & Lele [49] is that this treatment allows us to correctly enforce the prescribed perturbation at the inflow boundary without any visible wave reflection. At the outflow boundary, three treatments have been implemented: characteristic-based boundary conditions (cf. Poinsot & Lele [49]), a buffer domain approach (cf. Pruett *et al.* [52]) and a sponge layer approach (cf. Givoli [23], Israeli & Orszag [36]). The effectiveness of these boundary treatments was tested by simulating two- and three-dimensional instability waves and comparing the results with those of linear stability theory (LST) (Simen [60]), PSE (Bertolotti [6] Pruett & Chang [51]) and other DNS codes (Guo *et al.* [28], Pruett & Chang [51]). Our results have shown that two outflow treatments perform best: characteristic boundary conditions combined with a sponge layer, and a buffer domain approach plus a sponge layer. No visible inflow and outflow coupling or wave reflections are observed in the results. We find that these treatments work better than those which only use characteristic conditions (Poinsot & Lele [49]) or the buffer domain approach (Pruett & Chang [51]) alone.

Our second code is rather "unconventional" (Guo *et al.* [28]): the computational domain is not simply cut from the physical domain; instead a "spatial window function", $w(x)$, is used to truncate the domain in the streamwise direction, x. The governing equations in the computational domain then can be written as

$$\frac{\partial w(x)\mathbf{U}}{\partial t} = \frac{\partial w(x)\mathbf{F}}{\partial x} + \frac{\partial w(x)\mathbf{G}}{\partial y} + \frac{\partial w(x)\mathbf{H}}{\partial z} + w(x)\mathbf{Z} - \frac{dw(x)}{dx}\mathbf{F}\,, \qquad (4)$$

using usual notation (see Guo *et al.* [28]). When a rectangular window function, $w(x) = 1$ (within the domain of interest), is used, the standard Navier-Stokes equations are recovered from equation (4). Note that the concept of a "window function" has been widely used in digital signal processing for many years (cf. Guo [24], Harris [33]).

By properly designing the window function $w(x)$, equation (4) can be solved efficiently by Fourier spectral methods in the streamwise direction. (Note that a Fourier scheme is also used in the nonperiodic streamwise direction in Spalart's "fringe" approach [64, 65], but the concept and motivation of the fringe approach are quite different from those of the window approach.) The temporal and spatial discretizations in the wall-normal and spanwise directions are the same as those in the first code. Any type of grid stretching may be used in the streamwise direction, which is considered to be important in the DNS of boundary layer transition (Pruett *et al.* [52], Guo & Adams [25]). It can be shown that the accuracy of such a scheme only depends on the window function. Window functions which yield spectral accuracy have been given in Guo *et al.* [28]. No numerical inflow and outflow boundaries are present in this approach. They are instead replaced by the treatments of the inflow and outflow regions. These treatments have been designed to allow characteristic waves to pass with minimum reflections. Numerical results obtained with this code are in good agreement with those obtained by LST, PSE and other DNS codes (Simen [60], Bertolotti [6], Guo & Adams [25], Pruett & Chang [51]), with no sign of any wave reflection problem.

Figure 9 shows the comparison among our two spatial DNS codes and PSE. The amplitude functions of a linear second-mode instability wave at $M_\infty = 4.5$, $T_\infty = 61.15K$, $Re = 8000$ and $\omega = 1.76$ are shown in the figure. In our first DNS code, 121 grid points in the wall-normal direction and 16 grid points per wavelength in the streamwise direction were used. In the second DNS code, 121 points in the wall-normal direction and 10.4 points per wavelength in the streamwise direction were used. We can see that the agreement between our results and those of Pruett & Chang [51] is excellent.

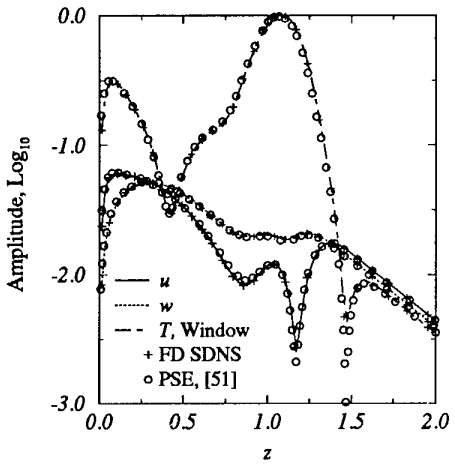

Figure 9: Amplitude functions of temperature (T), streamwise and wall-normal velocity components (u and v) of a linear second mode in a logarithmic scale at $x = 138$. (From [28], figure 3*b*.)

Figure 10 shows the comparison between our two DNS codes for a nonlinear second mode wave at $M_\infty = 4.5$. The flow parameters are identical to those in figure 9, except that the amplitude of the streamwise velocity of the second mode is about 1% of the freestream velocity. The computation of the nonlinear second mode was first carried out using the eigensolutions of LST as the inflow disturbance in the second DNS code. It uses 18.5 grid points per wavelength in the streamwise direction and 161 grid points in the wall-normal direction. Then the flow quantities sampled at $x = 111$ were used as the inflow conditions to start the first DNS code. The resolution used in the second computation is 32 grid points per wavelength in the streamwise direction and 161 grid points in the wall-normal direction. Again, the agreement between the two codes is perfect.

4.2 Modeling Nonparallel Effects in Temporal DNS

When a conventional temporal DNS approach (cf. Spalart & Yang [66]) is used to compute nonparallel boundary layer flows, there are two drawbacks: first it cannot consider nonparallel effects since it uses a parallel flow assumption in its formulation. Second, it cannot compute the mean flow quantities correctly, since it is a local procedure and thus cannot utilize the upstream information on these quantities to compute the downstream profiles. In this subsection, we first report on our new approach (presented in Guo *et al.* [29]), which allows us to model some nonparallel effects in a temporal DNS. The issue of the mean flow problem is addressed in the next subsection, with an application to supersonic turbulent boundary layers.

In a spatially evolving transitional boundary layer, the flow field at the downstream location $x = x_0$ can be represented by

$$\mathbf{u} = \sum_{l,m} \hat{\mathbf{u}}_{lm}(x,z) \exp[i \int_{x_0}^{x} (\alpha^r_{lm}(x) + i\alpha^i_{lm}(x))dx$$

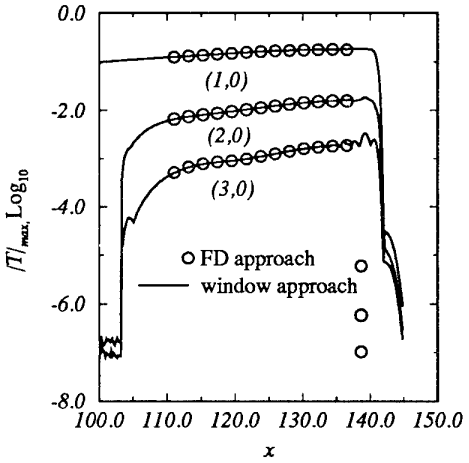

Figure 10: Temperature amplitude maxima of a nonlinear second mode and its first two harmonics are shown as a function of the streamwise distance. (From [28], figure 4a.)

$$+im\beta y - il\omega t] \,, \qquad (5)$$

where $\hat{\mathbf{u}}_{lm}$, α^r_{lm} and α^i_{lm} are the amplitude function, the streamwise wavenumber and spatial growth rate for the Fourier mode (l, m). The parameter β is the primary wavenumber in the spanwise direction, and ω is the primary temporal frequency. In equation (5), it can be seen that the variation of the flow field in the streamwise direction can be identified as a slowly evolving part, which is represented by the slow variation of $\hat{\mathbf{u}}_{lm}$, α^r_{lm} and α^i_{lm} with x, and a fast and small-scale fluctuation part, which is represented by the wave part of (5). The nonparallel effect of $\mathbf{u}$ is mainly contributed by the slowly evolving part. Using a multiple scale analysis similar to the one used in a PSE approach (cf. Bertolotti, Herbert & Spalart [7]), the slowly evolving part can be expanded into a Taylor series, and the nonparallel boundary layer flow can be written as (Guo *et al.* [29])

$$\begin{aligned}\mathbf{u} \;&= \mathbf{u}_0(x,y,z,t) + (x-x_0)\mathbf{u}_1(x,y,z,t) \\ &\quad +(x-x_0)^2\mathbf{u}_2(x,y,z,t) + \cdots \,, \end{aligned} \qquad (6)$$

where $(x - x_0)$ is the perturbation parameter which can be scaled with the streamwise wavenumber of instability waves. The functions $\mathbf{u}_i$ $(i = 0, 1, \cdots)$ are periodic in the streamwise and spanwise directions. When the wavelength of an instability wave is not too long and its frequency is not too small, the term $\mathbf{u}_i$ is usually one order smaller than $\mathbf{u}_{i-1}$ $(i > 2)$. Our further analysis shows that $\mathbf{u}_1$ contains mainly the information about the spatial growth rates of the instability waves, and $\mathbf{u}_2$ represents mainly the variation of the streamwise wavenumbers of the instability waves with x.

Substituting (6) into the Navier-Stokes equations, we can derive n sets of equations in the perturbation parameter space $(x - x_0)^i$ $(i = 0, 1, \cdots, n-1)$. The unknows in these equation sets are $\mathbf{u}_i$. When the streamwise and spanwise wavenumbers of $\mathbf{u}_i$ are prescribed, these equation sets are complete. Conceptually, a standard temporal DNS code can be modified to solve these equation sets. We refer to this approach as the extended temporal DNS approach.

Due to the complexity of the higher-order equations, only the first set of the equations $(i = 0)$ is considered in the present study. The governing equations then have the following form:

$$\frac{\partial \mathbf{u}}{\partial t} = \frac{\partial \mathbf{E}}{\partial x} + \frac{\partial \mathbf{F}}{\partial y} + \frac{\partial \mathbf{G}}{\partial z} + \mathbf{Z}_1 + \mathbf{Z}_2 + \mathbf{Z}_3 \,. \qquad (7)$$

The terms $\mathbf{Z}_1$, $\mathbf{Z}_2$ and $\mathbf{Z}_3$ are the terms resulting from our new formulation. The details of these additional terms can be found in Guo *et al.* [29]. When only the first set of the equations is solved, the solution of $\mathbf{u}$ will exhibit a temporal growth, since $\mathbf{u}_1$, which represents the spatial growth of $\mathbf{u}$, is not represented in the governing equations. In order to consider nonparallel effects of a boundary layer, it is better to do the computations in a reference frame, moving downstream with a velocity c_T, which is chosen as some average group velocity of the instability waves in the domain of interest.

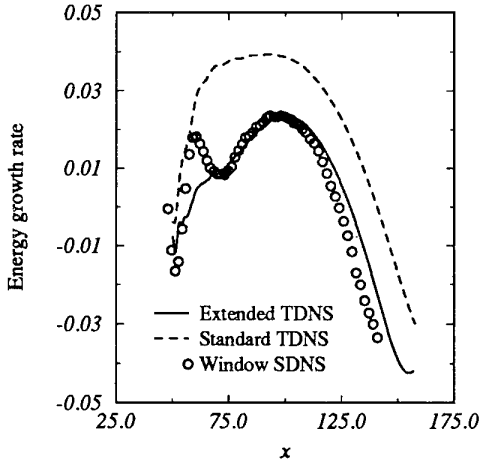

Figure 11: Spatial growth rates (defined by kinetic energy) for a linear second mode at $M_\infty = 4.5$. (From [29], figure 6.)

Figure 11 shows the spatial growth rates of a linear second mode wave obtained at $M_\infty = 4.5$, $T_\infty = 61.15K$, $Re = 8000$ and $\omega = 1.76$, by the conventional temporal DNS, the extended temporal DNS and a spatial DNS. The reference frame is moving downstream at a velocity $c_T = 0.815$, which is close to the average group velocity of the second mode. We can see that the results from the extended temporal DNS are quite close to those from spatial DNS, while the results from the standard temporal DNS are unacceptable. Our further computations show that the improvement of our extended temporal DNS is significant at high Mach number for both $2D$ and $3D$ waves (Guo *et al.* [30]).

Figure 12 shows the computation of the transition initiated by a pair of weakly nonlinear oblique waves at $M_\infty = 4.5$, $T_\infty = 61.15K$, $Re = 10000$ and $Pr = 0.7$. The frequency of the oblique wave is $\omega = 0.3878$. It has a spanwise wavenumber of $\beta = 0.83$ (oblique angle $\psi = 60^0$). In the extended TDNS, the streamwise wavenumber is chosen to be $\alpha = 0.48$. The frame velocity is $c_T = 0.82$, which is the average group velocity of the oblique waves. The maxima of the streamwise velocity amplitude functions of the leading modes are shown in the figure as functions of x. In the SDNS, the amplitude of the streamwise velocity component of the oblique waves in the inflow region is 1.5% of the freestream velocity, and the spatial window approach is used. In the TDNS, the initial amplitudes of the oblique waves are adjusted to match those in the SDNS. It can be seen that except for the spanwise modes $(0, 2)$ and $(0, 4)$, all the modes from

the extended TDNS agree very well with those from the SDNS when $x > 50$. In $x < 50$, the two approaches have different transients, which lead to slightly different solutions. The results obtained by the conventional TDNS are shown in figure 13. Compared to figure 12, one can clearly conclude that the extended TDNS performs better.

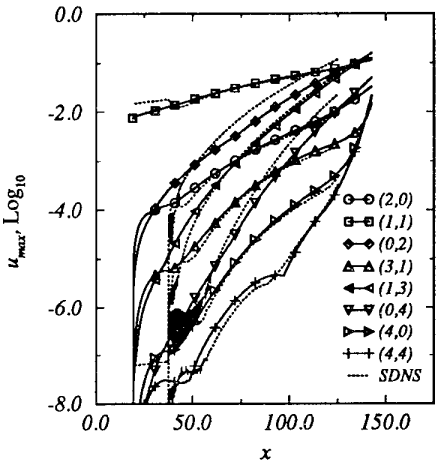

Figure 12: Maxima of the streamwise velocity amplitude functions of the leading modes in a logarithmic scale, obtained by the extended TDNS (symbols) and window SDNS approach. (From [30], figure 10.)

4.3 Computing Turbulent Boundary Layer with A Temporal DNS Approach

One major issue in computing turbulent boundary layers with a conventional TDNS approach is that mean flow quantities always exhibit temporal growth, making the collection of turbulence statistics rather difficult (note that this is not an issue for parallel flows such as channel flows in Coleman *et al.* [13]). To overcome this problem, Spalart & Leonard [61] and Spalart [62] assumed self-similarity both for the mean velocity and for the Reynolds stresses in their studies of equilibrium turbulent boundary layers and sink flows. These assumption are reasonable, but are strictly justified only in the case of sink flows. In Spalart [63], a more general approach was developed using a multiple-scale analysis to approximate the local effects of the streamwise growth of the flow. Satisfactory results have been obtained for boundary layer flows over flat plate.

However, a direct application of the multiple-scale analysis of Spalart [63] to compressible flow is rather tedious and difficult, due to the many nonlinear terms in the compressible Navier-Stokes equations. In order to avoid this problem, we have developed a different approach recently (cf. Guo & Adams [26]). In this approach, we make use of the fact that there exist two different scales in a turbulent boundary layer: mean flow quantities display large scales and slow variations in the streamwise direction, while turbulence quantities are generally fast and have small scales (cf. Spalart [63]). In a sense, mean flow quantities can be viewed as global quantities, carrying upstream information downstream. For example, the downstream profiles of mean flow quantities depend on their upstream values. Therefore these quantities cannot be solved by a local procedure without resorting to some similarity assumption. Turbulence quantities, on the other hand, are generally "local", being generated and dissipated within

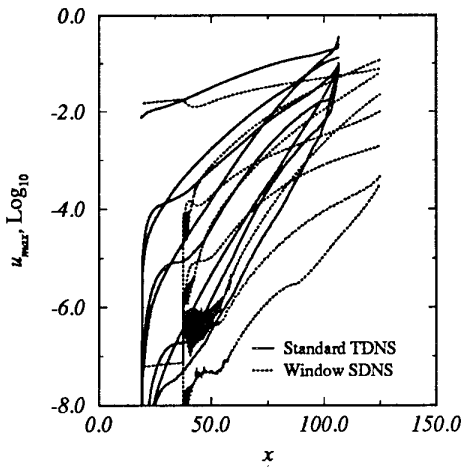

Figure 13: Comparison between standard TDNS and SDNS. The flow parameters are identical to those in figure 5. (From [30], figure 13.)

short time and small space. Intuitively, one would expect that it would be more efficient to compute these two different scales with different numerical approaches.

Motivated by the above observation, we developed an approach which computes the turbulence quantities locally with a TDNS approach, and computes the mean flow quantities globally by solving the Reynolds-averaged Navier-Stokes equations. A parabolization procedure (cf. Fletcher [22], Guo & Finlay [27]) has been applied to the Reynolds-averaged equations, which allows us to spatially march the mean flow quantities downstream efficiently. The nonparallel effects of the turbulent boundary layer on turbulence quantities are considered in the temporal DNS in the same way as we discussed in §4.2, except that here the validity of expansion (6) cannot be shown analytically, but has to be assumed. The justification of such an assumption has been discussed in Guo & Adams [26]. Only the first set of the equations ($i = 0$) is implemented in our current version of the code.

Figure 14 shows the time history of the skin friction coefficient, C_f, during the first three spatial steps at $M_\infty = 6$. It can be seen that at each station C_f tends to reach a statistically steady state. At the first step, a large variation of C_f is observed. We believe that this is due to the large transient caused by the initial conditions, which are rescaled from a simulation at $M_\infty = 4.5$. Since the initial data are not a solution of the parabolized Reynolds-averaged Navier-Stokes equations, spatial transients are expected in the first few steps. Usually, the transients diminish after a few steps. The spatial extent affected by the transient solutions depends on both the character of the Reynolds-averaged Navier-Stokes equations and the initial conditions. This issue is beyond the scope of the present paper.

It can be shown that the governing equations obtained from our approach for an incompressible boundary layer over a flat plate are identical to those of Spalart [63] when the coordinate transformation of Spalart [63] is not used. In a sense, our approach is similar to Spalart's in that both approaches utilize two scales. In our approach, the long scale analysis is explicitly applied to the *governing equations* for mean flow quantities, and the short scale analysis to the *governing equations* for turbulence quantities. When there are large streamwise streaks, e.g. in a three-dimensional boundary layer, our approach may be more

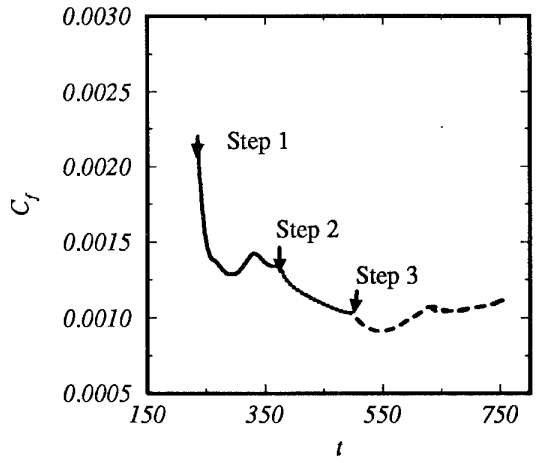

Figure 14: Time history of skin friction coefficient, C_f, in a $M_\infty = 6$ turbulent boundary layer. (From [26], figure $1a$.)

general, since the related governing equations or mean flow quantities are explicitly parabolized, making the use of spatial marching schemes more justifiable.

In Spalart [63], coordinate tilting has been introduced to model the nonparallel effects of boundary layers. In Guo *et al.* [29], our experience with transitional compressible boundary layer flows shows that the coordinate transformation technique does not guarantee an improved result, partly due to the difficulty in selecting a proper tilting angle. In this study, this technique is not used.

Compared to the PSE approach developed for transitional flows (cf. Bertolotti, Herbert & Spalart [7], Herbert [35]), we have the following comments. The PSE has been proven to be a very powerful tool in studying the transition process in spatially growing boundary layers up to the early stage of breakdown. The possibility of developing a PSE-type approach for turbulent boundary layers has been appealing (Zang [71]). To our understanding, the PSE relies on the spatial marching of shape functions (eigenfunctions) of all modes in the streamwise direction. This requires the spatial evolution of all shape functions to be slow in this direction. In turbulent boundary layers, only the mean flow and the stationary spanwise modes have slowly evolving shape functions in the streamwise direction. The shape functions of other modes do not have slow variations in the streamwise direction, and thus cannot be marched downstream by a spatial marching scheme. The method we described in this study has explored the possibility of marching downstream the shape functions of both the mean flow and the stationary spanwise modes, and computes the other modes locally using a temporal DNS approach. Thus it can be viewed as a version of PSE for turbulent boundary layer flows.

5. CONCLUDING REMARKS

In this report, we have reviewed recent progress made by our group in both temporal and spatial DNS of transition towards turbulence in compressible boundary layers. Temporal DNS results for both subharmonic transition at $M_\infty = 4.5$ and oblique wave breakdown at $M_\infty = 4.5$ and 2 have been outlined. Attention has been focused on our recent efforts in spatial DNS approaches and in modeling nonparallel effects in a temporal DNS approach. An extended temporal DNS approach has been developed, which can model some nonparallel effects of boundary layers. Extensive comparison between temporal and spatial approaches has shown that only this new formulation can achieve quantitative agreement with spatial approaches at high Mach number. In our efforts towards spatial DNS, two different codes have been developed: a conventional finite-difference/Fourier collocation approach and an unconventional spatial window approach. Both codes have been tested extensively. Our studies have shown that the treatment of inflow/outflow boundary conditions is crucial for high order non-dissipative schemes. The use of a sponge layer approach in the outflow region, combined with the outflow treatment in the unconventional window approach, or with characteristic outflow boundary condition or buffer domain approach in the conventional finite-difference code, is essential in achieving results which are free of inflow/outflow boundary coupling or wave-reflection.

Acknowledgement

We thank Christian Mielke for his help with $M_\infty = 4.5$ subharmonic breakdown simulation. Part of this work was funded by DFG, and collaboration was supported by ARC.

References

1. Adams, N.A., "Numerische Simulation von Transitionsmechanismen in kompressiblen Grenzschichten," *Doctoral Dissertation*, Technical University of Munich, Germany, 1993. Also DLR-FB 93-29, DLR, Germany.

2. Adams, N.A. & Kleiser, L., "Numerical simulation of fundamental breakdown of a laminar boundary-layer at Mach 4.5," *AIAA Paper* 93-5027, 1993.

3. Adams, N.A. & Kleiser, L., "Numerical simulation of transition in a compressible flat plate boundary layer," *Transitional and Turbulent Compressible flows - 1993*, ASME FED-Vol. 151, L.D. Kral, T.A. Zang (eds.), 1993, pp. 101–110.

4. Adams, N.A. & Kleiser, L., "Subharmonic transition to turbulence in a flat plate boundary layer at Mach number 4.5," *J. Fluid Mech.*, submitted, 1993.

5. D. Arnal., "Boundary layer transition: predictions based on linear theory," AGARD FDP/VKI Special Course on *Progress in Transition Modeling*, AGARD Report No. 793, 1993, pp. 2.1–2.63.

6. Bertolotti, F.P., "Compressible boundary layer stability analyzed with the PSE equations," *AIAA Paper* 91-1637, 1991.

7. Bertolotti, F.P., Herbert, Th. & Spalart, P.R. , "Linear and nonlinear stability of the Blasius boundary layer," *J. Fluid Mech.*, Vol. 242, 1992, pp. 441–471.

8. Bertolotti, F.P., "An introduction to the parabolized stability equations," *Transition: Experiment, Theory and Computation*, eds. T.C. Corke, G. Erlebacher, M.Y. Hussaini, Oxford University Press, 1994.

9. Boyd J.P., *Chebyshev & Fourier Spectral Methods.* Springer-Verlag, Berlin, 1989.

10. Canuto, C., Hussaini M.Y., Quarteroni A., Zang T.A., *Spectral Methods in Fluid Dynamics.* Springer-Verlag, Berlin, 1988.

11. Chang, C.L. & Malik, M.R., "Non-parallel stability of compressible boundary layers," *AIAA Paper* 93-2912.

12. Cheng, H.K., "Perspectives on hypersonic viscous flow research," *Annu. Rev. Fluid Mech.*, Vol. 25, 1993, pp. 455–484.

13. Coleman, G.N., Buell, J.G., Kim, J. & Moser, R.D., "Direct simulation of compressible wall-bounded turbulence," *Proc. 9th Symp. on Turbulent Shear flow*. Kyoto, Japan.

14. Delfs, J., "Numerische Simulation der transitionellen transsonischen Plattengrenzschichtströmung," ZLR-Forschungsbericht 93-20, Dissertation, Technical University of Braunschweig, 1993.

15. Dinavahi, S.P.G., Pruett, C.D. & Zang, T.A., "Direct numerical simulation and data analysis of a Mach 4.5 transitional boundary-layer flow," *Phys. Fluids*, Vol. 6, 1993, pp. 1323–1330.

16. Ducros, F., Comte, P. & Lesieur, M., "Ropes and lambda-vortices in direct and large-eddy simulation of a high-Mach number boundary layer over a flat plate," *9th Symp. on Turbulent Shear Flow*, Kyoto, Japan, 1993.

17. Eißler, W. & Bestek, H., "Spatial numerical simulation of nonlinear transition phenomena in supersonic boundary layers," FED-Vol. 151, *Transitional and Turbulent Compressible Flows*, L.D. Kral & T.A. Zang (eds.), ASME, 1993, pp. 69–76.

18. Erlebacher, G. & Hussaini, M.Y. , "Numerical experiments in supersonic boundary layer stability," *Phys. Fluids A*, Vol. 2, 1990, pp. 94–104.

19. Fasel, H., Rist, U. & Konzelmann, U., "Numerical investigation of the three-dimensional development in boundary-layer transition," *AIAA Journal* Vol. 28, 1990, pp. 29–37.

20. Fasel, H., Thumm, A., Bestek, H., "Direct numerical simulation of transition in supersonic boundary layers: oblique breakdown," ASME FED-Vol. 151, *Transitional and Turbulent Compressible Flows*, Kral, L.D., Zang, T.A. (eds.), 1993, pp. 77–92.

21. Fernholz, H.H., Finley, P.J., "A critical compilation of compressible boundary layer data with a survey of turbulent data," AGARDograph 263, 1977.

22. Fletcher, C.A.J., *Computational Techniques for Fluid Dynamics, Volume II*, 1988, Springer-Verlag, Berlin.

23. Givoli, D., "Non-reflecting boundary conditions," *J. Comput. Phys.*, Vol. 94, 1991, pp. 1–29.

24. Guo Y., "An analysis of repetitive signal by cepstrum," *J. of Beijing University of Science & Technology*, Vol. 9, 1987, pp. 48–56.

25. Guo, Y. & Adams, N.A., "A spectral/finite-difference algorithm for direct numerical simulation of spatially evolving compressible boundary layer transition," *Internal Report*, DLR-IB 221-93 A 26, DLR, Institute for Fluid Mechanics, Göttingen, Germany, 1993.

26. Guo, Y. & Adams, N.A., "A numerical investigation of supersonic turbulent boundary layers with high wall temperature," *Proc. of the Summer Program 1994*, Center for Turbulence Research, Stanford Univ./NASA Ames Research Center, U.S.A., 1994.

27. Guo, Y. & Finlay, W.H., Wavenumber selection and irregularity of spatially developing Dean and Görtler vortices. *J. Fluid Mech.*, Vol. 264, 1994, pp. 1–40.

28. Guo, Y., Adams, N.A. & Kleiser, L., "Direct numerical simulation of transition in a spatially growing compressible boundary layer using a new Fourier method," *Direct and Large-Eddy Simulation I*, eds. P.R. Voke, L. Kleiser, J.P. Chollet, 1994, Kluwer, London, pp. 249–259.

29. Guo, Y., Adams, N.A. & Kleiser, L., "Modeling of nonparallel effects in temporal DNS of compressible boundary layer transition," *Theoret. Comput. Fluid Dynamics*, in press, 1994.

30. Guo, Y., Kleiser, L. & Adams, N.A., "A comparison study of an improved temporal DNS and spatial DNS of compressible boundary layer transition," *AIAA paper* 94-2371.

31. Gustafsson, B., "The convergence rate for difference approximations to mixed initial boundary value problems," *Math. Comput.* Vol. 130, 1975, pp. 396–406.

32. Gustafsson, B., Kreiss, H.-O., Sundström, A., "Stability theory of difference approximations for mixed initial boundary values problems II," *Math. Comput.* Vol. 26, 1972, pp. 649–686.

33. Harris, F.J., "On the use of windows for harmonic analysis with the discrete Fourier transform," *Proc. IEEE*, Vol. 66, 1978, pp. 51–83.

34. Herbert, T., "Secondary instability of boundary layers," *Ann. Rev. Fluid Mech.*, Vol. 20, 1988, pp. 487–526.

35. Herbert, T., "Parabolized stability equations," AGARD FDP /VKI Special Course on *Progress in Transition Modeling*, AGARD Report No. 793, 1993, pp. 4.1–4.34.

36. Israeli, M. & Orszag, S.A., "Approximation of radiation boundary conditions," *J. Comput. Phys.*, Vol. 41, 1981, pp. 115–135.

37. Joslin, R.D., Streett, C.L. & Chang, C.-L., "Validation of three-dimensional incompressible spatial direct numerical simulation code," *NASA Technical Paper* 3205, 1992.

38. Kendall, J.M., "Supersonic boundary layer stability experiments," *Boundary Layer Transition Study Group Meeting*, Vol. II, BSD-TR-67-213, USAF, W.D. McCauley (editor), 1967, pp. 10-1–10-8.

39. Kleiser, L. & Zang, T.A., "Numerical simulation of transition in wall-bounded shear flows," *Ann. Rev. Fluid Mech.*, Vol. 23, 1991, pp. 495–537.

40. Kosinov, A.D., Maslov, A.A. & Shevelkov, S.G., "Experiments on the stability of supersonic laminar boundary layers," *J. Fluid Mech.*, Vol. 219, 1990, pp. 621–633.

41. Kufner, E., Dallmann, U. & Stilla, J., "Instability of hypersonic flow past blunt cones - effects of mean flow variations -," *AIAA Paper* 93-2983.

42. Lele, S.K., "Compact finite difference schemes with spectral-like resolution," *J. Comp. Phys.* Vol. 103, 1992, pp. 16–42.

43. Liu, C. & Liu, Z., "High order finite difference and multigrid methods for spatially evolving instability in a planar channel," *J. Comput. Phys.*, Vol. 106, 1993, pp. 92–100.

44. Mack, L.M., "Boundary-layer linear stability theory," *Special Course on Stability and Transition of Laminar Flow,* AGARD Report No. 709, 1984, pp. 3.1–3.81.

45. Mack, L.M., "Review of linear compressible stability theory," *Stability of Time Dependent and Spatially Varying Flow*, ed. D.L. Dwoyer, M.Y. Hussaini, 1987, pp. 164-187. New York: Springer-Verlag.

46. Mack, L.M., "On the inviscid acoustic-mode instability of supersonic shear flows. Part 1: Two-dimensional waves," *Theor. Comp. Fluid Dyn.*, Vol. 2, 1990, pp. 97–123.

47. Malik, M., Zang, T.A. & Bushnell, D., "Boundary layer transition in hypersonic flows," *AIAA Paper* 90-5232.

48. Ng, L., and Erlebacher, G., "Secondary instabilities in compressible boundary layers," *Phys. Fluids A* Vol. 4, 1992, pp. 710—726.

49. Poinsot, T.J. & Lele, S.K., "Boundary condition for direct simulation of compressible viscous flow," *J. of Comp. Phys.*, Vol. 101, 1992, pp. 104–129.

50. Pruett, C.D. & Zang, T.A., "Direct numerical simulation of laminar breakdown in high-speed, axisymmetric boundary layers," *Theoret. Comput. Fluid Dynamics*, Vol. 3, no. 6, 1992, pp. 345–367.

51. Pruett, C.D. & Chang, C.-L., "A comparison of PSE and DNS for high-speed boundary-layer flows," FED-vol. 151, *Transitional and Turbulent Compressible Flows*, L.D. Kral & T.A. Zang (eds.), ASME, 1993, pp. 57–67.

52. Pruett, C.D., Zang, T.A., Chang, C.-L. & Carpenter, M.K., "Spatial direct numerical simulation of high-speed boundary layer flows–Part I: algorithmic considerations and validation," *Theoret. Comput. Fluid Dynamics*, in press, 1994.

53. Pruett, C.D., & Chang, C.-L., "Spatial direct numerical simulation of high-speed boundary layer flows–Part II: transition on a cone in Mach 8 flow," *Theoret. Comput. Fluid Dynamics*, in press, 1994.

54. Rai, M.M. & Moin, P., "Direct numerical simulation of transition and turbulence in a spatially evolving boundary layer", *J. of Comp. Phys.*, Vol. 109, 1993, pp. 169–192.

55. Reed, H., "Direct numerical simulation of transition: the spatial approach," AGARD FDP/VKI Special Course on *Progress in Transition Modeling*, AGARD Report No. 793, 1993, pp. 6.1–6.46.

56. Sandham, N.D., and Adams, N.A., "Numerical simulation of boundary-layer transition at Mach two," *Applied Scientific Research*, Vol. 51, 1993, pp. 371–375.

57. Sandham, N.D., Adams, N.A. & Kleiser, L., "Direct simulation of breakdown to turbulence following oblique instability waves in a supersonic boundary layer," *Direct and Large-Eddy Simulation I*, eds. P.R. Voke, L. Kleiser, J.P. Chollet, 1994, Kluwer, London, pp. 213–223.

58. Saric, W.S., "Physical description of boundary-layer transition: experimental evidence," AGARD FDP/VKI Special Course on *Progress in Transition Modeling*, AGARD Report No. 793, Madrid: 22-25 March, Brussels: 29 March-1 April, 1993.

59. Saric W.S. & Reed H., "Leading edge receptivity to sound: experiments, DNS, and theory," *AIAA paper* 94-2222.

60. Simen, M, "Lokale und nichtlokale Instabilität hypersonischer Grenzschichtströmungen," *Doctoral Dissertation*, University of Stuttgart, Germany, 1993. Also DLR-FB 93-31, 1993, DLR, Germany.

61. Spalart, P.R. & Leonard, A., "Direct numerical simulation of equilibrium turbulent boundary layers," *Proc. 5th Symp. on Turbulent Shear Flows*, Ithaca, NY, August 7–9, 1985.

62. Spalart, P.R. , " Numerical study of sink-flow boundary layers," *J. Fluid Mech.*, Vol. 172, 1986, pp. 307–328.

63. Spalart, P.R. , " Direct simulation of a turbulent boundary layer up to $R_\theta = 1410$," *J. Fluid Mech.*, Vol. 187, 1988, pp. 61–98.

64. Spalart, P.R. , "Direct numerical study of leading-edge contamination," *Fluid Dynamics of Three-Dimensional Turbulent Shear Flows and Transition*, AGARD-CP-438, 1989, pp. 5.1-5.13.

65. Spalart, P.R., "Direct numerical study of crossflow instability," In *Laminar-turbulent Transition*, D. Arnal & R. Michel (eds.), Springer-Verlag, Berlin, 1989, pp 621–630.

66. Spalart, P.R. & Yang, K.S., "Numerical study of ribbon-induced transition in Blasius flow," *J. Fluid Mech.*, Vol. 178, 1987, pp. 345–365.

67. Spina, E.F., Smits, A.J. & Robinson, S.K., "The physics of supersonic turbulent boundary layers," *Ann. Rev. Fluid Mech.*, Vol. 26, 1994, pp. 287–319.

68. Stetson, K.F. & Kimmel, R.L., "On hypersonic boundary-layer stability," *AIAA Paper* 92-0737.

69. Thumm, A., Wolz, W. & Fasel, H., "Numerical simulation of spatially growing three-dimensional disturbance waves in compressible boundary layers," *Laminar-turbulent Transition*, D. Arnal, R. Michel (eds.), Springer, Berlin, 1989, pp. 303–308.

70. Wray A.A., "Very low storage time-advancement schemes," *Internal Report*, 1986, Nasa-Ames Research Center, Moffet Field, CA.

71. Zang, T.A., "Numerical simulation of the dynamics of turbulent boundary layers: perspective of transition simulator," *Phil. Trans. R. Soc. Lond. A*, Vol. 337, 1991, pp. 95–102.

72. Zang, T.A., Chang, C.L., & Ng, L.L., "The transition prediction toolkit: LST, SIT, PSE, DNS and LES," *Fifth Symposium on Numerical and Physical Aspects of Aerodynamic Flow*, January, 1992, CA. USA.

Simulation des Grandes Echelles d'Ecoulements Transitionnels

P. Comte, F. Ducros, J. Silvestrini, E. David, E. Lamballais, O. Métais & M. Lesieur
L.E.G.I./Institut de Mécanique de Grenoble *
B.P. 53 X, F38041 Grenoble Cedex, France
Tel: (33) 76 82 51 21, Fax: (33) 76 82 52 71, E-Mail: comte@img.fr

1. RÉSUMÉ
Deux nouveaux modèles de turbulence sous-maille sont proposés, sur la base du *modèle de la fonction de structure d'ordre 2 des vitesses* développé par Métais et Lesieur (*J. Fluid Mech.*, 1992, **239**, 157–194). Ils résultent de deux approches différentes visant à empêcher les fluctuations à grande échelles d'apporter de la viscosité turbulente. Des simulations de couches limites à Mach 0.5 sont présentées, montrant que ces deux modèles permettent de simuler la transition et l'atteinte d'un régime turbulent développé pour des coûts de calcul modérés, dans des configurations sensiblement différentes (plaque adiabatique et dièdre fortement chauffé).

2. INTRODUCTION
Malgré la continuelle augmentation des performances des supercalculateurs vectoriels et parallèles, la simulation de la transition à la turbulence demeure un défi technologique, même dans le cas d'écoulements en géométrie simple comme les couches limites se développant sur une plaque plane (voir Ref. [1] pour revue). Rai et Moin [2] sont récemment parvenus à reproduire en simulation numérique directe (DNS) des couches limites expérimentales quasi-incompressibles fortement bruitées (2.6% d'intensité turbulente à l'entrée, voir Refs. [3–5]) au prix de 800 heures de Cray-YMP par calcul. La simulation directe de couches limites sur des avions en vol (donc avec des niveaux de turbulence résiduelle plus faibles qu'en soufflerie) aurait largement excédé les ressources informatiques actuellement disponibles.

Ici, nous travaillons à des résolutions très inférieures, étant limités en pratique à des coûts de calcul de l'ordre de 50 heures par simulation, sur supercalculateurs de performances analogues. Dans nos simulations de couches limites, les mailles de calcul sont choisies suffisamment fines pour que les fonctions propres des modes les plus instables s'y discrétisent avec suffisamment de précision. Nous vérifions ce point en calculant le taux de croissance de ces modes pendant la transition. Les échelles plus petites – susceptibles d'être filtrées par le maillage – peuvent a priori provenir de trois origines :

- d'éventuels modes amortis ou peu amplifiés mais dont certains pourraient êtres nécessaires à la transition (modes circulaire ou *de Squire*, pouvant entrer en résonnance avec des modes plus instables).
- La turbulence à petite échelle qui se développe après la transition, dans la zone tampon ou la région logarithmique de la couche limite. Cette turbulence provient principalement du déferlement de couches de mélange locales au niveau de la pointe de tourbillons *en épingle à cheveux* organisés à plus grande échelle, et qui sont, eux, a priori résolus explicitement.
- Les tourbillons à petite échelle qui sont générés près de la paroi et qui exercent un transfert d'énergie inverse *(backscatter)* vers les tourbillons plus gros situés au-dessus.

Pour tous les écoulements que nous simulons (turbulence homogène, couches de mélange, jets, sillages, couches limites, écoulements en géométrie complexe...), nous modélisons la turbulence sous-maille à l'aide d'une viscosité turbulente. Nous proposons plusieurs modèles. Leurs constantes sont déterminées analytiquement dans le cas d'une turbulence homogène isotrope présentant une cascade de Kolmogorov de $k = 0$ à $k \longrightarrow \infty$. Nous présentons deux approches permettant de rendre ces modèles *sélectifs*, c'est-à-dire de les rendre aussi peu sensibles que ce soit aux gradients moyens et aux fluctuations de vitesse à grande échelle. Des exemples d'application montrent ensuite que ces deux approches sont prometteuses, en dépit de la rusticité des modèles et des résolutions employées.

3. MODÉLISATION SOUS-MAILLE
3.1 Les équations du mouvement
Le formalisme des simulations des grandes échelles étant bien connu en régime incompressible, nous nous plaçons ici dans le cas des écoulements compressibles. Les équations de Navier-Stokes et de l'énergie pour un gaz parfait polytropique s'écrivent, sous forme conservative et avec sommation sur les indices répétés,

$$\frac{\partial U}{\partial t} + \frac{\partial F_i}{\partial x_i} = 0 \quad , \tag{1}$$

avec

$$U = {}^T(\rho, \rho u, \rho v, \rho w, \rho e) \quad , \tag{2}$$

ρe étant l'énergie totale définie par

$$\rho e = \rho\, c_v\, T + \tfrac{1}{2}\rho(u_1^2 + u_2^2 + u_3^2) \quad . \tag{3}$$

Les flux F_i s'écrivent

$$F_i = \begin{pmatrix} \rho u_i \\ \rho u_i u_1 - \sigma_{i1} \\ \rho u_i u_2 - \sigma_{i2} \\ \rho u_i u_3 - \sigma_{i3} \\ \rho e u_i - u_j \sigma_{ij} - k\dfrac{\partial T}{\partial x} \end{pmatrix} \quad , \tag{4}$$

$k = \rho c_p \kappa$ étant la conductivité thermique. Les composantes σ_{ij} du tenseur des contraintes sont données par la loi de Newton

$$\begin{aligned} \sigma_{ij} &= -p\ \delta_{ij} + \lambda(\vec{\nabla}.\vec{u})\delta_{ij} + \mu\left[\frac{\partial u_j}{\partial x_i} + \frac{\partial u_i}{\partial x_j}\right] \quad , \\ &= -p\ \delta_{ij} + \underbrace{(\lambda + \tfrac{2}{3}\mu)}_{2^{ème}\ \text{viscosité}}(\vec{\nabla}.\vec{u})\delta_{ij} + \mu\tau_{ij} \quad , \end{aligned} \tag{5}$$

*Institut National Polytechnique de Grenoble (INPG), Université Joseph Fourier (UJF) et Centre National de la Recherche Scientifique (CNRS).

Paper presented at the 74th Fluid Dynamics Symposium on "Application of Direct and Large Eddy Simulation to Transition and Turbulence" held at Chania, Crete, Greece, in April 1994.

τ_{ij} étant la partie déviatrice du tenseur des déformations

$$\tau_{ij} = \left[\frac{\partial u_j}{\partial u_i} + \frac{\partial u_i}{\partial u_j} - \frac{2}{3}(\vec{\nabla}.\vec{u})\delta_{ij} \right] \qquad (6)$$

et l'on supposera la deuxième viscosité nulle (équilibre thermodynamique). On élimine la pression à l'aide de l'équation d'état des gaz parfaits $p = R\ \rho\ T$, avec $R = \frac{\mathcal{R}}{\mathcal{M}} = 287.06\ Jkg^{-1}K^{-1}$ dans le cas de l'air, ce qui donne

$$F_i = \begin{pmatrix} \rho u_i \\ \rho u_i u_1 + \rho RT\delta_{i1} - \mu\tau_{i1} \\ \rho u_i u_2 + \rho RT\delta_{i2} - \mu\tau_{i2} \\ \rho u_i u_3 + \rho RT\delta_{i3} - \mu\tau_{i3} \\ \rho(e + RT)u_i - \mu\tau_{ij}u_j - k\dfrac{\partial T}{\partial x} \end{pmatrix} \quad . \qquad (7)$$

La viscosité moléculaire $\mu(T)$ est donnée par la loi empirique de Sutherland et son extension habituelle pour les basses températures

$$\mu(T) = \begin{cases} \mu(273.15)\sqrt{\dfrac{T}{273.15}}\ \dfrac{1 + S/273.15}{1 + S/T} & \text{si } T \geq 120K \\ \quad \text{avec } \mu(273.15) = 1.711\ 10^{-5}\,Pl \\ \quad \text{et } S = 110.4K \\ \mu(120)\ T/120 & \text{si } T < 120K\ . \end{cases} \qquad (8)$$

La conductivité moléculaire $k(T)$ s'en déduit par l'intermédiaire du nombre de Prandtl $Pr = c_p\mu(T)/k(T)$ supposé constant égal à 0.7 (air).

3.2 Le filtrage

Le formalisme ci-dessus suppose toutes les variables du mouvement continues, sauf éventuellement dans les chocs. Lorsque l'on discrétise ces variables sur une grille, on procède à une opération de filtrage (passe-bas). A toute variable continue ϕ, on associe une variable discrète $\overline{\phi}(\vec{x}, t)$ définie en chaque point du maillage (ou en chaque point de collocation, lorsque l'on utilise des méthodes spectrales). Si l'on fait abstraction des erreurs introduites par les méthodes numériques, on peut montrer [6] que, dans presque tous les cas, l'opérateur $\overline{\ }$ commute avec les dérivées partielles temporelle et spatiales :

$$\overline{\frac{\partial \phi}{\partial t}} = \frac{\partial \overline{\phi}}{\partial t} \quad \text{et} \quad \overline{\frac{\partial \phi}{\partial x_i}} = \frac{\partial \overline{\phi}}{\partial x_i} \quad . \qquad (9)$$

Pour les écoulements compressibles, il est également commode d'introduire l'opérateur $\widetilde{\ }$ défini par

$$\widetilde{\phi} = \frac{\overline{\rho\phi}}{\overline{\rho}} \qquad \text{et} \qquad \phi'' = \phi - \widetilde{\phi} \quad , \qquad (10)$$

qui est à l'opérateur $\overline{\ }$ ce que les moyennes de Favre sont aux moyennes de Reynolds. La convolution du système (1) par le filtre $\overline{\ }$ donne alors, en utilisant les propriétés (9),

$$\frac{\partial \overline{U}}{\partial t} + \frac{\partial \overline{F_i}}{\partial x_i} = 0 \quad , \qquad (11)$$

avec

$$\overline{U} = {}^T(\overline{\rho}, \overline{\rho}\widetilde{u}, \overline{\rho}\widetilde{v}, \overline{\rho}\widetilde{w}, \overline{\rho}\widetilde{e}) \qquad (12)$$

l'*énergie totale résolue* $\overline{\rho e} = \overline{\rho}\widetilde{e}$ étant donnée par

$$\overline{\rho}\widetilde{e} = \overline{\rho}\ c_v\ \widetilde{T} + \tfrac{1}{2}\overline{\rho(u_1^2 + u_2^2 + u_3^2)} \quad . \qquad (13)$$

Les flux *résolus* $\overline{F_i}$ s'écrivent

$$\overline{F_i} = \begin{pmatrix} \overline{\rho}\widetilde{u_i} \\ \overline{\rho u_i u_1} + \overline{\rho}R\widetilde{T}\delta_{i1} - \overline{\mu\tau_{i1}} \\ \overline{\rho u_i u_2} + \overline{\rho}R\widetilde{T}\delta_{i2} - \overline{\mu\tau_{i2}} \\ \overline{\rho u_i u_3} + \overline{\rho}R\widetilde{T}\delta_{i3} - \overline{\mu\tau_{i3}} \\ \overline{\rho(e + RT)u_i} - \overline{\mu\tau_{ij}u_j} - k\dfrac{\overline{\partial T}}{\partial x} \end{pmatrix} \quad . \qquad (14)$$

certains termes n'étant pas calculables, ils doivent être modélisés.

3.3 La fermeture

Là encore, nous avons choisi l'option la plus simple : les termes faisant intervenir des coefficients de diffusion moléculaire (μ ou k) sont simplement remplacés par la quantité calculable d'expression la plus proche. On pose ainsi

$$\overline{\mu\tau_{ij}} \cong \widetilde{\mu}\widetilde{\tau_{ij}} \qquad (15)$$

et

$$\overline{\mu\tau_{ij}u_j} \cong \widetilde{\mu}\widetilde{\tau_{ij}}\widetilde{u_j} \qquad (16)$$

avec $\widetilde{\mu} = \mu(\widetilde{T})$ donné par la loi de Sutherland (8). On pose de même

$$\overline{k\frac{\partial T}{\partial x}} = \widetilde{k}\frac{\partial \widetilde{T}}{\partial x} \quad , \qquad (17)$$

avec $Pr = c_p\widetilde{\mu}/\widetilde{k} = 0.7$.

Les termes $\overline{\rho u_i u_j}$ et $\overline{\rho(e + RT)u_i}$ sont écrits comme somme de la quantité calculable d'expression la plus proche et d'un résidu non calculable, respectivement *tenseur des contraintes sous-maille* T_{ij} et *flux de chaleur sous-maille* Q_i.

$$\overline{\rho u_i u_j} = \overline{\rho}\widetilde{u_i}\widetilde{u_j} + \underbrace{[\overline{\rho u_i u_j} - \overline{\rho}\widetilde{u_i}\widetilde{u_j}]}_{T_{ij}} \qquad (18)$$

et

$$\overline{\rho(e + RT)u_i} = \overline{\rho}(\widetilde{e} + R\widetilde{T})\widetilde{u_i} + \underbrace{[\overline{\rho(e + RT)u_i} - \overline{\rho}(\widetilde{e} + R\widetilde{T})\widetilde{u_i}]}_{Q_i} \qquad (19)$$

L'hypothèse de Boussinesq (Refs. [7], [8]) consiste à supposer la partie déviatrice du tenseur des contraintes sous-maille T_{ij} proportionnelle à $\widetilde{\tau_{ij}}$, la partie déviatrice du tenseur des déformations résolu, le coefficient de proportionnalité étant une *viscosité turbulente* μ_t. Il est donc naturel d'introduire un autre coefficient λ_t reliant les parties isotropes de ces deux tenseurs, et de poser

$$\begin{aligned} T_{ij} &= \lambda_t(\vec{\nabla}.\vec{\widetilde{u}})\delta_{ij} + \mu_t\left[\frac{\partial \widetilde{u_j}}{\partial x_i} + \frac{\partial \widetilde{u_i}}{\partial x_j}\right] \quad , \\ &= (\lambda_t + \tfrac{2}{3}\mu_t)(\vec{\nabla}.\vec{\widetilde{u}})\delta_{ij} + \mu_t\widetilde{\tau_{ij}} \quad . \end{aligned} \qquad (20)$$

Le coefficient $(\lambda_t + \frac{2}{3}\mu_t)$ apparait ainsi comme une *deuxième viscosité turbulente* rendant compte d'un éventuel déséquilibre thermodynamique (au sens de la mécanique statistique) entre les degrés de liberté de la turbulence sous-maille. Vu que nous supposons que celle-ci suit une cascade de Kolmogorov traduisant une hypothèse d'équilibre énergétique, il est consistant d'imposer[1]

$$(\lambda_t + \tfrac{2}{3}\mu_t) \cong 0 \quad , \qquad (21)$$

ce qui revient à ne pas modéliser la partie isotrope de T_{ij}. Le choix (21) implique donc

$$\overline{\rho u_i u_i} \cong \overline{\rho}\widetilde{u_i}\widetilde{u_i} \quad , \qquad (22)$$

ce qui permet d'exprimer la *température résolue* $\widetilde{T}$ à partir de $\overline{U}$ grâce à (13). On obtient

$$\widetilde{T} = \frac{1}{c_v}\widetilde{e} - \frac{1}{2}(\widetilde{u_1}^2 + \widetilde{u_2}^2 + \widetilde{u_3}^2) \quad , \qquad (23)$$

ce qui permet de déterminer $\widetilde{\mu}$ et $\widetilde{k}$.

[1] voir à ce sujet la discussion sur la cascade de Kolmogorov et celle sur la deuxième viscosité dans Landau et Lifshitz [9].

Pour finir, le flux de chaleur sous-maille Q_i est modélisé en supposant qu'il suit un analogue turbulent de la loi de Fourier. De manière consistante avec l'hypothèse de Boussinesq, on pose

$$Q_i = -k_t \frac{\partial \widetilde{T}}{\partial x_i} \quad , \tag{24}$$

k_t étant un coefficient de conductivité turbulente relié à μ_t par l'intermédiaire d'un nombre de Prandtl turbulent

$$Pr_t = \frac{c_p \mu_t}{k_t} \quad . \tag{25}$$

En introduisant la *viscosité turbulente cinématique* $\nu_t = \mu_t/\overline{\rho}$ et la *diffusivité turbulente* $\kappa_t = k_t/c_p\overline{\rho}$, les flux résolus $\overline{F_i}$ se mettent finalement sous la forme

$$\overline{F_i} = \begin{pmatrix} \overline{\rho}\widetilde{u_i} \\ \overline{\rho}\widetilde{u_i}\widetilde{u_1} + \overline{\rho}R\widetilde{T}\delta_{i1} - (\widetilde{\mu} + \overline{\rho}\nu_t)\widetilde{\tau_{i1}} \\ \overline{\rho}\widetilde{u_i}\widetilde{u_2} + \overline{\rho}R\widetilde{T}\delta_{i2} - (\widetilde{\mu} + \overline{\rho}\nu_t)\widetilde{\tau_{i2}} \\ \overline{\rho}\widetilde{u_i}\widetilde{u_3} + \overline{\rho}R\widetilde{T}\delta_{i3} - (\widetilde{\mu} + \overline{\rho}\nu_t)\widetilde{\tau_{i3}} \\ \overline{\rho}(\widetilde{e} + R\widetilde{T})\widetilde{u_i} - \widetilde{\mu}\widetilde{\tau_{ij}}\widetilde{u_j} - (\widetilde{k} + \overline{\rho}c_p\kappa_t)\dfrac{\partial \widetilde{T}}{\partial x} \end{pmatrix} \quad , \tag{26}$$

avec

$$\widetilde{\tau_{ij}} = \left[\frac{\partial \widetilde{u_j}}{\partial u_i} + \frac{\partial \widetilde{u_i}}{\partial u_j} - \frac{2}{3}(\vec{\nabla}.\vec{\widetilde{u}})\delta_{ij} \right] \tag{27}$$

et

$$Pr_t = \frac{\nu_t}{\kappa_t} \quad . \tag{28}$$

3.4 Modèles éprouvés

3.4.1 Modèle(s) de Smagorinsky

Le modèle sous-maille le plus connu est le modèle de Smagorinsky [10] défini par

$$\nu_t(\vec{x}, t) = (C_s\Delta)^2 \sqrt{\tfrac{1}{2}\widetilde{\tau_{ij}}\widetilde{\tau_{ij}}} \quad , \tag{29}$$

toujours avec sommation sur les indices répétés. Δ est une échelle caractéristique de la taille de la maille de calcul, par exemple

$$\Delta = \sqrt[3]{\Delta x_1 \Delta x_2 \Delta x_3} \quad , \tag{30}$$

et C_s est une constante. Notons qu'il existe une variante moins connue de ce modèle, définie par

$$\nu_t(\vec{x}, t) = (C_v\Delta)^2 \sqrt{\vec{\widetilde{\omega}}.\vec{\widetilde{\omega}}} \quad , \tag{31}$$

$\vec{\widetilde{\omega}} = \vec{\nabla} \times \vec{\widetilde{u}}$ étant la vorticité résolue, et C_v une autre constante.

Si l'on considére une turbulence tridimensionnelle homogène isotrope incompressible suivant une cascade de Kolmogorov d'extension infinie, on trouve $C_s = 0.18$ pour une valeur de la constante de Kolmogorov $C_K = 1.4$. Deardorff [11], puis Moin et Kim [12] sont parvenus à simuler l'écoulement turbulent pleinement développé dans un canal en abaissant la valeur de C_s à 0.1 et en la multipliant par une fonction empirique d'amortissement $[1-\exp(y^+/25)]$. Ce modèle est en revanche trop dissipatif pour permettre de simuler la transition, sauf dans des cas fortement bruités [13]. Les ondes de Tollmien-Schlichting qui se développent pendant la transition créent des fluctuations de vitesse résolue $\vec{\widetilde{u}}$ à grande échelle (de l'ordre de 30 fois l'épaisseur de déplacement locale de la couche limite). Sans fonction d'amortissement, la dissipation occasionnée par le modèle peut alors atteindre 35% de la dissipation moléculaire. Avec fonction d'amortissement, elle est réduite à 7%, ce qui est encore excessif [14].

3.4.2 Modèle spectral

Le moyen d'éliminer radicalement ce problème est de se placer, lorsque c'est possible, dans un espace spectral adapté aux conditions aux limites et au maillage de la simulation (par exemple l'espace de Fourier si les conditions aux limites sont périodiques, ou celui des polynomes de Tchebischev si le maillage respecte la disposition des points de collocation). A chaque quantité $\phi(\vec{x}, t)$ correspond alors une unique représentation spectrale $\hat{\phi}(\vec{k}, t)$, en appelant $\vec{k}$ le vecteur d'onde dans l'espace spectral et k sa norme. On a alors accès directement aux plus petites échelles résolues, ce qui permet d'en déduire une viscosité turbulente de type *longueur de mélange*

$$\nu_t \propto \Delta.u'_\Delta \quad , \tag{32}$$

u'_Δ étant une estimation de l'écart-type des fluctuations de vitesse à la plus petite échelle résolue Δ. En turbulence homogène isotrope, on peut introduire le spectre d'énergie 3D isotrope $E(k, t)$ défini par

$$E(k, t) = 2\pi k^2 \langle \hat{u}_i(-\vec{k}, t)\hat{u}_i(\vec{k}, t) \rangle_{\|\vec{k}\|=k} \quad . \tag{33}$$

$\vec{\hat{u}}(\vec{k}, t)$ étant la transformée de Fourier 3D de $\vec{u}(\vec{x}, t)$. Une bonne estimation de u'_Δ est alors donnée par (voir Ref. [15])

$$u'_\Delta = \sqrt{k_c\ E(k_c)} \ , \text{ avec } \ k_c = \pi/\Delta \quad , \tag{34}$$

k_c étant le *nombre d'onde de coupure* associé à la taille de la maille Δ. Eq. (32) s'écrit alors

$$\nu_t = \nu_t^+ \sqrt{\frac{E(k_c, t)}{k_c}} \quad , \tag{35}$$

ν_t^+ étant une viscosité turbulente adimensionnelle. Il suffit alors de choisir ν_t^+ bornée pour garantir

$$\nu_t = 0 \Longleftrightarrow E(k_c, t) = 0 \quad . \tag{36}$$

Si la résolution est suffisante pour bien résoudre les instabilités qui se développent pendant les phases initiales de la transition, on aura $E(k_c, t) = 0$ et donc $\nu_t = 0$ jusqu'à l'apparition de turbulence à la plus petite échelle résolue.

Les modèles stochastiques de fermeture à deux points prédisent des fonctions $\nu_t^+(k/k_c)$ présentant toutes un plateau $\nu_t^+ = 0.267$ pour $k/k_c \longrightarrow 0$ et une brusque remontée *(cusp)* vers environ 0.7 au voisinage de la coupure. Un bon ajustement empirique est (voir [16])

$$\nu_t^+(k/k_c) = 0.267 + 9.21 \exp[-3.03(k/k_c)^{-1}] \quad , \tag{37}$$

donnant $\nu_t^+(1) = 0.712$ (voir Fig. 1).

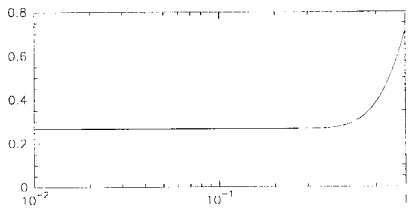

FIG. 1 - Courbe montrant $\nu_t^+(k/k_c)$ donné par eq. (37)

Ces modèles suggèrent également

$$Pr_t = \frac{\nu_t}{\kappa_t} \approx cte = 0.6 \quad , \tag{38}$$

ce que nous adopterons dans toute cette étude, bien que les simulations de Lesieur et Rogallo [17] aient mis en évidence une dépendance de Pr_t envers k/k_c. Le modèle spectral s'est révélé très bon pour simuler les écoulements turbulents isotropes ou non, mais aussi les écoulements cisaillés libres (voir par exemple les couches de mélange de Ref. [18], pour lesquelles l'écart-type des 3 composantes des fluctuations de vitesse est en bon accord avec les résultats expérimentaux, avec des spectres d'énergie en $k^{-5/3}$ au voisinage de k_c).

3.4.3 Modèle de la fonction de structure

L'idée de base ayant conduit à ce modèle était de transposer le modèle spectral dans l'espace physique, en essayant de préserver la propriété (38), qui garantit que le modèle ne perturbera pas la transition. Ceci n'est réalisable que de manière approchée, en raison du principe de Gabor,[2] qui interdit l'accès local à l'information simultanément dans l'espace physique et dans l'espace spectral.

Un bon candidat pour u'_Δ est la racine carrée de $\widetilde{F_{2\Delta}}$, la *fonction de structure d'ordre 2 des vitesses résolues* évaluée à l'échelle Δ, définie par

$$\widetilde{F_{2\Delta}}(\vec{x},t) = \left\langle \|\vec{\widetilde{u}}(\vec{x}+\vec{r},t)) - \vec{\widetilde{u}}(\vec{x},t)\|^2 \right\rangle_{\|\vec{r}\|=\Delta} \quad . \quad (39)$$

En effet, dans le cas de la turbulence homogène isotrope incompressible, Batchelor [19] a mis en évidence la relation

$$\langle F_{2r}(\vec{x},t)\rangle_{\vec{x}} = 4\int_0^\infty E(k,t)\left[1-\frac{\sin kr}{kr}\right]dk \quad , \quad (40)$$

entre la moyenne de la fonction de structure de la vitesse $\vec{u}$ *(non-filtrée)* à une échelle r donnée et le spectre isotrope d'énergie cinétique. Métais et Lesieur [20] en déduisirent le *modèle de la fonction de structure*, définissant une viscosité turbulente

$$\nu_t(\vec{x},t) = C\ \Delta\ \sqrt{\widetilde{F_{2\Delta}}(\vec{x},t)} \quad , \quad (41)$$

locale dans l'espace physique, la constante C valant $2C_S^2$, soit 0.063 pour $C_K = 1.4$.

La moyenne d'ensemble $\langle\rangle$ dans (39) porte sur les voisins immédiats du point $\vec{x}$. Lorsque l'on simule des écoulements libres ou non-cisaillés avec des mailles approximativement cubiques, on fait intervenir tous les six voisins. On a alors

$$\widetilde{F_{2\Delta}}(\vec{x},t) = \frac{1}{6}\Big[\|\vec{\widetilde{u}}(\vec{x}+\Delta\vec{x}_1,t) - \vec{\widetilde{u}}(\vec{x},t)\|^2 + \|\vec{\widetilde{u}}(\vec{x}-\Delta\vec{x}_1,t) - \vec{\widetilde{u}}(\vec{x},t)\|^2 + \|\vec{\widetilde{u}}(\vec{x}+\Delta\vec{x}_2,t) - \vec{\widetilde{u}}(\vec{x},t)\|^2 + \|\vec{\widetilde{u}}(\vec{x}-\Delta\vec{x}_2,t) - \vec{\widetilde{u}}(\vec{x},t)\|^2 + \|\vec{\widetilde{u}}(\vec{x}+\Delta\vec{x}_3,t) - \vec{\widetilde{u}}(\vec{x},t)\|^2 + \|\vec{\widetilde{u}}(\vec{x}-\Delta\vec{x}_3,t) - \vec{\widetilde{u}}(\vec{x},t)\|^2\Big] , \quad (42)$$

où $\Delta\vec{x}_i = \Delta x_i \vec{e}_i$ désigne le pas d'espace orienté dans la direction i.

Il est souvent nécessaire de resserrer le maillage dans la direction perpendiculaire au cisaillement moyen (ou à la paroi, dans le cas des couches limites). Lorsque cette direction coïncide avec une direction de maillage (x_2, par exemple), nous calculons la fonction de structure en ne faisant intervenir, outre le point central $\vec{x}$, que les 4 voisins situés dans le "plan de maillage" (x_1x_3) passant par $\vec{x}$ (voir Fig. 2, en maillage curviligne orthogonal).

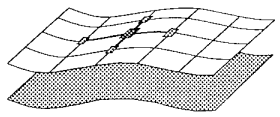

FIG. 2 - Points intervenant dans le calcul de $\widetilde{F_{2\Delta}}$ dans le cas des écoulements de paroi.

On prend alors

$$\widetilde{F_{2\Delta}}(\vec{x},t) = \frac{1}{4}\Big[\|\vec{\widetilde{u}}(\vec{x}+\Delta\vec{x}_1,t) - \vec{\widetilde{u}}(\vec{x},t)\|^2 + \|\vec{\widetilde{u}}(\vec{x}-\Delta\vec{x}_1,t) - \vec{\widetilde{u}}(\vec{x},t)\|^2 + \|\vec{\widetilde{u}}(\vec{x}+\Delta\vec{x}_3,t) - \vec{\widetilde{u}}(\vec{x},t)\|^2 + \|\vec{\widetilde{u}}(\vec{x}-\Delta\vec{x}_3,t) - \vec{\widetilde{u}}(\vec{x},t)\|^2\Big] . \quad (43)$$

La *longueur de mélange* Δ intervenant dans (39) est alors prise égale à

$$\Delta = \sqrt{\Delta x_1 \Delta x_3} \approx \Delta x_1 \approx \Delta x_3 \quad . \quad (44)$$

Dans notre équipe, nous avons constaté que le modèle de la fonction de structure, à 4 ou 6 points, se comportait légèrement mieux que le modèle de Smagorinsky (voir en particulier Fig. 16 de Ref. [21], montrant des profils d'énergie cinétique turbulente dans le cas de l'écoulement à l'aval d'une marche descendante, avec comparaison avec les résultats expérimentaux d'Eaton et Johnston [22]). Pour comparer formellement ces deux modèles, nous pouvons, au premier ordre, relier les incréments de vitesse de la fonction de structure à des dérivées. De

$$\vec{\widetilde{u}}(\vec{x}+\Delta\vec{x}_i,t) - \vec{\widetilde{u}}(\vec{x},t) = \Delta x_i\left(\frac{\partial\vec{\widetilde{u}}}{\partial x_i}\right)_{\vec{x}} + \mathcal{O}(\Delta x_i^2) \quad , \quad (45)$$

on peut déduire, dans le cas où $\Delta x_1 = \Delta x_2 = \Delta x_3 = \Delta$, et en supposant le champ de vitesse résolu $\widetilde{u}$ non-divergent,

$$\widetilde{F_{2\Delta}}(\vec{x},t) \underset{\Delta\to 0}{=} \frac{1}{6}\left[2\Delta x_1^2\left\|\frac{\partial\vec{\widetilde{u}}}{\partial x_1}\right\|^2 + 2\Delta x_2^2\left\|\frac{\partial\vec{\widetilde{u}}}{\partial x_2}\right\|^2 + 2\Delta x_3^2\left\|\frac{\partial\vec{\widetilde{u}}}{\partial x_3}\right\|^2\right][1+\mathcal{O}(\Delta)]$$

$$\underset{\Delta\to 0}{=} \frac{\Delta^2}{6}\left[\tfrac{1}{2}\widetilde{\tau_{ij}}\widetilde{\tau_{ij}} + \vec{\widetilde{\omega}}.\vec{\widetilde{\omega}}\right][1+\mathcal{O}(\Delta)] \quad . (46)$$

et donc

$$\nu_t(\vec{x},t) \underset{\Delta\to 0}{\sim} \sqrt{\frac{2}{3}}\,(C_s\Delta)^2\,\sqrt{\tfrac{1}{2}\widetilde{\tau_{ij}}\widetilde{\tau_{ij}} + \vec{\widetilde{\omega}}.\vec{\widetilde{\omega}}} \quad . \quad (47)$$

Dans la limite d'un pas d'espace infiniment petit, le modèle de la fonction de structure n'est consistant avec aucune des deux variantes du modèle de Smagorinsky, mais il se rapproche d'une combinaison des deux, moins dissipative que chacune d'elles dans les régions où vorticité et étirement s'excluent mutuellement (*i.e.* là où $\widetilde{\tau_{ij}}\widetilde{\tau_{ij}} = 0$ ou $\vec{\widetilde{\omega}}.\vec{\widetilde{\omega}} = 0$).

Fig. 3 montre une comparaison entre une simulation directe au nombre de Reynolds le plus élevé possible, et deux simulations des grandes échelles à nombre de Reynolds moléculaire infini. Ces résultats confirment que les simulations des grandes échelles permettent de simuler des écoulements plus turbulents que les simulations directes à même résolution.

[2] analogue du principe d'incertitude de Heisenberg en traitement du signal.

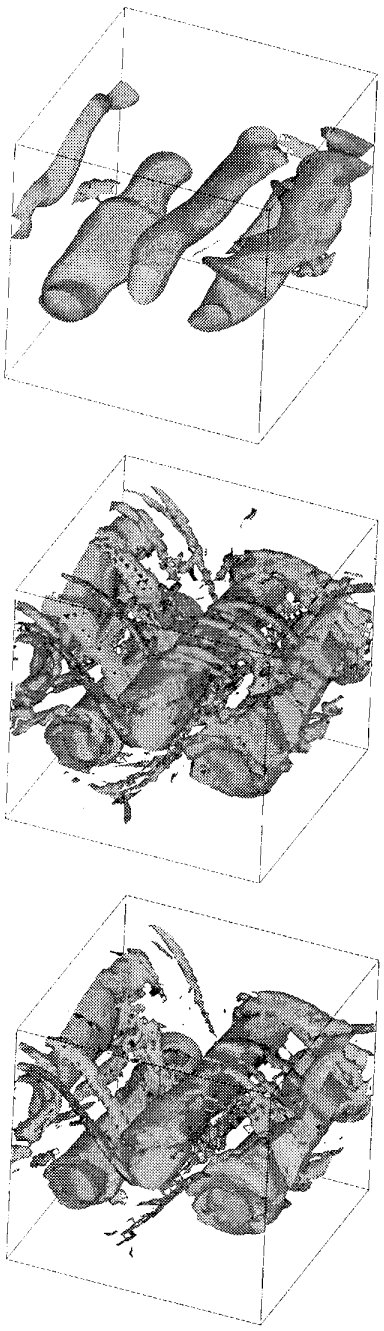

FIG. 3 - Sillage temporel incompressible simulé par méthodes spectrales avec une résolution de 48^3 modes de Fourier. De haut en bas :
- Simulation directe *(DNS)* at $R_e = U_m r_m/\nu = 200$
- Simulation des grandes échelles *(LES)* à $\mu = 0$, à l'aide du modèle de la fonction de structure (à six voisins)
- idem, avec le modèle de Smagorinsky.
Dans les 3 cas, l'image représente l'isosurface $\|\vec{\omega}\| = 0.5\ \omega_i$ à $t = 76 r_m/U_m$, en posant $\omega_i = \max\|\vec{\omega}(\vec{x},0)\|$. Les valeurs maximales de $\|\vec{\omega}\|$ à cet instant sont respectivement de 1, 2.2 et 2.1 ω_i pour la simulation directe, la simulation avec le modèle de la fonction de structure, et celle avec le modèle de Smagorinsky.

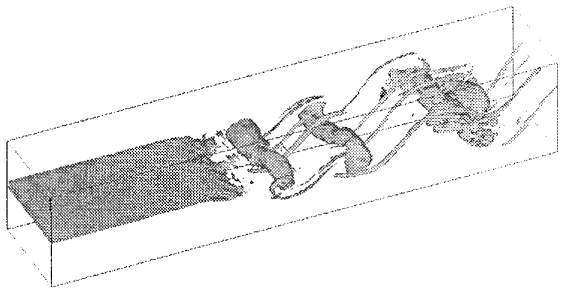

FIG. 4 - Couche de mélange incompressible se développant spatialement, en simulation des grandes échelles à l'aide du modèle de la fonction de structure *viscosité moléculaire* $\mu = 0$, *résolution :* $240 \times 48 \times 48$, *schéma numérique : compact ordre 6 & spectral, forçage amont : 2% de bruit 2D + 0.6% de bruit 3D (en intensité turbulente), quantité visualisée : isosurface* $\|\vec{\omega}\| = 0.6\ \omega_i$

Ils montrent que des modèles basés sur une hypothèse de cascade de Kolmogorov isotrope (comme le modèle de Smagorinsky avec $C_s \approx 0.2$ et le modèle de la fonction de structure) peuvent respecter les fins tourbillons longitudinaux – fortement anistotropes – dont le diamètre est proche de Δ. Ceci se confirme dans le cas des écoulements se développant spatialement, avec des schémas aux différences finies dans la direction longitudinale, et en employant la formulation (43) à 4 voisins (voir Fig. 4).

3.5 Nouveaux modèles

3.5.1 Modèle de la fonction de structure filtrée

Etant très local dans l'espace physique, le modèle de la fonction de structure ne peut pas être très local dans l'espace spectral. Ceci implique que le modèle ne sera pas influencé que par les plus petites échelles résolues. Ceci est assez peu sensible sur les écoulements dont les instabilités dominantes sont des instabilités des cisaillement inflexionnel (inviscides et fortment amplifiées, comme dans les couches de mélange, les jets, les sillages et les couches limites fortement chauffées ou à haut nombre de Mach).

En revanche, le modèle de la fonction de structure met – comme le modèle de Smagorinsky – de la viscosité turbulente dans les ondes de Tollmien-Schlichting (même si ces dernières sont bien résolues), au point d'empêcher les couches limites faiblement compressibles de transitionner si elles ne sont pas fortement forcées. Une solution pour y remédier est de rechercher pour u'_Δ un meilleur compromis que $\sqrt{\widetilde{F_2}_\Delta}$, moins local dans l'espace physique pour l'être davantage dans l'espace spectral. Nous avons recherché ce candidat parmi les fonctions *ondelette*, dont les propriétés d'orthogonalité sont attractives, mais dont la mise en œuvre reste lourde à trois dimensions [23].

Il est beaucoup moins coûteux de s'inspirer de la méthode d'enregistrement des disques microsillons, récemment devenus obsolètes : pour réduire la largeur du sillon, les fréquences graves du signal sont atténuées avant d'actionner le burin graveur *(accentuation)*.[3] Nous appliquons de même un filtre passe-haut au champ de vitesse résolu $\tilde{\vec{u}}$

[3] La correction inverse *(désaccentuation, ou correction RIAA)* est appliquée au niveau du préamplificateur pendant l'écoute.

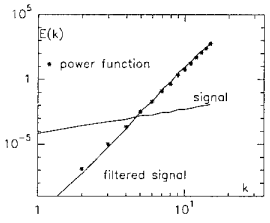

FIG. 5 - Preuve de la relation (50). Le signal d'entrée $\vec{\tilde{u}}$ est un bruit blanc discrétisé à 32^3 modes de Fourier. Son spectre $E(\vec{\tilde{u}})$ est en k^2 (la courbe libellée *signal*). Le spectre $E[\mathcal{L}^3(\vec{\tilde{u}})]$ est libellé *filtered signal*. Les points correspondent à $0.57\pi^{10.1}\ (k/k_c)^{10.1} E(\vec{\tilde{u}})$.

avant d'en calculer la fonction de structure. Il s'agit d'un filtre de type laplacien, discrétisé au second ordre à l'aide d'un schéma centré, et que l'on itère m fois :

$$\mathcal{L}^m(\vec{\tilde{u}}) = \underbrace{[\mathcal{L} \circ \ldots \circ \mathcal{L}]}_{m \text{ fois}}(\vec{\tilde{u}}) \qquad (48)$$

avec

$$\mathcal{L}(\vec{\tilde{u}}) = \sum_i \left[\vec{\tilde{u}}(\vec{x} - \Delta\vec{x}_i, t) - 2\vec{\tilde{u}}(\vec{x}, t) + \vec{\tilde{u}}(\vec{x} + \Delta\vec{x}_i, t)\right] \quad , \qquad (49)$$

$i \in \{1, 2, 3\}$ pour les écoulements libres et $i \in \{1, 3\}$ pour les couches limites. Le meilleur compromis efficacité-rapport signal/bruit est atteint pour $m = 3$ (voir Ref. [24]). Dans une boîte cubique avec des conditions aux limites périodiques dans les trois directions, nous avons alors obtenu

$$\frac{E[\mathcal{L}^3(\vec{\tilde{u}})]}{E(\vec{\tilde{u}})} \approx a\pi^p \left(\frac{k}{k_c}\right)^p \quad , \quad \forall k \in [0, k_c[\qquad (50)$$

avec $a = 0.57$ et $p = 10.1$, indépendemment du *signal d'entrée* $\vec{\tilde{u}}$ et de la résolution (Fig. 5). Un filtre tri-laplacien spectral ou exact aurait donné $a = 1$ et $p = 12$.

En reprenant *verbatim* les calculs ayant conduit au modèle de la fonction de structure [20] on obtient, avec les mêmes hypothèses,

$$\nu_t(\vec{x}, t) = C'_p\ \Delta\ \sqrt{\widetilde{\mathcal{F}_{2\Delta}}(\vec{x}, t)} \quad , \qquad (51)$$

avec

$$\widetilde{\mathcal{F}_{2\Delta}}(\vec{x}, t) = \left\langle \|[\mathcal{L}^3(\vec{\tilde{u}})](\vec{x} + \vec{r}, t)) - [\mathcal{L}^3(\vec{\tilde{u}})](\vec{x}, t)\|^2 \right\rangle_{\|\vec{r}\|=\Delta} \quad , \qquad (52)$$

et $C'_3 = 0.84\ 10^{-4}$ pour $C_K = 1.4$. Nous verrons que ce modèle permet, enfin, de simuler la transition à la turbulence d'une couche limite faiblement compressible sans forçage fort.

3.5.2 Modèle de la fonction de structure sélective

L'approche précédente consistait à augmenter la sélectivité du modèle de la fonction de structure en remplaçant $\widetilde{\mathcal{F}_{2\Delta}}$ par une fonction analysatrice plus sélective. Nous cherchons maintenant à développer un modèle sélectif adapté aux écoulements en géométrie complexe, où il se développe souvent des gradients à grande échelle dans des directions non-alignées avec le maillage (ondes de choc obliques, par exemple). Nous avons ici choisi de multiplier simplement la viscosité turbulente prédite par le modèle de la fonction de structure par une fonction filtre Φ, indépendante de l'orientation du maillage, valant 1 en présence de turbulence à la plus petite échelle résolue, et 0 sinon.

Le critère de tridimensionnalité à petite échelle que nous avons choisi est basé sur l'angle que fait, en chaque point $\vec{x}$ et à chaque instant, le vecteur vorticité résolu $\vec{\tilde{\omega}}(\vec{x}, t)$ avec sa moyenne instantanée sur un certain voisinage autour de $\vec{x}$. Une valeur élevée de cet angle, noté improprement $\langle\alpha\rangle_\Delta(\vec{x}, t)$ signifie que la direction de $\widetilde{\mathcal{F}_{2\Delta}}$ ne varie pas beaucoup dans la région de $\vec{x}$. L'écoulement y est donc laminaire ou bidimensionnel, et nous n'y appliquons pas de viscosité turbulente. Si cet angle est élevé, nous appliquons le modèle de la fonction de structure avec une constante réajustée pour tenir compte du filtre.

En pratique, on calcule un vecteur vorticité moyen $\langle\vec{\tilde{\omega}}\rangle_\Delta(\vec{x}, t)$ égal à la moyenne centrée de $\vec{\tilde{\omega}}$ en $\vec{x}$ et ses quatre (ou six) voisins. Pour la formulation à quatre voisins (la plus utilisée dans nos applications), on a donc

$$\langle\vec{\tilde{\omega}}\rangle_\Delta(\vec{x}, t) = \frac{1}{5}\left[\vec{\tilde{\omega}}(\vec{x}, t) + \vec{\tilde{\omega}}(\vec{x} + \Delta\vec{x}_1, t) + \vec{\tilde{\omega}}(\vec{x} - \Delta\vec{x}_1, t) + \vec{\tilde{\omega}}(\vec{x} + \Delta\vec{x}_3, t) + \vec{\tilde{\omega}}(\vec{x} - \Delta\vec{x}_3, t)\right] \quad . \qquad (53)$$

L'angle $\langle\alpha\rangle_\Delta(\vec{x}, t)$ est ensuite défini par

$$\langle\alpha\rangle_\Delta(\vec{x}, t) = \arcsin \frac{\|\vec{\tilde{\omega}}(\vec{x}, t) \wedge \langle\vec{\tilde{\omega}}\rangle_\Delta(\vec{x}, t)\|}{\|\vec{\tilde{\omega}}(\vec{x}, t)\|\ \|\langle\vec{\tilde{\omega}}\rangle_\Delta(\vec{x}, t)\|} \quad , \qquad (54)$$

et l'on pose

$$\nu_t(\vec{x}, t) = C''_{\alpha_0}\ \Phi_{\alpha_0}(\vec{x}, t)\ \Delta\ \sqrt{\widetilde{\mathcal{F}_{2\Delta}}(\vec{x}, t)} \quad , \qquad (55)$$

avec

$$\Phi_{\alpha_0}(\vec{x}, t) = \begin{cases} 1 & \text{si} \quad \langle\alpha\rangle_\Delta(\vec{x}, t) \geq \alpha_0 \\ 0 & \text{sinon} \end{cases} \quad . \qquad (56)$$

La valeur de α_0 a été choisie sur la base de dix simulations des grandes échelles de turbulence homogène isotrope incompressible, réalisées à l'aide du modèle de la fonction de structure (41) avec des conditions initiales différentes, à des résolutions de 32^3 et 48^3 modes de Fourier, comparables à celles que l'on utilise dans les simulations de couches limites. Après l'atteinte du régime de décroissance libre autosimilaire, les densités de probabilité de $\langle\alpha\rangle_\Delta(\vec{x}, t)$ ont montré un pic pour $\alpha_0 = 20°$ (voir Fig. 6 et [25]).

Nous avons aussi trouvé, pour toutes ces simulations,

$$\frac{\left\langle\sqrt{\widetilde{\mathcal{F}_{2\Delta}}(\vec{x}, t)}\right\rangle_{\vec{x}}}{\left\langle\Phi_{\alpha_0}(\vec{x}, t)\sqrt{\widetilde{\mathcal{F}_{2\Delta}}(\vec{x}, t)}\right\rangle_{\vec{x}}} \simeq cte = 1.56 \quad , \qquad (57)$$

indépendamment du temps, l'opérateur $\langle\rangle_{\vec{x}}$ désignant la moyenne sur l'ensemble du domaine de calcul. Pour que le modèle de la fonction de structure sélective donne à chaque instant la même valeur moyenne $\langle\nu_t(\vec{x}, t)\rangle_{\vec{x}}$ que le modèle de la fonction de structure (41), il suffit alors de fixer $C''_{20°} = 1.56\ C = 0.104$.

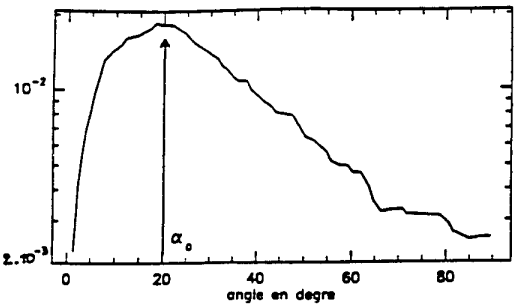

FIG. 6 - Densité de probabilité de $|\langle\alpha\rangle_\Delta(\vec{x},t)|$ calculée sur une des simulations des grandes échelles de turbulence homogène isotrope à 32^3, avec $\mu = 0$.

3.6 Évaluation des différents modèles

Comme pour les comparaisons présentées au chapitre 3.4, nous effectuons des simulations d'un écoulement cisaillé temporel, de manière à pouvoir utiliser un code de calcul pseudo-spectral, a priori plus précis qu'un code aux différences finies. Ceci permet aussi d'inclure le modèle spectral dans les comparaisons. Pour le modèle de la fonction de structure et ses dérivés, nous avons choisi la formulation à six voisins, plus consistante avec le modèle de Smagorinsky que celle à six voisisn. L'écoulement choisi est une couche de mélange incompressible, simulée à une résolution de 64^3 modes de Fourier, avec des conditions de glissement sans frottement dans la direction x_2, et des conditions périodiques suivant x_1 et x_3. La condition initiale est définie par

$$\vec{\tilde{u}}(\vec{x}, t=0) = U \left[\tanh\left(\frac{2x_2}{\delta_i}\right) \vec{e}_2 + 10^{-2} \vec{\psi}(\vec{x})\right] \quad , \tag{58}$$

δ_i étant l'épaisseur de vorticité initiale de la couche, U sa demi-différence de vitesse et $\vec{\psi}(\vec{x})$ étant une fonction aléatoire à divergence nulle, d'amplitude unitaire sur chacune des composantes. Nous présentons des visualisations de l'écoulement obtenu avec chacun des 5 modèles (sans viscosité moléculaire) au même instant ($t = 14\ \delta_i/U$). Il s'agit d'iso-surfaces des composantes longitudinale et transverse de la vorticité résolue, mettant repectivement en évidence les tourbillons longitudianaux et les tourbillons de Kelvin-Helmholtz primaires. Le seuil choisi est $\omega_i = 2U/\delta_i$, c'est-à-dire le maximum de la vorticité initiale.

Les extrema de vorticité longitudinale $\tilde{\omega}_1$ sont, pour les 5 simulations présentées Fig. 7, situés dans les tourbillons longitudinaux. Ils donnent une bonne mesure de la dissipation apportée par le modèle (voir la discussion sur la signification physique de ces extrema dans Ref. [26]). Les valeurs rapportées dans Figs. 7 et 8 confirment les impressions visuelles :

- Le modèle spectral apparait comme le moins dissipatif des modèles "éprouvés" : les isosurfaces représentées montrent que d'importants niveaux de vorticité (de l'ordre d'ω_i) sont concentrés dans les plus petites échelles résolues, ce qui est un signe de cascade d'énergie (confirmé par les spectres, non présentés ici). D'autre part, on voit nettement (sur les visualisations couleur en plein écran) les tourbillons longitudinaux s'enrouler autour des tourbillons primaires.
- Le modèle de la fonction de structure est légèrement moins dissipatif que le modèle de Smagorinsky, mais tous deux font pratiquement disparaitre les zones de reconnection entre les tourbillons longitudinaux et les tourbillons primaires, de même que la vorticité à petite échelle.
- Les deux nouveaux modèles se comportent tous deux de manière analogue au modèle spectral.

4 SIMULATION DES GRANDES ECHELLES DE COUCHES LIMITES COMPRESSIBLES

Un modèle sous-maille étant choisi, le système formé par les équations (11), (12), (23), (26), (27), (8), (38) est résolu par méthodes aux différences finies, à l'aide d'un schéma prédicteur–correcteur théoriquement d'ordre (2,4) [27]. Le code de calcul, développé par Normand, est décrit dans [28]. Les conditions aux limites, inspirées de [29] et [30], sont de type *non-réflectives* à la frontière supérieure et à la sortie du domaine. Les invariants de Riemann des caractéristiques rentrantes sont imposés à l'entrée. A la paroi (adiabatique ou isotherme, suivant les cas), on adopte des conditions d'adhérence pour la vitesse. Une condition de Neumann pour la pression est obtenue en considérant la composante suivant x_2 de (11) (voir [28] et [27] pour détails). Des conditions de périodicité sont imposées suivant l'envergure (direction x_3).

4.1 Couche limite faiblement compressible

Parmi les modèles formulés dans l'espace physique que nous avons présentés, les seuls qui sont susceptibles de permettre la transition sont les deux nouveaux modèles. Nous présentons ici une simulation de couche limite à nombre de Mach externe $M_\infty = 0.5$, se développant spatialement sur une plaque plane adiabatique. Le modèle sous-maille utilisé est le *modèle de la fonction de structure filtrée* présenté chapitre 3.5.1.

L'écoulement de base imposé à la frontière amont du domaine est une solution unidirectionnelle des équations de similitude en régime laminaire, à une distance $x_0 = 330\ \delta_i$ du bord d'attaque de la plaque (en appelant $\delta_i (x = x_0)$ l'épaisseur de déplacement de cet écoulement de base). La résolution est de $650 \times 32 \times 20$ points, pour un domaine de taille $812 \times 20 \times 22\ \delta_i$ en appelant $\delta_i = \delta_1(x_1 = 0)$ lépaisseur de déplacement de l'écoulement imposé à la frontière amont du domaine. Le nombre de Reynolds Re_{δ_i} basé sur δ_i est de 1000, ce qui positionne l'entrée du domaine à une distance

$$x_0 = \frac{Re_{\delta_i}}{(1.72\ f_{lam})^2}\ \delta_i = 330\ \delta_i \tag{59}$$

du bord d'attaque de la plaque (f_{lam} étant un facteur empirique de compressibilité très proche de 1 pour $M_\infty = 0.5$, voir [31] et [32]). Le domaine couvre donc une plage de $Re_x = (x/\delta_i + 330) Re_{\delta_i}$ comprise entre $3.3\ 10^5$ et $1.14\ 10^6$, ce qui englobe largement les points de transition observés expérimentalement pour des niveaux de bruit analogues aux nôtres : ici, nous perturbons le profil amont à chaque instant par

- un forçage déterministe bidimensionnel (ondes de Tollmien-Schlichting) d'amplitude $5\ 10^{-3}\ U_\infty$
- du bruit blanc 3D d'amplitude $8\ 10^{-3}\ U_\infty$.

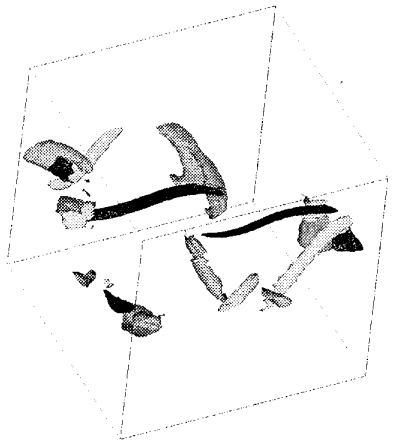

Modèle de Smagorinsky: $\max|\omega_1| = 2.92\ \omega_i$

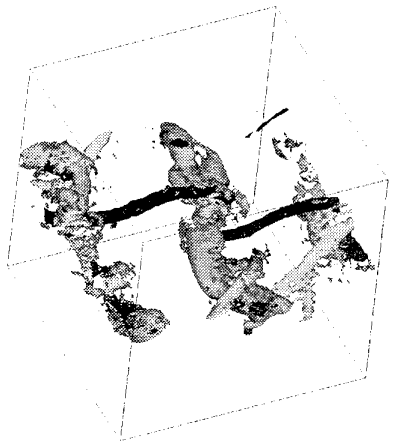

Modèle spectral: $\max|\omega_1| = 4.75\ \omega_i$

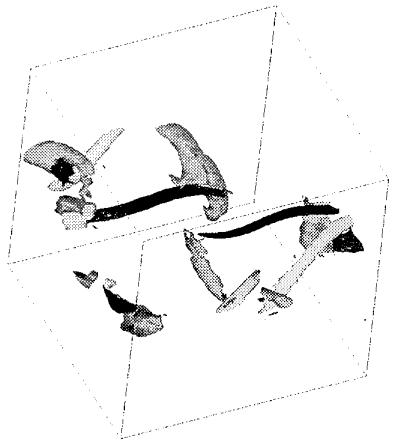

Modèle de la fonction de structure: $\max|\omega_1| = 2.86\ \omega_i$

FIG. 7 - Modèles "éprouvés": le modèle spectral est de loin le moins dissipatif.

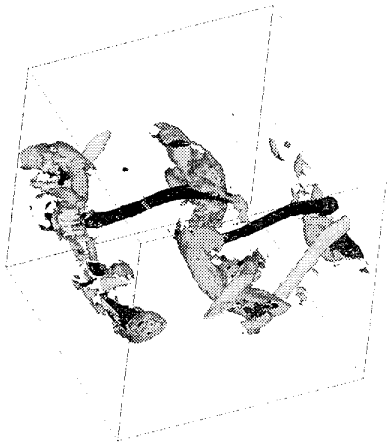

Modèle de la fonction de structure filtrée (Ducros): $\max|\omega_1| = 4.83\ \omega_i$

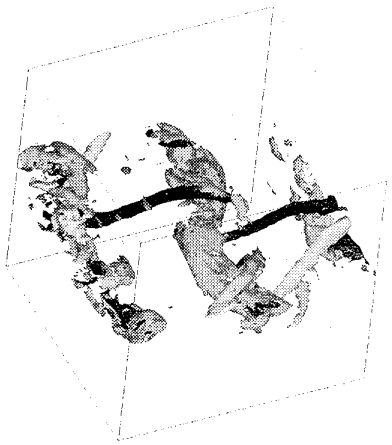

Modèle de la fonction de structure sélective (David): $\max|\omega_1| = 5.42\ \omega_i$

FIG. 8 - Nouveaux modèles: ils donnent des résultats très proches et consistants avec le modèle spectral.

Ce forçage a été choisi de manière à obtenir la transition le plus rapidement possible sans court-circuiter les mécanismes linéaires d'instabilité secondaire (modes obliques harmoniques et sous-harmoniques de l'onde TS la plus amplifiée). Il s'agit donc d'une expérience numérique de *transition contrôlée*, et l'on retrouve bien, sur Fig. 9, les tourbillons en Λ décalés prédits par Herbert [33].

FIG. 9 - Coupe horizontale à $x_2 = 0.27\ \delta_i$ de u_1, la composante longitudinale du champ de vitesse résolu. On voit ici deux images juxtaposées du domaine de calcul (artifice graphique – justifié par la périodicité des conditions aux limites suivant x_3 – permettant de mieux mettre en évidence l'organisation de l'écoulement dans le sens de l'envergure) On remarque la trace des ondes de T.S. forcées à l'entrée du domaine, des tourbillons en Λ en configuration décalée et des courants longitudinaux alternés *(streaks)*.

Au vu des profils longitudinaux de facteur de forme H_{12} et de frottement pariétal C_f (Fig. 10), on peut dire que la transition s'effectue vers $x \approx 280\ \delta_i$, c'est-à-dire pour $Re_x \approx 6\ 10^5$.

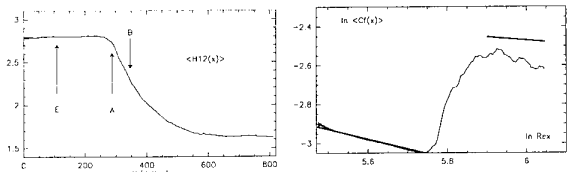

FIG. 10 - Facteur de forme H_{12} (à gauche). Coefficient de frottement (à droite, avec les 2 lois empiriques $C_{f_{lam}} = 0.0664 f_{lam} Re_x^{-1/2}$ et $C_{f_{turb}} = 0.0368 f_{turb} Re_x^{-1/6}$ tirées de Refs. [31] et [32]). Dans le cas présent, $f_{lam} \approx f_{turb} \approx 1$.

Plus en aval, des coupes verticales $(x_1 x_2)$ de $\widetilde{\omega}_3$ montrent clairement des éjections corrélés avec la pointe de tourbillons en épingle à cheveux *(hairpins)*, que l'on matérialise par des lignes vortex (Fig. 11).

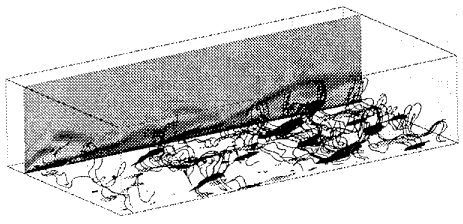

FIG. 11 - Zoom sur la portion du domaine comprise entre $x_1 = 474\ \delta_i$ et $553\ \delta_i$ (soit $Re_x \in [804\,000, 883\,000]$). Il s'agit donc du début de la région turbulente. La figure montre montrant des surfaces iso-vorticité longitudinale $\widetilde{\omega}_1 = 0.25\ U_\infty/\delta_i$ (gris clair) et $\widetilde{\omega}_x = -0.25$ (gris foncé), plus des lignes vortex visualisant les tourbillons en épingle à cheveux. Le plan de coupe montre les éjections et les éclatements.

C'est au niveau de ces éjections et des éclatements *(bursts)* qui en résultent que l'on trouve les plus fortes valeurs de la viscosité turbulente ν_t, montrant que le modèle de la fonction de structure filtrée agit avec parcimonie et à bon escient.

Les statistiques sont globalement en bon accord avec les résultats expérimentaux ([34], [35], [36]) et numériques [37] à nombre de Reynolds et niveau de perturbations comparables (Fig. 12), malgré une résolution plutôt marginale (dans la zone turbulente, l'ordonnée x_2 du premier point de grille correspond à $y^+ = 3$).

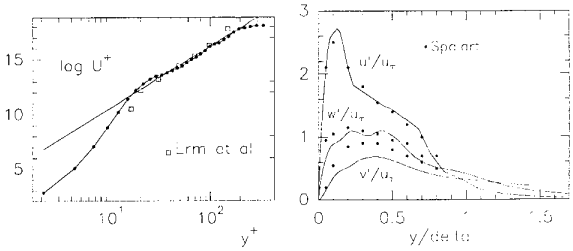

FIG. 12 - A gauche: Profil de vitesse en unités de paroi, pour $x_1 = 670\ \delta_i$, soit $Re_x = 10^6$ (ligne continue avec les points noirs). Les carrés correspondent à une expérience à Re_x comparable [34]. La ligne continue correspond á la loi classique $U^+ = ln(y^+)/0.41 + 5$.
A droite: écart-type des fluctuations de vitesse normalisées par la vitesse de frottement u_τ, toujours à $Re_x = 10^6$, comparées aux valeurs trouvées en simulation directe temporelle à plus haute résolution [37].

4.2 Transition d'une couche limite sur un dièdre chauffé

Outre l'étude fondamentale des mécanismes de transition à la turbulence, la motivation des simulations des grandes échelles est aussi, à terme, la prédiction et le contrôle du point de transition de couches limites sur des objets réels. Après les calculs présentés plus haut, l'étape suivante consiste à simuler l'établissement d'une couche limite depuis un bord d'attaque profilé, sur lequel souffle un écoulement uniforme, légèrement bruité. On pourra alors essayer de comprendre comment ces perturbations pénètrent dans la couche limite pour provoquer la transition (réceptivité). Pour simplifier au maximum la géométrie, nous nous sommes placés dans le cas d'un dièdre semi-infini à incidence nulle, en supposant l'écoulement symétrique. On n'en simule donc que la moitié (voir Fig. 13), à l'aide d'une adaptation en coordonnées curvilignes orthogonales du code de calcul utilisé pour les calculs de couche limite de plaque plane du chapitre précédent (voir [25] pour détails). Le modèle sous-maille utilisé ici est celui de la fonction de structure *sélective*, décrit chapitre 3.5.2.

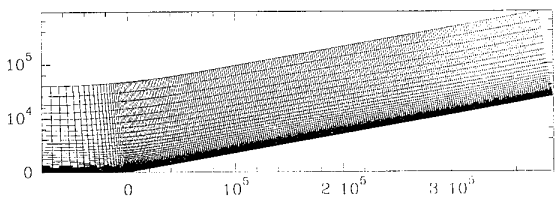

FIG. 13 - Section verticale du maillage $236 \times 30 \times 32$ utilisé pour simuler l'écoulement sur un dièdre chauffé (demi-angle au sommet 10°). Les échelles sont graduées en Re_x, compté à partir du bord d'attaque. Comparer le Re_x de sortie de ce domaine avec le Re_x à l'entrée du domaine précédent.

L'écoulement imposé à la frontière amont du domaine est uniforme en moyenne, à $M_\infty = 0.5$, avec une intensité turbulente de 10^{-3} provenant d'un bruit blanc tridimensionnel renouvelé à chaque pas de temps, comme pour la couche limite présentée précédemment. Le dièdre est supposé isotherme, chauffé à une température $T_w = 800K$, la température extérieure T_∞ étant de $270K$. Le paramètre pertinent à ce niveau est le rapport T_w/T_{ad} entre la température de paroi et la température de recouvrement adiabatique (celle qu'aurait la paroi si elle était adiabatique, en supposant que l'enthalpie totale se conserve à travers la couche limite). A Mach 0.5, T_{ad} est très proche de T_∞ et l'on a $T_w/T_{ad} = 2.9$. Ceci correspond à un chauffage fort, qui influence beaucoup la dynamique de l'écoulement : Figs. 14 et 15 montrent des signes évidents de transition à $Re_x \approx 250\,000$, soit 2.4 fois moins que pour la couche limite de plaque plane adiabatique précédente.

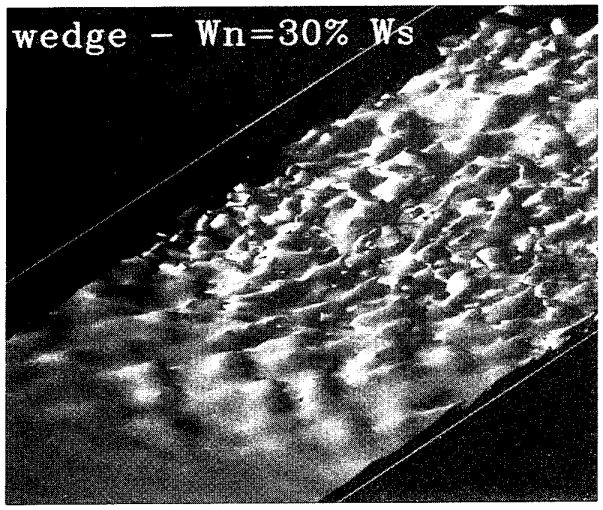

FIG. 14 - Dièdre chauffé. Zoom sur la moitié aval du domaine, montrant l'iso-surface $||\vec{\omega}|| = 0.30\, Max||\vec{\omega}||_{\vec{x}}$. On voit nettement des tourbillons en Λ et, plus en aval, des tourbillons en épingle à cheveux.

La raison en est dûe à la présence d'un point d'inflexion généralisé dans le profil de vitesse moyen qui s'établit avant la transition (voir Fig. 16). L'instabilité responsable de la transition est alors une instabilité de cisaillement inflexionnel de type Kelvin-Helmholtz de nature inviscide (comme dans les couches de mélange présentées au chapitre 3), beaucoup plus amplifiée que les instabilités visqueuses de type ondes de Tollmien-Schlichting rencontrées en couche limite sur paroi plane adiabatique.

Fig. 17 montre les profils longitudinaux moyennés en temps de coefficient de frottement C_f et nombre de Stanton St (flux de chaleur adimensionnel à la paroi). L'évolution du C_f en régime turbulent suit la loi empirique $C_f = 0.0368 f_{turb} Re_x^{-1/6}$ établie pour les couches limites de plaque plane. Dans le cas présent, f_{turb} vaut 0.63 (voir [32] pour détails). Le nombre de Stanton varie proportionnellement à C_f, comme le prédit l'analogie de Reynolds forte. Le coefficient de proportionnalité est, par contre, nettement inférieur aux valeurs empiriques communément admises (voir légende de Fig. 17). Ceci n'est pas forcément significatif, dans la mesure où ces formules empiriques résultent de la compilation de résultats d'expériences de plaque plane (et non de dièdres), toutes à des Re_x nettement plus élevés que les nôtres.

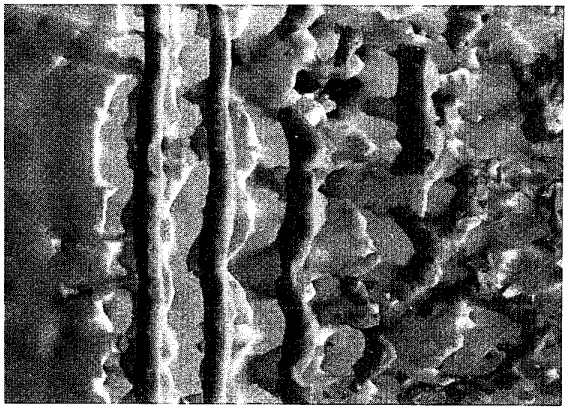

FIG. 15 - Dièdre chauffé. Zoom sur la région transitionnelle de l'écoulement, montrant l'émergence d'une instabilité bidimensionnelle, suivie de celle d'un mode oblique sous-harmonique *(H-mode)* donnant naissance aux tourbillons en Λ décalés. On montre ici une isosurface de basse pression (en noir), et, en clair, l'isosurface $||\vec{\omega}|| = 0.80\, Max||\vec{\omega}||_{\vec{x}}$, située plus près de la paroi que son homologue dans 14.

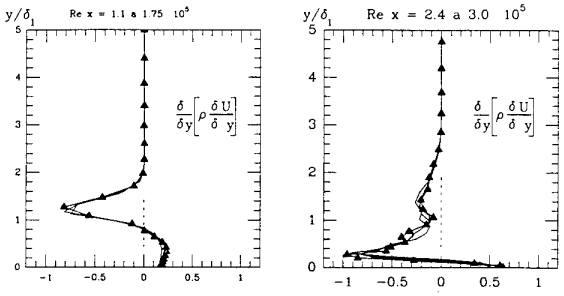

FIG. 16 - Profils moyennés en temps de $d/dx_2[\bar{\rho} d\bar{u}/dx_2]$ (en notant $\bar{\rho}(x_2)$ et $\bar{u}(x_2)$ les profils moyens de densité et de vitesse résolus), avant la transition (à gauche), et après (à droite). Le point d'inflexion généralisé y_S correspond au passage par zéro de ces profils. On le trouve $y_S = 0.9\ \delta_1$ avant la transition, et $y_S = 0.15\ \delta_1$ après, $\delta_1(x_2)$ étant l'épaisseur de déplacement locale.

Nous n'avons pas trouvé de références à des expériences sur un dièdre chauffé dans des conditions directement comparables aux notres. Les expériences qui s'y rapprochent le plus sont, à notre connaissance, celles de Cheng et Ng [38], qui concernent l'écoulement à faible vitesse ($U_\infty = 19m/s$) sur une plaque plane chauffée à 1100K. Le résultat majeur de cette publication est que le seul effet de ce chauffage sur les statistiques est une réduction de moitié des contraintes de Reynolds par rapport au cas non chauffé, ce que nous retrouvons dans notre simulation (Fig. 18).

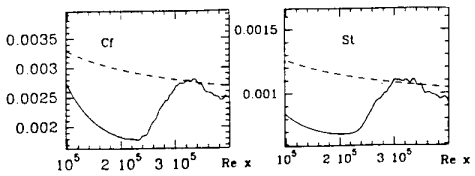

FIG. 17 - Dièdre chauffé: profils de C_f (à gauche) et de nombre de Stanton (à droite). La courbe pointillée dans le dessin de gauche correspond à $C_{f_{turb}} = 0.0368 f_{turb} Re_x^{-1/6}$, avec $f_{turb} = 0.63$ (déterminée à partir des formules empiriques tirées de Ref. [32]). La courbe pointillée dans le dessin de droite correspond à $St = (s/2)\, C_f$, avec $s = 0.8$, alors que la valeur communément acceptée pour ce *facteur d'analogie* est de 1.24.

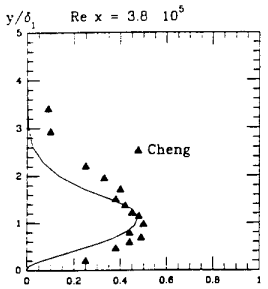

FIG. 18 - Profil de $-\rho u'v'/\rho_\infty u_\tau^2$ (contraintes de Reynolds normalisées) à $Re_x = 3.8\ 10^5$. En régime incompressible (non chauffé), le pic est à environ 1, avec la même valeur de u_τ (voir Ref. [39]). Les triangles montrent les valeurs obtenues par Cheng et Ng [38], à l'abscisse $x_1 = 183mm$ du bord d'attaque (celle pour laquelle l'accord avec notre simulation est le meilleur. Il s'agit de la position la plus en aval. Plus près du bord d'attaque, ils mesurent des profils plus proches du cas non chauffé, ce qui se comprend aisément, l'air ayant passé moins de temps au dessus de la plaque chaude.

5 CONCLUSION

Le modèle de la *fonction de structure filtrée* et celui de la *fonction de structure sélective* permettent tous deux de simuler la transition de couches limites à relativement faible coût, avec des résultats en accord acceptable avec les expériences. Ces résultats encourageants suggèrent qu' il n'est pas nécessaire de modéliser finement les termes sous-maille, l'essentiel étant d'empêcher le modèle d'amortir les instabilités responsables de la transition. Il semblerait donc que l'approche traditionnelle – où les constantes des modèles sont déterminées dans le cas d'école d'une cascade de Kolmogorov infinie – soit suffisante, peut-être en raison d'une certaine universalité (même approximative) de la turbulence. Cette hypothèse d'universalité est renforcée par l'indépendance de la turbulence des couches limites [4] envers les effets de compressibilité (chauffage, comme ici, ou bien nombre de Mach élevé, comme dans Ref. [40]).

6 REMERCIEMENTS

Le temps de calcul pour les simulations à haute résolution a gracieusement été alloué par l'Institut du Developpement et des Ressources en Informatique Scientifique.

[4] tant au niveau des visualisation que des statistiques

7 REFERENCES

[1] KLEISER L. & ZANG T.A. 1991 Numerical simulation of transition in wall-bounded shear flows. *Ann. Rev. Fluid Mech.*, **23**, pp. 495-537.

[2] RAI M.M. & MOIN P. 1993 Direct numerical simulation of transition and turbulence in a spatially evolving boundary layer. *J. Comp. Phys.*, **109**, pp.169-192.

[3] BLAIR, M.F. 1983 *J. Heat Transf.*, **105** 33

[4] SUDER, K.L., O'BRIEN, J.E. & RESHOTKO 1988 *NASA TM-100913.*

[5] SOHN, K.H. & RESHOTKO, E. 1991 *NASA CR-187068.*

[6] LEONARD, A. 1974 On the energy cascade in large-eddy simulations of turbulent fluid flows. *Adv. Geophys.*, **18A**, 237–248.

[7] BOUSSINESQ, J. 1877 Essai sur la théorie des eaux courantes. *Mémoire présenté à l'Académie des Sciences XXIII*, 46, Paris.

[8] BOUSSINESQ, J. 1896 Théorie de l'écoulement tourbillonnant et tumultueux des liquides dans les lits rectilignes à grande section (tuyaux de conduite et canaux découverts), quand cet écoulement s'est régularisé en un régime uniforme, c'est-à-dire moyennement pareil à travers toutes les sections normales du lit. *Comptes Rendus de l'Académie de Sciences CXXII*, 1290–1295.

[9] LANDAU, L. & LIFSHITZ, E.M. 1986 *Mécanique des fluides*, Editions Mir, Moscou.

[10] SMAGORINSKY J. 1993 General circulation experiments with the primitive equations, I. The basic experiment. *Mon. Weather Rev.*, **91**, 99–164.

[11] DEARDORFF, J.W. 1970 A three-dimensional numerical study of turbulent channel flow at large Reynolds numbers. *J. Fluid Mech.*, **41**, pp. 453-480.

[12] MOIN P. & KIM J. 1982 Numerical investigation of turbulent channel flow *J. fluid Mech.*, vol. **118**, pp. 341-377.

[13] VOKE P.R. & YANG, Z. 1993 Numerical studies of the mechanisms of bypass transition in the flat plate boundary layer *Proceedings of Turbulent Shear Flows 9*, Kyoto, Springer (sous presse).

[14] PIOMELLI U., ZANG, T.A., SPEZIALE. C.G. & HUSSAINI, M.Y. 1989 On the large-eddy simulation of transitional wall-boundeed flows, em ICASE Report 89–55.

[15] KRAICHNAN, R.H. 1976 Eddy viscosity in two and three dimensions. *J. Atmos. Sci.*,, **33**, 1521–1536.

[16] LESIEUR M. 1990 *Turbulence in Fluids* Second revised edition, Kluwer Academic Publishers.

[17] LESIEUR, M. & ROGALLO, R. 1989 Large-eddy simulation of passive scalar diffusion in isotropic turbulence. *Phys. Fluids*, **1**, 718–722.

[18] COMTE, P., LESIEUR, M. & FOUILLET. Y. 1989 Coherent structures of mixing layers in large-eddy simulation, *in* IUTAM Symposium on *Topological Fluid Dynamics*, Cambridge, Août 1989. Cambridge university Press, H.K. Moffatt ed., 649–658.

[19] BATCHELOR, G.K. 1953 *The theory of homogeneous turbulence*, Cambridge Unversity Press.

[20] MÉTAIS O. & LESIEUR M. 1992 Spectral large-eddy simulation of isotropic and stably stratified turbulence *J. Fluid Mech.*, **239**, 157–194.

[21] SILVEIRA N., GRAND D., MÉTAIS O. & LESIEUR M. 1993 A numerical investigation of the coherent structures of turbulence behind a backward-facing step, *J. Fluid Mech.*,, **256**, 1–25.

[22] EATON, J.K. & JOHNSTON, J.P., 1980 Turbulent flow re-attachment: an experimental study of the flow and structure behind a backward-facing step. *Stanford University, Rep. MD-39.*

[23] PRESTEMON, S., 1993, Evaluation de spectres locaux par transformée en ondelettes. Application aux simulations des grandes échelles de couches limites se développant spatialement. D.E.A. de l'Institut National Polytechnique de Grenoble, Octobre 1993.

[24] DUCROS F., COMTE P.& LESIEUR M. 1994 Large-eddy simulations of transition to turbulence in a weakly-compressible boundary layer over a flat plate, *Compuscrit I.M.G., pour soumission à J. Fluid Mech.*.

[25] DAVID E. 1993 Modélisation des écoulements compressibles et yypersoniques : une approche instationnaire. *Thèse* INPG.

[26] LESIEUR, M., 1993 Understanding coherent vortices through computational fluid dynamics, *Theoret. Comput. Fluid Dynamics*, **5**, 177–193.

[27] GOTTLIEB, D., & TURKEL, E. 1976 Dissipative two-four methods for time-dependent problems. *Math. Comp.*, **30** (136), 703–723.

[28] NORMAND X. & LESIEUR M. 1992 Direct and Large-Eddy Simulation of Transition in the Compressible Boundary Layer *Theor. and Comp. Fluid Dyn.*,vol. **3**, pp. 231.

[29] THOMPSON, K.W. 1987 Time-dependant boundary conditions for hyperbolic systems, *J. Comp. Phys.* **68**, 1–24.

[30] POINSOT, T.J. & LELE, S.K. 1992 Boundary conditions for direct simulations of compressible viscous reacting flows, *J. Comp. Phys.* **101**, 104–129.

[31] COUSTEIX, J. 1988 *Couche limite laminaire*, Cepadues-Editions.

[32] COUSTEIX, J. 1989 *Turbulence et couche limite*, Cepadues-Editions.

[33] HERBERT. T. 1988 Secondary instability of boundary layers. Ann. Rev. Fluid Mech., **20**, 487–526.

[34] ERM, L.P., SMITS, A.J. & JOUBERT, P.N. 1985 Low Reynolds number turblent boundary layers on a smooth flat surface in zero pressure gradient. *Proc. 5th Symp. on Turbulent Shear FLows*, Ithaca, NY, August 7-9.

[35] SABOT. J. & COMTE-BELLOT, G. 1976 Intermittency of coherent structure in the core region of fully developed turbulent pipe flow. *J. Fluid Mech,* vol **74,** pp 767-796.

[36] ECKELMANN, H. 1970 Experimentelle Untersuchungen in einer turbulenten Kanalströmung mit starken viskosen Wandschichten, Mitt. *MPI f. Strömungsforschung und AVA Göttingen Nr. 48.*

[37] SPALART P.R. 1988 Direct simulation of a turbulent boundary layer up to $R_\theta = 1410$ *J. Fluid Mech.*, **187**, 61–98.

[38] CHENG, R.K. & NG, T.T. 1982 Some aspects of strongly heated turbulent boundary layers flow. *Phys. Fluids*, **25**, 1333–1341.

[39] HINZE, J.O. 1975 *Turbulence*, McGraw Hill. New York.

[40] DUCROS F., COMTE P., LESIEUR M. 1993 Ropes and lambda-vortices in direct and large-eddy simulations of a high-Mach number boundary layer over a flat plate. *Proceedings of Turbulent Shear Flows 9*, Springer-Verlag.

Large Eddy Simulation of Channel Flow Using a Vorticity Transport Subgrid Model

Amy L. Rovelstad and Robert A. Handler
Remote Sensing Division
Naval Research Laboratory
Washington, DC 20375
USA

Peter S. Bernard and James M. Thomas
Department of Mechanical Engineering
University of Maryland
College Park, Maryland 20742
USA

SUMMARY

Vorticity transport concepts are applied to large eddy simulation (LES) techniques in two different contexts. In the first example, the LES equations of motion are reformulated by applying a spatial filter to the rotational rather than the momentum form of the Navier-Stokes equation, leading to the introduction of a subgrid-scale (SGS) vorticity flux tensor. A model originally developed using ensemble averaging is proposed and tested locally and instantaneously using simulations of full channel flow and a minimal channel calculation. The modeled and exact vorticity fluxes are found to generally agree, even for vorticity flux terms which are only present locally and instananeously.

The development of a vorticity transport based wall treatment using a deterministic vortex element approach is also outlined. Initial tests comparing the results of this approach to the zero pressure gradient and stagnation point boundary layer are compared to the Blasius and Falkner-Skan solutions and found to be in good agreement.

1. INTRODUCTION

Many common turbulent flows are known to be strongly influenced by the presence of large vortical structures. Flows of this type include wall-bounded flows [1], free surface turbulence[2], and shear layers. As a result, it is of interest to investigate the possibility of formulating a large eddy simulation (LES) model which is more closely tied to the vortical nature of these flows. One approach which appears to have promise is a subgrid-scale (SGS) model based on vorticity transport. In the present work we present an outline of how such a model can be formulated and present detailed flow visualizations which appear to indicate that this method is viable. *A priori* calculations comparing the exact and modeled vorticity transport terms are shown for a typical channel flow, as well as for minimal channel flow [3]. It is found that the actual and modeled vorticity flux are in fact closely correlated with quasi-streamwise structures, a result which is particularly well established by the minimal box calculations in which these structures are very well resolved. Finally, a new treatment for the wall region using discrete vortex sheets is outlined and some initial tests of the method for a Blasius boundary layer and a stagnation flow boundary layer are shown.

2. VORTICITY TRANSPORT ANALYSIS

The equations of motion for LES are typically formulated by spatially filtering the Navier-Stokes equations in momentum form, so that the effect of the unresolved scales appears as the SGS Reynolds stress, $\tau_{ij} = \overline{u_i u_j} - \overline{u}_i \overline{u}_j$. Here, a bar denotes a filtered quantity, u_i is the ith component of the velocity, and $i = (1,2,3)$ corresponds to the streamwise, wall-normal, and spanwise directions (x,y,z), respectively. One method of formulating a vorticity based LES is to filter the Navier-Stokes equations in rotational form to obtain the filtered equation,

$$\frac{\partial \bar{u}_i}{\partial t} + \frac{\partial}{\partial x_j}(\overline{u}_i \overline{u}_j) = -\frac{\partial P}{\partial x_i} + \epsilon_{ijk}\zeta_{jk} + \frac{1}{R_\tau}\frac{\partial^2 \bar{u}_i}{\partial x_j \partial x_j} + \delta_{i1}. \quad (1)$$

Here and in the following equations, the normalizing parameters are the friction velocity, $u_\tau = \sqrt{\tau_w/\rho}$, the channel height, h, a time scale, $t^* = h/u_\tau$, where the wall shear stress, τ_w, is defined by $\tau_w = \mu \left|\frac{\partial \bar{U}}{\partial y}\right|_{y=0}$, and $\bar{U}$ is the mean streamwise velocity. In addition $y^+ = u_\tau y/\nu$ is the nondimensionalized coordinate normal to the wall, $R_\tau = u_\tau h/\nu$ is the Reynolds number based on wall shear, and $P = \bar{p}/\rho + k + \tilde{k}$ is the modified pressure where

Paper presented at the 74th Fluid Dynamics Symposium on "Application of Direct and Large Eddy Simulation to Transition and Turbulence" held at Chania, Crete, Greece, in April 1994.

$k = \frac{1}{2}\overline{u_k u_k}$, and $\tilde{k} = \overline{\bar{u}_k \bar{u}_k}$.

The small scale motions in Eq. (1) are accounted for by the SGS vorticity flux tensor, $\zeta_{ij} = \overline{u_i \omega_j} - \overline{\bar{u}_i \bar{\omega}_j}$, rather than the SGS Reynolds stress tensor, so that in order to close the equations ζ_{ij} must be modeled. The model employed here was developed by applying a Lagrangian analysis to the vorticity transport equation [4,5,6]. Following that analysis, the vorticity flux, $\overline{u_i \omega_j}$, can be written:

$$\overline{u_i \omega_j} = -T_{ij} \overline{u_i u_k} \frac{\partial \bar{\Omega}_j}{\partial x_k} + Q_{ijk} u_i \overline{\frac{\partial u_j}{\partial x_k}} \bar{\Omega}_k \quad \text{(no sum on } i \text{ and } j\text{)} \tag{2}$$

Here the bar represents ensemble averaging, and Ω and ω represent the mean and fluctuating vorticity, respectively. The first term on the right hand side of Eq. (2) represents the transport of mean vorticity carried by a fluid the particle, while the second represents transport by vortex stretching and shearing. The scales T_{ij} and Q_{ijk} are the Lagrangian integral time scales defined by,

$$\overline{u_\alpha u_\beta} T_{\alpha\beta} = \int_{t_0-\tau}^{t_0} \overline{u_\alpha^a u_\beta(s)} ds \tag{3}$$

and

$$\overline{u_\alpha \frac{\partial u_\beta}{\partial x_\gamma}} Q_{\alpha\beta\gamma} = \int_{t_0-\tau}^{t_0} \overline{u_\alpha^a \frac{\partial u_\beta(s)}{\partial x_\gamma}} ds \tag{4}$$

where there is no summation on Greek indices, and the integrals are taken from time $t_0 - \tau$ to t_0. Note that in these expressions, the averaging is taken over a large number of fluid particles, and in principle the scales can be computed dynamically. (See [4,5,and 6] for further details on the definition of these scales.) For the purposes of this study, however, we assume constant scale values. It is possible, however, to divide the scales into two general types. For the T scales this is accomplished by dividing the terms into those associated with normal stresses, i.e., $\alpha = \beta$ in Eq. (3), and shear stress terms, $\alpha \neq \beta$. Similarly, the Q scales are classified by those associated with vortex stretching, i.e., $\beta = \gamma$ in Eq. (4), and those associated with vortex shearing, $\beta \neq \gamma$. We designate the first type of T scale as T_1, and the second type as T_2, while the Q scales become Q_1 and Q_2. It is proposed to extended this model directly to the SGS vorticity flux tensor using the relation

$$\begin{aligned} \zeta_{\alpha\beta} = & \\ & -C(\Delta)\,(T_1 \delta_{\alpha\beta} + T_2(1-\delta_{\alpha\beta}))\, \overline{\bar{u}_\alpha \bar{u}_k} \frac{\partial \bar{\Omega}_\beta}{\partial x_k} \\ & + \; C(\Delta)\,(Q_1 \delta_{\beta k} + Q_2(1-\delta_{\beta k}))\, \overline{\bar{u}_\alpha \frac{\partial \bar{u}_\beta}{\partial x_k}} \bar{\Omega}_k, \end{aligned} \tag{5}$$

where $C(\Delta)$ is a function that accounts for the effect of the grid scale, Δ, a bar now denotes spatial filtering, and $\delta_{\alpha\beta}$ is the Kronecker delta.

The validity of the model in a planar averaged sense in channel flow was examined previously [6]. In this case, the averaging procedure results in only four non-zero components of vorticity flux, $\overline{u\omega_3}$, $\overline{v\omega_3}$, $\overline{w\omega_1}$, and $\overline{w\omega_2}$ where $\mathbf{u} = (u, v, w)$ and $\omega = (\omega_1, \omega_2, \omega_3)$ are the velocity and vorticity components. These tests suggest that the modeled expression for the spatially filtered vorticity flux is able to adequately account for the exact value of filtered vorticity flux. Additionally, these tests suggest a relatively straightforward relation for $C(\Delta)$. A desired property of such a model is that it not only represent the SGS flux in an average sense but also in an instantaneous sense. It is also of considerable interest to examine the relationship between quasi-streamwise vortical structures and intense areas of vorticity flux so that an assessment can be made as to the physical accuracy of the model.

3. FLOW VISUALIZATIONS

3.1 Connection between vorticity flux and streamwise vortices

Instantaneous velocity fields taken from two direct numerical simulations were used to examine the relationship between vorticity transport and the streamwise-oriented structures. The first simulation (Case 1) was of channel flow with a Reynolds number $R_\tau = 125$ on a $48 \times 65 \times 64$ grid in a computational box measuring $1250 \times 250 \times 625$ viscous units in the streamwise, wall normal and spanwise directions, respectively. The second simulation was of a minimal channel flow with $R_\tau = 135.5$ on a $48 \times 129 \times 24$ grid in a computational box measuring $425 \times 171 \times 127$ viscous units (Case 2). The significantly increased resolution of this calculation enabled a much more detailed examination of the physical processes represented by the vorticity flux, as well as facilitating the ability to determine the viability of the proposed models.

In visualizing wall bounded turbulence it was found that plotting isosurfaces of streamwise vorticity gives a first estimate of the locations of many of the dominant quasi-streamwise vortices, though it is important to realize [1] that many of the smaller, but nevertheless important structures, are not isolated in this way. However, for the purposes of the present study, we will use this method since it is relatively efficient, and gives a reasonable first order impres-

sion of the location of these structures. With this in mind, Figure 1(a) shows isosurfaces of streamwise vorticity along with isosurfaces of $\overline{v\omega_3}$ for Case 1. Although reproduction of the 3-D color image as a monotone 2-D picture causes a great deal of detail to be lost, a careful examination of this visualization reveals that much of the instantaneous vorticity flux is typically associated with intense streamwise vortical structures, although there are also regions of the flow in which these particular structures are not evident but which still contribute to vorticity flux. In Figs. 1(b,c), contours of Ω_1 and $\overline{v\omega_3}$ across the channel at a fixed streamwise location are shown where solid lines and dashed lines indicate positive and negative values, respectively. The relationship between regions of intense streamwise vorticity and vorticity flux is evident. A clearer impression of the relationship between these structures and $\overline{v\omega_3}$ can be had using the highly resolved minimal channel data shown in Figs. 2(a,b,c). Here it is evident that a single clearly defined streamwise vortical structure, beneath which is a sheet of streamwise oriented vorticity of the opposite sign, is present on one wall. The isosurfaces of $\overline{v\omega_3}$ are clearly aligned with these areas of vorticity.

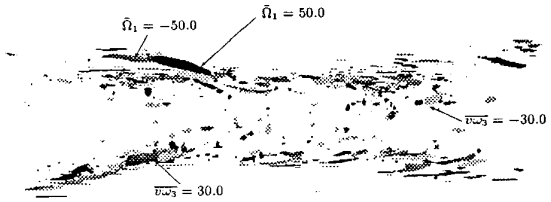

Figure 1a. Isosurfaces of Ω_1 and $\overline{v\omega_3}$ for Case 1.

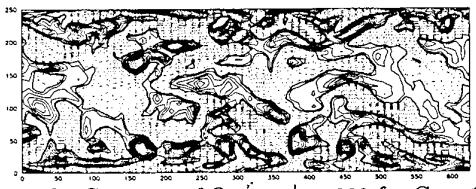

Figure 1b. Contours of Ω_1 at $x^+ = 390$ for Case 1, contour increment = 3.45.

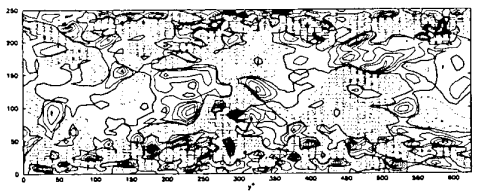

Figure 1c. Contours of $\overline{v\omega_3}$ at $x^+ = 390$ for Case 1, contour increment = 2.76.

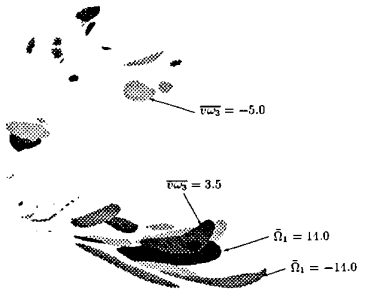

Figure 2a. Isosurfaces of Ω_1 and $\overline{v\omega_3}$ for Case 2.

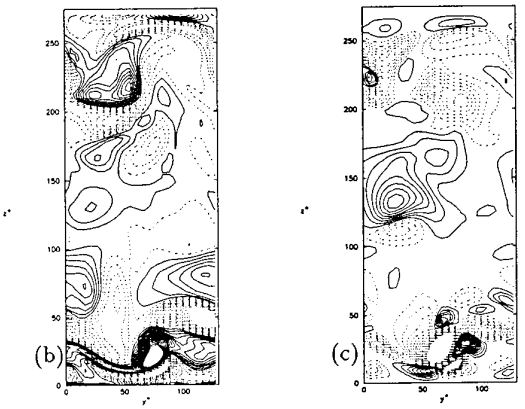

Figure 2b and c. Contours of (b) Ω_1 and (c) $\overline{v\omega_3}$ at $x^+ = 372$ for Case 2, contour increment = 0.862 (b), 0.276 (c).

The effect of these streamwise vortical structures can also be seen by comparing the isosurfaces of $\overline{v\omega_1}$ with those of Ω_1 in the channel and the minimal box (figures 3 and 4). Note that in this case $< \overline{v\omega_1} >= 0$, so that in the ensemble averaged or planar averaged equations this term does not appear. However, in the LES equations this term, along with $\overline{u\omega_2}$, whose planar average is also zero, accounts for the turbulent transport in the equation for the spanwise velocity. These terms are evidently significant locally, and in particular near vortical structures.

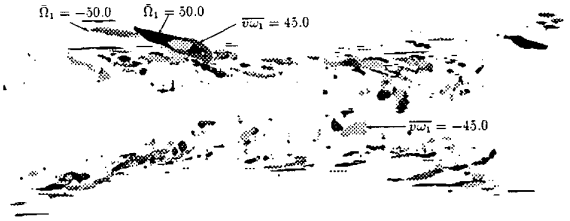

Figure 3a. Isosurfaces of $\overline{v\omega_1}$ for Case 1.

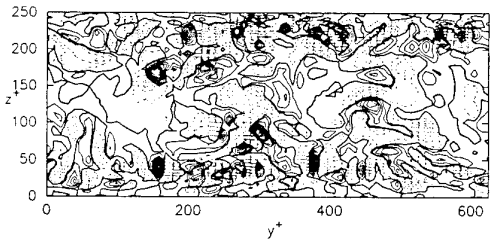

Figure 3b. Contours of $\overline{v\omega_1}$ for Case 1, contour increment = 3.45.

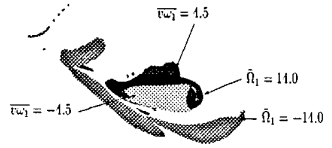

Figure 4a. Isosurfaces of $\overline{v\omega_1}$ for Case 2.

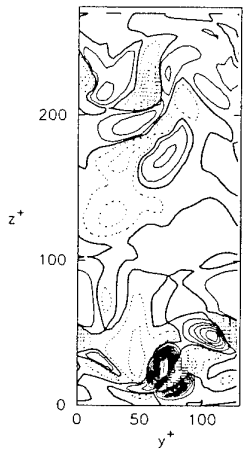

Figure 4b. Contours of $\overline{v\omega_1}$ for Case 2, contour increment = 0.414.

3.2 Visualization of the terms in the vorticity transport SGS model

The validity of the modeled equations used to represent the vorticity flux tensor can be examined using a similar technique. Figure 5 shows the isosurfaces of the modeled and exact $\overline{v\omega_3}$ using Eq. (5) with $T_1 = 4.0$, $T_2 = 0.1$, $Q_1 = 0.5$, and $Q_2 = 1.0$ and $C(\Delta) = 1.0$, while figure 6 show the results for the minimal box with $T_1 = 1.0$, $T_2 = 0.1$, $Q_1 = 3.0$, and $Q_2 = 2.0$, . While additional tuning could be done to improve the overall agreement, clearly the model is able to capture much of the actual vorticity flux.

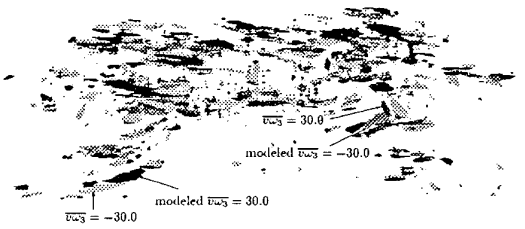

Figure 5. Isosurfaces of exact and modeled $\overline{v\omega_3}$, Case 1.

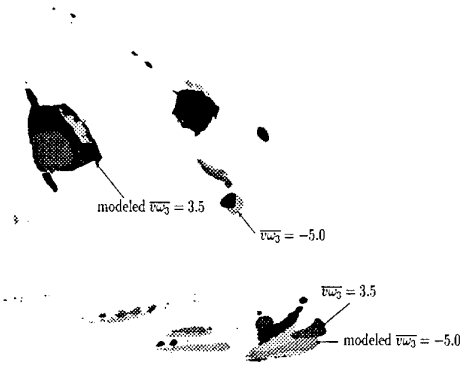

Figure 6. Isosurfaces of exact and modeled $\overline{v\omega_3}$, Case 2.

Figure 7 shows a similar comparison between $\overline{v\omega_1}$ and its modeled value. Again, while some of the details of the vorticity flux term are not captured by the model, the overall picture is promising.

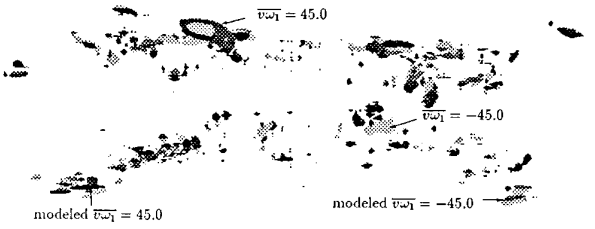

Figure 7. Isosurfaces of exact and modeled $\overline{v\omega_1}$, Case 1.

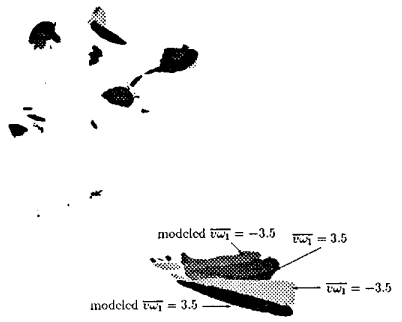

Figure 8. Isosurfaces of exact and modeled $\overline{v\omega_1}$, Case 2.

4. VORTEX METHOD TREATMENT OF THE WALL REGION

The vortical nature of the wall region flow dynamics is evident from Figures 1 - 8 and many previous studies, e.g. [1]. This suggests that it may be desirable, as well as feasible, to extend the Reynolds number range and efficiency of LES models by employing a vortex method to account for the flow nearest the wall. In particular, with an inexpensive vortex method representation of the highly organized motion of the wall region flow [1], it would be possible to vastly reduce grid point requirements near boundaries, and thus free up the LES model to pursue much higher Reynolds number flows. From this viewpoint, the vortex method can resolve the trade off between coarse resolution of the wall region flow and the need to capture the correct boundary physics.

Toward this end a deterministic vortex sheet method in two dimensions has been derived as the first step in modeling three-dimensional turbulent boundary layer flow. This is meant to accommodate the strong viscous diffusion near the wall surface. In current work, a three-dimensional vortex filament scheme is being added to account for the dynamics of vortical structures including the self-replication process. Our method is a non-random reformulation of the vortex sheet method of Chorin [7], with a viscous diffusion process based on the work of Fishelov [8]. Complete details of the analysis and results described here can be found in [9].

In the vortex sheet method, the flow field is represented through N vortex sheets or "tiles", of large aspect ratio l_i/h_i where $2l_i$ and $2h_i$ are the width and length of the ith tile. The tiles are assumed to have a uniform vorticity, and to convect undistorted with their center. The vortex sheet at the beginning of the calculation of a boundary layer is illustrated in Figure 9, which shows several layers of tiles above the solid surface, along with a layer of half tiles anchored along the surface. During the calculation, the sheets are allowed to convect according to a discretization of the kinematic condition

$$\frac{d\mathbf{x}_i}{dt} = \mathbf{u}(\mathbf{x}_i(t), t), \tag{6}$$

while vorticity diffusion is accounted for using a vorticity exchange method developed by Fishelov [8]. This models the Lagrangian form of the vorticity transport equation:

$$\frac{d\omega_i}{dt} = \frac{1}{R}(\nabla^2\omega)_i \tag{7}$$

where $\omega_i(t)$ is the strength of the ith tile. For an array of finite vortex sheets with smooth structure [10] this takes the form

$$\begin{aligned}\omega_i^{n+1} &= \omega_i^n + \frac{\Delta t}{R}\sum_j \frac{\gamma_{ij}\omega_j^n h_j}{\sqrt{\pi}\delta^3} \\ &\left[e^{-\frac{(y_i^n - y_j^n)^2}{\delta^2}} 16\left(\frac{(y_i^n - y_j^n)^2}{\delta^2} - \frac{1}{2}\right)\right. \\ &\left. +\sqrt{2}e^{-\frac{(y_i^n - y_j^n)^2}{2\delta^2}}\left(1 - \frac{(y_i^n - y_j^n)^2}{\delta^2}\right)\right] \end{aligned} \tag{8}$$

where $\gamma_{ij} \equiv m((x_i - l_i, x_i + l_i) \cap (x_j - l_j, x_j + l_j))/(2l_i)$ and $m(S)$ is the rectilinear measure of the set S. Thus $\gamma_{ij} = 1$ when $x_i = x_j$ and $l_i = l_j$, and $\gamma_{ij} = 0$ if $(x_i - l_i, x_i + l_i) \cap (x_j - l_j, x_j + l_j) = \emptyset$. The introduction of γ_{ij} follows a procedure adopted in [7] for calculation of the velocity field. For the present scheme, a discretization of the Biot-Savart integral may be used to compute velocities.

This approach has been successfully applied to zero pressure gradient Blasius boundary layer flow and the stagnation boundary layer flow corresponding to the Falkner-Skan similarity solution for a linearly increasing velocity field. Figures 10 and 11 show the results of calculations of the streamwise velocity at the dimensionless distance $x = 2.5$ from the leading edge. In contrast to the random vortex method, the instantaneous velocity fields agree closely with the exact solutions. Work is continuing on extending the method to account for spanwise velocities and to include the three-dimensional dynamics of vortical structures. It will then be tied into the LES scheme to permit preservation of the correct boundary layer physics in the context of coarsely resolved

high Reynolds number simulations of turbulent flow.

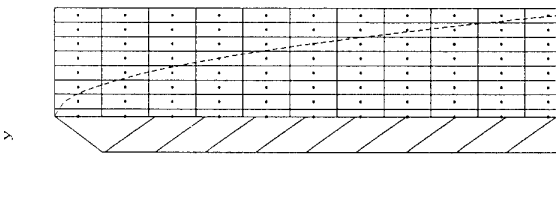

Figure 9. Initial configuration of sheets for boundary layer calculations.

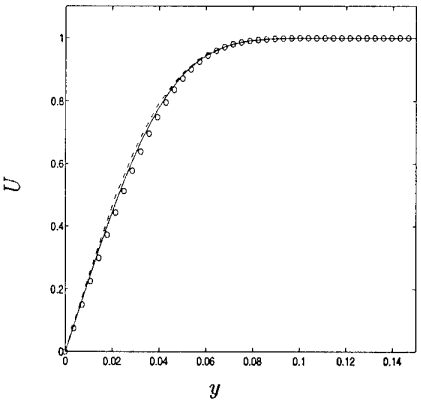

Figure 10. Comparisons of u predictions in the Blasius boundary layer - - -,N=1200: ——, N=2700; and o, Blasius solution.

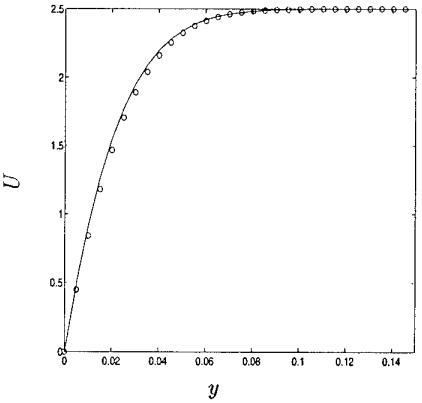

Figure 11. Comparisons of u predictions in stagnation flow boundary layer: ——, computed; o, Falkner-Skan solution.

CONCLUSION

A visual examination of vorticity flux using instantaneous realizations of channel flow have shown that these fluxes are intimately connected with quasi-streamwise vortical structures. Although this connection was evident in a marginally resolved flow, use of a more highly resolved minimal channel flow calculation which included only a limited number of vortical structures greatly clarified this relationship. Furthermore, the importance of these structures and the vorticity flux is evident even for vorticity flux terms which are zero in a planar averaged or ensemble averaged sense, thus emphasizing the importance of examining instantaneous quanitities. The models tested here, although not optimized, are generally able to represent the instantaneous location and intensity of the actual vorticity fluxes. Work on incorporating these models in a vorticity based LES to allow *a posteriori* comparisons is ongoing.

The influence of quasi-streamwise vortical structures also suggests a means for treating the wall that would better represent these structures in less well resolved flows is desirable. Towards this end, an approach using deterministic vortex sheet method is being developed. Application of this approach to boundary layer flows indicate that it has merit, and efforts to expand the method to three-dimensional turbulence are continuing.

ACKNOWLEDGEMENTS

This work was supported in part by Office of Naval Research contracts N00014-91-WX-24079 and N00014-93-10184. The first author was supported by a NRC fellowship.

REFERENCES

1. P. S. Bernard, J. M. Thomas and R. A. Handler, Vortex dynamics and the production of Reynolds stress, *J. Fluid Mech.* **253**, 385 (1993).

2. R. A. Handler, T. F. Swean, R. I. Leighton, and J.D. Swearingen,"Length scales and the energy balance for turbulence near a free surface," *AIAA J.*, **31** (11), pp. 1908-2007, 1993.

3. J. Jimenez and P. Moin, "The minimal flow unit in near-wall turbulence," *J. Fluid Mech.*, **225**, pp. 213-240, 1991.

4. P. S. Bernard, "Turbulent Vorticity Transport in Three Dimensions", *Theoretical and Computational Fluid Dynamics*, **2**, pp. 165 - 183, 1990.

5. A. Rovelstad, "Lagrangian Analysis of Vorticity Transport in a Numerically Simulated Turbulent Channel Flow", Ph. D. Thesis, University of Maryland, College Park, June, 1991.

6. A. Rovelstad, R. A. Handler, & P. S. Bernard, "Implications of Lagrangian Transport Analysis for Large Eddy Simulations", Proc. ASME

Fluid Eng. Conf. Washington, DC, pp. 13-21, June, 1993.

7. A. J. Chorin, "Vortex sheet approximation of boundary layers," *J. Comput. Physics*, **27**, p. 428, 1978.

8. D. Fishelov, "A new vortex scheme for viscous flows," *J. Comput. Physics*, **86**, p. 211, 1990.

9. P. S. Bernard, "A deterministic vortex sheet method for boundary layer flow," submitted to *J. Comput. Physics*, 1994.

10. T. Beale and A. Majda, "High order accurate vortex methods for computing 2D viscous flow," *J. Comput. Physics*, **58**, 188, 1985.

MODELLING ANISOTROPY AND BACKSCATTER EFFECTS IN THE SUBGRID SCALE STRESS TENSOR

T. GOUTORBE*, D. LAURENCE

EDF, Laboratoire National D'hydraulique,
BP 49 - 78401 CHATOU Cedex, France

**Ecole Centrale de Lyon / Université Claude Bernard - Lyon 1*
Laboratoire de Mécanique des Fluides et d'Acoustique, URA CNRS 263
ECL - BP 163 - 69131 ECULLY Cedex, France

SUMMARY

A new Subgrid scale (SGS) model used for Large-Eddy Simulation (LES) is developed by extending the scale-similarity hypothesis. Here a conventional Reynolds averaging is used instead of a test filter, resulting in using the resolved (large scale) part of the Reynolds stress tensor. This resolved Reynolds stress (RRS) model, without any eddy viscosity assumption, is shown to properly reproduce the drain and backscatter partition of energy exchange between resolved and subgrid scales (for a channel flow at moderate Reynolds numbers). After assessing these properties by a priori tests (filtering DNS results), LES computations are carried out, determining the model constants by an analytical approach and a dynamic approach. In both cases, backscatter effects can lead to instabilities which are finally cured by introducing a transport equation for the SGS energy. This is felt necessary because when backscatter occurs, both SGS production and Kolmogorov dissipation are negative, so SGS energy must vanish, thus ending backscatter. Only a transport equation for the SGS energy can account for this energy conservation principle which is violated by dynamic approaches, that impose an average procedure. Slight discrepancies appear in the buffer layer which may be attributed to the insufficient resolution of streak structures in the spanwise direction. Thus, an adaptation for the buffer-layer appears to be the last obstacle to construct a model accounting for the most important physical properties required for SGS modelling and applicable for practical applications at high Reynolds numbers.

1. INTRODUCTION

Large Eddy Simulations were originally applied to grid or shear flow turbulence where the SGS effect was modelled by an eddy viscosity to drain the energy transfer towards the smallest scales.

In a similar way, conventional (Reynolds averaged) turbulence models have first been applied to shear flows (boundary layers, jets & wakes). But for applications to more complex situations (such as impinging, curved or rotating flows), it has been often shown that strains and stresses are not always aligned, and can even lead to negative production (counter gradient stresses). Eddy viscosity models, which suppose both tensors to be aligned, proved to be insufficient in such cases.

The same trends appear for LES as we try to simulate more complex flows, but the situation is more drastic. Indeed, if in a shear flow the stresses are, in the mean, aligned to the strains, this situation is seldom true locally and instantaneously. The average value of the resolved flow dissipation is only a small fraction of its variance, meaning that there are often situations where stresses are opposed to the strains. This phase space (or local) backscatter is assumed to be related to the spectral backscatter which is the average of negative spectral transfer from small to large wave numbers (energy is flowing backwards from the subgrid scales to the resolved scales).

Aiming at including more physics in SGS modelling, many attempts have recently been made to replace or complete Smagorinsky's [1] model. For the present, it seems very difficult, with a deterministic model, to simulate the backscatter effect together with a correct mean rate of SGS dissipation ensuring a stable LES calculation.

Here we analyse a priori tests results to propose a new approach for SGS modelling that is shown to agree with local as well as mean SGS stresses.

2. MODELS

Let's consider the following filtered Navier Stokes equations:

$$\frac{\partial \overline{U_i}}{\partial t} + \frac{\partial (\overline{U_i}\,\overline{U_j})}{\partial x_j} = -\frac{\partial \bar{p}}{\partial x_i} + \nu \frac{\partial^2 \overline{U_i}}{\partial x_j^{\,2}} - \frac{\partial (\tau_{ij})}{\partial x_j} \qquad (1)$$

($\overline{\cdot}$) denotes a filter function of which variations in space and time are neglected. The subgrid stresses are defined as:

$$\tau_{ij} = \overline{U_i U_j} - \overline{U}_i \overline{U}_j \qquad (2)$$

The total velocity is thus decomposed as $U_i = \overline{U}_i + u'_i$, where $\overline{U}_i$ is the resolved flow.

2.1. Classical eddy viscosity formulation

Smagorinsky's model [1] uses information of the large scales through the only strain-rate tensor $\bar{S}_{ij} = \frac{1}{2}\left(\frac{\partial \overline{U}_j}{\partial x_i} + \frac{\partial \overline{U}_i}{\partial x_j}\right)$, and is written as:

$$\tau_{ij} = -\nu_t 2\bar{S}_{ij} + \tfrac{2}{3} k_{sgs} \delta_{ij} \qquad (3)$$

$$\nu_t = l^2 \sqrt{2\bar{S}_{ij}\bar{S}_{ij}} \quad , \quad k_{sgs} = \tfrac{1}{2}\tau_{kk} \qquad (4)$$

l is a mixing length defined from the grid spacing, e.g.: $l = C_s\ (\Delta x\ \Delta y\ \Delta z)^{1/3}$.

2.2. Drawbacks of the eddy viscosity approach

With this kind of formulation, SGS energy k_{sgs} is not known and must be reported in the pressure term. Therefore, the SGS stress tensor is not fully modelled, but only its deviator is available.

Paper presented at the 74th Fluid Dynamics Symposium on "Application of Direct and Large Eddy Simulation to Transition and Turbulence" held at Chania, Crete, Greece, in April 1994.

Let <.> be a statistical average (and in the numerical results presented hereafter, a global space-average). The total velocity is further decomposed as:

$$U_i = <\overline{U_i}> + u''_i + u'_i \quad (5)$$

where the resolved scale (RS) fluctuation is: $u''_i = \overline{U_i} - <\overline{U_i}>$.

Let's define the resolved Reynolds stress tensor R_{ij}^{rs} as:

$$R_{ij}^{rs} = \left(\overline{U_i} - <\overline{U_i}>\right)\left(\overline{U_j} - <\overline{U_j}>\right) = u''_i\, u''_j \quad (6)$$

It is important to correctly model $<\tau_{ij}>$, mainly because of its effect on the mean flow, but also to be able to calculate the mean value of the full Reynolds stress tensor:

$$R_{ij} = \left(U_i - <U_i>\right)\left(U_j - <U_j>\right) \quad (7)$$

by adding $<\tau_{ij}>$ to the average of the RRS tensor: $<R_{ij}> = <\tau_{ij}> + <R_{ij}^{rs}>$.

The dissipation of RS energy by the SGS stresses is defined as $\varepsilon_{sgs} = -\tau_{ij}\overline{S}_{ij}$ and has been shown by Piomelli et al. [2] and other authors to reach large negative values (backscatter), whereas it is always positive when using an eddy viscosity model:

$$\varepsilon_{sgs} = 2\nu_t \overline{S}_{ij}\overline{S}_{ij} \quad (8)$$

Piomelli et al. [2] and Härtel & Kleiser [3] pointed out that almost 40% of the locations in a channel flow are in a state of local backscatter, and mainly in the buffer layer or in the transitional stage. Furthermore, τ_{ij} variance itself is underestimated because of the high correlation between τ_{ij} and $\overline{S}_{ij}$, imposed by the eddy viscosity assumption.

2.3. Some other proposals

In order to get rid of this imposed stress-strain correlation, a first proposal was made by Bardina et al. [4] who assumed the scale-similarity and modelled τ_{ij} as $C_B(\overline{U_i} - \overline{\overline{U_i}})(\overline{U_j} - \overline{\overline{U_j}})$. This model was shown to represent quite well the subgrid stresses and especially the cross terms $C_{ij} = \overline{U_i}u'_j + \overline{U_j}u'_i$. But it led to a too low rate of subgrid scale dissipation, and so it was combined with (3) to form the "mixed model".

The standard mixed model was considered the most suitable for industrial applications (Laurence [5]), and has been continuously used at EDF during the past decade (Khoudli [6], Deutsch et al.[7]). Recently Horiuti & Mansour [8] proposed to improve Bardina's approach with a tensor eddy viscosity, and they accurately represented the mean normal stresses in a channel flow.

Concerning backscatter, Germano et al. [9] proposed to allow the eddy viscosity to vary through the dynamic approach, but first attempts to let it reach negative values led to instabilities. A different way was chosen by Leith [10] and Mason [11] introducing backscatter by random forcing but with little change in the overall prediction of $<\tau_{ij}>$.

3. A PRIORI TESTS

A priori tests are conducted by filtering velocity fields obtained from a direct numerical simulation (DNS) in order to yield SGS values of stresses and dissipation. The DNS channel flow results used hereafter were obtained with a fourth order finite difference procedure, presented and assessed in Lê & Maupu[12], and Maupu et al. [13] in comparison with the spectral results of Kim et al. [14-15] at the same Reynolds number, i.e. Re_τ=180 (based on friction velocity and channel half-width). The mesh used in this direct simulation is 161x209x63 points respectively in streamwise, spanwise and normal directions.

The filtering process was performed using a Gaussian filter function. The width of this filter is four times the grid spacing in x (or x_1 : streamwise) and y (or x_2 : spanwise). The filtered field obtained is therefore supposed to be the field that should yield a LES on a mesh 16 times coarser than the one aforementioned. Figure 1 displays profiles of $<\tau_{ij}>$ components obtained from a priori tests (and spatially averaged in planes of statistical homogeneity (x_1,x_2)). It shows that $<\tau_{11}>$ is much larger than the other components. In comparison, it is clear that the three diagonal components of $\overline{S}_{ij}$ (tensor used in eddy viscosity models) show zero mean values in this case.

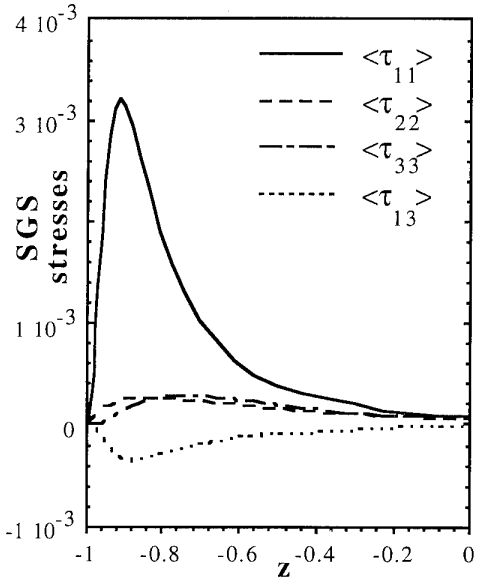

Figure 1: Mean values of the SGS stresses across half the channel width.

3.1 The Resolved Scale Reynolds Stress Tensor

A possible explanation for Bardina's [4] model to be insufficiently dissipative is that it only takes into account the smallest resolved scales which have too little correlation with $\overline{S}_{ij}$.

The RRS tensor R_{ij}^{rs} (eq. 6) might have a better correlation with $\overline{S}_{ij}$, and is also available in a LES. Figure 2, compared with figure 1 exhibits very similar tendencies between the mean values of the two tensors.

First, the curves relative to each component have the same shape for $<\tau_{ij}>$ and $<R_{ij}^{rs}>$ (except a slight shift of maxima). Secondly, the similar distribution of energy between the components (with a predominance of $<\tau_{11}>$ and $<R_{11}^{rs}>$ respectively) indicates the same orientation of the principal axes of the two tensors. This naturally leads to a modelling of the SGS stress tensor with respect to R_{ij}^{rs} rather than $\overline{S}_{ij}$.

In a general approach, it is proposed to model separately the trace and the deviator of the tensor as:

$$\begin{cases} \tau_{kk} = f_1\ R_{kk}^{rs} \\ {}^d\tau_{ij} = f_2\ {}^dR_{ij}^{rs} + f_3\left({}^dR_{ik}^{rs}\,{}^dR_{kj}^{rs} - \tfrac{1}{3}\delta_{ij}\,{}^dR_{mn}^{rs}\,{}^dR_{mn}^{rs}\right) \end{cases} \quad (9)$$

where $k_{rs} = \frac{1}{2} R_{ii}^{rs}$ is the RS energy, and ^{d}A denotes, for a tensor A, its dimensionless deviator part:

$$^{d}A_{ij} = \left(A_{ij} - \tfrac{1}{3} A_{kk}\delta_{ij}\right) \Big/ \tfrac{1}{2} A_{kk} .$$

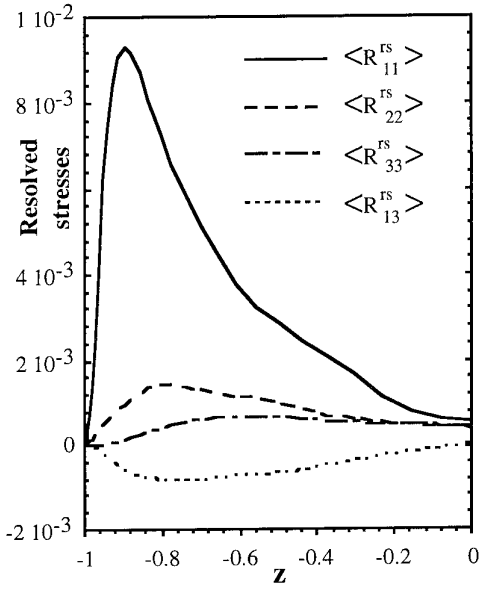

Figure 2: Mean values of the resolved scale Reynolds stresses.

To simplify the model, f_3 is first set to 0. A priori tests tend to show that the anisotropic parts of $<\tau_{ij}>$ and $<R_{ij}^{rs}>$ have the same order of magnitude at this low Reynolds number flow. So, in a first attempt, we set here $f_2 = 1$. Thus, $\tau_{ij} = f_1 R_{ij}^{rs}$, and only one parameter is to be determined: $f_1 = k_{sgs}/k_{rs}$.

3.2 Analytic RRS model

The ratio f_1 is available if one assumes a simple 2-slope spectral distribution, and a sharp cut-off filter in the spectral space. This schematic spectrum is represented on figure 3, where η_c is the cut-off wave number and η_1 the wave number that matches with the energy peak. Comte-Bellot's [16] measurements show that, for homogeneous turbulence, this wave number is close to $1/L_1$, L_1 being the integral scale .

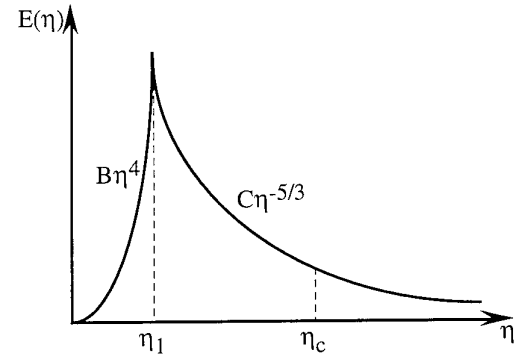

Figure 3: Simplified energy spectrum used for the analytic RRS model

Approximating $k_{rs} = \int_0^{\eta_c} E(\eta)d\eta$

and $k_{sgs} = \int_{\eta_c}^{\infty} E(\eta)d\eta$, one finds:

$$f_1 \approx \frac{1}{\frac{17}{15}\left(\eta_c/\eta_1\right)^{2/3} - 1} \qquad (10)$$

This formula shouldn't be considered exact for the entire channel flow, but has been used in a preliminary calculation to examine the main trends of the type of modelling we intend to test. In the following a priori calculation, the "analytic RRS model" uses eq. (10) with:

$\eta_c = \frac{2\pi}{\Delta_f}$, $\Delta_f = (\Delta x \Delta y \Delta z)^{1/3}$ (grid filter widths)

$\eta_1 = \varepsilon / k^{3/2}$, $k = k_{rs} + k_{sgs}$ and ε: molecular dissipation.

3.3 A priori backscatter prediction

Figure 4 shows a comparison of the distribution functions of $\tau_{ij}\bar{S}_{ij}$ calculated from a priori tests and obtained with various models at a fixed distance from the wall $z^+ = 8.6$. Whereas the backscatter effect actually exists in DNS results, it is found to be too large when using Bardina's model, leading to a too low rate of dissipation. This is not the case for the analytic RRS model, which, moreover, gives a correct mean value of ε_{sgs} .

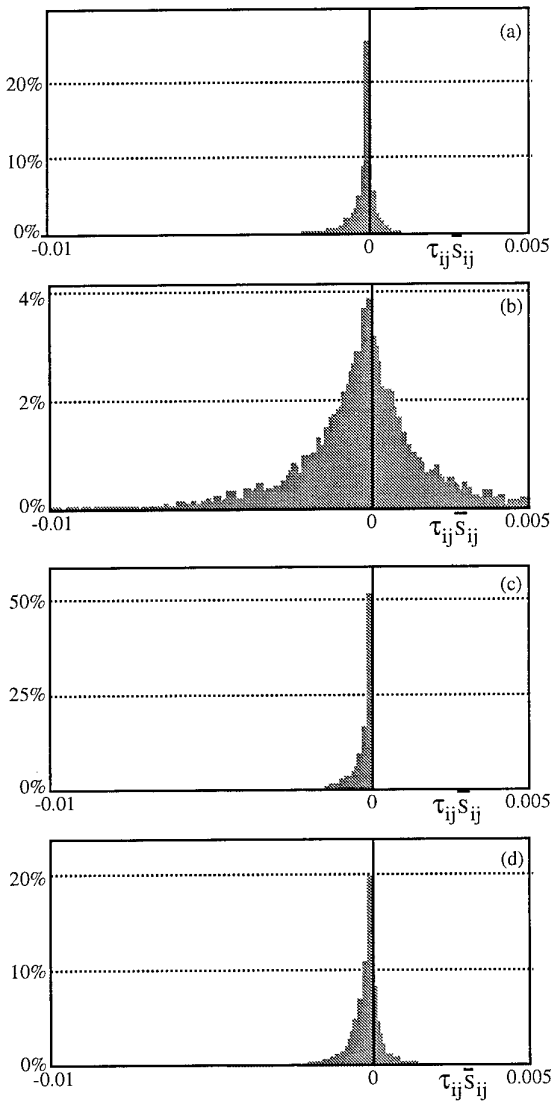

Figure 4: Probability density function of $\tau_{ij}\bar{S}_{ij}$ at $z^+ = 8.6$, obtained from a priori tests. a) "exact" DNS results ; b) Bardina's model ; c) Smagorinsky's model (C_S=0.1) ; d) analytic RRS model

4. LARGE-EDDY SIMULATION

When performing a real LES computation, the analytic RRS model is not so easy to implement. In the Kolmogorov equilibrium hypothesis, ε_{sgs} should be of the same order as ε. But when assuming this approximation for each point of the flow field, the large-scale wave number η_1 is clearly underestimated near the wall, leading to an increase in SGS energy.

4. 1 Dynamic RRSM

We then attempt to determine f_1 by the "dynamic approach", following in this way Germano's [9] idea for eddy viscosity models.

The filter induced by the LES grid is associated with the following set : $\{\ \bar{.}, \eta_c, k_{sgs}, k_{rs}, R_{ij}^{rs}\}$, respectively the filter, the cut-off wave number, the SGS energy, the RS energy and stresses.

A test-filter $\hat{}$ is introduced, of width $\hat{\Delta}$ larger than Δ, and associated with the set $\{\ \hat{.}, \eta_t, k_{\hat{}sgs}, k_{\hat{}rs}, R_{ij}^{\hat{}rs}\}$.

Applying the test-filter to (1) yields:

$$\frac{\partial \hat{\bar{U}}_i}{\partial t} + \frac{\partial(\hat{\bar{U}}_i \hat{\bar{U}}_j)}{\partial x_j} = -\frac{\partial \hat{\bar{p}}}{\partial x_i} + \nu \frac{\partial^2 \hat{\bar{U}}_i}{\partial x_j^{\,2}} - \frac{\partial(T_{ij})}{\partial x_j}; \qquad (11)$$

where $T_{ij} = \widehat{\bar{U}_i \bar{U}_j} - \hat{\bar{U}}_i \hat{\bar{U}}_j$ are the SGS stresses associated with the double-filtering.

The RRS model is assumed to be applicable to both filters:

$$\tau_{ii} = f_1(\eta_c)\ R_{ii}^{rs} \ \Leftrightarrow\ k_{sgs} = f_1(\eta_c) k_{rs} \qquad (12)$$

$$T_{ii} = f_1(\eta_t)\ R_{ii}^{\hat{}rs} \ \Leftrightarrow\ k_{\hat{}sgs} = f_1(\eta_t) k_{\hat{}rs} \qquad (13)$$

and from (10), f_1 varies as:

$$f_1(\eta) = \frac{1}{C_1\ \eta^{2/3} - 1} \qquad (14)$$

for $\eta = \eta_c$ or η_t. The constant C_1 is a local variable, but does not depend on the filter size.

Assuming that: $k_{\hat{}sgs} + k_{\hat{}rs} = k_{sgs} + k_{rs} = k$ (total turbulent energy), one finds:

$$\frac{k}{k_{\hat{}sgs}} = C_1\ \eta_t^{\,2/3}, \text{ and } \frac{k}{k_{sgs}} = C_1\ \eta_c^{\,2/3}. \text{ So: } \frac{k_{sgs}}{\hat{k}_{sgs}} = \left(\frac{\eta_t}{\eta_c}\right)^{2/3},$$

and finally:

$$f_1(\eta_c) = \frac{k_{sgs}}{k_{rs}} = \frac{1 - \frac{k_{\hat{}rs}}{k_{rs}}}{\left(\frac{\eta_c}{\eta_t}\right)^{2/3} - 1} \qquad (15)$$

Note that the ratios $\frac{k_{\hat{}rs}}{k_{rs}}$ and $\frac{\eta_c}{\eta_t}$ can be computed explicitly in a simulation. Thus, eq. (15) yields a complete closure for LES that is hereafter denoted as "dynamic RRS model".

A LES has been performed with the same code already used by Lê & Maupu [12], with a fourth order finite difference procedure. The mesh was chosen to match with the a priori tests mentioned in this paper, and contain 41x53x63 nodes respectively in x, y and z directions. The initial field was the one used in the a priori test, and obtained by filtering the DNS field. The mesh cells have a variable size in the normal direction, and a fixed size in the plane (x,y): Δx^+=44.8 and Δy^+=21.6. The run began with 100 time-steps with the original Smagorinsky model so as to ensure a mean energy drain from large to SGS scales. After that initialisation, the "dynamic" RRS model was initiated, using a test-filter width equal to twice the grid size in x and y directions.

A first attempt was made, computing $\frac{k_{\hat{}rs}}{k_{rs}}$ from eq. (15) at each grid point, but this yielded non-physical results. Indeed, $\frac{k_{\hat{}rs}}{k_{rs}}$ was found to be locally lower than 1, leading to negative energy! We then tried to determine the parameter $\frac{k_{\hat{}rs}}{k_{rs}}$ by plane-average, substituting (15) with:

$$f_1 = < f_1 > = \frac{1 - \frac{< k_{\hat{}rs} >}{< k_{rs} >}}{\left(\frac{\eta_c}{\eta_t}\right)^{2/3} - 1} \qquad (16)$$

giving a much more stable determination of $< f_1 >$.

In the initial stage, the LES computation yielded results similar to the a priori test, with backscatter taking place mostly in the buffer layer as noted by Piomelli et al. [2] and Härtel et al. [3]. But the dynamic RRS model led later to too much backscatter, and finally divergence. The explanation is found by looking, in figure 5 and 6, at the distributions of local SGS energy versus SGS dissipation over the plane where the maximum backscatter occurs (z^+=29). The a priori results (fig. 5) show that the locations of high energy are in a state of strong drain (ε_{sgs} >0), whereas the dynamic RRS model rapidly leads to the opposite trend (fig. 6). This contradicts a physical rule: if a location is in a state of backscatter, the SGS energy should decrease in time since it is no longer fed by the Kolmogorov cascade.

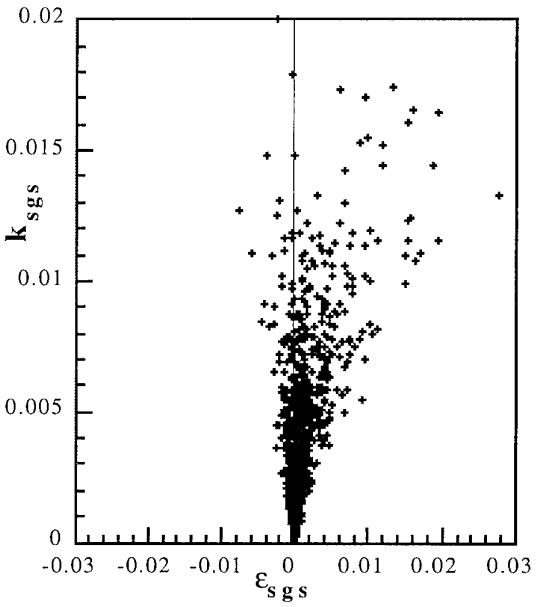

Figure. 5: Scatter plot of SGS energy versus SGS dissipation over one plane parallel to the walls (z^+=29). *A priori results.*

The theoretical "dynamic" determination of f_1 (eq. 15) is not clearly in contradiction with the physics, but this drawback is probably associated with the average procedure in (16). Since $f_1 = k_{sgs}/k_{rs}$ is calculated by plane average, this factor is the same on drain or backscatter locations.

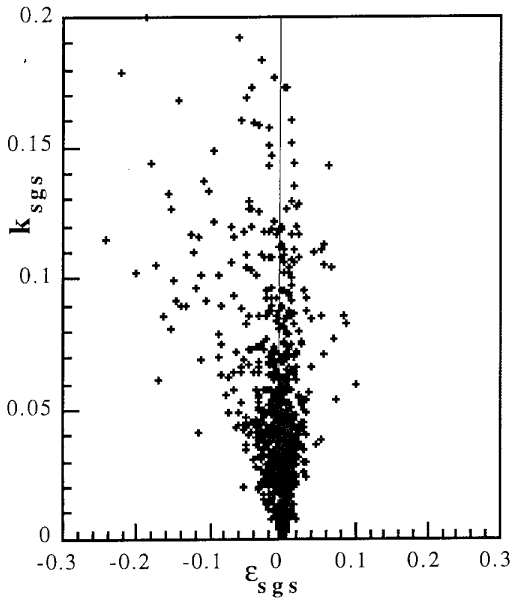

Figure. 6: Scatter plot of SGS energy versus SGS dissipation over one plane parallel to the walls (z^+=29). *Dynamic RRS model (after 50 time steps)*

This tends to show that a balance equation for the SGS energy is mandatory when models include backscatter, as pointed out by Ghosal et al. [19].

4.2 RRS model and SGS energy transport equation.

To avoid this kind of problem, the RRS model has been combined with a balance equation for the SGS energy. Following Schumann [17], this equation can be modelled as:

$$\frac{\partial k_{sgs}}{\partial t} + U_i \frac{\partial k_{sgs}}{\partial x_i} = -\tau_{ij}\bar{S}_{ij} + \frac{\partial}{\partial x_i}\left(\frac{1}{3} l_\Delta \sqrt{k_{sgs}} \frac{\partial k_{sgs}}{\partial x_i}\right) + \nu \frac{\partial^2 k_{sgs}}{\partial x_i^2} - c_\varepsilon \frac{k_{sgs}^{3/2}}{l_\Delta} \quad (17)$$

with $l_\Delta = \min\left(\Delta, c_\varepsilon z_w\right)$, z_w: distance from the wall

$c_\varepsilon = \pi\left(\frac{2}{3k_0}\right)^{3/2}$ and $k_0 = 1.6$ (Kolmogorov constant)

Thus, f_1 can be directly determined from $f_1 = k_{sgs}/k_{rs}$ at each grid point, and the SGS stresses are modelled as proposed originally: $\tau_{ij} = f_1 R_{ij}^{rs}$.

Starting from the same initial field as before, we calculated an initial SGS energy field with the dynamic RRS model. The run was then performed with the RRS model coupled with (17). This computation in no way exhibited instability and moreover yielded satisfactory results. Indeed, backscatter still occurs at the end of the calculation (after 2000 time-steps, i.e. 170 ν/u_τ^2) without an abnormal increase of SGS energy at these locations, so that the backscatter phenomenon seems well limited by the transport equation.

Figure 7 shows the mean SGS dissipation obtained at the end of this run, averaged on planes (x,y) and on the last 100 time units. Though the backscatter effect has been seen fairly large in this simulation, $<\varepsilon_{sgs}>$ has everywhere a positive mean value. When compared with a priori results, the mean SGS dissipation given by the RRS model, though slightly underestimated, is close to the DNS profile.

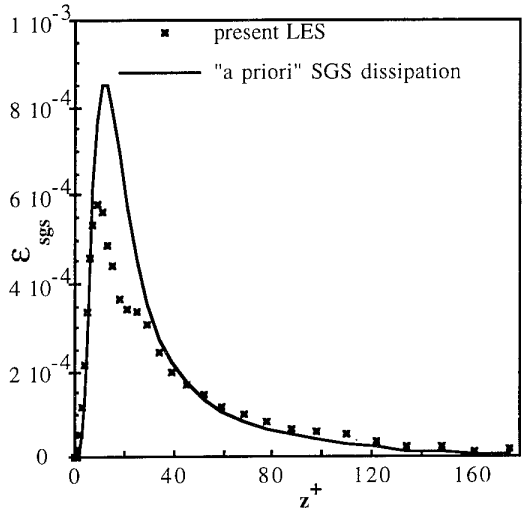

Figure 7: Comparison of subgrid-scale dissipation obtained from a priori-test and with RRS model coupled with transport equation for k_{sgs}.

Figure 8 gives an a posteriori validation of this LES. It shows that the sum of k_{rs} and k_{sgs} gives a total energy similar to the turbulent energy obtained in the DNS.

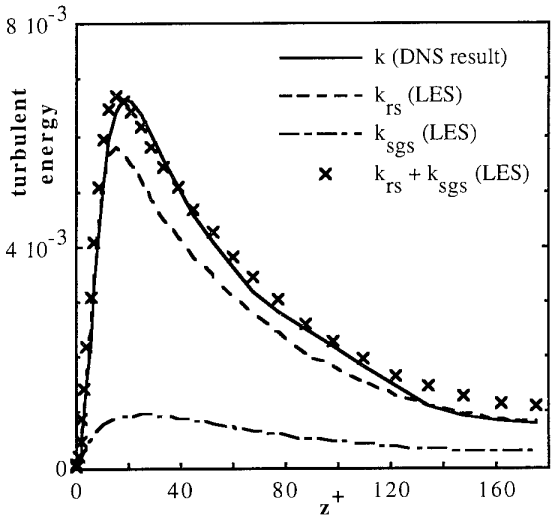

Figure 8: Comparison of total turbulent energy obtained from DNS and energy contained in resolved and subgrid scales from LES with RRS model coupled with transport equation for k_{sgs}.

The mean velocity profile given by this simulation is reported on figure 9. It follows the right law in the viscous sublayer. As far as the log-law is concerned, one can observe this behaviour in the layer z^+>50, but the additive constant is quite larger than the commonly accepted value (between 5 and 6). This may be attributed to a too short integration time compared with the turbulent time scale, but can also reveal a

shortage of the model to account for the phenomena occurring in the buffer layer when the grid resolution is too coarse. This question may be clarified by simulating a flow where this buffer layer can be more obviously considered as a separation zone.

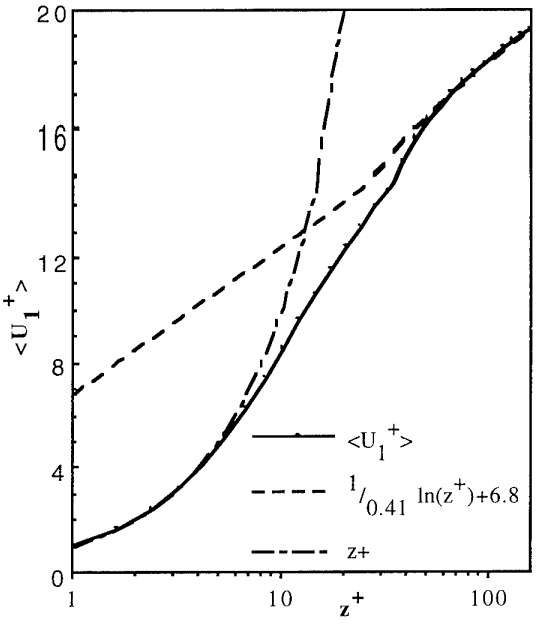

Figure 9: Mean velocity profile in wall coordinates. LES with the RRS model at Re_τ=180.

4.3 A higher Reynolds number simulation

The RRS model has been developed from the analysis of a DNS database of a rather low Reynolds number flow. One should wonder what occurs when the small scale anisotropy is known to be reduced by the longer inertial range of the energy spectrum. However the local similarity of structures at different scales previously observed by a priori tests at moderate Reynolds numbers has been recently confirmed with experimental results at high Reynolds numbers by Liu, Meneveau & Katz [18] using very high resolution PIV methods.

A simulation has been performed with the same initial field, but modifying Re_τ in decreasing the molecular viscosity. Re_τ has then been set to 550 and a steady state has been reached. The first conclusion pointed out by this calculation is that the RRS model still has a dissipative action in this case, and despite a quite coarse meshing ($\Delta x^+ \approx 135$ and $\Delta y^+ \approx 66$). Furthermore, the backscatter effect is also observed and doesn't involve instability. However, figure 10 confirms the need to improve this modelling. It shows that, though the log-layer seems well simulated, it appears that the velocity profile retains too large gradients in the buffer layer. This insufficient mixing is probably due to the fact that $\Delta y^+ \approx 66$ does not allow to represent the streak structures (the width of which is about 100 wall units) These particular structures cannot be modelled easily, particularly by scale similarity assumptions.

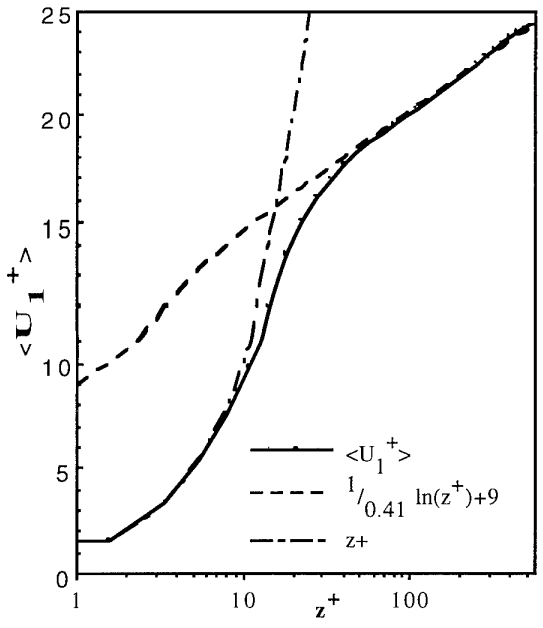

Figure 10: Mean velocity profile in wall coordinates. LES with the RRS model at Re_τ=550.

CONCLUSION AND OUTLOOK

A priori tests have revealed the ability of a new model based on the resolved Reynolds stress tensor to mimic the anisotropy of the subgrid scales and to accurately recover local backscatter effects. Difficulties were encountered in ensuring stability when such effects are predicted. Only the coupling of the RRS model with a transport equation for k_{sgs} proved stable in a complete LES computation.

The model, based on a scale-similarity assumption as Bardina's[4] model, has been shown dissipative enough to be used without any eddy viscosity hypothesis, even on a quite high Reynolds number flow. Improvements are needed to better simulate the buffer layer where streak structures do not follow a scale similarity law. Hence it might be necessary to develop models through "law of the wall" type boundary conditions at high Reynolds numbers. The "dynamic" procedure is promising, and could be applied simultaneously to the second model constant f_2 accounting for anisotropy reduction. A more complex flow situation should reveal the advantages of substituting the eddy viscosity assumption for other kinds of models, as is the case for conventional Reynolds averaged Navier Stokes equations.

Acknowledgements

The authors would like to thank Department ADEB (Application de l'Electricité dans les Bâtiments) of EDF for financial support allotted to the presentation of this work.

REFERENCES:

1 A. Smagorinsky: "General Circulation Experiment with the Primitive Equations: the basic experiment", Monthly Weather Review 91 n°3 (1963), pp. 99-164.

2 U. Piomelli, W. H. Cabot, P. Moin, S. Lee : "Subgrid-scale backscatter in turbulence and transitional flows", Phys. Fluids A3 (7), July 1991, pp.1766-1771.

3 C. Härtel, L. Kleiser: "Comparative testing of subgrid-scale models for wall bounded turbulent flows", Comp. F. Dynamics Vol.1 pp.215-222, Hirsch et al. (Editors), Elsevier 1992.

4 J. Bardina, J. H. Ferziger, W. C. Reynolds : "Improved subgrid-scale models for large eddy simulations", 1980, AIAA Paper N° 80-1357.

5 Laurence D.: "Advective Formulation of Large-Eddy Simulation for Engineering Flow" ; Euromech 199, Munich, Notes on Numerical Fluid Mechanics vol. 15, Vieweg(1985), pp. 147-160.

6 H. Khoudli, "Macrosimulation de turbulence homogène", Ecole Centrale Lyon thesis n° 88-23, 1988.

7 E. Deutsch, O. Simonin, "LES applied to the modelling of particulate transport coefficients in turbulent 2-phase flow", proc. 8th Tur. Shear Flow, Univ of Munich, 1991.

8 K. Horiuti & N.N. Mansour: "A normal SGS eddy viscosity model in LES", proc. 9th Tur. Shear Flow, Kyoto, 1993.

9 M. Germano, U. Piomelli, P. Moin, W. H. Cabot : "A dynamic subgrid-scale eddy viscosity model", Phys. Fluids A3 (7), July 1991, pp.1760-1765.

10 C. Leith: "Stochastic backscatter in a SGS model: plane shear mixing layer", Phys. Fluids A2(3) pp. 297-300,1990.

11 P.J. Mason, D.J. Thomson, "Stochastic backscatter in large eddy simulations of boundary layers", J. Fluid Mech. 242 (1992), pp.51-78.

12 T.H. Lê, V. Maupu : "Direct simulation of turbulent channel flow with finite difference schemes on non-staggered grids", 2nd Int. Symp. on Eng. Turbul. Modelling and Measurements, May 31 - June 2, 1993, Florence, Italy.

13 V. Maupu, T. Goutorbe, D. Laurence, "A finite difference direct numerical simulation of passive scalar transport in a turbulent channel flow", 5th International Symposium on Refined Flow Modelling and Turbulence Measurements, pp.343-350.

14 J. Kim, P. Moin, R. Moser, "Turbulent statistics in a fully developed channel flow at low Reynolds number.", J. Fluid Mech. 177 (1987), pp.133-166.

15 N.N. Mansour, J. Kim, P. Moin, "Reynolds-stress and dissipation-rate budgets in a turbulent channel flow.", J. Fluid Mech. 194 (1988), pp.15-44.

16 G. Comte-Bellot, S. Corrsin, "Simple eulerian time-correlation of full and narrow-band velocity signals in grid-generated "isotropic" turbulence", J. Fluid Mech. 48 (1971), pp.273-337.

17 U. Schumann, "Subgrid length-scales for large-eddy simulation of stratified Turbulence"; Theor. Comput. Fluid Dyn. 2, pp.279-290, 1991.

18 S. Liu, C. Meneveau & J. Katz, "Structure of subgrid scales in the far field of a turbulent round jet", First ERCOFTAC workshop on Direct and Large-Eddy Simulation, P. Voke ed., Kluwer, oct. 1994.

19 S. Ghosal , T. Lund, P. Moin, "A local dynamic model for LES", in CTR annual research briefs, CTR/Stanford U./NASA Ames 3-25.

Simulation of Pipe Flow

Y. Zhang, A. Gandhi, A.G. Tomboulides, S.A. Orszag
Fluid Dynamics Research Center, James Forrestal Campus
Princeton University, Princeton, New Jersey 08544-0710
USA

Abstract

In this paper we report simulations of low to moderate Reynolds number turbulent pipe flow, obtained using a 3-d spectral code. Here we describe features of flows at Reynolds numbers $Re = 2500$ and 4000 and compare with available data. It is noted that simulations with periodic inflow/outflow boundary conditions do not reproduce the turbulent puff and slug flows found in spatially evolving transitional flows. The goal is to coordinate the use of this code with the currently performed SuperPipe experiments now underway at Princeton University.

1 Introduction

As one of the simplest and most reproducible laboratory flows, turbulent pipe flow has been extensively studied, starting with the pioneering experiments of Osborne Reynolds in 1883. In the case of fully-developed turbulent pipe flow, the experiments by Reynolds (1883) [1], Nikuradse (1932) [2], Laufer (1954) [3], Towens (1971) [4], Lawn (1971) [5], and Perry (1975) [6] established the existence of multiple-scales with a viscous sublayer very close to the wall, an inertial sublayer far away from the wall and an "overlap" buffer layer in between. The flow field obeys different scaling laws inside each region.

Wygnanski & Champagne (1973) [7] and Wygnanski, Sokolov and Friedman (1975) [8] performed an extensive experimental study of transitional pipe flow. They identified two basic types of structures in pipe flow transition: turbulent slugs and puffs. If the inlet flow is slightly disturbed, transition occurs due to instability in the boundary layer which produces turbulent slugs. Turbulent slugs have clearly defined leading and trailing fronts and grow in length as they travel downstream. Turbulent puffs are generated by large disturbances in the pipe inlet region; when the flow Reynolds number is in the transitional regime - 2000 to 2700 - pipe flow is laminar interspersed with turbulent puffs.

The majority of pipe flow numerical simulations to date have studied stability and transition. Unlike other prototype wall-bounded shear flows, pipe flow is unique in that it is linearly stable over all Reynolds numbers (Salwen & Grosch, 1972 [9]). Davey & Nguyen, 1971 [10] performed a stability analysis of pipe flow subject to finite-amplitude axisymmetric disturbances but their results remain controversial (Itoh 1977 [11], Davey 1978 [12]). Orszag & Patera (1981 [13], 1983 [14]) also investigated the non-linear stability of pipe flow guided by their theory of secondary instability. They found that all axisymmetric finite-amplitude disturbances decay, but non-axisymmetric disturbances can be strongly unstable. Recent works by Henningson (1991) [15], O'Sullivan, Breuer and Sirovich (1991) [16] suggested another possible mechanism which might induce transition in pipe flow. They showed that the non-normality of the linearized Navier-Stokes equations in cylindrical co-

Paper presented at the 74th Fluid Dynamics Symposium on "Application of Direct and Large Eddy Simulation to Transition and Turbulence" held at Chania, Crete, Greece, in April 1994.

ordinates can lead to certain "optimal perturbations" which exhibit large transient growth even though they eventually decay. They observed in their simulations that the energy density of such initial structures can grow by a factor of as much as 160.

Relatively few direct numerical simulations (DNS) have yet been performed on high Reynolds number turbulent pipe flow. Nikitin (1993) [17] performed three-dimensional direct numerical simulations using mixed finite difference and spectral methods with maximum spatial resolution of $42 \times 63 \times 42$ (in the axial, radial and azimuthal directions respectively). He was able to obtain satisfactory agreement with experimental data in turbulent mean flow quantities inside the Reynolds number range of $2250 - 5900$. Unger, Eggels, Friedrich and Nieuwstadt (1992) [18] studied fully developed turbulent pipe flow using a second-order-accurate finite difference method for Reynolds number up to 6950. They obtained excellent agreement with the experiments of Westerweel *et al* (1993) [19] and Durst *et al* (1993) [20]. For example, they confirmed that pipe flow at low Reynolds number (less than 9600) deviates from universal logarithmic law, as indicated in the experiments of Durst *et al* [20].

However, there remain fundamental unresolved issues regarding pipe flow turbulence. It is not clear whether scaling laws continue to apply at very high Reynolds numbers; it is not known if "universal" constants still apply at these Reynolds numbers nor there exist accurate measurements of the von Karman constant or its possible dependence on Reynolds number. To seek the answers to the above questions, we have begun computational studies closely coupled to a new and novel pipe flow experiment [21]. The "SuperPipe" experimental facility at Princeton which has been designed to span the Reynolds number range from 10^3 to 4×10^7, allows turbulence measurements at Reynolds numbers roughly two orders of magnitude larger than previous measurements.

In this paper, we discuss initial results of direct numerical simulations of pipe flow at low to moderate Reynolds numbers. The present study is concentrated on the validation of our numerical method and construction of a DNS data base of turbulent pipe flow. Our initial results agree satisfactorily with both experiments and previous numerical simulations. We believe that the current DNS study will also provide a useful data base to explore turbulence transport models which are crucial to Large Eddy Simulation(LES) and Very Large Eddy Simulation(VLES) of turbulent pipe flow at high Reynolds numbers.

2 Numerical Formulation

The governing equations are the incompressible Navier-Stokes equations, which in rotational form are

$$\frac{\partial \mathbf{v}}{\partial t} + \boldsymbol{\omega} \times \mathbf{v} = -\nabla P + \nu \nabla^2 \mathbf{v} \qquad (1a)$$

$$\nabla \cdot \mathbf{v} = 0 \quad in \quad \Omega. \qquad (1b)$$

where $\mathbf{v} = (u, v, w)$ is the velocity field - u, v, w refer to streamwise, radial and azimuthal velocity components, respectively - $P = p + \frac{1}{2}\mathbf{v} \cdot \mathbf{v}$ is the total pressure, $\boldsymbol{\omega} = \nabla \times \mathbf{v}$ is the vorticity, and ν is the kinematic viscosity. The discretization of the equations is performed using spectral methods. Since the objective is the investigation of infinite pipe flow, Fourier expansions are introduced in the streamwise and azimuthal directions for all flow variables

$$u(z, r, \phi, t) = \sum_{k=0}^{K-1} \sum_{m=0}^{M-1} u_{mk}(r, t) e^{im\phi} e^{i\alpha kz} \qquad (2)$$

where m represents azimuthal Fourier modes, k streamwise modes, and $\alpha = L_z/2\pi$ the streamwise wavenumber. Substituting expansion (2) in

the governing equations, and applying the following change of variables

$$\tilde{v}_{mk} = v_{mk} + iw_{mk}; \quad \tilde{w}_{mk} = v_{mk} - iw_{mk} \quad (3)$$

the system of equations is diagonalized:

$$\frac{\partial u_{mk}}{\partial t} + \mathcal{F}_{mk}\left(\omega \times \mathbf{v}\right)_z = -ikP_{mk} + \nu\left(\nabla^2_{rz} - \frac{m^2}{r^2}\right)u_{mk} \quad (4a)$$

$$\frac{\partial \tilde{v}_{mk}}{\partial t} + \tilde{\mathcal{F}}_{mk}\left(\omega \times \mathbf{v}\right)_r = -\left(\frac{\partial P_{mk}}{\partial r} - \frac{m}{r}P_{mk}\right) + \nu\left(\nabla^2_{rz} - \frac{(m+1)^2}{r^2}\right)\tilde{v}_{mk} \quad (4b)$$

$$\frac{\partial \tilde{w}_{mk}}{\partial t} + \tilde{\mathcal{F}}_{mk}\left(\omega \times \mathbf{v}\right)_\phi = -\left(\frac{\partial P_{mk}}{\partial r} + \frac{m}{r}P_{mk}\right) + \nu\left(\nabla^2_{rz} - \frac{(m-1)^2}{r^2}\right)\tilde{w}_{mk} \quad (4c)$$

where

$$\nabla^2_{rz} = \frac{1}{r}\frac{\partial}{\partial r}\left(r\frac{\partial}{\partial r}\right) - \alpha^2 k^2$$

$$\tilde{\mathcal{F}}_{mk}\left(\omega \times \mathbf{v}\right)_r = \mathcal{F}_{mk}\left(\omega \times \mathbf{v}\right)_r + i\mathcal{F}_{mk}\left(\omega \times \mathbf{v}\right)_\phi$$

$$\tilde{\mathcal{F}}_{mk}\left(\omega \times \mathbf{v}\right)_\phi = \mathcal{F}_{mk}\left(\omega \times \mathbf{v}\right)_r - i\mathcal{F}_{mk}\left(\omega \times \mathbf{v}\right)_\phi$$

and $\mathcal{F}_{mk}$ refers to a Fourier transform in both ϕ and z. The coordinate singularity at $r = 0$ is removable, since it can be shown that the behavior of the Fourier coefficients of the velocity components close to the axis are

$$(u_m, v_m, w_m) \propto (\beta r^m, \gamma r^{m-1}, i\gamma r^{m-1}) \quad (5)$$

where β and γ are constants, [22], [23]. It can be verified that $\tilde{v}_{mk} = v_{mk} + iw_{mk}$ is zero at $r = 0$ for all m and it scales like $v_{mk} + iw_{mk} \propto r^{m+1}$; the latter is equivalent to the fact that the vorticity is also regular at $r = 0$. On the other hand, the variable $\tilde{w}_{mk} = v_{mk} - iw_{mk}$ has a non-zero value at $r = 0$ for $m = 1$; however, the coefficient of $\tilde{w}_{mk}$ for $m = 1$ is zero and so the singularity in (4c) is removed.

Numerically, however, there are still terms in the equations where both the numerator and the denominator goes to zero at the same rate close to the axis, which means that quantities of indeterminant form have to be treated. To do this, a special form of Jacobi polynomials is used as an expansion basis in the r direction adjacent to the axis, which in conjunction with L'Hôpital's rule results in a removal of the geometrical singularity, thus preserving the spectral convergence rate. The set of polynomials employed close to the axis correspond to the Jacobi polynomials $P^{(0,1)}$, with associated weights which are zero at $r = 0$.

For the time integration of equations (4a), (4b), (4c), we use a fractional step method, in conjunction with a mixed explicit/implicit stiffly stable scheme of second order of accuracy in time [24]. A consistent Neumann boundary condition is used for the pressure, based on the rotational form of the viscous term, which nearly eliminates splitting errors at solid (Dirichlet) velocity boundaries. The resulting Helmholtz equations are of the form

$$\frac{1}{r}\frac{\partial}{\partial r}\left(r\frac{\partial}{\partial r}u_{mk}\right) - \frac{m^2}{r^2}u_{mk} - \lambda^2 u_{mk} = g, \quad (6)$$

The constant λ^2 is 0 for the pressure equation and $\gamma_0/(\nu\Delta t) + \alpha^2 k^2$ for the velocity equations (γ_0 is a coefficient associated with the order of the time-integrating scheme used).

Our pipe flow code is capable of solving streamwise periodic flows as well as in-flow, out-flow flows. While the former set of boundary conditions is more efficient in the case of fully developed turbulent flow, the latter is indispensable when the simulation of spatially developing flow is required, a subject for future studies. In general, when the flow in the axial direction is not periodic, quadrilateral elements are employed. However, the current version of our code is designed to calculate fully developed turbulent pipe flow in the most efficient way, so streamwise periodicity is assumed and Fourier expansions are

employed as described in equation (2). As a result, the spatial discretization of the Helmholtz equation (6) is reduced to one dimension, and spatial discretization is performed using one dimensional spectral elements [25], [26]. In the element adjacent to the axis of symmetry we use Lagrange interpolants based on zeros of Jacobi $(0,1)$ polynomials, whereas in the rest of the elements Legendre-Lagrangian interpolants are employed [27]. The resulting matrix for the numerical solution of this one dimensional Helmholtz equation is essentially block diagonal and can be solved efficiently by the static condensation technique (with operation count approximately $K \times M \times K_e \times N^2$, where N is the number of grid points inside a single element and K_e the total number of elements (typically $K_e \leq 10$ and $N \leq 20$).

The numerical simulations we report here are from streamwise periodic flows. With fixed flowrate and spatial resolutions of $(4 \times 11) \times 64 \times 128$ and $(5 \times 15) \times 128 \times 128$, we report results at Reynolds numbers (based on pipe diameter $D = 2$ and bulk mean velocity $\bar{U} = 0.5$) of 2500 and 4000 respectively. The time step is 0.0075 for $Re = 2500$ and 0.005 for $Re = 4000$. The streamwise wave number is fixed at 0.5, which means that the pipelength is $2\pi D$. The pipe code is fully parallelized and all computations were performed on the IBM PVS parallel computer. For the maximum resolution, a speed of 8 sec per time step on a 32 processor machine is achieved, equivalent to about 240 MFlops.

3 Results and Discussion

Considerable effort was put in finding appropriate initial conditions which would eventually render the pipe flow turbulent. We found that non-axisymmetric disturbances with little or no variation in the streamwise direction (i.e. $\alpha k \approx 0$), experienced large transient growth before they eventually decayed, even for Reynolds numbers as high as 4000. On the other hand, initial perturbations in the form of a wave packet, localized in the streamwise direction, containing energy only in the first two ($m = 1, 2$) azimuthal modes, amplified rapidly and rendered the flow turbulent. An interesting finding is that even though the time it takes for the energy spectrum to build up is of the order of a few (less than 5) $D/\bar{U}$ time units, it takes considerably longer (of the order of $200 - 300$ such units) for the flow to reach a statistically steady state. Simulations at $Re = 2500$ were carried out to a statistically steady state, whereas in our preliminary computation of pipe flow at $Re = 4000$, the statistically steady state has not been reached; the skin friction coefficient computed from the available data at $Re = 4000$ is about 15% lower than the experimental data.

The dependence of the pipe skin friction coefficient upon Reynolds number is plotted in Figure (1). The data point at Re = 2500 agrees very well with the Blasius 1/4 law. However, our simulations do not reproduce the experimental finding that the value of C_f within the transitional Reynolds number range is between the laminar (Re^{-1}) and turbulent $(Re^{-1/4})$ laws. This disagreement can be explained as follows: pipe lengths in experiments are finite and the transitional flows observed are intermittent; large scale structures, such as turbulent slugs and puffs, which originate either from boundary layer instabilities in the inlet region or from large perturbations at the pipe inlet, are interspersed with laminar flow. As a consequence, the skin friction in a pipe with finite length, measured by the pressure drop between two downstream stations, is strongly dependent on the distance from the source of the disturbances. On the other hand, having imposed streamwise periodicity in our numerical pipe simulations, we effectively force disturbances to cover the whole pipe length, and it is not surprising that our computations will not produce spatially evolving transitional structures as observed in experiments. Similar observations have been reported in previous numerical simulations, e.g. Nikitin (1993) [17].

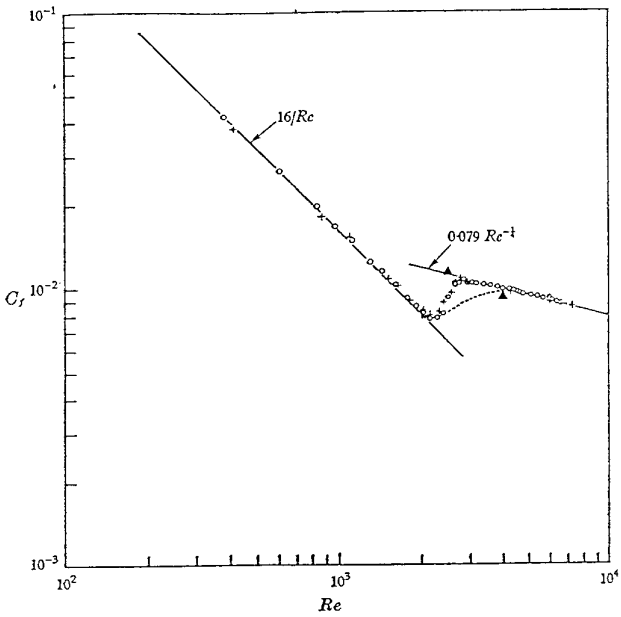

Figure 1: Skin friction coefficient C_f vs Re. Circles and crosses correspond to experiments by Patel & Head(1969), and Nikuradse(1932) respectively; triangles correspond to simulations

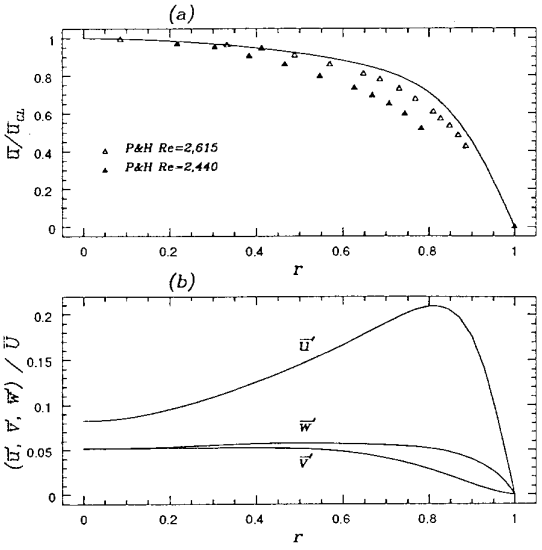

Figure 2: Mean (a) and rms (b) velocity distribution across the pipe for $Re = 2,500$

3.1 Turbulence statistics

Mean profiles and turbulence intensities

In Figure (2a), we plot the mean velocity profile *vs* pipe radius for $Re = 2500$. The computational mean velocity profile is fuller near the wall, indicating a larger skin friction coefficient than that observed experimentally by Patel & Head (1969) [28] at similar Re numbers. This discrepancy is expected since as mentioned earlier, the skin friction at $Re = 2500$ lies on the Blausius 1/4 curve and not on transitional curves observed in experiments. It should be mentioned that transition curves differ between different experiments, depending on experimental setup and disturbance level at the pipe inlet. The same profile of mean velocity, non-dimensionalized by the wall-shear velocity, is also plotted in Figure (3), in terms of the logarithm of wall units. The computational results agree with the law of the wall but disagree with the log-law at $Re = 2500$. This agrees with most experimental and numerical results which show that the log-law is not observable for $Re \leq 9600$. The mean velocity profile for $Re = 4000$ is shown in Figure (4a), together with experimental results from [7], [29], [30], [28]. It can be seen that the agreement in the core region of the pipe is satisfactory, whereas there is some discrepancy close to the wall. It is worth mentioning however, that there is considerable deviation among different sets of experimental data close to the wall; in addition, the mean flow statistics at $Re = 4000$ are only preliminary due to relatively short run times.

The rms values of all velocity components are plotted in Figures (2b) and (4b) for $Re = 2500$ and 4000 respectively. The rms of radial and azimuthal velocity components agree with the experimental data of Shemer,Wygnanski and Kit(1985) [30]. The rms of the streamwise component of the velocity agrees with the data except in the region very close to the wall due to the limited evolution time of our computation.

The Reynolds stress distribution for $Re = 2500$ is shown in figure (5). It can be observed that the distribution in the core region of the flow is very close to linear. The turbulent Reynolds stress distribution in the region very close to the wall re-

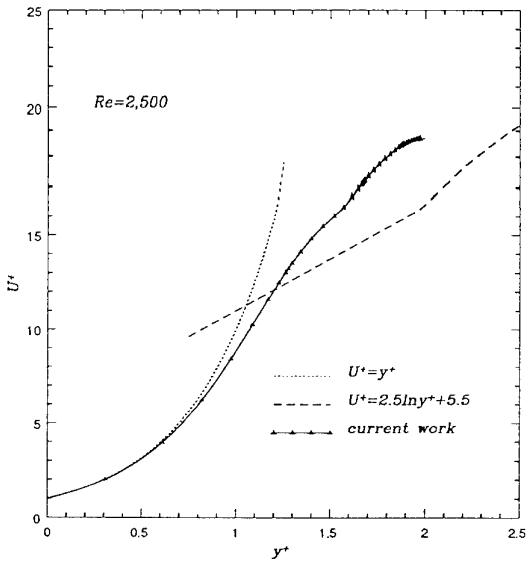

Figure 3: Mean velocity profile $U^+ = \bar{u}/u^*$ versus log-law for $Re = 2,500$

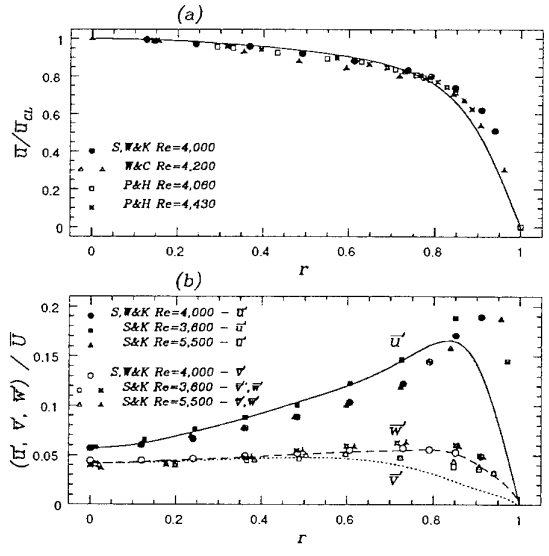

Figure 4: Mean (a) and rms (b) velocity distribution across the pipe for $Re = 4,000$

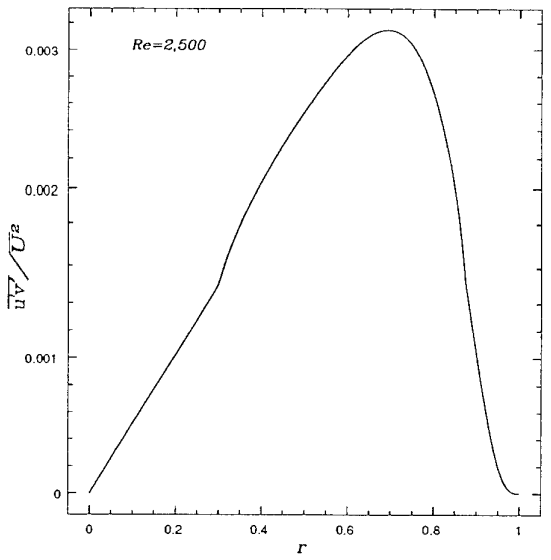

Figure 5: Reynolds stress distribution across the pipe for $Re = 2,500$

mains controversial (Kim, Moin and Moser, 1987 [31]). Their simulation results for turbulent channel flow indicate that the limiting wall behavior of the Reynolds stress takes the form: $\overline{u'v'} \sim y^3$. Our simulation results seem to agree with this y^3 behavior.

Vorticities

The distribution of the mean azimuthal vorticity for $Re = 2500$ and the root mean square values of all three vorticity components are plotted in Figure (6). Near the wall, the rms streamwise vorticity clearly shows a local minimum (at $y^+ \approx 4.2$) before reaching a maximum at the wall. In addition, visualization at $Re = 2500$ shows strong streamwise vortices appearing close to the wall in our pipe simulations as shown in Figure (7). These facts support the conjecture that streamwise vortices form near the wall, similar to the findings of Kim & Moin [31] in their channel simulations.

In Figure (8) we plot a cross-sectional view of streamwise vorticity on an axial-radial plane, for $Re = 2500$ and $Re = 4000$. Elongated vorticity streaks close to the wall, in the mean flow di-

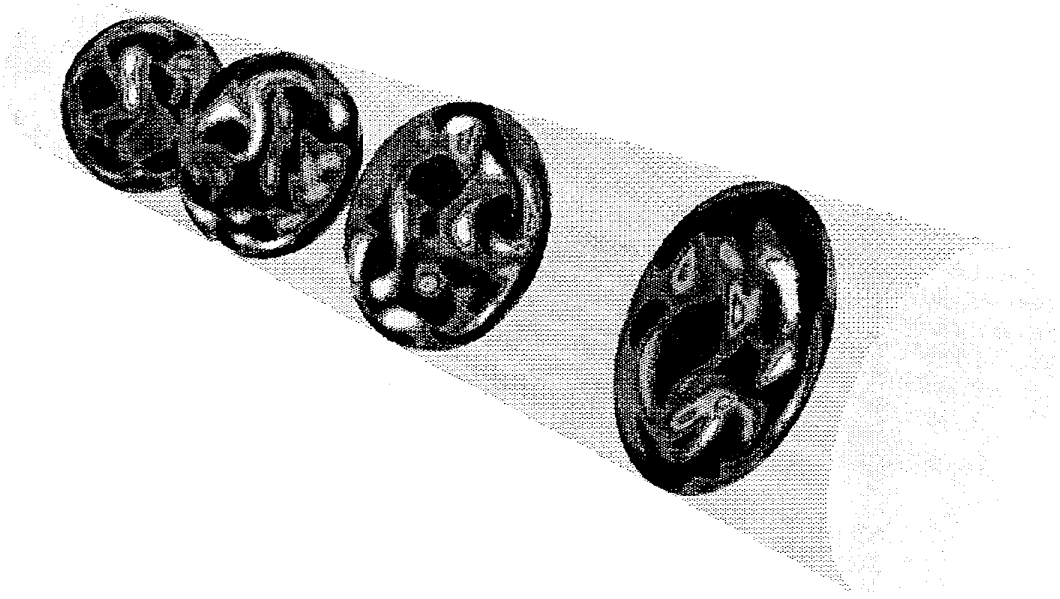

Figure 7: Streamwise vorticity across the pipe for $Re = 2,500$

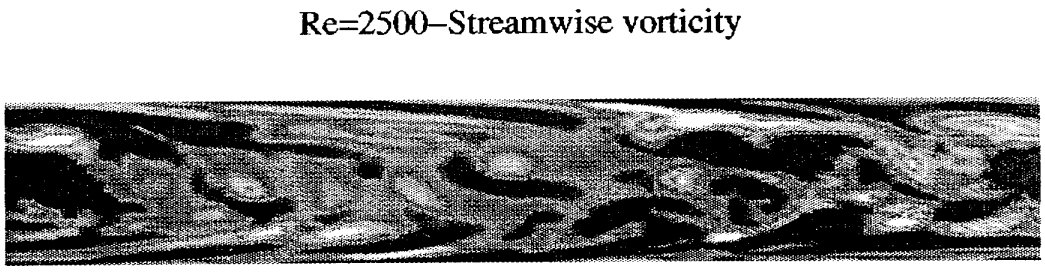

Figure 8: Streamwise vorticity along the pipe for a) $Re = 2,500$ and b) $Re = 4,000$

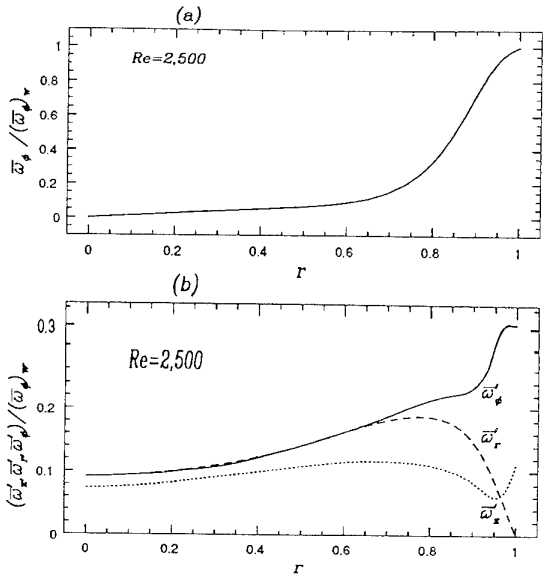

Figure 6: Mean (a) and rms (b) vorticity distribution across the pipe for $Re = 2,500$

rection, are clearly observed. These figures suggest the following dynamics: the wall shear generates rings of azimuthal vorticity close to the pipe surface. These azimuthal vorticity rings are extremely unstable because they are subject to strong stretching and tilting by the mean flow and shear. Once these azimuthal rings break up, they form elongated streamwise vorticity structures and are swept downstream by the mean flow.

This work was supported by ARPA and ONR under Contracts: N00014-92-J-1796 and N00014-92-C-0216.

References

[1] Reynolds O. An experimental investigation of the circumstances which determine whether the motion of water shall be direct or sinuous, and of the law of resistance in parallel channels. *Phil. Trans. Roy. Soc. Lond.*, 174:935, 1883.

[2] Nikuradse J. Laws of turbulent flow in smooth pipes. Technical Report TT F-10, 359, NASA, 1966.

[3] Laufer C.J. The structure of turbulence in fully developed pipe flow. Technical Report NACA Reports 1158-1209, NACA, 1954.

[4] H.W. Towens, J.L. Gow, R.E. Powe, and N. Weber. Turbulent flow in smooth and rough pipes. *Trans. ASME J. of Basic Engr.*, 6:353-362, 1972.

[5] C.J. Lawn. The determination of the rate of dissipation in turbulent pipe flow. *J. Fluid Mech.*, 48:477–505, 1971.

[6] A.E. Perry and C.J. Abell. Scaling laws for pipe-flow turbulence. *J. Fluid Mech.*, 67:257–271, 1975.

[7] I.J. Wygnanski and F.H. Champagne. On transition in a pipe part 1. the origin of puffs and slugs and the flow in a turbulent slug. *J. Fluid Mech.*, 59:281–335, 1973.

[8] I.J. Wygnanski, M. Sokolov, and D. Friedman. On transition in a pipe part 2. the equilibrium puff. *J. Fluid Mech.*, 69:283–304, 1975.

[9] H. Salwen and C.E. Grosch. Linear stability of Poiseuille flow. *J. Fluid Mech.*, 54:93–112, 1972.

[10] A. Davey and H.P.F. Nguyen. Finite-amplitude stability of pipe flow. *J. Fluid Mech.*, 45:701–720, 1971.

[11] N. Itoh. Non-linear stability of parallel flows with subcritical reynolds number. part 2. stability of pipe Poiseuille flow to finite axisymmetric disturbances. *J. Fluid Mech.*, 82:469–479, 1977.

[12] A. Davey. On Itoh's finite amplitude stability theory for pipe flow. *J. Fluid Mech.*, 86:695–703, 1978.

[13] A.T. Patera and S.A. Orszag. Finite-amplitude stability of axisymmetric pipe flow. *J. Fluid Mech.*, 112:467–474, 1981.

[14] Orszag S.A. and Patera A.T. Secondary instability of wall-bounded shear flows. *J. Fluid Mech.*, 128:347, 1983.

[15] D. Henningson. An eigenfunction expansion of localized disturbances. In *Advances in Turbulence, 3, Springer-Verlag A.V.Johansson and P.H. Alfredsson eds.*, pages 162–170, 1991.

[16] P. O'Sullivan, K.S. Breuer, and L Sirovich. The stability of finite amplitude three-dimansional disturbances in axisymmetric pipe flow. In *Bulletin of APS, Vol 36, No.10*, page 2695, 1991.

[17] N.V. Nikitin. Direct three-dimensional numerical simulation of turbulence and transition in a pipe-Poiseuille flow. In *Bulletin of APS, Vol 38, No.12*, page 2311, 1993.

[18] F. Unger, J.G.M. Eggels, R. Freidrich, and F.T.M. Nieuwstadt. On second and higher order statistics in fully-developed turbulent pipe-flow. In *Proc. 9th Symp. on Turbulent Shear Flows, Aug 16-18, Kyoto, Japan*, pages 2/1/1–2/1/6, 1993.

[19] J. Westerweel, R.J. Adrian, J.G.M. Eggels, and F.T.M. Nieuwstadt. Measurements with particle image velocimetry of fully turbulent pipe flow at low reynolds number. In *Proc. 6th Int. Symp. on Applications of Laser Techniques to Fluid Mechanics, July 20-23, Lisbon, Portugal*, 1992.

[20] F. Durst, J. Jovanovič, and J. Sender. Detailed measurements of the near wall region of turbulent pipe flows. In *Proc. 9th Symp. on Turbulent Shear Flows, Aug 16-18, Kyoto, Japan*, pages 2/2/1–2/2/6, 1993.

[21] M.V. Zagarola, A.J. Smits, G.L. Brown, V. Yakhot, and S.A. Orszag. Superpipe: a progress report. In *Bulletin of APS, Vol 38, No.12*, page 2317, 1993.

[22] Orszag S.A. Fourier series on spheres. *Monthly weather review*, 102:56, 1974.

[23] G.K. Batchelor and A.E. Gill. Analysis of the stability of axisymmetric jets. *J. Fluid Mech.*, 14:529–551, 1962.

[24] Karniadakis G.E., Israeli M., and Orszag S.A. High-order splitting methods for the incompressible Navier-Stokes equations. *J. Comput. Phys.*, 97:414, 1991.

[25] Patera A.T. A spectral element method for fluid dynamics; Laminar flow in a channel expansion. *J. Comput. Phys.*, 54:468, 1984.

[26] Maday Y. and Patera A.T. Spectral element methods for the Navier-Stokes equations. *ASME, State-of-the-art surveys in Computational Mechanics*, 1987.

[27] Tomboulides A.G. *Direct and Large-Eddy simulation of wake flows: Flow past a sphere.* PhD thesis, Princeton University, 1993.

[28] V.C. Patel and M.R. Head. Some observations on skin friction and velocity profiles in fully developed pipe and channel flows. *J. Fluid Mech.*, 38:181–201, 1969.

[29] L. Shemer and E. Kit. An experimental investigation of the quasisteady turbulent pulsating flow in a pipe. *Phys. Fluids*, 27,1:72–76, 1984.

[30] L. Shemer, I. Wygnanski, and E. Kit. Pulsating flow in a pipe. *J. Fluid Mech.*, 153:313–337, 1985.

[31] Kim J., Moin P., and Moser R. Turbulence statistics in fully developed channel flow at low Reynolds number. *J. Fluid Mech.*, 177:133–166, 1987.

Simulations of bypass transition for spatially evolving disturbances

A. Lundbladh[1], P.J. Schmid[2], S. Berlin[3] and D.S. Henningson[1,3]

[1]FFA, Box 11021, S-16111 Bromma, Sweden.
[2]Dept. Appl. Mathematics, University of Washington, Seattle WA 98195, USA.
[3]Department of Mechanics, KTH, S-10044 Stockholm, Sweden.

Abstract

The spatial evolution of disturbances in plane Poiseuille flow and zero pressure gradient boundary layer flow is considered. For disturbances governed by the linearized equations, potential for significant transient growth of the amplitude is demonstrated. The maximum amplification occurs for disturbances with zero or near zero frequencies. Spatial numerical simulations of the transition scenario involving a pair of oblique waves has been conducted for both flows. A fully spectral solver using a simple but efficient fringe region technique allowed the flows to be computed with high resolution into the fully turbulent domain. A modal decomposition of the simulation results indicates that non-linear excitation of the transient growth is responsible for the rapid emergence of low-frequency structures. Physically, this corresponds to streaky flow structures, as seen from the results of a numerical amplitude expansion. Thus, this spatial transition scenario has been found to be similar to the corresponding temporal one (Schmid & Henningson [1]). In the boundary layer simulations the streaks are seen to break down from what appears to be a secondary instability.

1 INTRODUCTION

We will present an investigation of *bypass* transition, i.e. transition emanating from linear growth mechanisms other than exponential instabilities. This definition is in line with the original idea of Morkovin [2], but is formulated in view of the results on non-modal transient growth by Butler & Farrell [3], Reddy & Henningson [4] and Trefethen, Trefethen, Reddy & Driscoll [5]. They found that significant growth of the disturbance energy was possible for certain two and three-dimensional disturbances in shear flows at subcritical Reynolds numbers, where the largest growth was obtained for the three-dimensional perturbations. Physically, the growth is due to the Orr and *lift-up* mechanisms (Orr [6] art. 8, Landahl [7]). Mathematically it can be explained by the fact that the linearized Navier-Stokes operator has non-orthogonal eigenfunctions, a necessary condition for subcritical transition to occur (Henningson & Reddy [8]).

In the investigation of Henningson, Lundbladh & Johansson [9] the lift-up mechanism was found to play an important role in the growth of both infinitesimal and finite amplitude localized disturbances. Similar results were obtained in a study of oblique breakdown by Schmid & Henningson [1]. In the latter study temporal simulations starting from a pair of oblique finite amplitude waves was performed. It was found that non-linearity rapidly excited components with zero streamwise wavenumber, i.e. streamwise vortices. By the lift-up effect the vortices generated large amplitude low and high-speed streaks in the streamwise velocity components. The breakdown to turbulence, which has recently been found to result from a secondary instability of the streaks (Kreiss, Lundbladh & Henningson [10]), occurs more rapidly than traditional transition initiated by the growth of two-dimensional waves.

The early phases of oblique transition have been simulated in the boundary layer on a flat plate (Fasel & Thumm [11], Chang & Malik [12] Joslin, Streett & Chang [13]). In the latter investigations the "streamwise vortex mode" also played an important role and the initial amplitude necessary to trigger transition was found to be lower than for comparable secondary instability scenarios. The oblique transition scenario was also observed in a study of a compressible confined shear layer by Gathmann, Si-Ameur & Mathey [14]. In their study the oblique waves appeared naturally from noise introduced at the inflow boundary.

In the present paper we report on the analysis and simulation of spatially evolving disturbances. First, the solution algorithm used in the spatial DNS is described. Second, the linearized equations are investigated for their potential of transient growth. Then,

Paper presented at the 74th Fluid Dynamics Symposium on "Application of Direct and Large Eddy Simulation to Transition and Turbulence" held at Chania, Crete, Greece, in April 1994.

numerical simulations are performed to probe the importance of the linear growth mechanism. For the channel flow the effect of this mechanism is assessed by a temporal-spanwise Fourier decomposition as well as a numerical amplitude expansion. For the boundary layer flow we demonstrate the similarity by a Fourier decomposition of the simulated flow.

2 SIMULATION ALGORITHM

We will use a numerical simulation program solving the full three-dimensional incompressible Navier-Stokes equations developed by Lundbladh, Henningson & Johansson [15]. The algorithm is similar to that of Kim, Moin & Moser [16], i.e. Fourier series expansion in the horizontal directions, Chebyshev series in the normal direction and pseudo-spectral treatment of the non-linear terms. The Chebyshev expansions have the novel feature that the second derivative of the variables are expanded instead of the variables themselves. This results in a better conditioned problem (see Greengard [17]), thus giving better numerical accuracy. The code has been thoroughly checked and has been used on a variety of supercomputers.

2.1 The fringe method

The simulation program has recently been modified to handle spatial development of disturbances in channel and boundary layer flows. Forcing terms were added to the Navier-Stokes equations in part of the computational domain to damp disturbances. The forcing was applied in the following manner.

$$\begin{aligned} \frac{\partial \mathbf{u}}{\partial t} &= NS(\mathbf{u}) + \lambda(x)(\mathbf{v}-\mathbf{u}) + \mathbf{g} \\ \nabla \cdot \mathbf{u} &= 0 \end{aligned}$$

where $\mathbf{u}$ is the solution fluid vector, x is the streamwise coordinate, y is the wall normal coordinate and z is the spanwise coordinate. $NS(\mathbf{u})$ is the RHS of the (unforced) momentum equations. $\mathbf{g}$ is a disturbance forcing. $\mathbf{v}$ is the prescribed inflow velocity vector which in general will fulfill the continuity equation. $\mathbf{v}$ may or may not fulfill the Navier-Stokes equations. Both $\mathbf{g}$ and $\mathbf{v}$ may depend on the three spatial coordinates and time. Here and in the following all quantities are non-dimensionalized by the channel half-height h and the undisturbed centerline velocity U_{cl} for the channel, the displacement thickness at the inflow δ_0^* and the free-stream velocity U_∞ for the boundary layer. From this the Reynolds number for the channel flow is defined as $R = U_{cl}h/\nu$ and for the boundary layer as $R = U_\infty \delta_0^*/\nu$, where ν is the kinematic viscosity.

$\lambda(x)$ is non-zero only in a small region at the end of the computed domain, termed the fringe region, hence λ will be denoted the fringe function. λ is a positive function whose magnitude determines the rate at which $\mathbf{u}$ approaches $\mathbf{v}$ in the fringe region.

Using this approach, inflow conditions can be prescribed and disturbances can flow freely out of the computational domain while the Fourier series representation in the streamwise direction is retained from the temporal simulation algorithm. This technique is similar to that described by Bertolotti, Herbert & Spalart [18].

A convenient form of the fringe function is as follows

$$\lambda(x) = \lambda_{max}[S(\frac{x - x_{start}}{\Delta_{rise}}) - S(\frac{x - x_{end}}{\Delta_{fall}} + 1)]$$

Here λ_{max} is the maximum strength of the damping, x_{start} to x_{end} the spatial extent of the region where the damping function is nonzero and Δ_{rise} and Δ_{fall} the rise and fall distance of the damping function. $S(x)$ is a smooth step function rising from zero for negative x to one for $x \geq 1$. We have used the following form for S, which has the advantage of having continuous derivatives of all orders.

$$S(x) = \begin{cases} 0 & x \leq 0 \\ 1/[1 + \exp(\frac{1}{x-1} + \frac{1}{x})] & 0 < x < 1 \\ 1 & x \geq 1 \end{cases}$$

The choice of the fringe parameters is governed by several factors. In general it would be desirable to minimize the length of the fringe region to improve the computational efficiency. An analysis of a simple wave equation yields that outflowing disturbances are damped by a factor

$$\begin{aligned} f_d &= \exp[\frac{1}{c}\int_{-\infty}^{\infty} \lambda(x)dx] \\ &= \exp[\frac{\lambda_{max}}{c}(x_{end} - x_{start} - \frac{\Delta_{rise} + \Delta_{fall}}{2})] \end{aligned}$$

where c is the convection velocity of the disturbance. The fringe parameters are chosen so that $f_d > 10^6$

with c taken as the maximum velocity of the laminar flow, to ensure that only a negligible amount of disturbances can pass through the fringe region. The simulation code uses a semi-implicit time stepping algorithm and the fringe forcing is applied in the explicit part. Thus λ_{max} is restricted due to stability considerations. Together with the requirement of damping this gives a lower limit for the length of the fringe region.

The damping and generation of the disturbances must not introduce small scales in the streamwise direction which would increase the resolution requirement beyond what is needed in the physical domain. In addition the fringe function should not rise to abruptly to avoid undesirable upstream influence.

The function $\mathbf{v}$ is used to prescribe the inflow conditions. For the channel flow it is simply the laminar parallel flow plus the desired disturbances. For the boundary layer flow it can be chosen as a parallel flow with the velocity profile taken from a boundary layer solution at the inflow. However, since the fringe forcing goes smoothly to zero over a distance Δ_{fall} the inflow velocity would not be exactly the desired. In addition, the decrease in boundary layer thickness from the outflow to the inflow value may start a few displacement thicknesses upstream of the fringe region. To remedy this problem and thereby reduce the region affected by the upstream influence the streamwise component v_1 is for the boundary layer case chosen as follows.

$$v_1(x,y) = U(x,y) + [U(x + x_{period}, y) - U(x,y)]\, S\left(\frac{x - x_{mix}}{\Delta_{mix}}\right)$$

$U(x,y)$ is typically a solution to the boundary layer equations, for zero pressure gradient it is the Blasius solution. x_{period} is the streamwise length of the simulation box. Here x_{mix} and Δ_{mix} are chosen so that the prescribed flow smoothly changes from the outflow velocity to the inflow velocity within the fringe region. S is as given above. The wall normal component v_2 is then calculated from the equation of continuity, and the spanwise velocity v_3 is set to zero for simulations where the mean flow is two dimensional. This choice of $\mathbf{v}$ ensures that the decrease in boundary layer thickness is completely confined to the fringe region, thus minimizing the upstream influence.

The solver for the spatial problem is apart from the introduced fringe forcing identical to the one used to simulate temporal problems. The efficiency is also the same with the only losses arising from the need to extend the computational domain by 10-30% to accommodate the non-physical fringe region, and the 5-10% extra time needed to apply the forcing in the fringe region.

2.2 Free stream boundary conditions

Since the simulation algorithm discretizes a finite domain in the wall normal direction, for the boundary layer simulations an artificial boundary condition must be applied at the top (free stream) boundary. Initial simulations were performed with Neumann boundary conditions on the velocities. However, it was found that more exact results could be achieved with the top boundary at a lower position if boundary conditions derived from the solution of the inviscid linearized equations were used. Thus the number of grid points in the wall normal direction could be reduced. These boundary conditions take the following form.

$$\frac{\partial \hat{\mathbf{u}}}{\partial y} + |k|\hat{\mathbf{u}} = \frac{\partial \hat{\mathbf{v}}}{\partial y} + |k|\hat{\mathbf{v}}$$

Here k is the absolute value of the horizontal wavenumber vector, $\hat{\mathbf{u}}$ and $\hat{\mathbf{v}}$ are the Fourier transforms of $\mathbf{u}$ and $\mathbf{v}$ defined above. These boundary conditions are a generalization of those used by Malik, Zang & Hussaini [19]. Since they are applied in Fourier space with different coefficients for each wavenumber, they are nonlocal in physical space.

Typically simulations with Neuman boundary condition require the upper boundary to be at 15-20 δ_0^*, whereas the improved boundary condition can be applied at 8-10 δ_0^*. The simulation of the oblique breakdown for the boundary layer used Neumann boundary conditions applied at 15 δ_0^*.

2.3 Code verification

The simulation algorithm has previously been verified on a number of temporal simulations, both by comparing to eigenfunction solutions and results generated by other simulation codes. A demonstration of the generation of inflow disturbances by the fringe method is given in figure 1. Here a pair of neutral oblique waves with a peak amplitude of 1×10^{-5} each,

are generated in a plane Poiseuille flow. Forcing is applied in the region $x = -9$ to $x = 0$ after which the waves have attained an amplitude of the prescribed value.

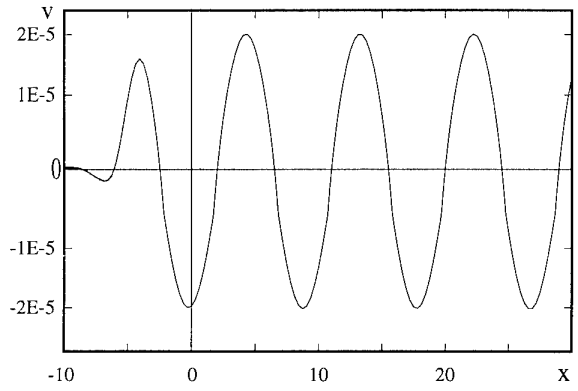

Figure 1. Forcing of two oblique neutral waves at $R = 8292$. Wall normal velocity at the channel centerline. The streamwise and spanwise wavenumbers are 0.7. The fringe region extends from $x = -9$ to $x = 0$ after which the forcing is zero. Note that the actual computational domain in this case extends beyond 30.

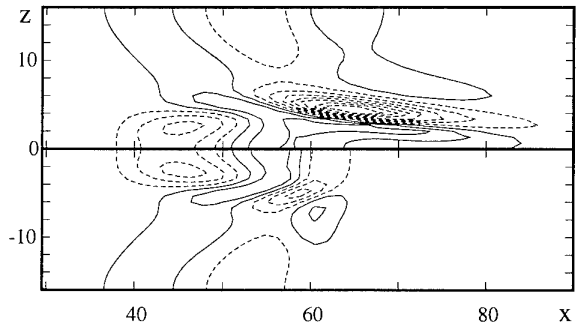

Figure 2. Damping of outflowing disturbance by the fringe region. R=950. Contours of wall normal velocity at $t = 117$. Top half : The fringe region starts at $x_{start} = 120$, bottom half : $x_{start} = 52.5$. Contours start at $v = -0.0065$ with spacing $v = 0.001$, negative contours dashed.

The results are shown for a spanwise position where the two waves are in phase, and hence the amplitudes add up. The forced waves are the full eigenmodes of the linearized equations, with nonzero velocity and normal vorticity. The use of a neutral eigenmode is practical for this test since the wave amplitude is constant downstream of the fringe function. In this case the prescribed velocity is:

$$\mathbf{v} = \begin{pmatrix} 1-y^2 \\ 0 \\ 0 \end{pmatrix} + ARe\{\mathbf{v}^{OS}(y)[e^{i(\alpha x+\beta z-\omega t)} + e^{i(\alpha x-\beta z-\omega t)}]\}$$

The first term is the undisturbed laminar Poiseuille flow. $\mathbf{v}^{OS}$ is an eigenvector of the linearized flow equations with frequency ω, streamwise wavenumber α and spanwise wavenumber β. Here and in the following A is the maximum value of the rms amplitude for the streamwise velocity of each wave.

The efficiency of the outflow damping is demonstrated in figure 2. Here we show a localized disturbance in a Blasius boundary layer flow computed for two different positions of the fringe region. The disturbance is seen to be damped out quickly with negligible change upstream of the start of the fringe region. The spanwise symmetric disturbance is generated at the origin at $t = 0$. Its exact form is given in Henningson, Lundbladh & Johansson [9].

2.4 Accuracy and computational resources

The computations of the full transition process requires large grids which places considerable requirements on the computational resources. Most of the calculations were performed on a CRAY-2 4/128. The performance on this machine was about 120 Mflops on a single processor or 450 Mflops parallelized on four processors, corresponding to about 7 and 1.8 micro seconds per grid point and temporal iteration. Part of the simulations were performed on a CRAY YMP and a CRAY C-90 which gave a performance 3/2 and 3 times that of the CRAY-2. The total simulation time was roughly 250 hours.

The simulation of breakdown in the channel flow used $600 \times 97 \times 128$ spectral modes in the streamwise, normal and spanwise directions, respectively. This was chosen to be approximately equal to corresponding temporal simulations where a grid refinement procedure showed convergence. Two calculations were performed of oblique breakdown in the boundary layer case. The first used $480 \times 97 \times 80$ spectral modes, and the second used $720 \times 121 \times 120$ spectral modes. As a test of convergence, four maxima of the wall normal shear of the streamwise velocity were compared between the two simulations ($x - x_0 \approx 200,250,300,350$, $y \approx 5$ in figure 9b). The differences in the shear at these points are less than 1%, although the position

of the last maximum is slightly different. For the channel flow the resolution gives a grid step of 6 wall units in the streamwise direction, 4 for the spanwise and 4 for the largest step in the wall normal direction, based on the wall friction in the turbulent region. Corresponding numbers for the boundary layer simulation with the higher resolution is 14, 6 and 4. Note that for all simulations the collocation points in the horizontal directions are actually placed at 2/3 of this spacing due to the dealiasing procedure. The spanwise symmetry was utilized in the simulations to reduce the number of computed modes to half of that given above.

3 SPATIAL INITIAL VALUE PROBLEM

Before we turn to the spatial DNS we consider the spatial evolution of infinitesimal perturbations in a parallel shear flow $U(y)$. The results will help us choose initial conditions as well as to interpret the simulation results.

A formulation of the linearized Navier-Stokes equations is chosen in terms of the spanwise and temporally Fourier transformed normal velocity $\hat{v}$ and and normal vorticity $\hat{\eta}$, i.e. $v = \hat{v}\exp(i\beta z - i\omega t)$ and $\eta = \hat{\eta}\exp(i\beta z - i\omega t)$. In this form the governing equations are

$$
\begin{aligned}
(i\omega - U\frac{\partial}{\partial x})(\mathcal{D}^2 - \beta^2 + \frac{\partial^2}{\partial x^2})\hat{v} + U''\frac{\partial}{\partial x}\hat{v} + \\
\frac{1}{R}(\mathcal{D}^2 - \beta^2 + \frac{\partial^2}{\partial x^2})^2\hat{v} = 0, \\
(i\omega - U\frac{\partial}{\partial x})\hat{\eta} - i\beta U'\hat{v} + \frac{1}{R}(\mathcal{D}^2 - \beta^2 + \frac{\partial^2}{\partial x^2})\hat{\eta} = 0
\end{aligned}
$$

where $\mathcal{D}$ and $'$ stands for the differential operator in the wall normal y-direction, ω denotes the frequency and β is the spanwise wavenumber. Together with the continuity equation and the definition of the normal vorticity $\hat{\eta}$, the above equations completely describe the evolution of three-dimensional infinitesimal disturbances. The streamwise and spanwise velocity components can be recovered as follows,

$$
\begin{aligned}
\frac{\partial^2\hat{u}}{\partial x} - \beta^2\hat{u} &= i\beta\hat{\eta} - \mathcal{D}\frac{\partial\hat{v}}{\partial x}, \\
\frac{\partial^2\hat{w}}{\partial x} - \beta^2\hat{w} &= -i\beta\mathcal{D}\hat{v} - \frac{\partial\hat{\eta}}{\partial x}.
\end{aligned}
$$

The substitution $\hat{v} = \tilde{v}\exp(i\alpha x)$ with $\alpha \in C$ transforms the above equations into an eigenvalue problem where the eigenvalue α appears up to the fourth power. A closer look at the viscous terms reveals that the eigenvalue appears equidimensional with respect to the differential operator $\mathcal{D}$. This suggests a transformation of the independent variable y of the form (Haj-Hariri [20])

$$
\begin{pmatrix} \tilde{v} \\ \tilde{\eta} \end{pmatrix} = \begin{pmatrix} \tilde{V} \\ \tilde{E} \end{pmatrix}\exp(-\alpha y)
$$

which will reduce the order of the nonlinear eigenvalue problem by two. The reduced equations read

$$
\begin{aligned}
(i\omega - i\alpha U)(\mathcal{D}^2 - 2\alpha\mathcal{D} - \beta^2)\hat{V} + i\alpha U''\hat{V} + \\
\frac{1}{R}(\mathcal{D}^2 - 2\alpha\mathcal{D} - \beta^2)^2\hat{V} = 0, \\
(i\omega - i\alpha U)\hat{E} - i\beta U'\hat{V} + \frac{1}{R}(\mathcal{D}^2 - 2\alpha\mathcal{D} - \beta^2)\hat{E} = 0.
\end{aligned}
$$

Casting the above equations into a *linear* eigenvalue problem using the companion matrix technique leads to

$$
\begin{pmatrix} -\mathbf{R}_1 & -\mathbf{R}_0 & 0 \\ \mathbf{I} & 0 & 0 \\ 0 & -\mathbf{S} & -\mathbf{T}_0 \end{pmatrix}\begin{pmatrix} \alpha\hat{V} \\ \hat{V} \\ \hat{E} \end{pmatrix} = \alpha\begin{pmatrix} \mathbf{R}_2 & 0 & 0 \\ 0 & \mathbf{I} & 0 \\ 0 & 0 & \mathbf{T}_1 \end{pmatrix}\begin{pmatrix} \alpha\hat{V} \\ \hat{V} \\ \hat{E} \end{pmatrix}
$$

with

$$
\begin{aligned}
\mathbf{R}_2 &= \frac{4}{R}\mathcal{D}^2 + 2iU\mathcal{D}, \\
\mathbf{R}_1 &= -2i\omega\mathcal{D} - \frac{4}{R}\mathcal{D}^3 + \frac{4}{R}\beta^2\mathcal{D} \\
&\quad -iU\mathcal{D}^2 + iU\beta^2\mathbf{I} + iU''\mathbf{I}, \\
\mathbf{R}_0 &= i\omega\mathcal{D}^2 - i\omega\beta^2\mathbf{I} + \frac{1}{R}\mathcal{D}^4 - \frac{2}{R}\beta^2\mathcal{D}^2 + \frac{1}{R}\beta^4\mathbf{I}, \\
\mathbf{T}_1 &= \frac{2}{R}\mathcal{D} + iU\mathbf{I}, \\
\mathbf{T}_0 &= -i\omega\mathbf{I} - \frac{1}{R}\mathcal{D}^2 + \frac{1}{R}\beta^2\mathbf{I}, \\
\mathbf{S} &= i\beta U'\mathbf{I}.
\end{aligned}
$$

A spectral collocation technique using Chebyshev polynomials was used to discretize the eigenvalue problem in the wall normal direction. Figures 3a and 3b show the spectrum of the spatial evolution operator for plane Poiseuille flow and two parameter combinations. The spectrum of the spatial evolution operator determines the growth or decay of infinitesimal disturbances far downstream ($x \rightarrow \infty$). Transient amplification can, however, occur before the asymptotic behavior is observed. To investigate this transient growth we reformulate the spatial problem as an initial-value-problem using an expansion in the eigenfunctions of the linearized operator. The spatial initial value problem may be written

$$\frac{d\kappa}{dx} = i\Lambda\kappa$$

where $\Lambda = \mathrm{diag}(\alpha_1, \ldots, \alpha_N)$ is a diagonal matrix consisting of the spatial eigenvalues and $\kappa(x)$ are the coefficients in the eigenfunction expansion

$$\begin{pmatrix} \hat{v} \\ \hat{\eta} \end{pmatrix} = \sum_{j=1}^{N} \kappa_j(x) \begin{pmatrix} \tilde{v} \\ \tilde{\eta} \end{pmatrix}_j$$

with $(\tilde{v}\ \tilde{\eta})_j^T$ as the j-th vector eigenfunction of the discretized spatial evolution operator. In order for the solution to be well posed only spatial eigenmodes propagating in the downstream direction can be included in the above expansion.

The local energy density defined in terms of the vector eigenfunction expansion can be written

$$\mathcal{E}(\kappa) = \kappa^H A \kappa = \kappa^H F^H F \kappa = \|F\kappa\|_2^2$$

where

$$A_{ij} = \frac{1}{2}\int_{-1}^{1} (\tilde{u}_i^* \tilde{u}_j + \tilde{v}_i^* \tilde{v}_j + \tilde{w}_i^* \tilde{w}_j)\, dy$$

Here the kinetic energy is used as a measure of the disturbance. Since we are not interested in the transfer of energy this choice will suffice. For a discussion of appropriate disturbance measures for spatial evolution problems, see Henningson & Schmid [21].

The maximum possible amplification G of energy density is then given as

$$G(x) = \sup_{\kappa_0} \frac{\mathcal{E}(\kappa)}{\mathcal{E}(\kappa_0)} = \|F \exp(i\Lambda x) F^{-1}\|_2^2$$

The above analysis follows the temporal analog and for further details the reader is referred to Reddy & Henningson [4].

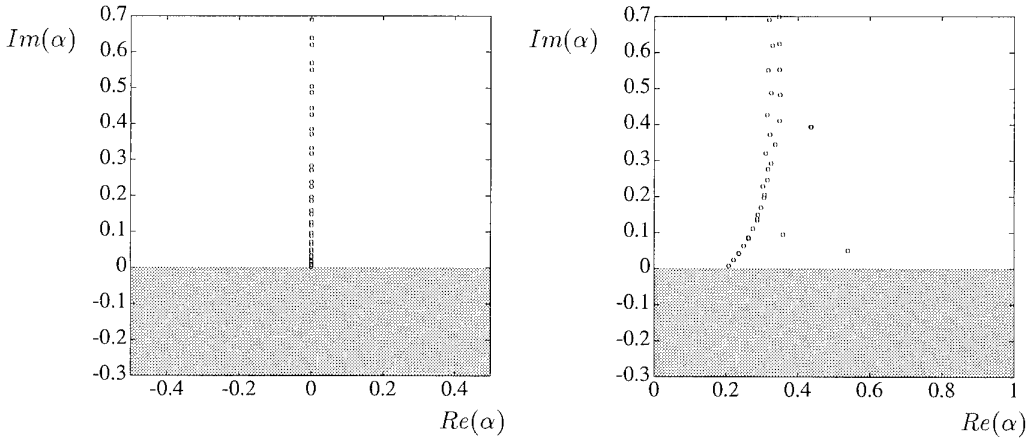

Figure 3. Spectrum of the spatial evolution operator for plane Poiseuille flow at $R = 2000$. (a) $\alpha = 1, \omega = 0$, (b) $\alpha = 1, \omega = 0.2$. The shaded half-plane corresponds to modes growing downstream.

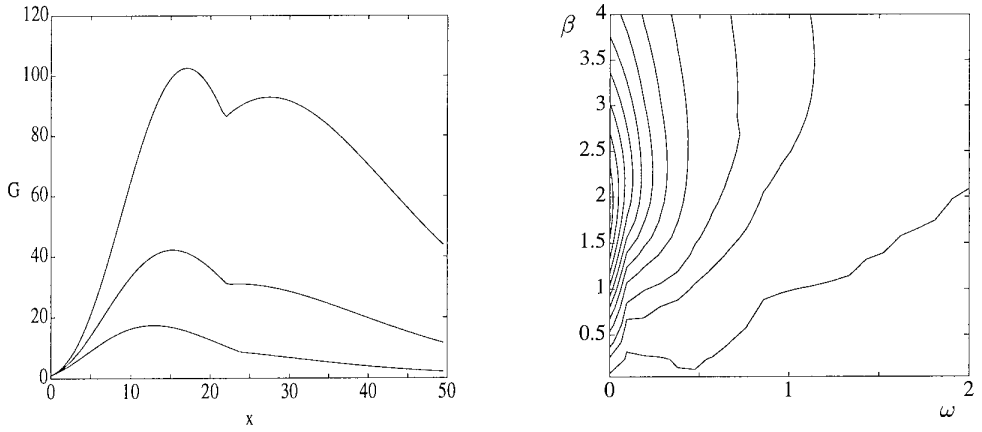

Figure 4. Transient amplification. (a) maximum amplification of energy density versus streamwise location for $R = 500, 1000, 2000$ and $\beta = 2, \omega = 0$. (b) $G_{\max}$ as a function of frequency ω and spanwise wavenumber β for $R = 2000$.. The contour levels are $5, 10, 20, ..., 100$. The irregularities in the contours are due to the limited number of wavenumbers investigated.

Figure 4a displays a plot of the maximum amplification $G(x)$ versus the streamwise location x for three different Reynolds numbers. Significant transient growth is observed before the onset of asymptotic decay of the disturbance. The curves in figure 4a are composed of two separate growth curves for symmetric and antisymmetric $\hat{v}$-disturbances and the cusps in Figure 4a stem from a switching of the optimally amplified perturbation from a symmetric to an antisymmetric $\hat{v}$-disturbance. The peak $G_{\max}$ of the amplification curves, i.e. $G_{\max} = \sup_{x \geq 0} G(x)$, has been plotted as a function of the frequency ω and the spanwise wavenumber β in Figure 4b. The Reynolds number is $R = 2000$, and $G_{\max}$ has been found to be determined by symmetric $\hat{v}$-perturbations. As can be seen in Figure 4b, the largest amplification is achieved by steady disturbances, i.e. disturbances with frequency $\omega = 0$. The maximum occurs for $\beta \approx 2$.

4 SIMULATION RESULTS

Spatial simulations of transition require a large computational domain to contain the entire growth and breakdown region. Thus, simulations of transition from initially two-dimensional waves, for which the growth rate is rather small, have not been able to follow the flow through the complete breakdown process. In contrast, the present computations are able to capture the complete transition process due partly to the rapidity of the bypass scenario, partly to the high efficiency of the spectral/fringe region technique.

4.1 Channel flow

We will now investigate the spatial analog of the oblique transition scenario presented by Schmid & Henningson [1]. For the first simulations a low amplitude is chosen which does not lead to transition but for which considerable non-linear effects appears. Figure 5 depicts the streamwise development of energy density in selected (ω, β)-modes where the integer pairs (m, n) denote the multiples of the fundamental frequency and spanwise wavenumber, respectively. The energy densities have been calculated by Fourier transforming time signals in the time and spanwise directions. The Reynolds number is 2000, and the inflow condition consists of $(1, \pm 1)$-modes with an amplitude of the maximum vertical velocity $A_v = 0.005$ in each wave. Higher modes are excited further downstream and a marked preference of modes with lower frequencies is observed, particularly the $(0, 2)$ mode. This suggests that the linear transient mechanism described earlier is responsible for the occurrence of low frequency disturbances. Additional evidence for this interpretation is the close correspondence between the spatial transition and the temporal case of Schmid & Henningson [1]. In the latter it was explicitly shown that the linear transient mechanism was responsible for the large growth of the $(0, 2)$ mode.

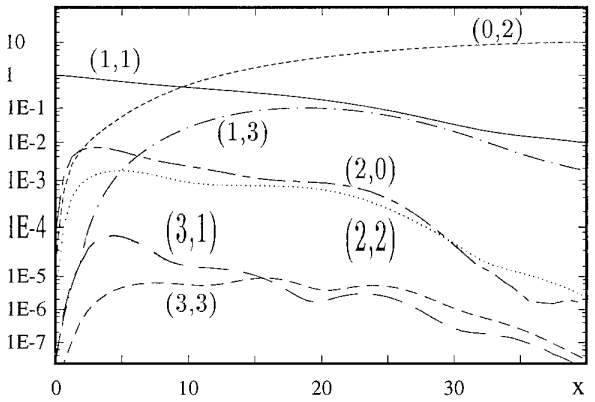

Figure 5. Spatial evolution of energy in (ω, β)-modes. Since the inflow has a spanwise symmetry which is upheld downstream by the flow equations the energies in $(\omega, \pm\beta)$ are equal. For $\beta \neq 0$ only the energy in the component with positive β is therefore displayed in the graph. The curves are normalized such that the energy of the (1,1) mode at inflow is set to unity.

Another tool to analyze the spatial evolution of disturbances is a numerical amplitude expansion. The disturbance velocity field is decomposed into a sum of flow fields weighted by powers of the initial amplitude.

$$\mathbf{u}'(A_v) = \sum_{j=1}^{N} \mathbf{u}_j A_v^j + \mathcal{O}(A_v^{N+1})$$

To solve for the N unknown flow fields $\mathbf{u}_j$ it is necessary to perform N simulations of the spatial transition process. The number of flow fields has been chosen as $N = 3$. This results in the following system of equations for the flow fields $\mathbf{u}_j$.

$$\begin{pmatrix} A_{v1} & A_{v1}^2 & A_{v1}^3 \\ A_{v2} & A_{v2}^2 & A_{v2}^3 \\ A_{v3} & A_{v3}^2 & A_{v3}^3 \end{pmatrix} \begin{pmatrix} \mathbf{u}_1 \\ \mathbf{u}_2 \\ \mathbf{u}_3 \end{pmatrix} = \begin{pmatrix} \mathbf{u}'(A_{v1}) \\ \mathbf{u}'(A_{v2}) \\ \mathbf{u}'(A_{v3}) \end{pmatrix}$$

The results of the amplitude expansion is shown in Figure 6. The streamwise velocity from the linear flow field $\mathbf{u}_1$ (Figure 6a) shows the decay of the incoming wave, whereas the quadratic flow field demonstrates a clear favoring of highly elongated structures. In the cubic field smaller scales are introduced. The combined flow fields $\mathbf{u}_1, \mathbf{u}_2$ and $\mathbf{u}_3$ (Figure 6d) shows a close resemblance with the full flow field.

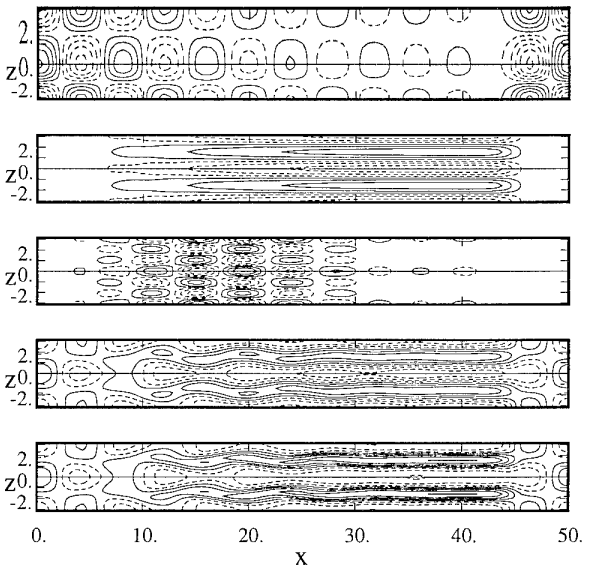

Figure 6. Flow fields from a numerical amplitude expansion for $R = 2000$. (a) linear, (b) quadratic and (c) cubic component; (d) sum of the first three terms of the amplitude expansion for $A_v = 0.005$; (e) original flow field corresponding to $A_v = 0.005$. Plotted is the streamwise disturbance velocity in a wall parallel plane at $y = -0.56$. The fringe region extends from $x = 42.5$ to $x = 50$. The contour levels in (a)-(c) are arbitrary, in (d) and (e) start at -0.0625, spacing 0.025, negative contours dashed.

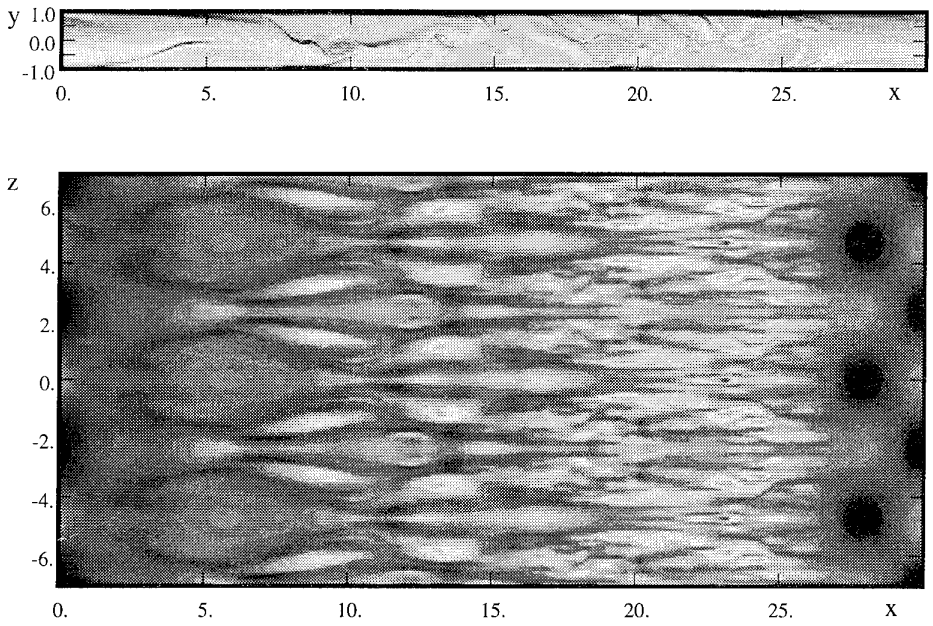

Figure 7. Instantaneous velocity fields for channel flow transition. Note the fringe region at the right part of the computational box. (a) Wall normal shear of the streamwise velocity at $z = 0$. (b) Streamwise velocity at $y = -0.9$, illustrating the downstream increase in skin friction. Three spanwise periods are shown.

Figure 7 displays the complete spatial transition and breakdown process starting with a pair of oblique waves. The waves are the least damped eigenmodes with zero normal vorticity for $\beta_0 = \pm 4/3$ and $\omega_0 = 0.410$. The amplitude of each wave is $A = 0.06$ and the Reynolds number $R = 2000$.

The rapidity of the transition scenario is apparent, and the formation of streaky structures as well as the occurrence of spikes and detached shear layers can be observed. On the right of the computational domain the effect of the fringe region which starts at $x = 22.5$ can be seen.

4.2 Boundary layer

The inflow conditions for the boundary layer simulation consists of the Blasius mean flow plus a pair of oblique waves. Here, the waves are the least damped eigenmodes with zero normal vorticity for $\beta_0 = 0.192$ and $\omega_0 = 0.08$. The amplitude of each wave is $A = 0.01$ and the Reynolds number at the inflow is 400.

Figure 8 shows the development of the coefficient of friction ($c_f = 2\tau_w/\rho U_\infty^2$, τ_w is the time and spanwise averaged wall shear stress) for the simulation. It is evident that the simulation captures the complete transition process, all the way into the turbulent regime.

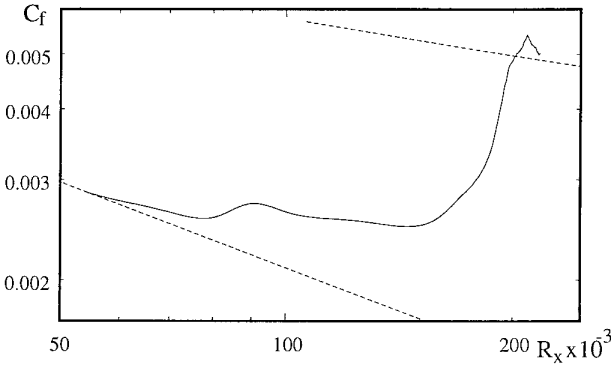

Figure 8. Coefficient of friction $c_f = 2\tau_w/\rho U_\infty^2$, τ_w is the averaged wall shear stress. $R_x = xU_\infty/\nu$ where x is the distance from the leading edge. Lower dashed line shows the value for a laminar Blasius boundary layer ($0.664R_x^{-1/2}$) and the upper curve is the turbulent friction $0.370(\log R_x)^{-2.584}$ by Shultz-Grunow (see Schlichting [22] p. 643)

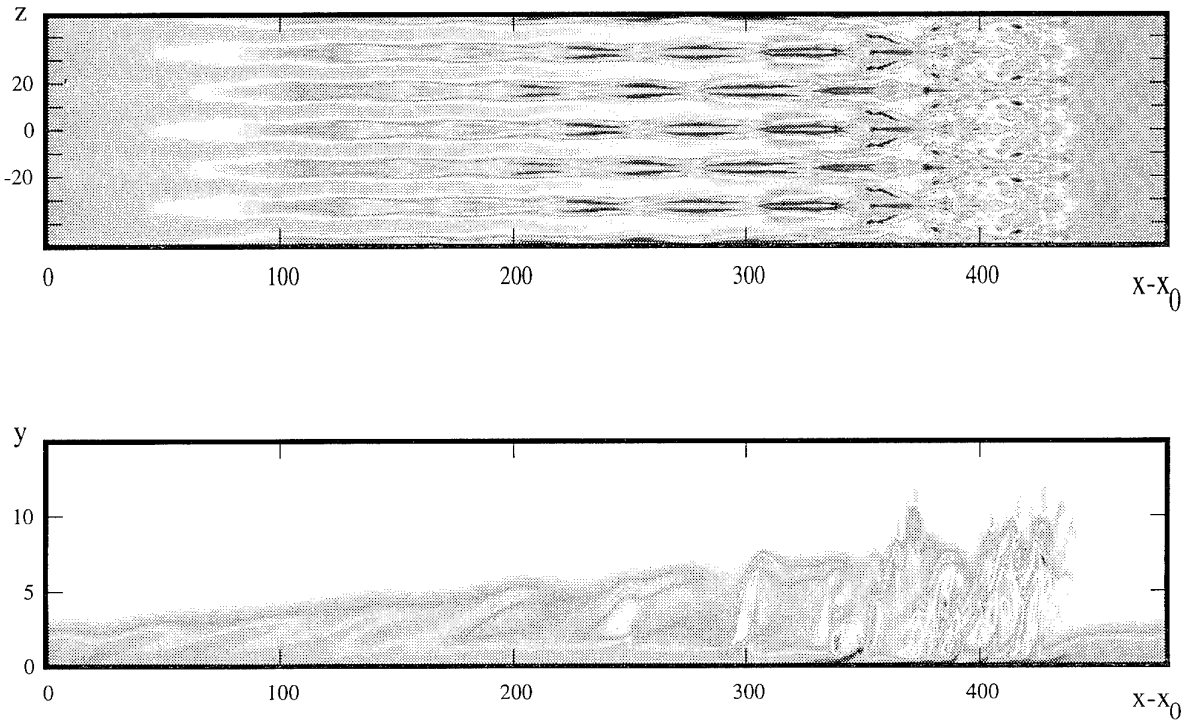

Figure 9. Instantaneous velocity fields for boundary layer transition. Note the fringe region at the right part of the computational box. (a) Streamwise velocity at $y = 2.93$. Values range from 0.34 to 1.08. Three spanwise periods are shown. (b) Streamwise shear at $z = 0$. Values range from -0.18 to 1.9.

Figure 9 shows an instantaneous view of the generated flow field. In figure 9a, which shows the streamwise velocity in a wall-parallel plane, the appearance of streamwise streaks is observed at about $x - x_0 = 50$. The streaks subsequently grow to a large amplitude and become unstable to a nonstationary disturbances, resulting in a breakdown to turbulence at about $x - x_0 = 350$. Figure 9b shows the streamwise shear in a side view of the boundary layer. Shear layers are seen to intensify and become unstable prior the breakdown, where the shear at the wall also increases substantially (cf. figure 8).

Figure 10 shows the energy in some of the excited Fourier components during the transition process.[1]. At $x - x_0 = 0$ only the $(1, \pm 1)$ components are excited. The $(1, \pm 1)$ modes show a rapid initial growth similar to that in the simulations by Schmid & Henningson [1], who also set the initial normal vorticity to zero.

The modes $(0, 0)$ $(0, \pm 2)$ $(2, 0)$ $(2, \pm 2)$ subsequently increase due to nonlinear effects, since they are directly generated by triad interactions from the $(1, \pm 1)$ modes. The $(0, \pm 2)$ mode grows more rapidly than the other modes and continues to grow rapidly until about $x - x_0 = 100$. The latter part of this growth was by Schmid & Henningson found to be due to a linear forcing of the streak (u-component) from the vortex (v, w-components) for the same wavenumber.

In contrast to the subcritical amplitude results in figure 5, a second phase of rapid growth starts for modes with nonzero ω, eventually completing the transition process. This second phase of growth can best be described as a secondary instability on the base flow with a spanwise variation given by the $(0, \pm 2)$ streak modes. A similar rapid growth of oblique modes from

[1] The flow was integrated until the whole flow field was periodic in time (approximately $t = 1000$), after which Fourier analysis was applied to 32 fields equally spaced within a period. The Fourier analysis was applied to the lower resolution calculation.

a state of streamwise streaks was found for temporal transition in plane Couette flow by Kreiss, Lundbladh & Henningson [10] and in plane Poiseuille flow by Lundbladh, Henningson & Reddy [23]. In the two latter studies the effect could be more unambiguously identified as a secondary instability since only the streak modes were significantly excited at the start of this phase.

After $x - x_0 = 408$ where the fringe damping is applied all Fourier components decay rapidly except the $(1, \pm 1)$ modes which are brought to their correct inflow value.

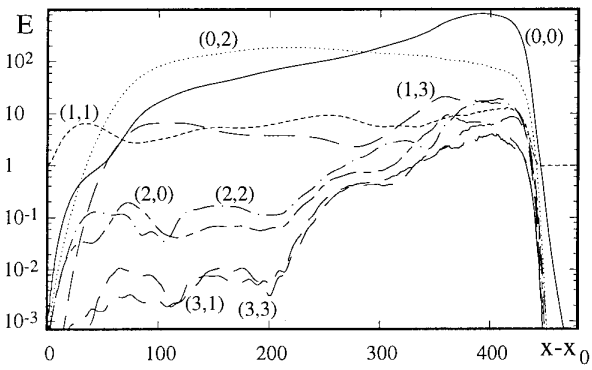

Figure 10. Energy in Fourier components with frequency and spanwise wavenumber $(\omega/\omega_0, \beta/\beta_0)$ as shown.

If we compare figure 10 with figure 8 we see that the region where the $(1, \pm 1)$ modes dominate (up to $x - x_0 = 60$ or $R_x = 80,000$) corresponds to a slow growth of the wall shear stress relative to the laminar value. The subsequent rapid increase of the friction coincides with the latter part of the growth for the $(0, \pm 2)$ modes. After the growth of these modes has leveled off the wall shear stress decays but more slowly and at a considerably higher level than the laminar value. The wall shear has a minimum at $R_x = 140,000$ or $x - x_0 = 220$ after which the friction increases rapidly during the secondary instability growth.

The simulation starts at a subcritical Reynolds number, and the result shows the possibility of oblique transition in the absence of exponential growth, as none of the modes involved pass through the unstable region in the frequency-Reynolds number plane. The transition process occupies about the same streamwise domain as in the simulations of secondary instability induced breakdown by Kloker & Fasel [24], in spite of the exponential growth of the two dimensional mode and higher input amplitude in the latter case. This is accentuated by the results of Spalart & Yang [25] who simulated an even larger domain by following a streamwise periodic box, accounting for the streamwise growth of the boundary layer and disturbance in an approximate manner. In spite of covering a larger Reynolds number range their simulations did not reach the turbulent state.

In the present investigation the wave amplitude at the inflow is low, resulting in a long growth region before breakdown. This initial amplitude represents the lowest amplitude disturbance of the chosen form, giving transition in this computational box. In a simulation with $A = 0.0086$ transition did not occur. In a study of oblique transition Joslin, Streett & Chang [13] did not find that the growth was sufficiently rapid to cause transition within their computational box, although the inflow is at a higher Reynolds number with the same initial amplitude as the one giving transition in the present study. The reason may be their use of complete eigenmodes as inflow condition (i.e. including the normal vorticity part of the eigenmode), which implies that they do not have the rapid transient growth of the oblique $(1, \pm 1)$ modes seen in the present case. The results of Lundbladh, Henningson & Reddy [23] indicate that the amplitude required for transition may be lowered even further if a linearly optimal distribution is used as initial data for the oblique modes.

5 CONCLUSIONS

The spatial transition scenario induced by a pair of oblique waves is qualitatively similar to its temporal analog. A linear mechanism plays a dominant role in amplifying the disturbance energy transiently, resulting in the preferred formation of highly elongated flow structures. If the amplitude is sufficiently high, these structures quickly break down to produce a turbulent flow.

The nonlinear generation of a vortex and the subsequent growth of streaks is quite similar to that seen in the temporal simulation by Schmid & Henningson [1]. In addition the streaks seem to break down due to the same secondary instability mechanism found in Kreiss, Lundbladh & Henningson [10]. In light of these findings, and those of other investigations discussed here, we conjecture that the following three stages occurs during oblique transition in shear flows:

- Initial non-linear generation of a streamwise vortex by the two oblique waves.
- Generation of streaks from the interaction of the streamwise vortex with the mean shear by the lift-up effect.
- Breakdown of the flow due to a secondary instability of the streaks, when these exceed a threshold amplitude.

Note that if the amplitude of the inflow disturbance is large enough the breakdown may be so rapid that the second and the third stage overlap. This is the reason the secondary instability is not so readily observed in the channel flow case.

We acknowledge the support and hospitality of the Institute for Computer Applications in Science and Engineering at the NASA Langley Research Center (LaRC), where part of this work was done. Computer time was provided by LaRC, the National Center for Supercomputer Applications, Urbana, IL, and the Pittsburg Supercomputer Center, Pittsburg, PA.

References

[1] P. J. Schmid and D. S. Henningson. A new mechanism for rapid transition involving a pair of oblique waves. *Phys. Fluids A*, 4:1986–1989, 1992.

[2] M. V. Morkovin. The many faces of transition. In C. S. Wells, editor, *Viscous Drag Reduction*. Plenum Press, 1969.

[3] K. M. Butler and B. F. Farrell. Three-dimensional optimal perturbations in viscous shear flow. *Phys. Fluids A*, 4:1637–1650, 1992.

[4] S. C. Reddy and D. S. Henningson. Energy growth in viscous channel flows. *J. Fluid Mech.*, 252:209–238, 1993.

[5] L. N. Trefethen, A. E. Trefethen, S. C. Reddy, and T. A. Driscoll. Hydrodynamic stability without eigenvalues. *Science*, 261:578–584, 1993.

[6] W. M. F. Orr. The stability or instability of the steady motions of a perfect liquid and of a viscous liquid. Part I: A perfect liquid. Part II: A viscous liquid. *Proc. R. Irish Acad. A*, 27:9–138, 1907.

[7] M. T. Landahl. Wave breakdown and turbulence. *SIAM J. Appl. Math*, 28:735–756, 1975.

[8] D. S. Henningson and S. C. Reddy. On the role of linear mechanisms in transition to turbulence. *Phys. Fluids*, 6:1396–1398, 1994.

[9] D. S. Henningson, A. Lundbladh, and A. V. Johansson. A mechanism for bypass transition from localized disturbances in wall bounded shear flows. *J. Fluid Mech.*, 250:169–207, 1993.

[10] G. Kreiss, A. Lundbladh, and D. S. Henningson. Bounds for threshold amplitudes in subcritical shear flows. TRITA-NA 9307, Royal Institute of Technology, Stockholm, Sweden (To appear in *J. Fluid Mechanics*), 1993.

[11] H. Fasel and A. Thumm. Direct numerical simulation of three-dimensional breakdown in supersonic boundary layer transition. *Bull. Am. Phys. Soc.*, 36:2701, 1991.

[12] C. L. Chang and M. R. Malik. Non-parallel stability of compressible boundary layers. AIAA Paper 93-2912, 1993.

[13] R. D. Joslin, C. L. Streett, and C. L. Chang. Spatial direct numerical simulations of boundary-layer transition mechanisms: Validation of PSE theory. *Theoret. Comput. Fluid Dyn.*, 4:271–288, 1993.

[14] R. J. Gathmann, M. Si-Ameur, and F. Mathey. Numerical simulations of three-dimensional natural transition in the compressible confined shear layer. *Phys. Fluids A*, 5:2946–2968, 1993.

[15] A. Lundbladh, D. S. Henningson, and A. V. Johansson. An efficient spectral integration method for the solution of the Navier-Stokes equations. FFA-TN 1992-28, Aeronautical Research Institute of Sweden, Bromma, 1992.

[16] J. Kim, P. Moin, and R. Moser. Turbulence statistics in fully developed channel flow. *J. Fluid Mech.*, 177:133–166, 1987.

[17] Leslie Greengard. Spectral integration and two-point boundary value problems. *SIAM J. Numer. Anal.*, 28:1071–1080, 1991.

[18] F. P. Bertolotti, T. Herbert, and P. R. Spalart. Linear and nonlinear stability of the Blasius boundary layer. *J. Fluid Mech.*, 242:441–474, 1992.

[19] M. R. Malik, T. A. Zang, and M. Y. Hussaini. A spectral collocation method for the Navier-Stokes equations. *J. Comp. Phys.*, 61:64–88, 1985.

[20] H. Haj-Hariri. Transformations reducing the order of the parameter in differential eigenvalue problems. *J. Comp. Phys.*, 77:472–484, 1988.

[21] D. S. Henningson and P. J. Schmid. A note on measures of disturbance size in spatially evolving flows. Proceedings from the 1993 ICASE/NASA Langley Workshop on the Transition to Turbulence, 1993.

[22] H. Schlichting. *Boundary layer theory.* McGraw-Hill, 1979.

[23] A. Lundbladh, D. S. Henningson, and S. C. Reddy. Threshold amplitudes for transition in channel flows. Proceedings from the 1993 ICASE/NASA Langley Workshop on the Transition to Turbulence, 1993.

[24] M. Kloker and H. Fasel. Numerical simulation of transition in a boundary layer with strong adverse pressure gradient. Ninth Symposium on Turbulent Shear Flows, Kyoto, Japan, 1993.

[25] P. R. Spalart and K. Yang. Numerical study of ribbon induced transition in blasius flow. *J. Fluid Mech.*, 178:345–365, 1987.

Direct numerical determination of the minimum bypass Reynolds number in boundary layers

Roque Corral and Javier Jiménez
School of Aeronautics, Universidad Politécnica
28040, Madrid, Spain

SUMMARY

It is argued that bypass transition on a flat plate can be interpreted as a consequence of the subcritical nature of the instability of the boundary layer, and that the minimum bypass Reynolds number should coincide with the one at which the turbulent layer relaminarises spontaneously. This threshold is found by direct numerical simulation of a spatially periodic turbulent layer in which spatial growth is modelled by a linear normal velocity. The computed mean profiles and integral properties agree well with experimental results at the higher Reynolds numbers, but diverge from them at the lower ones. While experiments turn away from the turbulent correlations below $Re_\theta \approx 300 - 500$, the computations follow them until relaminarising abruptly at $Re_\theta \approx 200$. The simulations use relatively small periodic computational boxes, holding only a few boundary layer thickness, and it is argued that this provides enough feedback to prevent the transitional effects observed in experiments and to result in an absolute relaminarisation threshold. The Reynolds number obtained in this way agrees with the onset of bypass transition in experiments with very high free stream turbulence levels, or with strong roughness tripping.

1. INTRODUCTION

It is common knowledge that some laminar flows can be tripped into turbulence at Reynolds numbers at which laminar stability theory predicts them to be stable. In some extreme cases, such as the circular pipe, the basic parallel flow is believed to be stable at *all* Reynolds numbers [1, pg. 515], while turbulence can be generated without difficulty, and occurs spontaneously in the right circumstances. In those cases it is typically true that the minimum Reynolds number at which turbulence appears depends on the perturbation applied (the "trip"), and is generally lower when the perturbation is more intense (see fig.2). It is of theoretical and practical interest to find whether there is an absolute minimum Reynolds number below which turbulence cannot be initiated, independently of the intensity of the trip, and to estimate it. That is the subject of the present paper.

It has been realised for some time that tripped ("bypass") transition is fundamentally different from the "regular" kind, in which background noise is amplified by linear instabilities and eventually grows to large amplitudes, leading to secondary breakdown and turbulence. Since in this case there is no linear instabilities, the same mechanisms cannot be involved, and there is no reason to expect that the same transitional structures should be present in both cases. The idea that the usual instability mechanisms are "bypassed" in subcritical transition has given this route to turbulence its name.

Bypass transition is specially prevalent in wall bounded flows. We have already mentioned the circular pipe. Plane channels also transition subcritically. While the first linear instability appears at a Reynolds number of 5772, based on the mean velocity and channel half width, it is known experimentally that turbulence can be promoted and maintained at $Re \approx 1500$ [2]. Another parallel flow, the boundary layer along the attachment line of swept wings, is also known to be subcritical, with linear and bypass transition Reynolds numbers $Re_S = U/(S\nu)^{1/2} = 545$ and 245, where S is the transverse strain at the stagnation line [3]. In these two flows the bypass Reynolds numbers seem to be absolute limits. Below them turbulence cannot be promoted and, if it is generated by massive perturbations, it decays. The same is true of the circular pipe, in which the minimum Reynolds number, based on the diameter, is around 2000 [4,5].

The distinction between classical and bypass transition is clarified when expressed in the language of modern bifurcation theory. Marginal linear instability can be interpreted as the point in parameter space in which two different solutions of the equations coexist: the equilibrium laminar one, and another solution, infinitesimally different and possibly unsteady, which is described by the instability eigenfunction. As we move away from marginal instability, e.g. by changing the Reynolds number, both solutions diverge and, while the equilibrium one remains laminar, the new solution becomes stronger and, possibly through a new series of bifurcations, leads to turbulence. There are two main kinds of elementary bifurcations. In the first one the new solution bifurcates *forward* in Reynolds number, and no turbulence is possible until the bifurcation threshold is reached. In the second, subcritical case, the "turbulent" solution branches towards Reynolds numbers *below* the bifurcation (fig. 1a), and only later, perhaps also after new bifurcations, turns forwards towards higher Reynolds numbers. Stable (attracting) solutions are marked in the figure as solid lines. In this case only the laminar solution below the

Paper presented at the 74th Fluid Dynamics Symposium on "Application of Direct and Large Eddy Simulation to Transition and Turbulence" held at Chania, Crete, Greece, in April 1994.

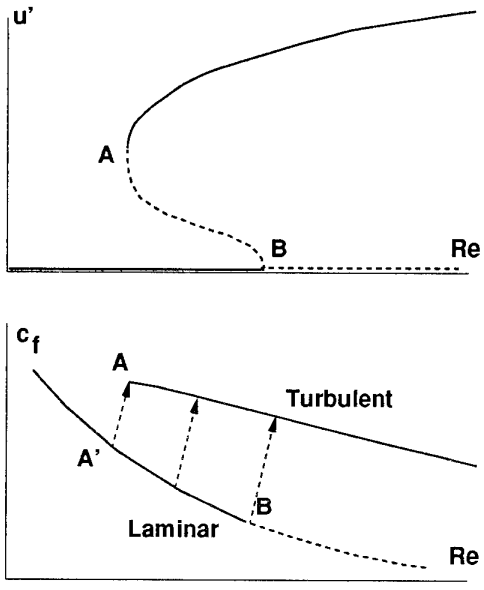

Figure 1. Sketches of subcritical transition. Solid segments mark attracting solutions, while dashed ones represent unstable (repelling) ones. (a) Generalised diagram; the vertical axis is perturbation amplitude with respect to laminar flow. The bifurcated branch models turbulent flow. (b) Friction coefficient behaviour in boundary layers; transition is assumed to occur with little change in Reynolds number.

bifurcation, and the turbulent one above the turning point, are attracting, and there are two different critical Reynolds numbers. Laminar flow can be maintained up to the bifurcation point B, if enough care is taken not to perturb it, but turbulent flow, the upper branch of the solution, can be tripped for all Reynolds numbers above A.

Figure 1b translates this model into the behaviour of a transitional boundary layer. The turbulent solution exists only for those Reynolds numbers above Re_A, and is always very different from the laminar solution. At the bypass Reynolds number the turbulent solution seems to end abruptly, since the solution branch linking it to the bifurcation point B is unstable and not observable. For any Reynolds number between A' and B, laminar flow can be tripped towards the turbulent branch by a perturbation large enough to carry it outside the basin of attraction of the laminar solution. Above Re_B transition occurs spontaneously. The point A', at the base of a trajectory carrying the flow to A, marks the lowest Reynolds number for which bypass transition is possible, and the easiest way to find it experimentally is to study the reverse transition from turbulent into laminar flow. Consider a process in which the Reynolds number of an existing turbulent flow is lowered slowly. As long as it stays above Re_A the flow will stay turbulent but, if it falls below that value, in the range for which no turbulent solution exists, the flow will relaminarise. This distinction between the spontaneous transition and relaminarisation limits was already noted by Reynolds [4].

It is important to realise that, once a flow has been made turbulent by a large disturbance, its fate is independent of the linear instability mechanisms. This is specially true of wall bounded flows for which the instabilities are viscous, with characteristic time scales of the order of $T_v = O(\delta^2/\nu)$, where δ is the boundary layer thickness. In contrast, the time scale of the turbulent fluctuations is given in terms of the friction velocity $u_\tau = (\nu\, \partial\overline{u}/\partial y|_{\rm wall})^{1/2}$, as $T_o = O(\delta/u_\tau)$, and are always fast with respect to the instability times, $T_o/T_v = \mathrm{O}(Re_\tau^{-1})$. The friction Reynolds number, $Re_\tau = u_\tau\delta/\nu$, is at least $O(100)$ in all transition situations. As a consequence the viscous instability mechanisms are too slow to be of importance once a vigorous turbulent motion is active, and turbulence survives or decays by itself, without reference to them.

1.1 Developing boundary layers

The discussion in the previous section applies to parallel flows, for which a unique Reynolds number can be defined which is applicable both to laminar and turbulent regimes. There are two reasons why the same model cannot be used directly for spatially developing boundary layers. First, there is no unique length scale on which to base a Reynolds number to be used as a bifurcation parameter. The obvious candidate, the boundary layer thickness, is a function of the velocity profile and depends on whether the flow is laminar or turbulent. It is therefore inconvenient to use as a test for subcriticality, since the transition and relaminarisation Reynolds numbers are based on different definitions. The alternative, to use as length scale the distance to the leading edge, has the disadvantage of being nonlocal and dependent on the development history of the layer.

The second difficulty is that any definition of Reynolds number depends on the development stage of the boundary layer and changes during the transition process. In a parallel flow, such as a pipe, there is no difference in quoting the Reynolds number at the beginning or at the end of the transition, since neither the mean velocity nor the pipe diameter change during the process, but in a developing boundary layer this is not so. The transition is not instantaneous and, by the time the new flow is established, its scales are different from those at the beginning. Any definition of a unique transition Reynolds number depends therefore on a model for the transition, and makes sense only if the process can be shown to be fast enough to be considered local with respect to the spatial development of the layer. In which sense this is true for the boundary layer on a flat plate is shown by the following estimates, which are based on the analyses in [6,7].

Consider relaminarisation. In a turbulent boundary layer, most of the velocity difference occurs in a sublayer whose thickness is $O(\theta)$, the momentum thickness, and turbulence generation and dissipation processes act on time scales $O(\theta/u_\tau)$. During that time the fluid is convected by the free stream velocity U_o across a distance $L_o = O(\theta U_o/u_\tau)$, which is the characteristic length for relaminarisation, since it describes the decay of turbulence left to itself. The streamwise development length of the layer is given by the momentum equation,

$$d\theta/dx = c_f/2 = (u_\tau/U_o)^2. \qquad (1.1)$$

The length needed for a significant change in the value of θ is $L_x = \theta/(d\theta/dx) = \theta(U_o/u_\tau)^2$, and the ratio of relaminarisation to development lengths is

$$\frac{L_o}{L_x} \sim \frac{u_\tau}{U_o} = \epsilon. \qquad (1.2)$$

This is a small parameter, typically $\epsilon \approx 0.05$ at the Reynolds numbers at which transition occurs, and determines in which sense relaminarisation depends only on the local characteristics of the boundary layer, and with which precision it makes sense to define a unique relaminarisation or transition Reynolds number. From the analysis that led to the above estimates, it follows that it also determines in which sense other aspects of the behaviour of the turbulent boundary layer can be considered local. It can be shown [6,7] that the characteristic thickness of the *full* boundary layer is $\delta/L_x = O(\epsilon)$, while the displacement and momentum thickness are $\delta^* \sim \theta \sim \epsilon\delta$. Therefore, even if the basic relaminarisation or bypass transition events are short compared to the streamwise development, $L_o \ll L_x$, the length needed for the transitional boundary layer to achieve equilibrium across its full thickness, $L_t = U_o\delta/u_\tau$, is comparable to the development scale.

Three different transition experiments for zero pressure gradient boundary layers, forced with different levels of free stream turbulence, are shown in figure 2. They show the characteristics discussed up to now. The transition Reynolds number decreases as the level of perturbation increases, and the transition process is fast, followed by a slower relaxation towards the equilibrium turbulent correlation. In this figure, the experiment corresponding to the highest forcing intensity is probably close to the absolute minimum transition threshold, since the free stream turbulent intensity (6%) is comparable to the fluctuation levels in fully developed turbulent boundary layers.

In the following sections we present numerical experiments on the behaviour of turbulent boundary layers at low Reynolds numbers, with the goal of determining the minimum relaminarisation threshold for the boundary layer on a flat plate without pressure gradient. In §2, the numerical scheme is introduced and the approximation of the developing layer by a parallel flow is analysed. The results are presented next, and compared to low Reynolds number experimental data.

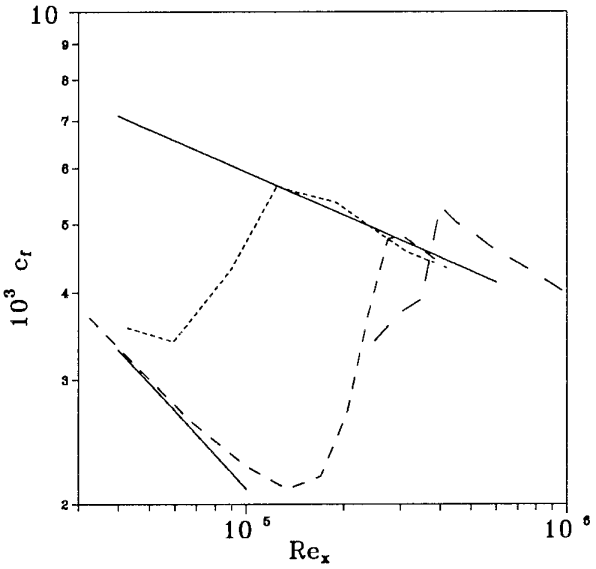

Figure 2. Friction coefficient as a function of $Re_x = U_o x/\nu$ for bypass transition on a flat plate at three different free stream turbulence levels. Long dashes: $u'/U_o = 2.6\%$ [8]. Short dashes and dots: $u'/U_o = 3\%$ and 6% [9]. Solid lines are turbulent and laminar correlations from [1, pg. 600].

The question of the internal time scales is then considered and, finally, conclusions on the bypass transition threshold are drawn and compared to experimental evidence.

2. THE NUMERICAL CODE

Our code simulates the complete Navier Stokes equations on a domain stretching from the wall, located at $y = 0$, to $y = \infty$. It is described in detail in [10], and is an adaptation to semi-infinite domains of the spectral code in [11]. The flow variables are assumed to be spatially periodic in the two homogeneous directions x and z, which are respectively parallel and normal to the mean velocity, and are expanded as Fourier series in $(x, z) \in (0, L_x) \times (0, L_z)$, and as Chebyshev series in $y \in (0, L_y{=}1)$. Since there is no physical boundary at $y = L_y$, only even or odd Chebyshev polynomials are used in the expansion, saving about half of the computational effort, as well as an artificial accumulation of grid points at that numerical boundary. Dealiasing by the 2/3 rule [12] is used in the two homogeneous directions, but not in y. Time stepping is third order explicit Runge-Kutta for the nonlinear terms and implicit Euler for the viscous ones.

The treatment of the boundary condition at infinity is novel [13]. An extra exponential basis function is added to the y-expansion of each Fourier component of the *velocity* variables, and its magnitude is computed as part of the time marching procedure. It is shown in [13] that the exponential accuracy of the spectral scheme is conserved as long as the *vorticity*, which carries no extra basis function, can be assumed to be

contained inside the computational box.

The code solves the initial value problem, in which the temporal evolution of some initial flow field is computed. In the simulations discussed here, an initially strong, essentially random, perturbation was introduced on a laminar profile and followed until either the flow settled to a statistically steady turbulent field, or decayed to laminar. In general, most cases were initialised with fields corresponding to statistically stationary turbulent conditions at neighbouring Reynolds numbers or box sizes. The mean y profiles of those initial conditions are approximately correct but, because flow field consistency is a function of box size, the details of most of them were wrong and did not satisfy continuity. Continuity is automatically enforced by the numerical code and restored after the first time step.

Most simulations were made with grids containing $24\times 97 \times 24$ spectral modes, after dealiasing. This corresponds to $\Delta x^+ \approx \Delta z^+ \approx 12$. A similar resolution in x was used in [11] for a turbulent channel, but with $\Delta z^+ \approx 7$. They cite previous simulations with resolutions 40% coarser in x and 20% coarser in z, without apparent effect in the low order statistics. Our resolution in y, with the first mesh point at $\Delta y_o^+ \approx 0.04$, is similar to theirs. For a boundary layer at $Re_\theta = 670$, Spalart [14] proved grid independence of the mean velocity profiles using $\Delta x^+ \approx 32$, $\Delta z^+ \approx 11$, $\Delta y_o^+ \approx 0.09$. We checked our mesh by running a few cases at an increased resolution of $\Delta x^+ \approx 10$, $\Delta z^+ \approx 8$. This did not result in a significant change in the statistical quantities ($< 5\%$, which is of the same order as the statistical uncertainty due to finite sampling time), but the instantaneous flow fields looked appreciably cleaner in the finer grids, and there was a slight trend towards decreasing c_f with higher resolution (see figs. 4 and 5). These high resolution tests could not be run for sufficiently long times to test for relaminarisation, but their statistics are included here for comparison. The profiles in figure 6 also belong to them.

The horizontal extent of the computational box was chosen so as to contain just a few copies of the basic flow structures, substituting the random distribution which occurs in natural flows by a doubly periodic array of identical flow units. The adequacy of this "minimal" approach was proven in [15] for the near wall region, and the boxes for our lowest Reynolds number experiments were scaled in wall units, (L_x^+, L_z^+ $\approx$ 250), and chosen so as to contain approximately two wall velocity streaks. This does not guarantee that the outer flow is well represented. It was found in [11] that the velocity correlation function in a channel at a somewhat higher Reynolds number decays to zero in the outer layer for $x/\delta \approx 2$, $z/\delta \approx 1.5$, and that a computational box of at least that size has to be used if the outer structures are to be well described [15]. At low Reynolds numbers the box size suggested by the wall scaling turns out to be sufficient for the outer flow L_x, $L_z > 2\delta \approx 20\,\theta$. At higher Reynolds numbers, $Re_\theta > 450$, this is no longer true, and we use computational boxes based on momentum thickness. As a consequence the wall region of those fields contain more independent structures than their low Reynolds number counterparts (see table 1).

It is argued below that the appearance of collective or intermittent effects at the lowest Reynolds numbers would require larger computational boxes to be adequately represented, and that they may be connected to the discrepancies observed between computations and experiments, as well as among different experiments, in the neighbourhood of transition.

2.1 The modelling of spatial growth

It is well known that, apart from exceptional cases, the velocity distribution for developing boundary layers varies with the streamwise coordinate x. The assumption of spatial periodicity is not valid, and *ad hoc* corrections have to be made. An artifice commonly used in transitional studies is to add a fictitious system of body forces in the streamwise direction so that the desired velocity profile becomes an exact steady solution of the Navier-Stokes equations. A spatially periodic solution is then superimposed on the flow. It has been argued convincingly by previous investigators [16] that this approach preserves the nonlinear structure of the flow instabilities during transition and that, if the size of the computational box is small with respect to the characteristic length scales of boundary layer growth, the errors are not locally large, although they could accumulate over long integration times.

While this method may be justified for the calculation of transition from small disturbances, in which the laminar profile is important, it is not useful to study relaminarisation where, as discussed above, the laminar profile is never realised and the time scales of turbulence are very far removed from those of viscosity. The real problem is to approximate locally a fully turbulent flow, and a better alternative is to follow directly the standard approximate similarity analysis of the turbulent boundary layer [6]. Our method is a simplified variant of the one used in [14].

The boundary layer can be separated into two zones. In the outer one the mean streamwise velocity is within $O(u_\tau)$ of that of the free stream, and the averaged momentum equation can be approximately written as

$$U_o \frac{\partial \overline{u}}{\partial x} = -\frac{\partial \overline{uv}}{\partial y}. \qquad (2.1)$$

There, the time scales of the largest turbulent eddies are of the same order as that of the downstream evolution of the flow, which has to be taken into account.

Equation (2.1) admits self similar solutions in which both $\overline{u}$ and $\overline{uv}$ are only functions of $\eta = y/\delta(x)$, where δ is some thickness representative of the the outer

layer. Equation (2.1) can then be written as

$$-\left(\frac{U_o}{\delta}\frac{d\delta}{dx}\right)\eta\frac{d\overline{u}}{d\eta}=-\frac{d\overline{uv}}{d\eta}, \qquad (2.2)$$

suggesting that a reasonable approximation to the self similar zero pressure gradient boundary layer would be to solve the full Navier-Stokes equations with an additional linear normal velocity,

$$v \rightarrow v - S\,\eta, \qquad S=-\left(\frac{U_o}{\delta}\frac{d\delta}{dx}\right), \qquad (2.3)$$

adjusted so as to model the left hand side of (2.2). It follows from the integral momentum equation (1.1) and from the estimate $\delta = O(\theta/\epsilon)$ [6], that

$$S = O(u_\tau^2/U_o\theta), \qquad (2.4)$$

which is of the order of the inverse of the slow development time scale for the boundary layer, and slower than the time scales for the turbulent fluctuations.

From the strain S it is possible to define a Reynolds number

$$Re_S = \frac{U_o}{(S\nu)^{1/2}}, \qquad (2.5)$$

which is the natural numerical parameter of the simulation.

It remains to analyse the wall region, in which convection effects are usually neglected, and where $\overline{u} = O(u_\tau)$ and $y = O(\nu/u_\tau)$. The momentum equation in this zone can be approximated by

$$\nu\frac{\partial\overline{u}}{\partial y}-\overline{uv}=u_\tau^2, \qquad (2.6)$$

and the neglected terms are $O(y\,\overline{u}\,\partial\overline{u}/\partial x)$. It follows from the previous estimates that, even if we keep in this zone the assumption that the mean flow satisfies self similarity in terms of outer variables, the convection terms in (2.6) are $O(\epsilon u_\tau^2/Re_\theta)$, and can be neglected safely. Finally, it can be shown that the errors introduced by the similarity assumption in the continuity equation result in velocity errors which are $O(\epsilon^2)$ in the outer region, and negligible near the wall.

It was noted in [14] that this mean flow analysis does not guarantee that the turbulent eddies are well represented. This can only be expected in the wall region, for which it was shown in the discussion leading to equation (1.2) that the turbulent time scales are much shorter than the evolution time S^{-1}. In the outer flow both scales are of the same order, and the self similarity assumption can only be qualitative. Spalart's analysis in [14] is similar to ours, but he carries his analysis of the mean flow to $O(\epsilon^2)$ while ours is only true to $O(\epsilon)$. In view of the uncertainty in the modelling of the outer turbulent eddies, and since the goal of our calculation is to determine the relaminarisation Reynolds number, which in a developing boundary layer can only be related to bypass transition within $O(\epsilon)$, we do not feel that the extra accuracy is necessary. The computer times needed for our model are considerable shorter than those in [14], and the whole computation can be carried in a large workstation.

Re_S	Re_θ	L_x^+	L_z^+	$1/\theta$	$10^3 c_f$	H
274	91	226	185	33.1	5.82	2.41
296	217	300	245	16.1	7.54	1.62
320	247	305	229	14.6	7.38	1.59
364	302	295	295	17.6	6.62	1.55
426	365	318	318	19.8	6.24	1.54
465	415	373	373	20.9	6.02	1.52
296	208	298	243	16.8	7.43	1.65
364	295	415	340	18.0	6.30	1.57
465	456	366	366	19.0	5.79	1.48
700	899	752	752	21.8	4.77	1.41

Table 1. Geometric parameters of the principal numerical experiments. All runs used 97 modes in the y direction. For (x, z), the cases in the upper block used (24×24) modes, after dealiasing. Those in the lower block (32×43). The lowest line (32×85). The upper line decayed to laminar, and table entries are based on laminar values.

3. NUMERICAL RESULTS

Table 1 contains a summary of the numerical experiments discussed in this paper. Each of them is characterised by a strain parameter, S, which controls the forcing velocity and the boundary layer thickness. Other inputs are the viscosity, and the size of the computational box. The top boundary condition is imposed at $y = 1$, and the velocity at infinity is $U_o = 1$. These choices fix the strain Reynolds number Re_S, while the rest of the parameters are measured from the solution. The statistics of the low resolution cases are accumulated at least over dimensionless times of 200, or until they remain stationary within 1-2%. Those of the higher resolution cases are only good within 5%. The values for L_x^+ and L_z^+ characterise the box size in terms of the inner structure, while $1/\theta$ relates the size of the largest eddies to the computational domain.

Three typical wall shear histories are shown in figure 3. In those cases in which turbulent flow can be maintained, the wall shear remains statistically stationary over long times, oscillating randomly on a time scale which will be discussed in the next section. In the cases which decay spontaneously, the decay is fast, on a time scale comparable to a single oscillation of the turbulent histories. The friction coefficients for different values of the numerical Reynolds number are given in figure 4. The threshold between turbulent and laminar ranges is sharp, with no intermediate "transitional" cases to connect the turbulent and laminar branches of the solution, in general agreement with the subcritical scenario outlined in the discussion of figure 1.

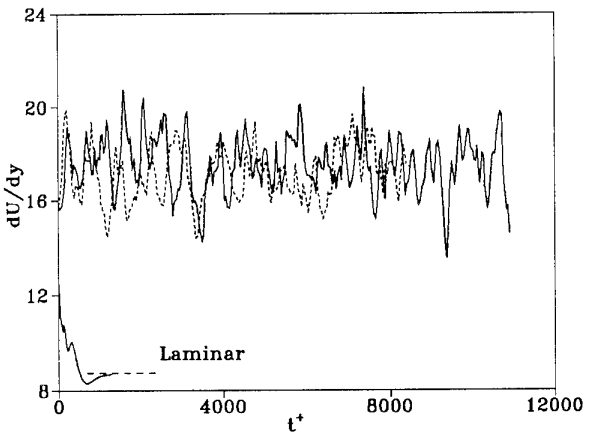

Figure 3. Time evolution of instantaneous wall shear averaged over the computational box. Long traces: $Re_S = 364$; box length for solid trace: $L_x^+ = 295$; dashed: $L_x^+ = 586$. Lower short trace, laminarising flow at $Re_S = 274$. Time is normalised with time-averaged wall shear $t^+ = t\partial\overline{u}/\partial y|_{\text{wall}}$.

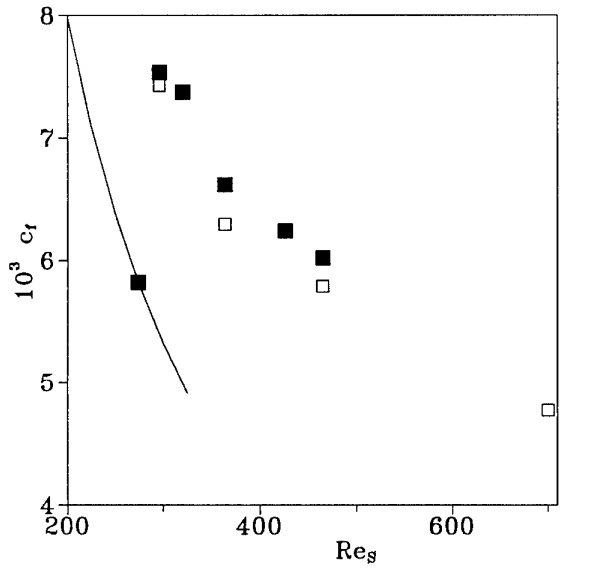

Figure 4. Friction coefficient of numerical fields versus Re_S. Solid symbols are low resolution cases. Open symbols, high resolution. Solid line is laminar solution of equation (2.2).

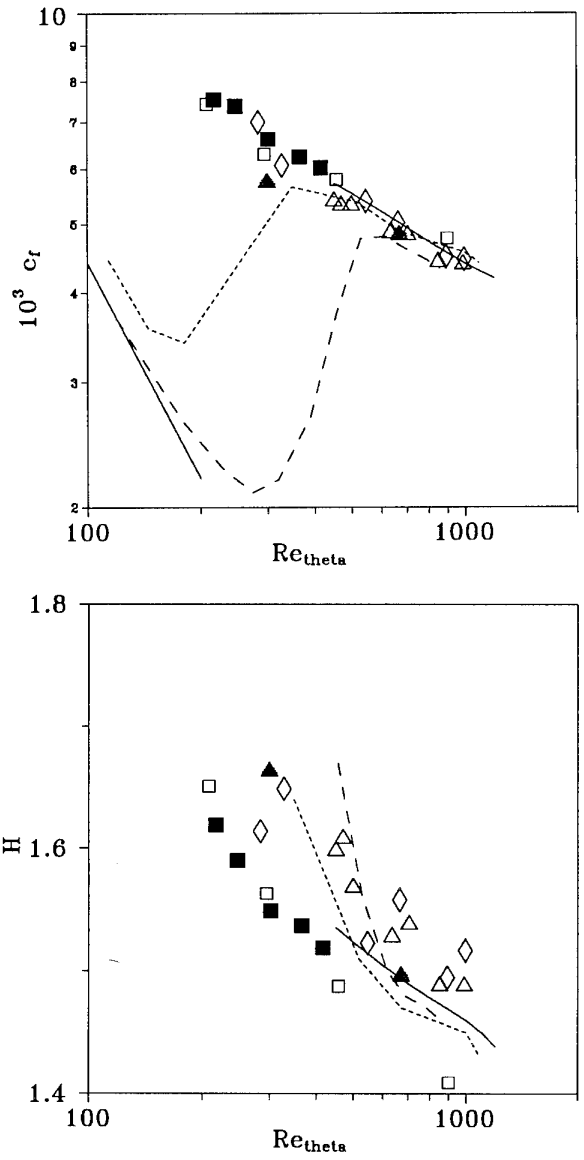

Figure 5. Boundary layer characteristics versus Re_θ. Top: friction coefficient, Bottom: form factor δ^*/θ. Dashed lines are transition development experiments, as in figure 2. Open triangles: experimental values [17]. Diamonds: resonant experiments [18]. Solid line: Coles [19] experimental correlation. Closed triangles: numerical simulation [14]. Squares: present simulation, as in figure 4.

The turbulent flow fields usually contain two or three low speed streaks at the wall, extending vertically for about half the boundary layer thickness. The outer flow is dominated by large horseshoe vortices, while the inner layer contains unsymmetrical or incomplete horseshoes, which seem to be related to the formation of the low velocity streaks [20, fig. 1]. All this is in general agreement with previous experimental and numerical evidence.

The bulk quantities of our numerical experiments are plotted in figure 5, together with values from experimental boundary layers, and with a few numerical results from [14]. The skin friction of the numerical fields is slightly higher than the experiments, while the form factors are a little low, but the disagreement is comparable to the experimental scatter, and is in any case within the expected errors of $O(u_\tau/U_o)$.

The largest discrepancies occur at the lowest Reynolds numbers. Except for the experimental values from [18], which will be discussed later, our turbulent fields

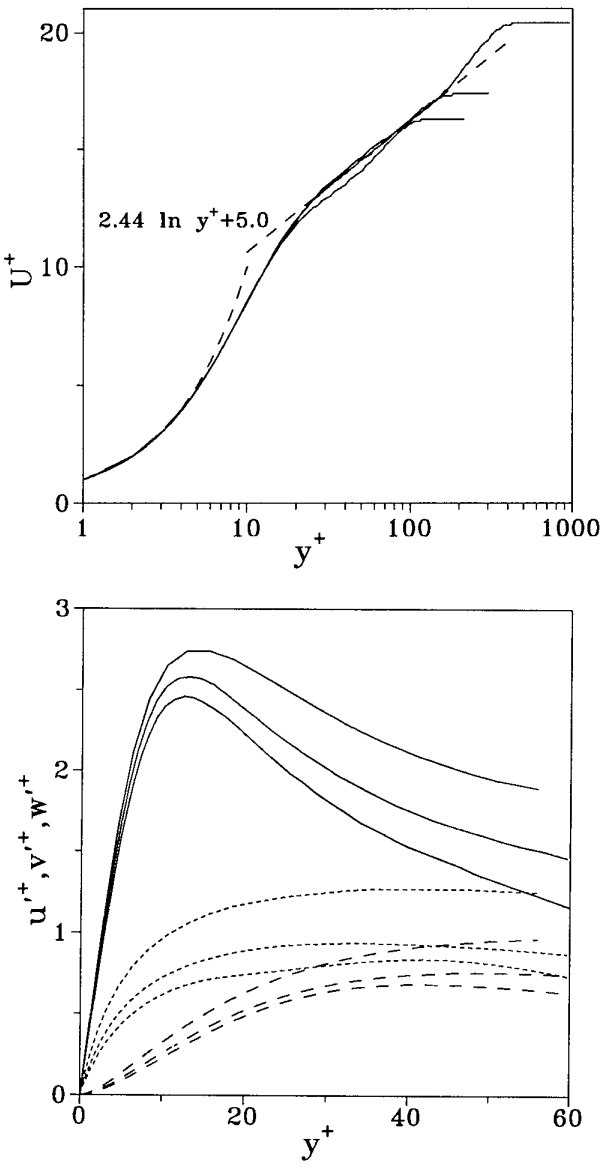

Figure 6. Boundary layer profiles from the high resolution simulations, expressed in wall variables. Top: mean velocity. Bottom: turbulent intensities; solid lines: u'; dashed: v'; dotted: w'. $Re_\theta = 208, 295, 899$, in order of increasing intensity.

survive at Reynolds numbers lower than those observed in experiments, and they do so while following the turbulent correlation obtained from higher Reynolds numbers. This is confirmed by the profiles in figure 6, which show that the law of the wall is well satisfied by our results for $Re_\theta > 300$, and still holds approximately at our lowest turbulent Reynolds number $Re_\theta = 208$. The peak location and approximate intensity of the fluctuation profiles agree with previous computations [11,14], but extend to lower Reynolds numbers.

Our results suggest a relaminarisation $Re_\theta \approx 200$, while the most often quoted lower limit for sustained turbulence in a boundary layer is $Re_\theta = 320$ [21]. It was noted by Spalart [14] that this latter estimate is doubtful, since Preston refers to "fully turbulent" flows, which are those satisfying the logarithmic law, and his limit is bound to be higher than that for self sustained turbulence. Spalart presented a turbulent profile at $Re_\theta = 300$ which does not exhibit a logarithmic region and which would thus not be considered turbulent by Preston, and he quotes self sustained turbulence at $Re_\theta = 225$, but shows no data. From figure 6a, our first "fully developed" simulation would be $Re_\theta = 302$. All these observation are in rough agreement with a minimum sustainable Re_θ of about 200, with classical velocity distributions appearing above 300.

3.1 Intermittency

Most previous experiments below $Re_\theta \approx 400$ have friction coefficients lower than those corresponding to the fully turbulent correlation, as well as form factors closer to the laminar ones. Since all low Reynolds number experiments are tripped, it is easy to understand how this could be an effect of the trip, or of the incomplete development of a transitional boundary layer (see the two transition curves in figure 5). References [19,17] carefully avoid this problem by using only measurements beyond the stage at which the profiles become independent of the tripping details. They are the ones closer to the fully turbulent correlation curves, but are restricted to $Re_\theta > 400$. Spalart's lowest Reynolds number ($Re_\theta = 300$) falls below the turbulent c_f, even if his simulation, like ours, is spatially periodic and unlikely to show effects of insufficient development. Our results follow the extrapolated turbulent correlations up to the limit of relaminarisation.

Transitional effects are also seen in the swept attachment line boundary layer, a parallel flow for which no development effects are expected, at Reynolds numbers below $Re_\theta \approx 300$, well above its relaminarisation limit of $Re_\theta \approx 200$ [3]. That flow and the flat plate boundary layer are closely related, as can be seen from equation (2.2). In the attachment line the main effect is a strain normal to the mean velocity, which can be modelled by a normal velocity $v = -Sy$, similar to the artificial term introduced in (2.2) by the spatial growth. Continuity, however, induces a transverse straining velocity $w = Sz$, whose effect on the large scale structures of the outer region is not negligible. Experimentally, the integral characteristics of both flows differ by only 20%, and their relaminarisation Reynolds numbers appear to be identical.

A similar transitional effect on the friction coefficient occurs in circular pipes, for which the experimental curves diverge from the turbulent law for Reynolds numbers below 3500, even if turbulence can be maintained above $Re \approx 2000$ [1, pg. 562].

In all these flows, large scale intermittency is known

to occur in various forms for Reynolds numbers below 1.5-2 times that of relaminarisation. The paradigm is forced transition in a circular pipe. At $Re \approx 2200$, the pipe becomes unstable to large perturbations, and tripping leads to the appearance of turbulent puffs, which reach a definite length of about 20 pipe diameters, and propagate downstream without change of shape or intensity [22]. Above $Re \approx 2300$ puffs grow with downstream distance and ultimately merge into larger structures (slugs) which at somewhat higher Reynolds number become the building blocks of fully turbulent flow [5]. Individual slugs can be observed, depending on the initial perturbation, for $Re < 3200$, close to the end of the transition range for the friction factor.

Similar phenomena have been observed in the attachment line boundary layer [3], in two dimensional channels [23], and in tripped boundary layers [24]. It is tempting to attribute at least part of the decrease in the friction coefficient, compared to its fully turbulent value, to the existence of occasional laminar regions in experimental boundary layers at low Reynolds numbers, and to attribute the lack of transitional effects in our simulations to the small size of our computational box. The length scale of most of the transitional structures mentioned above is large with respect to the boundary layer thickness, at least 10δ, and cannot be contained in our computational domain. In effect our turbulent flow triggers itself continuously, through the effect of the periodic boundary conditions, and intermittency is impossible. In contrast, Spalart's simulations, with computational boxes five times longer than ours, could show some intermittent effects at the lower Reynolds numbers. Such boxes are outside our computer capabilities, but a single experiment with a box twice as long as usual, at $Re_\theta = 300$, produced a decrease in the friction coefficient of about 3%, which is statistically significant but too small for definite conclusions.

Bandyopadhyay [18], reported an interesting experiment in which he was able to sustain a turbulent boundary layer over a transversely grooved surface which was hydraulically smooth, but which behaved as rough on account of a resonant interaction with the viscous sublayer. He could maintain a fully turbulent flow at $Re_\theta = 285$ whose bulk characteristics showed few transitional effects. His data are included as open diamonds in figure 5, and agree with our computations better than any of the others. Since part of the effect of his grooved surface is to constantly excite the layer, and thus to decrease intermittency, the agreement supports the idea that at least part of the discrepancy with other data is due to intermittent effects.

4. LAMINARISATION AND TRANSITION LENGTHS

The instantaneous skin friction, averaged over the whole computational box, shows a quasi-periodic variation

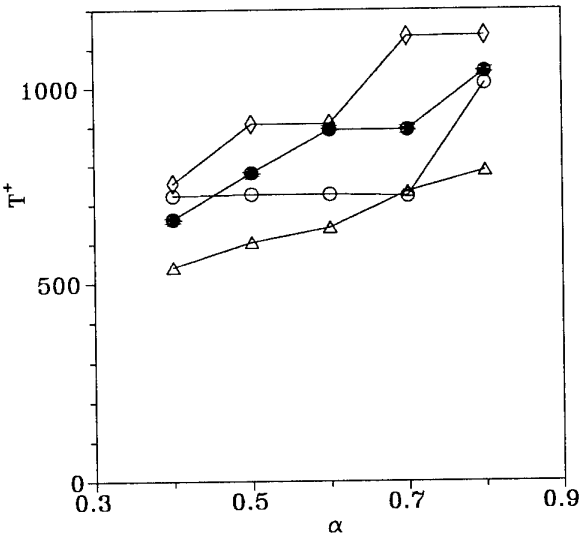

Figure 7. Average blooming period for several Re_θ, versus the hysteresis parameter, α, of the detection algorithm. See text for the detection method and for the normalisation of the data. ○: $Re_\theta = 247$, △: 299, ◇: 365, •: 502.

that was already identified and studied in [15] for the plane channel. In experimental flows, or in large computational boxes, this "blooming" cycle is not apparent because different points of the wall bloom at different moments and their contributions cancel out. In small systems, like those in the previously cited paper or the ones used here, only one or a few areas are active at each moment, and their high skin friction is seen in the average.

The length of these bursts of activity is an indication of the internal time scales of the boundary layer. Several skin friction histories are shown in figure 3. In general, these histories are always too short to measure the blooming frequency by standard spectral means, and only approximate values can be estimated. We have used a zero crossing counting technique with hysteresis, in which two thresholds are defined for the wall shear $\Omega = \partial\overline{u}/\partial y|_{\text{wall}}$, in terms of its temporal average $\overline{\Omega}$ and of its standard deviation σ. A zero crossing is defined whenever Ω crosses upwards the upper threshold $\overline{\Omega} + \alpha\sigma$ immediately after crossing downwards the lower threshold $\overline{\Omega} - \alpha\sigma$. The variation of the mean interval between crossings for several Reynolds numbers, as a function of the hysteresis parameter α, is shown in figure 7. It is normalised in wall variables with the mean wall shear $\overline{\Omega}$. Other normalisation were tried and found marginally less successful. The cycle length $\overline{\Omega}t \approx 800$, is comparable to the one identified in [15].

A history from a case just below the minimum Reynolds number for sustained turbulence is also included in Fig. 3. The flow decays to laminar, but a trace of the

blooming cycle can be found in the form of a slight waviness of the decay. More interestingly, the time scale of the decay is comparable to that of the turbulent cycle. It was shown in [15] that the cycle can be understood as the effect of a short triggering event followed by a more or less viscous decay. At low enough Reynolds numbers the trigger cannot overcome the effect of the decay, and the flow laminarises. According to that model the laminarising rate should be approximately similar to the decay rate of the blooming cycle, and the overall time scales should be comparable. The comparison of the two time histories in Fig. 3 is consistent with that view.

An interesting question is whether the length of the computational box influences the length of the blooming cycle. Two time histories for boxes whose lengths differ by a factor of two, are included in Fig. 3. The detection algorithm gives crossing periods which are about 40% longer for the long box than for the short one. The inspection of the histories suggests that this is not due to intrinsically longer cycles, some of which are almost coincident for the two boxes. The main effect seems to be that some minor cycles are missing in the long box, probably due to the statistical cancellation of their effects over the larger averaging area of the bigger box.

These considerations can be used to estimate how long a laminarising device (e.g. suction or acceleration) must be made to act on a boundary layer to damp the initial turbulence completely. The suggestion is that the total time that the device acts on a disturbance should be at least $\overline{\Omega}\Delta t \approx 800^{-1}$. Assuming a convection velocity $U_c \approx 0.5U_o$ for the important perturbations, and using values from table 1, the relaminarising length becomes $x/\theta \approx 300 - 400$. We have not been able to find experimental data for this quantity.

4.2 The bypass Reynolds number

We can now return to the original subject of this investigation, which was to compute the minimum Reynolds number at which a laminar boundary layer can be tripped into transition. The conceptual model is that the flow can be tripped if, after transition, the resulting Re_θ is within the existence range of the turbulent solution. During the transition process the momentum equation (1.1) applies, and since the friction coefficient cannot become negative without inducing separation, Re_θ cannot decrease. It follows that the minimum Reynolds number for which bypass transition can be induced coincides with the relaminarisation Reynolds number, $Re_\theta \approx 200$, and applies to perturbations which are large enough to carry the layer immediately to its turbulent state. Using the laminar relations for the Blasius profile, it corresponds to $Re_x \approx 9 \times 10^4$. Both values agree approximately with the onset of transition in the most strongly perturbed case of figures 2 and 5, and suggest that this case corresponds to the transition threshold for "infinitely" strong perturbations. That threshold also agrees approximately with the minimum Reynolds number for roughness induced transition, $Re_\theta = 230$, suggested by the results collected in [1, pg. 510].

5. CONCLUSIONS

In summary, we have developed a simple scheme for the direct numerical simulation of the flat plate turbulent boundary layer on a periodic box, and we have used it to compute the relaminarisation threshold for that flow.

Our computations give a relaminarisation Reynolds number which is consistent with available experimental estimates for the minimum Re_θ for bypass transition. Above that threshold, our flows show no transitional effects and remain fully turbulent. This is at variance with experimental results at very low Reynolds numbers, and we suggest that the difference might be connected to large scale intermittency effects that cannot be modelled within our small computational boxes. The agreement of our results with those of experiments on continuously forced boundary layers, which are expected to be relatively free from intermittency, supports that conclusion.

We have identified the time scale for turbulence growth and decay within the layer and we have related it to the minimum length over which relaminarisation devices should act to damp turbulence ($\sim 20\delta$).

6. ACKNOWLEDGEMENT

This work was supported in part by the Hermes programme of the European Space Agency, under contract to Dassault Aviation.

REFERENCES

[1] H. Schlichting. *Boundary layer theory.* McGraw-Hill, sixth edition, 1968.

[2] V.C. Patel and M.R. Head. Some observations on skin friction and velocity profiles in fully developed pipe and channel flows. *J. Fluid Mech.*, 38, 181–201, 1969.

[3] D.I.A. Poll. Transition in an infinite swept attachment line boundary layer. *Aero. Quart.*, 30, 607–629, 1979.

[4] O. Reynolds. An experimental investigation of the circumstances which determine whether the motion of water shall be direct or sinous, and of the law of resistance in parallel channels. *Phil. Trans.*, 174, 935, 1883.

[5] I.J. Wygnanski and F.H. Champagne. On transition in a pipe. Part I: The origin of puffs and slugs and the flow in a turbulent slug. *J. Fluid Mech.*, 59, 281–335, 1973.

[6] H. Tennekes and J.L. Lumley. *A first course in turbulence*, chapter 5. MIT Press, 1972.

[7] W.R.C. Phillips. The wall region of a turbulent boundary layer. *Phys. Fluids*, 30, 2354–2361, 1987.

[8] K.L. Suder, J.E. O'Brien, and E. Reshotko. Experimental study of bypass transition in a boundary layer. *NASA*, TM-100913, 1988.

[9] A.M. Savill. Synthesis of T3 test case computations. In O.Pironneau, W.Rodi, I.L.Rhyming, A.M.Savill, and T.V.Truong, editors, *Proc. 1st. ERCOFTAC Workshop*, Cambridge U. Press, 1990.

[10] R. Corral and J. Jiménez. *Direct numerical simulation of the subcritical boundary layer.* Tech. Note ETSIA/MF-921, School of Aeronautics, Madrid, 1992.

[11] J. Kim, P. Moin, and R. Moser. Turbulence statistics in fully developed channel flow at low Reynolds number. *J. Fluid Mech.*, 177, 133–166, 1987.

[12] C. Canuto, M.Y. Hussaini, A. Quarteroni, and T.A. Zang. *Spectral methods in fluid dynamics*, page 84. Springer, 1987.

[13] R. Corral and J. Jiménez. Fourier/Chebyshev methods for the incompressible Navier Stokes equations in infinite domains. In C.H.Hirsch, J.Periaux, and W.Cordulla, editors, *Computational Fluid Dynamics, 92*, pages 361–368, Elsevier, 1992. (submitted *J. Comput. Phys.*).

[14] P.R. Spalart. Direct numerical study of a turbulent boundary layer up to $Re_\theta = 1410$. *J. Fluid Mech.*, 187, 61–98, 1988.

[15] J. Jiménez and P. Moin. The minimal flow unit in near wall turbulence. *J. Fluid Mech.*, 255, 213–240, 1991.

[16] E. Laurien and L. Kleiser. Numerical simulation of boundary layer transition and transition control. *J. Fluid Mech.*, 199, 403–440, 1989.

[17] L.P. Purtell, P.S. Klebanoff, and F.T Buckley. Turbulent boundary layer at low Reynolds number. *Phys. Fluids*, 24, 802–811, 1981.

[18] P.R. Bandyopadhyay. Resonant flow in a row of small transverse cavities submerged in a turbulent boundary layer. *AIAA Paper*, 87-1235, 1987.

[19] D.E. Coles. The turbulent boundary layer in a compressible fluid. *Rand Rep.*, R403-PR, 1962.

[20] J. Jiménez. On the structure and control of near wall turbulence. *Phys. Fluids*, A 6, 944–953, 1994.

[21] J.H. Preston. The minimum reynolds number for a turbulent boundary layer and the selection of a transition device. *J. Fluid Mech.*, 3, 373–384, 1958.

[22] I.J. Wygnanski, M. Sokolov, and D. Friedman. On transition in a pipe. Part II: The equilibrium puff. *J. Fluid Mech.*, 69, 283–304, 1975.

[23] J. Jiménez. Transition to turbulence in two dimensional poiseuille flow. *J. Fluid Mech.*, 218, 265–297, 1990.

[24] I.J. Wygnanski, M. Sokolov, and D. Friedman. On a turbulent spot in a laminar boundary layer. *J. Fluid Mech.*, 78, 785–819, 1976.

A Flamelet Model for Turbulent Unpremixed Combustion.

V.R. Kuznetsov

Central Institute of Aviation Motors and Scientific Research Center ECOLEN
2, Aviamotornaya, 111250, Moscow, Russia.

1. Introduction.

Combustion theory is an applied science which is syntheses of several fundamental theories such as chemistry, heat and mass transfer theory, hydrodynamics, turbulence etc. Now the knowledge of these theories is adequate to make calculations for practical purposes. However some difficulties still remain unresolved. The most important one is associated with the steep dependence of chemistry on temperature. As a result chemistry is confined to very thin zones (flamelets). Hence very large memory and speed of computers are needed to resolve flamelets in DNS. This difficulty is aggravated by the large number of intermediate species.

The use of turbulence closures does not help since one has to assume that eddy diffusivities of reacting species and their pdf's (which are needed to average chemistry rates) are the same as that of conserved scalar. There are several examples indicating that these assumptions may lead to significant errors [1]. Therefore there is a need to develop some new approach.

2. Flamelet model for turbulent unpremixed flames.

As was shown in [1-5] the flamelet conception leads to drastic simplification of fluid dynamics equations. It will be considered here for unpremixed combustion. In this case the highest temperature and the highest chemistry rate are observed on the stoichiometric surface

$$z = \frac{St \cdot c_f - c_o + 1}{1 + St} = \frac{1}{1 + St} = z_s$$

where z is mixture fraction, c_f and c_o are mass fractions of fuel and oxidant and St is stoichiometric ratio. Quantity z would be equal to fuel concentration, if combustion were absent. It is calculated from the equation

$$\rho \frac{\partial z}{\partial t} + \rho u_k \frac{\partial z}{\partial x_k} = \nabla D \rho \nabla z \qquad (1)$$

Consider now heat and mass transfer equations

Paper presented at the 74th Fluid Dynamics Symposium on "Application of Direct and Large Eddy Simulation to Transition and Turbulence" held at Chania, Crete, Greece, in April 1994.

$$\rho\frac{\partial c_\alpha}{\partial t}+\rho u_k\frac{\partial c_\alpha}{\partial x_k}=\nabla D\rho\nabla c_\alpha+\rho W_\alpha \qquad (2)$$

where c_α is enthalpy or species mass fraction and ρW_α is the chemical source terms. Let us choose some frame moving with a velocity of some point located at the surface $z=z_s$. This velocity is equal to

$$w_k=-\frac{\partial z}{\partial t}\frac{\partial z}{\partial x_k}\Bigg/\left(\frac{\partial z}{\partial x_k}\right)^2 \qquad (3)$$

Using Eqs.(1) and (3) one has

$$w_k=u_k+\frac{\nabla D\rho\nabla z}{\rho\left(\frac{\partial z}{\partial x_k}\right)^2}\frac{\partial z}{\partial x_k} \qquad (4)$$

The last term in Eq.(4) has the Kolmogorov scaling. Hence each surface $z=const$ moves relatively to the media with the Kolmogorov velocity v_k. Hence in a moving frame the velocity within a flamelet would be an order of v_k Thus the left hand side of Eq.(2) is an order of $\rho_s c_\alpha^{(s)} v_k/\delta$ where δ is the flamelet thickness and subscript s denotes stoichiometric surface. On the other hand the first term on the right hand side of Eq.(2) is an order of $D\rho_s c_\alpha/\delta^2$. Comparing both estimates one can conclude that the left hand side of Eq.(2) can be neglected if $\delta\ll\eta$ where η is the Kolmogorov scale.

Since flamelets are thin one can neglect also variations of $D\rho$ and derivatives in the directions tangent to surface $z=z_s$. Therefore Eq.(2) is simplified as

$$D\frac{\partial^2 c_\alpha}{\partial z^2}+W_\alpha=0 \qquad (5)$$

where n is distance along the direction of normal to surface $z=z_s$. It is convenient to use z as an independent variable instead of n. Since dz/dn is almost constant within a flamelet one has final equation

$$N\frac{d^2 c_\alpha}{dz^2}+W_\alpha=0 \qquad (6)$$

where $N=D\nabla z^2$ is scalar dissipation.

Consider now the case $\delta\gg\eta$ using ideas of LES. All quantities should be averaged over distance which is somewhat less than δ and subgrid diffusivity should be

introduced. The derivation of Eq.(6) would be the same. The final result remains unchanged since a diffusivity is not present explicitly in Eq(6). There is but one difference: the scalar dissipation averaged over a flamelet should appear instead of true scalar dissipation. This difference plays a minor role since it was proved in [1] that the source term in all combustion systems is of such kind that solutions of Eq.(6) depended weakly on N.

Now boundary conditions should be formulated. This problem was analyzed in [6]. It was found that solutions are weakly dependent on N due to the small thickness of flamelets in z-space. Therefore boundary conditions can be posed at z=1 (pure fuel) and z=0 (pure oxidizer).

3. Scalar pdf.

Since the flamelet model was tested using turbulence closure there was a need to have the joint pdf of z and N. Theory [7] (see also [1]) was used for this purpose. It was based on assumption about independence of large-scale fluctuations (which affect the scalar field z) and small-scale fluctuations (which affect the field of scalar dissipation). This assumption inevitably led to intermittency since meaningful solution of the pdf equation had the following form

$$P(z) = (1-\gamma)\delta(z) + \gamma P_t(z)$$

where γ is intermittency factor and P_t denotes conditional pdf within a turbulent fluid where scalar fluctuations are observed.

Calculations were based on two particular solutions of the pdf equation. The first one was valid in the regions of negligible intermittency ($\gamma \approx 1$), where almost Gaussian pdf was obtained. The second one was valid in the intermittent region ($\gamma \ll 1$). It was expressed through the Airy function

$$\rho(z)P_t(z) = \frac{1.404}{\bar{z}_t}\,\mathrm{Ai}\left(\frac{1.788z}{\bar{z}_t} - 2.338\right)\rho(\bar{z}_t) \qquad (7)$$

where subscript t denotes conditional averaging over a turbulent fluid ($\bar{z}_t = \bar{z}/\gamma$).

There is one adjustable parameter in Eq.(7). Hence all the non-dimensional moments such as σ_t/z_t are some constants. Here $\sigma_t = \sqrt{\overline{(z-\bar{z}_t)^2}}$. They were found through the solution of eigen value problem for the pdf equation without any empirical information. In particular one has $\sigma_t/\bar{z}_t = 0.555...$ which is in close agreement with numerous experimental data (see a review in [1]). These data indicate also that $\sigma_t/\bar{z}_t$ is

almost constant through the whole intermittent region. Therefore very simple approximation of the pdf and intermittency factor can be found. One has

$$\overline{z^2} = \bar{z}^2(1+\sigma^2/\bar{z}^2) = \gamma\overline{z_t^2} = \gamma^{-1}\bar{z}_t^2(1+\sigma_t^2/\bar{z}_t^2)$$

or

$$\gamma = (1+\sigma_t^2/\bar{z}_t^2)/(1+\sigma^2/\bar{z}^2) \qquad (8)$$

Suppose now that σ and $\bar{z}$ are calculated. Since the nominator in Eq.(8) is known then γ can be calculated also. One has $\gamma>1$ if $\sigma<0.555\bar{z}$. Therefore Eq.(8) is valid only if $\sigma>0.555\bar{z}$ and the boundary between intermittent and non-intermittent regions can be defined using the relation $\sigma=0.555\bar{z}$. If $\sigma<0.555\bar{z}$ the Gaussian pdf should be assumed. Otherwise Eq.(7) should be used.

All assumptions of the theory as well as its predictions were verified experimentally (see [1] for more details).

Quantities $\bar{z}$, σ, $\overline{N}$ were calculated using turbulence closure based on equations for turbulence energy, eddy viscosity and σ (see [1] for more details).

Since solutions of Eq.(6) depend weakly on N, the scalar dissipation fluctuations were neglected, i.e. it was assumed that $N=\overline{N}_t$ in Eq.(6).

4. Some tests of the flamelet model.

These tests were performed in laboratory jet diffusion flames. The first one was calculation of hydrocarbon concentration. Since many hydrocarbons are observed in flames (which is due to pyrolisis) quantity c_f in C_3H_8 flame was calculated according to the rule

$$c_f = \sum_i \frac{12}{12+n_i} c_i$$

where c_i is concentration of i-th hydrocarbon and n_i is its H/C atoms ratio. Quantity c_f would be the initial fuel concentration in the absence of pyrolisis. There are some indirect evidences based on laminar premixed flame calculations [8] indicating that the rate of conversion of hydrocarbons to CO is much more than the rate of CO oxidation. So fast chemistry assumption was used to calculate c_f ($c_f=0$ if $z<z_s$, $c_f=(1-z)/(1-z_s)$ if $z>z_s$). Results are shown in Fig.1.

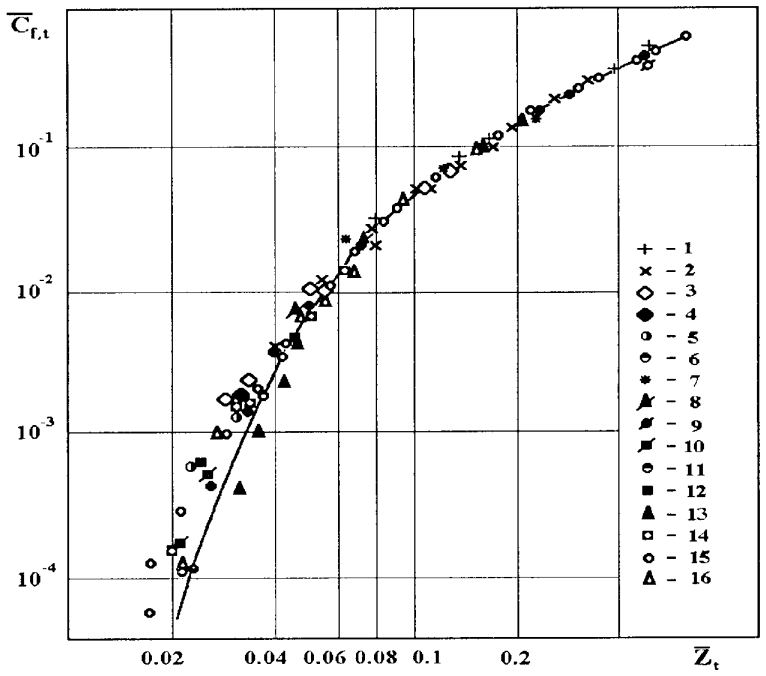

Figure 1. Quantity c_f in propane turbulent diffusion flames from [1] I- d=3mm, u_0=19.8m/s 1) x/d=40, 2) x/d=80, 3) x/d=120, 4) x/d=160, 5) x/d=200,6) x/d=240; II- d=6mm, u_0=10.7m/s 7) x/d=40, 8) x/d=80, 9) x/d=120, 10) x/d=160; III- d=3mm 11) u_0=19.8m/s, 12) u_0=14.2m/s, 13) u_0=28.2m/s;IV- d=6mm 14) u_0 =7.3m/s, 15) u_0=10.7m/s 16) u_0=14.9m/s. Symbols 1-10 correspond to radial profiles. Symbols 11-16 correspond to axial profiles. Solid line denotes calculations.

It is seen in Fig.1 that results depend neither on jet diameter nor on its velocity u_0. Hence the fast chemistry assumption is valid here. Therefore this was the test of the pdf model. Note that the far tails of the pdf are quite essential. For example the lowest calculated value of $c_{f,t}$ in Fig.1 would be an order of magnitude less if Gaussian pdf was used. Some other tests are shown in Figs.2-4.

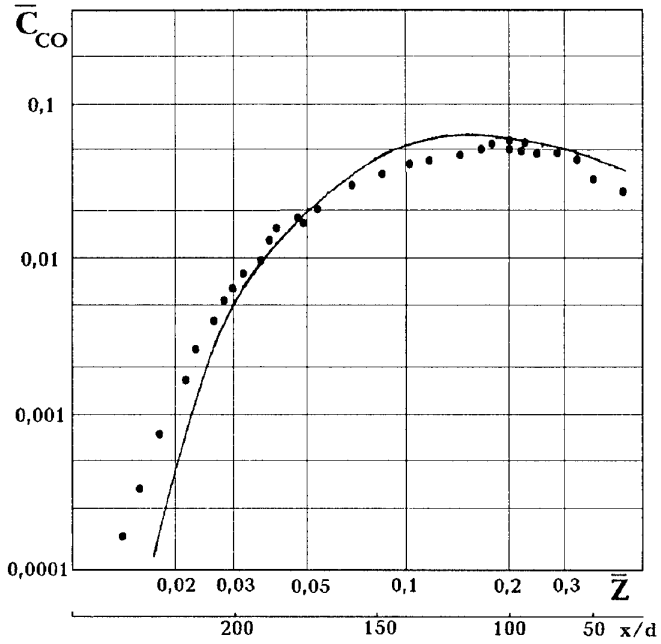

Figure 2. Axial profile of CO concentration in propane flame from data [1], d=3mm, u_0=19.8m/s. Solid line denotes calculations based on Eq.(6).

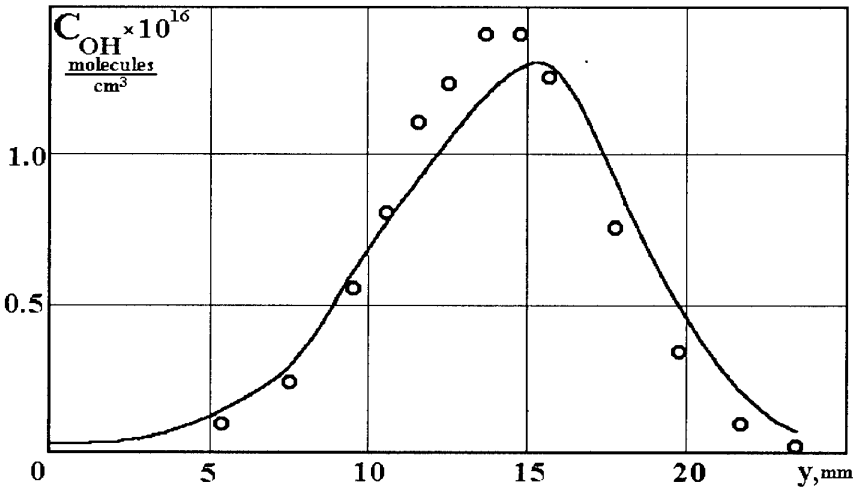

Figure 3. Hydroxyl concentration in H_2-air diffusion flame from data [9], d=3.18mm, u_0=285m/s, u_{air}=12.5m/s, x/d=50.

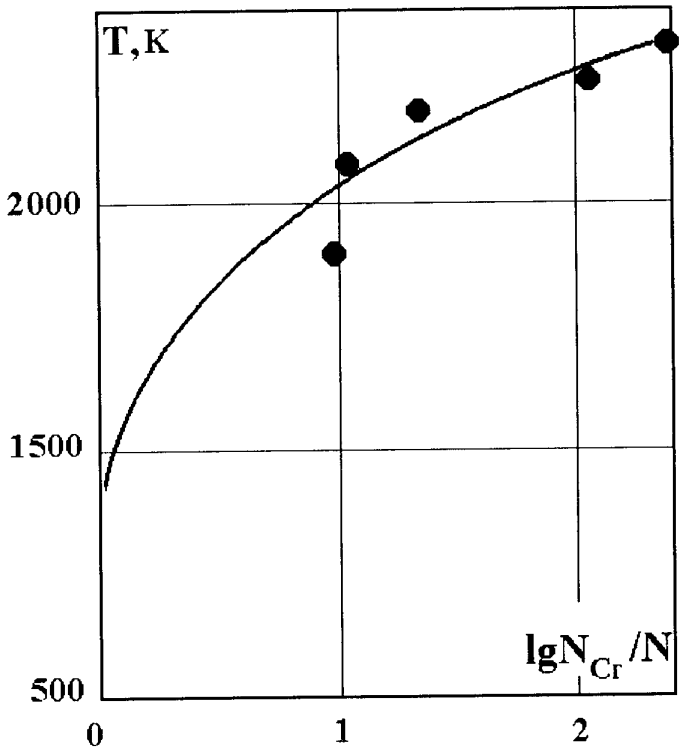

Figure 4. Conditionally averaged flame temperature in H_2-Ar-air system from data [10]. Condition is $z=z_s$. d=5.2mm, u_0=75-175m/s, u_{air}=9.2m/s, $N_{cr}=83s^{-1}$ is the value of N at flame extinction.

5. NOx formation.

Calculations of NO_x in C_3H_8 and H_2 flames were based on the Zeldovich mechanism using partial equilibrium assumption (two-body reactions were equilibrated). Flame radiation (which is quite important in laboratory flames) and buoyancy were taken into account (see [1] for more details). Results are shown in Fig.5 where No_m is maximum mass fraction of NO at the flame axis and $\tau=d/u_0$. It was found that when the scalar dissipation (or mixing rate) was increased then drop of flame temperature was accompanied by big rise of atomic oxygen concentration. The influence of both factors was almost counterbalanced due to the particular value of activation energy of reaction

$N_2 + O = NO + N$.

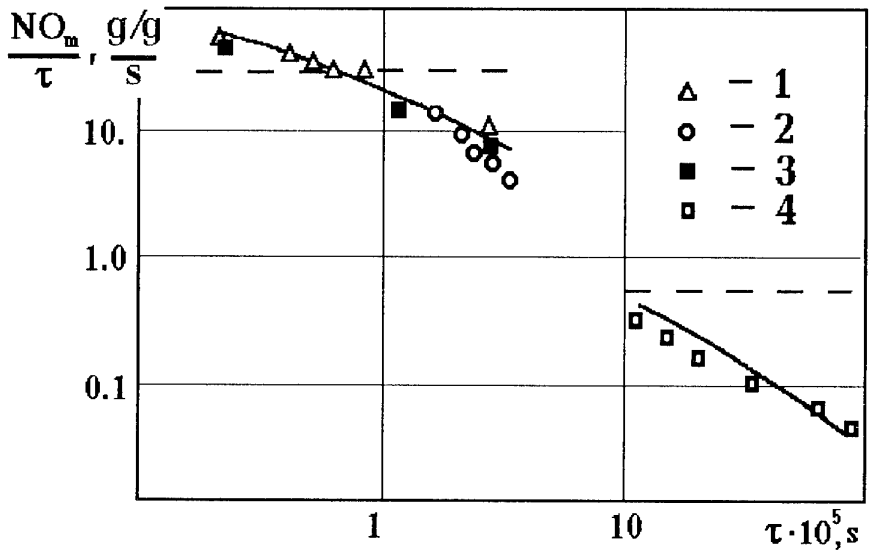

Figure 5. Maximum concentration of NO at the flame axis. 1- [1], H_2-air flame; 2- [11], H_2-air flame; 3- [12], H_2-air flame; 4- [1], C_3H_8-air flame. Solid lines denote calculations based on Eq.(6). Dotted lines denote calculations for adiabatic flames (where all species except NO are equilibrated).

Therefore the variation of N was relatively unimportant. The mixture fraction fluctuations were unimportant completely since the main NO_x production occurred in the vicinity of the surface $z=z_s$.

Therefore quite simple method was developed for calculation of NO_x pollution for industrial combustors. For this purpose N was assumed to be some constant (depending only on the combustor geometry) divided by the residence time. It was used for 15 aviation gas turbine combustors. Empirical constant for each combustor was fitted using NO_x emission data obtained at four regimes (from idle to take-off). Its variation from one combustor to another was not very large (no more than two times). Results are shown in Fig.6 where experimental NO_x emission index $EINO_x$ is plotted vs. calculated one.

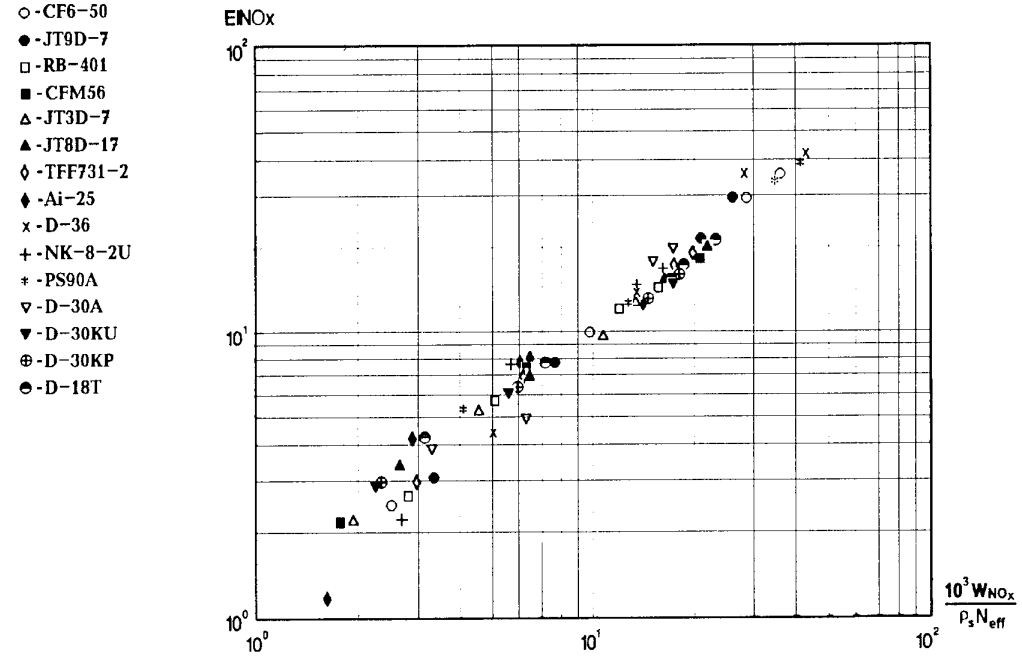

Figure 6. NO_x emission index in gas turbine combustors.

6. Conclusion.

The data presented in Secs.4 and 5 indicate that the flamelet model provides adequate description of turbulent unpremixed combustion. Therefore big simplification of the problem is obtained since Eq.(6) can be solved before the start of hydrodynamical calculations and there is no need to perform simultaneous hydrodynamical and chemical calculations. If turbulence closure is used then all the difficulties associated with the need to model reacting scalar pdf's and eddy diffusivities of reacting species can be avoided.

References.

1. Kuznetsov V.R., Sabelnikov V.A. Turbulence and Combustion (P.A.Libby, Ed.), Hemisphere, 1990.

2. Williams F.A. in Turbulent Mixing in Non-Reacting and Reacting Flows (S.N.B. Murthy, Ed.), Plenum, NY, 1975, 189.

3. Kuznetsov V.R. Mehan. Zhidkosti Gaza, 1977, 3, p.32

4. Kuznetsov V.R. Mehan. Zhidkosti Gaza, 1982, 6, p.3

5. Peters N. Progr. Ener. Combust. Sci., 1984, 10, p.319

6. Buriko Yu.Ya., Kuznetsov V.R., Volkov D.V., Zaitsev S.A., Uryvskiy A.F. Combustion and Flame, 1994,

7. Kuznetsov V.R. Mehan. Zhidkosti Gasa, 1972, 5, p.86.

8. Tsatsaronis G. Combustion and Flame, 1978, 33, p.217.

9. Drake M.C., Pitz R.W., Lapp M., Fenimore C.P. Twentieth Symp. (Int.) on Combustion, The Combustion Institute, 1984, p.327.

10. Magre P., Dibble R. AIAA Pap. 0378 (1978)

11. Bilger R.W., Beck R.E. Technical Note F-67, The Univ. of Sydney, 1974.

12. Lavoie G.A., Schlader A.F. Combust. Sci. Technol., 1974, 8, p.215.

Direct Numerical Simulation for Premixed Turbulent Combustion Modelling

R.S.Cant
Department of Mechanical Engineering,
UMIST,
PO Box 88, Manchester M60 1QD,
United Kingdom.

Summary

Recent advances in computer power have made it feasible to carry out Direct Numerical Simulation (DNS) of fundamental test problems in turbulent combustion. Nevertheless the requirements in terms of numerical grid resolution remain very severe and engineering computations will remain beyond the reach of DNS for some time to come. Thus there is an undiminished role for statistical modelling using traditional moment-closure techniques and DNS can be used to provide fundamental data in support of such modelling. The present paper describes a specific example of the use of DNS results to improve the quality of a well-established model of premixed turbulent combustion. A brief outline of the model formulation is given, followed by a short description of the DNS and post-processing techniques employed. Some results of immediate utility are presented in order to illustrate the usefulness of the approach, and the parameterisation of some further data is discussed in detail. The significance of the main improvements to the modelling is indicated and some remaining limitations are discussed. The prospects for future model refinement by improved DNS are examined and found to be excellent.

List of symbols

Roman

a_t	Tangential strain rate
C_u	Constant, eqn.(12)
C_τ	Constant, eqn.(10)
c	Reaction progress variable
c^*	Chosen value of c
g	Constant, eqn.(3)
h_m	Mean curvature of flamelet
I_0	Strain and curvature correction
k_t	Strain rate function
$\hat{L}_y$	Length scale of flamelet wrinkling
$\underline{N}$	Local flame normal vector
P	Probability density function
P_{11}	Autocorrelation on flame surface
p	exponent of ε
R	Radial autocorrelation offset
S_{ij}	Strain rate tensor
u_i	Fluid velocity i-component
u'	Rms turbulence intensity
u_L^0	Unstrained laminar flame speed
u_η	Kolmogorov velocity scale
W	Integrated reaction rate in flamelet
$\bar{w}$	Mean production rate of $\tilde{c}$
w_c	Instantaneous production rate of c
x, y, z	Cartesian coordinates
Y, Z	Cartesian autocorrelation offsets

Greek

η	Kolmogorov length scale
μ	Mean of $\ln \varepsilon$
ν	Kinematic viscosity
ρ	Density

Paper presented at the 74th Fluid Dynamics Symposium on "Application of Direct and Large Eddy Simulation to Transition and Turbulence" held at Chania, Crete, Greece, in April 1994.

Σ	Flame surface area per unit volume
σ_a	Standard deviation of strain rate
$\bar{\sigma}_y$	Flame orientation factor
σ_ε	Standard deviation of $\ln \varepsilon$
τ_η	Kolmogorov time scale

Overbars, etc.

$\bar{\phi}$	Reynolds average of quantity ϕ
$\tilde{\phi}$	Favre average of quantity ϕ
ϕ''	Favre fluctuation of quantity ϕ

Introduction

Turbulent combustion is a phenomenon of major technological importance. An overwhelming proportion of the world's energy production depends upon combustion in some form, and practical combustion systems almost invariably contain a turbulent gaseous flow field. The present work is concerned with premixed turbulent combustion in which the reactants are already mixed at the molecular level before combustion begins. This mode of combustion is relevant to spark-ignition automobile engines, to aero-engine reheat systems and to the analysis and prevention of accidental explosions in the petrochemical industry.

Turbulent combustion involves chemical reaction, heat release and transport of heat and mass by both molecular diffusive and bulk-convective motion. It is perhaps paradoxical that in general the small-scale molecular processes of reaction and diffusion are well understood while the larger-scale behaviour of the turbulent flow field still poses significant problems. More importantly, the details of the strong mutual interaction between the turbulence and the combustion chemistry remain obscure despite recent progress in experimental diagnostic techniques [1]. Nevertheless experimental observation has confirmed [2] that in many systems of practical interest premixed combustion takes place in so-called laminar flamelets. These occur when the timescales of the coupled molecular reaction and diffusion processes are at least as short as the shortest (Kolmogorov) timescales of the turbulence. Then all of the chemical reaction takes place in thin sheet-like interfaces separating unburned reactants from fully-burned products. Such reaction sheets have the same local structure as a wrinkled laminar flame subjected to straining and distortion by the turbulent flow field. This important finding offers a rational basis for the incorporation of combustion chemistry and heat release into turbulent combustion modelling based on traditional statistical moment- closure methods. A model formalism due to Bray, Moss and Libby (BML) [3] has proved successful in this regard, combining a second-moment (Reynolds stress) closure approach with a soundly-based framework for the construction of sub-models for the mean rates of molecular transport and chemical reaction. Existing sub-models are based on the best available understanding of the underlying physics, but a number of major uncertainties remain. Thus there is an urgent need for better statistical data in order to validate existing sub-models and to support the development of new ones.

Such data is best obtained by experiment wherever possible. In many cases, however, the required data is simply not accessible by means of current experimental techniques. An alternative approach, made feasible by recent advances in computer power, is to make use of Direct Numerical Simulation (DNS) of turbulent flames. This approach begins by accepting the need to resolve numerically the smallest length and time scales of both the turbulent motion and the reaction-diffusion zones within the flame. The largest problem that can be tackled is then set by the size of the available computing resources. This places a severe limit on the maximum attainable Reynolds number, but does al-

low for the collection of relevant and useful statistical data. In particular, DNS allows for the collection of data which by nature is three-dimensional and time-dependent.

The present paper describes the application of statistical results obtained from combustion DNS to the development of a mean turbulent reaction rate sub-model within the BML framework. The reaction rate sub-model is described and the need for supporting data is indicated. A brief outline is given of the DNS procedure and of the post-processing methods applied to the data. Results for the main quantities of interest are presented, and discussed in terms of the parameterisation necessary for modelling. The improved model formulation is explained in detail and is offered as an example of the usefulness of DNS in combustion modelling.

Model Formulation

Within the Bray-Moss-Libby model for premixed turbulent combustion modelling [3] the chemical state of the reacting medium is described by means of a reaction progress variable c defined to have the value zero in fresh reactants and the value unity in fully burned products. A precise definition of c may be given if required in terms of the mass fractions of individual chemical species present in the reacting mixture [4, 5]. The conservation equation for the Favre-averaged progress variable $\tilde{c}$ in Cartesian tensor notation is

$$\frac{\partial}{\partial t}\bar{\rho}\tilde{c} + \frac{\partial}{\partial x_k}\bar{\rho}\tilde{u}_k\tilde{c} = \bar{w} - \frac{\partial}{\partial x_k}\overline{\rho u_k'' c''} \quad (1)$$

where $\bar{\rho}$ is the mean density, $\tilde{u}_k$ is the Favre-mean velocity and $\overline{\rho u_k'' c''}$ is the turbulent flux of progress variable given within the BML formalism by a second-moment closure model. The principal source term is the mean turbulent reaction rate $\bar{w}$ is given within the flamelet formulation by the expression

$$\bar{w} = \rho_R u_L^0 I_0 \Sigma \quad (2)$$

where $\rho_R u_L^0 I_0$ represents the reaction rate per unit surface area of the flamelet and Σ is the flamelet surface area per unit volume. Each quantity in this expression must be determined separately. The unburned density ρ_R is either known or can easily be deduced from the available thermochemical data. The unstrained planar laminar burning velocity u_L^0 likewise depends on the thermochemical properties of the unburned gas mixture but not in any simple manner. In general values of u_L^0 must be obtained as a function of mixture strength, pressure and unburned gas temperature either by means of a correlation of experimental data [6] or by computation, solving numerically the large set of stiff equations describing the full laminar flame chemistry [7]. Both the flamelet surface area per unit volume Σ and the strain and curvature correction factor I_0 depend on the details of local interactions between the flamelet and the turbulent flow field. The former is a highly dynamic quantity described by its own exact balance equation [8, 9] containing terms relating mainly to strain and curvature effects. A simple algebraic expression for Σ is [10]

$$\Sigma = \frac{g\bar{c}(1-\bar{c})}{\bar{\sigma}_y \hat{L}_y} \quad (3)$$

where $\bar{c}$ is the Reynolds-averaged progress variable, g is a derived (not empirical) constant having a value of about 1.5 and $\hat{L}_y$ is an integral length scale associated with flame wrinkling. The quantity $\bar{\sigma}_y$ is an orientation factor given by the mean normal to the flame conditioned upon being on a surface of constant mean progress variable.

The factor I_0 accounts for the effects of straining and curvature on the local laminar flamelet. It is related to the properties of the laminar flame through the integral

$$I_0 = \int_{-\infty}^{\infty}\int_{-\infty}^{\infty} \frac{W(a_t, h_m)}{W(0,0)} \times P(a_t, h_m) da_t dh_m \quad (4)$$

where a_t is the hydrodynamic strain rate, i.e. the velocity divergence in the tangent plane of the flamelet, h_m is the geometrical mean curvature of the flamelet and $W(a_t, h_m)$ represents the integral of the reaction rate taken through the flamelet:

$$W(a_t, h_m) = \int_{-\infty}^{\infty} w_c(a_t, h_m; z)dz \quad (5)$$

The reaction rate w_c is the local and instantaneous production rate of the reaction progress variable c within the flamelet. Given a suitable definition of c in terms of species mass fractions it is possible using (4) and (5) to include chemistry of arbitrary complexity in the model formulation. In essence the evaluation of the integrated reaction rate W and hence the factor I_0 may be carried out in advance, and the results stored together with values of the unstrained burning velocity u_L^0 in a "flamelet library" for interpolation during a subsequent turbulent flame computation [4, 5].

In order to evaluate I_0 from W it is necessary to determine the joint pdf $P(a_t, h_m)$ and to parameterise it in terms of known model quantities. This is the principal subject of the remainder of the present paper.

Direct Numerical Simulation and Results

The data used to deduce the model improvements described in the preent paper were obtained by Direct Numerical Simulation of the propagation of a premixed flame propagating through isotropic turbulence [11]. The full three-dimensional Navier-Stokes equations were solved together with an equation for a reaction progress variable. One-step Arrhenius kinetics were used and heat release was assumed to be small. The computational domain consisted of 128 nodes in each spatial dimension with periodic boundary conditions. A pseudo-spectral technique was employed with second-order Runge-Kutta time advancement. Initialisation of the turbulence field was carried out using a prescribed spectral distribution of turbulence energy, and following a short settling period two planar laminar flames were initiated back-to-back near to the central $y - z$ plane of the domain. The flames propagated outwards in the positive and negative x-directions through the field of decaying turbulence until either the edge of the domain was reached or the turbulence length scale was judged to have become too large. Each run of the simulation took approximately 15 hours of CPU time on a Cray Y-MP and produced about 15 sets of full-field data on all variables. Data from four separate runs, made using different initial turbulence intensity, were studied at several different stages during the flame propagation [12]. In every case considerable distortion of the flames was observed, with the turbulent flame speed rising rapidly to a maximum before decaying slowly in time with the turbulence.

Extensive post-processing of the results was undertaken in order to extract quantities of interest. Surfaces of constant reaction progress variable were located by solving along grid lines at constant (y, z) for the locus $x(c = c^*), c^* = 0.1 \ldots 0.9$ using cubic-spline interpolation coupled with a bisection technique for root-finding. Each progress variable surface was found to be continuous and consisted of at least 128^2 sample points. Derivatives of progress variable and velocity were obtained in spectral space for best accuracy and were interpolated along grid lines onto surface points by means of cubic splines. The components of the local normal vector $\underline{N} = -\nabla c/|\nabla c|$ followed immediately, and the tangential strain rate a_t was computed by forming the full strain rate tensor $S_{ij} = 1/2(\partial u_i/\partial x_j + \partial u_j/\partial x_i)$ at each surface point and rotating it into surface coordinates by aligning one direction with the

local normal. Similarly, the local values of the two principal curvatures of the surface were obtained by forming the tensor of gradients of the normal vector, rotating it into surface coordinates and solving the resulting eigenvalue problem in two dimensions. Surface pdf data was collected by sampling each of the quantities of interest over all surface points. Results for the strain and curvature pdfs are shown in Figure 1. The pdf of surface strain rate (Fig.1a) has positive mean, indicating that the effect of straining is extensive on average, but there is a significant negative tail. In this constant-density simulation there is no dilatational straining and little variation of the pdf with progress variable through the flame. The mean curvature h_m is the arithmetic mean of the two principal curvatures of the surface and its surface pdf is shown in Fig.1b. The mean is zero, but there is slightly greater probability of large negative curvatures. This corresponds to the formation of highly-curved features left behind by Huygens-type propagation of the flame. For modelling purposes a most useful result is the surface joint pdf of strain and curvature shown as a contour plot in Fig.1c. This demonstrates that there is little or no correlation between strain and curvature at a surface point, so that the joint pdf may be decomposed as the product of the marginal pdfs of strain rate and mean curvature.

Due to the planar initial conditions and the periodic boundary conditions the turbulent flames remained statistically planar throughout. Thus, surfaces of constant mean progress variable $\bar{c} = c^*$ remained parallel to $y-z$-planes within the computational domain. These mean surfaces were located by averaging the progress variable over $y-z$ planes on the grid, interpolating and solving in the x-direction as before. This information enabled the collection of pdf data conditioned on mean progress variable, leading to the evaluation of corresponding conditional mean quantities. For example, the orientation factor $\bar{\sigma}_y$, defined as the mean of the local normal component in the direction of mean propagation, was obtained by constructing the pdf of the x-wise normal component conditioned on being on a surface of mean progress variable. A typical unconditional pdf of the x-wise component of $\underline{N}$ is shown in Fig.2a, yielding a mean value of 0.78, virtually independent of position in c-space. The corresponding conditional pdf is shown in Fig.2b, from which the mean $\bar{\sigma}_y$ was evaluated at 0.52, in this case virtually independent of $\bar{c}$ and in good agreement with experiment [13]. The roughness of the conditional pdf by comparison with the unconditional result is a reflection of the severe reduction in sample size suffered as a consequence of conditioning.

Finally, the length scale $\hat{L}_y$ was estimated using a procedure based on its definition [10, 13]. The procedure is a two-dimensional analogue of a technique for the interpretation of experimentally-obtained laser sheet photographs on which the flame appears as a line of constant instantaneous progress variable [13]. This instantaneous contour may be intersected by a contour of constant mean progress variable and the value of c obtained by running along the mean contour forms a square wave alternating rapidly between zero and unity. The length scale $\hat{L}_y$ is then given by the correlation length of the square wave, which may be interpreted as the integral length scale for flame surface wrinkling. In the present work, an instantaneous progress variable surface $x(c = c^*)$ was intersected in three dimensions by a selected $\bar{c}$-plane. This resulted in a two-dimensional square wave having the value unity for $c > \bar{c}$ and zero for $c \leq \bar{c}$. An example of one such square-wave is shown in Fig.3a. Each line within the plane pro-

duced a one-dimensional square wave similar to those in the previous experimental study. A two-dimensional autocorrelation of the two-dimensional square wave leads to the quantity

$$P_{11}(Y,Z) = \overline{c(y,z)c(y+Y,z+Z)} \quad (6)$$

A plot of the autocorrelation P_{11} is shown in Fig.3b where the strong exponential central peak is clearly visible. The isotropy of the distribution of c in the plane is reflected in the isotropy of the autocorrelation, which may be seen very clearly in the contour plot of P_{11} shown in Fig.3c. Thus the two coordinates Y and Z may be replaced by a single radius R, and an integration of P_{11} over R leads directly to $\hat{L}_y$:

$$\hat{L}_y = \int_0^\infty \frac{P_{11}(R) - \bar{c}^2}{\bar{c}(1-\bar{c})} dR \quad (7)$$

The autocorrelations and integrations were carried out numerically using standard routines, and yielded values for $\hat{L}_y$ close in magnitude to the integral length scale of the turbulence and largely independent of $\bar{c}$. Very few values could be computed from the available data and no firm conclusions could be drawn concerning the dependence of $\hat{L}_y$ on local turbulence quantities.

Parameterisation, Modelling and Discussion

The results shown in Fig.1 for the surface pdfs of strain and curvature are of direct relevance in modelling. The observed lack of correlation between the strain rate a_t and the mean curvature h_m implies that they may be assumed to be statistically independent and that the joint pdf $P(a_t, h_m)$ may be decomposed into the product of the marginal pdfs $P(a_t)$ and $P(h_m)$. Since the surface mean of the mean curvature is zero it is tempting to assume further that the net effect of curvature on the local laminar flamelet is zero. This is true only if the local integrated reaction rate (5) is an odd function of the curvature for all strain rates. There is evidence [14] to suggest that this is true at least for small values of the mean curvature: the net effect of straining appears to be rather larger. Integrating over h_m in (4) then yields

$$I_0 = \int_{-\infty}^{\infty} \frac{W(a_t)}{W(0)} P(a_t) da_t \quad (8)$$

where now it is necessary to parameterise only the marginal pdf of the strain rate a_t. An excellent representation for this pdf is the Gaussian distribution

$$P(a_t)da_t = \frac{1}{\sqrt{2\pi}\sigma_a} \exp\left[-\frac{(a_t - \bar{a}_t)^2}{2\sigma_a^2}\right] da_t \quad (9)$$

where the standard deviation σ_a is given in terms of the Kolmogorov time scale τ_η as

$$\sigma_a = C_\tau / \tau_\eta \quad (10)$$

In a similar manner the mean $\bar{a}_t$ is represented by

$$\bar{a}_t = k_t / \tau_\eta \quad (11)$$

where u_η is the Kolmogorov velocity and the function k_t is expressed as

$$\begin{aligned} k_t &= \bar{a}_{t0}, \quad 0 \le \frac{u_L^0}{u_\eta} \le 1; \\ k_t &= \bar{a}_{t0} \exp\left[C_u \left(1 - \frac{u_L^0}{u_\eta}\right)\right], \quad \frac{u_L^0}{u_\eta} > 1 \end{aligned} \quad (12)$$

Values of the constants C_τ, $\bar{a}_{t0}$ and C_u have been deduced from DNS results [12, 15] as 0.45, 0.28 and 0.25 respectively.

This parameterisation of the strain rate pdf in terms of Kolmogorov quantities leads to a formulation for closure of the turbulent reaction rate model. Standard expressions for the Kolmogorov length scale, time scale and velocity are

$$\eta = (\nu^3/\varepsilon)^{\frac{1}{4}}; \quad \tau_\eta = (\nu/\varepsilon)^{\frac{1}{2}}; \quad u_\eta = (\nu\varepsilon)^{\frac{1}{4}} \quad (13)$$

where ν is the kinematic viscosity and ε is the dissipation rate of turbulent kinetic energy. In a turbulent reacting flow field several uncertainties remain concerning the interpretation of these expressions. The sharp increase in temperature across the flamelet results in an order of magnitude increase in the kinematic viscosity, but any corresponding changes in the viscous dissipation rate are difficult to estimate due to the effects of thermal expansion on the local velocity field. Thus it is not clear whether ν and ε are to be taken as instantaneous values, or unconditional mean values, or some form of conditional mean values, conditioned for example on the instananeous thermochemical state as expressed through the reaction progress variable. Arguments based on experimental data may be advanced to support any or all of these viewpoints [14] and it is here that a major uncertainty remains. Nevertheless, for the purpose of modelling it is necesary to make some assumptions. It is at least probable that there will be a significant difference in the Kolmogorov length, time and velocity scales between reactants and products. Thus, at any point within the turbulent reacting flow field the Kolmogorov scales must be interpreted as local mean values:

$$\begin{aligned} \eta &= \nu^{(3/4)}\langle\varepsilon^{(-1/4)}\rangle \\ \tau_\eta &= \nu^{(1/2)}\langle\varepsilon^{(-1/2)}\rangle \\ u_\eta &= \nu^{(1/4)}\langle\varepsilon^{(1/4)}\rangle \end{aligned} \qquad (14)$$

In most current turbulent combustion models a balance equation is solved for the Favre-averaged viscous dissipation $\tilde{\varepsilon}$. Since this is a mass-weighted quantity it naturally favours the contribution to dissipation from the high-density unburned gas over that from the low-density fully-burned products. No method for decomposing $\tilde{\varepsilon}$ formally into reactant and product conditional mean values currently exists since these quantities themselves are unknown. Thus the unconditional Favre average is the best available estimate of $\langle\varepsilon\rangle$, and the present assumption is $\langle\varepsilon\rangle = \tilde{\varepsilon}$. A complication arises in the evaluation of the Kolmogorov quantities since these involve means of non-linear functions of ε. This is resolved by appealing to the lognormal distribution of ε postulated by Kolmogorov [16]:

$$P(\varepsilon)d\varepsilon = \frac{1}{\sqrt{2\pi}\sigma_\varepsilon \varepsilon}\exp\left[-\frac{(\ln\varepsilon - \mu)^2}{2\sigma_\varepsilon^2}\right]d\varepsilon \qquad (15)$$

where the mean μ of $\ln\varepsilon$ is given by

$$\mu = \ln\langle\varepsilon\rangle - \frac{1}{2}\sigma_\varepsilon^2 \qquad (16)$$

and the standard deviation σ_ε is taken to be constant. The mean of any power p of ε follows from the relation due to Oboukhov [16] obtained by integrating over the lognormal distribution

$$\langle\varepsilon^p\rangle = \langle\varepsilon\rangle^p \exp\left(-\frac{1}{2}p(1-p)\sigma_\varepsilon^2\right) \qquad (17)$$

The magnitude of the correction to the mean value is shown in Figure 4, and is seen to be fairly small over the range of fractional powers required here. Nevertheless it is sensitive to the value assumed for σ_ε which is taken as unity here. Further information about this quantity is required, either from DNS or from experimental data.

With the incorporation of the foregoing assumptions and corrections it is possible to evaluate the modelled strain rate pdf (9) for any value of the Favre-averaged dissipation $\tilde{\varepsilon}$. Note that the chemistry of the reacting mixture enters the pdf through the appearance of the unstrained laminar flame speed in (12). This evaluation has been performed for a number of different fuel/air mixtures and results are shown in Figure 5 for a stoichiometric methane/air mixture under typical experimental conditions. As the viscous dissipation rate increases the distribution tends to broaden markedly and to shift towards higher values of mean strain rate.

Combining this modelled distribution with values for the reaction rate ratio $W(a_t)/W(0)$ obtained by Rogg [4] for the same methane/air mixture it is possible to evaluate the factor I_0 from (8) over the same range of $\tilde{\varepsilon}$ and results are shown in Figure 6. The deviation from unity is not large, and reflects the relative insensitivity of this stoichiometric flame to the effects of turbulence.

Conclusions and Future Work

The usefulness of combustion DNS has been demonstrated through the application of DNS results to the refinement of an existing model of premixed turbulent combustion. Analysis of DNS data has yielded valuable physical insight and has led to a significant improvement in understanding. Statistical information not available from experiment has been obtained, shedding new light on important relationships between the key physical parameters. This in turn has led to improved modelling of the mean reaction rate in a premixed turbulent flame.

At the same time it is recognised that serious limitations remain. Nevertheless these are gradually being removed. More recent DNS techniques [17] are able to treat variable-density flows, while continued advances in computer power are extending the range of accessible Reynolds number. New numerical techniques based on finite differences [18] are proving especially suitable for combustion applications. Also, the need for data in support of combustion modelling is likely to grow as models become more sophisticated. It is clear that the potential for DNS in combustion is very great, and that its realisation promises to be an exciting task.

Acknowledgements

Financial suppport for this work was provided by the Center for Turbulence Research, Stanford University, by Shell Research Ltd. and by the UK Science and Engineering Research Coumcil.

References

[1] Becker, H., Monkhouse, P.B., Wolfrum, J., Cant, R.S., Bray, K.N.C., Maly, R., Pfister, W., Stahl, G., Warnatz, J.: 23rd Symposium (International) on Combustion, pp817-823, The Combustion Institute, 1990.

[2] Zur Loye, A.O., Bracco, F.V.: SAE paper 870454, 1987.

[3] Bray, K.N.C., Libby, P.A., Moss, J.B.: Combust. Flame **62**, 87-102, 1985.

[4] Cant, R.S., Rogg, B., Bray, K.N.C.: Combust. Sci. Tech. **69**, 53-61, 1990.

[5] Cant, R.S., Rogg, B., Kostiuk, L.W., Bray, K.N.C.: Combust. Sci. Tech., in press, 1994.

[6] Metghalchi, M., Keck, J.C.: Combust. Flame **38**, 143-154, 1980.

[7] Rogg, B.: Combust. Flame **73**, 45-65, 1988.

[8] Cant, R.S., Pope, S.B., Bray, K.N.C.: 23rd Symposium (International) on Combustion, pp809-815, The Combustion Institute, 1990.

[9] Cant, R.S.: Proceedings of the Joint Meeting of the British and German Sections of the Combustion Institute, Cambridge, 1993, pp48-51, The Combustion Institute, 1993.

[10] Bray, K.N.C., Libby, P.A., Moss, J.B.: Combust. Sci. Tech. **41**, 143-172, 1984.

[11] Rutland, C.J.: Ph.D. Thesis, Stanford University, 1989.

[12] Cant, R.S., Rutland, C.J., Trouvé, A.: Proc. of the 1990 Summer Program, pp271-279, Center for Turbulence Research, Stanford University, 1990.

[13] Chew, T.C., Bray, K.N.C., Britter, R.E.: Combust. Flame **80**, 65-82, 1990.

[14] Bray, K.N.C., Cant, R.S.: Proc. Roy. Soc. A **434**, 217-240, 1991.

[15] Girimaji, S.S. and Pope, S.B.: J. Fluid. Mech. **234**, 247-277, 1990.

[16] Kolmogorov, A.N.: J. Fluid Mech. **13**, 82-85, 1962.

[17] Trouvé, A. and Poinsot, T.: Proceedings of the 1992 Summer Program, pp325-343, Center for Turbulence Research, Stanford University, 1992.

[18] Gavrilakis, S., Tsai, H.M., Voke, P.R., Leslie, D.C.: "Direct and Large Eddy Simulation of Turbulence", eds. U. Schumann, R. Freidrich, pp105-118, F. Vieweg and Son, Braunschweig, 1986.

Figure 1. Statistical data for modelling. Examples of flame surface pdf data extracted from DNS. Taylor-scale Reynolds number of 6.4, $u'/u^0_L = 0.72$. Further details in [12].

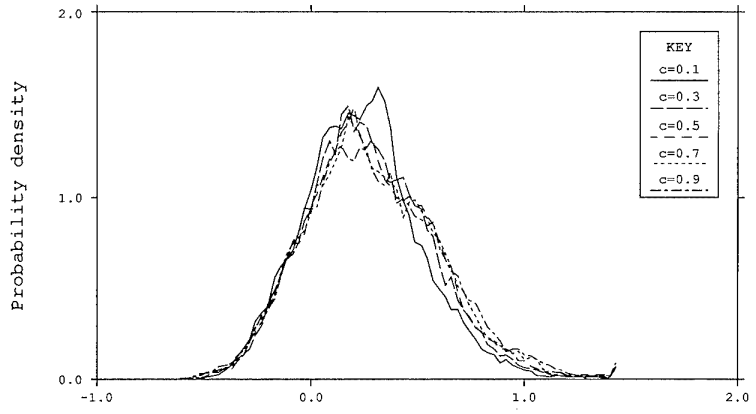

Fig. 1a) Strain rate pdf. Scale given in units of Kolmogorov time scale τ_η.

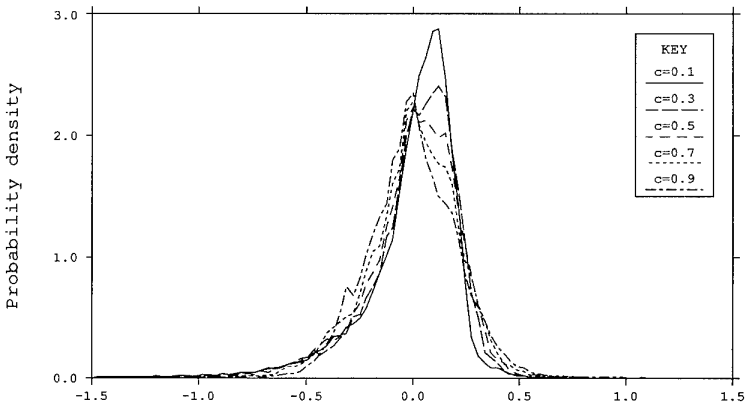

Fig. 1b) Mean curvature pdf. Scale given in units of Kolmogorov length scale η.

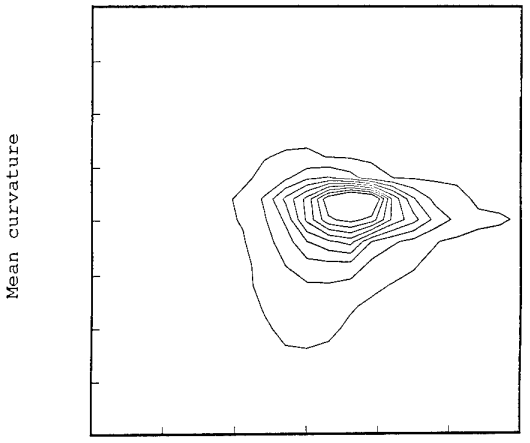

Fig. 1c) Joint pdf of strain rate and curvature. Scales as for (a) and (b).

Figure 2. Geometrical data for modelling. Same DNS dataset as Figure 1.

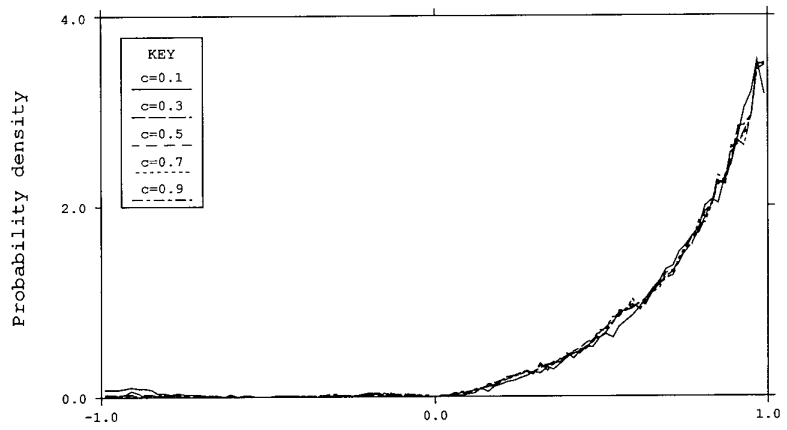

Fig. 2a) Unconditional pdf of the x-wise component of the flame normal vector. The mean is 0.78.

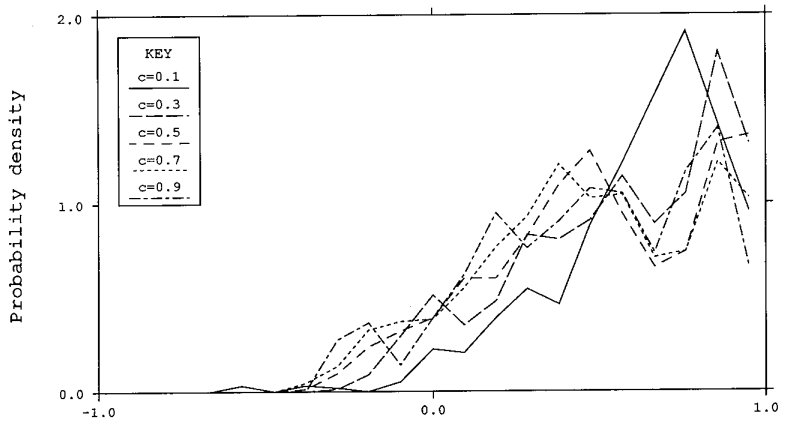

Fig. 2b) Conditional pdf of the x-wise component of the flame normal vector, conditioned on mean $\overline{c}$. The mean of the distribution $\overline{\sigma}_y$ is 0.52.

Figure 3. Determination of the flame wrinkling length scale $\hat{L}_y$. Same DNS dataset as Figure 1.

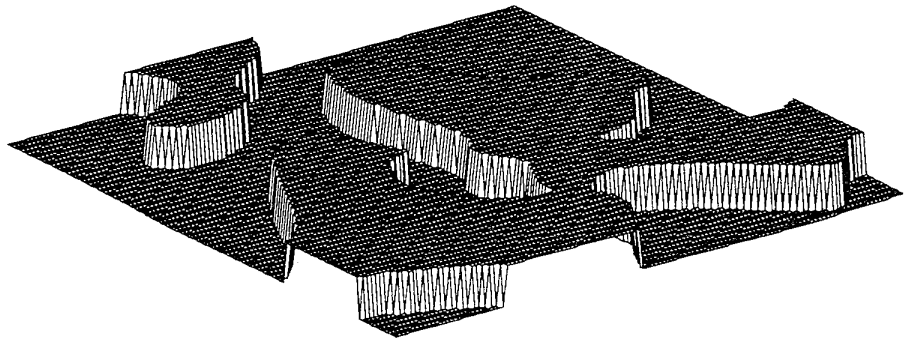

Fig. 3a) Square wave generated by intersecting the flame with a mean plane at $\overline{c}$ of 0.5.

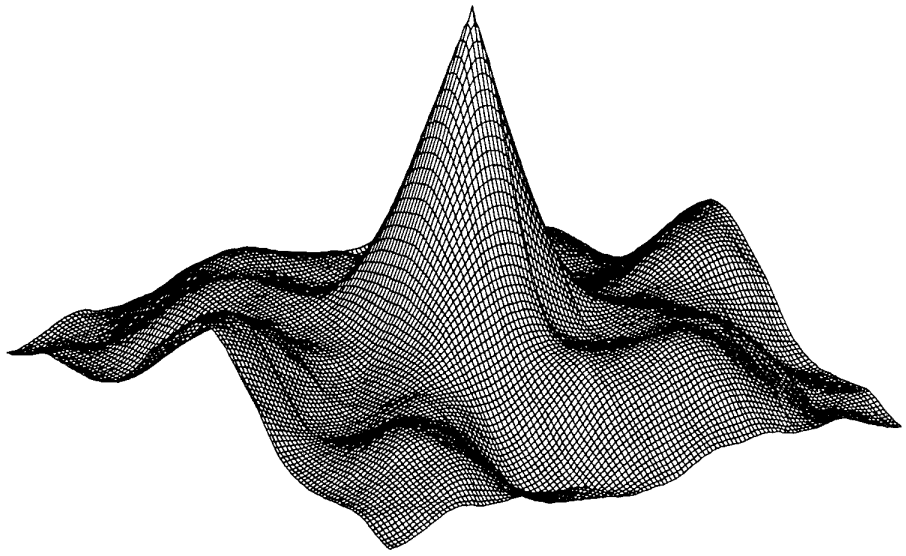

Fig. 3b) Autocorrelation of the square wave: perspective view.

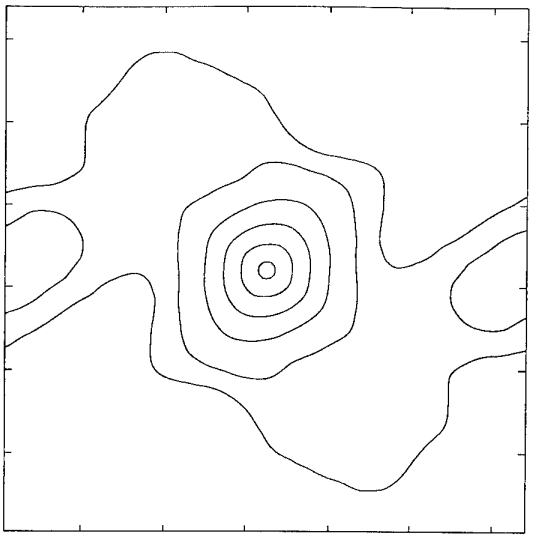

Fig. 3c) Autocorrelation of the square wave: contour plot.

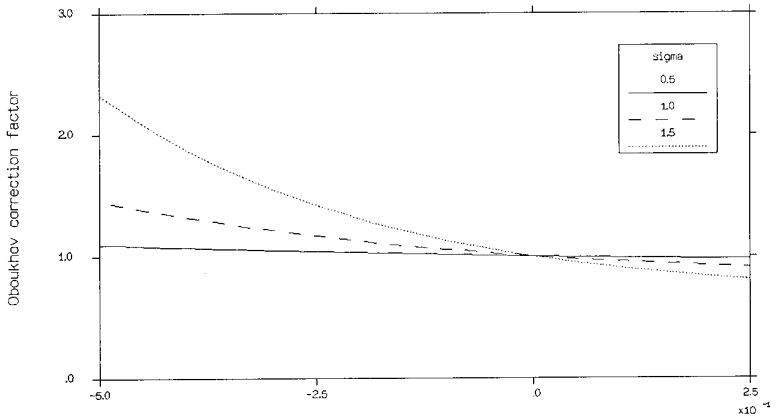

Figure 4. The Oboukhov correction factor i.e. the multiplier of $\langle \varepsilon \rangle^p$ required to produce $\langle \varepsilon^p \rangle$ in eqn.(17), evaluated for a range of the exponent p and three values of σ_ε.

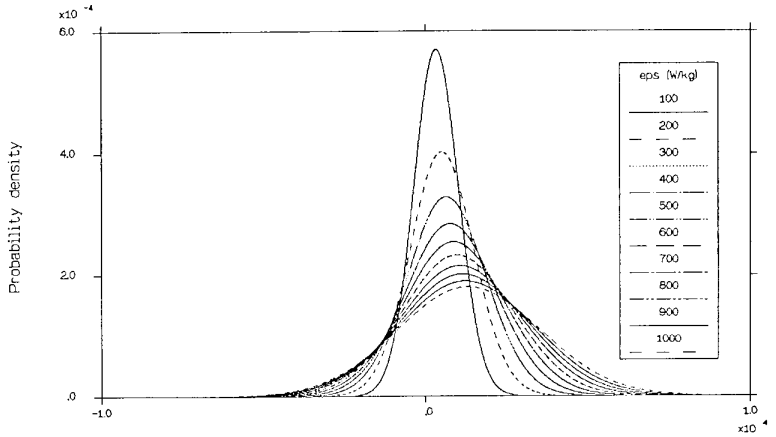

Figure 5. The modelled strain rate pdf, evaluated from eqn.(9) for $\sigma_\varepsilon = 1.0$ and a range of $\overline{\varepsilon}$. Value of u'_L is for a stoichiometric methane-air mixture under atmospheric conditions [4].

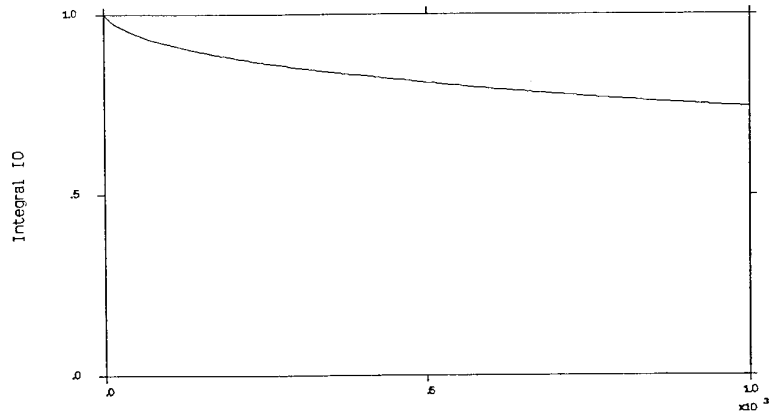

Figure 6. The function I_0 vs. $\overline{\varepsilon}$, evaluated from eqn.(8) for $\sigma_\varepsilon = 1.0$ using computed laminar flame data for W [4].

Entrainment in a Shear-Free Turbulent Mixing Layer

D. A. Briggs, J. H. Ferziger
Dept. of Mechanical Engineering
J. R. Koseff & S. G. Monismith
Dept. of Civil Engineering
Stanford University
Stanford CA, 94305-4020
United States

1. Abstract

Results from a direct numerical simulation of a turbulent mixing layer are presented. The flow evolves without shear and the mixing mechanisms associated with the turbulence are isolated. In the first set of simulations the turbulent mixing layer decays as energy is exchanged between the layers. In the second set, a forced mixing layer is simulated by continuously supplying energy to the higher energy side to maintain a stationary kinetic energy profile. Reynolds numbers based on the Taylor microscale of 28 and 38 are obtained in the decaying and forced simulations, respectively. The intermittency of the mixing layer is quantified by calculating the skewness and kurtosis of the velocity fields: results compare well with the shearless mixing layer experiments of Veeravalli & Warhaft[1]. Eddies of size of the integral scale ($k^{3/2}/\epsilon$) penetrate the mixing layer intermittently, transporting energy and governing the growth rate. The scalar dissipation rate, a measure of the mixing, peaks in the mixing layer. The triple correlation models proposed by Mellor & Yamada[2] and Launder[3] are applied to the inhomogeneous mixing layer and evaluated. The isotropic models tend to underpredict these correlations by as much as 60% while the more complicated anisotropic models are shown to be significantly more accurate. Both models for the pressure strain tensor are also shown to predict values that are incorrect by as much as 50%.

2. Introduction

Turbulent mixing layers occur in a wide variety of geophysical flows. For example, wind blowing over a lake or ocean generates a turbulent layer near the water surface which diffuses downward[4]. As a result, fluid is entrained from below by a variety of mechanisms such as engulfment and large scale stirring which can be driven by the turbulence or instabilities. The effects of shear on the entrainment rate are important and have been studied widely for unstratified[5,6] and stratified[7] flows but will not be considered in this paper. The entrainment process is further complicated when a stable density gradient and rotation are included[7]. Parameterizing the mixing rate in terms of the forcing and initial turbulence is necessary for developing turbulence models which can be used in geophysical flow applications. However, as described in Fernando[8], there is little consensus on the entrainment rate correlation and a more thorough description of the entrainment process is justified. In this paper we describe the results of a set of turbulent mixing layer simulations that evolve without shear. In this manner the entrainment mechanisms associated with the turbulence are isolated and the complications introduced by shear are avoided. In this context the mixing layer is defined as the region between two homogeneous layers of differing kinetic energy. Two simulations are discussed; in the first the turbulence decays while in the second the region with higher kinetic energy is continuously forced to maintain a steady state. The simulation results are compared to related experiments for validation and the structure of the mixing layers are further investigated. The last section of the paper evaluates the accuracy of standard turbulence models. The effects of stable stratification are currently being studied but are not presented here.

3. Mathematical details of the simulation

The three dimensional pseudo-spectral code originally developed by Rogallo[9] was used for the simulation. The governing equations are transformed into Fourier space (κ_1, κ_2, κ_3) and advanced using a second order Runge-Kutta method. Nonlinear terms are evaluated in physical space to save computation time. The solution consists of the Fourier coefficients representing the fluctuating velocity, $\hat{u}_i$, and fluctuating scalar, $\hat{\theta}$. The simulation is computed on an isotropic 128^3 grid (see Rogallo[9] and Holt[10] for details).

3.1 *Initial Conditions*

The flow field is initialized with a isotropic turbulent velocity field in the form of a pulse spectrum (Holt[10]). The mixing layer is created by Fourier transforming in the y direction and then imposing a prescribed profile,

Paper presented at the 74th Fluid Dynamics Symposium on "Application of Direct and Large Eddy Simulation to Transition and Turbulence" held at Chania, Crete, Greece, in April 1994.

$f(y)$, of the kinetic energy:

$$\hat{u}(k_x, y, k_z) = f(y)\ \hat{u}(k_x, y, k_z).$$

The flow becomes homogeneous in the horizontal plane and inhomogeneous in the vertical direction. Periodic boundary conditions are imposed in all directions. This requires that $f(y)$ be periodic and two mixing layers are actually created. Continuity is enforced before the flow is allowed to evolve. After about one eddy turnover time the nonlinear spectral transfer of energy associated with turbulence is apparent from the spectra. For clarity, in the remainder of the paper the two mixing layers will be averaged and we shall speak of a single mixing layer.

The decaying mixing layer evolves without turbulent production of any kind. In contrast, the forced mixing layer is maintained by continuously adding energy above the mixing layer. This produces a flow that is analogous to oscillating grid experiments. The energy is added locally in the vertical direction according to

$$\hat{u}(k_x, y, k_z) = \hat{u}(k_x, y, k_z)\ (1 + g(y)),$$

where $g(y)$ is a Gaussian function. The Fourier coefficients in the mixing layer and in the weakly energetic region below are largely unaffected.

3.2 *Statistical methods*

The horizontal planes are statistically homogeneous and turbulent quantities are computed by averaging over entire planes. Spectra are readily calculated from the Fourier coefficients. Integrating the three dimensional energy spectrum,

$$E_{ij} = (\hat{u}_i \hat{u}_j{}^* + \hat{u}_i{}^* \hat{u}_j)/2$$

over concentric rings in the $k_x - k_z$ plane yields a radial spectrum formed as function of y,

$$E_{ij}(\kappa, y) = \int E_{ij}[\kappa, y, A(\kappa)] dA(\kappa)$$

where κ is the radial wavenumber $(k_x^2 + k_z^2)^{1/2}$ and $A(\kappa)$ is a ring in that plane of thickness $dA(\kappa)$. This spectrum is used to study the dynamics of the mixing layer and to monitor the large scale development as the flow evolves: when energy in the lower wavenumbers becomes large the periodic boundary conditions become unrealistic and the computation is stopped. It is also desirable to keep the energy peak between $k = 5$ and 10 since this assures the resolution of many individual large scale structures.

The Taylor microscale is defined as

$$\lambda_{ij,\alpha} = \frac{u_i'}{\sqrt{\overline{(\partial u_j/\partial x_\alpha)^2}}}$$

and is used to form a Reynolds number, $Re_\lambda = q\lambda_{11,1}/\nu$ where $q^2 = \overline{u_i u_i}$. The transport equations for the Reynolds stresses are obtained from time averaging the fluctuating momentum equations and are written here for reference.

$$\begin{aligned}\frac{\partial \overline{(u^2+w^2)}}{\partial t} + \frac{\partial \overline{(u^2+w^2)v}}{\partial y} &= \frac{2}{\theta_o}\overline{p(\frac{\partial u}{\partial x} + \frac{\partial w}{\partial z})} \\ &- 2\nu(\overline{\frac{\partial u}{\partial x_k}\frac{\partial u}{\partial x_k}} + \overline{\frac{\partial w}{\partial x_k}\frac{\partial w}{\partial x_k}}) \\ &+ \nu\frac{\partial}{\partial y}\frac{\partial \overline{u^2}}{\partial y} + \nu\frac{\partial}{\partial y}\frac{\partial \overline{w^2}}{\partial y} \end{aligned} \quad (1)$$

$$\begin{aligned}\frac{\partial \overline{v^2}}{\partial t} + \frac{\partial \overline{v^3}}{\partial y} &= \frac{2}{\theta_o}\overline{p\frac{\partial v}{\partial y}} - 2\nu\overline{\frac{\partial v}{\partial x_k}\frac{\partial v}{\partial x_k}} + \nu\frac{\partial}{\partial x_2}\frac{\partial \overline{v^2}}{\partial x_2} \\ &- \frac{2}{\theta_o}\frac{\partial \overline{(pv)}}{\partial y} + 2\frac{g}{\theta_o}\overline{v\theta} \end{aligned} \quad (2)$$

$$\begin{aligned}\frac{\partial \overline{(q^2/2)}}{\partial t} &= -\frac{1}{2}\frac{\partial \overline{(u^2+v^2+w^2)v}}{\partial y} + \frac{1}{\theta_o}\frac{\partial \overline{(pv)}}{\partial y} \\ &- \nu\overline{\frac{\partial u_i}{\partial x_k}\frac{\partial u_i}{\partial x_k}} + \nu\frac{\partial}{\partial x_2}\frac{\partial \overline{(q^2/2)}}{\partial x_2} \end{aligned} \quad (3)$$

$$\begin{aligned}\frac{\partial \overline{uv}}{\partial t} + \frac{\partial \overline{uvv}}{\partial y} &= \frac{1}{\theta_o}\overline{p(\frac{\partial u}{\partial y} + \frac{\partial v}{\partial x})} - \frac{1}{\theta_o}\frac{\partial}{\partial y}\overline{pu} \\ &- 2\nu\overline{\frac{\partial u}{\partial x_k}\frac{\partial v}{\partial x_k}} + \nu\frac{\partial}{\partial x_2}\frac{\partial \overline{uv}}{\partial x_2} \end{aligned} \quad (4)$$

Similarly, a transport equation for the passive scalar correlation is derived from the fluctuating scalar transport equation

$$\begin{aligned}\frac{\partial \overline{(\theta^2/2)}}{\partial t} &= -\overline{v\theta}\frac{\partial \Theta}{\partial y} - \overline{v\frac{\partial \theta^2/2}{\partial y}} - 2\gamma\overline{\frac{\partial \theta}{\partial x_k}\frac{\partial \theta}{\partial x_k}} \\ &+ \gamma\frac{\partial}{\partial x_2}\frac{\partial \overline{(\theta^2/2)}}{\partial x_2} \end{aligned} \quad (5)$$

4. Results

4.1 *Unforced mixing layer*

The decaying or unforced mixing layer consists of two regions of approximately homogeneous turbulence, with a kinetic energy ratio of about seven, separated by a smooth interface (figure 1). As the kinetic energy decays the two regions exchange energy. The mechanisms associated with entrainment, such as engulfment due to large scale stirring, and turbulent diffusion are isolated from the effects of mean shear and gravitationally induced instabilities. Therefore, this flow provides a basis for understanding the growth of a mixing layer due to the turbulence alone.

The experiments of Veeravalli & Warhaft[1] (referred to as VW) provide thorough documentation of the statistical quantities in a shearless mixing layer and serve as a standard of comparison for our simulation. These experiments were performed in a wind tunnel with a composite grid that generated two regions of homogeneous turbulence. The composite grid consists of two sets of parallel bars of different diameter each spanning an equal area and spaced to produce equal solidity (other experiments used perforated plates, see VW for further details of the set-up and grid construction). Immediately downstream of the grid each region is characterized by a distinct kinetic energy. The mixing layer evolves as the flow is uniformly advected downstream. In the simulation the flow decays with time instead of distance downstream and any horizontal plane can be considered homogeneous.

The initial parameters of the simulation were chosen to match the 3.3:1 grid experiment of VW as closely as possible (the ratio is formed with the bar separation distances between the two grids). This experiment was chosen for its low microscale Reynolds number and data that includes results involving a passive scalar (Veeravalli & Warhaft[11]). The relevant parameters of the initial flow fields of each are shown in Table 1. As in the experiment, the simulated turbulent mixing layer is allowed to evolve from its source for about 1 or 2 eddy-turnover time-scales, $\tau = k/\epsilon$, before it is considered truly turbulent. The development time is required since both flows, in effect, evolve from a thin pulse spectrum. The radial spectra for the vertical (figure 2a) and horizontal (figure 2b) energy show that the flow is adequately resolved for this grid: both have approximately three decades of energy difference between the maximum and minimum levels throughout the mixing layer. The vertical velocity field is slightly less resolved since the smallest scales in the flow are associated with the vertical motion. The simulation differs from the experiment in that it develops from a smaller Re_λ but unlike the experiment, each horizontal plane can be considered statistically homogeneous.

4.1.1 *Decay rates*

The decay rate of homogeneous grid turbulence has been thoroughly documented. Data from early experiments was well described by a decay power law of the form (Batchelor[12])

$$k/k_o = A(t^* - t_o^*)^{-n}$$

where $n \approx 1$, k_o is the initial kinetic energy, A is a constant and t^* is a dimensionless evolution time. The virtual origin, t_o^* is adjusted to yield the best possible straight line that can be drawn through the data.

Table 1: Parameters of the simulation and experiments of Veeravalli & Warhaft (1989)

	Decaying Mixing Layer	VW
Initial parameters		
$k_1\,(\mathrm{cm}^2/\mathrm{s}^2)$	4.6	830.
$k_2\,(\mathrm{cm}^2/\mathrm{s}^2)$	.64	134.
$\epsilon_1\,(\mathrm{m}^2/\mathrm{s}^3)$	.0055	.641
$\epsilon_2\,(\mathrm{m}^2/\mathrm{s}^3)$	.00067	.103
$\lambda_1\,(\mathrm{cm})$	.091	49
$\lambda_2\,(\mathrm{cm})$	.097	48
$\Lambda_1\,(\mathrm{cm})$	.17	3.6
$\Lambda_2\,(\mathrm{cm})$	.075	1.49
$Re_{\lambda 1}$	28	78.1
$Re_{\lambda 2}$	11	29.8
$\tau_1 = k_1/\epsilon_1\,(\mathrm{s})$	.083	.13
$\tau_2 = k_2/\epsilon_2\,(\mathrm{s})$	.094	.13
Decay of turbulence: $k/k_o = A(t^* - t_o^*)^{-n}$		
n_1, n_2	1.7, 2.4	1.39, 1.42
t_{o1}^*, t_{o2}^*	1.7, 2.4	0., 0.
A_1, A_2	1., 1.	.27, .34

The subscripts 1 and 2 refer to the high and low energy sides of the mixing layer, respectively

More recent work (Riley[13], Gad-el-Hak & Corrsin[14], Bradshaw[15]) suggests n can be in the range 1.1 to 1.7 with a consensus for a value near 1.2. Decay rates for the simulation and the VW experiments are summarized in Table 1. The exponents are higher on both sides of the simulated mixing layer (1.7 and 2.4 for the high and low energy sides, respectively, compared to 1.39 and 1.42 for the experiment) and are probably due to the lower Re_λ of the simulations. For $Re_\lambda < 10$ the exponent of decay grows to 2.5 (Batchelor[12], Bennett & Corrsin[16]). The low energy side of the mixing layer

evolved in a range of Re_λ between 12.5 to 8: therefore, a higher exponent is expected. A common trend in both data sets is a higher exponent at lower Re_λ which lends further merit to this explanation. This trend is subtle for the 3.3:1 grid experiments but is more pronounced for the 3:1 perforated plate experiment. For this experiment the decay exponents are 1.25 and 1.43, associated with $Re_\lambda = 21$ and 44, respectively.

4.1.2 *Turbulence statistics*

The moments of the turbulence as functions of y were computed throughout the mixing layer development. A dimensionless evolution time t^* was created to relate the simulation and the experiment. The only relevant time scales in the flow are associated with the turbulence; therefore time was non-dimensionalized with the eddy turnover time. Statistical moments for both mixing layers collapse over $\Delta t^* \approx 0.66$. The normalized variance profiles for both the simulation and the experiment are shown in figure 3. The variance is normalized to lie between 0. and 1. The location where the mapped variance is .5 is designated as y_c and the half length, $l_{1/2}$, is defined as the vertical distance between the locations with mapped variance values .25 and .75.

The skewness, $S = \overline{u^3}/\overline{(u^2)}^{3/2}$, of the velocity field is one indicator of the intermittent nature of turbulent flows. In figure 4 the normalized skewness of the vertical velocity, S_v, is shown together with the experimental results. The Gaussian value of zero is obtained in both homogeneous regions while the mixing layer exhibits a significant negative deviation. This is attributed to large, intermittent structures penetrating downward from the higher energy region into the relatively weaker region below. Since the turbulence in the upper region is more energetic and of larger scale, the skewness is biased to the negative. The peak of the skewness appears below the center of the variance profile indicating the stronger influence of the higher energy region on the lower. The peak simulation skewness is -0.7 while that of the experiment is -1; both occur at approximately the same location. The difference between the simulation and the experiment is again believed to be a Re_λ effect. The skewness of the horizontal velocity, S_h, should be zero since this direction is homogeneous and turbulent eddies have no preferred horizontal direction. Figure 4(b) shows S_h throughout the mixing layer. Although the skewness has non-zero values, there is no perceivable trend in the simulation data. Averaging over a larger domain should reduce S_h. A small but inexplicable peak is noticed in the experimental S_h. This could be a side wall effect or some other secondary flow influence.

As a further indication of the intermittency in the mixing layer, the kurtosis, $K = \overline{u^4}/\overline{(u^2)}^2$ of the vertical and horizontal velocity fields, K_v and K_h, is calculated and shown in figure 5. Large values of the kurtosis are associated with a sample pool with a small number of values far from the mean. In the mixing layer K_v, and to a much lesser extent K_h, exhibit their respective maximum values. Outside the mixing layer both K_v and K_h retain the Gaussian value of 3. This is an indication that the eddies penetrating into the mixing layer are large and infrequent. As in the experiment the peak of K_v is much larger than that of K_h. Smoother data could be obtained with more averaging. However, this would require more grid points.

The structure of the mixing layer is visualized with vertical planar views of contours of kinetic energy. In figure 6 two vertical planes at $t^* = 2.5$ are shown. Structures of high kinetic energy (denoted by closely spaced contour lines) are typical of size of the same order as the integral scale, $\Lambda = k^{3/2}/\epsilon$, and can be seen throughout the mixing layer but appear less frequently on the weaker side. In regions with less energy these structures are separated by areas with little or no energy; they are responsible for the intermittency found in the statistics.

4.2 *Forced mixing layer*

The more complicated and geophysically relevant case of a forced mixing layer was also simulated. The energy profile is maintained by adding energy to the higher energy side of the mixing layer. A steady profile develops as energy is transported away from the source entraining adjacent fluid. A passive scalar profile with a sharp interface is constructed (figure 7) to simulate conditions in an ocean or lake thermocline. The vertical coordinate for the forced cases is centered at the interface and is normalized by the source half width $ls_{1/2}$, defined as the height difference that contains 50% of the source energy. The interface is far enough from the source to insure that the local turbulent kinetic energy there is derived almost entirely from transport. As in geophysical flows, the turbulence deforming the interface and mixing the scalar resides in a region with little turbulent production.

Turbulent entrainment again develops without shear in the forced mixing layer. Laboratory experiments use an oscillating grid to generate turbulence which then diffuses into the surrounding region (Hopfinger & Toly[17], Hannoun[18]). Energy is added isotropically and locally in the flow field by boosting the Fourier coefficients with an arbitrary distribution. When the total kinetic energy decays by 4 or 5% the boosting process is initiated. The stationary and boosted

variance profiles are shown in figure 7 and relevant initial parameters are displayed in Table 2.

The source cannot be too localized due to its spectral representation so a smooth boosting function concentrated in a small vertical region is used (as discussed above). Continuity is enforced in k-space after each boosting event causing the source to be slightly less localized. The spatial decay of the turbulence is exponential and placement of the scalar interface becomes a compromise between minimizing the effect of the source, by placing the interface far away, and maintaining a reasonable Re_λ. At the location chosen 18% of the energy dissipated is directly due to the source while the balance is from turbulent transport. This is acceptable in light of the fact that our spatial decay rates resemble those in experiments.

Table 2: Initial parameters of the forced mixing layer

$k\,(\mathrm{cm}^2/\mathrm{s}^2)$	16.
$\epsilon\,(\mathrm{m}^2/\mathrm{s}^3)$	.00356
$\lambda\,(\mathrm{cm})$	.07
$\Lambda\,(\mathrm{cm})$	.18
Re_λ	38
$\tau = k/\epsilon\,(\mathrm{s})$	.045

4.2.1 *Spatial decay and isotropy*

In figure 8 the horizontal rms velocity, u', decays with distance from the source as $u' \propto y^{*-n}$ where $n = 1.7$ and y^* is the vertical distance from the source offset by the virtual origin and normalized by the source half width. The virtual origin was determined as described in §4.1.1. The spatial decay rates in the experiments range from $n = 1.$ (Hannoun[18]) to $n = 1.25$ (Hopfinger & Toly[17]). Only a portion of the mixing layer is represented in figure 8, and it cannot be assumed that the same power law can be applied throughout (an observation also recognized by Hopfinger & Linden[19]).

Inside the mixing layer the ratio of the vertical rms velocity to the horizontal rms velocity peaks at a value of 1.2 (figure 9) before decaying to 0.8 in the low energy region. The experiments of Hannoun[18] and (Hopfinger & Linden[19]) yield values of 1.32 and 1.25, respectively. These values may be a manifestation of the vertically oscillated grid. However, the simulation, which forced the mixing layer isotropically, suggests that the anisotropy may be independent of the forcing and may be a feature of the mixing layer. This result is further substantiated by considering the normalized vertical kinetic energy flux, $\{\overline{(u^2+v^2+w^2)v}\}^{1/3}/u'$. Hannoun[18] found the value peaks in the mixing layer and then decays as distance from the source increases. This emphasizes the role of the vertical velocity in the mixing layer development.

4.2.2 *The velocity field and structure*

Compared to the decaying mixing layer, the intermittency is higher in the forced case, primarily because the kinetic energy ratio is much larger and Re_λ is slightly higher. Figures 10 and 11 show the skewness and kurtosis of the vertical and horizontal velocities. Near the source and below the mixing layer S_v and S_h are both nearly zero. The forced mixing layer is statistically stationary and averaging over time and horizontal planes gives smooth results. Peak values of S_v and K_v reach -1.5 and 12., respectively, and are biased towards the weaker side of the mixing layer as in the decaying case.

The mechanisms of entrainment can be studied by examining planar views of the scalar concentration and kinetic energy. Several features are observed in the two vertical planes shown in figure 12. As in the decaying case, large stirring structures that are of the size of the integral scale deform the interface. These eddies intermittently penetrate deeply into the interface and mix with fluid of different concentration (regions denoted by a). Fluid parcels are separated from other fluid of similar concentration (b). Mixing occurs at small scales once the large scales have done the stirring (c). The interface is highly contorted on the high energy side and relatively unperturbed on the opposite side. The interface thickness also varies with location and can be relatively thin (d). The profile of the scalar dissipation rate normalized by the mean gradient (figure 13) shows the peak of small scale mixing located at the center of the interface even though the energy is larger above.

5. Evaluation of Turbulence Models

The contributions to the growth of the forced mixing layer can be evaluated by considering the budget equations (1-5). The turbulent flux terms in the kinetic energy equation (the first two terms on the right hand side of (3)) are plotted in figure 14. Energy is transported away from the source by both the pressure and turbulent velocity fields towards the scalar interface as indicated by the negative and positive regions in figure 14. The transport by the turbulence is much larger than the contribution from the pressure field. Hopfinger & Linden[19] predict that both mechanisms are of the same order. However, this may only be valid at higher Re. The net transport at the interface is positive.

A commonly used turbulence model for geophysical flows was developed by Mellor & Yamada[2]. Versions

of this model include a complex, full Reynolds stress form and a simpler two equation version similar to the model proposed by Launder[3] (referred to here as LRR), the major difference being the determination of the length scale. Instead of solving a transport equation for the dissipation and forming a length scale from k and ϵ, a transport equation for the length scale, l, is formed directly and ϵ is derived from k and l. The Mellor-Yamada (MY) model uses assumptions first proposed by Rotta[20] to model the triple correlation terms. The constants in this model were evaluated using experimental data from homogeneous shear flows and regions of boundary layers where production is balanced by dissipation (buoyancy effects were absent). The model predicts the flows from which it was calibrated accurately however extensions to shear-less mixing layers may be inaccurate.

As described in LRR, the triple correlation, $\overline{u_i u_j v}$, is considered as a diffusive term and typically written as:

$$\overline{u_i u_j v} = -C_s \frac{k}{\epsilon}\left(\overline{u_i v}\frac{\partial \overline{u_j v}}{\partial y} + \overline{u_j v}\frac{\partial \overline{u_i v}}{\partial y} + \overline{v v}\frac{\partial \overline{u_i u_j}}{\partial y}\right) \quad (6)$$

or in isotropic form,

$$\overline{u_i u_j v} = -C_s \frac{k^2}{\epsilon}\frac{\partial \overline{u_i u_j}}{\partial y} \quad (7)$$

while the MY model uses

$$\overline{u_i u_j v} = (3/5) l q S_q \frac{\partial \overline{u_i u_j}}{\partial y}. \quad (8)$$

Only $\overline{u_i u_j v}$ is considered since this refers to the one inhomogeneous direction. S_q and C_s are model constants. The correlations $\overline{(u^2+w^2)v}$, $\overline{v^3}$ and $\overline{q^2 v}$ along with the isotropic MY and LRR model predictions (7) and (8) are shown in figure 15 using data from the forced mixing layer. The models predict $\overline{(u^2+w^2)v}$ fairly well but $\overline{v^3}$ is greatly underestimated. This error renders prediction of $\overline{(u^2+v^2+w^2)v}$ incorrect by about 40% in the mixing layer. In the decaying mixing layer the MY prediction of $\overline{(u^2+v^2+w^2)v}$ was inaccurate by 60%. The error results from the application of these models in a flow in which the skewness is large and where the eddies do not have a preferred direction of orientation (see figure 8). A structure with strong vertical motion will produce a large $\overline{v^3}$ while an equally energetic horizontal structure may not produce a large value of $\overline{(u^2+w^2)v}$. Consequently, in the mixing layer, $\overline{v^3} > \overline{(u^2+w^2)v}$. The isotropic models are not capable of describing the difference between $\overline{v^3}$ and $\overline{(u^2+w^2)v}$ when the anisotropy is weak. That is, while $\overline{(u^2+w^2)(y)} \approx 2\,\overline{v^2}(y)$, the differences between $\overline{v^3}(y)$ and $\overline{(u^2+w^2)v}(y)$ can be substantial. As shown in figure 16 the predictions with the anisotropic model (6) are a significant improvement. Figure 17 shows the effectiveness of the isotropic MY models for the triple correlations involving the scalar. These models are formulated similar to the velocity correlations

$$\overline{\theta v v} = -2\, l\, q\, S_{\theta v}\frac{\partial \overline{\theta v}}{\partial y} \quad (9)$$

$$\overline{\theta\theta v} = -l\, q\, S_{\theta\theta}\frac{\partial \overline{\theta\theta}}{\partial y} \quad (10)$$

where $S_{\theta u}$ and $S_{\theta\theta}$ are model constants. Again, the predictions of $\overline{\theta v^2}$ and $\overline{\theta\theta v}$ generally track their respective triple correlations but are quantitatively incorrect. Furthermore, the error cannot be improved with an adjustment in the isotropic coefficient.

The pressure strain tensor, Π_{ij}, can be decomposed into slow and rapid contributions,

$$\Pi_{ij} = \Pi_{ij}^{(s)} + \Pi_{ij}^{(r)}.$$

The first term on the right hand side is due to large scale correlations and the second is related to the mean shear. Both $\Pi_{ij}^{(s)}$ and $\Pi_{ij}^{(r)}$ are typically modeled as functions of the turbulent dissipation rate, the anisotropy tensor and the turbulent kinetic energy with the constraint that the tensor approach zero when the flow becomes isotropic (Speziale[21]). The form for Π_{ij} used in the MY model was adapted from a more complicated form of the LRR model but in the absence of shear both reduce to similar forms

$$\Pi_{ij} = -C_1 \epsilon b_{ij} \quad \text{(LRR)}$$

and

$$\Pi_{ij} = -C_2 \frac{q^3}{l} b_{ij} \quad \text{(MY)}$$

with $C_1 = 3.6$, $C_2 = 1.3$ and $l = k^{3/2}/\epsilon$. Although these forms are comparable, in practice they differ since ϵ and l are determined from different transport equations in the LRR and MY models. As shown in figure 18 the MY models for $\Pi_{11}+\Pi_{33}$, Π_{22} and Π_{12} yield correct trends but are quantitatively incorrect. As Re increases the pressure strain terms become more of a factor in the budget. Higher Re simulations will be made to evaluate the model in a more challenging regime.

6. Conclusions

The simulations agree well with experiments and can be used to further study the structure of the mixing layer and to evaluate turbulence models. The intermittency of the mixing layer, quantified by the skewness and kurtosis, is visualized with contours of the scalar field and offers insight into methods for improving turbulence models. Standard isotropic models for the triple correlations do not perform well for the simulated mixing layers since the gradients of $\overline{(u^2+w^2)}$ and $\overline{v^2}$ are too similar to account for the large difference between $\overline{(u^2+w^2)v}$ and $\overline{v^3}$. For example, the MY model predicts $\overline{(u^2+w^2)v}$ adequately but underpredicts $\overline{v^3}$ and $\overline{(u^2+v^2+w^2)v}$ by factors of 2. The anisotropic LRR model performs well but is complicated, requiring the evaluation of the cross correlations. Both the MY and LRR models of the pressure strain tensor are inaccurate but generally track the correlations.

Future simulations will include the effects of a stable density gradient. Increasing Re_λ will also be attempted since large scale entraining and engulfing mechanisms operate in these higher Re_λ regimes. It has been shown that for flows without shear the isotropic models yield poor predictions. Alternative parameterizations of these simpler models will be examined.

Acknowledgements

The authors wish to acknowledge the Office of Naval Research for support of this work through grant number N00014-92-J-1611.

Notation

b_{ij}	anisotropy tensor
E_{ij}	energy spectrum tensor
$E_{ij}(\kappa, y)$	radial energy spectrum tensor
k	$q^2/2$, turbulent kinetic energy
K	kurtosis
$l_{1/2}$	half length scale of the variance profile
$ls_{1/2}$	vertical distance containing 1/2 of the source
P, p	mean, fluctuating pressure
q	$\sqrt{\overline{u_i u_i}}$, turbulent velocity scale
Re_λ	$\lambda q/\nu$, microscale Reynolds number
S	skewness
t	time
u, v, w	fluctuating velocity components
x, y, z	spatial coordinates
y_c	height of the centered variance profile
y_I	height of the interface
y^*	dimensionless distance from the source

Greek

ϵ	$\epsilon_{ii}/2$, homogeneous dissipation rate of k
ϵ_{ij}	$2\nu\overline{u_{i,k}u_{j,k}}$, homogeneous dissipation rate tensor
γ	scalar diffusivity
Θ, θ	mean,fluctuating passive scalar concentration
Θ_o	reference scalar concentration
κ	radial wavenumber, $\sqrt{\kappa_1\kappa_1 + \kappa_3\kappa_3}$
κ_i	wavenumber vector
$\lambda_{ij,\alpha}$	Taylor microscale
Λ	$k^{3/2}/\epsilon$, integral length scale
ν	kinematic viscosity
Π_{ij}	pressure strain tensor, $\overline{p(u_{i,j} + u_{j,i})}$
τ	k/ϵ, eddy turnover time
χ	scalar dissipation rate

Primes denote rms quantities, overbars represent ensemble averages and $\hat{}$ denotes Fourier coefficients

REFERENCES

[1] VEERAVALLI, S. & WARHAFT, Z. 1989 The shearless turbulence mixing layer. *J. Fluid Mech.* **207,** 191-229.

[2] MELLOR, G. L. & YAMADA, T. 1986 Development of a turbulence closure model for geophysical fluid problems. *Rev. Geophys. Space Phys..* **20 No. 4,** 851-875

[3] LAUNDER, B. E., REECE, G. J., & RODI, W. 1975 Progress in the development of a Reynolds-stress turbulence closure. *J. Fluid Mech.* **68,** 537-566

[4] IMBERGER, J. & PATTERSON, J. C. 1990 *Physical Limnology. Advances in Applied Mechanics.* Academic Press. 303-475

[5] METCALFE, R. W., HUSSAIN, A. K. M. F. 1985 Coherent structures in a turbulent mixing layer: A comparison between direct numerical simulation and experiments. *Fifth symposium on turbulent shear flows. Held: Ithaca, NY, USA, Aug 7-9, 1985.*

[6] MEHTA, R. D. & BELL, J. 1991 Effect of velocity ratio on plane mixing layer development: Influence of the splitter plate. *Exp. Fluids.* **10(4),** 194-204

[7] THORPE, S. A. 1985 Laboratory observations of secondary structures in Kelvin-Helmholtz billows and consequences for ocean mixing. *Geophys. Astrophys. Fluid Dyn..* **34,** 175-99

[8] FERNANDO, H. J. S. 1991 Turbulent mixing in stratified fluids. *Ann. Rev. Fluid Mech.* **23,** 455-93

[9]ROGALLO, R. S. 1981 Numerical experiments in homogeneous turbulence. *NASA Tech. Memo. 81315.*

[10]HOLT, S. E., KOSEFF, J. R. & FERZIGER, J. H. 1992 A numerical study of the evolution and structure of homogeneous stably stratified sheared turbulence. *J. Fluid Mech.* **237,** 499-539.

[11]VEERAVALLI, S. & WARHAFT, Z. 1990 Thermal dispersion from a line source in the shearless turbulence mixing layer. *J. Fluid Mech.* **216,** 35-70.

[12]BATCHELOR, G. K. 1953 *The Theory of Homogeneous Turbulence.* Cambridge University Press, Cambridge, England

[13]RILEY, J. J., METCALFE, R. W. & WEISSMAN, M. A. 1981 Direct numerical simulations of homogeneous turbulence in density stratified fluids. *Non-linear Properties of Internal Waves (ed.B. J. West). AIP Conf. Proc. Vol 76*

[14]GAD-EL-HAK, M. & CORRSIN, S. 1974 Measurements of the nearly isotropic turbulence behind a uniform jet grid. *J. Fluid Mech.* **62,** 115

[15]BRADSHAW, P. 1975 *An Introduction to Turbulence and its Measurement.* Pergamon

[16]BENNETT, J. C. & CORRSIN, S. 1978 Small Reynolds number nearly isotropic turbulence in a straight duct and a contraction. *Phy. of Fluids.* **21(12),** 2129-2140

[17]HOPFINGER, E. J. & TOLY, J.-A. 1976 Spatially decaying turbulence and its relation to mixing across density interfaces. *J. Fluid Mech.* **78,** 155-175

[18]HANNOUN, I. A., FERNANDO, H. J. S., LIST E. J. 1989 Turbulence structure near a sharp density interface. *J. Fluid Mech.* **180,** 189-209

[19]HOPFINGER, E. J. & LINDEN, P. F. 1982 Formation of thermoclines in zero-mean-shear turbulence subjected to a stabilizing buoyancy flux. *J. Fluid Mech.* **114,** 157-173

[20]ROTTA, J. C. 1951 Statistische Theorie nichthomogener Turbulenz. *Z. Phys.* **129,** 547-72

[21]SPEZIALE, C. G. 1991 Analytical methods for the development of Reynolds-stress closures in turbulence. *Ann. Rev. Fluid Mech.* **23,** 107-57

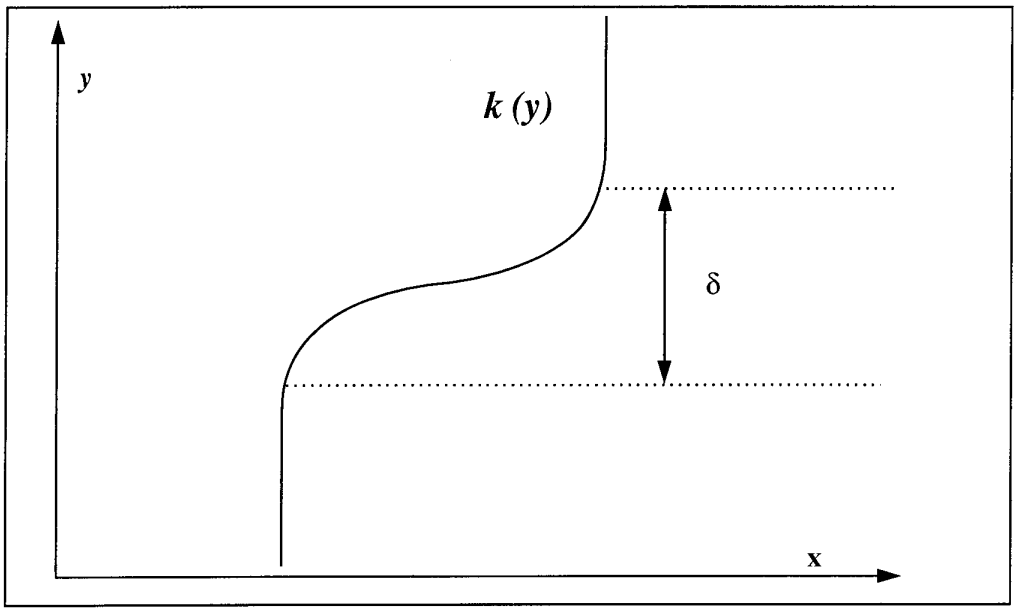

FIGURE 1. Initial kinetic energy profile with mixing layer thickness δ.

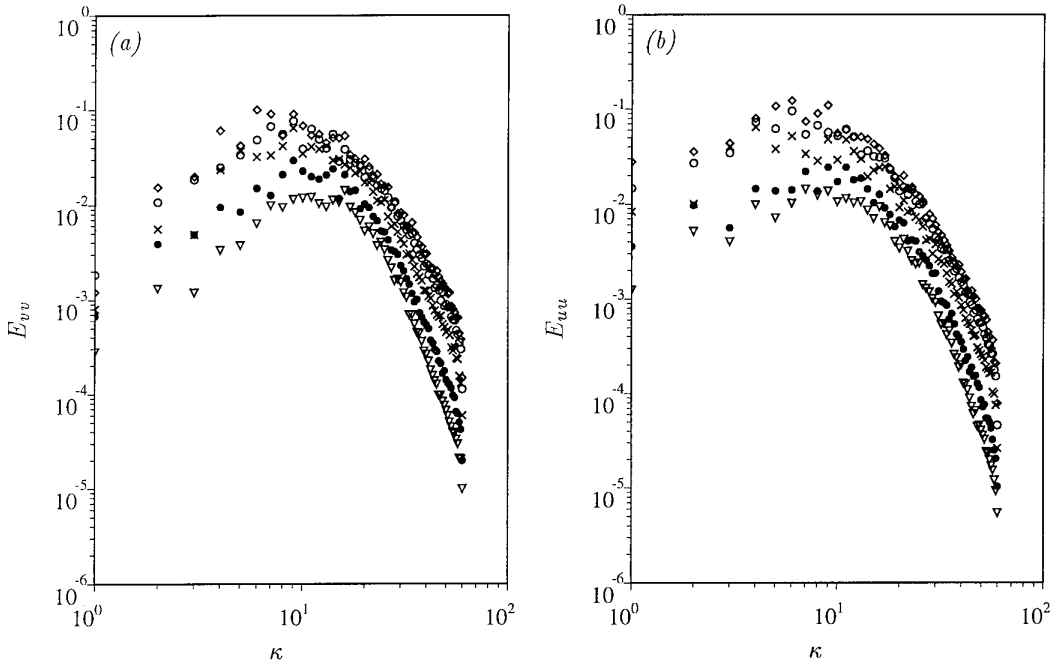

FIGURE 2. Radial spectra of the vertical (a) and horizontal (b) energy. Symbols denote positions throughout the mixing layer. $(y - y_c)/l_{1/2} = -1.3, -0.3, 0.0, 0.3, 1.3$; ∇ ,$\bullet$,$\times$,$\circ$,$\diamond$. The vertical dimension is offset by the center of the mapped variance profile, y_c and normalized by $l_{1/2}$ the half length of the mapped variance profile.

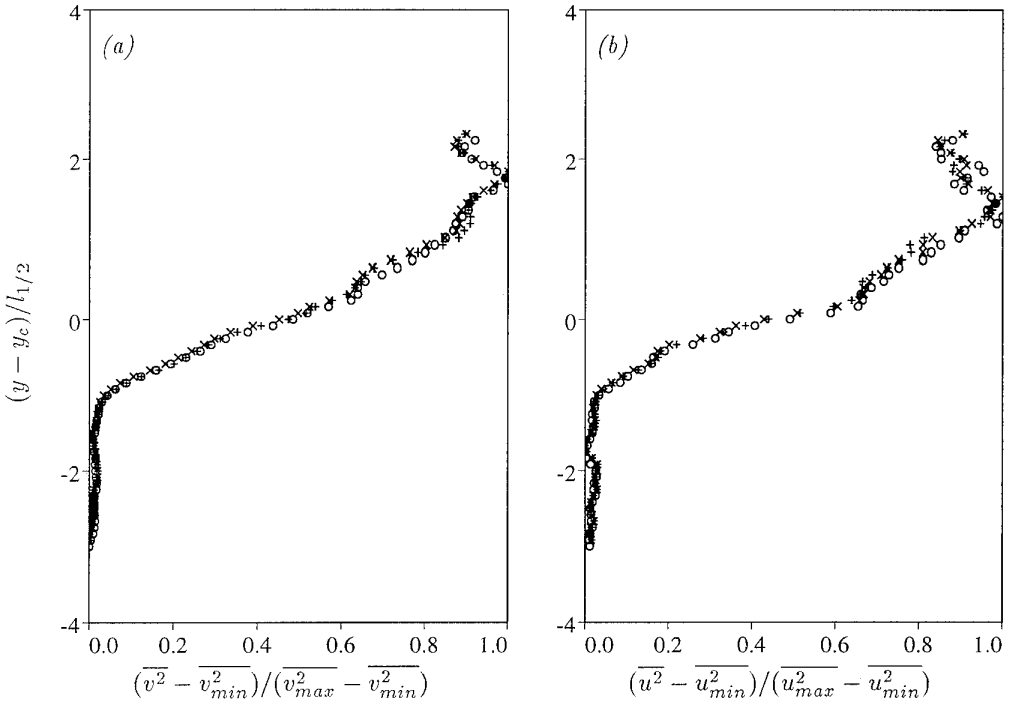

FIGURE 3. Variance of the vertical (a) and horizontal (b) velocity field for the decaying mixed layer. Symbols denote the turbulent evolution time normalized by the initial eddy turnover time; $\Delta t^* - t_o^* = 0.$; $\circ$, $\Delta t^* - t_o^* = 0.33$; $\times$, $\Delta t^* - t_o^* = 0.66$; $+$.

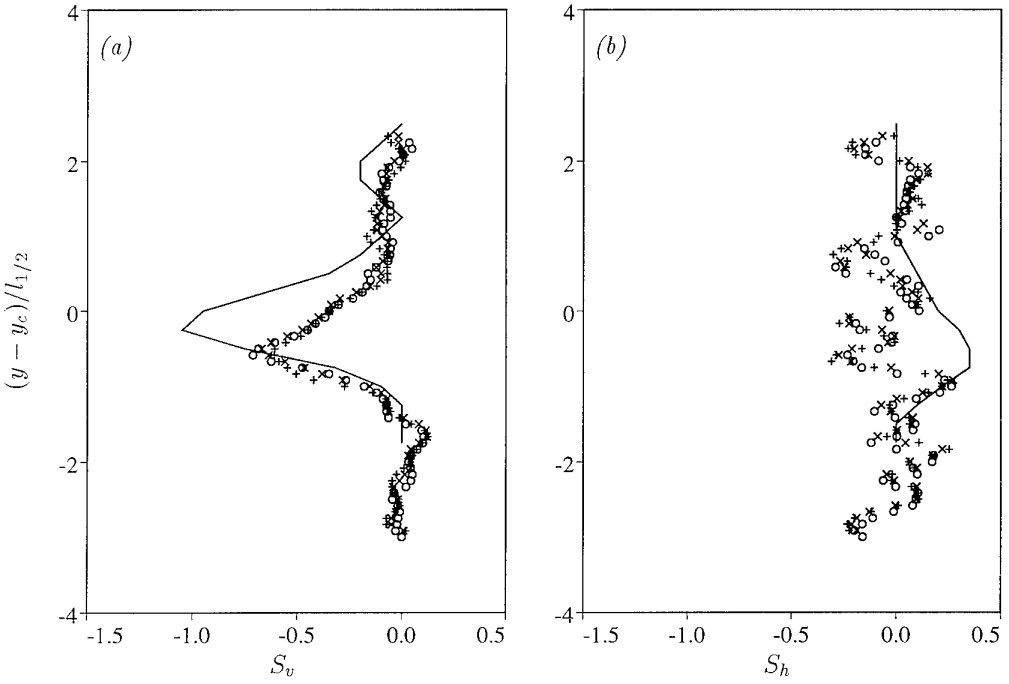

FIGURE 4. Normalized skewness of the vertical (a) and horizontal (b) velocity field for the decaying mixed layer. See figure 3 for the symbol description. Data from the experiments of Veeravalli & Warhaft (1989) are plotted for the same dimensionless times (——).

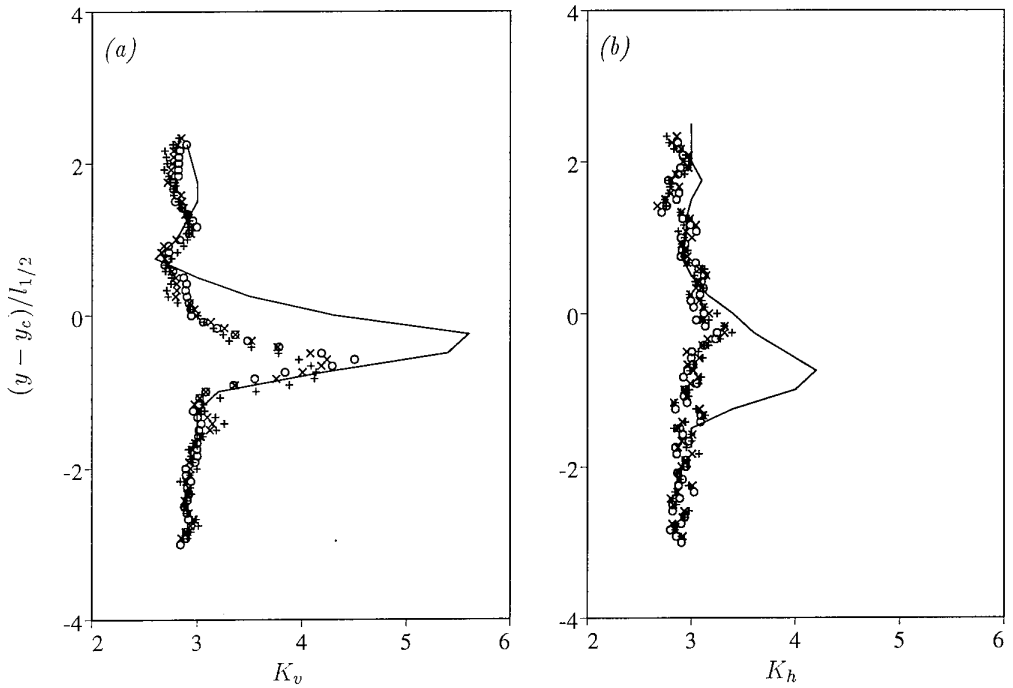

FIGURE 5. Normalized kurtosis of the vertical (a) and horizontal (b) velocity field for the decaying mixed layer. See figure 3 for the symbol description. Data from the experiments of Veeravalli & Warhaft (1989) are plotted for the same dimensionless times (——).

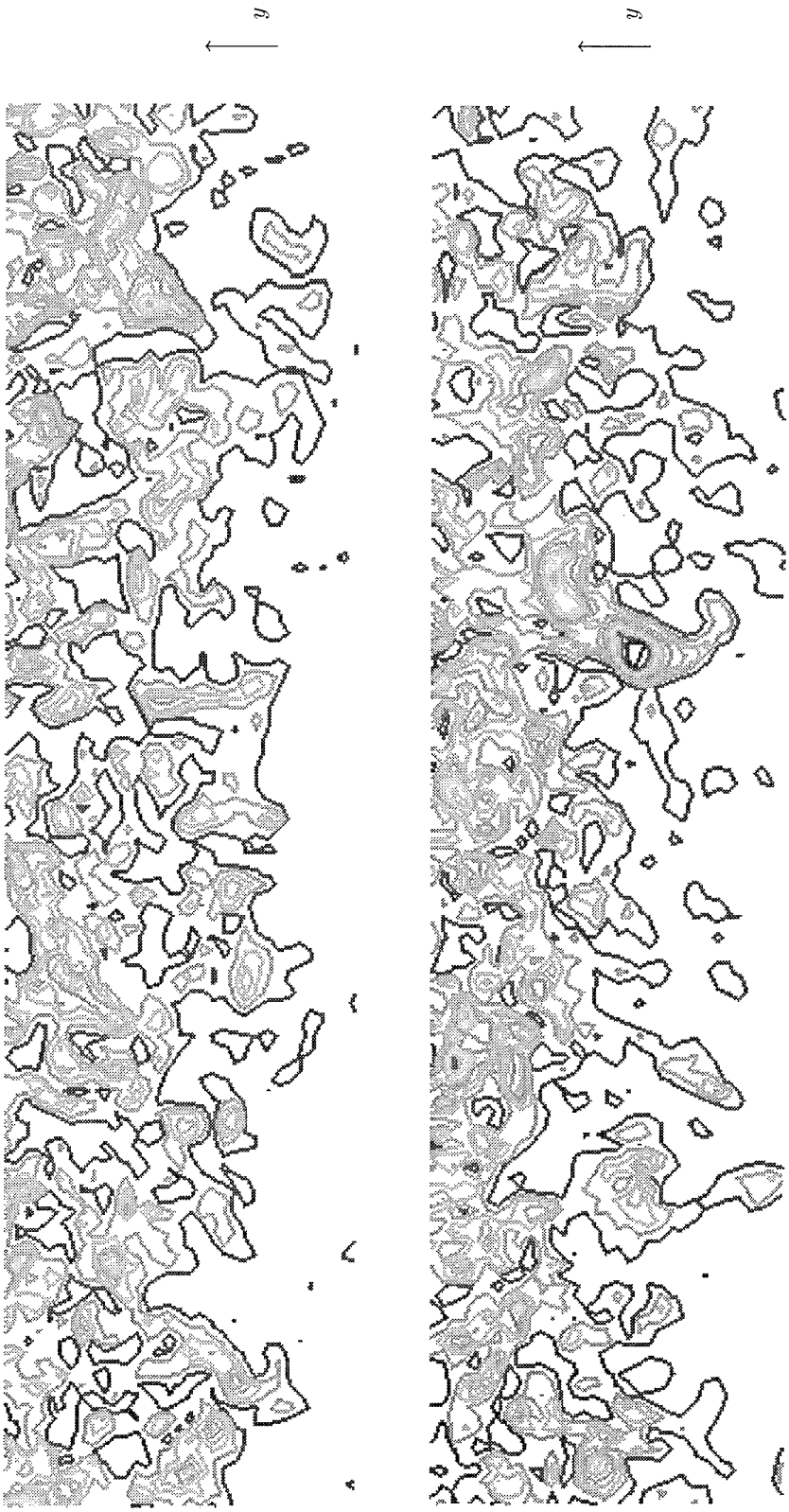

FIGURE 6. Kinetic energy contours in two vertical planes in the decaying mixing layer at $t^* = 2.5$. Closely spaced contours denote highly energetic regions.

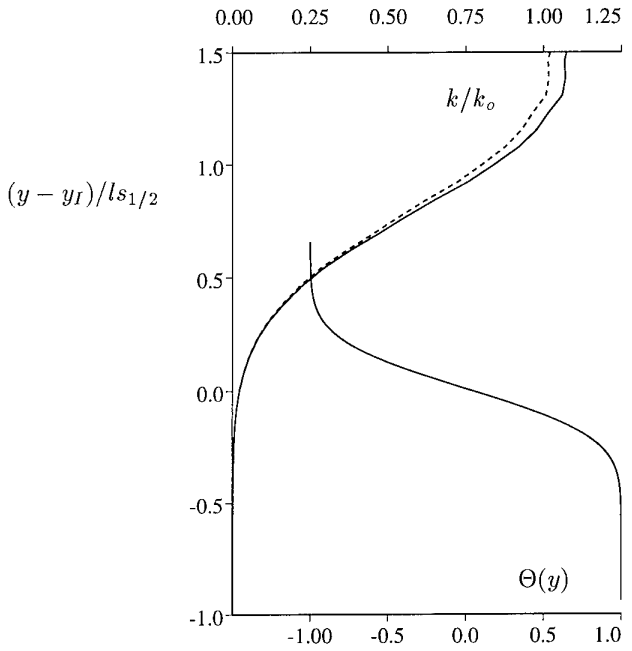

FIGURE 7. Horizontal rms velocity normalized by maximum value before (———) and after (----) a boosting event displaying the direct and local influence of the source. The vertical distance is offset by the interface height and normalized by the source half width. The scalar profile is also sketched for reference.

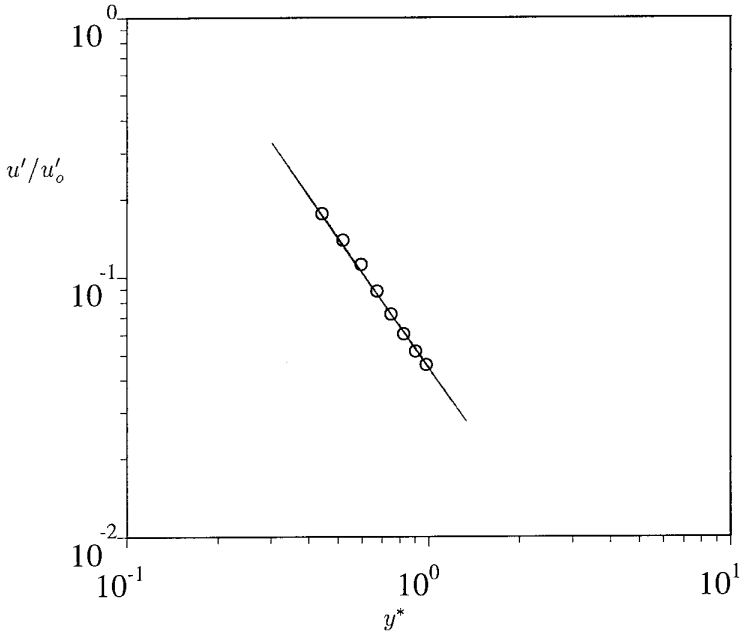

FIGURE 8. Decay of horizontal rms velocity with distance from the source. The rms velocity is normalized by its value at the center of the source.

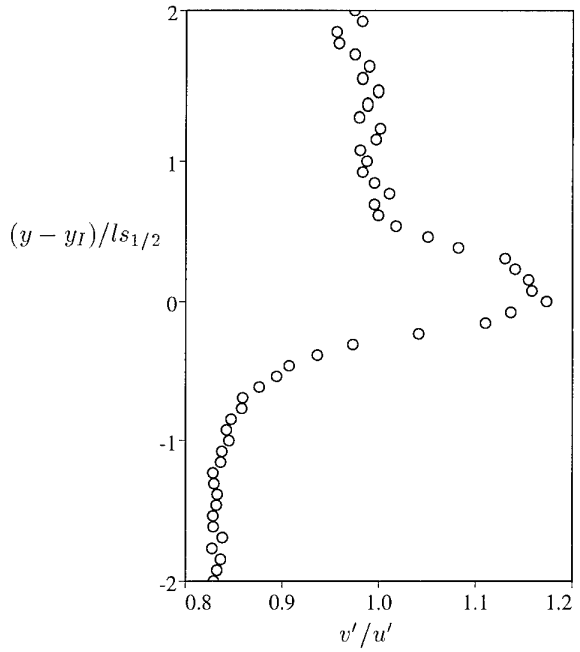

FIGURE 9. Anisotropy of velocity field as distance from the source increases.

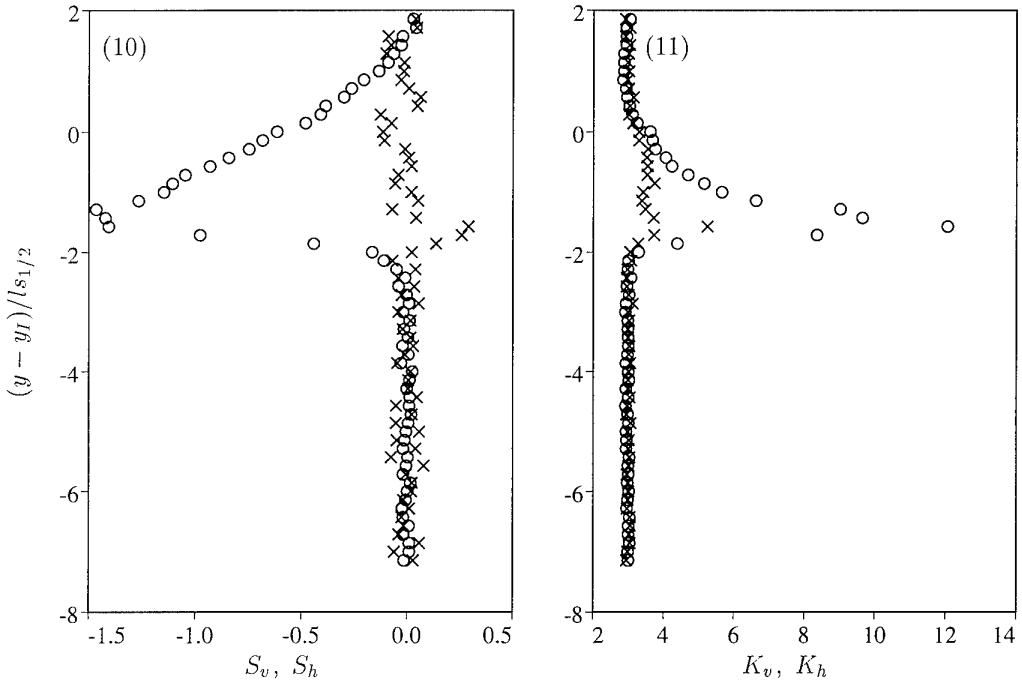

FIGURE 10,11. Skewness and kurtosis of vertical (o) and horizontal (×) velocity field for the force mixing layer after the kinetic energy profile has stabilized.

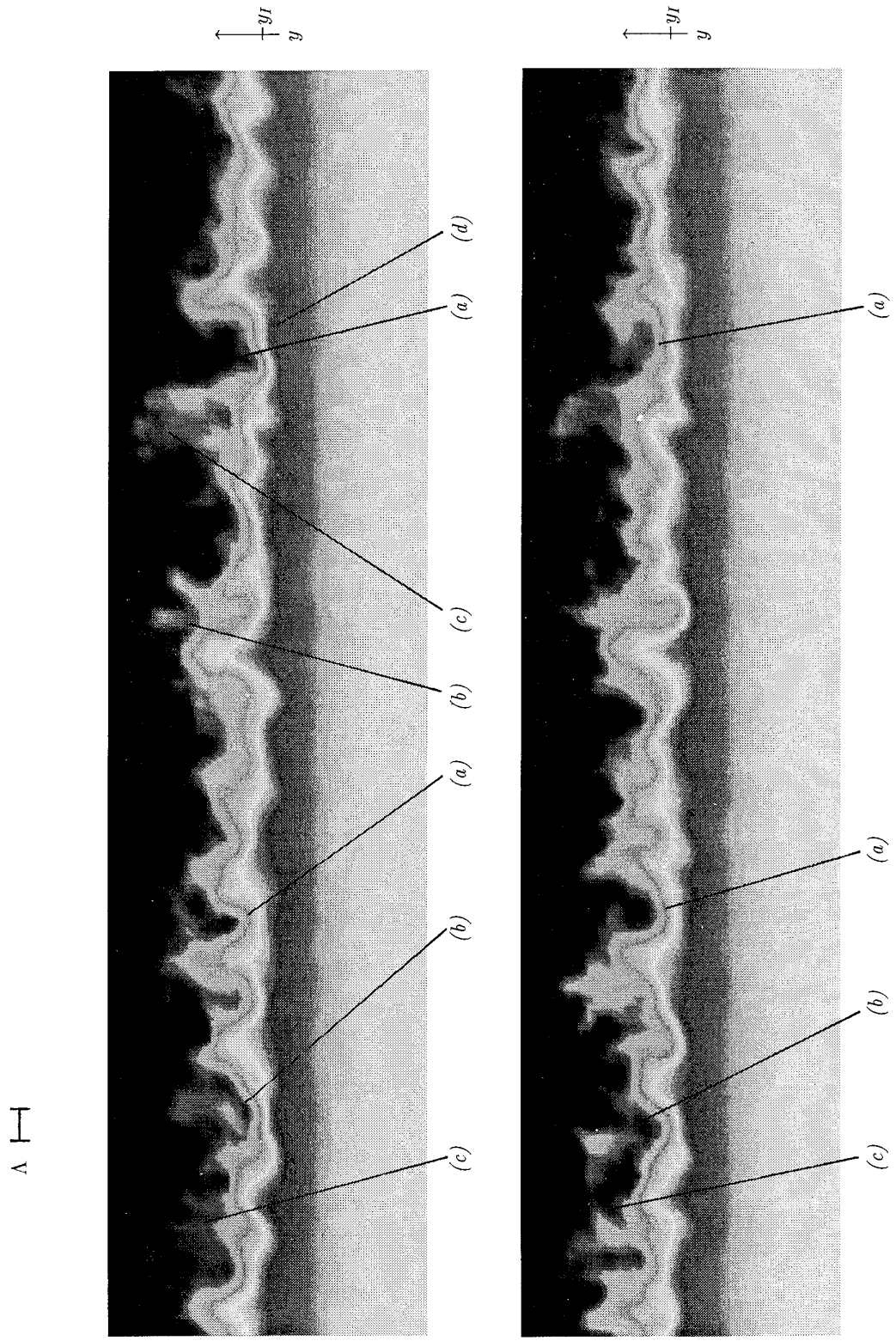

FIGURE 12. Scalar concentration in two vertical planes in the forced mixing layer. Regions with large scales (a); regions where engulfment has pinched off parcels of fluid of different concentration (b); regions marked by small scale mixing (c); regions where the interface has become thin (d). The integral scale is drawn as a scale reference.

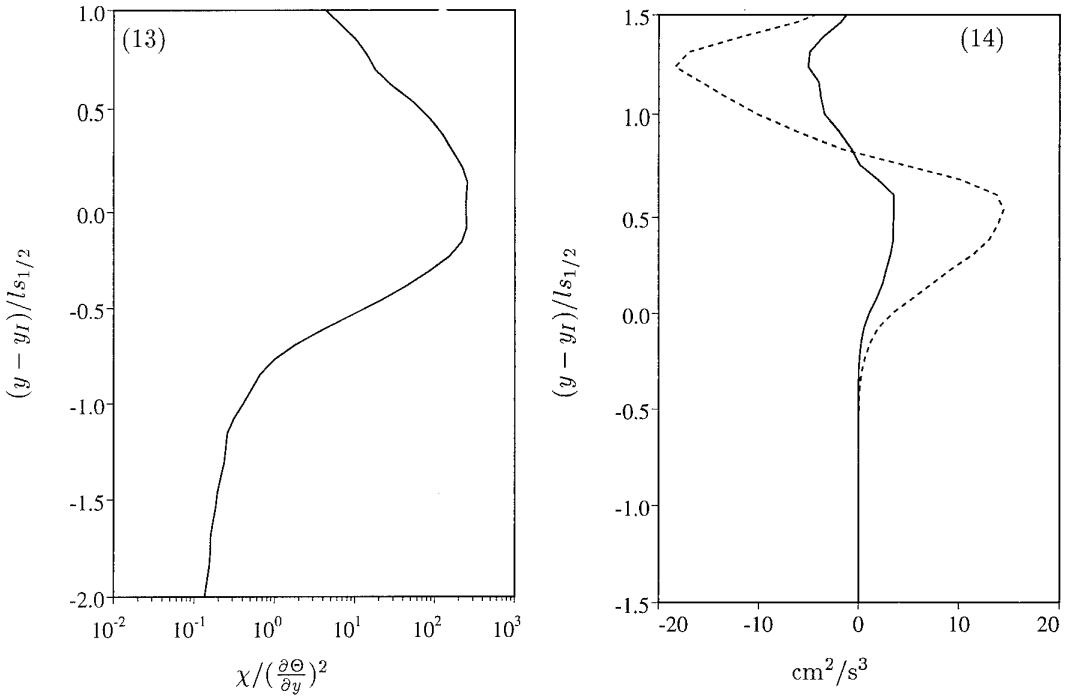

FIGURE 13. Normalized scalar dissipation rate as a function of y.

FIGURE 14. Transport terms in (3) for the forced mixing layer. The dashed line represents the vertical transport of kinetic energy by the turbulence $\overline{q^2 v}$ and the solid line represents the pressure transport $\overline{pv/\theta_o}$.

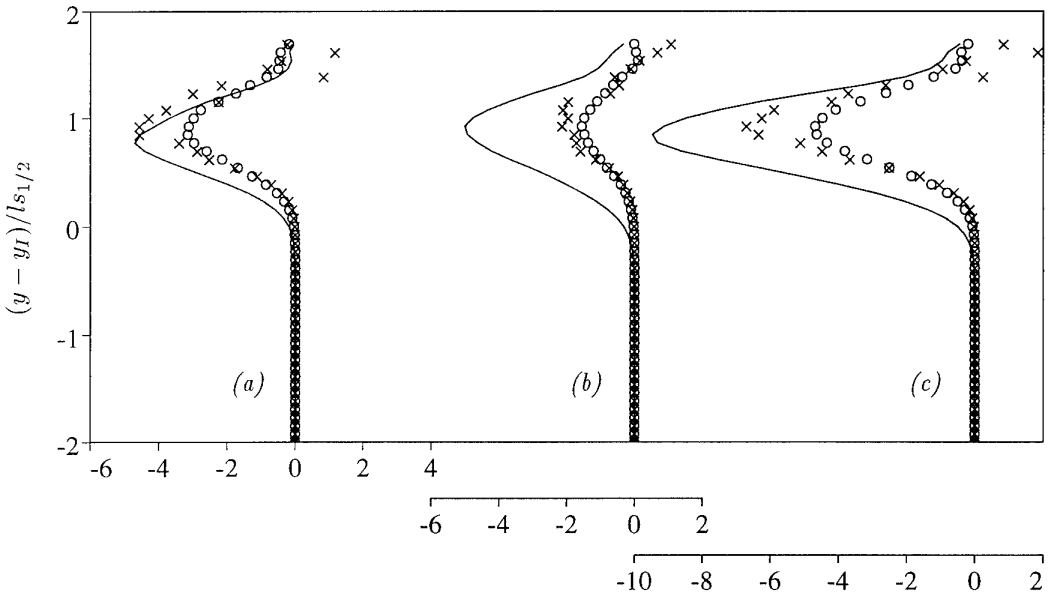

FIGURE 15. Vertical profiles of the triple correlations (cm^2/s^3) and corresponding isotropic models. Exact (———), Mellor-Yamada (○), LRR (×), *(a)*; $\overline{(u^2+w^2)v}$, *(b)*; $\overline{v^2 v}$, *(c)*; $\overline{(u^2+v^2+w^2)v}$

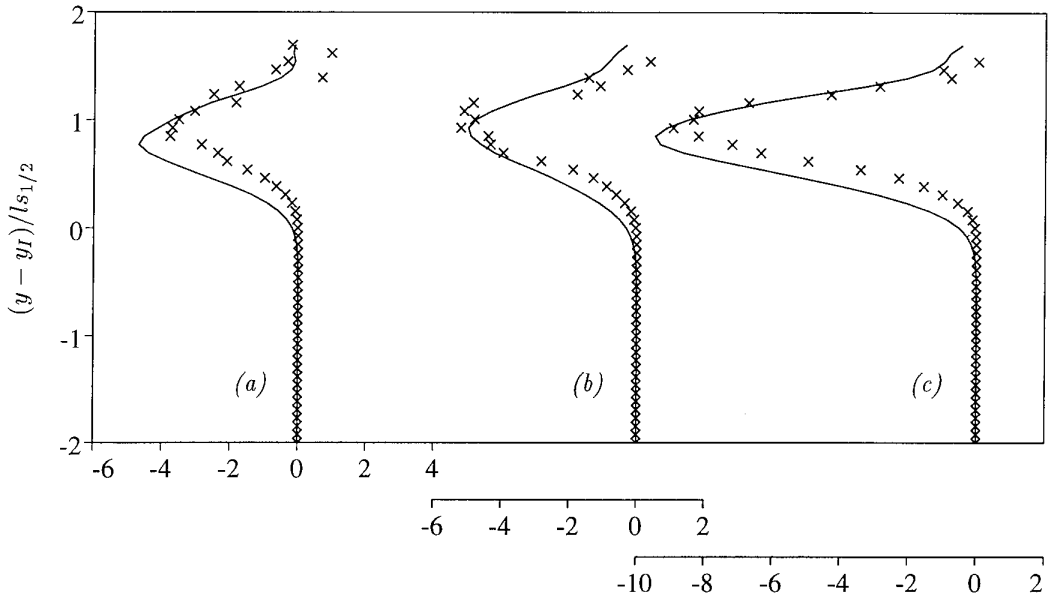

FIGURE 16. Vertical profiles of the triple correlations (cm^2/s^3). Exact (———) and anisotropic model of Launder, Reece & Rodi (×), *(a)*; $\overline{(u^2+w^2)v}$, *(b)*; $\overline{v^2 v}$, *(c)*; $\overline{(u^2+v^2+w^2)v}$

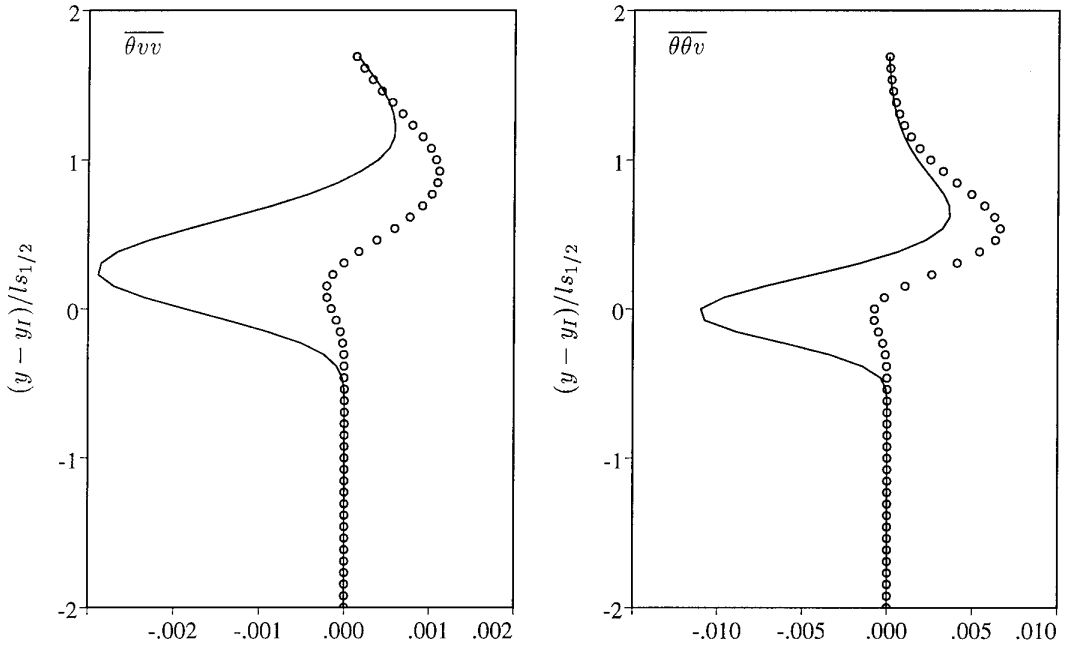

FIGURE 17. Scalar triple correlations (———) and Mellor-Yamada model (○).

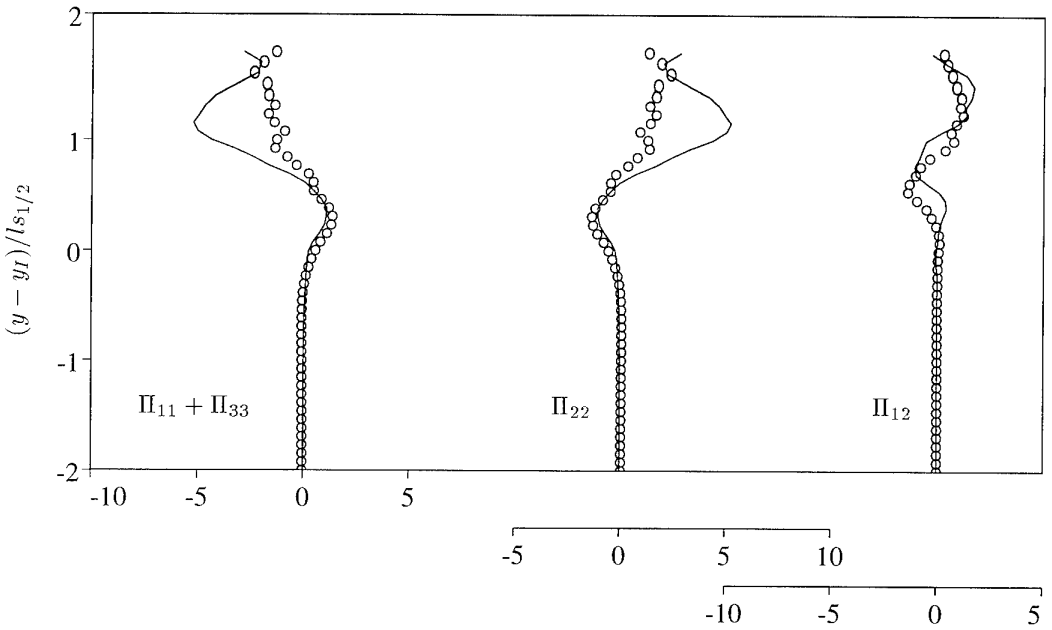

FIGURE 18. Vertical profiles of the pressure strain tensor (cm^2/s^3); exact (———) and predictions with Mellor-Yamada (○).

Direct Simulation of a Self-Similar Plane Wake

Robert D. Moser and Michael M. Rogers

NASA Ames Research Center
Moffett Field CA, 94035
USA

1. SUMMARY

Direct simulations of two time-developing turbulent wakes have been performed. Initial conditions for the simulations were obtained from two realizations of a direct simulation of a turbulent boundary layer at momentum thickness Reynolds number 670. In addition, extra two-dimensional disturbances were added in one of the cases to mimic two-dimensional forcing. The unforced wake is allowed to evolve long enough to attain self-similarity. The mass-flux Reynolds number (equivalent to the momentum thickness Reynolds number in spatially developing wakes) is 2000, which is high enough for a short $k^{-5/3}$ range to be evident in the streamwise one-dimensional velocity spectrum.

Several turbulence statistics have been computed by averaging in space and over the self-similar period in time. The growth rate in the unforced flow is low compared to experiments, but when this growth-rate difference is accounted for, the statistics of the unforced case are in reasonable agreement with experiments. However, the forced case is significantly different. The growth rate, turbulence Reynolds number, and turbulence intensities are as much as ten times larger in the forced case. In addition, the forced flow exhibits large-scale structures similar to those observed in transitional wakes, while the unforced flow does not.

2. INTRODUCTION

The plane wake studied here is one of several canonical free shear flows that are used as test flows for the development of turbulence models and turbulence control strategies. In addition, plane wakes are of particular interest in high-lift airfoil configurations, where one lifting surface (a flap) may be operating in or near the wake of an upstream surface. The numerical simulations reported here are the first of several to be performed to provide data for turbulence modeling relevant to such a configuration.

It is well known that a turbulent plane wake will approach a self-similar evolution, with thickness growing like $x^{1/2}$, where x is streamwise distance. However, the rate at which this growth occurs can vary considerably. For example, in the experiments of Wygnanski *et al.* ,[1] the growth rate $\frac{1}{\theta}\frac{db^2}{dx}$ (b is the half-width of the wake, defined below, and θ is the momentum thickness) varied from 0.29 to 0.41 depending on the details of the body that generated the wake. Even larger growth rates can be obtained using two-dimensional forcing.[1,2] Furthermore, as pointed out by George[3] and as observed by Wygnanski *et al.*,[1] even if the mean velocity profiles of various plane wakes are the same (when properly scaled), profiles of the turbulence statistics need not be.

As in many free-shear flows, the evolution of large-scale coherent structures in the plane wake has been of great interest (*e.g.* Refs. 4 and 5). Part of the reason for this interest is that the well-known features of transitional wakes (*e.g.* the Karman street) have been observed in the turbulent wake as well. However, the extent to which such structures are dynamically important, and how they might vary among different wakes is not clear.

The apparent non-uniqueness of the self-similar plane wake is a problem because it complicates the modeling of the flow. At the same time, it provides an opportunity to control the evolution of the wake. Progress in predicting and/or controlling the wake evolution will be facilitated by more detailed information on both the statistics and structures in plane wakes, how they are related, and how and why they vary among different wakes. Direct numerical simulation is an ideal tool for providing some of this information because it provides absolute control of the initial/inlet conditions and very detailed information about the flow. Two such simulations with differing initial conditions were performed to address these issues, and some of the preliminary results are reported here. The simulations are described in §3, a statistical description of the two flows is presented in §4, and the structural features of the flows are discussed in §5. Finally, some concluding remarks are given in §6.

3. THE SIMULATIONS

The numerical simulations discussed in this paper were performed by solving the three-dimensional time-dependent incompressible Navier–Stokes equations. For computational efficiency, a temporally evolving plane wake was simulated rather than the spatially evolving flow typical of experiments. The spatially and temporally evolving wakes differ in that different integral quantities are preserved. In the time-developing wake, the cross-stream integrated mass flux deficit $\dot{m} = -\int_{-\infty}^{\infty} \delta U \, dy$ is preserved (the velocity deficit is $\delta U = \overline{U} - U_\infty$, where $\overline{U}$ and U_∞ are the mean and free-stream velocities, respectively), while in the spatially evolving

Paper presented at the 74th Fluid Dynamics Symposium on "Application of Direct and Large Eddy Simulation to Transition and Turbulence" held at Chania, Crete, Greece, in April 1994.

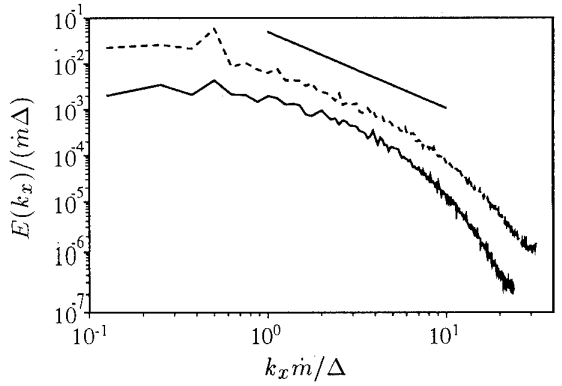

Figure 1. Streamwise one-dimensional energy spectra at $y = 0$ in the ——— unforced wake simulation at $t\Delta^2/\dot{m} = 91.5$ and - - - - the forced wake simulation at $t\Delta^2/\dot{m} = 50.0$. The straight line shows a $k^{-5/3}$ dependence.

wake, the integrated momentum flux deficit $U_\infty^2\theta = -\int_{-\infty}^{\infty}\delta U(U_\infty + \delta U)\,dy$ is preserved. In the limit of small deficits, the temporally evolving wake is equivalent to a spatially evolving wake viewed in a frame moving with the free stream, and in this limit, the mass flux deficit is given by $\dot{m} = U_\infty\theta$. In the time-developing wake, the free stream velocity is irrelevant, only the deficit is important. Thus, in what follows, nondimensionalization will be based on $\dot{m}$ and the initial magnitude of the velocity deficit, Δ. In both flows described here, the Reynolds number $Re_m = \dot{m}/\nu$ is 2000. This Reynolds number is high enough to produce a short $k^{-5/3}$ spectral range in the streamwise one-dimensional spectrum (figure 1).

In this study, the solution domain is periodic in the streamwise (x) and spanwise (z) directions with periods $50\dot{m}/\Delta$ and $12.5\dot{m}/\Delta$ respectively. These domain sizes were selected to correspond to those in the boundary layer simulations from which the initial conditions were obtained (see below). The domain is infinite in the cross-stream (y) direction. A Galerkin spectral method[6] was used to solve the equations.

Initial conditions were generated using two realizations of a turbulent boundary layer with a momentum thickness Reynolds number of 670, as computed by Spalart[7]. One boundary layer was used for each side of the wake, with equal free stream velocities attained at $y = \pm\infty$. Thus, the simulations represent a temporally evolving approximation to the wake of a zero-thickness flat plate with turbulent boundary layers at zero angle of attack. In addition to the boundary layers and their turbulence, one of the two simulations included extra two-dimensional forcing in the initial condition. This forcing was used to mimic the expected receptivity of the trailing edge of the plate to two-dimensional disturbances. To model the uncontrolled nature of the two-dimensional disturbances in a flat-plate wake, the forcing was introduced by amplifying all the two-dimensional modes in the boundary layer initial conditions by a factor of 20. In similar simulations in a mixing layer,[8] this amplification factor was needed to produce a significant effect. The amplification increased the total initial disturbance energy by a factor of 13, and the total energy per unit plan area added to the flow by the forcing was $0.7\dot{m}\Delta$.

4. SELF-SIMILARITY AND STATISTICS

Developed small deficit plane wakes evolve self-similarly, with thicknesses growing like $t^{1/2}$ (or $x^{1/2}$ in a spatially developing wake). Since in a time-evolving wake the total mass flux deficit $\dot{m}$ is constant, this implies that the maximum velocity deficit magnitude (U_0) decays like $t^{-1/2}$. In a spatially evolving wake, the momentum thickness θ is constant, which implies that a $x^{-1/2}$ decay of the deficit holds in this case. By scaling large-scale quantities with the local thickness and the velocity deficit, statistical profiles at different times (or different downstream locations in the spatially evolving flow) collapse onto a single curve. In what follows, the numerically simulated plane wake is examined for evidence of such self-similar evolution.

A variety of different thickness measures can be used to characterize the wake locally. To facilitate comparison to previous experimental data, we will use the half-width b, which is defined to be the distance between the y-locations at which the mean velocity is half of U_0 (note that some investigators take the half-width to be half this distance).

Shown in figure 2 are the time evolutions of b^2 and U_0^{-2} for the unforced and forced cases. Both these quantities should evolve linearly during self-similarity, and indeed in the unforced flow both have substantial periods of linear growth. The normalized growth rate (α) is

$$\alpha = \frac{1}{\dot{m}}\frac{db^2}{dt} = \frac{d(b\Delta/\dot{m})^2}{d\tau}\,, \qquad (1)$$

where the nondimensional time τ is given by $\tau = t\Delta^2/\dot{m}$. In the unforced flow $\alpha = 0.23$, which is significantly smaller than the experimental value of 0.34 in Ref. 9. In contrast, the forced case has no extended period of self-similar growth, though there are short periods during which b^2 and/or U_0^{-2} develop linearly. The best chance for self-similarity in the forced case occurs near the end of the simulation ($\tau > 40$). Here bU_0 (figure 2(c)) appears to be reaching a plateau indicating that b and U_0 are evolving together ($\alpha = 1.63$ at this time in the unforced flow). Furthermore the statistical profiles discussed below are roughly consistent with self-similarity.

Another global quantity that can be examined for evidence of self-similarity is

$$\mathcal{E} = \int_{-\infty}^{\infty}\epsilon\,dy\,, \qquad (2)$$

the integrated rate of dissipation of kinetic energy ($\epsilon = 2\nu\overline{S_{ij}S_{ij}}$, where S_{ij} is the strain-rate tensor and ν is the kinematic viscosity). This quantity has units of velocity cubed and therefore should scale with U_0^3. Thus $\mathcal{E}/U_0^3$ should be a constant during self-similarity. In figure 2(d), it is shown that $\mathcal{E}/U_0^3$ is indeed approximately constant for $40 \le \tau \le 90$ in the unforced case, but the evidence for

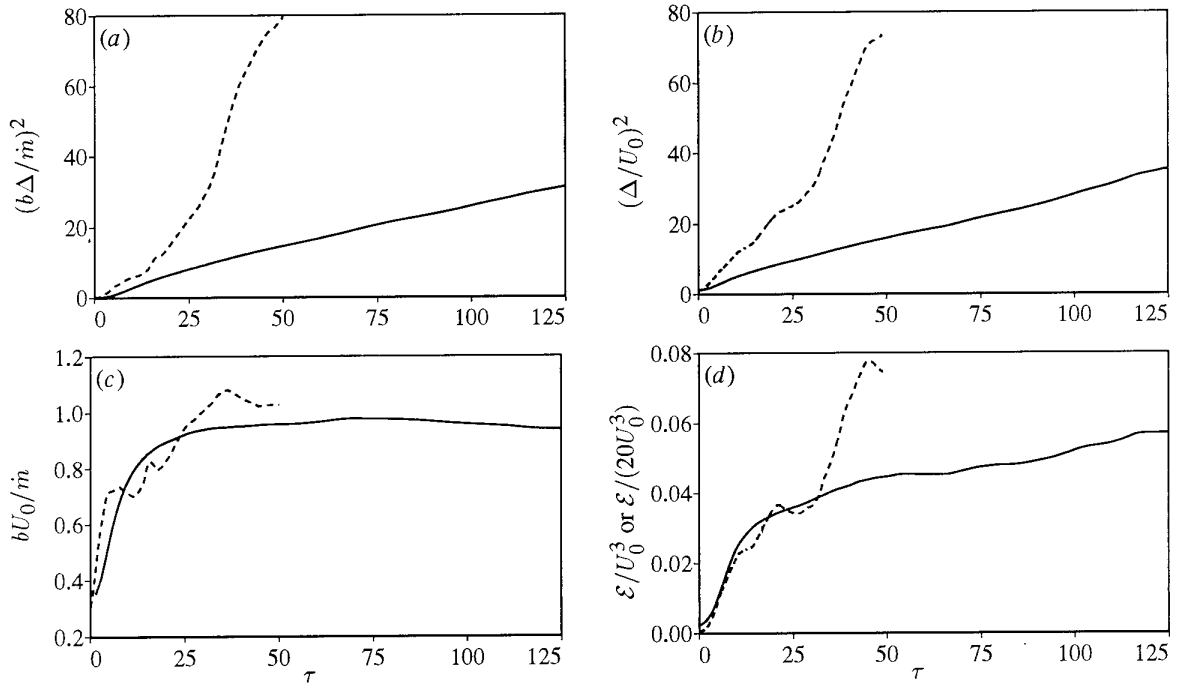

Figure 2. Evolution of (a) $(b\Delta/\dot{m})^2$, (b) $(\Delta/U_0)^2$, (c) $bU_0/\dot{m}$, and (d) $\mathcal{E}/U_0^3$ or $\mathcal{E}/(20U_0^3)$ in the —— unforced and ---- forced wake simulations, respectively.

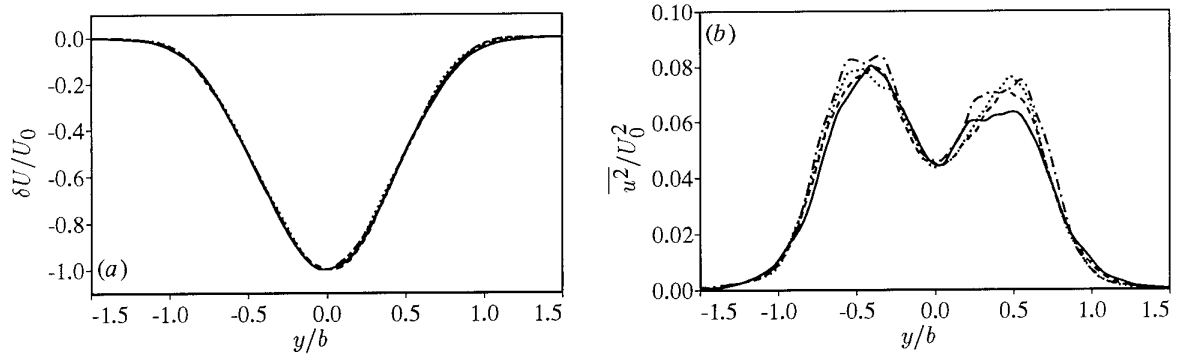

Figure 3. Collapse of (a) $\delta U/U_0$ and (b) $\overline{u^2}/U_0^2$ in scaled coordinates at four times during the self-similar period at —— $\tau = 42.8$, ---- $\tau = 56.6$, ····· $\tau = 71.7$ and —·— $\tau = 91.5$.

self-similarity is less convincing during the approximately self-similar period ($\tau > 40$) in the forced case.

The self-similarity of the unforced flow is further supported by the mean velocity and Reynolds stress profiles, when plotted in self-similar coordinates. Shown in figure 3 are the mean velocity and streamwise velocity variance at four times in the self-similar period ($42.8 \leq \tau \leq 91.5$) of the unforced flow. The collapse of these curves is good. Profiles from times outside of this period (not shown) do not collapse nearly as well. As in the mixing layer simulations in Ref. 8, the breakdown of self-similarity at late times appears to be caused by the finite size of the computational domain. In the forced flow, the mean and variance profiles also collapse quite well during the approximate self-similar period ($\tau > 40$).

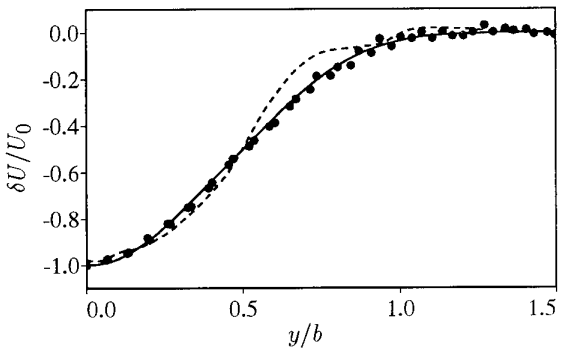

Figure 4. Comparison of time-averaged (in scaled coordinates) wake deficit profiles from ——, the unforced wake simulation, ---- the forced wake simulation, and • the experiments of Ref. 9.

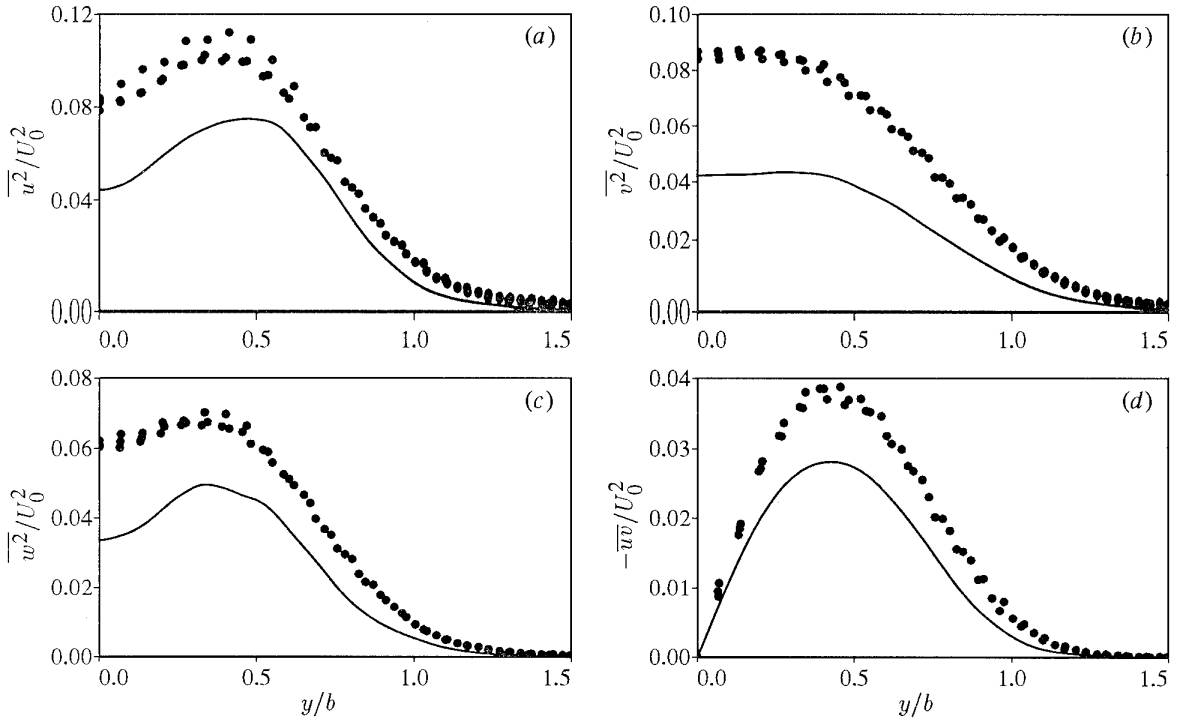

Figure 5. Comparison of the time-averaged (in scaled coordinates) components of the Reynolds stress tensor from ——, the unforced simulations, and • the experiments of Ref. 9.

Since the average quantities collapse in self-similar coordinates, they can also be averaged in time over the self-similar period, reducing the statistical noise in the profiles. The results of such averaging are shown in figures 4 and 5 for the mean velocity and Reynolds stress components, respectively. Also shown are the data from Ref. 9. Note that the magnitudes of the Reynolds stress components in the forced case are an order of magnitude larger than the curves shown in figure 5, and are therefore omitted (see figure 6). Since the wake is statistically symmetric, the statistical sample in these profiles has been increased by averaging the two sides of the wake together. Only half of each average profile is shown. The agreement between the experimental and unforced computational mean velocity is very good. However, the mean profile from the forced flow does not agree as well, and is not smooth. This is presumably because of the poor statistical sample of the large structures that dominate the forced flow (see §5). The components of the Reynolds stress tensor in the unforced computation shown in figure 5 have the same general shape as those measured in the Weygandt & Mehta[9] experiments, but the magnitudes are smaller.

Part of the reason for this difference in Reynolds stress magnitude is the difference in growth rates noted above. As was pointed out by George,[3] a variety of self-similar turbulent flows could occur in the same flow situation, and even if the (normalized) mean velocities are the same, the growth rates, Reynolds stresses, and dissipation rates (for example) can differ. In fact there is a direct relationship between the magnitude of the (normalized) Reynolds shear stress and the growth rate α. To see this, express the mean velocity and Reynolds shear stress in self-similar form:

$$\delta U = U_0 f(\zeta) \qquad -\overline{uv} = Rg(\zeta), \tag{3}$$

where $\zeta = y/b$, f and g are the self-similar profiles, and R is the scale for the Reynolds stress. In the time-developing wake, the mean velocity equation (in the inviscid limit) is

$$\frac{\partial \delta U}{\partial t} = -\frac{\partial \overline{uv}}{\partial y} . \tag{4}$$

Substituting the self-similar forms, evaluating the derivatives, and rearranging yields

$$f + \zeta f' = -\frac{2bR}{\dot{m}\alpha U_0} g' . \tag{5}$$

If two different wakes have the same f, then they must have the same g' profile and the scaling R must be given by

$$R = U_0^2 \alpha \frac{\dot{m}}{U_0 b} . \tag{6}$$

Since $\dot{m}/(U_0 b)$ is a shape factor of order one (see figure 2(c)), the Reynolds shear stress should scale like $U_0^2\alpha$. It is reasonable to assume that all components of the Reynolds stress tensor scale this way, and that at least some of the differences in the velocity variances shown in figure 5 are due to growth rate differences.

Profiles of the Reynolds stress tensor components normalized by $U_0^2\alpha$ are shown in figure 6 for both the simulations and the experiments of Ref. 9. This scaling with α has indeed reduced the differences among the different wakes. The unforced simulation and the experiments agree well with regard to the level of $\overline{u^2}$, $\overline{w^2}$, and $\overline{uv}$, but the level

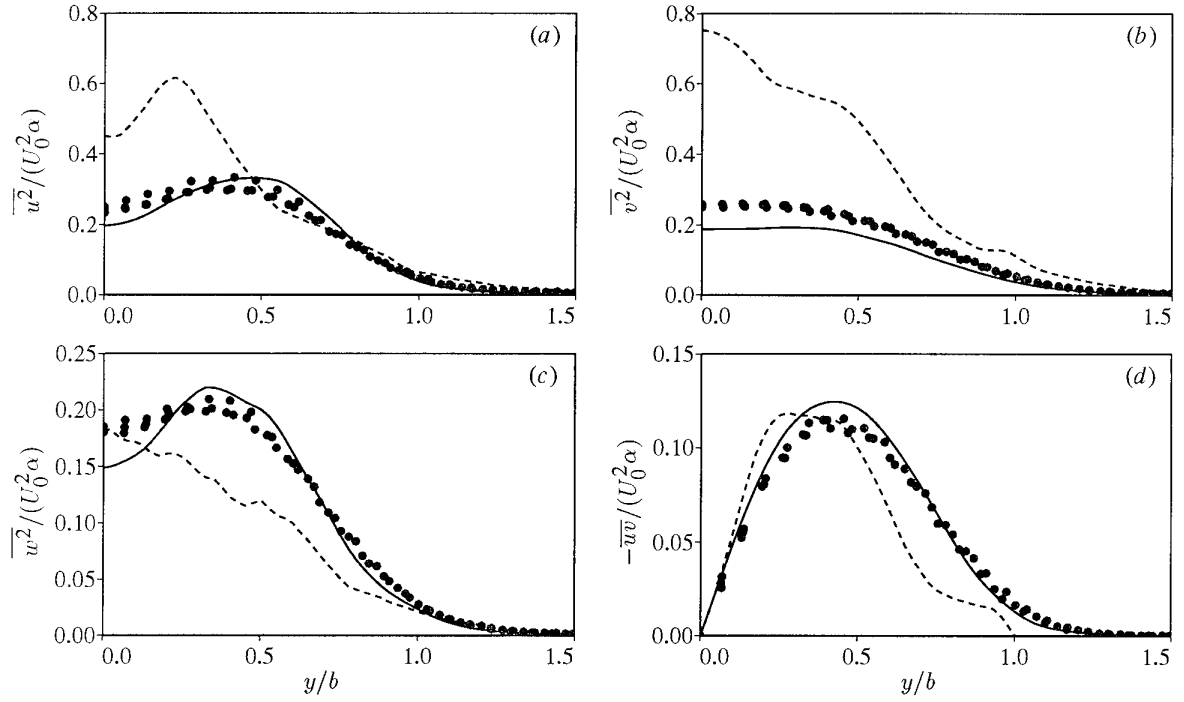

Figure 6. Comparison of the time-averaged (in scaled coordinates) profiles of $\overline{u^2}$, $\overline{v^2}$, $\overline{w^2}$, and $\overline{uv}$ normalized by $U_0^2\alpha$ from ——— , the unforced wake simulation, - - - - the forced wake simulation, and • the experiments of Ref. 9.

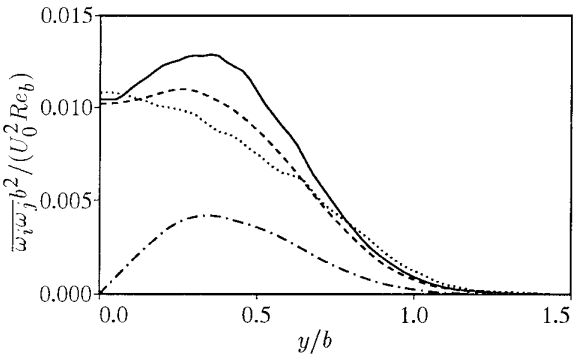

Figure 7. Time-averaged (in scaled coordinates) vorticity correlation tensor profiles $\overline{\omega_i\omega_j}$. ——— $\overline{\omega_1^2}$, - - - - $\overline{\omega_2^2}$, ····· $\overline{\omega_3^2}$, —·— $\overline{\omega_1\omega_2}$.

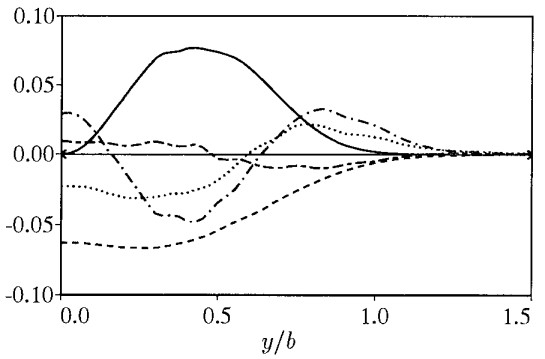

Figure 8. Terms in the $\overline{q^2}$ balance equation, scaled by U_0^3/b. ——— production - - - - dissipation ····· time derivative, —·— turbulent diffusion, and — - — pressure diffusion.

of $\overline{v^2}$ is still about 30% higher in the experiments. It is interesting that the levels of $\overline{u^2}$ and $\overline{v^2}$ in the forced case can be several times larger than those in the other data, while the $\overline{w^2}$ and $\overline{uv}$ profiles agree reasonably well for all three wakes when scaled with $U_0^2\alpha$. Apparently the strong forcing of the two-dimensional modes has produced a wake that is qualitatively different from the other two wakes (see §5). As pointed out in Ref. 3, the profiles of all the Reynolds stress tensor components are not expected to collapse perfectly in this scaling due to the unknown variation of the various terms in the Reynolds stress balance equations. A similar variation in the shapes of the $\overline{u^2}$ profiles in different wakes was reported in Ref. 1.

In addition to velocity statistics, vorticity statistics can be obtained from the simulations. As in Ref. 8, the scaling of $\mathcal{E}$ with U_0^3 implies that the vorticity variances should scale like $Re_b U_0^2/b^2$, where $Re_b = U_0 b/\nu$. However, since Re_b is a constant in a self-similar wake, the Reynolds number factor would only be important when comparing wakes at different Reynolds numbers. The vorticity variances averaged over the self-similar period in the unforced flow are shown in figure 7. The relative magnitudes of the variances of the vorticity components are in general agreement with those found in previous computations of homogeneous shear flows[10] and plane mixing layers[8].

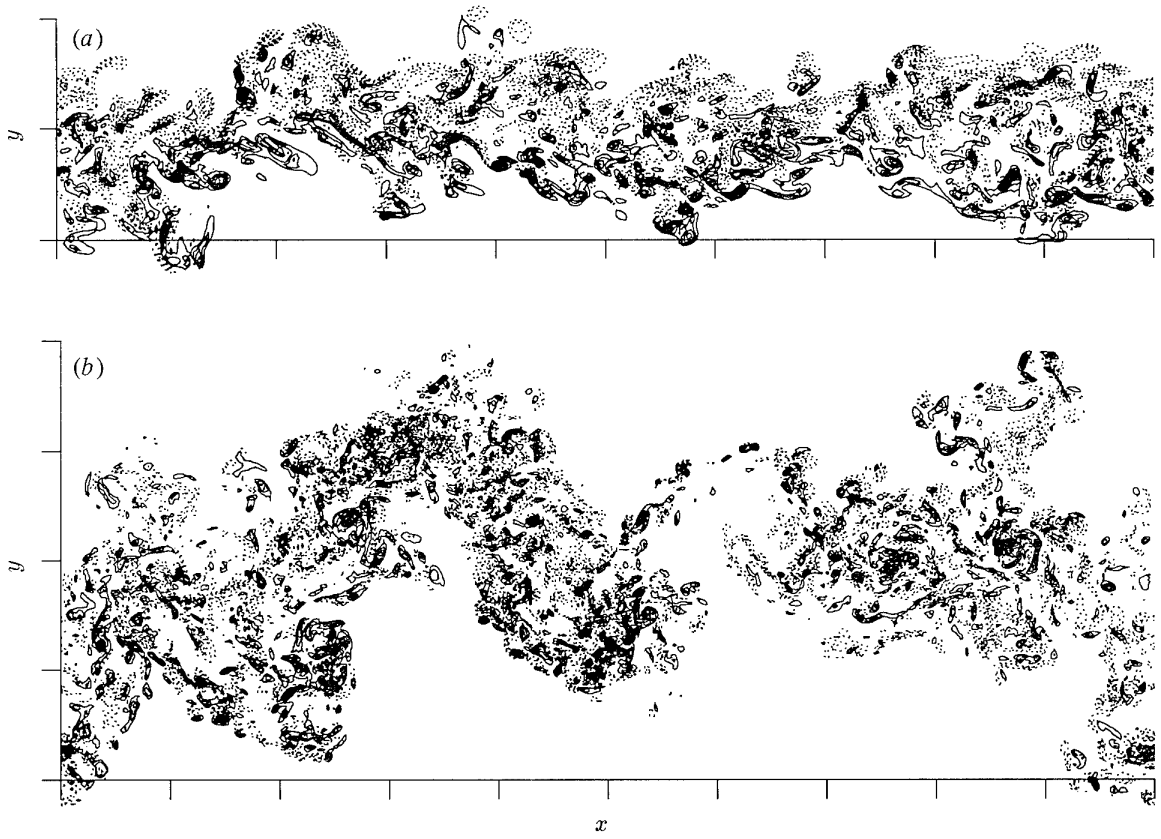

Figure 9. Contours of spanwise vorticity in an x–y plane in (a) the unforced flow at $\tau = 91.5$ and (b) the forced flow at $\tau = 50.0$. The contour increments are (a) $2.5U_0/b$ and (b) $20U_0/b$, and negative contours are dotted. Tic marks are at $5\dot{m}/\Delta$ intervals.

Some of the more difficult statistical quantities to determine experimentally are the terms in the balance equations for the Reynolds stresses. As an example, consider the equation for $\overline{q^2} = \overline{u_i u_i}$, which in this case of the time-developing wake is given by

$$\frac{\partial \overline{q^2}}{\partial t} = -2\overline{uv}\frac{\partial \delta U}{\partial y} - \frac{\partial \overline{q^2 v}}{\partial y} - \frac{\partial \overline{pv}}{\partial y} - \frac{2}{Re}\overline{\frac{\partial u_i}{\partial x_j}\frac{\partial u_i}{\partial x_j}} + \frac{1}{Re}\frac{\partial^2 \overline{q^2}}{\partial y^2} \tag{7}$$

The terms on the right hand side are interpreted (in order of appearance) as production, turbulent diffusion, pressure diffusion, dissipation, and viscous diffusion. The average of the terms in this equation over the self-similar period in the unforced flow are shown in figure 8.

Since the shear is zero at the center of the wake, the production is zero there. Production of $\overline{q^2}$ thus peaks in the maximum shear region and turbulent diffusion provides transport to the center of the wake. Turbulent diffusion also transports $\overline{q^2}$ to the edge of the wake, and is thus responsible for most of the growth in the width of the $\overline{q^2}$ profile. There is also a small transport from the edge of the wake to the center by pressure diffusion. The negative time derivative near the center of the wake produces the t^{-1} decay in the maximum $\overline{q^2}$, and the growth in the width of the turbulent region is reflected in the positive time derivative at the edge of the wake. For a self-similar wake, the time derivative can be computed directly from the $\overline{q^2} = U_0^2 h(\zeta)$ profile, with the result

$$\frac{b}{U_0^3}\frac{\partial \overline{q^2}}{\partial t} = -\frac{\dot{m}}{U_0 b}\alpha\left(h + \frac{1}{2}\zeta h'\right) . \tag{8}$$

At the centerline, $h = \overline{q^2}/U_0^2$ is 0.12 and the shape factor $\dot{m}/(U_0 b)$ is 1.04 (see figure 2(c)), resulting in a centerline value of the time derivative of 0.028. This is somewhat larger than the value (0.023) computed from the simulation data and plotted in figure 8. The discrepancy is a measure of the departure of the unforced simulation from self-similarity, and the adequacy of the statistical sample.

5. STRUCTURES

The large statistical differences between the forced and unforced wakes discussed in §4 are a manifestation of differences in the structure of the turbulence in these two flows. This difference can be seen in figure 9, where spanwise vorticity contours in x–y planes of both the forced and unforced flows are shown. In the forced case, there are concentrations of vorticity fluctuations that occur alternately on one side of the wake or the other, similar to the Karman street commonly observed in transitional wakes. By examining other x–y planes (not shown), one can determine that these large-scale features are spanwise coherent. The vorticity concentrations are also accompanied by large incursions of irrotational fluid into the

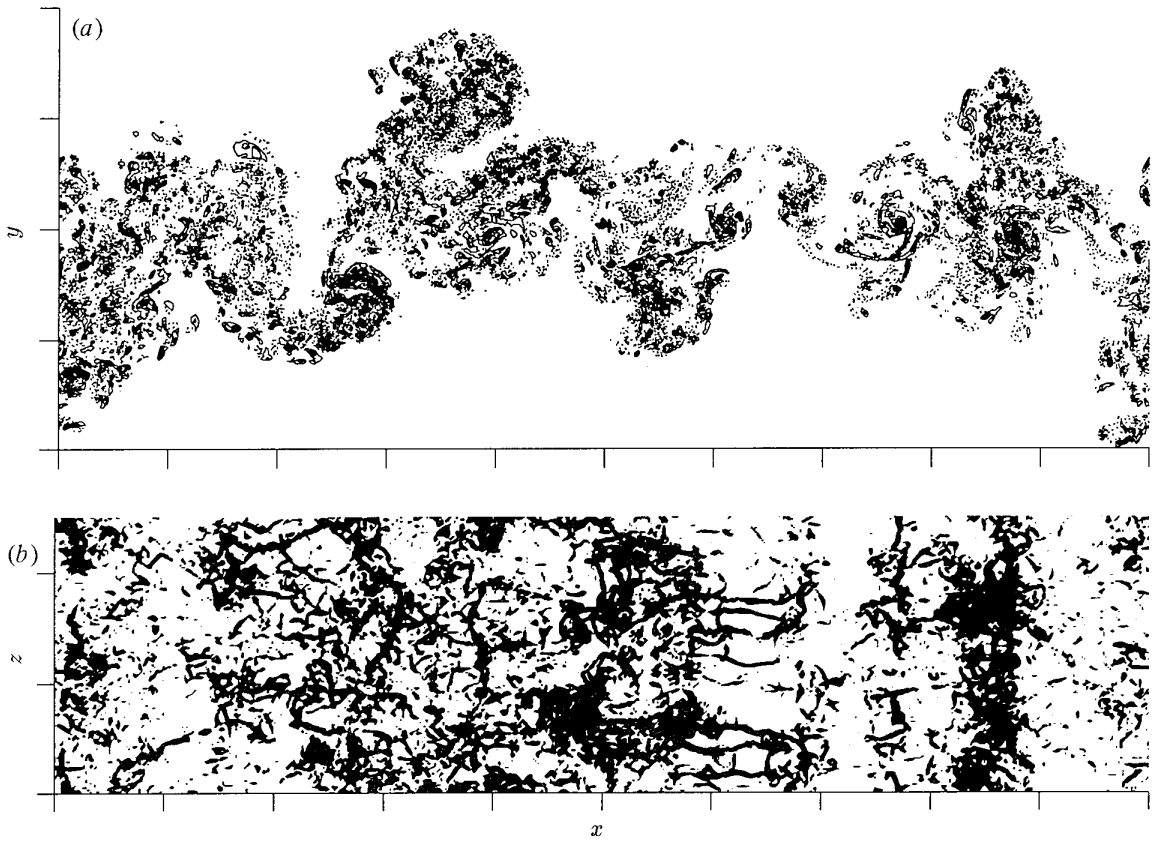

Figure 10. (a) Contours of spanwise vorticity in an x–y plane (contour increment of $10U_0/b$) and (b) top view of regions where enstrophy ($\omega_i\omega_i$) is larger than $8700U_0^2/b^2$ in the forced flow at $\tau = 26.3$. Tic marks are at $5\Delta/\dot{m}$ intervals.

wake. In contrast, the unforced wake exhibits no such vorticity concentrations, and relatively small incursions of irrotational fluid. It appears to consist of a slab of turbulence with undulating boundaries. Forcing was also found to produce large-scale structures similar to those in transitional flows in the turbulent mixing layers of Ref. 8.

Another striking difference between the two flows is that the forced flow appears to have vorticity fluctuations of much smaller scale. This is consistent with the appearance of the streamwise spatial spectra in figure 1 and the fact that finer spatial resolution was required to compute the forced flow. Comparing figure 9(a) and figure 9(b), it appears that the forced flow has a larger Reynolds number than the unforced flow since there are larger large-scale features, and smaller small-scale features. Indeed the centerline value of the turbulence Reynolds number $q^4/(\epsilon\nu)$ is an order of magnitude larger in the forced case than in the unforced case (4000 versus 460), this despite the fact that the Reynolds numbers based on $\dot{m}$ are the same in the two flows.

The mixing layer simulations of Rogers & Moser[8,11] suggest that whenever there is a flow region that is dominated by large-scale strain, but largely devoid of (spanwise) vorticity, it is likely that long coherent vortices aligned with the extensional strain (so-called rib vortices), will develop. Such a region might be expected between the vortices in a Karman Street, and indeed rib vortices have been observed in simulations of transitional wakes.[12] A strain-dominated region of this type appears to exist in the forced flow shown in figure 9(b)(at $x \approx 35\dot{m}/\Delta$), but no rib vortices were found at this time. However, at an earlier time ($\tau = 26.3$, figure 10), the strain-dominated region is also present and rib vortices occur there. The rib vortices can be seen in figure 10(b) as the long thin streamwise-oriented regions of large enstrophy at $x \approx 35\dot{m}/\Delta$. These vortices span the strain-dominated region, and do not occur elsewhere in the forced flow or anywhere in the unforced flow, which has no such strain-dominated regions. The reason for the disappearance of the rib vortices at later times has not yet been investigated.

6. CONCLUSIONS

Two turbulent time-developing plane wakes (forced and unforced) have been simulated numerically, and at least the unforced wake evolves self-similarly for a significant period. The growth rate of the unforced wake is low by 30% compared to experimentally observed growth rates. In the unforced flow, the magnitude of all the components of the Reynolds stress tensor except $\overline{v^2}$ are in general agreement with the experimental data of Ref. 9 when scaled by the growth rate. The vertical velocity variance is lower than the experiments by 30%.

The forced flow is not convincingly self-similar. But, toward the end of the simulation, it appears to be beginning a self-similar growth period. However, the growth rate α is an order of magnitude larger than in the unforced flow, and the turbulence levels are several times larger, even when the difference in growth rates is accounted for. Also, the turbulence Reynolds number is much larger than in the unforced flow, even though the bulk Reynolds numbers are the same. Finally, the forced flow exhibits large-scale structures similar to those observed in transitional wakes, though no such structures were present in the unforced flow. The strong forcing has resulted in a qualitatively different turbulent flow. It is not clear if this difference would be maintained if the flow could continue to evolve.

REFERENCES

1. I. Wygnanski, F. Champagne, and B. Marasli, "On the Large-scale Structures in Two-dimensional Small-deficit, Turbulent Wakes," J. Fluid Mech. **168**, 31 (1986).

2. B. Marasli, F. H. Champagne, and I. Wygnanski, "Effect of Travelling Waves on the Growth of a Plane Turbulent Wake," J. Fluid Mech. **235**, 511 (1992).

3. W. K. George, "The Self-Preservation of Turbulent Flows and its Relation to Initial Conditions and Coherent Structure," in *Advances in Turbulence*, edited by W. K. George and R. Arndt (Hemisphere, New York, 1989), pp. 39–73.

4. R. A. Antonia, L. W. B. Browne, and D. K. Bisset, "A Description fo the Organized Motion in the Turbulent Far Wake of a Cylinder at Low Reynolds Number," J. Fluid Mech. **184**, 423 (1987).

5. M. Hayakawa and F. Hussain, "Three-Dimensionality of Organized Structures in a Plane Wake," J. Fluid Mech. **206**, 375 (1989).

6. P. R. Spalart, R. D. Moser, and M. M. Rogers, "Spectral methods for the Navier–Stokes equations with one infinite and two periodic directions," J. Comp. Phys. **96**, 297 (1991).

7. P. R. Spalart, "Direct simulation of a turbulent boundary layer up to $R_\theta = 1410$," J. Fluid Mech. **187**, 61 (1988).

8. M. M. Rogers and R. D. Moser, "Direct Simulation of a Self-similar Turbulent Mixing Layer," Phys. Fluids **6**, 903 (1994).

9. J. H. Weygandt and R. D. Mehta, JIAA TR-110, Stanford University (1993).

10. M. M. Rogers and P. Moin, "The structure of the vorticity field in homogeneous turbulent flows," J. Fluid Mech. **176**, 33 (1987).

11. M. M. Rogers and R. D. Moser, "The three-dimensional evolution of a plane mixing layer: the Kelvin-Helmholtz rollup," J. Fluid. Mech. **243**, 183 (1993).

12. J. C. Lasheras and E. Meiburg, "Three-Dimensional Vorticity Modes in the Wake of a Flat Plate," Phys. of Fluids **2**, 371 (1990).

The Effect of Initial Conditions on the Development of Temporally Evolving Planar Three Dimensional Incompressible Wakes

Rolf Sondergaard
Dept. of Aeronautics and Astronautics
Stanford University
Stanford, CA, 94305
USA

Nagi N. Mansour
NASA-Ames Research Center
Mountain View, CA, 94035
USA

Brian J. Cantwell
Dept. of Aeronautics and Astronautics
Stanford University
Stanford, CA, 94305
USA

SUMMARY

A set of direct numerical simulations of temporally evolving incompressible plane wakes started from a variety of initial conditions have been performed. The intent is to explore the effect of initial conditions on the development of three dimensionality. It was found that the existence of an oblique disturbance at a streamwise wavelength equal to the two-dimensional subharmonic wavelength plays a very important role in the development of the wake. The Reynolds number and the presence or absence of longer wavelength disturbances were also found to be important at late times in the development of the flow. Disturbance phase was found to have an effect on the details of the structure of the wake, but has relatively little effect on the wake growth.

1 INTRODUCTION

The primary instability in plane wakes, the Kelvin-Helmholz instability which grows into the familiar Karman vortex street, has come to be relatively well understood. Secondary instability modes and eventual transition to turbulence, however, are still not well understood, and are the subject of ongoing research.

One of the key research issues has to do with the apparent non-uniqueness of the far field development of wakes. Experiments by Wygnanski, Champagne, and Marasli [1] showed that the asymptotic growth rate of incompressible plane wakes depended significantly on the specific geometry of the wake generator. Numerical calculations by Chen, Cantwell, and Mansour [2] showed that detailed features in the late stages of three-dimensional development of a compressible planar wake were sensitive to the relative phase of disturbance modes in the initial field.

The purpose of the present work is to examine the relationship between initial flow conditions and secondary development in incompressible plane wakes. A series of simulations were run on the massively parallel NAS Intel *iPSC/860*, located at the NASA-Ames Research Center. The simulations were used to explore the effects of various combinations and phasings of initial laminar disturbances on the development of three dimensionality and transition to turbulence. These disturbances included two- and three-dimensional modes from fundamental through sub-subharmonic streamwise wave-

Paper presented at the 74th Fluid Dynamics Symposium on "Application of Direct and Large Eddy Simulation to Transition and Turbulence" held at Chania, Crete, Greece, in April 1994.

lengths. The wake Reynolds numbers based on initial flow halfwidth and mean centerline defect velocity

$$Re \equiv \frac{\Delta u_{\mathbb{C}0}\, b_0}{\nu} \tag{1}$$

were between 119 and 2768. The low end of this range was chosen to match experiments on spatially evolving plane wakes by Corke, Krull, and Ghassemi [3]. The high end is intended to allow the study of moderately turbulent wakes, and is limited by the capabilities of the computational hardware used.

2 METHOD

The simulations were carried out using a newly developed code based on an algorithm similar to one introduced by Corral and Jiménez [4]. The algorithm allows Fourier spectral methods to be applied to problems with one infinite and two periodic directions without having to resort to nonlinear mapping of the infinite direction to a finite domain. This is accomplished by computing only the rotational region of the flow. The boundary conditions for the computed region are obtained by matching to known asymptotic solutions for the bordering irrotational regions.

The basic approach is to divide the flow into three domains in the non-periodic direction as shown in Figure 1. Domain I extends from $-\infty$ to $Y_1(t)$, domain II from $Y_1(t)$ to $Y_2(t)$, and domain III from $Y_2(t)$ to $+\infty$. The boundaries $Y_1(t)$ and $Y_2(t)$ are chosen such that domain II contains all the vorticity in the flow, and domains I and III are vorticity free. This choice of $Y_1(t)$ and $Y_2(t)$ requires that the vorticity magnitude and vorticity gradient at the top and bottom of domain II be zero (or in practice very small). This is the case for many flows of interest, particularly at high Reynolds number where the interface between rotational fluid and irrotational fluid is sharp. Choosing $Y_1(t)$ and $Y_2(t)$ in this way allows the vorticity in domain II to be treated as fully periodic. The vorticity equations governing the flow may then be solved with a pseudo-spectral technique which uses standard complex Fourier transforms in all three directions.

The inherent non-periodic nature of the flow only enters into the equations of motion through the nonlinear term of the momentum equation. The vorticity, ω_j, is not directly affected by the images of the flow vorticity created by artificially introducing periodicity in the non-periodic direction. It can accurately be treated as being periodic. The velocity, u_j, which is a solution of a Poisson equation involving the vorticity as a source term, is affected by the vorticity images and must be corrected to remove the effect of the artificial periodicity. This is accomplished by adding an incompressible, irrotational component to the velocity field in domain II which matches it to analytic asymptotic solutions for the velocity in domains I and III.

2.1 Numerical Algorithm

The vorticity form of the Navier-Stokes equations is

$$\omega_{j,t} + \epsilon_{jkl}(\epsilon_{lmn} u_n \omega_m)_{,k} = \nu \omega_{j,kk} \tag{2}$$

$$\omega_j = \epsilon_{jkl} u_{l,k} \tag{3}$$

where ω_j and u_j are the vorticity and velocity components in the j direction, and ϵ_{jkl} is the alternating unit tensor

$$\epsilon_{jkl} \equiv \begin{cases} 1, & \text{if } (j,k,l) = (1,2,3), (3,1,2), \\ & \quad \text{or } (2,3,1) \\ -1, & \text{if } (j,k,l) = (3,2,1), (1,3,2), \\ & \quad \text{or } (2,1,3) \\ 0, & \text{if } j = k,\ j = l, \text{ or } k = l. \end{cases} \tag{4}$$

In order to maximize the available resolution for a given number of grid points while at the same time keeping the vorticity at the edges of the resolved box small as required for the asymptotic matching, a growing uniform grid is used in the non-periodic x_2 direction. To implement this, the coordinates in each direction are rescaled to an interval of 2π, the "natural" interval for Fast Fourier Transforms.

$$\begin{aligned} \xi_1 &= 2\pi x_1 / L_1 \\ \xi_2(t) &= 2\pi (x_2 - Y_1(t)) / L_2(t) \\ \xi_3 &= 2\pi x_3 / L_3 \end{aligned} \tag{5}$$

where L_1 and L_3 are the fixed box lengths in the periodic x_1 and x_3 directions respectively and $L_2(t) = Y_2(t) - Y_1(t)$ is the time varying box size in the aperiodic x_2 direction.

Applying these coordinate transforms to the vorticity equations yields

$$\begin{aligned} \omega_{j,t} + \epsilon_{jkl}(\epsilon_{lnq} u^*_q \omega_n)_{,m} \Lambda_{mk} + \gamma \omega_j L_{2,t}/L_2 \\ = \nu \omega_{j,kl} \Lambda_{lm} \Lambda_{mk} \end{aligned} \tag{6}$$

$$\omega_j = \epsilon_{jkl} u^*_{l,m} \Lambda_{mk} = \epsilon_{jkl} u_{l,m} \Lambda_{mk} \tag{7}$$

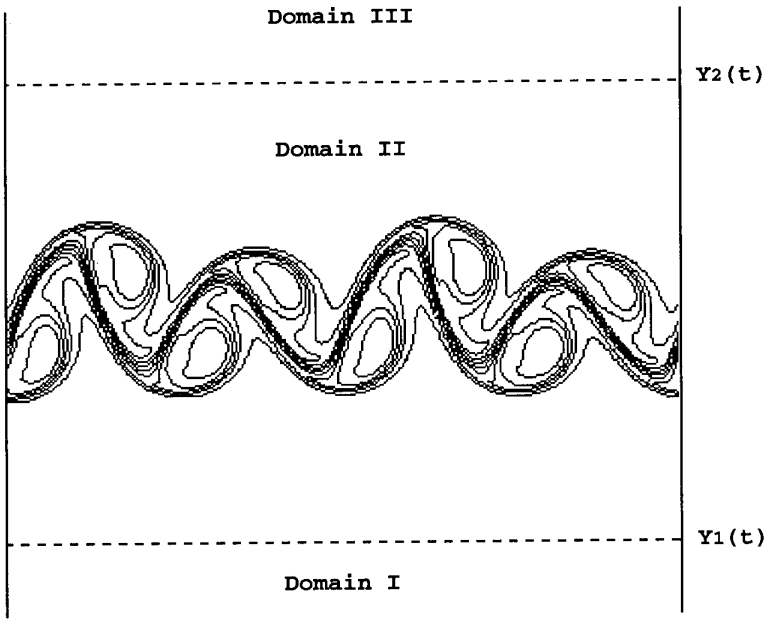

Figure 1: Numerical domains for computation

$$\Lambda_{jk} \equiv \begin{cases} 2\pi/L_j, & if \text{ j=k;} \\ 0, & \text{otherwise.} \end{cases} \quad (8)$$

$$\gamma \equiv \begin{cases} 1, & if \text{ j=1,3;} \\ 0, & \text{otherwise.} \end{cases} \quad (9)$$

where $u_j^* = u_j - L_{2,t}(t)\xi_2\delta_{2j}/2\pi$ is a grid stretching velocity.

The flow is periodic in the streamwise ξ_1 and spanwise ξ_3 directions

$$\Phi(\xi_1 + 2\pi, \xi_2, \xi_3; t) = \Phi(\xi_1, \xi_2, \xi_3; t) \quad (10)$$

$$\Phi(\xi_1, \xi_2, \xi_3 + 2\pi; t) = \Phi(\xi_1, \xi_2, \xi_3; t) \quad (11)$$

where Φ is any dependent variable. The vorticity is zero outside the resolved box

$$\omega_j = 0 \qquad \text{for } \xi_2 < 0 \quad \text{or} \quad \xi_2 > 2\pi \quad (12)$$

and the velocity perturbations go to zero at infinity

$$u_j(\xi_1, \xi_2, \xi_3; t) \overset{\xi_2 \to \pm\infty}{\longrightarrow} U_0. \quad (13)$$

The governing equations are solved in domain II using a standard Fourier pseudo-spectral technique treating the vorticity as periodic in the aperiodic direction ξ_2. Note that all of the terms in equation 6 can be treated as periodic since by construction $\omega_j \to 0$ at the top and bottom of the computational box.

The governing equations are advanced in wave space with nonlinear terms which are calculated in physical space at each timestep using a velocity which is the sum of the periodic velocity calculated from equation 7 and an aperiodic, irrotational velocity which matches the velocity and velocity gradient to asymptotic solutions outside the resolved domain.

Only one component of u_j need be solved for, since the remaining two components can be constructed from continuity and the definition of vorticity. It is convenient to solve for the cross-stream velocity u_2.

Taking the curl of equation 7 gives

$$u_{j,kl}\Lambda_{lm}\Lambda_{mk} = -\epsilon_{jkl}\omega_{l,m}\Lambda_{mk}. \quad (14)$$

The u_2 part of equation 14 is transformed in the two periodic (ξ_1 and ξ_3) directions, but not in the non-periodic direction giving the second order ordinary differential equation in ξ_2

$$\tilde{u}_{2,22}/L_2^2 + (k_1^2/L_1^2 + k_3^2/L_3^2)\tilde{u}_2 = -k_l\Lambda_{lj}\epsilon_{2jk}\tilde{\omega}_k/4\pi^2. \quad (15)$$

The general solution to equation 15 is

$$\tilde{u}_2 = \tilde{u}_2^P + \tilde{A}exp(L_2(k_1^2/L_1^2 + k_3^2/L_3^2)^{\frac{1}{2}}\xi_2) + \tilde{B}exp(-L_2(k_1^2/L_1^2 + k_3^2/L_3^2)^{\frac{1}{2}}\xi_2) \quad (16)$$

where $\tilde{u}_2^P$ is the particular solution of equation 15 (zero in domains I and III where the vorticity is zero, calculated numerically from the vorticity field in domain II), and $\tilde{A}$ and $\tilde{B}$ are functions of $K^2 = L_2^2(k_1^2/L_1^2 + k_3^2/L_3^2)$ to be determined by matching.

The solution for the velocity must be bounded at $\xi_2 = \pm\infty$, hence in the three domains

$$\tilde{u}_2 = \begin{cases} \tilde{A}_I e^{K\xi_2} & \text{I} \\ \tilde{u}_2^P + \tilde{A}_{II} e^{K\xi_2} & \\ \quad + \tilde{B}_I e^{-K\xi_2} & \text{II} \\ \tilde{B}_{II} e^{-K\xi_2} & \text{III.} \end{cases} \tag{17}$$

Matching the velocities and velocity gradients at the domain boundaries $\xi_2 = 0$ and $\xi_2 = 2\pi$ and solving for $\tilde{A}_{II}$ and $\tilde{B}_I$ gives

$$\tilde{u}_2 = \tilde{u}_2^P + \tfrac{1}{2}\Big((\tilde{u}_{2,2}^P(0)/K - \tilde{u}_2^P(0))exp(-K\xi_2) - (\tilde{u}_{2,2}^P(2\pi)/K + \tilde{u}_2^P(2\pi))exp(K\xi_2)\Big) \tag{18}$$

$$K \equiv L_2\left(\frac{k_1^2}{L_1^2} + \frac{k_3^2}{L_3^2}\right). \tag{19}$$

Solutions for $\tilde{u}_1$ and $\tilde{u}_3$ are constructed from the resulting solution for $\tilde{u}_2$ in domain II and the total solution for the velocity is transformed to physical space in the periodic directions. The cross product of the velocity and the vorticity is taken to form the periodic nonlinear term. The nonlinear term is then transformed back into wave space to advance the vorticity and scalar fields in time.

2.2 Time Advance and Dealiasing

The time advancement method used was the second order Runge-Kutta scheme

$$\Phi_{,t} = f(\Phi; t) \tag{20}$$

$$\Phi_\dagger^{n+1} = \Phi^n + \Delta t f(\Phi^n; t^n) \tag{21}$$

$$\Phi^{n+1} = \Phi^n + \tfrac{\Delta t}{2}(f(\Phi^n; t^n) + f(\Phi_\dagger^{n+1}; t^{n+1})) \tag{22}$$

where n is the time index.

Following the approach of Rogallo [5], aliasing was controlled with a combination of high wavenumber masking and phase shifting. All modes with wavenumbers such that

$$\frac{k_1^2}{N_1^2} + \frac{k_2^2}{N_2^2} + \frac{k_3^2}{N_3^2} > \frac{2}{9} \tag{23}$$

are set to zero. This eliminates all two- and three-dimensional aliasing, leaving only the one-dimensional aliasing term in each direction. The one-dimensional alias errors are dealt with by phase shifting the data a random fraction of a grid cell width in each direction at every other time substep followed by a further shift of exactly one half a grid cell width in each direction at the subsequent time substep. This random shifting cancels the aliasing error to second order in time, the same order as the time advancement algorithm. Using this dealiasing technique instead of a perfect (2/3 rule or multiple phase shift) technique reduces both memory requirements and operations per timestep.

2.3 Initial Conditions

All the simulations were initiated with a Gaussian mean streamwise velocity profile

$$\bar{u}_1 = U_0 - \Delta u_{\mathbb{C}0} \exp(-cx_2^2). \tag{24}$$

The centerline velocity defect, $\Delta u_{\mathbb{C}0}$, was chosen to be $0.692U_0$ and c was chosen to be 0.69315. This profile was used in the experiments of Sato and Kuriki [6], Corke et al. [3], and in the computations of Chen et al. [2]. It gives an initial wake halfwidth of $b_0 = 1.0$. The halfwidth is defined as as half the width of the mean velocity profile at half the maximum mean defect velocity. The mean profile is generated by averaging over x_1–x_3 planes.

Small disturbances which were periodic in the streamwise and spanwise directions were added to the mean flow.

$$\begin{aligned} \Phi(\xi_1, \xi_2, \xi_3; 0) = \bar{\Phi} \\ + \; & Real[\varepsilon_{100}\hat{\Phi}_{100}\exp(i\alpha\xi_1) \\ + \; & \varepsilon_{010}\hat{\Phi}_{010}\exp(i\frac{\alpha\xi_1 + \phi_{010}}{2}) \\ + \; & \varepsilon_{001}\hat{\Phi}_{001}\exp(i\frac{\alpha\xi_1 + \phi_{001}}{4}) \\ + \; & \varepsilon^{100}\hat{\Phi}^{100}\exp(i(\alpha\xi_1 \pm \beta\xi_3 + \phi^{100})) \\ + \; & \varepsilon^{010}\hat{\Phi}^{010}\exp(i\frac{\alpha\xi_1 \pm \beta\xi_3 + \phi^{010}}{2}) \\ + \; & \varepsilon^{001}\hat{\Phi}^{001}\exp(i\frac{\alpha\xi_1 \pm \beta\xi_3 + \phi^{001}}{4})] \end{aligned} \tag{25}$$

where Φ is any of the dependent flow variables, $\bar{\Phi} = \bar{\Phi}(\xi_2)$ is the mean flow, and $\hat{\Phi} = \hat{\Phi}(\xi_2)$ is a disturbance eigenfunction. The quantities α and β are streamwise and spanwise wavenumbers respectively, and ϕ is a disturbance phase an-

gle. Subscripts indicate a two-dimensional disturbance, superscripts indicate a three-dimensional disturbance, and the position of the "1"s indicate the streamwise wavelength of the mode. As an example, ε^{001} is the disturbance amplitude of the three-dimensional disturbance at the subsubharmonic streamwise wavelength.

The disturbance eigenfunctions correspond to the most unstable cross-stream eigenmode for the given disturbance angle and wavelength as determined by linear theory. All the simulations were initiated with two-dimensional disturbance modes at a wavelength equal to the fundamental (Karman) mode ($\varepsilon_{100} > 0$). The three dimensional disturbances were pairs of oblique waves with equal and opposite spanwise wavenumbers oriented 60° to the spanwise direction ($\beta/\alpha = tan(60°)$). This particular choice of three-dimensional modes was motivated by previous stability analysis by Lasheras and Meiburg [7] which suggested that the most unstable three dimensional modes should be wave pairs at angles near 60° at the subharmonic wavelength. Experimental observations by Cimbala, Nagib, and Roshko [8] and Corke et al. [3] supported these results.

The amplitude for each disturbance eigenfunction was chosen such that the integral over x_2 of the disturbance velocity eigenfunction for the given mode was equal to $0.02U_0b_0$ where U_0 is the freestream velocity and b_0 is the initial wake halfwidth.

In the following discussion, all quantities are normalized appropriately by U_0 and b_0. Initial disturbances will be referenced using the convention introduced above. For example, the A_{100}^{011} condition represents a two-dimensional fundamental plus 60° waves at the subharmonic and subsubharmonic streamwise wavelengths.

3 RESULTS

3.1 Flow Structure

Figure 2 shows perspective views of three-dimensional enstrophy isocontours for four times in the development of a $Re = 119$ wake started from the A_{100}^{010} condition (two-dimensional fundamental disturbance and a pair of oblique disturbances at the subharmonic wavelength). The freestream flow direction is from left to right. The contour level was chosen to be the maximum mean wake defect velocity divided by the wake halfwidth at each time, which is a rough measure of the mean gradient in the flow.

The development of this wake is typical of the wake computations initiated with a two-dimensional fundamental disturbance and a pair of oblique disturbances at the subharmonic wavelength. The initial development is primarily two dimensional, with the fundamental (Karman) mode growing strongly as predicted by linear theory. The flow develops well defined spanwise rollers with relatively weak streamwise structures stretching between rollers on the same side of the wake. Once the spanwise rollers are established, the three dimensional disturbances begin to grow strongly. The streamwise structures will become more intense on one side of the wake or the other, depending on the phase of the oblique subharmonic disturbance. This asymmetry, which is induced by the relative phase of the disturbances, was also observed by Chen et al. [2] in two-dimensional computations of a compressible wake initiated with disturbances at the fundamental and subharmonic wavelengths. In the case presented here, ($\phi^{010} = 0$) the streamwise structures on the top of the wake dominate, though the structures on the bottom of the wake are still strong. As the streamwise structures grow in strength, they begin to distort the spanwise rollers, and eventually become the dominant features in the flow.

Figure 3 is an enstrophy isocontour plot for a $Re = 346$ wake started from condition A_{100}^{010}, the same as the wake in figure 2. The flow is at a time corresponding to figure 2c. Note that the contour level for figure 3 is twice the maximum mean wake defect velocity divided by the wake halfwidth, so the structures in figure 3 have a much higher relative strength than those in figure 2c. This higher Reynolds number wake exhibits the same sort of flow structure, with strong streamwise structures running between distorted spanwise rollers. The streamwise coherent structures are much more intense than in the lower Reynolds number flow, and the spanwise rollers are far more convoluted. This is consistent with the increase in intensity of the vorticity and decrease in the smallest length scale expected with an increase in the Reynolds number.

In stark contrast is the flow in figure 4a. This is again a $Re = 119$ wake at a time corresponding to figure 2c, but started from condition A_{100}^{100}, $\phi^{100} = 0$, a two-dimensional fundamental distur-

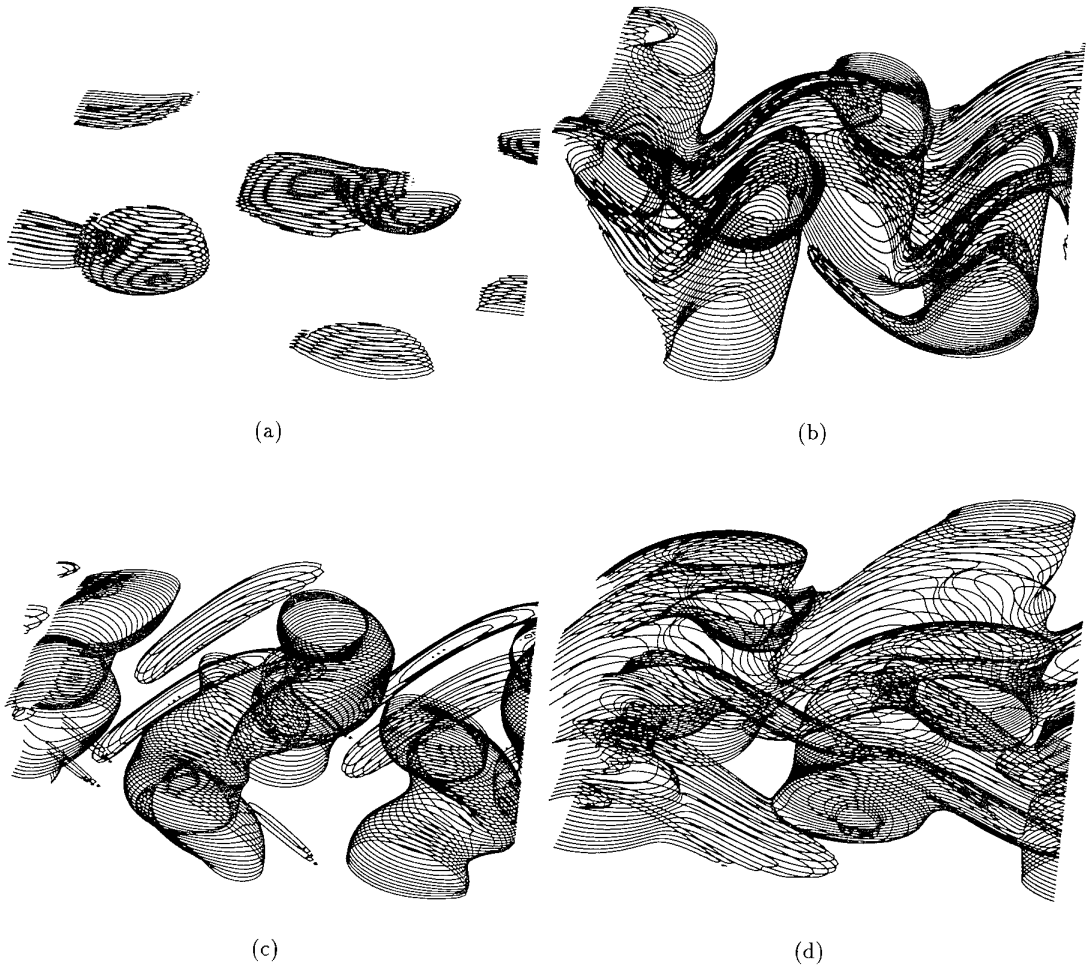

Figure 2: Enstrophy isocontour for $Re = 119$ wake, A_{100}^{010} condition. $\phi^{010} = 0$. (a) $t = 24.4$. (b) $t = 53.1$. (c) $t = 97.9$. (d) $t = 203.3$. Contour is $|\omega| = \max(\Delta\bar{u})/bi$.

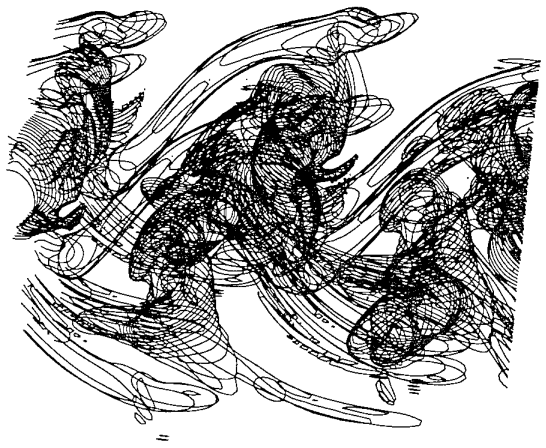

Figure 3: Enstrophy isocontour for $Re = 346$ wake, A_{100}^{010} condition. $\phi^{010} = 0$. $t = 102.7$. Contour is $|\omega| = 2\max(\Delta\bar{u})/bi$.

bance and a pair of oblique disturbances at the *fundamental* wavelength and zero relative phase.. The contour level is the maximum mean wake defect velocity divided by the wake halfwidth. With these initial conditions, the three dimensionality never develops to any significant extent. The streamwise structures are present, but at a very weak, dynamically insignificant level, far below the contour level shown. This is true even at much higher Reynolds numbers. Figure 4b is a flow started from the same conditions, but with $Re = 1384$. Though the streamwise structures are strong enough to appear at the contour level shown, and have a greater impact on the flow structure as evidenced by the visible corrugation in the spanwise rollers, they are still very weak and dynamically unimportant as compared to the streamwise structures in the flows started from

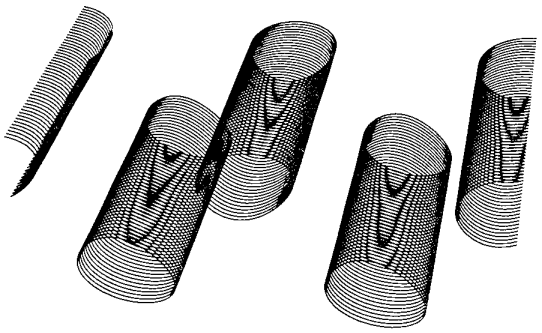

(a)

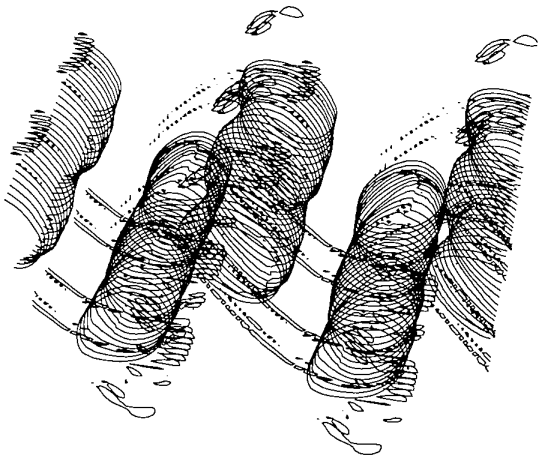

(b)

Figure 4: Enstrophy isocontours for wakes, A_{100}^{100} condition. $\phi^{100} = 0$. Contour is $|\omega| = \max(\Delta\bar{u})/bi$. (a) $Re = 119$, $t = 102.8$. (b) $Re = 1384$, $t = 100.2$.

Figure 5: Enstrophy isocontour for $Re = 119$ wake, A_{111}^{011} condition. All $\phi = 0$. $t = 102.8$. Contour is $|\omega| = \max(\Delta\bar{u})/bi$. Arrow identifies streamwsie structure from sub-subharmonic oblique disturbance.

the A_{100}^{010} condition. Similar results are found for computations started from the same set of initial disturbances, but with $\phi^{100} = \pi/2$. This result differs markedly from the compressible wake computed by Chen et al. [2], which showed strong three-dimensional development for one phase and only weak three-dimensional development for the other.

The effect of the addition of longer wavelength disturbances is illustrated by the flow in figure 5. This $Re = 119$ wake was started from the A_{111}^{011} condition, which is the initial condition for the flow in figure 2 with the addition of two-dimensional disturbances at the subharmonic and sub-subharmonic wavelengths and a pair of oblique disturbances at the sub-subharmonic wavelength. Note that the field shown is twice the size of the fields in the other figures (four fundamental wavelengths long instead of two). At the time shown, the wake has undergone a change in scale. The initial Karman vortex street, which contained four pairs of spanwise rollers, has evolved into a flow with two main spanwise structures at the subharmonic wavelength, each of which is composed of a pair of spanwise coherent structures of opposite sign of vorticity. These spanwise structures are the result of rollers on the same side of the wake merging together. The flow has the same general appearance as the other flows presented, with distorted spanwise structures connected by streamwise structures running between vortices on the same side of the wake. In this case the dominant streamwise structures (see arrow) are at a sub-subharmonic wavelength, with weaker streamwise structures at the subharmonic wavelength. Note that the streamwise structures in this case appear almost exclusively on the top side of the wake. This is a combined effect of the phasing between the two-dimensional fundamental and the oblique subharmonic, and the phasing between the two-dimensional subharmonic and the oblique sub-subharmonic, both of which favor the streamwise structures on the top side of the wake.

3.2 Effect of Initial Conditions on Wake Growth

Figure 6 shows a plot of the square of the wake halfwidth, b^2, versus non-dimensional time t for three simulation runs started from the A_{100}^{010} condition. The phasing between the two-dimensional disturbance and the oblique distur-

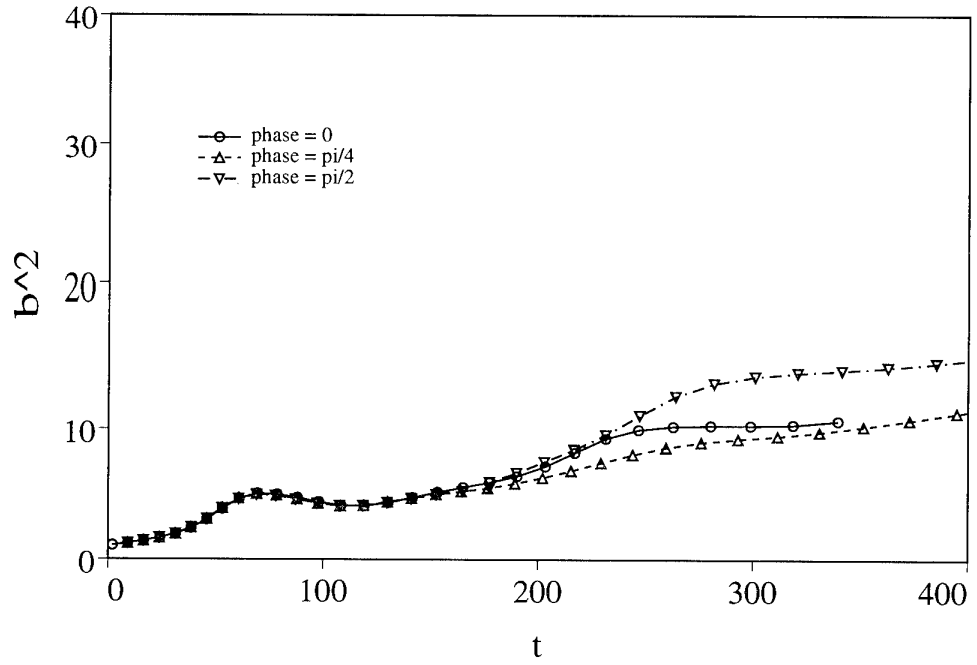

Figure 6: Square of normalized wake halfwidth v. normalized time for $Re = 119$ wakes with various disturbance phases, A_{100}^{010} condition. $\phi^{010} = 0$, $\frac{\pi}{4}$, and $\frac{\pi}{2}$

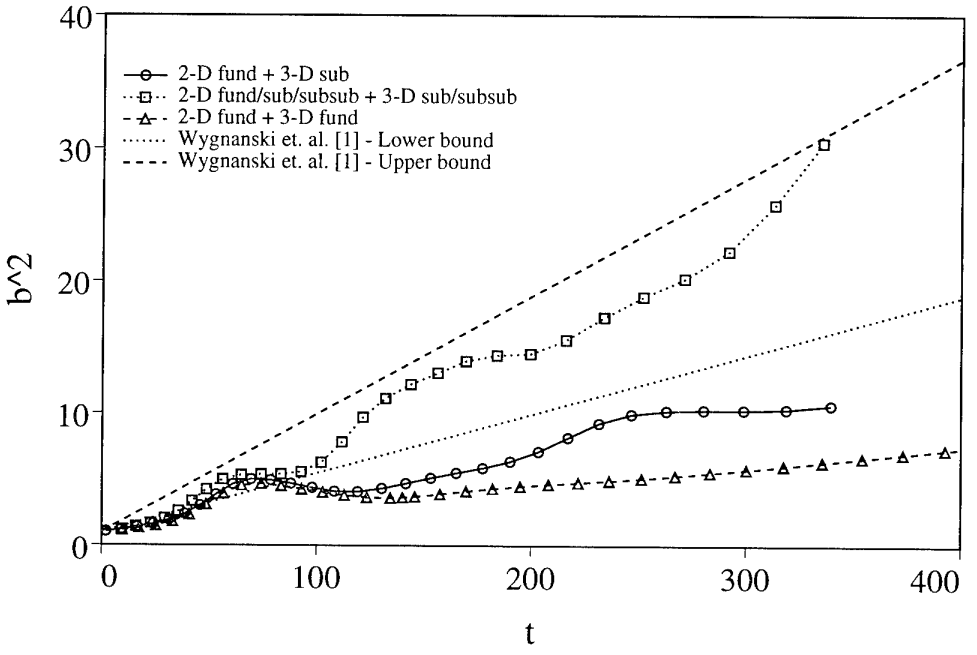

Figure 7: Square of normalized wake halfwidth v. normalized time for $Re = 119$ wakes, A_{100}^{010}, A_{111}^{011}, and A_{100}^{100} conditions. All $\phi = 0$.

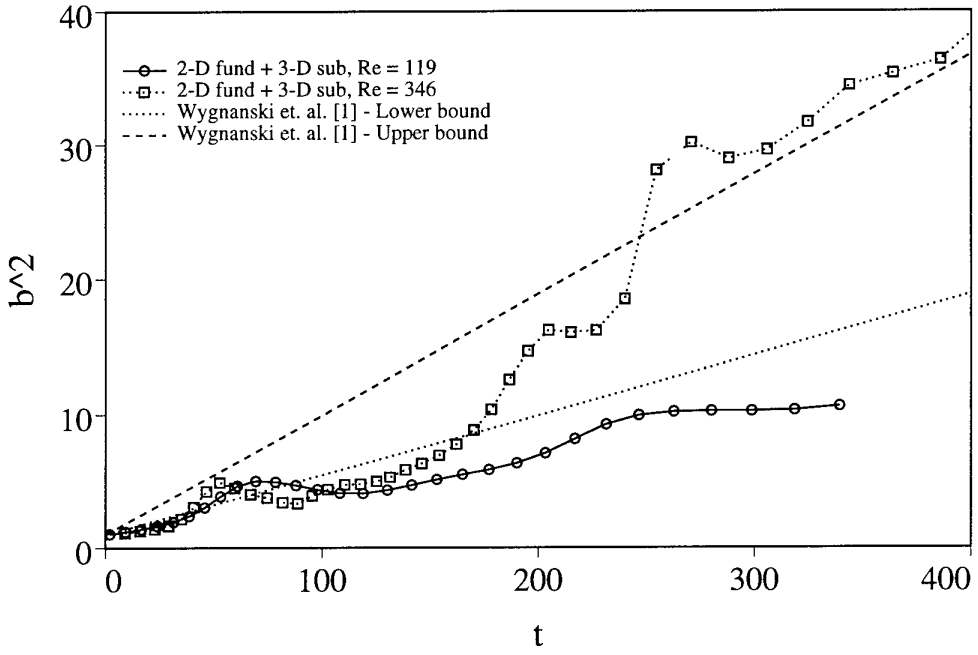

(a)

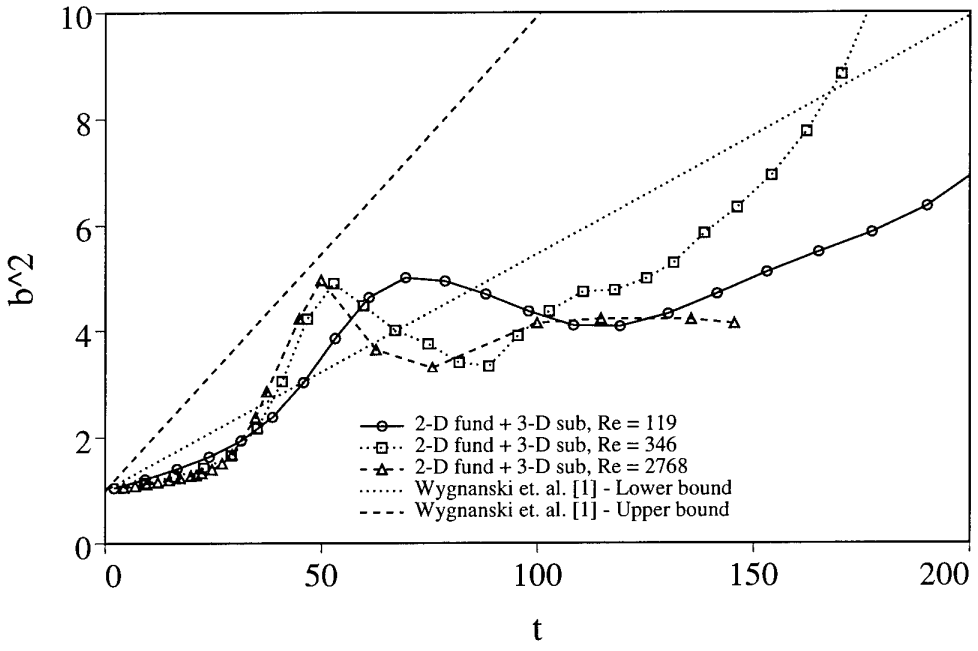

(b)

Figure 8: Square of normalized wake halfwidth v. normalized time for various Reynolds numbers, A_{100}^{010} condition, $\phi^{010} = 0$.

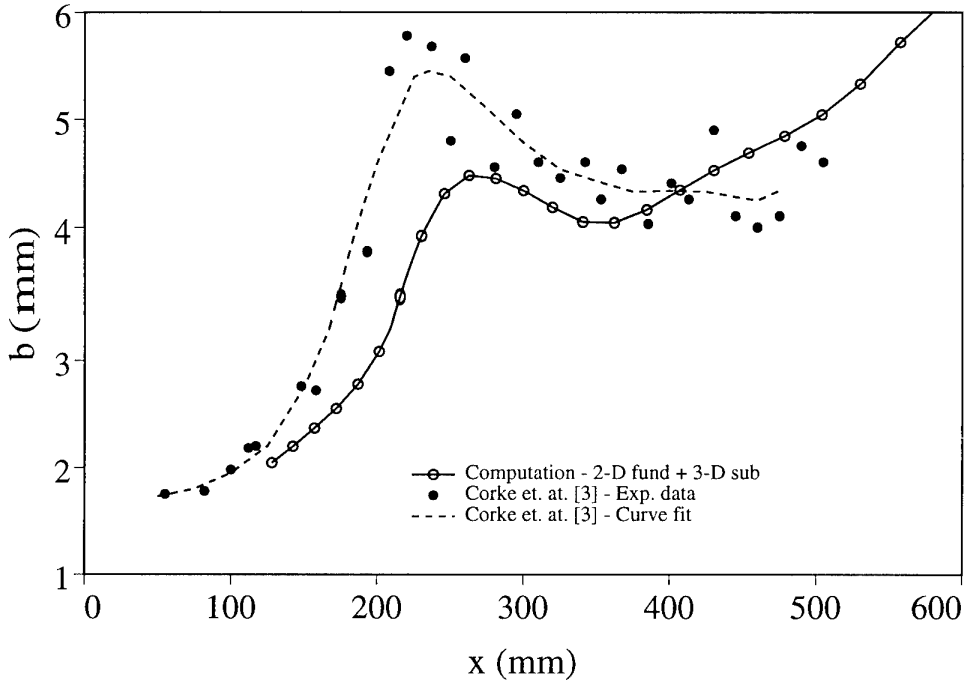

Figure 9: Comparison of halfwidth v. downstream distance for computed $Re = 119$ wake and experiments of Corke et al. [1]. Computed flow started from is A_{100}^{010} condition, $\phi^{010} = 0$. wavelength.

bances was varied between $\phi^{010} = 0$ (oblique disturbance crossing occurs at a maximum in the two-dimensional disturbance magnitude as for the flow in figure 2) and $\phi^{010} = \pi/2$ (oblique disturbance crossing occurs at a zero in the two-dimensional disturbance magnitude). Variation in phase of the oblique subharmonic disturbances has no discernible effect on the growth of the wake until very late times. At such late times the correspondence between the temporally evolving wake in the computation and a spatially evolving wake becomes poor. The computed flow is likely to be distorted by the confines of the finite computational domain, whereas in a spatially developing flow of infinite extent all possible subharmonics are available to break the periodicity and allow for further active growth.

Figure 7 shows a comparison of the square of the wake halfwidth versus time for three computations with different initial disturbances, all with $Re = 119$. The solid line is the 0° phase computation from figures 2 and 6 (A_{100}^{010} condition). The dotted line is the computation in figure 5 (A_{111}^{011} condition). The dashed line is the wake in figure 4a (A_{100}^{100} condition). All the disturbance phases are zero. After a time of approximately 75, the wake started from the A_{111}^{011} condition, which has the longer wavelength disturbances, has a growth rate approximately double that of the wake started from the A_{100}^{010} condition. This is due to the fact that the longer wavelength disturbances allow the wake to undergo an increase in streamwise scale as described above. In contrast, the wake started from the A_{100}^{100} condition, which never develops strong streamwise structures, exhibits only very weak growth after the initial rollup. The late time growth for this wake is almost entirely due to viscous diffusion.

Wygnanski et al. [1] studied a set of small defect turbulent plane wakes created with a variety of wake generators. The generators were carefully designed such that the momentum thickness, θ, was constant for all the experiments. The Reynolds number for the various wakes, based on freestream velocity and momentum thickness, varied between 640 and 3220. They found that the growth rate followed

$$\left(\frac{b}{\theta}\right)^2 = \Delta_0^2 \left(\frac{x - x_0}{\theta}\right) \tag{26}$$

where x is the streamwise coordinate and x_0 is a virtual origin. The coefficient Δ_0 was found to vary between 0.270 for a solid strip set perpendicular to the flow direction, and 0.382 for a flat plate with a trailing edge flap which was oscillated at the frequency of the Karman mode.

The straight lines in figure 7 indicate the upper and lower bounds for the growth rates observed

by Wygnanski et al. [1] transformed into the appropriate computational variables using $x - x_0 = U_0(t - t_0)$. Note that these lines have not been shifted to account for the virtual origins for the various flows. Only the slopes of the lines are significant.

Though none of the wakes in figure 7 are fully turbulent, the wakes started from the A_{100}^{010} and A_{111}^{011} conditions, both of which develop strong three-dimensionality, have late time growth rates comparable to the range of growth rates observed by Wygnanski et al. [1]. The A_{111}^{011} condition wake in fact grows faster than the highest growth rate in the range.

Figures 8a and 8b show a comparison of the square of the wake halfwidth versus time for three computations all started from the A_{100}^{010} condition, but at three different Reynolds numbers. The straight lines are again the bounds on the range of growth rates observed by Wygnanski et al. [1]. The solid line is the 0° phase computation from figure 2 which has $Re = 119$. The dotted line is the computation from figure 3 which has $Re = 346$. The dashed line (figure 8b only) is a computation with $Re = 2768$. At very early times increasing the Reynolds number initially reduces the wake growth rate. This is to be expected since at very early times the growth is dominated by viscous diffusion. After a time of approximately 25, as the disturbances grow to significant amplitudes, the growth rates of the $Re = 346$ and $Re = 2768$ cases rapidly outpace the growth rate of the $Re = 119$ case. After the first hump in the growth, the growth of the $Re = 346$ flow returns to a high rate whereas the growth of the lower Reynolds number flow becomes sluggish. The $Re = 2768$ flow, which has developed turbulent fine scales even before the first peak in the growth curve, closely follows the development of the $Re = 346$ wake up to a time of 50. Its width then appears to enter a cycle of growth and decay, with only a weak average growth rate.

This leads to the conclusion that at moderate Reynolds numbers, where streamwise structures grow strongly but do not immediately break down to turbulence, there exists a mechanism which allows rapid spreading of the wake. This growth mechanism is related to the fact that coherent streamwise structures in the moderate Reynolds number flows are very strong. These strong coherent three-dimensional structures dominate the growth dynamics at late times. At lower Reynolds numbers, the coherent structures are damped by viscous diffusion and are not as dynamically active.

At a Reynolds number of 2768, which is sufficiently high for the wake to break down to turbulence very quickly, the growth pattern in the early stages follows that of the $Re = 346$ wake, which is dominated by coherent structures. However, at later times, the growth rate is similar to that of the $Re = 119$ wake, which is dominated by diffusion. At early times, before the breakdown to turbulence occurs, the flow spreads rapidly under the influence of a nearly inviscid growth of the Karman mode and the initial development of the coherent streamwise structures. However, once the wake develops fine scales the coherent structures are destroyed. Once the fine scales, with their associated turbulent diffusion, disrupt the coherent structures, the wake reverts to a diffusion dominated state, with a relatively low rate of growth at the latest times calculated. It is possible that at later times, and with the addition of longer wavelength disturbances, the growth rate of the $Re = 2768$ wake will increase.

All of the flows in figures 6 through 8 which have oblique disturbances at the subharmonic wavelength have the common feature of undulations in the growth curve. This starts at a time of between 50 and 80 with a peak which corresponds to the rollup and saturation of the Karman mode. This is followed by a period of neutral or negative growth, followed by growth again. This cycle of strong growth followed by weak growth continues as the flow develops.

Corke et al. [3] studied this phenomenon in a $Re = 119$ spatially developing wake produced by a symmetric airfoil at zero angle of attack. They forced their wake with a two-dimensional disturbance at the fundamental frequency and a pair of oblique modes at the subharmonic in a manner similar to the computations presented here. They concluded that the fluctuations in the growth of the wake were due to a parametric resonance between the fundamental mode and the oblique subharmonic mode. The two-dimensional mode saturates and begins to feed energy into the three-dimensional oblique mode through a secondary instability mechanism. The oblique mode in turn saturates, and the two-dimensional mode begins to grow again.

Figure 9 shows a comparison between the wake width for the $Re = 119$, A_{100}^{010}, $\phi^{010} = 0$ case from

figure 6 and data from figure 4 from Corke et al. [3]. The computed flow has been renormalized to match momentum thickness and shifted to put the virtual origin for the computed flow at $x = 0$. The coordinates were transformed using $x/\theta_{Corke} = U_0(t - t_0)/\theta_{computation}$ and $(b/\theta)_{Corke} = (b/\theta)_{computation}$. This rescaling does not account for differences in forcing magnitude or for the virtual origin of the experimental wake. Nevertheless, the match between the computed flow and the experimental data is quite reasonable.

The results shown in figure 8 for the $Re = 346$ and $Re = 2768$ computations indicate that this resonant exchange of energy occurs at higher Reynolds numbers. Moreover it continues even at late times in the $Re = 346$ computation, when the streamwise structures dominate the flow.

Figures 5 and 7, which show the case with the long wavelength disturbances, indicate that this type of resonance continues even after a change in scale of the wake. When the streamwise scale of the flow doubles, the resonance begins to occur between the two-dimensional subharmonic and the three-dimensional sub-subharmonic. This accounts for the increasing magnitude of the three-dimensional sub-subharmonic as the wake continues to grow (cf. the discussion of figure 5). It is reasonable to assume that as one adds more and more subharmonics, this process of scale change and resonance should continue, at least for the moderate Reynolds numbers discussed here.

4 CONCLUSIONS

The results presented here indicate that oblique disturbances at the subharmonic wavelength are important to the initial development of strong three-dimensionality. Simulations started with a fundamental disturbance and a three dimensional disturbance at the subharmonic wavelength developed strong streamwise structures stretching between corrugated spanwise rollers on the same side of the wake. These structures create very high gradients in the velocity field of the wake and lead to strong growth. Simulations started with three dimensional disturbances at the fundamental wavelength only remain almost two-dimensional with very weak gradients and sluggish growth.

The Reynolds number has an effect on intensity and scale of the structures in the flow. Wakes with higher Reynolds number, but not so high as to immediately become turbulent, develop much stronger streamwise structures, which dominate the flow dynamically and serve to enhance the wake growth at later times. Wakes with Reynolds numbers sufficiently high to allow rapid breakdown to turbulence exhibit the same early growth patterns as lower Reynolds number wakes, which have highly coherent three-dimensional structures. However, at later times the turbulent motions disrupt the coherent structures and the growth rate becomes dominated by turbulent diffusion by the small scales.

The addition of longer wavelength disturbances allows for scale changes in the flow and augments the growth rate. This has implications for the interpretation of temporal simulations, where the flow is restricted to a maximum wavelength corresponding to the longest wavelength in the initial disturbance field. At late times in the simulation the flow will not follow a growth path which can be related to that of a spatially developing wake.

This result also has implications for experiments involving spatially developing wakes. Any experiment is by necessity limited by the dimensions of the facility in which the experiment is performed. The receptivity of the wake to subharmonic disturbances which has been observed in these computations suggests that the rate of growth of experimentally studied wakes may be sensitive to the low frequency spectral content of naturally occurring disturbances in the experimental facility.

5 Acknowledgements

The authors would like to acknowledge the support of the NASA-Ames Research Center and the Office of Naval Research, grant N00014-90-J-1976.

References

[1] I. Wygnanski, F. Champagne, and B. Marasli. On the large scale structures in two dimensional, small deficit, turbulent wakes. *J. Fluid Mech.*, 168:31–71, 1986.

[2] J. H. Chen, B. J. Cantwell, and N. N. Mansour. The effect of Mach number on the stability of a plane supersonic wake. *Phys. Fluids A*, 2 (6):984–1004, 1990.

[3] T. C. Corke, J. D. Krull, and M. Ghassemi. Three-dimensional-mode resonance in far wakes. *J. Fluid Mech.*, 239:99–132, 1992.

[4] R. Corral and J. Jiménez. Fourier/Chebychev methods for the incompressible Navier Stokes equations in infinite domains. *Comp. Fluid Dyn.*, 1:361–368, 1992.

[5] R. S. Rogallo. Numerical experiments in homogeneous turbulence. *NASA Technical Memorandum 81315*, 1981.

[6] H. Sato and K. Kuriki. The mechanism of transition in the wake of a thin flat plate placed parallel to a uniform flow. *J. Fluid Mech.*, 11:321–352, 1961.

[7] J. C. Lasheras and E. Meiburg. Three-dimensional vorticity modes in the wake of a flat plate. *Phys. Fluids A*, 2 (3):371–380, 1990.

[8] J. M. Cimbala, H. M. Nagib, and A. Roshko. Large structure in the far wakes of two-dimensional bluff bodies. *J. Fluid Mech.*, 190:265–298, 1988.

Simulation Directe du Sillage Tridimensionnel du Profil NACA0012

J. Dušek*, Ph. Fraunié†

Institut de Mécanique Statistique de la Turbulence
12, avenue Général Leclerc 13003 Marseille, France

SUMMARY

Direct numerical simulation of the tridimensional wake developping downstream a NACA 0012 wing has been performed using the spectral element code NEKTON. The onset of instability in the wake of an infinite NACA 0012 wing is investigated. The first bifurcation is studied in a two dimensional configuration with a mesh obtained using the numerical experience with a two dimensional unstable cylinder wake.
The second bifurcation accompanied by the onset of three-dimensionality is simulated on a three dimensional spectral element mesh obtained by extending the two-dimensional mesh spanwise. The onset of three-dimensionality is characterized by a deformation of the downstream and transverse velocity profiles in the spanwise direction and by the onset of an oscillating spanwise velocity. The critical Reynolds numbers are estimated for both bifurcations. The second bifurcation is shown to be characterized by a period doubling, i.e. the Strouhal frequency of the spanwise velocity is rather precisely equal to half the frequency of the transverse velocity oscillations. This result is in agreement with the numerical results of Karniadakis and Triantafyllou obtained for an infinite circular cylinder and confirms indirectly the experimental results of Williams-Stuber and Gharib showing that to obtain a Ruelle and Takens scenario in a wake, an external forcing is needed.

Furthermore, simulations in a geometrically three-dimensional configuration of a finite wing are performed. The development of the tip vortex of a finite wing is investigated. Comparisons are made with available experimental results performed at low Reynolds numbers. The structure of the three dimensional flow is found to be in good agreement with experiments. The simulations are carried out at supercritical Reynolds numbers at which the wake is unstable. The wake oscillations and tip vortex oscillations are evidenced and shown to be characterized by roughly the same Strouhal frequency although the computations could not be pushed until relaxation of transients.

1. RESUME

Une simulation numérique directe du sillage tridimensionnel en aval d'un profil NACA0012 par le solveur Navier-Stokes NEKTON utilisant une discrétisation en éléments spectraux est présentée.
Tout d'abord, l'apparition de l'instabilité de sillage pour une aile d'envergure infinie est étudiée.
La première bifurcation est analysée pour une configuration bidimensionnelle sur un maillage déduit de l'expérience acquise à propos de l'étude du cylindre. La seconde bifurcation, associée à l'apparition d'une tridimensionnalité, est obtenue sur un maillage tridimensionnel développé en envergure sur la base du maillage bidimensionnel précédent. Les valeurs critiques du nombre de Reynolds sont estimées pour les deux bifurcations. La seconde bifurcation est caractérisée par un doublement de période. Ce résultat est en accord avec ceux de Karniadakis and Triantafyllou obtenus dans le cas du cylindre circulaire et confirme indirectement les résultats expérimentaux de Williams-Stuber et Gharib, montrant que le scénario de Ruelle et Takens n'est pas spontanément rencontré dans le cas du sillage.

D'autre part, la configuration tridimensionnelle de l'aile d'envergure finie a été envisagée. La structure de l'écoulement à faible Reynolds, concernant notamment le tourbillon d'extrémité, est en conformité avec les résultats expérimentaux. Pour les nombres de Reynolds supercritiques, les oscillations du sillage et du tourbillon d'extrémité présentent apparamment la même fréquence de Strouhal, bien que les calculs n'aient pas pu être poussés jusqu'au développement complet des transitoires.

2. INTRODUCTION

2.1. Instationnarités des sillages 3D

L'étude présentée a pour objectif d'analyser le comportement spatio-temporel du sillage laminaire d'une aile. Dans le cas d'une configuration stationnaire, ce comportement est caractérisé, pour des nombres de Reynolds croissants, par l'apparition, d'une part, d'instationnarités et d'autre part, de structures conduisant à une disparition de symétries existantes. Dans le cas d'une configuration instationnaire, on observe une interaction nonlinéaire du forçage dû au mouvement de l'aile avec les instationnarités auto-induites propres aux sillages.
Les changements de la structure spatio-temporelle de l'écoulement interviennent aux bifurcations de Hopf [1, 2]. Chaque bifurcation de Hopf est caractérisée non seulement par l'apparition d'une nouvelle fréquence

*University of West Bohemia, Plzeň, Czech Republic
†LSEET, Université de Toulon et du Var

Paper presented at the 74th Fluid Dynamics Symposium on "Application of Direct and Large Eddy Simulation to Transition and Turbulence" held at Chania, Crete, Greece, in April 1994.

dans l'écoulement mais aussi par une brisure de symétrie si l'écoulement possède, au départ, un degré élevé de symétrie. L'intérêt pratique de l'étude des ces bifurcations réside dans la nécessité de prévoir les fréquences des instationnarités et les structures spatiales tourbillonnaires secondaires engendrées. D'un point de vue plus fondamental, les bifurcations de Hopf sont à la base des scénarii théoriques de la transition à la turbulence [2, 3, 4], leur étude pouvant apporter des éléments permettant de mieux comprendre ces mécanismes de la transition. Les travaux, d'un nombre relativement limité, traitant ce sujet [5, 6, 7, 8], n'ont pas encore permis de donner une réponse univoque à ce problème.
L'interaction non-linéaire d'un sillage avec un forçage externe [9, 10] est également importante du point de vue pratique et théorique. Des travaux expérimentaux [11] et numériques [9, 10] ont mis en évidence un comportement nonlinéaire ayant pour résultat le phénomène d'accrochage en fréquence, c'est à dire, pour des fréquences de forçage voisines mais distinctes de la fréquence propre du sillage, la sychronisation des oscillations du sillage avec celles du forçage. Un phénomène analogue s'est avéré être à l'origine des difficultés de mettre en évidence le scénario de transition propre aux sillages. Il semble, à l'heure actuelle, que les simulations numériques directes indiquent un doublement de période aux bifurcations successives dans les sillages [8, 12] alors que les premiers résultats expérimentaux [5] ont conduit à un scénario du type Ruelle, Takens, Newhouse. Ce désaccord peut être expliqué par une interaction aéroélastique intervenant dans la configuration expérimentale.

2.2 Présentation de la méthode numérique.

La méthode numérique adoptée [13, 8] considère la discrétisation spatiale des équations de Navier-Stokes incompressibles

$$\frac{\partial v_i}{\partial t} + v_j \frac{\partial v_i}{\partial x_j} - \nu \Delta v_i + \frac{\partial p}{\partial x_i} = 0$$

$$\frac{\partial v_j}{\partial x_j} = 0$$

($i, j = 1, 2, 3$ et Δ est l'opérateur laplacien) par éléments spectraux [13] implémentée dans le code Nekton [15].

Nous définissons le nombre de Reynolds en adimensionnant la viscosité par rapport à la vitesse à l'infini U_∞ et la corde de l'aile c:

$$Re = \frac{U_\infty c}{\nu}.$$

Parmi la variété de méthodes existantes, il est apparu que la méthode des éléments spectraux présentait un interêt particulier pour le calcul des sillages. Cet intérêt consiste en:

- la précision de la discrétisation spatiale (méthode pseudospectrale d'ordre de précision qui peut être adapté aux besoins),
- la décomposition du domaine en macroéléments qui permet une optimisation du maillage pour tirer le meilleur profit de la discrétisation spectrale (ceci est très important pour les écoulements inhomogènes)
- l'existence d'un code 3D disponible - Nekton [15]

3. ECOULEMENT AUTOUR D'UNE AILE NACA 0012 INFINIE

Pour étudier les phénomènes accompagnant les deux premières bifurcations, on a d'abord effectué [14] des simulations numériques dans une configuration géométrique très symétrique: celle d'une aile infinie, sans incidence.

3.1 Choix du maillage

Le domaine de calcul ainsi que la discrétisation choisie sont réprésentés sur la Figure 1. La frontière d'entrée a été placée à deux cordes en amont du profil, la frontière de sortie à sept cordes en aval. Les frontières latérales se trouvent à deux longueurs de corde du plan de symétrie de l'aile, ce qui correspond à 17 fois l'épaisseur du profil. Dans le cas des simulations tridimensionnelles, la dimension du domaine de calcul en envergure a été choisie de 14 cordes. Les conditions aux limites sur les frontières extérieures du domaine sont les suivantes:

- un profil de vitesse uniforme à l'entrée,
- une condition advective de sortie à la frontière aval et
- des conditions de périodicité spatiale sur les frontières latérales du domaine.

Pour comparer les dimensions du domaine de calcul à celles de Karniadakis et Triantafyllou [8], il faut se baser sur la corde du profil NACA. On constate alors que notre domaine est environ deux fois plus long et deux fois plus large dans le plan perpendiculaire à l'aile que le plus grand domaine de Karniadakis et Triantafyllou, ce qui réduit l'influence des conditions aux limites. Notre domaine possède moins d'éléments (28 contre 34 en 3D pour Karniadakis et Triantafyllou [8]) dans ce plan, mais ils sont disposés d'une manière beaucoup plus efficace. En effet, un travail de validation [16] de la méthode de discrétisation par éléments spectraux effectué dans le cas du sillage bidimensionnel d'un cylindre circulaire a conduit à la conclusion que la précision de la résolution de la couche limite de l'obstacle avait beaucoup moins d'importance que celle de la résolution du domaine occupé par le sillage.
La condition de périodicité en envergure ne traduit pas rigoureusement la configuration géométrique d'une aile infinie, mais elle a été choisie, de même que par Karniadakis et Triantafyllou, pour sa simplicité de mise en oeuvre. Quant à l'ordre des éléments, donné par le nombre de points de collocation par direction spatiale, il a été choisi relativement bas et fixé à six, ce qui

reste cependant comparable au choix de Karniadakis et Triantafyllou (1989) qui ont conservé 7 points de collocation.
Notre expérience acquise par des calculs bidimensionnels sur un cylindre circulaire indique que cet ordre d'éléments ne permet pas d'espérer une estimation avec une précision élevée des valeurs des fréquences des oscillations ni des nombres de Reynolds critiques des bifurcations. Le but de la présente étude étant limité à la mise en évidence qualitative de la transition à la tridimensionnalité et de l'apparition d'une nouvelle fréquence caractéristique, nous nous sommes contentés de la discrétisation décrite ci-dessus afin de ne pas alourdir le calcul au delà de la capacité des moyens disponibles. Pour la même raison, nous n'avons pas cherché non plus à optimiser davantage les frontières extérieures du domaine. En ce qui concerne l'influence des erreurs de discrétisation sur les caractéristiques de la première bifurcation du sillage bidimensionnel d'un cylindre infini, nous avons trouvé qu'avec une discrétisation analogue, l'erreur sur le nombre de Reynolds critique était de l'ordre de 10%, l'erreur sur le nombre de Strouhal étant bien inférieure. Compte tenu de l'absence de résultats expérimentaux de référence pour une aile infinie (en raison d'une configuration géométrique non réalisable expérimentalement), nous estimons que pour une étude qualitative de la deuxième bifurcation, la discrétisation retenue était suffisamment fine.
Enfin l'apparition de la tridimensionalité constitue un critère de finesse de la résolution de la troisième dimension (en envergure). En effet, le nombre de degrés de liberté retenu pour la discrétisation en envergure résulte de la nécessité de la mettre en évidence. Malgré des simplifications de la discrétisation spatiale, une étude temporelle très poussée est restée difficile, car la simulation d'une période de la nouvelle bifurcation exige un temps CPU considérable (quelques dizaines d'heures sur station de travail IBM RS 6000).

3.2 Simulation de la première bifurcation à incidence nulle

Dans un premier temps nous avons effectué une **simulation bidimensionnelle de la première bifurcation** de Hopf avec la décomposition en éléments spectraux correspondant à la section du domaine de la Figure 1 dans un plan perpendiculaire au plan de symétrie de l'aile. Pour tester la sensibilité des caractéristiques de la bifurcation à la discrétisation choisie, nous avons fait varier le nombre de points de collocation des éléments spectraux de 6 à 8. Les nombres de Reynolds critiques trouvés ont été, respectivement, de 440 et 470. Le nombre de Strouhal, qui est beaucoup moins sensible à la précision du calcul, a été trouvé voisin de l'unité dans les deux cas (0,996 et 0,998).
Du point de vue spatial, cette bifurcation est accompagnée d'une brisure de symétrie dans la direction transversale sous la forme de l'apparition d'une allée tourbillonaire bidimensionnelle. Le sillage reste bidimensionnel. Ceci a été confirmé par un calcul tridimensionnel à des nombres de Reynolds supérieurs au seuil de la première bifurcation et inférieurs à celui de la deuxième bifurcation vers une solution tridimensionelle. En effet les calculs 3D effectués, pour des nombres de Reynolds situés dans cet intervalle, à partir d'une solution initiale bidimensionnelle prolongée par translation en 3D ont montré la stabilité de la solution bidimensionnelle jusqu'aux nombres de Reynolds voisins de 3000. Le nombre de Strouhal a alors augmenté relativement peu dans cet intervalle, passant de 1 à 1,22. Ce comportement du nombre de Strouhal est en accord avec les résultats obtenus sur un cylindre circulaire [17].

3.3 Simulation de la seconde bifurcation à incidence nulle

La deuxième bifurcation de Hopf du sillage se manifeste par une transition à la tridimensionnalité, qui est ici apparue pour des valeurs du nombre de Reynolds situées entre 2500 et 3000. Les résultats présentés ci-dessous ont été obtenus pour $Re = 3500$.

Pour étudier les oscillations du sillage de l'aile, nous avons choisi dans le domaine de calcul six points particuliers en lesquels nous avons suivi l'évolution temporelle des caractéristiques du champ de l'écoulement. Quatre points sont situés dans le plan de symétrie de l'aile (caractérisé par $y = 0$). Deux de ces points ont été placés dans la couche limite au dessus de l'aile pour étudier l'interaction de la couche limite avec le sillage. L'axe des x étant orienté parallèlement à la vitesse à l'infini et l'axe des z dans le sens de l'evergure, la coordonnée z de tous ces points a été choisie égale à 7, c'est à dire à demi envergure, dans le plan de symétrie. Les coordonnées de ces points sont résumées dans le Tableau 1. Si nous appellons v la composante de la vitesse perpendiculaire au plan de symétrie de l'aile et w la composante dans le sens de l'envergure, la vitesse w devient non nulle (et instationnaire) à l'apparition de la tridimensionnalité (Figure 2) alors que la composante v devient déjà instationnaire à la première bifurcation mise en évidence au dessous de $Re = 500$.
Il s'agit donc ici de mettre en évidence l'apparition d'une composante w de la vitesse non nulle et de comparer les fréquences des deux composantes v et w. La Figure 3 montre le signal obtenu pour ces deux composantes de vitesse au point n° 4 situé sur l'axe à 1,7 cordes du bord de fuite (cf. Tableau 1).
De façon générale, le signal de la composante w comporte de fortes harmoniques supérieures, comme le montre la Figure 4 réprésentant la vitesse w dans la couche limite de l'aile (point n° 5). On remarque l'aspect saturé des amplitudes de la vitesse v et la naissance de l'instabilité de la vitesse w. Le coût de calcul nécessaire pour aboutir à la saturation de l'amplitude étant prohibitif, nous nous sommes bornés à l'analyse du signal dans un intervalle de temps correspondant à huit périodes de variation de w. L'échelle en temps étant la même pour les deux graphiques, on remarque que la fréquence des oscillations de la vitesse w est plus faible que la fréquence de base de la vitesse v.

Point	x	y	z
1	1,1175	0	7
2	1,3574	0	7
3	1,8825	0	7
4	2,7148	0	7
5	0,5	0,115	7
6	0,8272	0,1034	7

Tableau 1: Coordonnées des points en lesquels l'étude a été menée. (Les coordonnées du bord d'attaque est sont $x = 0, y = 0$).

Point	f_v	$f_{w,1}$	$f_{w,3}$	$f_{w,5}$	$\overline{f_w}$	$f_v/\overline{f_w}$
1	1,224	0,58	1,90	3,04	0,61	2,01
2	1,224	0,58	1,85	–	0,60	2,04
3	1,224	0,57	1.89	3,03	0,60	2,03
4	1,224	0,58	1,92	–	0,61	2,01
5	1,224	0,58	1,81	3,06	0,60	2,04
6	1,224	0,60	1,84	3,05	0,61	2,01

Tableau 2: Les fréquences des oscillations perpendiculaires au plan de symétrie de l'aile (f_v) et en sens de l'envergure ($\overline{f_w}$) et leur rapport. ($f_{w,1}$, $f_{w,3}$, $f_{w,5}$ - fréquences des harmoniques 1,2 et 3.)

Pour établir le rapport entre ces deux fréquences, nous avons procédé à une analyse spectrale sommaire de ces signaux. L'aspect de ces spectres est représenté, aux points n° 4 et 5 sur les Figures n° 5 et 6. Le pic correspondant à l'harmonique fondamentale du signal de v est très dictinct, situé dans ces deux cas très précisément au même nombre de Strouhal $St = 1,224$. Le signal de w contient plusieurs "harmoniques". Nous sommes obligés de mettre le mot "harmonique" en guillemets, car le signal n'est pas strictement périodique et de plus, les fréquences de ces "harmoniques" ne sont pas rigoureusement des multiples de l'harmonique fondamentale (cf. Tableau 2).

Ce phénomène s'explique par le fait que nous sommes encore loin de la saturation de la seconde bifurcation. Pour obtenir une base de comparaison avec les oscillations bien établies de la vitesse v, nous avons pris la moyenne des fréquences obtenues en divisant les fréquences des harmoniques supérieures observées par leur ordre respectifs. Par exemple, le signal de la figure 3 comporte des maxima aux nombres de Strouhal 0,57 (première harmonique), 1,89 (3^e harmonique) et 3,03 (5^e harmonique), ce qui donne une moyenne de 0,60. La première harmonique étant symétrique par rapport au plan z=7, on peut démontrer que les harmoniques paires doivent s'annuler aux points observés.

De plus, il convient de remarquer que les valeurs des fréquences croissent en fonction de l'amplitude. Les valeurs du Tableau 2 réprésentent ainsi des valeurs moyennes dans l'intervalle de calcul. A titre indicatif, nous avons trouvé par une analyse d'Hilbert du signal de w au point n° 4 que le nombre de Strouhal passe de 0,575 à 0,61 entre le début et la fin de la simulation. Les valeurs du Tableau 2 sont alors obtenues par défaut. Même sans correction, nous trouvons un rapport de fréquences des vitesses v et w très voisin de 2.

Les figures 3 et 4 montrent également que la fréquence sous harmonique commence à se manifester sur le signal de la composante transversale de la vitesse.

4 ECOULEMENT 2D ET 3D AUTOUR D'UNE AILE STATIONNAIRE EN INCIDENCE

4.1 Calculs bidimensionnels

L'étude de l'écoulement autour d'une aile stationnaire en incidence a d'abord été approchée par un calcul bidimensionnel. L'objectif de cette étape était principalement la validation de la méthode numérique basée sur une comparaisons aux résultats expérimentaux et numériques connus [18, 19]. Pour reproduire au plus près la configuration numérique de réf. [18] on a choisi l'angle d'incidence égal à 34°.

Le calcul en volumes finis de Daube et Ta Phuoc a été effectué pour un nombre de Reynolds basé sur la corde de 1000. Si l'on se base au maître couple à 34 degrés d'incidence (0,6), ceci correspond au nombre de Reynolds de 600. Les expériences sur une configuration analogue (cylindre circulaire) montrent que pour le même nombre de Reynolds l'écoulement est déjà turbulent. La méthode des éléments spectraux étant non-dissipative, un calcul à ce nombre de Reynolds ne converge pas. Par contre, on a pu effectuer des calcul aux nombres de Reynolds (basé sur la corde) de 200 et 500. La Figure 7 montre un bon accord de l'aspect du détachement tourbillonaire avec les résultats de Daube et Ta Phuoc [18]. A ce propos il est utile de mentionner également le résultat expérimental de Honji [19] au nombre de Reynolds de 200 et à l'incidence de 45° qui fait état d'une structure d'écoulement comparable à celle décrite par le cacul de Daube et Ta Phuoc. Pour expliquer le caractère très conservatif de la structure de l'écoulement sur une telle plage de nombres de Reynolds, on doit prendre en compte d'une part le caractère dissipatif de calculs en différences ou volumes finis où une viscosité numérique difficile à quantifier se superpose à la viscosité moléculaire définissant le nombre de Reynolds, et d'autre part le fait que les grosses structures tourbillonaires sont peu dépendantes de la dissipation moléculaire [20].

On a également effectué des calculs bidimensionnels aux incidences de 10° et 40° pour des nombres de Reynolds légèrement supercritiques. Le tabeau 3 montre que, à condition de rapporter les nombres de

angle	Section	Re	Re*	St	St*	$St_{cyl.}$
0°	0,12	500	60	1,00	0,12	0,12
10°	0,19	300	57	0,613	0,117	0,12
40°	0,65	110	71,5	0,292	0,19	0,145

Tableau 3: Les nombres de Strouhal réduits au maître couple pour de différentes incidences. (Maître couple - pour une corde égale à l'unité, Re, St - les nombres de Reynolds et de Strouhal basés sur la corde, Re*, St* - les valeurs réduites au maître couple, $St_{cyl.}$ - valeur du nombre de Strouhal pour un cylindre circulaire au Re=Re*.)

Reynolds et de Strouhal au maître couple, on retrouve sensiblement les mêmes résultats pour des incidences différentes. Ces résultats sont de plus comparables à ceux obtenus par Williamson pour un cylindre circulaire [17].

Ces résultats confirment que le sillage est relativement peu dépendant de la forme de l'obstacle [21].

4.2 Calculs tridimensionnels

Les calculs tridimensionnels à incidence nulle [14] et en incidence [22] ont été effectués sur la configuration réprésentée Figure 8. Il s'agit d'une aile NACA 0012 d'envergure finie en milieu non confiné. L'absence de confinement est simulé par une condition de symétrie par rapport au plan z=0 (l'axe z est orienté selon l'envergure de l'aile, fixée à six cordes) et par une condition d'écoulement libre dans le plan z=8. Les incidences considérées sont de 0°, 12°, 24° et 34°. L'objectif de cette étude était de simuler l'échappement tourbillonnaire de l'extrémité de pale, configuration pour laquelle on disposait d'un nombre important de références expérimentales [23, 24, 25, 26, 27, 28]. Les simulations ont été menées pour une configuration géométrique stationnaire (aile immobile) mais au dessus du seuil de la transition à l'instationnarité. Les nombres de Reynolds choisis correspondent sensiblement à un nombre de Reynolds basé sur le maître couple de 100. Les calculs et expériences pour des configurations infinies (aile, cylindre) montrent que ce nombre de Reynolds se situe entre la première et deuxième bifurcation de Hopf.
Les résultats obtenus, dont les détails sont donnés dans [22], ont permis de mettre en évidence un comportement spatio-temporel qui peut être résumé de façon suivante:

1) La structure spatiale tourbillonnaire obtenue par simulation numérique s'accorde avec celle obtenue expérimentalement. (Figure 9). En particulier le tourbillon de bout de pale est clairement observable et peut être comparé aux visualisations de Jouvaud [28].

2) Une étude de la structure spatiale du tourbillon de pale a été effectuée.

   a) La structure transversale a été trouvé en accord avec la théorie, en particulier celle de tourbillon visqueux [29] .

   b) La structure longitudinale a pu être analysée sur une distance de 7 cordes en aval de l'aile. L'aspect hélicoïdal de l'axe du tourbillon est comparable aux observations par visualisation [28].

3) L'évolution temporelle a été suivie en 8 points, dont 4 placés dans le sillage et 4 dans la zone du tourbillon de bout de pale.

   a) Les fréquences des caractéristiques de l'écoulement sont sensiblement les mêmes dans le sillage et dans le tourbillon de bout de pale.

   b) La structure spatiale hélicoïdale citée en 2.2 s'explique par l'instabilité de l'écoulement car elle oscille avec la fréquence du sillage.

5 CONCLUSIONS

5.1 Aile finie stationnaire

Dans la configuration de l'aile finie stationnaire à laquelle se réfèrent les résultats du paragraphe précédent, on envisage une étude du comportement temporel plus poussée.

1) Pour confirmer que les oscillations du sillage et du tourbillon marginal ont pour origine la même instabilité, on envisage de mener une étude de l'apparition de l'instabilité aux nombres de Reynolds plus bas (près du seuil).

2) Un certain nombre de résultats expérimentaux, numériques [30] et théoriques [2] indiquent qu'après la première bifurcation, l'écoulement tend vers un cycle limite caractérisé par une période universelle pour l'ensemble de l'écoulement. Cet état n'a pas été complètement atteint (cf. Fig. 15). L'explication pourrait être que l'écoulement n'a pas atteint la saturation de l'instabilité ou qu'il a traversé une autre bifurcation avec une fréquence incommensurable avec celle de la première bifurcation. Dans le second cas, moins vraissemblable, il s'agirait d'identifier les deux bifurcations et de comparer leurs fréquences respectives.

5.2 Aile finie instationnaire

Il existe des résultats expérimentaux concernant le comportement du tourbillon de bout de pale dans un régime instationnaire [31, 23, 24]. On envisage de placer l'aile finie aux différentes incidences dans un repère instationnaire pour simuler les mouvement de tamis et de pilonnement. On se trouvera ainsi en présence de deux fréquences, celle imposée par le mouvement de l'aile et celle propre au sillage. Mis à part des

effets non-linéaires sur le comportement temporel (accrochage des fréquences) d'un tel système, on s'attend également à des modifications profondes de la structure spatiale de l'écoulement qui restent à étudier.

Aknowledgements
This work was supported by the "Direction des Recherches, Etudes, Techniques" DGA grant 91/158. J. Dušek participation was made possible through a European grant within the program CST PECO - Individual Mobility.

References

[1] Landau L. D. & Lifshitz F. M. 1959, Fluid Mechanics, Course of Theoretical Physics, Vol 6., Pergamon Press.

[2] Manneville P. 1990, Dissipative Structures and Weak Turbulence, Academic Press, San Diego, London.

[3] M. J. Feigenbaum, 1979, "The onset spectrum of turbulence", *Phys. Lett.* **74A**. 375.

[4] D. Ruelle, F. Takens, 1971, "On the nature of turbulence", *Commun. Math. Phys.*, **20**, 167.

[5] K. R. Sreenivasan, 1985, "Transition and turbulence in fluid flows and low dimensional chaos", *Frontiers in Fluid Mechanics*, (ed. S.H. Davis & J.L.Lumley), pp 41-67, Springer Verlag.

[6] K. Williams-Stuber et M. Gharib, 1990, "Transition from ordre to chaos in the wake of an airfoil", *J. Fluid. Mech.*, **213**, 29.

[7] C.W. Van Atta and M. Gharib, 1987, "Ordered and chaotic vortex streets behind circular cylinders at low Reynolds numbers", *J. Fluid Mech.* **174**, 113.

[8] G.E. Karniadakis and G.S. Triantafyllou, 1992, "The three-dimensional dynamics and transition to turbulence in the wake of bluff objects", *J. Fluid. Mech.* **238**, 1.

[9] Karniadakis G.E. & Triantafyllou G.S. 1989, "Frequency selection and asymptotic states in laminar wakes", *J. Fluid Mech.*, **199**, 441.

[10] Li J., Sun J. & Roux B. 1992, "Numerical study of an oscillating cylinder in uniform flow and in the wake of an upstream cylinder", *J. Fluid. Mech.*, **237**, 457.

[11] Bishop, R. E. D. & Hassan, A. Y., 1964, The lift and drag forces on a circular cylinder oscillating in a flowing fluid. Proc. R. Soc. Lond. A **227**, 51.

Berger, E. & Wille, R., 1972, Periodic flow phenomena. *Ann. Rev. Fluid Mech*, **4**, 313.

Koopman, G. H., 1967, The vortex wakes of vibrating cylinders at low Reynolds numbers, *J. Fluid. Mech.*, **28**, 501.

Griffin, O. M. & Ramberge, S. E., 1975, On vortex strength and drag in bluff-body wakes, *J. Fluid. Mech.*, **69**, 721.

Bearman, P. W., 1984, Vortex shedding from oscillating bluff bodies, *Ann. Rev. Fluid Mech*, **16**, 195.

[12] Dusek, J., Fraunié, Ph., Seror S., Mise en évidence du doublement de période dans le sillage d'une aile NACA à la deuxième bifurcation de Hopf (soumis aux C.R.A.S.)

[13] Patera, A.T., 1984, A spectral element method for fluid dynamics: Laminar flow in a channel expansion, *J. Comp. Phys.* **54**, 468.

[14] S. Séror, 1992, Simulation numérique des équations de Navier-Stokes pour écoulements tridimensionnels incompressibles et instationnaire, *Rapport ENSAE.*

[15] Copyright © 1991, creare.x, Inc., Hanover, New Hampshire, USA.

[16] Dusek, J. & Fraunié Ph., 1993, Validation and error estimate of a spectral element discretization of a cylinder wake, *Numerical Methods in Laminar and Turbulent Flow*, **Vol VIII**, p. 15, Proceedings of the Eighth International Conference held at Swansea, 18th-23rd July, , C. Taylor, Editor.

[17] Williamson C.H.K. 1989, Oblique and parallel modes of vortex shedding in the wake of a circular cylinder at low Reynolds numbers, *J. Fluid Mech.* **206**, 579.

[18] Daube O., Ta Phuoc L., 1978, "Etude numérique d'écoulements instationnaires de fluide visqueux incompressible autour de corps profilés par une méthode d'ordre $O(h^2)$, $O(h^4)$.", *J. de Mécanique*, **vol 17**, pp 651-678.

[19] Honji, 1973, AFOSR Scientific Report 73-0640.

[20] Tennekes H., Lumley J.L., 1972, A first Course in Turbulence, MIT Press.

[21] Jackson C.P., , 1987, A finite-element study of the onset of vortex shedding in flow past variously shaped bodies, *J. Fluid. Mech.* **182**, 23.

[22] J.M. Carrat, 1993, Simulation directe de l'écoulement autour d'une extrémité d'aile en configuration stationnaire avec le code Nekton, *rapport ENSIMEV.*

[23] M.Maresca, M.Favier, 1987, " New simulation of airfoil dynamic stall due to velocity and incidence fluctuation". *AIAA J.*

[24] M.Ramos, 1991, "Etude du systme tourbillonnaire associé aux extrémités de pale d'un rotor en vol stationnaire", *Stage de DEA Université Aix-Marseille II.*

[25] M.Merigot 1992, "Etude de l'évolution temporelle d'un tourbillon d'extrémité d'aile", *Rapport de Stage de DEA*, ONERA.

[26] D. Jouvaud. 1981, "Faisabilité des mesures de vitesses au sein d'un tourbillon marginal d'extrémité de pale de rotor d'hélicoptère en vélocimétrie laser.", *Stage de DEA*, Université Aix-Marseille II.

[27] F. Beluche. 1983, "Contribution à l'étude de l'écoulement à l'extrémité d'un profil d'aile à bas Reynolds, *Stage de DEA*, Université Aix-Marseille II,

[28] D. Jouvaud. 1983, "Contribution l'étude de l'échappement tourbillonnaire à l'extrémité d'une aile", *Thèse de Doctorat*, Université Aix-Marseille II.

[29] Batchelor G.K., " Axial flow in trailing line vortex.". *J.Fluid Mech.*, **20**, $N^0 4$.

[30] Dusek J., Le Gal P. and Fraunié Ph., 1994, "A Numerical and Theoretical Study of the First Hopf Bifurcation in a Cylinder Wake", *J. Fluid Mech.*, **264**.

[31] Carr, L. W., McAllister, K. W., McCroskey, W. J., 1977, "Analysis of dynamic stall based on oscillating airfoil experiments", NASA.TN.D8382.

[32] Fraunié P., 1987, "Analyse des effets instationnaires sur un profil d'aile animé d'un mouvement de trajectoire circulaire", *thèse de Doctorat ès Sciences*, Université d'Aix- Marseille II.

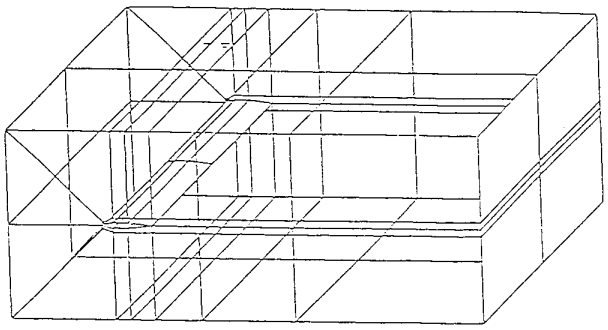

1) Le domaine de calcul et sa décomposition en éléments spectraux (longueur = 10 cordes, hauteur = 4 cordes, largeur en envergure = 14 cordes).
1) Computation domain and its decompostion into spectral elements (length = 10 chords, height = 4 chords, spanwise width = 14 chords).

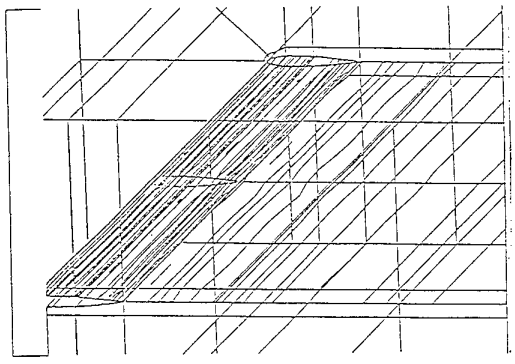

2) Courbes isobares dans le plan de l'aile indiquant l'apparition de la tridimensionalité
2) Isobars in the wing plane showing the onset of tridimensionality.

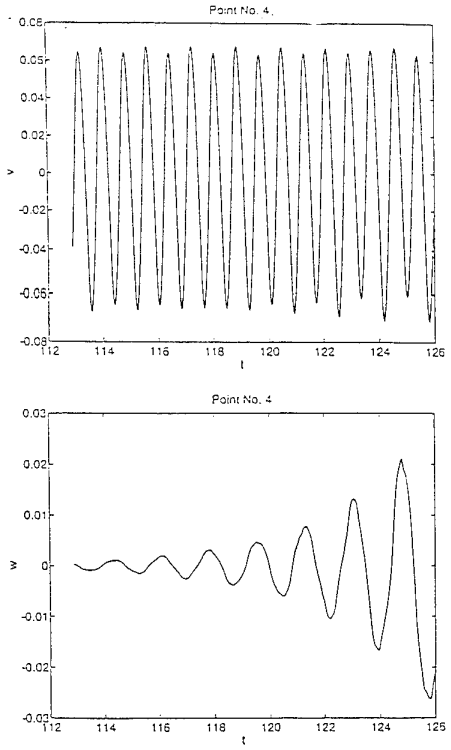

3) Signal de la vitesse transversale v (en haut) et en envergure w (en bas) au point n° 4.
3) The transverse velocity v (above) and spanwise velocity w (below) signal at the point N° 4.

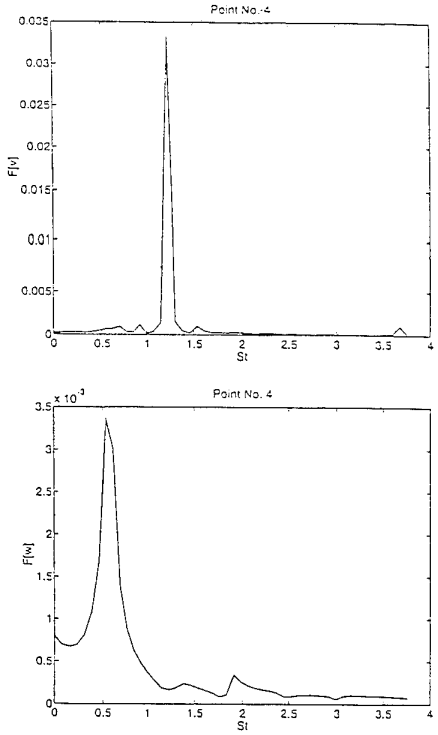

5) Spectre du signal de vitesse v et de vitesse w au point n° 4.
5) The v-velocity and w-velocity spectrum at the point N° 4.

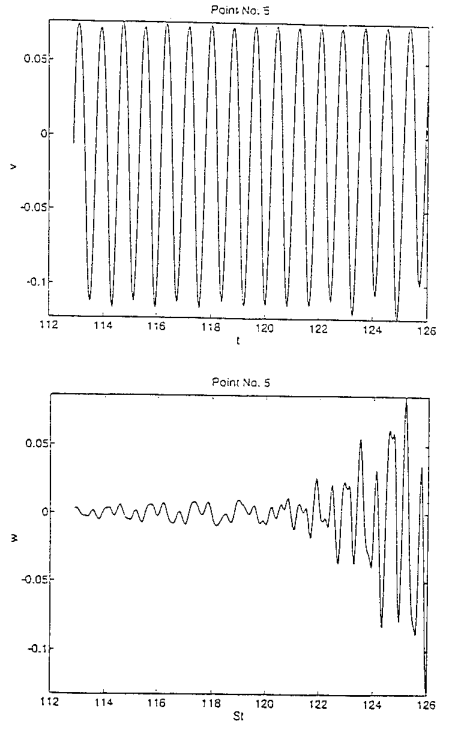

4) Signal de la vitesse transversale v (en haut) et en envergure w (en bas) au point n° 5.
4) The transverse velocity v (above) and spanwise velocity w (below) signal at the point N° 5.

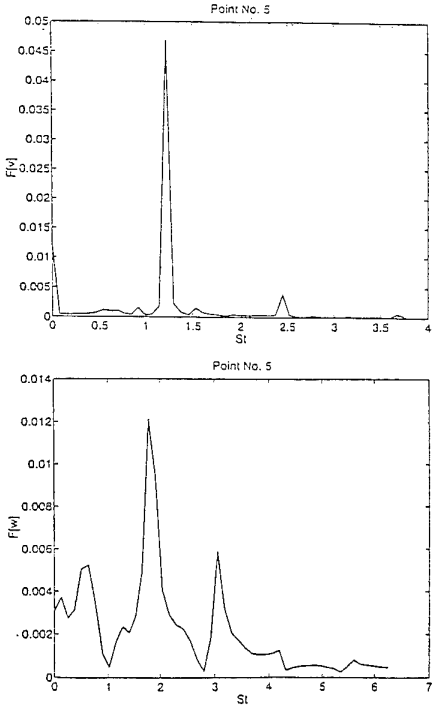

6) Spectre du signal de vitesse v et de vitesse w au point n° 5.
6) The v-velocity and w-velocity spectrum at the point N° 5.

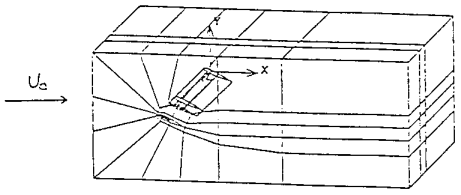

8) Configuration de l'aile finie avec incidence.
8) Finite airfoil with non zero angle of attack.

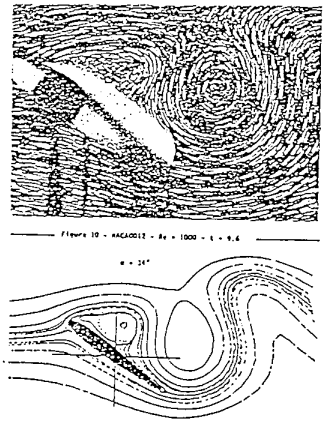

7) Comparaison du calcul 2D par volume finis au Re=1000 et par éléments spectraux au Re=500.
7) Comparison between computations using finite volumes (Re = 1000) and spectral elements (Re = 500).

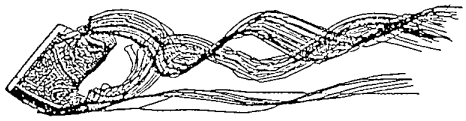

9) Lignes de courant du sillage de l'aile finie à l'incidence de 34°.
9) Streamlines in the airfoil wake with a 34° angle of attack.

Numerical Simulation of Spatially-Developing Planar Jets

Guy Hoffmann
Carlo Benocci
von Karman Institute for Fluid Dynamics
Chaussée de Waterloo, 72
B-1640 Rhode-St-Genèse
Belgium

Abstract

The flowfield of an impinging jet is investigated numerically by means of the LES technique. The numerical scheme uses a high order upwind biased formulation for the advective transport. A localized dynamic evaluation of the Smagorinsky constant is employed to avoid an empirical tuning of this value. A critical problem is the formulation of open boundary conditions. The set of boundary conditions presented here allows both the entrainment of fluid into the computational domain as well as the exit of the large vortical structures typical for this flow problem.

1 INTRODUCTION

Since the pioneering work of Deardorff [1] in the 70's, the large-eddy simulation (LES) approach to turbulence modeling has extensively been applied to homogeneous turbulence and wall-bounded shear layers, where *equilibrium* or *near-equilibrium* boundary conditions can be imposed in the streamwise direction (Schumann [2]). On the contrary, spatially-developing free shear layers have received much less attention. While some work exists on the plane mixing layer flow (Comte *et al.* [3], Pianese and Benocci [4]), jet flows have almost been neglected; the only literature found to exist at the beginning of the present investigation was a very preliminary work on planar free jets (Tsai *et al.* [5]) and an investigation of the impact of circular jets upon a wall (Risk and Menon [6]). This is somewhat surprising in view of the importance of jet flows in both fundamental and applied fluid dynamics. The present contribution gives LES results of an impinging jet flow and explains how specific problems can be overcome.

2 LARGE-EDDY MODEL

The LES method is based on the application of a filtering operation (denoted by an overbar) to the tridimensional time dependent Navier-Stokes equations. The scales larger than the typical size of the filter ('large scales') are resolved numerically, while the smaller ones have to be modeled. The incompressible conservation equations of mass and momentum written for the large scale variables ($\overline{u}_i$, P) are

$$\frac{\partial \overline{u}_i}{\partial x_i} = 0 \tag{1}$$

$$\frac{\partial \overline{u}_i}{\partial t} + \frac{\partial \overline{u}_i \overline{u}_j}{\partial x_j} = -\frac{\partial P}{\partial x_i} + \frac{1}{Re}\frac{\partial^2 \overline{u}_i}{\partial x_j \partial x_j} - \frac{\partial \tau_{ij}}{\partial x_j} \tag{2}$$

This formulation is consistent with a finite differences discretization over a staggered mesh (Schumann [7], Mason [8]). For the periodic channel, which is used as a benchmark, Re is the Reynolds number based on the average shear velocity $\langle u_\tau \rangle$ and the channel half height δ. In this case, the RHS of (2) contains an additional term $F_i = (F, 0, 0)$ which is a forcing term representing the average pressure drop in longitudinal direction. For the jet test case, the variables are nondimensionalized by the jet exit velocity U_0 and the orifice width b.

2.1 Subgrid-scale closure

In (2) τ_{ij} is the subgrid-scale term (SGS) describing the contribution of the unresolved small scales to the resolved large scale transport equation. This term has to be modeled and is given by

$$\tau_{ij} = \overline{u_i u_j} - \overline{u}_i \overline{u}_j \tag{3}$$

A widely used closure is the eddy viscosity model of Smagorinsky [9]

$$\tau_{ij} - \frac{1}{3}\tau_{kk}\delta_{ij} = -2\nu_t \overline{S}_{ij} = -2l^2 |\overline{S}| \overline{S}_{ij} \tag{4}$$

where $\overline{S}_{ij}$ is the strain rate of the resolved scales: $\overline{S}_{ij} = \frac{1}{2}(\frac{\partial \overline{u}_i}{\partial x_j} + \frac{\partial \overline{u}_j}{\partial x_i})$ and $|\overline{S}|$ the local strain rate. The length scale l characterizes the small eddies and is related to the length scale associated with the filtering procedure by the coefficient $C_s = C^{\frac{1}{2}}$

$$l = C^{\frac{1}{2}}\,\overline{\Delta} \tag{5}$$

In a finite difference procedure the filter is given by the mesh size Δ in the three coordinate directions, defining the grid filter width as

$$\overline{\Delta} = (\Delta_1 \Delta_2 \Delta_3)^{\frac{1}{3}} \tag{6}$$

The value of C_s can be derived for some exactly defined filters [10], but in practice the coefficient has to be tuned for the specific application. This is particularly problematic in test cases like the free or impinging jet, which include several types of turbulent flow and/or laminar regions. An attractive way around this problem is a dynamic evaluation of the coefficient C_s as proposed by Germano [11]. Here this approach is briefly summarized.
The basic idea is the local sampling of the smallest resolved scales applying a coarser test filter (denoted by a tilde). In a finite difference approach, this is done using a coarser test grid where the filter width $\widetilde{\overline{\Delta}}$ is defined analogously to (6). Following [11] a filter ratio $\widetilde{\overline{\Delta}}/\overline{\Delta} = 2$ is adopted. With this filter the SGS then reads

$$T_{ij} = \widetilde{\overline{u_i u_j}} - \widetilde{\overline{u}}_i \widetilde{\overline{u}}_j \tag{7}$$

Paper presented at the 74th Fluid Dynamics Symposium on "Application of Direct and Large Eddy Simulation to Transition and Turbulence" held at Chania, Crete, Greece, in April 1994.

Using again the Smagorinsky closure as in (4), T_{ij} is modeled as

$$T_{ij} - \frac{1}{3}T_{kk}\delta_{ij} = -2C\widetilde{\overline{\Delta}}^2 |\widetilde{\overline{S}}|\widetilde{\overline{S}}_{ij} \tag{8}$$

with

$$\widetilde{\overline{S}}_{ij} = \frac{1}{2}\left(\frac{\partial\widetilde{\overline{u}}_i}{\partial x_j} + \frac{\partial\widetilde{\overline{u}}_j}{\partial x_i}\right) \quad |\widetilde{\overline{S}}| = \left(2\widetilde{\overline{S}}_{ij}\widetilde{\overline{S}}_{ij}\right)^{\frac{1}{2}} \tag{9}$$

Subtracting the test grid average of τ_{ij} from T_{ij}, a relation for the resolved scales of motion between test and grid scale can be obtained

$$L_{ij} = T_{ij} - \widetilde{\tau}_{ij} = -\widetilde{\overline{u}_i}\widetilde{\overline{u}}_j + \widetilde{\overline{u_i}\overline{u}_j} \tag{10}$$

Substituting (4) and (8) into this relation yields an expression which contains the parameter C as the only unknown

$$L_{ij} - \frac{1}{3}L_{kk}\delta_{ij} = -2\,C\alpha_{ij} + 2\,\widetilde{C\beta_{ij}} \tag{11}$$

with

$$\alpha_{ij} = \widetilde{\overline{\Delta}}^2 |\widetilde{\overline{S}}|\widetilde{\overline{S}}_{ij} \quad \beta_{ij} = \overline{\Delta}^2 |\overline{S}|\overline{S}_{ij} \tag{12}$$

Assuming that C is locally no function of space, (11) can be written as

$$L_{ij} - \frac{1}{3}L_{kk}\delta_{ij} = 2\,CM_{ij} \tag{13}$$

with

$$M_{ij} = -\alpha_{ij} + \widetilde{\beta_{ij}} \tag{14}$$

This is a system of five independent equations in one unknown C. We use here the modification of Lilly [12] who proposed a contraction of (13) with M_{ij} to obtain

$$C = \frac{1}{2}\left(\frac{L_{ij}M_{ij}}{M_{ij}^2}\right) \tag{15}$$

As stated in [12], this is equivalent to a least squares approach, minimizing the error of C given by the five independent equations in (13). The result of this procedure is a local value of C obtained at each timestep. As pointed out by Ghosal *et al.* [13], the procedure to take C out of the filter operation in order to derive (13) is mathematically inconsistent. The error involved is a function of the residual E_{ij} which is neglected in the RHS of (13)

$$E_{ij} = 2\,\widetilde{C\beta_{ij}} - 2C\,\widetilde{\beta_{ij}} \tag{16}$$

The main problem arising when using (15) is that many local values of C become negative. This was found to lead to computational instability. To avoid this problem, the numerator and the denominator of (15) can be averaged along homogeneous directions ([11], [14]). This also removes the mathematical inconsistency mentioned above, as shown by Ghosal *et al.* [13], if the test filter is applied in these homogeneous directions only. For flows without homogeneous directions, this procedure can not be applied at all, and already for flows with only one homogeneous direction additional time averaging has to be used to stabilize the method [14]. A consistent local dynamic model is proposed by Ghosal *et al.* [13] which is based on a constrained variational formulation imposing a positive value of C.

The approach followed here is based on equation (15). Lund *et al.* [15] show that the numerical divergence is controlled by the RMS fluctuation level and the time correlation of negative eddy viscosities arising from (15). Here we try to minimize the occurrence of high RMS and long time correlation. The essential points can be summarized as follows:

- To obtain the test grid variables, a filter using only the 6 surrounding points is used (compared to 26 points in a volume-average approach). This results in a more localized value of C based on fewer samples.
- The values of C are computed from the test filtered variables defined for each grid cell. This reduces the time correlation of C compared to an approach where C is obtained at the test grid level.
- The strain rates on the test grid are obtained from definition (9).

To evaluate the influence of the inconsistency in the derivation of (13), C is recomputed using an estimation of E_{ij} based on the result of (15)

$$E_{ij} = 2\,\widetilde{\delta C\beta}_{ij} \tag{17}$$

where δC is the deviation of C with respect to the central point value where the filtering operation is defined. This gives a rough estimate of the error involved. The results indicate that relevant differences between both C fields exist only in a few grid points. In this approach, the errors resulting in locally large values of C are accepted. For the negative values, an *ad hoc* measure was preferred to a complete cut of the whole negative part. The negative C given by (15), using a least square on the full tensor, are recalculated leaving out the trace components. The value closer to or above zero is then retained in the computation.

In the procedure described above, the computation of C is based on the grid filter velocities interpolated at the cell centers from the velocity components defined on the staggered grid. To reduce the number of interpolations, the main code defines the turbulent viscosity ν_t in (4) at the location needed by each component of the momentum equation. The value of C defined in the cell center is transferred to these three positions by interpolation.

Results for the plane channel, using this localized dynamic model, are given in the section describing the advection scheme (Figure 1). In this test case, over 30% of the C values obtained by (15) are negative. After modification, over 20% of the C values remain negative. This gives rise to negative total viscosities in more than 10% of the grid points without causing numerical divergence. This means that the combination of RMS and time correlation of the negative C values and the resulting negative total viscosities stay in the stable region for the present numerical scheme.

3 NUMERICAL TECHNIQUES

For the incompressible Navier-Stokes equations, the density vanishes from the conservation equation for mass. This implies that mass conservation must now be interpreted as an additional constraint on the velocity field which has to be satisfied indirectly.

The approach followed here is the use of the pressure correction technique. The time advancement is done using a second order Adams-Bashforth scheme.

Rewriting the large scale momentum equations using H, defined as a space operator containing resolved terms, subgrid and molecular viscous stresses, leads to

$$\frac{\partial\overline{u}_i}{\partial t} = H(\overline{u}_i, \overline{u}_j) - \frac{\partial\overline{P}}{\partial x_i} \tag{18}$$

Now the numerical scheme for the time advancement can be summarized as follows

$$\frac{\overline{u}_i^* - \overline{u}_i^n}{\Delta t} = \frac{3}{2}H(\overline{u}_i, \overline{u}_j)^n - \frac{1}{2}H(\overline{u}_i, \overline{u}_j)^{n-1} - \frac{\partial\overline{P}^n}{\partial x_i} \tag{19}$$

$$\frac{\partial^2 \delta\overline{P}}{\partial x_i^2} = \frac{2}{\Delta t}\frac{\partial \overline{u}_i^*}{\partial x_i} \tag{20}$$

$$\frac{\overline{u}_i^{n+1} - \overline{u}_i^*}{\Delta t} = -\frac{1}{2}\frac{\partial \delta\overline{P}}{\partial x_i} \tag{21}$$

$$\overline{P}^{n+1} = \overline{P}^n + \delta\overline{P} \tag{22}$$

All terms in equations (19) to (22) except the advective term are discretized over a staggered grid using second order finite differences. On Cartesian grids this formulation is equivalent to a finite volume technique [16]. Mass conservation is enforced solving the pressure equation (20) at each time step with a direct Poisson solver [17]. The time step is chosen to respect the stability limits given by the advective and diffusive Courant-Friedrich-Levy numbers. The pressure term is treated as proposed by Van Kan [18].

3.1 Pressure boundary condition

The numerical solution of the pressure equation (20) requires Neumann boundary conditions for $\delta\overline{P}$. The consistent boundary condition for the pressure applied to the scheme described above ([19]) is given by

$$\frac{\partial \delta\overline{P}}{\partial N} = \frac{\overline{u}_\Gamma^* - \overline{u}_\Gamma^{n+1}}{\Delta t} N \tag{23}$$

where N is the direction normal to the boundary Γ. Easton [20] showed that the result is independent of $\overline{u}_\Gamma^*$ so that the following substitution can be made

$$\overline{u}_\Gamma^* = \overline{u}_\Gamma^{n+1} \tag{24}$$

Thus a homogeneous Neumann boundary condition is introduced for $\delta\overline{P}$.

3.2 Advective transport

The requirements for the discretisation of the advective term are the conservation of momentum and energy and the control of *aliasing errors*. Using a linear interpolation to obtain the convective fluxes at the center of the control surfaces in the staggered grid arrangement, a second order scheme is obtained which offers optimal conservation properties. In the jet test case, the aliasing error phenomenon can not be avoided completely. To control these, an upwind interpolation of the convective fluxes is applied. Second and third order upwind formulations were found to be too dissipative, but good results were obtained using a third order upwind-biased discretization, derived from the approach taken by Shirayama [21]. The scheme can be written as the sum of a forth order central scheme plus a forth order dissipation term given here for an advection velocity c and a generic transported variable f

$$\left(c\frac{\partial f}{\partial x}\right)_i = c_i(\alpha_1 f_{i-2} + \beta_1 f_{i-1} + \gamma_1 f_i + \delta_1 f_{i+1} + \epsilon_1 f_{i+2}) + \alpha|c_i|(\alpha_2 f_{i-2} + \beta_2 f_{i-1} + \gamma_2 f_i + \delta_2 f_{i+1} + \epsilon_2 f_{i+2}) \tag{25}$$

The coefficients α_1 to ϵ_1 and α_2 to ϵ_2 are obtained using Lagrangian interpolation formulas taking into account the grid stretching. The blending parameter α controls the magnitude of the forth order dissipation term. It allows the generation of a family of schemes from forth order central ($\alpha = 0$) over pure third order upwind ($\alpha = 1$) to upwind-biased schemes as proposed by Kawamura *et al.* [22] ($\alpha = 3$) or Shirayama [21] ($\alpha = 4$). On the boundaries the second order central scheme is retained. This reduces the overall precision to second order, but for the interior points the higher local precision is retained.
In the jet test case values of $\alpha = 0.25$ or $\alpha = 0.5$ were found to be sufficient to avoid wiggles. These result in the following interpolation formulas for the positive flux (given here for a positive advection velocity on a uniform grid)

$$(f_i)^+_{.25} = -.1041\overline{6}f_{i-1} + .6458\overline{3}f_i + .5208\overline{3}f_{i+1} - .0625f_{i+2} \tag{26}$$

$$(f_i)^+_{.5} = -.125f_{i-1} + .708\overline{3}f_i + .458\overline{3}f_{i+1} - .041\overline{6}f_{i+2} \tag{27}$$

The negative flux is obtained in a similar way, decreasing i by one. The overbar denotes numbers repeated infinitely. The standard forth order central scheme is given for comparison

$$(f_i)^+ = -.08\overline{3}f_{i-1} + .58\overline{3}f_i + .58\overline{3}f_{i+1} - .08\overline{3}f_{i+2} \tag{28}$$

In order to assess the combined effect of the turbulence model and numerical dissipation, simulations are performed using the plane channel at $Re_\tau = 1000$ as a benchmark. Approximate boundary conditions derived from the boundary layer equations are used as wall functions to model the solid walls. Details of this formulation will be given in [23]. The simulation uses $(40, 24, 26)$ grid points in a domain $(2.5\pi, 2., 2.)$ where (x_1, x_2, x_3) are the streamwise, periodic and wall normal directions respectively. In Figure (1) the effect of using the upwind discretisation with $\alpha = 0.25$ is compared to the solution using the forth order central scheme. The solid line is a LES by Piomelli [24] where the wall layer is resolved and which is used as a reference. As can be seen, there is a noticeable effect of the dissipation term on the turbulence intensities. To avoid this influence, further grid refinement is needed. Still the results, even on this coarse grid, are acceptable.

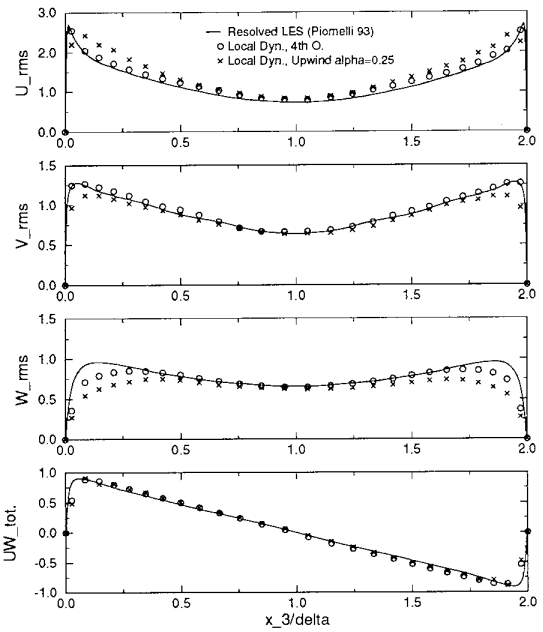

Fig. 1: *Turbulence intensities and total shear stress (based on $\langle u_\tau \rangle$). Plane channel Re=1000*

4 BOUNDARY CONDITIONS

The present simulation is concerned with a jet, issuing from a 2D slit in an infinite wall, impinging onto a flat plate as shown in Figure (2). As in the plane channel simulation, the solid walls are modeled by imposing the wall shear stress using approximate wall boundary conditions.

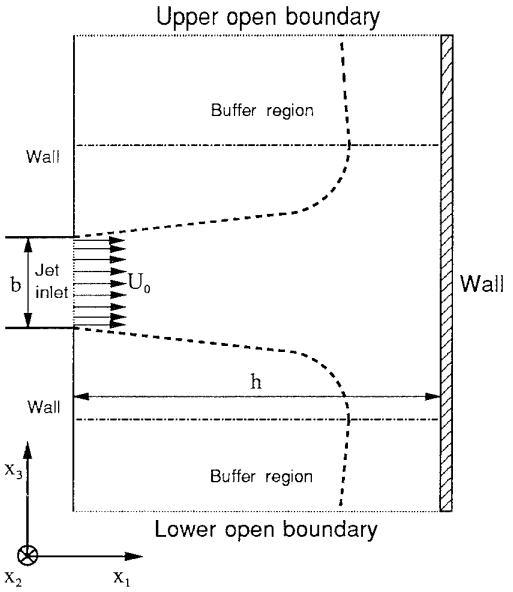

Fig. 2: *Impinging jet, geometry and coordinate system.*

4.1 Open; entrainment boundary conditions

The main difficulty related to the numerical simulation of a jet expanding into a flow at rest lies in the imposition of boundary conditions and is directly related to the numerical need to use a *finite* computational field to model a flowfield of theoretically *infinite* size. Therefore the boundary conditions are *purely numerical* ones and have to satisfy three basic requirements:

- to allow the entry of flow into the computational domain to balance the jet entrainment
- to allow the flow and in particular large turbulent structures to exit the computational domain without being deformed or reflected
- to model the physical connection between the top and bottom boundaries, in order to ensure a time-averaged symmetric development of the jet.

Modeling entrainment through the boundary is a critical problem in the jet simulation; in [6] is reported that the entrainment had to be artificially limited on the border to avoid instabilities.
In the frame of the pressure boundary condition treated above, the difficulty lies in the fact that at an open boundary the normal velocity at time step $n+1$ is unknown and not fixed as a boundary condition as it would be at a solid surface for example.
A stable way to specify $\overline{u}_\Gamma^{n+1}$ is to use a zeroth order extrapolation on the $\overline{u}_i^\star$ velocity field, (*i.e.* $\overline{u}_\Gamma^\star = \overline{u}_{interior}^\star$) which already contains $\partial\overline{P}^n/\partial x_i$ and differs from the $\overline{u}_i^{n+1}$ field by $\partial\overline{\delta P}/\partial x_i$ only. Alternative formulations have been investigated, but the tests carried out show that most standard conditions yield explosive instability, at least for the free and impinging jet test cases.
After the velocity field is updated using (21), the normal velocity components are calculated applying continuity to the last interior cell. The tangential velocity components at the fictitious cells outside the domain are obtained assuming a zero derivative of vorticity in the direction normal to the boundary.
An additional constraint has to be applied to the general procedure described above. The solution of the pressure equation (20) with Neumann boundary conditions requires that the following compatibility constraint is satisfied

$$\int_\Omega \Delta\overline{\delta P} dV = \oint_\Gamma \frac{\partial\overline{\delta P}}{\partial N} dS \qquad (29)$$

where the LHS represents a volume integral over the domain Ω and the RHS a surface integral along the boundary Γ. With (20) and (23) this condition can be written in the form

$$2\int_\Omega \frac{\partial\overline{u}_i^\star}{\partial x_i} dV = \oint_\Gamma (\overline{u}_\Gamma^\star - \overline{u}_\Gamma^{n+1}) N dS \qquad (30)$$

With (24) the RHS is equal to zero. This implies that (30) is equivalent to a constraint of global mass conservation which is satisfied by modifying uniformly the normal open boundary velocities at each timestep before solving equation (20).
The planar jet problem on a finite grid has to be stabilized using a far field condition which models the physical connection of top and bottom boundary. An ideal condition should ensure that the time mean pressure is the same at the top and bottom boundary.
In the present simulations, the average pressure over the top and bottom boundaries are kept constant at every timestep. This is done by adding a transversal pressure gradient to the pressure field P after the update (22). The δP field used to correct the predicted velocity field remains unchanged.
The boundary conditions must allow local inflow and outflow computed as part of the solution. In the presence of vortices the resulting inflow can cause an accumulation of errors at the boundary, leading to an unphysical development of the computation.
To solve this problem, the current approach uses the idea of a buffer domain, as proposed by Streett and Macaraeg [25], at the top and bottom boundary for the impinging jet problem.
This implies a smooth reduction to zero of the streamwise viscous term. The ingoing streamwise advection velocities are smoothly modified in order to involve a constant outgoing velocity obtained from the condition of global mass conservation. Outgoing advective velocities are not modified. The wall shear stress used to simulate the solid wall is smoothly reduced to zero in a similar way. The incompressibility constraint and the pressure boundary condition treatment are maintained as described above.

5 RESULTS

Figure (3) shows the instantaneous pressure field of an impinging jet at Reynolds number $10,000$, based upon the inlet width b and the initial jet velocity U_0. The total computational domain (x_1, x_2, x_3) is of dimension $(20, \pi, 40)$ with a grid resolution of $(80, 12, 80)$. The two buffer domains used at the top and bottom boundaries have a dimension of about 14 (using two times 12 grid points) in x_3-direction. The inlet velocity profile is uniform and constant in time. Figure (4) shows a close-up

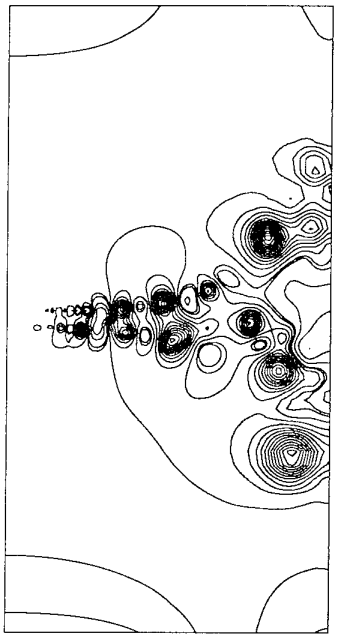

Fig. 3: *Instantaneous pressure contours. Impinging jet, Re=10,000*

view of the flowfield excluding the buffer regions and the wall area. As can be seen, the flow is characterized by the presence of large vortical structures. Following the time-evolution, vortex pairing/merging events can be observed. An analysis of the velocity fluctuations recorded

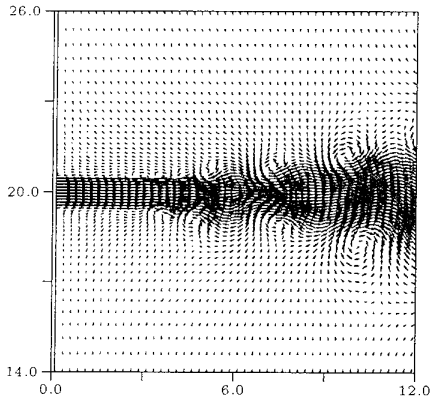

Fig. 4: *Detail, instantaneous velocity vectors. Impinging jet, Re=10,000*

at the end of the potential core, outside the shear layer of the jet, shows a dominant frequency corresponding to a Strouhal number (based upon b and U_0) of 0.2. This frequency characterizes the passage of vortices at this location. Fast Fourier transformation of the data taken at the centerline shows a frequency spectrum with peaks around 0.25. This compares well with the experimental range of 0.24 to 0.64 [26] and also with the value of 0.273 given in [27].

To obtain the mean velocities and the turbulence statistics, the flow is sampled over a period of 200 nondimensional time units. In Figure (5) the time averaged decay of the centerline velocity is compared to the law of the free and impinging jet obtained from experiment [28]. The numerical result is in quite good agreement with this data and displays clearly the two distinct regions.

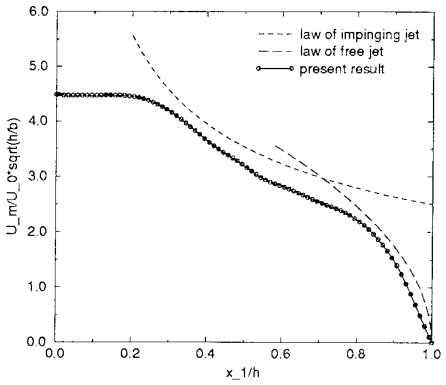

Fig. 5: *Decay of time mean centerline velocity. Impinging jet, Re=10,000*

Figure (6) shows the evolution of the streamwise turbulence intensities and the shear stress at different locations downstream the jet exit.

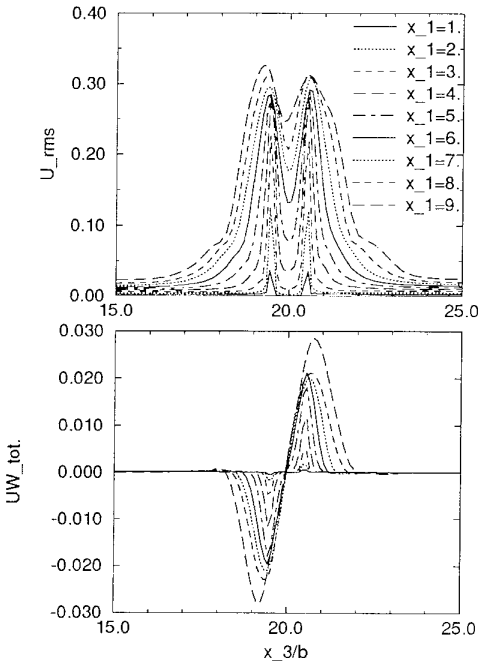

Fig. 6: *Turbulence intensities and shear stress (based on the jet exit velocity U_0) at x_1 locations 1. to 9.*

6 CONCLUSIONS

The present investigation has shown the feasibility to use LES for the study of spatially-developing jet flows. The choice of a high order upwind-biased discretization and the use of the buffer domain technique have made it possible to achieve results which are numerically stable and reproduce correctly the main physical features of the problem.

REFERENCES

[1] DEARDORFF, J.: A numerical study of three-dimensional turbulent channel flow at large Reynolds numbers.
J. Fluid Mech., Vol. 41, 1970.

[2] SCHUMANN, U.: Direct and large-eddy simulation of turbulence. Summary of the state-of-the-art 1991.
VKI LS 1991-02: Introduction to the modeling of turbulence. von Karman Institute for Fluid Dynamics, 1991.

[3] COMTE, P.; LESIEUR, M.; LAROCHE, H.; X., N.: Numerical simulation of turbulent plane shear layer.
Turbulent shear flows 6. Springer, 1989, pp 441–454.

[4] PIANESE, C.; BENOCCI, C.: Large-eddy simulation of spatially developing plane mixing layers.
Turbulent shear flows 8. Springer, 1991.

[5] TSAI, H.; VOKE, P.; LESLIE, D.: Large-eddy simulation of turbulent free shear flows.
Numerical Methods in Laminar and Turbulent Flow, Montreal, 1987, pp 363–373. Computational Mechanics Publications, Springer Verlag.

[6] RISK, M.; MENON, S.: Large-eddy simulations of axisymmetric excitation effects on a row of impinging jets.
Phys. Fluids, Vol. 31, No 7, July 1988.

[7] SCHUMANN, U.; GRÖTZBACH, G.; KLEISER, L.: Direct numerical simulation of turbulence.
VKI LS 1979-02: Prediction methods for turbulent flows. von Karman Institute for Fluid Dynamics, 1979.

[8] MASON, P.; N.S., C.: On the magnitude of the subgrid-scale eddy coefficient in large-eddy simulations of turbulent channel flow.
J. Fluid Mech., Vol. 162, 1986.

[9] SMAGORINSKY, J.: General circulation experiments with the primitive equations, i. the basic experiment.
Mon. Weather Rev., Vol. 91, 1963.

[10] MASON, P.: Large-eddy simulation of turbulent shear flows.
VKI LS 1989-03: Turbulent shear flows. von Karman Institute for Fluid Dynamics, 1989.

[11] GERMANO, M.; PIOMELLI, U.; MOIN, P.; CABOT, W.: A dynamic subgrid-scale eddy viscosity model.
Phys. Fluids A, Vol. 3, No 7, July 1991.

[12] LILLY, D.: A proposed modification of the germano subgrid-scale closure method.
Phys. Fluids A, Vol. 4, No 3, March 1992.

[13] GHOSAL, S.; LUND, T.; MOIN, P.: A local dynamic model for les.
Center for Turbulence Research, Annual Research Briefs 1992.

[14] YANG, K.-S.; FERZIGER, J. H.: Large-eddy simulation of turbulent obstacle flow using a dynamic subgrid-scale model.
AIAA Journal, Vol. 31, No 8, August 1993.

[15] LUND, T.; GHOSAL, S.; MOIN, P.: Numerical experiments with highly-variable eddy viscosity models.
ASME FED, Vol. 162, 1993.

[16] PEYRET, R.; TAYLOR, T.: Computational methods for fluid flows, Springer Verlag, Berlin, 1987.

[17] SCHMIDT, H.; SCHUMANN, U.; VOLKERT, H.: Three-dimensional, direct and vectorized elliptic solvers for various boundary conditions.
DFVLR Report DFVLR-mitt. 84-15, July 1984.

[18] VAN KAN, J.: A second-order accurate pressure-correction scheme for viscous incompressible flow.
J. Sci. Stat. Comp., Vol. 7, 1986.

[19] FLETCHER, C.: Computational techniques for fluid dynamics 1 & 2, Springer-Verlag, 1988.

[20] EASTON, C.: .
J. Comp. Phys., Vol. 9, 1972.

[21] SHIRAYAMA, S.: Construction of modified third-order upwind schemes for stretched meshes.
AIAA Journal, Vol. 30, No 5, May 1992.

[22] KAWAMURA, T.; TAKAMI, H.; KUWAHARA, K.: New higher-order upwind schemes for incompressible Navier-Stokes equations.
Lecture Notes in Physics 218. Springer Verlag, 1984.

[23] HOFFMANN, G.; BENOCCI, C.: Approximate wall boundary conditions derived from boundary layer equations and application in large-eddy simulation.
Fifth European Turbulence Conference, Siena, Italy, July 5-8 1994,

[24] PIOMELLI, U.: High Reynolds number calculations using the dynamic subgrid-scale stress model.
Phys. Fluids A, Vol. 5, No 6, June 1993.

[25] STREETT, C.; MACARAEG, M.: Spectral multi-domain for large-scale fluid dynamic simulations.
Applied Numerical Mathematics, Vol. 6, 1989/90.

[26] GUTMARK, E.; HO, C.: Preferred modes and the spreading rates of jets.
Phys. Fluids, Vol. 26, No 10, 1983.

[27] NAMER, I.; ÖTUGEN, M.: Velocity measurements in a plane turbulent air jet at moderate Reynolds numbers.
Exp. in Fluids, Vol. 6, 1988.

[28] BELTAOS, S.; RAJARATNAM, N.: Plane turbulent impinging jets.
J. Hydr. Research, Vol. 11, No 1, 1973.

Rib Vortices in Round Jets: Direct and Large Eddy Simulation

M. Fatica, R. Verzicco & P. Orlandi
Dipartimento di Meccanica e Aeronautica,
Università "La Sapienza",
Via Eudossiana 18, 00184, Roma, Italy

Abstract

Direct and Large Eddy simulations of temporal evolving round jets at low Reynolds numbers have been performed by a second-order finite difference scheme in cylindrical coordinates. The simulations have shown the formation of longitudinal structures whose number increases with the Reynolds number. The role of these structures in the spreading of the jet and in the creation of small scales has been analysed. LES models (Smagorinsky and dynamic models) permit to have satisfactory results with coarse grids.

1 Introduction

Illuminating works of Brown & Roshko [1], Winant & Browand [2], and more recently of Moser & Rogers [3], have shown for a plane mixing layer that the rib vortices are responsible for a drastic increase in the molecular mixing of a passive scalar. This result is relevant to combustion where the mixing of the reacting species controls the speed of the chemical reactions and then the efficiency of combustors. The effect of the streamwise vortices becomes even more important in round jets. In fact for a plane mixing layer the velocity jump is sustained by the undisturbed streams also far from the splitter plate. This implies that the streamwise vortices compete with large spanwise structures continuously strengthen by the potential streams. In contrast in a round jet the velocity difference between the ambient fluid and the high-speed core attenuates with the distance from the nozzle. The lack of an imposed constant shear makes stronger the interaction between the large spanwise structures and the streamwise vortices. These statements have been confirmed in many experimental and numerical studies (e.g. Liepmann & Gharib [4], Agüí & Hesselink [5], Verzicco & Orlandi [6]).

As stated in [3] in order to have the mixing transition, two ingedients are requested: a strong set of streamwise vortices and sufficiently high Reynolds and Schmidt numbers. This last requirement poses a strong limitation on the use of the direct simulation (hereafter referred to as DS) for flows of practical interest at Re much higher than those considered in [3], since the grid resolution required is unaffordable even by the modern supercomputers. On the other hand the necessity of describing the dynamics of intermediate structures, immediately rules out those methods based on Reynolds averages. Many recent works have shown that the most promising numerical technique is the large eddy simulation (hereafter referred to as LES) in which the large scales are explicitly computed and the sub-grid scales are modelled.

In this study we wish to analyse the dynamics of streamwise vortices, and the effect they have on the large vortex rings, through DS and LES for different values of the Reynolds number. Periodic boundary conditions are imposed along the axis of the jet. Such time-developing simulations, although different from real space developing jets, are able to describe the essential dynamics of vortical structures, using a reasonable number of grid points.

The paper is organised as follows: in the next section a short description of the numerical method is given, in §3 initial conditions and run parameters are described and the results are discussed in §4, closing remarks are in §5.

2 Numerical procedure

The numerical model discretizes on a staggered grid the time-dependent three-dimensional Navier-Stokes equations in primitive variables and in cylindrical coordinates. A detailed description of the numerical method and of the subgrid stress models has been given in previous works (Verzicco & Orlandi [7], Fatica Orlandi & Verzicco [8]); here it suffices to summarise the main points.

The equations are expressed by the quantities $q_\theta = v_\theta$, $q_r = r \cdot v_r$ and $q_z = v_z$. r is the radial coordinate and v_θ, v_r, v_z are respectively azimuthal, radial and axial velocities. The introduction of q_r, together with the use of a staggered grid, avoids the evaluation of the terms that become singular at $r = 0$ [7].

By the centreline velocity of the jet U_{cl} and a length scale L such that the jet radius is $R = 5L$, the dimensionless equations are:

$$\frac{\partial \overline{q}_r}{\partial r} + \frac{\partial \overline{q}_\theta}{\partial \theta} + r\frac{\partial \overline{q}_z}{\partial z} = 0. \qquad (1)$$

Paper presented at the 74th Fluid Dynamics Symposium on "Application of Direct and Large Eddy Simulation to Transition and Turbulence" held at Chania, Crete, Greece, in April 1994.

$$\frac{D\overline{q}}{Dt} = -\nabla\overline{P} + \nabla\cdot\left(\frac{1}{Re}\nabla\overline{\tau}\right) \qquad (2)$$

$\hat{\tau}_{ij}$ is the sum of the resolved ($\overline{\tau}_{ij}$) and the subgrid (τ'_{ij}) stresses. The lenght scale L for nondimensionalization is approximately equal to the vorticity thickness δ_ω, so that $Re = U_{cl}L/\nu$ is approximately equal to $Re = U_{cl}\delta_\omega/\nu$. All the quantities denoted by an overbar are defined as:

$$\overline{q}(r,\theta,z) = \frac{1}{r\Delta r\Delta\theta\Delta z}\int\int\int q(r',\theta',z')r'dr'd\theta'dz'$$

being the integration performed over the appropriate control volume for each variable. As usual for LES techniques, the total stresses are expressed through the following expression

$$\hat{\tau}_{ij} = (1+\nu_T Re)\overline{S}_{ij} = \hat{\nu}\overline{S}_{ij}, \qquad (3)$$

where $\overline{S}_{ij}$ is the resolved rate-of-strain tensor. The eddy viscosity ν_T is given by the Smagorinsky model [9]:

$$\nu_T = (C_s\Delta)^2|S| = (C_s\Delta)^2\left[2\overline{S}_{ij}\,\overline{S}_{ij}\right]^{1/2} \qquad (4)$$

or the dynamic model [10]:

$$\nu_T = C(\Delta)^2\left[2\overline{S}_{ij}\overline{S}_{ij}\right]^{1/2} \qquad (5)$$

for cylindrical coordinates it results $\Delta^2 = (r\Delta r\Delta\theta\Delta z)^{2/3}$. Despite the similar expressions for ν_T, the two models have a fundamental difference; in the first case the constant C_S is fixed and as suggested by Cain *et al.* [11] for mixing layers is $C_S = 0.1$. On the contrary for the dynamic model C is not given a priori but it is computed from the flow variables. The explicit expression for C is given in many papers (Germano *et al.* [10], Lilly [12]) and it is not reported here, however we wish to stress that the self-adaptive constant C allows the model to switch off when the grid resolves all the scales. The formulation proposed by Lilly [12] has been employed with an average along the periodic directions to stabilise the model.

Equations (1), (2) have been solved by a fractional-step method (Kim & Moin [13]) with the non-linear terms and the cross derivatives of the viscous terms computed explicitly and the other viscous terms implicitly. The Poisson equation for the scalar quantity necessary to correct both velocity and pressure fields (see [13]), has been directly solved by trigonometric expansions in the periodic directions and by a tridiagonal solver in the radial direction. The time integration scheme is a hybrid low-storage 3-order Runge-Kutta Crank-Nicolson scheme that, having a large stability limit, allows large time steps and CPU savings.

3 Initial Conditions

The initial mean velocity profile is the same as [6] and [8]

$$\overline{q}_z(r,\theta) = \left[1-\tanh\left(2.06\beta\log\left(\frac{r}{R(\theta)}\right)\right)\right]\frac{U_{cl}}{2} \qquad (6)$$

with $\beta = 5.5$, so that $R/\delta_\theta = 22.6$ (δ_θ is the momentum thickness). The azimuthal perturbation of the jet is given by a random radial displacement of $R(\theta)$:

$$R(\theta) = R + \epsilon_\theta\phi(\theta) \qquad (6a)$$

where $0 < \phi(\theta) < 1$ is a random number, and $\epsilon_\theta = .05$.

The azimuthal vorticity component ω_θ has been perturbed in z to initiate the instability leading to roll-up and successively to pairing; its distribution is:

$$\omega_\theta(z,r,\theta) = \frac{[q_z(r+\frac{\Delta r}{2},\theta) - q_z(r-\frac{\Delta r}{2},\theta)]}{\Delta r}\cdot\left[1+\epsilon_z sin(z)+\frac{\epsilon_z}{8}sin(z/2)\right].$$

This perturbation does not introduce ω_z, and ω_r is yielded by $\nabla\cdot\omega = 0$. The velocity field is obtained from the relationship $\nabla\times\omega = -\nabla^2\mathbf{U}$. The axial dimension of the computational domain was $L_z = 4\pi$, which is the minimal extension required for a pairing [6]. The free-slip radial boundary was located at $R_f = 10.66L$, that as checked in [6] does not affect the flow evolution.

Values of the Reynolds number of 200, 400, 600 and 800 have been considered for DS; for LES the simulations were performed at $Re = 200$ and $Re = 800$.

4 Results

Direct Simulation

Before discussing the role of the streamwise vortices it is worth to shortly describe the formation and evolution of the large rings.

The Kelvin-Helmholtz instability of the thin axisymmetric vorticity layer produces the roll-up of the layer. Regions where the vorticity is concentrated (rings) are separated by regions where the vorticity is depleted (braids) (Fig. 1a). Unless subharmonics of the fundamental wavelength are avoided, vortex rings interact to generate larger rings. In particular the upstream ring is strained below its downstream counterpart (Fig. 1b), wraps around (Fig. 1c) and merge (Fig. 1d). This process continues, provided that enough space is left between the ring and the axis of symmetry to allow another vortex ring to be strained below.

In this study we considered only the first pairing since Hussain and Zaman [14] observed that the vortex pairing produces a large amount of turbulent

stresses. Before the pairing, the braid region is subjected to the stretching induced by the large rings. This extensional strain is oriented at about $30° - 40°$ with respect to the axis of symmetry (see Martin and Meiburg [15]) and it causes the increase of radial and axial vorticity (Fig. 2) concentrated in couples of counterrotating streamwise vortices. This mechanism of formation of streamwise vortices is that suggested by Lin and Corcos [16] in plane mixing layers.

Fig. 2 shows how important are the three-dimensional effects by comparing the time evolution of the maxima of the vorticity field with those in the axisymmetric case. At Re=200 the diffusion prevents three-dimensionalities to grow and the flow remains axisymmetric also after the pairing ($t \approx 40$). At $Re = 800$ azimuthal instabilities are not damped so, when the pairing occurs, differences from the axisymmetric case are significant.

The bump at $t \approx 40$ (Fig. 3) in the time evolution of the momentum thickness δ_θ represents the pairing, which although is a pure axisymmetric event, is influenced by three-dimensional instabilities producing a greater spreading of the jet. This feature can be seen by comparing the evolution of momentum thickness at $Re = 200$ with that at $Re = 800$. In the first case, the axisymmetric and the three-dimensional cases do not differ, on the contrary at $Re = 800$, δ_θ is greater in the three-dimensional cases than in the axisymmetric case.

Contour plots of vorticity components on planes crossing the braid region (section a) and the core of the ring (section b) allow to have a picture of the way longitudinal vortical structures affect the jet. In Fig. 4 these plots are given at $Re = 200$ and $Re = 800$, for a $129 \times 91 \times 129$ simulation. In the sections through the braid, the same amount of radial and axial vorticity components shows that these longitudinal structures are inclined with respect to the axis of simmetry. The strength of these vortices increases with the Re and at $Re = 800$ the amount of ω_r and ω_z is comparable to ω_θ. This structures, at high Re in the section through the ring core, largely deform the shape of the jet producing intense azimuthal vorticity cups, with a consequent increase in the momentum thickness.

The dynamics of these structures does not substantially differ from that described in [6], when a "clean" perturbation with fixed azimuthal wavenumber was imposed. Then the description of the vorticty field is not repeated in the present paper, where on the contrary the analysis is focused on finding the most unstable wavenumber n^* and how it changes with Re; consequently the perturbation is random and n^* is selected by the flow itself. In this case the simulation is closer to the jet evolution in a laboratory, where Liepmann and Gharib [4] found that the most unstable wavenumber is higher than that for a single vortex ring. This is not surprising since the wavenumber of instability is strongly dependent on the strain field acting on the ring and in a jet the strain is not only that self-induced by the ring but there is the influence of close rings. This implies that in a jet, a vortex ring with a given circulation is subjected to a strain that is higher than if the same ring were isolated, with a consequent higher wavenumber of instability. As found by Shariff *et al.* [17] for vortex rings, there is not a single wavenumber but a band on unstable wavenumbers around the most unstable with the growth rate increasing with the Reynolds number (Fig. 5). The growth of the $n = 1$ wavenumber of the radial energy contribution, indicates that the jet is slightly moving off the axis (Fig. 5b). The $n = 0$ azimuthal energy contribution (Fig. 6) indicates a swirling motion as observed by Maxworty [18] in early turbulent vortex rings. The swirling motion also indicates the growth of helical modes, experimentally observed in the transitional region of jets. However before drawing solid conclusions on this last point it would be necessary to be more confident on the grid resolution at the latest stage of the evolution. From the development of ω_z for the $65 \times 91 \times 65$ and $129 \times 91 \times 129$ grid (Fig. 2b) we see that in the coarser simulation there is a sudden increase due to poor resolution and this legitimates the question whether the increase of ω_z observed in the latter grid is also due to insufficient resolution. We wish to point out that we were not able to assign the same initial conditions in simulations with different grids, using a random perturbation. The strong dependence on the initial perturbation was already reported for a mixing-layer by Moser and Rogers[3]. Fig. 7 shows sections of vorticity field at $Re = 800$ for a simulation, with the same resolution but with a different perturbation: in the simulation of Fig. 4, $\phi(\theta)$ in eq.(6a) was a random number, while in this one $\phi(\theta)$ is a combination of cosines with random phases (as in [8]). The two cases differ on the amount of energy in each wavenumber n. For the random phase perturbation the initial equipartition of energy among the first eigth wavenumbers, produces a strong asymmetry of the flow with the emergence of pronounced side jet as observed in experiment [4], [5]. The asymmetry is confirmed by the growth of the $n = 1$ mode in the energy spectra, whose effects on the field, when the initial contents of energy is the same in all the wavenumbers, are more pronounced.

LES simulation

LES simulations at Re=200 have been performed to emphasise the quality of the dynamic model to provide a turbulent viscosity only when necessary. This feature was previously investigated in transitional wall-bounded flows [10]. At this low Re the direct simulation has shown (Fig. 4) that the weak longitudinal vortices produce a distribution of azimuthal vorticity without cups. Then small three-dimensional scales do not form and a simulation by a $33 \times 91 \times 41$ grid is fully resolved. In Fig. 8 the $< v_r' v_z' >$ radial profile (the <> operator is an average in azimuthal

and axial direction) is given for simulations obtained without subgrid model, with the dynamic model and with the Smagorinsky model. The results by the dynamic model are almost identical to those by the direct simulation, indicating that the model does not act; on the contrary the Smagorinsky model produces an additional eddy viscosity with an excessive damping of the stresses. These arguments are an indirect proof that by the $33 \times 91 \times 41$ grid the flow field at $Re = 200$ is fully resolved. To prove definitely this statement we should have compared the $< v_r' v_z' >$ radial profile with that by the $129 \times 91 \times 129$ grid. As previously mentioned, this comparison was not possible since we were not able, with random initial conditions, to produce on different grids two initial disturbances with the same energy content at each azimuthal wavenumber. The large dependence of the time evolving jets on the initial conditions, caused different amount of the stresses at the later times.

Since the interest is to apply LES at high Reynolds numbers, simulations have been performed at $Re = 800$. As mentioned above, at this Reynolds number the $129 \times 91 \times 129$ simulation can not be considered fully resolved since it produces high vorticity levels at small scales, which are not adequately described by our spatial resolution. However we consider the fine grid simulation as a reference solution. LES have been performed with a grid $33 \times 65 \times 41$ without subgrid model, with the Smagorinsky model ($C_S = 0.1$) and with the dynamic model. To overcome the lack of initial conditions reproducibility, a random phase perturbation was applied. With this perturbation limited to the first eigth wavenumbers, the initial conditions on different grids have approximately the same energy distribution and the same evolution is expected.

Fig. 9a shows that without any subgrid model higher levels of $< v_r' v_z' >$ are generated close to the axis and smaller in the central region. These discrepancies have been also reported in [8] and are caused by the numerical eddy viscosity. When the Smagorinsky model is introduced (Fig. 9b), there is a slight production of subgrid stress in the central region and discrepancies between the LES and the DS seems to grow. A very good agreement could be obtained by appropriately tuning the value of the constant at each radial position. We believe that it is not an appropriate procedure since the optimum value of C_S requires a large number of simulations and the results of DS. Fig. 9c, on the other hand, shows that the dynamic model produces profiles of $< v_r' v_z' >$ in better agreement with that of the most refined grid. Improvements occur in the central region, characterized by large amount of vorticity but still, as for the Smagorinsky model, the results differ in the region near the axis. In the present simulation we found that the dynamic model strongly depends on the way the constant C is evaluated. We evaluted the constant by averaging in the θ direction, although we are aware of the small number of data. This lack of averaging data could be the cause of the absence of back scatter in the inner region. A first tentative to have more data by a further average in time brougth to worst results and this can be explained because this time average should be applied only to flows in a statistical steady state.

The LES has the features to be a more universal turbulence model with respect to the model based on the Reynolds average since it must capture the most important eddies. In the jet as well as in the mixing layer not only the rolls spanning in the azimuthal or in the spanwise directions are important but also the longitudinal vortices. In the previous subsection they role was analyzed by vorticity contour plots in planes normal to the flow direction and Fig. 4 shows that approximately eight couples of longitudinal vortices are generated. With only 32 points in the azimuthal direction we can not expect to capture this number of structures, however we expect to reproduce only some of the features of the DS. We observe in Fig. 10 that in the braid as in the DS (Fig. 4) the longitudinal vortices are weaker than in the centre of the roll. In the centre they are responsible for the production of cups of azimuthal vorticity. The role of the longitudinal vortices should largely contribute in combustion process to enhancing mixing of reactants and to combustion efficiency. Also in the LES the comparable magnitude of radial and axial vorticity in the braid region characterises the inclined orientation of the longitudinal vortices. This comparison of Smagorinsky and dynamic model results, shows that the dynamic model gives a better description of the streamwise vortices. As a final comment on Fig. 10 we think that the vorticity distribution around the centre region is quite well reproduced, on the contrary there is too much vorticity in the region around the axis.

5 Closing remarks

The aim of this paper was to analyse the role of axial vortices in the spreading of the jet, as in [6] but with an initial random perturbation, and the role of the pairing in the formation of these structures and in the production of turbulent stress. Our simulations have confirmed the strong dependence of this flow on the initial conditions as reported in [3] for a mixing layer. Further we found that there is a band of unstable azimuthal wavenumbers with a growth rate increasing with the Reynolds number as for a single vortex ring [17].

This paper was also devoted to show the feasibility of LES simulations in cylindrical coordinates of a temporal evolving round jet. The use of dynamic model gives an improvement of the results when coarse grids are used. The dynamic model, with the Lilly modification [12], seems more promising than the Smagorinsky model, due to the constant

computed from the flow field. In particular we have shown that the self-adaptive constant C allows the model to switch off when the grid adequately resolves all the scales of the flow. However also the dynamic model presents several aspects that need to be improved, first of all the excessive fluctuations, both in space and in time, of the coefficient C. More simulations have to be performed in order to determine a procedure of calculation of C closer to the physics of the flow. Work is in progress to develop a code for space developing round jets. Simulations of this flow are more interesting since very detailed comparisons with experimental data can be performed. Moreover in a space developing jet, there are at the same time laminar, transitional and turbulent regions and for LES simulations the use of an adaptive model, as the dynamic model, will be mandatory.

Acknowledgments

The authors would like to thank Prof. Ugo Piomelli for useful comments and suggestions.

The research was supported by a grant from Agenzia Spaziale Italiana.

References

[1] Brown, G.L. & Roshko, A.: 'On density effects and large structure in turbulent mixing layers', *J. Fluid Mech.* **64**, (1974), pp. 775–816.

[2] Winant, C.D. & Browand, F.K.: 'Vortex pairing: the mechanism of turbulent mixing layer growth at moderate Reynolds number', *J. Fluid Mech.* **63**, (1974), pp. 237–255.

[3] Moser, R.D & Rogers, M.M.: 'The three-dimensional evolution of a plane mixing layer: Pairing and transition to turbulence', *J. Fluid Mech.* **247**, (1992), pp. 275–320.

[4] Liepmann D. & Gharib M. ' The role of streamwise vorticity in the near-field entrainment of round jets', *J. Fluid Mech.* **191**, (1988), pp. 19–45.

[5] Agüí, J.C. & Hesselink, L.: 'Flow visualization and numerical analysis of a coflowing jet: a three-dimensional approach', *J. Fluid Mech.* **191**, (1988), pp. 19–45.

[6] Verzicco, R. & Orlandi, P.: 'Direct simulations of the transitional regime of a circular jet', *Phys. Fluid* **2**, (1994), pp. 751–759.

[7] Verzicco, R. & Orlandi, P.: 'A finite-difference scheme for the three-dimensional incompressible flows in cylindrical coordinates', *submitted to J. Comp. Phys.*

[8] Fatica, M. Orlandi, P. & Verzicco, R.: 'Direct and Large Eddy Simulation of Round Jet', to appear in Proceedings of First ERCOFTAC Workshop on Direct and Large Eddy Simulation, edited by Voke, Kleiser and Chollet, Kluwer

[9] Smagorinsky: 'General circulation experiments with the primitive equations. I. The basic experiment', *Monthly Weather Review*, **91**, (1963), pp. 99–164

[10] Germano, M., Piomelli, U., Moin, P., & Cabot, W.H.: 'A dynamic subgrid-scale eddy viscosity model', *Phys. Fluids A*, **1**, (1991), pp. 1061

[11] Cain, A.B., Reynolds, W.C., & Ferziger, J.H.: 'A three-dimensional simulation of transition and early turbulence in a time-developing mixing layer', *Report No TF-14.*, (1981), Stanford University.

[12] Lilly, D.K.: 'A proposed modification of the Germano subgrid-scale closure method', *Phys. Fluids A*, **4**, (1992), pp. 1061

[13] Kim, J. & Moin, P.: 'Application of a fractional step method to incompressible Navier-Stokes equations', *J. Comp. Phys.*, **59**, (1985), pp. 308

[14] Hussain, A.K.M.F. & Zaman, K.B.M.Q.: 'Vortex pairing in a circular jet under controlled excitation. Part 2. Coherent structure dynamics', *J. Fluid Mech.* **101**, (1980), pp. 493–544.

[15] Martin, J.E. & Meiburg, E.: 'Numerical investigation of three-dimensionally evolving jets subject to axisymmetric and azimuthal perturbations', *J. Fluid Mech.* **230**,(1991), pp. 271–318.

[16] Lin, S.J. & Corcos, G.M.: 'The three-dimensional evolution of a plane mixing layer: The Kelvin-Helmholtz roll-up', *J. Fluid Mech.* **141**, (1984), pp. 139–178.

[17] Shariff, K., Verzicco, R. & Orlandi, P.: 'A numerical study of three-dimensional vortex ring instabilities: viscous corrections and early nonlinear stage', *To appear in J. Fluid Mech.*, (1994).

[18] Maxworthy, T.: 'Some experimental studies of vortex rings', *J. Fluid Mech.* **81**, (1977), pp. 465–495.

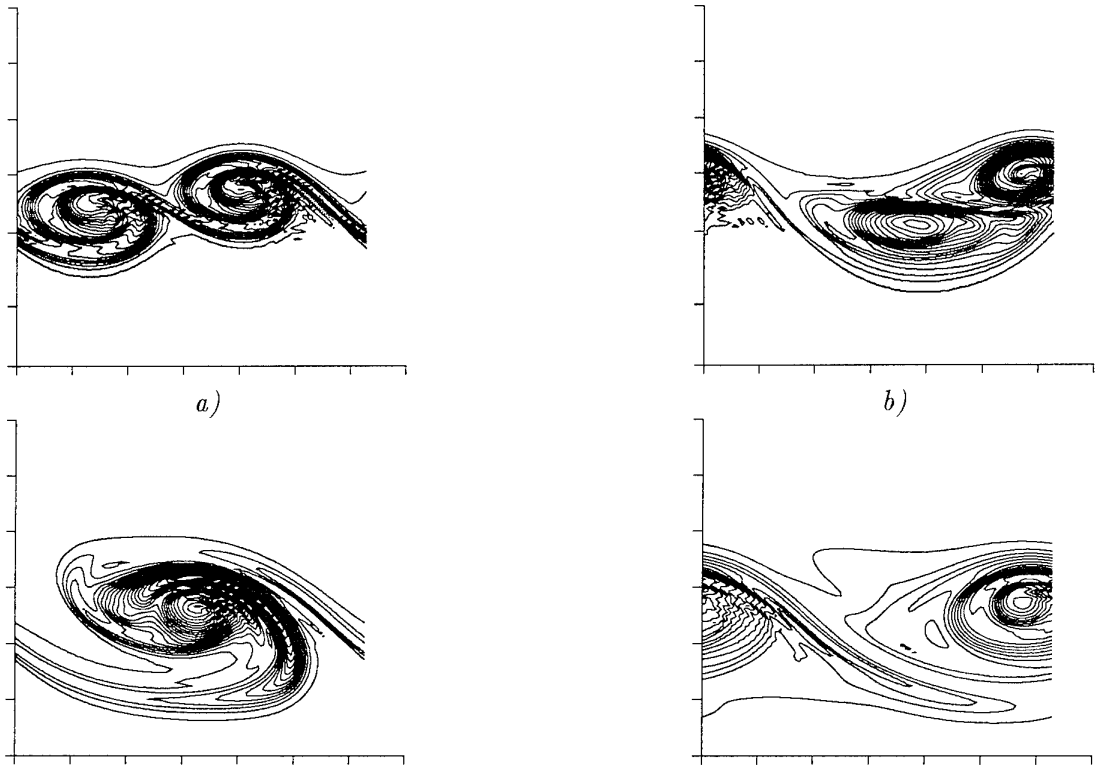

a) *b)* *c)* *d)*

FIGURE 1. DS axysimmetric: ω_θ at $Re = 800$ grid 91×129: *a)* t=24, *b)* t=32, *c)* t=48, *d)* t=80 ($\Delta = \pm 0.05$).

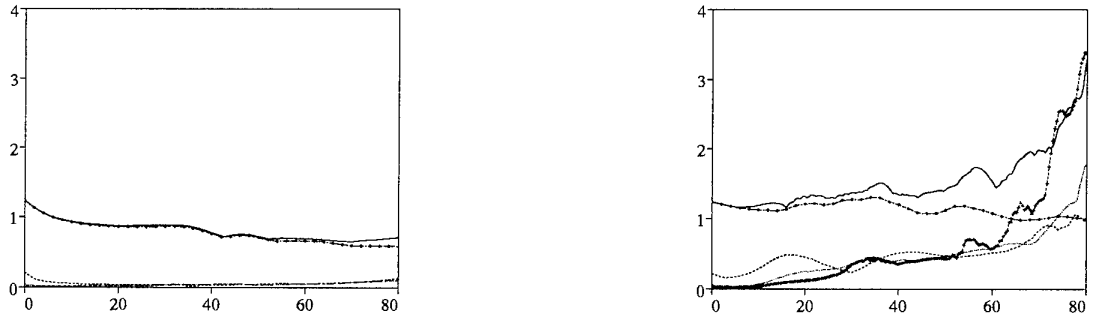

a) *b)*

FIGURE 2. Time evolution of the maxima vorticity components *a)* $Re = 200$, *b)* $Re = 800$. $\diamond$ axisymmetric ω_θ (91×129 grid), —— 3D ω_θ, ---- ω_r, ····· ω_z ($129 \times 91 \times 129$ grid); + ω_z ($65 \times 91 \times 65$ grid) only in *b)*.

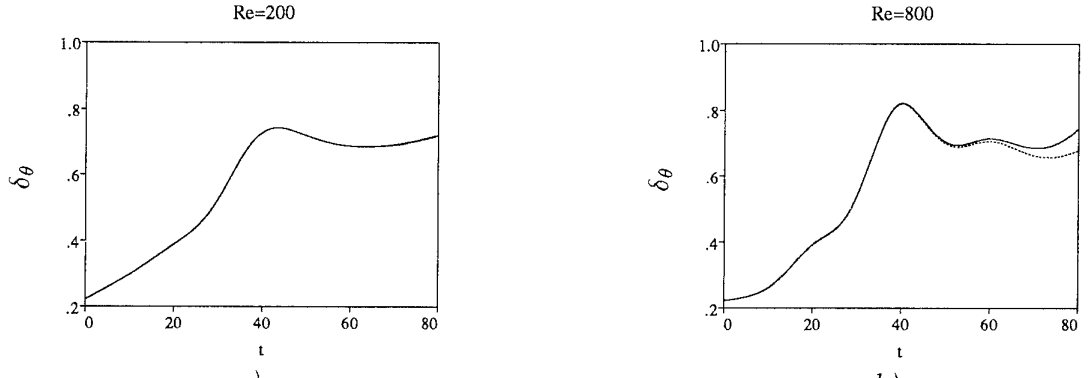

a) *b)*

FIGURE 3. Time evolution of the momentum thickness *a)* $Re = 200$, *b)* $Re = 800$. ---- axisymmetric (91×129 grid), —— 3D ($129 \times 91 \times 129$ grid).

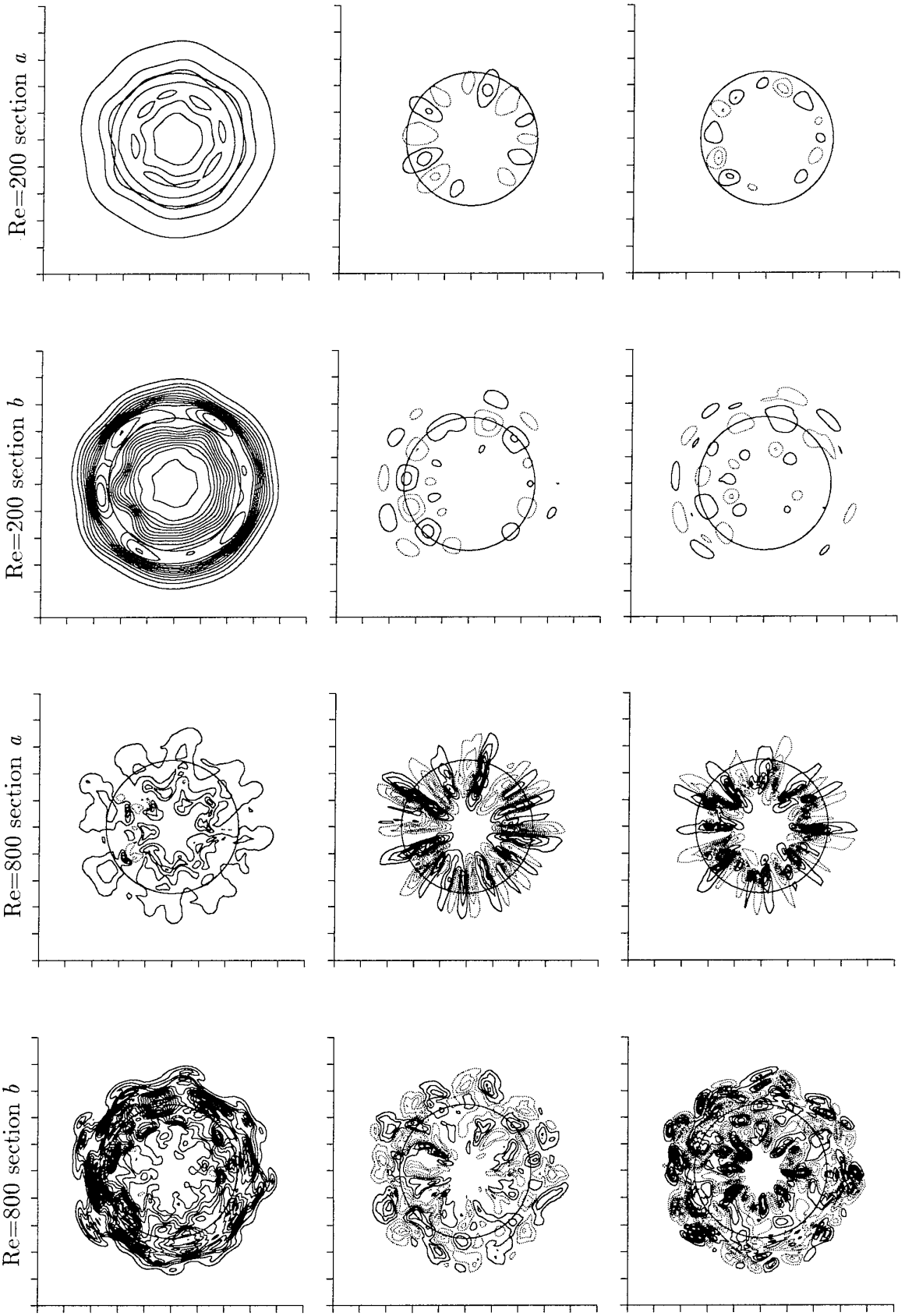

FIGURE 4. DNS grid $129 \times 91 \times 129$ at $t = 80$, $r - \theta$ planes, random perturbation. left column (ω_θ) middle column (ω_r) right column (ω_z), $Re = 200$ $\Delta = \pm 0.05$, $Re = 800$ $\Delta = \pm 0.1$ —— positive ····· negative values.

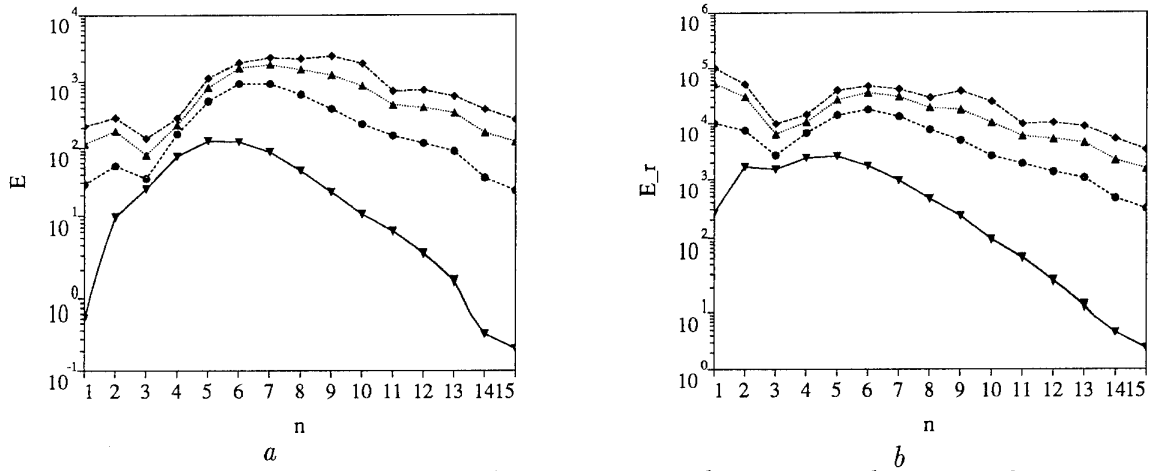

FIGURE 5. Ratio between energy modes at $t = 80$ and energy modes at $t = 0$, DS ($129 \times 91 \times 129$ grid):
∇ Re=200,$\circ$ Re=400,$\triangle$ Re=600 ;$\diamond$ Re=800. *a* total energy, *b* radial contribution.

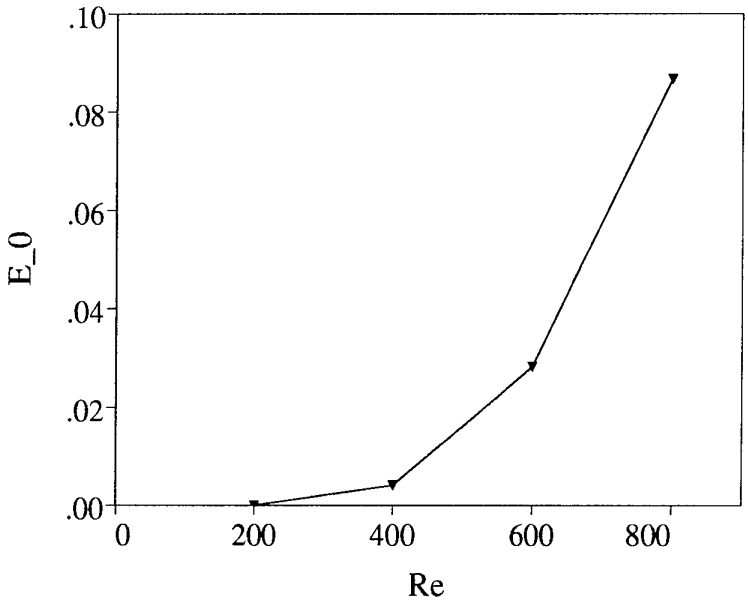

FIGURE 6. $n = 0$ azimuthal energy contribution at $t = 80$ *vs* Re, DS ($129 \times 91 \times 129$ grid).

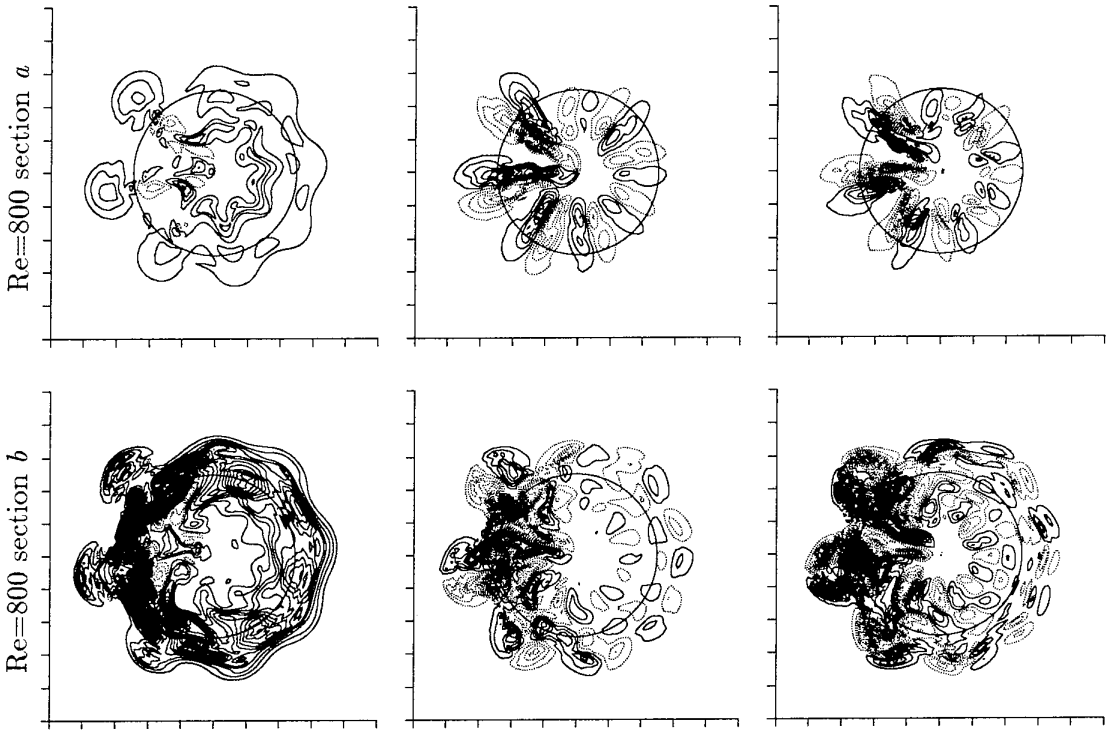

FIGURE 7. DNS grid $129 \times 91 \times 129$ at $t = 80$, $r - \theta$ planes, left column (ω_θ) middle column (ω_r) right column (ω_z), $\Delta = \pm 0.1$ —— positive ····· negative values. Random phases perturbation.

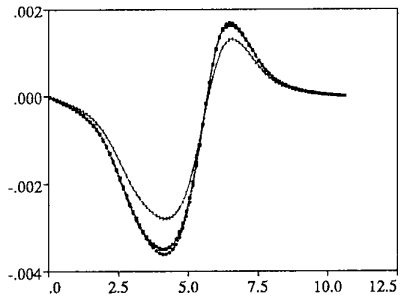

FIGURE 8. $< v_r' v_z' >$ *vs* r at $t = 80$ and $Re = 200$, ($33 \times 91 \times 41$ grid): • DS, □ dynamic model, | Smagorinsky model.

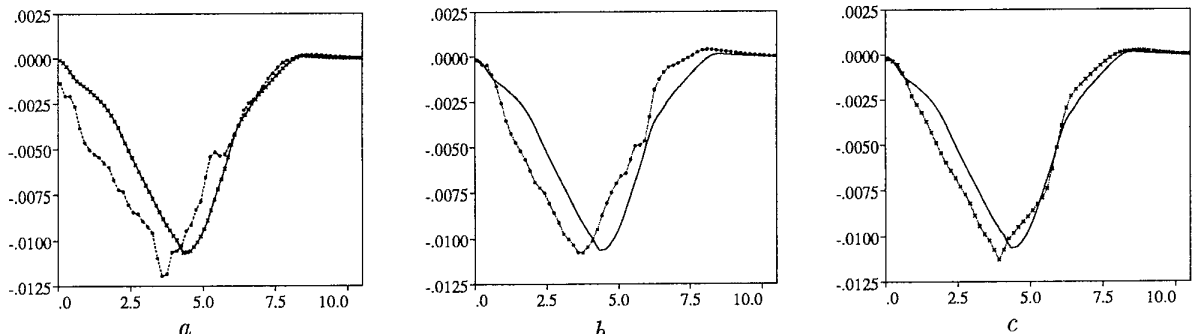

FIGURE 9. $< v_r' v_z' >$ *vs* r at $t = 80$ and $Re = 800$, —— DS ($129 \times 91 \times 129$ grid), *a* DS, *b* Smagorinsky model, *c* dynamic model ($33 \times 91 \times 41$ grid).

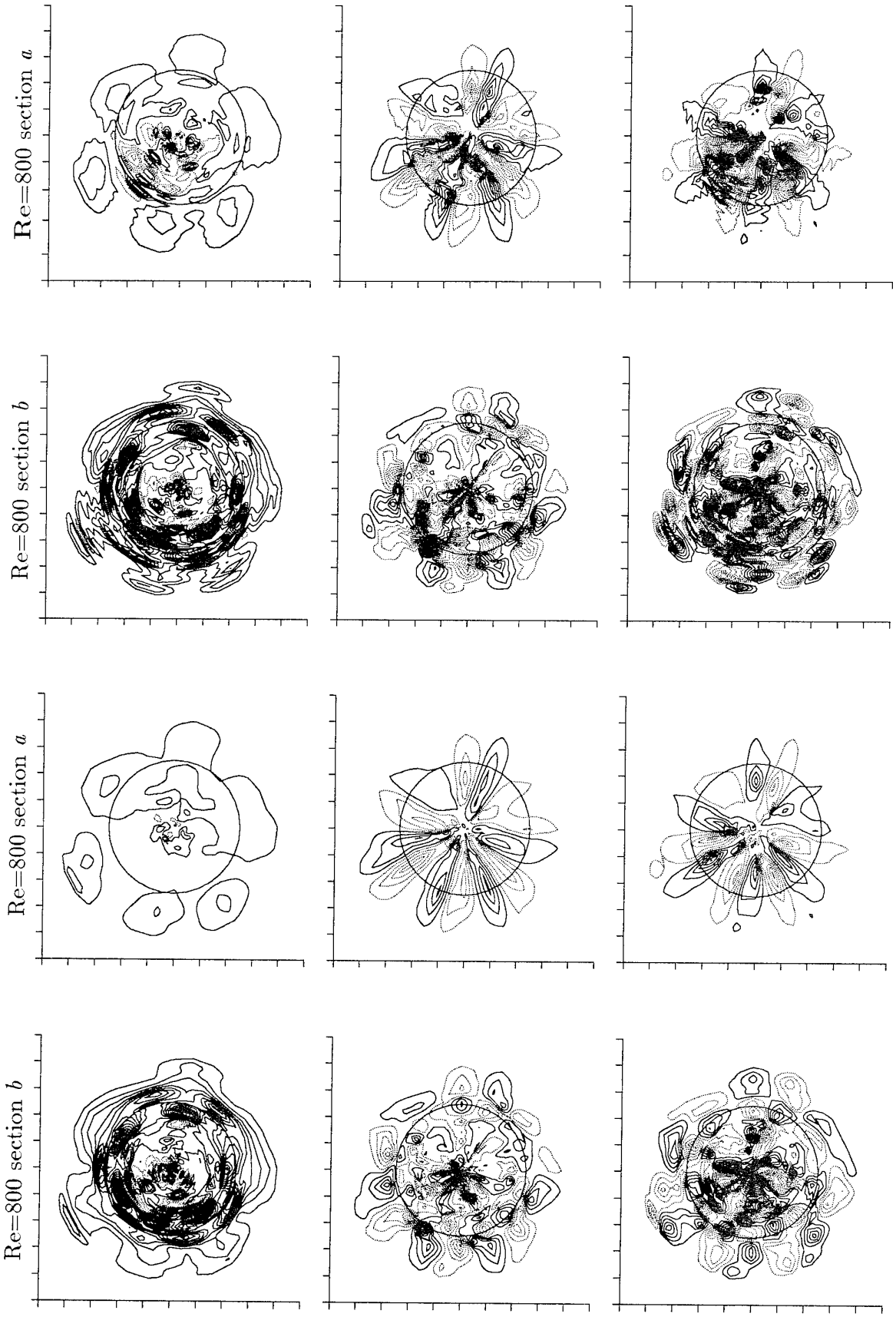

FIGURE 10. LES grid $33 \times 65 \times 41$ at $t = 80$, $r - \theta$ planes, left column (ω_θ) middle column (ω_r) right column (ω_z), $\Delta = \pm 0.1$ —— positive ····· negative values. (Upper Smagorinsky, lower dynamic model)

DIRECT NUMERICAL SIMULATION OF TRANSITION TO TURBULENCE FROM A HIGH-SYMMETRY INITIAL CONDITION

Oluş N. Boratav
Mechanical Engineering Department
Middle East Technical University of Ankara
Ankara 06531 Turkey
and Laboratoire Cassini
Observatoire de Nice
Nice 06304 France

Richard B. Pelz
Mechanical and Aerospace Engineering
Rutgers University
Piscataway, NJ 08855-0909, USA

1 Summary

The three-dimensional time evolution of a highly symmetrical vortex array [1] is simulated using a Fourier pseudospectral method for Re$= 1/\nu = 2000$ with an effective resolution of 1024^3 collocation points ($k_{max} = 340$). It is found that before the peak enstrophy is reached, there is a short stage when the local quantities increase sharply. The velocity derivative skewness and flatness values reach to 0.9 and 80 respectively. It is also found that during this interval, 6 vortex dipoles (at the origin) and 3 dipoles (at the $\pi/2$ corner) collapse towards two separate vorticity null points. The coherent vortices break up afterwards followed by sharp decrease in local quantities possibly due to dissipation. The singularity analysis shows that maximum vorticity scales as $(T - T_c)^{-1}$ shortly before the break up. The temporal evolution of the width of the analyticity strip shows that δ approaches zero but reaches a minimum positive value and starts to increase. This suggests that the solution remains uniformly analytic similar to the viscous Burgers equation.

2 Introduction

Taylor-Green flow [2] is a highly-symmetrical vortex array whose long-time-evolution has been examined in detail by numerical simulations [3–6]. It is found that at late times (after the peak in dissipation is reached), the energy spectra follows a power law in wave-number, the exponent being between 1.47 to 2.02 which is close to the scaling suggested by Kolmogorov for locally isotropic turbulence.

Perhaps the more interesting stage in the flow is the early time evolution; an interval before the peak in enstrophy and dissipation is attained. Viscous simulations show that during this interval the coherent, highly-symmetric vortices start to disintegrate. For the inviscid flow simulations, on the other hand, the question as to whether the smooth initial conditions will remain regular or not when the three-dimensional Euler equations are solved remains unanswered. Predictions using time series analysis and Padé approximants [7] gave hints that a singularity might develop spontaneously in the Taylor-Green flow. However, more recent work by Brachet et al. [4] using a more extended series could not confirm the existence of a finite time singularity. An alternate approach [8] is to examine the time evolution of the width of the analyticity strip δ (the distance to the real domain of the nearest singularity). Simulations by Brachet et al. [4,6] showed that δ decreases exponentially within the limits of resolution which suggests that the singularity will never occur in finite time.

An initial condition with even larger symmetries is the high-symmetry flow suggested by Kida [1]. The late time statistics of the flow have been examined by Kida and Murakami[9,10] and it is found that energy spectra is close to the Kolmogorov scaling, the exponent being between 1.5 to 1.7. However, the early time evolution of this initial condition is left unexamined. We expect that similar to the Taylor-Green vortex, the highly-symmetrical initial condition by Kida [1], would have a stage during which the coherent vortices would break up and questions on a possible singularity formation would arise. The present work focuses on this early stage of the flow.

Paper presented at the 74th Fluid Dynamics Symposium on "Application of Direct and Large Eddy Simulation to Transition and Turbulence" held at Chania, Crete, Greece, in April 1994.

3 Evolution

We examine the the evolution of the highly-symmetrical initial conditions by Kida [1] given by

$$u(x,y,z) = \sin x(\cos 3y \cos z - \cos y \cos 3z) \quad (1)$$

$$v(x,y,z) = \sin y(\cos 3z \cos x - \cos z \cos 3x) \quad (2)$$

$$w(x,y,z) = \sin z(\cos 3x \cos y - \cos x \cos 3y) \quad (3)$$

where u, v, w denote the velocity vector components in x, y, z directions. We solve the three-dimensional Navier-Stokes equations in rotational form using a pseudospectral Fourier method with the "2/3 rule" dealiasing [11]. We use the second-order accurate method of time-split fractional steps for time integration. By making use of the symmetries, it is possible to solve the flow in a subdomain (fundamental box) which is 1/4 th size of the whole domain. The highest resolution used in in our work is 1024^3 in the whole domain which is equivalent to a maximum Fourier mode of 340 after dealiasing. This resolution is higher than that of Kida and Murakami [10] (512^3) and Brachet et al. [6] (864^3). We use four different Reynolds numbers ($Re = 1/\nu$) in our simulations: 500, 1000, 2000 and 5000. We use the $Re = 5000$ run with two different resolutions (512^3 and 1024^3) to check our code by comparing our results with those given by Kida and Murakami[10]. The comparison gives perfect agreement in energy, enstrophy, Reynolds number based on Taylor microscale, dissipation and spectra. We use the $Re = 2000$ run for the early time behavior analysis in the present work. The detailed results of all runs will be given elsewhere.

In order to understand the early time evolution of the flow, we focus on two separate regions in the fundamental box where symmetries result in the formation of interesting vortex structures. These regions are; i) x, y, z = $\pi/2$ faces. ii) x, y, z = 0 faces. We will focus on the XY planes at z=$\pi/2$ and z=0 to describe these symmetries. Similar conclusions can be drawn for the other two planes.

For the XY plane z=$\pi/2$ the following symmetries exist:

$$\omega_x(x,y,\pi/2) = \omega_y(y,x,\pi/2) \quad (4)$$

$$\omega_z(x,y,\pi/2) = -\omega_z(y,x,\pi/2) \quad (5)$$

It is seen from the above equation that the normal vorticity (ω_z in plane XY) is an odd function with respect to y=z. This is nothing but a necessary condition to obtain a dipole along the line y=z.

The other regions of interest are the x, y, z =0 planes. We will consider z=0 plane to describe the symmetries. For this plane, we have

$$\omega_z(x,y,0) = -\omega_z(-x,y,0) \quad (6)$$

We see that the out-of-plane vorticity ω_z is an odd function with respect to the y axis and thus its image with respect to y axis will form a dipole. Similarly, we have another symmetry with respect to the x axis. This is given by

$$\omega_z(x.y,0) = -\omega_z(x,-y,0) \quad (7)$$

Then, due to the above odd symmetry with respect to the x axis, the image of the vortex with respect to the x axis will form another dipole.

To summarize, for the z = 0 plane, the vortex in the first quadrant ($0 \le x,y \le \pi/2$) will have an image vortex located below in the 4th quadrant ($0 \le x \le \pi/2$, ($-\pi/2 \le y \le 0$), with opposite sign, another image vortex located to its left (or right depending on the point of view) of opposite sign (quadrant 2) and finally the image vortex in quadrant 2 will have an image in quadrant 3. Therefore, totally, we have 4 vortices or 2 dipoles in the z=0 plane. A similar argument can be made for x=0 and y=0 planes giving 8 more vortices or 4 more dipoles. So, there are 12 vortices or 6 dipoles on the zero faces approaching the origin. We shall call this configuration a *dodecapole* since we can treat it as an entity.

We describe the evolution of the flow as the following:

1. Very rapidly, vortex dipoles are formed. Figure 1 displays a vorticity magnitude isosurface from two different views at t=0.75. Three of the dipoles are directed

towards the origin (Figure 2, top) and another three towards the point $x = y = z = \pi/2$. Both these points, due to symmetries, are constrained to have zero vorticity, i. e. they are vorticity null points. The dipoles (Figure 2, top) resemble flattened vortex sheets with sudden vorticity jumps across them (vorticity changes sign across the flattened dipole sheet). Least squares fitting to the energy spectra gives a k^{-4} power law around t=1.75. The configuration is similar to Saffman's [12] vorticity field with random two-dimensional vorticity discontinuities which also gives a k^{-4} scaling.

2. Between t=1.9 and t=2.2, we find drastic changes in certain local quantities. In this short interval, local maximum vorticity ω_{max} increases 13 times (Figure 3, top). Velocity derivative skewness and flatness take values as much as 0.9 and 80 respectively. The evolution of ω_{max}^{-1} shows that if the evolution continues with the pace it has around t=1.9, the function will hit the time axis and the local vorticity will diverge. We performed a least square fit in Figure 3 (bottom) for the region with the steepest slope and found that the time axis will be intersected at $T_c = 2.1077$. We also calculated the scaling between ω_{max} and $(T_c - T)$. Least squares fitting for between t=1.9640-2.0515 (using 8 data points) gives $\omega \sim (T_c - T)^{-1.09}$. This result is similar to the scaling calculated by Kerr [13,14] in his single dipole simulation. Recently, Bhattacharjee and Wang [15] have suggested an analytical model of three-dimensional Euler flows which gives a singularity on a line joining two vorticity nulls. It is found that vorticity diverges as $(T_c - T)^{-1}$.

   The vorticity isosurfaces show that the coherent structure breaks up into smaller pieces during the violent interval. The trend towards the singularity stops at a certain time. All the sudden increases in flow quantities are followed by sudden drops which are as sharp as the increase rates.

3. We find that the maximum vorticity is located at the zero planes of the flattened vortex tubes and more specifically in the *"head region"* of the vortices. We calculate that the vortex head deforms in a self-similar way until t=2.0. After this time, for example at t=2.062, the self-similarity is lost in the sense that the vorticity contour pictures can not be generated by only stretching and compressing the pictures at an earlier time. To quantify this process, we have calculated the distance between the location of the maximum vorticity and the origin. The results show that until t=1.939, the distance shrinks exponentially. But the trend changes after this time. The distance stays almost constant between t=1.939-2.0015. This surprising *"saturation"* is similar to the *"bouncing-off"* process of two vortex rings which are shot towards one another. In this interaction, there is a minimum intercentroid distance of the vortices after which the vortices change direction and divert their paths. The saturation process might also be related to a competition between the stretching and dissipation processes. There is an interval when these forces approximately balance each other and a local equilibria is attained as in the case of viscous Burgers vortex. However, it looks like the equilibria is not stable, the structure breaks down. The distance starts to decrease with a rate even faster than an exponential shrinkage $t > 2.0015$. The self-similarity is broken around this time.

4. We also investigate at which length scales the viscous time scales will be comparable to the convective (deformation) time scales in the problem. For this, we take an approximate exponential shrinkage time which is equal to $\Delta t \simeq 1.939 - 1.639 = 0.3$. We equate this to the viscous time scale given by $1/(\nu k^2)$ to obtain the wavenumber at which the dissipative forces have comparable time scale as the convective forces. This is found to be $k = 82$. The corresponding length scale can be eval-

uated using $L = 2\pi/k$ to obtain $L = 0.0766$. The grid size is given by $\Delta x = (\pi/2)/(2/3)256 = 0.0092$. Hence, the dissipative time scale becomes comparable to convective time scale at 8 grid-points. From the vorticity isosurfaces at z=0 section, we find that the 8 point limit is reached somewhere between $t = 2.0$ and 2.062. After then, viscous dissipation forces play a role against the singularity formation as rapidly as the convective forces play towards a singularity.

5. We calculated the temporal evolution of the analyticity width δ by least squares fitting to the high wavenumber end of the energy spectra. We used the wavenumber interval $100 < k < 340$ in the fittings and a spectra function having the form $\exp(-2\delta(t)k)$ at the high wavenumber end. Figure 4 gives the results in log-lin scale. The horizontal dashed line in this figure gives twice our effective resolution (after dealiasing). We find the existence of the regions of different slopes. After the first sharp drop in δ, there is a region of almost constant slope between t=1.789-1.9765 (recall that our predicted $T_c = 2.1077$ for this run) and another region with a steeper slope between t=1.98-2.1 after which the curve hits a minimum value at t=2.1265. The width starts to increase after this time. To check the influence of the selected wavenumber range on our results, we are currently performing a fitting assuming a shape function as $Ak^{\alpha}\exp(-2\delta(t)k)$ and $3.5 < k < 340$. The preliminary results are very similar and the results will be presented elsewhere.

   In two different studies by Brachet et al. [4,6], δ evolution with time seems to exhibit an exponential decrease. However, there are hints that such a trend might change after a certain time. Figure 5 in Reference 4 and Figure 2 in Reference 6 display certain points which fall below the exponential decrease line suggesting that there might be an interval with a faster δ decrease rate. Such an interval with a faster rate is what we observe in our simulations. In the absence of viscosity, there are strong hints in the current work to suggest that the local vorticity value might diverge and form a finite time singularity. We also find that δ has a non-zero minimum in our simulations. This suggests that the solution is uniformly analytic. This is the case for the viscous Burgers equation which also gives a δ decrease to a minimum and a subsequent linear increase (Figure 8 in Reference 8).

6. As the structure breaks down, the energy spectra evolves towards k^{-3} but continues to change. Therefore, k^{-3} scaling might be only a transient intermediate stage as the cascade evolves into the Kolmogorov regime at later times (A.Pouquet, private communication). We remind the reader that the peak enstrophy and dissipation in this run is reached around t=4, and Kolmogorov scaling is obtained around t=5.

7. In a recent work, Cantwell [16] has obtained an asymptotic solution of modified-Euler equations which gives a finite time singularity. Currently, we are investigating the time evolution of the Q-R invariants of the velocity gradient tensor and the alignment properties of the vorticity vector and eigenvectors of the strain-rate tensor. It will be interesting to check whether the pressure and the viscous term neglected in Cantwell's analysis [16] is also negligible in the current simulation due to the use of certain symmetries.

Acknowledgements

This work is fully supported by the Air Force Grant (AFOSR-91-0248). The authors would like to thank to R. Kerr, S. Kida, A. Bhattacherjee, A. Pouquet and N. Zabusky for the exciting discussions. M. Brachet kindly provided his code which we used as a guide in implementing the flow symmetries in the present work's initial condition. Computations were done on the Cray 2 at the Kirtland Supercomputer Center.

References

[1]S. Kida, "Three-Dimensional Periodic Flows with High-Symmetry", J. Phys. Soc. Jpn., **54(6)**, 2132 (1985)

[2]G. I. Taylor and A. E. Green, "Mechanism of the Production of Small Eddies from Large Ones", Proc. Roy. Soc. A **158**, 499 (1937)

[3]S. A. Orszag, "Numerical Simulation of the Taylor-Green Vortex", in Proc. Symp. on Computing Methods in Applied Sciences and Engineering (ed. R. Glowinski & J. L. Lions), part II, p.50, Springer-Verlag, 50 (1974)

[4]M. E. Brachet, D. I. Meiron, S. A. Orszag, B. G. Nickel, R. H. Morf, U. Frisch, "Small-scale Structure of the Taylor-Green Vortex", J. Fluid. Mech., **130**, 411 (1983)

[5]M. E. Brachet, "Direct Simulation of Three-Dimensional Turbulence in the Taylor-Green Vortex", Fluid Dy. Res., **8**, 1 (1991)

[6]M. E. Brachet, M. Meneguzzi, A. Vincent, H. Politano, P. L. Sulem, "Numerical Evidence of Smooth Self-Similar Dynamics for Three-Dimensional Ideal flows", Phys. Fluids, **4(12)**, 2845, (1992)

[7]R. H. Morf, S. A. Orszag and U. Frisch, "Spontaneous Singularity in Three-Dimensional Inviscid, Incompressible Flow", Phys. Rev. Letts., **44(9)**, 572 (1980)

[8]C. Sulem, P. Sulem and H. Frisch, "Tracing Complex Singularities with Spectral Methods", J. Comp. Phys., **50**, 138 (1983)

[9]S. Kida and Y. Murakami, "Kolmogorov's Spectrum in a Freely Decaying Turbulence", J. Phys. Soc. Jpn., **55(1)**, 9 (1986)

[10]S. Kida and Y. Murakami, "Kolmogorov Similarity in Freely Decaying Turbulence", Phys. Fluids, **30(7)**, 2030 (1987)

[11]S. A. Orszag, "Numerical Simulation of Incompressible Flows Within Simple Boundaries, I. Galerkin Representations", Stud. Appl. Math, **50**, 293 (1971)

[12]Saffman, P. G., "On the Spectrum and Decay of Random Two-Dimensional Vorticity Distributions at Large Reynolds Numbers", Studies App. Math., **50(4)**, 377 (1971).

[13]R. M. Kerr, "Evidence for a Singularity of the Three Dimensional, Incompressible Euler Equations", Topological Aspects of Dynamics of the Fluids and Plasmas, Moffat, Zaslavsky, Tabor, Comte (eds.), Kluwer Academic Pub., (1992).

[14]R. M. Kerr, "Evidence for a Singularity of the Three Dimensional, Incompressible Euler Equations", Phys. Fluids A, **5(7)**, 1725 (1993).

[15]Bhattacharjee, A. and Wang, X., "Finite-time Vortex Singularity in a Model of Three-Dimensional Euler Flows", Phys. Rev. Lett., **69(15)**, 2196 (1992).

[16]Cantwell, B., "Exact Solution of a Restricted Euler Equation for the Velocity Gradient Tensor", Phys. Fluids A, **4(4)**, 782 (1992).

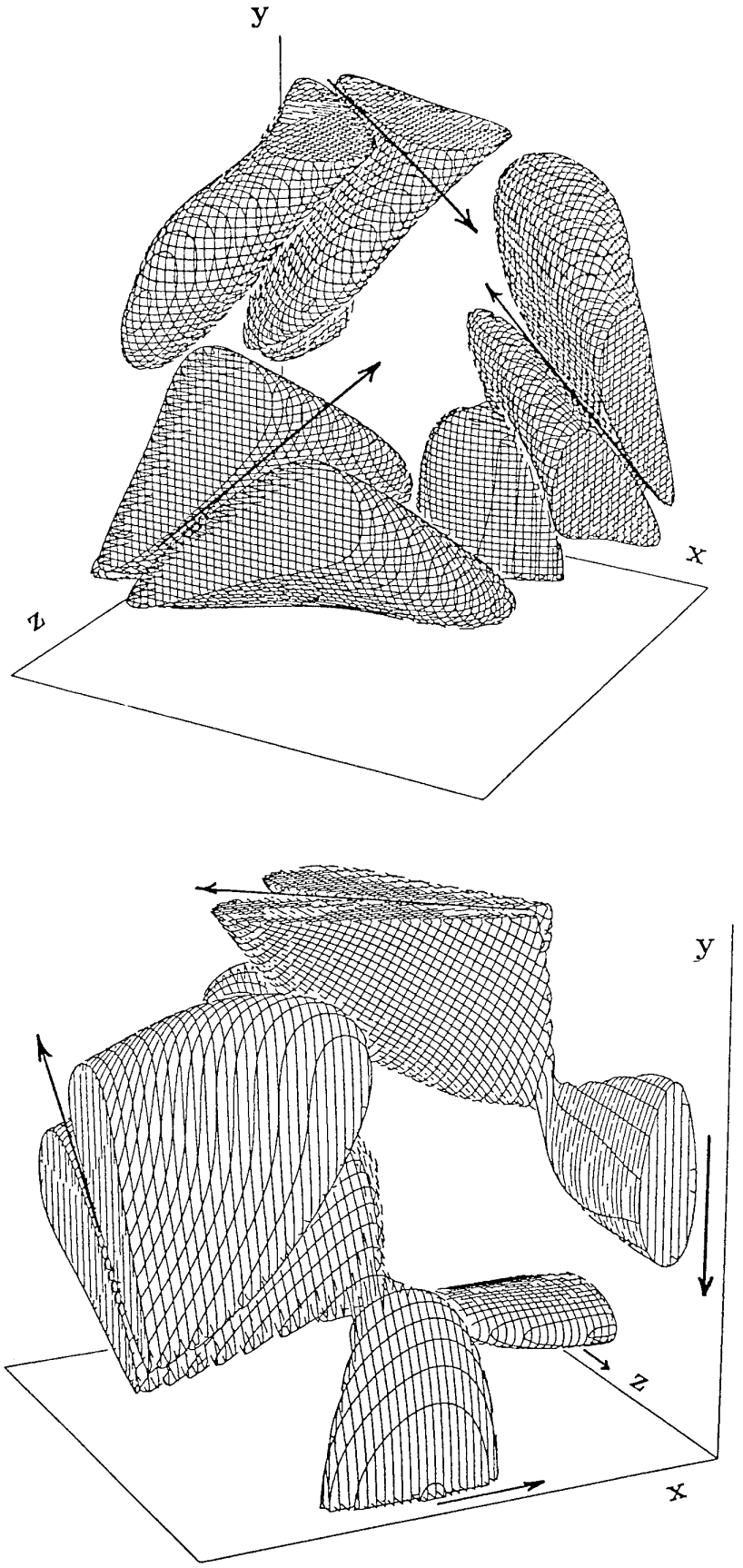

Figure 1: Vorticity magnitude isosurfaces at t=0.75. The selected isosurface magnitude is 63% of the initial maximum. Top view shows the $\pi/2$ planes and the bottom view shows the origin. Arrows indicate the direction of the motion of the dipoles.

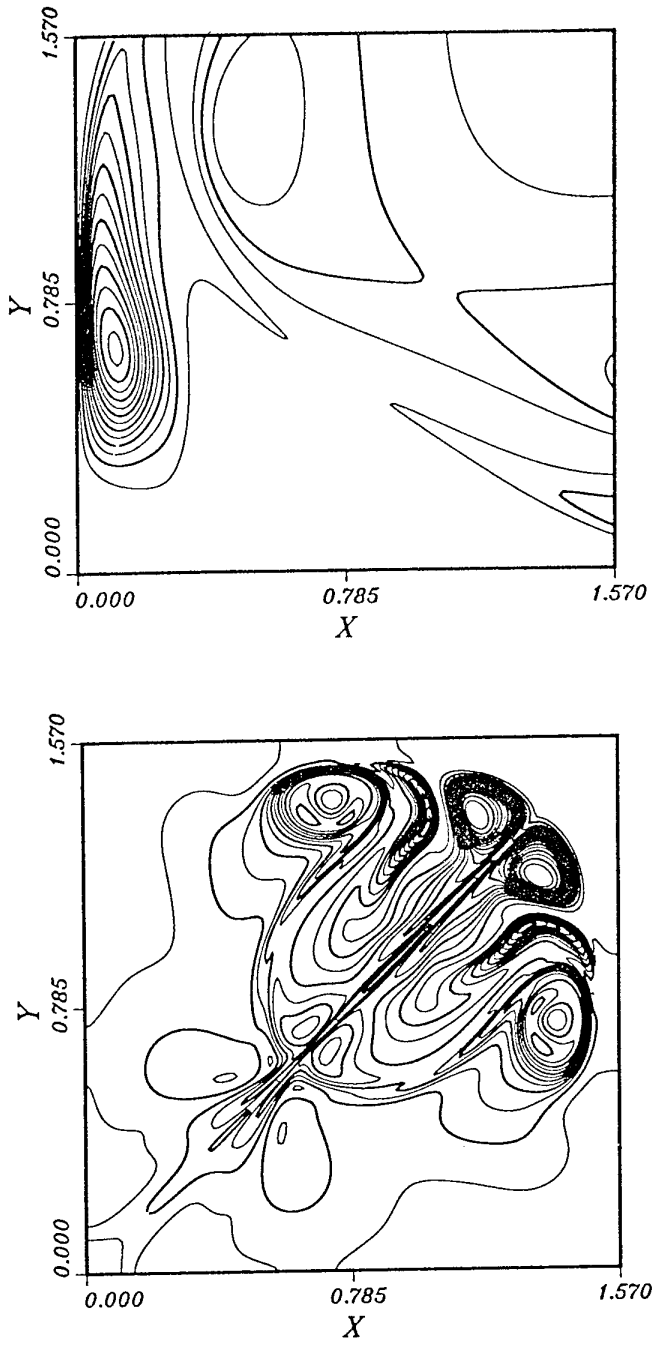

Figure 2: Vorticity magnitude contours at t=1.75, Top: z=0. Bottom: $z = \pi/2$ planes.

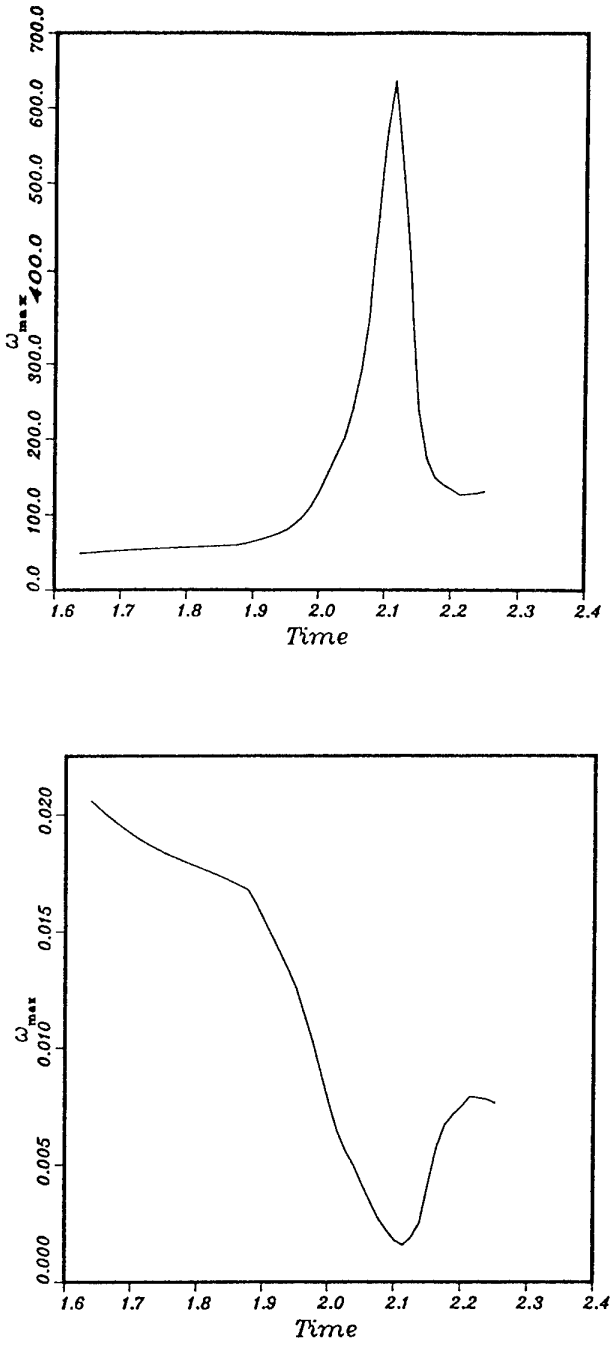

Figure 3: Evolution of maximum vorticity ω_{max} (top) and ω^{-1} (bottom).

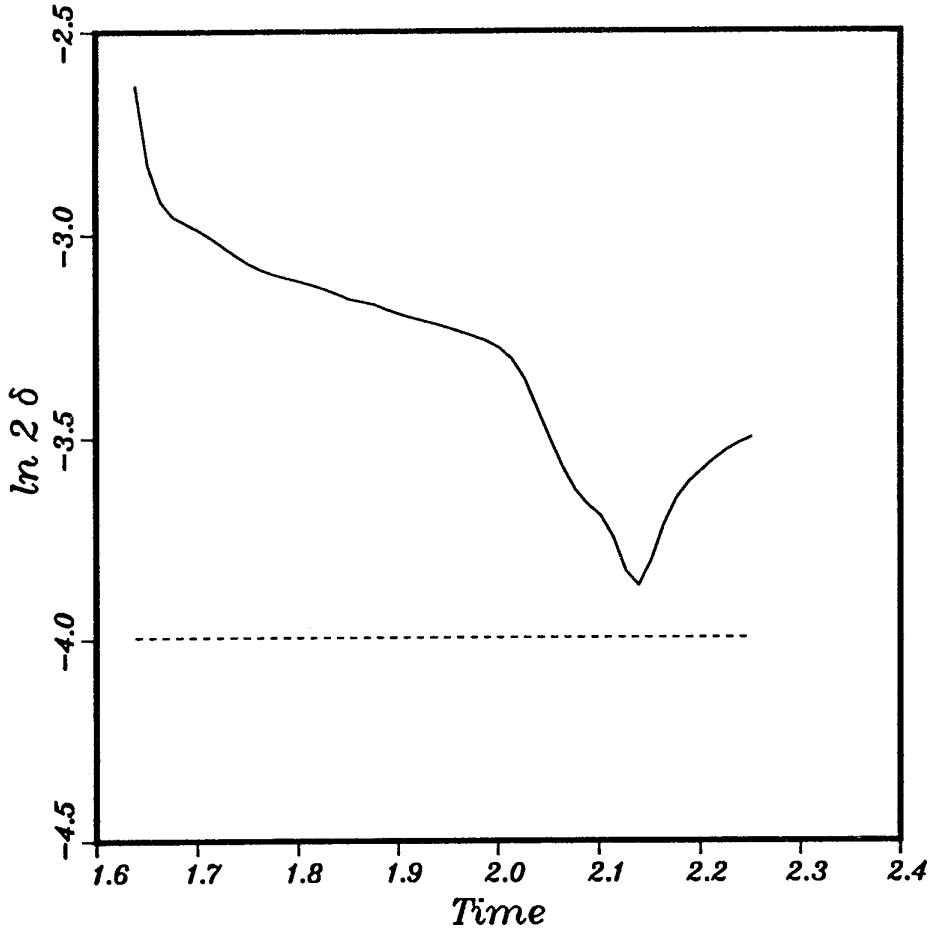

Figure 4: Evolution of the width of the analyticity strip δ. The dashed horizontal line indicates twice the effective grid size.

Direct Numerical Simulations of Leading-Edge Receptivity to Freestream Sound

David A. Fuciarelli
Helen L. Reed
Mechanical & Aerospace Engineering
Arizona State University
Tempe, Arizona 85287-6106
USA

1. SUMMARY

The objective of this paper is to review our efforts in spatial direct numerical simulations for modeling leading-edge receptivity to freestream sound and vorticity. These results begin to provide the link between the freestream and the initial boundary-layer response and can provide the upstream conditions for further simulations marching through the transition process toward turbulence.

2. INTRODUCTION

The current method of transition prediction involves the use of linear stability theory (e.g. Arnal 1993). However, this is an amplitude-ratio method and these free or self-excited oscillations described are generally initiated by some externally forced disturbances such as sound or freestream turbulence. Since receptivity defines the initial disturbance amplitude (that is, A_0), its role, not accounted for in linear stability theory, is key to the overall transition process. Without answering how freestream acoustic signals and turbulence enter the boundary layer and ultimately generate unstable T-S waves, transition to turbulence will never be successfully understood or predicted. Clearly then, the study of receptivity promises significant advance in practical transition-prediction methods.

In this paper, computational efforts to determine the process by which longer-wavelength external disturbances lead to instabilities in the boundary layer are reviewed with an emphasis on leading-edge effects. High-Reynolds-number asymptotics have identified that the conversion of long-wavelength freestream disturbances to shorter-wavelength instability waves takes place in regions where the mean flow locally exhibits rapid variations in the streamwise direction (Goldstein 1983, 1985; Kerschen 1990, 1991). Such regions include the leading edge, roughness, suction strips, discontinuities in surface slope and curvature, etc., anything that can scatter long-wavelength waves into shorter components that can match to instability waves in the boundary layer.

A combination of all the relevant effects, including, for example, roughness, geometry, associated pressure gradients (both favorable and adverse), vibrations, sound, and freestream turbulence, must be included in a determination of receptivity, and it is here that computations by spatial direct numerical simulation (DNS) excel. A variety of different geometric conditions and freestream disturbances can be implemented with this technique and the response of the boundary layer quantified and catalogued (Reed 1993).

3. REVIEW OF COMPLETED STUDIES ON LEADING-EDGE EFFECTS

Finite curvature can be included in the leading-edge region if a spatial computational method is used. This feature was left out of some early unsuccessful receptivity models. Use of an infinitely thin plate (zero thickness or computationally a straight line) to study leading-edge effects, although popular, is strongly discouraged. The attachment-line or stagnation region is a critical source of receptivity as large streamwise gradients occur there, and an infinitely thin plate features infinite vorticity there (per the simple Blasius solution). No computational simulation can resolve infinite vorticity. By stipulating the plate to have finite curvature at the leading edge, the singularity there is removed and a new length scale is introduced.

Experimentally, the most popular receptivity model has been the flat plate with an elliptic leading edge. Thus it is reasonable that computational models consider the same geometry. However, the curvature at the juncture between the ellipse and the flat plate is discontinuous and

Paper presented at the 74th Fluid Dynamics Symposium on "Application of Direct and Large Eddy Simulation to Transition and Turbulence" held at Chania, Crete, Greece, in April 1994.

provides a source of receptivity (Goldstein & Hultgren 1987). Lin et al. (1992, 1993) introduced a new leading-edge geometry based on a super-ellipse. The shape of this modified super-ellipse (MSE) is given by

$$[1-x/(AR\,L)]^{m(x)} + [y/L]^{n} = 1, \quad 0 < x/L < AR \quad (1)$$

$$m(x) = 2 + [x/(AR\,L)]^{2} \quad \text{and} \quad n = 2 \quad (2)$$

where L is the half-thickness of the plate and AR is the aspect ratio of the "elliptic" nose. For a usual super-ellipse, both m and n are constants. Super-ellipses have the advantage of continuous curvature (zero) at the juncture with the flat plate as long as $m > 2$ at $x/L = AR$. The MSE, with m(x) given above, has the further advantage of having a nose radius and geometry (hence a pressure distribution) close to that of an ordinary ellipse with $m = 2$ and $n = 2$.

To avoid singularities in the metric terms in the sensitive nose region, use of a C-grid rather than an H-grid is recommended. Again, it is important to include and resolve the attachment-line region accurately.

3.1 Receptivity to Freestream Sound

For low-speed flows, freestream-sound wavelength is typically one or two orders of magnitude larger that instability wavelengths in the boundary layer. Receptivity is defined to be the amplitude at Branch I normalized with the freestream-sound amplitude. The quantity U is the freestream speed.

To review previous numerical efforts, Murdock (1980, 1981) studied the receptivity of an incompressible boundary layer on both a flat plate with zero thickness and a parabolic body (favorable pressure gradient everywhere); he considered the boundary-layer response due to a plane sound wave parallel to the freestream direction. For the flat plate, his integration domain did not include the leading edge and he therefore had to impose an inflow boundary condition obtained by solving the unsteady boundary-layer equations. His numerical results were sensitive to the upstream-boundary location relative to the leading edge (see the first paragraph of Section 3). For a parabolic body, a sharper leading edge (smaller nose radius) was found to be more receptive, a result similar to that found theoretically by Hammerton & Kerschen (1991) for the parabolic body. Gatski & Grosch (1987) solved the full incompressible Navier-Stokes equations for flow over an infinitely thin, semi-infinite flat plate and found no clear development of T-S waves (again see the first paragraph of Section 3).

Lin et al. (1991, 1992, 1993, 1994) simulated the receptivity of the laminar boundary layer on a flat plate by solving the full Navier-Stokes equations in general curvilinear coordinates by a second-order finite-difference method with vorticity and stream function as dependent variables. They used a C-type orthogonal grid and included the finite-thickness leading edge and curvature. Geometries tested included elliptic, polynomial-smoothed elliptic, and MSE leading edges of different aspect ratios of 3, 6, and 9 (with smaller aspect ratio corresponding to a blunter nose). Various sound-like oscillations of the freestream streamwise velocity were applied along the boundary of the computational domain and allowed to impinge on the body. Problem parameters under investigation included disturbance amplitude and frequency, as well as leading-edge radius and geometry. They found the following:

(a) T-S waves appearing in the boundary layer could be linked to sound present in the freestream.

(b) Receptivity occurred in the leading-edge region where rapid streamwise adjustments of the basic flow occurred. Variations in curvature, adjustment of the growing boundary layer, discontinuities in surface geometry, and local pressure gradients there introduce length scales to diffract long freestream disturbances.

(c) The magnitude of receptivity and the disturbance response depended very strongly on geometry. As examples:

(i) For plane freestream sound waves, T-S - wave amplitude at Branch I decreased as the elliptic nose was sharpened.

(ii) When the discontinuity in curvature at the ellipse/flat-plate juncture was smoothed by a polynomial, receptivity was cut in half.

(iii) The disturbance originated from the location of the maximum in adverse pressure gradient.

(d) The receptivity to plane freestream sound appeared to be linear with freestream-disturbance

amplitude up to levels of about 5%U. Thus a linear Navier-Stokes solution could be used up to these levels.

3.2 Receptivity to Freestream Vorticity

The characteristic length scale for freestream spanwise vorticity is the convective wavelength which is approximately 3 times that of the amplified T-S wave at that frequency.

To review previous computational efforts, Kachanov et al. (1978) solved the incompressible flow over an infinitely thin flat plate, using the Navier-Stokes equations linearized for small disturbances, and considered both a transverse acoustic wave across the leading edge and a vortex street passing far above the plate surface. In the latter case, no evidence of T-S waves was found.

Buter & Reed (1992a,b, 1993, 1994) simulated the receptivity of the laminar boundary layer on a flat plate by solving the full Navier-Stokes equations in general curvilinear coordinates by a second-order finite-difference method with vorticity and stream function as dependent variables. They used a C-type orthogonal grid and included the finite-thickness leading edge and curvature. Geometries tested included an aspect-ratio-6 elliptic and polynomial-smoothed elliptic leading edge. A simple model of time-periodic freestream spanwise vorticity was introduced at the upstream computational boundary. This signal was decomposed into a symmetric and asymmetric streamwise velocity component with respect to the stagnation streamline. Then the computations were performed with these individual components specified as boundary conditions. For small disturbances, the results could then be linearly superposed. Moreover, the effect of a transverse-velocity component at the leading edge could be ascertained as the asymmetric-velocity case had this feature while the symmetric-velocity did not. Problem parameters under investigation included disturbance amplitude and orientation, as well as nose geometry. They found the following:

(a) As the disturbance convected past the body, it was ingested into the upper part of the boundary layer, decaying exponentially toward the wall. This was consistent with the findings of Kerschen (1989) and Parekh et al. (1991).

(b) Different wavelengths were evident in the boundary-layer response. Signals at the T-S wavelength were dominant near the wall, while toward the edge of the boundary layer, disturbances of the freestream convective wavelength were observed. This was consistent with the experimental observations of Kendall (1991).

(c) T-S waves appearing in the boundary layer could be linked to freestream vorticity acting near the basic-state stagnation streamline. Clear evidence of the T-S wavelength appeared aft of the location of the maximum surface pressure gradient.

(d) For the particular geometric and flow conditions considered in this study, receptivity to vorticity was found to be smaller than receptivity to sound by a factor of approximately three.

(e) Modifications to the geometry which increased the surface pressure gradient along the nose increased receptivity.

(f) For both the symmetric and asymmetric freestream velocity perturbations, the T-S response was linear with forcing over the range of amplitudes considered; symmetric: up to 4.2% U and asymmetric: up to 2.1% U.

(g) A superharmonic component of the disturbance motion was observed at all forcing levels for the asymmetric forcing. [See also Grosch & Salwen (1983).] This was initially observed in the stagnation region where the interaction of the asymmetric gust with the basic flow induced a large transverse velocity component which interacted with the adverse pressure gradient upstream of the nose to transfer disturbance energy to the superharmonic frequency. Depending upon geometry, flow conditions, and disturbance frequency and amplitude then, it is possible that this nonlinearity observed in the nose region could impact transition behavior. It is therefore unlikely that the linear response found in (f) for the asymmetric case will persist to the same level of freestream forcing as that observed for the symmetric case.

These results by our group began to provide the link between the freestream and the initial boundary-layer

response and can provide the upstream conditions for further simulations marching through the transition process toward turbulence. In this way, more realistic predictions and modeling of the turbulent flowfield downstream will be possible.

4. ONGOING WORK

In our previous work above, computational speed was prohibitively slow. This issue becomes even more important as we expand our studies to quantitatively compare with and complement the 20:1 and 40:1 MSE/flat-plate experiments of Saric et al. (1994) and the asymptotic theories (Goldstein 1983, 1985; Kerschen 1990, 1991) for lower frequencies and oblique sound waves. In this Section, we describe our recent efforts at formulating efficient algorithms to solve these more numerically sensitive situations.

4.1 Problem Formulation

In our work, the receptivity of a flat-plate boundary layer to freestream oblique sound is being investigated through the direct numerical simulation (DNS) of the Navier-Stokes equations in the leading-edge region. The chosen leading-edge geometry is the MSE, which has the property of continuous curvature at the flat-plate/leading-edge juncture. This allows us to concentrate the effort on the investigation of receptivity caused by the leading edge alone. The Reynolds number, based on leading-edge curvature, is to be varied parametrically along with the aspect ratio of the MSE in order to examine the stability of a wide variety of basic states. The use of various aspect ratios covers the range from a sharp leading edge to a blunt leading edge.

To improve computational speed over our previous efforts (described above), an alternating direction implicit (ADI) procedure is now being used to solve the governing equations in a general-curvilinear-coordinate system. Because of this, a hyperbolic-grid generator was developed recently to generate an orthogonal grid about a general shape; this eliminates cross-derivative terms in the governing equations. The inviscid solution is found using a source-panel method to provide far-field boundary conditions for the basic-state computation.

A hyperbolic grid-generation technique is used to produce a body-fitted general-curvilinear-coordinate system. The resulting grid is completely orthogonal and has finer resolution than the Cartesian system, thus reducing computational error. The grid is generated by solving an orthogonality condition and an equation governing the Jacobian. The two equations constitute a hyperbolic set of coupled nonlinear equations. The Jacobian function is set by using values from an algebraically generated grid which allows clustering of grid points at the leading edge and near the body. An example of a hyperbolically generated grid for a 6:1 MSE is shown in Figure 1.

The basic-state code is a 2-D incompressible Navier-Stokes solver in a general coordinate system. The governing equations, cast into a stream-function/vorticity form, are the vorticity-transport equation and the definition of vorticity which will be referenced below as the stream-function equation. The ADI method was chosen because of its simplicity and the fact that tridiagonal matrices result which can be solved efficiently. The governing system consists of two coupled equations. However, if the stream-function coefficients in the vorticity-transport equation are lagged, then the equations are effectively decoupled and each can be solved sequentially and independently. With the time-splitting method, the result is therefore four tridiagonal systems to be solved for each iteration.

Grid studies have been performed for the basic-state code. Figure 2 shows the wall vorticity along a 6-to-1 aspect-ratio MSE. Vorticity has been non-dimensionalized with the freestream velocity divided by the half thickness of the flat plate. For a grid resolution of 250 points in the streamwise direction and 125 points in the normal direction, the flow field is sufficiently resolved.

For the disturbance code, two approaches are being used. The first approach solves the unsteady disturbance equations directly using the same ADI method described above. This "time-marching" code has advantages in that it is nonlinear and shows the time evolution of the disturbances. The second approach is that of a "time-harmonic" implementation developed by Streett (1994). The dependent variables are expanded as follows:

$$\Delta(x,y,t) = \Delta(x,y)e^{i\omega t} + C.C. \qquad (3)$$

The disturbance equations are linearized and the above is substituted into them, resulting in a steady complex set of equations for the vorticity and stream-function waveforms. The advantage to this approach is that the code is converged to a quasi-steady-state solution directly

and therefore requires less computer resources. The disadvantages of this approach are that all disturbances must respond at the single frequency prescribed and that no nonlinear effects are incorporated. For the disturbance levels imposed and symmetric forcing (Buter & Reed 1994), these limitations are acceptable.

For the time-harmonic code, a buffer-domain technique is used to establish the downstream boundary conditions. The method used is that of Streett & Macaraeg (1989). The streamwise diffusion terms are multiplied by a factor that decreases with increasing distance inside the buffer zone. Specifically, that factor is given by:

$$f = 1 - \exp(-\gamma\, x_b^{\beta}) \qquad (4)$$

where $x_b = [\cosh(x)-\cosh(x_o)]/[\cosh(x_1)-\cosh(x_o)]$

x_o and x_1 are the beginning and end positions of the buffer zone and γ and β are control parameters. The buffer-zone technique ensures that the flowfield is convectively dominated in the streamwise direction and therefore prevents wave reflection from the downstream boundary.

The basic code was verified by a comparison with the experiments of Saric et al. (1994) on a 40:1 MSE; the chordwise pressure-coefficient distributions measured 14.8 mm above the flat plate are compared in Figure 3 and the agreement is exceptional. Figure 4 is a plot of the shape factors calculated from the basic state for a 20:1 MSE showing the trend towards Blasius flow.

Results from the disturbance code are encouraging and show quantitatively similar features with the work of Lin et al. (1992) as outlined in Section 3.1.

Indeed, ADI requires more iterations than competing methods (e.g. a strongly implicit procedure), but each iteration is performed much faster than for these other methods. To give some indication of efficiency, the current disturbance code was run on the CRAY-2 at the NASA Langley Research Center. The code ran at 205 Mflops and performed 4368 iterations in 600 CPU seconds on a 300 by 150 point grid. This computational speed was attained by utilizing a special tri-diagonal solver which solves each ADI sweep completely in one pass of the solver. By comparison, the old scalar code run on the same machine and grid, utilizing a standard solution procedure, performed 311 iterations in 600 CPU seconds. This is a factor of 14 speed improvement.

5. ACKNOWLEDGEMENT

This work is supported by NASA/Langley Research Center under a Graduate Fellowship in Aeronautics and the National Science Foundation under the Faculty Awards for Women in Science and Engineering.

6. REFERENCES

Arnal, D. 1993. Boundary layer transition: predictions based on linear theory, AGARD FDP/VKI Special Course on "Progress in Transition Modeling," AGARD Report No. 793, Madrid: 22-25 March, Brussels: 29 March-1 April.

Buter, T.A. and Reed, H.L. 1992a. Leading-edge receptivity to a vortical freestream disturbance: a numerical analysis, Instability, Transition, and Turbulence, (Hussaini, M.Y., Kumar, A., and Streett, C.L., eds.), Springer-Verlag, New York.

Buter, T.A. and Reed, H.L. 1992b. Boundary layer receptivity to a vortical freestream disturbance, Bulletin of the American Physical Society 37, 8, 1721.

Buter, T.A. and Reed, H.L. 1993. Numerical investigation of receptivity to freestream vorticity, AIAA-93-0073.

Buter, T.A. and Reed, H.L. 1994. Boundary-layer receptivity to freestream vorticity, Accepted Physics of Fluids A.

Gatski, T.B. and Grosch, C.E. 1987. Numerical experiments in boundary-layer receptivity, Proceedings of the Symposium on the Stability of Time-Dependent and Spatially Varying Flows, Springer-Verlag, 82-96.

Goldstein, M.E. 1983. The evolution of Tollmien-Schlichting waves near a leading edge, Journal of Fluid Mechanics 127, 59-81.

Goldstein, M.E. 1985. Scattering of acoustic waves into Tollmien-Schlichting waves by small streamwise variations in surface geometry, Journal of Fluid Mechanics 154, 509-530.

Goldstein, M.E. and Hultgren, L.S. 1987. A note on the generation of Tollmien-Schlichting waves by sudden surface-curvature change, Journal of Fluid Mechanics 181, 519-525.

Grosch, C.E. and Salwen, H. 1983. Oscillating stagnation point flow, Proceedings of the Royal Society of London, Series A 384, 175-190.

Hammerton, P.W. and Kerschen, E.J. 1991. The effect of nose bluntness on leading-edge receptivity, Bulletin

of the American Physical Society 36, 10, 2618.

Kachanov, Yu.S., Kozlov, V.V., Levchenko, V.Ya., and Maksimov, V.P. 1978. The transformation of external disturbances into the boundary layer waves, Sixth International Conference on Numerical Methods in Fluid Dynamics, (Cabannes, H., Holt, M., and Rusanov, V., eds.), 299-307, Springer-Verlag, Berlin.

Kendall, J.M. 1991. Studies on laminar boundary-layer receptivity to freestream turbulence near a leading edge, FED-Vol. 114, Boundary Layer Stability and Transition to Turbulence, (Reda, D.C., Reed, H.L., and Kobayashi, R., eds.), ASME.

Kerschen, E.J. 1989. Boundary layer receptivity, AIAA-89-1109.

Kerschen, E.J. 1990. Boundary layer receptivity theory, Applied Mechanics Review 43, 5, 2, S152-157.

Kerschen, E.J. 1991. Linear and nonlinear receptivity to vortical freestream disturbances, FED-Vol. 114, Boundary Layer Stability and Transition to Turbulence, (Reda, D.C., Reed, H.L., and Kobayashi, R., eds.), ASME.

Lin, N., Buter, T.A., Fuciarelli, D.A., and Reed, H.L. 1993. Computational aspects of nonparallel effects in boundary-layer receptivity, IUTAM Symposium on Nonlinear Stability of Nonparallel Flows, Clarkson University, July 26-30.

Lin, N., Reed, H.L., and Saric, W.S. 1991. Leading edge receptivity: Navier-Stokes computations, Boundary Layer Transition and Control Conference, 8-12 April, Peterhouse College, Cambridge, U.K.

Lin, N., Reed, H.L., and Saric, W.S. 1992. Effect of leading-edge geometry on boundary-layer receptivity to freestream sound, Instability, Transition, and Turbulence, (Hussaini, M.Y., Kumar, A., and Streett, C.L., eds.), Springer-Verlag, New York.

Lin, N., Reed, H.L., and Saric, W.S. 1994. Effect of leading-edge geometries on Tollmien-Schlichting wave generation, To be submitted.

Murdock, J.W. 1980. The generation of Tollmien-Schlichting wave by a sound wave, Proceedings of the Royal Society of London A 372, 517-534.

Murdock, J.W. 1981. Tollmien-Schlichting waves generated by unsteady flow over parabolic cylinders, AIAA-81-0199.

Parekh, D.E., Pulvin, P., and Wlezien, R.W. 1991. Boundary layer receptivity to convected gusts and sound, FED-Vol. 114, Boundary Layer Stability and Transition to Turbulence, (Reda, D.C., Reed, H.L., and Kobayashi, R., eds.), ASME.

Reed, H.L. 1993. Direct numerical simulation of transition: the spatial approach, AGARD Course in Transition Prediction and Modelling, VonKarman Institute and Madrid, March.

Saric, W.S., Wei, W., and Rasmussen, B. 1994. Boundary-layer receptivity: freestream sound on an elliptical leading edge, IUTAM Symposium on Laminar-Turbulent Transition, Sendai, Japan.

Streett, C.L. 1994. Personal communication.

Streett, C.L. and Macaraeg, M.G. 1989. Spectral multi-domain for large scale fluid dynamic simulations, Applied Numerical Mathematics 6, 1, 23.

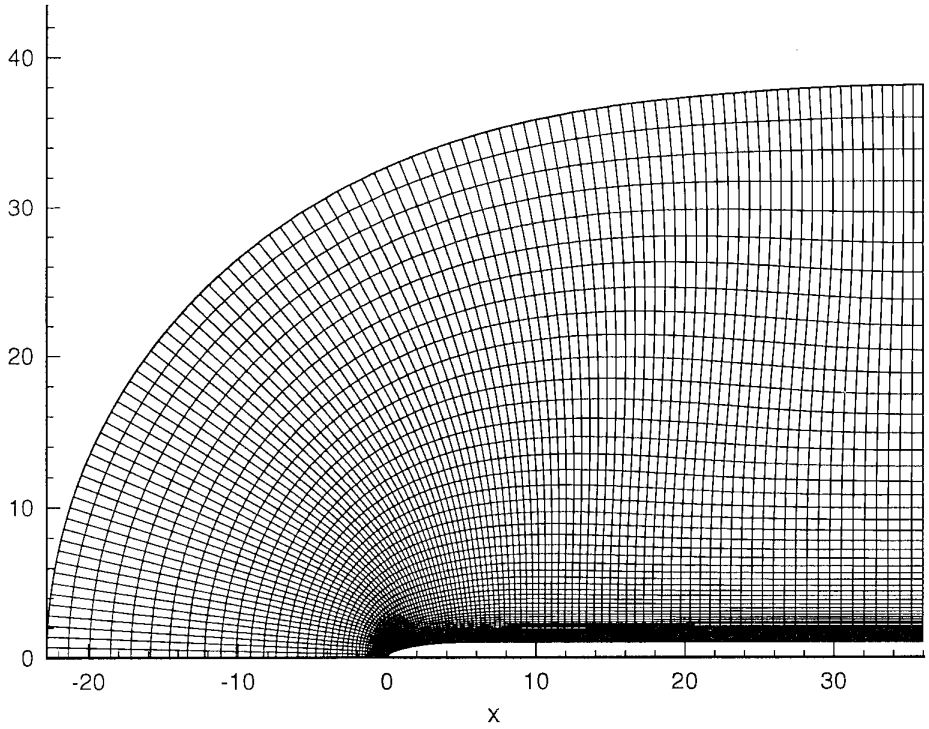

Figure 1. Hyperbolically Generated Grid.

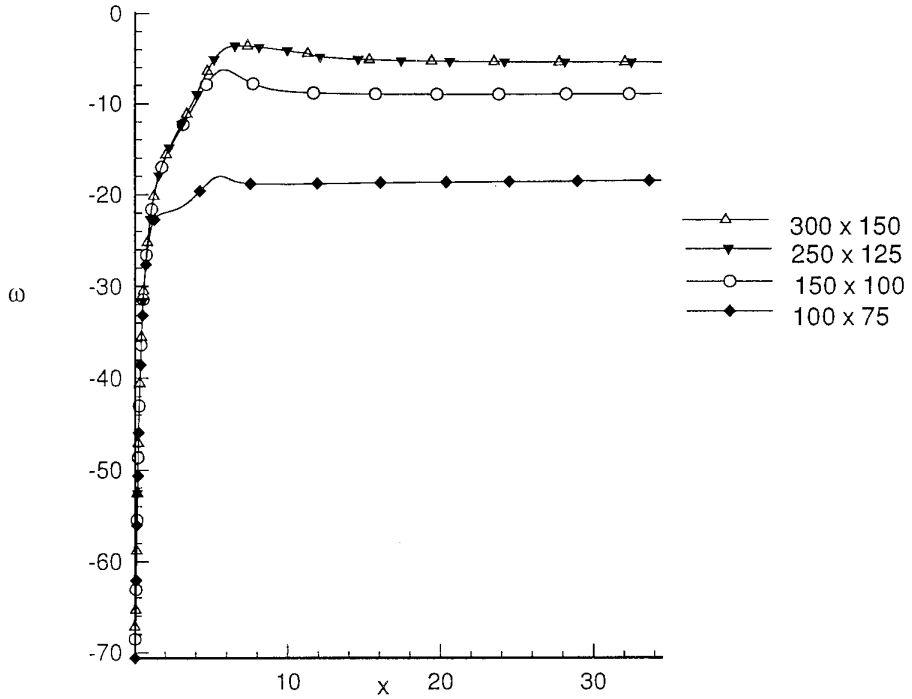

Figure 2. Wall Vorticity Along MSE.

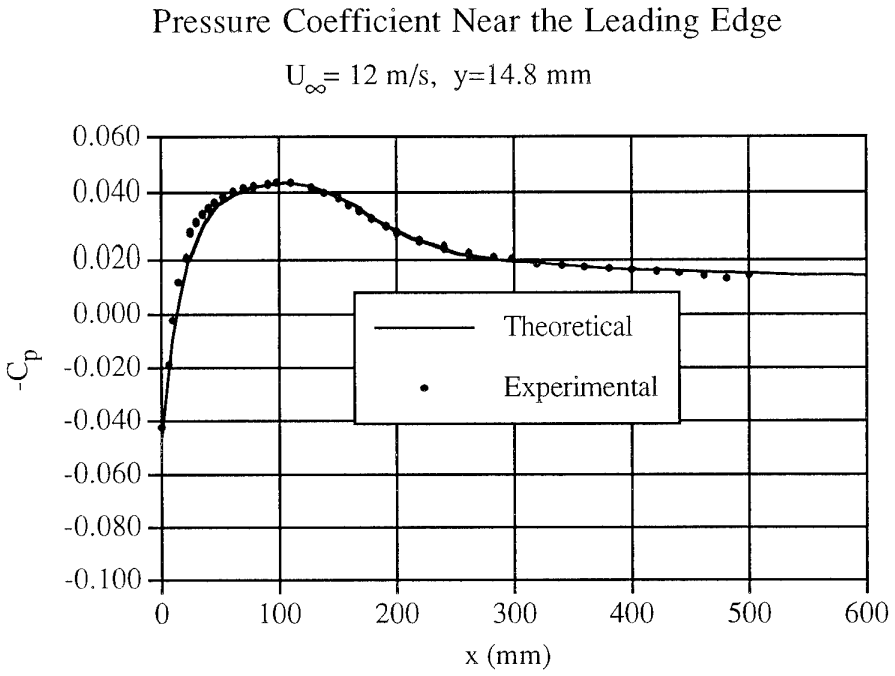

Figure 3. Comparison of Pressure-Coefficient Distribution for a 40:1 Modified Super Ellipse.

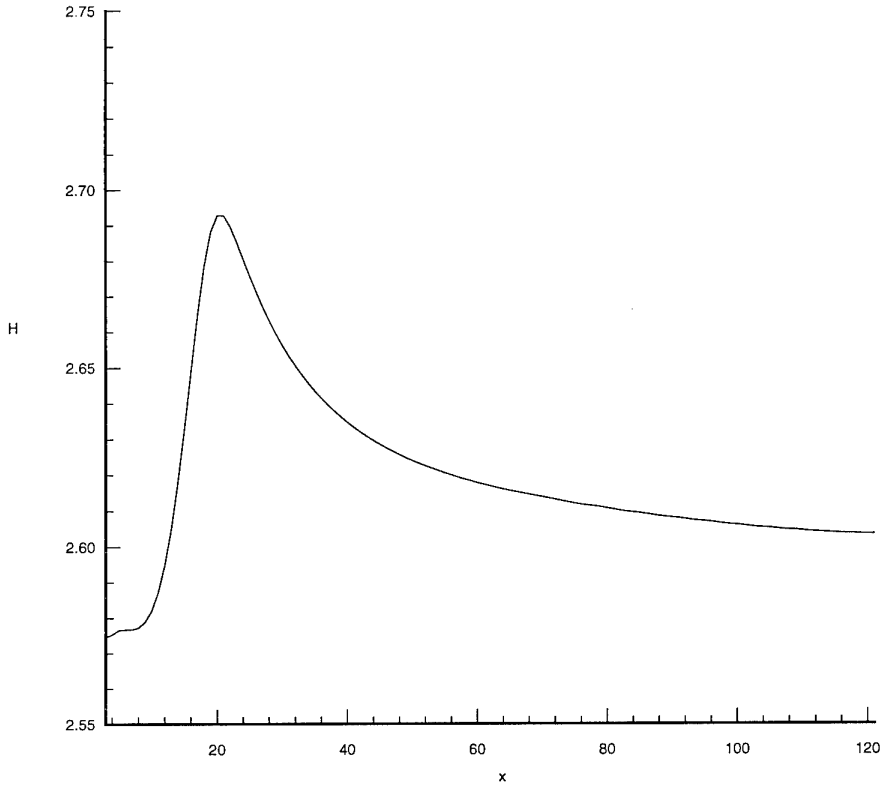

Figure 4. Shape Factor along MSE

Numerical Study of Realistic Perturbations in Three-Dimensional Boundary Layers

P. R. Spalart*
J. D. Crouch
L. L. Ng
Boeing Commercial Airplane Group
P.O. Box 3707, MS 7H-96
Seattle, WA 98124-2207
U. S. A.

1. SUMMARY

Direct Numerical Simulation is applied to a variety of small perturbations developing in a three-dimensional boundary layer. The basic flow is independent of the spanwise coordinate but incorporates a favorable and an adverse pressure gradient in the chordwise direction, similar to the leading-edge region of a swept wing. The edge velocity is analytically defined. Both Cross-Flow and Tollmien-Schlichting modes are amplified. Results focus on questions that are often open in three-dimensional transition-prediction codes, particularly "e^N" type codes. They include: non-parallel effects; choice of wave-vector; choice of propagation velocity and direction; and the effect of broad spectra, in either space direction and/or time. For this we survey a range of perturbations from pure waves to wave packets; the latter result from initial perturbations that are local in both space and time, and are arguably the richest type of disturbance. Quantitative results are offered for the validation of stability codes, and some are compared with Orr-Sommerfeld results.

2. INTRODUCTION

The prediction of boundary-layer transition, in an industrial context, necessarily relies on a highly-simplified representation of the relevant instabilities. Typically, the growth of a class of pure waves, harmonic in space and time and obeying linearized equations, is tracked. Current "e^N" methods estimate the transition location based on a correlation between an amplitude ratio and experimental data. These methods explicitly incorporate the growth rates of instabilities, but combine all other contributing factors into the value of N.

Future "amplitude" methods will provide an alternative to the e^N approach. These methods estimate the transition location based on disturbance amplitudes or some nonlinear byproduct of the finite disturbances (such as the departure of the wall shear stress from its laminar value). Initial amplitudes are given by receptivity theory, which relates the instability amplitudes to external sources such as free-stream disturbances, surface roughness, etc. These methods incorporate considerable additional physics, as compared to the amplitude-ratio methods. However, the accurate determination of the amplitude growth remains crucial.

For three-dimensional boundary layers the characterization of instability modes by the Orr-Sommerfeld (OS) equation leaves considerable freedom, and a wide variety of modes must be accounted for. In these boundary layers, the spatial-stability approach with fixed frequency leads to four unknowns (the wave-numbers α_r, α_i, β_r, β_i), while the dispersion relation provides only two real relationships. This requires two additional relationships in order to describe the instability evolution within a manageable class of modes. Nayfeh [1] and Cebeci & Stewartson [2] derived two such relationships based on the propagation of a disturbance along a real group line emanating from a localized source. Having used the condition that $\partial\alpha/\partial\beta$ is real to fix β_i, either the β_r domain can be partitioned and each wave number tracked separately, or the wave number β_r can be chosen locally based on maximum growth. This is typical of the decisions required for transition-prediction methods: the first approach seems more physically sound, but it is much more expensive. Drastic simplifications are routinely made, often with apparent impunity.

Gaster has given thorough discussions of wave packets [3], but apparently not a complete "recipe" for wave-vector selection in a prediction code. Conversely, Arnal and his group have emphasized the implementation and testing of complete methods over the mathematical aspects [4]. Faced with the same problems as Nayfeh and Cebeci & Stewartson, Mack [5] has instead suggested, for an infinite swept wing, the condition that the spanwise wave number β be real. Phase continuity then leads to the additional condition that the dimensional β_r remain constant in the chordwise direction (in non-infinite-swept situations, the more general condition is $\partial\alpha_r/\partial z = \partial\beta_r/\partial x$). The choice of conditions setting β

*Mainframe computer time provided by NAS

Paper presented at the 74th Fluid Dynamics Symposium on "Application of Direct and Large Eddy Simulation to Transition and Turbulence" held at Chania, Crete, Greece, in April 1994.

significantly influences the predicted growth characteristics of the instabilities [4].

In this paper, we study the propagation and growth of instabilities in an infinite-span three-dimensional boundary layer using direct numerical simulations (DNS). The instabilities are excited by localized or periodic sources. Their amplitude is small, and for this study we are not using the non-linear capability of DNS. The numerical challenge is instead related to the large flow domain and evolution times, the rather large amplitude ratios, the non-parallel basic flow, and the need for accurate growth rates. Our purpose is to provide guidance for the development of stability codes, whether of the amplitude-ratio or of the amplitude type.

Another motivation for this study is the need for criteria to distinguish Cross-Flow (CF) and Tollmien-Schlichting (TS) modes in regions where such modes coexist, an important distinction for amplitude-ratio methods when the mode types are assigned separate N factors. Stability codes sometimes encounter amplified waves that are difficult to classify because their wave-vectors are ambiguous in the traditional CF/TS context. Bringing out such "mixed" modes would be of keen interest and is within the capability of DNS, provided the input disturbance is "rich" enough. Depending on the mode definition, significant changes of the flow direction (or equivalently, straining in the plane of the wall) would presumably be instrumental in "converting" perturbations from CF- to TS-type, or vice-versa.

Many of the DNS results are compared to those of the Orr-Sommerfeld linear-stability theory. In the OS calculations, we consider spatial growth (real frequency) and assume that $\beta_i = 0$. This condition is motivated by the spanwise independence of the mean flow. β_r remains fixed, and the disturbance is partitioned into a spectrum of spanwise wave numbers, each of which grows independently. The dominant mode at any chordwise location depends on the growth history. This approach follows the work of Mack. As other readers may well prefer different assumptions, we attempt to provide usable and discriminating quantitative results from the DNS, without bias toward any particular stability approach.

For the DNS, the flow is governed by the Navier-Stokes equations with no-slip conditions at the wall, $y = 0$. Periodic conditions are used in the spanwise direction, z. In the case of pure waves, the spanwise period matches that of the wave. In the other cases, the domain is chosen large enough for the perturbation not to overlap with its periodic images (as verified in flow visualizations). This removes the effect of spanwise periodicity on the disturbances. Results are presented at specific times for the wave-packets (§6); for all the other cases, the simulation is conducted until a time-independent or time-harmonic global state is established. In the chordwise direction, x, the computational domain includes the neighborhood of the attachment line. As a result, inflow conditions are not needed within the boundary layer. We only specify that fluid approaching the wall from above is irrotational and matches the edge velocity described in §3. Perturbations are then explicitly introduced at some distance from the attachment line using a body force tailored for each perturbation type desired. Although not a realistic source of perturbations, a body force is fully versatile, and adequate for addressing the subsequent disturbance growth. The outflow condition relies on the "fringe method", which achieves a fully non-reflecting behavior when properly applied [6, 7, 8].

3. BASIC FLOW

The flow was designed to resemble the leading-edge region of a swept wing, save for surface curvature and compressibility, and to produce a level of CF and TS growth (without suction) that is manageable in global DNS. The accuracy of our DNS code typically limits the amplitude ratios to about 4 orders of magnitude [9, 7, 8]. Beyond that, unless a very large number of points is used, numerical contamination from the high-amplitude region ruins the accuracy in the low-amplitude region. The largest number of points we use here is 1600, in the x direction.

The spanwise edge velocity, W_∞, is used to normalize all velocities. The conventional attachment-line thickness $\delta_l \equiv \sqrt{\nu/(\partial U_e/\partial x)}$ is used to normalize all lengths. Here ν is the kinematic viscosity and the strain rate $\partial U_e/\partial x$ is taken over the attachment line. The attachment-line Reynolds number $\overline{R} \equiv \delta_l W_\infty/\nu$ is 250; therefore, small perturbations propagating in the z direction are damped [6]. The amplification occurs off the attachment line.

The edge velocity in the chordwise direction is given by

$$U_e = \frac{U_\infty}{\pi}\left[\tan^{-1}\left(\frac{x-x_0}{y_0}\right) + \tan^{-1}\left(\frac{x+x_0}{y_0}\right)\right] - rx$$

where $U_\infty = 1.5$, $x_0 = 104.44$, $y_0 = 164.06$, and $r = 1.4\times10^{-4}$. This is shown in Fig. 1. This function yields $dU_e/dx_{x=0} = 1/250$; so with $\nu = 1/250$ we indeed have $\delta_l = 1$ and $\overline{R} = 250$. The third derivative d^3U_e/dx^3

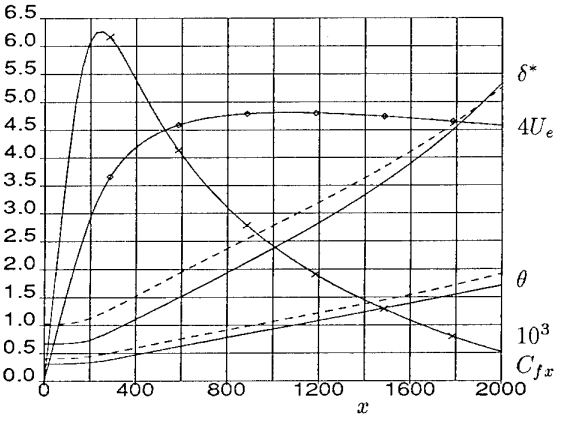

Figure 1: Edge velocity and thicknesses. $-\diamond-$, $4 \times U_e$; —, θ_x and δ^*_x; - - -, θ_z and δ^*_z; $-\times-$, $10^3 \times C_{fx}$.

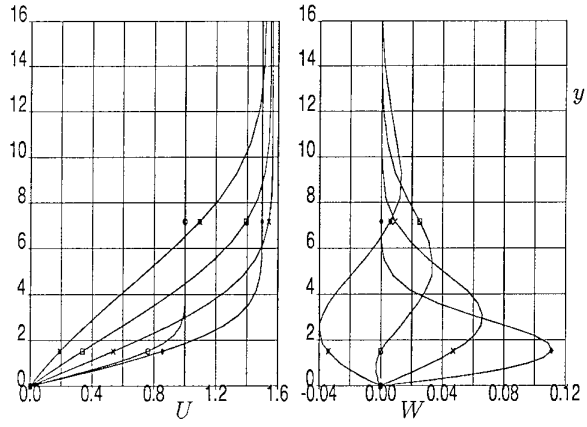

Figure 2: Velocity profiles. Left, streamwise profile; right, cross-flow profile. $\circ$, $x = 0$; $\diamond$, $x = 500$; $\times$, $x = 1000$; $\square$, $x = 1500$; $*$, $x = 2000$.

is 0 at $x = 0$, so that the flow is essentially identical to the Hiemenz flow ($U_e \propto x$) up to $x \approx 150$. This facilitates comparisons with other work. The factors U_∞ and r control the CF and TS amplification ratios, respectively. The $\tan^{-1}$ function allows a convenient extension into a Laplace solution in the region $y \gg \delta_l$, as needed for Navier-Stokes solutions.

Figure 1 also shows the momentum and displacement thicknesses associated with the projection of the velocity profiles in the x and z directions. The simulations cover the region $0 \leq x \leq 2000$. At the attachment line θ_z takes its well-known value of 0.404. By $x = 2000$, the boundary-layer thickness δ has increased by a factor of 5; this added to the numerical challenge, as our code is not adaptive. The shape factors $H_z = 2.73$ and especially $H_x = 3.08$ reflect the moderate adverse pressure gradient at $x = 2000$. The cross-flow profile, at $x = 2000$, is S-shaped. The Reynolds number $R_\times$ based on the integral of the cross-flow velocity [7] is returning through 0, back from its peak value of 81 near $x = 750$. Selected profiles, with respect to the local edge direction, are shown in Fig. 2.

The basic flow used for the OS calculations is obtained by solving the boundary-layer equations for the edge velocity U_e given above. The agreement between the DNS solutions and the boundary-layer solutions is very good for $x < 1800$, but beyond 1800 the wall-shear direction, in particular, deviates by several degrees between the two solutions. Although we have not totally ruled out numerical effects, we attribute this to the proximity of separation, indicated by the rapid drop of the streamwise skin friction (also shown in Fig. 1). At $x = 2000$, $C_{fx} \approx 0.5\ 10^{-3}$, based on W_∞, compared with a peak value of $6.2\ 10^{-3}$; the wall streamlines shown below (e.g., Fig. 7) illustrate the near-wall turning that ensues. Separation seems set to occur near $x = 2500$. The difference between the basic flows strongly impacts the TS growth rates; therefore, we limit the comparisons to $[0, 1800]$ for those modes.

4. PURE MODES

We call "pure modes" disturbances of the type $\widehat{f}(x, y) \exp(i[\beta z - \omega t])$. This harmonic dependence, with spanwise wave-number β and frequency ω (both real), is allowed by the basic flow. It is not identical to that of the "pure waves" of the OS equation, which is also harmonic in x. Throughout the paper, we take the convention that β_r is positive.

Even such simple perturbations lead to non-trivial tests of stability codes, associated with non-parallel effects and involving the streamwise growth rate and wave-number. Simple cases also build confidence before attempting more involved comparisons. Similar tests of the Parabolized Stability Equations (PSE) have been very successful, and non-parallel effects have lost much of their mystery [10, 11]; however, the present flow has more rapid variations, which could make it a harsher test for the PSE. In addition, many of the current prediction codes are not up to the PSE level.

Another reason to conduct inexpensive pure-mode simulations is to approach numerical resolution issues. For pure modes, there is no issue in the z direction, because of the harmonic dependence and the spectral numerical method. Solutions with 30 and 45 points in the y direction showed only subtle differences, and then limited to the basic flow. Nevertheless, 45 points were used for most cases. In the x direction, for pure CF modes we use a grid spacing of 2.5, in order to accommodate the CF vortex already near $x = 100$, where it makes a shallow angle with the z axis. Subsequent cases use a grid spacing of 5 in both x and z, which is sufficient considering that the shortest wave-lengths are of the order of 30 and that the growth over a period is not dramatic (typically, a ratio of 1.3). Recall that the discretization is spectral. The cases with harmonic forcing (at $\omega = 0.04$) use about 75 time steps per period, which is very accurate considering that a Runge-Kutta third-order time-stepping scheme is applied to the convection terms [9]. The wave-packet cases generate frequencies of the same order (ω between 0.02 and 0.05), so that the accuracy in time is again sufficient.

4.1 Pure CF modes

We generate stationary modes with spanwise periods $\lambda_z = 20$ and 15, which earlier work [7] showed to be rapidly amplified in the swept-Hiemenz region at $\overline{R} = 250$. Traveling modes are slightly more unstable, but are not qualitatively different from stationary ones. The instabilities are excited by a body force field centered at $x = 75$. Amplitudes are chosen to avoid both round-off errors and nonlinearity. The body force is of the type $\widehat{f}(x, y) \exp(i[\beta z - \omega t])$, the product of polynomial, Gaussian, and trigonometric functions in the various directions. It is divergence-free, and satisfies the same boundary conditions as the velocity field. Neither property is indispensable, but the former helps reduce the upstream influence (by not inducing a pressure field)

and the latter mitigates the formation of numerically disruptive boundary layers at the wall.

The x-z-dependence of the force is made to roughly fit an oblique wave, but its y-dependence is not particularly adjusted to generate a pure eigenmode. This is of interest, because an estimate of how rapidly the eigenmode establishes itself will help experimentalists that have had persistent difficulty extracting eigenmodes and growth rates consistent with linear theory. The term "eigenmode" is used loosely, as in any non-parallel flow [10]. Amplitudes for u' and v', based on the maximum with respect to y, are shown in Fig. 3. Only growth rates can be compared between the two cases, and not absolute levels, as the body-force magnitude is different. The magnitude of the growth-rate difference between u' and v' is of interest, because it is an effect the Orr-Sommerfeld equation could not be expected to capture. Smooth sustained growth is observed by $x \approx 200$; that is about 50 boundary-layer thicknesses downstream of the "wave-maker".

The $\lambda_z = 15$ case was expected to be of interest because stability codes often have serious trouble with CF modes in regions of decay. The DNS results do not show any dramatic changes in the growth rates, the streamwise wave-number, nor the disturbance profile in the y direction – in contrast, we have been unable to obtain consistent OS solutions over the whole domain. Beyond $x \approx 1700$, various eigenvalues appear to become so close to each other that the iterative eigensolver is unable to unambiguously extract an eigenvalue which we consider physically meaningful. A global eigensolver provides a spectrum, but selecting a meaningful eigenvalue is still a challenge. In many applications this poses no problems since the N-factor is based on the envelope. However, when there are regions of decay followed by growth, the N-factors can be significantly altered by errors in the decay region.

Tables Ia and Ib give quantitative results corresponding to Fig. 3, with the following notation. $\alpha_r(\partial u'/\partial y)$ means the wave-number extracted from the crests of $\partial u'/\partial y$ in a visualization such Fig. 5, below. The notation α is used for the DNS by analogy with the OS approach. These wave-numbers are local, and not extracted from the (global) spectrum of the spectral method. $\alpha(OS)$ is the Orr-Sommerfeld result. The growth rate $-\alpha_i(u')$ is based on the peak amplitude of u' as in Fig. 3.

The tables also give three angles: a_e is the angle $\tan^{-1}(U_e/W_\infty)$ the velocity vector at the edge of the boundary layer makes with the z axis; a_w is the angle $\tan^{-1}([\partial u/\partial y]/[\partial w/\partial y])$ of the wall streamline (or skin-friction line); and a_{CF} is the angle $-\tan^{-1}(\beta_r/\alpha_r)$ of the CF vortex itself (orthogonal to the CF wave-vector). The angles show that our earlier conclusion [7] that "the vortex direction lies between that of the free stream and that of the wall stress" is not general. It fails as soon as the flow enters the adverse pressure gradient. At the time we had only considered the swept Hiemenz flow.

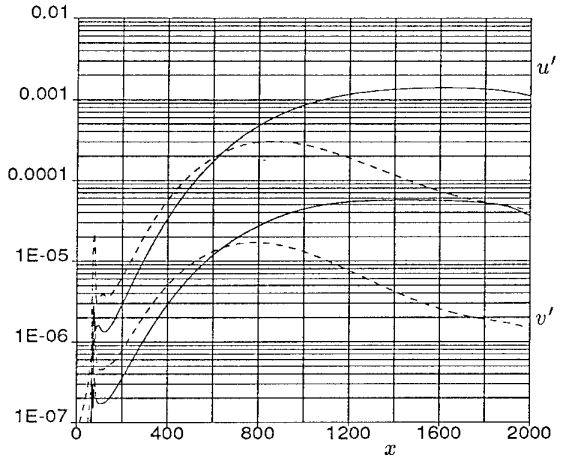

Figure 3: Amplitude of pure stationary CF modes, injected at $x = 75$. —, $\lambda_z = 20$; - - -, $\lambda_z = 15$. In each case, upper curve, u'; lower curve, v'.

Table Ia: pure CF mode, $\omega = 0$, $\lambda_z = 20$

x	400	1200	1700	2000
β_r	0.314	0.314	0.314	0.314
$\alpha_r(\partial u'/\partial y)$	–0.27	–0.27	–0.27	–0.27
$\alpha_r(OS)$	–0.26	–0.25	–0.27	
a_e	46°	50°	49°	49°
a_w	61°	53°	43°	35°
$a_{CF}(\partial u'/\partial y)$	49°	49°	49°	50°
$a_{CF}(OS)$	50°	51°	49°	
$-\alpha_i(u')$	0.0102	0.0010	–0.0001	–0.0013
$-\alpha_i(v')$	0.0088	0.0005	–0.0004	–0.0035
$-\alpha_i(OS)$	0.0075	–0.0004	–0.0007	

Table Ib: pure CF mode, $\omega = 0$, $\lambda_z = 15$

x	400	1200	1700	2000
β_r	0.419	0.419	0.419	0.419
$\alpha_r(\partial u'/\partial y)$	–0.36	–0.31	–0.34	–0.35
$\alpha_r(OS)$	–0.35	–0.33	–0.35	
a_e	46°	50°	49°	49°
a_w	61°	53°	43°	35°
$a_{CF}(\partial u'/\partial y)$	49°	54°	51°	50°
$a_{CF}(OS)$	50°	52°	50°	
$-\alpha_i(u')$	0.0091	–0.0023	–0.0016	–0.0014
$-\alpha_i(v')$	0.0075	–0.0030	–0.0016	–0.0018
$-\alpha_i(OS)$	0.0055	–0.0046	–0.0029	

Here, the vortex direction remains within 4° of the edge direction, whereas the wall direction is as much as 15° away from it, and on either side.

With pure waves, the comparison with Orr-Sommerfeld (OS) results reflects only non-parallel effects, as opposed to the effects of wave-vector choice. For CF modes, the non-parallel effects are found to be significant and destabilizing, consistent with previous PSE calculations of Malik & Li [11] and Stuckert *et al.* [12]; they are in quantitative agreement with the PSE results obtained by Malik & Li in the swept-Hiemenz region. In the adverse pressure gradient, the difference between DNS and OS results is of the same sign as in the favorable gradient, and even larger. With $\lambda_z = 20$, the N factor from $x = 200$ to the peak is 3.9 for the OS equation, while the DNS N factors are 6.2 and 5.1, for u' and v' respectively. Note that N factors could not be defined from Branch I in the DNS, because the body force was not far enough upstream for the transients to die out before Branch I. In any case the agreement between OS and DNS growth rates is quite poor. On the other hand, the direction of the vortices (or equivalently the chordwise wave-number α_r) shows good agreement. The non-parallel effects on CF modes are much more benign at $\overline{R} = 500$ [11].

4.2 Pure TS mode

The TS wave is also generated by a body force, now centered at $x = 500$; the spanwise wave-number is $\beta = 0.05236$ ($\lambda_z = 120$); the frequency is $\omega = 0.04$. These values were chosen to roughly match those that evolve naturally in wave packets (§6). Fairly smooth amplitudes are obtained around Branch I at $x \approx 1000$, as seen in Fig. 4. The subsequent growth is brisk, and at first is noticeably faster for v' than for u'. That trend reverses by $x = 1800$. The growth rates, shown in Table II, again show a de-stabilizing non-parallel effect, but smaller than for the CF modes. At $x = 2000$, the OS N factor is 5.7, while the DNS N factors are 5.9 and 6.4, for u' and v' respectively. A difference of 0.5 in N factor is quite tolerable in an engineering situation. The agreement on the wave-number α_r is good.

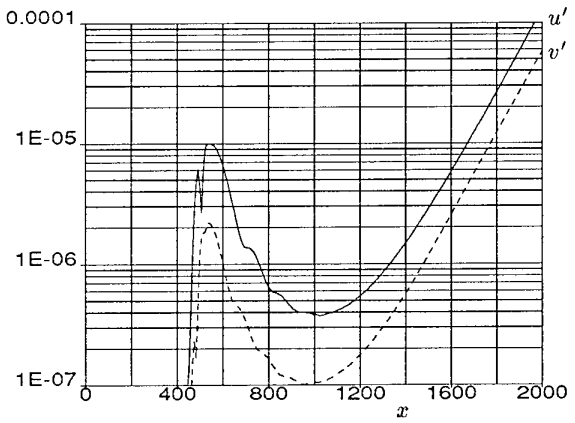

Figure 4: Amplitude of pure TS mode, injected at $x = 500$. —, u'; - - -, v'.

Table II: pure CF, $\omega = 0.04$, $\lambda_z = 120$

x	1400	1800
$\alpha_r(\partial u'/\partial y)$	0.055	0.050
$\alpha_r(OS)$	0.055	0.052
$-\alpha_i(u')$	0.0061	0.0078
$-\alpha_i(v')$	0.0069	0.0078
$-\alpha_i(OS)$	0.0058	0.0071

4.3 Assessment

Figs. 2, 3 and 4 together show that we have constructed a flow that sustains both types of instability, with N factors in the 6 to 8 range, and includes S-shaped profiles and decay regions. The lack of surface curvature and compressibility is not a major shortcoming, in that they are not known to have strong qualitative effects on the dispersion relation, at least up into the low-transonic range (we acknowledge their significant quantitative effects, usually damping). A Natural-Laminar-Flow design may have a higher $\overline{R}$ (although no higher than about 500) and would spread the TS growth over a much longer region. This would increase the numerical demands in all the spatial directions, and in time, leading to a considerable increase in cost. Thus, the present flow is a good compromise.

5. SPATIALLY LOCAL PERTURBATIONS

We now apply disturbances that are local in both the x and z directions, resulting in a full spanwise spectrum. The dynamics select the dominant β wave-number, which we estimate with the help of spectra, and visualizations using the "crests". The crests are defined as grid points at which the function considered (here, the wall value of $\partial u'/\partial y$) exhibits a local maximum with respect to the x direction or the z direction. This definition is only weakly dependent on the axes, and produces plausible results. Below we often refer to "the vortices", although the visualization in fact reflects the chordwise wall shear stress. This is fair, because the two are strongly correlated, the shear being high on the down-flow side of a vortex. Since only local maxima are retained, only one crest will appear per period, once the field exhibits fairly regular "waves". Thus, we estimate wave-lengths directly from the spacing between crests. Except in highly regular cases the wave-numbers cannot be unequivocally established to two significant digits. We provide the second digit because rounding to one digit would suppress too much information, but the uncertainty is often ±10%. Finally, crest points are retained only if the local function value is higher than the spanwise average by more than a threshold. This is necessary to weed out small oscillations (some of which represent numerical noise) and bring out the region of

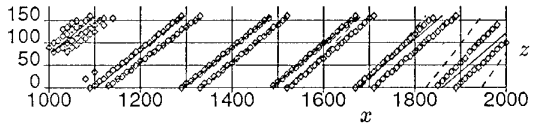

Figure 5: Visualization of CF vortex trailing an isolated source, at $x = 1000$. —, edge streamline; - - -, wall streamline; $\diamond$, crests of waves. DNS period $\lambda_z = 160$.

significant amplitude. The threshold at 5×10^{-5} is evident in Fig. 6; it is normally at least an order of magnitude smaller than the peak values. On the other hand, the threshold is arbitrary; the reader will keep in mind that the disturbed region does not have the abrupt edges our visualization technique may suggest.

5.1 CF modes

We again choose a stationary disturbance, and place it at $x = 1000$. Because the amplification is weak for $x > 1000$, the wake remains narrow and gives the clearest indication of the propagation direction, as shown by Fig. 5. The flow sustains only two crests of comparable magnitude. The presence of two crests, although convenient in terms of suggesting a wave-vector, is not significant in itself, because it results from the details of the body force we defined (which induces a region of up-flow between two regions of down-flow). Forces could be designed to induce one crest, or three.

The edge and wall streamlines originating at the disturbance ($x = 1000$, $z = 80$) are shown in Fig. 5, but are covered by the $\diamond$ symbols over much of the domain (they are more readable in later figures, such as 7 and 10). Each set of streamlines connects around the period of the DNS, $\lambda_z = 160$. The crests closely follow the edge-velocity direction, as opposed to the wall-shear direction, although the difference becomes noticeable only beyond $x \approx 1600$. The peak of the u' eigenfunction (on which the DNS and OS solutions agree) is consistently located near $y = 1.5\ \delta_x^*$, fairly high in the boundary layer, which explains why the change in orientation of the near-wall flow has little impact.

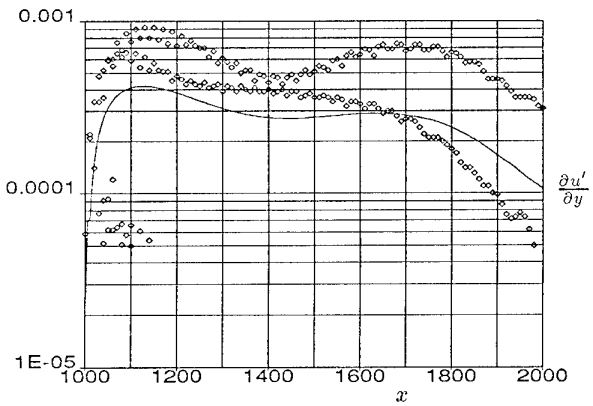

Figure 6: Amplitude of CF vortex trailing an isolated source, based on $\partial u'/\partial y$ at the wall. — rms ; $\diamond$, value at the wave crests.

Figure 6 shows the value of $\partial u'/\partial y$ on the two crests. The crest values run parallel to the root-mean-square values, but over most of the domain, one grows slowly, while the other decays slowly. This corresponds to a small mismatch between the direction of the phase lines and of the energy propagation, as seen before [7]. At $x = 1200$, Orr-Sommerfeld calculations for a perturbation with the wave-number observed in the DNS (i.e., $\beta = 0.23$) show the group-velocity direction to be within 1.5° of the edge streamline and −0.3° from the wave orientation.

The spanwise distance between crests varies from about 29 to about 45, larger values than the ones we chose in §4. This reflects the higher thickness of the boundary layer, but because of the lack of growth (and presumably of wave-number selection) the significance of these numbers is modest. Similar simulations with the force centered at $x = 500$ produced smaller spacings (at least in the region of highest amplitude), typically between 30 and 35 even at $x = 2000$. Growth rates are not shown, as Fig. 6 shows them to be of little size and interest. In particular, the rapid decay beyond $x \approx 1700$ is artificial, in that it results from a coincidence in the orientation of the vorticity perturbation with respect to the z axis; it also occurred around $x = 1600$ for the pure CF mode of Fig. 3, when the amplitudes u' and v' did not show a steep decay. The value of this case lies in the propagation direction, rather than in the wave-lengths and growth rates.

5.2 TS modes

The disturbance now has a frequency $\omega = 0.04$, as for the pure TS mode above. Up to about $x = 1500$, the visualization in Fig. 7 shows a mixed pattern. The CF mode is clearly indicated in terms of wave-vector ($\alpha_r \approx -0.16$, $\beta_r \approx 0.31$). However, around $(x, z) = (1300, 750)$ we also discern organized motion, in the form of short crests, that appears to stem from another region of the wave-vector space. The waves have $\alpha_r = 0$, $\beta_r = 0.10$, are fairly neutral in terms of amplification, and have a propagation angle of about 41° with respect to the z axis. Beyond $x = 1500$ we observe a more typical TS perturbation, and the $\alpha_r = 0$ waves smoothly merge into the TS wedge. We note that beyond $x = 1500$ the TS crests do not quite curve enough to become parallel to the x axis (implying $\alpha_r = 0$), but this is dependent on the threshold. In addition, $\beta_r \approx 0.10$ fits the edge of the TS wedge very well (as does the phase of the short crests). We conclude that the initial "isolation" of the $\alpha_r = 0$ crests is simply the result of the interference between CF and TS modes for $x < 1500$, and is *not* indicative of a neglected region of wave-vector space.

The figure also shows the location of the perturbation peak, with respect to z at a given x station. We call the locus of this peak the direction of energy propagation. Unlike in the (neutrally stable) CF case above, this device is needed to arrive at a narrow estimate of the best

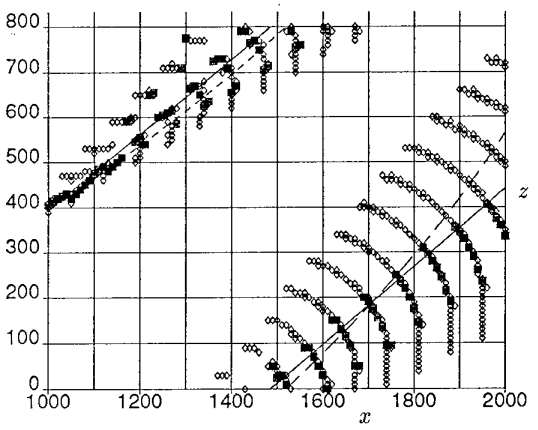

Figure 7: Visualization of TS mode trailing an isolated source. ◇, crests; •, peak versus z; —, edge streamline; - - -, wall streamline. DNS period $\lambda_z = 800$.

direction in which to integrate the growth of perturbations. A clear pattern is not established until $x \approx 1700$, because of the interference between modes, but then the band of peaks closely parallels the edge streamline, and not the wall streamline. Orr-Sommerfeld calculations based on the dominant mode (as predicted by the OS amplitude-ratio envelope) show the group-velocity direction is within 0.3° of the edge streamline at $x = 1500$ and 3° at $x = 1800$. At both locations, the group direction is bounded by the edge streamline and the wall streamline.

The DNS wave-vectors and growth rates are given in Table III, and the rms amplitude is shown in Fig. 8. The rms is defined with respect to the spanwise average, and a maximum is taken versus y. We distinguish the growth rate $-\alpha_i(u')$ based on this rms, and the growth rate $-\alpha_i(\partial u'/\partial y_{\max})$ based on the peak value of the wall-shear perturbation (shear taken at $y = 0$, and maximum taken versus z). These growth rates can be regarded as weighted averages of the growth rates of individual spanwise Fourier components (pure modes). As a result, $-\alpha_i(u')$ is always smaller than the highest pure-mode growth rate. The growth of the peak

Table III: localized TS mode, $\omega = 0.04$

x	1500	1800
α_r	0.071	0.066
β_r	0.041	0.036
$-\alpha_i(u')$	0.0032	0.0053
$-\alpha_i(v')$	0.0058	0.0075
$-\alpha_i(\partial u'/\partial y_{\max})$	0.0048	0.0067

value depends on phase relationships, and could briefly outpace the growth of pure modes. The evolution of the eigenfunction shape further differentiates the various growth rates. Only when the exponential growth is rapid enough to overwhelm the other factors (which are algebraic) are all the growth rates very close.

The wave-vectors were taken from the visualization, and near the peak amplitude. This peak amplitude is not centered within the packet; it is at lower z values than the center. The α_r wave-numbers are fairly well indicated by the visualization, but the β_r numbers are ambiguous, because of the curvature of the crests. The values shown for β_r were in fact calculated from α_r and the orientation of the crest at the amplitude peak (the angle $a_{TS}(\partial u'/\partial y)$, in the notation of Table I). In Fig. 8 the amplitude is time-dependent, unlike for pure modes (because here the force is not of the type $\widehat{f}(x,y)\exp(i[\beta z - \omega t])$) and shows significant periodic variation especially for $x < 1300$.

The β spectrum is shown in Fig. 9. Implicitly, we set $\beta_i = 0$ when Fourier-transforming the solution. The assumption of a "flat" spectrum used in theoretical treatments is fairly well satisfied at $x = 1100$; the question is obscured by the time-dependence of the spectrum. The subsequent wave-number selection, concurrent with the amplification, is evident. The most-amplified wave-number rapidly shifts to lower values, and the spectrum displays considerable history effects, which would

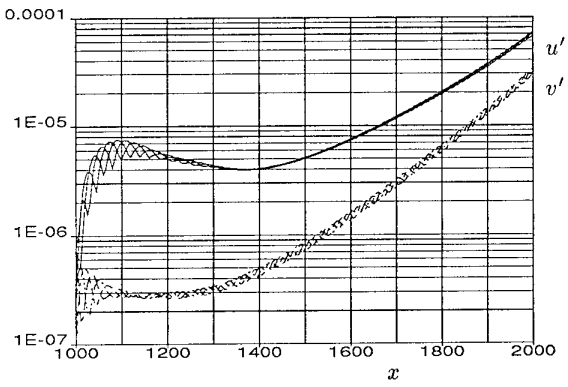

Figure 8: RMS amplitude of TS mode trailing an isolated source, at three phases within the period. —, u'; - - -, v'.

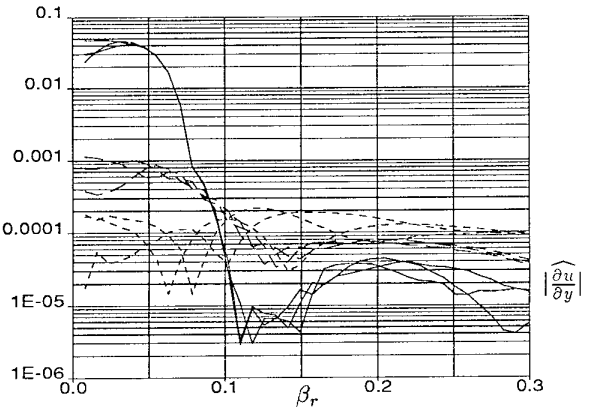

Figure 9: Spanwise spectrum of TS mode trailing an isolated source, at three phases within the period. - - -, $x = 1100$; — —, $x = 1500$; —, $x = 2000$.

be highly challenging for methods which select a single wave number based on local behavior. At $x = 2000$ the amplitude has been almost sustained near $\beta_r = 0.2$, and highly amplified near $\beta_r = 0.04$. However, the peak in the spectrum is still so wide that the algebraic factors in the amplitude growth cannot be negligible with respect to the exponential factors. Even a Gaussian model [3] would probably not be very accurate. The strong damping in the $[0.1, 0.15]$ interval provides a fair (although blurred) demarcation between CF and TS modes. The breadth of the spectrum accounts for the difficulty in extracting some wave-vectors from the visualizations, but we verify a good agreement between the dominant wave-number in the spectrum, when there is one, and that deduced from the visualization. At $x = 2000$ the spectrum indicates $\beta_r \approx 0.037$, and the visualization $\beta_r \approx 0.036$. On the other hand, at $x = 1500$ the spectrum is quite flat over $[0, 0.06]$, while the visualization indicates $\beta_r \approx 0.041$. The overall shape of the spectrum, on the log scale, is similar to the variation, versus β_r, of the growth rate $-\alpha_i$ predicted by the OS theory (not shown).

6. WAVE PACKETS

We now impose a disturbance that is localized both in space and time. If the localization is narrow enough, we are introducing about the same amount of energy for all wave-vectors and frequencies. As a result, the only overt parameter in this type of simulation, once the basic flow has been defined, is the location x_0 at which the disturbance was placed. However, our findings based on the crests in Fig. 5, and the spectrum at $x = 1100$ in Fig. 9, indicate that the shape of the body force (or other device) cannot be totally ignored, at least until a large amplitude ratio has been achieved.

We selected the case with $x_0 = 1000$ because it generated distinct TS and CF packets, which propagated at rather disparate velocities. This is revealed by Fig. 10. The $x_0 = 500$ and $x_0 = 1500$ cases led to the same conclusions. The edge and wall streamlines originating at the pulse point ($x = 1000$, $z = 200$) show that the edge streamline again indicates the appropriate propagation direction very well, and for both types of perturbations. Figure 11 shows the amplitude of the wave packet at a sequence of times.

Table IV gives quantitative information derived from Figs. 10 and 11 and companion figures, which are not shown (for instance, the frequency is extracted by comparing Fig. 10 and visualizations at different times). Δx and Δz are the distance traveled by the packets since the pulse was applied. The frequency ω, like the wave-numbers, is defined by analogy with pure modes. The phase velocities in the x direction, z direction, and the magnitude of the phase velocity are given by $c_{\phi x}$, $c_{\phi z}$, and $|c_\phi|$, respectively. The axis-dependent wave-numbers (such as β) and phase velocities (such as $c_{\phi z} \equiv \omega/\beta_r$) can be deceptive, as the wave-number can be artificially low and the velocity artificially high.

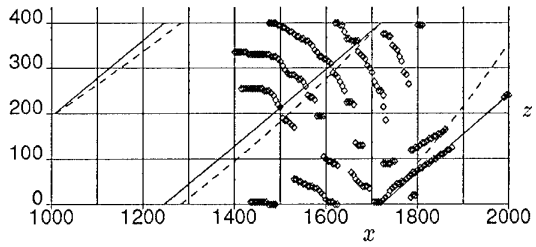

Figure 10: Visualization of wave-packet created at $x = 1000$. $\Delta t = 1200$. —, edge streamline; - - -, wall streamline. DNS period $\lambda_z = 400$.

The corresponding c_e velocities (such as $\overline{c_{ex}} \equiv \Delta x/\Delta t$) are defined a little loosely as "the velocity of the energy propagation". They denote the travel of the amplitude peaks and are much more meaningful than the separate phase velocities. The overline, as in $\overline{c_{ex}}$, indicates an average since the inception of the packet. The $|\ |$ signs, as in $|c_\phi|$, denote the magnitude of a vector.

The "apparent growth rate" $-\alpha_{i\ app}$ denotes the slope of the amplitude envelope with respect to x, extracted from Fig. 11. The TS apparent growth rate is lower than those in Table II. On the other hand, the positive CF apparent growth rate was unexpected, especially since $\beta_r = 0.13$ was damped in Fig. 9. It may result from favorable phase relationships, or from a more favorable frequency than those we imposed above. The CF packet indicates $\omega \approx 0.011$, whereas we used only 0 and 0.04.

The propagation of the TS packet is quite as expected. Referred to the edge streamline, the TS packet is quite symmetric and dominated by two-dimensional waves (in a rotated frame). This packet seems unaffected by the cross-flow. At $t = 1200$ the conditions are $R_{\delta^*} \approx 1500$, and a weak adverse pressure gradient. The phase velocity is 34%, and the energy velocity is 43% of the magnitude of the edge velocity. The wave number is 0.37, normalized by displacement thickness. This is fairly high, but not atypical for an adverse pressure gradient.

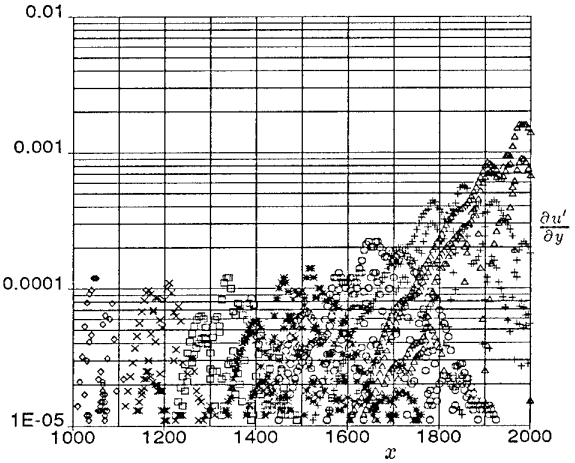

Figure 11: Amplitude of wave-packet created at $x = 1000$, at the following times, $\Delta t =$: ◇, 100; ×, 400; □, 700; ∗, 1000; ○, 1300; +, 1600; △, 1900.

Table IV: wave packet, $t = 1200$

Region	TS packet	CF packet
Δx	600	800
Δz	520	680
α_r	0.070	–0.08
β_r	0.059	0.13
$\sqrt{\alpha_r^2 + \beta_r^2}$	0.092	0.15
ω	0.048	0.011
$c_{\phi x}$	0.69	–0.14
$\overline{c_{ex}}$	0.50	0.67
$\overline{c_{ex}}(OS)$	0.49	0.64
$\overline{U_e}$	1.19	1.18
$c_{\phi z}$	0.81	0.08
$\overline{c_{ez}}$	0.43	0.57
$\overline{c_{ez}}(OS)$	0.43	0.50
W_e	1	1
$\lvert c_\phi \rvert$	0.52	0.16
$\overline{\lvert c_e \rvert}$	0.66	0.88
$\overline{\lvert c_e \rvert}(OS)$	0.65	0.81
$\sqrt{\overline{U_e^2 + W_e^2}}$	1.55	1.55
$\partial u'/\partial y_{\max}$	$1.9\ 10^{-4}$	$2.2\ 10^{-5}$
$-\alpha_{i\ app}$	0.0037	0.0042

The CF packet is more difficult to analyze. First, there is a weak "precursor" region that is at $(x, z) = (2000, 250)$ at $t = 1200$. Thus it has $(\Delta x, \Delta z) = (1000, 850)$. It has precisely followed the edge streamline, and the magnitude of its apparent energy velocity is 1.31. That represents 85% of the edge velocity, and we suspect that this perturbation is located high in the boundary layer. We based the estimates in Table IV on the stronger region of CF, located around $x = 1800$. This component traveled more slowly (57% of the edge velocity), but it retained more amplitude, as well as two crests. For these reasons, it was deemed more significant.

A detailed wave-packet comparison between the DNS and linear theory would require the tracking of a large number of linear modes, similar to the work of Gaster [14]. However, a small number of OS calculations can give an estimate of the ability of the linear theory to predict characteristics of the energy propagation. Using the dominant frequencies and spanwise wave numbers identified in the DNS, OS group velocities were calculated. The group velocity is given by the components $c_{ex} = \partial\omega/\partial\alpha_r$, $c_{ez} = \partial\omega/\partial\beta_r$. For the TS packet the OS results show a moderate change in $|c_e|$, approximately 14% over the region $1000 < x < 1600$. By contrast, the traveling CF mode has a velocity of $|c_e| = 0.94$ at $x = 1000$, which drops to $|c_e| = 0.58$ at $x = 1800$. The CF packet propagates ahead of the TS packet upstream of $x = 1600$; but downstream of $x = 1600$, the TS packet has a higher group velocity. The OS velocities given in the table are averaged over the propagation distance. The comparisons with the DNS show good agreement for TS waves. The agreement is not as good for the CF vortices; this could be attributed to errors near $x = 1800$, similar to those observed in pure CF comparisons.

7. DISCUSSION

We have generated by Direct Numerical Simulation a basic flow and a range of perturbations that exercise both the Cross-Flow and Tollmien-Schlichting instability mechanisms, in the linear régime, and are much more general than the perturbations encompassed by the Orr-Sommerfeld equation. We consider these perturbations as "realistic", although distributed random numbers would also be of interest [7, 8] and were not used here. We provided Orr-Sommerfeld results for several cases. Some cases should be within easy reach of the Parabolized Stability Equations, which we did not use here but has agreed very well with earlier DNS results, in terms of capturing non-parallel effects [10, 11]. Other cases are not accessible to inexpensive PSE calculations, of the kind that would be needed in a transition-prediction method. Therefore, we feel that these cases can test some of the ancillary components needed in a PSE-based prediction code. We also noted that future amplitude-based transition-prediction methods should find useful material in the present results.

The turning of the basic flow and the amplification of the perturbations occur over a rather short distance, compared with the boundary-layer thickness. This helped contain the cost of the simulations. On the other hand, the "non-parallel effects" are sizable, and in future work we may strive for a larger Reynolds number $\overline{R}$ and a longer region with weak adverse pressure gradient. However, much of the food for thought pertains to wave-vectors, which are much less affected by non-parallel effects than are growth rates. We may hope that the localized theories will fare better in a flow with larger streamwise extent and therefore weaker non-parallel effects. However, the attachment-line Reynolds number $\overline{R}$ is 250, and the streamwise Reynolds number R_x is between $0.5\ 10^6$ and 10^6, depending on the exact definition. These values are lower than in airliner applications, but not by an order of magnitude. Since non-parallel effects roughly scale with $R^{-1/2}$, it appears that they are not grossly exaggerated in the present flow, compared with likely applications.

For a range of excitation types and frequencies, CF- and TS-type perturbations were observed concurrently. They were always easy to distinguish based on wave-

vector magnitude and direction. We found no evidence of "energy transfer" between them (naturally, this would not apply in the non-linear régime) nor did we observe any significant "conversion" form one mode type to another. Therefore, our experience strongly supports the use of separate N factors. Our visualization approach (which is quite similar to those used in experiments) produces *interference* effects, which we believe could be mistaken for energy transfers, or for the emergence of an unexpected class of waves (§5.2). Visualization always invites caution. Results obtained elsewhere for a simple class of non-linear breakdowns also oppose the idea of an interaction between the two perturbation types in the linear or even the early non-linear régimes [13]. The wave-vector direction is extensively used for the CF/TS distinction in prediction codes, and there is a concern about possible hybrid instability modes (in terms of wave-vector) which could confuse the codes. In further work, we intend to seek regions of the parameter space (including different pressure gradients) in which such modes may play a role. It is of interest that they have not shown up here, even with the rich spatial and temporal spectra associated with wave packets.

Comparisons between the DNS and the OS equation (with $\beta_i = 0$, $\partial\beta_r/\partial x = 0$) indicate general agreement. Non-parallel effects are destabilizing and are qualitatively predictable based on earlier studies using the PSE. These effects are greatest for CF disturbances, especially in regions of decay. The dominant spanwise wave number, based on an integral of the OS growth rates, was in reasonable agreement with the observed DNS value. For a given frequency and spanwise wave number, the OS and DNS wave angles were very close. Group velocity calculations were also in good agreement with observed energy propagation for wave packets. The direction of the edge velocity of the boundary layer seems to provide a very good estimate of the propagation direction. This result could be important for flows without "infinite sweep", since the propagation direction then influences the final growth level.

When designing this study, we had hopes of obtaining firm indications of the most relevant wave-vectors. This would have represented a selective test for the more efficient "integration strategies" used in transition-prediction codes; these strategies typically track a single "mode" which characterizes the evolution of a packet. Unfortunately, the perturbations that were broad-banded initially remained so for the extent of the simulation, so that narrow wave-vector estimates were not obtained. We resorted to estimates taken from the region of highest amplitude, but their "error bars" are significant, so that their importance should not be over-stated. On the other hand, the DNS results do offer a rich test case for the different theoretical characterizations of the wave packet. We conclude that the relationship between pure-wave calculations and "real life" is a complex matter that will not be clarified by a small set of simulations, in spite of our efforts to generate "realistic" perturbations in a "realistic" basic flow.

References

[1] Nayfeh, A. H. 1980 "Stability of three-dimensional boundary layers". *AIAA J.* **18, 4**, 406-416.

[2] Cebeci, T, & Stewartson, K. 1980 "On stability and transition in three-dimensional flows". *AIAA J.* **18, 4**, 398-405.

[3] Gaster, M. 1981 "Propagation of linear wave packets in laminar boundary layers". *AIAA J.* **19, 4**, 419-423.

[4] Casalis, G., & Arnal, D. 1990 "Prediction of transition on a swept wing". Rech. Aérosp. no. 1990-1, 13-22.

[5] Mack, L. M. 1989 "Stability of three-dimensional boundary layers on swept wings at transonic speeds". IUTAM Symposium Transsonicum III, May 24-27, 1988, Göttingen, Germany.

[6] Spalart, P. R. 1989 "Direct numerical study of leading-edge contamination". AGARD CP 438; Symp. on Fluid Dyn. of 3D Turb. Shear Flows and Transition, Oct. 3-6 1988, Turkey.

[7] Spalart, P. R. 1990 "Direct numerical study of cross-flow instability". Third IUTAM Symp. on laminar-turbulent Transition, Sept. 11-15, 1989, Toulouse, France.

[8] Spalart, P. R. 1991 "On the cross-flow instability near a rotating disk". Boundary Layer Transition and Control Conference, Royal Aeronautical Society, Cambridge, April 8-11 1991.

[9] Spalart, P. R., Moser, R. D., & Rogers, M. M. 1991 "Spectral solvers for the Navier-Stokes equations with two periodic and one infinite direction". *J. Comp. Phys.* **96,2**, 297-324.

[10] Bertolotti, F. P., Herbert, Th., & Spalart, P. R. 1992 "Linear and nonlinear stability of the Blasius boundary layer". *J. Fluid Mech.* **242**, 441-474.

[11] Malik, M. R., & Li, F. 1993 "Transition studies for swept wing flows using PSE". AIAA-93-0077.

[12] Stuckert, G. K., Herbert, Th. & Esfahanian, V. 1993 "Stability and transition on swept wings". AIAA-93-0078.

[13] Spalart, P. R. 1993 "Numerical study of transition induced by suction devices", Int. Conf. on Near-Wall Turbulent Flows, Mar. 15-17, ASU, Tempe, AZ. Elsevier, pp. 849-858.

[14] Gaster, M. 1975 "A theoretical model for a wave packet in the boundary layer on a flat plate". *Proc. R. Soc. Lond. A* **347**, 271-289.

On Subcritical Instability of the Attachment Line Boundary Layer

VASSILIOS THEOFILIS
Department of Applied Mathematics, University of Twente, P.O. Box 217
7500 AE Enschede, The Netherlands

1. Summary

Subcritical instability in the two-dimensional incompressible attachment-line boundary layer remains a topic of debate, after the apparently contradictory results of Hall and Malik (1986) on one hand and Spalart (1988) and Jiménez *et al.* (1990) on the other. Direct Numerical Simulation (DNS) results are presented, aiming at addressing this question. Extensive numerical experimentation has been performed and all results obtained suggest that the two-dimensional model equations describing leading edge boundary layer (LEBL) flow do *not* support solutions growing subcritically in Reynolds number, although the nonlinear neutral loop is seen to bifurcate from its linear counterpart in a manner consistent with the predictions of the theory of Hall and Malik (1986). Nonlinear neutral loops have been obtained suggesting that the two-dimensional model LEBL flow is similar to the classical Blasius boundary layer in terms of the location, in parameter space, of the experimentally observed naturally occuring instability waves.

2. Introduction

The work of Hall *et al.* (1984) established that the eigenvalue problem (EVP) resulting from linear analysis of the generalised Hiemenz (1911) flow (Rosenhead, 1963) adequately predicts the behaviour of small-amplitude disturbances observed experimentally by Pfenninger and Bacon (1969) and Poll (1979). However, LEBL flow may become turbulent at Reynolds numbers well below the linear critical value, $\bar{R} \approx 583$, as observed, f.e., in the systematic experimental studies of Poll (1979, 1985) and three-dimensional DNS of Spalart (1988).

Receptivity being at its early stages of development (Morkovin and Reshotko 1989) deterministic analytical models that may yield predictions for finite-amplitude disturbances pivot about the Stuart-Watson weakly nonlinear analysis (Stuart, 1960; Watson, 1960). Hall and Malik (1986) were the first to apply weakly nonlinear analysis and DNS to the LEBL flow. Their theory predicted that this flow may be potentially destabilised by finite- amplitude disturbances and DNS results obtained by Hall and Malik, on a two-dimensional model, indeed yielded a value of critical $\bar{R} \approx 535$.

Spalart (1988), however, presented DNS results of instability and transition to turbulence without observing, in a number of three-dimensional runs performed, the subcritical behaviour predicted by the Hall and Malik computations. Spalart(1989) used no a-priori assumptions on the form of the perturbations, in contrast with all other work to-date, both theoretical and numerical, which invariably uses the Görtler-Hämmerlin (GH) form (Görtler, 1955; Hämmerlin, 1955). The simulations of Spalart, however, provided evidence that use of this form is permissible.

Jiménez *et al.* (1990) attempted to resolve the issue by considering, numerically, the two- dimensional limit of LEBL flow, since it is on this model that the Hall and Malik theory yields the prediction of (nonlinear) subcritical behaviour in both wave- and Reynolds number. Jiménez *et al.* took the (generalised Hiemenz) stagnation point flow subject to the GH assumption as a model for their base flow and, performing extensive experimentation, concluded that the two- dimensional flow does *not* support subcritical solutions; they suggested that the formally excluded (in view of the GH assumption) three-dimensional mechanisms may be responsible for the observed discrepancy between linear theory and experiment.

Theofilis (1988, 1993) formulated the two- dimensional LEBL flow as an initial-value-problem (IVP) and linearised about the generalised Hie-

Paper presented at the 74th Fluid Dynamics Symposium on "Application of Direct and Large Eddy Simulation to Transition and Turbulence" held at Chania, Crete, Greece, in April 1994.

menz profile using the GH assumption. He obtained results of the IVP that were in line with the EVP predictions of Hall *et al.* (1984). The model problem considered by Theofilis (1988) was shown, in the two-dimensional limit considered, to respond to blowing/suction of the boundary layer in the manner predicted by the EVP in Hall *et al.* (1984) and the three-dimensional DNS of Spalart (1988).

In the present paper we relax the condition of smallness imposed on the perturbations and solve the resulting nonlinear problem. The points on which the numerical procedures utilised herein differ to those presented in Theofilis (1993) are briefly discussed in §3, where an alternative numerical method is presented for the solution of the EVP. In §4 results on the EVP and both the linear and nonlinear IVP are presented. The significance of our nonlinear results with respect to the apparent disagreement between earlier two-dimensional stability results is highlighted. Concluding remarks are offered in §5.

3. Numerical Methods

The governing equations solved are those presented in Theofilis (1993) with the additional inclusion of the nonlinear terms, also presented therein. The temporal model is adopted throughout (Kleiser, 1993); a Fourier expansion is assumed in the homogeneous spanwise direction, treated as periodic, and second-order finite-differences on a stretched grid are used in the normal. The implementation of stretching in the normal direction, as opposed to the uniform grid used in Theofilis (1993), was decided on grounds of efficiency but also in view of the fact that a uniform grid might only be relevant in calculating the late nonlinear stages, which have not been addressed presently. Time-marching is performed by an implicit Crank-Nicolson scheme in view of (a) its stability properties and (b) the relatively short integration times in the present study. Further technical details may be found in Duck (1985) and Theofilis (1993).

The forcing of the simulations is provided by choosing the wall normal perturbation velocity in spectral space to be a smootlhy varying function of space and time. We have focussed on two forms of forcing, one jet-like, and one simulating ribbon excitation. The forms of these functions are given explicitly in Theofilis (1993). The former is a short-lived function of space and time while the latter is a function with a parametric dependence on the frequency of the maximally amplified linear mode. It should be mentioned here that the terms *jet* and, especially, *ribbon* are used to provide only qualitative description. Comparison of simulation results with experiments whose excitation is provided by, say, a vibrating ribbon, require the former to adopt the spatial model and three-dimensional calculations. Neither of the two falls into the scope of the present study.

Information on the EVP is desired for the nonlinear computations. It was thought appropriate to obtain this information by a numerical approach independent of that utilised for the simulations. The EVP system, of the Orr-Sommerfeld class, but *not* the Orr-Sommerfel equation (Poll, 1978; Arnal, 1992; Theofilis, 1994) is thus solved using spectral collocation based on Chebyshev polynomials. Of the results obtained the growth rate has been utilised to perform comparisons with those yielded by the IVP approach and the frequencies in order to force some of the nonlinear calculations described in the sequel.

4. Results

Results obtained may be classified as follows. Firstly, as mentioned, EVP results. Subsequently, linear IVP results which, when compared to the EVP results, provide validation of the IVP numerical approach. Finally, nonlinear results; the latter have been obtained under the two distinct forms of the forcing function discussed earlier. The amplitude of the forcing function was utilised as a parameter to control the size of the disturbances initially introduced into the numerical solution.

4.1. The Eigenproblem Revisited

Spectral collocation was selected to solve the eigenvalue problem in view of the favourable accuracy properties of spectral methods for smooth functions (Canuto *et al.* 1993). Within the context of collocation calculations Chebyshev polynomials were preferred to other spectral basis functions, based on arguments related to the minimax property of Clyebyshev polynomials used in conjunction with the standard Gauss and Gauss-Lobatto grids (Boyd, 1989). The grid refinement history at the neutral conditions (zero suction) $\bar{R} = 800, \beta = .3384638$ quoted by Hall *et al.* (1984) is presented in Table I.

Utilising $N = 160$ points, compact finite-differences, and asymptotic boundary conditions, Hall *et al.* (1984) predict that the neutral mode at

these conditions has a frequency $c_r = 0.3755134$.

N	c_r	c_i
16	0.3881956	-.0010554
32	0.3754382	-.0000697
64	0.3755143	-.0000007

TABLE I
Grid refinement history in our spectral collocation numerical solution of the EVP at $\bar{R} = 800, \beta = .3384638$.

It may be seen from the results of Table I that $N = 64$ collocation nodes suffice in order to produce converged EVP results. The smaller number of nodes utilised compared to compact finite-differences results in substantial savings when using the QZ algorithm (Wilkinson, 1965; NAG, 1992) to solve the eigenproblem.

Moreover, our results are obtained on a large (one-dimensional) integration domain, at both endpoints of which we impose the boundary condition of vanishing perturbations. This condition is more general than the prespecified exponential decay prescribed by Hall *et al.* (1994); the identical results obtained, however, justify use of the asymptotic behaviour of the perturbations assumed by Hall *et al.* (1994).

4.2. An IVP Formulation: Linear

In the IVP formulation of the stability problem we assume the decomposition of all flow quantities into base and perturbed flow. In the linear regime we expect the perturbations to be small compared to the $O(1)$ base flow and set quadratic in perturbations terms to be identically equal to zero. We subsequently march the solution in time and monitor the behaviour of the perturbed flow.

We utilise the jet-like excitation and obtain results typical examples of which are presented in figures 1 and 2 where the time dependence of the wall shear component in the streamwise direction u_y of an (almost) neutral and a decaying mode is plotted. After some transient, Tollmien-Schlichting (TS) waves emerge, whose growth or decay in time depends upon the combination of the Reynolds number and wavenumber parameter values.

The growth rate of an individual TS mode may be monitored in either real or transform space; the simulation is terminated when convergence of the growth rate has been achieved. The growth rate dependence on time for the results of figures 1 and 2 is also presented. The frequency of a TS mode is another result that may be directly calculated from the numerically obtained IVP linear results. Both frequency and growth rate linear results have been compared against the results of Hall *et al.* (1984) and those obtained by our collocation EVP approach with very good agreement resulting.

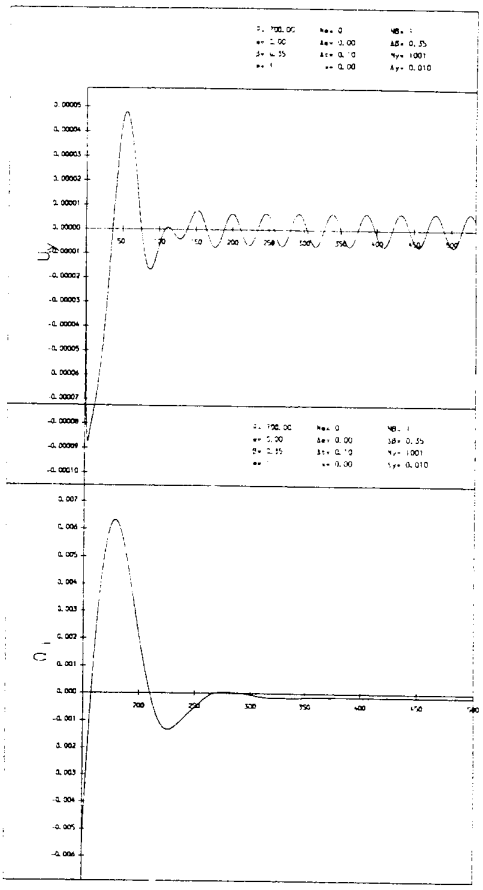

Fig. 1. An almost neutral linear TS mode at $\bar{R} = 700$, spanwise wavenumber $\beta = 0.35$. Upper: wall shear u_y against time t. Lower: growth rate ω_i against time t.

4.3. An IVP Formulation: Nonlinear

The smallness condition of the perturbed flow quantities is next relaxed and the resulting nonlinear system is solved numerically. We concentrate on the zero suction case and define our integration box according to the following criteria. In the wall-normal we truncate the domain at a distance large enough for imposition of the

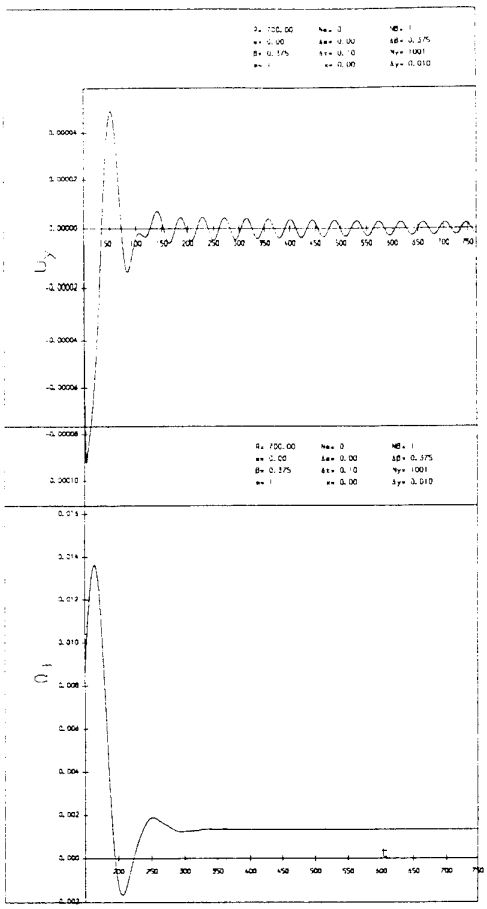

Fig. 2. A decaying linear TS mode at $\bar{R} = 700$, spanwise wavenumber $\beta = 0.375$. Upper: wall shear u_y against time t. Lower: growth rate ω_i against time t.

boundary condition of zero perturbations to be applicable. The reason for this choice is, again, our unwillingness to introduce an a-priori free-stream rate of decay on the perturbations. A large number of nodes, typically of $O(200)$ are taken in this direction in view of the extent of the domain and the low accuracy of the numerical method in this direction. In the spanwise direction a modest-to-large number of Fourier nodes, typically $O(100)$, may be devoted to either fine resolution of the fundamental or capturing of a number of subharmonics. In this study we have chosen the first course of action, concentrating on the domain suggested by the linear response.

Similarly to the linear IVP results, instability waves develop in the flow after some transient; a typical example is shown in figure 3. Values of the growth rate, ω_i, are calculated either through

$$\omega_i = \frac{1}{\hat{\phi}} \frac{d\hat{\phi}}{dt} \tag{1}$$

using the time signal of a spectral space flow quantity $\hat{\phi}$ (harmonic of the respective physical space quantity) or, equivalently, through monitoring a measure of the perturbation energy

$$E(\beta, t) = \int_0^{y_\infty} \{\hat{u}^2 + \hat{v}^2 + \hat{w}^2\} dy \tag{2}$$

$\hat{u}, \hat{v}$ and $\hat{w}$ indicating, respectively, perturbation velocity components in the streamwise, normal and spanwise directions, and calculating the slope of the function

$$\ln \sqrt{E(t)} \tag{3}$$

at a given wavenumber β value. The two definitions yield identical results.

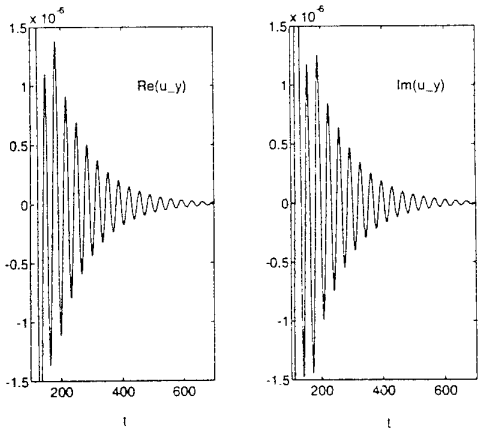

Fig. 3. Wave emerging at $\bar{R} = 550, \beta = 0.3$. Left: $\Re\{u_y\}$ against time. Right: $\Im\{u_y\}$ against time.

The quantity defined in (2) is, additionally, significant in that it measures the strength of an individual Fourier component and, as such, may be monitored in relation to resolution requirements of the simulation (Reed, 1993). Such a study has been performed in the course of the runs presented and a typical result is plotted in figure 4. Worth noticing here are, firstly, that the typical of spectral simulations linear dependence of the logarithm of energy on the number of nodes utilised is clearly exhibited. Secondly, it has been demonstrated (f.e. Zang *et al.*, 1989) that a minimum requirement for reliability of results obtained in transition simulation is the separation of the energy of the most-from the least-energetic (Fourier) modes by at least eight orders of magnitude; more than ten orders of magnitude separation is demonstrated

in figure 4. Moreover, the typical tail in the energy spectrum which denotes imminent loss of accuracy due to accumulation of energy in high-wavenumbers is absent from our calculations.

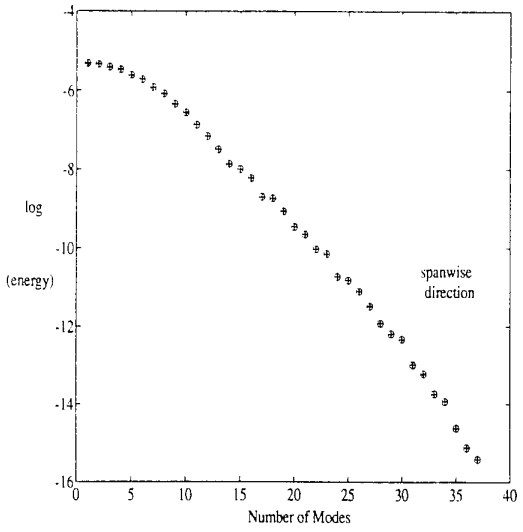

Fig. 4. Spanwise resolution quality test.

The issue of the link between resolution and de-aliasing has also been considered in the present nonlinear calculations. It was found to be irrelevant to actually invoke the dealiasing option in conjunction with the high resolutions utilised, although it was necessary to de-aliase our calculations during runs on more modest grids. This result appears to be in line with the emerging consensus that de-aliasing may be relevant for marginally resolved simulations (Spalart *et al.* 1991; Canuto *et al.* 1993). For the two-dimensional results presented herein, however, it is straightforward to resolve all scales at the early nonlinear stages considered.

We first compare our nonlinear IVP calculations against those yielded by the linear IVP approach. In figures 5 and 6 we present such a typical comparison between linear and nonlinear IVP results, the latter obtained under linear conditions, at a given set of parameters. Though undergoing different transient behaviour, the two sets of calculations yield, at convergence, identical frequency and growth rate results.

We next turn to nonlinear calculations and present in figure 7 a typical dependence of the perturbation energy function defined in (3) on the spanwise wavenumber and time at a given Reynolds number. This function becomes a linear function of time at a given wavenumber after some initial transient, indicating the onset of flow behaviour described by linear theory. The sign of the slope of an individual straight line determines growth or decay of the respective instability wave. Interpolation of the results at different wavenumbers determines the location in parameter space of the branches of the neutral loop. Repeating similar calculations at different Reynolds number values one obtains a complete (nonlinear) neutral loop.

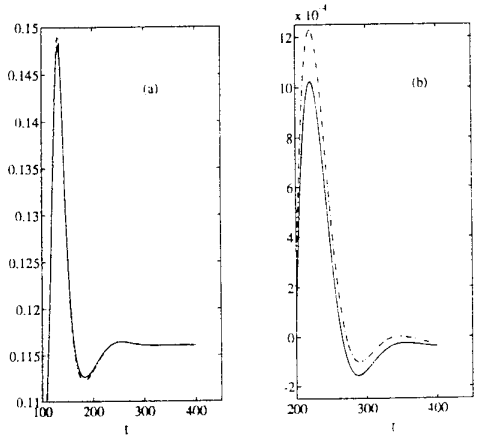

Fig. 5. Frequency in(a) and growth rate in(b) against time at $\bar{R} = 590$, spanwise wavenumber $\beta = 0.3$ predicted by linear and nonlinear numerical solution.

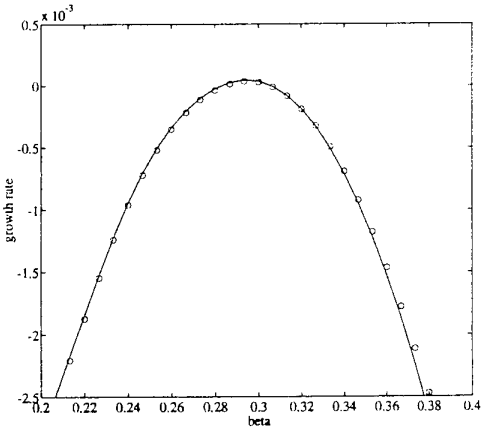

Fig. 6. Linear and nonlinear growth rate vs. wavenumber at $\bar{R} = 590$.

In order to address the issue of existence of two-dimensional nonlinear subcritical solutions we first obtain nonlinear solutions under linear conditions, namely small amplitude of the initially superimposed disturbance. Utilising the jet-like excitation we have scanned the Reynolds number parameter range in the neighbourhood of the neutral loop that linear theory delivers; all our results have been qualitatively similar to those

presented in figures 5 and 6, namely the flow returns to its linear behaviour after the initial transient.

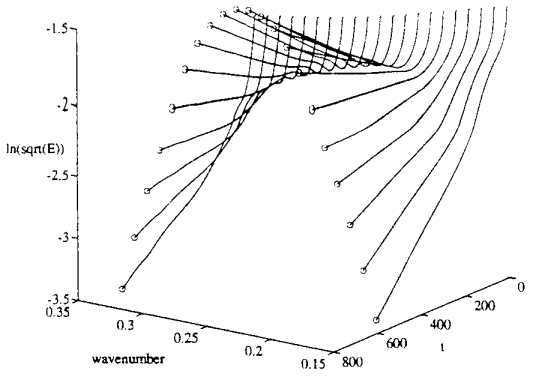

Fig. 7. Perturbation energy as function of time at $\bar{R} = 800, \beta \in [0.15, 0.35]$.

We then concentrate on a single Reynolds number value $\bar{R}$=550, which is approximately located in the middle of the disputed region and, keeping all other parameters the same, alter the form of the forcing. We consider the ribbon-like excitation which we apply for a number of TS cycles before abruptly removing it. We introduce periodic suction and blowing into the numerical solution choosing the frequency of the ribbon operation to be that of the most unstable (decaying) linear mode at the given Reynolds number value.[1] The result is presented in figure 8 from which two conclusions may be drawn. Firstly it may be seen that the ribbon sets up a (forced) neutral oscillation. Secondly, once the forcing is removed, the flow returns to its linear behaviour, namely (strongly) decaying oscillation. Incidentally it is worth noting that, although a sharp peak follows the removal of the forcing at $t = 750$, there is no lasting effect on the simulation stemming from this singular alteration in boundary conditions.

Keeping the same Reynolds number value and reverting to the jet-like excitation we progressivley increase the amplitude of the initially imposed perturbation. The effect of this action, as may be seen from the result presented in figure 9, is that a longer transient ensues in the nonlinear solution. In the course of this transient behaviour solutions corresponding to large initial excitation amplitudes spend time growing while their linear counterparts (the solutions which correspond to the lowest initial excitation amplitude) have long converged to their decaying state. However, this behaviour of the former solutions is only transient; eventually all calculations are seen to fall back to the linear result.

[1] This frequency was independently obtained from the EVP problem discussed in §3.1

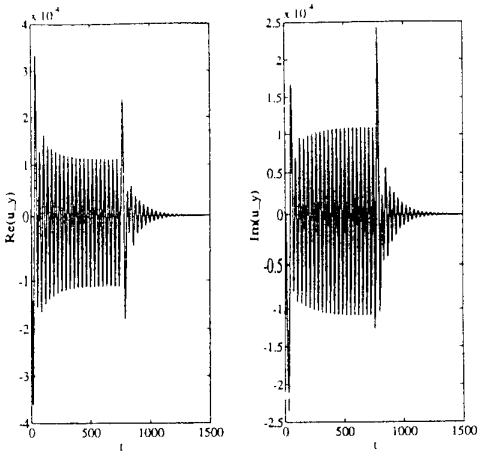

Fig. 8. Wall shear u_y dependence on time t using the ribbon-like forcing at $\bar{R} = 550$: initially a neutral wave of the imposed frequency is generated; after the forcing is being removed a decaying wave emerges.

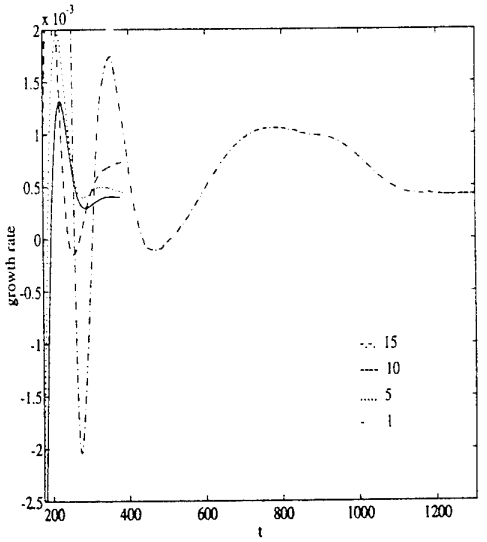

Fig. 9. Growth rates time history for increasing initial excitation amplitudes ε: Solid, $\varepsilon = 1$ (linear result); dashed, $\varepsilon = 5$; dash-dotted, $\varepsilon = 10$; dotted, $\varepsilon = 15$.

In the neighbourhood of the linear neutral loop, however, nonlinear solutions have been obtained that bifurcate (to different degrees) from the linear loop. A typical example is presented in figure 10 where the modal perturbation energy and respective growth rates of linear and nonlin-

ear computations are plotted against time at spanwise wavenumber increments of $\Delta\beta = 0.01$. This result is obtained at conditions favouring linear growth ($\bar{R} = 800$, in the neighbourhood of Branch I) utilising the jet-like form of forcing and a large initial excitation amplitude.

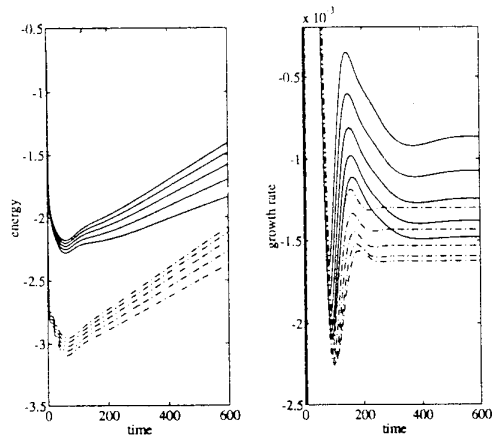

Fig. 10. Nonlinear (solid) vs. linear (dashed) results at $\bar{R} = 800$. Lower to higher: spanwise wavenumber $\beta = 0.15(.01)0.19$.

The growth rate dependence on wavenumber for both linear and nonlinear calculations is presented in figure 11; projected in figure 11 are also the (linearly interpolated) linear and nonlinear neutral loops, as well as the line of maximum amplification rate of the nonlinear calculation. Three results of significance may be observed in this figure.

Firstly, as may already be inferred from the results of figure 10, the nonlinear neutral loop is confined in a thin region around the linear loop. This result is similar to that obtained by Jiménez *et al.* (1990) and appears to support the theoretical prediction of Hall and Malik (1986).

Secondly, the consequence of the departure of the nonlinear neutral loop from the linear result is that the maximum amplification rate of the nonlinear neutral curve lies very close to the experimentally observed waves (c.f. Pfenninger and Bacon, 1969; Poll, 1979). To-date it has been assumed that the experimentally observed naturally occurring waves are Branch I instabilities. It is well known, however, that naturally occurring disturbances in Blasius flow peak near the theoretical maximum amplification and maximum amplitude ratio curves (see f.e. Poll, 1989). The present results appear to yield such a behaviour for the LEBL flow as well.

Finally, one may notice that the dependence of the maximum amplification rate on Reynolds number is very similar between the linear and nonlinear results. One may infer from the results presented in figure 11 that, in contrast with the numerical predictions of Hall and Malik (1986) and in line with a similar result of Jiménez *et al.* (1990), our nonlinear calculations on the present two-dimensional model yield a critical Reynolds number value close to that delivered by linear theory.

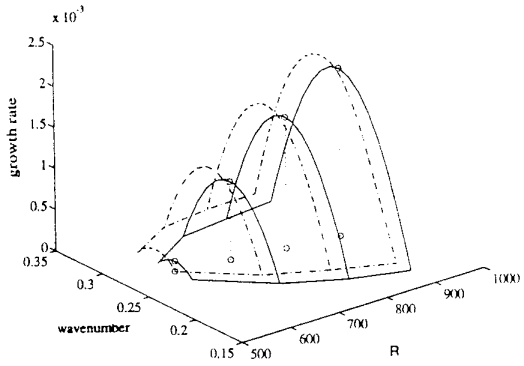

Fig. 11. Linear vs Nonlinear neutral loops; projected the line of maximum amplification rate.

5. Discussion

An effort has been made to address the issue of subcritical behaviour in incompressible two-dimensional attachment line flow. The initial-value-problem approach for the linear stability problem of Theofilis (1993) has been extended to allow for more general forms of perturbations, in an attempt to systematically relax the approximations under which the stability of incompressible leading edge boundary layer flow is studied.

In line with the numerical work of Jiménez *et al.* (1990) and contrary to the numerical conclusions put forward by Hall and Malik (1986), we failed to observe nonlinear solutions bifurcating subcritically in Reynolds number. The argument put forward by Spalart (1988) on the inability to draw conclusions on analytical models by a limited number of numerical runs still holds. However, the extent of the numerical experimentation performed on the two-dimensional model

considered presently appears to support the conclusion of Jiménez *et al.* (1990) that three-dimensional mechanisms are to be held responsible for the experimentally observed subcriticality.

The present nonlinear calculations have yielded neutral loops the location of which, in parameter space, suggests that the experimentally observed instability waves occur at (approximately) maximally amplified, rather than Branch I conditions. While work is in progress to quantify this conjecture, this result suggests that the attachment line boundary layer is, in this respect, akin to the classical Blasius flow.

References

1. Arnal, D., (1992). Boundary Layer Transition: Prediction, Application to Drag Reduction. *AGARD Rep. 786*, p.5-1.
2. Boyd, J. P., (1989). *Chebyshev and Fourier Spectral Methods*, Lecture Notes in Engineering **49**, Springer.
3. Canuto, C., Hussaini, M. Y., Quarteroni, A. and Zang, T. A., (1987). *Spectral Methods in Fluid Dynamics*, Springer Verlag, Berlin.
4. Duck, P. W., (1985). *J. Fluid Mech.* 160, p.465.
5. Görtler, H., (1955). Dreidimensionale Instabilität der ebenen Staupunktströmung gegenüber wirbelartigen Störungen. in *50 Jahre Grenzschichtforschung*, (H. Görtler & W. Tollmien eds.), p.304, Vieweg und Sohn, Braunschweig.
6. Hämmerlin G., (1955). Zur instabilitätstheorie der ebenen Staupunktströmung. in *50 Jahre Grenzschichtforschung*, (H. Görtler & W. Tollmien eds.), p.315, Vieweg und Sohn, Braunschweig.
7. Hall, P. and Malik, M. R., (1986). On the instability of a three-dimensional attachment-line boundary layer: weakly nonlinear theory and a numerical approach. *J. Fluid Mech.* , **163**, p.257.
8. Hall, P., Malik, M. R. and Poll, D. I. A., (1984). On the Stability of an Infinite Swept Attachment-Line Boundary Layer. *Proc. Roy. Soc.* **A 395**, p.229.
9. Hiemenz, K., (1911). *Dingl. Polytechn. J.* **326**, p.321.
10. Jiménez, J., Martel, C., Agüi, J. C. and Zufiria, J. A., (1990). Direct numerical simulation of transition in the incompressible leading edge boundary layer. *Techn. Note ETSIA* **MF-903**.
11. Kleiser, L., (1993). AGARD-FDP-VKI LS-06: *Progress in Transition Modelling*, VKI, Brussels, Belgium, March 29 - April 1.
12. Morkovin, M. V., and Reshotko, E., (1989). in I.U.T.A.M. SYMPOSIUM ON TRANSITION AND TURBULENCE, III, Toulouse, Springer Verlag.
13. NAG, (1992). Numerical Algorithms Group, *Mark 15*.
14. Pfenninger, W., and Bacon, J. W., (1969). Amplified laminar boundary layer oscillations and transition at the front of a 45° swept flat-nosed wing with and without boundary layer suction. in *Viscous Drag Reduction*, (C. S. Wells ed.), Plenum Press, p.85.
15. Poll, D. I. A., (1978). *College of Aeronautics* Rep. **7805**.
16. Poll, D. I. A., (1979). Transition in the infinite swept attachment line boundary layer. *The Aeronautical Quart.* **30**, p.607.
17. Poll, D. I. A., (1985). *J. Fluid Mech.* 150, p.329.
18. Poll, D. I. A., (1989). in *Computational Methods in Aeronautical Fluid Dynamics*, (P. Stow ed.), Oxford University Press, p.171.
19. Reed, H. L., (1993). AGARD-FDP-VKI LS-06: *Progress in Transition Modelling*, VKI, Brussels, Belgium, March 29 - April 1.
20. Rosenhead, L., (1963). *Laminar Boundary Layers*, Oxford University Press.
21. Spalart, P. R., (1988). Direct Numerical Study of Leading-Edge Contamination. *AGARD CP-438*, p.5-1.
22. Spalart, P. R., Moser, R. D., and Rogers, M. M. (1991). Spectral methods for the Navier-Stokes equations with one infinite and two periodic directions. *J. Comp. Phys.* **96**, pp. 297-324.
23. Stuart, J. T., (1960). *J. Fluid Mech.*, 9, p.352.
24. Theofilis, V., (1988). *M.Sc. Thesis*, Dept. of Mathematics, University of Manchester.
25. Theofilis, V., (1993). Numerical Experiments on the Stability of Leading Edge Boundary Layer Flow: A Two-Dimensional Study. *Int. J. Numer. Methods Fluids*, **16**, p.153.
26. Theofilis, V., (1994). The Discrete Temporal Eigenvalue Spectrum of the Generalized Hiemenz Boundary Layer Flow as Solution of the Orr-Sommerfeld Equation., *Journal Eng. Math.* , (to appear in Vol. **28**).
27. Watson, J., (1960). *J. Fluid Mech.*, 9, p.371.
28. Wilkinson, J. H., (1965). *The Algebraic Eigenvalue Problem*, Clarendon.
29. Zang, T. A., Krist, S. E., and Hussaini, M. Y., (1989). *J. Sci. Comp.*, **4**, vol. 2, pp.197-217.

SPATIAL DIRECT NUMERICAL SIMULATION OF BOUNDARY LAYER TRANSITION UNDER STRONG ADVERSE PRESSURE GRADIENT

H. Bestek, M. Kloker, W. Müller
Institut für Aerodynamik und Gasdynamik
Universität Stuttgart
Pfaffenwaldring 21
70550 Stuttgart, Germany

SUMMARY

Laminar-turbulent breakdown of a strongly decelerated Falkner-Skan-type boundary layer (Hartree-Parameter β_H=-0.18) is investigated by direct numerical simulations using the complete Navier-Stokes equations for three-dimensional incompressible flows. The numerical method is based on the so-called spatial model, and allows for simulations of spatially evolving three-dimensional disturbance waves in a two-dimensional growing boundary layer. Transition is initiated by 2-D and a pair of oblique 3-D waves, both with small amplitudes, excited periodically within a narrow disturbance strip at the plate surface. Their streamwise (linear and subsequent nonlinear) evolution resulting in the fundamental breakdown of laminar flow is simulated with high spatial resolution. It is observed that the fundamental breakdown process under adverse pressure gradient is dramatically more complex than the well-known K-breakdown in the Blasius flow: In addition to the (upper) high-shear layer on top of the lambda-vortex, a (lower) characteristic high-shear layer is formed simultaneously in between neighbouring lambda-vortices. This shear layer, induced by a secondary vortex system close to the wall, precipitates ultimate breakdown to turbulence.

Finally, some results of preliminary studies on the effect of suction on boundary-layer transition are presented that demonstrate the great potential of spatial direct numerical simulations for applied transition research in flows of practical interest.

1. INTRODUCTION

Transition in wall-bounded shear flows, such as boundary layers, flow through pipes and channels, etc., is a spatially evolving complicated process influenced by many factors. In natural boundary-layer transition this process is initiated by random environmental disturbances such as freestream turbulence, sound, vibrations etc. that enter the boundary layer and generate instability waves [1-3]. This first part of the transition process is called *receptivity* and is still not well understood. In the second part, the resulting disturbances grow while proceeding downstream in the unstable laminar boundary layer, and finally develop through several nonlinear stages of increasing complexity into a turbulent flow. The type of transition development that occurs is dependent on many parameters, such as nature, amplitude, and spectrum of initial disturbances, as well as on parameters affecting the stability properties of the basic flow (pressure gradient, roughness, wall curvature, sweep angle etc.).

In order to reduce the number of these parameters, transition research has focussed on "controlled" transition in simple model flows, such as the plane Poiseuille (channel) flow and the Blasius boundary-layer flow over a flat plate. In controlled experiments in flat-plate boundary layers (see [4-7], for example), a vibrating ribbon is used to periodically excite two-dimensional disturbance waves. The streamwise evolution of the disturbances into turbulent flow is then observed using flow visualization and hot-wire measurements. Several stages of disturbance development have been identified. Initially, small two-dimensional disturbances (Tollmien-Schlichting waves) are gradually amplified with growth rates adequately described by linear stability theory [8]. As soon as the TS-waves have gained sufficiently large amplitudes, the flow becomes unstable with respect to three-dimensional disturbances (secondary instability). Essentially two different secondary instability mechanisms have been identified by secondary stability theory, namely, subharmonic resonance and fundamental resonance [9]. For the fundamental-type breakdown, subsequent stages lead to peak-valley splitting, formation of lambda-shaped vortices together with high-shear layers, and breakdown of the high-shear layer as indicated by spikes in the disturbance velocity hot-wire signals. The lambda vortices are aligned along their peaks in streamwise direction, repeating every TS-wavelength until breakdown. In contrast, for the subharmonic-type breakdown, the lambda-vortices are staggered, repeating at a streamwise distance of twice the TS-wavelength.

In addition to experimental and theoretical work, direct numerical simulations based on the solution of the complete 3-D Navier-Stokes equations have played an increasingly important role in transition research in the past decade. The basic approach is similar to that of controlled experiments. Some regular perturbations are introduced into the integration domain, and their subsequent unstable, nonlinear development is calculated numerically. Two basically different kinds of numerical models are in use, the "temporal model" and the "spatial model". Both models have their own advantages and shortcomings, as discussed in the recent review by Kleiser & Zang [10].

In the temporal model it is assumed that the disturbances are periodic in streamwise direction and that the evolution occurs in time, while the base flow is assumed to be parallel. Due to the periodic boundary conditions, a short integration domain extending only over one or two disturbance wavelengths can be used. Numerical schemes are therefore much easier to develop and numerical computations using the temporal model are less expensive compared to simulations with the spatial model. The integration domain can be moved downstream with the disturbances to approximately model a possible streamwise change in the base flow and to somehow represent the spatial disturbance development observed in experiments. Most of the transition simulations reported in the literature are based on this temporal model (see [10]), where, for the case of controlled transition in plane Poiseuille and Blasius flow, good qualitative and to some extent quantitative agreement with experiments was achieved. However, the disadvantages of the temporal approach result from the underlying simplifying assumptions. Therefore, for base flows exhibiting strong streamwise variations (caused by pressure gradients, steps, etc.), the temporal model cannot be employed.

In contrast, in the spatial model the streamwise evolution of disturbances is simulated in a fixed integration domain extending over a large downstream distance. With this model realistic simulations of controlled experiments even in flows under strong adverse pressure gradient, as presented in this paper, are possible.

Paper presented at the 74th Fluid Dynamics Symposium on "Application of Direct and Large Eddy Simulation to Transition and Turbulence" held at Chania, Crete, Greece, in April 1994.

However, the development of a numerical method is much more difficult, especially due to the required outflow conditions and for reasons of numerical stability. Also, the demands on computer resources are very high. In both models periodicity of the flow in spanwise direction is assumed.

In the past several years numerical methods for solving the complete Navier-Stokes equations based on the spatial model have been developed and successfully applied for transition research at the University of Stuttgart [11-21]. The capability of these methods has been convincingly demonstrated by simulations of two different transition experiments. Rist [14, 16] performed a simulation of the vibrating-ribbon experiments by Kachanov et al. [6, 7] for the fundamental breakdown in a Blasius boundary layer, and Konzelmann [15, 17] simulated the nonlinear development of a three-dimensional wave packet in a Blasius boundary layer according to the wave-packet experiments by Gaster & Grant [22]. For both simulations, the numerical results showed excellent quantitative agreement with the experimental measurements.

The effects of a (strong) streamwise pressure gradient on the nonlinear evolution of the transition process are widely unknown. Controlled experiments have not yet been performed, due to the great difficulties arising from the proneness to separation and the strong disturbance growth in these flows. The instability mechanisms are now both of viscous and inviscid nature [8, 9]. In this paper, the simulation of a fictitious, controlled experiment of transition in such a flow, a strongly decelerated Falkner-Skan-type boundary layer, is presented.

Since the spatial model is capable to consider streamwise variations of the basic flow, it offers the possibility to investigate also the effects of other parameters on transition that may be present in flows of practical interest, as, for example, the effects of suction through porous strips. This is shown for the effect of a single suction strip on controlling the initial nonlinear stages of transition in a strongly decelerated Falkner-Skan-type boundary layer. It is demonstrated that the numerical method may also be applied to a boundary-layer flow over an airfoil with distributed suction.

2. NUMERICAL MODEL

As shown schematically in Fig. 1, a finite rectangular box is selected to represent a certain region of a boundary-layer flow on a flat plate. In the chosen coordinate system, the integration domain extends in the streamwise direction from $x=x_0$ to $x=x_N$, where x_0 is downstream of the leading edge of the flat plate. The integration domain in the normal direction extends from $y=0$ to $y=y_U$ and typically covers several boundary-layer thicknesses. In the spanwise direction, the flow is assumed to be periodic with the domain extending from $z=0$ to $z=\lambda_z$ (λ_z- basic spanwise wavelength).

The numerical method allows for simulations of spatially evolving, three-dimensional disturbance waves in a two-dimensional growing boundary layer. The simulation is performed in two steps. First, the steady two-dimensional base flow is calculated, i.e. a boundary layer under effect of a streamwise pressure gradient (and suction through a narrow suction strip, if applied).

Then, in the second step, disturbances are introduced through a narrow spanwise strip at the wall (shown schematically in Fig. 1). Whereas in most experiments disturbances are generated by a vibrating ribbon, in our simulations the disturbances are introduced by timewise periodic blowing and suction within the disturbance strip. With a given frequency and spanwise wavelength, different kinds of two-dimensional and pairs of three-dimensional oblique Tollmien-Schlichting waves as well as longitudinal vortices can be generated (see [13] for details). The streamwise evolution of these disturbances is calculated by solving the unsteady three-dimensional Navier-Stokes equations. The so-called non-parallel effects, and also all nonlinear effects involved in the transition process are included in the model. Thus, the numerical model can be regarded as a numerical simulation of a "controlled" transition experiment in which some sort of a wavemaker is used to generate controlled disturbance waves.

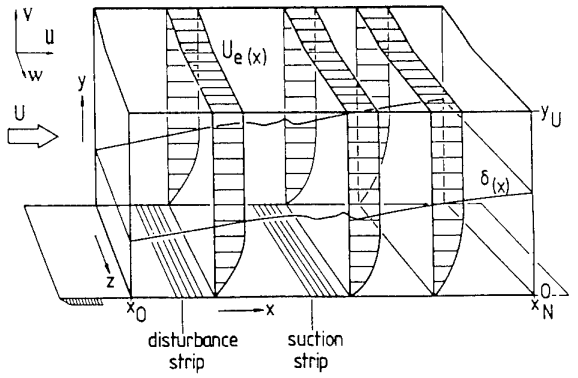

Fig. 1 Integration domain

2.1 Governing Equations

The numerical method is discussed in detail by Kloker et al. [20, 21]. Therefore, only the main features are given here. The numerical method is based on the three-dimensional Navier-Stokes equations for incompressible flow in vorticity-transport formulation. The vorticity components are denoted by ω_x, ω_y and ω_z, and u, v and w are the velocity components in the x, y and z directions, respectively (see Fig. 1). All variables are nondimensionalized with a reference length L and the free stream velocity U_∞. The nondimensional variables relate to the corresponding dimensional ones (denoted by bars) as

$$x = \frac{\bar{x}}{L}\,,\quad y = \frac{\bar{y}}{L}\sqrt{Re}\,,\quad z = \frac{\bar{z}}{L}\,,\quad t = \bar{t}\,\frac{U_\infty}{L}$$
$$u = \frac{\bar{u}}{U_\infty}\,,\quad v = \frac{\bar{v}}{U_\infty}\sqrt{Re}\,,\quad w = \frac{\bar{w}}{U_\infty}\,. \qquad (2.1)$$

The Reynolds number is $Re = U_\infty L/\bar{\nu}$ ($\bar{\nu}$ - kinematic viscosity). The three vorticity components are defined as

$$\omega_x = \frac{1}{Re}\frac{\partial v}{\partial z} - \frac{\partial w}{\partial y}$$
$$\omega_y = \frac{\partial w}{\partial x} - \frac{\partial u}{\partial z} \qquad (2.2)$$
$$\omega_z = \frac{\partial u}{\partial y} - \frac{1}{Re}\frac{\partial v}{\partial x}\,.$$

The flow variables are decomposed into those of the two-dimensional base flow (index B) and of the disturbance flow (denoted by a prime)

$$u = u_B + u', \qquad \omega_x = \omega_x',$$
$$v = v_B + v', \qquad \omega_y = \omega_y', \qquad (2.3)$$
$$w = w', \qquad \omega_z = \omega_z' + \omega_{zB}\,.$$

Consequently, for the steady base flow one vorticity transport equation for ω_{zB} and two Poisson-equations for u_B and v_B have to be solved. The calculation of

the disturbance flow is based on three vorticity transport equations (in conservative formulation) for the vorticity components and three Poisson-equations for the three velocity components. The detailed set of equations is given by Kloker et al. [20]. It is emphasized, that no simplifications are introduced using this formulation. A variation of the mean flow, as generated by nonlinear interactions, is represented by a non-vanishing time average of the disturbance flow.

2.2 Boundary Conditions

For the base flow, the streamwise pressure gradient is imposed by prescribing the streamwise velocity distribution $u_e(x)$ of the external flow at the freestream boundary, assuming inviscid flow. For the simulations discussed in this paper, $u_e(x)$ is chosen according to a strongly decelerated Falkner-Skan-type boundary layer with Hartree-Parameter β_H=-0.18. However, $u_e(x)$ may also be taken from an experiment to represent the velocity distribution of an airfoil as shown in section 5. At the inflow boundary, Falkner-Skan profiles corresponding to the imposed distribution of the streamwise pressure gradient are specified for the base flow variables. At the outflow boundary, all equations are solved neglecting the terms containing the factor 1/Re (second x-derivatives). At the wall, the velocity components are zero (except for the suction strip, if applied). The effect of suction through a porous strip is simulated by prescribing a normal velocity distribution $v_{B,0}(x)$ at the wall, as sketched in Fig. 10. One or more suction strips with variable spacing and different suction rates may be applied.

For the three-dimensional disturbance flow, all velocity components are zero at the wall, except within the disturbance strip, where the normal velocity component v' can be prescribed as a function of x, z, and t in order to introduce controlled time-periodic two- and three-dimensional disturbance waves. At the freestream boundary, vanishing vorticity fluctuations and an exponential decay of the velocity disturbances are assumed. At the inflow boundary, all velocity and vorticity disturbances are set to zero. As for the outflow boundary, the implementation of appropriate, non-reflecting outflow conditions is of crucial importance for the feasibility of numerically stable and reliable simulations up to late breakdown stages or developed turbulence. Here we use the newly introduced method of "artificial relaminarization" (see Kloker et al. [20]). An artificial decay of disturbances is enforced in a region somewhat upstream of the outflow boundary to substantially (orders of magnitude) reduce the disturbance level at this boundary. This is achieved by direct suppression of the disturbance vorticity vector. Thus, possible undue reflections caused by large amplitude, broad-band disturbances passing the outflow boundary are prevented.

2.3 Numerical Method

For the numerical solution of both the base flow and the disturbance flow equations a fourth-order accurate finite-difference discretisation on a uniform grid is employed in streamwise direction and normal to the wall, which allows a proper treatment of the effects of a varying boundary layer.

For the calculation of the base flow, the vorticity transport equation is solved with a semi-implicit, temporally dissipative time-stepping technique to march to steady state. The v_B-Poisson equation is solved with a vectorizable, stripe pattern Gauß-Seidel-like line iteration and the u_B-equation is directly solved.

The discretisation in spanwise direction for the disturbance flow is done by using a spectral ansatz

$$f'(x,y,z,t) = \sum_{k=-K}^{K} F_k(x,y,t)e^{ik\gamma z} \qquad (2.4)$$

to exploit the periodicity with respect to z, where the complex F_k represent all disturbance variables in spectral space, and γ is the basic spanwise wavenumber calculated from $\gamma = 2\pi/\lambda_z$. Since all flow variables are real, the relation $F_{-k} = F_k^*$ holds, where the asterisk denotes the complex conjugate. Additionally, for flow symmetry to z=0, the F_k's are purely real for u', v', ω_z' and purely imaginary for w', ω_x' and ω_y'.

For the disturbance flow, the integration in time is performed with a fourth-order accurate Runge-Kutta scheme. The four stages per time step of this scheme are coupled with a centered-upwind-downwind-(and vice versa)-centered discretisation for the x-convection terms. This technique ensures numerical stability by effective damping of high wavenumber (larger than aprox. $\pi/2\Delta x$) components in the solution, that are represented unacceptably inaccurate by the spatial discretisation on the used grid and lead, if undamped, to spurious, growing oscillations. The nonlinear terms are computed using a pseudospectral method. The v'-Poisson equation is solved with a multigrid method, using a vectorizable, stripe-pattern SOR line-iteration technique on each grid. The u'- and w'-Poisson equations are directly solved.

For all results presented in this paper, the Reynolds number is $Re=10^5$ (U_∞=9.09m/s, L=0.165m, $\nu=1.5*10^{-5}$ m^2/s), if not otherwise stated. The calculations were performed on the Cray-2 of the Stuttgart university computer center.

2.4 Code Validation

For controlled transition in boundary layers, the numerical method was carefully validated, both, for the Blasius flow and for flows with streamwise pressure gradient, by extensive comparisons with results from linear (spatial) stability theory and secondary stability theory (see [11, 18, 21]). The agreement for the spatial amplification rates, and for the amplitude and phase distributions, as obtained from Fourier-analysis of the unsteady flow-field data, was generally very good.

For the Blasius case, the simulation of the vibrating-ribbon experiments by Kachanov et al. [6, 7] showed quantitatively very good agreement with measured hot-wire data up to the appearance of multi-spikes in the u' time-signals [14, 16].

3. FUNDAMENTAL BREAKDOWN UNDER ADVERSE PRESSURE GRADIENT

The goal of this study was to explore the effects of a strong streamwise adverse pressure gradient on the evolution of the transition process. These effects are widely unknown, as controlled experiments have not yet been performed for this type of base flow, due to the great difficulties arising from the strong disturbance growth in these highly unstable flows. Therefore, the present study may be regarded as a numerical simulation of a "fictitious" vibrating-ribbon transition experiment performed in a strongly decelerated Falkner-Skan-type boundary layer (Hartree-Parameter β_H=-0.18, u_B-profile near separation), denoted subsequently by Case 2.

The numerical simulations were performed by M. Kloker and are discussed in more detail in his dissertation [21]. The results presented in this paper are of exemplary nature, and were selected in order to demonstrate that direct spatial simulations have reached a state of development where they can be used to explore flow phenomena that are not previously known from experiments. The results will also show the considerable details that can be captured with such simulations. We will concentrate here on comparing some of the complex flow structures associated with transition under strong adverse pressure gradient with the well-known structures in a transitional Blasius flow as obtained from a numerical simulation of the vibrating-ribbon experiments by Kachanov et al. [6, 7], denoted by Case 1. This simulation was originally performed by Rist [14, 16], however,

in this paper results from a more recent simulation of the same experiments are shown that was performed by Kloker (see [21]) using a much finer spatial resolution. The computer resource limits of the Cray-2 were fully exploited in this case. In both cases the fundamental-type breakdown is triggered by the input at the disturbance strip.

3.1 Reference Case: Fundamental Breakdown for Zero Pressure Gradient

In the experiments by Kachanov et al. the boundary layer flow over a flat plate was periodically disturbed by a vibrating ribbon at x = 250mm ($Re_{\delta_1} \approx 670$, δ_1=displacement thickness) distance from the flat-plate leading edge. A spanwise row of small pieces of tape was glued on the plate surface underneath the ribbon in order to induce three-dimensional disturbances with a fixed spanwise wavelength λ_z.

In fact, such a disturbance generates a system of small-amplitude longitudinal vortices. In direct succession, this system interacts nonlinearly with the large amplitude 2-D wave producing a pair of oblique 3-D waves with the frequency of the 2-D wave and spanwise wavelengths $\pm\lambda_z$. This phase-locked combination of fundamental disturbance waves grows while propagating downstream and generates higher harmonics in the frequency-spanwise-wavenumber spectrum. The disturbance amplitudes in physical space exhibit "peaks" and "valleys" in spanwise direction (see Fig. 5a), half a spanwise wavelength $\lambda_z/2$ apart.

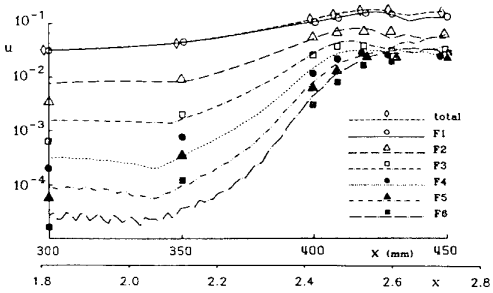

Fig. 2 Downstream amplitude development of various wave components at spanwise peak position for Case 1. Comparison with experiments (symbols [7]).

In the experiment the disturbance development was measured between x=300mm and x≈700mm using hot-wire probes. From these measurements a considerable amount of information about the spatial and temporal three-dimensional disturbance development is available through the detailed measurement and analysis of the u-velocity component, while there is no information about the v- and w-velocity components. The detailed information about one velocity component is very valuable for the validation of the numerical results. Once validated, on the other hand, the numerical simulation provides the complete flow field without the presence of extra disturbances caused by measuring devices.

In Fig. 2 results of the numerical simulation between x=300mm and x=450mm were compared with these measurements. The maximum amplitude of the downstream velocity disturbance component u' and its frequency harmonics are shown. The harmonic with primary frequency (i.e. the frequency of the vibrating ribbon) is labelled *F1*, while *F2* to *F6* denote the higher harmonics, with *F6* having six times the frequency of the fundamental, for example. As the disturbances in the numerical simulation are generated by periodic blowing and suction through the flat plate, they show a different initial behavior between x=300mm and x=350mm. Downstream of this region, the agreement between simulation and experiment is improving towards an excellent agreement. All harmonics show a steady increase until a maximum is reached near x=420mm to x=430mm, the position where the first spikes could be observed in the experimental hot-wire signals. More detailed comparisons with the experimental results are given by Rist [14].

An overall view of the dynamic processes involved in the K-breakdown process in the Blasius flow can be obtained from Fig. 3, where the instantaneous ω_z vorticity contours at the spanwise peak and valley positions are shown. At the peak position (Fig. 3a), the formation and subsequent breakdown of the instantaneous high-shear layer into smaller vorticity concentrations can be observed, leading to a totally chaotic motion resembling that of a turbulent boundary layer. In contrast, the disturbance development at the valley position (Fig. 3b) shows no outstanding characteristic structures at this stage. Correspondingly, the disturbance amplitudes at the valley position decrease at first, and start to grow fast not until downstream of the shear-layer breakdown at the peak position (see Fig. 5a).

As the numerical simulation yields more information about the flow field than the experiments, we are able to visualize the dominant flow structures of the transition process by a number of different visualization techniques. Some examples for such visualizations are given in Figs. 7a and 8a, where iso-surfaces of ω_x and ω_z are plotted in three-dimensional perspective view. The iso-surfaces consist of iso-contours $|\omega_x|$=const., and ω_z=const., respectively, calculated at successive downstream x positions and plotted in perspective view. The spanwise section considered here covers one wavelength λ_z, extending from z=0 to z=-λ_z. The spanwise peak position of the disturbance development is located at z=-$\lambda_z/2$, while the valley positions are at z=0 and z=-λ_z. The iso-surfaces $|\omega_x|$=const. in Fig. 7a visualize longitudinal vortical structures orientated in streamwise direction, which represent the "legs" of a developing lambda-vortex. The iso-surfaces ω_z=const. in Fig. 8a enclose the regions of high shear, and show a tongue-like structure of the high-shear layer, which is developing above the lambda-vortex. Both observations are in good agreement with other experimental observations.

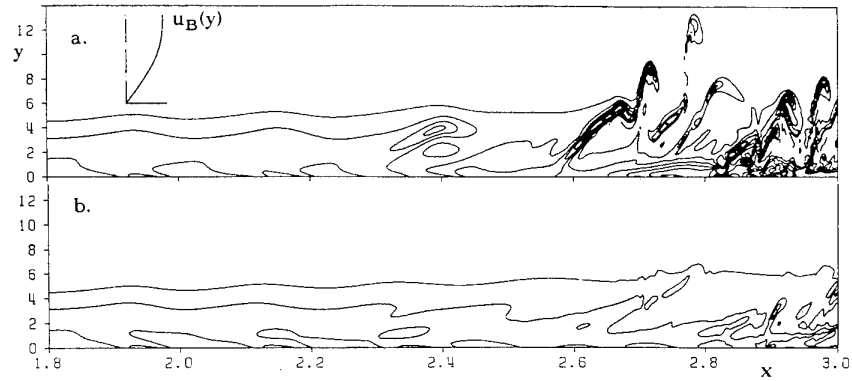

Fig. 3

Longitudinal sections of the flow field, showing instantaneous (t/T=11.4) spanwise vorticity (ω_z) contours at spanwise peak (a) and valley (b) position for Case 1 without pressure gradient (simulation of experiments by Kachanov et al. [6, 7]).

3.2 Fundamental Breakdown under Strong Adverse Pressure Gradient

For this simulation (Case 2) a strongly decelerated boundary layer with Hartree-Parameter β_H=-0.18 was chosen as the base flow and calculated as described in section 2. The corresponding flow configuration is shown in Fig. 4 together with the streamwise variation of the velocity profiles u_B and the vorticity profiles ω_{zB} of the base flow. The adverse pressure gradient causes a shift of the position of the maximum base-flow vorticity ω_{zB} away from the wall into the boundary layer and forces the flow to almost separate.

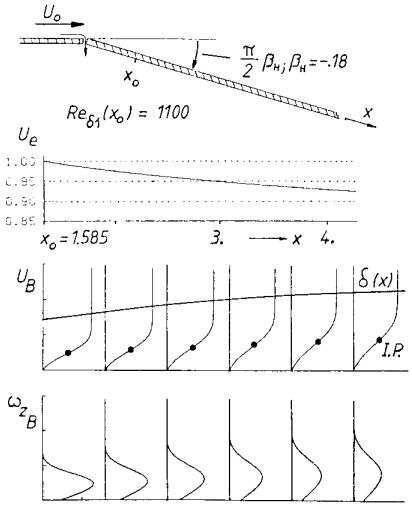

Fig. 4 A schematic of a strongly decelerated Falkner-Skan boundary layer (Hartree-Parameter β_H=-0.18) I.P. - Inflexional Points

For this simulation, up to 1850 grid points in the x-direction (corresponding to 80 points per initial wavelength λ_x), and 121 grid points in the y-direction were used. In the spanwise z-direction 40 de-aliased modes (K=40 in eq. (2.4)) were used. In the time direction, 19 periods of the disturbance frequency were calculated, with the intervals varied from 175 per period for the linear stages to 350 per period for the nonlinear stages of disturbance development, resulting in a total of calculated 5250 time steps.

Transition was initiated by introducing a 2-D wave with frequency F=1.08 ($F=\overline{\beta\nu}/U_\infty^2 * 10^4$) and a pair of oblique 3-D waves with identical frequency and γ=30.6 at the disturbance strip to enforce fundamental breakdown. The disturbances were introduced between x_1=2.08 and x_2=2.29 ($Re_{\delta_1}(x_2)$=1303) into the flow, both with very small amplitudes ($u'_{2D}/U_\infty=10^{-5}$, $u'_{3D}=2u'_{2D}$). At first, both modes grow according to linear instability, followed by the onset of fundamental resonant growth of the 3-D mode and the simultaneous, nonlinear generation of the so-called longitudinal vortex mode [18, 21]. It should be noted that, in the presence of a sufficiently large 2-D wave, the existence of a longitudinal vortex mode is inherently connected with the presence of a pair of oblique 3-D waves, and vice versa. Thus, if one mode is part of the disturbance input, the other is nonlinearly generated. Therefore, characteristic differences in the fundamental breakdown between the two cases investigated in this paper are not due to the disturbance input.

It was observed that the fundamental breakdown process under adverse pressure gradient evolves rapidly and quite different than in the Blasius flow. The streamwise evolution of the total u'-disturbance amplitudes at different spanwise positions for the two cases are compared in Fig. 5. From Fig. 5b it is obvious, that the terms "peak" and "valley" positions, as used for the Blasius flow to distinguish between spanwise regions of large and low disturbance amplitude growth in the fundamental breakdown process (Fig. 5a), seem to be not appropriate for the breakdown under adverse pressure gradient, as there are only minor differences in the disturbance growth along these spanwise positions. Therefore, we will use the term "co-peak" for this spanwise position (half a spanwise wavelength apart from the peak position), where the largest amplitudes occur except for those at the peak position.

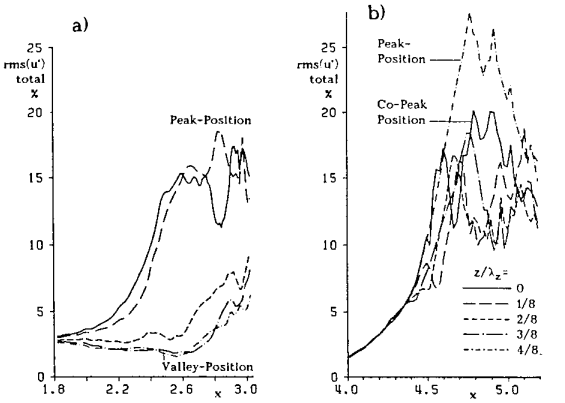

Fig. 5 Streamwise evolution of the total u'-distubance amplitudes at different spanwise positions z/λ_z for (a) Case 1 and (b) Case 2.

The final breakdown stages, visualized in the same manner by instantaneous ω_z-vorticity contours as in Fig. 3 for Case 1, are shown in Fig. 6. At the spanwise peak position, a qualitatively similar formation of a high-shear layer can be observed, albeit more intense due to the larger amplitudes (see Fig. 5), and undergoing a more rapid breakdown. Drastic differences, however, appear in the plane at the spanwise co-peak position, which is the valley plane in Case 1. Now, in addition to the "upper" high-shear layer at the peak position, a "lower inverted" high-shear layer evolves close to the wall. The inverted layer, generated by a downstream travelling, instantaneous separation zone (see the streamline plot inserted in Fig. 6b) merges with a second high-shear layer, both together crossing the entire boundary layer. Thus, they are separating very slow, partly recirculating fluid from the energetic motion above. The break-up of this very unstable layer into smaller structures occurs obviously *earlier*, i.e. further upstream, than the shear-layer decay at the peak position.

It is therefore not surprising that the flow structures associated with the nonlinear disturbance development are also different from those in the Blasius flow. In Figs. 7b and 8b, iso-surfaces $|\omega_x|$=const. and ω_z=const. visualize longitudinal vortical structures and instantaneous high-shear layers, respectively, at a comparable stage of disturbance development as shown for Case 1 in Figs. 7a and 8a. Without going into detail, from a comparison of the structures of both cases it is quite obvious that the breakdown to turbulence under adverse pressure gradient evolves much more dramatically with major differences with respect to the disturbance evolution in the "valley" and "co-peak" positions, respectively. In Fig. 8b the formation of a "lower" inverted high-shear layer at the co-peak position is clearly visible. This high-shear layer is induced by a secondary vortex system located underneath close to the wall, which is visible in Fig. 7b downstream of x≈4.57.

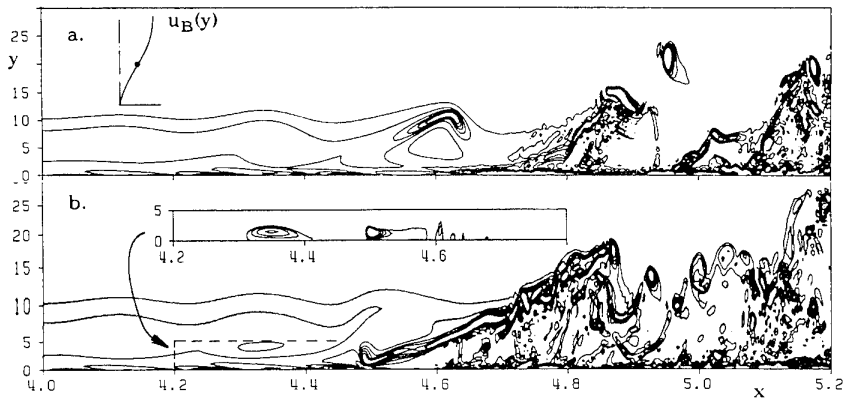

Fig. 6

Same as Fig. 3, now at t/T=18.4 for Case 2:
(a) peak station (z/λ_z=0.5)
(b) co-peak station (z=0).
Inserted in (b):
Instantaneous streamlines showing local separation zones.

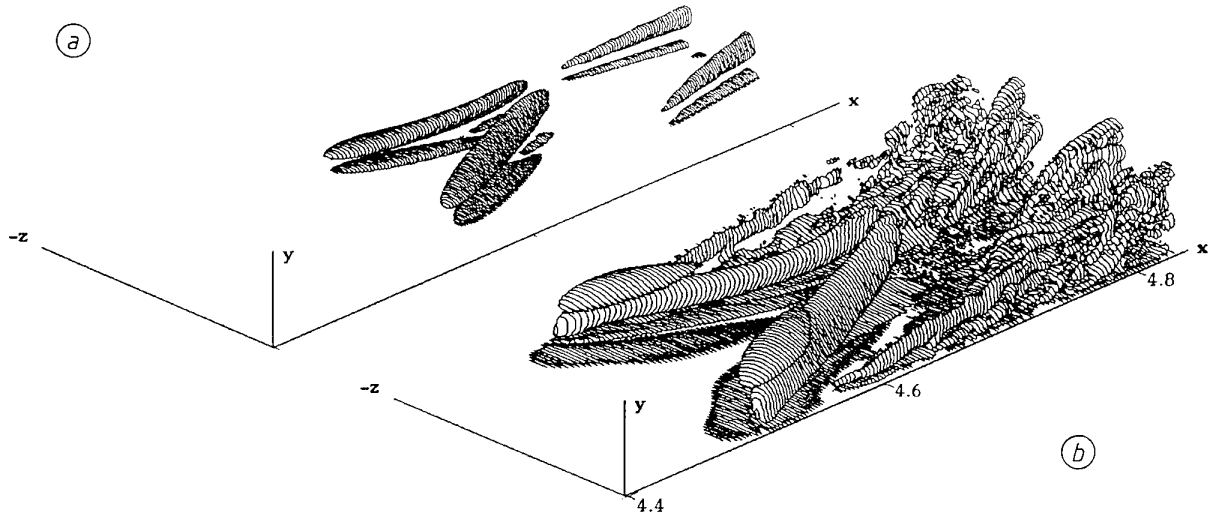

Fig. 7 Perspective view of instantaneous longitudinal vortical structures for the fundamental breakdown in (a) Case 1 and (b) Case 2.
Visualization by iso-surfaces $|\omega_x|$=0.08 in a streamwise domain covering Δx=0.45.

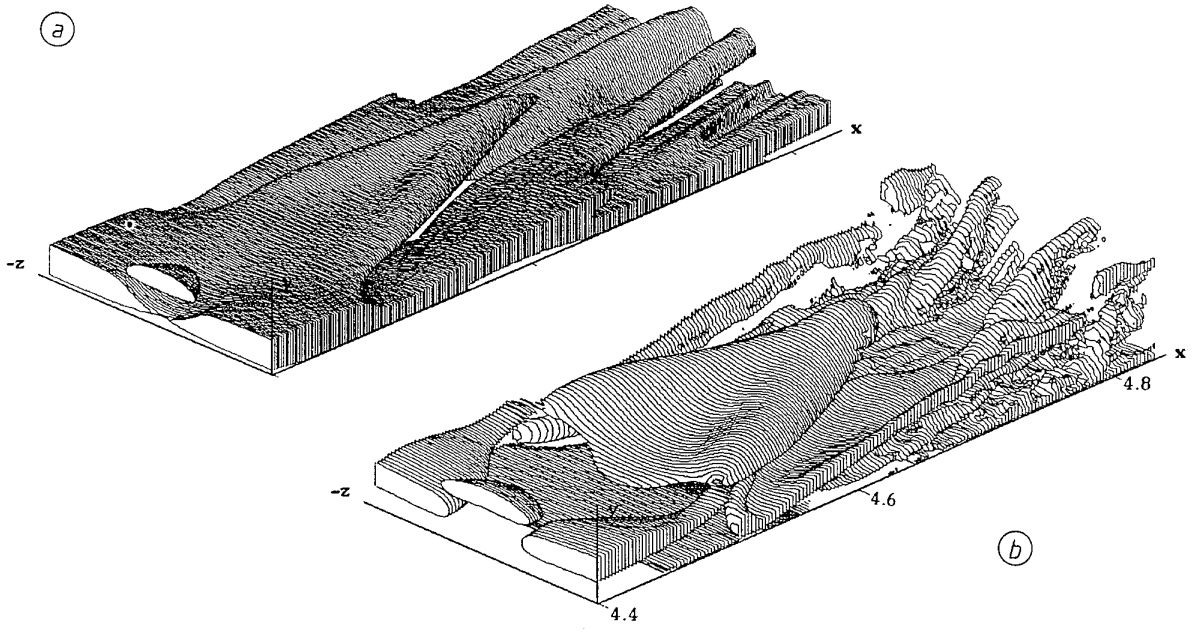

Fig. 8 Perspective view of instantaneous high-shear layers for the fundamental breakdown in (a) Case 1 and (b) Case 2.
Visualization by iso-surfaces ω_z=0.2 (a.) and iso-surfaces ω_z=0.1 (b.).

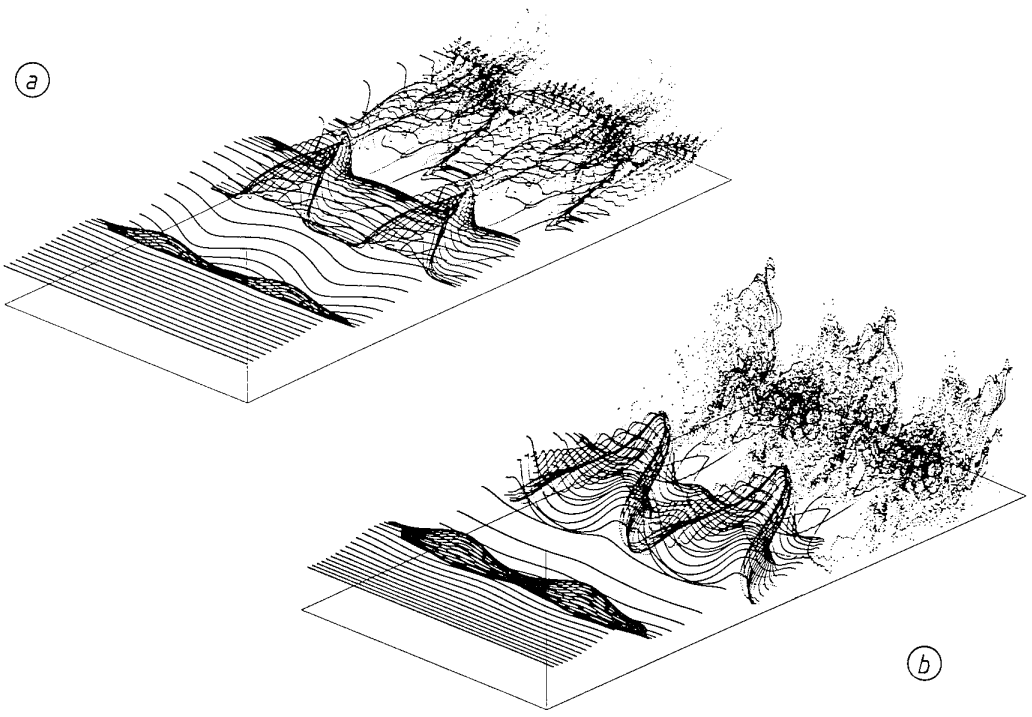

Fig. 9 Perspective view of instantaneous lambda-shaped vortices for the fundamental breakdown in (a) Case 1 and (b) Case 2.
Visualization by passive particles released from a horizontal wire in a streamwise domain covering $\Delta x=0.7$.

Finally, in Fig. 9, the flow structures are visualized by numerically generated particle-lines as they can be generated experimentally by the hydrogen bubble technique (in water flow) using a horizontal wire placed near the y-position of the critical layer. The particle-lines are plotted in perspective view likewise the iso-surfaces in Figs. 7 and 8, with the difference that the spanwise section considered here now covers two wavelengths λ_z. For Case 1, the numerically generated particle-lines develop into lambda-vortex structures that are separated by straight lines in the valley positions, while for Case 2, the formation of inverted lambda-shaped vortices are observed at these spanwise positions. The rapid spatial redistribution of particles in Case 2 documents the violent transition process.

Detailed investigations of the disturbance evolution, the formation of transitional structures, and the various flow phenomena observed from this simulation are discussed in [21].

3.3 Computational Aspects

The supercomputer resources needed for the calculation of the results presented in section 3 were very high. For Case 1, up to 4600 grid-points in x, 121 grid-points in y, and 15 (de-aliased) Fourier components in z have been used. With this discretisation 220 Megawords of memory of the Cray-2 were needed to run the simulation. The numerical integration of the Navier-Stokes equations was performed over 7160 discrete time levels, producing a total amount of ~2 Terabytes of flow-field information (of which only 1/1000 could be stored on tape). The cpu-time for the simulation added up to ~400 hours, which is equivalent to 17 days. Since it is impossible to continuously run such a large job during regular operation time of the supercomputer, the simulation had to be split into much smaller over-night and weekend jobs. Including the time necessary to analyse intermediate results (which is necessary to decide whether the simulation should be continued or not in the planned way), the simulation took more than half a year.

For Case 2, up to 1850 grid points in x, 121 in y, and 40 de-aliased modes in the z direction have been used. The necessary storage capacity was only 128 Megawords, namely due to (i) the use of an effective treatment of the outflow region using an "artificial relaminarization" zone [20] that enables a relatively short integration domain without undue upstream influence by the outflow boundary conditions, and (ii) due to the use of a special integration scheme improved with respect to numerical stability. The cpu-time for the simulation was 150 hours.

4. EFFECT OF A SINGLE SUCTION STRIP

Transition delay using wall suction is under consideration for laminar flow control (LFC) of aircraft wings. Suction is used to affect the initial stage of the transition process characterized by linear growth of small disturbances in the laminar boundary-layer flow. The application of suction acts to alter the mean-velocity profile in such a way that it is more stable with respect to the growth of small disturbances. The goal of LFC is to extend this regime of linear disturbance development as far downstream as possible to maintain laminar flow. Suction may be applied through spanwise slots or porous surfaces such as perforated plates. An array of spanwise porous suction strips located at suitable intervals allows for minimizing the amount of suction necessary to keep the boundary layer laminar. For the design of efficient strip configurations with the optimal number, spacing, and suction rate, the stability characteristics of the altered mean flow needs to be determined. For such calculations the mean flow must first be determined as accurately as possible. Nayfeh & El-Hady [23] used a nonsimilar boundary-layer code to

solve this problem. However, boundary-layer calculations fail to account for upstream influence. Reed & Nayfeh [24] proposed a numerical-perturbation scheme for determining the stability of flows over discrete suction strips using closed-form linearized triple-deck solutions of the flow due to the strips. Their results show good agreement with the experiments by Reynolds & Saric [25]. The effect of suction on the secondary instability in Blasius and Falkner-Skan flows was investigated in a recent paper by El-Hady [26] using primary and secondary instability-theory calculations.

The basic element of a suction configuration is a single suction strip. In the numerical model the effect of suction through a porous strip (see Fig. 1) is simulated by prescribing a normal velocity distribution $v_{B,0}(x)$ at the wall as sketched in Fig. 10. One or more suction strips with variable spacing and different suction rates may be applied. In order to validate the code for the effect of suction through porous strips, experiments by Reynolds & Saric [25] in a Blasius boundary layer with suction through discrete spanwise porous strips were simulated previously [19, 27]. Good agreement with the experimental data was observed for a case with one suction strip [19], as well as for a case with six suction strips [27] compared with theoretical results by Reed & Nayfeh [24]. With these thourough checks the suitability of the present numerical procedure to simulate the spatial disturbance development in a boundary layer with suction is emphasized.

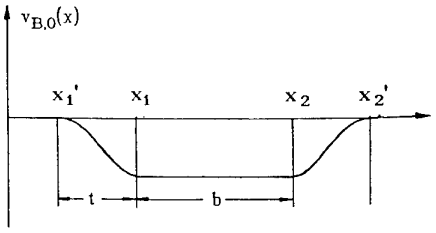

Fig. 10 Normal-velocity distribution at the wall for the simulation of a suction strip

In this section we present some results of preliminary numerical studies of the effect of a single suction strip on controlling the initial nonlinear stages of transition in a boundary layer with strong adverse pressure gradient. Emphasis is placed on investigating the upstream and downstream variation of the mean flow and its stability characteristics due to a single suction strip. The simulations were performed for the same simple model flow as used for Case 2 in section 3.2, i.e. a Falkner-Skan-type boundary layer with β_H=-0.18. However, whereas in Case 2 a fundamental-type breakdown was enforced by the disturbance input, here, we introduced a 2-D wave and a pair of oblique 3-D subharmonic waves at the disturbance strip. The effect of suction was observed from comparisons with previous simulations for subharmonic breakdown [18] without suction.

4.1 Calculation of Base Flows

Two different downstream locations of the suction strip are considered: For Case A, the center of the strip is fixed at x=2.9 (width $x_2'-x_1'$=0.12) and for Case B, further downstream at x=4.3. The nondimensional suction rate in both cases is chosen as q=-0.3, where $q=\int v_{B,0}(x)dx$ ($\overline{v}_{B,0\,max}/U_\infty$=-0.0075). The integration domain starts at Re_{δ_1}=1100 corresponding to x_0=1.58. A perspective view of the velocity components u_B, v_B and the vorticity ω_{zB} for Case A is given in Figure 11. The streamwise velocity profile $u_B(y)$ upstream of the suction strip shows an inflexion point due to adverse pressure gradient. Near the suction strip, the u_B-profile drastically changes its shape due to continuity, and further downstream it gradually returns to the inflexional shape. The normal-velocity distribution is dominated by the values prescribed at the wall; a remarkable upstream influence of the suction strip on the potential flow can be observed. The $\omega_{zB}(y)$-maximum (Fig. 11c) corresponds to an inflexion point in the $u_B(y)$-profile (Fig. 11a). The suction causes a shift of the ω_{zB}-maximum to the wall like a favourable pressure gradient.

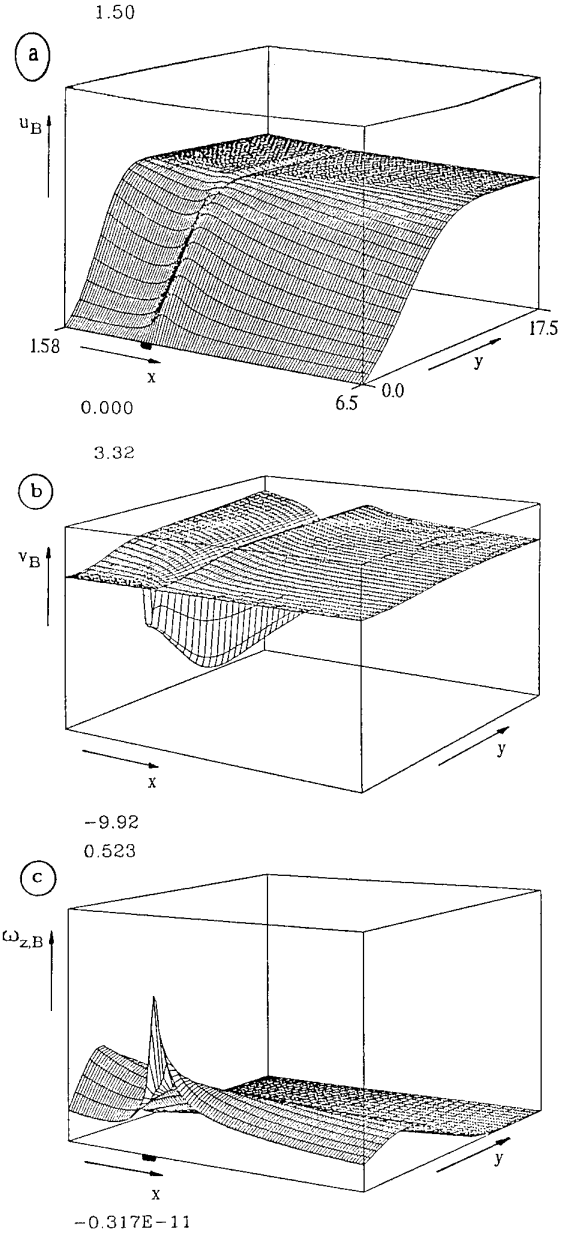

Fig. 11 Effect of local suction (Case A) on the mean-flow quantitives for a Falkner-Skan-type boundary layer with β_H=-0.18. Steady flow variables u_B, v_B, ω_{zB} vs. x and y in perspective view.

Quantitatively, the stabilizing effect of suction is exhibited by the development of the integral shape factor H_{12} (Fig. 12). In the vicinity of the suction strip the shape factor steeply falls below the Blasius value (indicated by the straight line) with a mimimum of $H_{12} \approx 2.3$, corresponding locally to a flow with β_H = +0.5. A noticeable upstream influence is also recognized. Downstream of the suction strip, the shape factor re-grows only slowly indicating a far-downstream influence on the base flow.

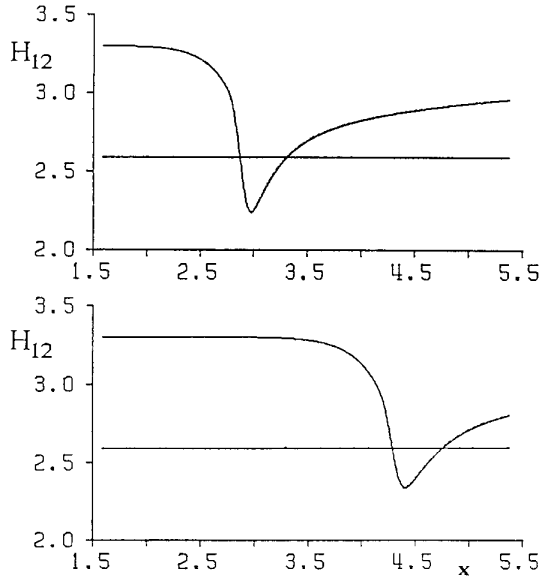

Fig. 12 Streamwise distribution of the shape factor H_{12} for Case A and Case B.

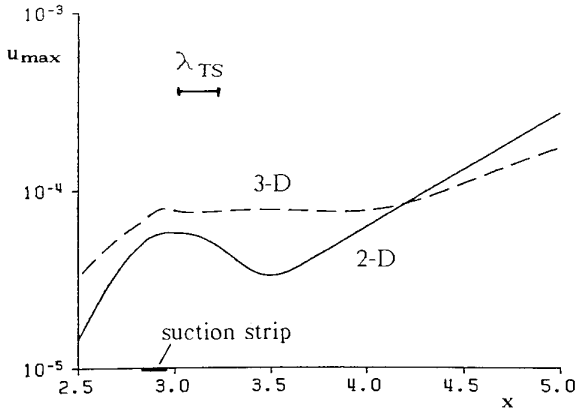

Fig. 13 Effect of early suction (Case A) on the streamwise 2-D and 3-D disturbance development.

4.2 Disturbance Development for Early Suction (Case A)
For the disturbance input, a nondimensional frequency F_{2D}=1.08 was chosen for the fundamental 2-D wave and, therefore, F_{3D}=0.54 for the subharmonic 3-D wave. The spanwise wavenumber was γ=30.6. The Fourier series for the spectral approximation of the numerical method was truncated at K=2. All parameters were chosen such to enable comparison with a case without suction [18]. The disturbance strip was located between x=1.98 and x=2.4, where a 2-D wave of half the amplitude of the 3-D wave was generated. For Case A, the center of the suction strip was located at x=2.9. The effect of early suction on the streamwise development of the 2-D and 3-D disturbance waves can be seen from Fig. 13 for the u-disturbance component (max. over y-direction). Upstream of the suction strip, the 2-D wave is more amplified than the 3-D wave but remains smaller due to its lower initial amplitude. Due to suction, the 2-D wave is damped between x=3.0 and x=3.5, and grows again exponentially further downstream. The 3-D wave is not damped as effectively as the 2-D wave but keeps its amplitude up to x=4.0, and continues growing downstream of x=4.0. The amplitude level remains below 0.2% up to x=5.0.

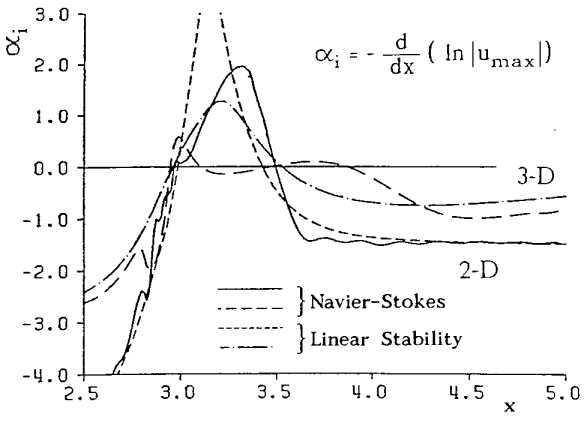

Fig. 14 Spatial amplification rate α_i vs. x of the 2-D and 3-D waves for Case A. Comparison of numerical simulation with results of linear stability-theory calculations.

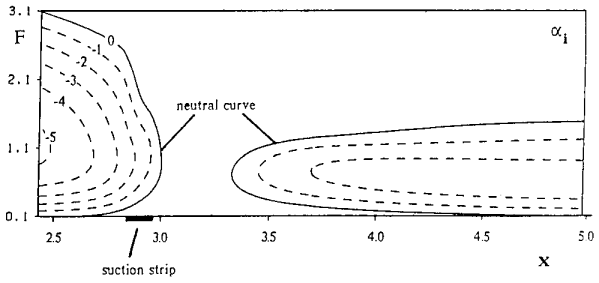

Fig. 15 Stability diagram for 2-D waves for Case A performed for the base-flow profiles taken from the steady Navier-Stokes solution.

A comparison of the amplification rates for both the 2-D and the 3-D wave with results of spatial linear stability theory is shown in Fig. 14. For the stability calculations, the base-flow profiles are taken from the Navier-Stokes simulation. The damping of both the 2-D and the 3-D wave within the suction strip region is clearly overestimated by linear theory. In Fig. 14, only one discrete 2-D frequency is considered. In order to gain a qualitative overview on the effect of a single suction strip on the spectrum of amplified frequencies of 2-D waves, we used spatial linear stability-theory calculations to determine a stability diagram for this base flow (Case A), as plotted in Fig. 15. The solid line indicates neutral stability, iso-amplification lines are dashed. Upstream of the suction strip a broad band of frequencies is amplified. As an effect of suction, all frequencies are damped up to x=3.3. In spite of inflexional velocity profiles only a narrow band of frequencies is amplified further downstream, i.e. for this case suction acts as a low-pass filter to disturbances. However, as can be seen from Fig. 14, the correct amplification (n-factor for e^n-method) can only be gained from a direct numerical simulation.

4.3 Disturbance Development for Late Suction (Case B)
For Case B, the suction strip was moved downstream to x=4.3 and therefore the development of the disturbances changes drastically. The effect of late suction on the streamwise disturbance development can be seen from Fig. 16 by comparison with the disturbance evolution without suction. The 2-D wave grows quickly to reach an amplitude of 3.5% at the location of the suction strip, whereas for the case without suction the

amplitude grows up to about 7%. As an effect of the upstream influence of the suction strip, as discussed before, the growth of the 2-D wave is retarded for 3.8<x<4.3, i.e. upstream of the suction strip. Downstream of the suction strip the amplitude of the 2-D wave is almost kept constant.

The 2-D wave exceeds and holds a threshold of about 0.7% (Kloker [18]) giving rise to a secondary instability mechanism: the 3-D wave undergoes enhanced amplification due to subharmonic resonance. For the suction case the growth of the 3-D wave is reduced due to lower 2-D wave amplitude, but it still grows up to 10% beyond the suction strip and then saturates. An important indicator of the final stage of transition is the change of the mean flow (mode (0, 0)). Without suction, the mean-flow distortion reaches a maximum amplitude of about 20% at x=4.8 (see Kloker [18]), whereas in the case with suction this development is delayed in streamwise direction (approximately by $\Delta x \approx 0.5$) but not prevented.

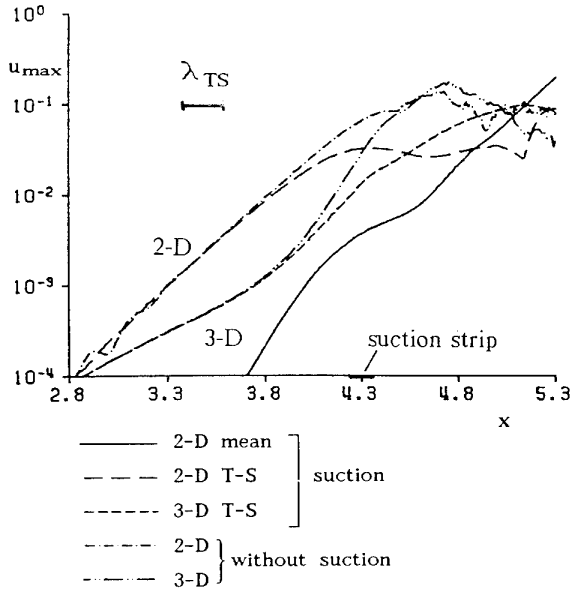

Fig. 16 Effect of late suction (Case B) on the streamwise 2-D and 3-D disturbance development. Comparison of calculations with and without suction.

A comparison between the calculated amplification rates and both, the linear and the secondary stability theory results, is performed in Fig. 17. Again, the stability calculations are performed for the base-flow profiles taken from the Navier-Stokes calculations. For the 2-D wave, linear theory is in good agreement with the simulation up to x=3.8, where suction starts to affect the flow. The 3-D wave is amplified according to linear theory up to x=3.3. Then, the amplification rate deviates from linear behaviour due to the onset of secondary instability. The symbols indicate results of a secondary stability analysis, where the required velocity profiles for both the disturbance and the base flow including mode (0, 0) were taken from the Navier-Stokes calculation. The calculated amplification rates for the 3-D wave are in good agreement with the results of the direct simulation. However, it is emphasized that the correct base flow and 2-D amplitude plus amplitude distribution were used, which can only be determined by direct simulation.

The results for the two cases have shown that suction applied in a region with linear disturbance development can considerably delay transition in this otherwise very

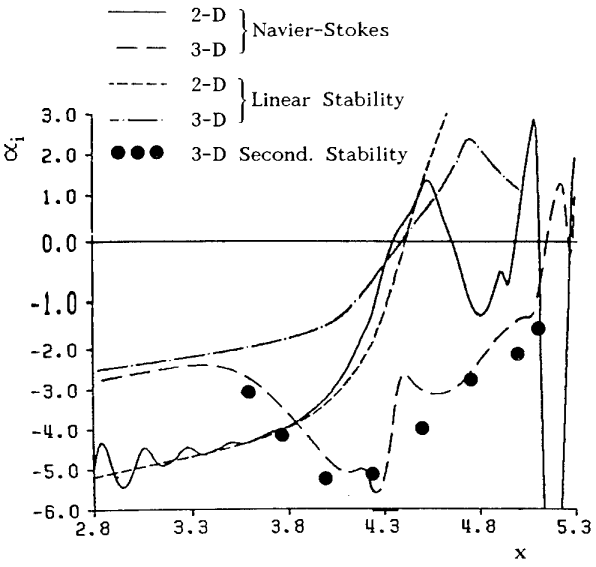

Fig. 17 Amplification rates α_i vs. x of the 2-D and 3-D waves for Case B. Comparison of numerical simulation with results of (primary) linear theory and secondary instability theory calculations.

unstable base flow. The influence of the suction strip extends far downstream. On the other hand, after the onset of subharmonic resonance, nonlinear development can only be weakly affected by suction. In particular, the growth of the 3-D wave depends strongly on the local amplitude of the 2-D wave. Since, in the investigated case, the amplitude of the 2-D wave does not fall below the threshold for nonlinear coupling, the growth of the 3-D wave is only slightly diminished. Thus, passive control in an already nonlinear stage of disturbance development cannot prevent transition to turbulence.

5. APPLICATION TO AN AIRFOIL WITH SUCTION

The results presented in this section shall demonstrate that the numerical method is also applicable for a 2-D boundary layer on a real airfoil with distributed suction. Therefore, we recalculated the base flow of experiments on an airfoil with suction performed by Van Ingen [28] in a wind tunnel.

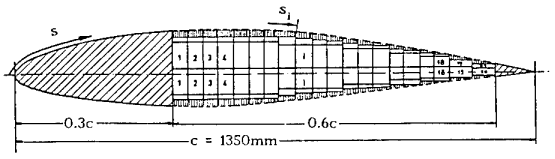

Fig. 18 NACA 64_2-A-215 airfoil with suctions chambers. Experimental investigation by Van Ingen [28].

For the flow over a NACA 64_2-A-215 airfoil (Fig. 18), Van Ingen investigated the prevention of flow separation with minimal viscous drag by suction through a porous surface with streamwise variable suction distribution. Between 30% and 90% chord the wing section was divided into 20 suction chambers, each adjustable separately. In the suction area the airfoil surface consisted of a filtering paper fixed on a honeycomb-like structure. A complete set of experimental data allows for the numerical simulation of the base flow. Due to the small ratio of boundary-layer thickness to surface curvature radius within the considered chord region the flat-plate assumption is well justified.

Navier-Stokes Simulations of the Effects of Suction Holes on a Flat Plate Boundary Layer

Hubert L. Meitz
Hermann F. Fasel
Department of Aerospace and Mechanical Engineering, University of Arizona
Tucson, Arizona 85721, USA

Abstract

Direct numerical simulations (DNS) of the Navier-Stokes equations are employed to explore the effects of suction holes on transition in a laminar flat plate boundary layer. The Navier-Stokes equations are cast in vorticity-velocity form. Periodicity is imposed in spanwise direction; all other spatial derivatives are discretized with fourth order compact differences. An explicit fourth order Runge-Kutta scheme is employed for the time-integration of the vorticity transport equations. Suction is applied through a row of holes aligned in spanwise direction. For low suction strengths, each hole generates a pair of stable streamwise vortices. When the suction strength exceeds a critical value, the vortices become unstable. For high suction strengths, vortex shedding occurs right at the suction holes. Our numerical findings agree well with experimental observations.

1 Introduction

Suction through the wall can be a very effective means to delay transition to turbulence. Linear stability theory (LST) analysis shows that continuous suction through the wall can substantially increase the critical Reynolds number of boundary layers, i.e. the distance from the leading edge up to which (infinitesimally) small disturbances are damped. In the theoretical limit, optimal wall suction applied to a two-dimensional boundary layer on a flat plate leads to the asymptotic suction profile with a critical Reynolds number $(U_\infty \delta_1/\nu)_{cr} = 70000$ which is more than 130 times larger than the critical value of the Blasius boundary layer [8]. These impressive theoretical results led to early application of wall suction in laminar flow control (LFC). However, for most aeronautical LFC applications a continous wall suction is impractical. It requires a permeable wall which cannot carry the structural loads of present aircraft skin panels. Thus, in practice wall suction for LFC is usually applied through slots or holes [5].

When suction holes are used, the wall normal velocity is zero over most of the surface and varies rapidly over the suction holes. This can give rise to undesired effects that can limit the efficiency of LFC and even lead to early transition: First, the receptivity of the boundary layer may be increased by the rapid flow variations near the suction holes, i.e. the boundary layer becomes more susceptible to external disturbances such as sound waves or freestream turbulence. Second, the streamwise vortices which emerge from the holes can be unstable to small perturbations in the flow. There is now ample evidence that even very weak streamwise vortices can have a dramatic effect on transition ([7, 2, 1]). Third, oscillations generated by the suction pump can feed into the boundary layer and generate disturbances. In addition, pre-existing disturbance waves inside the boundary layer may be scattered by the suction holes.

Theoretical or numerical studies of suction hole configurations are exceedingly difficult because of the vast disparity of length scales involved. Typically, the diameter of suction holes is only a fraction of the disturbance wavelength. Therefore, to date the bulk of data on suction holes is from experimental work.

1.1 The Northrop Experiments

In the 1950s, Goldsmith [4] performed a series of experiments at Northrop Aircraft to investigate the effects of suction holes on the boundary layer flow in the entrance region of a circular pipe. Suction was applied through one row of holes equally spaced along the circumference of the pipe. A schematic representation of this setup is given in Fig. 1.

Goldsmith found that for sufficiently low suction rates each hole generated a pair of steady streamwise vortices that extended downstream inside the boundary layer. If the suction strength exceeded a critical value, the vortices of adjacent holes merged to form horseshoe vortices that periodically shed in

Paper presented at the 74th Fluid Dynamics Symposium on "Application of Direct and Large Eddy Simulation to Transition and Turbulence" held at Chania, Crete, Greece, in April 1994.

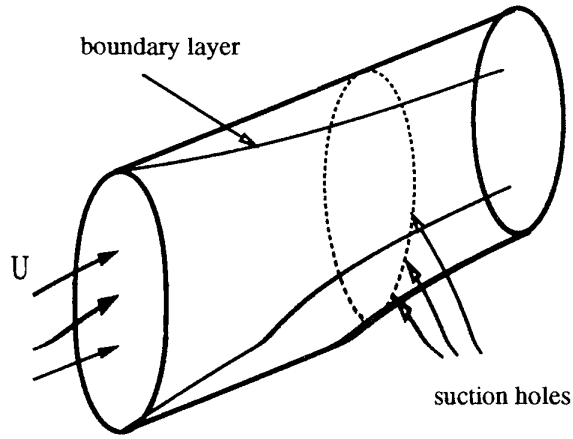

Figure 1: Experimental setup of Northrop experiments. Goldsmith [4]

downstream direction, which then lead to rapid transition to turbulence. The experiments showed that the effects of the suction could be satisfactorily decribed by two nondimensional parameters, a nondimensional wall shear

$$\mathcal{T} = \frac{s^2}{2\nu}\left(\frac{\partial u_B}{\partial y}\right)_{wall}\left(\frac{s-d}{s}\right)^{1.18} \qquad (1)$$

and a nondimensional suction flux

$$\mathcal{F} = \frac{1}{\nu}\frac{\Delta Q}{\Delta z}\left(\frac{s-d}{s}\right)^{0.62} \qquad (2)$$

where
u_B ... streamwise velocity of the unperturbed basic flow
ν ... viscosity
s ... spacing between centers of adjacent holes
d ... hole diameter
$\Delta Q/\Delta z$ ... suction flow volume per unit length along the circumference of the pipe.

For a given geometry and base flow, $\mathcal{T}$ is constant and $\mathcal{F}$ varies linearly with increasing suction strength.

For these two parameters Goldsmith found a "critical suction curve". A part of this curve is shown in Fig.2, with $\mathcal{F}$ on the abscissa and $\mathcal{T}$ on the ordinate axis.

For values of the parameters $\mathcal{T}$, $\mathcal{F}$ to the left of the critical suction curve, Goldsmith found stable vortices emerging from the holes and extending downstream in x-direction. For values $\mathcal{T}$, $\mathcal{F}$ in between the two branches of the curve, he found vortex shedding and transition to turbulence. For values $\mathcal{T}$, $\mathcal{F}$ to the right of the suction curve, he again found stable vortices, which, however, were aligned in the azimuthal direction.

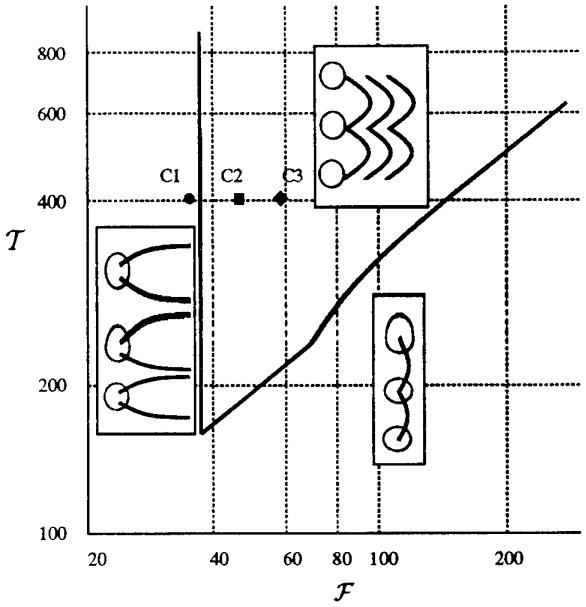

Figure 2: Critical suction curve. Goldsmith [4]

In addition to its possible effects on LFC, this phenomenon is very interesting from a stability point of view: Usually, boundary layers are only convectively unstable, i.e. disturbances are amplified (or damped) as they propagate downstream. In contrast, the vortex shedding observed in the experiment may be an indication of absolute instability.

1.2 Scope of the Present Work

A major finding of the experiments was that the critical suction curve is independent of the precise shape of the boundary layer profile, because only the wall vorticity appears in $\mathcal{T}$ of eq. (1). This allowed us to substitute in the numerical simulation a flat plate boundary layer for the pipe entrance boundary layer in the experiment, thus quasi "unrolling" the pipe onto a plate. To account for the finite circumference of the pipe, we imposed periodicity in the spanwise direction z (corresponding to the azimuthal direction θ in the experiments). In addition we imposed symmetry of the flow with respect to the $z = 0$ plane to reduce the memory and CPU-time requirements of the simulation.

With these assumptions, we performed three numerical simulations C1, C2, and C3, as indicated in Fig.2. In all three calculations, the nondimensional wall shear was $\mathcal{T} = 404$. In the calculation C1 (subcritical case) the nondimensional suction flux was $\mathcal{F} = 35$, corresponding to a point in the stable region to the left of the critical suction curve. In the calculation C2 (weakly supercritical case) the nondimen-

sional suction flux was $\mathcal{F} = 46$. This point is just inside the unstable region of the parameter space. It should be noted that there is considerable scatter of the original experimental data in this region. In the calculation C3 (strongly supercritical case) the nondimensional suction flux was $\mathcal{F} = 58$, which is well inside the unstable region.

2 Mathematical Model

2.1 Governing Equations

The governing equations are the incompressible, unsteady Navier-Stokes equations. Following the approach taken by Fasel et. al. [3], we adopted the vorticity-velocity formulation of these equations. They consist of three vorticity transport equations

$$\frac{\partial \omega_x}{\partial t} = -\frac{\partial a}{\partial y} + \frac{\partial c}{\partial z} + \frac{1}{Re}\nabla^2\omega_x \quad (3a)$$

$$\frac{\partial \omega_y}{\partial t} = \frac{\partial a}{\partial x} - \frac{\partial b}{\partial z} + \frac{1}{Re}\nabla^2\omega_y \quad (3b)$$

$$\frac{\partial \omega_z}{\partial t} = -\frac{\partial c}{\partial x} + \frac{\partial b}{\partial y} + \frac{1}{Re}\nabla^2\omega_z \quad (3c)$$

where

$$a = v\,\omega_x - u\,\omega_y + v_B\,\omega_x - u_B\,\omega_y \quad (4a)$$

$$b = w\,\omega_y - v\,\omega_z - v_B\,\omega_z - v\,\omega_{zB} \quad (4b)$$

$$c = u\,\omega_z - w\,\omega_x + u_B\,\omega_z + u\,\omega_{zB} \quad (4c)$$

and three velocity equations

$$\nabla^2 v = \frac{\partial \omega_x}{\partial z} - \frac{\partial \omega_z}{\partial x} \quad (5a)$$

$$\frac{\partial^2 w}{\partial x^2} + \frac{\partial^2 w}{\partial z^2} = \frac{\partial \omega_y}{\partial x} - \frac{\partial^2 v}{\partial y \partial z} \quad (5b)$$

$$\frac{\partial^2 u}{\partial x^2} + \frac{\partial^2 u}{\partial z^2} = -\frac{\partial \omega_y}{\partial z} - \frac{\partial^2 v}{\partial x \partial y} \quad . \quad (5c)$$

Here we define the vorticity as

$$\omega_x = \frac{\partial v}{\partial z} - \frac{\partial w}{\partial y} \quad (6a)$$

$$\omega_y = \frac{\partial w}{\partial x} - \frac{\partial u}{\partial z} \quad (6b)$$

$$\omega_z = \frac{\partial u}{\partial y} - \frac{\partial v}{\partial x} \quad (6c)$$

With the assumption of periodicity in spanwise direction z and symmetry w.r.t. $z=0$, we can expand the flow variables in sine- and cosine series

$$u(x,y,z) = \sum_{k=0}^{K} U_k(x,y)\cos(\gamma_k z) \quad (7a)$$

$$v(x,y,z) = \sum_{k=0}^{K} V_k(x,y)\cos(\gamma_k z) \quad (7b)$$

$$w(x,y,z) = \sum_{k=1}^{K} W_k(x,y)\sin(\gamma_k z) \quad (7c)$$

$$\omega_x(x,y,z) = \sum_{k=1}^{K} \Omega_{z\,k}(x,y)\sin(\gamma_k z) \quad (7d)$$

$$\omega_y(x,y,z) = \sum_{k=1}^{K} \Omega_{y_k}(x,y)\sin(\gamma_k z) \quad (7e)$$

$$\omega_z(x,y,z) = \sum_{k=0}^{K} \Omega_{z\,k}(x,y)\cos(\gamma_k z) \quad (7f)$$

where the spanwise wavenumber is

$$\gamma_k = 2\pi k/s$$

Substitution of these expansions into the vorticity transport equations (3a), (3b), (3c) and the velocity equations (5a), (5b), (5c) yields the governing equations in Fourier-space

$$\frac{\partial \Omega_{x\,k}}{\partial t} = -\frac{\partial A_k}{\partial y} - \gamma_k C_k + \frac{1}{Re}\nabla_k^2\Omega_{x\,k} \quad (8a)$$

$$\frac{\partial \Omega_{y_k}}{\partial t} = \frac{\partial A_k}{\partial x} + \gamma_k B_k + \frac{1}{Re}\nabla_k^2\Omega_{y_k} \quad (8b)$$

$$\frac{\partial \Omega_{z\,k}}{\partial t} = -\frac{\partial C_k}{\partial x} + \frac{\partial B_k}{\partial y} + \frac{1}{Re}\nabla_k^2\Omega_{z\,k} \quad (8c)$$

$$\frac{\partial^2 V_k}{\partial x^2} + \frac{\partial^2 V_k}{\partial y^2} - \gamma_k^2 V_k = \gamma_k \Omega_{x\,k} - \frac{\partial \Omega_{z\,k}}{\partial x} \quad (9a)$$

$$\frac{\partial^2 W_k}{\partial x^2} - \gamma_k^2 W_k = \frac{\partial \Omega_{y_k}}{\partial x} + \gamma_k \frac{\partial V_k}{\partial y} \quad (9b)$$

$$\frac{\partial^2 U_k}{\partial x^2} - \gamma_k^2 U_k = -\gamma_k \Omega_{y_k} - \frac{\partial^2 V_k}{\partial x \partial y} \quad (9c)$$

These equations are coupled through the nonlinear terms A_k, B_k, C_k, defined as

$$a(x,y,z) = \sum_{k=1}^{K} A_k(x,y)\sin(\gamma_k z) \quad (10a)$$

$$b(x,y,z) = \sum_{k=0}^{K} B_k(x,y)\cos(\gamma_k z) \quad (10b)$$

$$c(x,y,z) = \sum_{k=0}^{K} C_k(x,y)\cos(\gamma_k z) \quad . \quad (10c)$$

A crucial aspect of the vorticity-velocity formulation is the fact that the vorticity values at the wall cannot be computed from the vorticity transport equations (3a), (3b), (3c). Rather, they should be computed from the velocity fields, to maintain consistency and ensure overall conservation of mass and

zero-divergence of the vorticity. We used the following relations to evaluate the vorticity at the wall $y = 0$:

$$\frac{\partial^2 \Omega_{xk}}{\partial x^2} - \gamma_k^2 \Omega_{xk} = -\frac{\partial^2 \Omega_{yk}}{\partial x \partial y} \quad (11a)$$

$$- \gamma_k \left(\frac{\partial^2 V_k}{\partial x^2} + \frac{\partial^2 V_k}{\partial y^2} - \gamma_k^2 V_k\right)$$

$$\Omega_{yk} = 0 \quad (11b)$$

$$\frac{\partial \Omega_{zk}}{\partial x} = \gamma_k \Omega_{xk} \quad (11c)$$

$$- \frac{\partial^2 V_k}{\partial x^2} + \frac{\partial^2 V_k}{\partial y^2} - \gamma_k^2 V_k \quad .$$

Eq. (11b) follows from the definition of the normal vorticity (6b).

2.2 Boundary Conditions

The governing equations (8a), (8b), (8c), (9a), (9b), (9c) are solved inside the computational domain shown schematically in Fig.3.

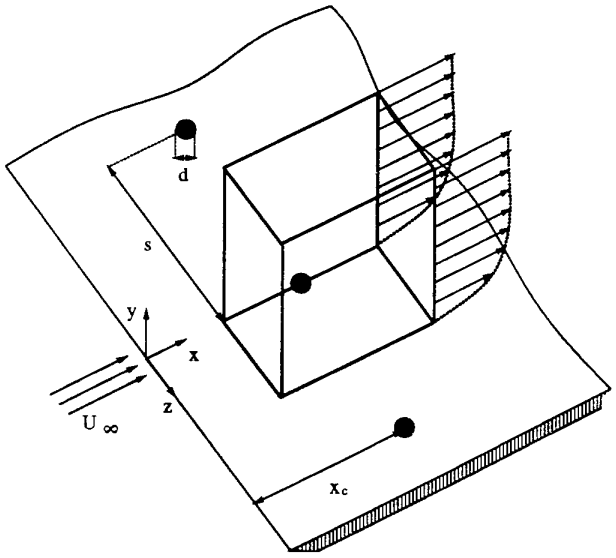

Figure 3: Computational domain.

At the **inflow boundary**, a Blasius boundary layer profile is imposed. At the **wall**, no-slip conditions are imposed on u and w. The normal velocity v is zero over the solid part of the wall and is imposed as $v = v_c \cos(\pi r/d)$ over the holes as shown in Fig.4. In addition, $\partial v/\partial y = 0$ is imposed to ensure conservation of mass. At the **freestream boundary**, a decay condition is imposed on v. Near the **outflow boundary**, we use a buffer domain technique similar to the one proposed by Kloker et.al. [6].

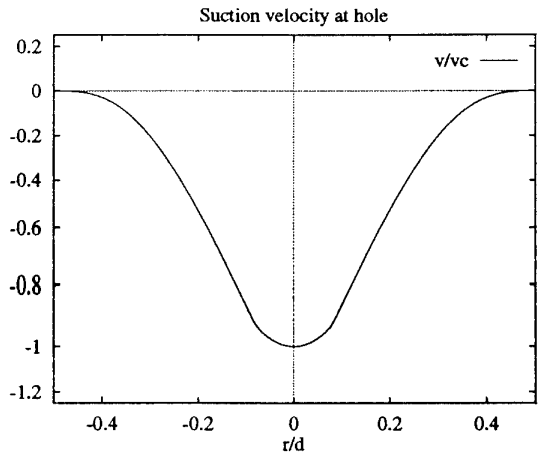

Figure 4: Plot of the suction velocity distribution v/v_c over one hole.

3 Numerical Method

In the governing equations, the spatial derivatives in x, y directions are discretized with 4th-order compact differences. The nonlinear terms A_k, B_k, C_k of the vorticity transport equations are evaluated pseudospectrally, using fast sine- and cosine transforms [10] to convert from physical space to Fourier space and back. The vorticity transport equations are integrated in time using a 4th order explicit Runge-Kutta method. At each Runge-Kutta substep, the calculation proceeds as follows:

1. integrate vorticity transport equations over one substep
2. solve V_k-Poisson equation with a direct Fast Fourier Transform method [9]
3. solve W_k, U_k Poisson equations
4. compute vorticities Ω_{xk}, Ω_{zk} at the wall

3.1 Computational Parameters

In our simulations, we used the following parameters:

U_∞ = 15 m/s ... freestream velocity

ν = 15×10^{-6} m^2/s ... dynamic viscosity

v_c = $0.6U_\infty$ (case C1) / $0.8U_\infty$ (case C2) / $1.0U_\infty$ (case C3), ... maximum suction velocity at hole center

v_{av} = 0.12 / 0.17 / 0.21 U_∞ ... average suction velocity over each hole

s = 2.007362 mm ... hole spacing

d = 1.0287 mm ... hole diameter

x_c = 506 mm ... distance of holes from leading edge.

In practical LFC applications, we expect average suction velocities of $\mathcal{O}(0.01U_\infty \ldots 0.1U_\infty)$, and a ratio hole of spacing to hole diameter (s/d) of $5 \ldots 10$.

In the computations, the integration domain was discretized with 961 gridpoints in x direction (one hole diameter = 14 Δx), and with 100 gridpoints in y direction (= 2 B.L. thicknesses). 11 Fourier modes were used for the spanwise discretization, with 17 collocation points used to compute the nonlinear terms.

4 Results

4.1 Subcritical Case C1

During the simulation of case C1, trailing vortices emerged from the holes as expected and extended downstream. Once the vortices had reached the outflow boundary, the flow field attained a steady state. This is in agreement with the experimental observations.

A three-dimensional contour plot of the magnitude of the streamwise vorticity $|\omega_x|$ is shown in Fig.5, with all lengths given in mm. Within the limits of the 3-D perspective, the region shown is drawn to scale in x, y, z. It extends from the centerplane of one suction hole at $z = 0$ to the centerplane of the adjacent suction hole to the right at $z = s$. In streamwise direction x, it extends approximately 1.5 hole diameters upstream of the hole centers and approximately 6 hole diameters downstream. In wall normal direction, the region extends to approximately one half boundary layer thickness. The streamwise vortices generated by the holes are clearly visible, and the shape of these vortices agrees well with the experimental observations.

Between the vortices is a small recirculation region, identified by contours of $u = 0$, which extends about three hole diameters downstream of the holes (see Fig.6).

From Fig.5 one can observe that vortices from adjacent holes are closer to each other than vortices from the same hole, as shown schematically in Fig.7.

Consequently, the main interaction between those vortices causes a mutual uplifting, i.e. as the vortices extend in downstream direction they move away from the wall. Fig.8 shows contours of the streamwise vorticity in the plane $z = s/3$. These plots

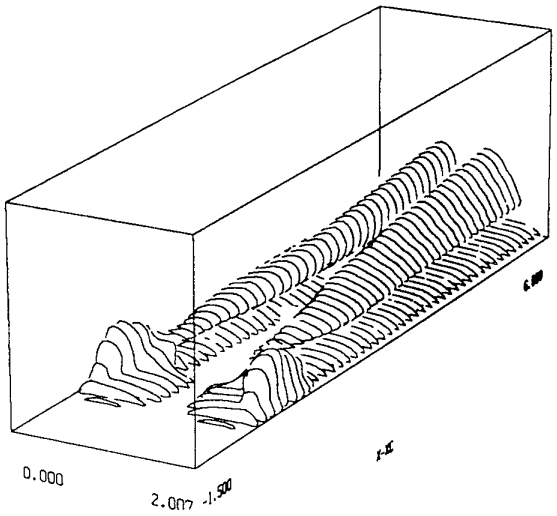

Figure 5: Case C1: Contourlines of $|\omega_x| = 30$, view from upstream.

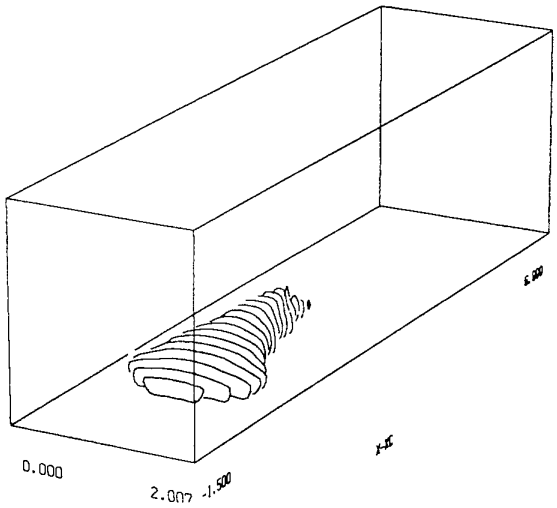

Figure 6: Case C1: Contourlines of $u = 0$, view from downstream.

essentially represent a cut through a vortex core. Superimposed on the vorticity contours are the velocity vectors (u, v) of the undisturbed boundary layer flow.

Near the holes, the vortices are still close to the wall, where the slope of the (undisturbed) boundary layer is fairly constant. Thus as the vortices are lifted up, they move into a fluid layer with increased mean streamwise velocity. This leads to vortex stretching, which results in an increase of vortic-

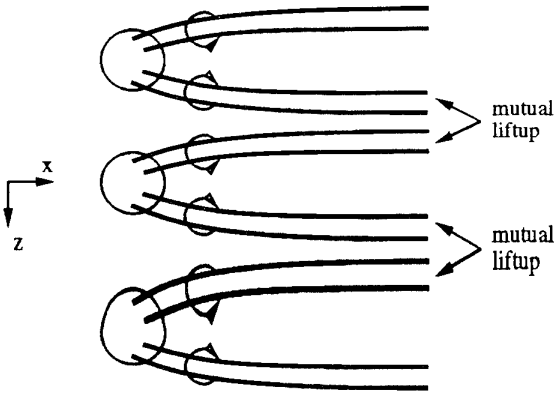

Figure 7: Schematic of holes with trailing vortices, view from top.

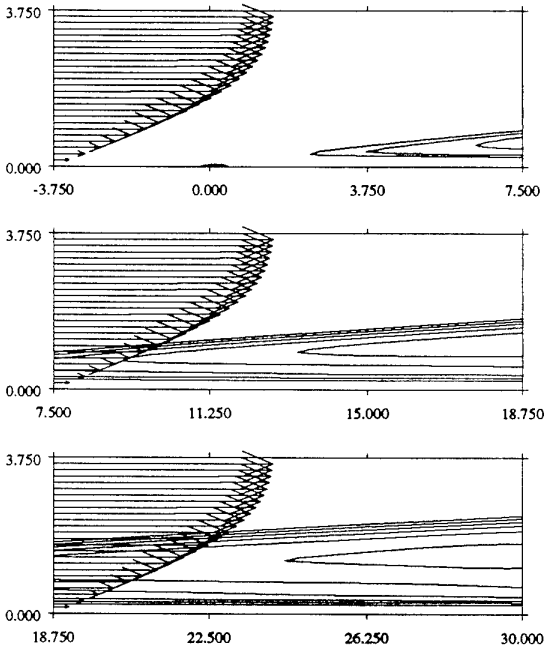

Figure 8: Sideview of vortices. Contours are levels of streamwise vorticity ω_x, arrows are velocity vectors of undisturbed boundary layer flow at left edge of plot. Drawn to scale in x, y (in mm); $x - x_c$ is distance from center of holes.

ity in downstream direction. Further downstream, as the vortices approach the edge of the boundary layer, the mean streamwise velocity no longer increases in vertical direction, and the growth of vorticity levels off. This behavior can be observed clearly from the next figure.

In Fig.9, the streamwise vorticity ω_x at the vortex core is plotted versus the downstream distance $x -$

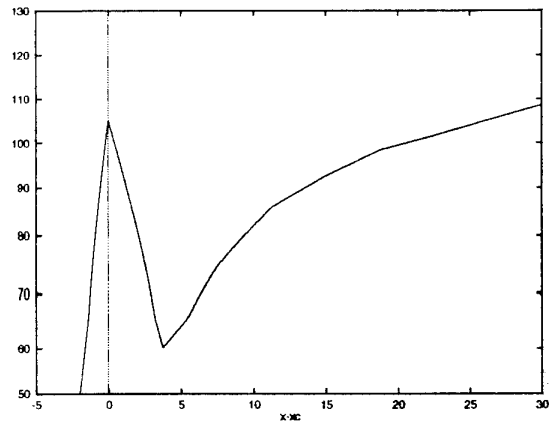

Figure 9: Case C1: Streamwise vorticity of the vortex cores, plotted over downstream distance $x - x_c$ (in mm).

x_c. At the holes, the vorticity attains a maximum and then falls off rapidly over a distance of three hole diameters. This distance is the same as the extent of the recirculation region mentioned above. From there on, the vorticity increases again, and grows approximately $\propto \sqrt{x}$. After 18 hole diameters, the vortices have risen to the edge of the boundary layer, and the growth becomes weaker.

4.2 Weakly Supercritical Case C2

For this case the flow field near the holes is qualitatively not very different from the previous case, as shown in Figs. 10 and 11. Two vortices emerge from each hole, and initially they appear steady. However, after 20 hole diameters downstream one can observe small fluctuations in the form of a periodic (both in space and time) thickening and thinning of the vortices. This is shown in Figs. 12 and 13. This behavior is reminiscent of the sinuous mode disturbances that are observed in vortex instabilities. Finally after 30 hole diameters the vortices break up (see Figs. 14 and 15).

A Fourier analysis of the fluctuations shows a distinct peak at 1714 Hz. In the usual nondimensional unit for stability investigations $F=2\pi f\nu/{U_\infty}^2 \times 10^4$, this corresponds to F=7.18. This is much higher than any frequency in the amplified TS-band for the Blasius boundary layer.

For further analysis, the phase of the ω_x Fourier mode corresponding to 1714 Hz was calculated near the y, z location of the vortex core. In Fig.16, this phase is plotted versus downstream distance $x - x_c$. The phase is fairly constant over the first 15 diameters downstream of the hole. From there on it ex-

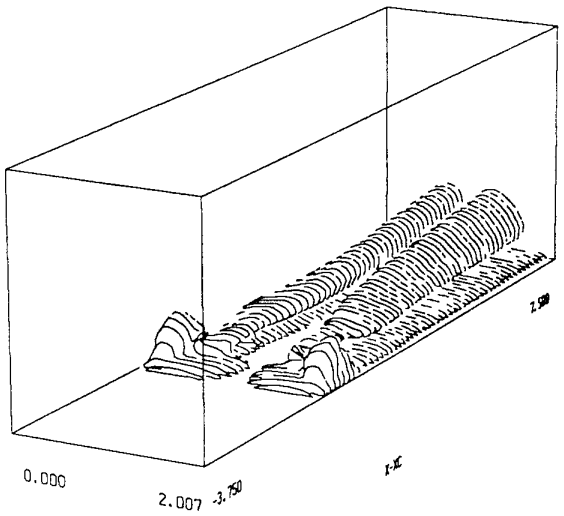

Figure 10: Case C2: Contours of $|\omega_x| = 30$, $x - x_c = -3.75 \ldots 7.5$.

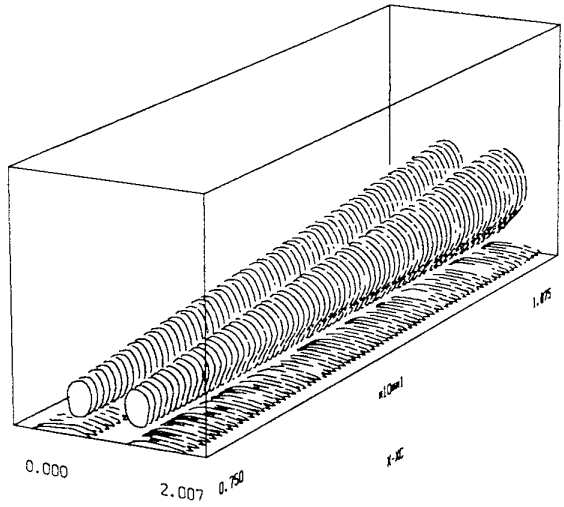

Figure 11: Case C2: Contours of $|\omega_x| = 60$, $x - x_c = 7.5 \ldots 18.25$.

hibits the typical pattern of a traveling wave, with the phase increasing by 2π over every wavelength. From the slope of the phase curve one can compute the phase speed of the fluctuations, which is about 45 % of the freestream speed.

In Fig.17, the Fourier amplitude corresponding to the phase in In Fig.16 is plotted versus $x - x_c$. After about 15 diameters downstream of the hole the amplitude begins to grow: This correlates with the change of the phase pattern in the previous figure.

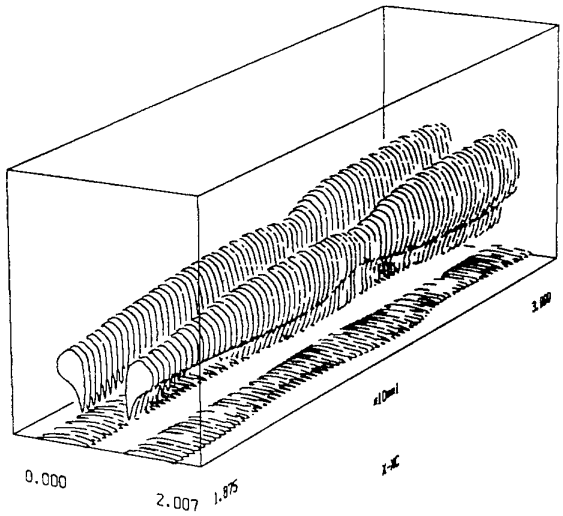

Figure 12: Case C2: Instantaneous contours of $|\omega_x| = 90$, $x - x_c = 18.25 \ldots 30.00$.

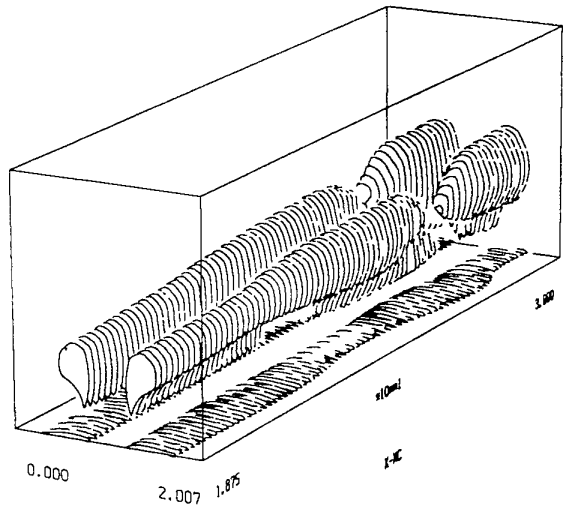

Figure 13: Case C2: Instantaneous contours of $|\omega_x| = 90$, $x - x_c = 18.25 \ldots 30.00$ at a later time.

4.3 Strongly Supercritical Case C3

For the third case C3, the flow is qualitatively very different from the first two cases. The fluctuations are strong already at the suction holes, and it appears that there is vortex shedding. This can be seen from the 3-D contour plots of the magnitude of the streamwise vorticity (Fig.18) and of the magnitude of the total vorticity (Fig.19).

Fig.20 shows timesignals of the spanwise vorticity at several downstream locations x, with $y, z =$

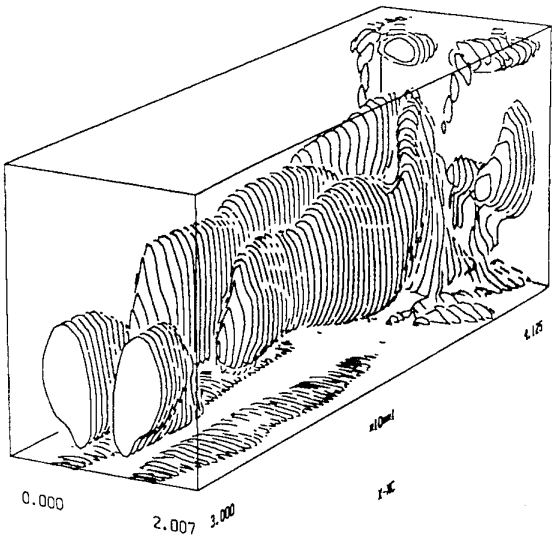

Figure 14: Case C2: Instantaneous contours of $|\omega_x| = 90$, $x - x_c = 30.00 \ldots 41.25$.

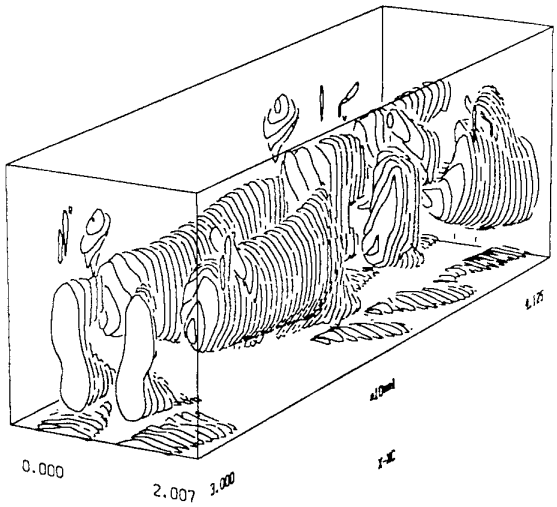

Figure 15: Case C2: Instantaneous contours of $|\omega_x| = 90$, $x - x_c = 30.00 \ldots 41.25$ at a later time.

constant. From these curves the periodicity of the vortex shedding near the holes is clearly discernible. Further downstream the timesignals resemble more and more those of a turbulent flow. (Note that in Fig.20 only every twenty-fifth computed point was used for the plotting).

Again a Fourier analysis of the fluctuations was performed. Now the frequency of the vortex shedding is approximately 735 Hz, which is much lower than the peak frequency in case C2. This correlates

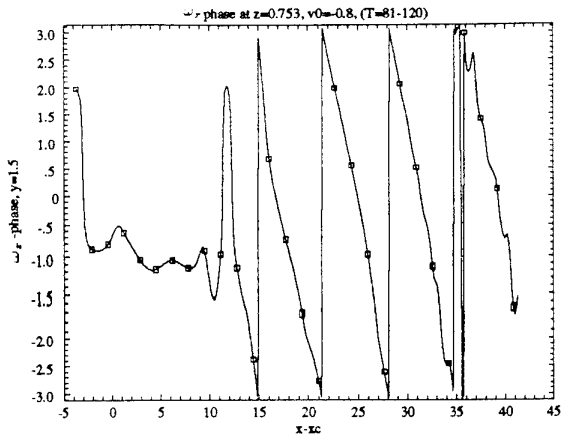

Figure 16: Case C2: Phase of ω_x Fourier component with frequency 1714 Hz, plotted versus x at constant $y = 1.5, , z = 0.753$

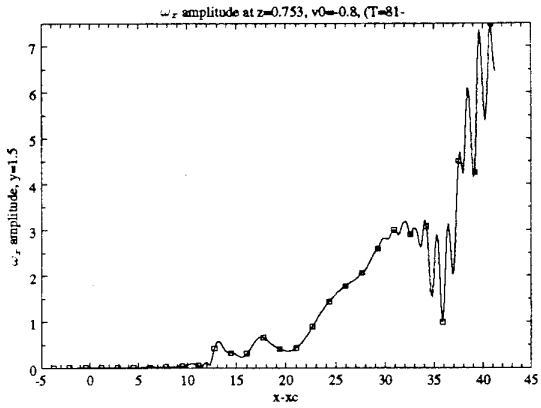

Figure 17: Case C2: Amplitude of ω_x Fourier component with frequency 1714 Hz, plotted versus x at constant $y = 1.5, , z = 0.753$

with Goldsmith's observation that the shedding frequency decreases with increasing suction strength. In Fig.21, the phase of the ω_z component of the 735 Hz fluctuation is plotted versus x. Contrary to the case C2, the phase exhibits a traveling wave pattern starting immediately at the holes. The phase speed, inferred from the slope, is about 45 % of the freestream speed.

5 Conclusions

The computational results are in good qualitative (for lack of quantitative data) agreement with the experimental results. Our calculations confirmed the location of the lower branch of the critical suction curve, and its universal character (i.e. the curve is applicable to both to pipe flow boundary layers and flat plate boundary layers.).

Of particular interest are the results of calculation

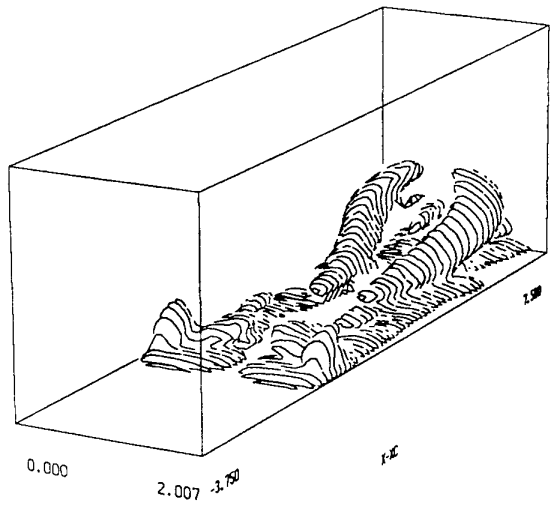

Figure 18: Case C3: Instantaneous contours of $|\omega_x| = 40$, $x - x_c = -3.75 \ldots 7.5$.

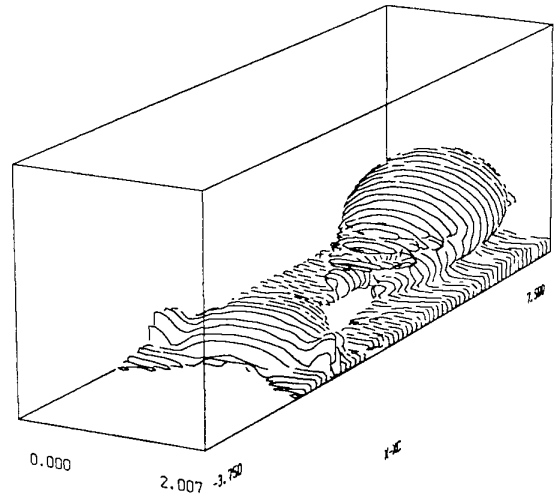

Figure 19: Case C3: Instantaneous contours of $|\omega| = 90$, $x - x_c = 7.5 \ldots 18.25$.

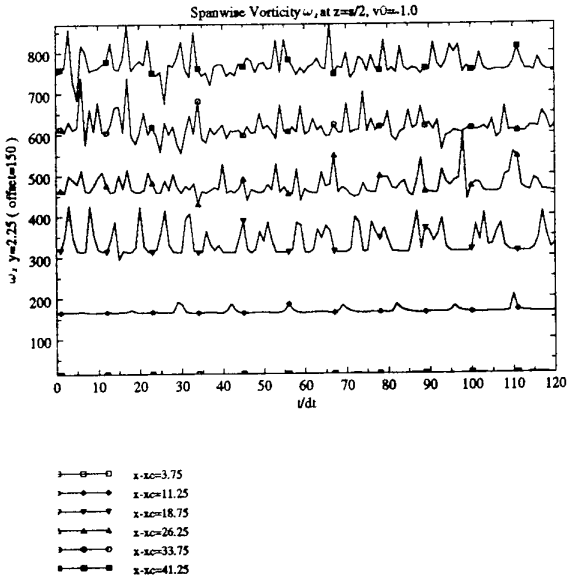

Figure 20: Case C3: ω_z plotted versus t, for several downstream locations x at constant $y = 2.25, , z = 1.003$

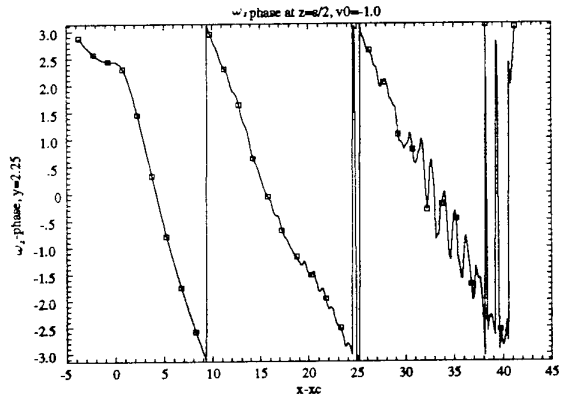

Figure 21: Case C3: Phase of ω_z Fourier component with frequency 735 Hz, plotted versus x at constant $y = 2.25, , z = 1.003$

C2, the weakly supercritical case. From the experimental data it was not quite clear how the transition from the stable to the unstable region in parameter space takes place. In principle, it could be either due to vortex instability, or due to an instability of the recirculation region that forms between the vortices. Goldsmith attributed the observed turbulence to vortex shedding from the hole, which sets in once the suction strength is above the critical threshold. In contrast, our calculations indicate that (at least in some region of the parameter space $\mathcal{F}, \mathcal{T}$) the transition is caused by a vortex instability.

As the suction strength is further increased, we expect the onset of instability growth in the vortices to move upstream and eventually to coalesce with the recirculation region, leading to the vortex shedding observed in the experiments (and in calculation C3).

A major difference between the pipe-entrance boundary layer and the flat plate boundary layer is

that the former is much more stable (in fact a useful neutral stability curve has yet to be established for this flow). Indeed, Goldsmith did not observe transition in the absence of suction. In contrast, with the parameters used in the simulations, the Blasius boundary layer is unstable to small disturbances. We would expect transition to turbulence to occur sufficiently far downstream, even with the lowest suction strength (case C1). In view of this, the critical suction curve assumes a different character for the flat plate boundary layer: It separates regions where transition is guaranteed to occur due to suction effects alone (vz. in between the two branches) from those where transition may be caused by other effects.

Acknowledgements

This work is supported by the National Aeronautics and Space Administration under NASA-Langley Contract No. NAG-1422.

References

[1] Bertolotti, F., 1991, "Linear and Nonlinear Stability of Boundary Layers with Streamwise Varying Properties," *PhD Dissertation,* Ohio State University.

[2] Butler, K., Farrell, B., 1992, "Three-dimensional optimal perturbations in viscous shear flow," . *Phys. Fluids A,* Vol. 4 (8), pp. 1637–1650.

[3] Fasel, H., Rist, U., Konzelmann, U., 1990, "Numerical investigation of the three dimensional development in boundary layer transition," *AIAA Journal,* Vol. 28, No. 1, p.29.

[4] Goldsmith, J., 1957, "Critical Laminar Suction Parameters for Suction into an Isolated Hole or a Single Row of Holes," *Northrop Aircraft Report* No. BLC-95.

[5] Harris, C. D., Brooks, C. W., Clukey, P. G., Stack, J. P., 1992, "The NASA Langley Laminar-Flow-Control Experiment on a Swept, Supercritical Airfoil," *NASA Technical Memorandum* 4309.

[6] Kloker, M., Konzelmann, U., Fasel, H., 1993 "Outflow boundary conditions for spatial Navier-Stokes simulations of transitional boundary layers," *AIAA Journal,* Vol. 31, No. 4, pp. 620–628.

[7] Nayfeh, A. H., 1981, "Effect of streamwise vortices on Tollmien-Schlichting waves," *J. Fluid Mech.,* Vol. 107, pp.441–453.

[8] Schlichting, H., 1987, "Boundary Layer Theory," seventh edition, McGraw-Hill, pp. 506–509

[9] Swarztrauber, P. N., 1977, "The Methods of Cyclic Reduction, Fourier Analysis and the FACR Algorithm for the Discrete Solution of Poisson's Equation on a Rectangle," *SIAM Review,* Vol. 19, No. 3, pp. 490–501.

[10] Swarztrauber, P. N., 1982, "Vectorizing the FFTs," *Parallel Computations* (G. Rodrigue, ed.), Academic Press, pp. 51–83.

Direct Numerical Simulation of 2-D and 3-D Instability Waves in a Laminar Separation Bubble

Ulrich Rist
Ulrich Maucher
Institut für Aerodynamik und Gasdynamik
Universität Stuttgart
Pfaffenwaldring 21
70550 Stuttgart
Germany

1. SUMMARY

Direct Numerical Simulations of a laminar separation bubble are presented, where the bubble is generated by prescribing a locally decelerated free-stream velocity along a flat-plate. Controlled disturbances are introduced into the flow field upstream of the bubble by suction and blowing through the wall in order to study the linear and nonlinear stability characteristics of the flow. A number of generic cases with different two-dimensional (*2-D*) and three-dimensional (*3-D*) initial disturbance amplitudes are investigated, (i) a linear case, (ii) a case subject to secondary instability (strong amplification of 3-D disturbances by resonance with a large amplitude 2-D wave), (iii) a 3-D nonlinear case (interaction of two oblique waves), and (iv) a nonlinear case combining the interaction of two oblique waves with a 2-D wave. Good quantitative agreement of the numerical results with (local) linear stability theory is observed throughout case (i) and for the initial disturbance development of the priming waves in the other cases despite the nonparallel base flow. For the nonlinear disturbance development, however, unexpected results are obtained: Secondary instability is hard to distinguish from primary instability and apparently breaks down as soon as the priming 2-D disturbances saturate. However, the nonlinear mechanism identified in cases (iii) and (iv), is obviously much more likely to produce large amplitude 3-D disturbances necessary for the generation of a transitional laminar separation bubble. The mechanism leads to a nonlinearly saturated regime with reasonably turbulent mean-flow characteristics as well as longitudinal vortices in the reattachment zone.

2. INTRODUCTION

Laminar separation bubbles may occur at low Reynolds number under certain operating conditions, especially on laminar-flow airfoils (cf. [1]). Due to a strong adverse pressure gradient downstream of the minimum pressure point the laminar boundary layer may separate before undergoing transition. Most separation bubbles are transitional, i.e., the bubble is closed by turbulent reattachment. Improving flight and performance characteristics of laminar-flow airfoils and compressor blades requires an accurate prediction of separation bubbles. However, all present models used for the prediction of separation bubbles rely on empirical relations derived from experiments, since the flow physics are not yet fully understood. Turbulence models good enough for predicting transitional flows are not available and most Direct Numerical Simulations (*DNS*) of laminar separation bubbles are, so far, only based on the 2-D Navier-Stokes equations. 2-D investigations were justified due to the observation of 2-D effects dominating the flow in the separation zone and inside the bubble. For the generation of turbulence, however, 3-D effects are necessary. In addition, longitudinal vortices have been observed in some experiments (e.g., [2]) in the reattachment zone behind the bubble.

The present work is a continuation of earlier (2-D) investigations by Gruber et al. [3] (2-D) and Rist [4] (3-D) with the aim of obtaining deeper insight into the transition and reattachment process in laminar separation bubbles. Based on the experience gained from the DNS of flat-plate boundary-layer transition [5] where transition in a low turbulence environment is initiated by a sequence of instabilities, e.g., primary instability (instability of the base flow versus Tollmien-Schlichting waves) and secondary instability (instability of the flow in the presence of finite-amplitude 2-D waves versus small amplitude 3-D disturbances), a number of generic disturbance combinations are investigated in the present paper.

3. NUMERICAL METHOD

Only a general outline of the method will be given here, details are available in [5] - [9]. The latest version of the DNS-scheme developed by Fasel et al. [5], improved by Kloker et al. [6] and more recently by Kloker [7], is used. It is based on the numerical solution of the complete 3-D Navier-Stokes equations in vorticity-velocity formulation for incompressible unsteady flow. The flow is split into a two-dimensional steady base flow and a three-dimensional unsteady disturbance flow in such a way that *no* linearization occurs. This allows the calculation of different base flows by prescribing different free-stream velocity distributions without altering the boundary conditions for the calculation of the disturbance flow. Thus, compared to earlier simulations of boundary layer instability and transition, only the base flow had to be changed for the calculations presented in this paper.

3.1 Governing equations

The flow over a flat plate is considered (see Figure 1) where the streamwise, wall normal, and spanwise directions are denoted by x, y, and z, respectively with their relevant velocity components denoted by u, v, and w. All variables are nondimensionalized by the free-stream velocity $\overline{U}_\infty$ upstream of the separation bubble and by a reference length $\overline{L}$, where overline denotes dimensional variables

$$x = \frac{\overline{x}}{\overline{L}}, \quad y = \sqrt{Re}\frac{\overline{y}}{\overline{L}}, \quad z = \frac{\overline{z}}{\overline{L}}, \qquad (1)$$
$$u = \frac{\overline{u}}{\overline{U}_\infty}, \quad v = \sqrt{Re}\frac{\overline{v}}{\overline{U}_\infty}, \quad w = \frac{\overline{w}}{\overline{U}_\infty},$$

and $Re = \overline{U}_\infty \overline{L}/\overline{\nu}$ is the global Reynolds number. For all investigations presented here, $Re = 10^5$ ($\overline{U}_\infty = 30m/s$, $\overline{\nu} = 1.5 \cdot 10^{-5} m^2/s$, and $\overline{L} = 0.05m$).

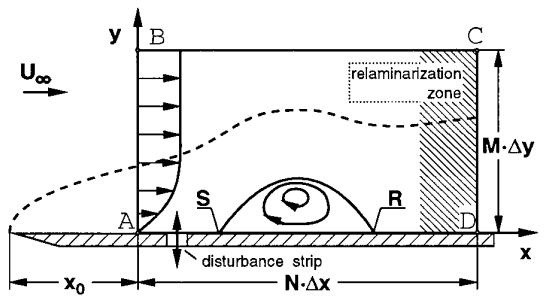

Figure 1: Integration domain for the DNS of a laminar separation bubble. S = separation point, R = reattachment point.

Paper presented at the 74th Fluid Dynamics Symposium on "Application of Direct and Large Eddy Simulation to Transition and Turbulence" held at Chania, Crete, Greece, in April 1994.

With the vorticity defined as $\vec{\omega} = -rot(\vec{u})$, the vorticity transport equations for the calculation of the x-, y-, and z-vorticity components are

$$\begin{aligned}
\frac{\partial\omega_x}{\partial t} + \frac{\partial}{\partial y}(v\omega_x - u\omega_y) - \frac{\partial}{\partial z}(u\omega_z - w\omega_x) &= \tilde{\Delta}\omega_x, \\
\frac{\partial\omega_y}{\partial t} - \frac{\partial}{\partial x}(v\omega_x - u\omega_y) + \frac{\partial}{\partial z}(w\omega_y - v\omega_z) &= \tilde{\Delta}\omega_y, \quad (2) \\
\frac{\partial\omega_z}{\partial t} + \frac{\partial}{\partial x}(u\omega_z - w\omega_x) - \frac{\partial}{\partial y}(w\omega_y - v\omega_z) &= \tilde{\Delta}\omega_z,
\end{aligned}$$

where

$$\tilde{\Delta} = \frac{1}{Re}\frac{\partial^2}{\partial x^2} + \frac{\partial^2}{\partial y^2} + \frac{1}{Re}\frac{\partial^2}{\partial z^2}. \quad (3)$$

The velocity components are calculated from

$$\begin{aligned}
\frac{\partial^2 u}{\partial x^2} + \frac{\partial^2 u}{\partial z^2} &= -\frac{\partial\omega_y}{\partial z} - \frac{\partial^2 v}{\partial x \partial y}, \\
\tilde{\Delta} v &= \frac{\partial\omega_x}{\partial z}, -\frac{\partial\omega_z}{\partial x} \quad (4) \\
\frac{\partial^2 w}{\partial x^2} + \frac{\partial^2 w}{\partial z^2} &= \frac{\partial\omega_y}{\partial x} - \frac{\partial^2 v}{\partial y \partial z}.
\end{aligned}$$

Next, the flow is split into a steady, two-dimensional base flow (index B), and an unsteady, three-dimensional disturbance flow (denoted by primes)

$$\begin{aligned}
u = u_B + u', \quad v = v_B + v', \quad w = w', \quad (5) \\
\omega_x = \omega_x', \quad \omega_y = \omega_y', \quad \omega_z = \omega_{zB} + \omega_z'.
\end{aligned}$$

Inserting equation (5) into equations (2 – 4) and sorting out the equations to be fulfilled by the base flow yields two sets of equations for the calculation of the base and for the disturbance flow, respectively. The boundary conditions are split accordingly, and both flows are computed separately, as described in the next two sections.

3.2 Calculation of the base flow

The integration domain is divided into N and M equally spaced intervals in x and y direction, as shown in Figure 1. Blasius boundary layer profiles are prescribed at the inflow boundary A–B, the no-slip boundary condition applies at the plate's surface at $y = 0$, and at outflow (C–D) the governing equations are solved with the assumption of $1/Re \cdot \partial^2 f/\partial x^2 = 0$, where $f = [u_B, v_B, \omega_{zB}]$. The "relaminarization zone" and the "disturbance strip" shown in Figure 1 are not used for the calculation of the base flow. Along the upper boundary B–C a free-stream velocity distribution is prescribed containing a smooth step by Δu_M between x_1 and x_2 (cf. Figure 2). A steady finite difference solution to the 2-D base flow equations is seeked by using an $\mathcal{O}(\Delta x^4, \Delta y^4, \Delta t^2)$-accurate finite difference x-implicit, y-explicit splitting method.

3.3 Calculation of the disturbance flow

After the base flow has been calculated, disturbances are introduced into the integration domain by timewise periodic blowing and suction upstream of the bubble within the "disturbance strip", and their downstream development is obtained by solving the 3-D disturbance flow equations.

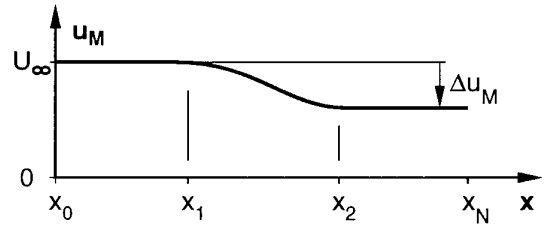

Figure 2: Velocity distribution along the free-stream boundary of the integration domain.

Periodicity in spanwise direction is assumed, and an effective pseudospectral/finite difference scheme is constructed by using a Fourier ansatz in z-direction

$$f(x,y,z,t) = \sum_{k=-K}^{K} F_k(x,y,t) e^{ik\gamma z}, \quad (6)$$

where $f = [u', v', w', \omega_x', \omega_y', \omega_z']$, $F_k = [U_k, V_k, W_k, \Omega_{xk}, \Omega_{yk}, \Omega_{zk}]$, and $\gamma = 2\pi/\lambda_z$ is the spanwise wave number. Since f in equation 6 is a real quantity, only those modes with $k \geq 0$ need to be calculated, the others are defined by $F_{-k} = \overline{F_k}$, where $\overline{\ }$ stands for the complex conjugate. $\mathcal{O}(\Delta x^4, \Delta y^4)$-accurate finite difference expressions are used for discretization on the grid already used in section 3.2 for the calculation of the base flow. Time integration is performed by an explicit, $\mathcal{O}(\Delta t^4)$-accurate four stage Runge-Kutta scheme using central, upwind, downwind, and again central finite differences for the x-convection terms, in each stage, respectively. The sequence of upwind and downwind differences is altered for every time step. It can be shown that this technique effectively damps out small scale oscillations that cannot be accurately discretized on a given grid [7].

The boundary conditions for the disturbance flow are: no disturbances at inflow (A–B), no slip at the plate (A–D), except for the wall-normal velocity within the disturbance strip

$$V_k(x,0,t) = A_k\sqrt{Re}\, v_w(x) \sin(\beta t), \quad (7)$$

where $v_w(x)$ is a "wall-forcing function", and β is the dimensionless frequency related to the frequency parameter $F = \overline{\beta\nu}/\overline{U}_\infty^2 \cdot 10^4$ usually used in boundary-layer stability theory by $\beta = F \cdot Re \cdot 10^{-4}$. $v_w(x)$ is zero everywhere, except within the disturbance strip, where a point-symmetric amplitude distribution with respect to the strip's center is constructed from the 5^{th}-order polynomial $v_w(\xi) = 20.25 \cdot \xi^5 - 35.4375 \cdot \xi^4 + 15.1875 \cdot \xi^3$ with ξ running from 0 to 1 in the first and from 1 to 0 in the second half of the disturbance strip.

The vorticity at the wall is calculated from

$$\begin{aligned}
\left.\frac{\partial^2\omega_x}{\partial x^2}\right|_{y=0} + \left.\frac{\partial^2\omega_x}{\partial z^2}\right|_{y=0} &= -\left.\frac{\partial^2\omega_y}{\partial x \partial y}\right|_{y=0} + \left.\frac{\partial}{\partial z}\tilde{\Delta} v\right|_{y=0}, \\
\left.\omega_y\right|_{y=0} &= 0, \quad (8) \\
\left.\frac{\partial\omega_z}{\partial x}\right|_{y=0} &= \left.\frac{\partial\omega_x}{\partial z}\right|_{y=0} - \left.\tilde{\Delta} v\right|_{y=0}.
\end{aligned}$$

At the upper boundary of the integration domain (B–C) an exponential decay of the disturbances in y-direction is allowed, and hence a relatively small integration domain of only a few boundary layer thicknesses can be used. Starting already upstream of the outflow boundary (C–D), the disturbances are forced to decay by gradual suppression of the disturbance vorticity (with x) [6]. This technique has been carefully tested, it works for boundary layers as well as for strongly nonparallel base flows, like e.g., free shear layers or bluff body wakes.

4. NUMERICAL RESULTS

The integration domain shown in Figure 1 begins at $Re_{\delta_1} = 1.72077\sqrt{x_0 \cdot Re} = 331$, extends over $18\delta_1$ in y-direction (until $y = 18.84$) and from $x_0 = 0.37$ to $x_N = 5.06$. A velocity step by $\Delta u_M = 9\%$ is prescribed between $x_1 = 0.71$ and $x_2 = 2.43$ according to Figure 2. Except where noted, 697 and 96 equally sized intervals are used for discretization in x- and y-direction, respectively for a discretization using approx. 25 grid points per TS-wavelength in x-direction and 100 time steps per period. With the disturbance strip placed between $x = 0.55$ and $x = 0.70$ and the "relaminarization zone" beginning at $x_{rz} = 4.67$, the spanwise wave number in equation (6) is set to $\gamma = 20$.

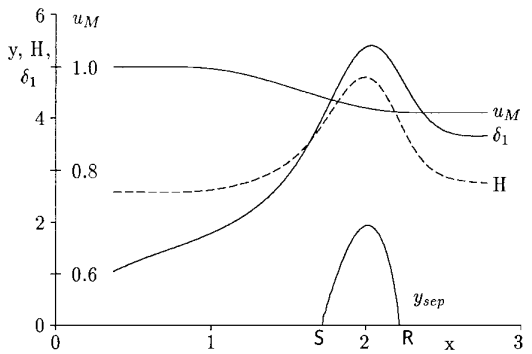

Figure 3: Base flow parameters: free-stream velocity u_M, shape factor H, displacement thickness δ_1, separation streamline y_{sep}, separation point S, and reattachment point R.

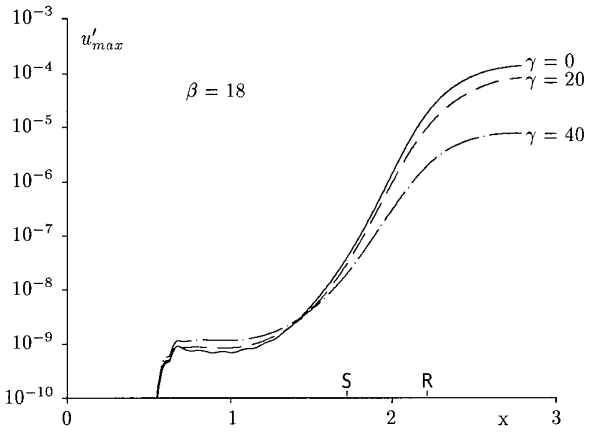

Figure 4: Amplification curves for small-amplitude disturbances (case **L**), β = frequency, γ = spanwise wave number.

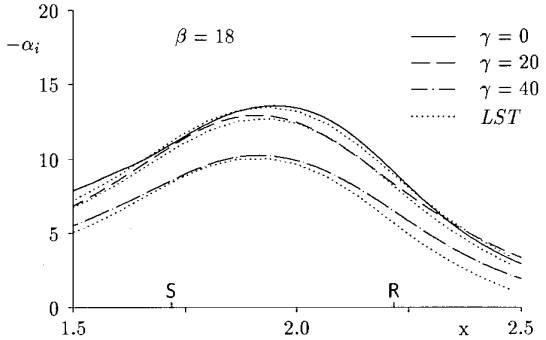

Figure 5: Comparison of DNS-amplification rates from case **L** with Linear Stability Theory (*LST*), β = frequency, γ = spanwise wave number.

4.1 Base flow

Characteristic features of the base flow are given in Figure 3. They allow the comparison of the prescribed free-stream velocity $u_M(x)$ with the displacement thickness $\delta_1(x)$, the shape factor $H(x)$ (displacement thickness/momentum thickness), and the separation streamline corresponding to $\Psi = 0$ where Ψ is the (2-D) stream function. Here and in all subsequent figures S and R mark the separation and reattachment of the base flow, they are repeated to facilitate comparison between different figures. The shape factor starts with the Blasius value $H = 2.59$ at inflow, increases to a maximum around 4.8, and decreases again in the reattachment region. The strong increase of δ_1 and hence H begins already upstream of the bubble. Separation and reattachment, however, occur downstream of the largest gradient of $u_M(x)$ at those positions where $H \approx 4$. With $\delta_{1S} \approx 4.0$ at separation according to Figure 3, the Reynolds number based on the displacement thickness at separation $Re_{\delta_1 S} = \sqrt{Re} \cdot \delta_{1S} \approx 1265$ turns out to be quite large compared to the Blasius value of $Re_{\delta_1} = 1.72077\sqrt{x_S \cdot Re} \approx 715$ for the same x. Behind the bubble, the flow asymptotically recovers to a Blasius boundary layer indicating that the laminar separation bubble has primarily a local effect on the base flow. Since δ_1 decreases downstream of the bubble until the decrease is superseded by the growth of the flat-plate boundary layer, Re_{δ_1} would also decrease and the presentation of the results further down, based on a local normalization by δ_1 would be equivocal. It is therefore better to keep to the "global normalization" introduced in equation (1).

4.2 Choice of disturbance frequency

Linear Stability Theory (*LST*) calculations based on the Orr-Sommerfeld equation and using u_B-velocity profiles calculated in the previous section, revealed that the flow was most unstable with respect to 2-D disturbances with frequencies around $\beta = 18$ ($F = \beta/Re \cdot 10^4 = 1.8$ in the stability diagram). This was verified in the DNS with small amplitude wave packets centered at $\beta = 7, 14$, and 28, respectively. In all three cases the most amplified disturbance occured at $\beta \approx 18$. The disturbance frequency for all subsequent studies using periodical forcing was therefore set to $\beta = 18$.

4.3 Discussion of Results

Depending on the choice of the disturbance amplitudes A_k in equation (7), different cases can be investigated: a "linear" case (**L**) with a 2-D and two pairs of 3-D TS-waves each with such a small amplitude that no relevant nonlinear interactions occur; a "fundamental" case (**F**) with a large amplitude 2-D TS-wave together with small amplitude 3-D TS-waves; an "oblique" case (**O**), where only one large-amplitude 3-D wave pair is introduced; and a "combined" case (**C**), where an equally large 2-D TS-wave is introduced together with the oblique wave pair of case **O**. In the first two cases, the spectral ansatz (6) is truncated at $K = 2$, and disturbances are introduced for $k = 0$, 1, and 2, i.e., $\gamma = 0$, 20, 40, respectively. In the other two cases, eqn. (6) is truncated at $K = 4$ or larger.

4.3.1 *Linear case*

Amplification curves of the u'-disturbance maxima vs. x are shown in Figure 4 for the 2-D wave and the 3-D wave pairs. Generated at the disturbance strip ($0.55 \leq x \leq 0.70$) with $A_0 = A_1 = A_2 = 10^{-10}$ in (7), the waves undergo a strong amplification over several orders of magnitude, starting already upstream of the separation point. The amplification is strongest for the flat wave, it decreases with increasing spanwise wave number. Downstream of the bubble, the amplification is reduced due to the relaxation of the base flow to a Blasius boundary layer. It is important to note that the magnitude of the amplification rate $\alpha_i = -d/dx(\ln u'_{max})$ is more than ten times larger in presence of the bubble than without it. In addition, 3-D waves are nearly as amplified as 2-D waves.

A quantitative comparison of the amplification rates extracted from Figure 4 with results of LST using local base flow profiles, i.e., parallel-flow assumption, is given in Figure 5. Remarkably good quantitative agreement is observed, small differences can be attributed to the nonparallel base flow, since the disturbance amplitudes are too small for nonlinear effects ($\mathcal{O}(10^{-4})$). Closer investigation of these nonparallel effects showed that the v'-disturbance maximum agrees better with LST in the downstream part of the bubble, whereas u'_{max} agrees better in the upstream part. Such qualitative behavior is plausible, since the streamlines have different (concave/convex) curvature before and after the bubble. On the whole, nonparallel effects are surprisingly small.

4.3.2 *Fundamental case*

The only difference of this case to the previous one is a much larger amplitude of the 2-D wave at the disturbance input, $A_0 = 10^{-5}$ (compare above). The intention is to simulate a combination that will lead to K-type transition in a Blasius

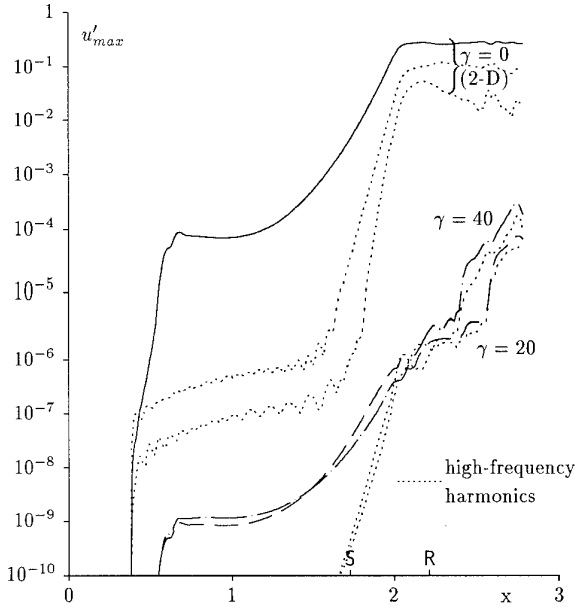

Figure 6: Amplification curves for large 2-D and small 3-D disturbance amplitudes (case **F**), γ = spanwise wave number.

boundary layer. In such a case, a tenfold increase of the 3-D amplification rates can be expected due to secondary instability [10]. As long as the amplitudes of the 3-D disturbances are very small, no interaction is expected among these, and the simultaneous introduction of two oblique wave pairs is considered an effective means of getting an idea about the sensitivity of the expected resonance to the spanwise wave number.

Except for the larger amplitude of the 2-D wave, the 2-D and 3-D disturbances in Figure 6 initially develop in the same way as in Figure 4. However, when the 2-D wave attains amplitudes of $u'_{max}/U_\infty \approx 20\%$, nonlinear effects are responsible for its saturation which persists downstream of the bubble. As already shown in [4] and as will be shown further down, the flow is qualitatively reasonable for $x > 2.0$, despite the possible deterioration of the numerical results due to insufficient numerical resolution for $x > 2.0$.

High-frequency harmonics ($\beta = 36$ and $\beta = 54$ for the 2-D wave, $\beta = 36$ for the 3-D waves) have been included in Fig. 6 as dotted lines in order to give an additional indication of nonlinear effects. Saturation of disturbance amplitudes at a high level and generation of higher harmonics are typical nonlinear phenomena which can also be observed in other base flows, e.g., in a Blasius boundary layer [8], [9]. In case **L**, where no saturation is observed, all higher harmonics stay below 10^{-7}.

As regards the 3-D disturbances, which were supposed to get in resonance with the 2-D wave and strongly amplified by secondary instability (cf. Herbert [10]) after the 2-D wave has attained sufficiently large amplitudes ($\mathcal{O}(1\%)$), an unexpectedly reduced growth of the 3-D waves is observed as soon as the 2-D wave saturates. This could again be due to nonlinear effects since the 3-D higher harmonics shown have approximately the same amplitude as the fundamentals. However, the reduced amplification may also be explained by nonlinear deformation and stabilization of the mean flow due to the action of the 2-D nonlinear disturbances, as already shown in [4].

In order to validate this surprising result, case **F** has been re-computed using smaller grid sizes in x and time (i.e., ≈50 grid points per wavelength, and 120 intervals/period, respectively). No differences were observed.

Next, the simulation was repeated using larger 3-D disturbance amplitudes. Results of this simulation are shown in

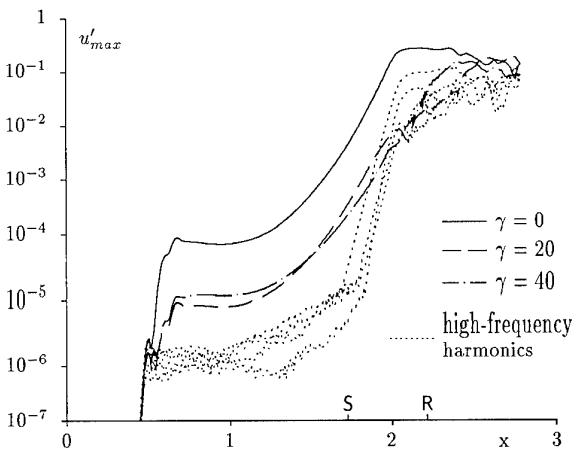

Figure 7: Effect of increasing the 3-D disturbance amplitude compared to Figure 6, γ = spanwise wave number.

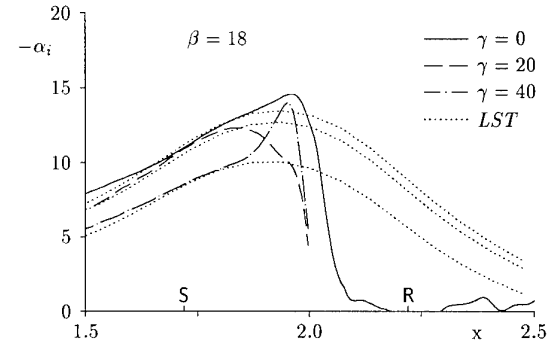

Figure 8: Comparison of DNS-amplification rates from case **F** with Linear Stability Theory (*LST*), β = frequency, γ = spanwise wave number.

Figure 7 in the same way as in Figure 6. Apart from larger numerical noise upstream of the bubble, depicted by the high-frequency harmonics, no significant differences occur for the 2-D and 3-D waves compared to the preceding investigation. So far, no important contribution of secondary instability to the transition process could be observed for the laminar separation bubbles under investigation, even after changing the scenario from "fundamental" to "subharmonic resonance", as reported in [4].

When looking at the amplification rates $-\alpha_i$ in Figure 8, calculated from the data shown in Figure 6, an initially rather close quantitative agreement between the DNS and LST is again observed as for the linear case in Figure 5. For clarity the 3-D α_i curves are not shown for $x > 2.0$, since α_i would overemphasize local oscillations of the amplitudes vs. x in Figure 6. Starting at $x \approx 1.85$, the amplification rates begin to deviate from LST and all waves shown turn towards a neutral behavior. The 2-D wave experiences a short distance with slightly increased amplification while the 3-D wave with the larger spanwise wave number ($\gamma = 40$) attains a rather large amplification rate before it decreases.

Comparisons with stability calculations for secondary instability at $x = 1.8$, where the 2-D disturbance amplitude is approximately 1%, yield increased 3-D amplification rates for $\gamma = 40$, thus indicating indeed a possible secondary instability just before the nonlinear saturation of the 2-D disturbances. However, identification of a secondary instability in the DNS results is very difficult in the present case due to its small difference to primary instability, as far as amplification rates are concerned. In addition, the secondary instability breaks down soon after its emergence. Similar observations are made in the subharmonic case **S** [4].

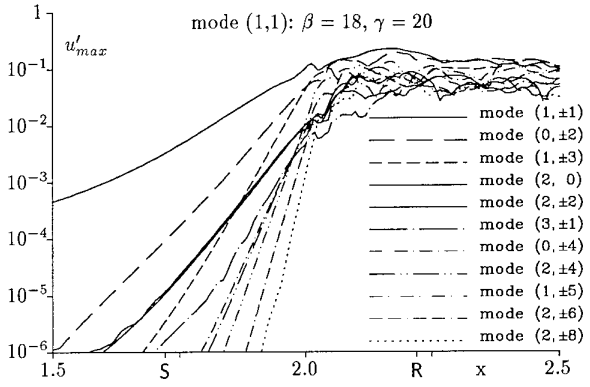

Figure 9: Amplification curves for large 3-D disturbance amplitudes (case **O**), β = frequency, γ = spanwise wave number.

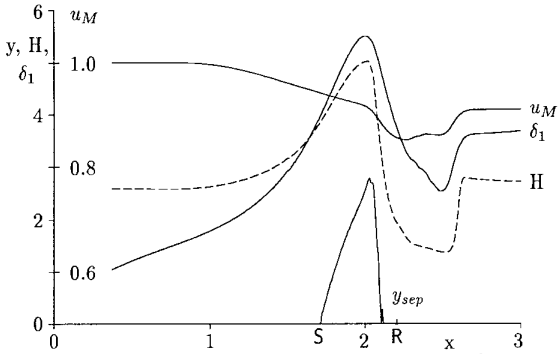

Figure 10: 2-D mean-flow parameters in case **O**: free-stream velocity u_M, shape factor H, displacement thickness δ_1, separation streamline y_{sep}. S, R: separation and reattachment of the undisturbed base flow.

4.3.3 *Oblique case*

In the past years, a new 3-D amplification mechanism was found, initially in the transonic flow regime (e.g., [11]) where 3-D waves are equally or even more amplified than 2-D waves. A somewhat similar situation appears here in the separation bubble: 3-D (linear) disturbances are approximately as amplified as 2-D disturbances (cf. Fig. 4 and 5). Therefore, a 3-D instability (now called *oblique breakdown*) might be of relevance here. This possibility is investigated in case **O** by means of a pair of oblique waves with $\beta = 18$ and $\gamma = \pm 20$ (i.e., $A_k = 0$, for $k \neq 1$, and $A_1 = 10^{-5}$ in eqn. (7)).

In this case, additional nonlinear effects are expected to occur among different modes in spanwise direction. Therefore, in addition to using a finer resolution in x and t (≈50 grid points/wavelength, and 200 time steps/period, resp.), K in equation (6) is increased compared to the simulations above. In order to save some computer time, the beginning of the "relaminarization zone" and the end of the integration domain are placed at $x_{rz} = 2.52$ and $x_N = 3.17$, respectively. In addition, case **O** is performed as a "spatial continuation simulation" using two integration domains overlapping in downstream direction, and $K = 4$ and $K = 8$ in the two grids, respectively. Periodic inflow conditions for the disturbances calculated on the second grid beginning at $x = 1.5$, are extracted from the results of the first grid at the same x. x_0 of the first grid and the height of the integration domain in y-direction are not altered compared to the simulations discussed so far, but the number of grid points in x-direction is reduced to 498 in spite of the finer resolution.

Amplification curves u'_{max} vs. x from case **O** are shown in Figure 9 for some typical spectral modes. A typical feature of the oblique breakdown is the amplification of modes (n,k)[1], where $n + k$ is even. These modes include 2-D disturbances, e.g., mode (2,0), and longitudinal vortices, e.g., mode (0,±2). The amplitudes of corresponding oblique wave pairs (denoted by ±k9 are added to form single curves in Figure 9. Two observations are important: first, modes (1,±1) are amplified according to LST until nonlinear effects lead to saturation around $x \approx 2.0$, and second, all other modes are generated by nonlinear interactions, e.g., modes (0,±2), (2,±2), and (2,0) by modes (1,±1). The second observation is confirmed by the amplification rates between $x = 1.5$ and $x = 2.0$ in Figure 9: the nonlinearly generated waves belonging to the interaction just mentioned, are all amplified with the same rate which is approximately twice the rate of the forcing waves. Higher-order nonlinear modes start at an initially lower amplitude with even larger amplification rates, e.g., (1,±3). It turns out that the local amplitudes of all nonlinearly generated modes solely depend on the local amplitude of modes (1,±1) [11].

In principle, the "oblique breakdown" mechanism is operative for any spanwise wave number $\gamma > 0$ as long as the corresponding oblique wave pair is amplified. From the observations in connection with case **L**, however, a "preferred" or "optimal" spanwise wave number γ_p can be expected: Decreasing γ from γ_p to $\gamma = 0$, the amplification of the 3-D waves can no longer increase, since the amplification of the 2-D wave is the largest possible, but at the same time the "oblique" mechanism somehow must decrease due to its absence in 2-D. Increasing γ beyond γ_p must also decrease the strength of the mechanism due to the reduced amplification of oblique primary waves with increasing spanwise wave number. Taking α_i of modes (0,±2) between $x = 1.5$ and $x = 2.0$ as a reference, a number of test calculations were performed using different (global) spanwise wave numbers γ in eqn. (6), and the largest amplification of modes (0,±2) was found near $\gamma_p \approx 20$. The "preferred" spanwise wavelength of the longitudinal vortices represented by modes (0,±2) ($\gamma \approx 40$) is thus $\lambda_{zp} \approx 0.157$. With $\delta_{1S} \approx 4$ from Figure 3, λ_{zp} can be expressed as $\lambda_{zp} \approx 12.4\delta_{1s}$, when the stretching in y-direction by $\sqrt{Re}$ is taken into account.

As already observed in case **F**, additional nonlinear effects lead to the saturation of all disturbance amplitudes at $x > 2.0$. Although the resolution is still not adequate to resolve all aspects of the flow in that region, a number of interesting qualitative mean-flow features can be observed, as will be shown in the next two figures.

The downstream development of the free-stream velocity u_M, the shape factor H, the displacement thickness δ_1, and the separation streamline y_{sep} for the mean flow from case **O** are given in Figure 10 for comparison with the base flow (i.e., the undisturbed steady flow) in Figure 3. No differences occur for $x < 1.85$ in agreement with the small disturbance amplitudes observed further above. In the rearward part of the bubble, however, everything is different from the undisturbed flow: Reattachment occurs earlier, the bubble's outline resembles a triangle, the shape factor and the displacement thickness both decrease to very low values, and even the free-stream velocity is decreased. The retardation of the outer flow is thus increased by additional 5% relative to U_∞ by the action of the disturbances, which have reached such a large amplitude that they have finite amplitude at y_M, despite their exponentially fast decay with increasing y. Such a large change of the velocity at the upper boundary of the integration domain could cause undue influences of the chosen height of the domain on the flow, especially for $x > 2.1$. This would be clarified by additional simulations using different distances y_M of the upper boundary from the flat plate. Other investigations using a viscous-inviscid interaction model of the kind proposed in [12] are also of interest, they would further remove possible effects of a finite height of the integration domain.

The sudden jump of all curves back to the undisturbed values at $x \approx 2.52$, however, is due to the artificial suppression of the disturbances in the "relaminarization zone" beginning at $x_{rz} = 2.52$. This shows the efficiency of the "relaminarization

[1] n = frequency index (relative to $\beta = 18$), k = spanwise wave number index (relative to $\gamma = 20$).

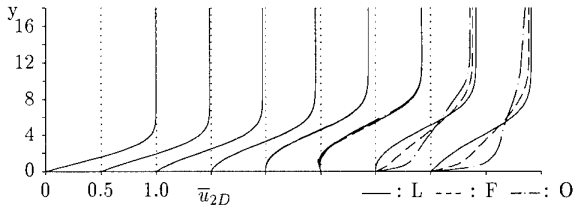

Figure 11: Comparison of 2-D mean-flow profiles at $x = 1.0$, 1.2, 1.4, ..., 2.4.

zone". Compared to case **L**, and to the influence of the bubble on the base flow described in connection with Figure 3, where only a local influence of the bubble on the flow was observed, the influence of the large-amplitude disturbances is not local, since, once amplified and saturated, a quasi-turbulent flow would persist for all x downstream of the bubble if no relaminarization were enforced.

The downstream evolution of the 2-D mean-flow profiles for the three cases **L/F/O** are compared in Figure 11. For $x < 2.0$, there is no difference due to the small disturbance amplitudes. Further downstream in the reattachment zone, the most striking differences appear: the profiles according to cases with large-amplitude disturbances have different curvature and a much larger $\partial u/\partial y$ close to the wall. Qualitatively these profiles look like turbulent boundary layer profiles, and indeed, calculation of the shape factor H in the reattachment zone for the nonlinear cases yields $H \approx 2.0$, and $H \approx 1.4$ in case **F**, and **O**, respectively. Thus, the qualitative and quantitative resemblance of the mean flow behind the bubble to a turbulent mean flow is most pronounced in case **O** (a typical shape factor for turbulent flat-plate boundary layers is $H \approx 1.5$). The apparent difference between case **F** and case **O** is due to different 3-D disturbance amplitudes: the flow in case **F** is dominant 2-D and therefore qualitatively more distinct from 3-D turbulence than in case **O**.

In summary, the separation bubble in case **O** yields the best qualitative agreement with a transitional laminar separation bubble. In addition, longitudinal vortices which have already been observed in experiments (e.g., [2]) might be due to the occurence of modes (0,±2). The calulation of λ_{zp} further above gives an estimate for the spanwise wavelength of such vortices. What happens to case **O** if an even large amplitude 2-D disturbance is present, is investigated in the next section.

4.3.4 *Combined case*

The results presented in sections 4.3.2, and 4.3.3 show that a large amplitude 2-D disturbance will not immediately drive small amplitude 3-D disturbances to large-amplitude saturation, the mutual interaction of 3-D disturbances seems to be much better suited for that purpose, instead. A problem with case **O**, however, is that the flow is dominated by 3-D disturbances whereas experiments show a dominance of 2-D effects.

Until reliable receptivity studies are available, the initial disturbance spectrum must be estimated and different generic combinations must be investigated, as it is done here. Due to the convective nature of the instabilities observed above, the flow downstream of the separation bubble depends on the disturbance spectrum introduced further upstream. In order to check the relevance of case **O**, a number of additional simulations were performed, where large-amplitude subharmonic, fundamental or higher harmonic 2-D disturbances were added to the initial 3-D disturbance in case **O**. The most "dangerous" combination found, was that using fundamental disturbance frequency, since that frequency is the only one that is comparably amplified as the forcing 3-D modes (1,±1) already in the "linear region" upstream of the bubble.

The simulation presented in this section is performed using ≈50 grid points/wavelength, 200 time steps/period, $\gamma = 20$, $K = 4$ in equation (6), and 594 grid points in x. Disturbances are generated with $\beta = 18$, $A_0 = 1.1 \cdot 10^{-5}$, and $A_1 = 10^{-5}$

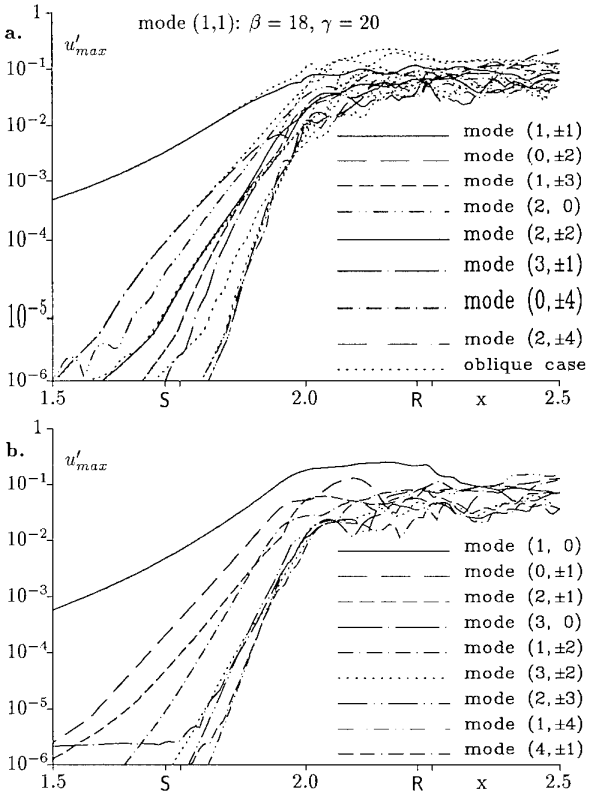

Figure 12: Amplification curves for large 2-D and 3-D disturbance amplitudes (case **C**). (**a.**) n+k even, (**b.**) n+k odd. Dotted lines in (a) represent the results already shown in Figure 9.

in eqn. (7), and x_0 and the height of the integration domain are left unchanged compared to the simulations already described. The amplitudes A_0 and A_1 are chosen so that mode (1,0) and the superposition of mode (1,1) with mode (1,-1) start with equally large disturbance amplitudes at the disturbance strip.

Amplification curves for the new simulation (case **C**) are presented in Figure 12. Figure 12(a) contains only those (even) modes (n,k) which are also present in case **O** with the results from Figure 9 replotted as dotted lines. Compared to case **O**, some modes (e.g., (2,0) and (3,±1)) are initially larger while others remain unchanged until $x \approx 1.85$. Downstream of this x-station, the even modes are generally smaller than in case **O**, this is especially apparent for the longitudinal vortex modes (0,±2) and obviously due to the presence of large-amplitude odd modes shown in Figure 12(b). For $x > 1.85$ two major qualitative differences between case **C** and case **O** arise from the quantitative differences observed further upstream: (i) the flow is dominated by the 2-D wave (1,0) in a manner qualitatively similar to that in case **F**, and (ii) the longitudinal vortices are represented by modes (0,±1) instead of modes (0,±2), i.e., their spanwise wavelength is halfed.

As already observed in case **O** (Figure 9), some modes are again equally amplified between $x = 1.5$ and $x = 2.0$, e.g., modes (0,±2), (2,0), and (2,±2) in Figure 12(a), and modes (0,±1) and (2,±1) in Figure 12(b). Such wave pair triples or pairs thus belong to the same nonlinear combination interaction mechanism, i.e., mode (1,1) with its complex conjugates in the first case, and mode (1,0) with modes (1,±1) in the second case. Even the increased amplitudes of some modes (e.g. (2,0)) can be explained by wave (mode) interaction: compared to case **O**, where it is generated solely by (1,1) and (1,-1), a self interaction of mode (1,0) also contributes to this mode in case **C** and provides for an increased amplitude.

Although the even modes in case **C** are somewhat smaller than in case **O** for $x > 1.85$, and despite the existence of odd modes, the underlying instability mechanism appears to be the same. Namely, the nonlinear interaction of modes in the frequency-spanwise-wave-number-spectrum. Thus, the inclusion of 2-D disturbances into the "oblique breakdown" model does not alter the principle found there.

5. CONCLUSIONS

Inclusion of 3-D disturbances in the DNS of an arbitrarily chosen laminar separation bubble gave a number of unexpected results. Since only one specific base-flow configuration has been investigated so far, it is not yet clear to what extent the present results may be generalized. Further investigations using other base flow parameters, e.g., larger free-stream velocity drop Δu_M, larger Reynolds number at separation $Re_{\delta_1 S}$, larger integration domain in y-direction, etc. are therefore necessary.

6. ACKNOWLEDGEMENTS

Without the financial support provided by the Deutsche Forschungsgemeinschaft (DFG) under contract Ri 680/1-1 and by the University of Stuttgart, the present investigations would not have been possible. The support of both institutions is therefore greatly appreciated. Special thanks go to Wolfgang Müller for taking the "burden" of attending the conference and presenting part of the present results, while the first author was sick.

7. REFERENCES

[1] Muller, T.J. (ed.), "Low Reynolds Number Aerodynamics", Springer Lecture Notes in Eng., Springer, New York, 1989.

[2] Althaus, D., "Drag measurements on airfoils", XVII OSTIV-Congress, Paderborn, Germany, 1981.

[3] Gruber, K., Bestek, H. and Fasel, H., "Interaction between a Tollmien-Schlichting wave and a laminar separation bubble", AIAA Paper 87-1256, 1987.

[4] Rist, U., "Nonlinear effects of 2-D and 3-D disturbances on laminar separation bubbles", *in* S.P. Lin (ed.), Proc. "IUTAM-Symp. Nonlin. Instab. of Nonpar. Flows", Springer, New York, 1994, pp 324–333.

[5] Fasel, H., Rist, U. and Konzelmann, U., "Numerical investigation of the three-dimensional development in boundary layer transition", AIAA J., *28*, 1, January 1990, pp 29–37.

[6] Kloker, M., Konzelmann, U. and Fasel, H., "Outflow boundary conditions for spatial Navier-Stokes simulations of transitional boundary layers", AIAA J., *31*, 4, May 1993, pp 620–628.

[7] Kloker, M., "Direkte Numerische Simulation des laminar-turbulenten Strömungsumschlages in einer stark verzögerten Grenzschicht", Dissertation Universität Stuttgart, 1993.

[8] Rist, U. "Numerische Untersuchung der räumlichen, dreidimensionalen Störungsentwicklung beim Grenzschichtumschlag", Dissertation Universität Stuttgart, 1990.

[9] Rist, U. and Fasel, H., "Direct numerical simulation of controlled transition in a flat-plate boundary layer", submitted to J. Fluid Mech., September 1993.

[10] Herbert, Th., "Secondary instability of boundary layers", Ann. Rev. Fluid Mech., *20*, 1988, pp 487–526.

[11] Thumm, A., "Numerische Untersuchungen zum laminar-turbulenten Strömungsumschlag in transsonischen Grenzschichtströmungen", Dissertation Universität Stuttgart, 1991.

[12] Veldman, A.E.P., "New, quasi-simultaneous method to calculate interacting boundary layers", AIAA J., *19*, 1, January 1981, pp 79–85.

Investigation of Shear Layer Transition Using Various Turbulence Models

Kaldellis J.K.[1], Georgantopoulos G.A.
Hellenic Air Force Academy, Dept. of Aerodynamics
52 G. Kolokotroni Street
11741 Athens
Greece

Abstract

The accurate prediction of shear layer transition plays an important role in the performance amelioration of modern aero-mechanical devices, since transitional shear layers are frequently observed on axial turbomachine blades and other low Reynolds number airfoils.

In the present work some of the most famous existing turbulence models are used in order to analyze a large variety of well documented experimental transitional shear flows. Particular attention is paid to the estimation of the transition length and to the calculation of loss evolution inside the transition area.

Finally interesting conclusions of the proposed analysis are summarized in the last part of the paper, where the behaviour of several transitional blade shear layers is examined, applying the most reliable of the above tested turbulence models.

NOMENCLATURE

e	total energy per unit volume
k	thermal conductivity
p	static pressure
q^2	turbulent kinetic energy
Re	Reynolds number based on reference conditions
t	time
T	temperature
(u,v)	velocity components
u_e	free stream velocity
(x,y)	coordinates of a Cartesian system
y+	$y(\rho.\tau_w)^{1/2}/\mu$
γ	intermittency factor
δ	shear layer thickness
θ	momentum thickness
ρ	density
τ_{ij}	tensor of total viscous stresses (i,j=x,y)
Ω	vorticity vector

Subscripts

w	value at the wall

1. INTRODUCTION

The accurate prediction of shear layer transition plays an important role in the performance amelioration of modern aero-mechanical devices, since transitional shear layers are frequently observed on axial turbomachine blades and other low Reynolds number airfoils.

Up to now boundary layer transition is not yet fully understood. Therefore this lack of accurate information on boundary layer transition poses serious constraints in the application of computer aided design procedures for the design of high performance compressors and turbines, Kaldellis (1993), Douvikas et al (1989). Additionally the prediction of the 3-D loss distribution is also based on the correct estimation of behaviour of the transitional shear layers, Katramatos and Kaldellis (1991).

In the present work a two-dimensional compressible numerical code is developed and used to investigate the evolution of the main flow parameters of some transitional compressor and turbine blade shear layers. During this effort some of the most famous simple turbulence models are used in order to check the influence of the turbulence model upon the loss evolution inside the transition area, see also Kaldellis and Kodossakis (1992).

For this purpose the proposed method is first checked over a wide range of experimental data by Gostelow and Blunden (1988) and Walker and Gostelow (1989). Then it is applied to analyze the behaviour of several transitional blade shear layers. Some interesting conclusions of the proposed analysis are summarized in the last part of the paper.

2. PRINCIPLES OF NUMERICAL ALGORITHM

The numerical method is based on the non-dimensional 2-D compressible Navier-Stokes equations written in conservative form. These equations can

(1) also Technological Educational Institute of Piraeus; Permanent address: Pontou 58, 16777 Greece.

Paper presented at the 74th Fluid Dynamics Symposium on "Application of Direct and Large Eddy Simulation to Transition and Turbulence" held at Chania, Crete, Greece, in April 1994.

be expressed as:

$$\frac{\partial U}{\partial t}+\frac{\partial E}{\partial x}+\frac{\partial F}{\partial y}=0 \qquad (1)$$

where:

$$U=\begin{bmatrix}\rho\\ \rho u\\ \rho v\\ \rho e\end{bmatrix} \qquad (2)$$

$$E=\begin{bmatrix}\rho u\\ \rho u^2+p-\frac{1}{Re}\cdot\tau_{xx}\\ \rho uv-\frac{1}{Re}\cdot\tau_{xy}\\ u(e+p)-\frac{1}{Re}\cdot(u\tau_{xx}+v\tau_{xy}+k\frac{\partial T}{\partial x})\end{bmatrix} \qquad (3)$$

and

$$F=\begin{bmatrix}\rho v\\ \rho uv-\frac{1}{Re}\cdot\tau_{xy}\\ \rho v^2+p-\frac{1}{Re}\cdot\tau_{yy}\\ v(e+p)-\frac{1}{Re}\cdot(u\tau_{xy}+v\tau_{yy}+k\frac{\partial T}{\partial y})\end{bmatrix} \qquad (4)$$

where "Re" is the Reynolds number based on reference conditions. The above form of equations does not take into account external heat exchange and body forces, while "e" is the total energy per unit volume given as:

$$e=\rho(i+\frac{u^2+v^2}{2}) \qquad (5)$$

and "i" is the internal energy per unit mass.

Finally the two equations of state must also be used, i.e:

$$p=p(\rho,T) \qquad (6)$$

$$i=i(p,T) \qquad (7)$$

Note that for the initial test cases the perfect gas assumption is adopted.

For turbulent flows it is convenient to use the Reynolds-averaged form of N-S equations employing also the Boussinesq approximation, see Anderson et al (1984). Thus the components of the shear stress tensor are expressed as:

$$\tau_{xx}=(\lambda+2\mu_e)\frac{\partial u}{\partial x}+\mu_e\frac{\partial v}{\partial y} \qquad (8)$$

$$\tau_{yy}=(\lambda+2\mu_e)\frac{\partial v}{\partial y}+\mu_e\frac{\partial u}{\partial x} \qquad (9)$$

$$\tau_{xy}=\mu_e(\frac{\partial u}{\partial y}+\frac{\partial v}{\partial x}) \qquad (10)$$

where the effective viscosity "μ_e" takes into account the molecular "μ" and the eddy viscosity "μ_t" using also the transition intermittency factor "γ", i.e:

$$\mu_e=\mu+[(1-\gamma)\cdot\mu+\gamma\cdot\mu_t]\Rightarrow \qquad (11)$$
$$\mu_e=\mu+\gamma\cdot\mu_t$$

The coefficient of bulk viscosity "λ" is generally negligible except in the study of shock and acoustic waves, which is not our case. The effective thermal conductivity "k" is calculated using the turbulent Prandtl number and the transition intermittency factor "γ".

Since the emphasis of this paper is not on the numerical method, the main points of the algorithm are briefly described below. The numerical solution of the system of equations is obtained using a typical time-marching technique. The governing equations are treated using MacCormack's method which is a predictor-corrector version of the Lax-Wendroff scheme, see also Anderson et al (1984). Several numerical techniques are also used (e.g. multigrid stage, local time-stepping, artificial viscosity terms) to ensure and accelerate the convergence of the algorithm, see also Kaldellis (1992).

The grids used in the present version of the method are H-C grids, which are the most commonly used grids for viscous flow computations in cascade flows. H-O-H grids are also under development in order to improve the accuracy of the method particularly at the trailing edge. The grid generation procedure is decomposed in three main steps; domain definition and allocation of the points on domain boundaries, filling of the domains and finally orthogonalisation of the mesh. Note that the mesh size must be very fine near the solid boundaries (due to thin laminar and transitional shear layers) in order to capture viscous effects.

3. TURBULENCE MODELS

3.1 Baldwin-Lomax Model

Baldwin-Lomax's (1978) model is one of the most widely used models for engineering calculations and was devised to avoid the necessity of finding the edge of the boundary layer. It is a two-layer model and the eddy viscosity is given by the following expression:

$$\mu_t = \min[(\rho \cdot l^2 \cdot D^2 \cdot |\Omega|), (\rho \cdot \alpha \cdot C_{cp} \cdot F_{max} \cdot y_{max} \cdot \Gamma)] \quad (12)$$

where:

$$l = K \cdot y \quad (13)$$

and "Γ(y)" is a modified Klebanoff intermittency function, i.e:

$$\Gamma(y) = \frac{1}{1+5.5(C_{kleb} \cdot y / y_{max})^6} \quad (14)$$

Note that "y_{max}" is the value of y where the function F(y), i.e:

$$F(y) = y \cdot |\Omega| \cdot D(y) \quad (15)$$

reaches its maximum value "F_{max}". Note that "K" is the Von Karman constant (K=0.41) and "D" is the Van Driest damping function which ensures the correct asymptotic behaviour of the Reynolds stress near the wall, i.e.:

$$D(y) = 1 - \exp(-y^+/A^+) \quad (16)$$

Finally "α", "A^+", "C_{cp}" and "C_{Kleb}" are constants chosen to fit experimental data (i.e. α=0.016, A^+=26, C_{cp}=1.6 and C_{Kleb}=0.3).

3.2 One-Half Equation Model

The second turbulence model is based on a modified form of the Cebeci-Smith turbulence model, using also the transport ordinary differential equation for the mixing length proposed by Malik and Pletcher (1978), in order to take into account the influence of the large eddy structure upon the mixing length values in the outer part of the flow field. More precisely:

$$\mu_t = \rho \cdot l^2 \cdot |\Omega| \quad (17)$$

For flow along solid surfaces good results are observed by evaluating "l" according to:

$$l = K \cdot y \cdot (1 - \exp(-y^+/A^+)) \quad (18)$$

in the inner region closest to the solid boundaries.

In the outer part of the flow the mixing length is calculated according to:

$$l = C_1 \cdot L \quad (19)$$

where "L" is determined by the solution to an ordinary differential equation. The final form of this transport equation (Malik and Pletcher,1978) can be written as:

$$u_e \cdot \frac{\partial L}{\partial x} = C_2 \cdot \left| \frac{\tau_w}{\rho_w} \right|^{1/2} \cdot \left[\frac{L}{\delta} - \left(\frac{L}{\delta} \right)^2 \right] \quad (20)$$

The switching from equation (18) to (19) is performed when "l" from eq.(18) first exceeds the corresponding value from eq.(19). Finally C_1 and C_2 are constants which take the value 0.12 and 1.25 respectively.

3.3 One-Equation Model

The third model consists of an one-equation turbulence model, where an extra differential equation for the turbulent kinetic energy "q^2" is solved in addition to the system of equations (1). This transport partial differential equation is developed for "q^2" from the Navier-Stokes equations. For compressible two-dimensional shear flows the equation by Hassid and Poreh (1975) takes the form:

$$\frac{\partial(\rho \cdot q^2)}{\partial t} + \frac{\partial(\rho \cdot u \cdot q^2)}{\partial x} + \frac{\partial(\rho \cdot v \cdot q^2)}{\partial y} = \frac{\partial}{\partial x}\left(\mu_e \cdot \frac{\partial q^2}{\partial x}\right) + \frac{\partial}{\partial y}\left(\mu_e \cdot \frac{\partial q^2}{\partial y}\right) + P - \epsilon \quad (21)$$

where the turbulent kinetic energy production term "P" is given by:

$$P = \mu_t \cdot \left[2\left(\frac{\partial u}{\partial x}\right)^2 + 2\left(\frac{\partial v}{\partial y}\right)^2 + \left(\frac{\partial u}{\partial y} + \frac{\partial v}{\partial x}\right)^2 \right] \quad (22)$$

and the dissipation term "ε" is given as:

$$\epsilon = (C_3 \cdot \mu_t + C_4 \cdot \mu) \cdot \frac{q^2}{L_\epsilon^2} \quad (23)$$

The turbulent viscosity "μ_t" is given by the following relationship:

$$\mu_t = C_5 \cdot \rho \cdot [1 - \exp(C_6 \cdot Re_q)] \cdot \sqrt{q^2} \cdot L_\epsilon \quad (24)$$

where:

$$Re_q = \frac{\rho \cdot \sqrt{q^2} \cdot L_\epsilon}{\mu} \quad (25)$$

and C_3, C_4, C_5, C_6 are numerical constants with values 0.299, 0.336, 0.548, 0.029 respectively.

Finally the dissipation length scale "L_ϵ" is estimated using the three layer formulation developed by Birch (1987). According to this formulation:

$$L_\epsilon = \begin{cases} K \cdot y \cdot D(y) \\ 0.11 y_{max} \cdot \Gamma(y) \\ L_\epsilon^* \end{cases} \quad (26)$$

where "y_{max}" is the distance from the

wall to the maximum of the function "$F_\omega(y)$", given by:

$$F_\omega(y) = y^2 \cdot |\Omega| \qquad (27)$$

and "L_ϵ^*" is a specified constant freestream length scale.

4. TRANSITION MODELLING

Several workers have attempted to correlate the combined influence of pressure gradient and freestream turbulence level on transition, which is of great interest to turbomachine and airfoil designers, see also Katramatos and Kaldellis (1991). However even today advanced computational methods are based on "point transition" or predict unrealistic (excessive) transition lengths and they do not take into account the influence of freestream turbulence level.

The proposed model is based on information given by Abu-Ghannam and Shaw (1980), by Narasimha (1985), by Walker (1987) and by Walker and Gostelow (1989). According to the proposed model transition is started when the local boundary layer momentum thickness Reynolds number "Re_ϑ" exceeds some critical value "Re^*", given by:

$$Re^* = a + \exp\left[H(\lambda_\vartheta) - \frac{H(\lambda_\vartheta)\cdot \bar{T}_u}{b}\right] \qquad (28)$$

where:

$$\begin{aligned} H(\lambda_\vartheta) &= b + d_1\cdot\lambda_\vartheta + d_2\cdot\lambda_\vartheta^2 \qquad (\lambda_\vartheta \le 0) \\ H(\lambda_\vartheta) &= b + d_3\cdot\lambda_\vartheta + d_4\cdot\lambda_\vartheta^2 \qquad (\lambda_\vartheta > 0) \end{aligned} \qquad (29)$$

with a=163, b=6.91, d_1=12.75, d_2=63.64, d_3=2.48, d_4=-12.27, and

$$\lambda_\vartheta = \frac{\rho\cdot\vartheta^2}{\mu}\cdot\frac{du_e}{dx} \qquad (30)$$

the Pohlhausen parameter. The average turbulence intensity "T_u" is the mean value between the initial "in" and the corresponding turbulence value at the start "s" of transition, i.e:

$$\bar{T}_u = 0.5\,(\bar{T}_{u_{in}} + \bar{T}_{u_s}) \qquad (31)$$

The length of transition is predicted using the Walker's (1987) minimum transition length model in combination with the arbitrary pressure gradient transition model by Walker and Gostelow (1989). Therefore the length of transition is given as:

$$\frac{L_T}{L_{T_{min}}} = \frac{0.14 + 20\exp(100\lambda_{\vartheta_s})}{0.33 + 3\exp(100\lambda_{\vartheta_s})}\cdot g(\bar{T}_u) \qquad (32)$$

where:

$$Re_{L_{T_{min}}} = 5.2\,Re_s^{0.75} \qquad (33)$$

and $g(\bar{T}_u)$ is an empirical function taking into account the experimental information concerning the influence of the freestream turbulence level on the length of transition. More precisely according to various experiments "L_T" is observed to increase with turbulence level up to T_u=1.4% and then tend to decrease for higher values of T_u.

Finally the intermittency factor "γ" is expressed as:

$$\begin{aligned} &\gamma = 0.0 && (x < x_s) \\ &\gamma = 1 - \exp(-0.412\xi^2) && (x_s \le x \le x_s + L_T) \\ &\gamma = 1.0 && (x > x_s + L_T) \end{aligned} \qquad (34)$$

where "ξ":

$$\xi = \frac{x - x_s}{l} \qquad (35)$$

and "x_s" is the streamwise distance to the start of transition. The "l" parameter describes the distance between γ=0.25 and γ=0.75 intermittency. The numerical value of "l" is predicted from the following equation by Chen and Thyson (1971):

$$Re_l = 22\,Re_s^{0.67} \qquad (36)$$

5. CALCULATION RESULTS

Using the above described algorithm an important number of transitional shear flows has been investigated and selected results are presented here.

Gostelow and Blunden Transitional Flow

For the purposes of evaluating the three turbulence models a number of calculations has been performed, concerning the experimental transitional flows presented by Gostelow and Blunden (1988) and Gostelow and Walker (1990) for various turbulence levels and a wide range of pressure gradients.

According to Gostelow and Blunden (1988) the investigations were conducted in their octagonal section open circuit tunnel with working section of 608mmx608mm. The boundary layer measurements were made on the top surface of a flat aluminum plate of 1500x608x25mm mounted in the working section and the maximum velocity used

is U_o=40m/sec. For the series of measurements involving variable pressure gradients a fairing having a variable-angle straight flap was mounted above the flat plate. Although it is quite difficult to impose the desired pressure gradient using a simple linear fairing, the velocity distributions showed that the deviations are not serious. The turbulence levels required for the experiments were generated by using square array bi-planar grids, mounted at a fixed distance upstream of the plate leading edge.

The test case analyzed here concerns a shear layer developed under a very strong adverse pressure gradient (λ_θ=-0.0575) at a remarkable turbulence intensity (Tu≈2.1%). The experimental freestream velocity distribution is given in figure [1] along with the corresponding velocity distribution imposed in the numerical solution. Due to the thin shear layers investigated the refinement of the mesh near the solid surfaces is mandatory, if the details of the shear flow are to be properly resolved. For this purpose a simple algebraic numerical grid is adopted which clusters the grid points near the wall, while emphasis is given to ensure that some points always lay in the viscous sublayer.

The calculated velocity profiles for two selected station (x=190mm, γ=0.055 and x=220mm, γ=0.699) are given in figures [2] and [3]. The stations presented are located near the beginning and the end of the transition area and the calculation results of all three models are favourably compared with the experimental data. After a closer examination of the results one can say that the second model (using the ODE for the mixing length) represents better the physics than the other two models. Although it is somewhat unexpected the one-equation model does not give really better results than the Baldwin-Lomax model, despite the remarkable additional computational effort needed.

Taking into account the entire calculation results it is obvious that the simple turbulence models used here along with the corresponding transition model give reasonable results for all test cases examined. However the one-half equation model gives superior predictions for the most test cases and with less computational effort than the one-equation model. The reason for this may be that in most cases, an improvement in the specification of the mixing length will have more effect than a change in the turbulence kinetic energy.

Using in the following the one-half equation model as the standard model in the complete numerical algorithm the evolution of the flow field throughout the transition area is well predicted, see also figures [4a] and [4b]. According to these velocity profiles one can study the flow transformation from laminar to turbulent, while the computational data describe realistically the whole process.

Transitional Flow on a Transonic High Turning Turbine Blade

The second test case examined here is a transonic turbine cascade with a remarkable flow turning of 111° and a very high exit Mach number of 0.92 at design point. This cascade was extensively tested by Mee et al. (1990) who provided us detailed measurements of the flow quantities. It is well known that the flow in a turbine is predominately accelerating, therefore the study of the transition area is quite important, either in cases where the delay of natural transition is desirable to maximise the length of laminar flow or in cases where fast transition is preferable in order to prevent flow separation.

At design conditions the inlet angle is 42.8° while the exit Reynolds number is almost 1,000,000. The blade chord of the turbine is 300mm and the blade span is also 300mm. At the leading edge of the blade the turbulence level was measured to be 4.3%, a typical value for turbomachinery applications. The geometry of the blade is schematically given in figure [5] and the numerical grid used contains 189x212 points. Since our effort is concentrated in the transition area, more than the half of the grid points are placed there. Several numerical test cases are carried out for design and off-design conditions and no more than 4500 iterations are necessary to obtain convergence in any case investigated.

Due to space limitation calculation results are given only at design point in comparison with the experimental measurements by Mee et al. (1990). According to the calculation results transition is detected at S/S_o=0.387, while the length of transition is L_T/S_o=0.379. The corresponding experimental results suggest that transition takes place from S/S_o=0.4 to 0.8, slightly later than indicated in calculations. In figures [6a], [6b], [6c] and [6d] the calculated velocity profiles are favourably compared with the experimental ones for the transi-

tional area of the blade suction side, points A, B, C and D of figure [5].

Finally, the suction surface shape factor distribution is presented in fig.[7], and the numerical prediction describes quite well the experimental points. The evolution of the shape factor across the blade is in accordance with the beginning and the end of transition, since the maximum value of H_{12} is located between 36.3% (numerical results) and 41.4% (experimental results) of the total surface length "S_o" of the suction side of the blade.

Profile Loss Prediction for NACA Compressor Cascades

The next test case is the NACA 65-(12) 10 compressor cascade which has been analyzed for various solidity values and for a wide range of incidence angles. The same test was analyzed by Kaldellis (1992) using a fast viscous-inviscid (V-I) interaction method. That method based on a system of integral shear layer equations gives in most cases remarkable results with minimum computational effort. One of the most serious drawbacks of that method is the way of handling the transition. The integral method used is based on a point transition model, therefore the transition process is almost neglected.

Using as a numerical example the case of figure [8] with solidity value of σ=0.50 and a high off-design positive incidence angle (i=2°, β_1=60°), the behaviour of both suction and pressure side shear layers can be analyzed. For the suction side blade shear layer (figure [9a]) the transition area is located between S=0.0044m and S=0.0161m, while the transition point of the V-I method is placed at S=0.0067m. Note that due to the better description of the transition shear layer the corresponding turbulent shear layer has a smooth evolution of its momentum shape factor especially near the trailing edge. On the other hand the pressure side shear layer is laminar for about 3/4 of the blade chord. According to the present method the transition is situated between S=0.033m and S=0.0502m, while the changes of the momentum shape factor are quite small, see also figure [9b].

The results of the proposed analysis, focused mainly in the transition area, are summarized in figures [10] and [11], where the predicted profile loss coefficient is given in comparison with experiments by Herring et al (1957) and other calculations for the complete incidence operation range of the blade for two extreme solidity values. The overall agreement between the calculated and the experimental results is ameliorated especially for negative incidence angles, where the impact of the transition phenomena is very important. For positive incidence angles the results are also good, although no flow separation is detected in contrary with the V-I method, which predicts trailing edge flow separation for σ=0.5 and i=+2°. Of course the results obtained using the semi-empirical correlations by Lieblein (1960) give only a qualitative picture of the loss distribution, since the application of the De Haller criterion leads always to prediction of early separation.

Comparing the results of figures [10] and [11] one can say that the proposed numerical method gives quite better results in cases where the transition plays an important role. Even if time and computational restraints are a prerequisition, one can use either the proposed or the V-I method (giving acceptable results), since the developed N-S algorithm needs only one order of magnitude more computational power than the corresponding V-I method.

6. CONCLUSIONS

In this paper the first version of a robust and fast enough compressible N-S code developed by the authors is presented and subsequently used to analyze a variety of transitional shear flows. The flow cases investigated include shear layers developed under favourable and adverse pressure gradients and various turbulence levels. Additionally some application results concerning compressor and turbine transitional blade shear layers are favourably compared with the corresponding experimental data.

Three turbulence/transition models have been incorporated and tested into the complete algorithm giving acceptable results for all transitional flow cases examined. However, the one-half equation model seems to give better results at least for the tests analyzed. For all cases investigated the transition area is well described and the start and the length of the transition is predicted with remarkable accuracy. As a direct outcoming of this improvement the corresponding profile loss is better predicted, especially in cases where transition plays an important role in the complete flow pattern. Of course additional effort has to be spent to incorporate an O-

grid in the present algorithm and to use a two-equation turbulence model, without to significantly increase the computational requirements of the method.

Consequently, taking into account the quality of the results obtained and the numerical behaviour of the algorithm, we believe that the above described method constitutes an attractive and reliable engineering tool for low Reynolds compressible and incompressible blade design purposes, able to investigate compressor and turbine transitional flows at various turbulence levels at design and off-design operational points.

REFERENCES

1. **Abu-Ghannam B.J., Shaw R., 1980**, *"Natural Transition of Boundary Layers - the Effects of Turbulence, Pressure Gradient and Flow History", Journal of Mech. Eng. Science, Vol. 22, No.5.*

2. **Anderson D.A, Tannehill J.C., Pletcher R.H., 1984**, *"Computational Fluid Mechanics and Heat Transfer", Hemisphere Publ. Corporation, London.*

3. **Baldwin B.S., Lomax J., 1978**, *"Thin Layer Approximation and Algebraic Model for Separated Turbulent Flows", AIAA Paper 78-257.*

4. **Birch N.T., 1987**, *"Navier-Stokes Predictions of Transition, Loss and Heat Transfer in a Turbine Cascade", ASME Paper 87-GT-22, Anaheim, California.*

5. **Chen K.K., Thyson N.A, 1971**, *"Extension of Emmons' Spot Theory to Blunt Bodies", AIAA Jr., Vol.9, pp.821-825.*

6. **Douvikas D., Kaldellis J., Papailiou K.D.,1989**, *"Secondary Flow Calculations for Axial and Radial Compressors", presented in AGARD Propulsion and Energetics Panel PC 74B on Secondary Flows in Turbomachines, Luxembourg, Volume One, September 1989.*

7. **Gostelow J.P., Blunden A.R., 1988**, *"Investigations of Boundary Layer Transition in an Adverse Pressure Gradient", ASME Paper 88-GT-298, Amsterdam.*

8. **Gostelow J.P., Walker G.J., 1990**, *"Similarity Behaviour in Transitional Boundary Layers Over a Range of Adverse Pressure Gradients and Turbulence Levels", ASME Paper 90-GT-130.*

9. **Hassid S., Poreh M., 1975**, *"A Turbulent Energy Model for Flows with Drag Reduction", ASME Journal of Fluid Engineering 97, pp.234-241.*

10. **Herring L.J., Emery J.C., Erwin J.R., 1957**, *"Systematic 2D Cascade Tests of NACA 65-series Compressor blades at low speeds", NACA TN 3916.*

11. **Kaldellis J., 1992**, *"Convergence Acceleration of a Viscous - Inviscid Interaction Method in the Presence of Flow Separation", presented at the 1st National Congress on Computational Mechanics, Athens, Greece, September 1992.*

12. **Kaldellis J., Kodossakis D.,1992**, *"The Impact of the Turbulence Terms on the Calculation of Fully Separated Subsonic and Supersonic Shear Flows, Including Shock-Shear Layer Interaction", presented at the 3rd National Congress on Mechanics/IUTAM, Athens, Greece, June, 1992.*

13. **Kaldellis J.,1993**, *"Parametrical Investigation of the Interaction Between Turbulent Wall Shear Layers and Normal Shock Waves, Including Separation", published in ASME Transactions, Journal of Fluids Engineering, Vol.115, pp.48-55.*

14. **Katramatos D., Kaldellis J.,1991**, *"3-D Loss Prediction Based on Secondary Flow and Blade Shear Layer Interaction", ASME Paper 91-GT-59, Florida, USA, June 1991.*

15. **Lieblein S., 1960**, *"Incidence and Deviation Angle Correlation for Compressor Cascades", ASME Jr. of Basic Eng., Vol.82.*

16. **Malik M.R., Pletcher R.H., 1978**, *"Computation of Annular Turbulent Flows with Heat Transfer and Property Variations", Heat Transfer 1978, Proc. Sixth Int. Heat Transfer Conference, Vol.2, Hemisphere, Washington D.C., pp.537-542.*

17. **Mee D.J., Baines N.C., Oldfield M.L.G., 1990**, *"Detailed Boundary Layer Measurements on a Transonic Turbine Cascade", ASME Paper 90-GT-263, Brussels, Belgium.*

18. **Narasimha R., 1985**, *"The Laminar-Turbulent Transition Zone in the Boundary Layer", Prog. in Aerospace Sci., Vol.22, pp.29-80.*

19. **Walker G.J., 1987**, *"Transitional Flow on Axial Turbomachine Blading", AIAA Paper No 87-0010.*

20. **Walker G.J., Gostelow J.P., 1989**, *"Effects of Adverse Pressure Gradients on the Nature and Length of Boundary Layer Transition", ASME Paper 89-GT-274, Toronto, Canada.*

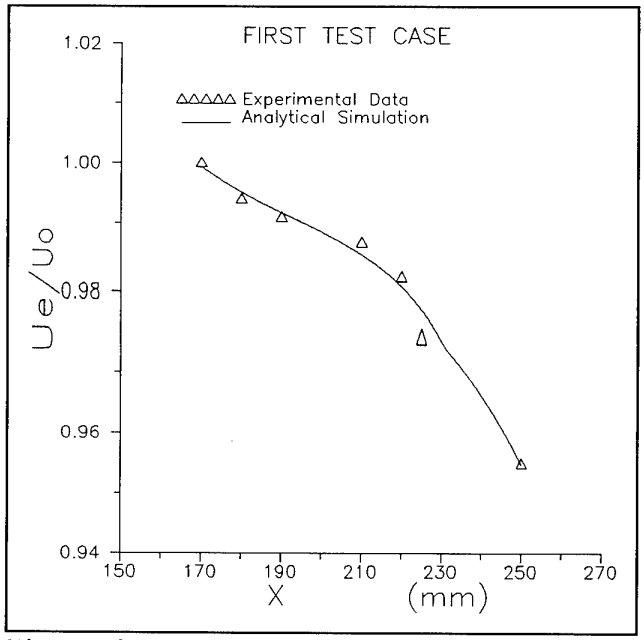

Figure 1: Streamwise external velocity distribution.

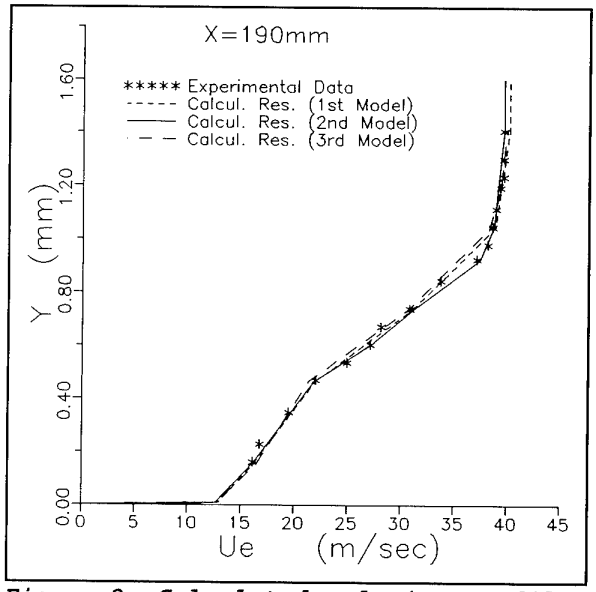

Figure 2: Calculated velocity profiles using various turbulence models, x=190mm, γ=0.055.

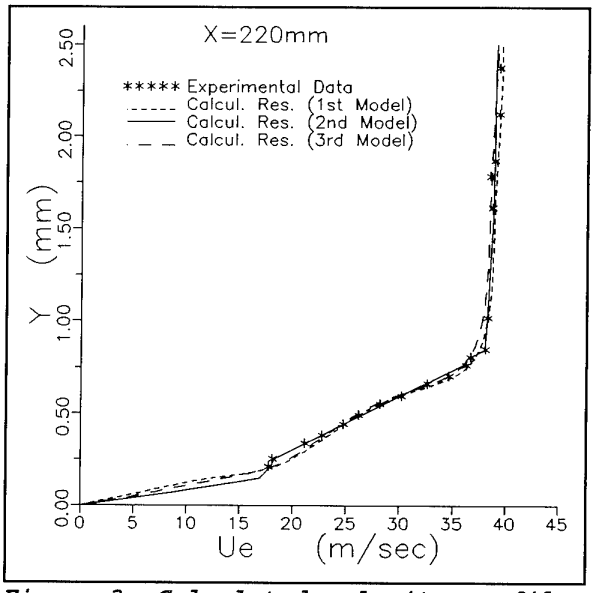

Figure 3: Calculated velocity profiles using various turbulence models, x=220mm, γ=0.699.

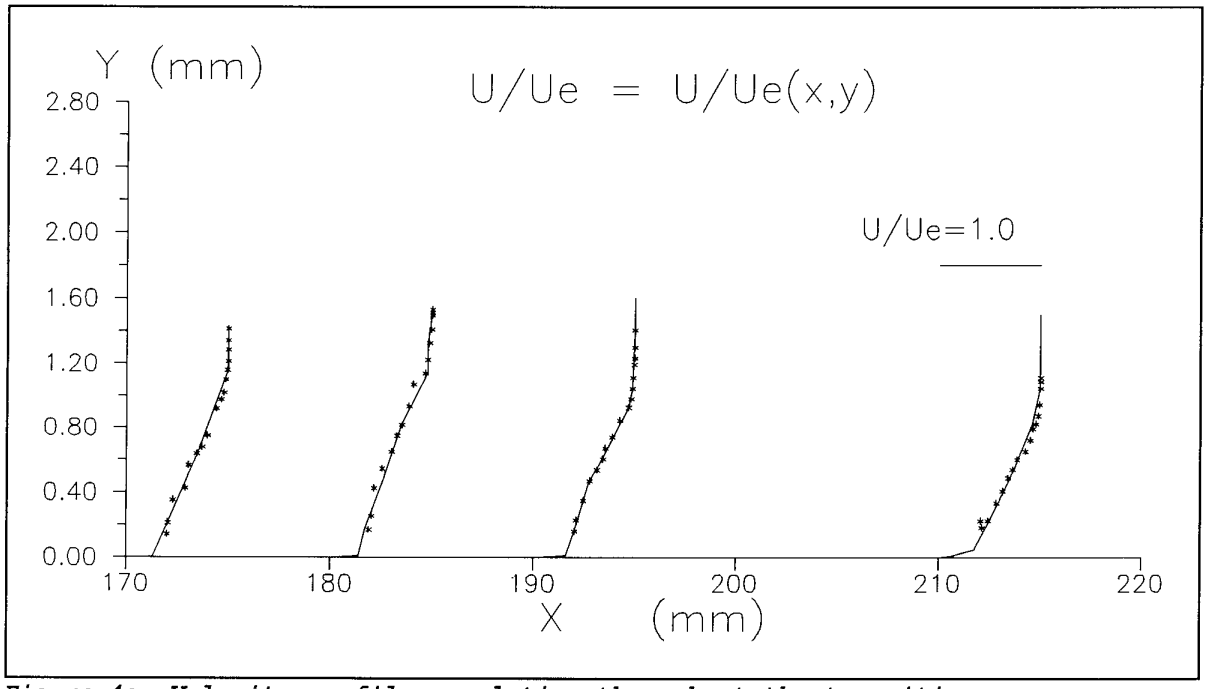

Figure 4a: Velocity profiles evolution throughout the transition area.

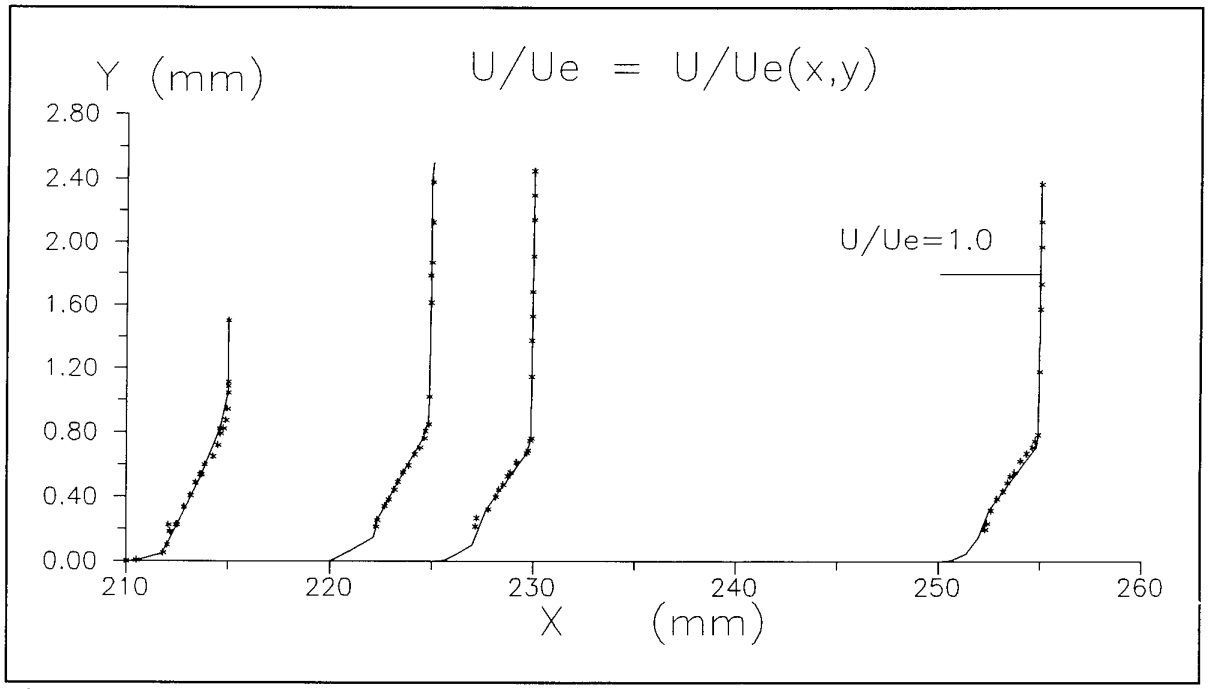

Figure 4b: Velocity profiles evolution throughout the transition area.

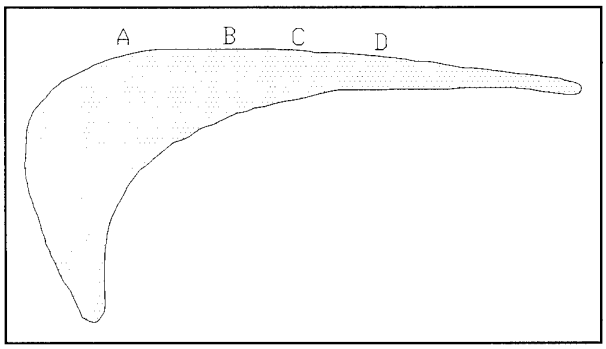

Figure 5: Schematical view of the turbine blade.

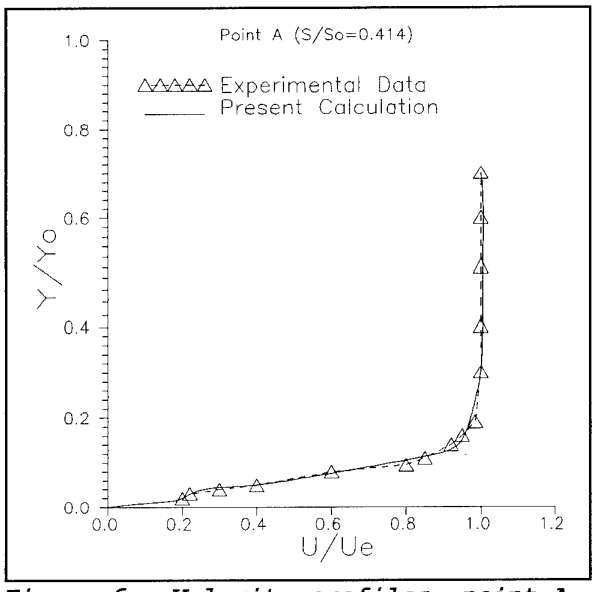

Figure 6a: Velocity profiles, point A.

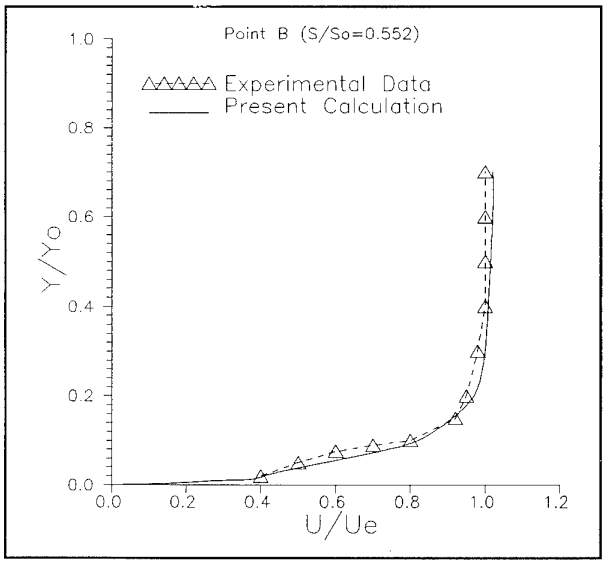

Figure 6b: Velocity profiles, point B.

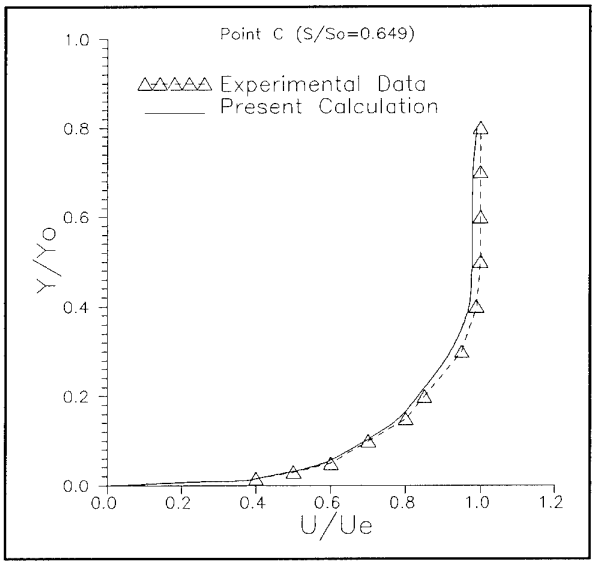

Figure 6c: Velocity profiles, point C.

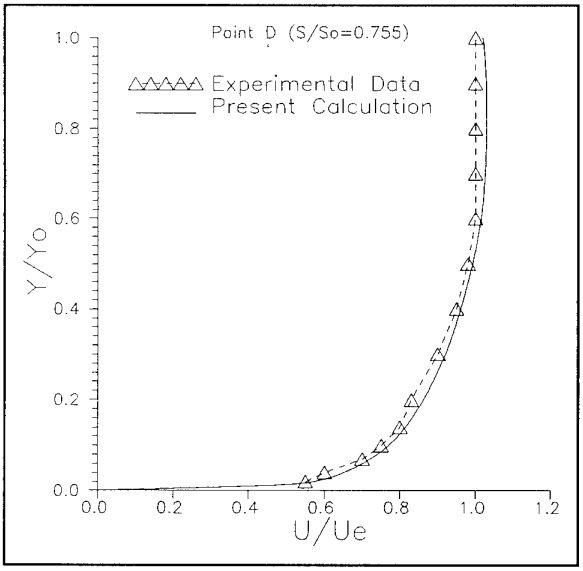

Figure 6d: Velocity profiles, point D.

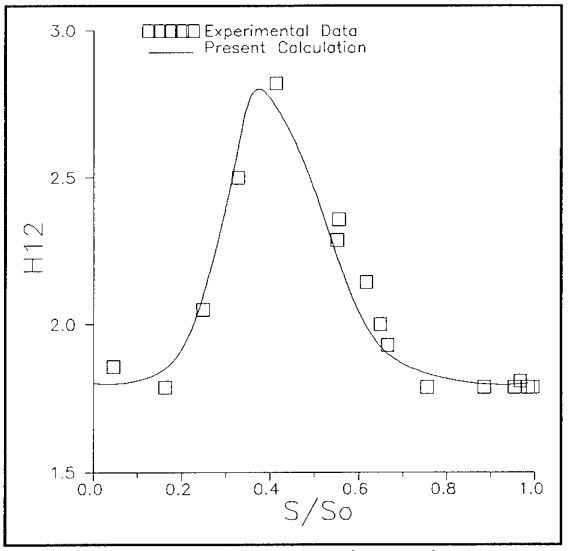

Figure 7: Turbine suction side shape factor.

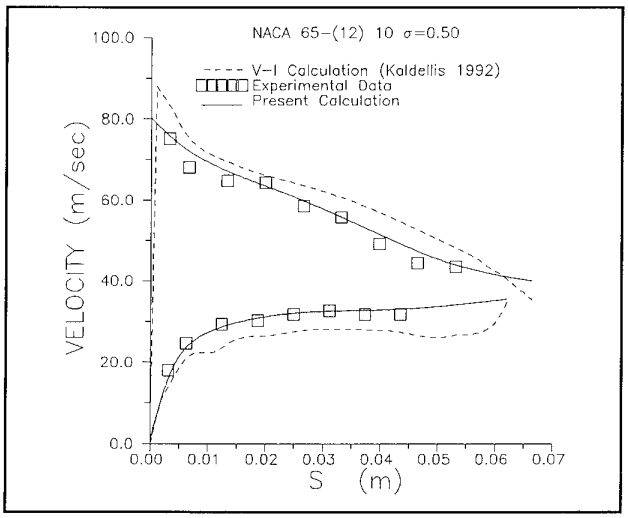

Figure 8: Velocity distribution for NACA 65-(12)10 compressor cascade, i=2°, β_1=60°.

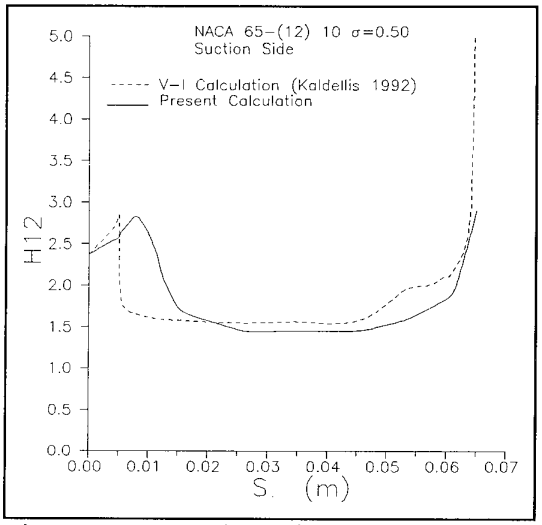

Figure 9a: Suction side shape factor, NACA 65-(12)10, σ=0.5, i=2°, β_1=60°.

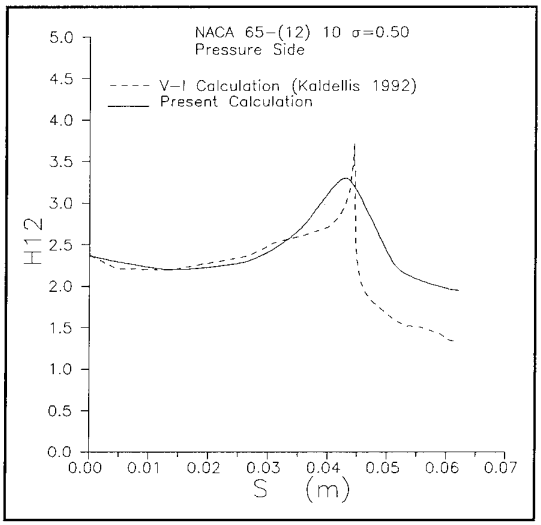

Figure 9b: Pressure side shape factor, NACA 65-(12)10, σ=0.5, i=2°, β_1=60°.

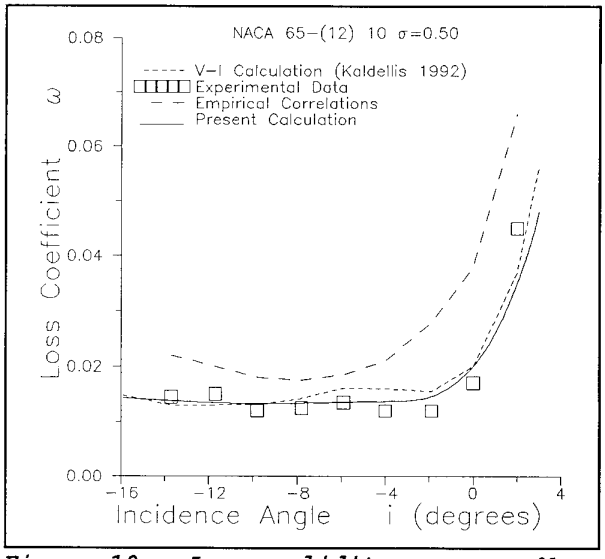

Figure 10: Low solidity case. Mean profile loss coefficient.

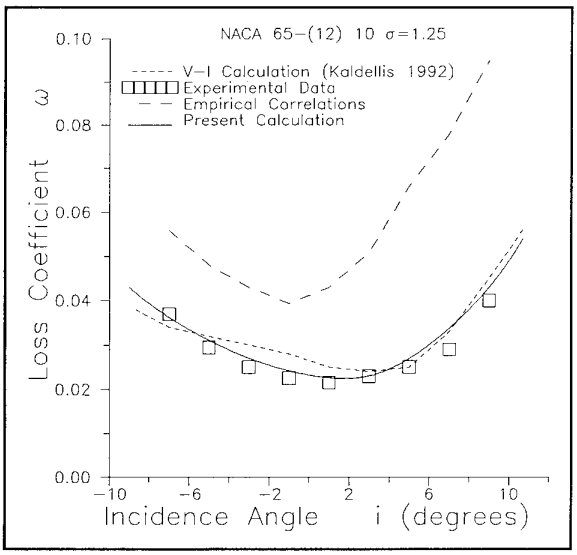

Figure 11: High solidity case. Mean profile loss coefficient.

DNS of Turbulent Flow in a Driven Cavity and their Analysis Using Proper Orthogonal Decomposition

W. Cazemier, R.W.C.P. Verstappen and **A.E.P. Veldman**
Department of Mathematics, University of Groningen
P.O.Box 800, 9700 AV Groningen, The Netherlands

1 SUMMARY

Direct Numerical Simulation (DNS) of 2D and 3D lid-driven cavity flows have been performed. The results have been analyzed using Proper Orthogonal Decomposition (POD). POD has been applied to a 2D driven cavity at Reynolds number 22,000 and to a 3D at $Re = 10,000$. The POD-basis-functions have been computed using the so-called 'snapshot' method of Sirovich. The 2D basisfunctions are used for a Galerkin projection of the Navier-Stokes equations. This results in a relatively low (20 to 80) dimensional dynamical system, that shows (almost) the same dynamical behaviour, in short and long term, as the DNS. Moreover, if the Reynolds number is set to 11,000, the 80-dimensional dynamical system has (almost) the same periodic solution as the 2D Navier-Stokes equations have at $Re = 11,000$.

2 INTRODUCTION

Coherent structures are present in virtually every flow visualization study. But, what is precisely meant by 'coherent structures', and how can one decompose an arbitrary turbulent or transitional flow into a coherent and an incoherent part? An unbiased answer to these questions is given by Lumley [1]. He defined coherent structures using the concept of Proper Orthogonal Decomposition (POD for short). Loosely speaking POD is a technique to extract a set of basisfunctions from the two-point correlation tensor, that is superior to any other set, e.g. to Fourier-modes, in the sense that any other decomposition of the flow in an equal number of modes captures less energy. To make this paper self-contained, we have outlined the basic ideas of POD in Section 4 (for a more detailed discussion the reader is referred to [2], e.g.).

The computation of POD basisfunctions requires large amounts of flow data (either measured or numerically simulated). A direct numerical computation of the basisfunctions from our numerically obtained data sets would more than exhausts the largest available computing resources. POD is feasible, however, when using the so-called snapshot method of Sirovich [3]. The snapshot method is a relatively cheap way to approximate the eigenfunctions of the two-point correlation tensor (see Section 5 for details).

The snapshots have been taken from direct numerical simulation (DNS) of driven cavity flows, both in two and three spatial dimensions. Direct numerical simulations are numerical solutions of the unsteady (here: incompressible) Navier-Stokes equations that compute the evolution of all dynamically significant scales of motion (without using any turbulence model). The way in which these numerical solutions have been computed is described in the next section. Results in 2D and 3D are presented in the Sections 7.1 and 7.2 respectively.

Having an unbiased way to educe coherent structures in a transitional or turbulent flow, the next question that can be posed, reads: how do these structures move, interact, survive, ...

To unravel the dynamics of coherent structures, low-dimensional dynamical flow models have been proposed and studied. These low-dimensional descriptions can be derived by a Galerkin projection of the Navier-Stokes equations on a space spanned by a relatively few number of global modes. They, i.e. low-dimensional flow models, form an active field of research, see for instance [4], [5], [6], [7] and [8].

POD-basisfunctions seem to be well-suited as basis for the Galerkin projection, since they do converge optimally fast (in L^2-norm). All references mentioned in the paragraph above, except Noack and Eckelmann [8] (who use 'mathematical' modes), have applied POD. Aubry *et al.* [4] were among the pioneers. They used POD to derive a low-dimensional dynamical system for the motion of coherent structures in the wall region of a turbulent boundary layer. Deane *et al.* [5] applied the method to grooved channels and circular cylinders; Glauser *et al.* [6] to an axisymmetric jet mixing layer; Rempfer [7] to a flate-plate boundary layer.

We have used the POD of the flow in a 2D driven cavity at Re =22,000 to derive a low-dimensional dynamical system for this case, with the aim to evaluate how well the dynamics of the this system mimics the dynamics of the Navier-Stokes equations. The

Paper presented at the 74th Fluid Dynamics Symposium on "Application of Direct and Large Eddy Simulation to Transition and Turbulence" held at Chania, Crete, Greece, in April 1994.

outcomes of the DNS and the integration of the low-dimensional dynamical system are compared in Section 7.4.

The 3D flows in [4], [5], [6] and [7] were assumed to be periodic in one direction. As a consequence of this assumption, it is sufficient to compute a two-dimensional POD: the basisfunctions in the periodical direction are simply Fourier-modes, and need not be computed explicitly. Here, no-slip conditions have been applied at all walls of the cavity and, in 3D, a full 3D POD has been computed (Section 7.5).

3 DNS OF DRIVEN CAVITY FLOWS

The incompressible Navier-Stokes equations

$$\begin{aligned} \nabla \cdot U &= 0 \\ \frac{\partial U}{\partial t} + \nabla \cdot (UU^T) &= -\nabla P + \frac{1}{Re}\Delta U \end{aligned} \quad (1)$$

are solved numerically using the Marker-and-Cell method [9]. The pressure gradient and the incompressibility constraint are treated implicitly; the convective and viscous terms are treated explicitly. The spatial discretisations are second-order accurate. The discrete Poisson equation for the pressure is solved using the conjugate gradient method with modified incomplete Choleski preconditioning. The ICCG code is fully vectorized by explicitly reordering the unknowns along diagonals of the grid, and is optimized using Eisenstat's implementation (cf. [10] and references therein).

In two dimensions, the flow in a lid-driven cavity converges to a steady state for Reynolds numbers up to 10,000 [11]. For larger Reynolds numbers, 2D driven cavity flows undergo a transition to unsteadiness. Our 2D direct simulations (see [12] for more details) on 333^2-grids exhibit that the flow converges to a periodically oscillating state at $Re = 11{,}000$, that a second bifurcation has taken place at $Re = 16{,}000$ and that the dynamics has become chaotic (that is: some of the Lyapunov exponents are positive) at $Re = 22{,}000$. Data from the latter run has been used to evaluate the POD technique.

It may be emphasized that the physical relevance of the 2D simulations is limited. Reliable physical experiments [13] reveal that the flow in a 3D cube, lid-driven cavity is already unsteady at $Re = 3,200$ and that the power spectrum has a $-5/3$ slope at $Re = 10,000$. Thus, the first instability in the 3D flow is certainly not two-dimensional: the experimentally observed instability is associated with 3D Taylor-Görtler-like vortices. In conclusion, fluid flows in the direction perpendicular to the lid-motion are significant and have to be computed to simulate the physics.

We have performed 3D DNS with no-slip conditions at all walls of the cavity at both $Re = 3,200$ and $Re = 10,000$. The 3D incompressible Navier-Stokes equations are solved numerically on a stretched, staggered 100^3 grid. The CPU-time per gridpoint and time-step is 0.6μs on one processor of NLR's NEC SX-3.

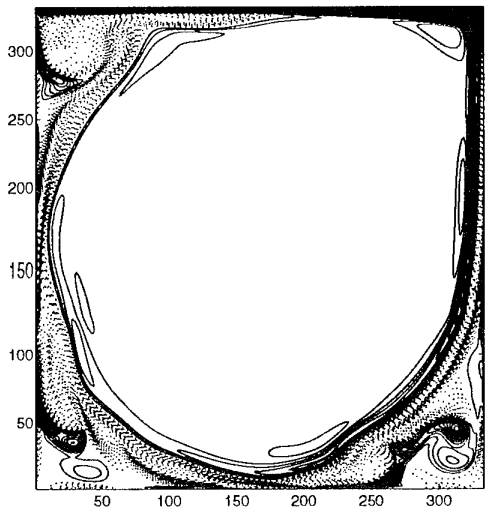

Figure 1: *Snapshot of the vorticity in a 2D driven cavity at Re = 22,000. Here, and in all figures of the 2D driven cavity to follow, the upper-lid of the cavity is driven from the left to the right.*

As an illustration of the structures in the flow, Figure 2 shows an instantaneous vorticity field in the 3D cavity. More results can be found in Section 7.2.

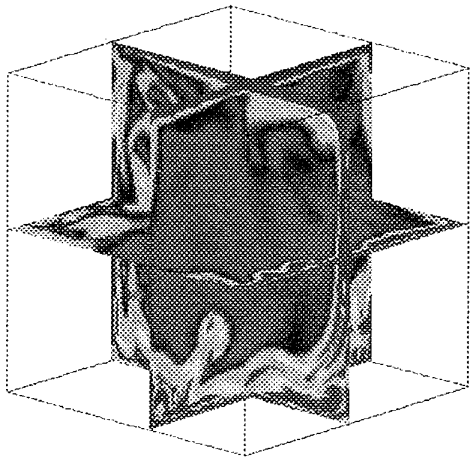

Figure 2: *Snapshot of the vorticity in a 3D driven cavity at Re = 10,000. The orientation of the cavity is such that the upper-plane is driven from the left/back to the right/front.*

The data of this 3D simulation has been used for the 3D POD.

4 PROPER ORTHOGONAL DECOMPOSITION

The basic idea, introduced by Lumley [1], consists of finding a basis of say N 'structures' σ^i $(i=1,2,..,N)$, that is optimal compared to all other sets of N functions in the sense that any other decomposition (e.g. in N Fourier-modes) captures less kinetic energy, i.e. the basisfunctions σ^i are determined successively such that the projection

$$\frac{\langle (\sigma^i, u)^2 \rangle}{(\sigma^i, \sigma^i)}, \tag{2}$$

is maximal for $i=1,2,..,N$. Here, u denotes the fluctuating part of the velocity field U, $\langle \cdot \rangle = \lim_{T\to\infty} \int_0^T \cdot \, \mathrm{d}t$, and $(f,g) = \int_\Omega f\bar{g}\mathrm{d}\Omega$; Ω is the flow domain.

The maximalization problem (2) can, by calculus of variations [14], be written as

$$\int_G R(x,x')\sigma^i(x')\,\mathrm{d}x' = \lambda_i \sigma^i(x), \tag{3}$$

where R is the auto-correlation tensor:

$$R(x,x') = \langle u(x)u(x') \rangle.$$

The eigenvalue problem (3) is a Fredholm integral equation of the second type, with a positive definite Hermitian kernel [15]. The properties of this integral equation are given by the Hilbert-Schmidt theory which states that there exists a denumerable set of orthonormal basisfunctions σ^i, and that the corresponding eigenvalues λ_i are real and positive. Moreover, the flow field can be reconstructed from the basisfunctions,

$$u = \sum_{i=1}^{\infty} a_i \sigma^i, \tag{4}$$

where the time-dependent coefficients a_i are uncorrelated, i.e.

$$\langle a_i a_j \rangle = \delta_{i,j} \lambda_i.$$

This implies that an eigenvalue is equal to the average amount of turbulent kinetic energy in the 'direction' of the corresponding basisfunction. The total turbulent kinetic energy is, in average, given by the sum of the eigenvalues.

The POD basisfunctions are divergence-free and satisfy the boundary conditions. These properties ease the Galerkin projection of the Navier-Stokes equations (see Section 6).

It may be remarked that the POD technique can also be applied to the entire velocity field, instead of to the fluctuating part. In that case the zeroth basisfunction is (approximately) equal to the mean velocity.

5 APPROXIMATION OF THE BASISFUNCTIONS

Today's computing resources are (by far) insufficient to compute POD basisfunctions directly from (3). For this reason, we have used the so-called snapshot method of Sirovich [3]. This method reduces the computational complexity to that of an eigenvalue problem of dimension M, where $M \geq N$ is the number of snapshots that is used to approximate the auto-correlation tensor R. A snapshot $u^{(n)}(x) = u(x, n\,dt)$ is a realization of the fluctuating flow field.

The snapshot method is formally based on the ergodic hypothesis, which justifies to rewrite the auto-correlation tensor R as an infinite series,

$$R(x,x') = \lim_{M\to\infty} \frac{1}{M} \sum_{n=1}^{M} u^{(n)}(x) u^{(n)}(x'),$$

provided that the time-spacing dt in between successive snapshots is large enough for the snapshots to be uncorrelated. This series is truncated after M terms. The truncated series is substituted into the integral equation (3) and thus an integral equation with a degenerate kernel is obtained. Since the snapshots are linearly independent the solutions of this integral equation are of the form

$$\sigma^i(x) = \sum_{n=1}^{M} q_n^i u^{(n)}(x),$$

where the vector q^i of the M unknown coefficients q_n^i forms the solution of the eigenvalue problem

$$Qq^i = \lambda q^i \quad \text{with} \quad Q_{ij} = \frac{1}{M}\langle u^{(i)}, u^{(j)} \rangle.$$

A priori, we do not know how large M should be taken for a fair approximation of the basisfunctions. In fact, we have no alternative but to try different values of M and thus to estimate the speed of convergence; see Section 7.3. It may be remarked that we have to restrict ourselves to two spatial dimensions here, since it is yet practically impossible - due to a shortage of computing power - to perform a 3D DNS that provides sufficient uncorrelated snapshots to study the convergence of the basisfunctions as function of the number of snapshots.

6 A LOW-DIMENSIONAL SYSTEM

We decompose the velocity field U into the mean velocity $\bar{U}$ and the fluctuating velocity u: $U = \bar{U} + u$. The Galerkin projection of the Navier-Stokes equations (1) on the basisfunction σ^i reads

$$\begin{aligned}(\sigma^i, \frac{\partial u}{\partial t}) = \; & -(\sigma^i, \nabla\cdot(\bar{U}u)) - (\sigma^i, \nabla\cdot(u\bar{U})) \\ & -(\sigma^i, \nabla\cdot(uu)) - \tfrac{1}{Re}(\nabla\sigma^i, \nabla u).\end{aligned}$$

Here we have made use of two properties of the basisfunctions, viz. their divergence is zero and they satisfy the boundary conditions. Substitution of the truncation, after N terms, of the expansion (4) into the above expression gives

$$\frac{da_i}{dt} = -A_{i,k,l}a_k a_l - B_{i,k}a_k - D_i, \qquad (5)$$

where $i,j,k = 1,..,N$, and $A_{i,k,l}$, $B_{i,k}$ and D_i depend on the mean flow $\bar{U}$ and the basisfunctions σ^i:

$$\begin{aligned} A_{i,k,l} &= (\sigma^i, \nabla\cdot(\sigma^k\sigma^l)) \\ B_{i,k} &= \frac{1}{Re}(\nabla\sigma^i, \nabla\sigma^k) + (\sigma^i, \nabla\cdot(\sigma^k\bar{U})) \\ &\quad +(\sigma^i, \nabla\cdot(\bar{U}\sigma^k)) \\ D_i &= (\sigma^i, \nabla\cdot(\bar{U}\bar{U})) + \frac{1}{Re}(\nabla\sigma^i, \nabla\bar{U}) \end{aligned}$$

It may be noted that we have closed the system (5), by simply neglecting all contributions related to basisfunctions with an index larger than N. Later, in Section 7.4, we will discuss other ways of treating the unresolved modes.

The evolution of the coefficients $a_i(t)$ in the expansion (4) is governed by the ordinary differential equations (5). The underlying idea is that due to the optimal fast convergence (in L^2-norm) of the basisfunctions, the dimension of the dynamical system (5) can be kept relatively low. And that from this system the motion of the large structures can be simulated both cheaply and accurately. To what extend this holds, will be investigated in Section 7.4.

7 RESULTS

This section describes results of the direct numerical simulations of 2 and 3D flows in driven cavities and their analysis using proper orthogonal decomposition.

7.1 2D DNS

Figure 3 shows the mean flow in the driven cavity at $Re = 22,000$. It takes roughly 5 seconds for the core to turn around. We call this period a large-eddy turnover-time.

At $Re = 22,000$ the motion of vortical structures has become chaotic and isn't so confined in space as at lower Reynolds' number, e.g. as at $Re = 11,000$ where the motion of vortical structures is periodic and confined to small regions near the corners of the cavity. At $Re = 22,000$ one can observe vortical structures moving seemingly chaotically around in the cavity along trajectories that stay relatively close to the walls of the cavity. Figure 1 shows a snapshot.

The 2D DNS of the driven cavity flow at $Re = 22,000$ consists of two separate simulations that

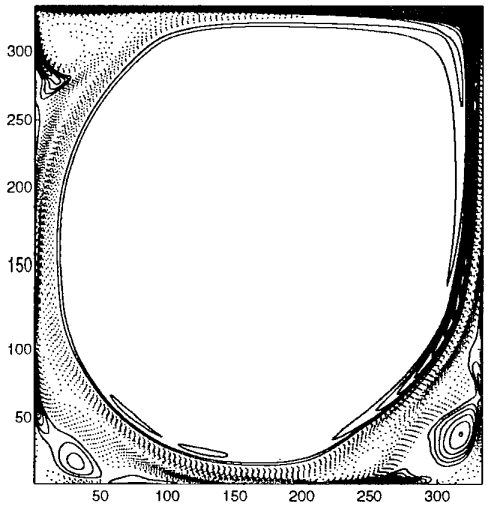

Figure 3: *The vorticity of the mean flow, as obtained from a 2D DNS of a lid-driven cavity flow at* $Re = 22,000$.

start from different initial conditions. Both start from earlier computed velocity fields that are statistically in equilibrium. The first run covers 500 seconds; the second one last six times longer. So, in total, 700 large-eddy turnover-times have been computed. The kinetic energy as obtained from both runs is shown in Figure 4. The first 500 seconds correspond to the first run; the rest (from 500 to 3500 seconds) belongs to the second run.

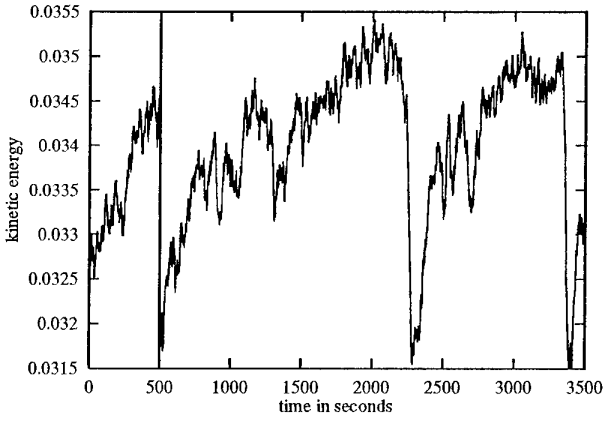

Figure 4: *Time-series of the total kinetic energy in a 2D driven cavity (Re=22,000).*

The fluctuating kinetic energy of both runs is shown in Figure 5.

One can observe two sharp peaks in the fluctuating kinetic energy and two deep valleys in the kinetic energy at $\pm$ 2300 seconds and at $\pm$ 3400 seconds. These extremely rare events correspond to an eddy penetrating the core region of the cavity. Figure 6 catches such an intruder in the act. Afterwards it

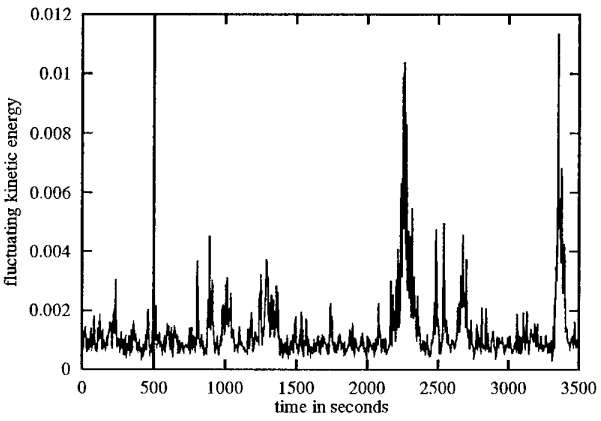

Figure 5: *Time-series of the total fluctuating kinetic energy in a 2D driven cavity (Re=22,000).*

dissipates. The fluctuating kinetic energy is relative large when the core is altered, since the flow pattern is fairly different from the mean flow then. It is to be emphasized that Figure 6 shows a rarity: this has happened only twice during 700 large-eddy turnover-times.

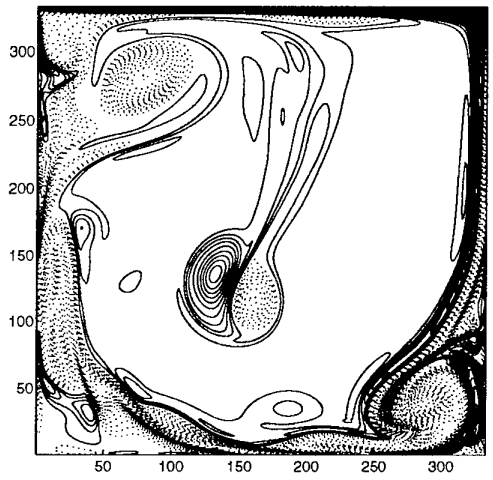

Figure 6: *A rarity: an eddy has penetrated the core region of the lid-driven cavity. This figure shows the vorticity; Re=22,000.*

7.2 3D DNS

Prasad and Koseff [13] have conducted a series of physical experiments in three-dimensional lid-driven cavities. In particular, they have measured turbulent flows in lid-driven cube cavities at $Re = 3,200$ and $Re = 10,000$. We have performed 3D DNS of these turbulent flows using no-slip conditions at all walls of the cavity. The results of the 3D DNS reproduce the experimentally observed Taylor-Görtler-like vortices. As an illustration of the structures in the flow, Figure 2 shows an instantaneous vorticity field in the 3D cavity at $Re = 10,000$.

The Navier-Stokes equations are integrated sufficiently long in time to compute both mean and rms velocities. The experimental data in [13] consists of mean and rms velocities at lines in the symmetry plane. The computed mean velocities at the symmetry plane agree well with those that have been measured, and also the rms velocity profiles are similar; see Figure 7 for a comparison.

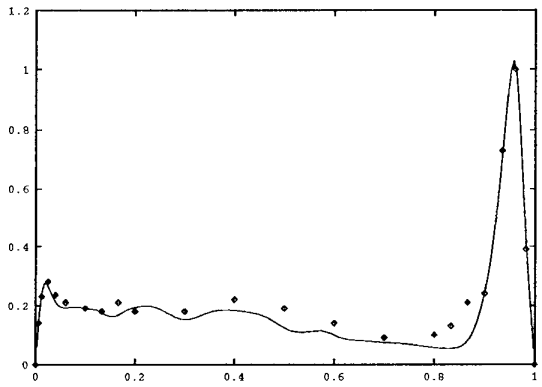

Figure 7: *Comparison of the rms velocity* $\overline{v'v'}$ *at the symmetry plane. This figure shows* $10 * \sqrt{(\overline{v'v'})}$ *versus* x *at Re= 10,000 along the vertical line in the symmetry plane through the geometric center of the cavity. The symbols denote measured values; the continuous line represents the computed rms velocity* $10 * \sqrt{(\overline{v'v'})}$.

Moreover, the power spectrum computed from the DNS data at $Re = 10,000$ has a part with a $-5/3$ slope.

7.3 2D POD

The 2D POD is approximated using snapshots of the 2D DNS of a driven cavity flow at $Re = 22,000$. Results of this DNS have been shown in Section 7.2.

The snapshot method of Sirovich (see Section 5) requires that the snapshots are uncorrelated. In 2D we can satisfy this requirement by taking 5 seconds, i.e. one large-eddy turnover time, in between successive snapshots (see Figure 8).

The 2D DNS covers 3500 seconds. Thus, 700 uncorrelated snapshots are available and up to 700 basisfunctions can be computed. Figure 9 shows the convergence of the eigenvalues as a function of the number of snapshots. We can see that the eigenvalues have not fully converged yet. Partly, this may be explained by eddies that enter the core region at extreme long time-intervals (see Figure 6). This

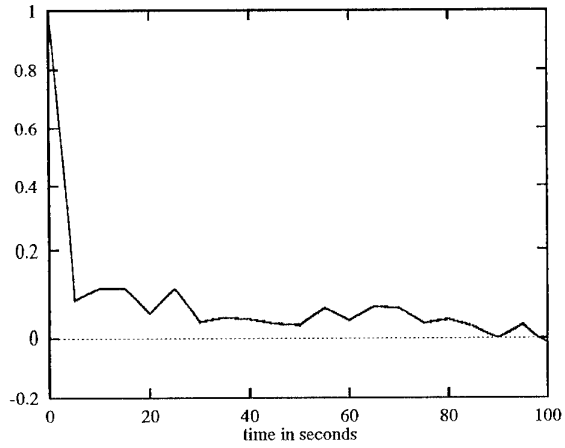

Figure 8: *Correlation of the snapshots.*

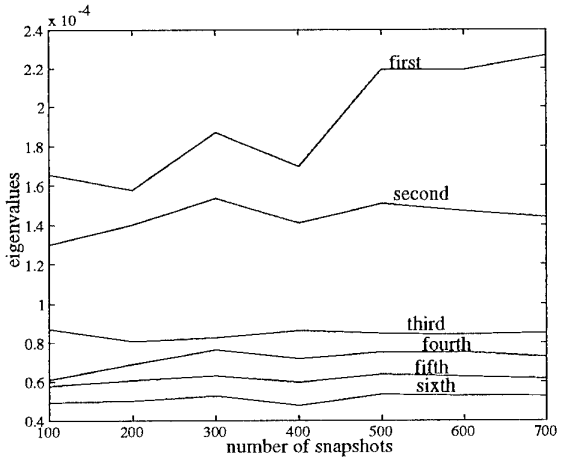

Figure 9: *Convergence of the eigenvalues as function of the number of snapshots.*

phenomenon is certainly not represented accurately in the basisfunctions. For that it occurs too infrequently: of the 700 snapshots only a few will contain information about this rare phenomenon. It may be observed that the eigenvalues with the higher indices seem to have converged somewhat better than the first two. This supports the idea that long-wave phenomena have not fully converged yet.

The basisfunctions that have been computed by the snapshot method have not fully converged, and thus may not be as optimal as the exact POD basisfunctions are. They do, however, converge rapidly, and that is the crux of the matter. The first few of them contain most of the fluctuating kinetic energy. To illustrate this, some eigenvalues are listed in Table 1. Note that the average amount of turbulent kinetic energy in the 'direction' of a basisfunction is equal to the corresponding eigenvalue. The first basisfunction contains 18% of the fluctuating kinetic energy. The first 20, 40 and 80 basisfunctions contain (in time-average) 78%, 89% and 95% of the total fluctuating kinetic energy, respectively.

index	λ_i	% energy
1	$2.31\,10^{-4}$	18
2	$1.44\,10^{-4}$	30
3	$8.56\,10^{-5}$	36
4	$7.29\,10^{-5}$	42
5	$6.17\,10^{-5}$	47
6	$5.35\,10^{-5}$	51
7	$4.46\,10^{-5}$	55
8	$3.82\,10^{-5}$	58
9	$3.07\,10^{-5}$	60
10	$2.95\,10^{-5}$	62
20	$1.28\,10^{-5}$	78
40	$4.13\,10^{-6}$	89
80	$1.15\,10^{-6}$	95

Table 1: *Some characteristic eigenvalues of the POD of the 2D driven cavity at Re=22,000. The right column shows the relative energy of the projection of the fluctuating velocity field on the first i basisfunctions (in time average).*

POD basisfunctions are optimal in the sense that every other set of N basisfunctions contains less energy (in time average) than the first N POD basisfunction do. To illustrate this we have compared POD with Fourier. For that purpose a $333 * 333$ Fourier-transform of the fluctuating flow field has been computed. The $333 * 333$ Fourier-coefficients are ordered by magnitude; the largest first. The energy contained by the first N Fourier-modes is significantly smaller than the energy contained by the first N POD-modes (see Figure 10). As expected, the POD basisfunctions converge much faster than the Fourier modes.

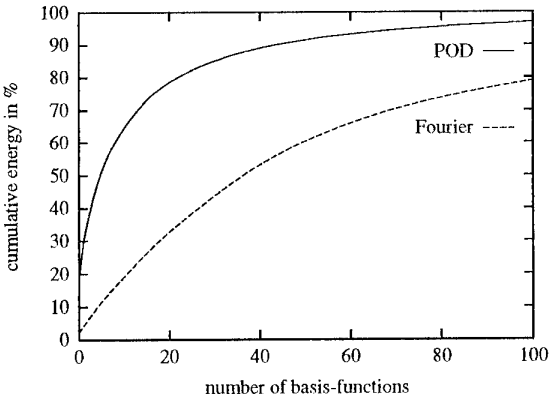

Figure 10: *Comparison of POD and Fourier-modes.*

The first four basisfunctions are shown in Figure 11. It is well-known that Fourier-modes can be grouped in pairs, e.g. $\sin(x)$ and $\cos(x)$ form a pair; they differ by a shift over one quarter of their period, and form a basis for a complete description of the

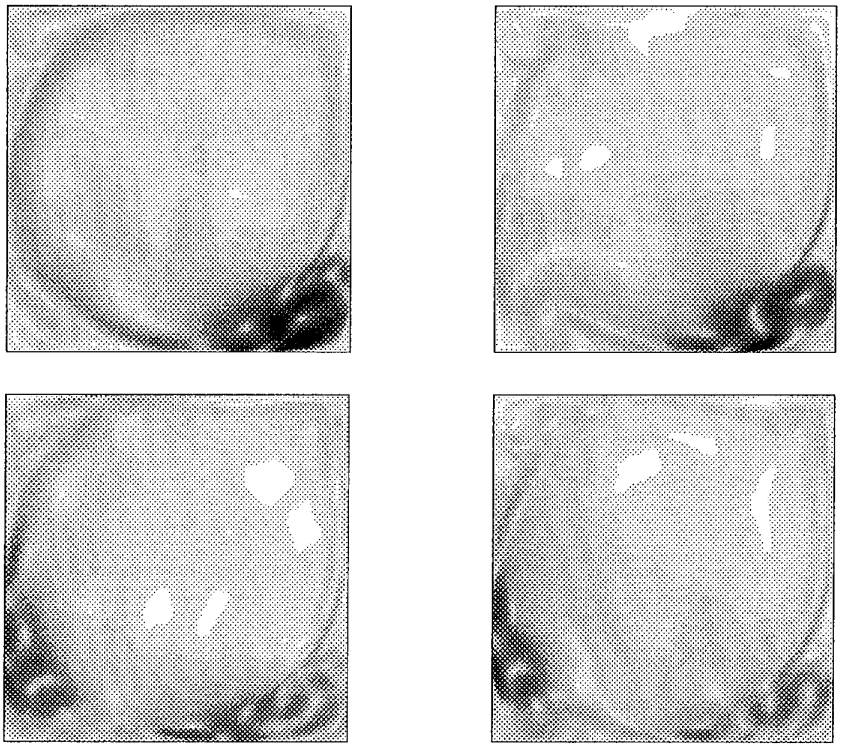

Figure 11: *The first 4 basisfunction from upper left to lower right. This figure shows the vorticity of the POD-basisfunctions in a 2D driven cavity (Re=22,000).*

evolution of a 'cosine-wave'. Figure 11 suggests that POD-modes can be grouped in pairs, too. The first two form a pair. The second one is approximately a quarter out of phase compared to the first one. With the first two basisfunctions only, a motion of an eddy in the lower right corner of the cavity can be represented. Moreover, the third and fourth form a pair. With them an eddy moving in the lower part of the cavity can be represented.

7.4 DYNAMICAL SYSTEM VS. DNS

In this section we use at most 80 of the 700 basisfunctions to construct the low-dimensional dynamical system (5). The coefficients in this system are integrals. These integrals have been computed using the same kind of spatial discretisations as those that have been used for the direct simulation. For the time integration we have applied a fourth-order Runge-Kutta method, for the short-time integrations, and a fifth-order DOPRI method with variable step-size (see e.g. [16]) for the longer integration. It may be noted that in our case DOPRI is substantially faster than Runge-Kutta.

The convergence of the solution of the 20, 40 and 80 dimensional dynamical systems (5) to the solution of the Navier-Stokes equations is shown in Figure 12. Here, all integrations (i.e. of the Navier-Stokes equations and of the 20, 40 and 80 dimensional system) have been started from identical initial conditions. The initial field is an arbitrary velocity field from the DNS time-series that has been projected on the first 20 basisfunctions. For the 40 and 80 dimensional dynamical system the coefficients of last 20 and last 60 basisfunctions have initially been set to zero. In Figure 13 the coefficient of the first basisfunction is shown during one large-eddy turnover-time.

The Figures 12 and 13 demonstrate the potential of the low-dimensional dynamical system (5) to approximate the Navier-Stokes equations for relatively short times.

For larger times the solutions of the dynamical system and the Navier-Stokes equation will always diverge due the fact that both systems are chaotic, i.e. very sensitive to small disturbances. The long-time integrations of the 20, 40 and 80 dimensional dynamical system (5) at $Re = 22,000$ showed that we need a model that takes into account the energy transport to the unresolved modes, or we need to increase the number of resolved modes. We took the former option.

The model that we have used for the long-time integrations is similar to the model that has been proposed by Rempfer in [7]. It consists of adding ar-

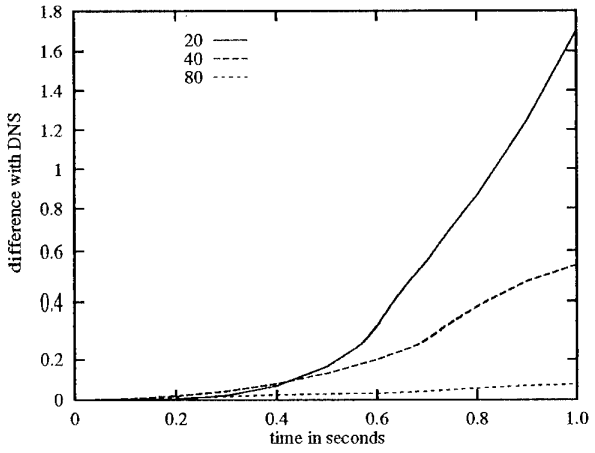

Figure 12: *Difference between the numerical solution of the 20, 40 and 80 dimensional dynamical system and the solution of the Navier-Stokes equations. This figure shows the time-integral of the absolute difference of the projections a_1 of the numerical solution of the Navier-Stokes equations and of the dynamical systems on the first basisfunction σ^1 versus the time.*

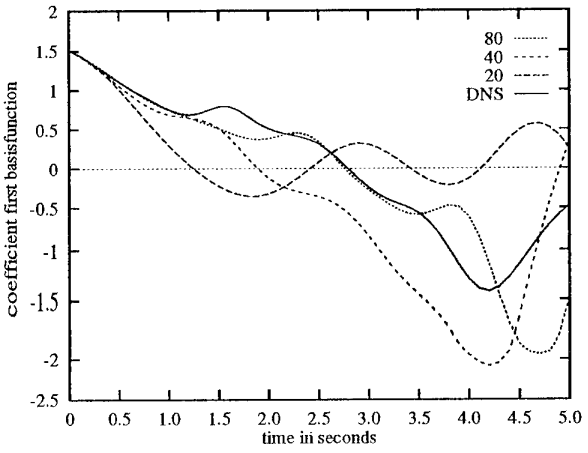

Figure 13: *The projection a_1 of the solution on the first basisfunction during one large-eddy turnover-time.*

tificial dissipation. The artificial dissipation is zero for the first basisfunction and increases linearly with the number of the basisfunctions. The artificial dissipation ϵ_k for the k^{th} basisfunction is given by

$$\epsilon_k = 1.5 \cdot 10^{-2} k \frac{\nabla^2 u}{Re}, \qquad (6)$$

where the coefficient $1.5 \cdot 10^{-2}$ has been determined by trial and error.

The energy spectra as obtained from the integrations over 350 large-eddy turnover-times of both the 80-dimensional dynamical system (with model) and the Navier-Stokes equations are compared in Figure 14. The agreement is fairly good, only the 16^{th} basisfunction and the tail have too much energy in comparison to the DNS. Likely, the agreement can be improved by applying more sophisticated models.

A low-dimensional dynamical system governing a driven cavity flow, opens the door to apply tools from dynamical systems theory to study bifurcations, transition scenario's, etc., provided that this system approximates the flow for a wide range of Reynolds numbers. To investigate whether this condition holds or not, we have integrated the low-dimensional dynamical system (5) with $Re = 11,000$. The POD into basisfunctions has been computed at $Re = 22,000$. The time-series obtained from the DNS at Re=22,000 exhibits chaotic behaviour. We have employed the method proposed in [17] and [18] to analyze the time-series: the (correlation) dimension of the attractor is approximately 2.8, and the Kolmogorov entropy is approximately 3. Thus, at $Re = 22,000$ the flow is chaotic.

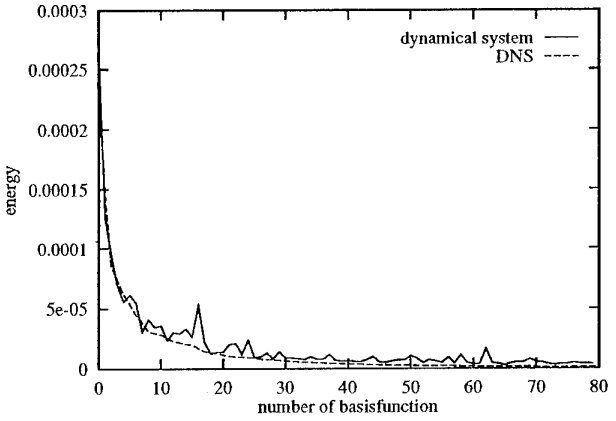

Figure 14: *Comparison of spectra of DNS and the 80-dimensional dynamical system (with closure model (6)). The energy spectra have been obtained from integrations over 350 large-eddy turnover-times.*

DNS's have revealed that the driven cavity flow converges to a periodical state at $Re = 11,000$, see [19] or [12]. All integrations, of the 20, 40 and 80 dimensional model, with and without closure model (6), yield a periodical solution when the Reynolds number is set to 11,000. The periodic solution of the 80-dimensional dynamical system gives the best match with the DNS: its period is 1.7 seconds and its amplitude differs less than 10% from the DNS result. In conclusion, also in this case, the solution of the 80-dimensional dynamical system (5) matches the DNS - that has been performed on a 333^2 grid, i.e. has approximately 10^5 degrees of freedom - strikingly well. Figure 15 shows the origination, motion and merging of eddies near three corners of the cavity during one full period, as obtained from the 80-dimensional dynamical system.

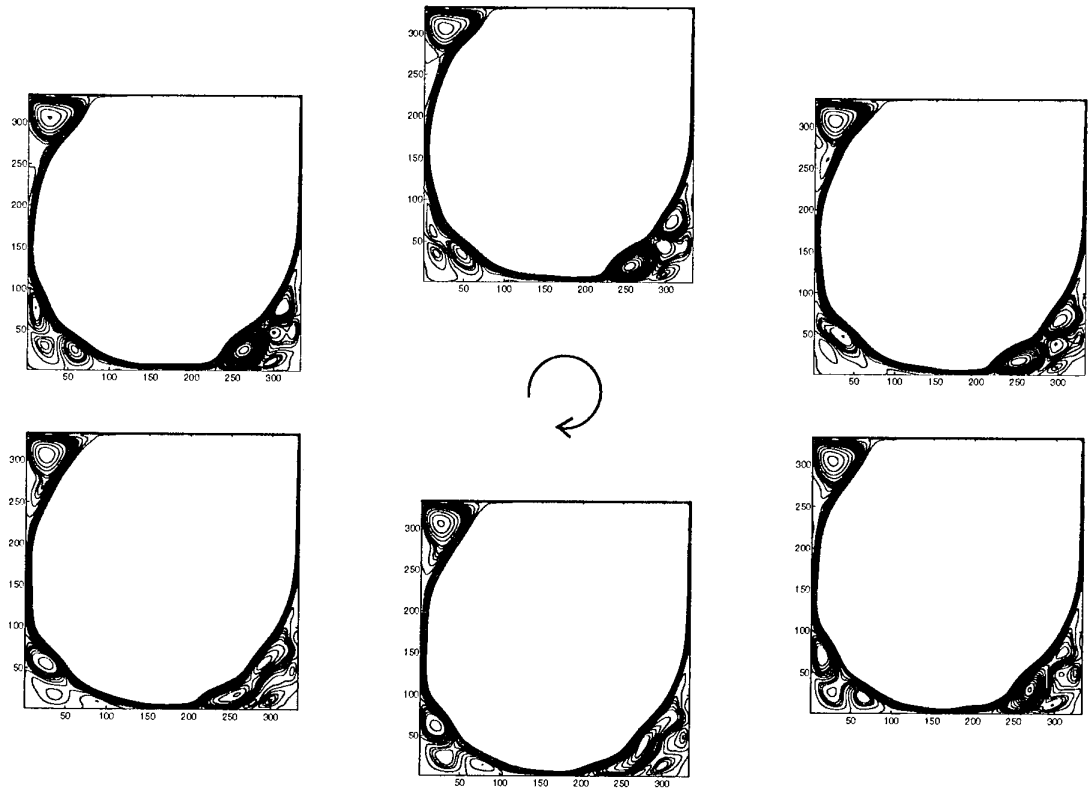

Figure 15: *One full period of streaklines of the periodic solution of the 80-dimensional dynamical system at Re=11,000.*

index	λ_i	% energy
0	$1.52\,10^{-2}$	91.7
1	$1.63\,10^{-4}$	92.7
2	$1.37\,10^{-4}$	93.5
3	$8.52\,10^{-5}$	94.0
9	$4.44\,10^{-5}$	96.0

Table 2: *Eigenvalues of 3D POD; Re=10,000. Here, the right column shows the relative energy of the entire velocity field, and not of the fluctuating part (as in Table 1).*

7.5 3D POD

For the 3D POD 40 uncorrelated snapshots of the DNS of the flow in a cube lid-driven cavity ($Re = 10,000$) have been used. The eigenvalues of the basisfunctions are listed in Table 2. In this case we have not subtracted the mean field: we have computed the POD-expansion of the entire velocity field and not of the fluctuating part, like in 2D. Here, the zeroth basisfunction is (approximately) the mean field. Iso-surfaces of the energy of this basisfunction are shown in Figure 16. The next two basisfunctions are also shown in Figure 16. It may be noted that these two basisfunctions form a pair (like in 2D).

ACKNOWLEDGEMENTS

Both the Stichting Nationale Computerfaciliteiten (National Computing Facilities Foundation, NCF) with financial support from the Nederlandse Organisatie voor Wetenschappelijk Onderzoek (Netherlands Organization for Scientific Research, NWO) and the National Aerospace Laboratory NLR are gratefully acknowledged for the use of supercomputer facilities.

REFERENCES

1. Lumley, J.L., "The Structure of Inhomogeneous Turbulent Flows", *in* "Atmospheric Turbulence and Radio Wave Propagation", A. M. Yaglom, V. I. Tararsky, eds., Moscow, Nauka, 1967, pp 166-178.

2. Berkooz, G., Holmes, P. and Lumley, J.L., "The Proper Orthogonal Decomposition in the Analysis of Turbulent Flows", Annu. Rev. Fluid Mech. *25*, 1993, pp 539-575.

3. Sirovich, L., "Turbulence and the Dynamics of Coherent Structures", Quart. Appl. Math. *45*, 1987, pp 561-590.

4. Aubry, N., Holmes, P., Lumley, J.L. and Stone, E., "The dynamics of coherent structures in the

wall region of a turbulent boundary layer", J. Fluid Mech. *192*, 1988, pp 115-173.

5. Deane, A.E., Kevrekidis, I.G., Karniadakis, G.E. and Orsag, S.A., "Low-Dimensional Models for Complex Geometry Flows: Application to Grooved Channels and Circular Cylinder", Phys. Fluids A *3*,10, 1991, pp 2337-2354.

6. Glauser, M.N., Leib, S.J., George, W.K., "Coherent Structures in the Axisymmetric Turbulent Jet Mixing Layer", *in* "Turbulent Shear Flows 5", F. Durst *et al.*, eds., New York, Springer-Verlag, 1987.

7. Rempfer, D., "Kohärente Structuren und Chaos beim laminair-turbulenten Grenzschichtumschlag", Ph.D.-thesis, Stuttgart, Germany, Institut für Aerodynamik und Gasdynamik der Universität Stuttgart, 1991.

8. Noack, B.R. and Eckelmann, H., "A Low-Dimensional Galerkin Method for the Three-Dimensional Flow Around a Circular Cylinder", Phys. Fluids *6*, 1, 1994, pp 124-143.

9. Harlow, F.H. and Welsh, J.E., "Numerical Calculation of Time-Dependent Viscous Incompressible Flow of Fluid With Free Surface", Phys. Fluids *8*, 1965, pp 2182-2189.

10. Dongarra, J.J., Duff, I.S., Sorensen, D.C. and Van der Vorst, H., "Linear System Solving on Vector and Shared Memory Computers", Philadelphia, SIAM, 1991, pp 167-192.

11. Ghia, U., Ghia, K.N. and Shin, C.T., "High-Re Solutions for Incompressible Flow Using the Navier-Stokes Equations and a Multigrid Method", J. Comp. Phys. *48*, 1982, pp 387-411.

12. Verstappen, R., Wissink, J.G. and Veldman, A.E.P., "Direct Numerical Simulation of Driven Cavity Flows", Appl. Sci. Research *51*, 1993, pp 377-381.

13. Prasad, A.K. and Koseff, J.R., "Reynolds Number and End-Wall Effects on a Lid-Driven Cavity Flow", Phys. Fluids A *1*, 2, 1989, pp 208-218.

14. Lumley, J.L., "Stochastic Tools in Turbulence", New York, USA, Academic Press, 1970.

15. Mikhlin, S.G., "Integral Equations, and their Applications to Certain Problems in Mechanics, Mathematical Physics and Technology", Pergamon Press, 1957.

16. Hairer, E., Norsett, S.P. and Wanner, G., "Solving Non-linear Differential Equations I" Berlin, Germany, Springer-Verlag, 1987.

17. Grassberger, P. and Procaccia I., "Characterization of Strange Attractors", Phys. Rev. Lett. *50*, 5, 1983, pp 346-349.

18. Grassberger, P. and Procaccia I., "Estimation of the Kolmogorov Entropy from a Chaotic Signal", Phys. Rev. A *28*, 4, 1983, pp 2591-2593.

19. Shen, J. "Hopf Bifurcation of the Unsteady Regularized Driven Cavity Flow" J. Comp. Phys. *95*, 1991, pp 228-245.

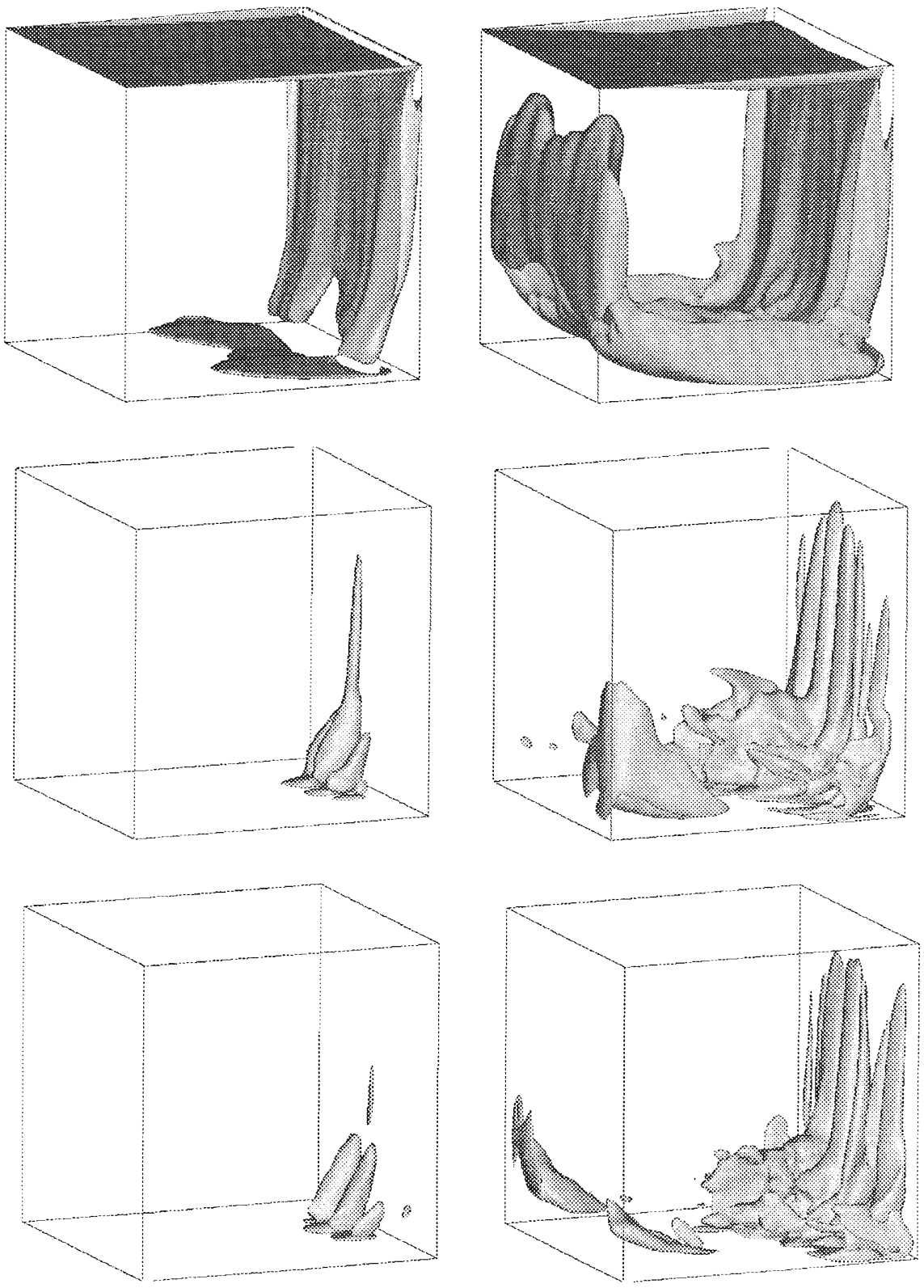

Figure 16: *Iso-surfaces of the energy of the first three basisfunctions of the 3D POD. The first row shows two iso-surfaces of the zeroth basisfunction. The next row shows the first basisfunction; the lower row shows two iso-surfaces of the second basisfunction.*

Direct Simulation and Graphics Post–Processing of Three–dimensional Turbulent Flows *

J. Ryan†, P. Leoncini‡, U. Berrino‡, B. Troff†
†ONERA, BP 72, 92322 Chatillon Cedex, France
‡CIRA, Via Maiorise, 81043–CE Capua, Italy

Abstract

Direct Simulations involve huge amounts of time dependent data and are expensive to run fully even on supercomputers. A thousand hours of CRAY to obtain valid results is in the order of things. Such costs can be significantly reduced by MIMD machines . To be able to analyse the computed results many and various visualization techniques are also essential.

This paper presents work that was done at ONERA to parallelise a Navier–Stokes solver PEGASE and development of an interactive visualization tool at CIRA applied to numerical turbulent flow fields generated by the solver. This work was partly achieved within the framework of the European RACE/PAGEIN project which was aimed at demonstrating the feasibility of Direct Numerical Simulation techniques for future industrial developments, implying modern supercomputer technology, high performance computing networking and massive data transfers between vector and/or parallel supercomputers.

The first part of this paper presents the essential characteristics of version 1.0 of PEGASE implemented on a vector machine, the second part describes modifications in algorithms and coding in order to implement it efficiently on the IPSC860 and on a PARAGON. Numerical results and comparisons in costs between the three machines are given. The third part describes the graphics post-processing developed at CIRA.

1 MAIN FEATURES OF PEGASE 1.0 ON CRAY

A Navier-Stokes solver PEGASE has been developed at ONERA Aerodynamics Department for Direct simulation of turbulent incompressible flows. The numerical method is performed in such a way to ensure good numerical properties (stability , consistency), to get a good accuracy of the solution and to reduce the number of operations and the computation cost. It has first been implemented on a vector machine such as the Cray YMP. A full description is to be found in [1], and [2]. The basic equations of fluid motion are the unsteady incompressible three–dimensional Navier–Stokes equations, in velocity-pressure formulation. To these equations, initial and boundary conditions (Dirichlet, Neumann, or periodic) are associated.

The equations are discretized on a non-staggered grid: velocity components and pressure are located at the same node, which greatly alleviates the coding burden and enhances the applicability of the method.

The convective term is discretized in time by an explicit second order accurate Adams–Bashforth scheme and the diffusion term by an explicit first order Euler scheme.

Space derivatives are approximated by fourth order accurate finite difference schemes, centered at the inner nodes and non–centered at boundary nodes. An implicit residual smoothing technique is used to reduce stability constraints on the time step when small grid spacing is employed. It does not change the accuracy of the scheme.

When the equations are discretized, they are combined to give a Poisson–like equation for the pressure which is solved iteratively, with a multi-gradient solver.

The operator to be solved is the gradient operator, followed by the smoothing operator (factorized in the three directions of space and stored once and for all in LU form, as each factor contains only three diagonals), followed by the divergence operator. Once pressure is thus implicitly obtained, velocity is semi-explicitely computed.

The main cost of the code resides in the pressure computation.

2 PARALLELIZING PEGASE FOR AN MIMD MACHINE

The strategy chosen for parallelization of three–dimensional calculations is that of non–overlapping pencils over a two–dimensional array of processors. This configuration seemed the most efficient for the implementation of the iterative method used to compute pressure. Though this technique implies more modifications of the original CRAY code than the choice of overlapping pencils, it allows a greater number of points in the physical domain and less computations for the same amount of communications.

In order to limit the amount of communications, the original smoothing operator L^{-1} has been modified,

*Paper presented at "APPLICATION OF DIRECT AND LARGE EDDY SIMULATION TO TRANSITION AND TURBULENCE", AGARD Symposium, 18–21 April 1994, Chania, Crete, Greece

Paper presented at the 74th Fluid Dynamics Symposium on "Application of Direct and Large Eddy Simulation to Transition and Turbulence" held at Chania, Crete, Greece, in April 1994.

where L is :

$$L = (1. - \eta\Delta\ ) \tag{1}$$

- (i) Instead of being applied to all the physical domain, which implies communication between neighbouring subdomains, it has been restricted to inner points of each subdomain with a boundary condition $(1. + \eta\Delta\ )$. Thus only one communication is needed.

  This simplification has been shown not to modify stability and precision of the global algorithm, [3].

- (ii) Moreover, in order to use the vectorization possibilities of each processor at its most , the inversion of the smoothing operator is not done by Lower-Upper decomposition, but by a steepest descent iterative technique. One or two iterations of the steepest descent is quite sufficient and efficient in this case, as the matrices involved are strongly diagonally dominant, and that accuracy of the smoothing operator is not of first importance .

Computation of spatial derivatives (fourth order finite differences) has been rewritten.

- Contributions of border points to computations of derivatives of points situated in other processors are first computed, and asynchronously sent. Derivatives at inner points are computed, then border points derivatives are computed, the necessary contributions having also been read asynchronously. (By asynchronous, one means that the send and receive calls return immediately, allowing the program to do further work while the message is processed.)

2.1 Results

In the following are given cost results for the three machines on which PEGASE was implemented.

- On Cray YMP, with one processor, PEGASE runs at approximatively 200 Mflops, and costs 10^{-5}s per point and per time step (including 10 iterations in the pressure solver);

- On iPSC860, for a 64 bit precision (double precision on the iPSC860), the modified code is six times less expensive when using the 128 processors, thus a performance of 1,200 Mflops is reached. Cost does not increase much with the number of processors as communications are mostly local.

- On Paragon, performances are improved over the iPSC860 by a ratio of 25% as message passing and processors are optimized.

3 GRAPHICS POST-PROCESSING

Visualization plays an important role in CFD simulations. There are several classical techniques for visualising scalar data variables inside volume grids, like cutting planes and isosurfaces [18]. These instantaneous representations can be directly applied to a sequence of time-dependent flow solutions in order to display the inherent time-related behaviour of a scalar field.

Two basic representations apply instead to vector fields: vector plots and particle tracing.

A vector plot consists in drawing a vector glyph in certain points of a flow field whose arrow points towards the local direction of the vector field, usually the velocity. While the ambiguity arising from application to 3D surfaces in a volume can be solved using lighted solid vector glyphs, vector plots are totally inadequate for full volume plots or for applying to time-dependent flow data, given the quantity of local information that has to be conveyed to the analyst.

Three characteristic curves, streamlines, pathlines and streaklines, can help to depict an intuitive picture of the fluid motion, each of them putting in evidence particular aspects.

A streamline in a flow field is a curve whose tangent is everywhere parallel to the direction of flow at a given instant of time. The use of streamlines in steady cases is very helpful in analysing computational flow simulations. It represents the trajectory through a given velocity field V(P)

$$\frac{dP}{dt} = V(P)$$

and can be computed by numerically integrating. Streamlines are often the only means of understanding complex 3D flow patterns such as may result from vortical flows. Starting from streamline data, a ribbon can be visualized as a strip centered over the streamline whose rotational orientation is based on the local vorticity.

A pathline is the path or trajectory traced out by a moving fluid particle. It is made visible by identifying a fluid particle, e.g. by use of smoke or dye, at a given instant of time and then following it through its subsequent motion. It would not normally be helpful to plot the pathline, but one may plot the particle's position at any time. Nevertheless since pathlines allow to follow the particles in their motion when the time goes by, they represent the temporal history of generic particle.

3.1 Streaklines

Instead of identifying a single particle, one may identify a number of particles which pass through one fixed location in space. The line joining the various fluid particles is defined as a streakline. Streaklines at a generic instant define the position occupied by the particles which previously passed through a particular point of

the flow field. In numerical simulation the temporal frequency of particle passage through a fixed point of space controls the accuracy of streakline; if the frequency of passage increases the computational efforts are bigger.

If we inject with continuity in a point of the flow field an aggregate of coloured particles with the same physical characteristics of the fluid, a photo taken at the fixed instant of time will show on the photographic slide a line representing in that time the streakline produced in that point.

Experimental visualization techniques have been effectively used to present a qualitative view of the fluid motion. In unsteady flows, streamlines, pathlines and streaklines are all different and the interpretation of patterns obtained by flow visualization calls for care, because it may not be easy to infer instantaneous flow patterns from the observations. In unsteady flows the aggregates of streaklines vary at the different instant of time, in steady flows they are the same at all time (in this case streamlines, pathlines and streaklines are identical).

3.2 Direct Volume Rendering

Direct volume rendering is a visualization method that aims at providing information about the whole volume in a single image. For such representation a 3D sampled scalar volume is supposed, like the one usually available in CFD simulation grids. Volume samples are mapped to color and opacity and directly rendered by accumulation to the screen pixels. Two basic techniques apply in order to reduce 3D grid data to images: ray-casting and projection.

Though projection methods can also be used for image-space techniques, it is recently referred to by relating it to the capability of reaching rendering times ever closer to interactivity. It consists of projecting volume cells to the screen by reduction to a collection of polygons (usually triangles). These can then be rendered using fast graphics hardware available on mid and high-end 3D graphics workstations. The results of such projections are usually referred to as splats. In rectilinear grids one can take advantage from cell coherence and an implicit ordering for splatting, leading to relatively simple and fast rendering.

Once a cell is splatted, color and opacity have to be associated to the samples in order to render it. Projection-based methods rely on graphics hardware for blending. SGI workstations have a blend function that permits the incoming color components to be scaled by the incoming alpha (opacity) value, and the framebuffer contents to be scaled by one minus the incoming alpha value. Thus incoming alpha is correctly thought of as a material opacity, ranging from 1 (completely opaque) to 0 (completely transparent). Polygons representing cell faces can be drawn using Gouraud shading (linear interpolations of color components and alpha), that most of the graphics hardware offers. When using alpha blending, the drawing of polygons have to be performed from back to front with respect to the current view axis in order to correctly compose opacity.

3.3 Visualization of PEGASE Turbulent Flow Data

Turbulence is the irregular regime for fluid motion which randomly varies with space and time. It is a three-dimensional, rotational, irregular, diffusive and dissipative phenomenon. The above described data representations can be effectively combined in order to visualise turbulent phenomena. Displaying them in animation is then the most natural to exploit the inherent time-dependence of turbulence data.

When a turbulent flow field is being investigated by means of cutting planes or isosurfaces, analysts use such representations as probes. Their surface nature is helpful when the phenomenon is well identified by one or few data values (e.g. shock waves), otherwise meaningful feature-oriented information can remain hidden, possibly lying between discrete surface values. Nevertheless isosurfaces of well-selected data variables may give a rough shape of coherent structures.

Streaklines are the most helpful means to understand and to show main characteristics in numerical unsteady turbulent flows, with particular emphasis on the important dynamic aspects of turbulence, since the discrete nature of moving particles is able to capture the essence of fluid motion. The approach for rendering streaklines have to be carefully decided, in order to avoid thousands of particles concurrently in the 3D scene leading to an unreadable image. Lighted spheres may be used to remove spatial ambiguities; mapping their color to the time the particles were released has been found useful to depict diffusion, as well as making them ever more translucent as time goes on.

By conveying global insight in volume data, direct volume rendering may be used as a feature-oriented data representation. Wherever a phenomenon has its interesting regions, a proper combination of the scalar variable to be directly rendered, the opacity transfer function (usually an exponential or a gaussian) and possibly multiple thresholding values can be arranged in order both to emphasize hidden characteristics and to remove meaningless graphics. Furthermore a higher degree of realism has been reached by modifying vertex color by applying additional gradient lighting, resulting in more solid-looking structures. Scalars to which volume rendering has been helpfully applied were the streamwise velocity component, energy, vorticity, enstrophy and helicity.

Post-processing of results from the PEGASE code has been carried out in a visualization environment, named NOVA, developed at CIRA within the CEC-RACE II PAGEIN (Pilot Applications on a Gigabit European Integrated Network) project. The unsteady particle tracer has been developed by DRA (UK) and CIRA, by extending the Eurovis multiblock particle tracer developed within the Garteur AD AG 16 on

visualization for CFD. For cutting planes and isosurfaces, PEGASE data has been visualized with FLOVIS, an interactive 3D graphic post-processor developed at CIRA running on high-performances graphics workstations. Both NOVA and FLOVIS allow time-dependent data to be dynamically displayed in animation, during which the user has still the possibility to interact with 3D objects.

Data produced with PEGASE by direct simulation of a vortex breakdown were used for the proposed images (fig. 1,2). In this case candidate particle sources are a series of points located on a line of the boundary grid surface representing the incoming flow. As new particles are injected from each starting point they tend to depict a streak surface swirling according to the vortex that originates by the rotating flow initial condition; such surface suddendly loose its roughly regular shape as the vortex breaks down.

4 CONCLUSIONS

The PAGEIN prototype is of great interest for massive data generating and analyzing codes. The possibility of interactive visualization and computation allows better control of the process. Implementation of several time-dependent flow visualization techniques has shown that the streakline tracer is the most natural tool for the analysis of turbulent flow fields, and that particle-based representations can be effectively combined with direct volume rendering of well-suited flow-related scalars, the latter helping to concurrently depict important flow characteristics through its global insight capability.

However safegards such as on-line time dependent measurement of error [5] should be devised so that the beauty of the visualizations does not affect the accuracy of the results.

Acknowledgements

The work described in this article was partially supported by the CEC RACE II program PAGEIN project (R2031).

We wish to thank the EUROVIS Group and the PAGEIN Consortium for their collaboration, suggestions and encouragement.

Special mention is due for Mr D. Catherall of DRA, who is a co-author of the particle tracer.

References

[1] B. Troff, T.H. Le, T.P. Loc: "A numerical method for the the three-dimensional unsteady incompressible Navier-Stokes equations.", J. Compt. and Appl. Math. Vol. 35, 1991 pp. 311-318.

[2] T.H. Le, Ph. Mege, Y. Morchoisne: "Détermination de critères d'éclatement tourbillonaire par résolution des equations d'Euler et de Navier-Stokes". AGARD Conference Proceedings 494 on Vortex Flow Aerodynamics, 1990.

[3] T.H. Le, J. Ryan, K. Dang Tran: "Direct simulation of incompressible viscous flow through a rotating square channel.",9^{th} Gamm Conf. Lausanne, Sept. 25-27, 1991.

[4] K.C. Le Than: "Résolution des equations de Navier-Stokes incompressible instationnaire tri-dimensionnelles par une méthode de sous-domaines", These de doctorat, Paris VI, Specialite Analyse Numerique,2-12-91.

[5] Zienkiewicz O. C. and Zhu J. Z. : "The Three R's of Engeneering Analysis and Error Estimation and Adaptivity", Computer Methods in Applied Mechanics and Engeneering 82 (1990) 95-113, North-Holland.

[6] G. Volpe: "Streamlines and Streamribbons in Aerodynamics", AIAA paper 89-0140, Reno NV, January 1989.

[7] Catherall, D. "The Use of Graphics in Analysing CFD Results". RAE TR 89035, Farnborough (UK), July 1989.

[8] Berrino, U.; Kassies, A.; Renzoni, P.; Westenberg, G. "EUROVIS requirements document". NLR TR 91007 L, Amsterdam (NL), January 1991.

[9] Berrino, U.; Leoncini, P.; Lucignano, F. "FLOVIS (FLOw VISualizer) 2.6", User Manual. *Lecture Series: Computer Graphics and Flow Visualization in CFD*, Von Karman Institute, Brussel (B), 16-20/9/1991.

[10] RACE 2031 PAGEIN. "Technical Annex". ONERA, Chatillon (F), June 1992.

[11] Berrino, U.; Leoncini, P.; Lucignano, F. "Distributed Multimedia for Technical–Scientific Cooperation". *I.Co.Graphics '93 Conference*, Milan (I), 9-12/3/1993.

[12] E. M. Murman, K. G. Powell: "Trajectory Integration in Vortical Flow", AIAA Journal, Vol. 27 No. 7, July 1989.

[13] P. G. Buning, J. L. Steger: "Graphics and Flow Visualization in Computational Fluid Dynamics", AIAA paper 85-1507, Cincinnati OH, July 1985.

[14] Y. Levy, D. Degani, A. Seginer: "Graphical Visualization of Vortical Flows by Means of Helicity", AIAA Journal, Vol. 28 No. 8, August 1990.

[15] D. A. Lane: "Visualization of Time-Dependent Flow Fields", IEEE Visualization '93 Conference, San Jose CA, October 1993.

[16] A.J.S. Hin, F. H. Post: "Visualization of Turbulent Flow with Particles", IEEE Visualization '93 Conference, San Jose CA, October 1993.

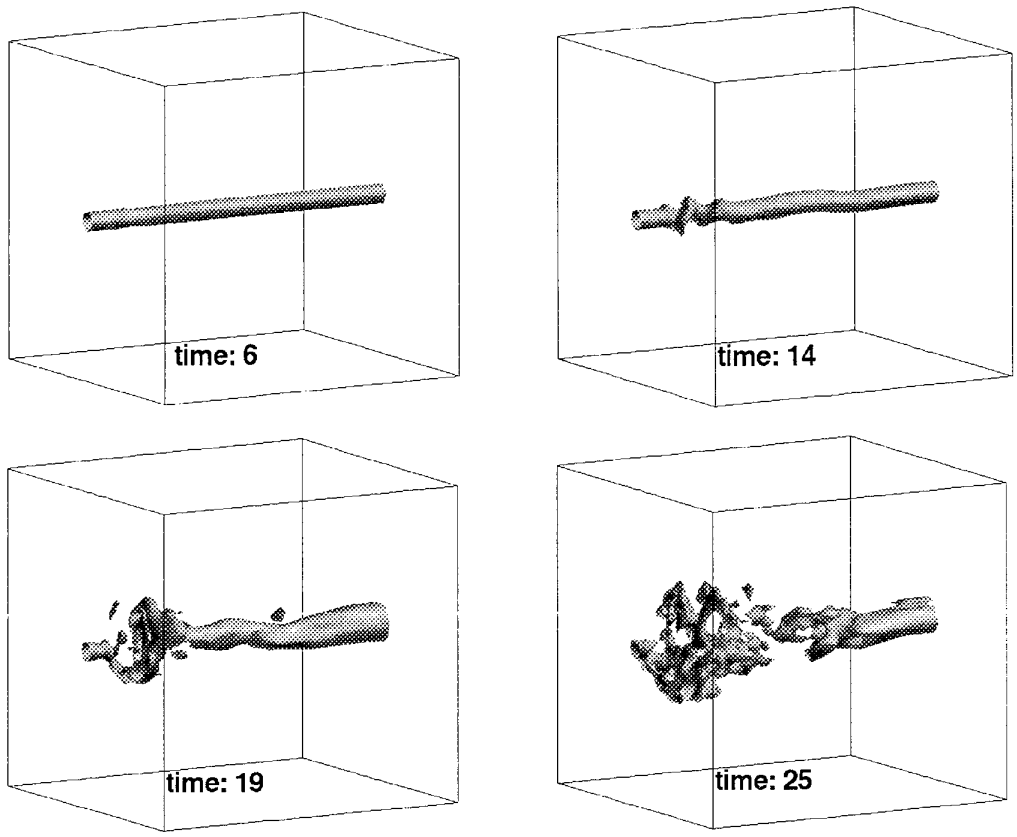

Fig. 1 Four time steps in the vortex breakdown simulation (Reynolds 2300, Rossby 0.47) showing the shape of the isolated axi–symmetrical vortex by means of the isosurface of the z–velocity component at value 1.2.

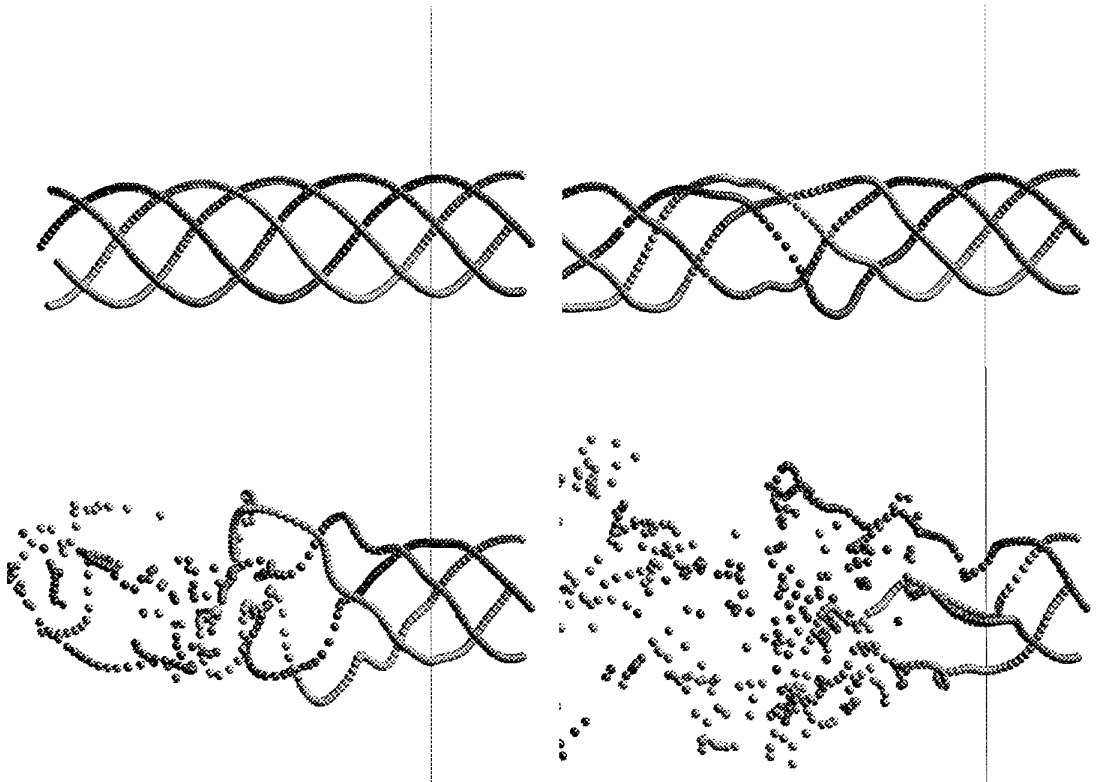

Fig. 2 Close view of the region where the vortex breaks down in the same flow as Fig. 1. Particles are injected from four positions symmetrically distributed around the vortex symmetry axis.

[17] A. Van Gelder, J. Wilhelms: "Rapid Exploration of Curvilinear Grids Using Direct Volume Rendering (Extended Abstract)", IEEE Visualization '93 Conference, San Jose CA, October 1993.

[18] W. Lorensen, H. Cline: "Marching Cubes: A High Resolution 3D Surface Construction Algorithm", ACM Computer Graphics, Vol. 21 No. 4, 1987.

General Discussion

Professor Cantwell, Stanford University, USA
In this session, we will hear remarks from the Technical Evaluator. These will be followed by a general discussion of the meeting. I want to remind all speakers to be aware that the session is being translated. In this circumstance, as the translators do not have a text to work from, it is especially important to try to speak as clearly, slowly and carefully as possible. In addition, when you get up to ask a question or to speak, I would appreciate it if you would identify yourself and your affiliation.

May I now introduce the Technical Evaluator, John Lumley, Willis H. Carrier Professor of Aerospace and Mechanical Engineering at Cornell University. Professor Lumley is one of the best known workers in turbulence, not just in the United States, but around the world. He began his academic career at Penn State where he spent 18 years; he has now been 17 years at Cornell University and is the recipient of many awards and recognitions. He is a member of the National Academy of Engineering, the American Academy of Arts and Sciences; he is a winner of the Timoshenko medal, a winner of the Fluid Dynamics Prize of the American Physical Society, which is probably the most prestigious prize given in the U.S. for fluid dynamics; he is also winner of the AIAA Fluid and Plasma Dynamics Award; the author of a number of books, one of which probably almost everyone here would have encountered at one time or another. It was the book that I first used as a student to learn about turbulence entitled, "A First Course in Turbulence", by Tennekes and Lumley. Without any further remarks, I will ask Professor Lumley to take the floor.

Professor Lumley, Cornell University, USA
See Table of Contents for Technical Evaluation Report

Professor Cantwell, Stanford University, USA
Thank you Professor Lumley for your remarks. These were good strong opinions which I am sure have stimulated plenty of people in the audience. Now I would like to throw the discussion open to the audience and call for any comments. The comments may be on Professor Lumley's report or may be with respect to a given paper; they may be general comments, philosophical, or specific. This is an open discussion and anything is fair game. Like all open discussions of this type, they tend to start slowly, nobody wants to speak first. Now we have got three here. State your name and affiliation and speak as clearly as possible for the translators.

Tharos Nehaus, University of Solenniki
I thought I would raise my hand and speak first because I am an outsider to this Conference. I am doing experimental work and I would like to say something that is not to be interpreted as a criticism, but I heard many authors mention negative viscosities and eddy viscosities. I am just thinking that after 25 years of coherent structural work, supposedly to understand physics, why are we talking about negative viscosities. It may be a technicality, and I am leaving it up to you to respond.

Professor Cantwell, Stanford University, USA
I think there are a number of people here who could have used a list of definitions. There is a lot of jargon in this field. I think that is probably not surprising given the relatively new nature of the field and the fact that things are changing rapidly. Every investigator has their own set of

terminology that they like best. Sometimes, these terms become common to various groups but sometimes not. It can be difficult, I agree.

Professor Moin, Stanford University, USA
Unfortunately, I missed the talk by Comte, but John commented on the applications of the structure function model. I would like to pick that up as one of the models that has been put forward (in addition to the dynamic model that we have seen here) and have a discussion on the importance or the utility of the structure function model. In my opinion, and this is backed by spectral analysis of the structure function model, this model is essentially a glorified Smagorinsky model. In fact, it scales to the Smagorinsky model with the right coefficient, which is 0.267. You get the same thing with the standard value of the Smagorinsky coefficient. I do not see that the structure function model added anything beyond Smagorinsky. Also, it has the same type of problems close to the wall. Dr. Comte himself established at the CTR that the structure function model has the improper limiting behavior very close to the wall. I would like to know if anyone else has had any experience with the structure function model and whether they agree with my comments about it.

Professor Cantwell, Stanford University, USA
Let's take that up as a point. Does anyone have a response to that?

Dr. Comte, Institut de Mécanique de Grenoble, France
About the consistency between the structure-function model, I mean the original Métais-Lesieur model, and the Smagorinsky model, it is written in paper #14 that the structure-function model is fairly close to the Smagorinsky model. In fact, to the first order, it can be recast as a mixture between the strain and the vortex versions of the Smagorinsky model. When you do that, you end up with a value of the constant of the structure-function model equal to twice the square of the Smagorinsky model times the square root of 2/3. In practice, the structure-function model is a bit less dissipative than the Smagorinsky model. I showed some comparisons in the case of temporal wakes and mixing layers.

As far as the behaviour close to the wall is concerned, I think that the recent developments — which made this model maybe not dynamic, but either filtered or selective — certainly do not cure the problem but at least bring some sort of improvement.

Professor Cantwell, Stanford University, USA
Could I ask just a clarification question about the structure function model? Does that model assume that the subgrid scale stress and local strain tensors are aligned?

Dr. Comte, Institut de Mécanique de Grenoble, France
Basically yes, because there is an eddy-viscosity. But in the case of the selective structure-function model, you have a filter which is non-linear: it is based upon the angle between the instantaneous local vorticity vector and some sort of local average of it over a certain neighbourhood. This gives to this model the property of not putting any eddy-viscosity in the laminar regions, which is basically what we aimed at.

To come back to the fundamental difference between the original structure-function model and the Smagorinsky model, the most important I can find is that the structure-function model only features velocity increments, whereas the Smagorinsky model involves derivatives to discretize. It is well known that finite-difference evaluation of derivatives behave somewhat differently from exact derivatives, especially at high wave-numbers.

Dr. Kleiser, DLR, Gottingen, Germany
Just a few comments on the question about experiences with the structure function model. In work not presented at this meeting, we have done some apriori tests of various models, including the

structure function model and the classical Smagorinsky model. We did not find any superiority of the structure function model with respect to the near wall behavior which we investigated, in particular, concerning the back-scatter of energy from the non-resolved scales to the resolved ones. Maybe my colleague wants to comment some more on these details.

Mr. Haertel, DLR, Gottingen, Germany
We did some comparisons but other people have done the same and basically our experiences are similar to those that have been made at CTR with the structure function model. We repeated that work but also looked at some further quantities, more than were considered that time in the CTR report. In principle, there were no qualitative differences between the various models. At least, we haven't found any.

Professor Orlandi, University of Rome, Italy
I would like to know if somebody thinks that this structure function model can be improved by using the notion of self-extended similarity. This notion recently has received some interest since in experiments and in numerical simulations by the research group of physicists led by Prof. Benzi, it has been observed that there is a very good scaling both in the inertial and in the dissipative range of the structure function of arbitrary order when plotted versus the third order structure function. I would like to know whether somebody thinks that this similarity can help to account for the back-scatter in subgrid models based on the structural function. The third order structure function, in fact, is related to the energy transfer.

Dr. Comte, Institut de Mécanique de Grenoble, France
I don't know about the work by Robert Benzi, but the person in Grenoble you mentioned is probably Yves Gagne, who did essentially one-point measurements using Taylor's hypothesis to measure structure functions. I had quite a few discussions with Yves Gagne and Bernard Castaing, who proposed intermittency corrections and scaling models. They told me that as far as second-order moments are concerned (for example, the second-order structure-function we use in our models), we could heavily rely upon the Kolmogorov 1941 theory to derive the constants of our models, and that there was no need for intermittency corrections.

Professor Jiménez, University of Madrid, Spain
More than a comment, I want to raise a point that has not been discussed here. This is a meeting in which there is a large number of people who are not specialists in this specific area because of the presence of the AGARD Panel. A question that we should address here is whether anything has happened in this meeting which allowed us to put an error bar in the results of DNS or LES. Can we go to an industrial user or to somebody trying to predict what is going to happen with an experiment, and say that we are doing this within 10%? I don't know whether John Lumley or anybody else wants to address that.

Professor Cantwell, Stanford University, USA
Actually, I think Professor Poll had a question after Professor Kleiser's invited talk which might bear on what you are describing. Professor Kleiser described several different types of transition that were being studied. Professor Poll pointed out that if he goes into his wind tunnel he measures transition with a hot wire and he sees intermittency, he sees switching back and forth. It seems to me that what you are raising is a similar issue; to what degree do simulations, particularly LES as well as DNS reproduce the real world and to what degree do we know what disturbances are required to fully define a flow in a DNS or an LES computation. You have precise control over all boundary and initial conditions. In a real experiment you don't. Worse than that, you don't really know precisely what conditions are going to be important. We keep finding that small effects play a significant roll more and more. Perhaps Professor Poll could comment on that issue and expand on his point from one of the earlier sessions.

Professor Poll, University of Manchester, UK

The point was that it is very nice to see a complete calculation, but the question that I raised was one that related to what we actually see in experiments. It is not yet clear to me that the complete calculations we have actually represent behaviour in the real world. The question really is how much would you have to put in at the input phase in order to reproduce phenomena which are generally observed by first year students in their first morning in the lab. The other point that I would like to make is that, although I didn't see all the papers by any means, many of the models were being compared with graphs taken from books like Schlichting which is 50 years old. I think it would be rather more realistic if the theoreticians made a special effort to use the best experimental data that is available, not simply Blasius law for a pipe, for example, which under low Reynolds number conditions may not be accurate at all. What may appear to be good agreement may in fact be misleading. So, if you do a very good calculation, please compare it with the very best data that you can find, not simply something out of an old undergraduate textbook.

Professor Moin, Stanford University, USA

If I may go back to Professor Jimenez' comment, I think he has a very good point. One of the advantages that you have in a large eddy simulation, in contrast to the Reynolds averaged approach, is that the models should be designed, and they are usually designed, so that if you refine the resolution you approach the proper limit, that is the Navier-Stokes equations. If you want to give an answer to someone in industry, regarding the uncertainty of your calculation, as with all good CFD, you should always do a grid refinement study. It is only with a grid refinement study that you can know about the uncertainty or the accuracy of your calculation. With LES we know that if you refine the mesh you get more accurate results and if the quantity that you are interested in, say such as skin friction or pressure coefficient, don't change when you do the grid refinement, then you can trust your result.

Dr. Kleiser, DLR, Gottingen, Germany

I think actually we can be quite confident about accuracy and about reliability of our DNS results. Of course, if you are asking what these results have to do with the real world, the question is what is the real world? Let us take the example of the classical vibrating-ribbon transition experiment in a Blasius boundary layer. I think this is a reasonably well-defined physical problem. I believe that DNS today is at a stage where this process can be computed to any desired level of accuracy. With respect to comparing the data, see, for example, the talk by Bestek from the Stuttgart group. They compared their data including maybe the first 10 or 12 harmonics of their time signals with the very detailed measurements of Katchanov and really obtained a very convincing agreement. It is now time to stop *unnecessary* doubts about the validity of computations. Of course, computations need to be done with the appropriate care and with the appropriate amount of comparisons with the real world or with some sensible model problems. In the LES, on the other hand, we still have the modelling problem even if we have fine grids. This is quite a different issue which is also present in the Reynolds averaged Navier-Stokes computation. But in DNS, I believe, as Professor Lumley has mentioned, the state of the art is quite mature.

Professor Meier, DLR, Gottingen, Germany

I would like to comment on the role of numerics and experiment in this context. I am not against any numerical results also presented here in the Conference, especially against Kleiser's results because we are from the same institute, but I think we have to consider that the numerics is nowadays still restricted to some simple cases of application. For instance, the whole range of high Reynolds number is not covered really by numerical methods in such a way that you can simply trust the result which is obtained by an application of a well-known method on a not very well established case. One result of this Conference is that the numerical work presented here gives a really good three-dimensional view and the physical background of shear layer instability, stagnation line instabilities, Tollmien-Schlichting type, cross-flow instability and all the special

supersonic modes of instability in simple geometry at low Reynolds numbers. This is the main advantage of numerical methods having a higher definition and higher accuracy than an experiment to clarify the physical behavior in the beginning non-linear range of flow instabilities. At higher Reynolds number and complex geometries the experiment gives the better global result. In any case, the experiment will be needed for validation of all cases. One cannot decide right now who has won the race, the experiment or the numerics. I think that both sides have advantages, but my prediction is that in the more realistic cases which have been announced in some previous comments, the experiment will come up in the future.

Professor Cantwell, Stanford University, USA

I guess I also have a comment on this discussion. In the case of the wakes which Prof. Lumley referred to during his remarks, we saw an example of a flow which, even at moderate Reynolds number, may not be entirely computable. We don't know what the very long time asymptotic behavior of a plane wake will be unless we can compute for immensely long times which may in fact turn out to be impractical. So, the uniqueness issue connected with the asymptotic behavior of the wake is one which I think will not be solved for quite a while. Papers 25 and 26 which Lumley referred to were papers which looked at plane wakes, and I might remark that most real wakes are three-dimensional in the far field. In fact this issue is more severe in the case of a three-dimensional wake. The reason for this is that in the plane wake, if you go far enough downstream, you can at least make an Oseen approximation to the flow and make an argument for the existence of self-similarity. You can do this because the Reynolds number of a plane wake is a constant and at high Reynolds number the properties of the wake are independent of viscosity. In the case of a three-dimensional wake you still have to go far downstream to make the similarity argument, but the three-dimensional wake has the property that the Reynolds number goes down with distance. So by the time you get to the far wake where the Oseen approximation may begin to be valid, you have got a low Reynolds number flow, one which is relaminarizing, in which the argument that the wake is independent of viscosity doesn't work. So, in three-dimensional wakes, it may be even more difficult to compute the asymptotic behavior than in two-dimensional wakes. In fact, in a three-dimensional wake at moderate Reynolds numbers there may simply be no region of self-similarity. There is a whole series of issues here that we don't have any understanding about. That is a separate issue from the one that we have been discussing. There are certain problems which challenge our ability to compute at all.

Professor Reshotko, Case Western Reserve, USA

Since no one has brought this matter up since John Lumley's talk, I would like to add my support for his comments about the need for looking at an analytic foundation for a lot of the numerical work that is being done. In order to understand the physics, one has to have some hypothesis to investigate by one experiment or another. Analysis lays out the hypotheses which can then be tested by good numerical experiments. I also think that computations, especially by DNS and LES methods have a lot of information available that is mostly not used. A DNS or LES calculation may have a hundred thousand or even a million nodes in a computational domain with many pieces of information available at each node. I think of the experimentalist who could never dream of having a hundred thousand probes and so many pieces of information at each probe station and what that experimenter might do if he had that amount of capability. So, I therefore urge the people who do computations to think a little more as if they were experimentalists and try to extract from their data the quantitative physical information that we are all seeking, and not simply present pictures or pleasant movies with music.

Professor Moin, Stanford University, USA

I would like to follow up on that primarily for the other members of the AGARD Panel and others who are not really familiar with DNS/LES work that has been going on. From Eli's comments and part of John's remarks, one might get the impression that people who have been doing DNS and

LES have been just running these codes. The record of contributions to turbulence physics and theory by the people who have been doing DNS is very rich. This has been going on for 15 years. I would say that in the past 10 years, the understanding that has been gained from analysis of direct numerical simulation flow fields has been far more than that gained from experiments. So, good people who have been doing good DNS, were doing it not for the sake of doing DNS, but to extract physics from it. The records of what they have learned have been archived in the Journal of Fluid Mechanics, the Physics of Fluids and other first rate journals.

Professor Cantwell, Stanford University, USA

I would also comment, I guess we don't have any diagnostic developers here, but there are people developing flow diagnostics who do actually conceive of having a million flow points and a million measurements in a flow using holographic and particle imaging techniques.

Professor Lumley, Cornell University, USA

I just want to make clear after Parviz's remarks, I was trying not to embarrass anybody — of course, many people have been doing, from the beginning, all the things that I suggested. It is just that there are a few that haven't been doing them. (Comment by Moin.) But you don't have to defend yourself, I'll defend you.

Professor Cantwell, Stanford University, USA

I have another comment on the experimental side and that is that there is no question that simulations have led experiments for the last 10 years in finding new physics because of the fact that our experimental tools are so limited. There are, on the horizon, three-dimensional techniques which, when perfected, will be able to make measurements in experimental flows with a great deal of density. Presumably, they will be very fast. So, it is not clear that computer simulations will remain in the lead. I guess what people call DES, Direct Experimental Simulation, is beginning to be thought of as a seriously possible thing to do. Who knows, may be 10 years from now we may be looking at experiments, trying to use simulations to see if we can match them.

Professor Slooff, NLR, Netherlands

I have a comment and a question from an applied computational fluid dynamicist's point of view and it touches on one of the points made by Professor Lumley. That is, he said that, like with some other research, there is a lot of work being done on it but very little with it. I am not quite sure whether that is the situation we have here, but from my perspective the promise of both DNS and LES was, amongst others, that they would give us better information on detailed flow structures that would lead to better turbulence models for Reynolds averaged Navier-Stokes simulations. LES also had the promise that it would by-pass the necessity of having various different turbulence models for different kinds of flows; with a good basic subgrid scale model we would be able to circumvent that problem.

Now I have witnessed only about half of the papers here, but in those I have not really seen much evidence of progress with respect to the first point. The associated question is: have DNS and LES simulations already led to better turbulence models for Reynolds averaged Navier-Stokes simulations or do we still think that that promise is still there?

I have also noticed that there are already quite a number of subgrid scale turbulence models. Not quite as many yet as for Reynolds averaged Navier-Stokes, and my impression certainly is that the differences between the various models are smaller than those between full turbulence models for the Reynolds-averaged Navier-Stokes equations. Nevertheless, it has created some doubt, at least in my mind, whether the original promise, as we saw it 5 or 10 years ago, will eventually be fulfilled. I would like the experts to comment on both these points.

Professor Moin, Stanford University, USA
As far as the contribution of DNS to turbulence modelling, I think it is important to put things in perspective. DNS generates data like experiments do. It does provide you with better data and more data than experiments. It gives you, for example, pressure fluctuations that are not accessible in the laboratory. The data that DNS provides can be archived. Then you can use that data to validate the models. But the tough part, that is coming up with better models, requires thinking and creativity and that is not what we get from DNS. All DNS can do is give you data. The modelling part has been in the hands of a handful of people who have made creative contributions to the modelling arena. As we get better and better computers, we just do bigger DNS, higher Reynolds numbers and more cases, but in the final analysis, better models have to come from creative people. That has nothing to do with DNS. Regarding your remarks about LES' promise and its status, it should first be noted that there are not many LES models. I think the field of LES did not progress for a decade. I would say for the entire '80s it gave way to DNS. Former LESers got excited about DNS and used it to study the physics of turbulent flows. LES is now coming back again and there are two or three models around right now. We do not have a plethora of models out there. These models are being very quickly pushed to their limits. People are conducting experiments with them, doing different flows and configurations. And, I think the results of all of these numerical experiments will come to light in the next year or two and we will be able to see where we stand with LES. There is a healthy and vigorous activity right now in evaluating LES and some of the new ideas in LES. But remember, up to 1990 there really weren't that many new ideas in LES except the Smagorinsky model and some models that were derived from the statistical theories of turbulence which were only for homogeneous flows. It is now that we have some new ideas to handle inhomogeneous flows.

Professor Cantwell, Stanford University, USA
Even now, to a large degree, the dynamic localization models are still Smagorinsky in nature.

Professor Moin, Stanford University, USA
That is right. There are other variants of it that don't rely on the Smagorinsky. There is the mixed model, for example, which has been applied to complex flows. The K-equation is being looked at which brings in the history effect as John pointed out. We should keep evaluating more cases, especially the cases where Reynolds averaged models have had problems: massively separated flows, flows with curvature, adverse pressure gradient — these tests are being carried out.

Professor Poll, University of Manchester, UK
I know of no guarantee, no theorem, that tells us that turbulence modelling is something which can be developed to the point where it reproduces what we actually see. The Navier-Stokes equations are equations of motion, but a hundred years ago when Reynolds did his celebrated averaging, he realized that, by doing averaging, he was rejecting information with no guarantee that any amount of modelling could ever bring it back. So whilst it is perfectly satisfactory to talk about direct numerical solutions to produce data, it is not at all satisfactory to expect these data to improve turbulence modelling, because, ultimately, turbulence modelling may well be a blind alley. It doesn't matter to what level of complexity we go, there is no guarantee that, at the end, you will get better solutions.

Professor Cantwell, Stanford University, USA
Maybe I could make a few comments about this issue. This has some history in connection with this symposium. When we were first beginning to think about having a symposium in this area, we were aware of an effort which was basically a world-wide effort on collaborative testing of turbulence models which was being led by Professor Bradshaw at Stanford, Professor Lumley at Cornell and Professor Launder at Manchester. One of the ways we were able to argue to AGARD that they should run such a meeting was that we also realized that part of that effort involved

disseminating simulation data to people who were going to try to use that data to develop improved mean-flow Reynolds-averaged models. When we set out the call for papers for this meeting, the call was written in such a way that we would get such papers, that is papers in which a mean-flow turbulence model was developed using simulation data. I have to say that we really didn't get any papers like that and I am curious to know what was the outcome of that collaborative testing effort.

Professor Lumley, Cornell University, USA

The collaborative testing: if you talk to Peter Bradshaw, you will find it has not been terribly satisfactory. It did not promote the development of new models. It did not promote the participation of many of the groups that we had hoped to have. What we have now is an encyclopedia of runs of standard models against a number of demanding test cases, which is useful. What we had hoped, which is the development of better models will have to wait for creative people.

Dr. Kleiser, DLR, Gottingen, Germany

I would like to come back to one of the remarks that Professor Lumley has made, namely, the use of low-dimensional models for transition and turbulence studies. In fact, such work for transition has been done already. There is such work at the University of Stuttgart, and maybe in the meantime also at some other groups. Rempfer has been working for about 3 or 4 years on that problem and he has actually derived finite dimensional models which are able to reproduce transition phenomena in a flat plate boundary layer in a similar way as the paper we just heard. So, such activities are actually underway. A more general comment is that I do not see this meeting here as fully representative of all of the work that is going on in the area. A lot of activities that have been commented as missing are actually existing. On the use of these low dimensional models, this may perhaps be seen a bit critically. Before you can work with them you first have to generate all these eigenfunctions. To do that you have to first obtain the data, so in effect it is a means of post-processing the data. I do not know if it is reasonably possible to arrive at a state where we can interpolate between a few such simulations and make predictions of flow states that are in between and that have not been produced by DNS themselves. Also from what I have heard from the Stuttgart group, it may happen that the computation of these eigenfunctions is more expensive than the actual DNS. It is probably not, in general, a cheap and quick tool which saves us doing the actual computations.

Professor Saric, Arizona State University, USA

I should like to make a couple of comments, one of which will support the comments of Reshotko and in them some way ask for a clarification of a comment made by the chair that said that for the last 10 years DNS has been leading the experimental work. In the low speed case for sure, there is not an experiment that has been superseded by any DNS. I would say that there is always some experimental work now that is exceeding the capabilities of DNS. The examples that Kleiser gave of doing the vibrating ribbon experiment. That goes back to Schubauer in the 1940's. But we are doing things now that DNS cannot do, and we are guided really by analytical modelling. That is what is driving experimental work these days and it seems to be ahead of the computational work. So to echo Reshotko, perhaps the DNS people should also be inspired by the analytical modelling of these same sort of flows. In the supersonic case, just by virtue of the lack of facilities and capabilities we can't do those kinds of experiments, but certainly in the low speed case, I think the experiments are far ahead of any computational technique.

Professor Moin, Stanford University, USA

I cannot comment on the low speed case, I will leave that to Kleiser perhaps to talk about the transition issue. As far as the fully developed turbulent flows are concerned, it wasn't until the numerical simulations stepped in and, in fact, identified precisely the kind of coherent structures that were present in low Reynolds number turbulent boundary layers. Some of the old concepts that had emerged from turbulent boundary layer structure research proved to be wrong. For example,

examination of DNS databases has revealed the nature of the bursting process, the structure of hairpin vortices and the associated or lack of symmetries. These clarifications were made on the coherent structure front. As far as turbulence modelling is concerned, for the first time we saw the terms in the Reynolds stress equations that cannot be obtained experimentally, terms like pressure-strain correlations and the dissipation tensor.

Professor Saric, Arizona State University, USA
My official position is that I know nothing about turbulence, so I was just confining myself to problems of transitional boundary layers.

Professor Cantwell, Stanford University, USA
OK, so both our statements were a little too broad. I admit mine was probably too broad. I think that in transition you may have a good point. 1 think in moderate Reynolds number turbulent flows the things Prof. Moin pointed out are all true. We have learned things about the pressure field, and we have learned things about the dissipation field. There have been valiant attempts to measure dissipation at a few points in a turbulent flow but these are very difficult experiments to do and very limited bits of information come out of them. Simulations have given us the ability to look at these quantities in great detail, far beyond what experiments have done. I would restrict my comments to that. In another area which is very high Reynolds number turbulent flows, clearly experiments have led because simulation simply can't get there.

Dr. Kleiser, DLR, Gottingen, Germany
I have been asked to add a few comments on the question of experiments versus DNS. I think to build up a controversy between them is totally superfluous, it doesn't help anything. I would say that the majority of the problems that exist in fluid mechanics still must be tackled by experimental methods. The DNS has a relatively small segment of the problems that we are studying that can be reasonably worked on. Suppose that we have a transitional flat plate boundary layer, and we make a few little scratches, or grooves, or we put riblets on. So immediately we have to work for two more years to develop a new DNS code, and even if it is well written, it may be 5 or 10 times more expensive to run than the smooth surface code. There is clearly no need for saying one is ahead of the other. There are just some special problems where you can, I believe, obtain more data and more detailed information from DNS. On the other hand, I think it has been briefly mentioned already that experimental techniques are making great progress towards providing detailed flowfield data, including maybe in the future even three-dimensional data. Thus, there is much room for the development of both techniques. Certainly for my lifetime and for probably many generations, we will very much need experiments.

Dr. Spalart, Boeing Commercial Airplane Group
To add to the controversy with experiments, I think the inability to measure stationary cross flow vortices or to cleanly generate travelling ones, which is a worldwide inability, should be an embarrassment to the experimental community. Another example is the non-parallel effects in the Blasius boundary layer which the theoretical and applied math people have been "chasing" for 20 years. I think we have understood a lot of things by direct simulation. The experimental limitations did waste the time of the theoreticians.

Dr. Bestek, University of Stuttgart, Germany
I do not see any controversy between experiments and DNS as far as transition research is concerned. In my group we are using DNS mostly but we also have a laminar water channel where we are doing controlled transition experiments. There we found that to do a controlled experiment is at least as difficult as to develop a spatial DNS code and apply this for spatial simulations. Prof. Saric put together some important points on transition experiments a couple of years ago at the Langley transition workshop. You first have to define the base flow. For example, if you try to

generate a simple Blasius boundary layer experimentally, you will never reach it. You always will do an experiment in a flow with a pressure gradient that you have to determine carefully. For a numerical model, it is easy to generate a proper Blasius flow. However, the situation is quite different for a more complicated geometry, as, for example, transition induced by a hump. So both methods have advantages and disadvantages, both can be applied in situations where the other cannot be used without great difficulties. I do not see any controversy between experiment and DNS.

Professor Saric, Arizona State University, USA

Please let me clarify my situation. I was only responding to the chairman's comments that somehow DNS has been leading the experimental work in the past 10 years. In the transitional case, I don't think that was true. I, probably more than anybody else, appreciate the computational work, I married Helen for that reason. We do indeed work closely. I think that the secret is that experimental and computational work goes together. But the point of fact is that low speed transitional work has been driven by analytical modelling and not by the DNS work. That is the main point that I wanted to make. If the DNS work is also driven by analytical modelling, I think it could be a much richer type of environment.

Dr. Woodward, DRA, UK

I find I got rather bored with this discussion, so can I take it in a different direction? As a practical aerodynamicist, the two papers that I found most interesting were the paper which attempted to calculate the flow through the suction holes and Helen Reed's paper on receptivity. It seems to me that if we actually understood the receptivity issue that she outlined, then we would be able to design pressure distributions on airfoils which minimized the way in which the disturbance got into the boundary layer — we would have a minimum disturbance boundary layer. Then the understanding that came from calculating the suction flow through the hole seemed to me would lead us in the direction which would enable us to design practical suction systems for a possible laminar flow airplane. I wondered whether, having outlined what I found interesting, anyone else would like to comment on this and its application to a practical aircraft situation?

Professor Meier, DLR, Gottingen, Germany

I would like to come back on the remark of Professor Slooff who is complaining about the lack of presentation of good models here in this meeting. We have considered the role of experiments and numerics, but I think that there is another side which has to be covered more elaborately in the future. This is the pure physical theory of the systems, up to the mathematical background. We are talking here in a mathematical meaning on highly non-linear systems, especially in the case of fully developed turbulence. In connection with the model question, we have to be aware of the fact that it is an unsolved problem if you can model these highly undefined non-linear systems with a lot of degrees of freedom by simple models with a low number of parameters. What has been shown here are cases of instability where the systems are not branched up too much. In these cases, you can numerically calculate and you can expect simple models, for instance, of transitional systems. But the more you go to the turbulent case where the systems become more chaotic, the modelling will be really difficult and questionable, and I wonder if we don't find here a wall which is too high to climb over in the near future.

Mr. Haertel, DLR, Gottingen, Germany

I don't want to comment on that, but I would like to bring the focus back to LES. One of the speakers before talked about the promise, which has been given years ago, that LES one day might be a very cheap and efficient tool to accurately compute a lot of turbulent flows. I think that this promise in some sense has been kept, at least in the area of geophysical flows, where in fact LES frequently is the only thing you have available. DNS for atmospheric boundary layers, e.g., is simply impossible. Now, people try to compute more engineering type of flows, but there one

encounters flow regions where really all the turbulent motions are genuinely inhomogeneous, the near-wall region, for example, or highly strained turbulence, etc. The physics there is completely different from what you typically encounter in free-shear flows with rather small rates of strain. I think it is not very surprising that the simple SGS models which were developed in the geophysical community now are found to have their drawbacks in these other types of flows. The models so far are still based on something like an eddy-viscosity assumption, but the physics definitely are not eddy-viscosity physics, but something completely different. The data which are necessary to improve the models or to tune them, can only come from direct simulations because for experiments they aren't accessible at all and it's just now that such data became available to a much larger number of researchers. Maybe you have to come up with a much more sophisticated model for parts of the flow, including a couple of transport equations, for example, or you directly have to go to DNS for such flow regimes where current SGS models, for physical reasons are not really applicable. Just as Professor Moin pointed out, one of the future paths might be to have an LES for the free flows and something like a DNS in the near-wall regime.

Professor Cantwell, Stanford University, USA
I think that when we talk about the challenges of turbulence modelling we sometimes lose sight of the complexity of the flows that we can do something about. In fact, even with relatively crude turbulence models we have reached the point today where we can begin to approach problems that would have been undreamed of 10 years ago. So, we forget our successes and concentrate on our failures. I think perhaps in turbulence modelling it is probably something that we do to a great degree. The future is actually going to be very bright, particularly when we begin to contemplate the kinds of tools, both experimental and computational tools, that we are going to have 5 or 10 years from now. Perhaps, when we gather again for a future symposium on turbulence, we will be even more amazed at the degree of our capabilities.

It is about time to bring this meeting to a close. I want to thank all the members of the Program Committee who worked hard to bring this meeting together, but especially to the local organizers. I think that everyone who has stayed in this hotel this past week has been very impressed with the hospitality, kindness and attention of all the people that work at the hotel. This has been a wonderful venue for this meeting. I want to thank Professor Panaras and Professor Georgantopoulos for their hard work in finding the venue and setting it up and arranging things, Colonel Metochianakis and Captain Kormas who were the ones who did much of the real work in the local organization and made the whole meeting go smoothly. We all give them great thanks and I would like to give them a round of applause. Now I would like to turn the meeting over to Mr. Dujarric, Chairman of the Fluid Dynamics Panel, who will give some closing remarks.

Mr. Dujaric, Chairman FDP
Thank you. I must now close this 74th Session of the Fluid Dynamics Panel. We have been very fortunate to have had so many high quality presentations.

It is also possible that the agreeable venue has contributed to this success. It is not by chance that we have been able to have a well structured meeting and the discovery of such an exceptional site. I would like to say a special thank you in addition to those also stated by Brian and in particular to thank the Co-Chairmen of the Program Committee, Brian Cantwell himself, Javier Jimenez and Spiro Lekoudis. I would like to thank the technical evaluator for this meeting, Dr. Lumley, for the remarks he presented to us and for the evaluation that he will prepare for us in writing. I would like to thank the authors who have presented papers at this symposium and particularly those authors who have responded to the invitation from the Program Committee, Mr. Moin and Mr. Kutnetsov as well as the two authors who have, in a very short time, prepared replacements for withdrawn papers, Mr. Fasel and Mr. Kaldellis. I would like to thank all the participants who have posed careful questions during this last session and have contributed to the lively discussion. I would like

also on behalf of the Panel to thank Dr. Panaras and Dr. Georgantopoulos for their work in organizing this symposium. I would like to thank the translators, Mr. de Liffiac, Mrs. Atzitiris and Mrs. Photiadis who have really stood up to the high level discussion of the speakers. I want also to thank the assistants and the technicians, M. Brolet and M. Hector as well as Mr. Ayvali at the reception. Thanks again to our Executive Mr. Jack Molloy and his secretary Anne-Marie Rivault.

Before leaving, I would like to present to you the activities planned for 1995 as well as for the end of 1994. We will have a Symposium on Rotor Aerodynamics and Acoustics which is planned from 10 - 13 October in Berlin, Germany, and next week a special course on the Optimum Methods for Aerodynamic Design. This course will take place at the von Karman Institute, Brussels, Belgium. There will also be a course from the 6th to 10th June at the von Karman Institute and from the 13th to the 17th June in Ankara on the Aerodynamics of Missiles. Next year our Spring Symposium will take place in Turkey and it will be on Aerodynamics and Integration of Stores and Their Separation. This Symposium will be classified. In autumn, we will have a Symposium in Spain on the Progress and Challenges of CFD Methods and Algorithms. We have also planned special courses on Parallel Calculations in CFD which will be presented at VKI and at NASA Ames as well as Aerothermodynamics and the Integration of the Propulsion for Hypersonic Vehicles. This will take place in the spring at the VKI. Thank you for your attention.

REPORT DOCUMENTATION PAGE

1. Recipient's Reference	2. Originator's Reference	3. Further Reference	4. Security Classification of Document
	AGARD-CP-551	ISBN 92-836-0006-1	UNCLASSIFIED

5. Originator Advisory Group for Aerospace Research and Development
North Atlantic Treaty Organization
7 rue Ancelle, 92200 Neuilly-sur-Seine, France

6. Title

Application of Direct and Large Eddy Simulation
to Transition and Turbulence

7. Presented at

The 74th Fluid Dynamics Symposium held at Chania, Crete, Greece,
in April 1994

8. Author(s)/Editor(s)	9. Date
Multiple	December 1994
10. Author's/Editor's Address	**11. Pages**
Multiple	418

12. Distribution Statement There are no restrictions on the distribution of this document. Information about the availability of this and other AGARD unclassified publications is given on the back cover.

13. Keywords/Descriptors

Computational fluid dynamics
Eddies
Turbulent flow
Transition flow
Mathematical models
Computerized simulation
Aerodynamic configurations
Turbulence

14. Abstract

The papers prepared for the AGARD Fluid Dynamics Panel (FDP) Symposium on "Application of Direct and Large Eddy Simulation to Transition and Turbulence", which was held 18-21 April 1994 in Chania, Crete, Greece are contained in this report. In addition, a Technical Evaluator's Report aimed at assessing the success of the Symposium in meeting its objectives, and an edited transcript of the General Discussion held at the end of the meeting are also included.

During the past two decades significant progress has been made in the numerical simulation of turbulent flows. Vast improvements in speed and memory size of modern supercomputers, and recent progress in simulation algorithms and parallel computation have put us on the threshold of being able to simulate flows in configurations of engineering interest. The purpose of this Symposium is to disseminate the accumulated experience in this fast moving field which can be expected to play a vital role in future aeronautical developments.

AGARD-CP-551
Advisory Group for Aerospace Research and Development
North Atlantic Treaty Organization
APPLICATION OF DIRECT AND LARGE EDDY SIMULATION TO TRANSITION AND TURBULENCE
Published December 1994
418 pages

The papers prepared for the AGARD Fluid Dynamics Panel (FDP) Symposium on "Application of Direct and Large Eddy Simulation to Transition and Turbulence", which was held 18-21 April 1994 in Chania, Crete, Greece are contained in this report. In addition, a Technical Evaluator's Report aimed at assessing the success of the Symposium in meeting its objectives, and an edited transcript of the General Discussion held at the end of the meeting are also included.

AGARD-CP-551

Computational fluid dynamics
Eddies
Turbulent flow
Transition flow
Mathematical models
Computerized simulation
Aerodynamic configurations
Turbulence

AGARD-CP-551
Advisory Group for Aerospace Research and Development
North Atlantic Treaty Organization
APPLICATION OF DIRECT AND LARGE EDDY SIMULATION TO TRANSITION AND TURBULENCE
Published December 1994
418 pages

The papers prepared for the AGARD Fluid Dynamics Panel (FDP) Symposium on "Application of Direct and Large Eddy Simulation to Transition and Turbulence", which was held 18-21 April 1994 in Chania, Crete, Greece are contained in this report. In addition, a Technical Evaluator's Report aimed at assessing the success of the Symposium in meeting its objectives, and an edited transcript of the General Discussion held at the end of the meeting are also included.

AGARD-CP-551

Computational fluid dynamics
Eddies
Turbulent flow
Transition flow
Mathematical models
Computerized simulation
Aerodynamic configurations
Turbulence

AGARD-CP-551
Advisory Group for Aerospace Research and Development
North Atlantic Treaty Organization
APPLICATION OF DIRECT AND LARGE EDDY SIMULATION TO TRANSITION AND TURBULENCE
Published December 1994
418 pages

The papers prepared for the AGARD Fluid Dynamics Panel (FDP) Symposium on "Application of Direct and Large Eddy Simulation to Transition and Turbulence", which was held 18-21 April 1994 in Chania, Crete, Greece are contained in this report. In addition, a Technical Evaluator's Report aimed at assessing the success of the Symposium in meeting its objectives, and an edited transcript of the General Discussion held at the end of the meeting are also included.

AGARD-CP-551

Computational fluid dynamics
Eddies
Turbulent flow
Transition flow
Mathematical models
Computerized simulation
Aerodynamic configurations
Turbulence

AGARD-CP-551
Advisory Group for Aerospace Research and Development
North Atlantic Treaty Organization
APPLICATION OF DIRECT AND LARGE EDDY SIMULATION TO TRANSITION AND TURBULENCE
Published December 1994
418 pages

The papers prepared for the AGARD Fluid Dynamics Panel (FDP) Symposium on "Application of Direct and Large Eddy Simulation to Transition and Turbulence", which was held 18-21 April 1994 in Chania, Crete, Greece are contained in this report. In addition, a Technical Evaluator's Report aimed at assessing the success of the Symposium in meeting its objectives, and an edited transcript of the General Discussion held at the end of the meeting are also included.

AGARD-CP-551

Computational fluid dynamics
Eddies
Turbulent flow
Transition flow
Mathematical models
Computerized simulation
Aerodynamic configurations
Turbulence

During the past two decades significant progress has been made in the numerical simulation of turbulent flows. Vast improvements in speed and memory size of modern supercomputers, and recent progress in simulation algorithms and parallel computation have put us on the threshold of being able to simulate flows in configurations of engineering interest. The purpose of this Symposium is to disseminate the accumulated experience in this fast moving field which can be expected to play a vital role in future aeronautical developments.

ISBN 92-836-0006-1

During the past two decades significant progress has been made in the numerical simulation of turbulent flows. Vast improvements in speed and memory size of modern supercomputers, and recent progress in simulation algorithms and parallel computation have put us on the threshold of being able to simulate flows in configurations of engineering interest. The purpose of this Symposium is to disseminate the accumulated experience in this fast moving field which can be expected to play a vital role in future aeronautical development.

ISBN 92-836-0006-1

During the past two decades significant progress has been made in the numerical simulation of turbulent flows. Vast improvements in speed and memory size of modern supercomputers, and recent progress in simulation algorithms and parallel computation have put us on the threshold of being able to simulate flows in configurations of engineering interest. The purpose of this Symposium is to disseminate the accumulated experience in this fast moving field which can be expected to play a vital role in future aeronautical developments.

ISBN 92-836-0006-1

During the past two decades significant progress has been made in the numerical simulation of turbulent flows. Vast improvements in speed and memory size of modern supercomputers, and recent progress in simulation algorithms and parallel computation have put us on the threshold of being able to simulate flows in configurations of engineering interest. The purpose of this Symposium is to disseminate the accumulated experience in this fast moving field which can be expected to play a vital role in future aeronautical development.

ISBN 92-836-0006-1

AGARD

NATO OTAN

7 RUE ANCELLE • 92200 NEUILLY-SUR-SEINE

FRANCE

Télécopie (1)47.38.57.99 • Télex 610 176

DIFFUSION DES PUBLICATIONS

AGARD NON CLASSIFIEES

Aucun stock de publications n'a existé à AGARD. A partir de 1993, AGARD détiendra un stock limité des publications associées aux cycles de conférences et cours spéciaux ainsi que les AGARDographies et les rapports des groupes de travail, organisés et publiés à partir de 1993 inclus. Les demandes de renseignements doivent être adressées à AGARD par lettre ou par fax à l'adresse indiquée ci-dessus. *Veuillez ne pas téléphoner.* La diffusion initiale de toutes les publications de l'AGARD est effectuée auprès des pays membres de l'OTAN par l'intermédiaire des centres de distribution nationaux indiqués ci-dessous. Des exemplaires supplémentaires peuvent parfois être obtenus auprès de ces centres (à l'exception des Etats-Unis). Si vous souhaitez recevoir toutes les publications de l'AGARD, ou simplement celles qui concernent certains Panels, vous pouvez demander à être inclu sur la liste d'envoi de l'un de ces centres. Les publications de l'AGARD sont en vente auprès des agences indiquées ci-dessous, sous forme de photocopie ou de microfiche.

CENTRES DE DIFFUSION NATIONAUX

ALLEMAGNE
Fachinformationszentrum,
Karlsruhe
D-76344 Eggenstein-Leopoldshafen 2

BELGIQUE
Coordonnateur AGARD-VSL
Etat-major de la Force aérienne
Quartier Reine Elisabeth
Rue d'Evere, 1140 Bruxelles

CANADA
Directeur, Services d'information scientifique
Ministère de la Défense nationale
Ottawa, Ontario K1A 0K2

DANEMARK
Danish Defence Research Establishment
Ryvangs Allé 1
P.O. Box 2715
DK-2100 Copenhagen Ø

ESPAGNE
INTA (AGARD Publications)
Pintor Rosales 34
28008 Madrid

ETATS-UNIS
NASA Headquarters
Code JOB-1
Washington, D.C. 20546

FRANCE
O.N.E.R.A. (Direction)
29, Avenue de la Division Leclerc
92322 Châtillon Cedex

GRECE
Hellenic Air Force
Air War College
Scientific and Technical Library
Dekelia Air Force Base
Dekelia, Athens TGA 1010

ISLANDE
Director of Aviation
c/o Flugrad
Reykjavik

ITALIE
Aeronautica Militare
Ufficio del Delegato Nazionale all'AGARD
Aeroporto Pratica di Mare
00040 Pomezia (Roma)

LUXEMBOURG
Voir Belgique

NORVEGE
Norwegian Defence Research Establishment
Attn: Biblioteket
P.O. Box 25
N-2007 Kjeller

PAYS-BAS
Netherlands Delegation to AGARD
National Aerospace Laboratory NLR
P.O. Box 90502
1006 BM Amsterdam

PORTUGAL
Força Aérea Portuguesa
Centro de Documentação e Informação
Alfragide
2700 Amadora

ROYAUME-UNI
Defence Research Information Centre
Kentigern House
65 Brown Street
Glasgow G2 8EX

TURQUIE
Millî Savunma Başkanliği (MSB)
ARGE Dairesi Başkanliği (MSB)
06650 Bakanliklar-Ankara

Le centre de distribution national des Etats-Unis ne détient PAS de stocks des publications de l'AGARD.
D'éventuelles demandes de photocopies doivent être formulées directement auprès du NASA Center for AeroSpace Information (CASI) à l'adresse ci-dessous. Toute notification de changement d'adresse doit être fait également auprès de CASI.

AGENCES DE VENTE

NASA Center for
AeroSpace Information (CASI)
800 Elkridge Landing Road
Linthicum Heights, MD 21090-2934
Etats-Unis

ESA/Information Retrieval Service
European Space Agency
10, rue Mario Nikis
75015 Paris
France

The British Library
Document Supply Division
Boston Spa, Wetherby
West Yorkshire LS23 7BQ
Royaume-Uni

Les demandes de microfiches ou de photocopies de documents AGARD (y compris les demandes faites auprès du CASI) doivent comporter la dénomination AGARD, ainsi que le numéro de série d'AGARD (par exemple AGARD-AG-315). Des informations analogues, telles que le titre et la date de publication sont souhaitables. Veuiller noter qu'il y a lieu de spécifier AGARD-R-nnn et AGARD-AR-nnn lors de la commande des rapports AGARD et des rapports consultatifs AGARD respectivement. Des références bibliographiques complètes ainsi que des résumés des publications AGARD figurent dans les journaux suivants:

Scientific and Technical Aerospace Reports (STAR)
publié par la NASA Scientific and Technical
Information Division
NASA Headquarters (JTT)
Washington D.C. 20546
Etats-Unis

Government Reports Announcements and Index (GRA&I)
publié par le National Technical Information Service
Springfield
Virginia 22161
Etats-Unis
(accessible également en mode interactif dans la base de
données bibliographiques en ligne du NTIS, et sur CD-ROM)

Imprimé par le Groupe Communication Canada
45, boul. Sacré-Cœur, Hull (Québec), Canada K1A 0S7

AGARD

NATO OTAN

7 RUE ANCELLE • 92200 NEUILLY-SUR-SEINE

FRANCE

Telefax (1)47.38.57.99 • Telex 610 176

DISTRIBUTION OF UNCLASSIFIED

AGARD PUBLICATIONS

AGARD holds limited quantities of the publications that accompanied Lecture Series and Special Courses held in 1993 or later, and of AGARDographs and Working Group reports published from 1993 onward. For details, write or send a telefax to the address given above. *Please do not telephone.*

AGARD does not hold stocks of publications that accompanied earlier Lecture Series or Courses or of any other publications. Initial distribution of all AGARD publications is made to NATO nations through the National Distribution Centres listed below. Further copies are sometimes available from these centres (except in the United States). If you have a need to receive all AGARD publications, or just those relating to one or more specific AGARD Panels, they may be willing to include you (or your organisation) on their distribution list. AGARD publications may be purchased from the Sales Agencies listed below, in photocopy or microfiche form.

NATIONAL DISTRIBUTION CENTRES

BELGIUM
Coordonnateur AGARD — VSL
Etat-major de la Force aérienne
Quartier Reine Elisabeth
Rue d'Evere, 1140 Bruxelles

CANADA
Director Scientific Information Services
Dept of National Defence
Ottawa, Ontario K1A 0K2

DENMARK
Danish Defence Research Establishment
Ryvangs Allé 1
P.O. Box 2715
DK-2100 Copenhagen Ø

FRANCE
O.N.E.R.A. (Direction)
29 Avenue de la Division Leclerc
92322 Châtillon Cedex

GERMANY
Fachinformationszentrum
Karlsruhe
D-76344 Eggenstein-Leopoldshafen 2

GREECE
Hellenic Air Force
Air War College
Scientific and Technical Library
Dekelia Air Force Base
Dekelia, Athens TGA 1010

ICELAND
Director of Aviation
c/o Flugrad
Reykjavik

ITALY
Aeronautica Militare
Ufficio del Delegato Nazionale all'AGARD
Aeroporto Pratica di Mare
00040 Pomezia (Roma)

LUXEMBOURG
See Belgium

NETHERLANDS
Netherlands Delegation to AGARD
National Aerospace Laboratory, NLR
P.O. Box 90502
1006 BM Amsterdam

NORWAY
Norwegian Defence Research Establishment
Attn: Biblioteket
P.O. Box 25
N-2007 Kjeller

PORTUGAL
Força Aérea Portuguesa
Centro de Documentação e Informação
Alfragide
2700 Amadora

SPAIN
INTA (AGARD Publications)
Pintor Rosales 34
28008 Madrid

TURKEY
Millî Savunma Başkanliği (MSB)
ARGE Dairesi Başkanliği (MSB)
06650 Bakanliklar-Ankara

UNITED KINGDOM
Defence Research Information Centre
Kentigern House
65 Brown Street
Glasgow G2 8EX

UNITED STATES
NASA Headquarters
Code JOB-1
Washington, D.C. 20546

The United States National Distribution Centre does NOT hold stocks of AGARD publications.
Applications for copies should be made direct to the NASA Center for AeroSpace Information (CASI) at the address below.
Change of address requests should also go to CASI.

SALES AGENCIES

NASA Center for
AeroSpace Information (CASI)
800 Elkridge Landing Road
Linthicum Heights, MD 21090-2934
United States

ESA/Information Retrieval Service
European Space Agency
10, rue Mario Nikis
75015 Paris
France

The British Library
Document Supply Centre
Boston Spa, Wetherby
West Yorkshire LS23 7BQ
United Kingdom

Requests for microfiches or photocopies of AGARD documents (including requests to CASI) should include the word 'AGARD' and the AGARD serial number (for example AGARD-AG-315). Collateral information such as title and publication date is desirable. Note that AGARD Reports and Advisory Reports should be specified as AGARD-R-nnn and AGARD-AR-nnn, respectively. Full bibliographical references and abstracts of AGARD publications are given in the following journals:

Scientific and Technical Aerospace Reports (STAR)
published by NASA Scientific and Technical
Information Division
NASA Headquarters (JTT)
Washington D.C. 20546
United States

Government Reports Announcements and Index (GRA&I)
published by the National Technical Information Service
Springfield
Virginia 22161
United States
(also available online in the NTIS Bibliographic
Database or on CD-ROM)

Printed by Canada Communication Group
45 Sacré-Cœur Blvd., Hull (Québec), Canada K1A 0S7

ISBN 92-836-0006-1